The sedimentary recordings of the tsunamis triggered by the 1883-Krakatau eruptions on the littoral South of Sunda Strait in the region of Ujung Kulon, Java Island, Indonesia, and the role of the coastal morphology on the organisation and the characteristics of the deposits

Yan Iskandarsyah

UNIVERSITÉ DE STRASBOURG

UNIVERSITÉ DE STRASBOURG

Image Ville Environnement

ÉCOLE DOCTORALE DES SCIENCES DE LA TERRE, DE L'UNIVERS, ET DE L'ENVIRONNEMENT (ED-413)

LABORATOIRE IMAGE, VILLE, ENVIRONNEMENT (LIVE – UMR 7362)

THESIS

Presented by :

T. Yan W. M. ISKANDARSYAH

Defence on : **29/09/2015**

To obtain the degree of : **Doctor of Université de Strasbourg**

Disciplin/Speciality : Earth Science – Physical Geography

The sedimentary recordings of the tsunamis triggered by the 1883-Krakatau eruptions on the littoral South of Sunda Strait in the region of Ujung Kulon, Java Island, Indonesia, and the role of the coastal morphology on the organisation and the characteristics of the deposits

THESIS directed by :	**M. Dominique SCHWARTZ** (Prof., Université de Strasbourg)
RAPPORTEURS :	**M. Hervé Regnauld** (Université Rennes 2) **M. Emmanuel Gilles** (Université Metz)
EXAMINERS :	**M. Franck Lavigne** (Prof., Université Paris 1) **M. Patrick WASSMER** (Université de Strasbourg, encadrant) **M. Mathieu Schuster** (Université de Strasbourg)
INVITED EXAMINER :	**M. Ildrem Syafri** (Universitas Padjadjaran, Indonésie)

UNIVERSITÉ DE STRASBOURG

UNIVERSITÉ DE STRASBOURG

ÉCOLE DOCTORALE DES SCIENCES DE LA TERRE, DE L'UNIVERS, ET DE L'ENVIRONNEMENT (ED-413)

LABORATOIRE IMAGE, VILLE, ENVIRONNEMENT (LIVE – UMR 7362)

THÈSE

Presentée par :

T. Yan W. M. ISKANDARSYAH

Soutenance le : **29/09/2015**

Pour obtenir le grade de : **Docteur de l'Université de Strasbourg**

Discipline/Spécialité : Sciences de la Terre – Géographie Physique

Les enregistrements sédimentaires des tsunamis générés par l'éruption du Krakatau en 1883 sur le littoral sud du détroit de la Sonde dans la région de Ujung Kulon, l'île de Java, Indonésie et le rôle de la morphologie côtière sur l'organisation et les caractéristiques des dépôts

THÈSE dirigée par : **M. Dominique SCHWARTZ** (Prof., Université de Strasbourg)

RAPPORTEURS : **M. Hervé Regnauld** (Université Rennes 2)
M. Emmanuel Gilles (Université Metz)

EXAMINATEURS : **M. Franck Lavigne** (Prof., Université Paris 1)
M. Patrick WASSMER (Université de Strasbourg, encadrant)
M. Mathieu Schuster (Université de Strasbourg)

EXAMINATEUR INVITÉ: **M. Ildrem Syafri** (Universitas Padjadjaran, Indonésie)

Je dédie ce travail à ma femme bien aimée, Henny SARIYATI

Sans toi, je suis un grain de poussière

ABSTRACT

The giant tsunamis generated by the tremendous eruptions of Krakatau in 1883 were recorded along the coasts of Sunda Strait. Eyewitnesses testimony, tidal and pressure gauges recorded at Batavia (Jakarta), and tsunami signatures left by such event have been mostly used by researchers to evidencing the occurrence of the 1883-Krakatau tsunami around the Sunda Strait. Yet, there was still gap in knowledge when talking about the evidences of the 1883-Krakatau tsunami in the southern part of Sunda Strait and around Indian Ocean, due to the lack of eyewitness and a fact that some of the coasts is mostly noted as the remote areas. Laban Isthmus, one of the intriguing coastal landforms located 80 km to the south of Krakatau and connect Ujung Kulon Peninsula to Java Island, displayed the potential to record marine flooding events issuing from Sunda Strait and Indian Ocean. This study demonstrated however that the isthmus has recorded 4 (four) tsunami events related to the eruptions. Based on a new combination approach of sedimentary and micro-fossils analyses with the Anisotropy of Magnetic Susceptibility (AMS) technique, the result of the study evidenced that each wave was recorded twice: *i*) by a direct flow coming from the Sunda Strait in straight line, *ii*) by a wave coming from the Indian Ocean, delayed in time after having been refracted around the West-end of Ujung Kulon Peninsula (near Panaitan Island). Such evidence was unique and could be related to the exceptional geomorphological context of the Ujung Kulon Peninsula, including the isthmus and its V-shape bays, which made it one of the most remarkable traps of tsunami deposits.

Keywords : *tsunami, Krakatau, evidence, coast, Ujung Kulon Peninsula, isthmus, deposits*

ACKNOWLEDGEMENTS

Praise and gratitude to God for giving me a chance to complete the thesis with a title “The sedimentary recordings of the tsunamis triggered by the 1883-Krakatau eruptions on the littoral South of Sunda Strait in the region of Ujung Kulon, Java Island, Indonesia, and the role of the coastal morphology on the organisation and the characteristics of the deposits”. This thesis is dedicated to my wife (Henny Sariyati), my children (Teuku Riza Muhammad Iskandarsyah and Cut Reyna Ananda Keumaladewi), my parents (Teuku Hasan Basry Lizam and Prof. Poniah Andayaningsih), and my families for their understanding, sacrifice, and supports during my study in Fance.

A number of people and organizations should be acknowledged for their contributions in this study. Firstly, I am very sincerely grateful to my thesis director (directeur de thèse) whom I greatly respect, Dominique Schwartz, and particularly to Patrick Wassmer, for all things he has demonstrated over the years. Many thanks are also given to members of the jury for their contributions to the improvement of the manuscript.

Then, I would like to thank to Prof. Ganjar Kurnia, former Rector of Universitas Padjadjaran, Indonesia, and Prof. Hendarmawan, Dean of Fakultas Teknik Geologi (FTG), Universitas Padjadjaran, Indonesia, that have given a permission to study in France. I am also indebted to :

1. Martine Trautmann and Marc Diraison from Ecole et Observatoire des Sciences de la Terre (EOST), Université de Strasbourg (UdS), France, for the grain-size and AMS analyses.
2. Lia Djurnaliah and Yoga A. Sendjaja from FTG, Universitas Padjadjaran, Indonesia, for the discussion of foraminifera and XRF-analysis.
3. Cindy A. Firdausiah and Ria Fitriany for the identification of foraminifera.
4. Hilman Damanhuri for the microscopic examination of minerals.

5. Dian H. Saputra, M. Nursiyam Barkah, and Rama B. Herawan for their assistances in collecting the samples and producing the maps.
6. All of the field investigation members for their assistances, supports, and constructive discussion.

My appreciation is delivered to Balai Taman Nasional Ujung Kulon (BTNUK) Indonesia for allowing the work in Ujung Kulon National Park and to Lembaga Ilmu Pengetahuan Indonesia (LIPI) for providing technical support in the field investigation. I am also grateful to the Government of Indonesia which have given the scholarship and to Laboratorium Geologi Lingkungan dan Hidrogeologi, FTG, Universitas Padjadjaran, Indonesia, which have funded the research of the study.

Finally, I cannot forget all of the kindness of my colleagues, for their supports during my study, i.e. M. Sapari D. Hadian, Bombom R. Suganda, Yuyun Yuniardi, R. Irvan Sophian, and Yudhi Listiawan (FTG, Universitas Padjadjaran, Indonesia), Nurul Jadid (ITS Surabaya, Indonesia), Dedy K. Halim (UPH Jakarta, Indonesia), Putu Mahendra (CNRS-Paris, France), Andri Abdurrochman (Université de Strasbourg/FMIPA, Universitas Padjadjaran, Indonesia), Dedy E. Septiadi, Filsa Bioresita, Carla Claudia Silitonga, Gianto, and Husneni M. Lutfi (Université de Strasbourg, France), Ade Kadarisman (Université Paris 2/Fikom, Universitas Padjadjaran, Indonesia), Barbora Vyslouzilova (Czech), and Hugo Goett and Quentin Lejeune (France). Also to all parties that cannot be mentioned one by one.

TABLE OF CONTENTS

LIST OF FIGURES

LIST OF TABLES

RÉSUMÉ (Executive Summary in French)

1. Introduction

Un tsunami est constitué par une série de vagues créés lorsqu'une masse d'eau, océanique ou lacustre, est déplacée brutalement. Ce phenomene peut etre déclenché par un séisme, un glissement de terrain sous-marin, un mouvement de masse d'origine continentale ou insulaire, de nature volcanique ou non, arrivant en mer ; une éruption volcanique sous marine ou encore l'impact d'un astéroïde en mer. En raison des volumes d'eau déplacés et de l'énergie cinétique libérée, le tsunami peut avoir un impact dévastateur sur les zones côtières adjacentes. Le Tsunami de l'Ocean Indien (IOT), survenu le 26 décembre 2004 a été généré par un des plus importants tremblements de terre jamais enregistré dans la partie Nord de la province d'Aceh - Indonésie, et le tsunami du Tohoku le 11 mars 2011, à Miyako, Iwate Prefecture, Tohoku et dans la région de Sendai, au Japon, ont largement montrés à quel point ces phénomènes pouvaient être dévastateurs, détruisant les villes ou villages sur les zones côtières et tuant des milliers de personnes, malgré l'existence d'un système d'alerte précoce (Japon). Dans les temps historiques, la gigantesque éruption du volcan Krakatau, le 27 août, 1883, a provoqué des tsunamis dont les vagues de certains ont atteint une quarantaine de mètres de hauteur. Plus de 36.000 personnes ont perdu la vie au cours de cet évènement sur les zones côtières adjacentes du pourtour du détroit de la Sonde, entre Java et Sumatra, en Indonésie.

Les vagues de tsunami ont laissé de nombreuses traces de leurs passages. Ce sont des signatures sous forme de dépôt sédimentaires sur les zones côtières telles que des couches intercalées de sédiments marins, la presence de foraminifères en abondance, des blocs de corail noyés dans du sable, des grands blocs de corail, et les turbidités (Bryant, 2008; Dawson et Shi, 2000). Ces éléments sont très utiles pour reconnaître les caractéristiques de

tsunami et identifier leur présence dans le passé (Chagué-Goff et al., 2011). Dans l'étude de tsunami volcanique, la présence de matières volcaniques dans les séquences du tsunami peut devenir un élément supplémentaire important (Paris et al., 2014a, 2014b), qui a été identifié très tot par les nombreux chercheurs qui ont travaillé sur ces dépôts de tsunami volcanique du Krakatau en 1883 (Umbgrove, 1947; Verstappen, H. Th, 1956; Ongkosongo, 1985; Bronto, 1990; Camus et al., 1992; Cita et al, 1996; Cita et Aloisi, 2000; Carey et al, 2001; van den Bergh et al, 2002, 2003; van der Kaars et van den Bergh, 2004; Boer et al., 2006; Atmadja, 2007; Paris et al, 2014b). L'étude des tsunamis générés par le Krakatau est particulièrement intéressante en raison des nombreux témoignages disponibles qui permettent de relier les phénomènes éruptifs qui se sont succédés avec des enregistrements sédimentaires souvent bien conservés le long des côtes, notamment dans les zones où la faible pression anthropique a permis leur conservation.

Située au Sud du Krakatau, la région d'Ujung Kulon possède un fort potentiel d'enregistrement et de conservation des archives sédimentaires des tsunamis produits par l'éruption du Krakatau en 1883. Ceci est principalement dû à la morphologie côtière tout à fait particulière des côtes du sud du détroit de la Sonde. La baie de Selamat Datang avec sa morphologie en V ouvert vers le Nord et pointé au Sud sur l'isthme de Laban, trait d'union entre le détroit de la Sonde et l'Océan Indien sur lequel s'ouvre la baie de Karang Ranjan. Ces deux possibilités rendent ce site unique comme enregistreur des paleotsunamis issus du detroit mais aussi de l'Ocean Indien. Toutefois, seules les personnes habitant les côtes de Java et de Sumatra localisées dans le centre et le Nord du détroit de la Sonde ont été en mesure de fournir des témoignages visuels sur les éruptions volcaniques et les phénomènes tsunamis qui ont eu lieu durant les événements du Krakatau en août 1883. Les rivages rocheux et l'austère du Sud, particulièrement dans la région de la péninsule de Ujung Kulon, ont toujours été libres de populations. On ne dispose donc d'aucune connaissance sur le nombre et les caractéristiques des inondations des tsunamis sur les côtes de la péninsule de Ujung Kulon. Seule une exploration fine et détaillée des dépôts sédimentaires dans cette région de Ujung Kulon permettra de comprendre la façon dont ces signatures sédimentaires laissées par les tsunamis générés par les différentes phases éruptives du Krakatau en 1883 ont été mis en place.

Quatre questions scientifiques liées à cet objectif sous-tendent cette démarche de recherche :

- Est-que les dépôts de tsunami trouvés le long des côtes de la péninsule de Ujung Kulon ont été mis en place par les tsunamis générés par l' éruption du Krakatau en 1883 ?
- Si les dépôts trouvés dans ce secteur sur les côtes de l'océan Indien sont liés aux tsunamis du Krakatau, alors, quels sont les processus qui pourraient expliquer leur mise en place sur des littoraux non exposés au Krakatau ?
- Est-ce que la configuration des dépôts de tsunami trouvés dans la zone d'étude pourrait être liée aux différentes phases éruptives du Krakatau en 1883 ?
- Quel est l'effet du relief côtier sur la configuration des dépôts de tsunamis ?

2. Etat de l'art dans l'étude du tsunami de Karakatau

Le tsunami correspond à un train d'ondes (10 vagues ou plus) de grande à très grande longueur d'onde. Contrairement aux vagues produites par le vent, la longueur d'onde du tsunami peut se situer entre 10 et 250 km, en raison de la profondeur de l'océan qui est finie et du mécanisme de génération des ondes. Le tsunami est caractérisé par une période, qui correspond au temps mis par deux crêtes de vagues successives pour passer en un même point. Elle peut varier entre 15 minutes et une heure. La vitesse des ondes est d'environ 800 km/h lorsque la profondeur du fond est de 5000 m, elle se réduit à 36 km/h pour un fond de 10 m.

Lorsque le tsunami se rapproche des côtes, les ondes peuvent subir des réflexions, des diffractions ou des réfractions selon la morphologie du fond de l'océan ou du littoral, complexifiant le nombre et l'orientation des ondes enregistrées. Lorsque les vagues progressent en milieu peu profond, la dispersion d'énergie sur le fond génère une réfraction autour des obstacles comme les iles ou les reliefs sous-marins. Le long d'un rivage irrégulier, l'énergie des vagues se concentre sur les promontoires, provoquant l'érosion, et se disperse dans les baies, qui entraîne le dépôt (Thurman et al., 1999). En revanche, une barrière verticale, comme une digue ou un rocher, peut réfléchir la vague de tsunami dans l'océan avec peu de perte d'énergie. Ce processus est appelé réflexion des ondes. D'autre part, un obstacle sur le trajet d'un onde de tsunami (par exemple, une digue ou une île) peut provoquer une diffraction. Les vagues, après le passage de l'île, se transforment et transportent l'énergie des vagues dans la région située derrière l'île qui est appelée la zone d'ombre. Le changement d'orientation des vagues est dû à des changements dans la hauteur d'une même vagues le long de la crête.

Une fois sur le continent, la hauteur des vagues équivaut à l'épaisseur de l'écoulement de l'eau ou hauteur d'inondation. Cette valeur est difficile à mesurer et par conséquent, la hauteur perspective (*run-up*) a été utilisée pour décrire l'intensité des vagues de tsunami. La hauteur perspective est différente de la hauteur maximale de l'inondation. Il constitue la hauteur verticale maximale atteinte sur le rivage au dessus du niveau de la mer par l'inondation du tsunami. Plus cette hauteur perspective est grande, plus grand est le tsunami et plus importants sont les volumes d'eau transportés sur le rivage (Hills et Mader, 1997). La distance maximale d'inondation est affectée par la rugosité du paysage côtier. Cette rugosité est représentée par le *n* de Maning, où *n* est égal à 0,015 pour la topographie très lisse, 0,03 pour les terrains aménagés, et 0,07 pour un paysage fortement boisée.

Sur la terre, les événements d'inondation de tsunami se composent de trois phases, à savoir *uprush*, *slack*, et *backwash*, qui affectent la mise en place des sédiments (Wassmer et al., 2010). L'uprush ou le flux est une soudaine poussée vers le haut qui se forme immédiatement après qu'une vague de tsunami déferle, avec une forte énergie dans la zone proximale (proche du littoral). L'énergie diminue quand la vague progresse vers l'intérieur des terres, atteignant alors l'extension maximale de l'inondation dans la zone distale. Le slack est une période de faible activité (énergie zéro) avant la reprise d'écoulement de backwash (Dawson et Stewart, 2007). Durant cette phase, les substrats de boue et les foraminifères seront abondamment déposés. Le backwash débute par un écoulement lent à partir de la zone distale. L'eau accélère ensuite progressivement en se rapprochant de la mer et il se produit souvent, en raison de l'augmentation de l'énergie, une reprise des sédiments déposés. Les conditions de ces trois phases sont modifiées par le profil général de la pente côtière sur laquelle les vagues déferlent. Lorsque les pentes sont raides, la succession de trois phases se produit pour chaque vague individuelle du train de vague. Lorsque la topographie est très plane tous les sédiments sont mis en place au cours d'une seule longue phase d'uprush suivie par un backwash. Le retrait complet de l'eau des surfaces inondées peut prendre plus d'une dizaine d'heures (Lavigne et al, 2009; Wassmer et al, 2010). La direction de l'uprush varie en fonction des reliefs côtiers et de la propagation initiale de la vague, alors que le backwash est toujours perpendiculaire à la côte et guidé par la topographie (rivière, vallées).

Sur les côtes, un tsunami laisse en général de nombreuses traces de son passage, notamment des dépôts sédimentaires. Ces derniers correspondent à des couches de

sédiments marins discordantes sur les dépôts continentaux, on note la présence de foraminifères marins en abondance dans les dépôts et on peut observer des blocs hétérométriques pris dans une matrice sableuse. Les dépôts sédimentaires sont habituellement caractérisées par une série de séquences superposées. La granulométrie moyenne des matières déposées et l'épaisseur moyenne des couches diminuent vers l'intérieur des terres. Les dépôts affichent souvent un contact basal érosif et intègrent des fragments de rip-up boueux à la partie inférieure du dépôt. Ces rip-up résultent de processus d'érosion des écosystèmes estuariens boueux, lagunaire, ou des sédiments des marais dans la zone d'érosion près des plages (la zone proximale) (Atwater, 1987; Morton et al, 2007). Les coquilles, les coraux, et les matériaux à base de plantes terrestres sont souvent trouvés dans les dépôts (Bondevik et al., 1997; Goff et al., 2004; Hawkes et al, 2007; Kortekaas et Dawson, 2007). Des dunes sont mises en place et de gros blocs de coraux sont transportés et s'imbriquent au moment de leur dépôt à la terre. Côté océanique, le retour des vagues vers la mer peut générer des turbidités. Ces signatures sont très utiles pour reconnaître les caractéristiques des tsunamis et identifier les événements passés.

Wassmer et al. (2007) ont étudié les rôles respectifs de l'uprush et du backwash sur les signatures sédimentaires du 2004-IOT, pour décrire le comportement de l'inondation. L'étude a révélé une différenciation forte des faciès de dépôts du tsunami de la partie proximale à la zone distale. Les dépôts qui ont situés près du rivage (la zone proximale) ont été jugés grossiers et indifférenciés, alors que la fréquence de séquences de grano-classement normal stratifiés, avec une base grossière qui devient peu à peu plus fine vers le haut, augmente vers la terre (Wassmer et al., 2007). Ils correspondent à la diminution générale de l'énergie des vagues de la zone proximale à la zone distale pendant la phase uprush alors que l'énergie augmente de plus en plus de la zone distale à la zone proximale au cours de la phase de backwash. Les signatures ont été bien conservés dans la zone distale à cause de la très faible énergie des vagues pendant la phase de slack, soit à la fin du uprush et au début du backwash (Wassmer et al., 2007, 2010).

L'étude de paléo-tsunamis doit être un effort multidisciplinaire au-delà des approches sédimentologique et stratigraphique (Goff et al., 2010, 2012). L'application de l'anisotropie de la susceptibilité magnétique (ASM) dans l'étude des dépôts de tsunami développé par Wassmer et al. (2010) a été bien testée et acceptée comme une méthode appropriée pour déterminer les conditions hydrodynamiques et paléo-courants de sédiments mise en place

(Chagué-Goff et al., 2011). Une autre étude de Chagué-Goff et al. (2012) montre que les indicateurs géochimiques dans les dépôts de tsunami sont très utiles pour déterminer l'ampleur des événements de paléo-tsunamis historiques. Les deux ASM et méthode géochimique sont menées conjointement avec l'analyse granulométrique. Parfois, l'identification des diatomées et les foraminifères sont effectuées avec la granulométrie, l'ASM, et l'analyse géochimique. Dans l'étude des tsunamis générés par les éruptions volcaniques, la présence de matériaux pyroclastiques dans les séquences du tsunami constitue un élément d'identification supplémentaire important (Waythomas and Neal, 1998; Carey et al., 2001; Nishimura et al., 2005; Bruins et al., 2008; Paris et al., 2014a, 2014b). Les matériaux pyroclastiques peuvent présenter des couches intercalées avec des unités de sable par le tsunami et / ou mélangé avec du sable comme des unités de sable ponceuses. Ceci a été bien décrits dans les dépôts de tsunami du Krakatau en 1883 dans le détroit de la Sonde (Paris et al., 2014b). Les téphras non consolidés, tels que les cendres fines, les cendres grossières, et les lapilli avec de la pierre ponce, des scories, et d'autre éléments de fragments de juvéniles produits par des écoulements pyroclastiques, une poussée pyroclastique, ou des retombées pyroclastique (McPhie et al., 1993) sont souvent trouvés dans les dépôts de tsunami volcaniques. La mise en relation des enregistrements sedimentaires de tsunamis avec les processus d'éruptions volcaniques peut être un élément decisif pour identifier les événements passés de tsunamis volcanogènes. Paris et al. (2014b) ont ainsi couplé histoire de l'éruption et l'enregistrement du tsunami avec une étude des éruptions du Krakatau en 1883, dans laquelle une partie de la thèse a été impliquée. Il a ouvert la voie pour le développement de la recherche concernant des événements passés du Krakatau en 1883 sur la base de certains dépôts de tsunami exceptionnels le long des plaines côtières du détroit de la Sonde.

Les grandes explosions paroxysmiques du complexe volcanique de Krakatau se sont produites au matin du lundi 27 août 1883. Commencée par une explosion du Mont Perbuwatan à 05h30, elle s'est poursuivie par celle du Mont Danan à 06h44, et finalement par les énormes explosions du Mont Rakata à 10h02 et 10h52 (heure locale) qui ont détruit la plus grande partie de l'île de Krakatau (Verbeek, 1884, 1 885; Hurlbut et Verbeek, 1887. Symons et al 1888; Simkin et Fiske, 1983). Ces évènements ont en outre eu des répercussions planétaires. Les dernières explosions de Mont Rakata ont produit le plus grand bruit d'explosion volcanique jamais entendu par l'humanité avec une énergie totale libérée équivalent à 200 mégatonnes de TNT (Bryant, 2008). Le son a atteint les îles de

Rodriguez dans l'océan Indien, Ceylan, et Elsey Creek, Territoire du Nord, Australie (Verbeek, 1884, 1885. Symons et al 1888; Blong, 1984). Les explosions du Krakatau ont éjectés 18 - 21 km^3 de volume de juvenile dacitiques (les ponces et les cendres volcaniques) qui se propagent a plus de 50 km de la source (Verbeek, 1884, 1885;. Symons et al, 1888; Soi et Rampino, 1981; Simkin et Fiske , 1983). Ces dépôts pyroclastiques sont devenus une preuve très précieuse pour reconstruire les éruptions du Krakatau en 1883. La dernière explosion énorme acréé un grand bassin ou une nouvelle caldeira de 7 km de large et plus de 100 mètres de profondeur (Verbeek, 1885; Hurlbut et Verbeek, 1887. Symons et al 1888; Simkin et Fiske, 1983). Mont Perbuwatan et Mont Danan, ont sombrés dans les profondeurs et ne restait plus que le flanc sud du Mont Rakata avec une magnifique falaise abrupte plus de 800 m de haut et 10 m^2 de roche presque au milieu de la nouvelle caldeira (Verbeek, 1884, 1885). Les énormes changements qui ont touché le complexe volcanique du Krakatau pendant cette séquence éruptive ont été responsables des perturbations successives de l'eau de mer conduisant à la formation de vagues de tsunami.

Les vagues de tsunami puissantes produites lors de l'éruption du Krakatau en 1883 ont été plus meurtrière que l'éruption elle-même. Ces tsunamis ont détruit de nombreux villages dans les zones côtières à travers le détroit de la Sonde, tuant 36,417 peuples sur les côtes occidentales de Java (Merak, Anyer et Caringin) et les côtes Sud de Sumatra (Verbeek, 1885; Hurlbut et Verbeek, 1887; Symons et al, 1888. Simkin et Fiske, 1983). Au Sud du détroit, les tsunamis ont inondés les côtes de la péninsule de Ujung Kulon. L'eau se précipita sur l'étroite bande de terre de l'isthme de Laban, rasa au sol les arbres de la forêt tropicale, et se déversa dans l'océan Indien. Le run-up maximum atteint par le tsunami (environ 42 m) a été enregistré à Merak, île de Java. Les mécanismes de génération de tsunamis lors des éruptions gigantesques de Krakatau en 1883 ont été largement explorés par les chercheurs. Cependant, ces mécanismes sont encore débattus et les spéculations et de controverses abondent. Ils pourraient être liés à :

- La coulée pyroclastique entrant dans la mer (Verbeek, 1884, 1885; Latter, 1981; Soi et Rampino, 1981; Francis, 1985; Sigurdsson et al, 1991; Nomanbhoy et Satake, 1995; Bryant, E., 2008; Maeno et Imamura. , 2011).
- L'explosion sous-marine phréatomagmatique (Yokoyama, 1987; Nomanbhoy et Satake, 1995; Bryant, E., 2008).
- L'effondrement de la caldeira (Verbeek, 1884, 1885. Soi et Rampino, 1981; Francis, 1985; Sigurdsson et al, 1991).

La coulée pyroclastique entrant dans la mer est considéré par de nombreux auteurs comme l'hypothèse la plus logique dans le déclenchement des grandes vagues de tsunami. Nonobstant, on ne sait pas si la coulée pyroclastiques dans la mer est le seul mécanisme de la génération des tsunamis du Krakatau ou si elle ne déclenche que les dernières grandes vagues de tsunami.

Une jauge de pression à l'usine à gaz à Batavia peut être utilisée pour identifier les tsunamis du Krakatau en 1883 (Symons et al., 1888). Les variations de pression de l'air enregistrée au manomètre peut être mise en relation avec les éruptions du Krakatau et aurait pu être liée aux grandes vagues de tsunami. Cinq vagues de tsunami observées, entre le 26 – 27 août, peuvent être bien connectés avec certaines des ondes inscrits à la jauge de pression (Symons et al 1888). Bien que seulement certaines vagues d'air aient été connectées de manière plausible, ces dossiers d'enregistrements sont très précieux pour appuyer l'interprétation des événements après l'éruption du Krakatau.

3. Zone d'étude et méthodologie

Les côtes Sud du détroit de la Sonde dans la région de Ujung Kulon ont fait par le passé l'objet de recherches axées sur la reconstitution de la forêt tropicale, rasée par les tsunamis générés par l'éruptions du Krakatau en 1883. En revanche, rien n'a été fait dans ce secteur sur les sédiments mise en place par les tsunamis. Toutefois, situé au Sud du Krakatau au fond d'une baie caractérisée par une morphologie côtière en «piège a vagues», l'isthme étroit de Laban, reliant la péninsule de Ujung Kulon avec l'ile de Java, dispose d'un potentiel important pour enregistrer et conserver les signatures sédimentaires des tsunamis générés par le volcan Krakatau.

En ce qui concerne la morphologie du littoral, la zone de Ujung Kulon affiche un relief côtier unique qui peut avoir joué un rôle sur la distribution de l'énergie des vagues et en particulier lorsqu'on considère les deux grands forme de «V» de morphologies des côtes de la baie de Bienvenue et la baie de Cidaun. La baie de Bienvenue est délimitée par les étroites plaines côtières avec une grande zone de marée peu profonde (la profondeur d'eau d'environ 500 mètres de la zone est inférieure à 50 cm), contrairement à la baie en face de Karang Ranjang avec un large plaines côtières (50 - 100 m) et une zone intertidale étroite. Alors que la baie de Cidaun est plus petite que la baie de Bienvenue et pas directement ouverte vers le détroit de la Sonde et le complexe volcanique de Krakatau, en raison de la

présence de l'île de Peucang. Cette baie est caractérisée par les étroites plaines côtières et zone intertidale. Cependant, elle peut également conserver un dépôt de tsunami remarquable au fond de la baie de Cidaun. La forme d'entonnoir des côtes concentre habituellement l'énergie des vagues en fond de baie (Baldock et al, 2007; Okayasu et al, 2011; Yamanaka et al, 2013.). Pour la zone d'étude, cette configuration «piège a vague» est doublée dans chacune de ces baies par un grand stock sédimentaire (des boues de sable très épaisses dans la baie de Bienvenue et des sables grossiers dans la baie de Cidaun) qui auraient pu être responsable d'un dépôt de tsunami important sur l'isthme de Laban et la zone de Cidaun. En raison de sa position à la convergence de la forme en «V» du relief côtier de la baie de Bienvenue, qui fait face au détroit de la Sonde au Nord, et de la baie de Karang Ranjang, ouverte sur l'Océan Indien au Sud, l'isthme de Laban était potentiellement en mesure d'enregistrer des événements d'inondations marine générées à partir des deux côtés de l'isthme: le tsunami induit par le volcanisme du Nord et le tsunami déclenché par des séismes du Sud. Le contexte géologique est ensuite utilisé pour déterminer les couches de base de pré-1883 ci-dessous les dépôts de tsunami. Dans les plaines côtières et l'isthme, la couche de base est constituée par de l'argile (la boue) et le sable des dépôts alluviaux. Ainsi, à la base, le premier dépôt du tsunami doit être mélangé avec ces sédiments quaternaires. Dans la région du Mont Honje, la plaine côtière est délimitée par des rochers volcaniques et sédimentaires tertiaires exposés aux falaises de la crête. Par conséquent, le dépôt de tsunami sera mélangé avec des matériaux plus grossiers comme des galets, du gravier, du sable, et des ponces, donc, le dépôt pourrait être plus facilement érodé (Hjulstrom, 1939). En conséquence, l'isthme de Laban ou de la peninsule de Ujung Kulon constitue probablement de loin le meilleur emplacement dans le détroit de la Sonde pour les enregistrements des paleotsunamis du Krakatau.

L'objectif de la thèse est de reconstruire les relations entre la morphologie côtière unique de la péninsule de Ujung Kulon et l'hydrodynamique des tsunamis du Krakatau en 1883. Pour atteindre cet objectif, trois méthodes d'analyse de texture et de composition sont appliquées, à savoir l'analyse de distribution granulométrique, l'identification des microfaunes et l'Anisotropie de la Susceptibilité Magnétique (ASM). Au début, une interprétation image satellite a été réalisé pour sélectionner les sites d'investigation qui peuvent avoir conservé des dépôts de tsunami.

Sur la base des sites potentiels sélectionnés, vingt-et-un sites d'investigation ont été observés entre juillet et août 2011 et en mai 2012. Les sites d'observation ont été principalement distribués sur les côtes Est (Mont Honje région) qui ont été anthropisées et sont plus accessibles. Alors que les côtes Ouest (la péninsule de Ujung Kulon) sont constituées de forêt ou des arbustes étaient localement assez impénétrable (entre 12 et 15 m/h avec une machette), même si elle montre quelques sites potentiels pour les enregistrements sédimentaires de tsunami. Deux sites potentiels dans la partie centrale des baies, à savoir Cidaun et Laban, ont été étudiés. Un transect a ensuite été fait le long de l'isthme, composé de 6 sites d'observation de forage (U-01 à U-06), afin de reconstituer les caractéristiques de la sédimentation liée aux tsunamis du Krakatau en 1883 à travers l'isthme plat et d'identifier les dépôts potentiels à partir d'une source de l'océan Indien. À la péninsule de Ujung Kulon, seul la méthode de carrotage a été autorisé, en raison de la réglementation du gouvernement sur toutes les activités dans un parc national (UU n° 5/1990 à propos de la conservation des ressources naturelles et écosystème). La profondeur maximale de l'investigation était de 3,0 mètre et plus bas seulement de l'argile et le sable des alluvions anciennes ont été trouvés. Ils correspondent aux couches de base pré-1883.

Indépendamment, les échantillons de l'ASM ont été recueillis en utilisant des boites cubiques (2 cm de cote) non- magnétiques le long des sections verticales des dépôts de tsunami dans le tube de carrotage. Les boîtes d'échantillonnage ont ensuite été orientées, selon l'orientation du carrotage, et scellées après le retrait pour éviter leur dessiccation. Les sédiments prélevés ont été limités au sable fin, aux limons et a l'argile présentant une bonne cohésion pour conserver la fabrique des sédiments (Wassmer et al., 2010). Par conséquent, les sédiments grossiers n'ont pas été échantillonnés en raison de leur perturbation lors de l'échantillonnage. Dans la partie orientale de Ujung Kulon, la plupart des signatures de tsunami ont été observées sur des affleurements, donc, la méthode de tranchée a été réalisée sur le site U-17 pour l'échantillonnage de l'ASM.

L'analyse granulometrique a été effectuée pour les échantillons avec 2 mm (-1 φ) de granulométrie maximale en utilisant un appareil de LS-230 Beckman Coulter au Laboratoire d'Analyses des Sols et Formations Superficielles, EOST, Université de Strasbourg (UdS), France. Les paramètres granulométriques tels que la moyenne, la variance, la déviation standard, l'asymétrie (*skewness*), et l'aplatissement (*kurtosis*) ont été déduits de cette analyse. La moyenne (Mφ ou μ) montre une moyenne de taille des grains,

la variance ($\sigma\varphi^2$) et la déviation standard ($\sigma\varphi$) indiquent le degré de triage, tandis que l'asymétrie ($Sk\varphi$ ou γ_1) et l'aplatissement ($K\varphi$ ou γ_2) montrent la forme de la répartition des grains (Boggs Jr, 1992). Selon les caractéristiques des dépôts de tsunami décrits par Chagué-Goff et al. (2011), les dépôts ont une distribution granulométrique qui s'étend des blocs aux sediments fins. Les sédiments diminuent généralement de taille vers l'intérieur des terres et vers le haut dans les dépôts. La répétition de séquences de grano-classement normal, l'asymétrie et l'aplatissement ont été utilisés pour déterminer les séquences du tsunami dans le dépôt à chaque profil / section. Le triangle textural adopté à partir de Brady et Weil (1999) a été utilisé pour attester les limites entre les séquences. Dans le dépôt de tsunami, ces limites sont généralement caractérisées par des sables fins / limons déposés par la queue d'une vague mélangé avec des gravier / sables grossiers mis en place par le front d'une autre vague (Chagué-Goff et al., 2011). Les paramètres granulométriques ont également été utilisées pour interpréter la condition de l'hydrodynamique en vigueur pendant le dépôt des sédiments en utilisant les diagrammes de CM, dans lequel le *C* est le percentile de la distribution granulométrique (C99) dans les dépôts et le *M* est la médiane (Passega, 1957). Pour éviter l'effet statistique de la présence d'un grain anormalement grossier au sein de la distribution granulométrique, le cinquième percentile de la distribution (C95) a été utilisé dans cette étude, comme proposé par Allen (1971).

Les échantillons, au sein des carottes U-03, U-04 et U-05 de l'isthme de Laban, ont été étudiés sous un microscope binoculaire, dans Laboratorium Palaeontologi, Fakultas Teknik Geologi (FTG), Universitas Padjadjaran (UNPAD), en Indonésie, pour obtenir des données qualitatives et quantitatives sur les assemblages de microfaune. Les foraminifères benthiques sont la majorité des espèces de microfaune utilisées pour déterminer une profondeur maximale du fond marin érodé par les vagues du tsunami (Bahlburg et Weiss, 2007; Chagué-Goff et al, 2011;. Dawson et Shi, 2000; Phleger, 1951). Les foraminifères sont exprimées par quantité d'individus par volume de l'échantillon, comme communément appelé *la densité*. La densité a été utilisé pour déterminer un biofaciès à travers la méthode d'analyse de cluster (Abbene et al., 2006). Le biofaciès résulté est une partie d'une unité stratigraphique caractérisé par les assemblages de fossiles qui est limitée à un certain faciès et un environnement spécifique (Allaby, 2013).

La mesure de l'ASM fournit des informations sur les fabriques magnétiques des dépôts de tsunami, en relation avec les caractéristiques hydrodynamiques lors de la mise en

place (Wassmer et al., 2010). Les échantillons ont été testés à l'aide d'un dispositif de MFK1-A Kappabridge, à l'Institut de Géologie, EOST, Université de Strasbourg (UdS), France, pour mesurer les axes maximum (K_1), intermédiaire (K_2), et minimum (K_3) de l'ellipsoïde d'anisotropie. Ces axes ont été utilisés pour évaluer la relation entre les processus de dépôt et la fabrique magnétique à travers le calcul des paramètres de l'ASM (Jelinek, 1981), à savoir le volume moyen essentiel de susceptibilités magnétiques (K_m), la linéation magnétique ($L = K_1 / K_2$), la foliation magnétique ($F = K_2 / K_3$), le paramètre de forme (T), le degré corrigé de l'anisotropie (P_j), le paramètre d'alignement (F_s), et le facteur de forme (q). L'ellipsoïde de l'anisotropie est caractérisée par trois axes définis comme K_1 (l'axe long) > K_2 > K_3. L'azimut de l'axe de K_1 et son inclinaison indiquent la direction du flux lors de la mise en place des sédiments (Wassmer et al., 2010). La fabrique magnétique est coaxiale avec la fabrique des sédiments (Tarling et Hrouda, 1993) qui se caractérise par la foliation magnétique (oblat, $K_1 \sim K_2 > K_3$ et $1 > T > 0$) et la linéation magnétique (allongé, $K_1 > K_2 \sim K_3$ et $0 > T > -1$). Le paramètre de forme (T), qui représente le type de fabrique magnétique, est lié à l'état des environnements sédimentaires. La force relative de la fabrique magnétique est représentée par le degré d'anisotropie (P_j) (Hrouda, 1982), tandis que le développement linéaire d'une fabrique est exprimé par le paramètre d'alignement (F_s) (Ellwood, 1975). Basé sur des mesures en laboratoire, les valeurs des paramètres magnétiques constituent les textures primaires de dépôt de sédiments naturels si le facteur de forme (les valeurs q) est compris entre 0,06 et 0,7 avec les angles d'imbrications (I; l'inclinaison de K_1) inferieurs à 20° (Hamilton et Rees, 1970).

L'analyse pétrographique a été effectuée afin d'identifier la teneur en minéraux dans les matériaux volcaniques trouvés avec les dépôts de tsunami comme un critère important pour reconnaître des dépôts de tsunami produits par les éruptions du Krakatau en 1883. Cette analyse a été effectuée sous un microscope polarisant, sous 40x à 100x, dans le Laboratorium Petrologi - Mineralogi, Fakultas Teknik Geologi (FTG), Universitas Padjadjaran (UNPAD), en Indonésie. Considérant que la plupart des échantillons sont des matériaux non consolidés, des sections minces ont été préparées par la méthode des montures de grains. Les minéraux identifiés dans les échantillons sélectionnés ont ensuite été comparés avec le résultat de l'examen microscopique de la cendre volcanique du Krakatau en 1883 décrit par Verbeek (1884, 1885), afin de confirmer que les dépôts observés ont été effectivement résultés des éruptions du Krakatau.

L'analyse géochimique a été réalisée afin d'identifier les éléments majeurs (SiO_2, TiO_2, Al_2O_3, Fe_2O_3, MnO, MgO, CaO, Na_2O, K_2O, et P_2O_5) ainsi que les proportions de bioclastes, exprimées par teneur en matière organique et de carbonate et de *loss on ignition*/LOI, contenus dans les dépôts de tsunami. L'analyse de la fluorescence X (XRF) a été appliquée en raison de sa méthode précise, facile à utiliser et rapide sans préparation d'échantillon, même pour les matériaux non consolidés. Pourtant, les échantillons doivent être bien conservés et non contaminés. Les échantillons de couches sélectionnées ont été analysées par un Rigaku RIX 2000 - XRF spectromètre au Département de Géosciences de l'Université de Shimane, au Japon, en utilisant des méthodes établies (Kimura et Yamada, 1996). Comme l'analyse pétrographique, les résultats de l'analyse XRF ont été comparés avec la composition chimique de la cendre volcanique du Krakatau décrit par JW Retgers dans Verbeek (1885) et Symons et al. (1888).

Finalement, six profils stratigraphiques à l'isthme de Laban, le long du transect d'investigation, ont été corrélés à partir du site U-01 au Nord (une zone proximale pour l'invasion marine du détroit de la Sonde, mais une zone distale pour l'invasion marine de l'océan Indien) jusqu'au site U-06 au Sud (une zone distale du détroit de la Sonde, mais une zone proximale de l'océan Indien). Cette section stratigraphique a été faite par une nouvelle approche combinant la distribution granulométrique, les foraminifères, et l'analyse d'ASM, pour laquelle la technique d'ASM est devenue une clé primaire fiable dans la corrélation. Le scénario des tsunamis du Krakatau en 1883 à Ujung Kulon a été reconstruit selon la corrélation stratigraphique.

4. Résultats

La zone de Ujung Kulon est un emplacement optimal pour les enregistrements des tsunamis dans le détroit de la Sonde. Ses deux baies en forme d'entonnoir , la position de la péninsule entre le détroit de la Sonde et l'océan Indien, l'état de ses couches de base, et le fait que cette région est un parc national constituent les facteurs d'influence pour les bons enregistrements des tsunami sédimentaires et leur préservation dans les sites sélectionnées. Beaucoup de signatures de dépôts de tsunamis ont été trouvées dans la zone de Ujung Kulon et de ses environs. Un dépôt de tsunami incroyable avec des blocs de corail embarqués dans le sable, y compris des couches de sable bioclastique et l'unité de sable ponceux a été trouvé à l'isthme de Laban, dans la partie centrale en forme de V de la

morphologie côtière de la péninsule de Ujung Kulon. Les couches de sédiments observées ont été caractérisées par une série de séquences de grano-classement normal empilées l'une sur l'autre et l'intégration de fragments de rip-up de sédiments argileux. Les foraminifères ont également été trouvés en abondance dans les sections distales de l'isthme. A l'Est, le long de l'étroite plaine côtière à l'avant du Mont Honje, le dépôt des sables de tsunami atteint jusqu'à 50 cm d'épaisseur, en sandwich entre un matériels de corail et des graviers fins. Localement, les dépôts en vrac et des gros blocs de corail ont été trouvés loin dans les terres.

Les résultats des investigations de terrain montrent que la péninsule de Ujung Kulon montre des enregistrements remarquables de tsunamis. Ces évidences sont bien conservées en raison de la situation de la péninsule comme une réserve naturelle de l'UNESCO ou un parc national. En revanche, les signatures de dépôt de tsunami sur l'étroite plaine côtière du Mont Honje ne sont pas bien conservées, parce que cette plate-forme littorale a été profondément transformée en rizières. Seule une mince couche du dépôt de tsunami est restée à certains endroits, avec des gros blocs de corail. Même la plupart des affleurements montrent seulement le socle rocheux des dépôts volcaniques et sédimentaires tertiaires. Ce dernier indique que les sédiments meubles dans cette région sont facilement effaçable soit par voie naturelle ou anthropique. Selon l'analyse granulométrique chaque section montre une répétition vers le haut des séquences de grano-classement normal ainsi qu'une tendance a la diminution d'épaisseur du dépôt vers les terres.

Nous avons constaté que les foraminifères benthiques ont été concentrés à une profondeur comprise entre 100 - 240 cm, soit environ 11 à 28 espèces et 564 individus jusqu'à 21,888 les individus. La densité la plus faible est à la profondeur entre 15 - 60 cm, soit environ 4 - 10 espèces et 5 - 90 individus / dm3, en raison des conditions de conservation très mauvaises au niveau du sol. Nous avons vu ensuite que l'isthme de Laban a peut-être fait l'objet d'inondations par le tsunami des deux cotés de l'isthme: du Nord, du détroit de la Sonde sur la base de la dominance de *Elphidum lessonii* et *Streblus beccarii* dans les sections U-03 et U-05 (jusqu'à 5,184 les individus / dm3) et du Sud, de l'océan Indien sur la base de la dominance de *Planulina wuellerstorfi* dans les sections U-04 et U-05 (jusqu'à 5.056 les individus / dm3). En outre, l'analyse de cluster statistique montre que les couches de sédiments peuvent être divisés en cinq biofaciès (biofaciès A, B, C, D, E) qui se distinguent par le nombre d'espèces et d'individus dans chaque échantillon

(Abbene et al., 2006; Patterson, 1990). Le biofaciès A consiste en une ou plusieurs couches de sédiments contenant une petite quantité d'espèces et les individus apparentés. Les biofaciès suivantes (B, C, D, E) correspondent à une augmentation progressive du nombre des espèces et des individus. Ces biofaciès peuvent refléter l'énergie des vagues (Gallagher et al., 1999). Les biofaciès A et B peuvent avoir été produits par les vagues de haute énergie et turbulentes de l'uprush lorsque les sédiments ont été mises en place. Les biofaciès C, D, et E sont probablement produits par les vagues les plus faiblement énergiques lorsque la grande quantité de sédiments a été mise en place loin dans les terres. La fluctuation des biofaciès C, D, et E est survenue aux sections U-04 et U-05 qui se trouvent plus à l'intérieur. Les changements latéraux de biofaciès sont clairement observés en comparant U-03 U-04 et U-05, dans lequel ces biofaciès évoluent et indiquent que l'énergie des vagues est plus réduite à l'intérieur des terres.

La technique d'anisotropie de la susceptibilité magnétique (ASM) permet de mettre en évidence la fabrique magnétique interne des dépôts. En général les valeurs L, F, et T indiquent que la fabrique magnétique est essentiellement oblat ($L < M$, ou $K_1 \sim K_2 > K_3$ et $0 < T < 1$), avec une variation de leur composante allongée ($L > F$, ou $K_1 > K_2 \sim K_3$ et $-1 < T < 0$). Les variations verticales de P_j et F_s sont toujours cohérentes entre elles et représentent le degré d'alignement de contrôle du degré d'anisotropie. Il indique les fluctuations de l'intensité du courant au cours de la sédimentation (Wassmer et al., 2010). En relation avec les vagues de tsunami, les axes de K_1 montrent que les sédiments ont été mises en place par deux directions générales d'écoulement. Une première direction Sud, à partir du détroit de la Sonde, entre N104° et N262°. Une seconde dans la direction opposée de l'océan Indien propagation entre N280° et N80°. En commençant par une direction Sud, les deux directions en évidence par l'ASM alternent avec une régularité surprenante dans toutes les séquences sédimentaires.

Lors de l'examen microscopique de la cendre volcanique recueillies auprès U-01, U-02, U-03, U-06, U-08 et U-13, des fragments de verre, la roche, et certains minéraux ont été identifiés. Les particules de verre et des morceaux microscopiques de pierre ponce, ne sont pas présents en grande abondance (<10%) et sont apparemment modifiés dans les minéraux argileux. Les minéraux identifiés sont le feldspath, l'orthopyroxène et des minéraux opaques (par exemple l'ilménite, magnétite, etc), en conformité avec les descriptions précédentes des dépôts pyroclastiques du Krakatau en 1883 (Paris et al .,

2014; Renard, A., 1883; Symons et al, 1888. Verbeek, 1885, 1884). Enfin, les résultats des analyses géochimiques montrent que les dépôts ont une composition similaire avec les examens antérieurs des cendres volcaniques du Krakatau recueillies immédiatement après les éruptions en 1883.

La corrélation stratigraphique est alors utilisée comme un outil pour la reconstruction de la mise en place des sédiments et les paléocourants. L'isthme de Laban peut présenter une meilleure séquences tsunami que d'autres endroits. Six sections différentes décrites à l'isthme ont des similitudes de preuves entre les séquences. Une corrélation stratigraphique a été alors reconstruite du Nord au Sud sur la base des séquences identifiées. Deux sources opposées de dépôts de tsunami mises en évidence par les changements des axes de K_1 ont provoqué une variation des séquences de tsunami à chaque section. La séquence au Nord de l'isthme peut avoir une direction différente de la mise en place des sédiments que la même séquence au Sud. Dans certaines sections les dépôts pourraient avoir été mélangé verticalement. De chaque source, quatre séquences de tsunami ont été identifiées respectivement. Ainsi, l'isthme a été probablement noyé huit fois (deux fois pour chaque séquence de tsunami).

5. Disscussion and conclusion

Les résultats de ces analyses ont démontré que l'isthme de Laban à Ujung Kulon a enregistré pas moins de 8 (huit) séquences d'invasions marines provoquées par l'éruption. Nous avons pu montrer que ces huit invasions correspondaient en fait à 4 (quatre) tsunamis et que chacun de ces tsunamis avait été doublement enregistré a Laban : 1) par un flux direct provenant du détroit de la Sonde en ligne droite, et 2) par une vague indirecte venant de l'océan Indien, retardée dans le temps après avoir été réfractée le long des côtes de l'extrémité ouest de la péninsule de Ujung Kulon (près de l'île Panaitan). Cet enregistrement unique et original pourrait être lié au contexte géomorphologique exceptionnel de la péninsule de Ujung Kulon, et notamment de l'isthme et de ses baies en forme de V, qui en font l'un des pièges les plus remarquables de dépôts de tsunami autour du détroit de la Sonde.

Le comportement particulier des tsunamis sur l'isthme produit une signature sédimentaire alternée (*inter-fingering*) originale, qui est étroitement liée aux processus impliqués lors de l'éruption du Krakatau en 1883. L'épaisseur des dépôts peut refléter

l'énergie des vagues du tsunami et de l'intensité de l'éruption, par exemple, la plus grande vague de tsunami généré par la plus grande explosion à 10h02, le 27 août, est représenté par le dépôt de tsunami le plus épais. L'épaisseur des dépôts provenant du détroit de la Sonde (directement du Krakatau) sont plus épais que les dépôts provenant de l'océan Indien (réfractée le long des côtes de la péninsule). Ces caractéristiques montrent que la topographie côtière a joué un rôle sur l'épaisseur des dépôts de tsunami et, certainement, les changements de l'énergie du tsunami. La remarquable conservation de ces enregistrements multiples tsunami sédimentaires doit être liée à l'épaisseur importante des dépôts et sur le fait que cette zone n'a jamais été occupée par les hommes depuis 1883. Tout cela rend de l'isthme de Laban comme un site des plus exceptionnels d'enregistrements de tsunami sur la terre.

Cette étude fournit une clé importante pour la détermination de l'effet des reliefs côtiers sur l'inondation par des tsunamis dans la région de Ujung Kulon. En utilisant les connaissances les plus récentes et en mettant en œuvre les techniques développées à la suite des deux évènements majeurs de ces dernières années, l'étude des dépôts de tsunamis constitue une entreprise multidisciplinaire associant la sédimentologie, la stratigraphie l'étude du magnétisme des dépôts, de leur minéralogie et de leur géochimie. Cette approche permet d'identifier avec une grande précision la séquence des évènements tsunamis lies à l'éruption du Krakatau. Dans cette reconstruction, les apports de la technique ASM, sont déterminants pour déceler la fabrique magnétique et mettre en évidence l'orientation des flux qui ont mis en place les dépôts. Cette méthode prend tout son sens lorsque les dépôts ne présentent pas de structures sédimentaires visibles. Elle permet alors d'étalonner d'autres méthodes sédimentaires pour permettre de distinguer chaque vague du train d'ondes. La mise en évidence par cette technique d'une orientation de l'écoulement opposée au sens « normal » (en l'occurrence vers la source du tsunami), sur l'isthme de Laban a été confirmée par l'étude des foraminifères. Ces éléments ont permis de montrer que les vagues du tsunami en provenance du Krakatau avaient subi une réfraction le long des côtes occidentales de la péninsule de Ujung Kulon et que les dépôts de tsunamis se trouvant sur les rivages Sud de Ujung Kulon n'étaient pas à mettre en relation avec des tsunamis d'origine sismique générés dans l'océan Indien mais étaient bien synchrones de l'éruption du Krakatau. Cette découverte a ainsi permis de confirmer les zones d'inondations des tsunamis du Krakatau en 1883 telles qu'elles avaient été identifiées par Verbeek en 1885.

Cependant, cette étude peut avoir des insuffisances et des limitations. La méthode de forage pour collecter les échantillons d'ASM qui a été appliquée pour la première fois dans cette étude, a des limites dues à l'imprécision de la mesure de l'azimut du tube d'échantillon avant le forage et la possibilité de perturbation des échantillons au cours du forage. Cette imprécision peut être responsable d'une dispersion non contrôlée des azimuts des courants ayant déposé les sédiments. Une autre limitation de la méthode concerne l'échantillonnage de l'ASM dans les sédiments mal triés avec une fraction de particules grossières dominante comme cela a été quasi systématique dans les sections proximales. L'échantillonnage de l'ASM dans ces conditions est impossible, car les particules grossières peuvent perturber la fabrique initiale des sédiments lors de l'enfoncement des boites échantillons. Cette limitation pourrait être levée en utilisant des boites plus grandes mais cela nécessiterait un dispositif de mesure adapté aux grandes boîtes.

Les limitations, qui résultent de cette étude, ouvrent de nouvelles possibilités pour effectuer une étude plus poussée et une corrélation stratigraphique plus large autour de ce site unique et exceptionnel pour les enregistrements de tsunamis. L'échantillonnage sous marin pourrait également constituer un apport très précieux et complémentaire pour valider l'analyse des foraminifères dans les dépôts de tsunami qui ont été déposés loin à l'intérieur des terres. Tous ces éléments vont enrichir l'étude des tsunamis qui ont étés déclenchées le 27 août 1883 par les différentes phases éruptives du mythique volcan Krakatau.

INTRODUCTION

Tsunami is constituted by series of waves created when a body of water, on the ocean or lake, is suddenly displaced. This phenomenon can be generated by earthquakes, mass movements above or below water, volcanic eruptions, large asteroids impact, or other underwater explosions. Some meteorological phenomena, such as swells and storm surge, are not classified as tsunami waves.

Due to the immens volumes of water displaced and the kinetic energy released, tsunami can have a devastating impact to the adjacent coastal areas. Indian Ocean Tsunami (IOT) on December 26, 2004, one of the largest earthquakes ever recorded in the northern part of Aceh - Indonesia, and Tohoku Tsunami on March 11, 2011 in Miyako, Tōhoku's Iwate Prefecture and in the Sendai area, Japan, have widely opened the public insight that tsunami is one of the terrible phenomena destroying the towns or villages on the coastal areas and killing thousands people, although, the early warning system has been adopted. In historical time, the gigantic eruption of Krakatau Volcano on August 27, 1883 has been recorded causing the great waves of tsunami and killing ± 36,000 local peoples on the adjacent coastal areas around the Sunda Strait, between Java and Sumatra, Indonesia. Even 3500 years before present, the largest eruption of Santorini Volcano, a volcanic island in the southern Aegean Sea, about 200 km Southeast of Greece's mainland, may have led indirectly to the collapse of the Minoan civilization, on the island of Crete 110 km to the South, through the resulted gigantic tsunami. The last two are volcanic tsunami that are characterised by short-period waves and greater dispersion compared to earthquake tsunami (Paris et al., 2014a), like the 2004-IOT and the 2011-Tohoku Tsunami. Krakatau and Santorini tsunamis occurred when the recording devices were not as sophisticated as present. Thus, in order to reconstruct the intensity of these paleotsunamis, we can only rely on the observations and eyewitness accounts that were collected during and after the events, and also on the traces left by the waves.

Tsunami waves left many depositional signatures on the shoreland such as sandwiched marine sediment layers, foraminifera abundance, coral boulders embedded in sand, large coral boulders, and turbidites (Bryant, 2008; Dawson and Shi, 2000). These elements are very useful to recognize the tsunami characteristics and identify their occurrence in the past (Chagué-Goff et al., 2011). In the study of volcanogenic tsunami, the presence of volcanic materials within the tsunami sequences become an important additional element (Paris et al., 2014a, 2014b). Recently, Krakatau volcanogenic tsunami

signatures have been identified by many researchers (Umbgrove, 1947; Verstappen, H. Th., 1956; Ongkosongo, 1985; Bronto, 1990; Camus et al., 1992; Cita et al., 1996; Cita and Aloisi, 2000; Carey et al., 2001; van den Bergh et al., 2002, 2003; van der Kaars and van den Bergh, 2004; Boer et al., 2006; Atmadja, 2007; Paris et al., 2014b). The Krakatau tsunami study is particularly interesting because of the many testimonials available that allow age to relate the eruptive phenomena that have succeeded each with sedimentary records often well preserved along the coasts, particularly in areas where low anthropogenic pressure allowed their conservation.

Located South of the Krakatau with an incredible coastal morphology between Sunda Strait and Indian Ocean, Ujung Kulon Peninsula has an important potential to record and preserve the sedimentary records of the 1883-Krakatau tsunamis along the coastal area in the Sunda Strait, but also, because of its configuration, the tsunami records on the coastal area of Indian Ocean. These two possibilities render this site unique as an incredible past-tsunami recorder. However, only the people at the coasts of Java and Sumatra localized in the center and northern part of the Sunda Strait provided many visual testimonies about the volcanic eruptions and tsunamis phenomena at the events of August 1883. While, the rocky shores and austere South, particularly the region of Ujung Kulon Peninsula, have always been free of populations. So there are gaps in knowledge about the number and characteristics of tsunami flooding on the coasts of Ujung Kulon Peninsula.

The objective of this study is to explore and understand the way in which the tsunami generated by the various eruptive phases of the 1883-Krakatau eruptions occurred at Ujung Kulon on the basis of sedimentary recording along the South coasts of Sunda Strait. There are four scientific questions related to the objective such as follows:

1. Whether the tsunami deposits found at Ujung Kulon, including the deposits at the South coasts, are emplaced by the 1883- Krakatau tsunamis ?
2. If the deposits at the South coasts are emplaced by the 1883- Krakatau tsunamis, then, how is the scheme in case they could be deposited at the coasts which is not open to the Krakatau ?
3. Could the configuration of the tsunami deposits found at the study area be linked to the various eruptive phases of the 1883-Krakatau eruptions ?
4. How is the effect of coastal landforms to the configuration of the tsunami deposits (multiple sedimentary recording) ?

In order to respond those questions, three methods of textural and compositional analyses were applied, i.e. grain-size distribution analysis, foraminiferal identification, and Anisotropy of Magnetic Susceptibility (AMS) analysis. Grain-size distribution analysis were performed to recognize the tsunami sequences. Foraminiferal assemblages was identified to determine the origin of the sediments emplaced, whether they came from Sunda Strait or from Indian Ocean. While AMS technique is the method relied to recognize the paleocurrent or the orientation of sedimentary fabric within the deposits. This method could be expected to separate the layers coming from the opposite directions. Petrographical and geochemical analyses were also performed to compare the composition of materials within the tsunami deposits with the volcanic materials produced by the 1883-Krakatau eruptions. The combination of all the methods above constitute one of the new approach in the study of tsunami.

The results are then written in 9 chapters, which 2 chapters are presented in international journals, such as follows :

PART I : State of the art in the study of Karakatau tsunami

- **Chapter 1 :** Tsunami and its recordings
  Generally describes the characteristics of tsunami, its generation and classification, its sedimentary records, and its role for identifying past events.
- **Chapter 2 :** The 1883-Krakatau tsunami
  Describes the 1883-Krakatau eruptions and their tsunami sequences resulted from the eruptions.
- **Chapter 3 :** The 1883-Krakatau tsunami sedimentary recordings
  Describes in general the result of the previous studies on Krakatau tsunami deposits, gaps in knowledge, and fascinationg study of the 1883-Krakatau tsunami deposits.

PART II : Scientific approach

- **Chapter 4 :** The study area
  Describes the study area in the point of view of its oceanographic conditions, its geomorphological features, and its geological setting.
- **Chapter 5 :** Methods section
  Explains in detail the methodology used in this study, such as satellite image interpretation, field investigations, laboratory and data analyses.

PART III : Results

- **Chapter 6 :** The data collected

  Presents all of data collected from the field investigations and laboratory analyses, includes the result of data analyses.

- **Chapter 7 :** Synthesis

  Presents the reconstruction of volcanic phases of the 1883-Krakatau eruptions and tsunamis based on the sedimentary deposits and also the tsunami generation and its characteristics around the Sunda Strait.

PART IV : Discussion and conclusion

- **Chapter 8 :** Discussion

  Discuss all of the results, synthesis, highlight the positive items of the thesis, making the link with the literature presented in the state of the art, and also talking about the negative items resulted in the study.

- **Chapter 9 :** Conclusion

  Concludes the results of the study in general and its perspectives to filling the gaps in knowledge that might have not been achieved due to the limitation of this study.

Some data in Chapter 6 have been presented in an article "**Coupling the eruption and tsunami records: the 1883 Krakatau case-study, Indonesia**" published in Bulletin of Vulcanology and Geothermal Research (2014). Independently, the data of Laban Isthmus have been presented as an article "**Exceptional records of 1883 Krakatau tsunamis behaviour at Laban Isthmus**" submitted in Nature Publishing Group (NPG). Part I and II have been presented in the 2nd Southeast Asian Gateway Evolution Meeting, on March 11-15, 2013, Berlin, Germany. While, Part III and IV was presented in the 8th IAG-International Conference on Geomorphology, on August 27-31, 2013, Paris, France.

This study is supported by Directorate General of Higher Education, Ministry of Education and Culture, Government of Indonesia, and Laboratorium Geologi Lingkungan dan Hidrogeologi, Fakultas Teknik Geologi, Universitas Padjadjaran, Indonesia. Some data presented in international journal are derived from a collaboration with the ANR-VITESSS (Volcano-Induced Tsunamis: Sedimentary Signature and numerical Simulation), responsible R. Paris.

PART I
State of the art in the study of Krakatau tsunamis

Chapter 1
Tsunami and its recordings

Tsunami is a Japanese term, i.e. *tsu* means a harbour and *nami* means a wave, which is widely used in the scientific terminology for a wave or series of waves generated by the sudden displacement of a column of water that often develop as resonant phenomena in harbours. In fact, this wave is different from tidal and wind-generated waves. The tsunami wave breaks at the shoreline, whereas tidal and ordinary wind waves break at the surf zone. Thus, the tsunami can run up to greater heights, or sometimes further inland, than the tidal and wind waves (including storm waves). Tsunami is a high-magnitude phenomenon which has the potential to affect strongly the coastal areas, e.g. coastal landform modification, perturbation of the sedimentary balance, catastrophic destruction of human settlements, and ecological perturbation. Yet, it has also the potential to leave many erosional and depositional signatures on its paths near the coastlines and sometimes up to several kilometers depending on the coastal morphology context. The sediments emplaced inland by tsunamis constitute the sedimentary signature or sedimentary recording of the event and can be used to determine the characteristics and the occurrence of tsunami by the past. This chapter describes the characteristics of tsunami, the trigerring mechanisms at the origin of tsunami generation, and the tsunami recordings along the coastlines. It includes the recent evolution of deciphering science for tsunami sedimentary recordings developed thanks to the last decade strong events, e.g. 2004-Indian Ocean and 2011-Tohoku tsunamis.

1.1. Tsunami characteristics

Tsunami and wind-generated waves (e.g. swell and storm waves) can be distinguished on the base of their characteristics. The terminology used to describe tsunami characteristics is the same as the one used for wind waves, i.e. the wavelength, the period, the velocity, the water depth, the wave height, and the run-up height, see Figure 1-1 (Blong, 1984; Myles, 1985; Okal, 1988; Camfield, 1994; Satake, 1995; Pelinovsky, 2006; Bryant, 2008; Ward, 2008; Mori et al., 2011). A tsunami corresponds to a wave train (it may consists of 10 or more waves) from large to very large *wavelength*, i.e. the horizontal distance between any two corresponding points on successive waveforms. In contrast to the wind waves, tsunami

wavelength can lie between 10 to 500 km, due to the finite ocean depth and the mechanism of wave generation. The tsunami *wave period* is the time it takes for a pair of wave crests to pass by a point. This period can ranges between 100 to 2,000 seconds and the order of one hour (Bryant, 2008), while wind waves may have a period of about 10 seconds for a wavelength of 150 m (Thurman et al., 1999). Due to the long wavelength and periods, tsunami has a *velocity* about 250 m/second (900 km/hour) in the open ocean and 10 m/second (36 km/hour) at shore (Bryant, 2008). This velocity is faster than wind waves which travel at about 20 – 90 km/hour (Thurman et al., 1999). The relationship between wave velocity (V), wavelength (L), and period (T) is expressed by a simple function such as follows:

$$V = \frac{L}{T}$$

As a result of the very small ratio between its long wavelength and the oceans depth that never exceed 5 km, the majority of tsunamis behave as shallow-water waves (Wu, 1981; Mei and Agnon, 1989; Bryant, 2008). In this case, the trigonometric functions characterizing sinusoidal waves (the simplest form of tsunami wave in the open ocean, see Figure 1-1) dissapear and the wave velocity becomes a simple function of the *water depth* (d) and the *gravitational acceleration* (g), as follows:

$$V = \sqrt{gd}$$

The water depth is measured from mean sea level or *zero energy level*, i.e. the level of the water in the open ocean if there are no waves, to ocean floor (Figure 1-1). Zero energy level constitutes a halfway between the crests and the troughs of the waves, in which the vertical distance between a crest and a trough is called the *wave height* (Thurman et al., 1999).

While tsunami waveform in the open ocean is sinusoidal in shape, it becomes more peaked when it crosses a continental shelf. As a tsunami approaches shore, the wave trough dissapears and the tsunami becomes a solitary wave which lies above mean sea level, i.e. the wave height (H) becomes a *solitary wave height* (H_s), see Figure 1-1. Yet, many observations of tsunami noted that the exceptional tsunami waves have a component below mean sea level, featured by 'N-wave', when approaching the shore. In many cases, the water is generally draw down before the wave crest arrives. This N-wave characteristic is caused by nonlinear effects that produce a trough in front of the wave (Tadepalli and Synolakis, 1994; Satake, 1995; Geist and Dmowska, 1999; Carrier et al., 2003; Geist and Parsons, 2006; Pelinovsky, 2006). Nonlinear effects can also cause the tsunami waves overriding the land as a bore, e.g. 2004-Indian Ocean tsunamis (Glimsdal et al., 2006; Grue et al., 2008; Lavigne et al., 2009;

Paris et al., 2010; Nandasena et al., 2011) and 2011 Tohoku tsunamis (Mori et al., 2011; Wilson et al., 2012; Mori et al., 2013).

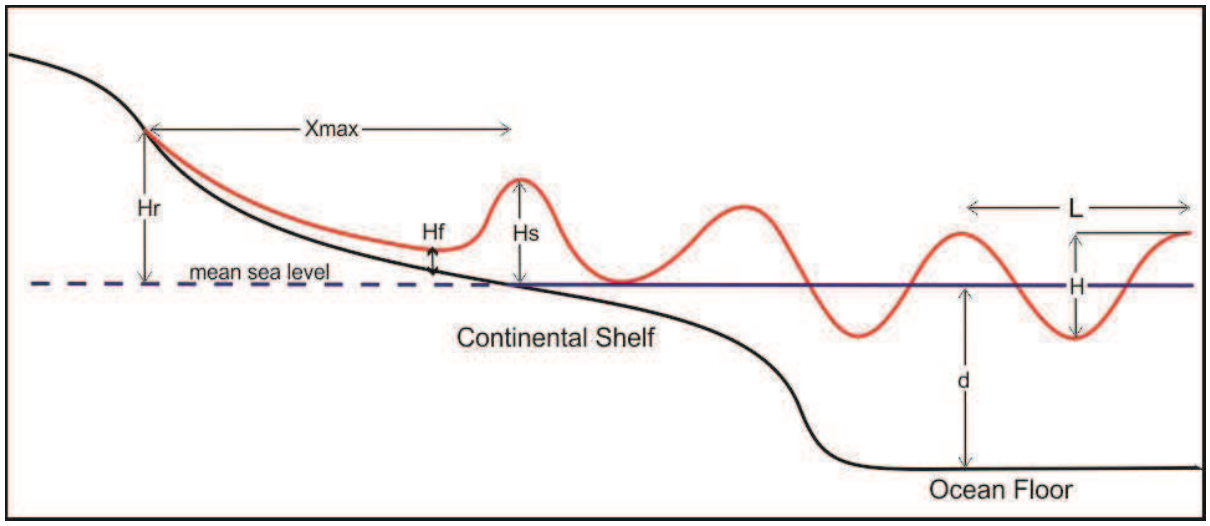

Figure 1-1. Tsunami characteristics used in the text (modified after Bryant, 2008): L is the wavelength (m), H is the tsunami wave height or crest to trough wave height (m), d is the water depth (m), H_s is the wave height at shore (m), H_f is the flooding height inland (m), H_r is the run-up height above sea level (m), and X_{max} the maximum distance of flooding (m).

When tsunami approaches the shorelines, it can undergo shoaling, refraction, reflection, and diffraction, depend on the morphology of the ocean floor or the coast, complexifying the number and orientation of the waves recorded. *Shoaling* occurs when the wave enter the shallow marine zone, in which it becomes slow down (Thurman et al., 1999). Under stationary conditions, the wavelength is reduced, the velocity decreases with the reduction of water depth, the wave energy and the wave height increases. When the crest of wave becomes too steep, it becomes unstable, curling forward and breaking. Tsunami wave reach shore without breaking and bring tremendous power to bear on the coastline.

As a shallow water wave, tsunami can feel the ocean bottom at any depth and the wave crest undergo *refraction* or bending around higher seabed topography, such as islands chains, rises, and seamounts. The wave bends because the depth under a wave crest varies along the crest. Along an irregular shoreline, the wave energy is concentrated on headlands, causing erosion, and dispersed in bays, resulting in deposition (Thurman et al., 1999). While, a vertical barrier, such as a seawall or a rock ledge, can reflect tsunami wave back into the ocean with little loss of energy, i.e. a process called *wave reflection*, creating unusual waveforms. On the other hand, a surface-piercing obstacle (e.g. a breakwater or an island) can

cause *difraction*. The waves, after passing the island, turn and carry the wave energy into the region behind the island called shadow zone, e.g. the 2004-Indian Ocean tsunami observed in Sri Lanka Island where the waves heading to the west circumvented the south coast of the island taking a northbound orientation in the shadow of the island. The turning of the waves is due to the changes in wave height in the same wave along the crest.

Once tsunami wave reaches the land, then the wave height equates with the depth of water flow over land or *flooding height*/H_f (Blong, 1984; Camfield, 1994; Yeh* et al., 1994; Nott, 1997). It is not easy to measure the flooding height, Lavigne et al. (2009) have evaluated this height by measuring the position of palm branches hanging on tamarin trees or broken branches on casuarina trees. However, most of the paleotsunami studies used *run-up height* (H_r) to describe the intensity of tsunami waves. Run-up height is different from the maximum flooding height. It constitutes the maximum vertical height reached onshore above sea level by the flooding of tsunami (tsunami inundation). The greater the run-up height the bigger the tsunami and the greater the volume of water carried onshore (Hills and Mader, 1997).

The *maximum distance of flooding* (X_{max}) is affected by coastal landscape roughness. Roughness is represented by Maning's *n*, where *n* equals 0.015 for very smooth topography, 0.03 for developed land, and 0.07 for a densely treed landscape (Figure 1-2).

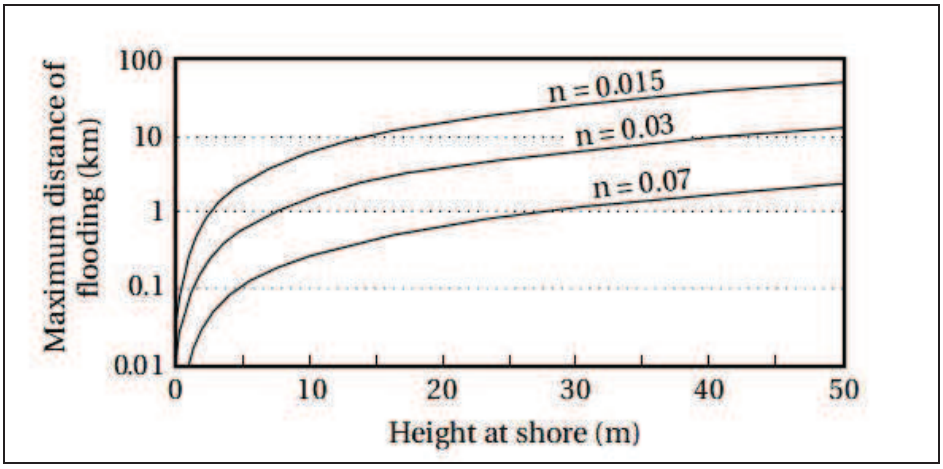

Figure 1-2. Varying coastal landscape roughness curves (Hills and Mader, 1997): Roughness represented by Maning's *n* are resulted from the relationships between maximum distance of flooding on a flat coastal plain (km) and tsunami height at shore (m). The values of *n* are explained in the text.

A different condition of roughness can also influence the velocity of tsunami waves (Camfield, 1994; Yeh* et al., 1994; Nott, 1997). This situation is expressed by an equation as follows:

$$v_r = H_t^{0.7} [\tan (\beta_w)]^{0.5} n^{-1}$$

where H_t is wave height (meter) and β_w is slope of the water surface (degree).

The slope of the water surface, i.e the angle of the water surface relatives to the horizontal, may be a difficult parameter to estimate. It can only be determined after an event, e.g. by measuring the water lines on buildings or trees. It may or may not be parallel to the coastal landscape and generally ranges between 0.001 – 0.0025.

On land, tsunami inundation events consist of three phases, i.e. *uprush*, *slack*, and *backwash*, that affect the sediment emplacement (Wassmer et al., 2010). Uprush is a sudden upward surge or flow that forms immediately after a tsunami wave breaks, with the strong energy at the proximal zone (near offshore). The energy decreases when the wave progressing inland, then reaching the flooding maximum extension at the distal zone (onshore). Slack, a period of little activity (zero energy) prior to backwash flow (Dawson and Stewart, 2007), occurs at this zone without energy and velocity at all. In this phase, mud substrates and foraminifera will be abundantly deposited. Afterwards, backwash begins to flow from the distal zone to the offshore, with the velocity acceleration and sediment mixing. Uprush velocity is greater than the backwash, but its duration is shorter (Masselink and Puleo, 2006). The conditions of these three phases are modified by the general profile of the coastal slope on which the waves surge. When the slope are steep, the three phases succession occurs for each single wave within the tsunami wave-train. When the slope is very flat all the sediments are emplaced during a single long uprush phase eventually followed by a low backwash and the complete receding of the water needs tens of hours (Lavigne et al., 2009; Wassmer et al., 2010). The direction of the uprush varies depend on the coastal landforms and the initial propagation of the wave, whereas the backwash is always perpendicular to the coastline and guided by the topography (river, valleys).

1.2. Tsunami generations and classifications

Tsunami generation is thought of as a product of submarine seismic disturbance (earthquake-generated tsunami), a mass movement (landslide) above or below water, a

volcanic eruption (volcano-induced tsunami), and a large asteroid impact in the ocean. These phenomena are commonly called geological hazards.

The relationship between such geological hazards and tsunami generations are displayed in Figure 1-3 with some examples explained below.

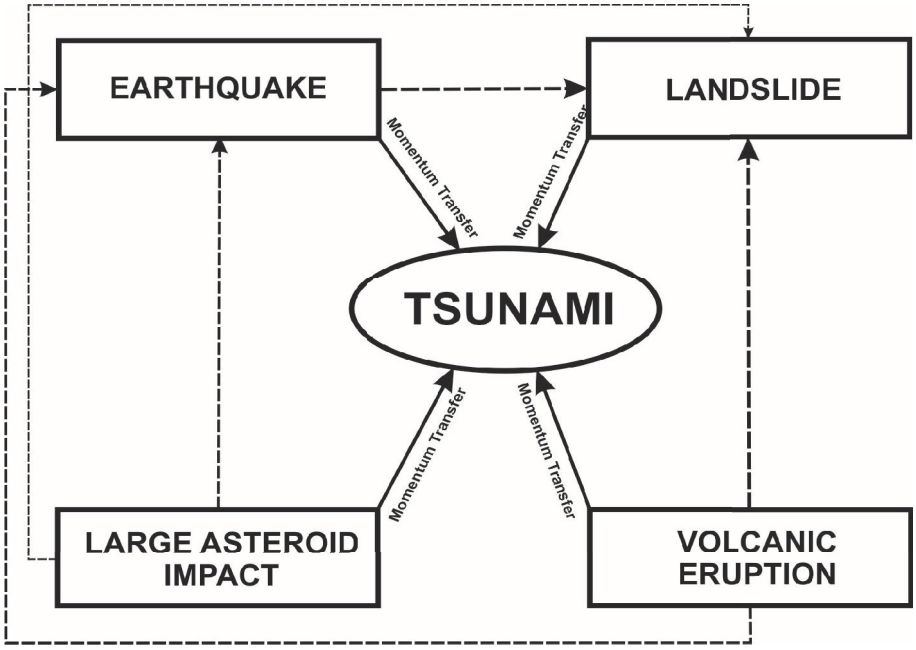

Figure 1-3. Flow chart showing the relationship between geological hazards and tsunami generations. Tsunami can be generated by earthquake, landslide, volcanic eruption, and large asteroid impact (indicated by arrow lines). Such geological hazards-induced tsunamis affect one another (phenomena filiation are indicated by dashed lines).

a. Earthquake-generated tsunami

In general, the majority of tsunamis are typically seismic events, thus, tsunami is also called *seismic sea waves* (Thurman et al., 1999). Submarine seismic disturbances will generate earthquakes-induced tsunamis. Underwater vertical fault movement is one of submarine seismic disturbances which could trigger a large tsunami. It displaces Earth crust, generates earthquakes, and produces a sudden change in water level at the ocean surface. Since 1964, the main part of tsunami events have been triggered by submarine earthquakes (NOAA Center for Tsunami Research, 2014). However, only earthquakes of magnitude 7.0 or greater were related to the significant tsunamis (Iida, 1963; Geist, 1999; NOAA Center for Tsunami Research, 2014).

Indian Ocean tsunami on December 26, 2004 (2004-IOT), one of the largest tsunamis ever recorded, was triggered by earthquakes with a moment magnitude, M_w, ranging around 9.1 – 9.3. The rupture affected the fault on 1200 km with throws reaching locally 15 m. This tsunami event swept across the northern Indian Ocean and killed 229,867 people (United Nations, 2006, in Bryant, 2008). Due to its distribution and fatalities (Table 1-1), 2004-IOT is the largest tsunami event ever recorded in historical times. It has a maximum run-up height of 50.9 or $\pm$ 51 m asl, which was an exception occurrence of tsunami run-up caused by a significant non-hydrostatic effect when through a narrow saddleback morphology between Labuhan Hill and Ritieng Hill, in Lok Ngha, Aceh (Choi et al., 2006; Lavigne et al., 2009; Kim et al., 2013).

Table 1-1. Distribution and fatalities of Indian Ocean Tsunami in 2004 (2004-IOT).

Parameter	*2004-IOT Data*
Date	December 26, 2004
Cause	Submarine earthquake
Source	Underwater fault movement below Andaman Islands, Indian Ocean
$H_{r\ max}$ (m asl)	50.9 ($\pm$ 51)
Distant areas affected	All Indian Ocean coasts, Callao – Peru (Pacific Ocean), and Rio de Janeiro – Brazil (Atlantic Ocean)
Fatalities (people)	229,867

Source: based on Choi et al. (2006); Lavigne et al. (2009).

b. Landslide-induced tsunami

Earthquakes can also generate landslides, both submarine and terrestrial landslides. Submarine landslide is commonly associated with tsunami, while terrestrial landslide falling into a body of water may be locally significant. A large landslide can displace a large volume of water, thus, the tsunami wave resulted from this event is most probably larger than the wave of earthquake-tsunami.

A large earthquake (with a magnitude of 7.9) caused by tectonic movements along Fairweather Fault, in the Southeastern Alaska, on July 9, 1958, triggered a giant rockslide at the headland of Lituya Bay (near Gilbert Inlet). The rockslide with a volume of 40 million cubic yards ($\approx 30.5 \times 10^6$ m^3) acting as a monolith impacted with great force the bottom of

Gilbert Inlet. The impact created a radial crater which displaced sediments and resulted in water splashing action generating a huge solitary tsunami wave which swept the main body of the bay. The run-up of tsunami reached the southeast spur of Gilbert Inlet with a height of 1,720 - 1,740 feet (≈ 530 meter) above sea level, and a wave height ranging around 30 m. (Miller, 1960; Pararas-Carayannis, 1999).

Other landslide-induced tsunamis can be generated by slope instability at volcanoes (Paris et al., 2014a). Yet, it can also be categorized as a volcanic-induced tsunami because it usually occurs during eruption. The slopes of a volcano are unstable during eruptions and can form a debris avalanche with velocity about 100 m/sec (Bryant, E., 2008). In many cases, the resulting landslides were localized enough to generate small tsunami, however, they caused the greatest death tolls. For examples; i) The collapse occurred on the flank of Mayuyama Volcano, which is one of the dacite lava dome of Unzen Volcanic Complex in Japan, on May 21, 1792, in which 0.34 km^3 of material sloughed off its flank without warning, generated a tsunami with run-ups 35 – 65 meter above sea level (m asl) in the Ariake Sea, and killed 14,524 people. ii) The landslide of Ili Werung Volcano in Lembata Island, Indonesia, on July 18, 1979, in which 0.05 km^3 of volcanic materials entered the sea, generated a tsunami with run-up 9 m asl, and killed 500 people (Gillespie and Clague, 2009).

c. Volcanic eruption-induced tsunami

Volcanic tsunami constitutes a high wave or surge of water produced by a variety of eruptive or non-eruptive processes at volcanoes during their activities (Begét, 2000). The volcanoes must lie in the ocean, sea, or near the lakes, so the energy released during eruptions can be transmitted and generated impulsive waves (Begét, 2000). This process is usually called *momentum transfer* (see Figure 1-3).

Latter (1981) defined ten processes at volcanoes which can generate tsunami wave, i.e. volcanic earthquakes, pyroclastic flows, submarine explosions, caldera formation, volcanic landslides, basal surges, avalanches of hot rock, lahars, atmospheric pressure wave, and lava flows (Figure 1-4). Volcanic earthquakes (22 %), pyroclastic flows (20 %), and submarine explosions (19 %) dominated the volcanic tsunami events since 3,500 years BP when the eruption of Santorini in Mediterranean Sea has been recorded as a major event of volcano-induced tsunami (Latter, 1981).

Santorini eruptions in Late Bronze Age and Krakatau eruptions in 1883 are two examples of the large explosive eruptions of volcanic islands which produced huge tsunami

waves in the ocean/sea. Karymsky Volcano eruptions in Kamchtka Peninsula is, since 1996, the best example of subaquatic volcanic explosions that generated giant tsunamis in a lake.

Santorini Volcanic Island, situated in the northeastern part of Mediterranean Sea between Greece and Turkey, erupted 3,500 BP and generated a giant tsunami which was probably the largest volcanic tsunami in the historical times, based upon the deposited seaborne pumice on the island of Anaphi, East of Santorini, at an altitude of 40 to 50 meters above present sea level (LaMoreaux, 1995; McCoy and Heiken, 2000; Pareschi et al., 2006; Goodman-Tchernov et al., 2009). The tsunami destroyed all the towns along the eastern Mediteranean coasts of and was likely responsible of the brutal extinction of the Minoean civilisation in the surrounding islands.

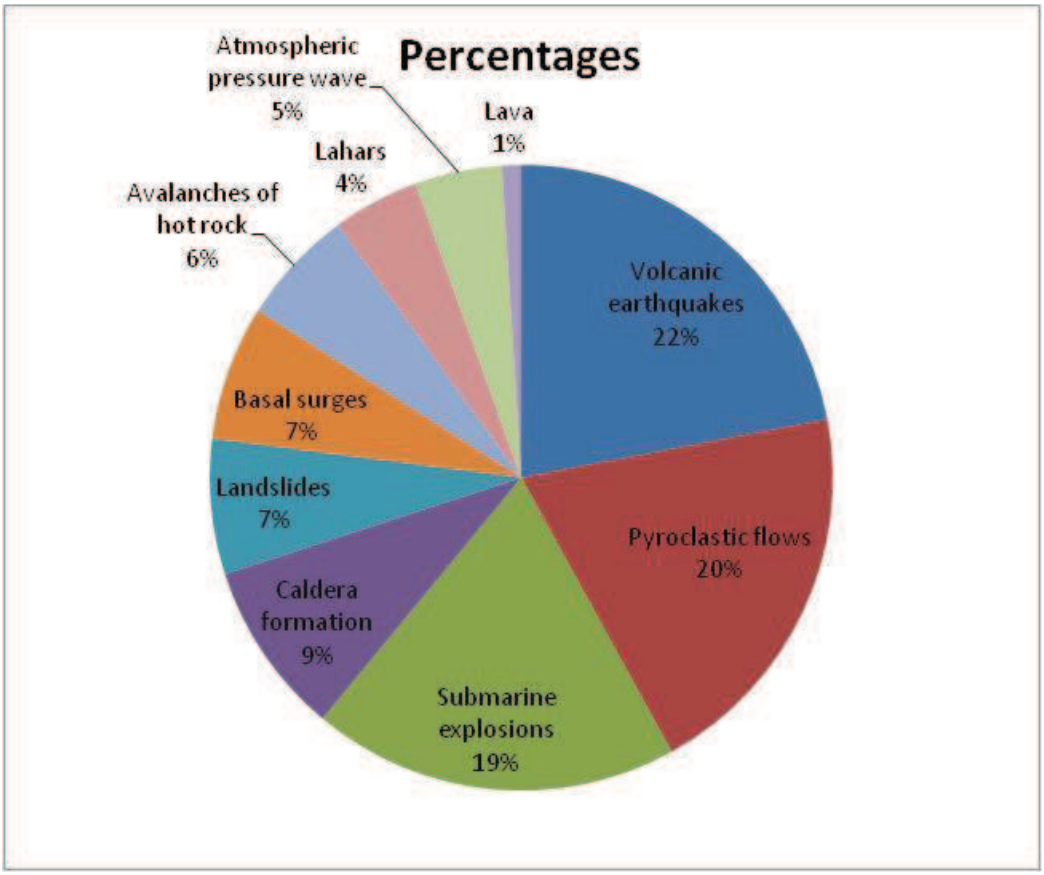

Figure 1-4. Generation mechanisms of vocanic tsunamis: a pie chart displays the frequences of volcanic events induced tsunami waves since the eruption of Santorini, Mediterranean, in Late Bronze Age or about 3,500 BP (based on Latter, 1981).

The gigantic eruptions of Krakatau Volcanic Island, located in the centre part of Sunda Strait, Indonesia, occurred on August 26 - 27, 1883 and generated giant tsunami waves which propagated almost all over the world. The waves swept all of the coastal areas around the

Sunda Strait reaching a maximum run-up height of 42 m asl in Merak, the northwestern tip of Java Island, and killed ± 36,000 people (Verbeek, 1884, 1885; Hurlbut and Verbeek, 1887; Symons et al., 1888; Simkin and Fiske, 1983). Some papers mentioned that the major tsunamis of Krakatau were allegedly generated by pyroclastic flow entering the sea (Verbeek, 1884, 1885; Latter, 1981; Self and Rampino, 1981; Francis, 1985; Sigurdsson et al., 1991; Nomanbhoy and Satake, 1995; Bryant, E., 2008; Maeno and Imamura, 2011), underwater phreatomagmatic explosion (Yokoyama, 1987; Nomanbhoy and Satake, 1995; Bryant, E., 2008), and caldera collapse (Verbeek, 1884, 1885; Self and Rampino, 1981; Francis, 1985; Sigurdsson et al., 1991). The world wide distribution of Krakatau tsunamis were most probably caused by atmospheric pressure wave (Verbeek, 1884, 1885; Symons et al., 1888; Bryant, E., 2008). Due to its distribution and fatalities, the 1883-Krakatau tsunami constitutes one of the largest volcanic-tsunamis ever recorded in historical times. Table 1-2 shows the impact of the 1883-Krakatau tsunami.

In contrast with the 2004-IOT, the maximum run-up of Krakatau tsunami recorded in Merak (Verbeek, 1885) was not related to a specific coastal morphology. However, the principal difference between volcanic tsunami and earthquake tsunami lies in the fact that the wavelength is shorter for the first case. Despite this shorter wavelength and a greater dispersion, the volcanic tsunami can potentially produce a larger damage area (Paris et al., 2014b).

Table 1-2. Distribution and fatalities of the 1883-Krakatau tsunami.

Parameter	*The 1883-Krakatau Tsunami Data*
Date	August 26-27, 1883
Cause	Volcanic eruption
Source	Krakatau, Sunda Strait
$H_{r\,max}$ (m asl)	42
Distant areas affected	Port Elizabeth-South Africa (Indian Ocean), West Coasts of America (Pacific Ocean), and Le Havre-France & Caribbean Sea (Atlantic Ocean)
Fatalities (people)	36,417

Source: based on Verbeek (1885); Choi et al. (2003).

Meanwhile, the 1996 subaquatic explosive eruption of Karymsky Volcano, near the northern shore of Karymskoye Lake in Kamchatka Peninsula, Rusia, is an example of volcanic eruption that generated multiple tsunamis around the 4 km diameter of Karymskoye Lake (Belousov et al., 2000). The most important of the processes during eruptions were the deposition of pyroclasts into the lake and the decrease of outflow from the lake as a result of the blokage of the Karymskaya River outlet by the pyroclastic dam. The level of the lake was then rising during eruptions and tsunamis run-up reached the maximum height at 30 m asl (Belousov et al., 2000).

d. Large asteroid impact-induced tsunami

One of the largest impact-induced tsunami is allegedly produced by a large asteroid impact on Chicxulub, Mexico, 65 million years ago at the Creatacious – Tertiary boundary (K/T boundary). This event is considered as the best candidate for the K/T mass extinction recorded in the geological archives and is probably responsible for the extinction of the last dinosaurs still present on Earth at this time. The resulting tsunami, more than 100 m in height, swept over 300 km inland around the shore of ancient Gulf of Mexico (Bourgeois et al., 1988; Smit et al., 1996; Matsui et al., 2002). The evidence of this event is attested by a geological record and was probably one of the largest threat to the life on Earth.

1.3. Tsunami signatures

On land, tsunamis leave several types of evidences (signatures/recordings) on their paths from which tsunamis characteristic and occurrence can be determined (Dawson and Shi, 2000; Dawson and Stewart, 2007; Bryant, E., 2008; Bourgeois, 2009; Chagué-Goff et al., 2011; Paris et al., 2010). The signatures of tsunami will be related to the coastal landscape (the source of sediments and geomorphic features) and behaviour of the flooding. Masselink et al. (2014) have classified the coastal landscape in following categories: coastal deltas, estuaries, littoral coasts (the shoreface, beaches, and barriers), coastal sand dunes, and rocky coasts, and described them such as follow (some part can be seen in Figure 1-5):

1. Coastal deltas are discrete accumulations of terrigenous sediment deposited where rivers enter into the sea, consist of fine to coarse-grained deltas.
2. Estuaries are the seaward portion of a drowned valley system which receives sediment from fluvial and marine sources where the central zone of estuaries can be dominated by

salt marshes or mangrove flats composed of predominantly muddy sediments (Dalrymple et al., 1992).

3. The shoreface-beaches-barriers environments are linked by sediment transport pathways caused mainly by wave processes where sands and gravels are found dominantly.
4. Coastal sand dunes are accumulations of wind-blown sand usually found in association with sandy beaches and estuaries.
5. Rocky coasts are strongly controlled by geologic processes and composed of fragments of rock and corals.

Wassmer et al. (2007) have studied the respective roles of the uprush and backwash on the sedimentary signatures of the 2004-IOT, as reflection of behaviour of the flooding. The study revealed a sharp facies differentiation of tsunami deposits from proximal to distal zones (see Figure 1-5 for the zonation). The deposits located near the shoreline (proximal zone) were found to be coarse and ungraded, whereas the frequency of stratified normally graded sequences, with a coarse base evolving gradually to a finer top, increases landward (Wassmer et al., 2007). They corresponded to the general decrease of wave energy from proximal to distal zones during the uprush phase and the energy increasing from distal to proximal during the backwash phase. The signatures were well preserved in the distal zone due to the very low wave energy during the slack phase, i.e. in the end of the uprush and beginning of the backwash (Wassmer et al., 2007, 2010).

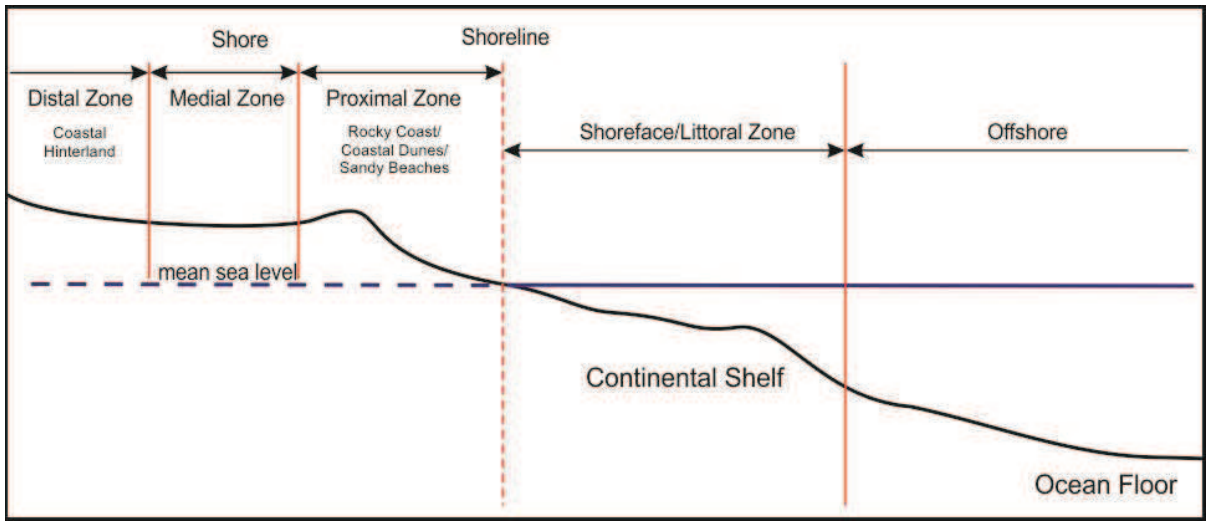

Figure 1-5. A coastal profile showing the zonation of coastal areas used in the text (modified after (Masselink et al., 2014): Based on the distance to the source of sediments, a depositional zone of tsunami deposits on land (*onshore*) can be divided into proximal, medial, and distal zones.

Many depositional and erosional signatures are produced by the tsunami waves when they begin to hit and penetrate inland. Buried sand, foraminifera, boulder floaters in sand, large coral boulders, dump deposits, dunes, and turbidites are some examples of depositional signatures of tsunami (Bryant, E., 2008). On the other hand, scoured depressions through beach ridges and vegetation-soil stripping are the examples of the tsunami erosional signatures (Bourgeois, 2009).

Buried sand, as the commonest signature of tsunami, is a layer of marine sand unit between finer material and peat on flat coastal plains (Atwater, 1987; Darienzo and Peterson, 1990; Dawson et al., 1991; Clague and Bobrowsky, 1994; Minoura et al., 1994; Paris et al., 2010). This sand unit is usually characterized by a series of fining upward sequences stack once upon each other. The mean grain-size of the deposited materials and the mean thickness of the layers decrease landward. The deposits often display an erosional basal contact and incorporate muddy rip-up clasts at the bottom part of tsunami deposit, as a product of erosional process of muddy estuarine, lagoonal, or marsh sediments in the zone of erosion near the beach (proximal zone) (Atwater, 1987; Morton et al., 2007). Shell, coral, and land-based plant materials are often found within the deposit (Bondevik et al., 1997; Goff et al., 2004; Hawkes et al., 2007; Kortekaas and Dawson, 2007).

Material emplaced by tsunami inland often contain abundance of foraminifera, which constitute a strong criterion to identify sedimentary signature (Dawson and Shi, 2000; Chagué-Goff et al., 2011). Their presence in the deposits, especially species with a narrow range of environmental conditions, are a precious indicator of the submarine origin of deposited sediments (Chagué-Goff et al., 2011). Loeblich and Tappan (1964) show that foraminifera, can live suspended either in water column (planktonic) or on the seafloor (benthonic/benthic). Because tsunami wave can move water from a number of distinctive habitats, thus foraminifera within the deposit can be provided by marine planktonic and benthic, intertidal, and terrestrial environments.

In some cases, for a tsunami deposit that lies far inland, boulders with a size less than 0.5 m can be found floating or embedded in sand (Bryant et al., 1992, 1996). The boulders often constitute less than 0.1 % of the deposits volume. Due to the position of boulders buried beneath the surface, they cannot be found unless a trenching or drilling investigation is applied. In contrast, the large coral boulders moved by tsunami waves lie on the surface (Scheffers and Kelletat, 2003; Paris et al., 2010). These coral boulders can have a size up to 750 m^3 or 1,500 tonnes as found on the reefs of Rangiroa, Tuamotu Archipelago, in the

southeastern part of Pacific Ocean (Bourrouilh-Le Jan and Talandier, 1985). The boulders can also be found in groups, e.g. scaterred boulders which were deposited across the reef on the eastern side of Miyako Island, south of Ryukyu Island, Japan (Kawana and Nakata, 1994; Goto et al., 2010), and deposited into imbricated piles, e.g. imbricated sandstone boulders along the cliffs (33 m asl) at Mermaids Inlet, Jervis Bay, Australia (Bryant et al., 1996, 1997).

Besides moving the boulders, tsunami waves can bring a variety of materials and sediment sizes from cliffs, coastal platforms, and coral reefs, when the waves overwashed rocky environments. This chaotic sediment mixture are deposited far inland as a dump deposit (Bryant et al., 1992, 1996; Nott and Bryant, 2003; Scheffers and Kelletat, 2004; Switzer et al., 2005). The broken fragile particles (e.g. foraminifera, shells) are often found within deposits.

The tsunami waves can also build sand dunes, in different forms and sizes. The beach-ridge dunes in the Northeast Japan (between Lake Jusan and Japan Sea) can reach 150 m in width and 1,200 m in length (Minoura and Nakaya, 1991). Large parabolic sand dunes in the south end of Jervis Bay form a V-shaped dunes called *chevrons*, that may be stacked relative to each other (Bryant et al., 1997; Kelletat and Scheffers, 2003). Another example is dune bedforms in the north of the entrance of Jervis Bay, Australia, i.e. a series of undulatory to linguoidal giant ripples with a relief of 6.0 – 7.5 meters and spaced 160 m apart as a product of large asteroid impact-induced tsunami (Bryant et al., 1997; Kelletat and Scheffers, 2003). In the southern Madagascar, a similar chevron bedforms was described as a tsunami deposit related probably to the Burckle meteorite impact about 5,000 years ago (Abbott et al., 2006; Gusiakov et al., 2010). Yet, this interpretation has been disputed by Bourgeois (2009) which clarified that the chevron bedforms explained by tsunami waves were unfounded speculation. Bourgeois and Weiss (2009) have also examined that the tsunami wave modeled in the South of Madagascar is inconsistent with the chevron orientation. They agree with other Earth scientists who have interpreted this chevron bedforms as aeolian or storm waves products. In contrast, the orientation of chevrons in Australia do not match with the wind-blown dunes (Kelletat and Scheffers, 2003). Due to the debatable signature, therefore, the chevrons bedforms are still unable to represent the signature of mega-tsunami worldwide.

One important tsunami signature that is not linked with the landward tsunami deposit is *turbidites*. This signature is most related to the submarine landslides in a deep sea, either close to or far from the source of tsunami, e.g. volcaniclastic turbidites correlated with the Canary Islands landslides in Agadir Basin and Madeira Abyssal Plain (Wynn and Masson, 2003) and the large volume mega-turbidites produced by Santorini tsunami in the abyssal plains as well

as on the floors of small basins of the Mediterranean and Calabrian Ridges (Cita et al., 1996; Cita and Aloisi, 2000). Another possibility is a backwash flow in submarine environments (Dawson and Stewart, 2007; Shanmugam, 2012), such as turbidites on the floor of Okushiri Basin, Taisei, Japan, deposited by 1993 Hokkaido-Nansei-oki tsunami (Nanayama and Shigeno, 2006). Turbidites are deepwater sediments produced by turbidity current as a type of gravity flow and characterized by fining-up intervals from pebble conglomerates at the bottom part to the fine grained shales at the top (Bouma, 1964). Their evidences must be traced using a submarine investigation, such as a scuba diving and a deep sea core sampling, except if they are exposed as geological imprints at the surface. In the case of geological imprints, they can be used as a proxy to study paleotsunamis occurred in the pre-Quaternary record (Dawson and Stewart, 2007; Bourgeois, 2009). Notwithstanding, it is difficult to distinguish catastrophic-tsunami events with other depositional processes based on the sedimentological features alone without historical informations (Shanmugam, 2012).

Like turbidites, some erosional signatures (scoured depressions and vegetation-soil stripping) cannot be used alone to evidence the tsunami events if they are not supported by other tsunami informations. An appropriate example is a report from Richmond et al. (2012) explaining the 2011-Tohoku tsunami involvement on erosion, deposition, and associated landscape change along the coastal plains near Sendai, Japan. There are few tsunami studies linked to the erosional features due to the geomorphic aspects of tsunami which are considered in less than 5 % of pre-historic cases (Bourgeois, 2009). However, they have received considerable attention in the literature. Cavitation features, V-shaped grooves, flutes, humocky topography, sculpture headland features, truncated cliffs, raised platforms, and eroded barier remnants are also erosional features due to the involvement of water (Young and Bryant, 1992; Aalto et al., 1999). Yet, it is still debatable whether they were formed by tsunami or storm waves, even other processes (Bourgeois, 2009).

1.4. Tsunami deposits for identifying past events

Currently, tsunami events can be well recorded and documented visually through sophisticated devices, e.g. at the light of the numerous video footages of the 2004-IOT and the 2011-Tohoku tsunami. Moreover, the oral testimonies of the survivors shortly after the events render the recordings of present tsunamis more reliable. While for the study of past tsunami events, we will rely heavily on the tsunami signatures and only base our interpretation on the

rare recordings. Even for the very old tsunami events, before the historical times, the study can only be based on proxies established on the basis of present tsunamis.

The detail informations of tsunami signatures, especially tsunami deposits, can give a reliable and accepted set of diagnostic criteria (proxies) for identifying past events (Atwater, 1987; Bourgeois et al., 1988; Cita et al., 1996; Smit et al., 1996; Dawson and Shi, 2000; Scheffers and Kelletat, 2004; Dawson and Stewart, 2007; Bryant, E., 2008; Bourgeois, 2009; Lavigne et al., 2009; Goto et al., 2010; Paris et al., 2010; Chagué-Goff et al., 2011; Shiki et al., 2011; Goff et al., 2012; Shanmugam, 2012; Paris et al., 2014b). Tsunami deposits (the term *tsunamiite* is also sometimes used (Shiki et al., 2011)), as explained before, are all of the sedimentary unit deposited by tsunami waves, either left onshore during the uprush-slack-backwash phases or offshore during the backwash phase only. Some papers have listed and explained the proxies that can be used to study tsunami deposits, although the so-called "toolbox" proposed by Chagué-Goff (2011) is still under development and many questions are still unanswered (Morton et al., 2007; Goff et al., 2010; Peters and Jaffe, 2010; Chagué-Goff et al., 2011; Goff et al., 2012).

A summary of most the commonly used proxies of tsunami deposits were described and modified by Chagué-Goff et al. (2011) in a "*toolbox for tsunami studies*", such as follows:

1. Grain-size of the deposits range from boulders to fine mud.
2. Sediments generally fining inland and upwards within the deposits, although coarsening upwards can be present.
3. A distinct sedimentary unit or laminated sub-units can be formed by each wave.
4. Sometimes a distinct upper and lower sub-units, representing uprush and backwash, can be identified.
5. Lower contact is unconformable or erosional.
6. Rip-up clasts of reworked material (natural and anthropogenic) can be present.
7. Loading structures can be associated at the base of deposits.
8. AMS combined with grain-size analysis provides informations on hydrodynamic conditions during sediments emplacement.
9. Heavy mineral laminations often present near base of unit/sub-unit, but source dependent.
10. The deposits can be associated with abundance of marine to brackish diatoms, in which a greater percentage of reworked terrestrial diatoms presences at the upper part. Large number of broken valves reflects a turbulent flow. Variation in diatom affinities indicate a source area and magnitude event.

11. The deposits are marked with the changes in foraminiferal assemblages. Deeper water species may be introduced and/or increase in foraminiferal abundance and breakage of tests. Composition relates to shore (near shore vs offshore).
12. In the deposits, pollen concentrations are often lower due to the marine origin and high percentage of coastal pollen (e.g. mangroves). Changes of pollen above deposit caused by vegetation changes are associated with saltwater flooding.
13. Increases in elemental concentrations of sodium, sulphur, chlorine (paleosalinity indicator), calcium, strontium, magnesium (from shell and coral), titanium, zirconium (associated with heavy minerals) occur within tsunami deposits relative to under and overlying sediments. Indicates saltwater inundation, and/or high marine shell/coral content, and/or high energy environment (heavy minerals, source dependent). Preservation issues to be considered in particular for salt (downward leaching), but uptake and preservation in wetlands/soil.
14. The deposits are possible contaminated by heavy metals and metalloids.
15. Geochemical and microfossil evidences often extend further inland than landward maximum extent of sedimentary deposit.
16. Individual shells and/or shell-rich units are often present in the tsunami deposits. Often more intact shells as opposed to shell hash. Small, fragile shells, and shellfish can be found near the upper surface of the deposits.
17. The deposits are often associated with buried vascular plant material, buried soil, and/or skeletal remains.
18. Shell,woods, and less dense debris are often found rafted near the top of sequences.
19. The tsunami deposits are often associated with archaeological remains and/or oral record.
20. Based on all the characteristics above, the tsunami deposits can postulate and identify the known local or distant tsunamigenic sources.

As complementary, Chagué-Goff et al. (2011) have added geomorphological aspect as supporting tool for the identification of tsunami inundation in the past.

The study of paleotsunami must be a multidisciplinary endeavour beyond the sedimentology and stratigraphy approaches (Goff et al., 2010, 2012). The application of anisotropy of magnetic susceptibility (AMS) in the study of tsunami deposits developped by Wassmer et al. (2010) has been well tested and accepted as an appropriate method to determine the hydrodynamic conditions and paleocurrents of sediment emplacement (Chagué-Goff et al., 2011). Another study from Chagué-Goff et al. (2012) shows that geochemical

indicators within tsunami deposits are very useful for identifying the extent of historical paleotsunami events. Both AMS and geochemical methods are carried out together with grain-size analysis. Occasionally, the identification of diatom and foraminifera assemblages is performed together with the grain-size, AMS, and geochemical analyses.

For the volcanogenic tsunamis, the presence of pyroclastic materials become an important additional diagnostic criterion (Waythomas and Neal, 1998; Carey et al., 2001; Nishimura et al., 2005; Bruins et al., 2008; Paris et al., 2014a, 2014b). The pyroclastic materials may present as intercalated layers with tsunami sand units and/or mixed with sand as pumiceous sand units, such as well described in the 1883-Krakatau tsunami deposits around the Sunda Strait (Paris et al., 2014b). Unconsolidated tephra, such as fine ash, coarse ash, and lapilli with pumice, scoria, and other juvenile clasts content, produced by pyroclastic flow, pyroclastic surge, or pyroclastic fall (McPhie et al., 1993) are often found within volcanic tsunami deposits.

Coupling the proxy toolkit of tsunami records with the volcanic eruption processes can be a remarkable endeavour for identifying past volcanogenic tsunami events. Paris et al. (2014b) have well coupled the eruption's history and tsunami records with a case study from the 1883-Krakatau eruptions, in which a part of the thesis has been involved. The Krakatau tsunami deposits collected from field investigations were characterized using a combination approach, including sedimentological (grain-size distributions and AMS analysis), geochemical (ICP-AES and loss on ignition analyses), and georeferenced database from previous observations (GIS database). Paris et al. (2014b) demonstrated quite well that the study of Krakatau tsunami provides information for reconstructing the past eruption in 1883. It paved the way for developing the research of the 1883-Krakatau past events based on some exceptional tsunami deposits along the coastal plains of Sunda Strait.

Chapter 2
The 1883-Krakatau tsunamis

Before the 1883-eruptions, Krakatau Volcanic Complex was the main island of the small archipelago situated in the center of Sunda Strait, Indonesia, between Java and Sumatra. This archipelago was composed of Verlaten (Sertung) Island at the northwest, Long (Panjang) Island at the northeast, De Poolsche Hoed (Polish Hat) Islet at the north, and the Krakatau Volcanic Complex (Rakata) at the south (Verbeek, 1885; Hurlbut and Verbeek, 1887; Symons et al., 1888; Simkin and Fiske, 1983). This later was composed of three active volcanoes: Mount Perbuwatan at the north, Mount Danan at the center, and Mount Rakata at the south (Verbeek, 1884, 1885; Hurlbut and Verbeek, 1887; Symons et al., 1888; Simkin and Fiske, 1983), see Figure 2-1.

Figure 2-1. Krakatau Archipelago after the 1883-eruptions with Sertung, Panjang, Polish Hat, and Krakatau Volcanic Complex (dashed line indicates the island before August 26, 1883) underlying the location of an old previous caldera rim (Verbeek, 1885; Symons et al., 1888; Simkin and Fiske, 1983). At the center, Anak Krakatau developed from a remained rock since 1927 (Stehn et al., 1929).

The base of ancient Krakatau was composed of basaltic andesite to andesite (augite-enstatite andesite) which had ever been erupted in 1680, producing an andesitic-lava. However, it was still a slight convulsion (Renard, A., 1883; Verbeek, 1885; Hurlbut and Verbeek, 1887; Symons et al., 1888; Self and Rampino, 1981). After 200 years of quietude, the Krakatau Volcano erupted in 1883, with the largest explosions recorded in historical times after the explotions of Tambora Volcano in Sumbawa Island, Indonesia, in 1815 (Rampino and Self, 1982; Stothers, 1984; Oppenheimer, 2003) and Samalas Volcano on Lombok Island, Indonesia, in 1257 (Lavigne et al., 2013). The radius of the circle, within which the sound of the explosion was heard, was twice the size of the 1815-Tambora explosion (Verbeek, 1884, 1885). For a better understanding of the tsunamis generation related to the different eruption phases, we described briefly the remarkable events of the 1883-Krakatau eruptive and tsunami sequences in Section 2.1 and Section 2.2.

2.1. The 1883-Krakatau eruptive sequence

Mount Krakatau had shown a sign for subsequently enormous phenomena since May 1883. The volcano began to erupt on Sunday 20th of May, between 10.00 am and 11.00 am (Verbeek, 1884, 1885; Hurlbut and Verbeek, 1887). Many eyewitnesses from the vessels, which had passed through the Sunda Strait, reported that the eruptions of Krakatau occurred during May 20 – 23, 1883. Even on May 27, when J. A. Schuurman (a mining engineer from Batavia/Jakarta) visited the Krakatau Island, some explosions with interval between 5 and 10 minutes still occurred (Hurlbut and Verbeek, 1887). According to the report of Schuurman, three craters were formed on the island of Krakatau during May and August 1883.

On August 26, 1883, large explosions of Krakatau occurred within 10 minutes of interval (Verbeek, 1885; Hurlbut and Verbeek, 1887; Symons et al., 1888). Volcanic ash was ejected up to 34 km heigth above the islands. The loud and violent explosions could be heard throughout the islands of Java and Sumatra. During the night of August 26 – 27, the sounds became formidable and reached the maximum in the morning of August 27.

On Monday morning, August 27, 1883, larger paroxysmal explosions occurred. Started by an explosion of Mount Perbuwatan at 5.30 am, then Mount Danan at 6.44 am, and eventually the tremendous explosions of Mount Rakata at 10.02 am and 10.52 am (local time) destroyed the most part of Krakatau Island (Verbeek, 1884, 1885; Hurlbut and Verbeek, 1887; Symons et al., 1888; Simkin and Fiske, 1983), see Figure 2-1. These last horrific explosions

produced the largest sound of volcanic explosion ever heard by humanity with a total energy released equivalent to 200 megatons of TNT (Bryant, 2008). The radius of the circle within which the sound heard was estimated about 30° (Verbeek, 1884). The sound reached the islands of Rodriguez in the Indian Ocean, Ceylon, and Elsey Creek, Northern Territory, Australia (Verbeek, 1884, 1885; Symons et al., 1888; Blong, 1984). Air vibration that accompanied the eruptions was felt in Pasuruan, 830 km away from Krakatau.

The Krakatau explosions ejected 18 - 21 km^3 volume of dacitic juvenile (pumices and volcanic ash) that spread more than 50 km from the source (Verbeek, 1884, 1885; Symons et al., 1888; Self and Rampino, 1981; Simkin and Fiske, 1983). These pyroclastic deposits became a very valuable evidence for reconstructing the Krakatau eruptions. Verbeek (1884) displayed the result of microscopic examination of the volcanic ash collected from Buitenzorg (Bogor), located in West Java at 330 m asl, as follows:

1. *Glass*; microscopic pieces of pumice which were always present in large abundance with in innumerable irregular fractured particles. In some particles the glass threads were bent.
2. *Feldspar*; generaly in single crystals, all seems to be plagioclase and no potash. Glass, apatite, augite, and magnetite were present as inclusions.
3. *Pyroxene*; monoclinic augite, partly green and brown, oblique, sometimes transitions from brown to green tints occurred. Glass, apatite and magnetite were present as inclusions.
4. *Magnetite*; as the oldest component part, present in grain and octahedra.Their quantity in the ashes decreased as they fell further from Krakatau.

Moreover, J. W. Retgers in Verbeek (1885) provided a detail description by separating the particles of glass from the crystalline minerals, such as given in the following table.

Table 2-1. Chemical composition of the 1883 Krakatau ash collected in Buitenzorg (Bogor).

(wt) %	**Glass** (with specific gravity < 2.6)	**Feldspar** (average of all kinds present)	**Enstatite** (ferriferous)	**Augite**	**Magnetite** (with Ilmenite)
Silica	68.12	58.29	52.30	48.60	-
Titanic Acid	0.18	-	-	-	6.70
Alumina	15.81	27.19	6.10	8.20	-
Ferric Oxide	-	-	-	-	56.00
Ferrous Oxide	5.01	-	27.70	14.00	37.30
Manganous Oxide	-	-	trace	-	-
Lime	2.78	8.27	2.20	18.90	-
Magnesia	1.18	-	13.60	11.60	-
Potash	1.06	1.22	-	-	-
Soda	5.09	5.82	-	-	-
Total	99.23	100.79	101.90	101.30	100.00

Modified from Verbeek (1885); Symons et al. (1888).

The last tremendous explosion created a large basin or new caldera with 7 km wide and more than 100 meter deep (Verbeek, 1885; Hurlbut and Verbeek, 1887; Symons et al., 1888; Simkin and Fiske, 1983). The Polish Hat Islet in the north disappeared, while Sertung Island in the northwest and Panjang Island in the northeast became larger than before. To the northern part of Krakatau Island, Mount Perbuwatan and Mount Danan, have sunk in the depths and remained only the southern flank of Rakata Volcano with a magnificent precipitous cliff more than 800 m high and a 10 m^2 rock almost in the middle of the new caldera (Verbeek, 1884, 1885). This rock, then, developed since 1927 became a new islet that is well known as Anak Krakatau (Krakatau's Child in Indonesian language) at present (Stehn et al., 1929). The enormous changes that affected Krakatau Volcanic Complex during this eruptive sequence were responsible for succesive disruptions of the sea water leading to the formation of tsunami waves.

2.2. The 1883-Krakatau tsunami sequence

A remarkable phenomenon during the Krakatau eruption in 1883 was the formation of powerful tsunami waves, which were more deadly than the eruption itself. As it has been explained in Chapter 1, the volcanic tsunamis produce the worst volcanic disasters (Latter, 1981; Begét, 2000). Krakatau tsunamis with run-up heigth between 1 - 2 meter has swept adjacent coastal areas in Sunda Strait since August 26, 1883 (Verbeek, 1885; Hurlbut and Verbeek, 1887; Symons et al., 1888). These tsunamis were recorded during the evening of August 26 in Vlakke Hoek and Beneawang, Southwest Sumatra (Latter, 1981).

The giant waves of tsunami were generated on August 27. These phenomena destroyed many villages in the coastal areas around the Sunda Strait, killing 36,417 peoples at the western coasts of Java (Merak, Anyer, and Caringin) and the southern coasts of Sumatra (Verbeek, 1885; Hurlbut and Verbeek, 1887; Symons et al., 1888; Simkin and Fiske, 1983). To the south of the strait, tsunamis inundated the coasts of Ujung Kulon Peninsula. The water rushed over the narrow strip of land of Laban Isthmus, shaving to the ground the trees of the rainforest, and poured into Indian Ocean (Figure 2-2). The maximum run-up of tsunami (about 42 m asl) was recorded at Merak. At Anyer the run-up ranged between 11 – 36 m asl, at Caringin 23 m asl, at Teluk Betung 22 m asl, at Ketimbang (around Rajabasa) 24 m asl, at Sebuku Island 30 m asl, and 15 m asl at the northern part of Panaitan Island (Verbeek, 1885; Hurlbut and Verbeek, 1887; Symons et al., 1888; Simkin and Fiske, 1983), see Figure

2-2. Moreover, the Krakatau eruptions caused series of waves that were recorded along the coasts of Africa, Australia, New Zealand, Alaska, West Coast of America, Chili, West Coast of France, and South Georgia (near the East Coast of Argentina) 10,000 km away (Verbeek, 1885; Hurlbut and Verbeek, 1887; Symons et al., 1888).

Figure 2-2. Map of tsunami inundation in the Sunda Strait and its vicinity: The Krakatau Volcanic Complex, marked by a red circle, is situated in the center part of the strait. The coastal areas inundated by the 1883 Krakatau tsunamis are indicated by black colour, while height of run-up indicated in meter (based on Verbeek, 1885; Hurlbut and Verbeek, 1887; Symons et al., 1888; Simkin and Fiske, 1983).

The mechanisms of giant tsunamis generation during the gigantic eruptions of Krakatau in 1883 have been widely explored by researchers. They could be related to:

- pyroclastic flow entering the sea (Verbeek, 1884, 1885; Latter, 1981; Self and Rampino, 1981; Francis, 1985; Sigurdsson et al., 1991; Nomanbhoy and Satake, 1995; Bryant, E., 2008; Maeno and Imamura, 2011)

- underwater phreatomagmatic explosion (Yokoyama, 1987; Nomanbhoy and Satake, 1995; Bryant, E., 2008)
- caldera collapse (Verbeek, 1884, 1885; Self and Rampino, 1981; Francis, 1985; Sigurdsson et al., 1991).

These possibilities corresponds to three reasonable trigerring mechanisms of the 1883-Krakatau tsunamis. Lateral blast may have occurred to a small degree on Krakatau eruptions (Camus and Vincent, 1983). Yet, its effect on tsunami generation is not known, even it has been discounted due to the invalid evidences for supporting the model of a northward-directed lateral blast and debris flow (Francis, 1985; Sigurdsson et al., 1991).

The generation mechanisms of Krakatau tsunamis, however, are still debated in which speculations and controversies abound. Caldera collapse hypothesis, which is assumed as a sudden subsidence of Krakatau edificie (Verbeek, 1884, 1885; Francis, 1985; Sigurdsson et al., 1991), is difficult to accept because the duration of actual caldera collapse is about hours until days, e.g. the 1991-Pinatubo eruption (Wolfe and Hoblitt, 1996). Moreover, some modelling have demonstrated that this mechanism underestimates tsunami wave heights and did not match with the tide-gauge records at Batavia (Nomanbhoy and Satake, 1995; Maeno and Imamura, 2011).

Underwater phreatomagmatic explosion, which is modeled as an incorporation of the series of surge-producing explosions occurring over 30 minutes period, could have generated an initial large wave (Yokoyama, 1987). Le Méhauté and Wang (1996) showed that a water dome or a water crater produced by phreatomagmatic explosion, with a high energy explosion, should occur very rapidly in a shallow marine environment. Van Guest, a Dutch volcanologist, described this feature as a bolt of yellow suddenly opened in the ocean running across the strait and flooded by all of the seawater, when he was observing the remaining Krakatau Island at 10.00 am, August 27 (Bryant, E., 2008). Nomanbhoy and Satake (1995) then numerically simulated this hypothesis by assuming an initial upward displacement of immense volume of water over a period of 1 to 5 minutes as if it was pushed up by a piston. Yet, there is no detailed explanation about this initial condition and neither does the condition for a longer explosion period.

Pyroclastic flow entering the sea is considered by many authors as the most logical hypothesis in triggering the large tsunami waves. Maeno and Imamura (2011) has compared the three tsunami generation mechanisms using numerical simulations and validated them

with the observation and other trustworthy tsunami data. They then concluded that a pyroclastic flow entering the sea was the most plausible mechanism in triggering the 1883-Krakatau tsunami. Previously, Nomanbhoy and Satake (1995) has also compared the tsunami generation mechanisms numerically, but have not considered the detailed physical processes as used by Maeno and Imamura (2011) in examining the hypothesis of pyroclastic flow entering the sea. Maeno and Imamura (2011) used two types of two layer shallow water models, dense and light types of pyroclastic flow, to evaluate the effect of flow density. The result displayed that pyroclastic flow entering the sea could generate a tsunami height as well as the historical records from Verbeek (1884, 1885), which were measured immediately after the eruptions at some coastal areas around the Sunda Strait, including the tidal gauge records at Batavia. The model of pyroclastic flow entering the sea from Maeno and Imamura (2011) gave an appropriate explanation about the generation of the 1883-Krakatau tsunamis that is much better than other hypotheses. Although it can still be debated, this model at least is in line with many investigations on submarine and inland tsunami deposits around the Sunda Strait. Even the submarine deposits around the ancient Krakatau are mainly composed of pumice and ash produced by pyroclastic flow entering the sea rather than material from submarine phreatomagmatic explosion (Self and Rampino, 1981; Sigurdsson et al., 1991; Carey et al., 1996; Mandeville et al., 1996). Notwithstanding, it is not clear whether the pyroclastic flow entering the sea is the only mechanism of Krakatau tsunamis generation or if it only triggered the last largest tsunami waves.

Nomanbhoy and Satake (1995), in a different conclusion, proposed that the largest tsunami was generated by a submarine explosion while the smaller tsunamis might have been produced by the entry of pyroclastic flows into the sea. If we agree with Maeno and Imamura (2011) and the fact that the largest tsunami wave was associated with the climactic Krakatau eruption at 10.00 am, August 27, thus, the conclusion should be changed to be: “The largest tsunami wave was generated by a pyroclastic flow entering the sea and the smaller tsunami waves might have been produced by submarine phreatomagmatic explosion or by the other pyroclastic flow entering the sea”. Caldera collapse, that probably came late in the eruptions (Self and Rampino, 1981), may also have caused a tsunami after the largest one due to an evidence found by Deplus et al. (1995) which explained that a depressed area on the seafloor of ancient Krakatau was produced by a sudden collapse of volcanic edifices.

Considering the location of the source and the location of the tidal gauge at Batavia, the movements of tsunami waves recorded probably include refracted waves. There were

eighteen such waves observed at Batavia tidal gauge on August 27 (Verbeek, 1885; Hurlbut and Verbeek, 1887). Some eyewitnesses also observed that a great wave inundated the fish market at Batavia after mid-day and the second wave arrived less than 20 minutes later (Hurlbut and Verbeek, 1887). Symons et al. (1888) concluded that one event of the 1883 Krakatau tsunami consists of two or more waves following one another at rapid intervals about 5 to 15 minutes. Therefore, on the basis of Krakatau case study, Paris et al. (2014b) proposed the volcanic tsunamis as a series of waves with a shorter period than earthquake tsunamis.

Besides the tidal gauge, a pressure gauge at the gasworks in Batavia can be used to identify the 1883 Krakatau tsunamis (Symons et al., 1888). The air wave registered at the Batavia pressure gauge giving the nearest record of Krakatau eruptions which might have related to the great tsunami waves. Five observed tsunami waves, during August 26 – 27, can be well connected with some of the air waves registered at the pressure gauge (Symons et al., 1888), see Table 2-2. Although only certain air waves were plausibly connected, these records are very valuable for supporting the interpretation of events after the climactic eruption of Krakatau.

Table 2-2. Estimated tsunami waves based on air wave recorded at Batavia pressure gauge.

Air wave in Batavia				Time estimated if seawaves left Krakatau	Observed tsunamis (location & time)
Time		Excess of indicator reading above estimated normal (mm)	Barometric equivalent (inches)		
26th	17.20	13	0.08	17.07	Teluk Betung, Merak, Caringin at 18.00 – 19.00
27th	01.55	20	0.12	01.42	Sirik after 01.00
	02.38	21	0.12	02.25	-
	04.56	22	0.13	04.43	-
	05.43	41	0.24	05.30	Anyer at 06.30 Teluk Betung at 06.00 – 07.00
	06.57	41	0.24	06.44	Anyer at 07.30
	09.42	29	0.17	09.29	-
	10.15	63	0.37	10.02	Merak, Anyer, Caringin, Teluk Betung after 10.00
	11.05	40	0.23	10.52	-

Modified from Symons et al. (1888).

The well historical records and geological evidences of Krakatau past events in 1883 offer an opportunity to develop the study of volcanic tsunami, avoiding an excessive speculation or an endless controversy. Many observations from eyewitnesses and from the field recorded immediately after the 1883-Krakatau eruptions, including tide and pressure gauge records (Verbeek, 1884, 1885; Hurlbut and Verbeek, 1887; Symons et al., 1888), have been remarkably connected with the present analysis of near-field pyroclastic deposits (around the ancient Krakatau Island), geological features, and numerical simulations (Self and Rampino, 1981; Francis, 1985; Yokoyama, 1987; Sigurdsson et al., 1991; Camus et al., 1992; Deplus et al., 1995; Nomanbhoy and Satake, 1995; Carey et al., 1996; Mandeville et al., 1996; Carey et al., 2000; Legros and Druitt, 2000; Maeno and Imamura, 2011).

Chapter 3

The 1883-Krakatau tsunami sedimentary recordings

Tsunami deposits have been identified in some coastal plains around the Sunda Strait (Ongkosongo, 1985; Carey et al., 2001; Paris et al., 2014b), as well as in a shallow marine of Teluk Banten (van den Bergh et al., 2002, 2003; van der Kaars and van den Bergh, 2004; Boer et al., 2006). These deposits were then well connected to the Krakatau eruptions in 1883. This chapter will present some new insight based on recent investigations of sites displaying high potential for the 1883-Krakatau tsunami sedimentary recordings.

3.1. Previous studies

Pyroclastic deposits found on the islands of Lagoendi, Sebesi, Sebuku, and the coasts of Sumatra, in the north of Krakatau Volcanic Complex (Carey et al., 1996, see Figure 3-1) contained rounded pumice-lapilli that were recognized, based on fractal analysis, as a product of Krakatau tsunamis run-up (Carey et al., 2001). These deposits were associated with the poorly sorted coral-bearing silty to sandy layers found on Sebesi and the coasts of Sumatra, which have similar characteristics with the common tsunami deposits.

The 1883-Krakatau tsunami deposits have been described by Ongkosongo (1985) and Bronto (1990), as unsorted and structureless gravel overlying pyroclastic deposits on the coasts of Java and Sumatra. Ongkosongo (1985) and Atmadja (2007) have also interpreted some large coral boulders on the coastal plains of Anyer (Java) and Gubug Garam (Sumatra) as a result of tsunami waves. At the South of Anyer, these coral boulders were deposited on *the wave cut platform* (intertidal zone), even some boulders were found on the sea floor near a reef front (Ongkosongo, 1985), see Figure 3-2. The largest 300 m^3 coral boulder found at Anyer (Verbeek, 1885; Ongkosongo, 1985; Atmadja, 2007), evidences that a giant tsunami wave was a plausible mechanism to move it far inland. To the South of the strait, such coral boulders were found on the coastal plains of Ujung Kulon Peninsula (Umbgrove, 1947; Verstappen, H. Th., 1956).

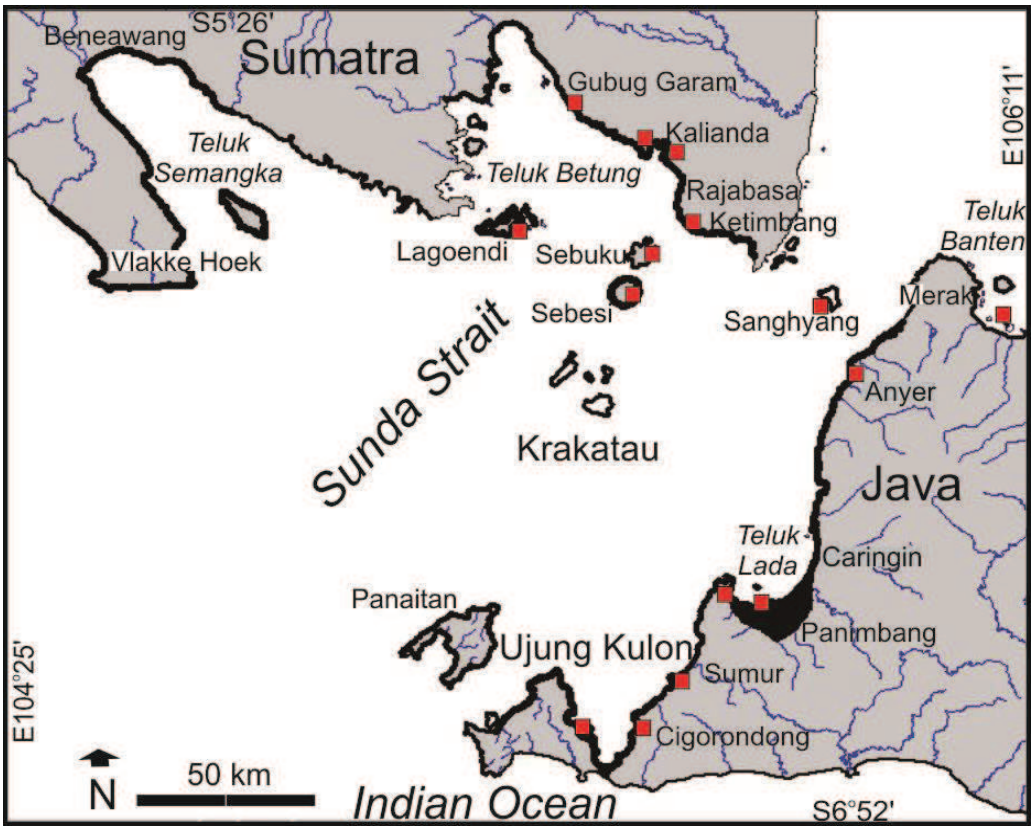

Figure 3-1. Map of distribution sites of the previous studies on the 1883-Krakatau tsunamis in Sunda Strait and its vicinity: The study sites symbolized by quadrangle shapes spread on the inundated coastal areas which are indicated by black shades (Verbeek, 1885; Umbgrove, 1947; Verstappen, H. Th., 1956; Ongkosongo, 1985; Bronto, 1990; Carey et al., 2001; van den Bergh et al., 2002, 2003; van der Kaars and van den Bergh, 2004; Boer et al., 2006; Atmadja, 2007; Paris et al., 2014b)

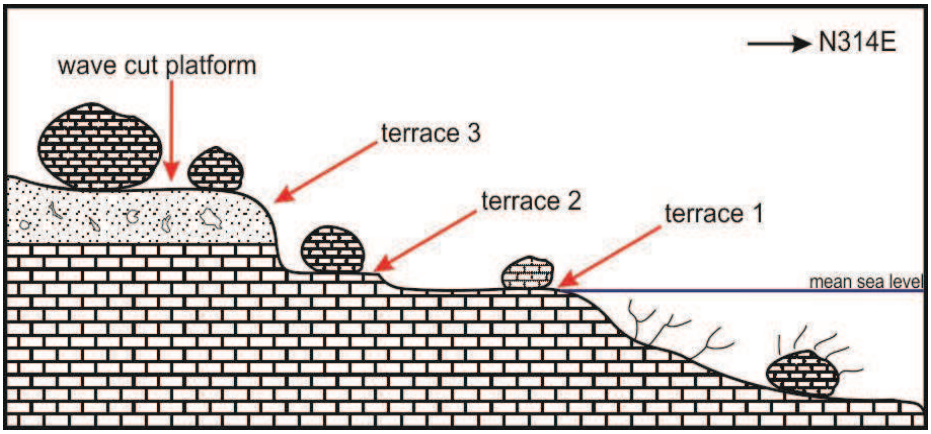

Figure 3-2. Cross section of large coral boulders emplaced by tsunami waves on the coastal plain of Anyer Kidul (modified from Ongkosongo, 1985): Some coral boulders were deposited on *the wave cut platform*. Such coral boulders were distributed on different terraces and also on the seafloor.

The 1883-Krakatau tsunami deposit was also found in a shallow marine of Teluk Banten (*Banten Bay*). The deposit was recorded in the submarine cores collected from the seafloor of Teluk Banten (van den Bergh et al., 2002, 2003; van der Kaars and van den Bergh, 2004; Boer et al., 2006). Van den Bergh et al. (2002, 2003) identified this tsunami deposit as a poorly sorted sandy layer with abundant bioclasts, pumices, and the typical crystal assemblages related to the 1883-Krakatau eruptions. Land-derived components were incorporated within the tsunami deposit emplaced in the shallow bay when the tsunami backwash occurred.

In a recent study, Paris et al. (2014b) have well coupled the eruptions and tsunami records for the case of Krakatau eruptions in 1883. Five sedimentary facies related to the 1883-Krakatau events were identified at some coasts around the Sunda Strait, i.e. *bioclastic tsunami sand unit*, *pumiceous tsunami sand unit*, *rounded pumice lapilli reworked by tsunami*, *pumiceous ash fall deposit*, and *pyroclastic surge deposit*. Bioclastic tsunami sand unit found at the bottom part of stratigraphic sections on the coasts of Java and Sumatra (see Table 3-1) were deposited before plinian phase of the eruption, on August 26. Pumiceous tsunami sand unit overlaid the bioclastic sand indicating the onset of plinian phase, on August 27. Rounded pumice lapilli associated with the pyroclastic falls were reworked by tsunami and most probably deposited by the backwash. Pumiceous ash deposits were identified at the middle part in almost all of the sections corresponding to the eruptions during the afternoon of 26th and the early morning of 27th. Finally, pyroclastic surge deposits overlying the uppermost tsunami deposits, but only found on the coasts of Sumatra due to the northward direction of pyroclastic surges on climactic eruption of August 27 (Table 3-1). This latter study gave a great contribution for the study of tsunami deposit and particularly for the reconstruction of past Krakatau events. It can be used as a main reference for the study of Krakatau tsunami deposits.

Many other places around the Sunda Strait have a potential for preserving tsunami deposits related to the 1883-Krakatau eruptions, accordingly with the tsunami inundation zone delineated by R. D. M. Verbeek (Verbeek, 1885; Hurlbut and Verbeek, 1887; Symons et al., 1888). Amongst these locations, Ujung Kulon Peninsula, the peneplain of Panimbang, and the southwestern coasts of Sumatra (Vlakke Hoek and Beneawang in Semangka Bay, South of Sumatra), have not been subject for more detailed investigations. It was probably caused by the fact that the pyroclastic surges as well as pyroclastic flow that induced Krakatau tsunamis occurred in northward direction. However, study of tsunami deposits in the southern places

will undoubtedly give a significant contribution for reconstructing the past events in the Sunda Strait.

Table 3-1. Distribution of sedimentary facies associated with the 1883-Krakatau events along the coasts of Sunda Strait, see Figure 3-1 for the locations. The distribution is symbolized by (+) if present and (-) if not present.

Locations	The presence of sedimentary facies				
	Bioclastic sand	Pumiceous sand	Rounded pumice lapilli	Pumiceous ash	Pumiceous surge deposit
Ujung Kulon	+	+	+	+	-
Cigorondong	+	+	+	+	-
Sumur	+	+	+	+	-
Panimbang	+	+	+	+	-
Anyer	-	+	+	+	-
Sanghyang Island	+	+	+	-	-
Kalianda	+	+	+	+	-
Gubug Garam & PLTU Taharan	+	+	+	+	+

Source: based on Paris et al. (2014b).

3.2. Gaps of study

Many studies, both on Krakatau eruptions and Krakatau tsunamis, have been undertaken in the Sunda Strait and its vicinity. A bibliographic database of *Scopus* provides about 127 references related to Krakatau-1883, in which only 27 references (about 21 %) examined the 1883-Krakatau tsunamis since 1981. Almost all of the study of Krakatau tsunamis were carried out near the ancient Krakatau Volcano and in the northern part of Sunda Strait, along the small islands and the coasts of Java and Sumatra. In the South of the strait, as well as the northwestern part, only the study of Paris et al. (2014b) and the ancient studies from Verbeek (1884, 1885), Umbgrove (1947) and Verstappen (1956) have been recognized. This gap of study is apparently caused by several factors such as follows:

1. The historical records mostly reported the damages caused by the 1883-Krakatau tsunamis in the northern part of Sunda Strait, e.g. Merak, Anyer, Caringin, Ketimbang, Rajabasa, and Teluk Betung (Verbeek, 1884, 1885; Hurlbut and Verbeek, 1887; Symons et al., 1888; Latter, 1981; Simkin and Fiske, 1983).

2. Some geological features, e.g. dissapearance of the northern part of Krakatau Island and submarine distribution of ignimbrites to the northward (Verbeek, 1885, 1884; Self and Rampino, 1981; Simkin and Fiske, 1983; Sigurdsson et al., 1991), supported the supposition that the effect of Krakatau tsunami waves would be more devastating to the northern part of the strait.
3. Mostly the eyewitnesses observed the tsunami waves lived in the towns or villages along the northern coasts of Sunda Strait, even some vessels reported the 1883-Krakatau events when they passed the northern part of the strait (Verbeek, 1884, 1885; Hurlbut and Verbeek, 1887; Symons et al., 1888).
4. The reports of tsunami damage scarce in the southern and northwestern coasts of the strait might have been related to the rare inhabitant in these areas, even Ujung Kulon Peninsula and Vlakke Hoek has never been occupied by men before and after 1883.
5. In the region of Ujung Kulon Peninsula, scientific research has focused on the recovery of the rainforest after the 1883-Krakatau eruptions (Hommel, 1990; Whittaker et al., 1997).

Actually, some locations in the southern and the northwestern part of Sunda Strait potentially preserved the tsunami deposits better than the northern coasts. The tsunami deposits along the northern coasts of Sunda Strait are often reworked through slope processes, settlements, fish ponds, resorts, agriculture, and industrial areas. In contrast, in the remote area along the southern and the northwestern coasts of the strait, tsunami deposits will be well preserved. From many potential sites in those areas, Ujung Kulon Peninsula is believed to have a remarkable potential for tsunami records and preservation of tsunami deposits, due 1) to the presence of an important sediment stock in the bottom of Welcome Bay, 2) to its funnel-shaped morphology able to concentrate the waves energy, and 3) to its position as a nature reserve part of the UNESCO world heritage.

3.3. Fascinating site to record the 1883-Krakatau tsunamis

Study of tsunami deposits related to the 1883-Krakatau eruptions in the southern part of Sunda Strait constitutes a breakthrough endeavour to fill the gaps of the study of Krakatau tsunami as mentioned above. Ujung Kulon Peninsula and the western part of Ujung Kulon National Park (Mount Honje), connected by an isthmus, are the regions selected for this study rather than other places like Panimbang and Beneawang or Vlakke Hoek, see Figure 3-1. Ujung Kulon has a unique coastal landform situated between Sunda Strait and Indian Ocean.

Some bays in the peninsula that resemble a funnel shape morphology may concentrate the energy of tsunamis coming from Krakatau. Such feature can increase the energy of tsunamis entering the bay, like it is clearly shown on the modelling from Baldock et al. (2007) in some bays of tsunami prone all over the world or when the 2011-Tohoku tsunami penetrated the bays of Iwate Prefecture, Japan (Okayasu et al., 2011; Yamanaka et al., 2013). Moreover, the flat narrow isthmus located in the central part of the large bay between Ujung Kulon Peninsula and Mount Honje region can constitutes an exceptional sedimentary recorder for the waves coming from Sunda Strait as well as from Indian Ocean.

Panimbang, near Teluk Lada (*Lada Bay*), was largely inundated by the 1883-Krakatau tsunamis (Verbeek, 1885; Hurlbut and Verbeek, 1887; Symons et al., 1888; Simkin and Fiske, 1983), but the tsunami deposits are not well preserved due to the developed agricultures at the present time. Beneawang, in the centre part of Teluk Semangka (*Semangka Bay*), has also a similar condition with Panimbang. While Vlakke Hoek, in the southwestern end of Sumatra, may have preserved the tsunami deposits. Yet, its coastal landform is not a bay and by then, lack of sediments prone to be mobilized to realize a good recording.

As the numerical simulation from Yokoyama (1987) and also from Maeno and Imamura (2011) displayed the refraction of Krakatau tsunami propagation in the southern part of Sunda Strait, when the tsunami waves entered the Indian Ocean, the zone of inundation on the southern coasts of Ujung Kulon Peninsula delineated by Verbeek (1885) is still plausible (Figure 3-1). Unfortunately, nothing has been done on the sedimentary record of the tsunamis in the southern coasts of Ujung Kulon Peninsula. The inundation of Krakatau tsunamis on the South coasts of Ujung Kulon Peninsula is still poorly understood. In this case, the AMS analysis performed over the peninsula isthmus might evidence the flow orientation of sediment emplaced from Sunda Strait, as well as from Indian Ocean. Since it has been succesfully applied by Wassmer et al. (2010) to decipher the tsunami deposits on the eastern coast of Banda Aceh, Indonesia, the AMS technique can accurately evidence the sedimentary fabric of tsunami sand unit and the flow orientation of sediment emplacement. This analysis will be completed by the foraminiferal assemblages, in which some species may indicate a specific origin from an Indian Ocean continental margin. Therefore, the result of this study is expected to be able to fill the gaps in knowledge concerning the sedimentary record of the tsunamis occurred 132 years ago at the South coasts of Ujung Kulon Peninsula. This will constitute a new insight on the 1883-Krakatau tsunami study.

PART II
Study area and Methodology

Chapter 4

Characteristics of the study area

As mentioned in Chapter 3 (Part 1), the region of Ujung Kulon National Park in the western tip of Java Island, Indonesia, has been selected to be the study area in reason of a high potential for recording and preservation of tsunami sedimentary signatures. Located between latitude S 6°27' - S 6°54' and longitude E 104°55' - E 105°42', the investigation zone is restricted along the eastern coasts of Mount Honje region, the western coasts of Ujung Kulon Peninsula, and the narrow isthmus of Laban in the central part of Ujung Kulon National Park (see Figure 4-1).

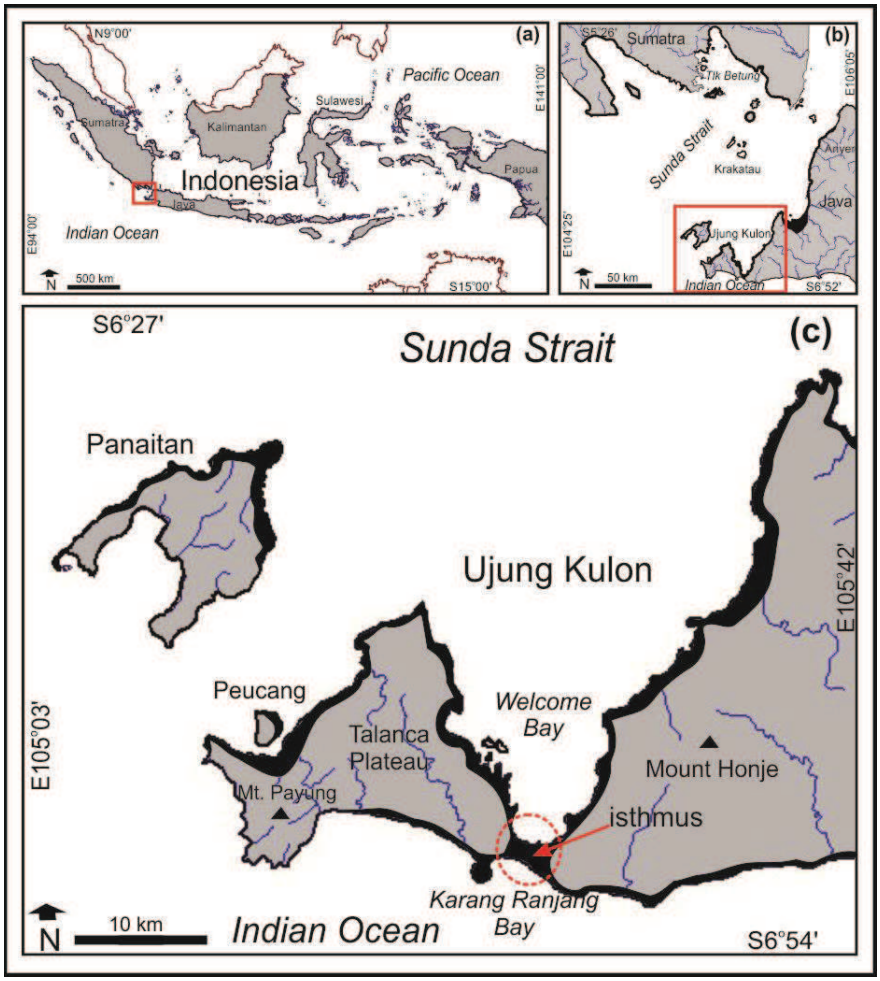

Figure 4-1. Location of the study area; (a) Map of Indonesia, showing the location of Sunda Strait within quadrangle between Java and Sumatra islands (enlarged in fig-b). (b) Map of Sunda Strait, showing the location of Ujung Kulon within quadrangle (enlarged in fig-c). (c) The region of Ujung Kulon, with a red circle pointing out Laban Isthmus.

Situated between Sunda Strait and Indian Ocean, Ujung Kulon has a unique coastal landform which likely affects the distribution of Krakatau tsunami deposits. The slowing down, the acceleration, and the entrapment of tsunami waves are influenced by the features of submarine and coastal morphology and the landscape roughness, which will be described in the section of geomorphological features. While the initial condition of the pre-1883 base layers can be determined from its regional geological setting. All these investigations allow to identify morphological and sedimentological contexts prone to good sedimentary recordings and their preservation in the selected sites area.

4.1. Geomorphological features

4.1.1. Submarine conditions

In general, the conditions of bathymetry around Ujung Kulon area after the Krakatau eruptions in 1883, as described by Verbeek (1885) and (Simkin and Fiske, 1983; Verbeek, 1885)are not different with the present bathymetry (Susilohadi et al., 2009). In contrast, the northern part of Sunda Strait has been changed by a large mass of pyroclastic deposits entering the sea (Mandeville et al., 1996; Self and Rampino, 1981; Sigurdsson et al., 1991). Contemporary Dutch and British Admiralty charts, which were well charted before the 1883-Krakatau eruptions (Simkin and Fiske, 1983; Verbeek, 1885), were referred to determine the bathymetric conditions around Ujung Kulon area (Figure 4-2).

The seafloor between the South of Krakatau and Ujung Kulon is a shallow marine zone with a depth less than 100 meter below sea level (m bsl). To the West of the strait, the seafloor drops drastically to more than 200 m bsl. In the Indian Ocean, the depth of seafloor increases gradually from 500 m bsl in a continental margin to a deep ocean floor of more than 1500 m bsl (Figure 4-2). Around Panaitan Island and the West coasts of Ujung Kulon Peninsula, the slope of seafloor becomes steep to very steep (presumably more than 30°).

This bathymetric conditions influence the distribution of marine organisms, where the most abundant and scientifically important groups of marine organisms are foraminifera. Foraminifera are a large phylum of amoeboid protozoans (single celled) with reticulating pseudopods, fine strands of cytoplasm that branch and merge to form a dynamic net (Loeblich and Tappan, 1964). The majority of foraminifera species live on or within the seafloor

sediment (benthic) with a small number of species known to be floaters in the water column at various depths (planktic).

In the shallow marine between Krakatau and Ujung Kulon, the most abundant benthic foraminifera found are *Amphistegina radiata* and *Eponides rephandus* (Rositasari, 2001). To the westward, planktic foraminifera such as *Globigerina bulloides* and *Pulleniatina aqualateralis* become dominant. Other benthic species in Indian Ocean, to the closure of Indonesian seaway, such as *Uvigerina proboscidea, Cibicides lobatulus, Cibicides wuellerstorfi, Bulimina aculeata, Bulimina alazanensis, Stilostomella lepidula, Oridorsalis umbonatus,* and *Gyroidinoides cibaoensis* indicate a deep sea environment (Rai and Singh, 2012).

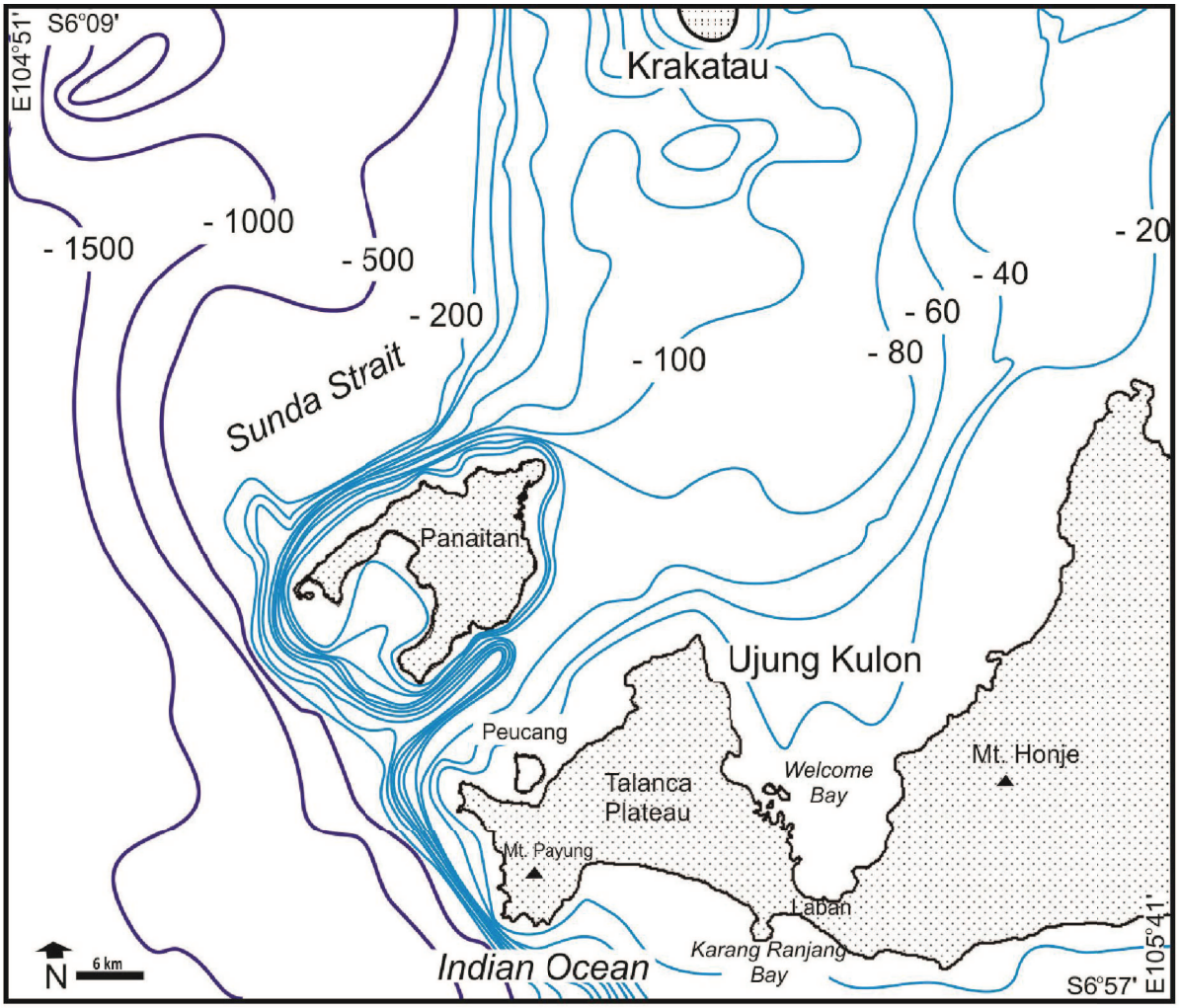

Figure 4-2. Regional Bathymetric Map of the Ujung Kulon area which referred to the contemporary Dutch and British Admiralty charts (Simkin and Fiske, 1983; Verbeek, 1885) and the present bathymetry (Susilohadi et al., 2009); Light contour lines represent a shallow marine zone, while the dark contour lines represent a deeper seafloor. The negative values of contour lines express the depth of sea in meter below sea level (m bsl).

Transported by the tsunami waves with the sediments eroded on the sea floor (for benthic species), the presence of foraminifera within the tsunami sedimentary records can reflect the depth of the wave action on the sea floor. At Laban Isthmus, this approach can be used to determine whether the tsunami deposit was derived from the Sunda Strait or from the Indian Ocean.

4.1.2. Coastal landforms

Ujung Kulon area is located at the Southwest tip of Java Island. To the East, Mount Honje (a part of hilly morphological unit of Bayah Zone) is culminating at 620 m asl (see Figure 4-3). The surrounding hilly topography decreases gently in altitude to the West as the extremity of Java Island narrow at Laban. With less than 2 km wide and 3 km long, Laban Isthmus connects Mount Honje area to the East with Ujung Kulon Peninsula to the West. This peninsula correspond to a 25 km sided isosceles triangle, the base of which is oriented WSW-ESE. The WSW extremity of this triangle correspond to Tanjung Layar (Java First Point), Sanghyang Sirah, and Mount Payung Volcano culminating at 480 m; ESE extremity to the West end of Laban Isthmus while the NNW extremity point out the Krakatau volcanic complex located 80 km further North (Figure 4-3).

The middle part of peninsula has been strongly eroded to be a peneplain ((Bemmelen, 1949). This part is a large region of wilderness known as the Talanca Plateau which reaches 140 m asl (see Figure 4-3), however, most consist of low rolling terrain seldom more than 50 m asl. The surroundings coastline of the peninsula are molded by the sea around them. Battered by Indian Ocean; the long sandy beaches of the South coasts are backed by dunes, lagoons, and rocky outcrops. The West coast's reef-lined shore has cliffs, promontories, sands, and boulders, creating the most spectacular coastline of Ujung Kulon. On the North coasts, the coastal plains consist of white sands and coral banks with small islands, estuaries, swamps, and forest lined shores.

The Ujung Kulon area is mostly covered by a dense tropical rain-forest. A condition that strongly affects the velocity of tsunami waves ashore and the maximum distance of flooding (see Chapter 1). According to (Hills and Mader, 1997), such condition constitutes a coastal landscape roughness with Maning's n equals 0.07, in other words, the effect of tsunami waves can be minimized in this region. The height of trees in this dense forest are also important to calibrate the elevation on SRTM (*Shuttle Radar Topographic Mission*) map used in this study, which apparently constitute the canopy of vegetation. The low terrain, such

as Laban Isthmus, is dominated by *Arenga obtusifolia* (palm tree) with a height up to 16 m (Hommel, 1990). The Talanca Plateau is dominated by scrubs and a dense secondary forest, e.g. *Nicolaia speciosa* with a height less than 5 m. While Mount Honje and Mount Payung are covered by a dense primary forest characterizing mountainous vegetation such as *Vitex pubescens*, with a height up to 25 m. Using these heights, we can determine the real elevation of the area, e.g. the 25 m asl elevation of Laban Isthmus determined by an SRTM 90m Digital Elevation Data is actually less than 9 m asl after correction.

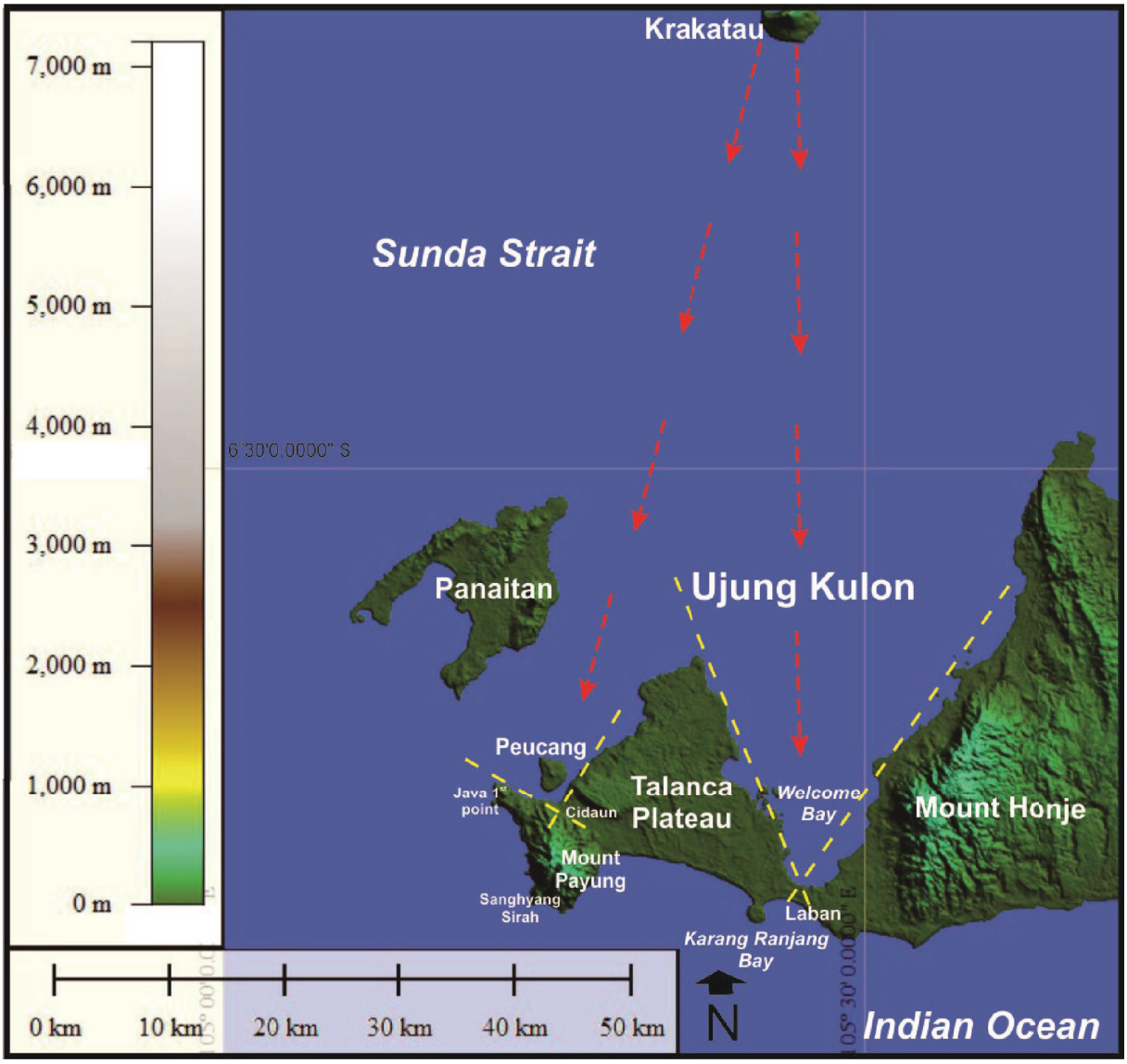

Figure 4-3. Digital Elevation Map of Ujung Kulon area (source: SRTM 90m Digital Elevation Data, CGIAR-CSI, 2009); Showing the location of V-shape bays indicated by dashed lines. Arrow lines represented the direction of possible tsunami waves from Krakatau Volcanic Complex.

Regarding the coastline morphology, Ujung Kulon area displays a unique coastal landform that may have played a role on wave energy distribution and particularly when considering the two large "V" shape morphologies of the coasts of Welcome Bay and Cidaun Bay (Figure 4-3). Welcome Bay is bounded by the narrow coastal plains with a large shallow tidal zone (the water depth around 500 meter of the zone is less than 50 cm), in contrast to the opposite Bay of Karang Ranjang with a wide coastal plains (50 – 100 m) and a narrow intertidal zone. While Cidaun Bay is smaller than the Welcome Bay and not directly open toward the Sunda Strait and Krakatau Volcanic Complex in reason of the presence of Peucang Island (Figure 4-3). This later bay is characterized by the narrow coastal plains and intertidal zone. However, it may also preserve a remarkable tsunami deposit in the center end of Cidaun Bay. The funnel shaped coastal landform usually concentrate the wave energy in the center end of the bay (Baldock et al., 2007; Okayasu et al., 2011; Yamanaka et al., 2013). For the study area, this 'wave trap' configuration is doubled up as each of these bays displays a large sediment stock (very thick sandy sludges in Welcome Bay and fine to coarse sands in Cidaun Bay) that might have been responsible for a significant tsunami deposits on Laban Isthmus and Cidaun area.

Additionnaly, due to its position at the convergence of the remarkably large V-shape coastal landform of Welcome Bay, which faces the Sunda Strait at the North, and the Bay of Karang Ranjang, open to the Indian Ocean at the South, Laban narrow strip of land was potentially able to record marine flooding events generated from both sides of the isthmus: volcanic-induced tsunami from the North and earthquake-induced tsunamis from the South. By then, Laban Isthmus constitutes probably by far the best location in Sunda Strait for past tsunami recordings preservation.

4.2. Geological setting

Sunda Strait lies between an oblique subduction zone that extends parallel to the western coast of Sumatra, and a frontal subduction zone in the southern part of Java (Harjono et al., 1991; Pramumijoyo and Sebrier, 1991; Malod et al., 1995; Susilohadi et al., 2009). Semangko and Mentawai Strike-slip Faults were involved in the deformation of Sunda Strait with a velocity of about 4 mm/years (Figure 4-4). They formed an undulating to steep topography on the seabed and shore (Malod et al., 1995).

This tectonical setting was responsible for the formation of Krakatau Volcanic Complex and for the still active strong volcanic activity as attested by the numerous eruptions of Anak Krakatau which is one of the most active volcanoes in Indonesia (Sutawidjaja, 1997; Agustan et al., 2012). It also formed the funnel-shaped (V-shape) morphology of Welcome Bay, widely open to the North and the Krakatau Volcanic Complex, between Ujung Kulon Peninsula and Mount Honje region, see Figure 4-5. The peninsula, formerly, was an island attached to the mainland of Java (Mount Honje region) by a depositional isthmus (Verstappen, H. Th., 1956). Thus, the isthmus must be characterized by sedimentary deposits from the peninsula itself and Mount Honje region.

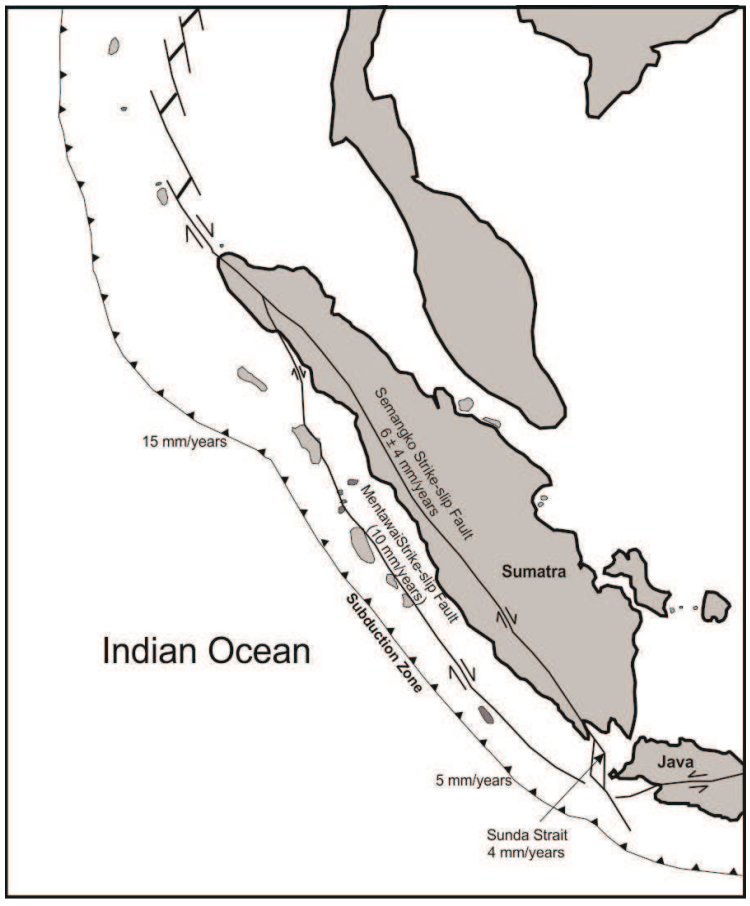

Figure 4-4. Regional structure of Sumatra and the western part of Java (Malod et al., 1995); Subduction zone is indicated by the lines with triangular symbols, while strike-slip faults are represented by the lines with arrows symbols.

Stratigraphically, Ujung Kulon area is composed of Miocene to Pliocene sedimentary/volcanic deposits and Quaternary alluvial deposits (Atmawinata and Abidin, 1991; Sudana and Santosa, 1992; Susilohadi et al., 2009), see Figure 4-5. The western part of

Ujung Kulon (the peninsula) is composed of Miocene volcanic deposits from Cikancana Formation at the base, i.e. volcanic breccia, tuff (consolidated volcanic ash) with andesitic-lava intercalation, sandy tuff, calcareous tuff, and limestone at some locations (Atmawinata and Abidin, 1991). This unit was overlaid by Pliocene deposits which consist of calcareous sandstone, tuffaceous sandstone, pumiceous tuff, and andesitic breccia with tuffaceous claystone from Ciramea Formation. Volcanic rocks were deposited around Mount Payung, in the soutwestern end of peninsula. In Peucang Island, Handeuleum Island, and other little islands, Quaternary coral reef limestones are found (Verstappen, H. Th., 1956; Atmawinata and Abidin, 1991). Most of the deposits have been covered by alluvial deposits, such as pebble, gravel, sand, silt, and mud. On the coastal plains, volcanic ash and tsunami sand unit from the-1883 Krakatau eruptions were then deposited above the alluvial deposits, when tsunamis washed over Ujung Kulon. Even the isthmus was entirely covered by these deposits (Verbeek, 1885).

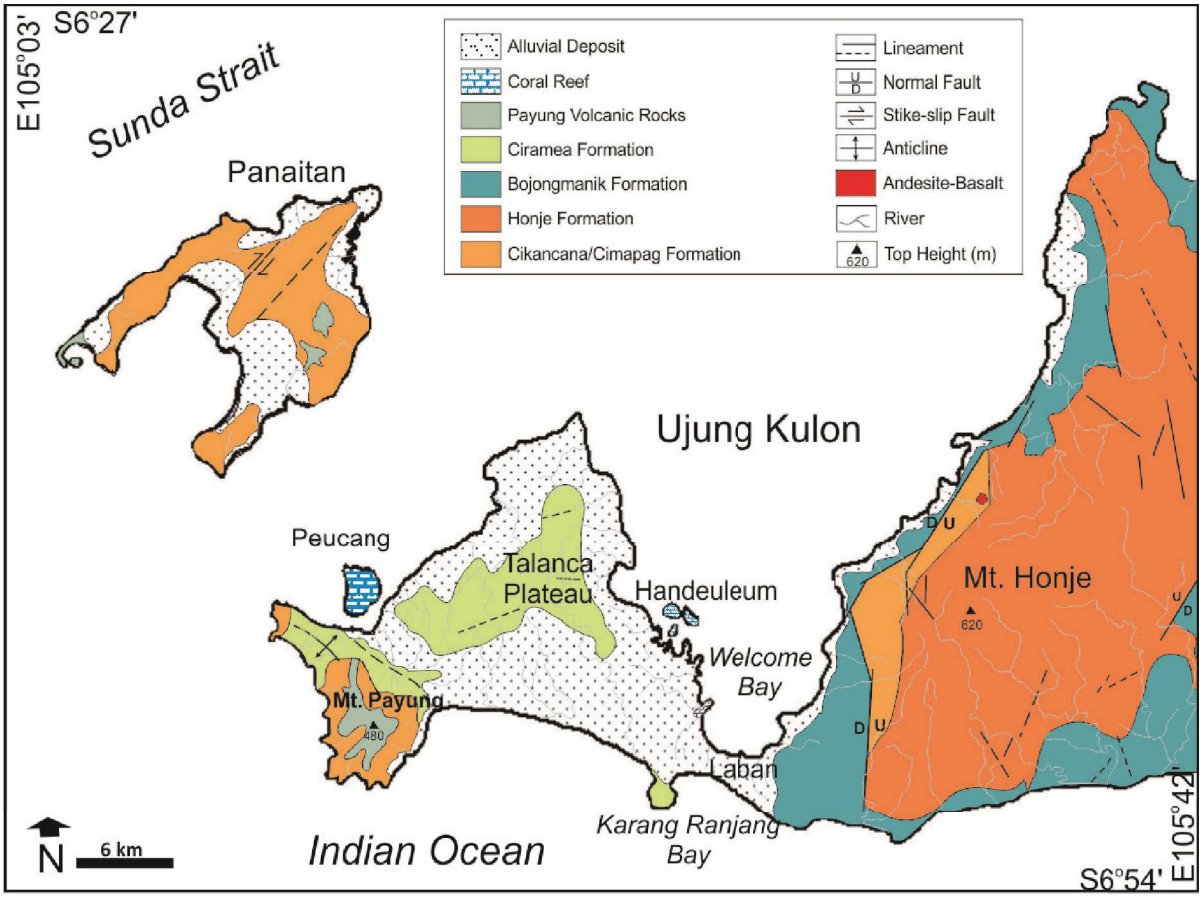

Figure 4-5. Regional geological map of the Ujung Kulon area (modified after (Atmawinata and Abidin, 1991; Sudana and Santosa, 1992); The deposits are symbolized by colours and patterns displayed in a box, from the oldest (at the bottom part) to the youngest (at the upper part). The detail informations are explained in the text.

The eastern part of Ujung Kulon (Mount Honje region), see Figure 4-5, is composed of Miocene deposits from Cimapag Formation at the base. It consists of polymict breccia, altered andesitic-lava, tuff, sandstone, claystone, limestone, conglomerate, and aglomerate (Sudana and Santosa, 1992). Volcanic debris deposits from Honje Formation, i.e. volcanic breccia, tuff, andesitic – basaltic lavas, alternating of sandstone and shally claystone, with intercalation of marl, tuff, conglomerate, limestone, and lignite from Bojongmanik Formation then overlaid the Cimapag Formation. The Pliocene corresponds only to intrusive andesitic and basaltic rocks. Much of underlying rocks, particularly on the coastal plain, were covered by Quaternary alluvial deposits and Sunda Strait tidal accumulations, i.e. pebble, gravel, sand, silt, clay, mud, pumice, and coral reef limestone or shells of moluscs (Sudana and Santosa, 1992). The surface of these alluvial deposits underwent a pedogenesis process and were locally capped with volcanic ash and tsunami sand unit resulting from the-1883 Krakatau eruptions.

This geological setting is then used to determine the pre-1883 base layers below the tsunami deposits. At the coastal plains and the isthmus, the base layer consists of clay (mud) and sand from the alluvial deposits. Thus, at the base, the first tsunami deposit must be mixed with these Quaternary sediments. At Mount Honje region, the coastal plain is bounded by Tertiary volcanic and sedimentary rocks exposed at the cliffs of the ridge. Consequently, the tsunami deposit will be mixed with coarser materials like pebble, gravel, sand, and pumice, therefore, the deposit might be more easily eroded (Hjulstrom, 1939).

These morphological and sedimentological contexts demonstrate how Ujung Kulon area was potentially able to record tsunami flooding events. Two funnel shape bays, a large amount of coastal sediments prone to erosion and the position of the peninsula between the shallow marine environment of Sunda Strait and the continental slope of Indian Ocean render this region as one of the best location for tsunami recordings. The pre-1883 base layers can be used to determine the lower boundary of the 1883-Krakatau tsunami deposits. Considering such conditions, an appropriate approach must be implemented in this location. A multi-proxies approach, including among others the recently adapted AMS technique and foraminiferal identification, may give the best hypothesis for the sediment sources.

Chapter 5
Methods section

Induction scientific problem solving was used in this study, in which a set of observations was made prior to hypothesize an explanation related to all of the observations (Stadler, 2004; Trochim, 2006). An interpretation of satellite image was realized to select the investigation sites that may have preserved tsunami deposits. Grain-size distribution, foraminiferal assemblages, and AMS analyses were then performed on the samples collected from the field in order to attempt to reconstruct the 1883-Krakatau tsunamis behaviour when inundated Ujung Kulon. This chapter explains all the methods used from preparation, field investigation, laboratory analysis, and data analysis.

5.1. Satellite image interpretation

Satellite image interpretation conducted in this study do not correspond to an extraction of qualitative and quantitative information in the form of a map. It has been performed as an image reading (an elemental form of image interpretation) that corresponds to simple identification of objects, in this case, answering to the following question: “is the potential site indicating a possibility of tsunami sedimentary recording?”. Using a common product of satellite images, i.e. Google Earth, the interpretation was performed based on shape, size, pattern, texture, colour, shadow, and other associated relationships.

Google Earth (EarthViewer 3D) is a virtual globe, map and geographical information obtained from satellite imagery, aerial photography, and Geographical Information System (GIS) 3D globe. The new Google Earth version, which has been updated by SIO, NOAA US Navy, NGA, and GEBCO since January 31, 2010, was used to avoid a significant misinterpretation caused by environmental changes in identifying sites with high sedimentary recordings potential for a field investigation. Certain number of the sites were identified on the base of the topographic conditions favouring sediment erosion and deposition on the coastal area, the presence of a sediment stock on the seashore (large sandy beaches, sand dunes, etc), the presence of “wave traps” coastal morphology (i.e. bays wide open toward the Krakatau, funnel shaped bays able to concentrate wave energy, etc), the inland flats allowing

a good recording in the medial and distal part, the existence of topographic lows favouring the sediment trapping (lagunas, ponds, interdunes lows, etc)

5.2. Field investigations

On the base of the potential sites selected, twenty-one investigation sites were observed on July to August 2011 and May 2012 (Figure 5-1). The observation sites were mostly distributed at the East coasts (Mount Honje region) that was anthropized and more accessible. While the West coasts (Ujung Kulon Peninsula) constituted of forest or shrubs were locally quite impenetrable (between 12 and 15 m/hour with a machete), although it shows some potential sites for the tsunami sedimentary recordings.

Notwithstanding, two potential sites in the central part of funnel shaped bays, i.e. Cidaun and Laban, have been investigated. Because of the particular coastal morphology and a significant sediment stock at the bottom of the bay (see Chapter 4), Laban Isthmus quickly appears as the most important site to investigate. A transect was then made along the isthmus, consisting of 6 drilling observation sites (U-01 to U-06), in order to reconstruct the characteristics of the sedimentation related to the 1883-Krakatau tsunamis through the flat isthmus and to potentially identify deposits from an Indian Ocean source.

At Ujung Kulon Peninsula, only hand-auger equipment was allowed to use, to realize the cores for tsunami deposits investigations, due to the government regulation for all activities within a National Park (UU No. 5/1990 about the Conservation of Natural Resources and Ecosystem). Considering the characteristic of sub-soil materials in this area (that consists of soft and cohesive layers) and to get a minimal disturbance of collected samples, a modified auger was used for this study, i.e. combining riverside auger and gouge auger, a pestle, and sample tube of 50 cm in length and 7 cm in diameter. Before the drilling, sample tube was oriented. The maximum depth of investigation was 3.0 meter and further down was only found clay and sand from the old alluvial deposits, as the pre-1883 base layers.

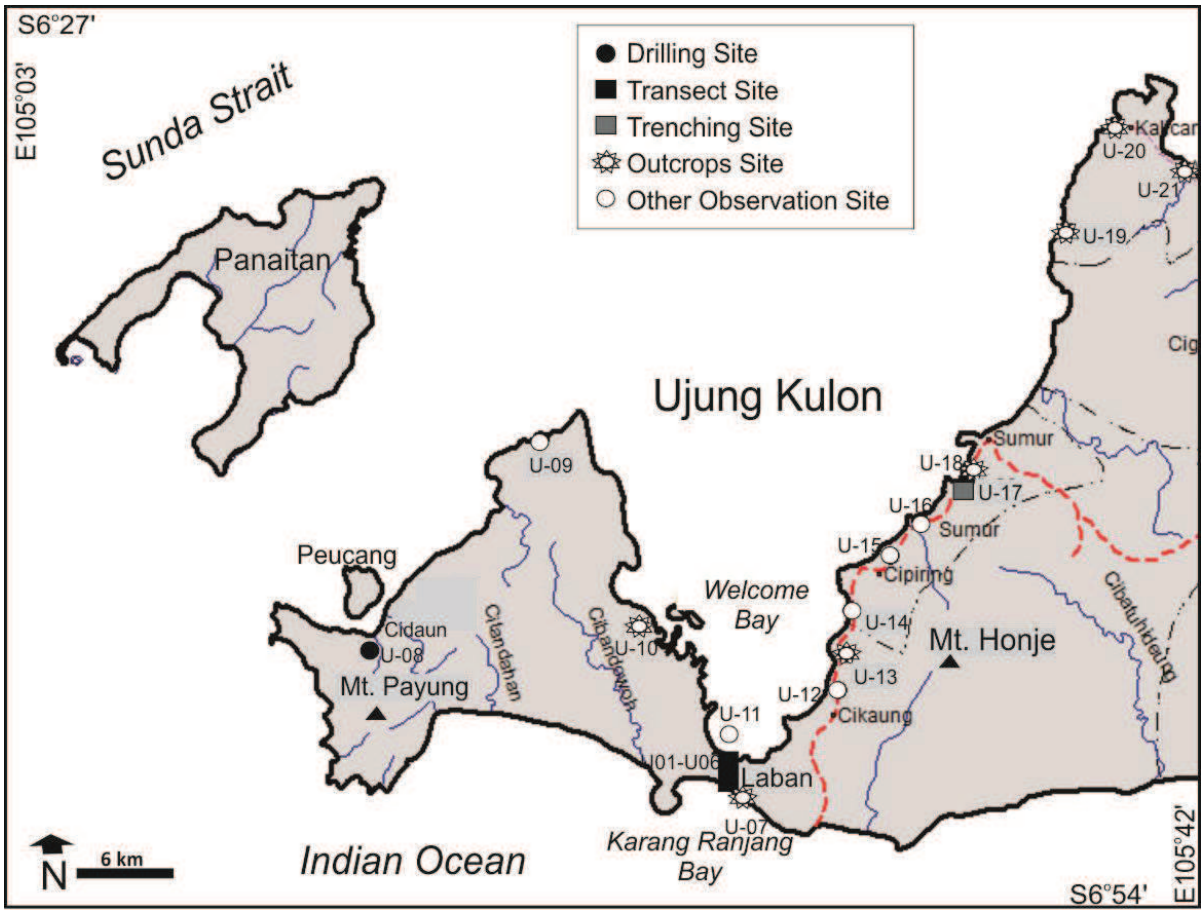

Figure 5-1. Field investigation sites symbolized in a legend; Transect Site at Laban Isthmus consists of 6 drilling observation sites. Outcrops Sites are locations where a portion of bedrock or other stratum appears at the surface of the Earth. Other Observation Sites consist of an observation of coastal landform and tsunami signatures such as sand dunes, coral boulders, and dump deposits.

Independently, the AMS samples were collected by 2 cm wide cubic plastic of non-magnetic boxes, along the vertical sections of tsunami deposits in the auger tube (see Figure 5-2). The sampling boxes were then oriented, according to the orientation of the auger during coring, and sealed after removing from the cores to avoid desciccation. The sediments sampled were limited to the fine sand, silt, or clay, with a good cohesion to retain the fabric (Wassmer et al., 2010). The disturbance of the sedimentary fabric must be avoided to get an excellent result of AMS parameters as a proxy of hydraulic characteristics during emplacement. Consequently, coarse grain sediments were not sampled because their fabric could be disturbed during sampling.

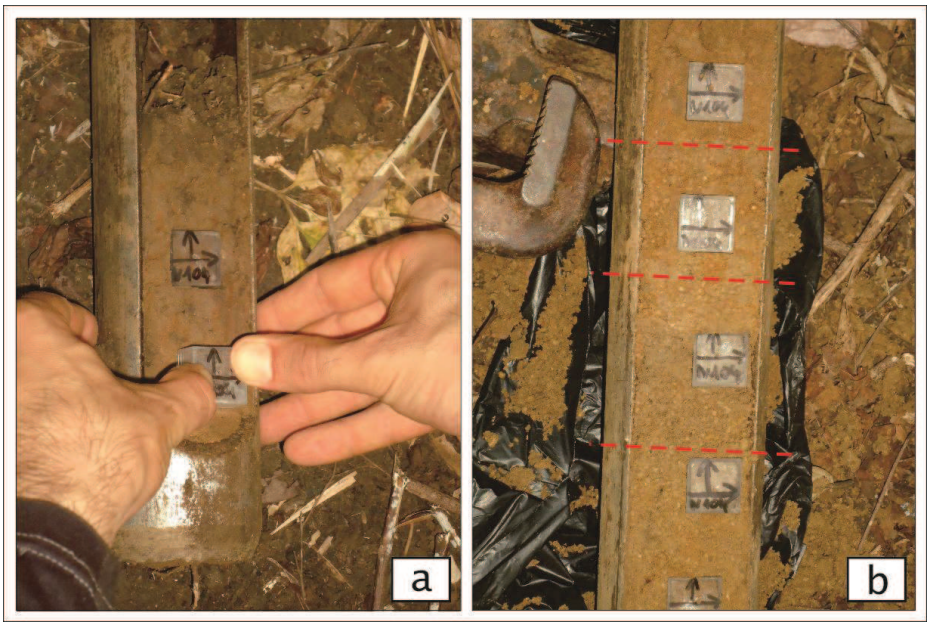

Figure 5-2. AMS sampling procedures; (a) An example of sampling technique at U-06 observation site; the boxes were plugged in the moist sediments along the vertical section of auger tube. b) The dashed lines mark the transition between two layers. The boxes were oriented (azimuth and tilting of the plugging axis) to measure AMS axes.

In the eastern part of Ujung Kulon, most of the tsunami signatures were observed on outcrops. Trenching method was performed at site U-17 with a size of wall about 70 - 100 cm depth and 5 m length (Figure 5-3). Samples were collected for grain-size analysis on each layer based on visual changes in texture and composition of the sediments, while for AMS only the fine sediment layers were sampled. All samples were then analysed in laboratory.

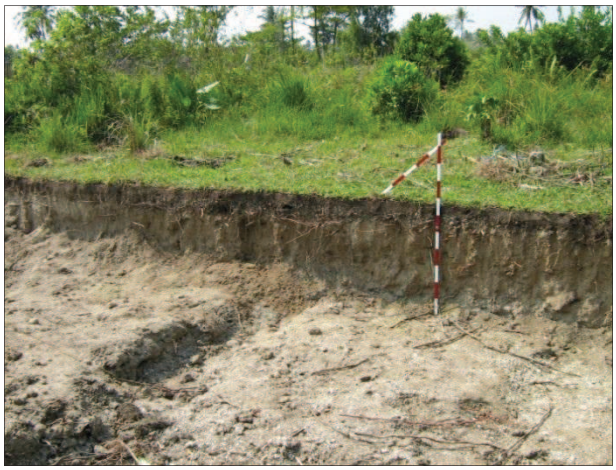

Figure 5-3. Location of entrenchment at site U-17; The deposit was exposed by an excavation for local settlement.

5.3. Laboratory and data analyses

5.3.1. Grain-size distribution analysis

Grain size analysis was performed for the samples with a 2 mm (-1 ϕ) maximum grain-size using a Beckman Coulter LS-230 device in Laboratoire d'Analyses des Sols et Formations Superficielles, EOST, Université de Strasbourg (UdS), France. It consists of a laser optical bench associated with the fluid module (1.7 L) or a dry route module (mostly soft sediments and sands). The detection range extending from 0.04 µm to 2000 µm for the 117 classes of particles.

Previously, the samples must be prepared through several treatments such as follows:

- The sands were separated by T-34 sieve size, for refusing the particles more than 2000 µm
- The destruction of organic matter; attacked with H_2O_2 or hydrogen peroxide.
- The elimination of flocculant ion; washed with KCl or HCl.
- The dispersion of the samples by sodium hexametaphosphate.
- Rotary agitation between 4 to 6 hours.

Granulometric parameters such as mean, variance, standard deviation, skewness, and kurtosis were then resulted from this analysis. Mean (M_φ or μ) shows an average of grain-size, variance (σ_φ^2) and standard deviation (σ_φ) indicate the degree of sorting, while skewness ($S_{k\varphi}$ or γ_1) and kurtosis (K_φ or γ_2) show the shape of the grain-size distribution (Boggs Jr, 1992). These parameters were defined mathematically considering all of the grain-size class intervals.

According to the proxies of tsunami deposits described by (Chagué-Goff et al., 2011), the deposits have the grain-size distribution from boulders to fine mud. Sediments generally fining inland and upwards within the deposits. Thus, the grain-size distribution was used to determine the tsunami sequences in the study area. The grain-size were classified on the basis of (Wentworth, 1922), with the values of phi (ϕ) as conventionally used by sedimentologists (Krumbein, 1938), see Table 5-1. Phi grade scale is an arithmetic-size scale that can be easily divided into smaller units with limits of integer value in order to provide an adequate number of experimentally determined points for analytic purposes. Standard deviation, skewness, and kurtosis resulted from laboratory analysis were calculated on the basis of classifications from (Folk and Ward, 1957), see Table 5-2. These classifications were adopted to get optimal

information on transport and emplacement mechanisms of tsunami deposits (Blott and Pye, 2001).

Controlled by textural triangle, the mean grain-size were expressed at the stratigraphic profiles for all investigation sites. Each profile displays sumperimposed fining upward (normal grading) and coarsening upward (reverse grading) sequences. The normal grading repetition, skewness and kurtosis were used to determine tsunami sequences within the deposit at each profile/section. Textural triangle adopted from (Brady and Weil, 1999), see Figure 5-4, was used to evidence boundaries between sequences. In tsunami deposit, these boundaries are usually characterized by fine sands/silts deposited by the tail of a wave mixed with gravel/coarse sands emplaced by the front of another wave (Chagué-Goff et al., 2011).

Table 5-1. Grain-size scale adopted from (Wentworth, 1922) and (Krumbein, 1938).

Grain Size		Descriptive Terminology
Phi (ϕ)	Mm	
-11	2048	Cobbles
-10	1024	
-9	512	
-8	256	
-7	128	
-6	64	Pebbles
-5	32	
-4	16	
-3	8	
-2	4	Granules
-1	2	
0	1	Very Coarse Sand
1	0.5	Coarse Sand
2	0.25	Medium Sand
3	0.125	Fine Sand
4	0.063	Very Fine Sand
5	0.031	Silt
6	0.016	
7	0.008	
8	0.004	
9	0.002	Clay

Table 5-2. Grain size parameters and their classifications adopted from (Folk and Ward, 1957).

Parameters	Equation	Values	Terminology
Standard Deviation (Sorting)	$\sigma_1 = \frac{\emptyset_{84} - \emptyset_{16}}{4} + \frac{\emptyset_{95} - \emptyset_5}{6.6}$	< 0.35 0.35 – 0.50 0.50 – 0.70 0.70 – 1.00 1.00 – 2.00 2.00 – 4.00 > 4.00	Very Well Sorted Well Sorted Moderately Well Sorted Moderately Sorted Poorly Sorted Very Poorly Sorted Extremely Poorly Sorted
Skewness	$Sk_1 = \frac{\emptyset_{16} + \emptyset_{84} - 2\emptyset_{50}}{2(\emptyset_{84} - \emptyset_{16})} + \frac{\emptyset_5 + \emptyset_{95} - 2\emptyset_{50}}{2(\emptyset_{95} - \emptyset_5)}$	1.0 to 0.3 0.3 to 0.1 0.1 to -0.1 -0.1 to -0.3 -0.3 to -1.0	Very Fine Skewed Fine Skewed Symmetrical Coarse Skewed Very Coarse Skewed
Kurtosis	$K_G = \frac{\emptyset_{95} - \emptyset_5}{2.44(\emptyset_{75} - \emptyset_{25})}$	< 0.67 0.67 – 0.90 0.90 – 1.11 1.11 – 1.50 1.50 – 3.00 > 3.00	Very Platykurtic Platykurtic Mesokurtic Leptokurtic Very Leptokurtic Extremely Leptokurtic

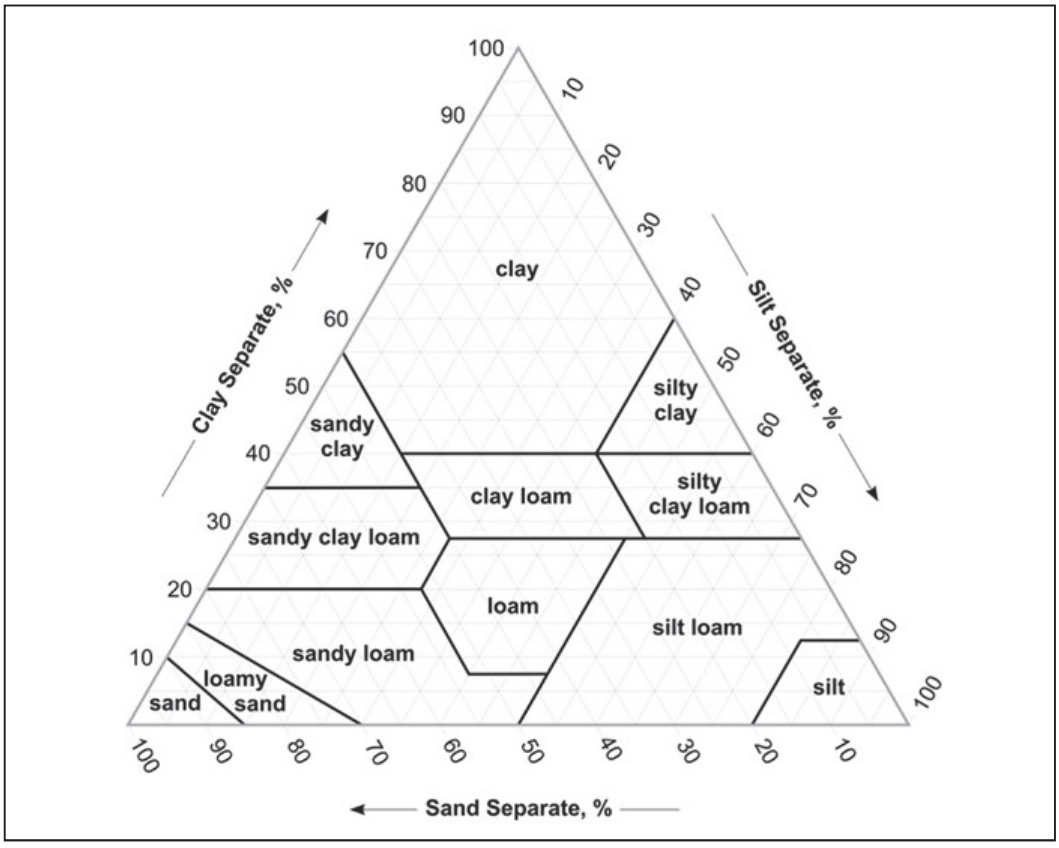

Figure 5-4. The textural triangle diagrams adopted from (Brady and Weil, 1999). Each class has particular characteristics based on their sand, silt, and clay percentages.

Grain-size parameters were also used to interpret the hydrodynamics condition prevailing sediment during deposition by using *CM* diagrams, in which *C* is the one percentile of the grain-size distribution (C99) in the deposits and *M* the median (Passega, 1957). To avoid the statistical effect of the presence of an abnormally coarse grain within the grain-size distribution, fifth percentile of the distribution (C95) was used in this study, as already proposed by Allen (1971). The values of the median (C50) and C95 parameters were extrapolated from the calculated cumulative curves, expressed by μm, for the construction of CM diagrams in order to correlate grain-size data with transport and emplacement mechanisms. The highest median and C95 values indicate a rolling along the ground, which corresponds to the highest energy conditions. When energy gradually decreases, the mechanisms are the graded suspension (that usually leads to normal grading during deposition) followed by uniform suspension for the transport of finer particles. The lowest C95 values correspond to the conditions of pelagic suspension. Above 500 μm C95 indicate a bedload transport, whereas pure suspension transport occurs below this limit in weakest current conditions.

5.3.2. Foraminiferal identification

Samples were studied under a binocular microscope, in Laboratorium Palaeontologi, Fakultas Teknik Geologi (FTG), Universitas Padjadjaran (Unpad), Indonesia, to obtain qualitative and quantitative data on microfaunal assemblages. Benthic foraminifera are the majority of microfaune species used to determine a maximum depth of seafloor eroded by tsunami waves (Bahlburg and Weiss, 2007; Chagué-Goff et al., 2011; Dawson and Shi, 2000; Phleger, 1951). Prior to identification, benthic foraminifera must be separated from the sand grains by soaking the samples with H_2O_2 30% and NaOH. After soaking, the samples were washed and then dried in a temperature ranging between 100 – 120 °C.

The samples were then sprinkled sparsely across a picking tray and examined under a binocular microscope of 40x magnification. Individual foraminifera specimens were picked and mounted for permanent reference. Any foraminifera specimens encountered on the picking tray were captured using the wetted tip of an artist's brush and transfered to the glued slide, i.e. a recessed area in an 18-ply cardboard slide with a black background and a water-soluble glue. At any time, the specimen was wetted to release the glue so that the specimen can be turned and viewed from different perspectives.

(Kitazato, 1988) has classified benthic foraminifera into 4 types based on their way of life, i.e. anchored on a seaweed, crawl around a seaweed, attached on a sediment substrate, and live on/in a sediment substrate. Benthic foraminifera attached on and live in a sediment substrate can be used for identifying the tsunami sequences, rather than the benthic anchored or crawl on a seaweed which may be displaced by a tidal wave. Benthic foraminifera within a sediment substrate may have remained intact, when the tsunami wave erodes a seafloor and emplaces a substrate far inland. In the study area, only foraminifera within cores U-03, U-04, and U-05 from Laban Isthmus were plausible to be analysed, due to their location that were far inland and away from the tidal influence (see Figure 5-1).

Benthic foraminiferal assemblages can be used as proxy to determine the maximum depth of bathymetry as source of tsunami deposits (Bahlburg and Weiss, 2007; Chagué-Goff et al., 2011; Phleger, 1951) and the environmental changes (Abbene et al., 2006). A diagram of bathymetric zone was then used to describe the origin of benthic foraminifera. This diagram appropriately displays the oceanic region of Indian Ocean that consists of continental shelf, continental slope, and ocean floor from littoral to abyssal zones (see Figure 5-5). While the shallow marine environment of Sunda Strait is a part of the continental shelf and only consists of littoral and neritic zones.

The foraminiferal assemblages are expressed by amount of individuals per sample volume, as commonly called as *density*. Their density in the samples collected from the study area were measured by considering the auger tube size (ø $\pm$7 cm) and the collected samples interval. The density was used to determine a biofacies through cluster analysis method (Abbene et al., 2006). Biofacies resulted from statistical cluster analysis method is a part of a stratigraphic unit characterized by the fossil assemblages that is restricted to a certain facies and a specific environment (Allaby, 2013). In this study, a multivariate method of Q-mode cluster analysis was applied to define biofacies using the Statistical Package for the Social Sciences (IBM-SPSS, version 22). The Q-mode analysis ranked and grouped together the samples with similar species composition based on the relative frequencies of the most common species. This cluster analysis calculated a simple Euclidean distance coefficient between every possible pair of samples, and amalgamated the samples into a *dendrogram*, i.e. a branching diagram that hierarchically nests objects into increasingly more inclusive groups, using averaged linkage between groups. The resulted clusters separate quantitatively the samples into assemblages based on their species composition (Abbene et al., 2006).

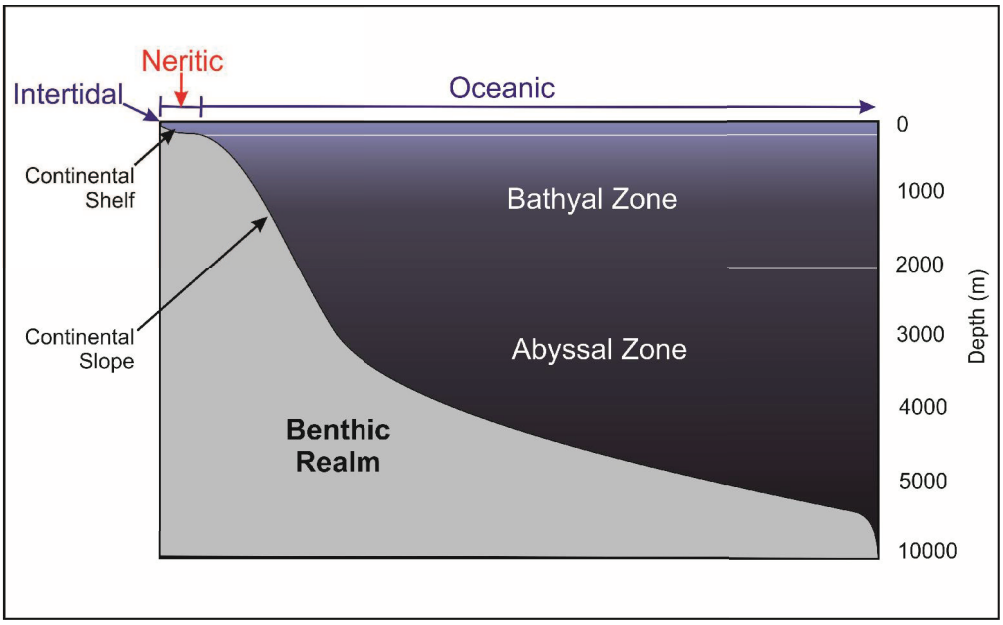

Figure 5-5. Diagram of bathymetric zones showing various regions of the ocean; i) Continental shelf is the sea floor adjacent to a continent and extending to an average depth of about 180 m where the continental slope began. ii) Continental slope is the edge of the continent, the slope descends from the continental shelf and increases in depth more rapidly than does the continental shelf. iii) Intertidal (littoral) zone is the region along the shoreline covered by the sea at high tide but exposed to air at low tide. iv) Neritic zone is sub-littoral zone overlying the continental shelf. v) Bathyal zone is the benthic region along the upper continental slope between the edge of the continental shelf and the abyssal benthic region. vi) Abyssal zone is a region of the ocean floor below 2,000 m depth.

5.3.3. Anisotropy of Magnetic Susceptibility (AMS) measurement

The measurement of AMS delivers informations on the magnetic fabrics of tsunami deposits, in relation with hydraulic characteristics during emplacement (Wassmer et al., 2010). The samples were tested using a MFK1-A Kappabridge device, in Institut de Géologie, EOST, Université de Strasbourg (UdS), France, to measure the maximum (K_1), intermediate (K_2), and minimum (K_3) AMS axes. These axes were used to evaluate the relationship between depositional processes and magnetic fabrics through the calculation of AMS parameters (Jelinek, 1981), i.e. mean bulk volume of magnetic susceptibilities (K_m), magnetic lineation ($L = K_1/K_2$), magnetic foliation ($F = K_2/K_3$), shape parameter (T), corrected degree of anisotropy (P_j), alignment parameter (F_s), and shape factor (q).

Each box sample was marked and measured in three perpendicular positions (see Figure 5-6). The Kappabridge was zeroed after inserting the specimen into a measuring coil, so that susceptibility differences were measured during specimen spinning (64 measurements were made during one spin) which resulted in very sensitive determination of the anisotropic

component of the susceptibility tensor profiting from the measurement on the lowest possible and therefore most sensitive range (AGICO, 2009). Then, one bulk susceptibility value was measured along one axis and the complete susceptibility tensor was combined from these measurements.

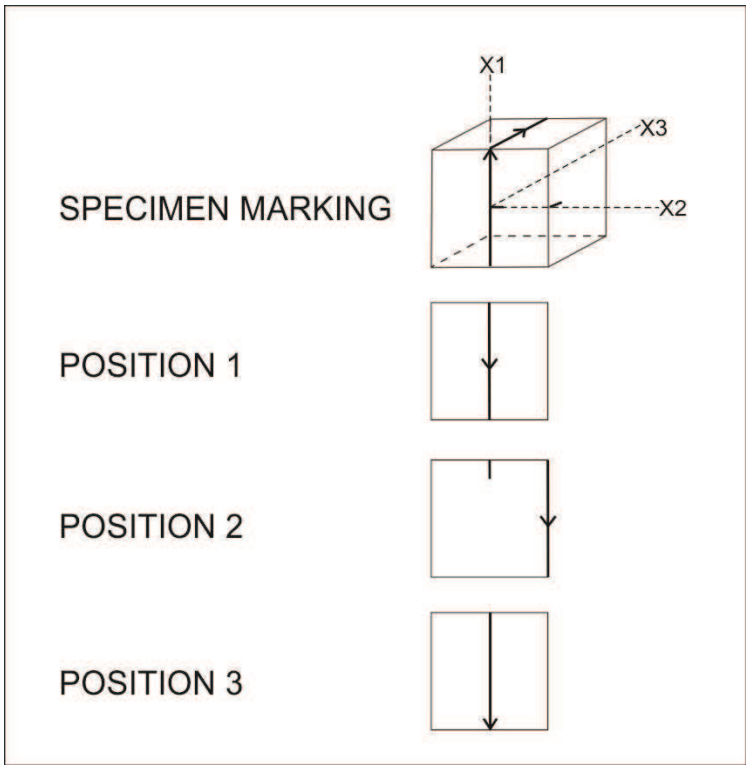

Figure 5-6. AMS measuring positions (AGICO, 2009); a) Specimen marking; top of specimen = trend/azimuth of core axis (X1), side of specimen = plunge/inclination of core axis (X3), and mark 90° clockwise from plunge line (X2). b) Position 1 is spinning about axis X1 which points towards us. c) Position 2 is spinning about axis X2, 90° counter clockwise from Position 1. d) Position 3 is spinning about axis X3 which gets away from us.

AMS measures the crystallographic fabric of the grains constituting the deposit (Tarling and Hrouda, 1993). The crystalline main axis, more resistant to attrition, determines sediment particles long axis and in conjunction with subsequent measure the ovoid shape of the grains. In a deposit, the long axis of the grain is parallel the flow directions with an imbrication (tilting) dipping upstream (Hamilton and Rees, 1970). The AMS was then used as a proxy to retrieve the internal magnetic fabric of the deposits that reflects the preferential organisation of the grains. An oriented sample is exposed to a succession of electromagnetic signals from various directions, from which the inducted magnetic field is measured to retrieve the

particles' fabric (Wassmer et al., 2010). The ellipsoid of anisotropy is characterized by three axes defined as K_1 (long axis) > K_2 > K_3. K_1 axis azimuth and tilting indicate flow direction during sediment emplacement (Wassmer et al., 2010).

The magnetic fabric is coaxial with the sediment fabric (Tarling and Hrouda, 1993) which is characterized by the magnetic foliation (oblate, $K_1 \sim K_2 > K_3$ and $1 > T > 0$) and the magnetic lineation (prolate, $K_1 > K_2 \sim K_3$ and $0 > T > -1$). The shape parameter (T), represents the type of magnetic fabric, is related to the condition of sedimentary environments. The relative strength of magnetic fabric is represented by the degree of anisotropy (P_j) (Hrouda, 1982), whereas the development of a linear fabric is expressed by the alignment parameter (F_s) (Ellwood, 1975). Based on laboratory measurements, the magnetic parameter values constitute the primary depositional fabrics of natural sediments if shape factor (q values) range as $0.06 < q < 0.7$ with the imbrication angles (I; inclination of K_1) are less than 20° (Hamilton and Rees, 1970). To visualize the magnetic fabric characteristics in the study area, some parameters such F, L, T, and F_s were then plotted versus depth using binary diagram.

5.3.4. Petrographic Analysis

In this study, petrographic analysis was performed to identify the mineral content within volcanic materials found along with the tsunami deposits as an important criterion for recognizing the tsunami deposits produced by the 1883-Krakatau eruptions. This analysis was carried out under a polarizing microscope, under 40x to 100x magnification, in Laboratorium Petrologi - Mineralogi, Fakultas Teknik Geologi (FTG), Universitas Padjadjaran (Unpad), Indonesia. Considering that most of the samples are unconsolidated materials, thin sections were prepared by *grain mounts method*. Grains were cleaned of any heavy liquids used in their separation, washed and dried before mounting.

Unfortunately, majority of the samples collected have been mixed between bioclasts and pyroclastic materials. Even some samples have underwent pedogenesis processes causing the alteration of minerals content. Thus, only some samples from selected layers were examined under the polarizing microscope. The identified minerals within the samples were then compared with the result of microscopic examination of the 1883-Krakatau volcanic ash described by Verbeek (1884, 1885), in order to confirm that the observed deposits were actually resulted from the 1883-Krakatau eruptions.

5.3.5. Geochemical Analysis

Geochemical analysis was performed to identify the major elements (SiO_2, TiO_2, Al_2O_3, Fe_2O_3, MnO, MgO, CaO, Na_2O, K_2O, and P_2O_5) and the trace elements (Ba, Ce, Cr, Ga, Nb, Ni, Pb, Rb, Sc, Sr, Th, V, Y, and Zr) as well as the proportions of bioclasts, expressed by organic and carbonate content in loss on ignition/LOI, contained within the tsunami deposits. X-ray fluorescence (XRF) analysis was applied due to its accurate method, easy to use and fast without sample preparation, even for unconsolidated materials. Yet, the samples must be well preserved and uncontaminated. The samples from selected layers were analysed through a Rigaku RIX 2000 - XRF spectrometer at Department of Geoscience, Shimane University, Japan, using established methods (Kimura and Yamada, 1996). Like petrographic analysis, the result of XRF analysis were compared with the chemical composition of the 1883-Krakatau volcanic ash described by J. W. Retgers in Verbeek (1885) and Symons et al. (1888).

5.3.6. A new approach in stratigraphic correlation

Six stratigraphic profiles at Laban Isthmus, along the investigation transect, were correlated from site U-01 at the north (a proximal zone for Sunda Strait marine invasion but a distal zone for Indian Ocean marine invasion) to site U-06 at the south (a distal zone for Sunda Strait but a proximal zone for Indian Ocean). This stratigraphic cross section was made by a new approach combining grain-size distribution, foraminiferal assemblages, and AMS analysis, for which the AMS technique became a reliable primary key in the correlation. The sequences, resulted from grain-size distribution and foraminiferal assemblages, were laterally connected one to another on the basis of K_1 (long axis) azimuth. The presence of pyroclastic materials within the sections were compared with the composition of the 1883-Krakatau volcanic ash from previous studies, to prove that the tsunami deposits were synchronous with Krakatau eruptions.

The scenario of the 1883-Krakatau tsunami at Ujung Kulon was reconstructed according to the stratigraphic correlation. Hydrodynamic conditions during the emplacement of tsunami deposits were determined using the relationships between CM diagram, biofacies, and AMS data. The propagation of Krakatau tsunami waves were determined through a calculation using the formulas as explained in the Part I and the modeling made by Yokoyama (1987) and Maeno and Imamura (2011). Digital Elevation Model (DEM), generated from a variety of satellite images, was used to support the identification of tsunami propagation on

the basis of height information (after correction with the height of vegetation), terrain roughness, coastal morphological shapes, and 3D representation of a terrain's surface. The source of the DEM used in this study is a SRTM (*Shuttle Radar Topographic Mission*) 90m Digital Elevation Data from CGIAR-CSI (2009), a Consortium for Spatial Information. Moreover, this scenario was connected with the field recorded immediately after the 1883-Krakatau eruptions, including tide and pressure gauge records at Batavia, by (Verbeek, 1884, 1885) and also with the previous related studies (Hurlbut and Verbeek, 1887; Symons et al., 1888; Umbgrove, 1947; Verstappen, H. Th., 1956; Latter, 1981; Paris et al., 2014).

PART III
Results

Chapter 6
Data collected

Ujung Kulon area, that has been well described in Chapter 4, is one of the best location for tsunami recordings in Sunda Strait. Its two funnel shaped of bays, the position of peninsula between Sunda Strait and Indian Ocean, the condition of its base layers, and a fact that this region is a national park constitute the influence factors for the good tsunami sedimentary recordings and their preservation in the selected sites area. Many depositional signatures of tsunami have been found in Ujung Kulon area and its vicinity. An incredible tsunami deposit with coral boulders embedded in sand including layers of bioclastic sand and pumiceous sand unit was found at Laban Isthmus, at the central part of the V-shape coastal morphology of Ujung Kulon Peninsula. In order to understand the spatial evolution of the deposit emplaced from seashore to distal area, the cores realized were investigated along a transect crossing the isthmus from North to South as mentioned in Chapter 5 (Sections U-01 to U-06). The observed sediment layers were characterized by a series of fining upward sequences stacked one upon the other and incorporate rip-up clasts of clayey sediment. Foraminifera were also found abundant in the distal sections of the isthmus. To the East, along narrow coastal plain in the front of Mount Honje, the deposit of tsunami sands is up to 50 cm in thickness, sandwiched between finer material and coral gravels. Locally, dump deposits and large coral boulders were found far inland. All the description of the cores collected from the field investigations and the data from laboratory analyses of the sediments, grain size and AMS, will be exposed in this chapter.

6.1. Field investigation results

6.1.1. Drilling investigations

Drilling investigations were performed to observe the sediment layers within the area of Ujung Kulon National Park. At Laban Isthmus, six drilling sites were plotted along a North – South transect, from the proximal section of Sunda Strait to the opposite proximal section of Indian Ocean (Figure 6-1). At the western part of peninsula (Cidaun), another

drilling site selected has allowed to evidence the sediment layers deposited by the 1883-Krakatau tsunamis.

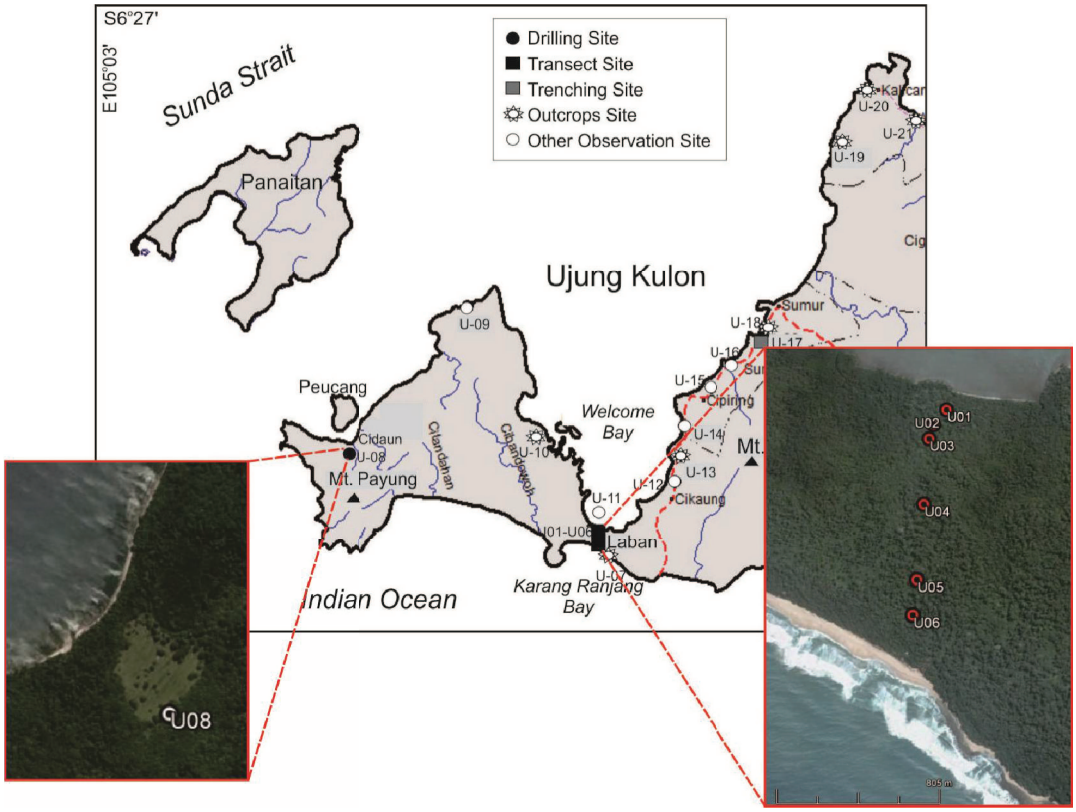

Figure 6-1. Map of the drilling and transect sites; The transect site is situated at Laban Isthmus, consists of 6 drilling sites from U-01 to U-06 (right inset map). Another driling site, U-08, was done at Cidaun, 400 m from the coast (left inset map).

a. Laban Isthmus transect site (site U-01 to U-06)

Laban Isthmus is situated 80 km to the South of the Krakatau Islands, in the region of Ujung Kulon Peninsula at the very bottom of the V-shaped morphology of Welcome Bay. A transect along this narrow isthmus (less than 2 km wide) was made from North (site U-01) to South (site U-06). All the sections presented below will be described from base to top and depth values are given in cm from the surface.

Site U-01 is located at 6°49'42.30" S and 105°27'09.40" E, 200 m from the shoreline of Sunda Strait. Section U-01, see Figure 6-2, consists at the base of massive clay layers (> 200 cm) from the older deposits (alluvial deposits produced from Ciramea and Bojongmanik Formations). These clays are grey in colour and one can note the presence of bioclasts near the top of layer.

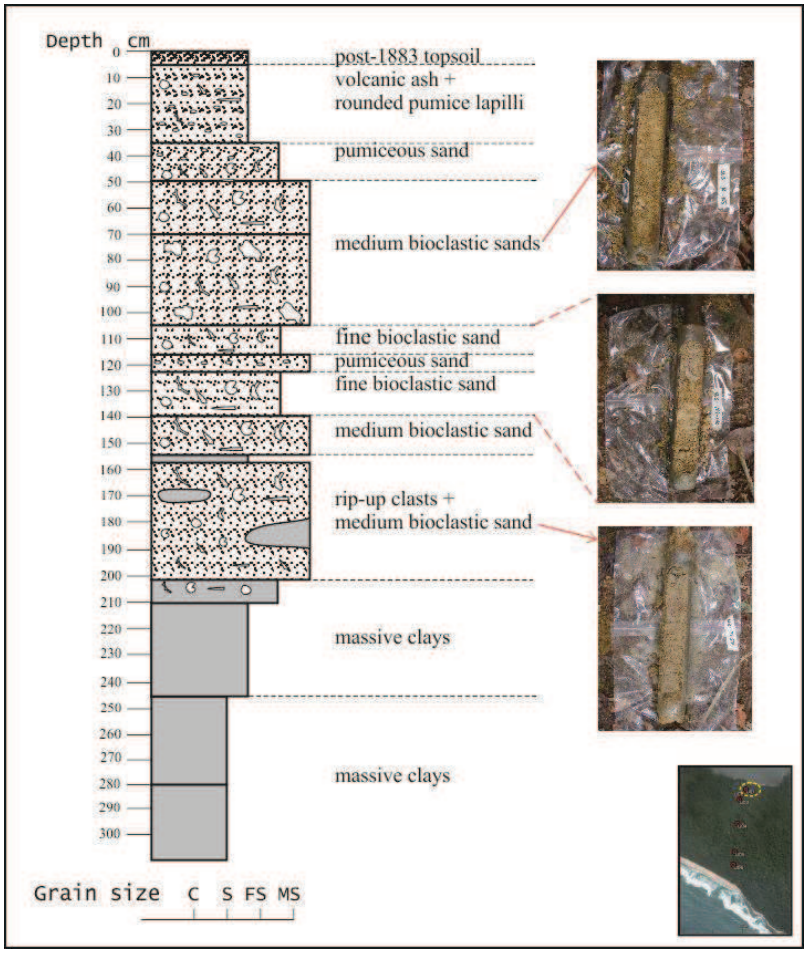

Figure 6-2. Stratigraphic profile of Section U-01; The site shown by a yellow circle line in the North on the inset map is located 200 m from the coast.

At a depth within 200 and 155 cm a thick marine sediment layer composed of grey sands with abundant bioclasts (mostly shells) displays at the base rip-up clasts of clayey sediment. Above, at a depth of 155 - 105 cm, a layer composed of coral gravels and bioclasts mixed with medium sand at the bottom evolves upward to fine sand. At a depth of 125 - 120 cm, this bioclastic sand unit is interrupted by a light-brown pumiceous sand layer. Between 105 and 50 cm, a light-brown bioclastic sand layer mixed with coral gravels of a diameter up to 3.5 cm was identified, covered by a layer of light-brown pumiceous sand (50 to 35 cm) mixed with bioclasts at the bottom part. The 35 last cm correspond to a layer of volcanic ash containing abundant pumice lapilli. This latter underwent pedogenesis processes in the upper part.

Site U-02 is located at 6°49'45.40" S and 105°27'07.30" E, 120 m southward from U-01. Section U-02, see Figure 6-3, consists of massive silt to clay layers from the older deposits at the base (> 240 cm). Dark grey in colour, this material contains a weak amount of bioclasts near the top of layer. The base of the nest layer (240 – 180 cm) is characterized by rip-up clasts of clayey sediment mixed with yellowish coarse to fine sands and abundant bioclasts. The layer above (180 - 120 cm) is composed of a lower part of coral gravels and bioclasts mixed with gravels interrupted between 145 and 140 cm by a light-brown pumiceous sand and an upper part of coarse sand. Between 120 - 40 cm stays a yellow-white bioclastic sand layers mixed with coral gravels. At the base, it consists of bioclastic granules at the bottom and coarse bioclastic sand at the upper part. Covering the coarse bioclastic sand layer, a 40 cm dark to yellow-brown soil (the post 1883 soil) with a silty texture displays in the middle a pumice and bioclasts layer.

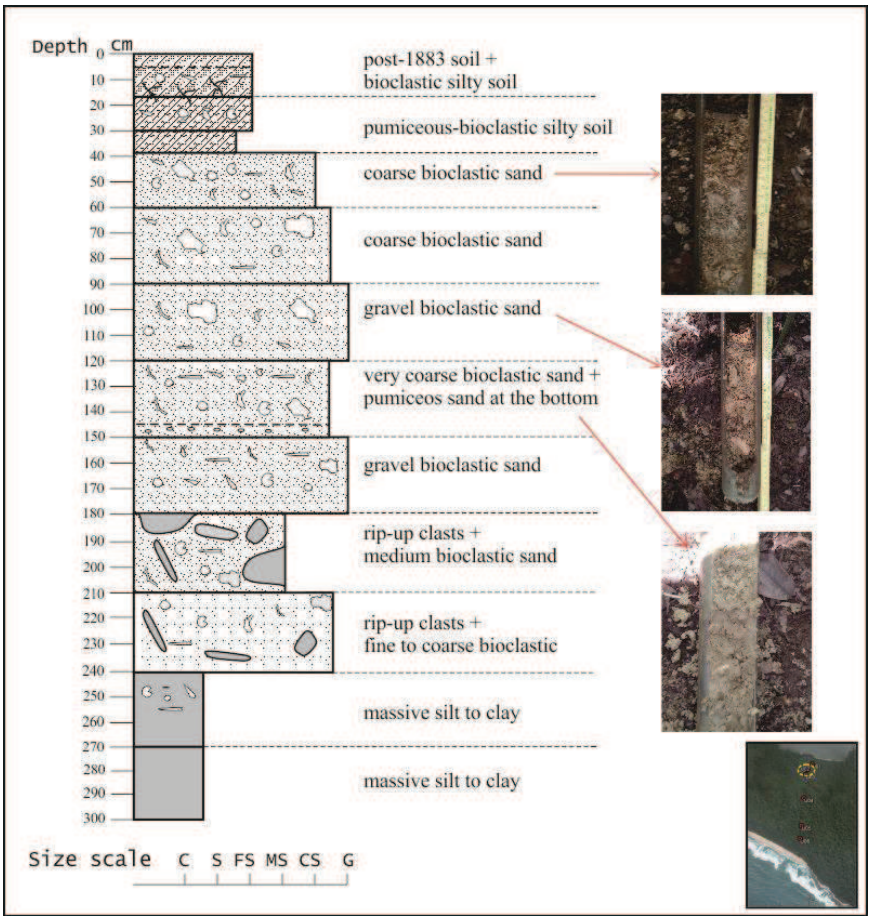

Figure 6-3. Stratigraphic profile of Section U-02; The site shown by a yellow circle line in the inset map is located 120 m from Site U-01.

Site U-03 is located at 6°49'48.30" S and 105°27'06.70" E, 90 m southward from U-02. Section U-03, see Figure 6-4, consists of grey silt to clay layers from the older deposits at the base (> 225 cm). Like for U-02, abundant bioclasts were found within the upper layer. Above, in a layer between 225 and 180 cm, rip-up clasts of clayey sediment are mixed with light-brown to yellow medium to fine sands and abundant bioclasts. Within the next layer (180 - 165 cm) rip-up clasts of clayey sediment are still present. They are mixed with yellow coarse sand. Above (165 – 150 cm), the layer is composed of fine bioclastic sand mixed with coral gravels. From 165 to 150 cm lays a gravel sand unit. Above, a layer of fine bioclastic sand (150-132.5 cm) is overlain by a coarse bioclastic sand mixed with abundant coral gravels (132.5-120 cm). Between 120 - 30 cm, three layers composed of light-grey bioclastic sand mixed with coral gravels are stacked one upon the other. From 120 to 190 cm, coarse sands, from 90 to 60 cm, medium sands, and from 60 – 30 cm, fine sands. At the surface (0-30 cm), the yellow-brown silty soil is, at the bottom, mixed with pumice and bioclasts.

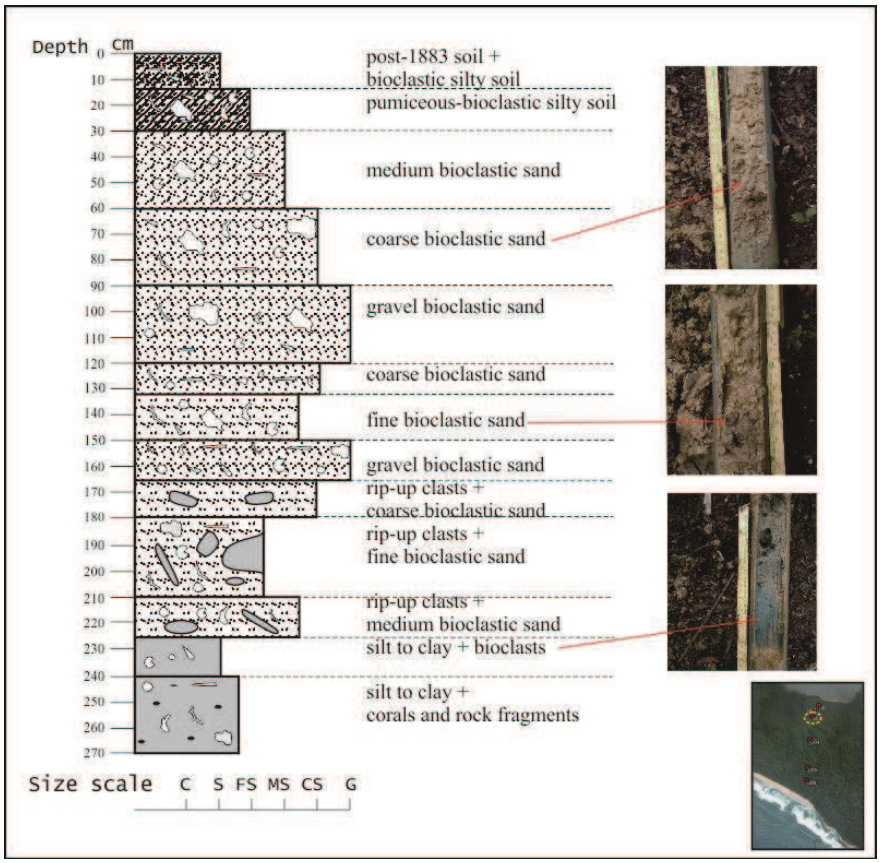

Figure 6-4. Stratigraphic profile of Section U-03; The site shown by a yellow circle line in the inset map is located 90 m from Site U-02.

Site U-04 is located at 6°50'01.50" S and 105°27'07.00" E, 400 m southward from U-03. Section U-04, see Figure 6-5, consists of a layer of sand with abundant rock fragments from the older deposits at the base (> 240 cm). Again the first layer above (240-220 cm) displays rip-up clasts of clayey sediment mixed with grey to white medium sand and abundant bioclasts.The next layers (220 - 175 cm) is composed of three sub-layers evolving from light-brown fine sand at the bottom to grey-greenish very fine sand at the top. Rip-up clasts of clayey sediment are present in all the layer. Between 175 – 135 cm, coral boulders (ϕ up to 30 cm) are present, embedded in the light-grey silty bioclastic sand layers. These layers can be divided in three: rip-up clasts within fine bioclastic sand at the base (175-170 cm), very fine sand at the middle with coral boulders (170-155 cm), and silty to fine sand bioclastic at the top (155-135 cm).

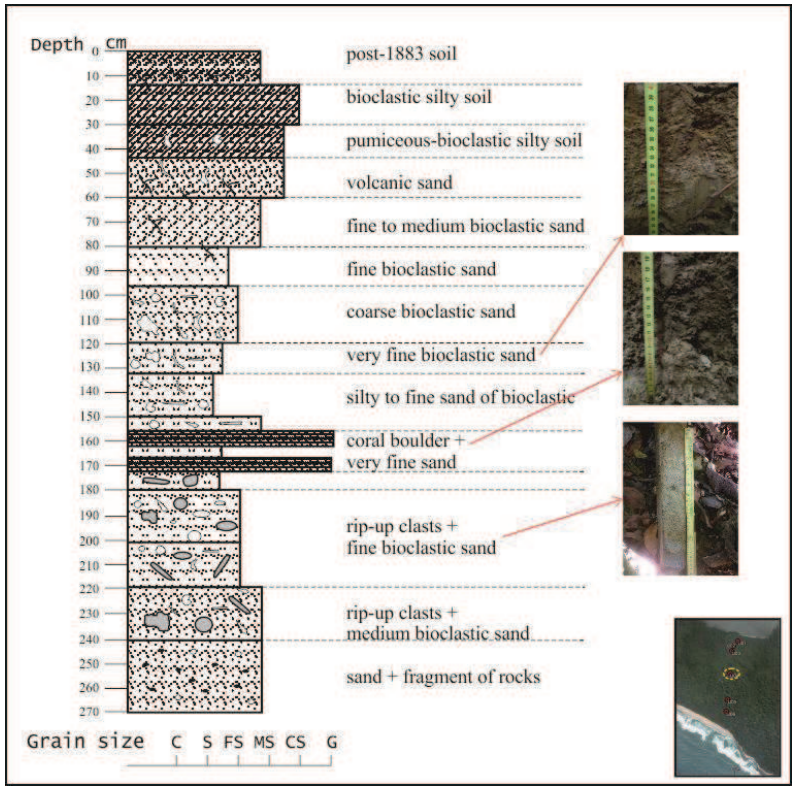

Figure 6-5. Stratigraphic profile of Section U-04; The site shown by a circle line in the inset map is located 400 m from Site U-03.

Very fine bioclastic sand mixed with coral gravels overlay these remarkable layers (at a depth of 135 - 120 cm). Between 120 and 80 cm, grey to dark yellow bioclastic sand unit can be divided in two: coarse sand at the base with coral gravels (120-97 cm) and fine

sand at the top (97-80 cm). Above, a trace of roots was found in a fine to medium yellow bioclastic sand unit (80 - 60 cm). A part of this layer has been weathered. This material is covered by a layer of volcanic sand (60-45 cm). At 45-30 cm, a yellow silty soil mixed with pumice and bioclasts is overlain by a soil, the texture of which is fining upward.

Site U-05 is located at 6°50'15.60" S and 105°27'07.10" E, 450 m southward from U-04. Section U-05, see Figure 6-6, starts at 295 cm with a 55 cm thick layer composed at the base by a sub-layer of fine welded sands containing pumice shards (ϕ 2-6 cm) followed by a medium welded sand containing pumices and rock fragments from the older deposits.

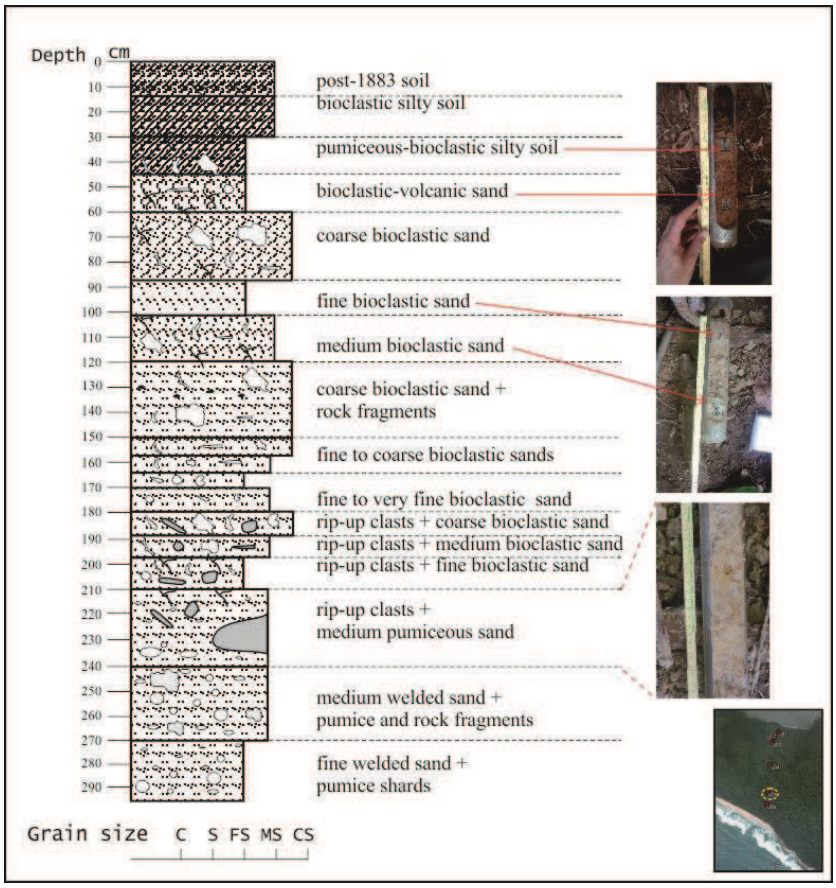

Figure 6-6. Stratigraphic profile of Section U-05; The site is located 450 m from Site U-04.

Above 240 cm, the layer characterized by rip-up clasts content was found after the base layer (at a depth between 240 – 180 cm). The first layer (at a depth of 240 – 210 cm) constitutes rip-up clasts of clayey sediment mixed with grey to white medium pumiceous sand. The next layer between 210 and 180 cm is characterized by smaller rip-up clasts

content mixed with brown sand and abundant bioclasts. This layer can be subdivided on a grain-size evolution in three: rip-up clasts mixed with fine bioclastic sand (210-197.5 cm), rip-up clasts mixed with medium bioclastic sand (197.5-188 cm), and rip-up clasts mixed with coarse bioclastic sand (188-180 cm).

A similar pattern of gradation can be evidenced above in a layer between 180 and 150 cm, where grain-size evolution allow distinguishing 4 sub-layers: fine bioclastic sand (180-170), very fine bioclastic sand (170-164), fine bioclastic sand (164-157), and coarse bioclastic sand (157-150). Above, from 150 to 120 cm, a layer of coarse bioclastic sand contains rock fragments. Between 120 and 87.5 cm, a layer of bioclastic sand can be divided in a base (120-101 cm) of medium sand and a top of fine sand (101-87.5 cm). The following layer, from 87,5 to 60 cm, is composed of yellow to brown bioclastic sand mixed with coral gravels ($\phi > 4$ cm). It displays traces of roots. A brown volcanic sand layer mixed with bioclast and showing traces of roots (60-45 cm) is then overlain by a light-brown homogenous silty soil. This soil contain pumices and bioclasts at the base (45-30 cm) and a layer rich in bioclasts (30-15 cm).

Site U-06 is located at 6°50'21.50" S and 105°27'07.00" E, 200 m southward from U-05 and 300 m from the shoreline of Indian Ocean. Section U-06, see Figure 6-7, consists of welded sand layers from the older deposits at the base (> 200 cm). These base layers are overlain by light-brown to grey sandy clay layers at a depth between 200 – 155 cm. Above, a layer of brown sand can be divided in two sub-units: at the base (155-125 cm) is very fine sands with inclusions of rip-up clasts of clayey sediment and debris of potery, at the top (125-100 cm) is a layer of fine sands including rip-up clasts.

The next layers (100-80 cm) corresponds to brown coarse bioclastic sand and contains smaller rip-up clasts. A unique layer of coarse to medium pumiceous sand mixed with trace of roots and terrigenous materials at the upper part was found at a depth of 80 - 60 cm. Above, a greyish-brown bioclastic sand layers (60-30 cm), can be divide in three sub-layers. At the base (60-47 cm) medium bioclastic sand, from 47 to 36 cm fine bioclastic sand, and at the top (36-30cm) a layer of silt. At the top of the sequence, a layer of light-brown fine volcanic sand containing bioclasts (30-10 cm) has underwent a pedogenesis and the silty soil displays traces of roots.

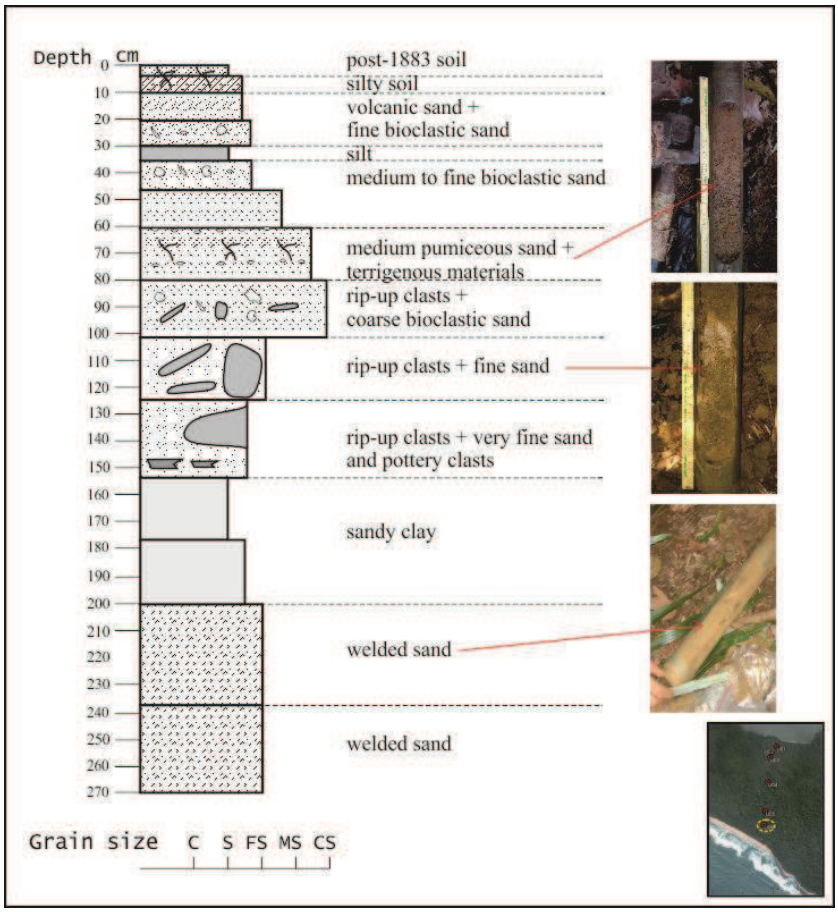

Figure 6-7. Stratigraphic profile of Section U-06; The site is located 200 m from Site U-05.

b. Cidaun drilling site (site U-08)

Cidaun is situated at the very bottom of V-shaped morphology of Cidaun Bay, in the western part of Ujung Kulon Peninsula (South of Peucang Island). One drilling site was selected at 6°45'46.55" S and 105°15'59.79" E, 400 m southeastward from the shoreline. Section U-08 resulted from a drilling core up to 350 cm below the surface can be seen in Figure 6-8.

The top of a silty soil layer was evidenced at 350 cm. This soil surface is covered by a layer of silty-clay containing a weak amount of bioclasts (350-315 cm).The top of this layer constituted the ante-1883 surface. From 315 to 280, stays a layer of fine to medium bioclastic sand which contains rip-up clasts of clayey sediment of different sizes. Above is met a grey medium bioclastic sand at a depth between 280 and 245 cm. These two marine sediment layers are overlain by volcanic grey ash containing abundant dark minerals mixed with wood remains at the bottom (245-210 cm).

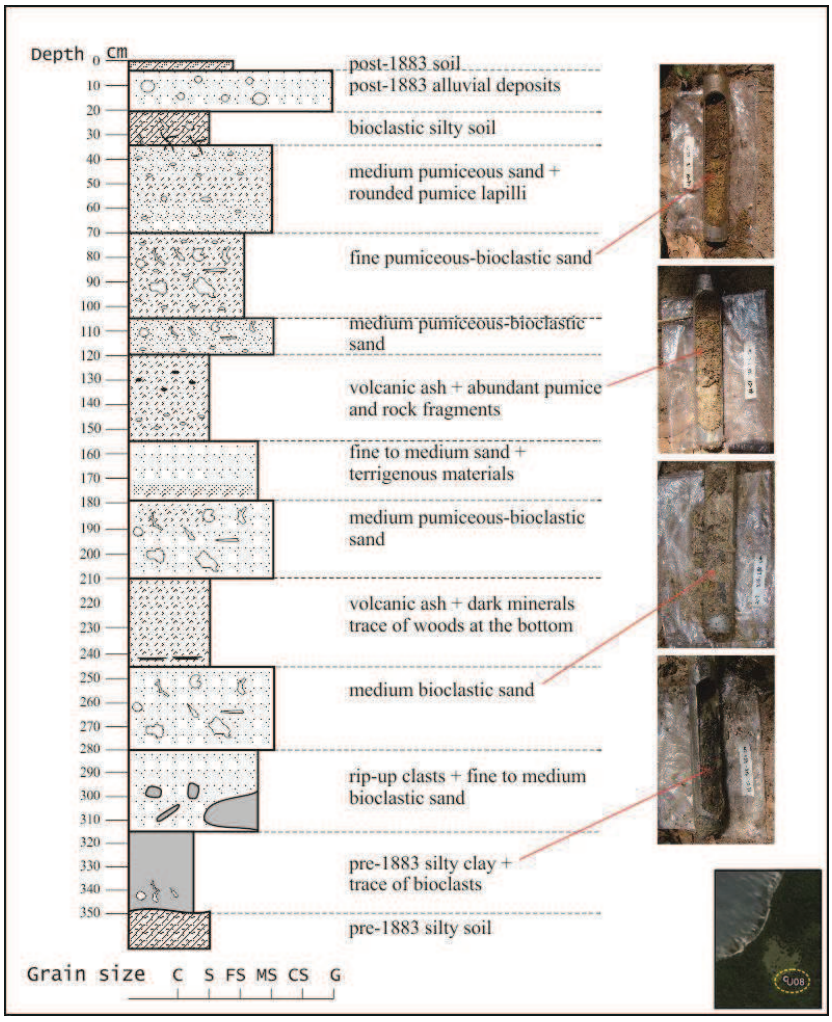

Figure 6-8. Stratigraphic profile of Section U-08; The site shown by a circle line in the inset map is located 400 m from the coast.

The second sand unit is between 210 and 156 cm. It is composed of a lower layer (210-180 cm) of greyish-brown medium pumiceous-bioclastic sand and an upper layer (180-156 cm) of fine to medium sand displaying discontinous layer of terrigenous materials. Above, stays a layer of volcanic ash with abundant pumice and rock fragments (156-120 cm).

The third sand unit is found at a depth between 120 and 35 cm. It consists of three sub-units as follow: yellowish medium pumiceous-bioclastic sand (120-105 cm), fine pumiceous-bioclastic sand (105-70 cm), and medium sand mixed with rounded pumice lapilli (70-35 cm). This sandy unit is characterized by an increasing abundance of pumice and a correlative decreasing abundance of bioclasts upward. A silty soil containing

numerous bioclasts is developed at the top of this sandy sequence between 35 and 20 cm. This layer is covered by recent alluvial deposits and on which a recent thin (4 cm) sandy soil is evolving.

6.1.2. Outcrops observations

a. Karang Ranjang coastal outcrop (site U-07)

An outcrop of sandstone was found at the coast of Karang Ranjang Bay, a bay at the South side of Laban Isthmus that open to the Indian Ocean. This geological evidence is situated at 6°50'31.90" S and 105°27'09.20" E. The outcrop corresponds to alternating layers of calcareous sandstone containing clay nodule and tuffaceous sandstone from the Tertiary sedimentary deposit of Bojongmanik Formation (Figure 6-9a).

At the base (110 – 40 cm), a light-brown medium to coarse tuffaceous sandstone contains bioclasts and rock fragments. At the upper part (< 40 cm), a coarse grey calcareous sandstone has been compacted and mixed with clay nodules, bioclasts, quartz minerals, and rock fragments. Clay nodules were characterized by a colour of dark grey to green.

b. Cigenter River outcrop (site U-10)

A remarkable deposit was exposed along the River of Cigenter, in the northeastern part of Ujung Kulon Peninsula, near Handeuleum Island. The selected site has been profiled as Section U-10, at 6°45'00.20" S and 105°23'50.80" E, 300 m southwestward from the shoreline, see Figure 6-9b.

Section U-10, consists of a grey to brown volcanic ash at the base (at a depth deeper than 100 cm). Above is a layer of brown medium pumiceous-bioclastic sand (100-60 cm) overlain by a grey fine pumiceous-bioclastic sand (60-17.5 cm). At the top of this latter layer, a soil developped post-1883 event. The overall, sequence is strongly weathered.

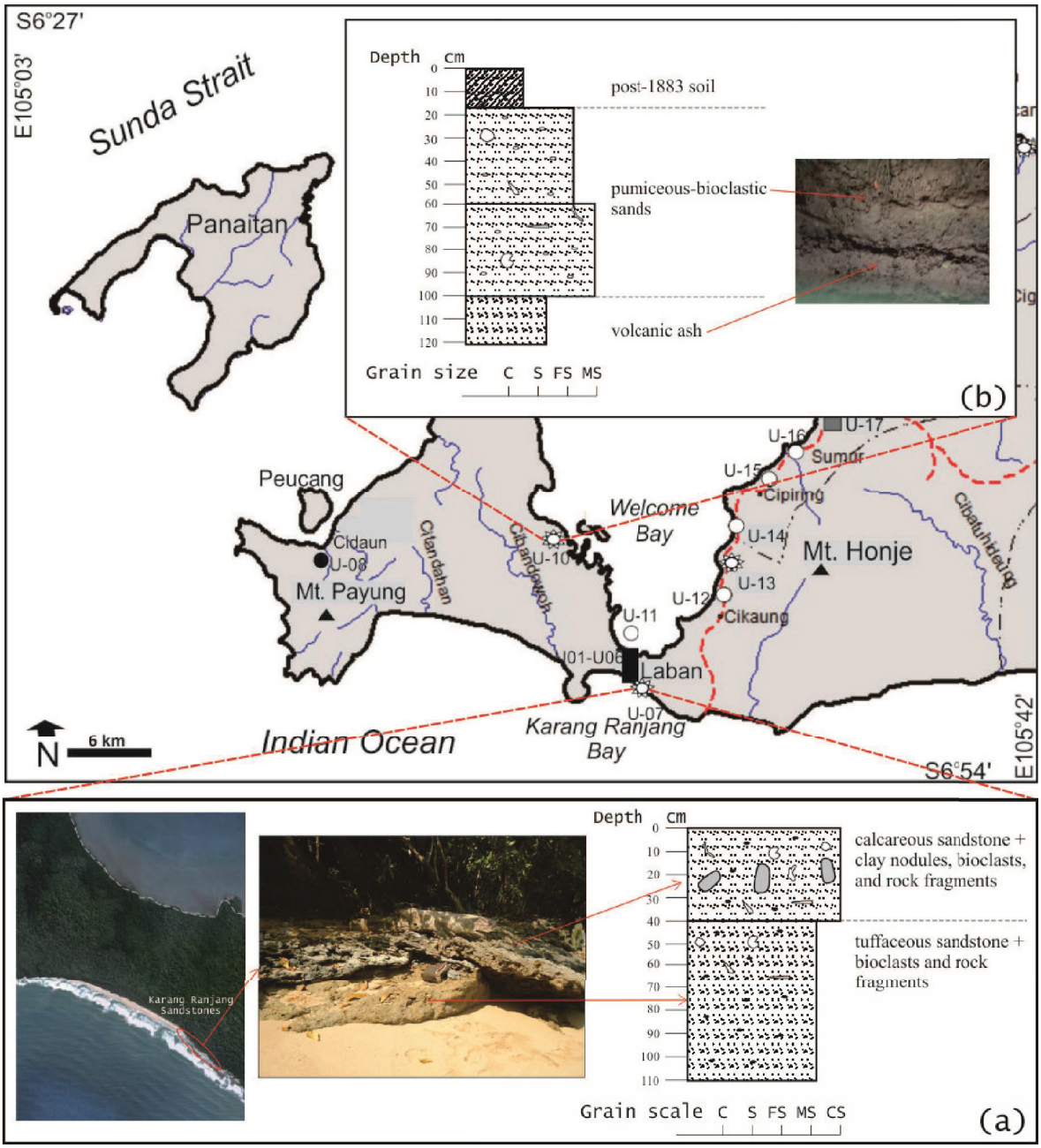

Figure 6-9. Stratigraphic profiles of Sections U-07 and U-10; (a) Section U-07 is a coastal outcrop of Karang Ranjang located at the south side of Laban Isthmus. (b) Section U-10 was made from an outcrop along the River of Cigenter, 300 m from the shoreline.

c. Tamanjaya outcrop (site U-13)

Tamanjaya outcrop is a natural outcrop on the bank of a small river between Cikaung Village and Cipiring Village, at 6°46'18.00" S and 105°30'31.60" E, 550 m eastward from the shoreline (Figure 6-10). Section U-13, then, can be described as follow:

- A light brown sandy soil considered as the 1883-surface was found at the base (> 270 cm deep).
- Above the soil, a layer of sediments mixed with grey ash (270-215 cm), contains numerous clayey rip-up clasts.
- Between 215 and 170 cm, a layer of brown to grey fine bioclastic sand displays rip-up clasts at the base.
- Above, brown to grey pumiceous ash are mixed with abundant rock fragments (170-70 cm).
- At top, this volcanic unit is overlain by alluvial deposits, heteroimetric material (from silt to cobble) and is covered by a soil.

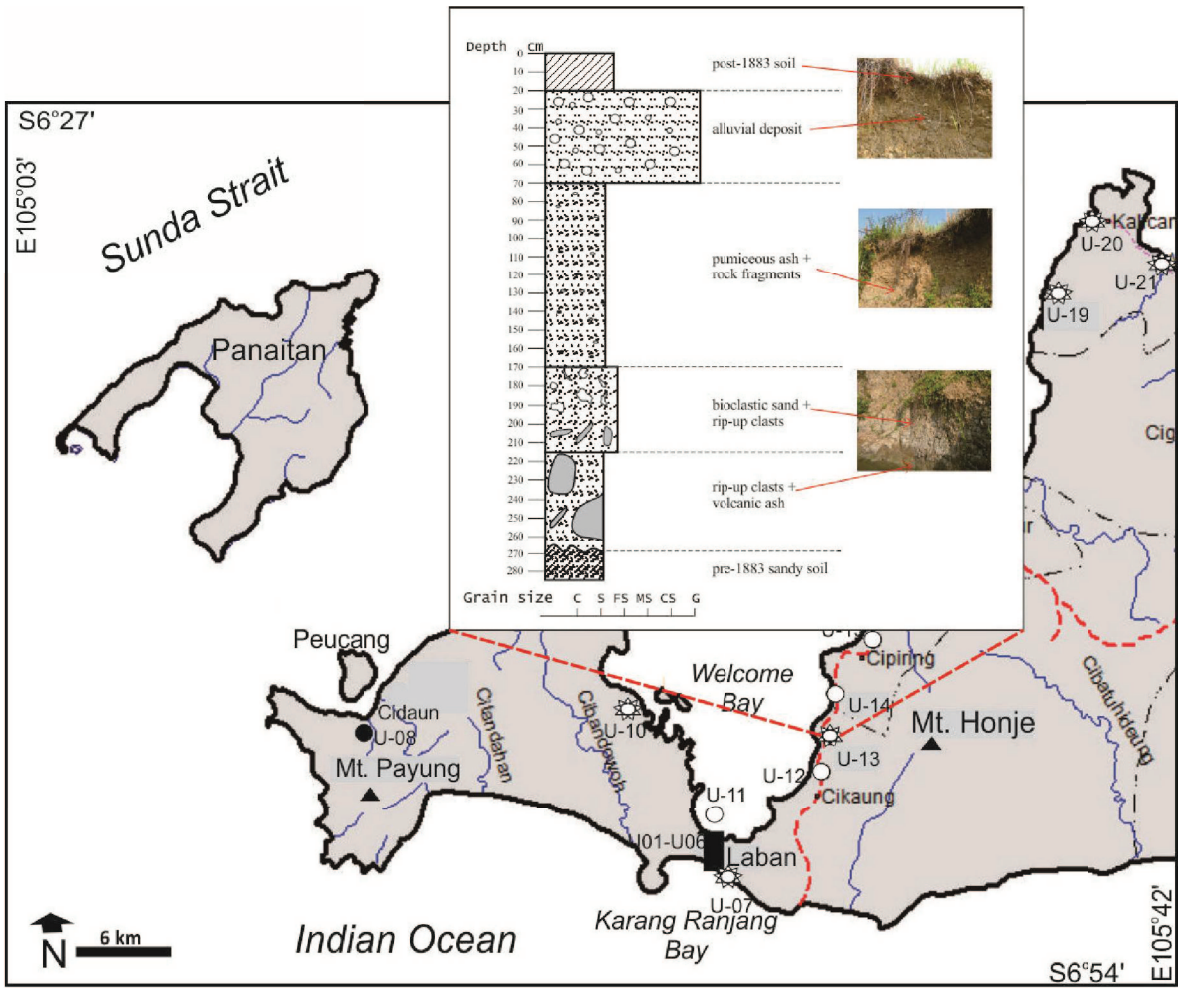

Figure 6-10. Stratigraphic profiles of Section U-13; The section shown by an inset figure was based on the outcrop located 550 m from the shoreline. The outcrop is situated on the bank of small river between Cikaung Village and Cipiring Village.

d. Sumur entrenchment (site U-17)

An existing local entrenchment near the Village of Sumur, about 70 - 100 cm depth and 5 m length, was used to observe the Krakatau tsunami deposits (Figure 6-11a). This trench is located at 6°40'57.70" S and 105°34'16.60" E, 150 m eastward from the shoreline. Stratigraphic profile of Section U-17 can be described as follow: Between 80 and 55 cm, a coarsening upward layer of grey pumiceous ash layers, with abundant mafic minerals at the base (> 70 cm deep). Above this 70 cm limit, a thin layer (70-65 cm) of medium bioclastic sand interrupted the sequence. A grey fine pumiceous-bioclastic layer (55-45 cm) overlain a coarsening upward grey sand with abundant trace of roots (45-20 cm). At the surface, a grey to dark brown fine bioclastic sand underwent a post-1883 pedogenesis.

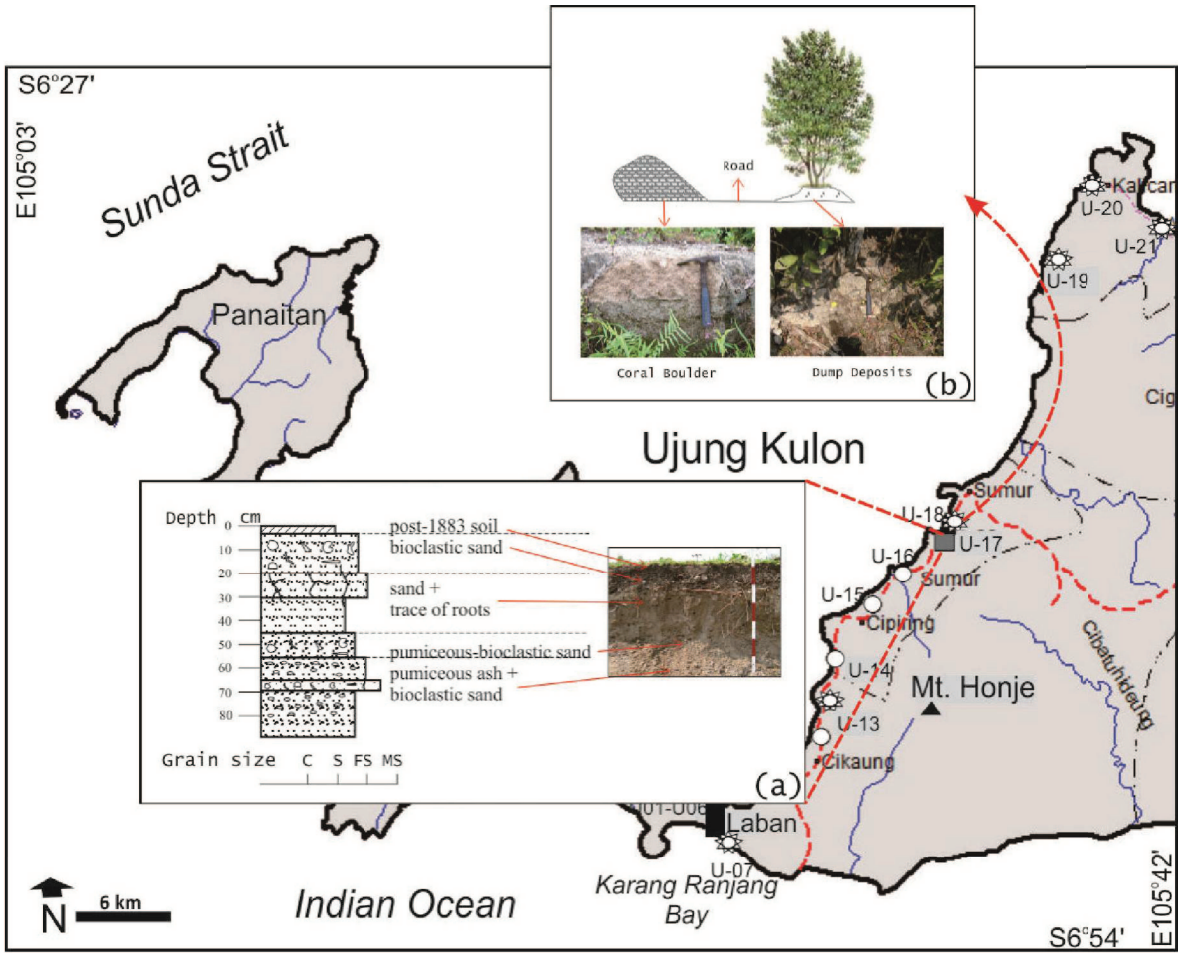

Figure 6-11. Stratigraphic profiles of Sections U-17 and U-18; (a) Section U-17 is an existing entrenchment located near the Sumur Village. (b) Section U-18 is a dump deposit and a large coral boulder found along the roadside near the Sumur Village.

e. Sumur dump deposit (site U-18)

Dump deposit was found at site U-18 (6°40'35.70" S and 105°34'22.80" E), 200 m from the shoreline, near the Village of Sumur (Figure 6-11b). The deposit consists of marine molluscs, such as Pelecypoda (Bivalvia) and Gastropoda, mixed with coral gravels, cobbles, pebbles, sand, clay, grey ash, pumice, and rock fragments. Large coral boulders (ϕ 1 - 2 m) was also found along with this dump deposit.

f. Tanjungjaya outcrops (sites U-19, U-20, and U-21)

Tanjungjaya outcrops are scattered along a cross road of Tanjungjaya (a region near the western tip of Teluk Lada or *Pepper Bay*) to Sumur Village. Three sections were made on the basis of the outcrops exposed at the roadside, i.e. sections U-19, U-20, and U-21.

Section U-19 located at 6°31'43.70" S and 105°37'37.40" E, 100 m from the shoreline, was identified as the Tertiary volcanic deposits from Honje Formation (Figure 6-12a). A white to dark grey tuff was found below 20 cm from the surface with the thickness more than 100 cm. Above this layer, a 20 cm brown silty soil was developed from tuff surface.

Section U-20 contains remaining of tsunami deposit emplaced in this region (Figure 6-12b). Located at 6°29'55.70" S and 105°38'55.00" E, 350 m from the shoreline, the section consists of a brown to dark brown very fine sand at the base (at a depth more than 40 cm), a thin layer of white to grey coarse pumiceous-bioclastic sand (40-20 cm), and above, the post-1883 silty soil.

Section U-21 located at 6°31'14.90" S and 105°41'06.30" E, 150 m from the beach of Pepper Bay, was identified as the Tertiary volcanic deposits from Cimapag Formation at the base and the sedimentary deposits from Bojongmanik Formation at the upper part (Figure 6-12c). A yellow matrix supported tuff breccia was found below 205 cm from the surface with a thickness more than 200 cm. Above this layer, at a depth of 205 – 175 cm, a yellow fine to medium pumiceous tuff overlain the tuff breccia. This unit was then covered by a yellowish-brown fine to medium sandstone (at 175 -155 cm). A thin layer of black to brown fractured claystone was found between 155 – 140 cm. At the upper part, between 140-20 cm, a reddish-brown claystone displays parallel lamination. This layer is partly weathered, even at the top, where a clayey soil has been developed.

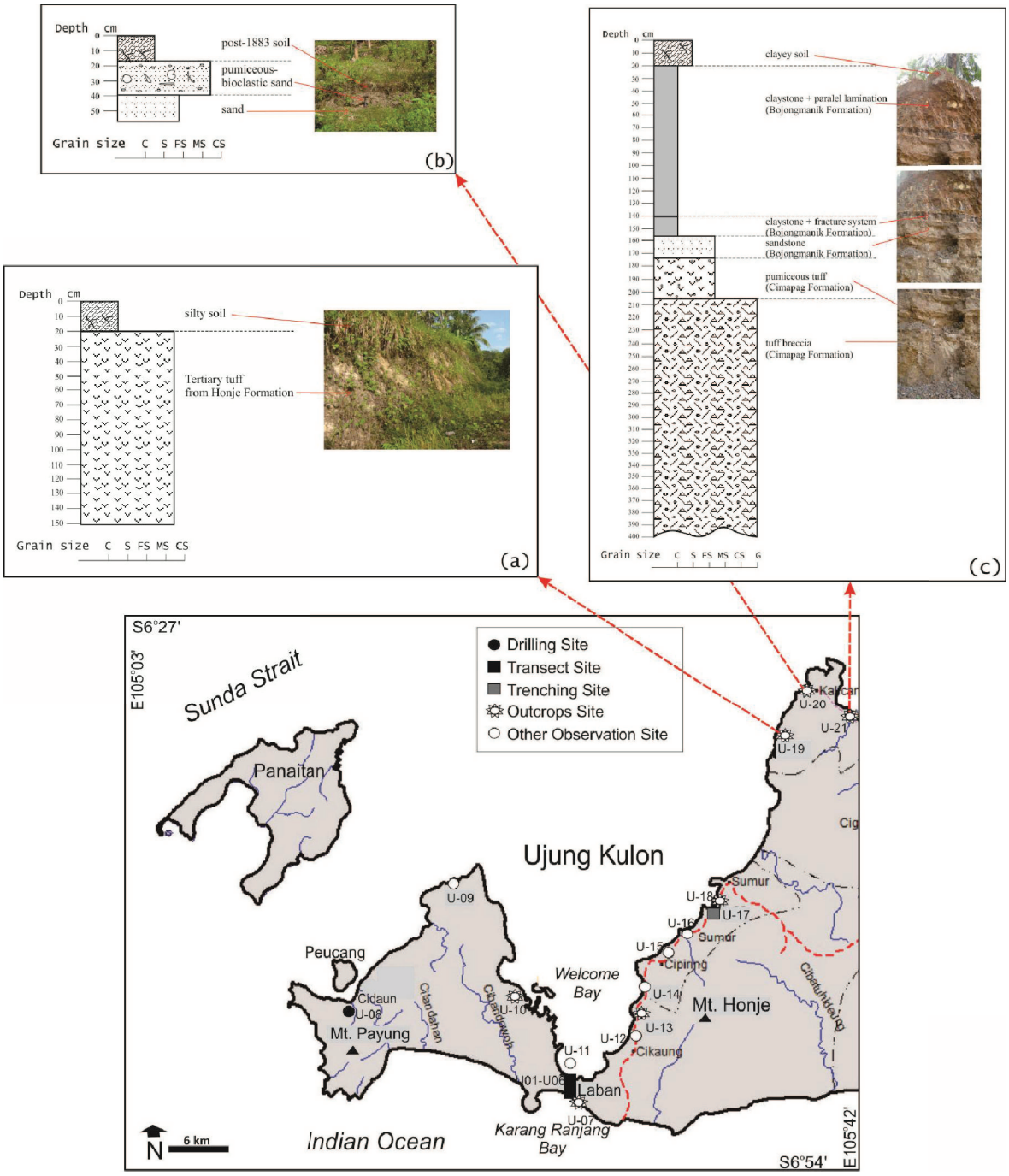

Figure 6-12. Stratigraphic profiles of Sections U-19, U-20, and U-21; (a) Section U-19 is an outcrop of old volcanic deposit from Honje Formation, located at the cross road between Tanjungjaya - Sumur. (b) Section U-20 is a thin layer of remaining tsunami deposit found at the roadside near Tanjungjaya Village. (c) Section U-21 is an outcrop of Tertiary deposits from Cimapag Formation and Bojongmanik Formation located near the western coast of Pepper Bay – Panimbang, 150 m from the shoreline.

6.1.3. Other observations

a. Sand dunes (sites U-07 and U-09)

Sand dunes were identified at the coast of Karang Ranjang (site U-07), and Tanjung Alang-alang (site U-09: at 6°39'11.22" S and 105°21'54.25" E). In general, the dunes were composed of white to light-brown very loose beach sands mixed with coral gravels, shells, pumice, quartz, mafic minerals, and rock fragments. The dimension of Karang Ranjang sand dune was about 2 – 3 m in height and 10 – 20 m in width, while the larger Tanjung Alang-alang sand dune was 4 – 5 m high and 40 – 50 m wide (Figure 6-13).

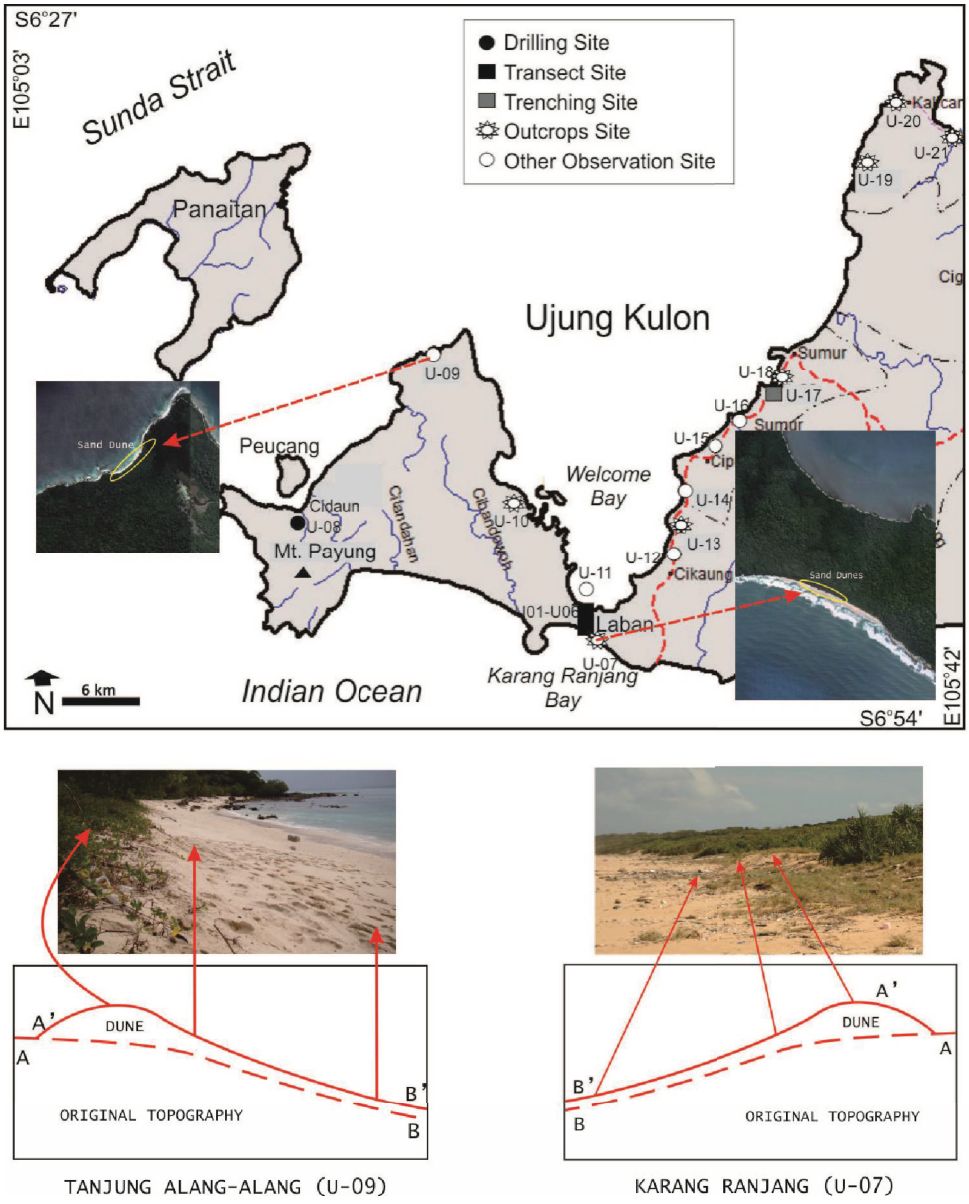

Figure 6-13. Sand dunes and their profiles at sites U-07 and U-09; The Karang Ranjang sand dune (U-07) is smaller than the dune at Tanjung Alang-alang.

b. Large coral boulders (sites U-09 and U-15)

Coral boulders with diameter more than 2 m were found lying on the coast of Tanjung Alang-alang (U-09). At site U-15 (6°43'14.50" S and 105°31'55.10" E), near Cipiring Village, the large coral boulders were scattered on the middle part of a paddy field, up to 700 m from the shoreline (Figure 6-14). This region is a part of Mount Honje narrow coastal plain, usually called "shore platform". This latter was defined as wave-cut platform by Ongkosongo (1985) in his figure of coral boulders emplaced by tsunami waves in Anyer Kidul.

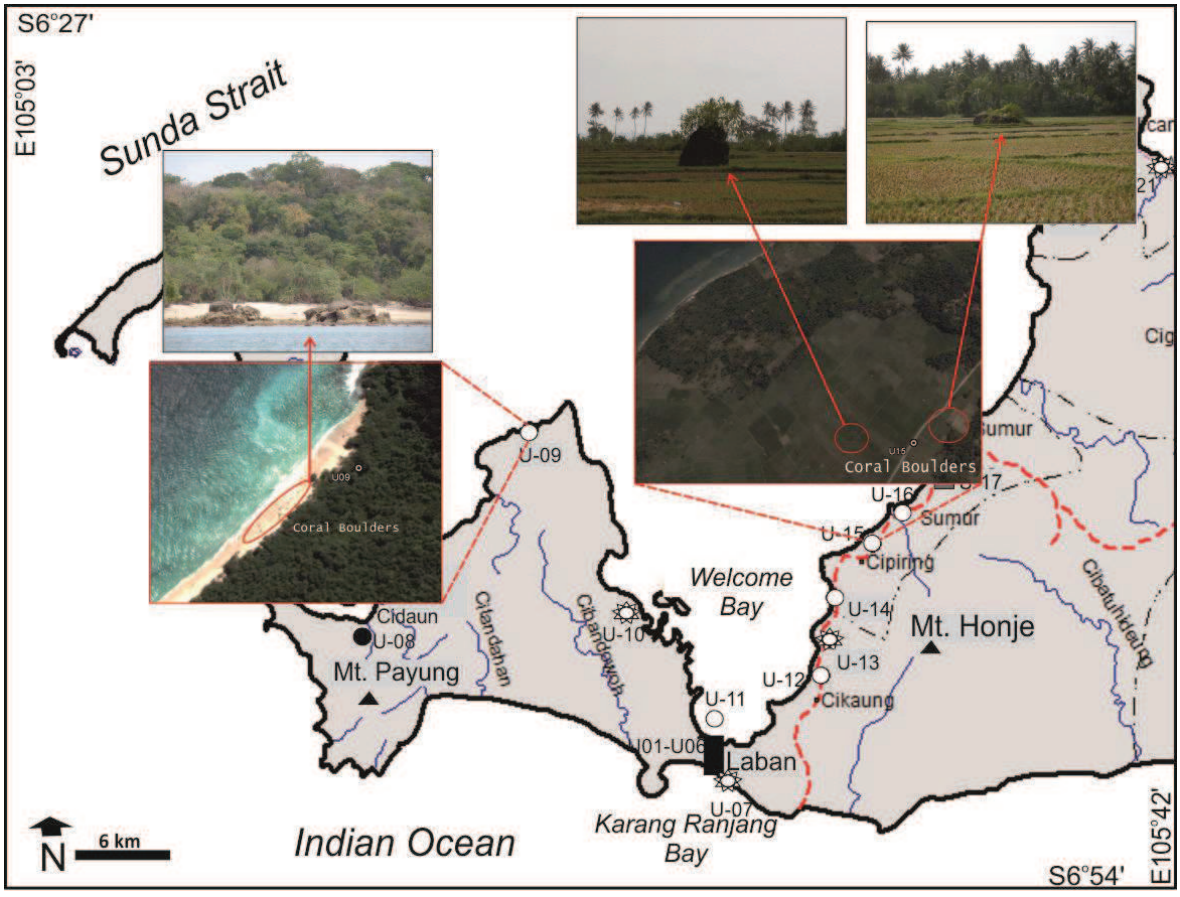

Figure 6-14. Large coral boulders at sites U-09 and U-15; The boulders are scattered on the coast of Tanjung Alang-alang (U-09) and on the middle part of paddy field near Cipiring Village (U-15).

c. Coastal landforms (sites U-11, U-12, U-14, and U-16)

V-shape morphology of Welcome Bay is delineated by the coastline of Ujung Kulon Peninsula in the western part, the tidal zone of Laban Isthmus in the center, and the narrow coastal plain of Mount Honje region in the eastern part. The peninsula and the isthmus

were identified as a peneplain produced by fluvial erosion that would, in the course of geologic time, reduce the land almost to baselevel (sea level), leaving so little gradient that essentially no more erosion could occur (Davis, 1889).

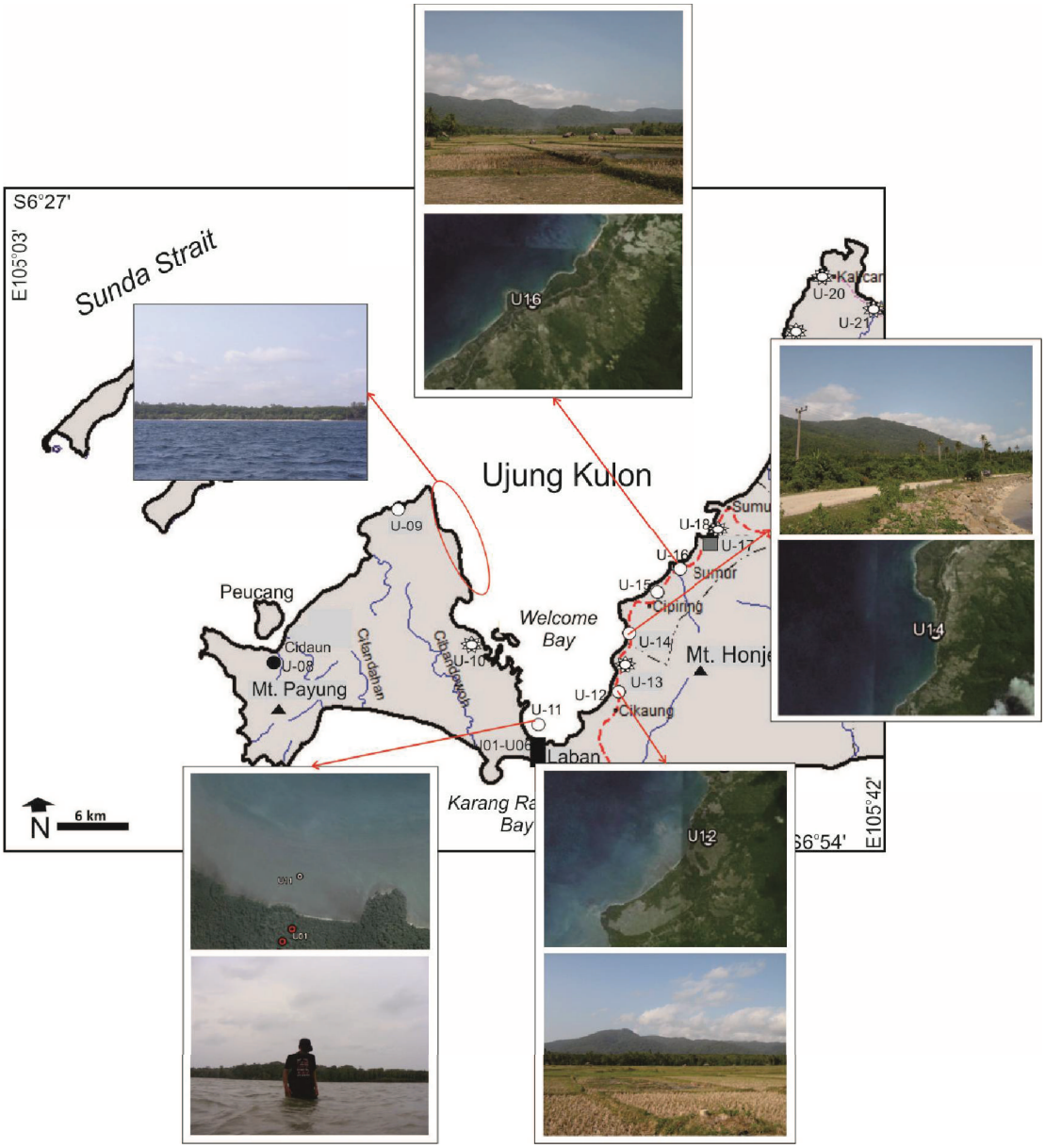

Figure 6-15. Coastal landforms of Welcome Bay observed from the vessel, at sites U-11, U-12, U-14, and U-16; The western part of the bay constitutes a peneplain of Ujung Kulon Peninsula, including the isthmus in the extreme tip of this V-shape bay, while the eastern part of the bay is a shore platform of Mount Honje region.

From site U-11 (6°49'27.90" S and 105°27'09.90" E) recorded on a wide tidal zone of Laban Isthmus, i.e. a zone of mean sea level with more than 500 m wide in the northern

part of the isthmus including the silty sediments accumulated in the bottom of the bay, Ujung Kulon Peninsula was seen almost featureless plain with a dense tropical rain-forest dominated by *Arenga obtusifolia* (palm tree) with homogen height up to 16 m (Hommel, 1990), see Figure 6-15 above.

The narrow coastal plain in the eastern part of V-shape bay was identified as a shore platform, i.e. an erosional feature developed by a combination of processes, including wave action, subaerial weathering and biogenic activity (Masselink et al., 2014). The platforms were lowered and extended through time. At sites U-12 (6°47'25.40" S and 105°30'18.30" E), U-14 (6°44'56.80" S and 105°30'43.10" E), and U-16 (6°42'12.00" S and 105°32'50.00" E), the shore platforms have been mostly changed to be a paddy field (Figure 6-15).

The results of field investigations show that Ujung Kulon Peninsula displays remarkable recordings of tsunamis, e.g. thick deposits of tsunami sand unit, coral boulders embeded in sand, and large coral boulders scattered far inland. These evidences are well preserved due to the situation of Ujung Kulon Peninsula as a UNESCO natural reserve or a National Park. In contrast, the depositional signatures of tsunami on the narrow coastal plain of Mount Honje are not well preserved, because this shore platform has been mostly and deeply transformed in paddy fields. Only a thin layer of tsunami deposit has remained at some places, along with large coral boulders (the smaller ones have been broken and used to realize house foundations in the villages), and dump deposits. Even most of the outcrops only display the basement rock from the Tertiary volcanic and sedimentary deposits. This latter indicates that the unconsolidated sediments in this region are easily erasable whether by natural or anthropic action.

6.2. Grain-size laboratory analysis

Grain-size analysis were performed for all sediment samples collected from Ujung Kulon Peninsula, including the isthmus, and some selected samples from Mount Honje region. The results presented in Table 6-1 show that the deposits consist of coarse sand to silt. The frequency grain-size curves evidence unimodal distribution, i.e. a distribution with one clear peak or most frequent value.

Table 6-1. Grain-size distribution parameters for the samples collected from the study area.

Samples Code	Mean Depth	Mean Grain-size ϕ	Mean Grain-size μm	Standard Deviation	Skewness	Kurtosis
U-01 001	17.5	5.46	22.73	2.54	-0.44	0.85
U-01 002	42.5	2.05	241.45	2.69	-0.41	1.32
U-01 003	60.0	1.20	435.90	1.85	-0.33	1.16
U-01 004	87.5	1.47	361.74	2.27	-0.42	1.61
U-01 005	110.0	2.28	206.67	2.76	-0.40	1.64
U-01 006	120,0	1.29	409.63	1.65	-0.21	1.41
U-01 007	150.0	1.11	463.81	2.08	-0.47	1.27
U-01 008	192.5	1.42	373.10	1.88	-0.31	1.23
U-01 009	205.0	1.60	329.51	1.96	-0.12	1.14
U-01 010	245.0	1.69	309.61	2.13	-0.05	1.08
U-01 011	0.0	0.93	525.30	1.25	-0.29	1.82
U-02 001	7.5	3.98	63.40	2.23	-0.34	2.14
U-02 002	25.0	3.98	63.42	1.75	-0.46	1.81
U-02 003	35.0	4.56	42.33	3.11	-0.34	1.13
U-02 004	50.0	1.33	397.05	1.88	-0.24	1.38
U-02 005	75.0	1.11	463.83	1.50	-0.28	1.39
U-02 006	105.0	1.06	478.49	1.52	-0.37	1.54
U-02 007	135.0	1.11	463.92	1.73	-0.38	1.46
U-02 008	160.0	1.06	478.43	1.39	-0.26	1.02
U-02 009	180.0	1.06	478.43	1.39	-0.26	1.02
U-02 010	195.0	2.45	182.42	2.78	-0.27	1.05
U-02 011	225.0	1.15	449.61	1.96	-0.39	1.14
U-03 001	7.5	5.73	18.86	2.12	-0.17	0.98
U-03 002	25.0	5.41	23.45	2.47	-0.26	1.16
U-03 003	45.0	3.58	83.87	3.75	-0.43	0.79
U-03 004	75.0	1.29	409.63	1.77	-0.24	1.70
U-03 005	105.0	0.97	509.26	1.65	-0.30	1.51
U-03 006	125.0	1.42	373.19	2.47	-0.42	1.92
U-03 007	140.0	3.35	98.01	3.66	-0.27	0.82
U-03 008	160.0	1.11	463.77	1.63	-0.27	1.38
U-03 009	170.0	1.87	273.42	2.52	-0.46	1.29
U-03 010	195.0	1.60	329.47	1.48	-0.07	1.47
U-03 011	195.0	4.34	49.45	2.02	-0.61	1.53
U-03 012	217.5	2.41	188.28	2.23	-0.02	1.13
U-03 013	232.5	5.95	16.15	2.59	-0.32	1.29
U-03 014	255.0	2.59	166.22	3.01	-0.39	0.90
U-04 001	7.5	5.06	30.07	1.89	-0.55	1.37
U-04 002	25.0	3.67	78.83	1.97	-0.42	1.56
U-04 003	45.0	4.38	47.943	1.76	-0.61	1.58
U-04 004	80.0	5.06	30.07	4.06	0.08	0.72
U-04 005	75.0	5.37	24.19	2.23	-0.62	1.13
U-04 006	95.0	5.64	20.07	2.59	-0.42	0.92
U-04 007	110.0	5.50	22.03	3.08	-0.32	1.21
U-04 008	125.0	5.86	17.18	2.66	-0.47	0.89
U-04 009	135.0	5.77	18.28	2.62	-0.49	0.89
U-04 010	155.0	5.06	30.07	3.82	-0.05	1.00
U-04 011	165.0	5.19	27.394	3.08	-0.40	1.09
U-04 012	165.0	6.04	15.17	3.31	-0.13	1.03
U-04 013	175.0	6.13	14.258	2.86	-0.24	0.85
U-04 014	195.0	5.64	20.07	2.66	-0.49	0.96
U-04 015	205.0	5.55	21.354	3.20	-0.22	1.07
U-04 016	225.0	5.28	25.74	3.00	-0.37	1.18
U-05 001	7.5	4.38	47.94	2.46	-0.68	1.80
U-05 002	25.0	4.52	43.67	2.22	-0.60	1.09
U-05 003	45.0	5.86	17.18	2.45	-0.60	1.10
U-05 004	75.0	3.67	78.83	2.44	-0.61	2.27
U-05 005	95.0	5.28	25.74	2.63	-0.68	1.23
U-05 006	110.0	4.25	52.61	2.50	-0.57	1.69
U-05 007	135.0	3.35	97.99	2.80	-0.35	1.85
U-05 008	155.0	3.22	107.59	2.90	-0.42	1.84
U-05 009	160.0	5.77	18.28	2.62	-0.50	0.93
U-05 010	167.5	6.22	13.40	2.69	-0.42	0.86
U-05 011	175.0	4.70	38.55	2.67	-0.59	1.16
U-05 012	185.0	4.38	47.93	2.91	-0.49	1.18
U-05 013	195.0	5.82	17.73	3.08	-0.29	1.02
U-05 014	205.0	6.72	9.52	2.33	-0.16	0.99
U-05 015	225.0	5.41	23.45	3.29	0.10	0.96
U-05 016	255.0	5.46	22.73	4.13	0.17	0.71
U-05 017	282.5	6.58	10.45	3.01	-0.16	0.96
U-06 001	1.5	4.56	42.33	2.86	-0.23	1.15
U-06 002	11.5	3.62	81.31	2.54	-0.26	1.55
U-06 003	25.0	3.58	83.89	1.59	-0.37	2.42
U-06 004	34.0	4.65	39.77	2.20	-0.58	1.54
U-06 005	39.5	3.58	83.90	2.69	-0.32	1.52
U-06 006	42.5	2.23	213.20	2.46	-0.24	1.35
U-06 007	49.5	2.90	133.69	2.04	-0.45	2.12
U-06 008	65.0	2.36	194.23	1.65	-0.19	1.74
U-06 009	81.0	1.96	256.89	1.75	-0.20	1.81
U-06 010	81.0	2.50	176.92	2.63	-0.59	2.28
U-06 011	102.0	2.63	161.13	1.83	-0.30	1.73
U-06 012	102.0	6.49	11.12	3.29	-0.49	0.76
U-06 013	132.0	3.68	78.82	2.40	-0.43	1.79
U-06 014	132.0	4.61	41.04	3.85	-0.56	0.95
U-06 015	162.0	5.95	16.14	3.67	-0.42	1.04
U-06 016	192.0	4.07	59.57	2.90	-0.63	1.42
U-06 017	222.0	2.54	171.51	2.52	-0.62	2.33
U-07 001	0.0	1.92	264.99	0.52	0.14	1.15
U-07 002	0.0	2.14	226.91	0.52	-0.07	1.15
U-08 001	17.5	1.42	373.15	1.35	-0.30	1.42
U-08 002	52.5	1.69	309.57	1.71	-0.41	2.30
U-08 003	87.5	2.05	241.43	2.39	-0.61	1.93
U-08 004	112.5	1.69	309.61	2.24	-0.61	1.59
U-08 005	130.0	1.92	265.06	2.64	-0.69	1.14
U-08 006	148.0	1.69	309.66	2.10	-0.55	1.76
U-08 007	165.5	1.78	290.96	2.31	-0.60	1.34
U-08 008	192.5	2.23	213.20	2.73	-0.52	1.12
U-08 009	227.5	2.23	213.21	2.52	-0.24	1.04
U-08 010	252.0	2.99	125.71	3.32	-0.25	0.85
U-08 011	269.5	3.53	86.54	3.37	-0.18	0.84
U-08 012	297.5	2.14	226.91	2.23	0.11	0.99
U-08 013	0.0	1.51	350.62	0.90	0.26	0.96
U-09 001	0.0	0.84	558.97	0.83	0.07	0.87
U-10 001	110.0	6.36	12.21	2.50	-0.27	0.91
U-13 001	85.0	7.43	5.79	3.14	-0.01	0.82
U-13 002	185.0	6.45	11.47	3.00	-0.27	0.75
U-13 003	0.0	2.01	249.10	0.74	0.20	1.17
U-17 001	2.5	4.47	45.05	3.27	-0.35	0.89
U-17 002	15.0	1.83	282.06	2.55	-0.46	1.41
U-17 003	25.0	1.47	361.68	1.71	-0.37	1.61
U-17 004	35.0	2.68	156.26	3.06	-0.47	1.04
U-17 005	50.0	2.05	241.43	2.42	-0.52	1.29
U-17 006	0.0	0.88	541.83	1.32	-0.41	0.82
U-20 001	5.0	7.34	6.16	2.12	-0.17	0.99
U-20 002	25.0	0.93	525.23	2.16	-0.53	2.42
U-20 003	45.0	4.52	43.67	3.39	-0.30	0.93

The mean grain-size for the samples collected from the sites around the Sunda Strait (U-01, U-02, U-03, U-08, U-09, U-10, U-11, U-13, U-17, U-20) ranges from 0.84 ϕ (558.97 μm) to 7.43 ϕ (5.79 μm), yet, in general the mean grain-size is not bigger than 5 ϕ. In contrast, the samples collected from the sites near Indian Ocean (U-05, U-06, U07) display mean grain-size between 1.92 ϕ (264.99 μm) and 6.72 ϕ (9.52 μm) with a general mean grain-size is 3 - 6 ϕ. This latter is almost similar with the mean grain-size in section U-04, in the middle of Laban Isthmus, between 3.67 ϕ (78.83 μm) and 6.13 ϕ (14.26 μm).

Each section shows a fining upward repetition as well as a trend of deposit fining landward. The sediments inland (within the sections U-04 and U-05) are finer than in other sections that are generally situated near the shoreline. The coarsest sediment (0.84 ϕ) was collected from the deposit at Cigenter River (section U-10), in the northeastern part of Ujung Kulon Peninsula. While the finest sediment (7.43 ϕ) was collected from the pumiceous ash layer exposed at the small river between CikaungVillage and Cipiring Village (section U-13), in the Mount Honje region. Yet, this layer cannot be considered as a 1883-tsunami deposit due to its position that is overlain by the old alluvial deposits in the bank of river. It is probably associated to the ash emplaced by pre-1883 eruptive activity. Therefore, the finest sediment of tsunami deposit is about 7.34 ϕ which was collected from a thin layer of remaining tsunami deposit found at Tanjungjaya Village (U-20).

The standard deviation ranges from 0.52 to 4.13 (classified as interval 1.00 to >4.00), indicating the poorly to extremely poorly sorted sediment layers (Blott and Pye, 2001; Folk and Ward, 1957), as commonly found in debris flow (Major, 1997) and tsunami deposits (Kortekaas and Dawson, 2007). The skewness for all deposits ranges from -0.69 to 0.26 showing that the sediment layers are generally composed of very coarse to fine particles (Blott and Pye, 2001; Folk and Ward, 1957). Very coarse particles with skewness between -1.0 and -0.3 (coarse skewed) are dominant at sections U-01, U-05, and U-06 (see Figure 6-16 for example), whereas at U-02, U-03, and U-04 the skewness fluctuate vertically between coarse and fine skewed (see Figure 6-17 for example). The range of kurtosis (0.71-2.42) displays the curves between platykurtic (0.67-0.90) and very leptokurtic (1.50-3.00) (Blott and Pye, 2001; Folk and Ward, 1957). In general, the kurtosis of the sediments are dominated by leptokurtic and very leptokurtic (1.11-3.0) with negatively skewed curves indicating that the most frequently appearing grain-size (mode) has a significant differences with the central portions (median and mean grain-size). It means that the

sediment layers are poorly sorted and correspond to a dominance of coarse particles (Blott and Pye, 2001; Okeyode and Jibiri, 2012). By contrast, platykurtic curves from sections U-13, U-17, and U-20 demonstrate that most of the values share about the same frequency with median and mean grain-size (see Figure 6-18).

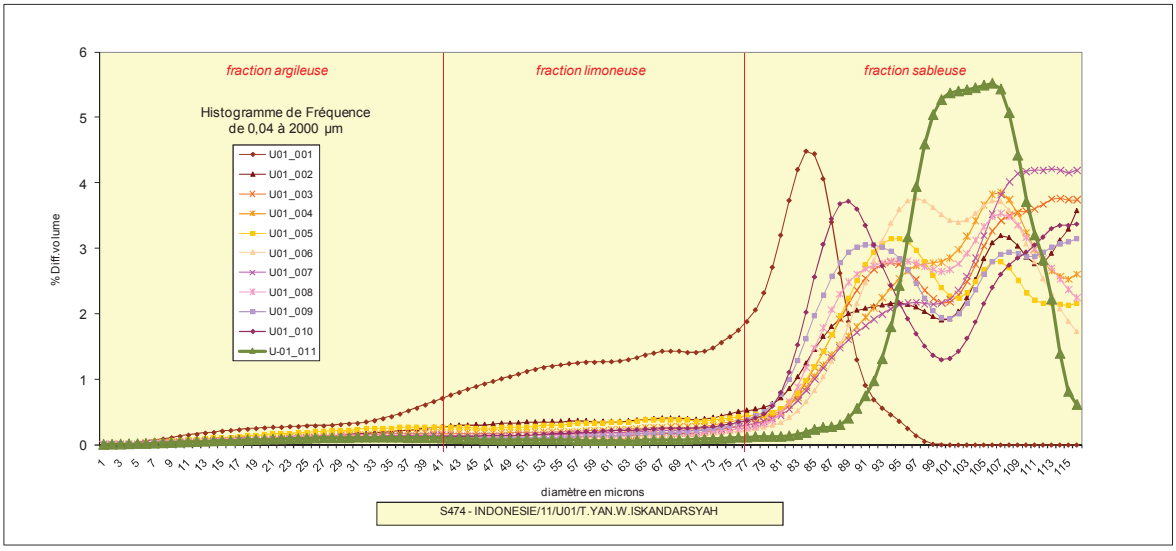

Figure 6-16. Histogram for the grain-size analysis of the samples collected from section U-01. The curves display negative skewness (coarse to very coarse skewed) and kurtosis from leptokurtic to very leptokurtic.

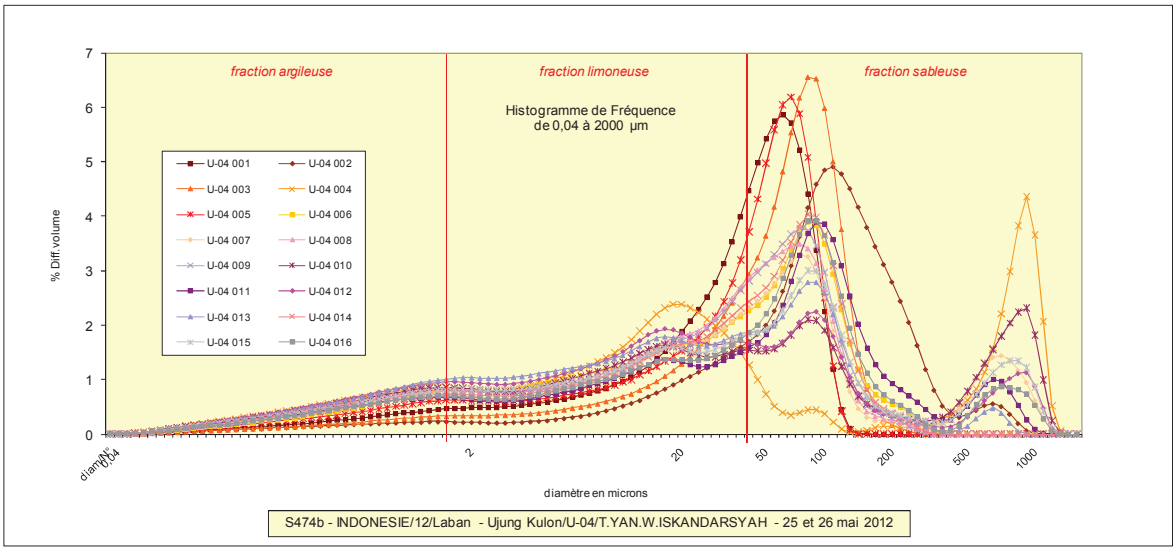

Figure 6-17. Histogram for the grain-size analysis of the samples collected from section U-04. The curves display a dominance negative skewness that has begun to change into symmetrical and positive skewness (fine skewed) and kurtosis from mesokurtic to very leptokurtic.

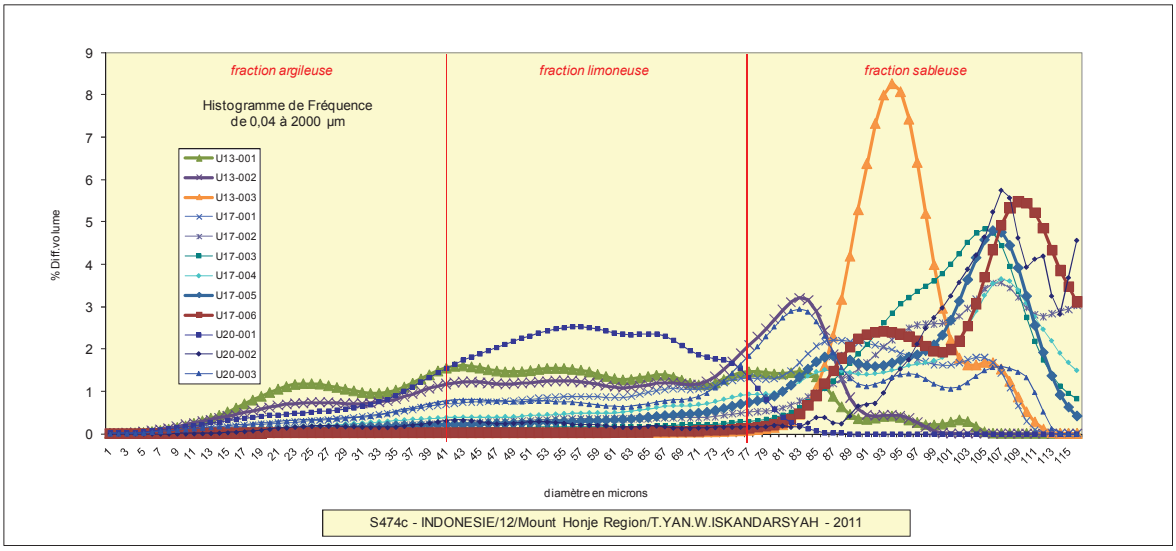

Figure 6-18. Histogram for the grain-size analysis of the samples collected from section U-13, U-17, and U-20. The curves display negative skewness (corase to very coarse skewed) and kurtosis from a dominant platykurtic to very leptokurtic.

As described in method sections, CM diagram is used to correlate grain-size data with transport and emplacement mechanisms. C is fifth percentile (C95) obtained from the values of D-95 and M is the median obtained from D-50. In the diagram, the values of D-95 and D-50, which were extrapolated from the calculated cummulative curves, are expressed by μm. Table 6.2 shows the values of D-95 and D-50 expressed in φ and μm. The fifth percentile ranges from -0.73 ϕ (1660.00 µm) to 4.52 ϕ (43.66 µm), whereas the median ranges from 0.48 ϕ (716.90 µm) to 7.48 ϕ (5.61 µm).

The values of D-95 and D-50 also express the tendency of the results of grain-size laboratory analysis, in which the sediments in the distal sections (sections U-04, U-05) are finer than in the proximal sections (e.g. sections U-01, U-02, U-08). This tendency, however, will correlate to the emplacement mechanisms that rely on the energy of the waves and the condition of the sites. The finer sediments (in sections U-04 and U-05) are resulted from uniform to ground suspension, while the coarser (e.g. in sections U-01, U-02, U-03, U-08 and U-17) are produced by rolling mechanism or rolling and ground suspension (section U-06). The relationship between the fifth percentile (D-95) and the median (D-50), expressed in the CM diagrams, for demonstrating the difference of sediment emplacement mechanisms between proximal and distal sections and also between the peninsula and Mount Honje region are presented in three selected figures (Figure 6-19 to 6-21). The remaining can be seen in Appendix 1-a.

Table 6-2. D-95 and D-50 values for the samples collected from the study area.

Samples Code	Mean Depth	D-95		D-50		Samples Code	Mean Depth	D-95		D-50	
		φ	μm	φ	μm			φ	μm	φ	μm
U-01 001	17.5	2.77	146.80	4.79	36.24	U-05 011	175.0	2.09	234.10	3.71	76.43
U-01 002	42.5	-0.73	1660.00	1.56	339.80	U-05 012	185.0	1.02	493.60	3.44	92.09
U-01 003	60.0	-0.73	1660.00	1.02	493.60	U-05 013	195.0	0.88	541.90	5.06	30.07
U-01 004	87.5	-0.73	1660.00	1.15	449.70	U-05 014	205.0	3.44	92.09	6.54	10.78
U-01 005	110.0	-0.60	1512.00	1.83	282.10	U-05 015	225.0	0.21	863.90	5.73	18.86
U-01 006	120,0	-0.60	1512.00	1.29	409.60	U-05 016	255.0	-0.06	1041.00	6.27	12.99
U-01 007	150.0	-0.73	1660.00	0.75	594.90	U-05 017	282.5	1.56	339.80	6.13	14.26
U-01 008	192.5	-0.60	1512.00	1.29	409.60	U-06 001	1.5	0.75	594.90	4.25	52.63
U-01 009	205.0	-0.73	1660.00	1.69	309.60	U-06 002	11.5	0.48	716.90	3.44	92.09
U-01 010	245.0	-0.73	1660.00	1.96	256.80	U-06 003	25.0	1.83	282.10	3.44	92.09
U-01 011	0.0	-0.46	1377.00	0.88	541.90	U-06 004	34.0	2.50	176.80	3.98	63.41
U-02 001	7.5	0.48	716.90	3.58	83.90	U-06 005	39.5	0.08	948.20	3.17	111.00
U-02 002	25.0	2.36	194.20	3.71	76.43	U-06 006	42.5	-0.60	1512.00	2.09	234.10
U-02 003	35.0	0.21	863.90	3.84	69.62	U-06 007	49.5	0.48	716.90	2.50	176.80
U-02 004	50.0	-0.73	1660.00	1.29	409.60	U-06 008	65.0	0.21	863.90	2.36	194.20
U-02 005	75.0	-0.60	1512.00	1.02	493.60	U-06 009	81.0	-0.19	1143.00	1.96	256.80
U-02 006	105.0	-0.60	1512.00	0.88	541.90	U-06 010	81.0	0.21	863.90	1.83	282.10
U-02 007	135.0	-0.73	1660.00	0.88	541.90	U-06 011	102.0	0.48	716.90	2.50	176.80
U-02 008	160.0	-0.73	1660.00	0.88	541.90	U-06 012	102.0	2.90	133.70	5.32	24.95
U-02 009	180.0	-0.73	1660.00	0.88	541.90	U-06 013	132.0	0.75	594.90	3.17	111.00
U-02 010	195.0	-0.60	1512.00	2.23	213.20	U-06 014	132.0	0.35	786.90	3.04	121.80
U-02 011	225.0	-0.73	1660.00	0.88	541.90	U-06 015	162.0	0.48	716.90	4.65	39.77
U-03 001	7.5	2.90	133.70	5.59	20.70	U-06 016	192.0	0.88	541.90	2.90	133.70
U-03 002	25.0	1.96	256.80	5.06	30.07	U-06 017	222.0	0.35	786.90	1.83	282.10
U-03 003	45.0	-0.60	1512.00	2.50	176.80	U-07 001	0.0	0.88	541.90	1.96	256.80
U-03 004	75.0	-0.60	1512.00	1.29	409.60	U-07 002	0.0	1.15	449.70	2.09	234.10
U-03 005	105.0	-0.73	1660.00	0.88	541.90	U-08 001	17.5	-0.19	1143.00	1.29	409.60
U-03 006	125.0	-0.73	1660.00	1.15	449.70	U-08 002	52.5	0.21	863.90	1.56	339.80
U-03 007	140.0	-0.73	1660.00	2.90	133.70	U-08 003	87.5	-0.19	1143.00	1.29	409.60
U-03 008	160.0	-0.73	1660.00	1.02	493.60	U-08 004	112.5	-0.19	1143.00	1.02	493.60
U-03 009	170.0	-0.73	1660.00	1.29	409.60	U-08 005	130.0	-0.60	1512.00	0.75	594.90
U-03 010	195.0	-0.46	1377.00	1.69	309.60	U-08 006	148.0	-0.33	1255.00	1.15	449.70
U-03 011	195.0	2.50	176.80	3.71	76.43	U-08 007	165.5	-0.46	1377.00	1.02	493.60
U-03 012	217.5	-0.46	1377.00	2.63	161.20	U-08 008	192.5	-0.46	1377.00	1.42	373.10
U-03 013	232.5	2.50	176.80	5.46	22.73	U-08 009	227.5	-0.60	1512.00	2.09	234.10
U-03 014	255.0	-0.73	1660.00	1.96	256.80	U-08 010	252.0	-0.73	1660.00	2.63	161.20
U-04 001	7.5	3.31	101.10	4.52	43.66	U-08 011	269.5	-0.60	1512.00	3.31	101.10
U-04 002	25.0	1.42	373.10	3.31	101.10	U-08 012	297.5	-0.73	1660.00	2.63	161.20
U-04 003	45.0	2.77	146.80	3.84	69.62	U-08 013	0.0	-0.06	1041.00	1.69	309.60
U-04 004	80.0	-0.19	1143.00	5.59	20.70	U-09 001	0.0	-0.46	1377.00	0.88	541.90
U-04 005	75.0	3.31	101.10	4.52	43.66	U-10 001	110.0	3.31	101.10	6.00	15.65
U-04 006	95.0	2.63	161.20	4.92	33.00	U-13 001	85.0	2.77	146.80	7.48	5.61
U-04 007	110.0	0.35	78.690	4.65	39.77	U-13 002	185.0	2.90	133.70	6.00	15.65
U-04 008	125.0	3.04	121.80	5.06	30.07	U-13 003	0.0	0.48	716.90	2.09	234.10
U-04 009	135.0	2.90	133.70	4.92	33.00	U-17 001	2.5	0.48	716.90	3.71	76.43
U-04 010	155.0	-0.06	1041.00	5.06	30.07	U-17 002	15.0	-0.73	1660.00	1.29	409.60
U-04 011	165.0	0.75	594.90	4.25	52.63	U-17 003	25.0	-0.33	1255.00	1.29	409.60
U-04 012	165.0	0.35	786.90	5.59	20.70	U-17 004	35.0	-0.60	1512.00	1.83	282.10
U-04 013	175.0	2.50	176.80	5.73	18.86	U-17 005	50.0	-0.33	1255.00	1.42	373.10
U-04 014	195.0	2.77	146.80	4.79	36.24	U-17 006	0.0	-0.73	1660.00	0.48	716.90
U-04 015	205.0	0.21	863.90	4.92	33.00	U-20 001	5.0	4.52	43.66	7.21	6.76
U-04 016	225.0	0.48	716.90	4.38	47.93	U-20 002	25.0	-0.73	1660.00	0.61	653.00
U-05 001	7.5	2.23	213.20	3.44	92.09	U-20 003	45.0	0.21	863.90	3.84	69.62
U-05 002	25.0	2.36	194.20	3.71	76.43						
U-05 003	45.0	3.44	92.09	4.92	33.00						
U-05 004	75.0	1.15	449.70	2.90	133.70						
U-05 005	95.0	2.90	133.70	4.11	52.77						
U-05 006	110.0	1.42	373.10	3.44	92.09						
U-05 007	135.0	-0.33	1255.00	2.90	133.70						
U-05 008	155.0	-0.19	1143.00	2.63	161.20						
U-05 009	160.0	3.04	121.80	4.92	33.00						
U-05 010	167.5	3.17	111.00	5.46	22.73						

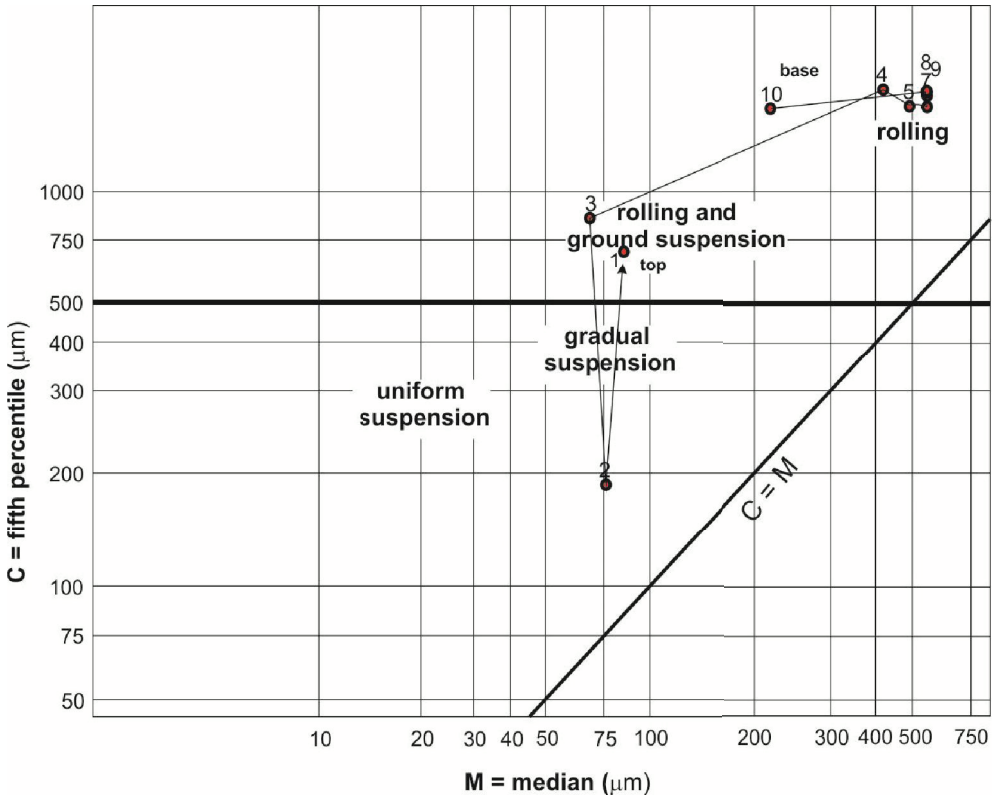

Figure 6-19. CM diagram (C = D-95 and M = D-50, in μm) for the samples from section U-01. Numbers refer to the samples for each section displayed in Table 6-2, thin arrow line showing the evolution of energy from base to top of the deposit.

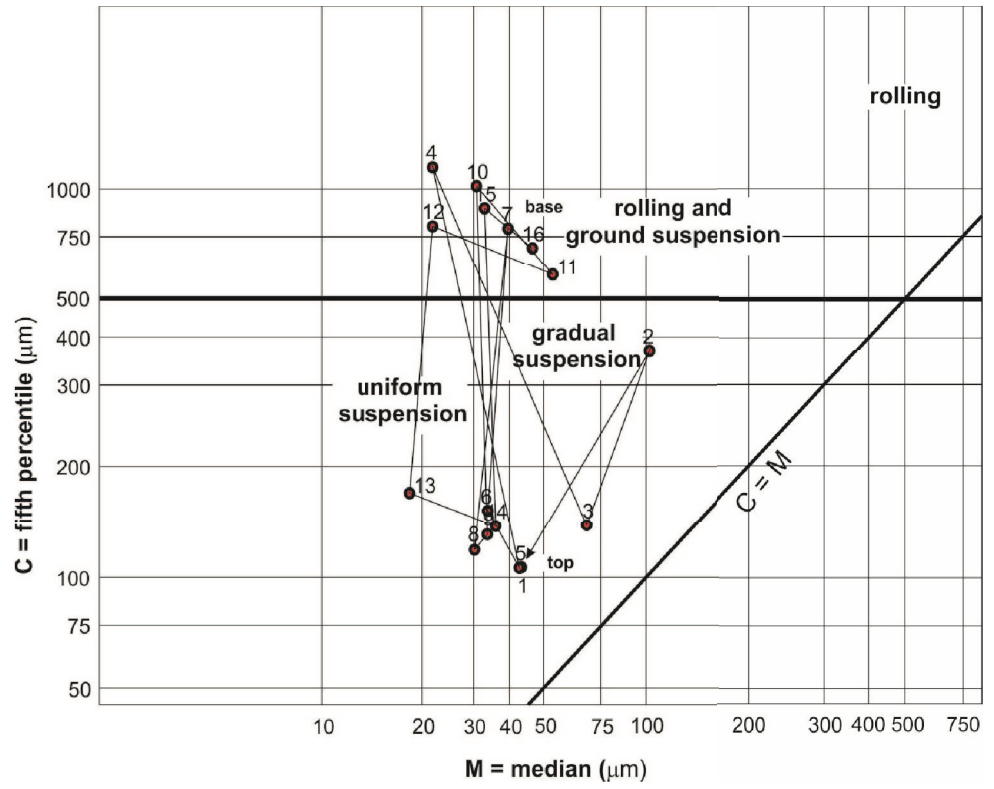

Figure 6-20. CM diagram (C = D-95 and M = D-50, in μm) for the samples from section U-04.

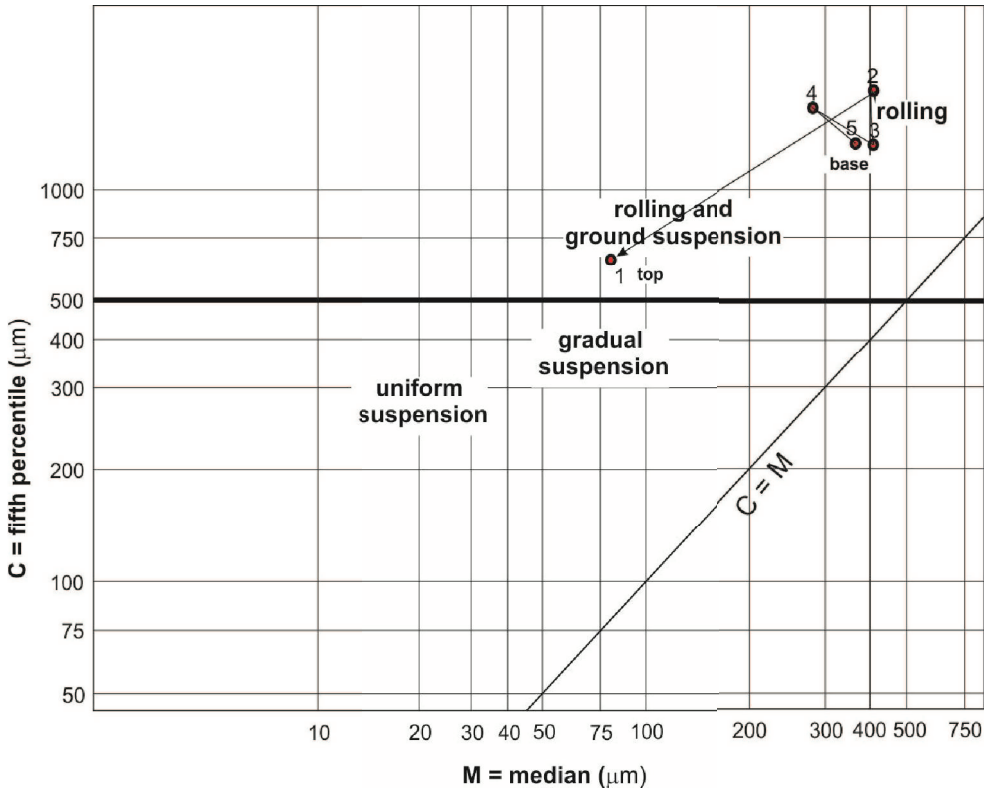

Figure 6-21. CM diagram (C = D-95 and M = D-50, in μm) for the samples from section U-17 (Mount Honje region).

6.3. Foraminiferal assemblages

Benthic foraminifera were identified to determine a maximum depth at which seabed was eroded by tsunami waves. At Laban Isthmus and Ujung Kulon Peninsula, most of benthic foraminifera remained intact and could be used to identify the tsunami sequences, especially in sections U-03, U-04, and U-05 that are far inland and out of reach of the tidal influence.

We found that benthic foraminifera were concentrated at a depth between 100 - 240 cm, i.e. about 11 - 28 species and 564 individuals (section U-03:005) up to 21,888 individuals (section U-05:010), see Table 6-3 to 6-5. The lowest density is at the depth between 15 - 60 cm, i.e. about 4 - 10 species and 5 - 90 individuals/dm^3 (section U-04:002), due to the very bad conservation conditions at the soil level.

Table 6-3. Foraminiferal assemblages in section U-03, including their bathymetric origins.

Benthonic Name	Number of Individuals in Each Sample														Total of Individuals
	U-03 001	U-03 002	U-03 003	U-03 004	U-03 005	U-03 006	U-03 007	U-03 008	U-03 009	U-03 010	U-03 011	U-03 012	U-03 013	U-03 014	
	0-15 cm	15-30 cm	30-60 cm	60-90 cm	90-120 cm	120-130 cm	130-150 cm	150-170 cm	170-180 cm	180-210 cm	180-210 cm	210-225 cm	225-240 cm	240-270 cm	
Amphicoryna proxima **Silvestri**	2											32			34
Amphistegina lessonii **d'Orbigny**	38		2		8	4	246	96	64	64	4	112		96	734
Anomalina globulosa **Chapman & Parr**													32		32
Asterorotalia trispinosa **Thalmann**				2		4	32			64		16		32	150
Bigenerina nodosaria **d'Orbigny**										192		80	64		336
Bolivina nitida **Brady**			2												2
Bolivina sphatulata **Williamson**	12		2	4	24	8	672	80	288	256	16	208	320	192	2082
Bolivinella elegans **Parr**										32		16			48
Bolivinellina translucens **Phleger & F.L Parker**	16				16		64	48	96	160		96	96	96	688
Bulimina marginata **d'Orbigny**					12	8	64	16	64	384	4	208	160	64	984
Bulimina pupoides **d'Orbigny**					8				32	128		48	96		312
Elphidium lessonii **d'Orbigny**	56		34	108	96	96	1024	384	672	1056	104	752	3296	2208	9886
Elphidium macellum **Fichtel & Moll**	12			4					48	64	8	32	96		264
Epistominella exigua **Brady**									144	896	12	48	544	416	2060
Eponides umbonatus **Reuss**													32		32
Euuvigerina peregina **Cushman**				2	4		96	32		192		32	128	32	518
Fissurina laevigata **Reuss**			2												2
Gavelinonion barleeanum **Williamson**						4	32	16		64			32		148
Hyalinea balthica **Schroeter**			2	6	12	4	224	64	192	288	8	208	224	64	1296
Hypermina cylindrica **Parr**	6											16			22
Lagena hispidula **Cushman**	2									32		16			50
Lagena laevis **Montagu**						4							32		36
Loxostomina mayori **Cushman**	4														4
Neoconorbina terquemi **Rzehak**									32	64					96
Neouvigerina porrecta **Brady**	22			2											24
Nonion scaphum **Fichtel & Moll**	14						32		32	96	4	80	64	96	418
Oolina globosa **Montagu**			4												4
Oolina opiculata **Reuss**				2					16						18

Table 6-3 (continued)

Benthonic Name	Number of Individuals in Each Sample														Total of Individuals
	U-03 001	U-03 002	U-03 003	U-03 004	U-03 005	U-03 006	U-03 007	U-03 008	U-03 009	U-03 010	U-03 011	U-03 012	U-03 013	U-03 014	
	0-15 cm	15-30 cm	30-60 cm	60-90 cm	90-120 cm	120-130 cm	130-150 cm	150-170 cm	170-180 cm	180-210 cm	180-210 cm	210-225 cm	225-240 cm	240-270 cm	
Patellinella jugosa **Brady**	10				12		64	48				48			182
Planulina wuellerstorfi **Schwager**	50		2	6	24	12	224	64	240	448	12	96	352	160	1690
Quinqueloculina auberiana **d'Orbigny**														32	32
Quinqueloculina granulocostata **Germeraad**												16		32	48
Quinqueloculina lamarckiana **d'Orbigny**										64		32	64		160
Quinqueloculina parkeri **Brady**													32		32
Quinqueloculina seminulum **Linnaeus**	10						64	32	112	192	8	32		32	482
Quinqueloculina tropicalis **Cushman**	16						64	32	48			96	268	128	652
Rectobolivina columellaris **Brady**	4			4	8	8			16		4			96	140
Reophax nodulosus **Brady**							32			32			32		96
Robulus thalmani **Hessland**	10			4	12		64		64	288	4	16	32	64	558
Siphotextularia crispata **Brady**	10		2						32			32			76
Streblus becarii **Linnaeus**	30		38	94	308	148	640	688	752	1408	92	1712	1696	416	8022
Textularia agglutinans **d'Orbigny**	4						32						32	32	100
Trifarina brady **Cushman**	10			4	16		96	32	64	64			64		350
Uvigerina canariensis **d'Orbigny**					4		96	32	96	96	4	224	224	64	840
Total of Individuals in Each Sample	338	0	90	242	564	300	3862	1664	3104	6624	284	4304	8012	4352	**33740**
Number of Species	21	0	10	13	15	11	20	15	21	26	14	27	26	20	44
Dominance (%)	*E. lessonii*	-	*S. becarii*	*E. lessonii*	*E. lessonii*	*S. becarii*	*E. lessonii*	*S. becarii*	*S. becarii*	*S. becarii*	*E. lessonii*	*S. becarii*	*E. lessonii*	*E. lessonii*	*E. lessonii*
	16,57	0,00	42,22	44,63	17,02	49,33	26,51	41,35	24,23	21,26	36,62	39,78	41,14	50,74	29,30

LEGEND:

	Littoral - Neritic	0 - 200 mbsl
	Upper Bathyal	200 - 600 mbsl
	Middle Bathyal	600 - 1000 mbsl
	Lower Bathyal	1000 - 2000 mbsl
	Abyssal	> 2000 mbsl

Table 6-4. Foraminiferal assemblages in section U-04, including their bathymetric origins.

Benthonic Name	Number of Individuals in Each Sample																Total of Individuals
	U-04 001	U-04 002	U-04 003	U-04 004	U-04 005	U-04 006	U-04 007	U-04 008	U-04 009	U-04 010	U-04 011	U-04 012	U-04 013	U-04 014	U-04 015	U-04 016	
	0-15 cm	15-30 cm	30-60 cm	80 cm	60-90 cm	90-100 cm	100-120 cm	120-130 cm	130-150 cm	150-160 cm	160-170 cm	160-170 cm	170-180 cm	180-210 cm	200-210 cm	210-240 cm	
Ammobaculites agglutinans **d'Orbigny**	1																0
Amphicoryna proxima **Silvestri**						16	16					64	32		32		160
Amphicoryna separans **Brady**					4		32					64	32	32			164
Amphistegina lessonii **d'Orbigny**				100	16	80	512	96	672	512	288	256	512	304	768	160	4276
Amphistegina quoyii **d'Orbigny**	3																0
Bigenerina nodosaria **d'Orbigny**							16		32				32				80
Bolivina nitida **Brady**	2			16		16		192		128	96			16		64	528
Bolivina spathulata **Williamson**	1			20	8	48	144		128	128	64	64	64	80	128	32	908
Bolivinellina translucens **Phleger and F.L. Parker**				12	12	80	96		96	256	96	128	128	272	160	256	1592
Bulimina marginata **d'Orbigny**							64						128		64	32	288
Bulimina pupoides **d'Orbigny**	1			8	8	16	64			320					64		480
Calcarina venusta **Brady**	1				2		32										34
Cancris auriculus **Fichtel & Moll**				20		32	16		128		32			48	320	96	692
Cancris oblongus **Williamson**	1								32								32
Cyclammina trullissata **Brady**	1			20	4									16			40
Dentalina subsoluta **Cushman**					2		32		32					16			82
Discorbinella bodjongensis **Leroy**				12	16		64		64			64		48	96	64	428
Elphidium crispum **Linnaeus**	4				34	128				64	192						418
Elphidium lesonii **d'Orbigny**	3			80			272	192	256			128	256	176	416		1776
Elphidium macellum **Fichtel & Moll**	1			12			192		192	128	64	64	96	96	96	96	1036
Elphidium orbidulare **Brady**		1															1
Eponides schreibersi **d'Orbigny**	4																0
Eponides umbonatus **Reuss**																32	32
Euuvigerina peregrina **Cushman**	1			8	2			96	64					16			186
Fissurina circularis **Todd**						16						64			32		112
Gavelinonion barleeanum **Williamson**				12	20	96	128	64		128		64	192		128	96	928
Gyroidina neosoldanii **Brotzen**	1			28				128		768							924
Hoglindina elegans **d'Orbigny**							112	128	288	448	96	128	384	288	544	384	2800
Hyalinea baltnica **Schroeter**	2			16	6		48										70
Hypermina cylindrica **Parr**								32	96	128	32		64	16			368
Karreriella bradyi **Cushman**														16			16
Lagena gracilima **Seguenza**					2												2

Table 6-4 (continued)

Benthonic Name	Number of Individuals in Each Sample																Total of Individuals
	U-04 001	U-04 002	U-04 003	U-04 004	U-04 005	U-04 006	U-04 007	U-04 008	U-04 009	U-04 010	U-04 011	U-04 012	U-04 013	U-04 014	U-04 015	U-04 016	
	0-15 cm	15-30 cm	30-60 cm	80 cm	60-90 cm	90-100 cm	100-120 cm	120-130 cm	130-150 cm	150-160 cm	160-170 cm	160-170 cm	170-180 cm	180-210 cm	200-210 cm	210-240 cm	
Lagena hispidula **Cushman**													64			32	**96**
Loxostomum sp. **Nov**	1				2											32	**34**
Neoconorbina terquemi **Rzehak**	1			8		64				64					64		**200**
Neouvigerina porrecta **Brady**						80	16			192		64	128	80	64	64	**688**
Nonion cf. asterizans **Fichtel and Moll**	3																**0**
Nonion scaphum **Fichtel and Moll**	1			8	12	48	96	32	32		288	192	160	64	320		**1252**
Operculina ammonoides **Gronovius**					2												**2**
Patellinella jugosa **Brady**								96	96				64		96	32	**384**
Planulina wuellerstorfi **Schwager**	2	1		120	130	560	1312	768	1504	1408	1248	768	1472	1184	2176	896	**13547**
Quinqueloculina auberiana **d'Orbigny**			1		4												**5**
Quinqueloqulina pygmaea **Reuss**				20			64			64		64	160	48			**420**
Quinqueloqulina seminulum **Linnaeus**	1				8	64	160		64		32				192	608	**1128**
Rectobolivina columellaris **Brady**							16							16			**32**
Rectoglandulina comatula **Cushman**						16			32		32				64		**144**
Robulus thalmani **Hessland**	4			56	2	112		320	352		384	128	352	224	576	320	**2826**
Sigmoilina tenuis **Czjzek**	1																**0**
Siphotextularia crispata **Brady**					4	32	128		64	128				32			**388**
Sphaeroidina bulloides **d'Orbigny**				4													**4**
Streblus becarii **Linnaeus**	8		2	48	36	48	384	352	128	640	128	256	576	160	288	416	**3462**
Textularia agglutinans **d'Orbigny**							64		32		32				64		**192**
Trifarina bradyi **Cushman**						16	32								96	64	**208**
Uvigerina canariensis **d'Orbigny**				16			176	64	64								**320**
Uvigerina cushmani **Todd**																32	**32**
Total of Individuals in Each Sample	**49**	**2**	**3**	**644**	**336**	**1568**	**4288**	**2560**	**4448**	**5504**	**3104**	**2560**	**4896**	**3248**	**6848**	**3808**	**43817**
Number of Species	24	2	2	22	23	20	28	14	23	17	16	17	20	23	24	21	55
Dominance (%)	*S. becarii*	-	*S. becarii*	-	*P. wuellerstorfi*	*P. wuellerstorfi*	*P. wuellerstorfi*	*P. wuellerstorfi*	*P. wuellerstorfi*	*P. wuellerstorfi*	*P. wuellerstorfi*	*P. wuellerstorfi*	*P. wuellerstorfi*	*P. wuellerstorfi*	*P. wuellerstorfi*	*P. wuellerstorfi*	*P. wuellerstorfi*
	16,33	0,00	66,67	0,00	38,69	35,71	30,60	30,00	33,81	25,58	40,21	30,00	30,07	36,45	31,78	23,53	30,92

LEGEND:

	Littoral - Neritic	0 - 200 mbsl
	Upper Bathyal	200 - 600 mbsl
	Middle Bathyal	600 - 1000 mbsl
	Lower Bathyal	1000 - 2000 mbsl
	Abyssal	> 2000 mbsl

Table 6-5. Foraminiferal assemblages in section U-05, including their bathymetric origins.

Benthonic Name	Number of Individuals in Each Sample																	Total of Individuals
	U-05 001	U-05 002	U-05 003	U-05 004	U-05 005	U-05 006	U-05 007	U-05 008	U-05 009	U-05 010	U-05 011	U-05 012	U-05 013	U-05 014	U-05 015	U-05 016	U-05 017	
	0-15 cm	15-30 cm	30-60 cm	60-90 cm	90-100 cm	100-120 cm	120-150 cm	150-160 cm	160 cm	160-170 cm	170-180 cm	180-190 cm	190-200 cm	200-210 cm	210-240 cm	240-270 cm	270-295 cm	
Amphistegina lessonii **d'Orbigny**	none	reworked	reworked	reworked		896	704		576	640	1088	1280	256	56	24	208	640	**6368**
Anomalina colligera **Chapman and Parr.**	none	reworked	reworked	reworked							64							**64**
Anomalina globulosa **Chapman and Parr.**	none	reworked	reworked	reworked													32	**32**
Anomalinella rostrata **Brady**	none	reworked	reworked	reworked														**0**
Asterorotalia trispinosa **Thalmann**	none	reworked	reworked	reworked	32													**32**
Astrononion fijiense **Cushman and Edwards**	none	reworked	reworked	reworked											8			**8**
Bolivina spathulata **Williamson**	none	reworked	reworked	reworked	192	2368	1984	1344	1728	1728	832	2240	592	56	16	32	96	**13208**
Bolivinella elegans **Parr.**	none	reworked	reworked	reworked													32	**32**
Bolivinellina translucens **Phleger and F.L. Parker**	none	reworked	reworked	reworked						128	64	64		24		16	224	**520**
Buccella frigid **Cushman**	none	reworked	reworked	reworked		64												**64**
Bulimina marginata **d'Orbigny**	none	reworked	reworked	reworked	416	3136	3264	1216	1152	1792	1024	2944	368	16		16		**15344**
Bulimina pupoides **d'Orbigny**	none	reworked	reworked	reworked			64			64						16		**144**
Calcarina calcar **d'Orbigny**	none	reworked	reworked	reworked		64						64						**128**
Calcarina venusta **Brady**	none	reworked	reworked	reworked				64					16				32	**112**
Cancris oblongus **Williamson**	none	reworked	reworked	reworked													32	**32**
Cassidulina teretis **Tappan**	none	reworked	reworked	reworked	32	448	64		384				16					**944**
Chrysalidinella dimorpha **Brady**	none	reworked	reworked	reworked												16		**16**
Cibicides subhaidingerii **Parr.**	none	reworked	reworked	reworked									48					**48**
Conorboides advena **Cushman**	none	reworked	reworked	reworked										8				**8**
Cyclammina trullissata **Brady**	none	reworked	reworked	reworked									32					**32**
Dentalina subsoluta **Cushman**	none	reworked	reworked	reworked			64		64	64							32	**224**
Elphidium craticulatum **Fichtel and Moll**	none	reworked	reworked	reworked	192													**192**
Elphidium crispum **Linnaeus**	none	reworked	reworked	reworked		1792		192										**1984**
Elphidium lessonii **d'Orbigny**	none	reworked	reworked	reworked			704			2112	2624	3008	288	256	136	64		**9192**
Elphidium orbidulare **Brady**	none	reworked	reworked	reworked	352	256												**608**
Eponides (?) procera **Brady**	none	reworked	reworked	reworked			64											**64**
Eponides schreibersi **d' Orbigny**	none	reworked	reworked	reworked											8			**8**
Eponides (?) tenera **Brady**	none	reworked	reworked	reworked				64				64	16		32			**176**
Euuvigerina peregrina **Cushman**	none	reworked	reworked	reworked	160	832	2880	768	576	1664	1536	2688	192	64	32	16		**11408**
Gyroidina neosoldanii **Brotzen**	none	reworked	reworked	reworked			192											**192**
Hyalinea balthica **Schroeter**	none	reworked	reworked	reworked	160	1408	1792	1856	1024	3392	1856	1280	688	72	72		832	**14432**
Jaculella acuta **Brady**	none	reworked	reworked	reworked								64						**64**
Lagena hispidula **Cushman**	none	reworked	reworked	reworked													32	**32**

Table 6-5 (continued)

Benthonic Name	Number of Individuals in Each Sample																	Total of Individuals
	U-05 001	U-05 002	U-05 003	U-05 004	U-05 005	U-05 006	U-05 007	U-05 008	U-05 009	U-05 010	U-05 011	U-05 012	U-05 013	U-05 014	U-05 015	U-05 016	U-05 017	
	0-15	15-30	30-60	60-90	90-100	100-120	120-150 cm	150-160	160	160-170	170-180	180-190	190-200	200-210	210-240	240-270 cm	270-295 cm	
Lagena laevis **Montagu**	none	reworked	reworked	reworked								64						**64**
Lagena sulcata **Walker and Jacob**	none	reworked	reworked	reworked								64			8			**72**
Lenticulina calcar **Linnaeus**	none	reworked	reworked	reworked					512		384	256	96					**1248**
Lenticulina Formosa **Cushman**	none	reworked	reworked	reworked									32					**32**
Nonion cf. asterizans **Fichtel and Moll**	none	reworked	reworked	reworked	64	512	576	320							8			**1480**
Nonion scaphum **Fichtel and Moll**	none	reworked	reworked	reworked					192	320	128	320	64	8	40	32	64	**1168**
Patellinella jugosa **Brady**	none	reworked	reworked	reworked		128						128						**256**
Planulina ariminensis **d'Orbigny**	none	reworked	reworked	reworked		64	256											**320**
Planulina wuellerstorfi **Schwager**	none	reworked	reworked	reworked		1472	1792	1664	1024	5056	1152	192	544	152	16	544	992	**14600**
Pleurostomella brevis **Schwager**	none	reworked	reworked	reworked			128			128	64		16					**336**
Quinqueloculina pygmaea **Reuss**	none	reworked	reworked	reworked		128			64							64	96	**352**
Quinqueloculina seminulum **Linnaeus**	none	reworked	reworked	reworked							64				112			**176**
Quinqueloculina tropicalis **Cushman**	none	reworked	reworked	reworked												16		**16**
Rectobolivina virgula **Brady**	none	reworked	reworked	reworked								64						**64**
Rectoglandulina comatula **Cushman**	none	reworked	reworked	reworked						64	64			16				**144**
Reophax nodulosus **Brady**	none	reworked	reworked	reworked										8				**8**
Robulus thalmani **Hessland**	none	reworked	reworked	reworked		512	576	128	128	192		832	320	24			672	**3384**
Rosalina sp. **Nov.**	none	reworked	reworked	reworked				64			64							**128**
Stilostomella fistuca Schwager	none	reworked	reworked	reworked												8		**8**
Streblus becarii **Linnaeus**	none	reworked	reworked	reworked	1472	6208	2304	2624	1280	5184	3456	5376	928	408			64	**29304**
Tubinella funalis **Brady**	none	reworked	reworked	reworked		64												**64**
Uvigerina canariensis **d'Orbigny**	none	reworked	reworked	reworked								64						**64**
Uvigerina peregrina **Cushman**	none	reworked	reworked	reworked													32	**32**
Total of Individuals in Each Sample	**0**	**0**	**0**	**0**	3040	19456	16704	10304	8128	21888	13312	19776	4256	1112	480	840	3232	**122528**
Number of Species	0	0	0	0	10	18	17	12	13	15	16	20	18	14	13	13	16	56
Dominance (%)	-	-	-	-	*S. becarii*	*S. becarii*	*B. marginata*	*S. becarii*	*B. spathulata*	*S. becarii*	*S. becarii*	*S. becarii*	*S. becarii*	*S. becarii*	*E. lessonii*	*P. wuellerstorfi*	*P. wuellerstorfi*	*S. becarii*
	0	**0**	**0**	**0**	48,42	31,91	19,54	25,47	21,26	23,68	25,96	27,18	21,80	36,69	28,33	64,76	30,69	23,92

LEGEND:

	Littoral - Neritic	0 - 200 mbsl
	Upper Bathyal	200 - 600 mbsl
	Middle Bathyal	600 - 1000 mbsl
	Lower Bathyal	1000 - 2000 mbsl
	Abyssal	> 2000 mbsl

We have seen above (Table 6-3 to 6-5) that Laban area may have been subject to tsunami floodings from both parts of the isthmus, North from Sunda Strait and South from Indian Ocean. The dominance of *Elphidum lessonii* and *Streblus beccarii* in sections U-03 and U-05 (up to 5,184 individuals/dm^3) indicate that the sediment layers mostly originate from the sub-littoral zones, at a depth between 0 – 200 meter below sea level/mbsl (Bahlburg and Weiss, 2007; Nanayama and Shigeno, 2006), yet, it cannot be discriminant to identify the sediment source because these environments are found in Sunda Strait as well as in Indian Ocean. By contrast, *Planulina wuellerstorfi*, dominant in sections U-04 and U-05 (up to 5,056 individuals/dm^3), indicates that the sediments were entrained from a bathyal environment, at the depth between 200 – 600 mbsl (Holbourn et al., 2013; Phleger, 1951). Such environment cannot be found in Sunda Strait. This latter species can be considered a specific characteristic of an Indian Ocean continental margin source (Lutze and Coulbourn, 1984). Consequently, it appears that an alternating sedimentation process from two different sources has occured at Laban Isthmus.

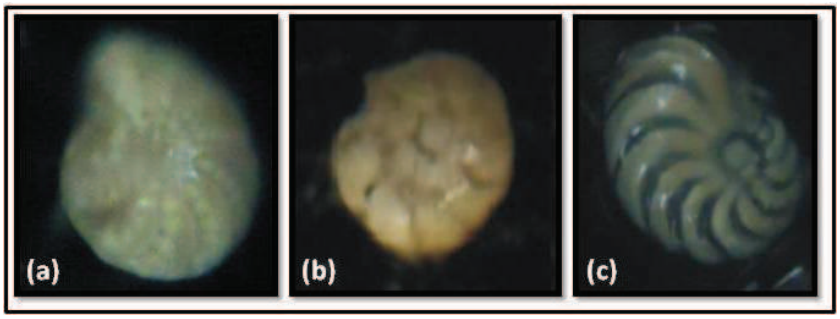

Figure 6-22. Photograps of the dominant species of benthic foramnifera found within the samples from sections U-03, U-04, and U-05: (a) *Elphidum lessonii* **d'Orbigny**, (b) *Streblus beccarii* **Linnaeus**, (c) *Planulina wuellerstorfi* **Schwager**.

The foraminiferal assemblages in sections U-03, U-04, and U-05 were then statistically clustered to determine biofacies. The sediments containing these foraminifera were classified based on biofacies to recognize the hydrodynamic conditions of sediments emplacement. Figure 6-23 to 6-25 display the result of statistical cluster analysis expressed in dendogram. Furthermore, this statistical cluster analysis shows that the sediment layers can be divided into five biofacies (Biofacies A, B. C, D, E) which are distinguished by the number of species and individuals in each sample (Abbene et al., 2006; Patterson, 1990).

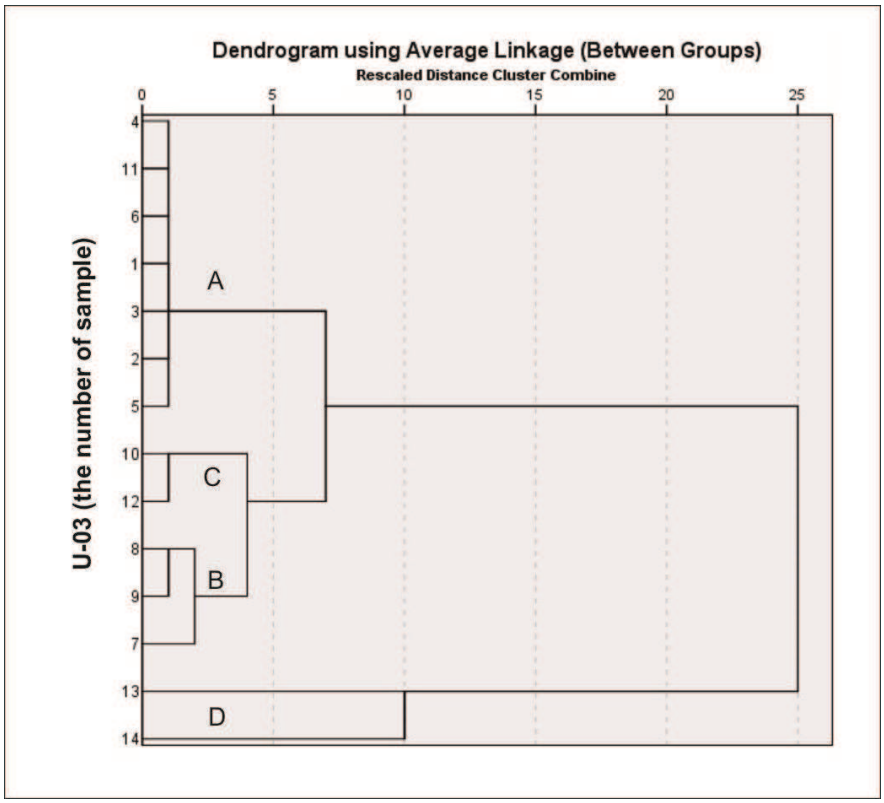

Figure 6-23. A dendogram of biofacies resulted from the clustering of foraminiferal assemblages at section U-03.

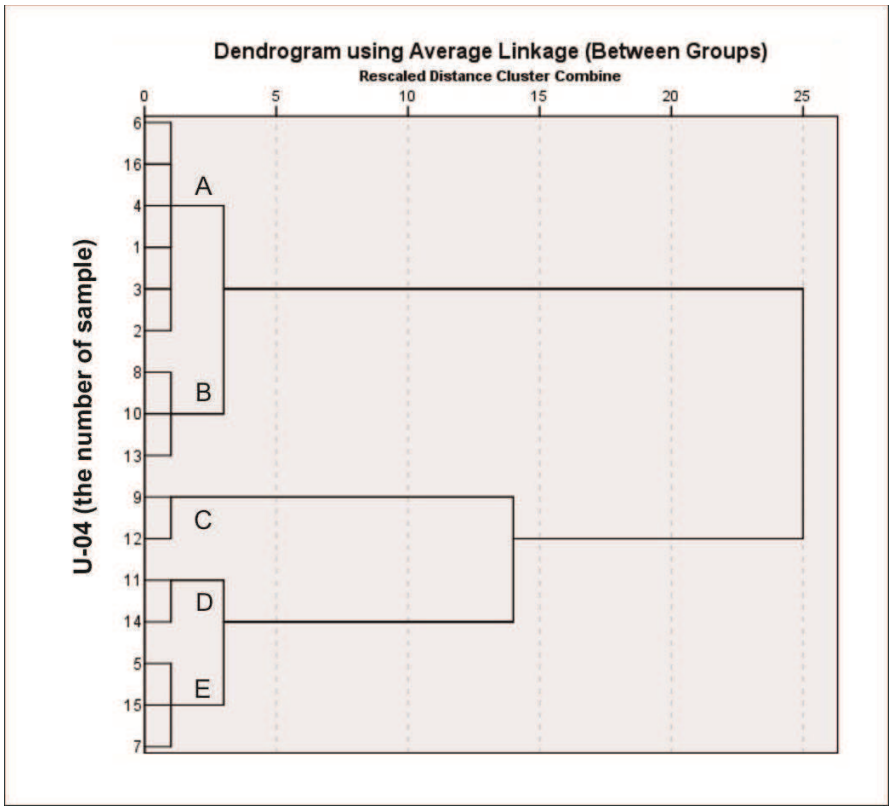

Figure 6-24. A dendogram of biofacies resulted from the clustering of foraminiferal assemblages at section U-04.

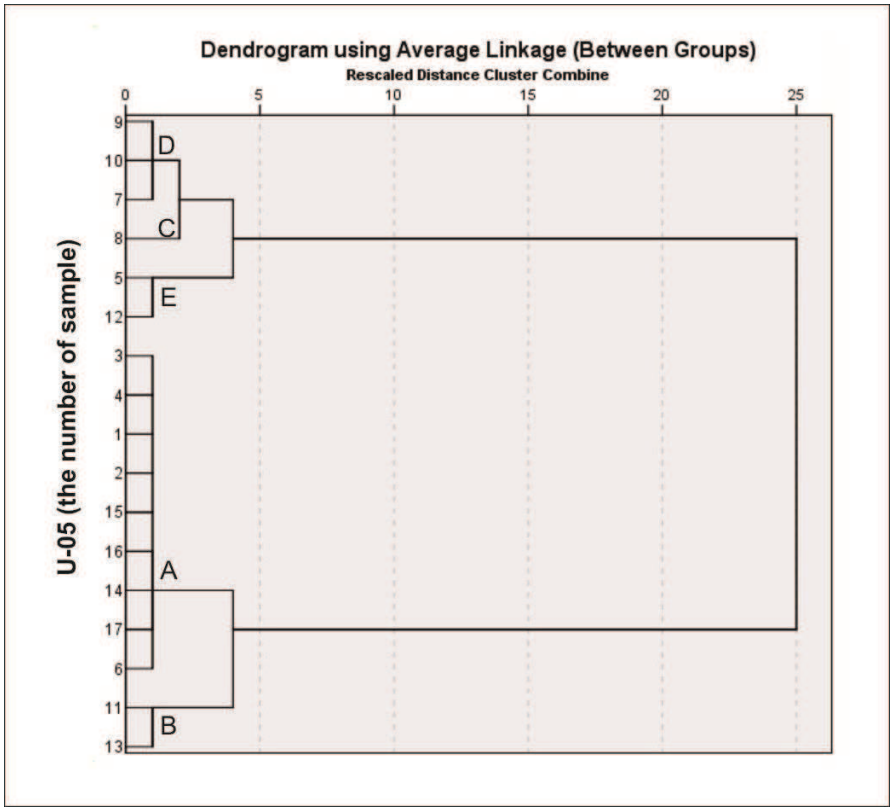

Figure 6-25. A dendogram of biofacies resulted from the clustering of foraminiferal assemblages at section U-05.

In general, Biofacies *A* consists of one or more sediment layers containing a small amount of species and related individuals. The following biofacies (*B, C, D, E*) correspond to a progressive increase of the number of species and individuals.

However, determining biofacies is not that simple. In some cases, a sample with a large number of individuals and species can be grouped into the same biofacies with the sample containing a small amount of individuals and related species. For example, sample U-05:006 with 19,456 individuals and 18 species is clustered to be Biofacies *A* with samples containing 480 – 3,232 individuals and species ranging between 13 – 16. This complexity is most probably affected by the type of species that constitutes one of the parameters used in determining biofacies.

Biofacies can reflect the energy of the waves (Gallagher et al., 1999). Biofacies *A* or *B* might have been produced by the high energy waves of the turbulence of the uprush water when the sediments were emplaced. Biofacies *C*, *D*, and *E* are most probably produced by the lowest energetic waves when the large amount of sediments emplaced far

inland. Figure 6-26 shows that the fluctuation of Biofacies *C*, *D*, and *E* occurred at sections U-04 and U-05 found farther inland rather than at section U-03. Lateral biofacies changes are clearly observed by comparing U-03 with U-04 and U-05. In section U-03, Biofacies A and B dominate the tsunami deposits. At a depth between 180 - 100 cm, these biofacies evolve into Biofacies C, D, and E as the waves energy decreases farther inland.

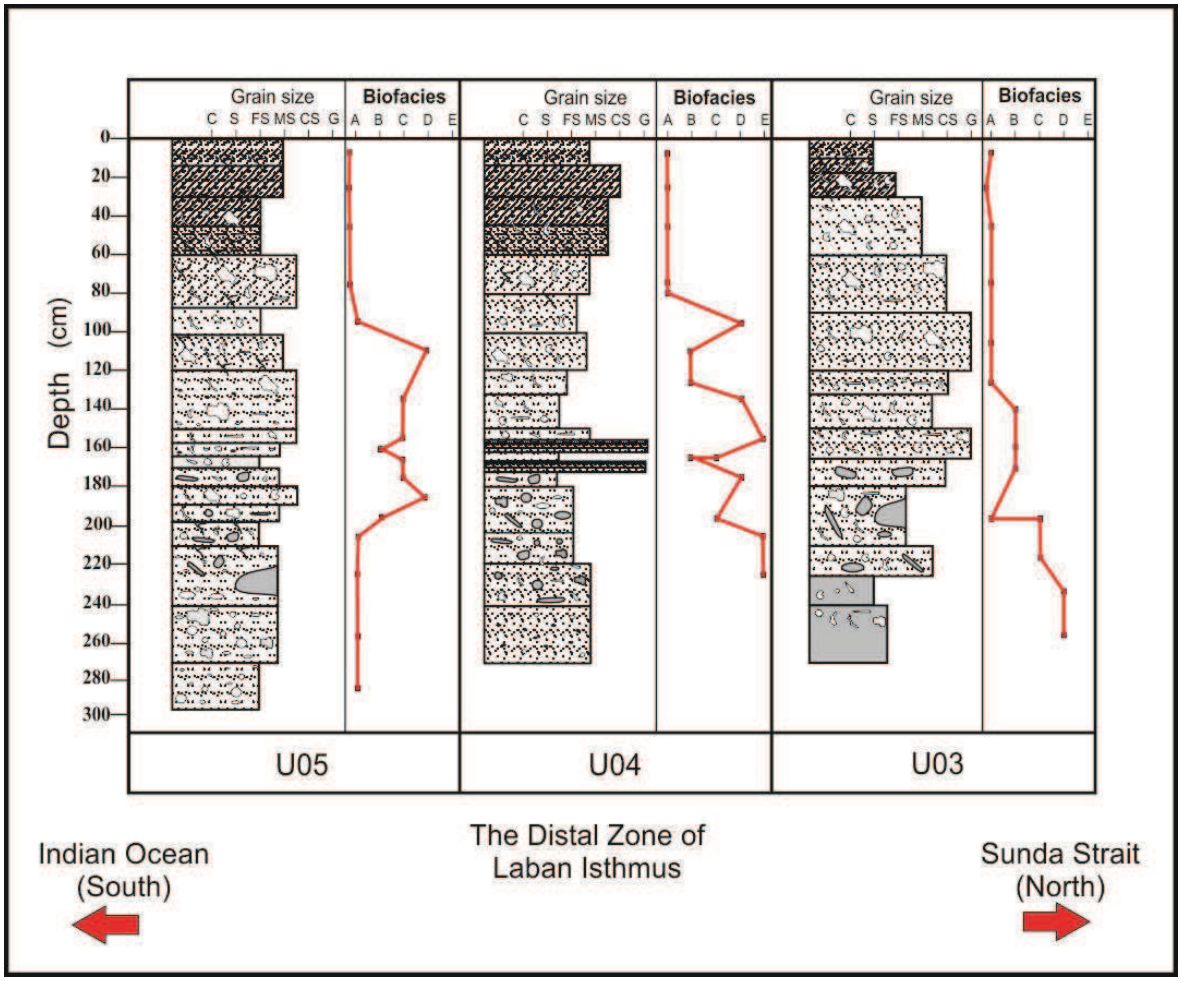

Figure 6-26. Biofacies distribution for section U-03 (right), U-04 (centre), and U-05 (left); The lines in the graphs can represent a fluctuation of tsunami wave energy. Lateral biofacies changes are clearly observed by comparing U-03 with U-04 and U-05.

6.4. Anisotropy of Magnetic Susceptibility (AMS)

The Anisotropy of Magnetic Susceptibility (AMS) technique allows evidencing the internal magnetic fabric of the deposits. Table 6-6 presents the different sediment sources and related AMS parameters. The different sources for sediment layers determined a

significant variation of AMS parameters. Mean bulk volume of magnetic susceptibilities (K_m), affected by the minerals composition of sediments, ranges from 0.534 x 10^{-4} to 41.730 x 10^{-4} SI unit. Yet, there is no significant relationship between the evolution of K_m with the axis changes. In general, the values of K_m at section U-03 are generally lower than other sections. On the contrary, the values of K_m at section U-06 are higher than the others. The differences of K_m values at the opposite coastal zones suggest that the source of sediment layers may not be the same. The highest K_m at section U-06 indicates that the deposits are composed of material with abundant heavy minerals originated from continental margin (Nechaev and Isphording, 1993), a condition which might be found at Indian Ocean.

K_{max} (K_1) ranges from 1.0022 to 1.0453, K_{int} (K_2) ranges from 0.9922 to 1.0152, and K_{min} (K_3) is between 0.9545 and 0.9980. From proximal to the distal zones, two parameters of axis display a normally lateral change, i.e. when K_1 values (as the longest axis of AMS ellipsoid) increase, as consequence, K_3 values (the shortest axis) decrease.

At proximal sections of the isthmus (U-01, U-03, U-06), lineation (*L*) ranges from 1.001 to 1.025, foliation (*F*) ranges from 1.009 to 1.046, shape parameter (*T*) ranges from -0,529 to 0.965, corrected degree of anisotropy (*Pj*) ranges from 1.016 to 1.058, and alignment parameter (*Fs*) is between 1.016 and 1.075. At distal sections (U-04, U-05), *L* ranges from 1.002 to 1.045, *F* ranges from 1.008 to 1.058, *T* ranges from -0,488 to 0.891, *Pj* ranges from 1.015 to 1.095, and *Fs* between 1.021 and 1.145. From base to top, the sections in the isthmus display fluctuation *L*, *F*, *T*, *Pj*, and *Fs* values. At Cidaun, section U-08 shows *L* ranges from 1.007 to 1.015, *F* ranges from 1.010 to 1.022, *T* ranges from 0,070 to 0.266, *Pj* ranges from 1.018 to 1.038, and *Fs* between 1.026 and 1.054. While at Mount Honje region (section U-17), *L* ranges from 1.001 to 1.009, *F* ranges from 1.002 to 1.005, *T* ranges from -0,471 to 0.575, *Pj* ranges from 1.004 to 1.013, and *Fs* between 1.007 and 1.022. From base to top, the section display fluctuation *L*, *F*, *T*, *Pj*, and *Fs* values. However, the values at Mount Honje region are lower than those at Laban Isthmus.

In general, *L*, *F*, and *T* values indicate that the magnetic fabric are mainly oblate ($L < F$, or $K_{max} \sim K_{int} > K_{min}$ and $0 < T < 1$), with variation in their prolate component ($L > F$, or $K_{max} > K_{int} \sim K_{min}$ and $-1 < T < 0$). The vertical changes of *Pj* and *Fs* are still consistent with one another and represent that the degree of alignment control the degree of

anisotropy. It indicates the fluctuations in the current strength during sedimentation (Wassmer et al., 2010).

Table 6-6. Anistropy of Magnetic Susceptibility parameters for sediment layers at Ujung Kulon.

Code of Samples	Mean Depth (cm)	K_m (in 10^{-4})	K_1	K_2	K_3	K_1 Axis		K_3 Axis		L	F	T	Pj	Fs	Q
						D^0	I^0	D^0	I^0						
U-01 004	91	0.535	1.0098	1.0040	0.9862	315	36	219	8	1.006	1.018	0.510	1.025	1.030	0.282
U-01 006	126	0.534	1.0168	0.9987	0.9845	348	34	90	18	1.018	1.014	-0.109	1.033	1.052	0.775
U-01 007	155	0.970	1.0063	1.0049	0.9888	122	15	27	17	1.001	1.016	0.842	1.020	1.019	0.083
U-01 008	181	2.702	1.0182	0.9980	0.9838	262	19	135	60	1.020	1.014	-0.164	1.035	1.056	0.830
U-01 009	202	2.153	1.0198	0.9946	0.9857	278	24	18	21	1.025	1.009	-0.471	1.036	1.061	1.171
U-01 010-a	217	3.087	1.0130	1.0026	0.9844	235	16	115	61	1.010	1.018	0.281	1.029	1.040	0.443
U-01 010-b	231	6.041	1.0176	1.0135	0.9689	286	27	124	62	1.004	1.046	0.835	1.056	1.055	0.088
U-03 002-a	15.5	13.990	1.0102	0.9969	0.9929	187	41	294	19	1.013	1.004	-0.529	1.018	1.031	1.241
U-03 002-b	18.5	14.410	1.0087	1.0025	0.9888	230	25	72	63	1.006	1.014	0.383	1.021	1.026	0.368
U-03 002-c	21	16.290	1.0134	0.9992	0.9874	0	26	260	20	1.014	1.012	-0.089	1.026	1.041	0.755
U-03 002-d	23.5	16.010	1.0134	1.0098	0.9769	248	7	139	68	1.004	1.034	0.806	1.041	1.041	0.104
U-03 002-e	29	10.630	1.0161	1.0152	0.9687	88	5	358	4	1.001	1.048	0.965	1.056	1.050	0.018
U-03 003	45	5.278	1.0109	1.0006	0.9885	329	26	188	58	1.010	1.012	0.088	1.023	1.033	0.595
U-04 002-a	15	20.890	1.0130	1.0058	0.9812	13	1	136	89	1.007	1.025	0.554	1.034	1.040	0.254
U-04 002-b	21	15.260	1.0223	1.0036	0.9741	343	3	224	83	1.019	1.030	0.235	1.050	1.069	0.482
U-04 003-a	40	11.940	1.0116	1.0095	0.9789	161	7	15	81	1.002	1.031	0.877	1.037	1.036	0.065
U-04 003-b	46	11.550	1.0257	1.0122	0.9621	7	3	252	83	1.013	1.052	0.585	1.070	1.080	0.238
U-04 003-c	48.5	11.150	1.0232	1.0054	0.9714	36	13	186	75	1.018	1.035	0.324	1.054	1.072	0.415
U-04 003-d	51	11.400	1.0267	0.9979	0.9754	19	19	165	67	1.029	1.023	-0.112	1.053	1.083	0.782
U-04 003-e	54	10.180	1.0453	1.0002	0.9545	17	1	279	81	1.045	1.048	0.030	1.095	1.145	0.660
U-04 005-a	71	6.590	1.0136	1.0059	0.9805	139	14	285	74	1.008	1.026	0.542	1.035	1.042	0.263
U-04 005-b	84	3.857	1.0184	1.0100	0.9716	76	25	306	55	1.008	1.039	0.647	1.052	1.057	0.198
U-04 007-a	100	2.515	1.0120	1.0086	0.9794	351	9	132	79	1.003	1.030	0.792	1.037	1.037	0.111
U-04 007-b	104	2.323	1.0109	1.0062	0.9828	356	12	109	62	1.005	1.024	0.671	1.031	1.033	0.182
U-04 007-c	110	3.329	1.0163	1.0049	0.9788	156	15	13	71	1.011	1.027	0.398	1.039	1.050	0.360
U-04 007-d	114	4.031	1.0112	1.0095	0.9793	21	21	228	67	1.002	1.031	0.891	1.037	1.034	0.057
U-04 009-a	133.5	8.044	1.0218	0.9981	0.9801	13	3	109	60	1.024	1.018	-0.127	1.043	1.067	0.794
U-04 009-b	136	5.881	1.0219	0.9993	0.9788	18	10	226	78	1.023	1.021	-0.035	1.044	1.068	0.708
U-04 009-c	139	4.501	1.0256	0.9927	0.9816	189	7	302	73	1.033	1.011	-0.488	1.047	1.080	1.195
U-04 009-d	142.5	6.978	1.0090	1.0030	0.9880	236	1	328	71	1.006	1.015	0.432	1.022	1.027	0.334
U-04 011	163.5	3.882	1.0103	0.9988	0.9909	231	8	329	42	1.012	1.008	-0.188	1.020	1.031	0.850
U-04 013	172	1.932	1.0245	1.0035	0.9720	34	1	291	84	1.021	1.032	0.211	1.054	1.076	0.501
U-04 014	193	3.574	1.0334	0.9922	0.9744	192	6	76	76	1.042	1.018	-0.384	1.062	1.105	1.073
U-04 015-a	200	4.168	1.0241	1.0038	0.9722	187	5	304	80	1.020	1.033	0.229	1.054	1.075	0.487
U-04 015-b	203.5	5.449	1.0233	1.0025	0.9742	9	12	207	77	1.021	1.029	0.165	1.051	1.072	0.537
U-04 016-a	222	6.563	1.0162	1.0049	0.9789	29	10	154	73	1.011	1.027	0.401	1.039	1.050	0.358
U-04 016-b	225	7.236	1.0170	1.0052	0.9778	208	2	319	83	1.012	1.028	0.410	1.041	1.052	0.352
U-04 016-c	227.5	9.779	1.0129	1.0013	0.9857	359	5	176	85	1.012	1.016	0.155	1.028	1.040	0.541
U-04 016-d	230	9.689	1.0104	1.0024	0.9872	181	0	74	88	1.008	1.015	0.315	1.024	1.032	0.417
U-04 016-e	232.5	11.460	1.0113	1.0003	0.9884	8	10	191	80	1.011	1.012	0.048	1.023	1.034	0.630
U-05 002	23	18.330	1.0166	1.0084	0.9749	16	7	157	81	1.008	1.034	0.613	1.045	1.051	0.218
U-05 003-a	40	18.180	1.0271	1.0059	0.9670	152	1	246	81	1.021	1.040	0.309	1.063	1.085	0.428
U-05 003-b	47	16.080	1.0102	1.0061	0.9837	324	7	164	83	1.004	1.023	0.698	1.029	1.031	0.165
U-05 003-c	51	16.320	1.0090	1.0013	0.9898	280	5	113	85	1.008	1.012	0.201	1.020	1.027	0.503
U-05 004-a	71	11.820	1.0384	1.0010	0.9606	93	15	282	75	1.037	1.042	0.057	1.081	1.121	0.633
U-05 004-b	79	10.590	1.0247	1.0114	0.9639	270	12	34	70	1.013	1.049	0.570	1.067	1.077	0.247
U-05 004-c	82	10.420	1.0208	1.0059	0.9732	318	20	161	69	1.015	1.034	0.384	1.050	1.065	0.371
U-05 005-a	97	11.790	1.0261	0.9996	0.9744	104	9	335	77	1.027	1.026	-0.012	1.053	1.081	0.689
U-05 005-b	100	8.597	1.0284	0.9984	0.9733	211	0	301	57	1.030	1.026	-0.075	1.057	1.088	0.748
U-05 006	103	7.444	1.0205	1.0037	0.9758	217	24	22	65	1.017	1.029	0.259	1.046	1.063	0.463
U-05 007	122	5.416	1.0069	1.0008	0.9922	158	35	347	55	1.006	1.009	0.175	1.015	1.021	0.522
U-05 012	189	5.380	1.0188	1.0011	0.9801	255	5	153	67	1.018	1.021	0.092	1.040	1.058	0.595
U-05 013	196	6.464	1.0212	1.0012	0.9776	247	3	151	65	1.020	1.024	0.095	1.045	1.066	0.593
U-05 017-a	282	1.453	1.0266	1.0144	0.9590	350	9	199	80	1.012	1.058	0.647	1.075	1.083	0.199
U-05 017-b	285	1.363	1.0266	1.0141	0.9593	270	10	70	79	1.012	1.057	0.639	1.075	1.083	0.204
U-06 002-a	7.5	16.060	1.0094	1.0009	0.9897	130	33	298	56	1.008	1.011	0.142	1.020	1.029	0.550
U-06 002-b	12	19.280	1.0190	1.0043	0.9767	24	2	283	80	1.015	1.028	0.314	1.044	1.059	0.421
U-06 003	28	18.120	1.0204	1.0032	0.9763	1	6	157	83	1.017	1.028	0.229	1.046	1.063	0.485
U-06 004	33	18.350	1.0242	1.0069	0.9690	18	5	146	83	1.017	1.039	0.384	1.058	1.075	0.372
U-06 005	38	19.180	1.0155	1.0105	0.9740	163	10	346	80	1.005	1.037	0.764	1.047	1.048	0.128
U-06 006	43	36.750	1.0117	1.0054	0.9828	37	2	289	85	1.006	1.023	0.568	1.031	1.036	0.245
U-06 007	48	33.430	1.0116	1.0042	0.9842	58	20	254	70	1.007	1.020	0.463	1.029	1.035	0.314
U-06 008-a	60	36.670	1.0115	1.0073	0.9812	21	2	123	79	1.004	1.027	0.724	1.034	1.035	0.151
U-06 008-b	63	37.870	1.0117	1.0031	0.9852	80	26	220	58	1.009	1.018	0.355	1.027	1.036	0.388
U-06 008-c	66	40.180	1.0054	1.0038	0.9908	197	3	51	86	1.002	1.013	0.787	1.016	1.016	0.113
U-06 008-d	70	36.020	1.0146	1.0036	0.9817	338	16	104	64	1.011	1.022	0.337	1.034	1.045	0.403
U-06 011	101	41.730	1.0120	1.0073	0.9808	1	5	177	85	1.005	1.027	0.702	1.034	1.037	0.163
U-06 012	107	35.640	1.0226	1.0014	0.9760	194	5	25	85	1.021	1.026	0.100	1.048	1.070	0.590

Table 6-6 (continued)

Code of Samples	Mean Depth (cm)	K_m (in 10^{-4})	K_1	K_2	K_3	K_1 Axis		K_3 Axis		L	F	T	Pj	Fs	Q
						D^0	I^0	D^0	I^0						
U-08 007-a	166	5.039	1.0175	1.0020	0.9805	258	17	116	69	1.015	1.022	0.174	1.038	1.054	0.527
U-08 007-b	170	7.506	1.0087	1.0017	0.9896	175	7	298	77	1.007	1.012	0.266	1.020	1.026	0.453
U-08 008	194	4.694	1.0089	1.0004	0.9907	291	34	200	1	1.008	1.010	0.070	1.018	1.027	0.609
U-17 002-a	17	13.130	1.0022	0.9998	0.9980	140	76	296	13	1.002	1.002	-0.164	1.004	1.007	0.822
U-17 002-b	19.5	11,000	1.0024	1.0006	0.9969	167	55	279	15	1.002	1.004	0.332	1.006	1.007	0.402
U-17 003-a	22	12.060	1.0045	0.9998	0.9957	89	45	256	44	1.005	1.004	-0.065	1.009	1.014	0.727
U-17 003-b	26.5	11.780	1.0033	0.9997	0.9971	34	25	275	46	1.004	1.003	-0.144	1.006	1.010	0.803
U-17 003-c	27	10.970	1.0028	1.0007	0.9964	318	31	133	59	1.002	1.004	0.352	1.007	1.009	0.388
U-17 004	31.5	11.440	1.0072	0.9980	0.9948	14	60	141	20	1.009	1.003	-0.471	1.013	1.022	1.167
U-17 005-a	46	8.326	1.0030	1.0005	0.9965	201	18	298	20	1.003	1.004	0.214	1.007	1.009	0.490
U-17 005-b	56	6.750	1.0054	0.9988	0.9958	192	43	294	13	1.007	1.003	-0.381	1.010	1.016	1.057
U-17 005-c	71	9.408	1.0024	1.0011	0.9965	191	58	38	29	1.001	1.005	0.575	1.006	1.007	0.239

Note: see Part II, Chapter 5, for the explanation of AMS parameters

In accordance with the laboratory measurements for primary depositional fabrics of natural sediments (Hamilton and Rees, 1970), the shape factor (q) ranges between 0.006 and 0.700, although minimum and maximum values reaching 0.018 and 1.241 respectively. The imbrication angles (I; inclination of K_1) are commonly less than 20°, with some variation between 21° and 41°. Thus, the AMS data can be used for analysis of depositional processes of tsunami deposits and their flow directions (Hamilton and Rees, 1970). However, exceptional imbrication angles measured at section U-17, ranges between 18° and 76°, must be considered in those analysis.

In relation with the tsunami waves, K_1 axes show that the sediments were emplaced by two general flow directions, see Table 6-6. A first southward direction, from Sunda Strait, spreading between N104°E and N262°E. A second in the opposite direction from Indian Ocean spreading between N280°E and N80°E. Starting with a southward direction, the two directions evidenced by AMS alternate with a surprising regularity within the whole sedimentary sequence investigated. The southward direction is in accordance with the propagation of Krakatau direct tsunamis waves. The northward direction is more surprizing, especially because it appears have been synchronous of the Krakatau tsunami events. A strong backwash is hard to imagin in this very flat topographic context. This finding evidenced by AMS confirm the flooding of Ujung Kulon Peninsula South coastal areas described by Verbeek (1885) but it's origin must be explained.

6.5. Mineral and chemical composition

In the microscopic examination of the volcanic ash collected from U-01, U-02, U-03, U-06, U-08, and U-13 (Figure 6-27 to 6-32), glass, rock fragments, and some minerals were identified. The glass particles, microscopic pieces of pumice, are not present in large abundance (< 10%) and are apparently altered in clay minerals. The identified minerals are feldspar (mostly plagioclase, but K-feldspar is also present in some samples), orthopyroxene, and opaque minerals (e.g. ilmenite, magnetite, etc), in accordance with the previous descriptions of 1883 Krakatau pyroclastic deposits (Paris et al., 2014; Renard, A., 1883; Symons et al., 1888; Verbeek, 1885, 1884).

The samples from proximal sections (U-01, U-02, U-03, U-06) were selected due to an assumption that the deposits at distal sections must be derived from the same sources with those at the proximal sections. From section U-08, a layer at a depth between 35 - 70 cm was chosen due to its texture that shows the best characteristics of volcanic deposit. Below are the detailed descriptions of thin sections realized on the material of the volcanic ash sampled from the selected layers, i.e. the volcanic deposits or tsunami deposits containing pumice and volcanic ash.

1. Thin section of U-01 from a depth of 0 - 35 cm (volcanic ash deposit, see also Figure 6-2) shows a brownish white tint, contains subrounded grains, medium sorted, and matrix supported. This section is composed by groundmass (25%, microcrystalline, interference color; 1st order white), rock fragments (30%, subangular sediment fractions), volcanic glass (10%, rounded pumice), and other minerals such as quartz (10%, interference color; 1st order white), plagioclase (5%, albite-carlsbad twin, interference color; 1st order white), K-feldspars (3%, interference color; 1st order white), and opaque minerals (17%, black, neither transparent nor translucent).
2. Thin section of U-02 from a depth of 0 – 30 cm (pumiceous-bioclastic silty soil unit, see also Figure 6-3) shows a yellowish white tint, contains subangular grains, poorly sorted, and matrix supported. This section is composed by groundmass (50%, microcrystalline, interference color; 1st order white), rock fragments (15%, subangular sediment fractions), and other minerals such as quartz (10%, interference color; 1st order white), plagioclase (9%, albite twin, interference color; 1st order white), K-feldspars (10%, interference color; 1st order white), pyroxene (5%, interference color; 2nd order light blue), and clay minerals (1%, interference color; 3rd order green).

3. Thin section of U-03 from a depth of 0 – 30 cm (pumiceous-bioclastic silty soil unit, see also Figure 6-4) shows a yellowish white tint, contains subangular to angular grains, poorly sorted, and matrix supported. This section is composed by groundmass (40%, microcrystalline, interference color; 1st order white), rock fragments (15%, subangular sediment fractions), volcanic glass (5%, rounded pumice), and other crystal minerals such as quartz (10%, interference color: 1st order white), plagioclase (20%, carlsbad twin, interference color; 1st order white), K-feldspars (5%, interference color; 1st order white), and orthopyroxene (5%, interference color; 2nd order light blue).
4. Thin section of U-06 from a depth of 55 – 75 cm (pumiceous sand unit, see also Figure 6-7) shows a yellowish white tint, contains subrounded grains, poorly sorted, and matrix supported. This section is composed by groundmass (40%, microcrystalline, interference color; 1st order white), rock fragments (20%, subangular sediment fractions, e.g. clay), and other minerals such as quartz (8%, interference color; 1st order white), K-feldspars (25%, interference color; 1st order white), and pyroxene (7%, interference color; 2nd order light blue).
5. Thin section of U-08 from a depth of 35 – 70 cm (pumiceous sand unit, see also Figure 6-8) shows a brownish white tint, contains subangular grains, poorly sorted, and matrix supported. This section is composed by groundmass (50%, microcrystalline, interference color; 1st order white), rock fragments (28%, subangular sediment fractions), and other minerals such as quartz (10%, interference color; 1st order white), plagioclase (5%, albite twin, interference color; 1st order white), K-feldspars (5%, interference color; 1st order white), and clay minerals (2%, interference color; 3rd order green).
6. Thin section of U-13 from a depth of 85 cm (pumiceous ash and bioclastic sand unit, see also Figure 6-11) shows a brownish white tint, contains subrounded grains, medium sorted, and matrix supported. This section is composed by groundmass (50%, microcrystalline, interference color; 1st order white), rock fragments (30%, subangular sediment fractions, e.g. clay), and other minerals such as quartz (8%, interference color; 1st order white), K-feldspars (5%, interference color; 1st order white), pyroxene (2%, interference color; 2nd order light blue), and opaque minerals (5%, black, neither transparent nor translucent).

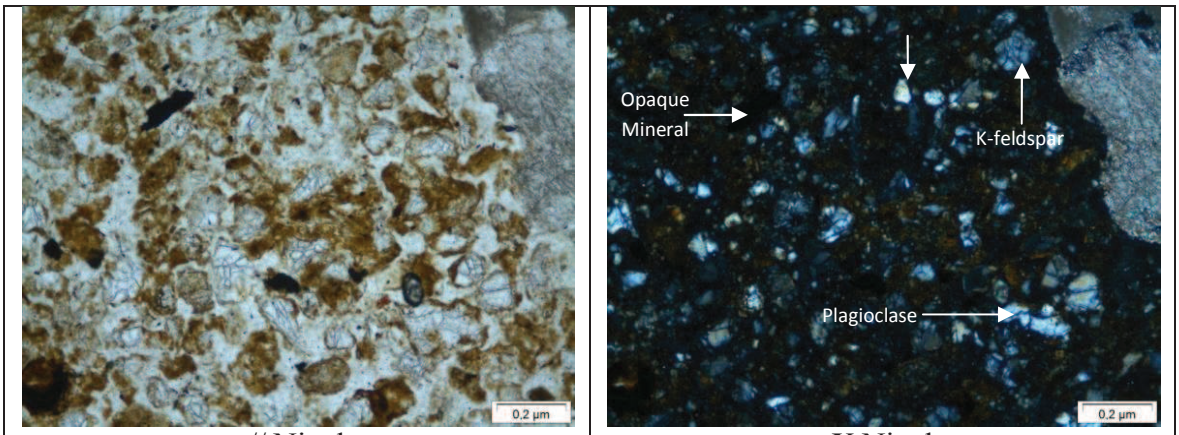

// Nicol | X Nicol

Figure 6-27. Photomicrograph of U-01 (0-35 cm) thin section displayed in *parallel nicol* or plane-polarized light (left) and *crossed nicol* or cross-polarized light (right). Crossed nicol is mainly used to recognize the type of minerals through their birefringence (interference color) and twinning characteristics.

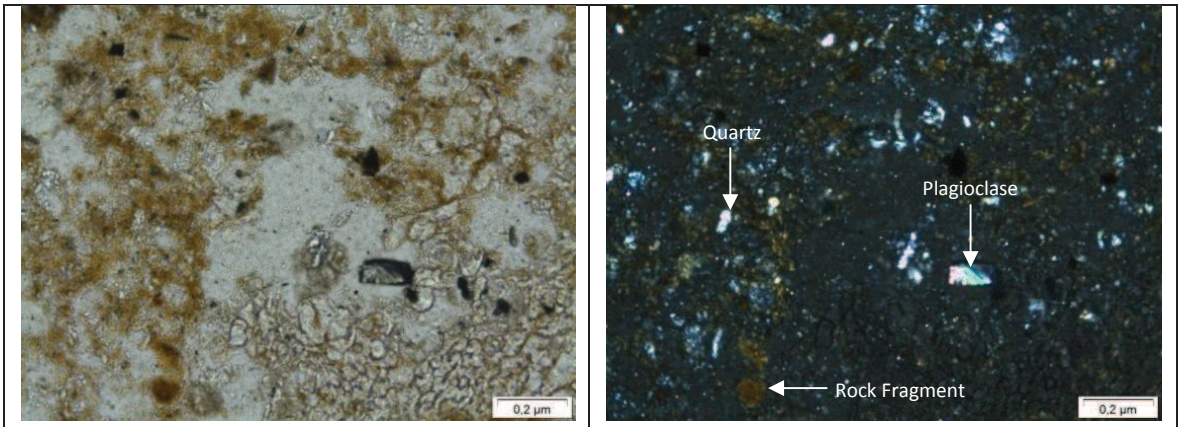

// Nicol | X Nicol

Figure 6-28. Photomicrograph of U-02 (0-30 cm) thin section displayed in *parallel nicol* or plane-polarized light (left) and *crossed nicol* or cross-polarized light (right).

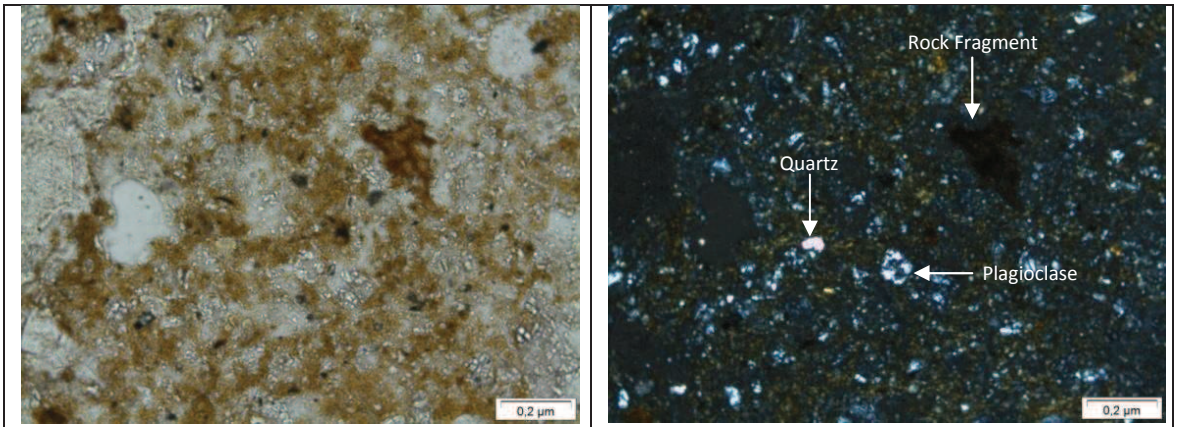

// Nicol | X Nicol

Figure 6-29. Photomicrograph of U-03 (0-30 cm) thin section displayed in *parallel nicol* or plane-polarized light (left) and *crossed nicol* or cross-polarized light (right).

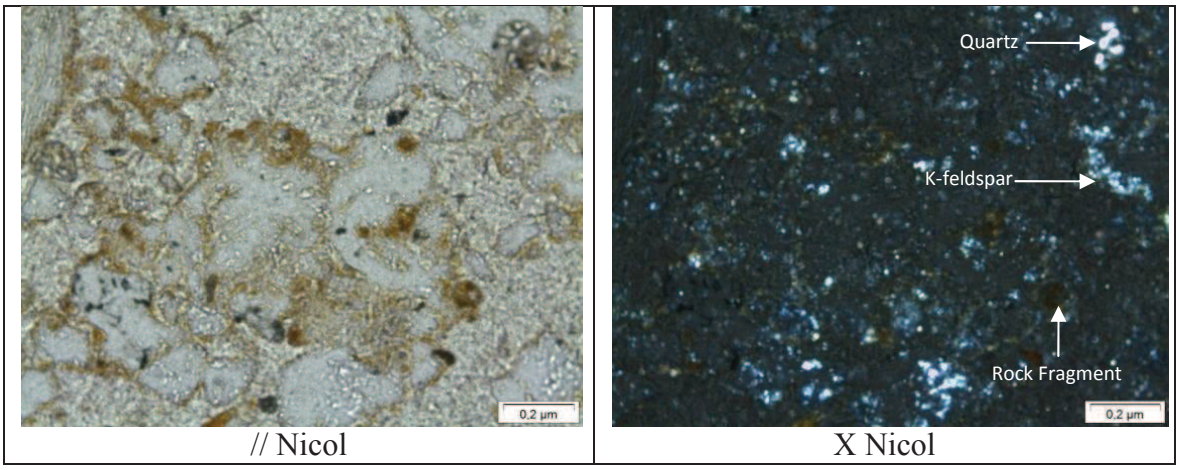

Figure 6-30. Photomicrograph of U-06 (55-75 cm) thin section displayed in *parallel nicol* or plane-polarized light (left) and *crossed nicol* or cross-polarized light (right).

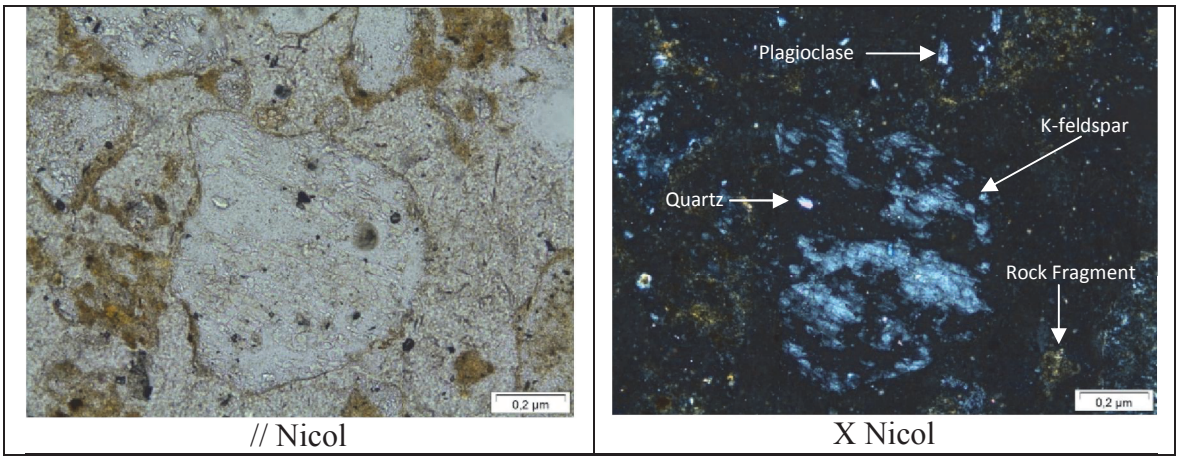

Figure 6-31. Photomicrograph of U-08 (35-70 cm) thin section displayed in *parallel nicol* or plane-polarized light (left) and *crossed nicol* or cross-polarized light (right).

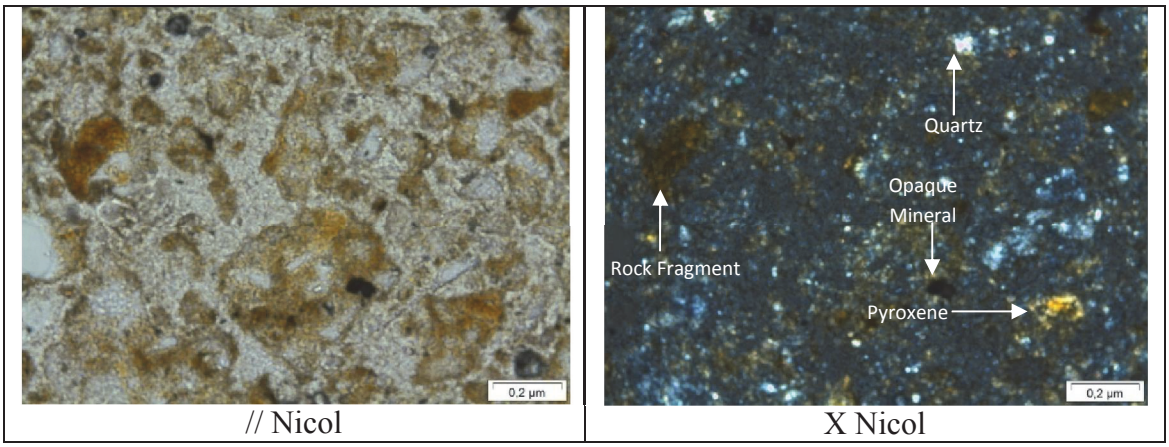

Figure 6-32. Photomicrograph of U-13 thin section displayed in *parallel nicol* or plane-polarized light (left) and *crossed nicol* or cross-polarized light (right).

Samples composed of coarse sands to coral gravels mixed with abundant bioclasts were also examined under polarizing microscope to recognize the composition of minerals and their origin environment. The main components are groundmass, shell fragments, rock fragments, and crystal minerals such as quartz, plagioclase, K-feldspars, and pyroxene that are present in various amounts. Groundmass (composed of microcrystalline) and rock fragments (composed of subrounded to subangular sediment fractions) are of volcaniclastic origin. Abundant shell fragments in the samples constitute the remnant fragments of molluscs or foraminifera, with very minor siliceous sponge spicules, as indicator of a marine environment origin.

Only four representative sections were examined, section U-01 (proximal section of Laban Isthmus), U-4 (distal section of Laban Isthmus), U-08 (Cidaun at the western part of Ujung Kulon Peninsula), and U-17 (Mount Honje region). Fine bioclastic sand layer from section U-01 at a depth of 117 – 122 cm and from section U-17 at a depth of 0 – 10 cm and 40 -50 cm were selected due to their best chracteristics of tsunami sand unit. Rip-up clasts mixed with bioclastic sand layer from section U-04 at a depth of 180 – 210 cm was selected to recognize the composition of organic shells and minerals. A layer from section U-08 at a depth of 175 – 210 cm was also selected due to its unique characteristic, i.e. bioclastic sand unit mixed with pumice and terrigenous materials. The detailed descriptions of thin sections from U-01, U-04, U-08, and U-17 (see Figure 6-33 to 6-37) are explained as the following:

1. Thin section of U-01 from a depth of 117 – 122 cm shows a yellowish brown tint, contains subangular grains, poorly sorted, and matrix supported. This section is dominated by shell fragments (60%, the remnant of organic shells), groundmass (20%, microcrystalline, interference color; 1st order white), rock fragments (15%, pale and subangular sediment fractions), and other minerals such as quartz (3%, interference color; 1st order white) and pyroxene (7%, interference color; 2nd order light blue).
2. Thin section of U-04 from a depth of 180 – 210 cm shows a yellowish white tint, contains subangular grains, poorly sorted, and matrix supported. This section is dominated by shell fragments (55%, the remnant of organic shells), groundmass (20%, microcrystalline, interference color; 1st order white), and other minerals such as quartz (7%, interference color; 1st order white), plagioclase (7%, carlsbad twin, interference color; 1st order white), K-feldspars (5%, interference color; 1st order white), and opaque minerals (6%, black, neither transparent nor translucent).

3. Thin section of U-08 from a depth of 175 – 210 cm shows a brownish white tint, contains subrounded grains, poorly sorted, and matrix supported. This section is composed of shell fragments (25%, the remnant of organic shells), groundmass (30%, microcrystalline, interference color; 1st order white), rock fragments (15%, subrounded sediment fractions), and other minerals such as quartz (12%, interference color; 1st order white), plagioclase (5%, carlsbad twin, interference color; 1st order white), K-feldspars (10%, 1st order white), and pyroxene (7%, 2nd order light blue).
4. Thin section of U-17 from a depth of 0 – 10 cm shows a yellowish white tint, contains subrounded – angular grains, poorly sorted, and matrix supported. This section is composed of shell fragments (15%, the remnant of organic shells), groundmass (60%, microcrystalline, interference color; 1st order white), rock fragments (5%, subrounded - subangular sediment fractions), and other minerals such as quartz (10%, interference color; 1st order white), plagioclase (3%, albite twin, interference color; 1st order white), K-feldspars (3%, 1st order white), and pyroxene (4%, 2nd order light blue).
5. Thin section of U-17 from a depth of 40 – 50 cm shows a yellowish white tint, contains subangular grains, poorly sorted, and matrix supported. This section is composed of shell fragments (25%, the remnant of organic shells), groundmass (40%, microcrystalline, interference color; 1st order white), rock fragments (20%, subangular sediment fractions), and other minerals such as quartz (5%, interference color; 1st order white), plagioclase (5%, albite twin, interference color; 1st order white), and K-feldspars (5%, 1st order white).

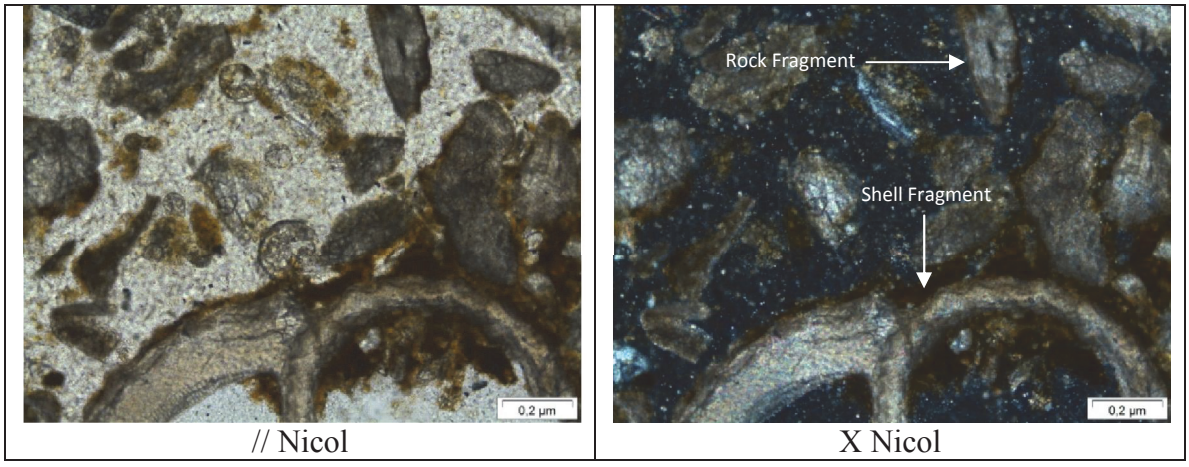

Figure 6-33. Photomicrograph of U-01 (117-122 cm) thin section displayed in *parallel nicol* or plane-polarized light (left) and *crossed nicol* or cross-polarized light (right).

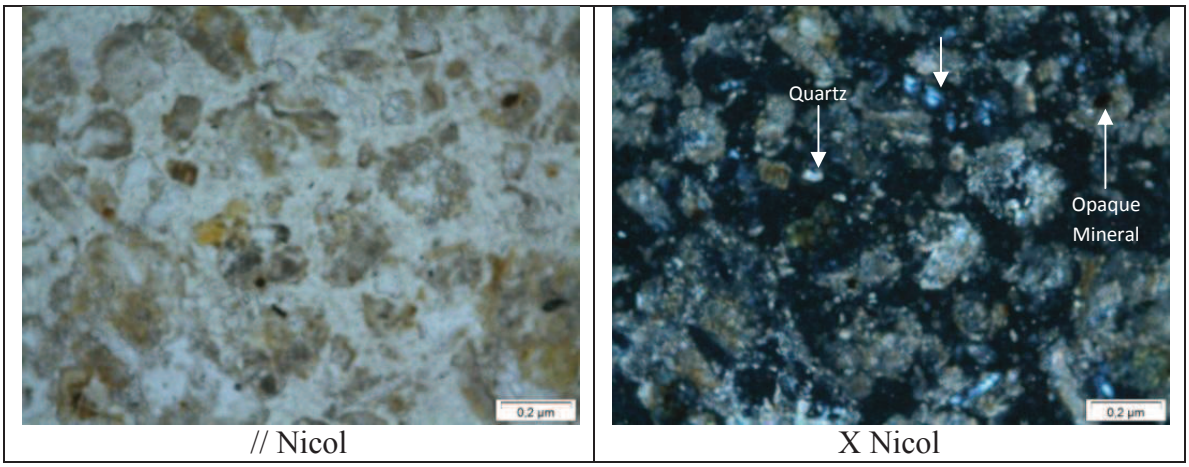

Figure 6-34. Photomicrograph of U-04 (180-210 cm) thin section displayed in *parallel nicol* or plane-polarized light (left) and *crossed nicol* or cross-polarized light (right).

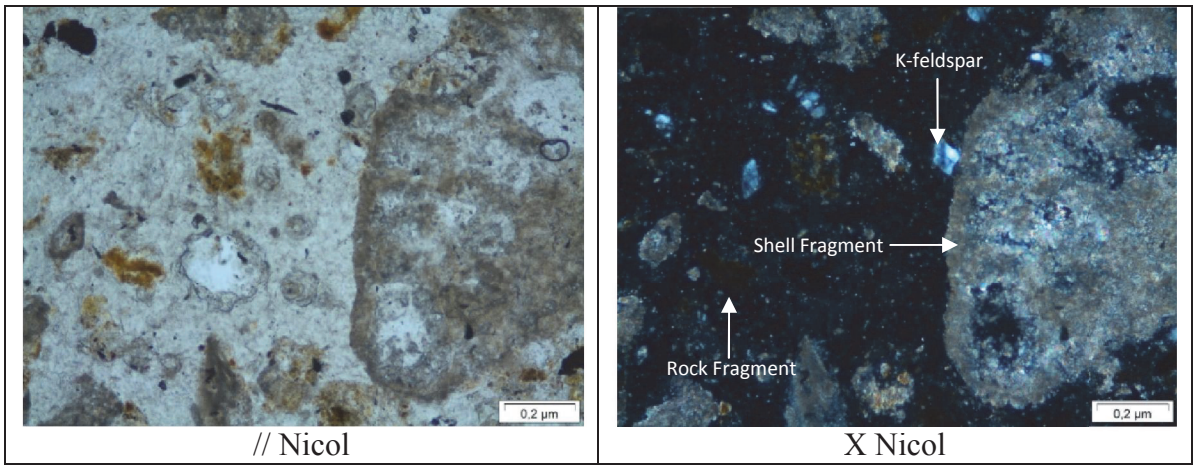

Figure 6-35. Photomicrograph of U-08 (175-210 cm) thin section displayed in *parallel nicol* or plane-polarized light (left) and *crossed nicol* or cross-polarized light (right).

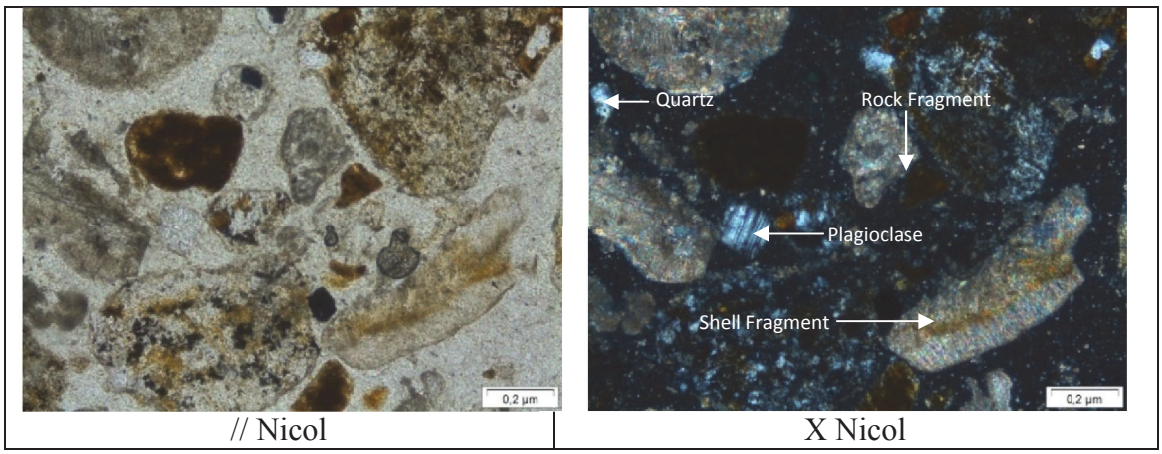

Figure 6-36. Photomicrograph of U-17 (0-10 cm) thin section displayed in *parallel nicol* or plane-polarized light (left) and *crossed nicol* or cross-polarized light (right).

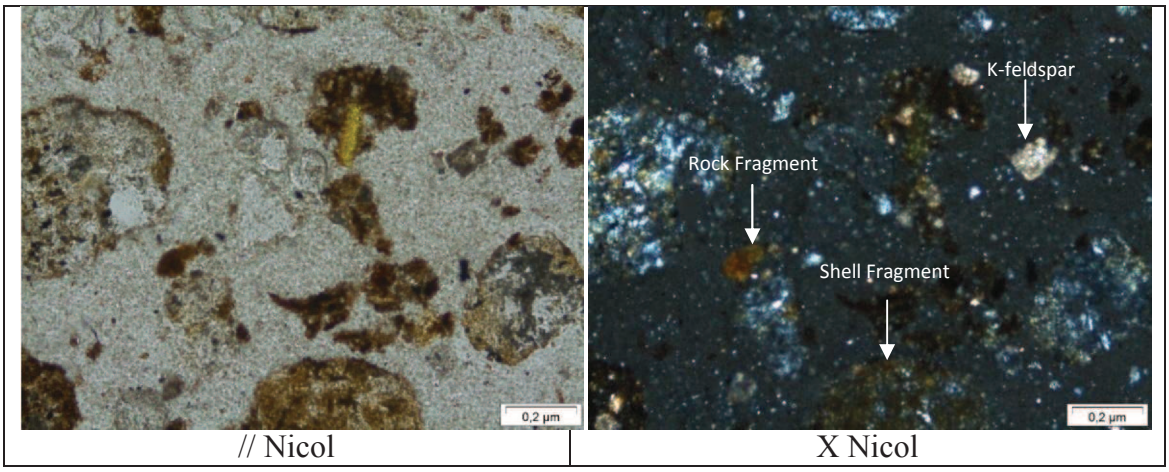

Figure 6-37. Photomicrograph of U-17 (40-50 cm) thin section displayed in *parallel nicol* or plane-polarized light (left) and *crossed nicol* or cross-polarized light (right).

Besides petrographic analysis, chemical analysis (XRF) was performed in order to distinguish bioclastic sand unit, pumiceous sand unit, and volcanic ash ejected from 1883 Krakatau eruptions. Three representative layers were sampled from Laban's transect, i.e. a layer from setion U-03 at a depth between 0 – 30 cm, a layer from section U-06 at a depth between 55 – 75 cm, and a layer from section U-04 at a depth between 180 – 210 cm. Samples from U-03 (0-30 cm) and U-06 (55-75 cm) represent pumiceous sand/volcanic ash deposit at proximal sections, whereas sample from U-04 (180-210 cm) constitutes one of the best representative layers of bioclastic sand at distal sections.

Major elements, i.e. SiO_2, TiO_2, Al_2O_3, Fe_2O_3, MnO, MgO, CaO, Na_2O, K_2O, and P_2O_5, and the proportions of bioclasts, expressed by organic and carbonate content in loss on ignition (LOI), were used in this comparison, in which SiO_2, CaO, and LOI become the key of comparison due to their significant differences. In relation to the common research of tsunami deposits, trace elements (Ba, Ce, Cr, Ga, Nb, Ni, Pb, Rb, Sc, Sr, Th, V, Y, and Zr) were not used in the comparison.

U-03 (0-30 cm) has 66.74 wt% of SiO_2 and U-06 (55-75 cm) has 76.50 wt% of SiO_2, while U-04 (180 -210 cm) has only 24.59 wt% of SiO_2. Notwithstanding, sample of U-04 contains significant CaO and LOI, i.e. about 33.80 wt% and 27.19 wt% respectively. On the contrary, U-03 has only 1.51 wt% of CaO and 9.45 wt% of LOI. As well as the sample from U-06 which only contains 1.97 wt% of CaO and 2.80 wt% of LOI.

Table 6-7. Chemical analysis comparison of pumiceous sand unit or volcanic ash deposits (U-03 and U-06) and bioclastic sand unit (U-04).

weight %	U-03 (0-30)	U-04 (180-210)	U-06 (55-75)
SiO_2	66.74	24.59	76.50
TiO_2	1.04	0.41	1.18
Al_2O_3	12.72	6.40	9.78
Fe_2O_3	6.15	4.14	5.17
MnO	0.11	0.05	0.08
MgO	1.03	2.10	0.87
CaO	1.51	33.80	1.97
Na_2O	1.10	0.74	1.62
K_2O	0.78	0.42	0.60
P_2O_5	0.14	0.12	0.11
LOI	9.45	27.19	2.80
Total	**100.74**	**99.94**	**100.68**

The results of field investigations and laboratory analyses demonstrate that tsunami sedimentary recordings are better preserved at Ujung Kulon Peninsula than on the narrow coastal plain of Mount Honje region. Six drilling sections along a North – South transect at Laban Isthmus, Ujung Kulon Peninsula, display a great complexity and lateral variations of sedimentary signatures. The sections, that are separated one to the other within a distance between 100 to 400 m, indicate a similarity of texture and composition at certain layers from base to top. Rip-up clasts of clayey sediment constitutes the base layer of the sections. Above, a thick bioclastic sand unit is almost found at several depths. These similarities can be used to reconstruct a stratigraphic correlation between proximal and distal sections. Fining upward repetition of the grain-size at each section recognized from laboratory analysis and CM diagram confirming an emplacement under high energy of the

waves (rolling and rolling-ground suspension) can be used to synthesize tsunami sequences at each section before correlating one to the other. The identification of foraminiferal assemblages within the deposits, e.g. identifying a stenoecious species (foraminifera strongly linked to restricted environment) such as *Planulina wuellerstorfi* (linked to a continental margin environment), has given a significant contribution to confirm flooding of the isthmus by the South. This finding is then supported by AMS analysis evidencing repetition of surprising floodings from the South during the Krakatau tsunami sequence recordings. Finally, the results of mineralogy and geochemical analyses show that the deposits have a similarity composition with the previous examinations of Krakatau volcanic ash collected immediately after 1883 eruptions.

Chapter 7
Synthesis

This chapter contains a combination of data collected that constitutes the recognition of tsunami sequences and their stratigraphic correlation. The stratigraphic correlation is then used as a tool for reconstructing the palaeocurrent and sediment emplacement. It will contribute to a better understanding of the scenario of tsunamis penetrating far inland along Ujung Kulon coastal plains, and particularly, at Ujung Kulon Peninsula with its remarkable V-shape bays and its narrow isthmus between Sunda Strait and Indian Ocean. Different from Chapter 6, the below descriptions of tsunami sequences are based on a combination of sedimentological data (core descriptions and grain-size analysis) to allow evidencing the quantity of sequences at each section. This synthesis may significantly change due to the K_1 axis changes (in a deposit, this axis is parallel the flow directions). Thus, a sequence determined by the first synthesis can be changed to two or three sequences in the later synthesis.

7.1. Tsunami sequences

7.1.1. Tsunami sequences at Laban Isthmus (from U-01 to U-06)

At distal sections (U-04 and U-05), the grain-size parameters show more important fluctuations than at the proximal sections (except U-06). According to their normal grading repetition, skewness, kurtosis, bioclasts, pyroclastics content, rip-up clasts characterizing the base of an uprush phase, four sequences of tsunami deposits have been identified at sections U-01, U-02, U-03, U04, and U-06, and five sequences at sections U-05 (Figure 7-1a to 7-6a). The boundaries between sequences, linked to material texture, are controlled by textural triangle adopted from Brady and Weil (1999). Some deposits display the sequence boundaries characterized by fine sands/silts mixed with gravel/coarse sands, or, in the textural triangle ranging between loamy sand/sandy loam and loam/silt loam (Figure 7-1b to 7-6b). Loam is a deposit composed mostly of sand and silt, and a smaller amount of clay.

These boundaries are important because they correspond to the interface between two sequences and correspond to the superposition between two processes: at the base the top of a sequence of the previous tsunami is characterised by low energy processes leading to deposition of fine material, and atop, strong energy processes at the base of the new sequence emplacing coarser material within rip-up, scouring sometimes the basal layer and mixing the interface material. This thin contact zone confirms the contact between two tsunami sequences.

First tsunami sequence at section U-01 is characterized by the presence of rip-up clasts of clayey sediment mixed with normally graded medium to fine sands (subrounded and poorly to extremely poorly sorted). Second tsunami sequence consists of subrounded to subangular poorly sorted coarse to fine sands with a thin layer of pumiceous sand. Third sequence consists of poorly sorted coarse to fine sands mixed with bioclasts. Fourth sequence in this section is constituted by a pumiceous sand layer.

Similar with section U-01, first tsunami sequence at section U-02 displays rip-up clasts of clayey sediment mixed with normally graded medium to fine sands (subrounded and poorly to extremely poorly sorted). Second tsunami sequence consists of subrounded to subangular poorly sorted coarse to fine sands. Third sequence at this section consists of poorly sorted coarse to fine sands mixed with bioclasts. Fourth sequence consists of pumiceous silty soil containing bioclasts.

At section U-03, the first tsunami sequence shows rip-up clasts of clayey sediment mixed with normally graded coarse to fine sands (subrounded to subangular and poorly to extremely poorly sorted). Second sequence consists of poorly sorted coarse to fine sands mixed with bioclasts. A reverse grading is present at the upper part of the sequence. Third sequence is composed of bioclastic sands which normally graded (coarse to fine) sands. Fourth sequence corresponds to a pumiceous-bioclastic silty soil.

Like previous sections, rip-up clasts of clayey sediment mixed with normally graded medium to fine sands (subrounded and poorly to extremely poorly sorted) constitutes the first tsunami sequence at section U-04. Second tsunami sequence in this section consists of subrounded to subangular and poorly sorted coarse to fine sands mixed with rip-up clasts and large coral boulders embedded in sands. Third sequence consists of poorly sorted coarse to fine sands mixed with bioclasts. Fourth sequence is composed by volcaniclastic sand units at the base and silty soil containing pumice and bioclasts at the top.

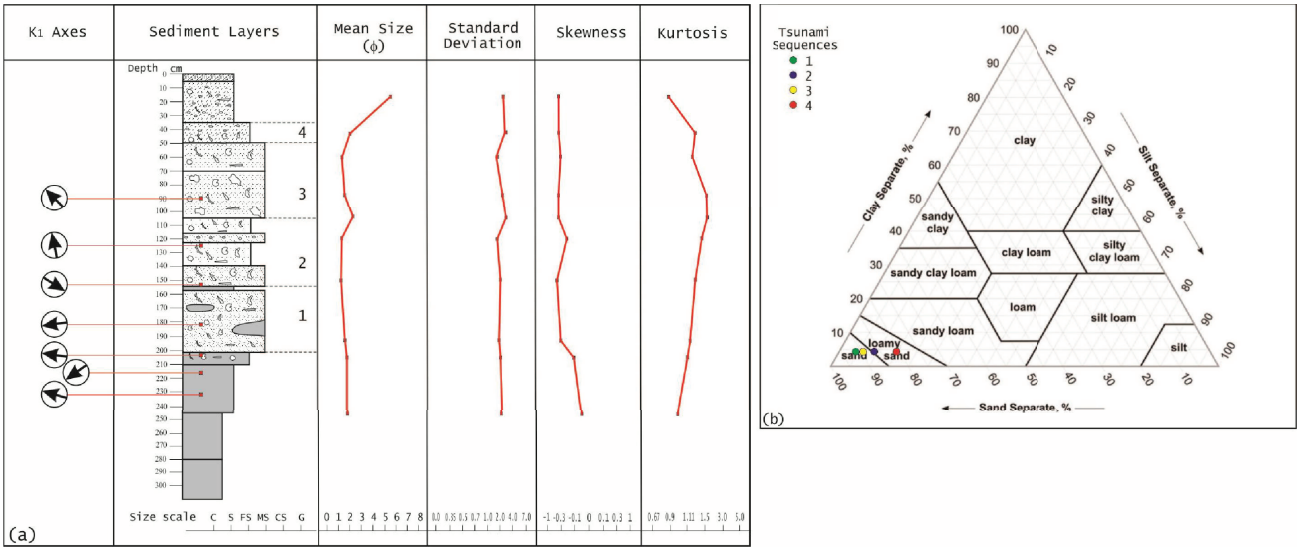

Figure 7-1. (a) Log profile of section U-01 with its grain-size distribution curves. Four sequences of tsunami deposit are marked numerically from base to top. (b) Textural triangle adopted from Brady and Weil (1999) showing the compositional texture of the sequence boundaries.

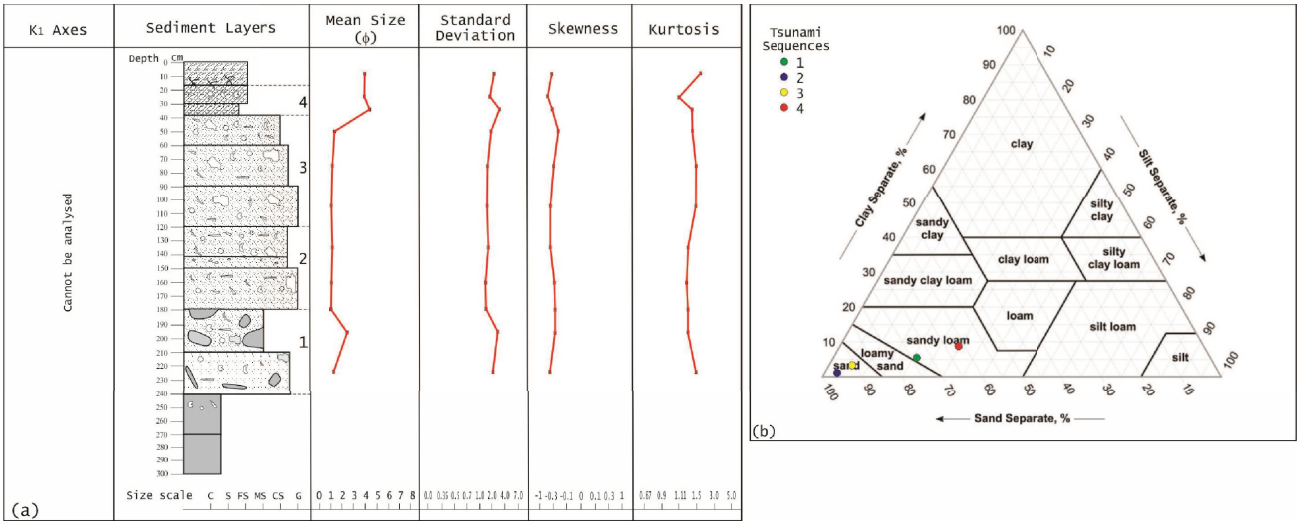

Figure 7-2. Log profile for section U-02 with its grain-size distribution curves. Four sequences of tsunami deposit are marked numerically from base to top. (b) Textural triangle adopted from Brady and Weil (1999) showing the compositional texture of the sequence boundaries.

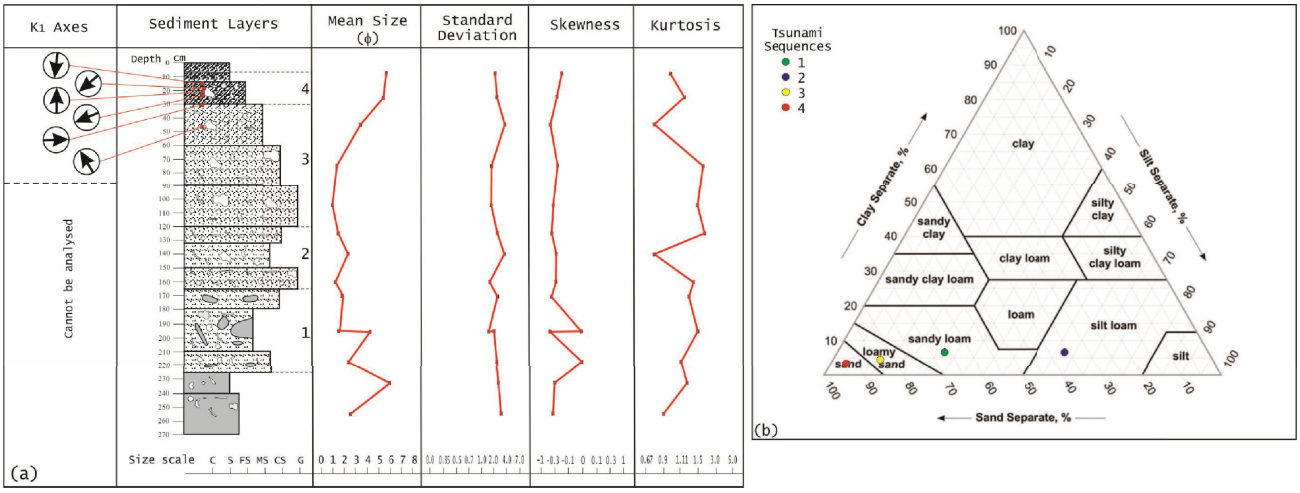

Figure 7-3. (a) Log profile of section U-03 with its grain-size distribution curves. Four sequences of tsunami deposit are marked numerically from base to top. (b) Textural triangle adopted from Brady and Weil (1999) showing the compositional texture of the sequence boundaries.

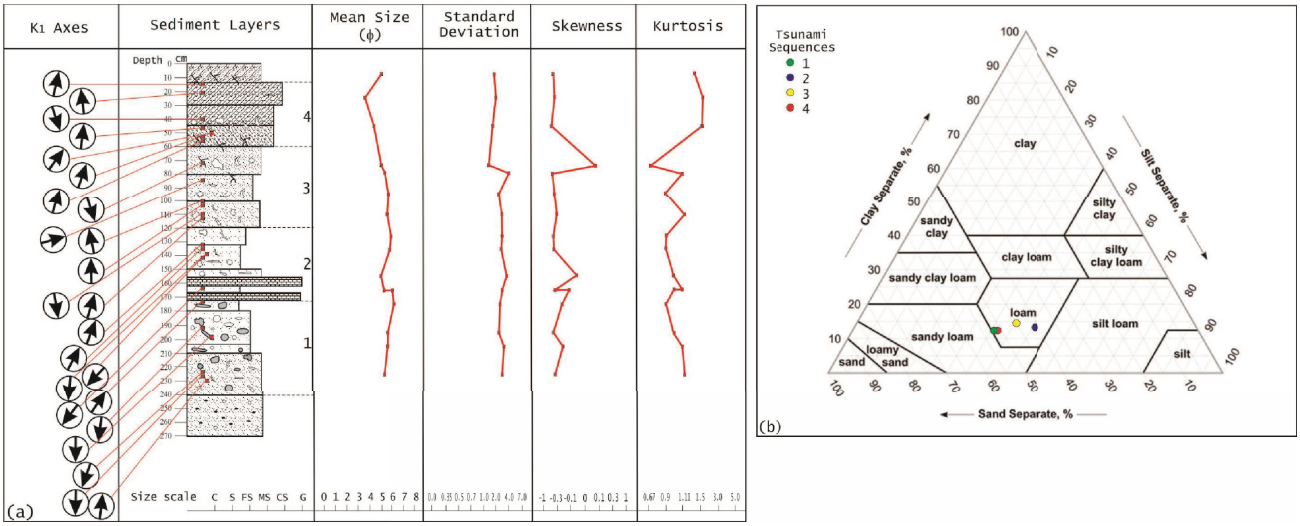

Figure 7-4. (a) Log profile of section U-04 with its grain-size distribution curves. Four sequences of tsunami deposit are marked numerically from base to top. (b) Textural triangle adopted from Brady and Weil (1999) showing the compositional texture of the sequence boundaries.

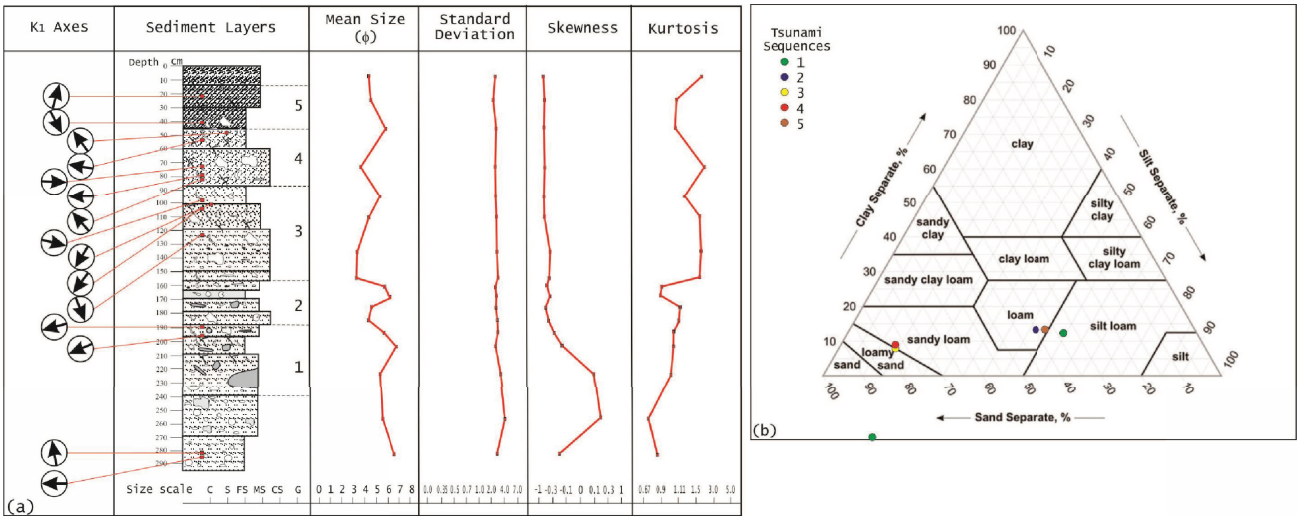

Figure 7-5. (a) Log profile of section U-05 with its grain-size distribution curves. Five sequences of tsunami deposit are marked numerically from base to top. (b) Textural triangle adopted from Brady and Weil (1999) showing the compositional texture of the sequence boundaries.

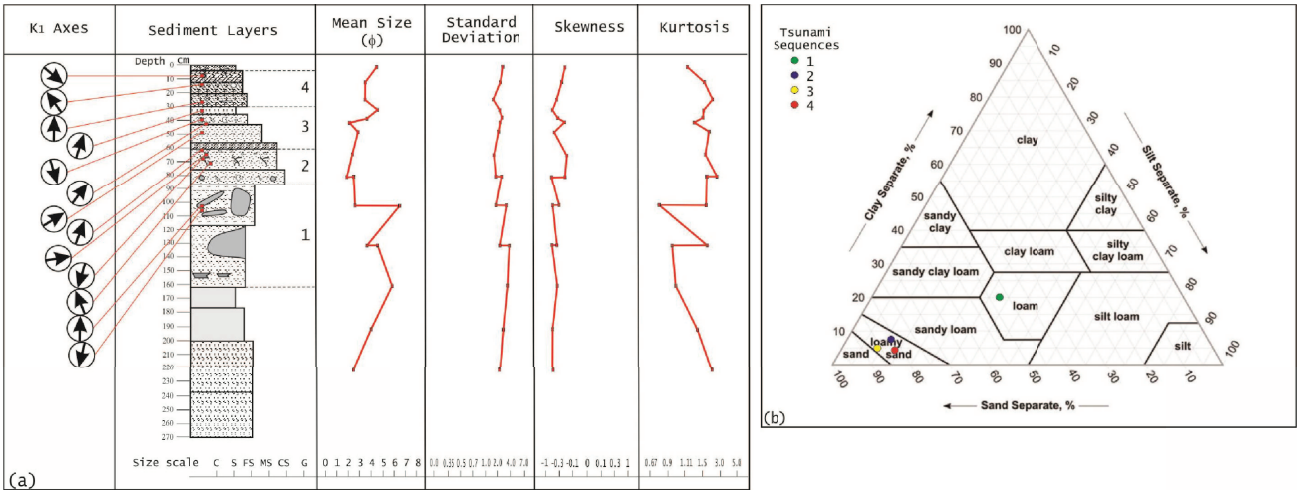

Figure 7-6. (a) Log profile of section U-06 with its grain-size distribution curves. Four sequences of tsunami deposit are marked numerically from base to top. (b) Textural triangle adopted from Brady and Weil (1999) showing the compositional texture of the sequence boundaries.

Section U-05 is almost similar with section U-04. First sequence at this section displays rip-up clasts of clayey sediment mixed with normally graded medium to fine sands (subrounded and poorly to extremely poorly sorted). Second tsunami sequence consists of subrounded to subangular poorly sorted coarse to fine sands mixed with rip-up clasts and bioclasts. Third tsunami sequence is composed of bioclastic sands which normally graded (coarse to fine sands). Fourth sequence is composed of volcaniclastic sand units mixed with abundant bioclasts. The last (fifth) sequence found at this section shows similar characteristic than those of section U-04, consist of pumiceous-bioclastic silty soil.

First tsunami sequence at section U-06 contains rip-up clasts of clayey sediment mixed with fine to medium sands (subrounded and poorly to extremely poorly sorted) displaying a discrete reverse grading. Second tsunami sequence, generally, consists of subrounded to subangular poorly sorted coarse to fine sands. Rip-up clasts of clayey sediment is also present at this sequence. Third sequence consists of normally graded and poorly sorted coarse to fine sands mixed with bioclasts. Fourth sequence at this section corresponds to a bioclastic silty soil layer without volcanic materials involved.

7.1.2. Tsunami sequences at Cidaun (Site-08)

Site U-08 is located in the western part of Ujung Kulon Peninsula (Cidaun, near Peucang Island). Based on their normal grading repetition, skewness, kurtosis, bioclasts, pyroclastics content, and rip-up clasts, three sequences of tsunami deposits have been identified (Figure 7-7a). First sequence, at a depth between 315 - 245 cm, consists of rip-up clasts of clayey sediment at the bottom layer, coral gravels mixed with fine grey sands (subrounded and very poorly sorted) and abundant bioclasts at the upper part.

Second tsunami sequence lies at depth between 210 - 180 cm. It consists of coral gravels mixed with fine sands, bioclasts, and volcanic ash at the upper part. The sandy material is characterized by subrounded to subangular shape and is very poorly to extremely poorly sorted.

Third sequence lies at a depth between 120 - 35 cm. It consists of normally graded medium to fine sands mixed with pumiceous-lapilli and pumiceous ash, bioclasts, and other organic materials. Sands at this sequence are subrounded and very poorly sorted. A discrete reverse grading is present at the upper part of the sequence, which consists of medium sand mixed with coral gravels and abundant bioclasts.

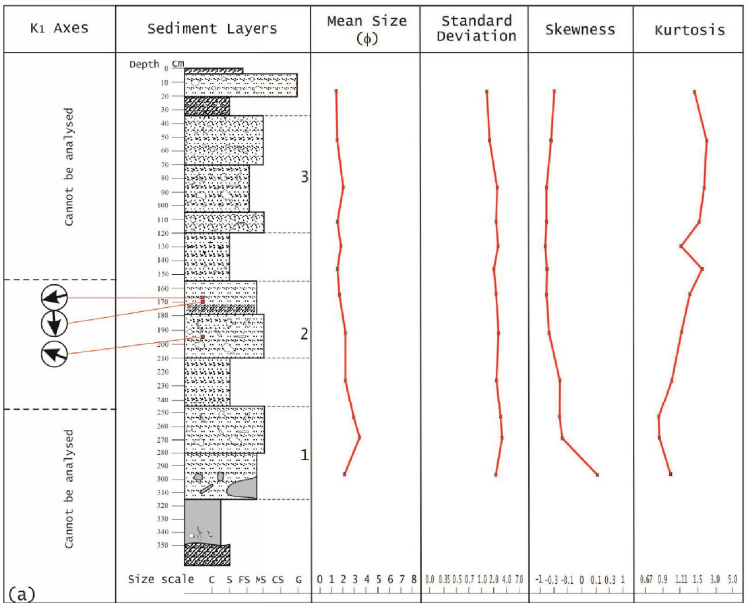

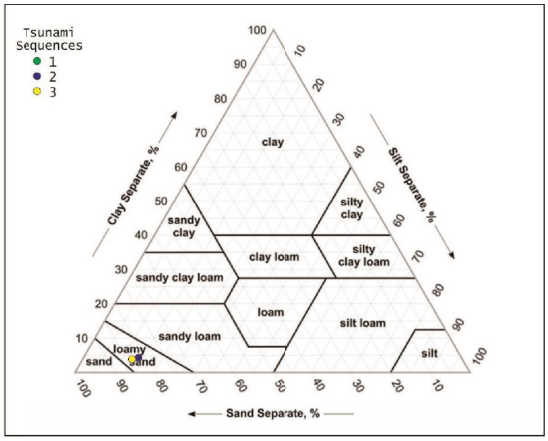

Figure 7-7. (a) Log profile of section U-08 with its grain-size distribution curves. Three sequences of tsunami deposit are marked numerically from base to top. (b) Textural triangle adopted from Brady and Weil (1999) showing the compositional texture of the base of the sequences.

Because there is no direct interface between two sequences, in which the sequences are separated by volcanoclastic deposits, the textural triangle is used to recognize the base of the new sequence emplacing coarser material within rip-up. The base of the sequences are then characterized by fine sands/silts mixed with gravel/coarse sands and categorized as loamy sand (see Figure 7-7b).

7.1.3. Tsunami sequences at Sumur coastal plain (Sites U-17 and U-20)

In the eastern part of Ujung Kulon National Park (Mount Honje region), along the coastal plain of Sumur, tsunami deposits are not well preserved. The coastal plains are narrow and bounded by the ridges of Mount Honje. This flat areas are today occupied by paddy field. However, a pit wall investigation at Site U-17 shows the presence of two relatively thin tsunami sequences in this area (Figure 7-8a).

First tsunami sequence lies at a depth between 70 - 45 cm. This normally graded sequence consists of a thin layer of pumiceous sand containing abundant dark minerals and volcanic glass at the bottom. Coral gravels mixed with fine grey sands (subrounded), and abundant bioclasts characterize the upper part. The second sequence corresponds to a layer of bioclastic sand that lies at a depth between 5 - 30 cm. It consists of fine to medium sands (subrounded and very poorly sorted) mixed with corals and shells. The textural triangle was used to evidence that the clayey sediments from the bottom layer are still present in the coarse sand unit, *loamy sand* in the diagram (see Figure 7-8c).

Another outcrop found at the cross road of Tanjungjaya (section U-20) show a thin sequence of tsunami deposit (Figure 7-8b). The sequence is constituted by coarse and very poorly sorted pumiceous bioclastic sands, with the presence of loamy sand in the base. Similar with section U-17, the clayey sediments from the bottom layer are still present in the coarse sand unit (see Figure 7-8c).

The descriptions of tsunami sequences demonstrated above give significant contribution to the understanding of the tsunami behaviour at Ujung Kulon. Laban Isthmus have a better tsunami sequences than other places. Six different sections described at the isthmus have evidence similarities between the sequences. A stratigraphic correlation was then reconstructed from North to South based on the sequences identified. In this correlation, the sequences at each section may increase due to the K_1 axis changes.

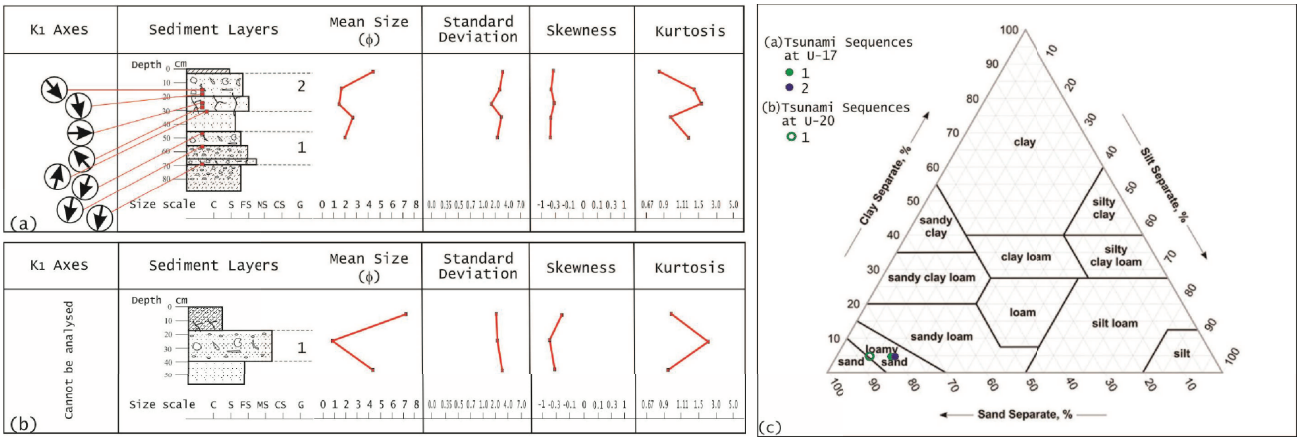

Figure 7-8. (a) Log profile of section U-17 with its grain-size distribution curves. Two sequences of tsunami deposit are marked numerically from base to top. (b) Log profile of section U-20 with its grain-size distribution curves. One single sequence of tsunami deposit is shown in this section. (c) Textural triangle adopted from Brady and Weil (1999) showing the compositional texture of the base of the sequences for sections U-17 and U-20.

7.2. Effect of coastal landforms on tsunami sequences

Before correlating the sequences, we have to find out the effect of coastal landforms on tsunami sequences. This is very important to assure that Laban Isthmus is an appropriate site to demonstrating the 1883-Krakatau tsunami behaviour. The result of an interpretation of satellite images and field investigations show the differences of coastal landforms and characteristics of tsunami sequences on two contrasting coastal plains following the giant tsunami waves on August 27, 1883: the plain of Ujung Kulon Peninsula on the western part of Ujung Kulon National Park and the Mount Honje narrow coastal plain in the East of National Park (see Figure 7-9).

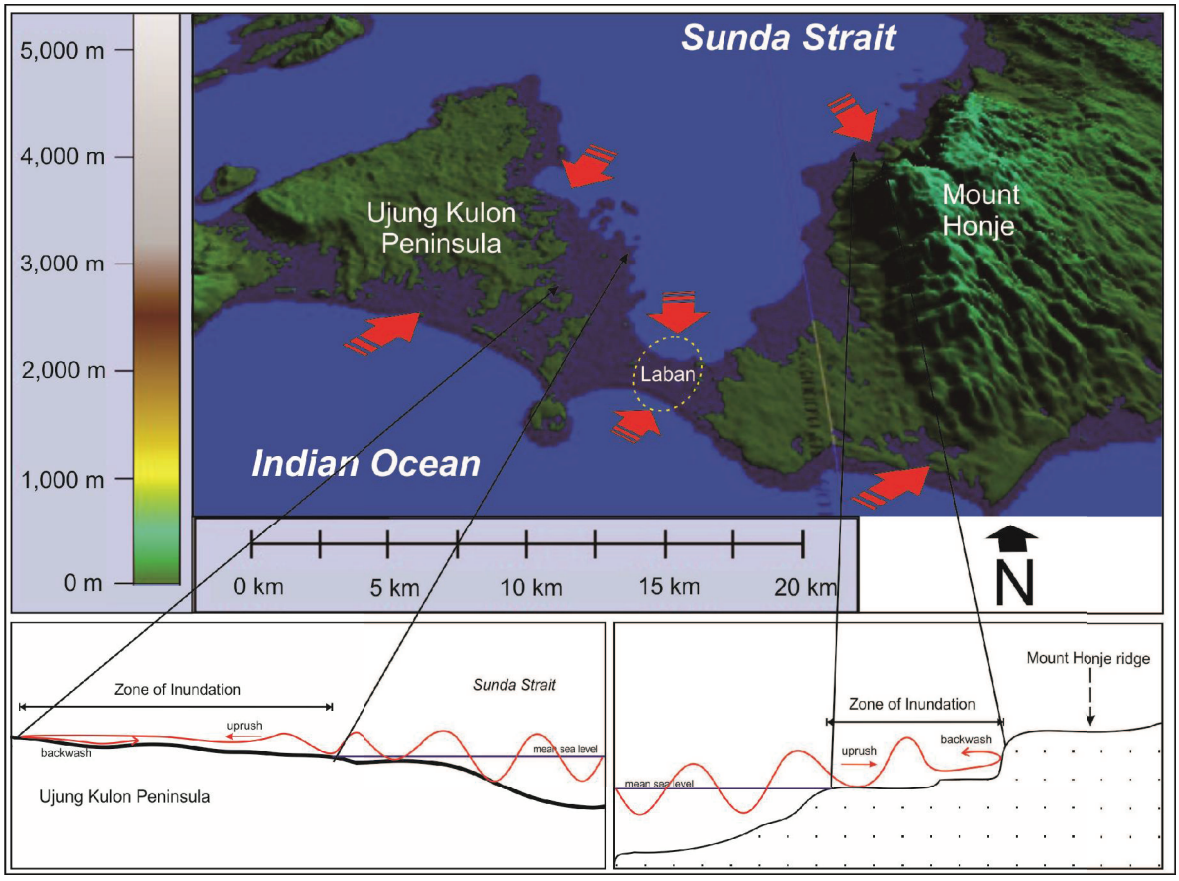

Figure 7-9. An oblique image of Ujung Kulon area; Stripes arrows represent the tsunami flow directions. The estimate zone of inundations of the 1883-Krakatau tsunamis are displayed by a dark (blue) shadow and described by two inset pictures: (i) right-below; tsunami propagation and inundation on Mount Honje coastal plain, (ii) left-below; tsunami propagation and inundation on Ujung Kulon Peninsula.

The landforms of the peninsula coastal plain are characterized as alluvial plain or peneplain with a plateau (Talanca Plateau) in the central parts and strand plain with beach ridges in the southwestern part (Mount Payung region). The narrow coastal plain of Mount Honje region is characterized as a strand plain dominated by the wave cut platform (a narrow flat area often found at the base of a sea cliff or along the shoreline of a bay that was created by the erosion of waves) and limited landward by steep slopes. This difference of landform has affected the zone of inundation on Ujung Kulon coastal plain (Figure 7-9) and has been responsible of a shorter period of inundation on Mount Honje coastal plain compared to the peninsula coastal plain. It seems to be one of the causes of the tsunami deposits in the eastern part are relatively thin and not completely recorded.

At the central part of V-shape bays, the run-up tsunami flow invaded areas more than 2 km from the coast, e.g. the 2 km wide Laban Isthmus has been inundated by tsunami waves washover (see Figure 7-9 and Figure 7-10 to 7-13). Strong tsunami flow severely damaged the tidal plain and the landforms along the coasts except coastal dunes in the northwest of peninsula (Tanjung Alang-alang). Most of the landforms except sand dunes along the coasts had almost no effect on the protection against the tsunami, but the higher micro-landforms such as beach ridges (near Mount Payung region) and the narrow coastal landform like the wave cut platform prevented the flow of the tsunami from its invasion far inland (see Figure 7-9). A strong backwash was then generated by the slopes limiting the plain. This latter phase reworked and deleted the material emplaced by the uprush phase, in which the strong energy of the uprush might not have allowed high amount of sediments deposited at these sites.

According to Wassmer et al. (2007, 2010) described in Chapter 1, the narrow coastal plains at the foot of Mount Honje and Mount Payung (in the Southwest of peninsula) can only preserve tsunami deposits at the proximal zone. This zone is dominated by coarse and ungraded materials resulted from rolling to ground suspension of sediment emplacement processes, in line with the sequences shown in sections U-17 and U-20 (Mount Honje region). By contrast, the peneplain of Laban Isthmus and the peninsula show a facies differentiation of tsunami sequences between proximal, medial, and distal zones. They correspond to the general decrease of wave energy from proximal to distal zones during the uprush phase and the energy increasing from distal to proximal during the backwash phase. At Laban Isthmus, the backwash phase might not have occurred due to the uprush coming

from the opposite direction. Consequently, the sequences at distal zone (U-04) are dominated by finer materials that fluctuates vertically between coarse and fine sands resulted from uniform to gradual suspension of sediment emplacement. At the North of Laban Isthmus, a zone of mean sea level with more than 500 m wide contains the silty sediments accumulated in the bottom of the bay. The sediments are potentially eroded during tsunami propagation within this wide tidal zone. At the isthmus, rip-up clasts of clayey sediment found at the base of all sections were most probably originated from this zone.

Due to the flat plain morphology of Laban Isthmus, the 1883-Krakatau tsunami inundation then spread out over the entire isthmus with an average run-up height about 6 - 9 m asl. The direction of run-up flow was almost perpendicular to the coastline, whereas backwash flow directions were controlled by topography. Backwash flow was concentrated in the proximal zone of the plain (near shore), for example in section U-01 (evidenced by K_1 between N315°E and N348°E). Because the isthmus is situated between Sunda Strait and Indian Ocean, two general uprush flow directions have penetrated Laban Isthmus. The characteristics of these uprush phases were controlled by local topography and waves energy and are reflected by sediment fabric and grain-size. A first southward direction of Krakatau tsunami, from Sunda Strait, spreading between N122°E and N236°E (the ranges of general southward direction expressed by K_1 axes is N104°E - N262°E). A second in the opposite direction from Indian Ocean spreading between N318°E and N58°E (the general northward direction is N280°E - N80°E). The existence of this narrow and flat isthmus which is affected by tsunamis originated from two water bodies corresponds well with the distribution of thick tsunami deposits. The source of the sediments emplaced is double: fine sands and silts from the bottom of Welcome Bay and medium to coarse sands from Karang Ranjang Bay on the Indian Ocean side. Coastal erosion of the plain caused by the direct attack of tsunami waves is reflected by incorporation of rip-up clasts of clayey sediments at the base of the first tsunami sequence.

Two opposite sources of tsunami deposits evidenced by K_1 axes changes have caused a variation of tsunami sequences at each section. The sequence at the North of the isthmus may have a different direction of sediment emplacement than the same sequence at the South. In certain section they might have been mixed vertically. From each source, four tsunami sequences were identified respectively. Thus, the isthmus was probably flooded eight times (two for each tsunami sequence), see Figure 7-10 to 7-13.

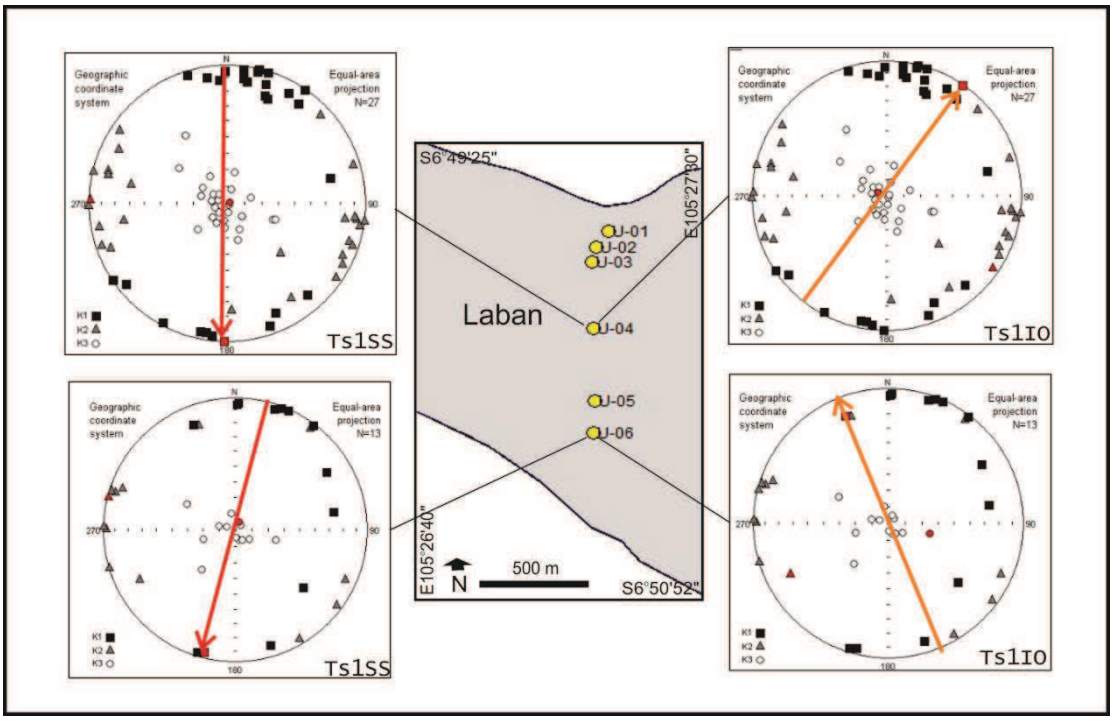

Figure 7-10. First projection of K_1, K_2, and K_3 (AMS ellipsoid axes) onto a diagram of lower hemisphere for the Laban Isthmus; Observation sites (U01 – U06) on the map are symbolized by circles. Line arrow in the diagram indicates the directions of K_1 axis for the first tsunami sequence at section U-04 (at a depth of 230 cm and 172 cm) and section U-06 (107 and 70 cm).

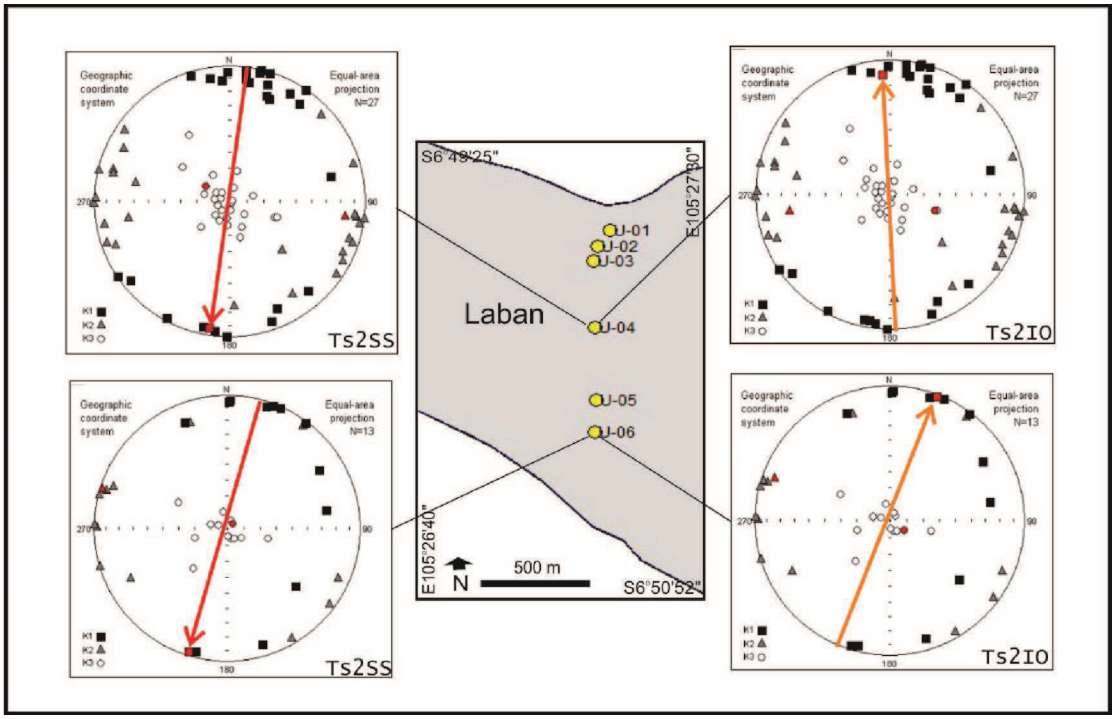

Figure 7-11. Second projection of K_1, K_2, and K_3 (AMS ellipsoid axes) onto a diagram of lower hemisphere for the Laban Isthmus; Observation sites (U01 – U06) on the map are symbolized by circles. Line arrow in the diagram indicates the directions of K_1 axis for the second tsunami sequence at section U-04 at a depth of 139 cm and 104 cm and at section U-06 at 66 and 60 cm.

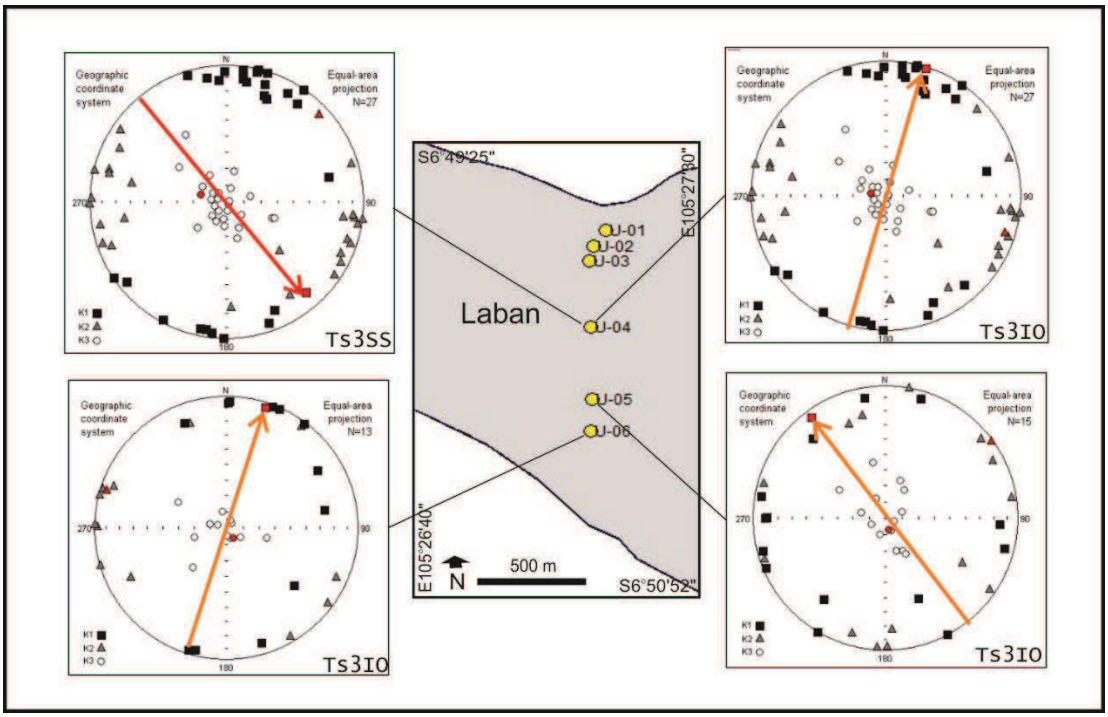

Figure 7-12. Third projection of K_1, K_2, and K_3 (AMS ellipsoid axes) onto a diagram of lower hemisphere for the Laban Isthmus; Observation sites (U01 – U06) on the map are symbolized by circles. Line arrow in the diagram indicates the directions of K_1 axis for the third tsunami sequence at section U-04 at a depth of 71 cm and 54 cm, U-05 at 47 cm, and at section U-06 at 33 cm.

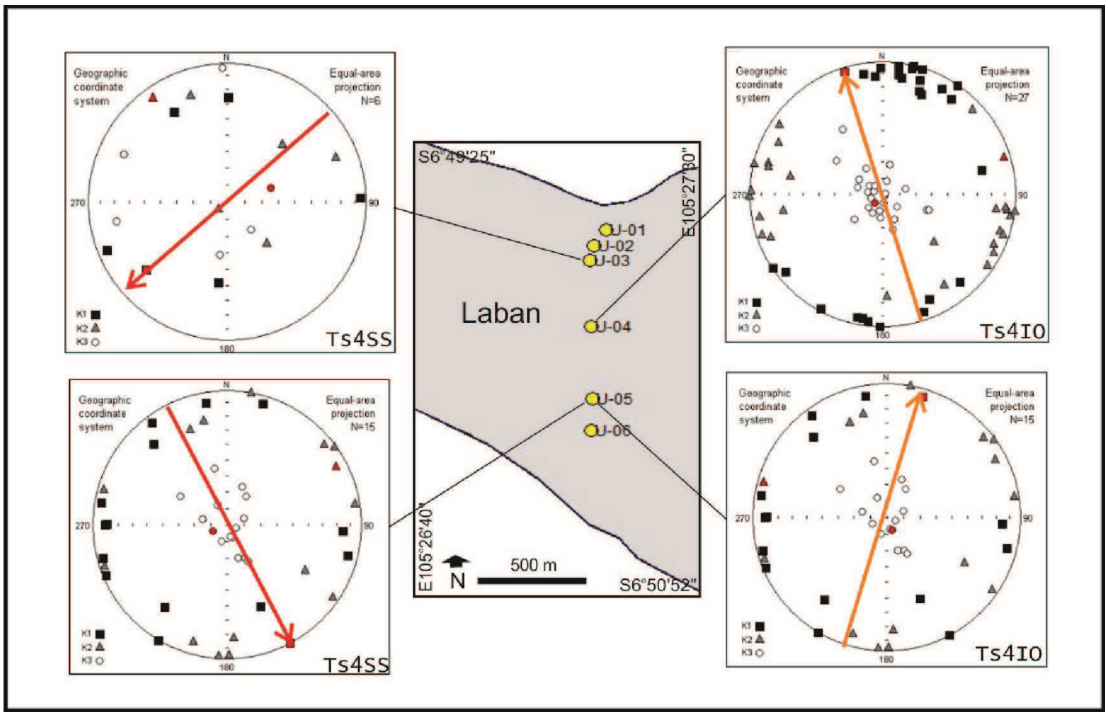

Figure 7-13. Fourth projection of K_1, K_2, and K_3 (AMS ellipsoid axes) onto a diagram of lower hemisphere for the Laban Isthmus; Observation sites (U01 – U06) on the map are symbolized by circles. Line arrow in the diagram indicates the directions of K_1 axis for the third tsunami sequence at section U-03 at a depth of 18.5 cm, U-04 at 21 cm, and U-05 at 40 and 23 cm.

7.3. Stratigraphic correlation

As mentioned above that Laban Isthmus was completely overflooded by the 1883-Krakatau tsunamis. These successive floodings are responsible for the emplacement of an incredible tsunami sedimentary record laying beneath the recent topsoils. Relying on the K_1 axis changes and foraminiferal assemblages, the tsunami sequences identified by the grain-size analysis can be changed significantly. Four until five sequences of tsunami deposit recognized at sections U-04, U-05, and U-06 were modified to be six, seven, and eight sequences respectively. This modification is based on a fact that a sequence can be divided into two different sequences emplaced from two opposite direction.

A stratigraphic cross section was then reconstructed from the core alignment to reveal the emplacement process of each tsunami sequence. Figures 7-14 to 7-19 demonstrate a North - South cross section of Laban Isthmus since before the 1883-Krakatau eruption (a condition of base layer, Figure 7-14) until after 1883 event (a complete stratigraphic section after pedogenesis process, Figure 7-19). The layers of tsunami deposits, both from Sunda Strait (symbolized by TsSS) and from Indian Ocean (symbolized by TsIO), basically show the same sediment texture and composition. They only have a difference of foraminiferal assemblages. The description below represents a characteristic of TsSS and TsIO for each tsunami deposit.

Stratigraphically, the first tsunami deposits from Sunda Strait (Ts_1SS) overlain the pre-1883 alluvial deposits, i.e. clay and sand (Figure 7-14 and 7-15). With a thickness of 20 - 60 cm, Ts_1SS is composed of clayey rip-up clasts mixed with coral gravels and bioclasts which indicate a deposit produced by a high flooding energy at the proximal areas. Some pumice shards were found at the base of Ts_1SS. The rip-up clasts in the distal section (U-04) are finer than in the proximal sections. This layer is characterized by K_1 axes between N181°E and N235°E, some part are more than N235°E expressing the dynamics of the surging waves during the flooding (Wassmer et al., 2010). This Sunda Strait southward direction is evidenced by the present of *Streblus beccarii* originated from shallow marine. Ts_1IO then overlain Ts_1SS, coming from the South and reaching the central part of Laban Isthmus. Ts_1IO has similar characteristics with opposite K_1 axes direction between N338°E and N29°E. This northward direction is also confirmed by the abundance of *Planulina wuellerstorfi* originated from Indian Ocean continental margin.

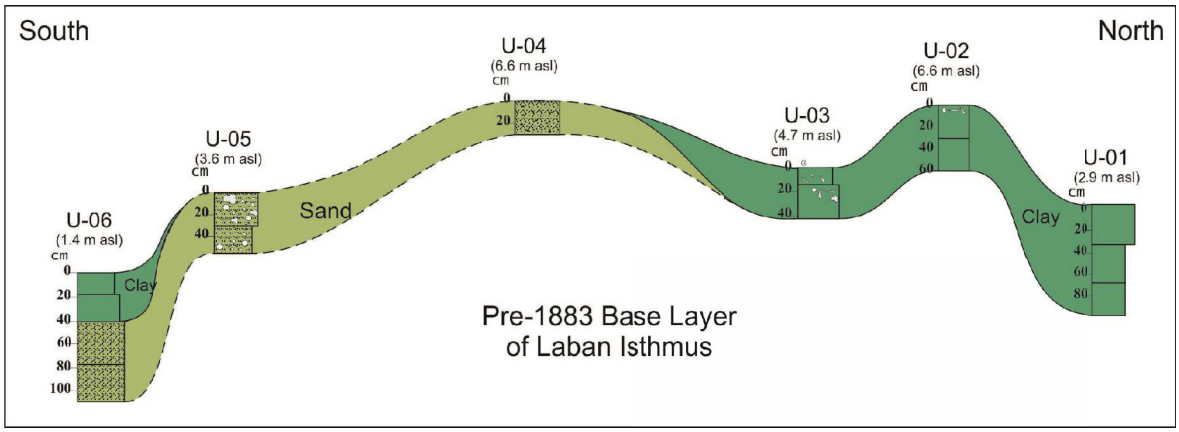

Figure-7.14. A Stratigraphic Cross Section of Laban Isthmus, from North (Sunda Strait) to the South (Indian Ocean), reconstructed from U-01, U-02, U-03, U-04, U-05, and U-06 profiles, displaying the pre-1883 base layer.

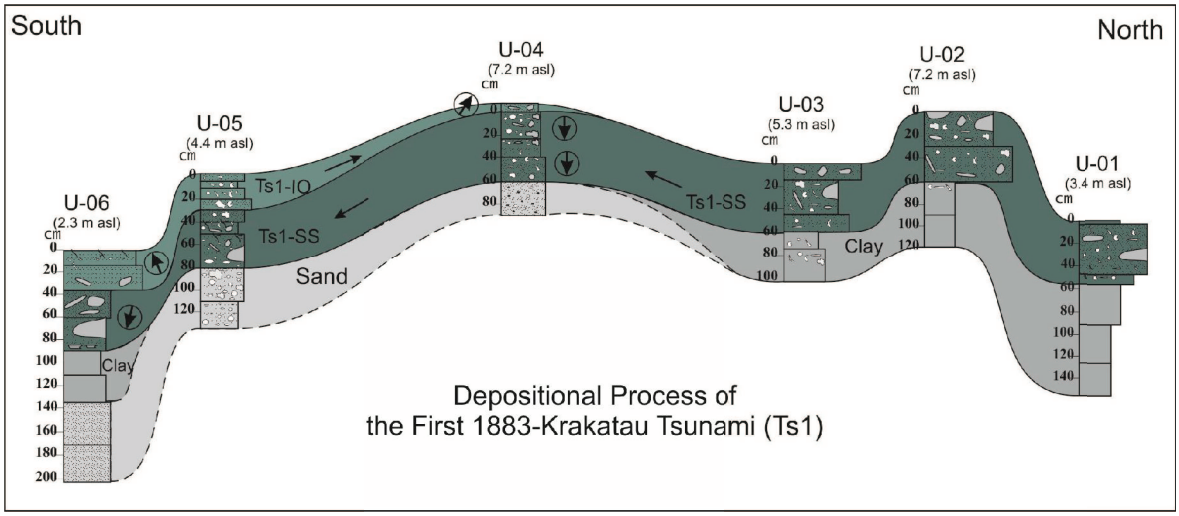

Figure 7-15. A stratigraphic cross section that displays a succession of the first tsunami deposits and their flow directions, both from Sunda Strait (represented by a symbol of **TsSS** and darker colour) and from Indian Ocean (represented by **TsIO** with a lighter colour).

Thick layer Ts_2SS (40 - 80 cm) covered the first tsunami deposits (Figure 7-16). This tsunami deposit is characterized by abundant shells and foraminifera and the presence of coral boulders embedded in sand (evidenced by Biofacies D/E and 27.19 wt% loss on ignition/LOI), that was likely produced by the highest tsunami wave energy. In the northern part, a thin layer of small rounded pumice lapilli intersperses the tsunami sand unit. Ts_2SS has K_1 axes between N122°E and N236°E, in line with the main southward direction. This layer was then overlain by Ts_2IO (a thickness up to 40 cm) with similar characteristics and K_1 axes between N318 - N58 °E (northward direction). *Bolivina spathulata* found at the top of Ts_2IO can be used as fossil index of an Indian Ocean origin.

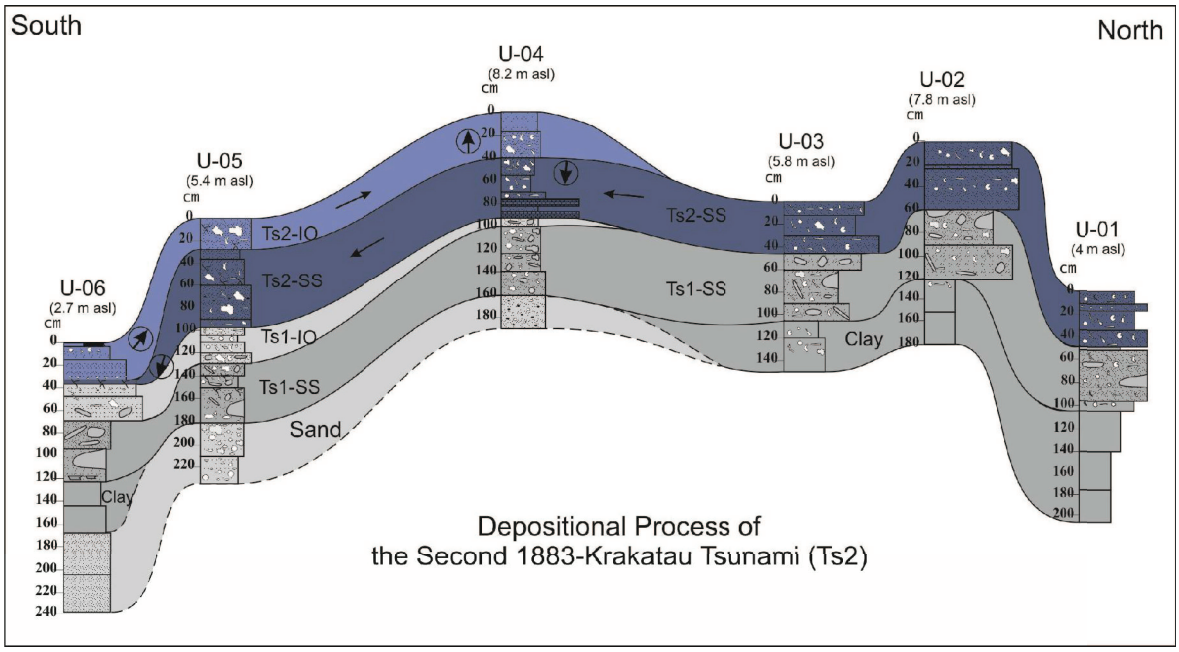

Figure 7-16. A cross section displaying a succession of the second tsunami deposits and their flow directions from Sunda Strait (**TsSS**) and from Indian Ocean (**TsIO**).

Ranging between 20 - 85 cm, Ts_3SS, is the thickest tsunami deposit at Laban Isthmus (see Figure 7-17). It is characterized by normal grading with abundant bioclasts and coral gravels (50 - 60 %), yet, its biofacies (Biofacies A) shows a scarcity of foraminifera. The range of K_1 axes in this layer are too wide, which were most probably caused by inaccurate AMS sampling on very coarse unconsolidated materials. According to Wassmer et al. (2010), the sediments sampled for AMS technique were limited to the fine sand, silt, or clay, with a good cohesion to retain the fabric. Only K_1 axis on fine to medium bioclastic sands at the distal section (N139°E) displays the southward direction. On the contrary, Ts_3IO is one of the thinnest deposit (10 - 20 cm) with K_1 axes between N324°E and N36°E. Ts3IO is composed of silty soil mixed with bioclasts and volcanic ash and characterized by Biofacies A with insignificant content of foraminifera.

The fourth tsunami deposits, i.e. Ts_4SS and Ts_4IO, constitute the surface topography (Figure 7-18). The whole part of Ts_4SS has been partly reached by the weathering and has undergone a beginning of pedogenesis. Ts_4SS is composed of silty soil, bioclasts, volcanic ash, and pumice (9.45 wt% LOI and 66.74 wt% SiO_2) with K_1 axes between N130°E and N230°E. With similar characteristics, Ts_4IO overlain Ts_4SS from the South (K_1 axes between N343°E and N16°E). The upper part of Ts_4IO might have been digested by the pedogenesis processes.

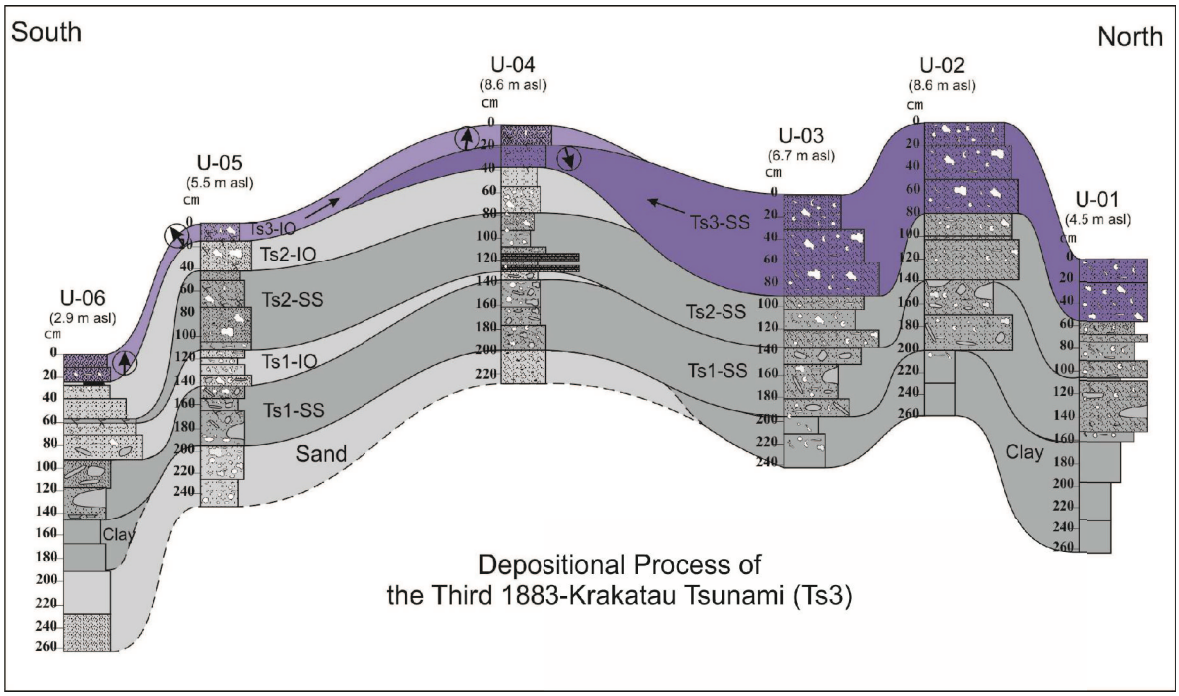

Figure 7-17. A cross section displaying a succession of the third tsunami deposits and their flow directions from Sunda Strait (**TsSS**) and from Indian Ocean (**TsIO**).

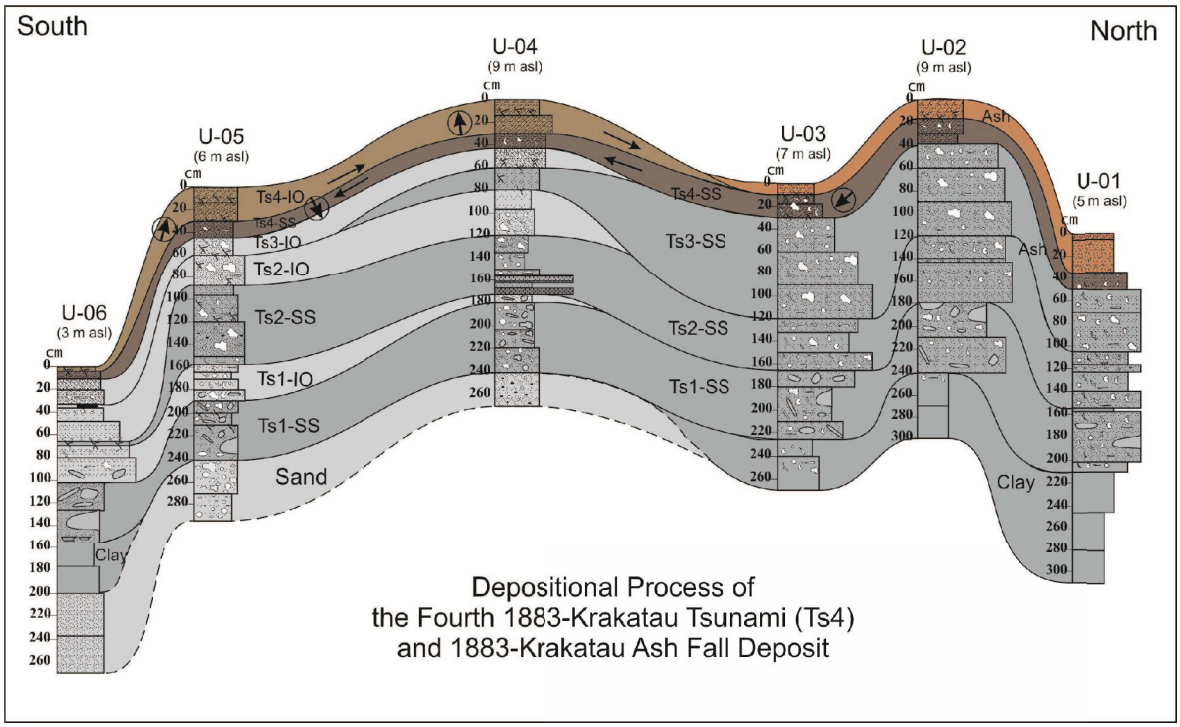

Figure 7-18. A cross section displaying a succession of the fourth tsunami deposits and their flow directions from Sunda Strait (**TsSS**) and from Indian Ocean (**TsIO**), and also the depositional of volcanic ash at the northern part of the isthmus.

Finally, the northern part section of Ts_4SS was overlaid by light brown pumiceous ash with a thickness up to 30 cm. This unit contains juvenile grains (pumice/glass 10%, fresh crystals 35%, and microcrystalline 25%) mixed with rock fragments (30%). The pedogenesis process has also affected the upper part of the layer.

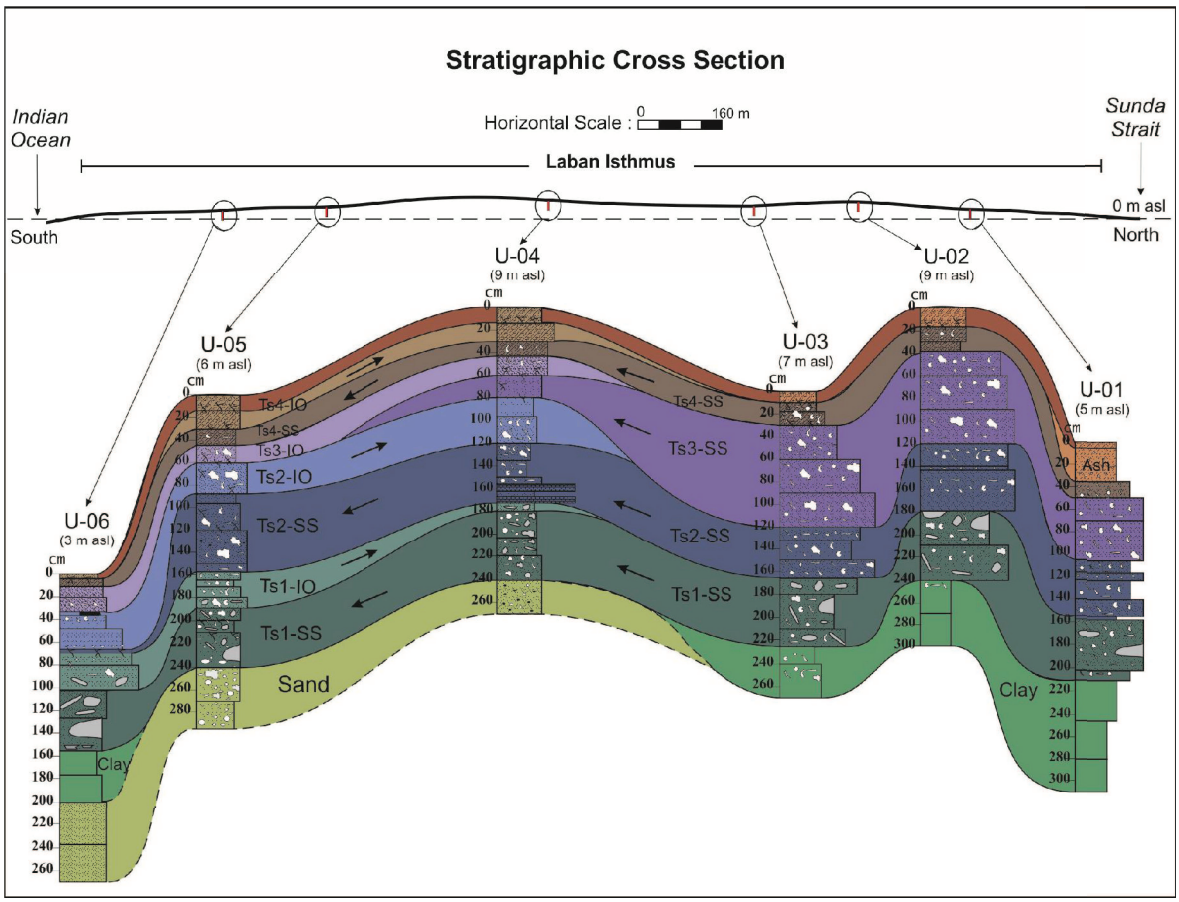

Figure-7.19. A complete Stratigraphic Cross Section of Laban Isthmus, displaying the succession of the 1883-Krakatau tsunami sequences and their flow directions and a condition of the isthmus after 1883.

All the synthesis above revealed that Laban Isthmus, a part of fascinating morphology of Ujung Kulon Peninsula, has a great sedimentary recording of tsunamis induced by the 1883-Krakatau eruption. The recording displays four double layers of tsunami deposits coming from Sunda Strait (TsSS) and from Indian Ocean (TsIO). This incredible tsunamis signature found at the central part of a large V-shape morphology of Welcome Bay can be used to evidence the scenario of devastating tsunamis generated by the 1883-Krakatau eruptions at Ujung Kulon. It will be described more detail in Part IV.

PART IV
Disscussion and Conclusion

Chapter 8
Discussion

A detailed treatment of data collected, allows at this stage to discuss ideas to understand the way in which the tsunamis, generated by the various eruptive phases of the 1883-Krakatau eruptions, occurred at Ujung Kulon. The discussion, indubitably, points out the role played by coastal landforms on the behaviour of tsunami waves in the study area and its correlation with the sedimentary recordings found along the narrow isthmus of Laban, between Sunda Strait and Indian Ocean. Reconstruction of past tsunami events by correlating coastal morphology with the sedimentary records at this isthmus is expected to fill the gaps in knowledge about the number and characteristics of tsunami flooding on the coasts of Ujung Kulon Peninsula.

8.1. Characteristics of the tsunami deposits and their origin

Due to the local flat morphology, there was very minor or almost no erosion between successive waves at Ujung Kulon Peninsula, especially at Laban Isthmus with its flat topography from proximal to distal zones (this weak reworking of the material already emplaced by the following waves was also mentioned on the eastern coast of Banda Aceh for the 2004 IOT event by Wassmer et al. (2007)). In contrast, at Mount Honje narrow coastal plain, a probable erosion and an important reworking process occurred during the Krakatau tsunami events due to the rapid shuttle movements (up-rush / backwash) on this wave cut platform. Additionally, a post-depositional tidal erosion may have occurred in reason of the proximity of this area with the post-tsunami coastline.

Consequently, in reason of an ideal natural context (flat area and important sediment sources) favouring the emplacement of a thick and differentiated sediment layer, the deposits within the isthmus might have recorded the successive steps of the 1883-Krakatau tsunamis floodings. The behaviour of the 1883-Krakatau tsunami waves that penetrated Ujung Kulon can be determined by identifiying the characteristics of tsunami deposit in this isthmus.

The main characteristic of the 1883-Krakatau tsunami deposits is the presence of stacked individual sequences represented by a fining upward (normally graded) of bioclastic sand unit and pyroclastic materials content within some sequences. They correspond to the generation of volcanogenic tsunami (Paris et al., 2014a, 2014b). Except the grain-size evolution from base to top, no traction current structures were observed within the sequences. The sedimentary sequences in each section very likely recorded the flooding by some tsunami events and the arrival of the successive tsunami waves are expressed by their vertical succession.

Fining upward sequences expressed the uprush phase of tsunami flooding event are mostly dominant at each section. While reverse grading (coarsening upward) sequences expressed the backwash phase are not found within the sections. This is due to the uprush coming from the opposite direction that caused the coarsening upward sequences were not completely recorded. The mixing process between backwash phase and the opposite uprush (that only differ $\pm$ 10 minutes interval of flooding periods) is evidenced by a flow direction perpendicular to K_1 axis overall azimuth (southward or northward directions) at some sections. This process was concentrated on the South proximal to distal zones (U-06, U-05, U-04). Such condition may also cause the absence of mud drapes at the top of sequences, the time interval necessary to form them being closer to hours than to minutes.

The perpendicular K_1 axes were also dominant at the North proximal zone (Section U-01). This is due to the fact that this zone is still affected by a high energy of tsunami wave. Under high energy, the sediment particles do not underwent an imbrication but roll along their long axis (see CM diagrams in Chapter 6), producing a magnetic fabric with a K_1 axis perpendicular to the flow direction (Wassmer et al., 2010, 2015; Wassmer and Gomez, 2011).

The presence of *Planulina wuellerstorfi* as dominant benthic foraminifera at the South coasts of Ujung Kulon become an important criterion for evidencing the northward direction of tsunami wave coming from Indian Ocean, due to the environment of the species that characterize a continental margin source and cannot be found in Sunda Strait. In most cases, *Elphidum lessonii* and *Streblus beccarii* contained within the deposits are used as proxies to identify a maximum depth of seabed eroded by tsunami waves in Sunda Strait, due to their origin from the sub-littoral zones at a depth between 0 – 200 meter below sea level.

However, the opposite tsunami wave directions have also formed two opposite proximal zones at Laban Isthmus that are characterized by different wave energies. Based on the grain-size distribution, the tsunami wave energy coming from the northern part (Sunda Strait) is stronger than from the southern part (Indian Ocean). This difference can be explained by the fact that the first are comming straight from the Krakatau when the second are refracted along the peninsula coasts, but also by the coastal morphologies (Figure 8-1). The northern part of the coastal plain is constituted by a large and shallow continental shelf. The V-shape morphology of the bay may increase the energy of the wave comming from the North, concentrating it in the center end of the bay (Baldock et al., 2007; Okayasu et al., 2011; Yamanaka et al., 2013). On the contrary, morphology of the southern coasts consist of a narrow continental shelf and steep submarine slope that may reduce the threshold shear velocity of the tsunami waves (Wassmer et al., 2010).

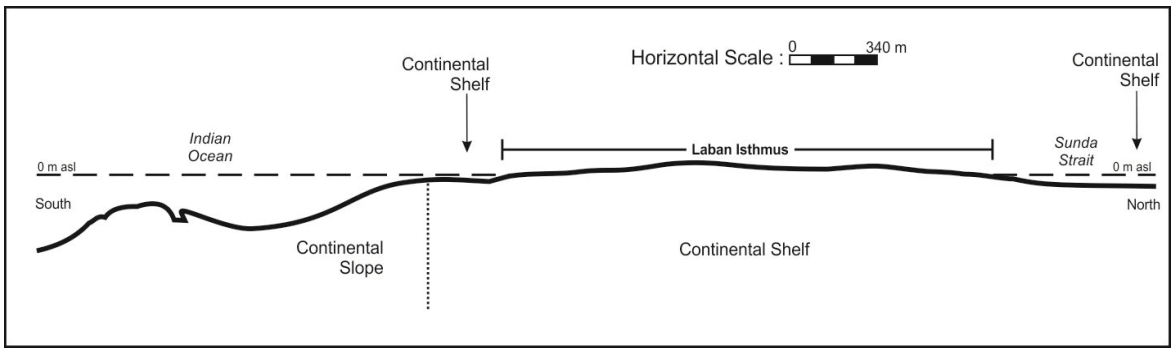

Figure 8-1**.** Cross section of Laban Isthmus from Indian Ocean continental slope to the continental shelf of Sunda Strait.

Another characteristic of the tsunami deposits found at Laban Isthmus is the clayey rip-up clasts found at the base of tsunami sequences at all sections. This signature was likely produced by erosion of the mudier sediments at the base of mangrove forests on the sea front. The massive clays from the old alluvial deposits at the base of each sequence is probably able to provide such clayey clasts. They may have been collected on the sea front where no deposit occurred during the successive tsunamis, in reason of a strong energy in this very proximal zone. As a consequence, the source remains active during all the tsunami sequences.

Along with coral gravel and bioclastic sands that are commonly found in all sections, the rip-up clasts and vertically normal grading repetition of grain-size are the most

commonly used proxies to identify tsunami deposits (Chagué-Goff et al., 2011). Where these materials are mixed with a large coral boulder embedded in sand found at Section U-04 or abundance foraminifera at Sections U-03, U-04, and U-05, it forms one of the strongest evidence of the tsunami depositional signatures at Ujung Kulon, due to the fact that only tsunami washover can emplace sand, boulders, and abundance foraminifera together on a beach (Bryant, 2008).

The presence of pyroclastic materials within the tsunami deposits are also the strongest evidence for the 1883-Krakatau tsunamis (Paris et al., 2014b). At Ujung Kulon, based on thin sections examination from selected samples, the proportion of juvenile clasts (pumices or volcanic glass) resulted from the 1883-Krakatau eruption within the bioclastic sand units ranges between 5 % and 10 %. In some sections, the pyroclastic materials (volcanic ash and lapilli) overlie the bioclastic sand unit. These compositions indicate that the sediments were emplaced by the tsunami waves before the onset of ash falls related to the Plinian phase of the 1883-Krakatau eruption. Such condition is almost similar with the volcanic-tsunami deposits that are poor in juvenile grains found in Japan, i.e. sand and gravel beneath fine ash massive pumice deposits from the 1640-Komagatake eruption (Nishimura and Miyaji, 1995), and in Turkey, i.e. a tsunami deposit without juvenile material and overlain by felsic ash fall deposits from Minoan eruption of Santorini (Minoura et al., 2000).

The pyroclastic materials preserved along with tsunami deposits at Ujung Kulon coastal areas is dominated by ash, even if lapilli are also quite common. Rounded pumice lapilli was found in some sections. The rounded pumice lapilli has been described by Carey et al. (2001) on Sebesi Island and Paris et al. (2014b) on the South coasts of Sumatra, i.e. the rafted pumice lapilli on the sea surface that are then abraded during tsunami up-rush and deposited inland after tsunami backwash. The presence of these pyroclastic materials are important for diagnosing the tsunami deposits related to the volcanic eruption (Nishimura et al., 2005; Paris et al., 2014a). In our case, their presence confirm that the tsunami deposits are associated to the 1883-Krakatau eruptions. Except juvenile (the glass particles or microscopic pieces of pumice in microscopic examination) that are not present in large abundance (< 10%) and apparently altered to be clay minerals, the identified minerals such as feldspar, pyroxene (enstatite, augite, etc.), and opaque minerals (e.g. ilmenite, magnetite, etc) are in accordance with the previous descriptions of

the 1883-Krakatau pyroclastic deposits (Renard, A., 1883; Verbeek, 1884, 1885; Symons et al., 1888; Paris et al., 2014b). Nevertheless, the chemical composition of glass particles is almost similar with the composition of volcanic ash collected from Sections U-03 and U-06, see Table 8-1.

Table 8-1. Chemical analysis of volcanic ash from selected depth of Sections U-03 and U-06 compared with the composition of glass from the dust fell at Buitenzorg (Bogor) which was analysed by J.W. Retgers (Verbeek, 1885; Symons et al., 1888).

wt %	Ujung Kulon volcanic ash		The chemical composition of dust fell at Buitenzorg				
	U-03 (0-30)	U-06 (55-75)	Glass	Feldspar	Enstatite	Augite	Magnetite
SiO_2	66.74	76.50	68.12	58.29	52.30	48.60	-
TiO_2	1.04	1.18	0.18	-	-	-	6.70
Al_2O_3	12.72	9.78	15.81	27.19	6.10	8.20	-
Fe_2O_3	6.15	5.17	5.01	-	27.70	14.00	93.30
MnO	0.11	0.08	-	-	Trace	-	-
MgO	1.03	0.87	1.18	-	13.60	18.90	-
CaO	1.51	1.97	2.78	8.27	2.20	11.60	-
Na_2O	1.10	1.62	5.09	5.82	-	-	-
K_2O	0.78	0.60	1.06	1.22	-	-	-
P_2O_5	0.14	0.11	-	-	-	-	-
LOI	9.45	2.80	-	-	-	-	-
Total	**100.74**	**100.68**	**99.23**	**100.79**	**101.90**	**101.30**	**100.00**

Moreover, a comparison between the volcanic ash collected from those sections and the dust fell at varying distances from Krakatau in 1883 shows that their chemical compositions are also similar (Symons et al., 1888), see Table 8-2. Due to these similar characteristics of tsunami sequences within all sections found at Ujung Kulon, it can be assumed that the 1883-Krakatau eruptions is the only source of tsunami deposits recorded at Ujung Kulon coastal areas.

The values of SiO_2 increase with distances from the source. It might have been related to the increasing number of fine grained materials of the volcanic ash/dust. El-Hasan (2006) has examined a geochemical dissociation of major oxides and trace elements between bed and slime sediments. He evidenced that the spatial distribution of major oxide concentrations along the stream drainage exhibited a slight increase with distance, due to

the abundance of fine grained materials at the end of drainage where the slowing of sedimentation rate would enhance the adsorption of various metals.

Table 8-2. Chemical analysis of volcanic ash from selected depth of Sections U-03 and U-06 compared with the composition of the dust fell in 1883 at varying distances from Krakatau which was analysed by C. Winkler (Symons et al., 1888).

wt %	Ujung Kulon volcanic ash		The chemical composition of dust analysed by C. Winkler	
	U-03 (0-30)	U-06 (55-75)	Fell near Krakatau	Fell at Buitenzorg (Bogor)
SiO_2	66.74	76.50	61.36	66.77
TiO_2	1.04	1.18	1.12	0.67
Al_2O_3	12.72	9.78	17.77	16.44
Fe_2O_3	6.15	5.17	6.10	4.78
MnO	0.11	0.08	0.41	0.38
MgO	1.03	0.87	2.32	1.67
CaO	1.51	1.97	3.45	2.90
Na_2O	1.10	1.62	4.98	4.14
K_2O	0.78	0.60	2.51	2.25
P_2O_5	0.14	0.11	-	-
LOI	9.45	2.80	-	-
Total	**100.74**	**100.68**	**100.02**	**98.00**

Yet, Section U-06 in the study area (82 km from Krakatau) has a higher SiO_2 content than the one measured at Buitenzorg/Bogor (>150 km from Krakatau), see Figure 8-2. It evidences that the bursts of volcanic materials of the 1883-Krakatau eruption were mostly northward to westward directions. Thus, the grained materials within volcanic ash fell at the northern and western part of Krakatau are most probably coarser than those that fell at areas located at the same distances in the southern part of Krakatau, i.e. at Ujung Kulon region. A high *wt %* of SiO_2 at Section U-06 indicates that many pumice have been weathered to clay minerals that would enhance the adsorption process. In contrast, the volcanic material fell at Section U-03 which is still rich in fresh crystals (volcanic glass) like those that fell at some locations around the Sunda Strait (Symons et al., 1888; Paris et al., 2014b).

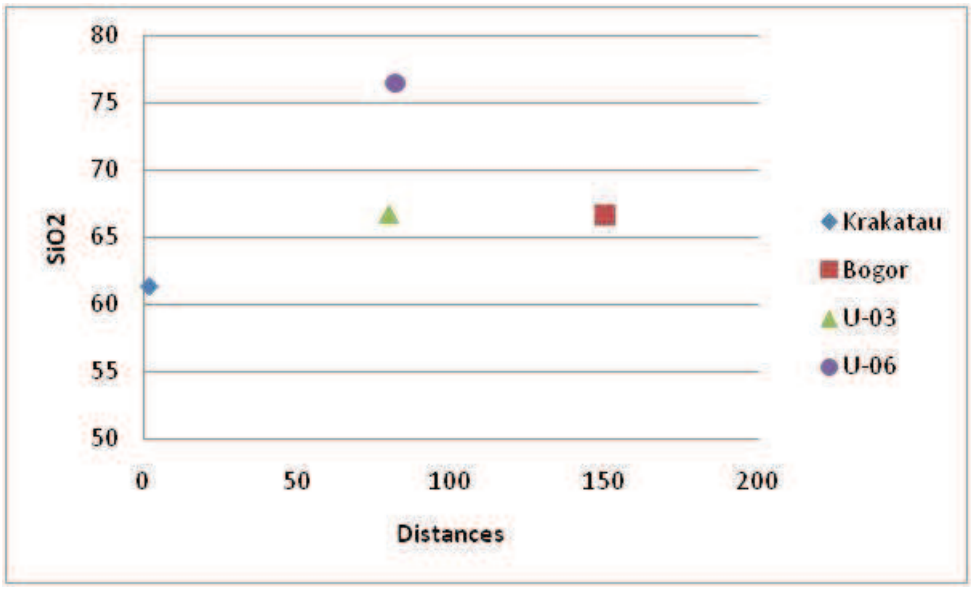

Figure 8-2. Graph of relationship between the values of SiO_2 (*wt %*) within the volcanic ash/dust and the distances of location from Krakatau where samples were collected (km).

8.2. Hydrodynamic of sediment emplacement

Combined data of grain-size distribution, foraminiferal assemblages, and AMS parameters can be used to reconstruct sedimentation processes during tsunami inundation. A normal grading of the grain-size from base to top is commonly produced by a single tsunami wave (Dawson and Shi, 2000). This feature reflects the progressive decrease of the tsunami wave energy. In the study area, the general decreasing of the grain-size from base to top that occurred at each section is reflected by the curves of mean grain-size. This is in accordance with the progressive reduction of hydrodynamic energy.

On the contrary, standard deviation does not attest for a better sorting of the sediments and skewness displays a relatively constant negative curves (indicating a tail of coarser particles). These intriguing features can be interpreted as the effect of the two opposite directions of tsunami waves and also by the occurence of backwash in some part of the inundation zone. In such conditions, each successive wave reached an already flooded area. The sediment resuspended during the light reworking by the previous wave (after the slack phase) was mixed with the sediment reworked by the next wave (uprush phase). Thus, the sediment became more mixed and the material emplaced was then still poorly to extremely poorly sorted with a domination of coarse particles. The mixing

texture between fine sands/silts and gravel/coarse sands occurred at the sequence boundaries which can be seen in the textural triangle (ranging between loamy sand/sandy loam and loam/silt loam, see Chapter 7). In particular, the sedimentation area at Laban Isthmus remained inundated during the whole tsunami events, then, the water was also contaminated by the fine grained sediments (clay or fine silt) eroded from surrounding soils between each successive wave. This "pollution by the fines" was already mentioned by Wassmer et al. (2010). Shi et al. (1995) suggest based on grain-size distribution analysis from tsunami deposits in Flores, Indonesia, that the fine grained sediments are removed from soils during backwash flow after the inundation event.

Moreover, Laban Isthmus displays an effect of more mixing process by two opposite directions of tsunami waves from Sunda Strait and Indian Ocean. The medial and distal sections (U-03, U-04, and U-05) show more variable values of standard deviation and skewness than the proximal sections (U-01, U-02, and U-06). However, the mean grain-size of the sediments at the medial and distal zones are finer than the sediments at the proximal areas of deposition, as a consequence of the less energetic sediment reworking farther inland (Figure 8-3).

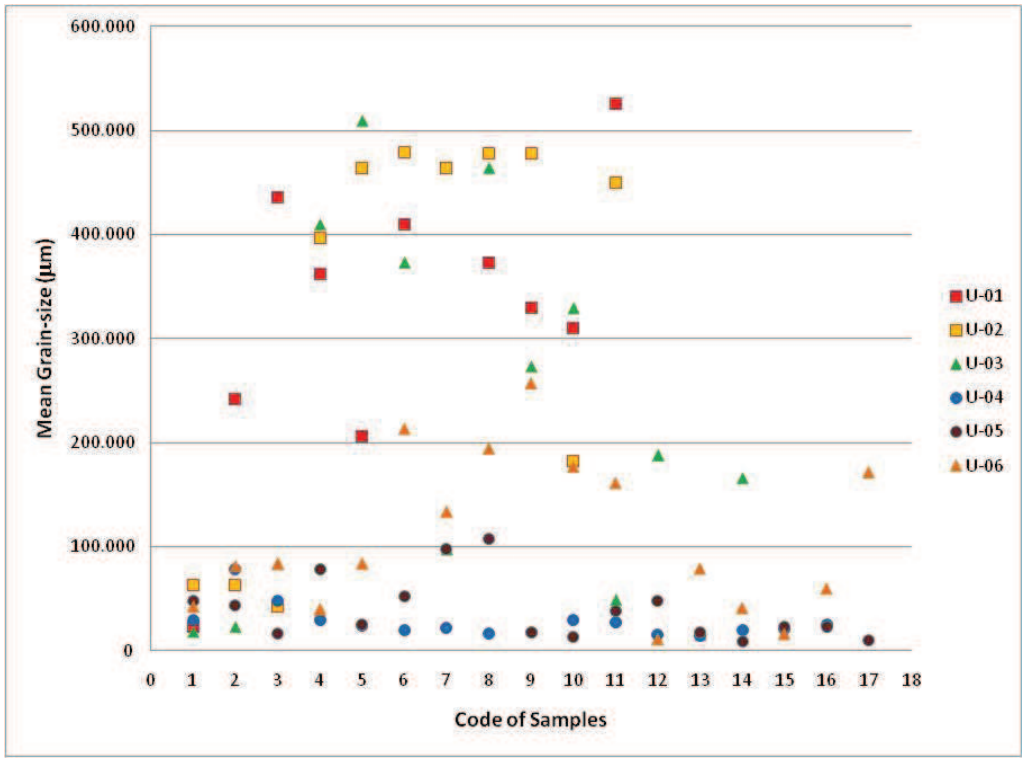

Figure 8-3. Scatter plot of the mean grain-size fluctuation of the sediments at Laban Isthmus, Ujung Kulon Peninsula, from proximal to distal sections.

Hydrodynamic fluctuation of tsunami waves, in fact, can be expressed by *CM* diagrams. The diagrams displayed in Chapter 6 indicate that the dominant transport mechanism at the proximal zone is rolling to ground suspension, while at the medial and distal zones are more variable between rolling and ground suspension to uniform suspension. For each wave cycle at the distal section, the energy during the sedimentation of the basal is higher than the energy during the emplacement of the top of the tsunami sequence which is revealed by the rapid change in transport mechanisms from rolling and ground suspension to gradual or uniform suspension. Bottom traction (rolling and saltation) of the materials as the major transport process for the basal layers is also evidenced by the presence of boulders embedded in sand at Section U-04.

The variations of hydrodynamic conditions can also be identified based on the vertical evolution of AMS parameter (Wassmer et al., 2010). The vertical evolution of magnetic lineation (*L*) and magnetic foliation (*F*) express the fluctuations of current transport from traction to the settling process during sedimentation. Traction, represented by the values of magnetic lineation, is a current transport of sand grains and larger clasts (bedload transport) that occurred as rolling, sliding, or saltation along the bottom of each successive wave. The coarser the grain-size the higher the lineation values. When there is no current, then, suspension settling expressed by the values of magnetic foliation might replace the traction process at the end of tsunami inundation. The finer the grain-size the higher the foliation value. These characteristics are supported by the mainly oblate values of the shape parameter of the AMS ellipsoids (*T*) which indicates the dominant settling during emplacement of the tsunami deposits.

The fluctuations in the current strength during sedimentation are also indicated by the consistent vertical changes of *Pj* and *Fs* (Wassmer et al., 2010), when the degree of alignment of the magnetic particles (*Fs*) controls the degree of anisotropy of the deposits (*Pj*). As well as the magnetic foliation values, the evolution of the *Fs* follows the variations of the mean grain-size. The finer the grain-size the higher the *Fs* value. Consequently, an increase of the *Fs* value indicate a decrease of the current power. It certainly attests to the progressive increase of the settling versus traction process during sediment emplacement related to the successive waves.

From proximal to distal sections, the magnetic foliation, the degree of alignment of the magnetic particles, and the degree of anisotropy of the deposits are variable. The most

proximal sections have a weak and contrasting variation of values, while the distal sections display a better organization of the sediment emplacement of the tsunami deposits. The emplacements explained by such parameters are in accordance with the hydrodynamic fluctuation of tsunami waves expressed by *CM* diagrams. A calmer condition of hydrodynamic at the distal zone (see Figure 8-4) constitutes a good environment for the foraminiferal abundance. The result of biofacies analysis of benthic foraminifera from the selected sections shows that a progressive increase of the number of species and individuals occurred farther inland rather than near the zone of proximal.

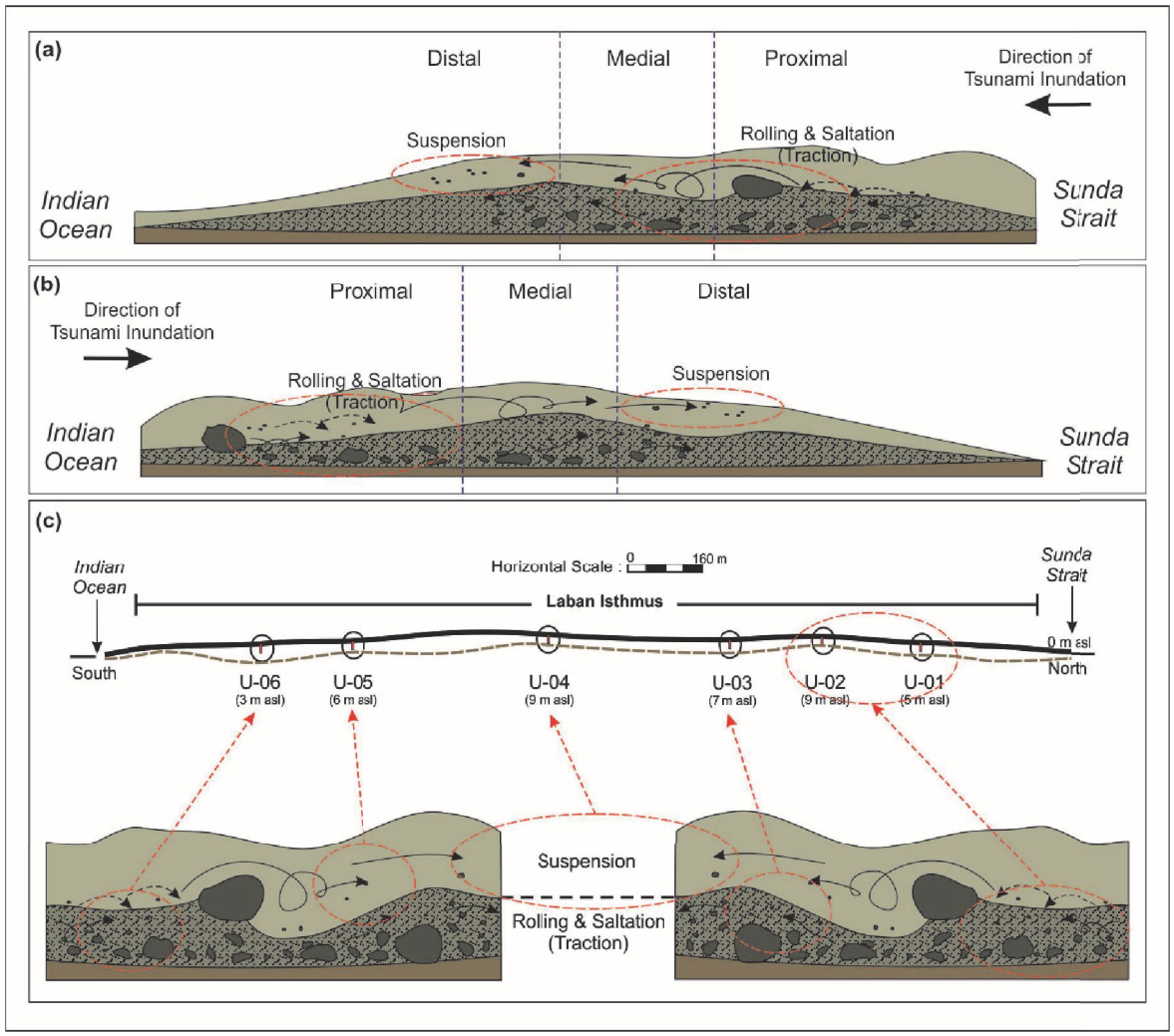

Figure 8-4. The hydrodynamic of sediment emplacement occurred at Laban Isthmus, Ujung Kulon Peninsula, from proximal to distal sections (both from the Sunda Strait and from the Indian Ocean); (a) Illustration of inundation process from the North (Sunda Strait), (b) Illustration of inundation process from the South (Indian Ocean), (c) A combination figure shows the hydrodynamic process occurred at each section.

The calmer hydrodynamic condition of the wave at the distal zone is also caused by the decreasing of the tsunami velocity when penetrates landward. Once the velocity decreases, then the suspended load of the sediments becomes dominant and the flooding maximum extension occurs at the distal zone. At this zone, the tsunami has no energy and velocity at all (*slack phase*) and consequently, mud drapes and foraminifera should have been abundantly deposited. Unfortunately, the mud drapes are not always present at the top of sequences due to the effect of two opposite tsunami wave directions with a rapid interval of flooding periods. This effect can be evidenced through a fluctuation of mean grain-size at each section vertically produced by an exchange of energy processes, e.g. Section U-02 located at proximal zone (if the wave is coming from the North) with strong energy processes, at another moment, can be situated at distal zone with suspension sedimentation process (if the wave is coming from the South), see Figure 8.4.

The landscape of Laban Isthmus is covered by palm tree (Hommel, 1990), thus, it may have a Maning's *n* between 0.07 (*n* for a densely forested landscape) and 0.03 (*n* for developed land). Consequently, the maximum distance of flooding for the biggest tsunami wave coming from Sunda Strait at this isthmus (20 m in height, based on numerical modelling from Maeno and Imamura (2011)) cannot exceed 2 km, see Figure 8-5.

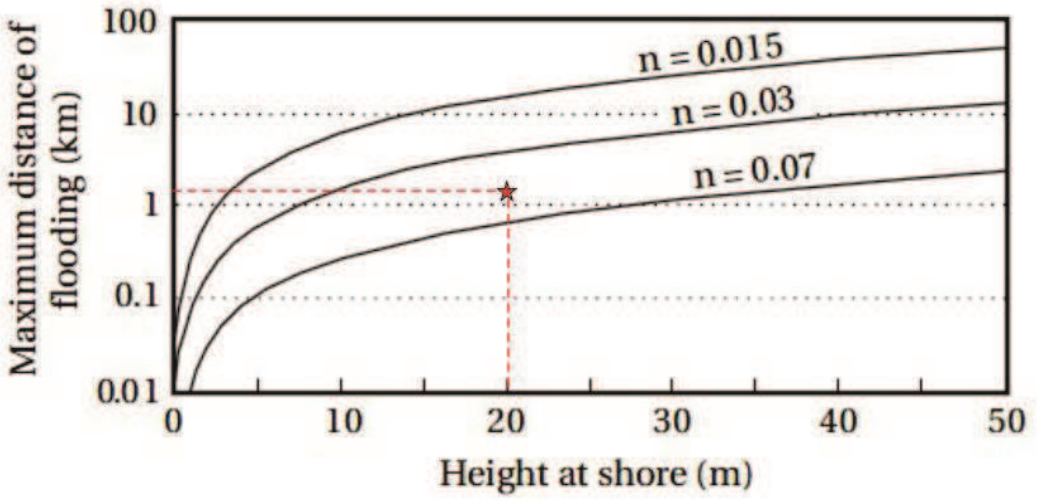

Figure 8-5. Plotting of Laban Isthmus coastal landscape (symbolized by a star) on the roughness curves after Hills and Mader (1997) and the relationships between maximum distance of flooding on the isthmus (km) and tsunami height at shore (m) expressed by dashed line. The values of *n* is explained in the text.

This maximum distance is equal to the minimum width of the isthmus, thus, the zone of slack might only reach near shore of the Indian Ocean. Surprisingly, as mentioned above, this area is also a proximal zone for the tsunami coming from Indian Ocean. It reveals the intriguing feature of section U-06 for which the sediments are dominantly produced by the bedload transport, yet, they are factually able to contain abundant foraminifera.

8.3. Scenario of tsunamis at Laban Isthmus

According to the stratigraphic correlation (Chapter 7), Laban Isthmus was presumably inundated by four tsunami events. The Krakatoa Committee of The Royal Society (1888) reported such possibility of four tsunami sequences based on a pressure gauge at the Batavia gasworks (Symons et al., 1888). Despite the registered air wave could only be connected with certain tsunami waves, these records can be used to evidence that tsunami waves might reach the isthmus more than one time.

As seen at Figure 7-15 to 7-18 in Chapter 7, one inundation event actually consists of inland penetrations of two tsunami waves from opposite directions, i.e. an initial penetration from Sunda Strait followed by a penetration delayed in time from Indian Ocean produced by refracted waves along Ujung Kulon Peninsula (Figure 8-6). This means that Ts_1SS and Ts_1IO were produced by a same and unique tsunami event, see Figure 7-15. Each following tsunami waves (Ts_2, Ts_3, and Ts_4) produced the same double signature (Figure 7-16 to 7-18).

Accordingly with the result of this study, recent numerical simulations of tsunami propagation during the 1883-Krakatau eruptions show that the tsunami waves going out of Sunda Strait were refracted toward the east along Ujung Kulon Peninsula (Yokoyama, 1987; Nomanbhoy and Satake, 1995; Maeno and Imamura, 2011), see Figure 8-6. Paris et al. (2014b) reported that Ujung Kulon Peninsula (Java's First Point) has been affected by the Krakatau tsunamis since August 26, 1883. They evidenced tsunami sand unit below ash fall deposit at the base of the sections. These tsunami evidences are not recorded at Laban sections, their traces might have been eroded by a larger subsequent tsunami. Pumice shards found within rip-up clasts at the base of Ts_1SS attests for this erosional process.

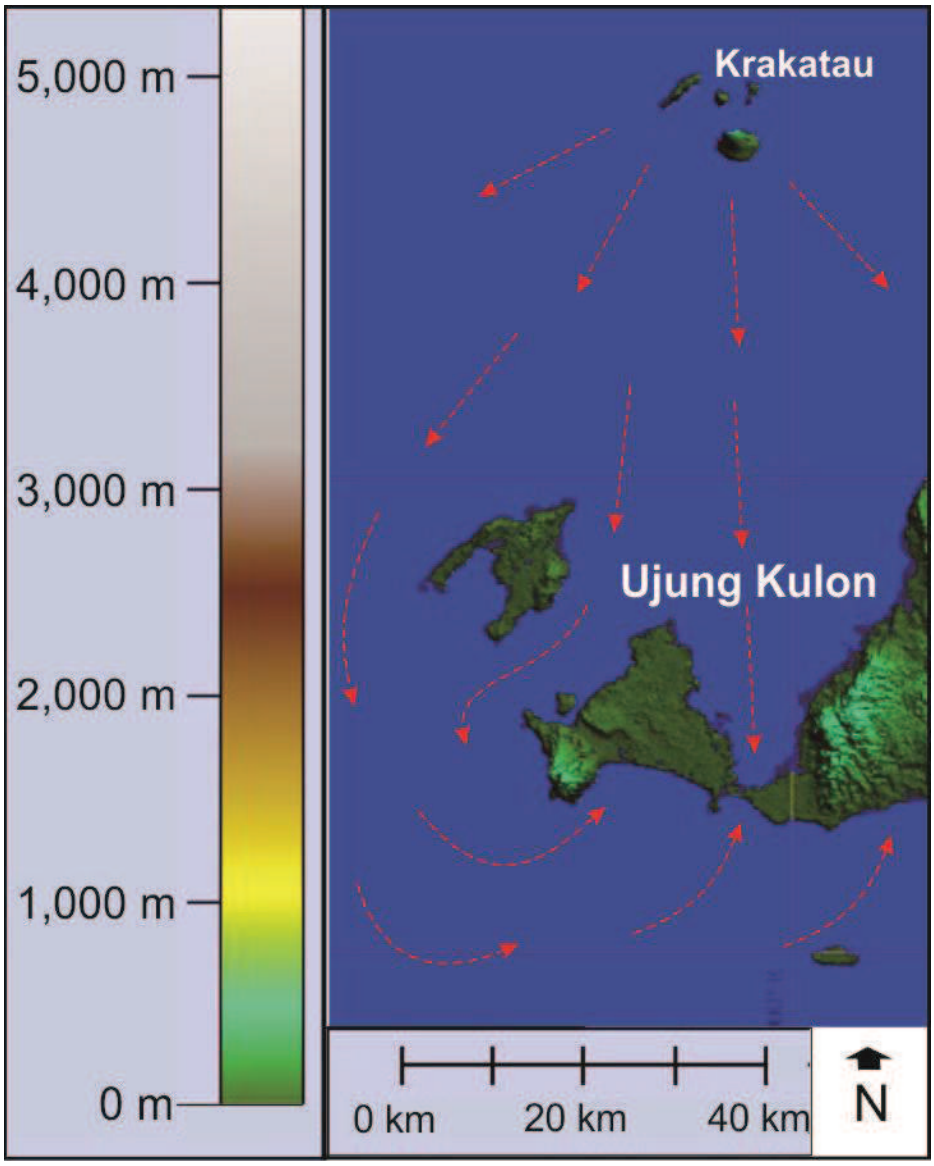

Figure 8-6. A regional map (source: SRTM 90m Digital Elevation Data, CGIAR-CSI, 2009) showing the southward directions of Krakatau tsunami waves and their refracted around Ujung Kulon Peninsula to Indian Ocean, indicated by dashed arrow lines.

The first tsunami deposits recorded at Laban Isthmus (Ts_1SS/Ts_1IO) were most probably deposited by the early morning tsunami wave on August 27. It might have been generated by the explosion of Mount Perbuwatan at 05.30 am. This early large explosion of Krakatau is considered to be quite able to induce tsunami wave (Latter, 1981; Self and Rampino, 1981; Bryant, 2008). This wave, as reported in the previous reports (Verbeek, 1884, 1885; Symons et al., 1888), destroyed the town of Anyer after 06.00 am. Those reports calculated very well the arrival times of tsunami waves at some coastal plains

around the Sunda Strait. Considering these arrival times and recent modelling of Krakatau tsunami propagation, in which Anyer was destroyed 30 minutes after the explosion and Teluk Betung (Sumatra) at 06.30 am (Verbeek, 1884, 1885; Latter, 1981; Yokoyama, I., 1987; Nomanbhoy and Satake, 1995; Maeno and Imamura, 2011; Paris et al., 2014b), we can estimate that the tsunami wave for Ts_1SS penetrated Laban Isthmus from the North between 06.00 - 06.30 am and the Ts_1IO wave might have inundated the southern part of the isthmus 5 - 10 minutes after the depositional of Ts_1SS (Figure 8-7(a) and (b)). This diagnostic short time gap indicates that, in Indian Ocean, the velocity of the wave-train increased due to the deeper ocean floor (Verbeek, 1884, 1885; Symons et al., 1888; Latter, 1981; Bryant, 2008).

Ts_2SS and Ts_2IO can be associated with the tsunami waves between 06.30 - 09.00 am, which were recorded at Merak, Anyer, Caringin, and Teluk Betung (Verbeek, 1885; Symons et al., 1888; Latter, 1981; Paris et al., 2014b). These waves were most probably generated by Mount Danan explosion at 06.44 am (Symons et al., 1888; Self and Rampino, 1981; Bryant, 2008). If the tsunami wave reached Anyer at 07.30 am and Teluk Betung at 07.45 am (Symons et al., 1888), thus Ts_2SS was likely deposited by the same tsunami between 07.30 - 07.45 am and Ts_2IO after 07.45 am (Figure 8-7(c) and (d)). The presence of coral boulders embeded in sand at the centre of the isthmus, indicates that the wave energy was higher than the previous tsunami.

A tremendous explosion of Mount Rakata at 10.02 am, August 27, propelled the largest tsunami wave (Verbeek, 1885; Symons et al., 1888; Latter, 1981; Yokoyama, I., 1987; Nomanbhoy and Satake, 1995; Maeno and Imamura, 2011; Paris et al., 2014b). This huge wave (up to 42 m of run-up at Merak) is believed to corresponds with the depositional of Ts_3SS between 10.30 - 11.00 am and Ts_3IO 5 - 10 minutes later, see Figure 8-7(e) and (f). The thickness of Ts_3SS (up to 85 cm) is consistent with the largest tsunami wave.

Eventually, the last tsunami which deposited Ts_4SS and Ts_4IO might correspond with the 11.05 am air wave recorded at Batavia pressure gauge (Verbeek, 1885; Symons et al., 1888) and deposited after 11.20 am (Figure 8-7(g) and (h)). The barometric pressure between this air wave and the air waves connected tsunamis are equivalent (Symons et al., 1888). The last explosion of Krakatau on August 27, at 10.52 am, was most probably connected with this tsunami. However, it only left the thin layers of tsunami deposits

which might have been related to the low energy of the uprush, as confirmed by the grain size distribution, foraminiferal assemblages, and AMS data. In the northern part, this deposit was overlaid by pumiceous ash resulted from the depositional of floating pumice on the Sunda Strait after the final eruptions (Verbeek, 1885; Symons et al., 1888; Carey et al., 1996).

Indeed, the last tsunami after the final eruption phase was not recorded along the other coastal sections described by previous studies (Ongkosongo, 1985; Carey et al., 2001; Paris et al., 2014b). The deposit was most probably reworked through erosional processes, agricultures, resorts settling, and industries. Unfortunately, the eyewitness after the climactic eruption were not trustworthy, due to the darkness and great alarm condition (Verbeek, 1884, 1885).

Figure 8-7 shows the illustrations of the 1883-Krakatau tsunami inundation at Laban Isthmus, from (a) Ts_1SS to (h) Ts_4IO. In the case of (a) as well as (c) and (g), wave energy was so strong that no distal domain existed, tsunami with fine sediments and abundant foraminifera pourred in the Indian Ocean. Scheme (b) shows a boundary of distal zone near shore of the Sunda Strait, as well as (d), (f), and (h). While, for scheme (e) the boundary of distal zone is near shore on the Indian Ocean side.

An interesting thing concerning the schemes mentioned above is that the biggest tsunami (e) could not reach Indian Ocean. This is likely due to the increasing of Maning's value when the palm trees on the isthmus were uprooted and swept by the strongest energy of tsunami wave. The bed roughness would be close to 0.07 and, consequently, the maximum distance of flooding could not exceed 2 km or might only reach near shore of the Indian Ocean.

The uprush from Sunda Strait can flow with abundant foraminifera across the Laban Isthmus into Indian Ocean for three of the four cases. By contrast, due to the lower energy of the tsunami waves, the uprush from Indian Ocean cannot bring abundant foraminifera and never cross the isthmus. These schemes, however, can confirm the foraminiferal abundance within Section U-05 that is higher than Section U-04 and also the lack of foraminiferal assemblages within Section U-03.

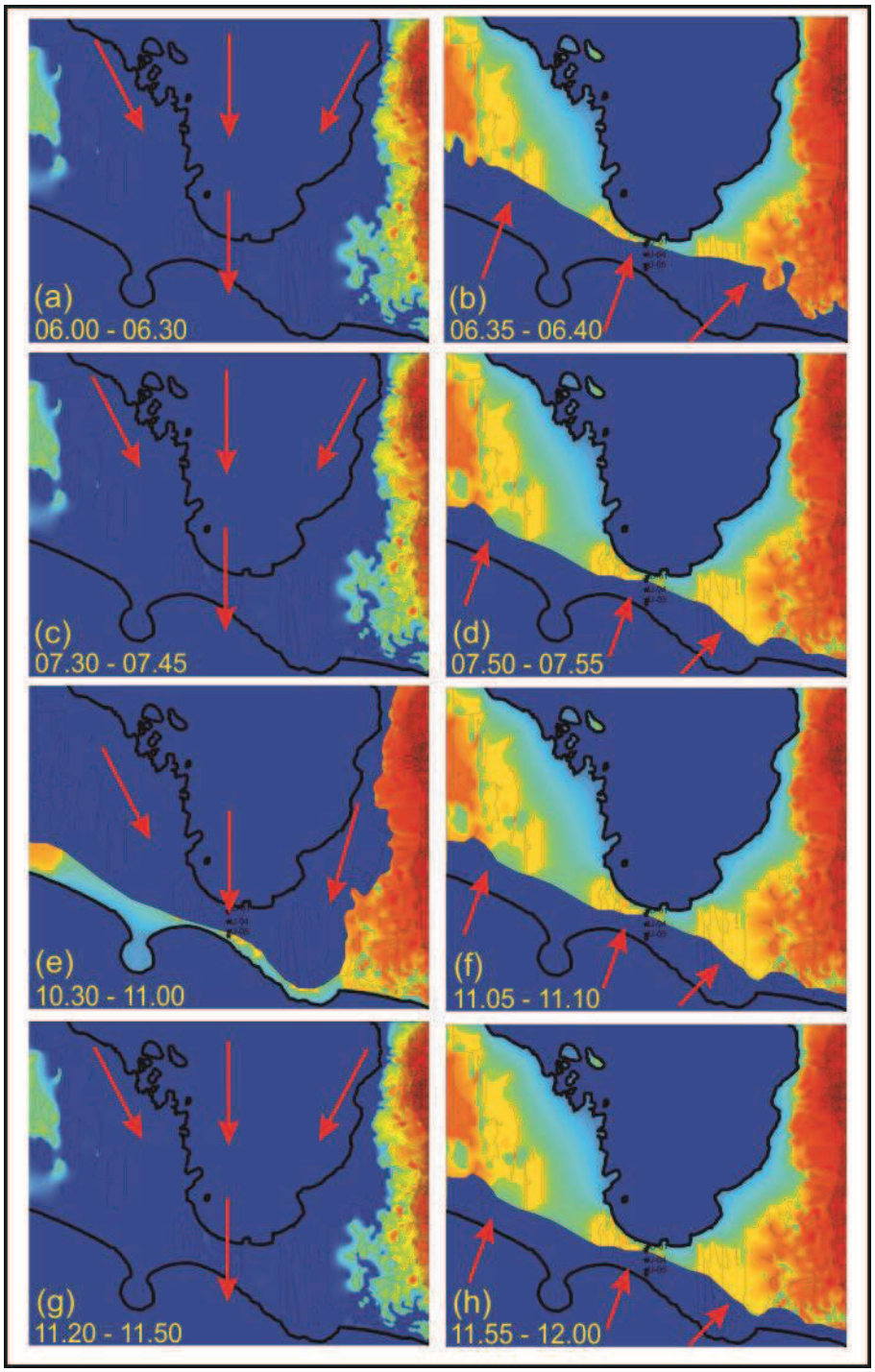

Figure 8-7. An estimated chronology of tsunami inundation occurred at Laban Isthmus on August 27, 1883. Each map showing the direction of the wave (symbolized by arrows) and the zone of inundation (coloured by a dark blue shadow as well as marine) for each tsunami event, a previous inundation zone is ignored. Eight tsunami flooding events have been reconstructed as displayed in the figure, see text for explanation; (a) The first tsunami flooding event that deposited Ts_1SS, (b) The northward direction of tsunami flooding event for Ts_1IO, (c) The second event deposited Ts_2SS, (d) The northward direction for Ts_2IO, (e) The third event deposited Ts_3SS, (f) The northward direction for Ts_3IO, (g) The fourth event deposited Ts_4SS, (h) The northward direction for Ts_4IO.

It is difficult to constrain clearly the generation mechanisms of tsunami waves during eruptions (Paris et al., 2014a). However, some informations about the elevation and the thickness of tsunami deposits, which reflect the tsunami run-up, can be used as references for identifying the tsunami generations. At Laban Isthmus, the elevations of the distal section before the inundation are estimated not less than 6 m asl (Figure 8-8), therefore, the tsunami run-up height must be more than 6 m asl. This run-up height was recorded more than 1 km from the shoreline of Sunda Strait as the main scene of the 1883-Krakatau tsunamis.

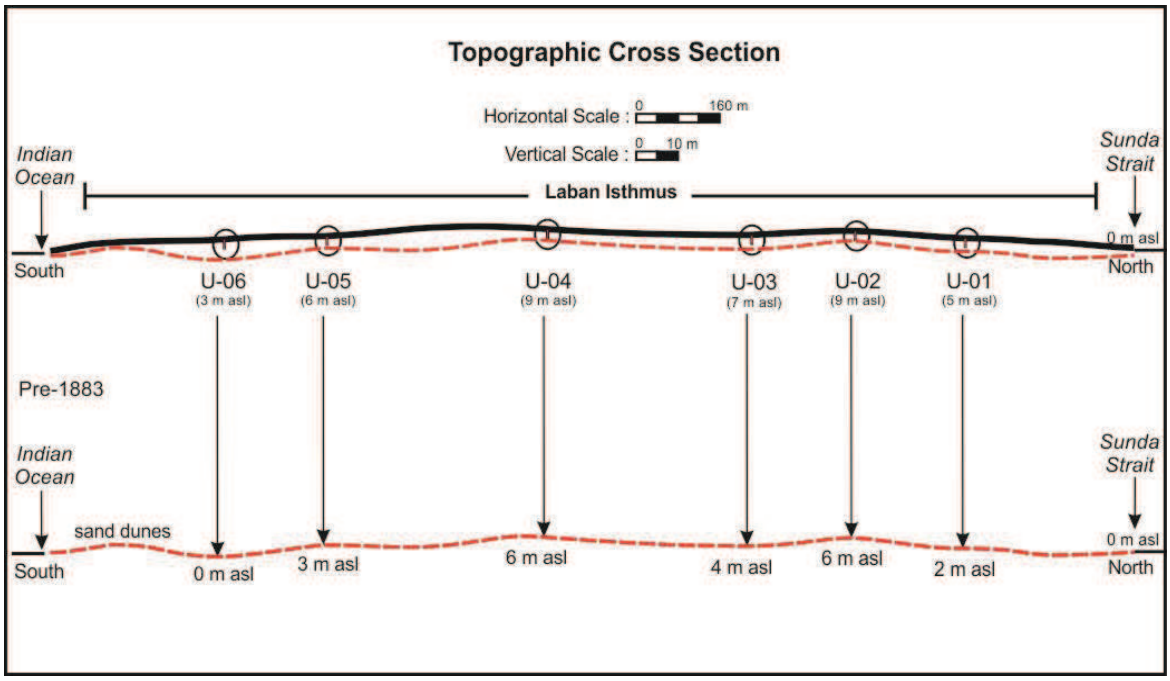

Figure 8-8. Cross sections showing the difference of elevation of Laban Isthmus between present topography (above) and pre-1883 landform indicated by dashed lines (below).

According to the roughness curves after Hills and Mader (1997), see Figure 8-5, the North coast of Laban Isthmus may be hit by a 20 m high tsunami wave. Maeno and Imamura (2011) have modelled the largest tsunami propagations using three different generation mechanisms (pyroclastic flow entering the sea, caldera collapse, and phreatomagmatic explosion), for which only the pyroclastic flow entering the sea produced a tsunami height over 20 m at Welcome Bay 30 minutes after the eruptions. The pyroclastics content within the tsunami sand units can be an indicator for a mixing process when pyroclastic flow induced tsunami waves. Thus, the largest tsunami waves (the third

tsunami) penetrated Laban Isthmus was most probably caused by the entry of pyroclastic flows into the sea.

We could analogize the generation mechanisms of the first and the second tsunamis to the scenario above, because the entry of pyroclastic flows into the sea might have been generated at each volcanic eruption. Self and Rampino (1981) mentioned in their outstanding paper that there were more than one pyroclastic flow during Krakatau eruptions in 1883. While caldera collapse which came late in the eruption is most probably a trigger for the last tsunami (the fourth tsunami) recorded at Laban Isthmus. Nevertheless, these analogies must be confirmed by other evidences or by more accurate simulations.

This study shows that the coastal morphology of Ujung Kulon Peninsula, combined with the tsunamis generated by the August 27, 1883, Krakatau eruptions, resulted in the recording of not less than four tsunami events at Laban Isthmus. Each of the tsunamis directly related to the main Krakatau eruption phases is double-recorded:

- a first southbound flooding of Laban Isthmus by direct waves trapped by the V-shape morphology of Welcome Bay,
- a northbound second flooding lightly delayed in time by waves refracted along the Ujung Kulon Peninsula coasts taking advantage of the low Karang Ranjang Bay to penetrate Laban Isthmus.

The particular behaviour of tsunami at the isthmus produced an original inter-fingered sedimentary signature, which is tightly linked to the processes involved during the Krakatau eruption. The thickness of the deposits can reflect the energy of the tsunami waves and the eruption intensity, e.g. the largest tsunami wave generated by the largest explosion at 10.02 am, on August 27, is represented by the thickest tsunami deposit (Ts_3SS). The thickness of the deposits coming from Sunda Strait (straight from the Krakatau) are thicker than the deposits coming from Indian Ocean (refracted along the peninsula coasts). Such features reveal that the coastal landform played a role on the thickness of the tsunami deposits and, certainly, the changes of tsunami energy. The remarkable preservation of these multiple tsunami sedimentary recordings must be related to the important thickness of the deposits and on the fact that this zone has never been occupied by men since 1883. All of this renders Laban Isthmus one of the most exceptional sites of tsunami recordings on Earth.

Chapter 9
Conclusions

Tsunami deposits and primary volcanic material emplaced around the Sunda Strait during the 1883-Krakatau eruptive sequence were not preserved everywhere. Around the coastal plain of the eastern part of Ujung Kulon National Park (Mount Honje region), they were most probably reworked by bioturbation, slope processes, agriculture, and tourist resorts. At the South of the strait, in the region of Ujung Kulon Peninsula and particularly at Laban Isthmus, the sediments deposited by the tsunamis triggered by the Krakatau tremendous eruption were surprisingly well preserved, probably in reason of the fact that this zone has never been occupied by men since 1883. Displaying an intriguing coastal landform, Laban Isthmus constitutes an exceptional site that recorded very well and preserved the succsessive deposits emplaced by tsunami waves during Krakatau eruptions in 1883.

The sedimentological approach to the multiple tsunami sedimentary recordings at Laban Isthmus supported by other tsunami signatures around Ujung Kulon National Park demonstrated some important conclusions such as follows:

1. The main characteristic of the-1883 Krakatau tsunami deposits found at Ujung Kulon is the presence of stacked individual sequences represented by normally graded bioclastic sand units and volcanic materials content within some sequences. This volcanic materials present within the tsunami sequences correspond to interbeded layer with the bioclastic sand unit, pumiceous sand unit or pumiceous ash fall deposit. Petrographic and geochemical examinations of the volcanic ash from selected layers demonstrated a similar composition in mineral and major elements with the volcanic ash collected near Krakatau and Bogor in 1883. The presence of these volcanic materials mixed with marine sediments allow to link without ambiguity the tsunami deposits, both from Sunda Strait and Indian Ocean, with the 1883-Krakatau eruption sequence.
2. Multiple sequences of tsunami deposits have been identified at Ujung Kulon Peninsula. The boundaries between sequences are mostly characterized by fine sands/silts mixed with gravel/coarse sands, or, in the textural triangle ranging between loamy sand/sandy loam and loam/silt loam. The tsunami deposits display structural, grain-size and

magnetic fabric characteristics that recorded the hydrodynamic conditions of tsunami inundation at Ujung Kulon during Krakatau eruptions in 1883. Each flooding event was recorded by a normally graded sequence with a coarse base layer resulted from bedload transport within the head of the wave evolving gradually to a top layer resulted in the settling of the finer particles that were transported within the tail of the wave. These sediment transport mechanisms are well confirmed by the CM diagrams from proximal to distal sections. The fluctuations of grain-size data (mean grain-size, standard deviation, and skewness) at the distal sections of Laban Isthmus indicate that a mixing process occurred between two different phases of sediment transport from Sunda Strait and Indian Ocean. When the settling process of the wave coming from Sunda Strait was still ongoing, another wave coming from Indian Ocean with the bedload transport mechanism surged on this area, producing an intriguing feature of tsunami deposit.

3. The occurrence of two different flooding directions from Sunda Strait and from Indian Ocean at Laban Isthmus is evidenced by the characteristics of magnetic fabric resulted from Anisotropy of Magnetic Susceptibility (AMS) method. K_1 axes displayed two general flow directions with their slightly variations. A first southward direction, from Sunda Strait, spreading between N122°E and N236°E. A second in the opposite direction from Indian Ocean spreading between N318°E and N58°E. Variations in their orientations are both related to the current strength, the mean grain-size, and the local topographic control. Due to its geographic position, the isthmus became an ideal location for the optimal preservation of the remarkable tsunami signatures deposited from Sunda Strait and Indian Ocean. The presence of *Planulina wuellerstorfi* as dominant benthic formanifera at the South coasts of Ujung Kulon also evidenced the northward direction of tsunami wave coming from the Indian Ocean, confirming the flow direction evidenced thanks to the help of AMS technique. While, *Elphidum lessonii* and *Streblus beccarii* contained within the deposits were mainly derived from the shallow marine environment of the Sunda Strait. The more surprizing northward direction of the waves evidenced by their magnetic fabrics and foraminiferal assemblages is then explained as a part of the 1883-Krakatau tsunami propagation that refracted around Panaitan Island, near the westend of Ujung Kulon Penisula. Indubitably, it reveals the origin of the flooding at the South coasts of Ujung Kulon Peninsula charted by (Verbeek, 1885).

4. A stratigraphic correlation reconstructed on the basis of grain-size distribution, texture and structure of the sequence, foraminiferal assemblages, and characteristics of the magnetic fabric including its orientations evidenced alternately four layers of tsunami deposits both from Sunda Strait and from Indian Ocean. This stratigraphic correlation revealed that four tsunami events have overridden Laban Isthmus and Ujung Kulon Peninsula and that each tsunami event appears to have been constituted of two opposite wave penetrations. The correlation allows to establish a scenario of the 1883-Krakatau tsunamis in the South part of Sunda Strait. The stratigraphic records were produced during the Krakatau eruptions and can be linked to the report of Krakatoa Committee of The Royal Society (1888) about the possibility of tsunami waves based on pressure gauge at the Batavia gasworks (Symons et al., 1888). Two tsunami events observed before the paroxysm might have been linked to the first August 27, 1883 explosion of Mount Perbuwatan, at 5.30 am and the second, Mount Danan, at 6.44 am. The other two were associated with the large explosion of Mount Rakata at 10.02 am and 10.52 am.
5. The tsunami deposits observed at Laban Isthmus and Ujung Kulon Peninsula were most probably emplaced by the large tsunami events that might have been generated by pyroclastic flows or landslides produced by the volcanic edifice. According to the numerical simulation from Maeno and Imamura (2011), the pyroclastic flow entering the sea can generate a tsunami height over 20 m at Welcome Bay 30 minutes after the eruptions. The model also demonstrated that no other tsunami generation mechanisms can produce a wave height up to 20 m at such bay in 30 minutes. The huge tsunami waves that penetrated Laban Isthmus are evidenced by the thick tsunami deposits from proximal to distal sections and the presence of the large coral boulders embeded in sand at distal section.
6. Remarkable tsunami signatures discovered in this area were resulted from the exceptional coastal configuration of the isthmus and surrounding coasts. Laban Isthmus is situated at the convergence of the large V-shape coastal landform of Welcome Bay which faces the Krakatau Volcanic Complex (80 km to the north of Laban Isthmus) and Karang Ranjang Bay on the South side of the isthmus which is open to the Indian Ocean. This unique coastal landform have concentrated and increased the energy of the Krakatau tsunami waves entering the Welcome Bay, allowing them to overpass the isthmus and to pour into the Indian Ocean at Karang Ranjang Bay. The refraction of the direct waves along Ujung Kulon generates a less energetic northward flooding from

Karang Ranjang Bay. As a consequence, these northbound floodings never reached the Sunda Strait coasts. Another V-shape bay behind Peucang Island, in the western part of Ujung Kulon Peninsula, also shows a thick tsunami deposit emplaced 400 m far inland from Cidaun coastal area as the centre part of the bay.

7. The contrasting coastal landforms of two littoral plains at Ujung Kulon National Park, i.e. the peneplain of Ujung Kulon Peninsula in the western part and the Mount Honje narrow coastal plain in the eastern part display significant characteristics differences between tsunami sequences recorded. This landform differences have affected the behaviour of the flooding. At Mount Honje, in reason of the small size of the plain, the uprush flow reached quickly the foothills that generated a strong backwash flow affecting all the area. As a consequence, the flooding duration was short. At Laban, backwash was quite absent and in reason of the flattness of the topography, except in the nearshore area while the duration of the flooding was more important. Reworked by bioturbation, slope processes, agriculture, and tourist resorts (like the other sites around the Sunda Strait) the deposits preservation potential was also reduced at Mount Honje compared to Laban.

This study provides an important key of determination of the coastal landforms effect to the tsunamis inundation at Ujung Kulon area. The key is a learning from the characteristics of tsunami deposits, i.e. their normal grading repetition, skewness, kurtosis, bioclasts, pyroclastics content, rip-up clasts characterizing the base of an uprush phase, and magnetic fabric properties, in some places with an intriguing coastal landforms. Using current knowledge in tsunami study that constitutes a multidisciplinary endeavour beyond the sedimentology and stratigraphy approaches, i.e. analyses of the grain-size, the foraminiferal assemblages, and the magnetic fabric, the tsunami sequences can be accurately identified. The AMS technique, appears to be an effective method to determine the magnetic fabric and the flow orientation that emplaced the deposits. It is possible to evidence the speed variations of water waves in a single event (Wassmer et al., 2015). It becomes an essential method in the study of paleo-tsunami, particularly when the sediments are lacking of any visible sedimentary structures and when the foraminiferal assemblages cannot confirm the origin of the sediments coming from the same environment. It can also be used to calibrates other sedimentary methods in distinguishing each successive wave within a single event. The opposite flow orientation detected by this

technique and confirmed by foraminiferal assemblages at Laban Isthmus have evidenced that the tsunami waves coming from Krakatau were refracted along the West end of Ujung Kulon Peninsula.

Notwithstanding, this study may have inadequacies and limitations. A drilling method for AMS collecting samples was applied for the first time in this study. The method has some limitations due to inaccuracy of the azimuth measurement of the sample tube before the drilling and the possibility of samples disturbance during the drilling. Therefore, it must be carefully done with an appropriate auger when applying this method. Another limitation of the method concerns the AMS sampling in poorly sorted sediments with a dominant fraction of coarse bioclastic particles which were mostly found in the proximal sections. AMS sampling in these conditions is impossible especially when sequences contain very coarse bioclastic particles, because it can bias the bulk volume susceptibility of the sample itself. This resulted in a loss of precision due to the impossibility to extract the information from some sediment layers. This limitation can be circumvented if the AMS is measured with the larger sample boxes. As a consequence, the device of measurement must be more adapted for the larger boxes with the coarse materials inside.

In spite of some inadequacies, the results of the study can respond the scientific questions mentioned in the Introduction. The tsunami deposits found at the South coasts of Ujung Kulon are emplaced by the refracted 1883-Krakatau tsunamis. These deposits are not related to the past earthquake tsunamis occurred in Indian Ocean. The 1883-Krakatau tsunami inundation zone delineated by Verbeek (1885) confirms this finding.

However, besides augmenting the samples collected, an additional transect should be made on the other possible sites to calibrate the result of stratigraphic correlation at Laban Isthmus. Hence, the limitations resulted from this study open new opportunities for performing an advanced study and a wider stratigraphic correlation around this unique and exceptional site for the tsunami recordings. Submarine sampling will also be a very valuable endeavour for validating the analysis of foraminiferal assemblages within tsunami deposits found far inland. All of these will enrich the study of past tsunami events in Ujung Kulon, in relation with the tsunamigenic eruption generated by the mythic Krakatau in 1883. For instance this thesis, at least, has added a contribution to the development of knowledge on this legendary eruption and its consequences on the Sunda Strait.

REFERENCES

Aalto, K.R., Aalto, R., Garrison-Laney, C. E., Abramson, H.F., 1999. Tsunami(?) Sculpturing of the Pebble Beach Wave-Cut Platform, Crescent City Area, California. J. Geol. 107, 607–622. doi:10.1086/jg.1999.107.issue-5

Abbene, I.J., Culver, S.J., Corbett, D.R., Buzas, M.A., Tully, L.S., 2006. Distribution of Foraminifera in Pamlico Sound, North Carolina, Over the Past Century. J. Foraminifer. Res. 36, 135–151. doi:10.2113/36.2.135

Abbott, D., Martos, S., Elkinton, H., Bryant, E.F., Gusiakov, V., Breger, D., 2006. Impact craters as sources of mega-tsunami generated chevron dunes, in: Geological Society of America Abstracts with Programs. p. 299AGICO, 2009. MFK1-FA/CS4/CSL, MFK1-A/CS4/CSL, MFK1-FB, MFK1-B: User's Guide, Ver. 4.0. ed. Advance Geoscience Instrument Co., Brno, Czech Republic, Czech Republic.

AGICO, 2009. MFK1-FA/CS4/CSL, MFK1-A/CS4/CSL, MFK1-FB, MFK1-B: User's Guide, Ver. 4.0. ed. Advance Geoscience Instrument Co., Brno, Czech Republic, Czech Republic.

Agustan, Kimata, F., Pamitro, Y.E., Abidin, H.Z., 2012. Understanding the 2007–2008 eruption of Anak Krakatau Volcano by combining remote sensing technique and seismic data. Int. J. Appl. Earth Obs. Geoinformation 14, 73–82. doi:10.1016/j.jag.2011.08.011

Allaby, M., 2013. A Dictionary of Geology and Earth Sciences. Oxford University Press.

Allen, G.P., 1971. Relationship Between Grain Size Parameter Distribution and Current Patterns in the Gironde Estuary (France). J. Sediment. Res. 41.

Atmawinata, S., Abidin, H.Z., 1991. Geological map of the Ujung Kulon quadrangle, West Java.

Atmadja, S., 2007. Onshore Boulder Deposits Near Krakatau Volcano, Indonesia. AGU Spring Meet. Abstr. -1, 03.

Atwater, B.F., 1987. Evidence for great Holocene earthquakes along the outer coast of Washington State. Science 236, 942–944.

Bahlburg, H., Weiss, R., 2007. Sedimentology of the December 26, 2004, Sumatra tsunami deposits in eastern India (Tamil Nadu) and Kenya. Int. J. Earth Sci. 96, 1195–1209. doi:10.1007/s00531-006-0148-9

Baldock, T.E., Barnes, M.P., Guard, P.A., Hie, T., Hanslow, D., Ranasinghe, R., Gray, D., Nielsen, O., 2007. Modelling tsunami inundation on coastlines with characteristic form, in: Proc. 16th Australasian Fluid Mechanics Conf.(AFMC). pp. 939–942.

Begét, J.E., 2000. Volcanic tsunamis. Encycl. Volcanoes 1005–1014.

Belousov, A., Voight, B., Belousova, M., Muravyev, Y., 2000. Tsunamis Generated by Subaquatic Volcanic Explosions: Unique Data from 1996 Eruption in Karymskoye Lake, Kamchatka, Russia. Pure Appl. Geophys. 157, 1135–1143. doi:10.1007/ s000240050021

Bemmelen, R.W., 1949. The geology of Indonesia. US Government Printing Office.

Blott, S.J., Pye, K., 2001. GRADISTAT: a grain size distribution and statistics package for the analysis of unconsolidated sediments. Earth Surf. Process. Landf. 26, 1237–1248. doi:10.1002/esp.261

Blong, R.J., 1984. Volcanic hazards. A sourcebook on the effects of eruptions.

Boer, W., van den Bergh, G.D., de Haas, H., de Stigter, H.C., Gieles, R., van Weering, T.C.E., 2006. Validation of accumulation rates in Teluk Banten (Indonesia) from commonly applied 210Pb models, using the 1883 Krakatau tephra as time marker. Mar. Geol. 227, 263–277. doi:10.1016/j.margeo.2005.12.002

Boggs Jr, S., 1992. Petrology of Sedimentary Rocks Macmillan. N. Y. 707.

Bondevik, S., Svendsen, J.I., Mangerud, J., 1997. Tsunami sedimentary facies deposited by the Storegga tsunami in shallow marine basins and coastal lakes, western Norway. Sedimentology 44, 1115–1131. doi:10.1046/j.1365-3091.1997.d01-63.x

Bouma, A., 1964. Turbidites, in: A.H. Bouma and A. Brouwer (Ed.), Developments in Sedimentology, Turbidites. Elsevier, pp. 247–256.

Bourgeois, J., 2009. Geologic effects and records of tsunamis. The sea 15, 55–91.

Bourgeois, J., Weiss, R., 2009. “Chevrons” are not mega-tsunami deposits; A sedimentologic assessment. Geology 37, 403–406. doi:10.1130/G25246A.1

Bourgeois, J., Hansen, T.A., Wiberg, P.L., Kauffman, E.G., 1988. A Tsunami Deposit at the Cretaceous-Tertiary Boundary in Texas. Science 241, 567–570. doi:10.1126/science.241.4865.567

Bourrouilh-Le Jan, F.G., Talandier, J., 1985. Sedimentation et fracturation de haute energie en milieu recifal: Tsunamis, ouragans et cyclones et leurs effets sur la sedimentologie et la geomorphologie d’un atoll: Motu et hoa, a rangiroa, Tuamotu, Pacifique SE. Mar. Geol. 67, 263–333. doi:10.1016/0025-3227(85)90095-7

Brady, N.C., Weil, R.R., 1999. The nature and properties of soil 12th ed. Prentice-Hall Inc. Upper Saddle River, New Jersey.

Bronto, S., 1990. Gunung Krakatau. Dir. Vulkanol. Edisi Khusus No. 133, 5h.

Bruins, H.J., MacGillivray, J.A., Synolakis, C.E., Benjamini, C., Keller, J., Kisch, H.J., Klügel, A., van der Plicht, J., 2008. Geoarchaeological tsunami deposits at Palaikastro (Crete) and the Late Minoan IA eruption of Santorini. J. Archaeol. Sci. 35, 191–212. doi:10.1016/j.jas.2007.08.017

Bryant, E., 2008. Tsunami: The Underrated Hazard. Springer.

Bryant, E.A., Young, R.W., Price, D.M., Wheeler, D.J., Pease, M.I., 1997. The Impact of Tsunami on the Coastline of Jervis Bay, Southeastern Australia. Phys. Geogr. 18, 440–459. doi:10.1080/02723646.1997.10642629

Bryant, E.A., Young, R.W., Price, D.M., 1996. Tsunami as a major control on coastal evolution, southeastern Australia. J. Coast. Res. 12, 831–840.

Bryant, E.A., Young, R.W., Price, D.M., 1992. Evidence of Tsunami Sedimentation on the Southeastern Coast of Australia. J. Geol. 100, 753–765.

Bubenshchikova, N., Nürnberg, D., Lembke-Jene, L., Pavlova, G., 2008. Living benthic foraminifera of the Okhotsk Sea: Faunal composition, standing stocks and microhabitats. Mar. Micropaleontol. 69, 314–333. doi:10.1016/j.marmicro.2008.09. 002

Camfield, F.E., 1994. Tsunami effects on coastal structures. J. Coast. Res. 177–187.

Camus, G., Diament, M., Gloaguen, M., Provost, A., Vincent, P., 1992. Emplacement of a Debris Avalanche during the 1883 eruption of Krakatau (Sunda Straits, Indonesia). GeoJournal 28, 123–128. doi:10.1007/BF00177224

Camus, G., Vincent, P.M., 1983. Discussion of a new hypothesis for the Krakatau volcanic eruption in 1883. J. Volcanol. Geotherm. Res. 19, 167–173.

Carey, S., Morelli, D., Sigurdsson, H., Bronto, S., 2001. Tsunami deposits from major explosive eruptions: An example from the 1883 eruption of Krakatau. Geology 29, 347–350. doi:10.1130/0091-7613(2001)029<0347:TDFMEE>2.0.CO;2

Carey, S., Sigurdsson, H., Mandeville, C., Bronto, S., 2000. Volcanic hazards from pyroclastic flow discharge into the sea: Examples from the 1883 eruption of Krakatau, Indonesia. Geol. Soc. Am. Spec. Pap. 345, 1–14. doi:10.1130/0-8137-2345-0.1

Carey, S., Sigurdsson, H., Mandeville, C., Bronto, S., 1996. Pyroclastic flows and surges over water: an example from the 1883 Krakatau eruption. Bull. Volcanol. 57, 493–511. doi:10.1007/BF00304435

Carrier, G.F., Wu, T.T., Yeh, H., 2003. Tsunami run-up and draw-down on a plane beach. J. Fluid Mech. 475, 79–99. doi:10.1017/S0022112002002653

Chagué-Goff, C., Andrew, A., Szczuciński, W., Goff, J., Nishimura, Y., 2012. Geochemical signatures up to the maximum inundation of the 2011 Tohoku-oki tsunami — Implications for the 869 AD Jogan and other palaeotsunamis. Sediment. Geol., The 2011 Tohoku-oki tsunami 282, 65–77. doi:10.1016/j.sedgeo.2012.05.021

Chagué-Goff, C., Schneider, J.-L., Goff, J.R., Dominey-Howes, D., Strotz, L., 2011. Expanding the proxy toolkit to help identify past events — Lessons from the 2004 Indian Ocean Tsunami and the 2009 South Pacific Tsunami. Earth-Sci. Rev., The 2009 South Pacific tsunami 107, 107–122. doi:10.1016/j.earscirev.2011.03.007

Choi, B.H., Hong, S.J., Pelinovsky, E., 2006. Distribution of runup heights of the December 26, 2004 tsunami in the Indian Ocean. Geophys. Res. Lett. 33.

Choi, B.H., Pelinovsky, E., Kim, K.O., Lee, J.S., 2003. Simulation of the trans-oceanic tsunami propagation due to the 1883 Krakatau volcanic eruption. Nat. Hazards Earth Syst. Sci. 3, 321–332.

Cita, M.B., Aloisi, G., 2000. Deep-sea tsunami deposits triggered by the explosion of Santorini (3500 y BP), eastern Mediterranean. Sediment. Geol. 135, 181–203. doi:10.1016/S0037-0738(00)00071-3

Cita, M.B., Camerlenghi, A., Rimoldi, B., 1996. Deep-sea tsunami deposits in the eastern Mediterranean: New evidence and depositional models. Sediment. Geol., Marine

Sedimentary Events and Their Records 104, 155–173. doi:10.1016/0037-0738(95)00126-3

Clague, J.J., Bobrowsky, P.T., 1994. Tsunami deposits beneath tidal marshes on Vancouver Island, British Columbia. Geol. Soc. Am. Bull. 106, 1293–1303. doi:10.1130/0016-7606(1994)106<1293:TDBTMO>2.3.CO;2

Cuven, S., Paris, R., Falvard, S., Miot-Noirault, E., Benbakkar, M., Schneider, J.-L., Billy, I., 2013. High-resolution analysis of a tsunami deposit: Case-study from the 1755 Lisbon tsunami in southwestern Spain. Mar. Geol. 337, 98–111. doi:10.1016/j.margeo.2013.02.002

Dalrymple, R.W., Zaitlin, B.A., Boyd, R., 1992. Estuarine Facies Models: Conceptual Basis and Stratigraphic Implications: PERSPECTIVE. J. Sediment. Res. 62.

Darienzo, M.E., Peterson, C.D., 1990. Episodic tectonic subsidence of Late Holocene salt marshes, northern Oregon Central Cascadia Margin. Tectonics 9, 1–22. doi:10.1029/TC009i001p00001

Davis, W.M., 1889. The rivers and valleys of Pennsylvania. National Geographic Society.

Dawson, A.G., Stewart, I., 2007. Tsunami deposits in the geological record. Sediment. Geol., Sedimentary Features of Tsunami Deposits - Their Origin, Recognition and Discrimination: An Introduction 200, 166–183. doi:10.1016/j.sedgeo.2007.01.002

Dawson, A.G., Shi, S., 2000. Tsunami Deposits. Pure Appl. Geophys. 157, 875–897. doi:10.1007/s000240050010

Dawson, A.G., Foster, I.D.L., Shi, S., Smith, D.E., Long, D., 1991. The identification of tsunami deposits in coastal sediment sequences. Sci. Tsunami Hazards 9, 73–82.

Deplus, C., Bonvalot, S., Dahrin, D., Diament, M., Harjono, H., Dubois, J., 1995. Inner structure of the Krakatau volcanic complex (Indonesia) from gravity and bathymetry data. J. Volcanol. Geotherm. Res. 64, 23–52. doi:10.1016/0377-0273(94)00038-I

El-Hasan, T., 2006. Geochemical dissociation of major and trace elements in bed and suspended sediment phases of the phosphate mines effluent water, Jordan. Environ. Geol. 51, 621–629. doi:10.1007/s00254-006-0357-3

Ellwood, B.B., 1975. Analysis of emplacement mode in basalt from Deep-Sea Drilling Project Holes 319A and 321 using anisotropy of magnetic susceptibility. J. Geophys. Res. 80, 4805–4808. doi:10.1029/JB080i035p04805

Folk, R.L., Ward, W.C., 1957. Brazos River bar [Texas]; a study in the significance of grain size parameters. J. Sediment. Res. 27, 3–26.

Francis, P.W., 1985. The origin of the 1883 Krakatau tsunamis. J. Volcanol. Geotherm. Res. 25, 349–363. doi:10.1016/0377-0273(85)90021-6

Gallagher, S.J., Jonasson, K., Holdgate, G., 1999. Foraminiferal biofacies and palaeoenvironmental evolution of an Oligo-Miocene cool-water carbonate succession in the Otway Basin, southeast Australia. J. Micropalaeontology 18, 143–168. doi:10.1144/jm.18.2.143

Geist, E.L., Parsons, T., 2006. Probabilistic Analysis of Tsunami Hazards*. Nat. Hazards 37, 277–314. doi:10.1007/s11069-005-4646-z

Geist, E.L., 1999. Local tsunamis and earthquake source parameters. Adv. Geophys. 39, 117–209.

Geist, E.L., Dmowska, R., 1999. Local Tsunamis and Distributed Slip at the Source, in: Sauber, J., Dmowska, R. (Eds.), Seismogenic and Tsunamigenic Processes in Shallow Subduction Zones, Pageoph Topical Volumes. Birkhäuser Basel, pp. 485–512.

Gillespie, R.G., Clague, D.A., 2009. Encyclopedia of Islands. University of California Press.

Glimsdal, S., Pedersen, G.K., Atakan, K., Harbitz, C.B., Langtangen, H.P., Lovholt, F., 2006. Propagation of the Dec. 26, 2004, Indian Ocean Tsunami: Effects of Dispersion and Source Characteristics. Int. J. Fluid Mech. Res. 33, 15–43. doi:10.1615/ InterJFluidMechRes.v33.i1.30

Goff, J., Chagué-Goff, C., Nichol, S., Jaffe, B., Dominey-Howes, D., 2012. Progress in palaeotsunami research. Sediment. Geol. 243–244, 70–88. doi:10.1016/j.sedgeo.2011.11.002

Goff, J., Pearce, S., Nichol, S.L., Chagué-Goff, C., Horrocks, M., Strotz, L., 2010. Multi-proxy records of regionally-sourced tsunamis, New Zealand. Geomorphology 118, 369–382. doi:10.1016/j.geomorph.2010.02.005

Goff, J., McFadgen, B.G., Chagué-Goff, C., 2004. Sedimentary differences between the 2002 Easter storm and the 15th-century Okoropunga tsunami, southeastern North Island, New Zealand. Mar. Geol. 204, 235–250. doi:10.1016/S0025-3227(03)00352-9

Goodman-Tchernov, B.N., Dey, H.W., Reinhardt, E.G., McCoy, F., Mart, Y., 2009. Tsunami waves generated by the Santorini eruption reached Eastern Mediterranean shores. Geology 37, 943–946. doi:10.1130/G25704A.1

Goto, K., Kawana, T., Imamura, F., 2010. Historical and geological evidence of boulders deposited by tsunamis, southern Ryukyu Islands, Japan. Earth-Sci. Rev. 102, 77–99. doi:10.1016/j.earscirev.2010.06.005

Grue, J., Pelinovsky, E.N., Fructus, D., Talipova, T., Kharif, C., 2008. Formation of undular bores and solitary waves in the Strait of Malacca caused by the 26 December 2004 Indian Ocean tsunami. J. Geophys. Res. Oceans 113, C05008. doi:10.1029/2007JC004343

Gusiakov, V., Abbott, D.H., Bryant, E.A., Masse, W.B., Breger, D., 2010. Mega Tsunami of the World Oceans: Chevron Dune Formation, Micro-Ejecta, and Rapid Climate Change as the Evidence of Recent Oceanic Bolide Impacts, in: Beer, T. (Ed.), Geophysical Hazards, International Year of Planet Earth. Springer Netherlands, pp. 197–227.

Hamilton, N., Rees, A.I., 1970. The use of magnetic fabric in paleocurrent estimation. Palaeogeophysics 445–464.

Harjono, H., Diament, M., Dubois, J., Larue, M., Zen, M.T., 1991. Seismicity of the Sunda Strait: Evidence for crustal extension and volcanological implications. Tectonics 10, 17–30.

Hawkes, A.D., Bird, M., Cowie, S., Grundy-Warr, C., Horton, B.P., Shau Hwai, A.T., Law, L., Macgregor, C., Nott, J., Ong, J.E., Rigg, J., Robinson, R., Tan-Mullins, M., Sa, T.T., Yasin, Z., Aik, L.W., 2007. Sediments deposited by the 2004 Indian Ocean Tsunami along the Malaysia–Thailand Peninsula. Mar. Geol., Quaternary Land-Ocean Interactions: Sea-Level Change, Sediments and Tsunami 242, 169–190. doi:10.1016/j.margeo.2007.02.017

Hills, J.G., Mader, C.L., 1997. Tsunami Produced by the Impacts of Small Asteroids. Ann. N. Y. Acad. Sci. 822, 381–394. doi:10.1111/j.1749-6632.1997.tb48352.x

Hjulstrom, F., 1939. Transportation of Detritus by Moving Water: Part 1. Transportation 142, 5–31.

Holbourn, A., Henderson, A.S., Macleod, N., 2013. Atlas of Benthic Foraminifera. John Wiley & Sons.

Hommel, P.W.F.M., 1990. A phytosociological study of a forest area in the humid tropics (Ujung Kulon, West Java, Indonesia). Vegetatio 89, 39–54. doi:10.1007/BF00134433

Hrouda, F., 1982. Magnetic anisotropy of rocks and its application in geology and geophysics. Geophys. Surv. 5, 37–82. doi:10.1007/BF01450244

Hurlbut, G.C., Verbeek, R.D.M., 1887. Krakatau. J. Am. Geogr. Soc. N. Y. 233–253.

Iida, K., 1963. Magnitude, energy and generation mechanisms of tsunamis and a catalogue of earthquakes associated with tsunamis, in: Proceedings, Tsunami Meetings Associated with the Tenth Pacific Science Congress. pp. 7–18.

Jelinek, V., 1981. Characterization of the magnetic fabric of rocks. Tectonophysics 79, T63–T67. doi:10.1016/0040-1951(81)90110-4

Kawana, T., Nakata, T., 1994. Timing of Late Holocene Tsunamis Originated around the Southern Ryukyu Islands, Japan, Deduced from Coralline Tsunami Deposits. J. Geogr. 103, 352–376.

Kelletat, D., Scheffers, A., 2003. Chevron-shaped accumulations along the coastlines of Australia as potential tsunami evidences. Sci. Tsunami Hazards 21, 174–188.

Kim, D.C., Kim, K.O., Choi, B.H., Kim, K.H., Pelinovsky, E., 2013. Three-dimensional runup simulation of the 2004 Indian Ocean tsunami at the Lhok Nga twin peaks. J. Coast. Res. 65, 272–277.

Kimura, J., Yamada, Y., 1996. Evaluation of major and trace element XRF analysis using a flux to sample ratio of two to one glass beads. J. Mineral. Petrol. Econ. Geol. 91, 62–72.

Kitazato, H., 1988. Locomotion of some benthic foraminifera in and on sediments. J. Foraminifer. Res. 18, 344–349.

Kortekaas, S., Dawson, A.G., 2007. Distinguishing tsunami and storm deposits: An example from Martinhal, SW Portugal. Sediment. Geol., Sedimentary Features of Tsunami Deposits - Their Origin, Recognition and Discrimination: An Introduction 200, 208–221. doi:10.1016/j.sedgeo.2007.01.004

Krumbein, W.C., 1938. Size Frequency Distributions of Sediments and the Normal Phi Curve. J. Sediment. Res. 8.

LaMoreaux, P.E., 1995. Worldwide environmental impacts from the eruption of Thera. Environ. Geol. 26, 172–181. doi:10.1007/BF00768739

Latter, J.H., 1981. Tsunamis of volcanic origin: Summary of causes, with particular reference to Krakatoa, 1883. Bull. Volcanol. 44, 467–490. doi:10.1007/BF02600578

Lavigne, F., Degeai, J.-P., Komorowski, J.-C., Guillet, S., Robert, V., Lahitte, P., Oppenheimer, C., Stoffel, M., Vidal, C.M., Surono, Pratomo, I., Wassmer, P., Hajdas, I., Hadmoko, D.S., Belizal, E. de, 2013. Source of the great A.D. 1257 mystery eruption unveiled, Samalas volcano, Rinjani Volcanic Complex, Indonesia. Proc. Natl. Acad. Sci. 110, 16742–16747. doi:10.1073/pnas.1307520110

Lavigne, F., Paris, R., Grancher, D., Wassmer, P., Brunstein, D., Vautier, F., Leone, F., Flohic, F., Coster, B.D., Gunawan, T., Gomez, C., Setiawan, A., Cahyadi, R., Fachrizal, 2009. Reconstruction of Tsunami Inland Propagation on December 26, 2004 in Banda Aceh, Indonesia, through Field Investigations. Pure Appl. Geophys. 166, 259–281. doi:10.1007/s00024-008-0431-8

Le Méhauté, B., Wang, S., 1996. Water waves generated by underwater explosion. World Scientific.

Legros, F., Druitt, T.H., 2000. On the emplacement of ignimbrite in shallow-marine environments. J. Volcanol. Geotherm. Res. 95, 9–22. doi:10.1016/S0377-0273(99)00116-X

Loeblich, A.R., Tappan, H.J.R., 1964. Foraminiferal classification and evolution. J Geol Soc India 5, 5–40.

Lutze, G.F., Coulbourn, W.T., 1984. Recent benthic foraminifera from the continental margin of northwest Africa: Community structure and distribution. Mar. Micropaleontol. 8, 361–401. doi:10.1016/0377-8398(84)90002-1

Maeno, F., Imamura, F., 2011. Tsunami generation by a rapid entrance of pyroclastic flow into the sea during the 1883 Krakatau eruption, Indonesia. J. Geophys. Res. Solid Earth 1978–2012 116.

Major, J.J., 1997. Depositional Processes in Large-Scale Debris-Flow Experiments. J. Geol. 105, 345–366. doi:10.1086/jg.1997.105.issue-3

Malod, J.A., Karta, K., Beslier, M.O., Zen Jr., M.T., 1995. From normal to oblique subduction: Tectonic relationships between Java and Sumatra. J. Southeast Asian Earth Sci. 12, 85–93. doi:10.1016/0743-9547(95)00023-2

Mandeville, C.W., Carey, S., Sigurdsson, H., 1996. Sedimentology of the Krakatau 1883 submarine pyroclastic deposits. Bull. Volcanol. 57, 512–529. doi:10.1007/BF00304436

Masselink, G., Hughes, M., Knight, J., 2014. Introduction to Coastal Processes and Geomorphology, Second Edition. Routledge.

Masselink, G., Puleo, J.A., 2006. Swash-zone morphodynamics. Cont. Shelf Res., Swash-Zone Processes 1st International Workshop on Swash-Zone Processes 26, 661–680. doi:10.1016/j.csr.2006.01.015

Matsui, T., Imamura, F., Tajika, E., Nakano, Y., Fujisawa, Y., 2002. Generation and propagation of a tsunami from the Cretaceous-Tertiary impact event. Spec. Pap.-Geol. Soc. Am. 69–78.

McCoy, F.W., Heiken, G., 2000. Tsunami Generated by the Late Bronze Age Eruption of Thera (Santorini), Greece. Pure Appl. Geophys. 157, 1227–1256. doi:10.1007/s000240050024

McPhie, J., Doyle, M., Allen, R., Allen, R.L., 1993. Volcanic textures: a guide to the interpretation of textures in volcanic rocks. CODES-University of Tasmania.

Mei, C.C., Agnon, Y., 1989. Long-period oscillations in a harbour induced by incident short waves. J. Fluid Mech. 208, 595–608. doi:10.1017/S0022112089002958

Miller, D.J., 1960. The Alaska earthquake of July 10, 1958: Giant wave in Lituya Bay. Bull. Seismol. Soc. Am. 50, 253–266.

Minoura, K., Imamura, F., Kuran, U., Nakamura, T., Papadopoulos, G.A., Takahashi, T., Yalciner, A.C., 2000. Discovery of Minoan tsunami deposits. Geology 28, 59–62. doi:10.1130/0091-7613(2000)028<0059:DOMTD>2.0.CO;2

Minoura, K., Nakaya, S., Uchida, M., 1994. Tsunami deposits in a lacustrine sequence of the Sanriku coast, northeast Japan. Sediment. Geol. 89, 25–31. doi:10.1016/0037-0738(94)90081-7

Minoura, K., Nakaya, S., 1991. Traces of Tsunami Preserved in Inter-Tidal Lacustrine and Marsh Deposits: Some Examples from Northeast Japan. J. Geol. 99, 265–287.

Mori, N., Cox, D.T., Yasuda, T., Mase, H., 2013. Overview of the 2011 Tohoku Earthquake Tsunami Damage and Its Relation to Coastal Protection along the Sanriku Coast. Earthq. Spectra 29, S127–S143. doi:10.1193/1.4000118

Mori, N., Takahashi, T., Yasuda, T., Yanagisawa, H., 2011. Survey of 2011 Tohoku earthquake tsunami inundation and run-up. Geophys. Res. Lett. 38, L00G14. doi:10.1029/2011GL049210

Morton, R.A., Gelfenbaum, G., Jaffe, B.E., 2007. Physical criteria for distinguishing sandy tsunami and storm deposits using modern examples. Sediment. Geol., Sedimentary Features of Tsunami Deposits - Their Origin, Recognition and Discrimination: An Introduction 200, 184–207. doi:10.1016/j.sedgeo.2007.01.003

Myles, D., 1985. Great waves: Tsunami. McGraw-Hill Book Company.

Nanayama, F., Shigeno, K., 2006. Inflow and outflow facies from the 1993 tsunami in southwest Hokkaido. Sediment. Geol. 187, 139–158. doi:10.1016/j.sedgeo.2005.12. 024

Nandasena, N.A.K., Paris, R., Tanaka, N., 2011. Numerical assessment of boulder transport by the 2004 Indian ocean tsunami in Lhok Nga, West Banda Aceh (Sumatra, Indonesia). Comput. Geosci. 37, 1391–1399. doi:10.1016/j.cageo.2011.02.001

Nechaev, V.P., Isphording, W.C., 1993. Heavy-mineral assemblages of continental margins as indicators of plate-tectonic environments. J. Sediment. Res. 63, 1110–1117. doi:10.1306/D4267CB7-2B26-11D7-8648000102C1865D

Nishimura, Y., Nakagawa, M., Kuduon, J., Wukawa, J., 2005. Timing and Scale of Tsunamis Caused by the 1994 Rabaul Eruption, East New Britain, Papua New Guinea, in: Satake, K. (Ed.), Tsunamis, Advances in Natural and Technological Hazards Research. Springer Netherlands, pp. 43–56.

Nishimura, Y., Miyaji, N., 1995. Tsunami deposits from the 1993 Southwest Hokkaido earthquake and the 1640 Hokkaido Komagatake eruption, northern Japan. Pure Appl. Geophys. 144, 719–733. doi:10.1007/BF00874391

NOAA Center for Tsunami Research, 2014. Recent and Historical Tsunami Events and Relevant Data [WWW Document]. URL http://nctr.pmel.noaa.gov/database_devel. html (accessed 5.15.14).

Nomanbhoy, N., Satake, K., 1995. Generation mechanism of tsunamis from the 1883 Krakatau Eruption. Geophys. Res. Lett. 22, 509–512. doi:10.1029/94GL03219

Nott, J., 1997. Extremely high-energy wave deposits inside the Great Barrier Reef, Australia: determining the cause—tsunami or tropical cyclone. Mar. Geol. 141, 193–207. doi:10.1016/S0025-3227(97)00063-7

Nott, J., Bryant, E., 2003. Extreme Marine Inundations (Tsunamis?) of Coastal Western Australia. J. Geol. 111, 691–706. doi:10.1086/jg.2003.111.issue-6

Okal, E.A., 1988. Seismic parameters controlling far-field tsunami amplitudes: A review. Nat. Hazards 1, 67–96. doi:10.1007/BF00168222

Okayasu, A., Shimozono, T., Sato, S., Tajima, Y., Liu, H., Takagawa, T., Fritz, H.M., 2011. 2011 Tohoku Tsunami Runup Distribution and Damages around Yamada Bay, Iwate. AGU Fall Meet. Abstr. -1, 02.

Okeyode, I.C., Jibiri, N.N., 2012. Grain Size Analysis of the Sediments from Ogun River, South Western Nigeria. Earth Sci. Res. 2. doi:10.5539/esr.v2n1p43

Ongkosongo, O.S.R., 1985. Coastal geomorphology of Cilegon-Labuan, West Java, in: Proceedings of the Symposium on 100 Years Development of Krakatau and Its Surroundings, Jakarta, 23-27 August 1983. Indonesian Institute of Sciences, p. 147.

Oppenheimer, C., 2003. Climatic, environmental and human consequences of the largest known historic eruption: Tambora volcano (Indonesia) 1815. Prog. Phys. Geogr. 27, 230–259. doi:10.1191/0309133303pp379ra

Pararas-Carayannis, G., 1999. Analysis of mechanism of the giant tsunami generation in Lituya Bay on July 9, 1958, in: Tsunami Symposium, Honolulu, Hawaii, 11p.

Pareschi, M.T., Favalli, M., Boschi, E., 2006. Impact of the Minoan tsunami of Santorini: Simulated scenarios in the eastern Mediterranean. Geophys. Res. Lett. 33, L18607. doi:10.1029/2006GL027205

Paris, R., Switzer, A.D., Belousova, M., Belousov, A., Ontowirjo, B., Whelley, P.L., Ulvrova, M., 2014a. Volcanic tsunami: a review of source mechanisms, past events and hazards in Southeast Asia (Indonesia, Philippines, Papua New Guinea). Nat. Hazards 70, 447–470. doi:10.1007/s11069-013-0822-8

Paris, R., Wassmer, P., Lavigne, F., Belousov, A., Belousova, M., Iskandarsyah, Y., Benbakkar, M., Ontowirjo, B., Mazzoni, N., 2014b. Coupling eruption and tsunami records: the Krakatau 1883 case study, Indonesia. Bull. Volcanol. 76, 1–23. doi:10.1007/s00445-014-0814-x

Paris, R., Fournier, J., Poizot, E., Etienne, S., Morin, J., Lavigne, F., Wassmer, P., 2010. Boulder and fine sediment transport and deposition by the 2004 tsunami in Lhok Nga (western Banda Aceh, Sumatra, Indonesia): A coupled offshore–onshore model. Mar. Geol. 268, 43–54. doi:10.1016/j.margeo.2009.10.011

Passega, R., 1957. Texture as Characteristic of Clastic Deposition. AAPG Bull. 41, 1952–1984.

Patterson, R.T., 1990. Intertidal benthic foraminiferal biofacies on the Fraser River delta, British Columbia; modern distribution and paleoecological importance. Micropaleontology 36, 229–244.

Pelinovsky, E., 2006. Hydrodynamics of Tsunami Waves, in: Grue, J., Trulsen, K. (Eds.), Waves in Geophysical Fluids, CISM International Centre for Mechanical Sciences. Springer Vienna, pp. 1–48.

Peters, R., Jaffe, B., 2010. Identification of tsunami deposits in the geologic record; developing criteria using recent tsunami deposits. U. S. Geological Survey.Phleger, F.B., 1951. Displaced Foraminifera Faunas.

Phleger, F.B., 1951. Displaced Foraminifera Faunas.

Pramumijoyo, S., Sebrier, M., 1991. Neogene and quaternary fault kinematics around the Sunda Strait area, Indonesia. J. Southeast Asian Earth Sci. 6, 137–145. doi:10.1016/0743-9547(91)90106-8

Rai, A.K., Singh, V.B., 2012. Response of eastern Indian Ocean (ODP Site 762B) benthic foraminiferal assemblages to the closure of the Indonesian seaway. Oceanologia 54.

Rampino, M.R., Self, S., 1982. Historic eruptions of Tambora (1815), Krakatau (1883), and Agung (1963), their stratospheric aerosols, and climatic impact. Quat. Res. 18, 127–143. doi:10.1016/0033-5894(82)90065-5

Renard, A., 1883. Les cendre volcanique de l'eruption du Krakatau: Tombee a Batavia, le 27 aout 1883. Bull. Acad. R. Belg. Brux., III VI/11.

Richmond, B., Szczuciński, W., Chagué-Goff, C., Goto, K., Sugawara, D., Witter, R., Tappin, D.R., Jaffe, B., Fujino, S., Nishimura, Y., Goff, J., 2012. Erosion, deposition and landscape change on the Sendai coastal plain, Japan, resulting from the March 11, 2011 Tohoku-oki tsunami. Sediment. Geol., The 2011 Tohoku-oki tsunami 282, 27–39. doi:10.1016/j.sedgeo.2012.08.005

Rositasari, R., 2001. Karakteristik foraminifera di Paparan Selat Sunda. LIPI Pustaka IPTEK Nas.

Satake, K., 1995. Linear and Nonlinear Computations of the 1992 Nicaragua Earthquake Tsunami, in: Imamura, D.F., Satake, D.K. (Eds.), Tsunamis: 1992–1994, Pageoph Topical Volumes. Birkhäuser Basel, pp. 455–470.

Scheffers, A., Kelletat, D., 2004. Bimodal tsunami deposits–a neglected feature in paleo-tsunami research. Coastline Rep. 1, 67–75.

Scheffers, A., Kelletat, D., 2003. Sedimentologic and geomorphologic tsunami imprints worldwide—a review. Earth-Sci. Rev. 63, 83–92.

Self, S., Rampino, M.R., 1981. The 1883 eruption of Krakatau. Nature 294, 699–704. doi:10.1038/294699a0

Shanmugam, G., 2012. Process-sedimentological challenges in distinguishing paleo-tsunami deposits. Nat. Hazards 63, 5–30. doi:10.1007/s11069-011-9766-z

Shi, S., Dawson, A.G., Smith, D.E., 1995. Coastal Sedimentation Associated with the December 12th, 1992 Tsunami in Flores, Indonesia, in: Imamura, D.F., Satake, D.K. (Eds.), Tsunamis: 1992–1994, Pageoph Topical Volumes. Birkhäuser Basel, pp. 525–536.

Shiki, T., Tsuji, Y., Minoura, K., Yamazaki, T., 2011. Tsunamiites - Features and Implications. Elsevier.

Sigurdsson, H., Carey, S., Mandeville, C., Bronto, S., 1991. Pyroclastic flows of the 1883 Krakatau eruption. Eos Trans. Am. Geophys. Union 72, 377–381. doi:10.1029/90EO00286

Simkin, T., Fiske, R.S., 1983. Krakatau, 1883--the volcanic eruption and its effects. Smithsonian Inst Pr.

Smit, J., Th. B. Roep, W. Alvarez, A. Montanari, P. Claeys, J. M. Grajales-Nishimura, J. Bermudez, 1996. Coarse-grained, clastic sandstone complex at the K/T boundary around the Gulf of Mexico: Deposition by tsunami waves induced by the Chicxulub impact? Cretac.-Tert. Event Catastr. Earth Hist. 307, 151.

Stadler, F., 2004. Induction and Deduction in the Sciences. Springer.

Stehn, C.E., van Leeuwen, W.M., Dammermann, K.W., 1929. Krakatau.

Stothers, R.B., 1984. The Great Tambora Eruption in 1815 and Its Aftermath. Science 224, 1191–1198. doi:10.1126/science.224.4654.1191

Sudana, D., Santosa, S., 1992. Geological map of the Cikarang, Jawa.

Susilohadi, S., Gaedicke, C., Djajadihardja, Y., 2009. Structures and sedimentary deposition in the Sunda Strait, Indonesia. Tectonophysics 467, 55–71. doi:10.1016/j.tecto.2008. 12.015

Sutawidjaja, I.S., 1997. The activities of Anak Krakatau Volcano during the years of 1992 - 1996. Kyoto Daigaku Bōsai Kenkyūjo Nenpō 13–22.

Switzer, A.D., Pucillo, K., Haredy, R.A., Jones, B.G., Bryant, E.A., 2005. Sea Level, Storm, or Tsunami: Enigmatic Sand Sheet Deposits in a Sheltered Coastal Embayment from Southeastern New South Wales, Australia. J. Coast. Res. 655–663. doi:10.2112/04-0177.1

Symons, G.J., Symons, G.J., Judd, J.W., Strachey, S.R., Wharton, W.J.L., Evans, F.J., Russell, F.A.R., Archibald, D., Whipple, G.M., 1888. The eruption of krakatoa: And subsequent phenomena. Trübner & Company.

Tadepalli, S., Synolakis, C.E., 1994. The Run-Up of N-Waves on Sloping Beaches. Proc. R. Soc. Lond. Ser. Math. Phys. Sci. 445, 99–112. doi:10.1098/rspa.1994.0050

Tarling, D., Hrouda, F., 1993. Magnetic Anisotropy of Rocks. Springer.

Thurman, H.V., Trujillo, A.P., Abel, D.C., McConnell, R., 1999. Essentials of oceanography. Prentice Hall.

Trochim, W.M.K., 2006. Deduction and Induction. http://www.socialresearchmethods.net/kb/dedind.php.

Umbgrove, J.H.F., 1947. Coral Reefs of the East Indies. Geol. Soc. Am. Bull. 58, 729–778. doi:10.1130/0016-7606(1947)58[729:CROTEI]2.0.CO;2

Van den Bergh, G.D., Boer, W., de Haas, H., van Weering, T.C.E., van Wijhe, R., 2003. Shallow marine tsunami deposits in Teluk Banten (NW Java, Indonesia), generated by the 1883 Krakatau eruption. Mar. Geol. 197, 13–34. doi:10.1016/S0025-3227(03)00088-4

Van den Bergh, G.D., van Weering, T.C.E., de Haas, H., 2002. 1883 Krakatau Tsunami Deposits In Teluk Banten (nw Java, Indonesia), in: EGS General Assembly Conference Abstracts. Presented at the EGS General Assembly Conference Abstracts, p. 4233.

Van der Kaars, S., van den Bergh, G.D., 2004. Anthropogenic changes in the landscape of west Java (Indonesia) during historic times, inferred from a sediment and pollen record from Teluk Banten. J. Quat. Sci. 19, 229–239. doi:10.1002/jqs.804

Verbeek, R.D.M., 1885. Krakatau, 495 pp. Gov Press Batavia Indonesia.

Verbeek, R.D.M., 1884. The Krakatoa Eruption. Nature 30, 10–15. doi:10.1038/030010a0

Verstappen, H. Th., 1956. Landscape development of the Udjung Kulon Game Reserve. Penggemar Alam 36, 37–51.

Ward, S.N., 2008. Tsunami Balls A Granular Approach to Tsunami Runup. Commun. Comput. Phys., 1 3, 222–249.

Wassmer, P.C., Gomez, C.A., Iskandasyah, T., Lavigne, F., Sartohadi, J., 2015. Contribution of Anisotropy of Magnetic Susceptibility (AMS) to reconstruct flooding characteristics of a 4220 BP tsunami from a thick unconsolidated structureless deposit (Banda Aceh, Sumatra). Front. Earth Sci. 3, 40.

Wassmer, P., Gomez, C., 2011. Development of the AMS method for unconsolidated sediments. Application to tsunami deposits. Géomorphologie n° 3, 279–290. doi:10.4000/geomorphologie.9491

Wassmer, P., Schneider, J.-L., Fonfrège, A.-V., Lavigne, F., Paris, R., Gomez, C., 2010. Use of anisotropy of magnetic susceptibility (AMS) in the study of tsunami deposits: Application to the 2004 deposits on the eastern coast of Banda Aceh, North Sumatra, Indonesia. Mar. Geol. 275, 255–272. doi:10.1016/j.margeo.2010.06.007

Wassmer, P., Baumert, P., Lavigne, F., Paris, R., Sartohadi, J., 2007. Sedimentary facies and transfer associated with the December 26, 2004 tsunami on the north eastern littoral of Banda Aceh (Sumatra, Indonesia). Geomorphol.-RELIEF Process. Environ. 335–346.

Waythomas, C.F., Neal, C.A., 1998. Tsunami generation by pyroclastic flow during the 3500-year B.P. caldera-forming eruption of Aniakchak Volcano, Alaska. Bull. Volcanol. 60, 110–124. doi:10.1007/s004450050220

Wentworth, C.K., 1922. A Scale of Grade and Class Terms for Clastic Sediments. J. Geol. 30, 377–392. doi:10.2307/30063207

Whittaker, R.J., Jones, S.H., Partomihardjo, T., 1997. The rebuilding of an isolated rain forestassemblage: how disharmonicis the flora of Krakatau? Biodivers. Conserv. 6, 1671–1696. doi:10.1023/A:1018335007666

Wilson, R., Davenport, C., Jaffe, B., 2012. Sediment scour and deposition within harbors in California (USA), caused by the March 11, 2011 Tohoku-oki tsunami. Sediment. Geol., The 2011 Tohoku-oki tsunami 282, 228–240. doi:10.1016/j.sedgeo.2012.06. 001

Wolfe, E.W., Hoblitt, R.P., 1996. Overview of the eruptions. Fire Mud Erupt. Lahars Mt. Pinatubo Philipp. 3–20.

Wu, T.Y., 1981. Long Waves in Ocean and Coastal Waters. J. Eng. Mech. 107, 501–522.

Wynn, R.B., Masson, D.G., 2003. Canary Islands Landslides and Tsunami Generation: Can We Use Turbidite Deposits to Interpret Landslide Processes?, in: Locat, J., Mienert, J., Boisvert, L. (Eds.), Submarine Mass Movements and Their Consequences, Advances in Natural and Technological Hazards Research. Springer Netherlands, pp. 325–332.

Yamanaka, Y., Tajima, Y., Sato, S., Liu, H., 2013. Dynamic Behaviors of the 2011 Tohoku Tsunami in Ryori Bay. Major Disaster Resil. Soc. 14.

Yeh*, H., Liu†, P., Briggs‡, M., Synolakis§, C., 1994. Propagation and amplification of tsunamis at coastal boundaries. Nature 372, 353–355. doi:10.1038/372353a0

Yokoyama, I., 1987. A scenario of the 1883 Krakatau tsunami. J. Volcanol. Geotherm. Res. 34, 123–132. doi:10.1016/0377-0273(87)90097-7

Young, R.W., Bryant, E.A., 1992. Catastrophic wave erosion on the southeastern coast of Australia: Impact of the Lanai tsunamis ca. 105 ka? Geology 20, 199–202. doi:10.1130/0091-7613(1992)020<0199:CWEOTS>2.3.CO;2

APPENDICES

1. GRAIN-SIZE ANALYSIS

Analyse granulométrique par voie fluide : fraction 0,040 µm - 2000 µm

Echantillon :	INDONESIE/11/PANTAI/U-01/0-35/T.Yan W. ISKANDARSYAH
Date :	19/01/2012 14:58
Opérateur :	MT
Fichier :	U01-001

Commentaires :	prof. : 0-35 cm Destruction MO à H2O2 -élimination des ions floculants - hexa + US

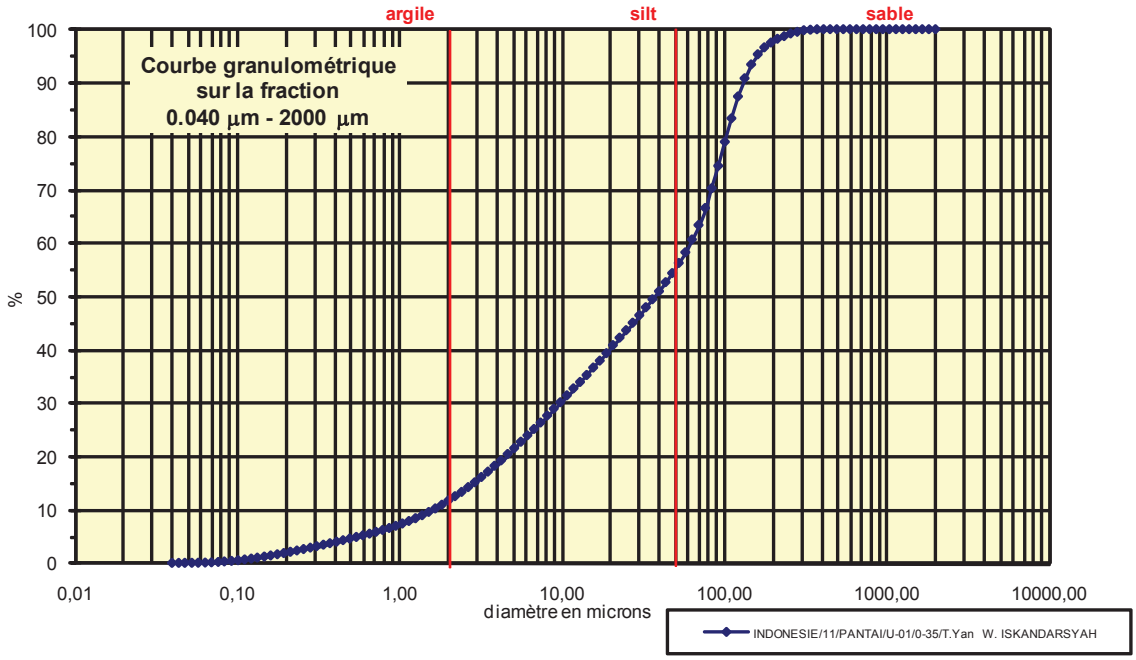

Fractiles	Taille (µm)	Taille (ϕ)
d_5	0,545	10,84
d_{10}	1,520	9,36
d_{16}	2,920	8,42
d_{25}	6,158	7,34
d_{30}	8,944	6,80
d_{50}	36,240	4,79
d_{60}	57,770	4,11
d_{75}	92,090	3,44
d_{84}	111,000	3,17
d_{90}	121,800	3,04
d_{95}	146,800	2,77

% Argile inférieur à 2µ	**A**	**10,90**
% Silts de 2µ à 50µ	**LT**	**43,40**
limons fins 2µ à 20µ	LF	28,40
limons grossiers 20µ à 50µ	LG	15,00
% Sables 50µ à 2000 µ	**ST**	**45,70**
sables fins 50µ à 200µ	SF	43,20
sables fins 50µ à 100µ	SF1	20,10
sables fins 100µ à 200 µ	SF2	23,10
sables grossiers 200µ à 2000µ	SG	2,50
sables grossiers 200µ à 500µ	SG1	2,50
sables grossiers 500µ à 1000µ	SG2	0,00
sables grossiers 1000µ à 2000µ	SG3	0,00

Indice de classement	
Trask, S_o	3,867
Krumbein, Q_d	-1,951
Inman, σ_ϕ	-2,624
Folk & Ward, σ_ϕ	-2,535
Hazen, C_u	38,007

Moyenne	
Trask, M	49,124
Inman, M_ϕ	5,796
Folk & Ward, M_z	5,459

Coefficient de dissymétrie	
Skew ness, S_{k-1}	0,432
Skew ness, S_{k-2}	0,657
Inman, $\alpha_{\phi-1}$	-0,385
Inman, $\alpha_{\phi-2}$	-0,769
Folk & Ward, Sk_I	-0,442

Coefficient d'acuité (Kurtosis)	
Krumbein & Petijohn, K	0,357
Inman, K_ϕ	0,538
Folk & Ward, K_G	0,848

Coefficient de courbure	
C_c	0,911

Analyse granulométrique par voie fluide : fraction 0,040 µm - 2000 µm

Echantillon :	INDONESIE/11/PANTAI/U-01/35-50/T.Yan W. ISKANDARSYAH
Date :	19/01/2012 15:26
Opérateur :	MT
Fichier :	U01-002

Commentaires :	prof. : 35-50 cm Destruction MO à H2O2 -élimination des ions floculants - hexa + US

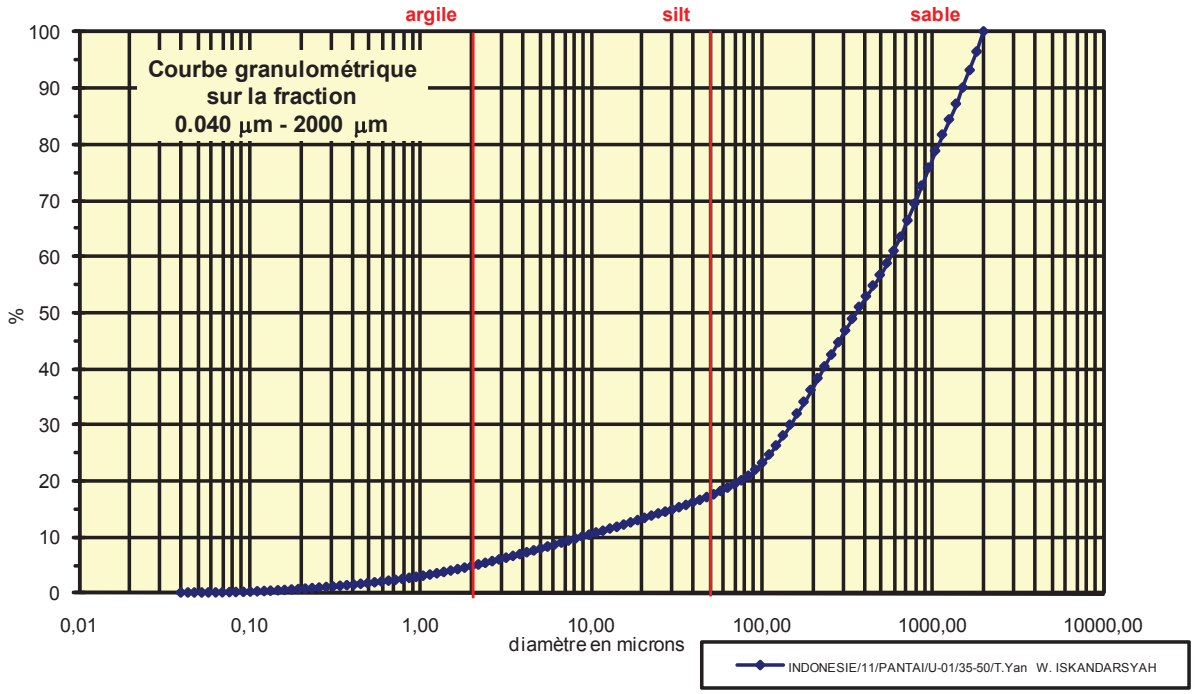

Fractiles	Taille (µm)	Taille (ϕ)
d_5	2,207	8,82
d_{10}	8,944	6,80
d_{16}	36,240	4,79
d_{25}	111,000	3,17
d_{30}	146,800	2,77
d_{50}	339,800	1,56
d_{60}	541,900	0,88
d_{75}	863,900	0,21
d_{84}	1143,000	-0,19
d_{90}	1512,000	-0,60
d_{95}	1660,000	-0,73

% Argile inférieur à 2µ	**A**	**4,43**
% Silts de 2µ à 50µ	**LT**	**12,57**
limons fins 2µ à 20µ	LF	8,47
limons grossiers 20µ à 50µ	LG	4,10
% Sables 50µ à 2000 µ	**ST**	**83,00**
sables fins 50µ à 200µ	SF	19,10
sables fins 50µ à 100µ	SF1	4,90
sables fins 100µ à 200 µ	SF2	14,20
sables grossiers 200µ à 2000µ	SG	63,90
sables grossiers 200µ à 500µ	SG1	20,50
sables grossiers 500µ à 1000µ	SG2	19,10
sables grossiers 1000µ à 2000µ	SG3	24,30

Indice de classement	
Trask, S_o	2,790
Krumbein, Q_d	-1,480
Inman, σ_ϕ	-2,490
Folk & Ward, σ_ϕ	-2,692
Hazen, C_u	60,588

Moyenne	
Trask, M	487,450
Inman, M_ϕ	2,297
Folk & Ward, M_z	2,050

Coefficient de dissymétrie	
Skew ness, S_{k-1}	0,831
Skew ness, S_{k-2}	0,911
Inman, $\alpha_{\phi-1}$	-0,297
Inman, $\alpha_{\phi-2}$	-1,000
Folk & Ward, Sk_i	-0,409

Coefficient d'acuité (Kurtosis)	
Krumbein & Petijohn, K	0,250
Inman, K_ϕ	0,919
Folk & Ward, K_G	1,323

Coefficient de courbure	
C_c	4,446

Analyse granulométrique par voie fluide : fraction 0,040 µm - 2000 µm

Echantillon :	INDONESIE/11/PANTAI/U-01/50-70/T.Yan W. ISKANDARSYAH
Date :	19/01/2012 15:39
Opérateur :	MT
Fichier :	U01-003

Commentaires :	prof. : 50-70 cm Destruction MO à H2O2 -élimination des ions floculants - hexa + US

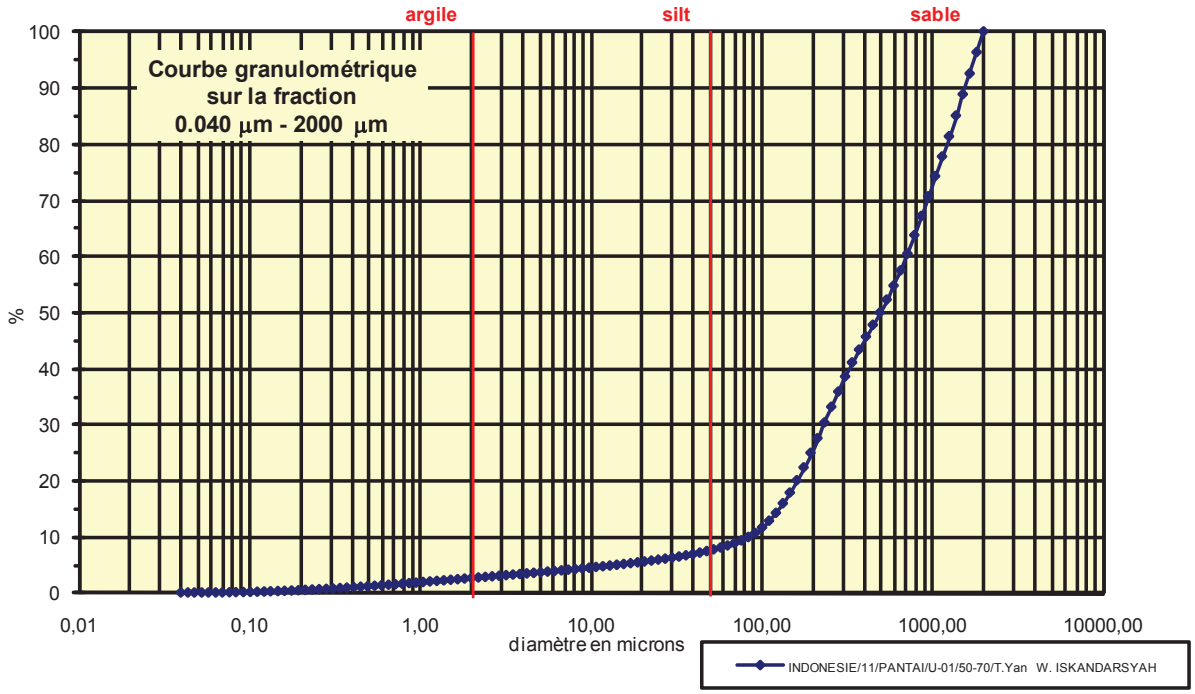

Fractiles	Taille (µm)	Taille (ϕ)
d_5	14,260	6,13
d_{10}	83,900	3,58
d_{16}	133,700	2,90
d_{25}	194,200	2,36
d_{30}	213,200	2,23
d_{50}	493,600	1,02
d_{60}	653,000	0,61
d_{75}	1041,000	-0,06
d_{84}	1255,000	-0,33
d_{90}	1512,000	-0,60
d_{95}	1660,000	-0,73

% Argile inférieur à 2µ	**A**	**2,48**
% Silts de 2µ à 50µ	**LT**	**4,90**
limons fins 2µ à 20µ	LF	2,89
limons grossiers 20µ à 50µ	LG	2,01
% Sables 50µ à 2000 µ	**ST**	**92,62**
sables fins 50µ à 200µ	SF	17,52
sables fins 50µ à 100µ	SF1	3,22
sables fins 100µ à 200 µ	SF2	14,30
sables grossiers 200µ à 2000µ	SG	75,10
sables grossiers 200µ à 500µ	SG1	25,00
sables grossiers 500µ à 1000µ	SG2	20,70
sables grossiers 1000µ à 2000µ	SG3	29,40

Indice de classement	
Trask, S_o	2,315
Krumbein, Q_d	-1,211
Inman, σ_ϕ	-1,615
Folk & Ward, σ_ϕ	-1,848
Hazen, C_u	7,783

Moyenne	
Trask, M	617,600
Inman, M_ϕ	1,288
Folk & Ward, M_z	1,198

Coefficient de dissymétrie	
Skew ness, S_{k1}	0,830
Skew ness, S_{k2}	0,911
Inman, $\alpha_{\phi-1}$	-0,167
Inman, $\alpha_{\phi-2}$	-1,041
Folk & Ward, Sk_i	-0,328

Coefficient d'acuité (Kurtosis)	
Krumbein & Petijohn, K	0,296
Inman, K_ϕ	1,124
Folk & Ward, K_G	1,161

Coefficient de courbure	
C_c	0,830

Analyse granulométrique par voie fluide : fraction 0,040 µm - 2000 µm

Echantillon :	INDONESIE/11/PANTAI/U-01/70-105/T.Yan W. ISKANDARSYAH
Date :	25/01/2012 15:39
Opérateur :	MT
Fichier :	U01-004

Commentaires :	prof. : 70-105 cm Destruction MO à H2O2 -élimination des ions floculants - hexa + US

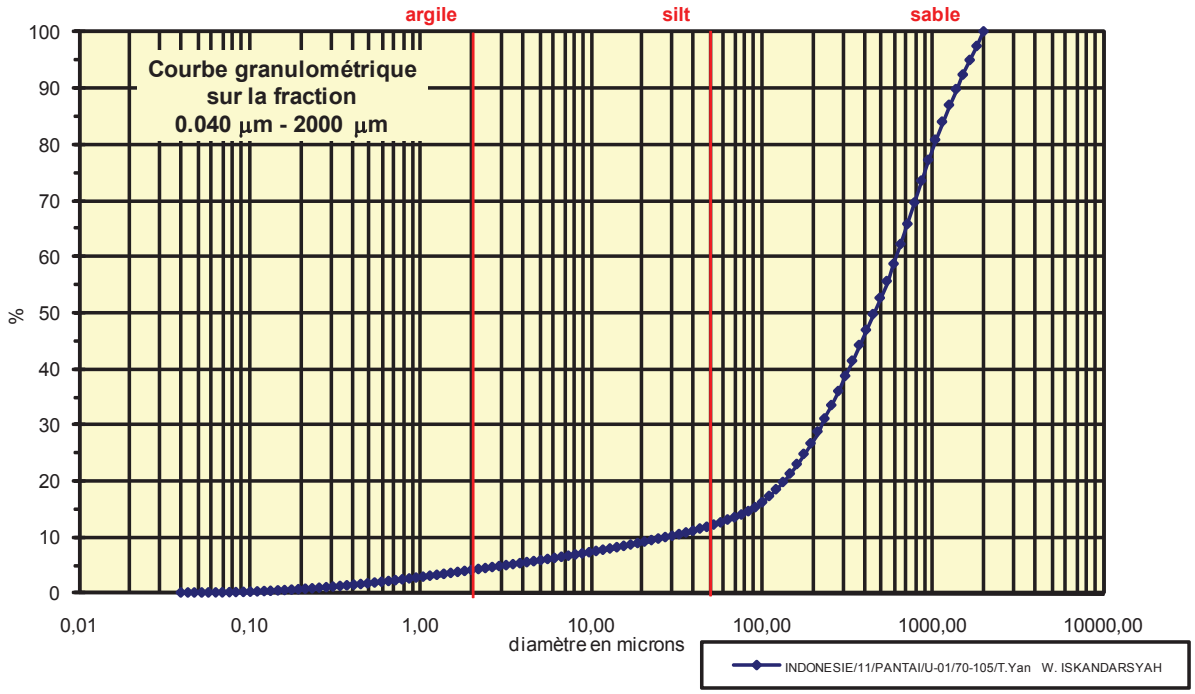

Fractiles	Taille (µm)	Taille (ϕ)
d_5	3,206	8,29
d_{10}	27,380	5,19
d_{16}	92,090	3,44
d_{25}	176,800	2,50
d_{30}	213,200	2,23
d_{50}	449,700	1,15
d_{60}	594,900	0,75
d_{75}	863,900	0,21
d_{84}	1143,000	-0,19
d_{90}	1377,000	-0,46
d_{95}	1660,000	-0,73

% Argile inférieur à 2µ	**A**	**3,84**
% Silts de 2µ à 50µ	**LT**	**7,86**
limons fins 2µ à 20µ	LF	4,97
limons grossiers 20µ à 50µ	LG	2,89
% Sables 50µ à 2000 µ	**ST**	**88,30**
sables fins 50µ à 200µ	SF	14,90
sables fins 50µ à 100µ	SF1	3,50
sables fins 100µ à 200 µ	SF2	11,40
sables grossiers 200µ à 2000µ	SG	73,40
sables grossiers 200µ à 500µ	SG1	25,90
sables grossiers 500µ à 1000µ	SG2	24,60
sables grossiers 1000µ à 2000µ	SG3	22,90

Indice de classement	
Trask, S_o	2,211
Krumbein, Q_d	-1,144
Inman, σ_ϕ	-1,817
Folk & Ward, σ_ϕ	-2,274
Hazen, C_u	21,728

Moyenne	
Trask, M	520,350
Inman, M_ϕ	1,624
Folk & Ward, M_z	1,467

Coefficient de dissymétrie	
Skew ness, S_{k1}	0,755
Skew ness, S_{k2}	0,869
Inman, $\alpha_{\phi-1}$	-0,259
Inman, $\alpha_{\phi-2}$	-1,444
Folk & Ward, Sk_I	-0,421

Coefficient d'acuité (Kurtosis)	
Krumbein & Petijohn, K	0,255
Inman, K_ϕ	1,481
Folk & Ward, K_G	1,614

Coefficient de courbure	
C_c	2,791

Analyse granulométrique par voie fluide : fraction 0,040 µm - 2000 µm

Echantillon :	INDONESIE/11/PANTAI/U-01/105-115/T.Yan W. ISKANDARSYAH
Date :	25/01/2012 15:44
Opérateur :	MT
Fichier :	U01-005

Commentaires :	prof. : 105-115 cm Destruction MO à H2O2 -élimination des ions floculants - hexa + US

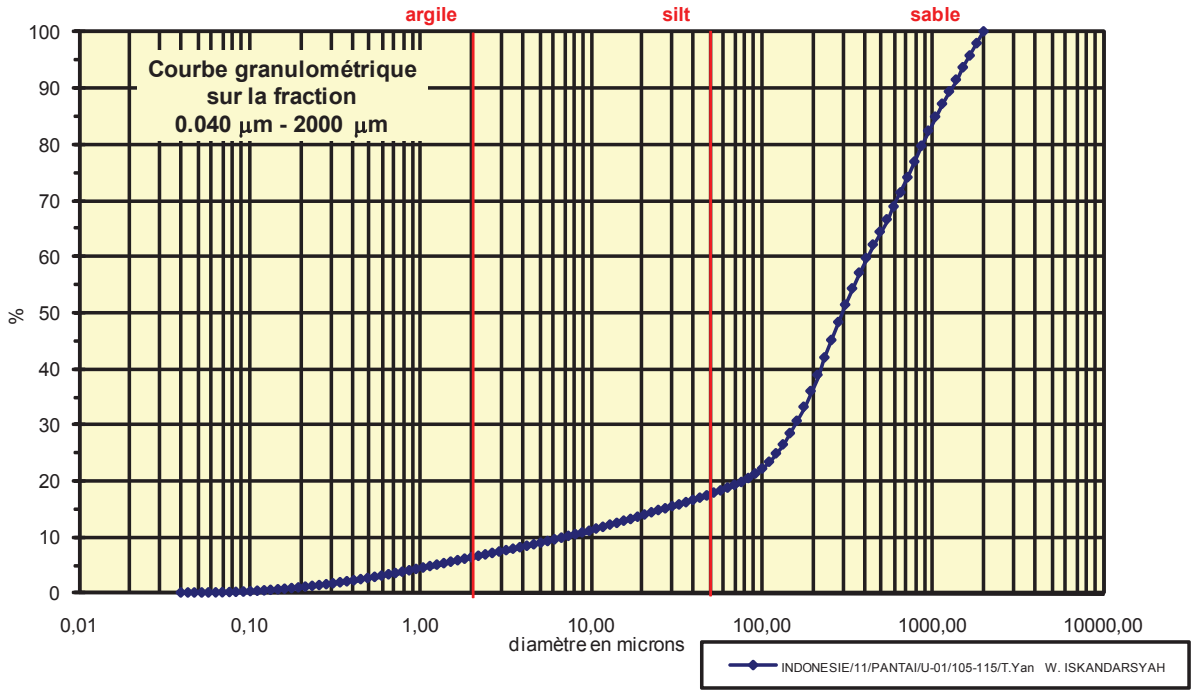

Fractiles	Taille (µm)	Taille (ϕ)
d_5	1,261	9,63
d_{10}	6,761	7,21
d_{16}	33,000	4,92
d_{25}	121,800	3,04
d_{30}	146,800	2,77
d_{50}	282,100	1,83
d_{60}	409,600	1,29
d_{75}	716,900	0,48
d_{84}	948,200	0,08
d_{90}	1255,000	-0,33
d_{95}	1512,000	-0,60

% Argile inférieur à 2µ	**A**	**6,02**
% Silts de 2µ à 50µ	**LT**	**11,28**
limons fins 2µ à 20µ	LF	7,48
limons grossiers 20µ à 50µ	LG	3,80
% Sables 50µ à 2000 µ	**ST**	**82,70**
sables fins 50µ à 200µ	SF	18,60
sables fins 50µ à 100µ	SF1	3,90
sables fins 100µ à 200 µ	SF2	14,70
sables grossiers 200µ à 2000µ	SG	64,10
sables grossiers 200µ à 500µ	SG1	28,40
sables grossiers 500µ à 1000µ	SG2	18,00
sables grossiers 1000µ à 2000µ	SG3	17,70

Indice de classement	
Trask, S_o	2,426
Krumbein, Q_d	-1,279
Inman, σ_ϕ	-2,422
Folk & Ward, σ_ϕ	-2,761
Hazen, C_u	60,583

Moyenne	
Trask, M	419,350
Inman, M_ϕ	2,499
Folk & Ward, M_z	2,275

Coefficient de dissymétrie	
Skew ness, S_{k1}	1,097
Skew ness, S_{k2}	1,047
Inman, $\alpha_{\phi-1}$	-0,278
Inman, $\alpha_{\phi-2}$	-1,111
Folk & Ward, Sk_I	-0,402

Coefficient d'acuité (Kurtosis)	
Krumbein & Petijohn, K	0,238
Inman, K_ϕ	1,111
Folk & Ward, K_G	1,639

Coefficient de courbure	
C_c	7,782

Analyse granulométrique par voie fluide : fraction 0,040 µm - 2000 µm

Echantillon :	INDONESIE/11/PANTAI/U-01/117-122/T.Yan W. ISKANDARSYAH
Date :	25/01/2012 15:43
Opérateur :	MT
Fichier :	U01-006

Commentaires :	prof. : 117-122 cm Destruction MO à H2O2 -élimination des ions floculants - hexa + US

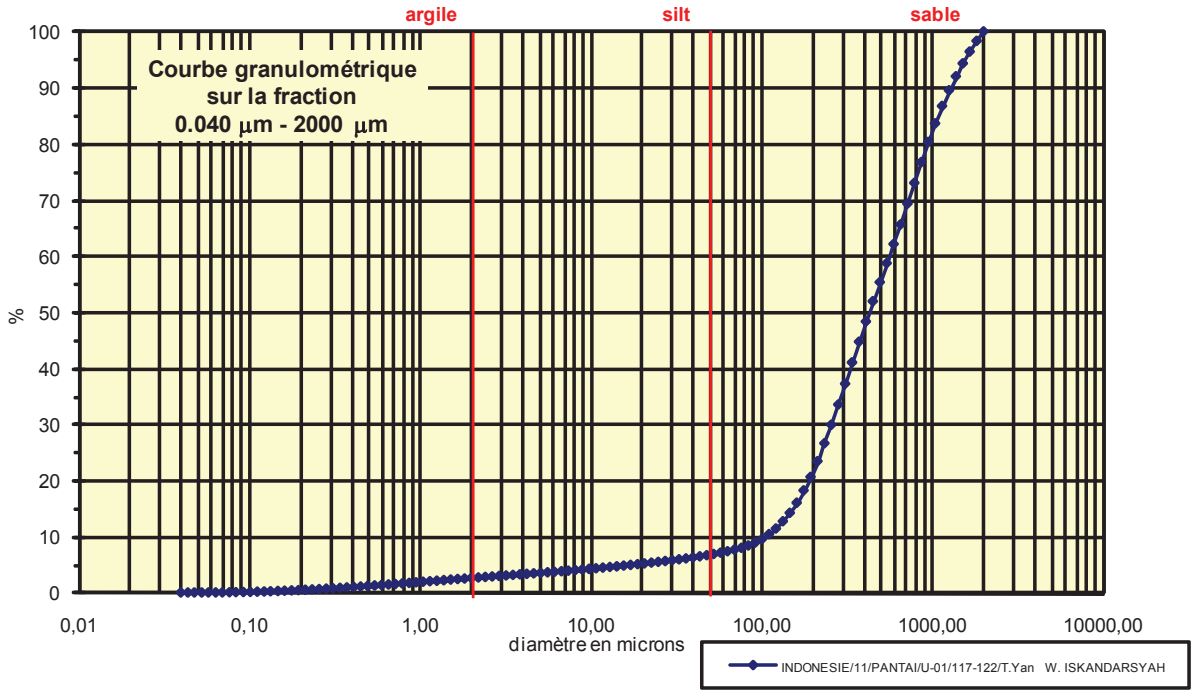

Fractiles	Taille (µm)	Taille (ϕ)
d_5	17,180	5,86
d_{10}	101,100	3,31
d_{16}	161,200	2,63
d_{25}	213,200	2,23
d_{30}	256,800	1,96
d_{50}	409,600	1,29
d_{60}	541,900	0,88
d_{75}	786,900	0,35
d_{84}	1041,000	-0,06
d_{90}	1255,000	-0,33
d_{95}	1512,000	-0,60

% Argile inférieur à 2µ	**A**	**2,49**
% Silts de 2µ à 50µ	**LT**	**4,15**
limons fins 2µ à 20µ	LF	2,56
limons grossiers 20µ à 50µ	LG	1,59
% Sables 50µ à 2000 µ	**ST**	**93,36**
sables fins 50µ à 200µ	SF	13,96
sables fins 50µ à 100µ	SF1	2,25
sables fins 100µ à 200 µ	SF2	11,71
sables grossiers 200µ à 2000µ	SG	79,40
sables grossiers 200µ à 500µ	SG1	34,70
sables grossiers 500µ à 1000µ	SG2	25,00
sables grossiers 1000µ à 2000µ	SG3	19,70

Indice de classement	
Trask, S_o	1,921
Krumbein, Q_d	-0,942
Inman, σ_ϕ	-1,346
Folk & Ward, σ_ϕ	-1,651
Hazen, C_u	5,360

Moyenne	
Trask, M	500,050
Inman, M_ϕ	1,288
Folk & Ward, M_z	1,288

Coefficient de dissymétrie	
Skew ness, S_{k-1}	1,000
Skew ness, S_{k-2}	1,000
Inman, $\alpha_{\phi-1}$	0,000
Inman, $\alpha_{\phi-2}$	-1,000
Folk & Ward, Sk_I	-0,208

Coefficient d'acuité (Kurtosis)	
Krumbein & Petijohn, K	0,249
Inman, K_ϕ	1,400
Folk & Ward, K_G	1,405

Coefficient de courbure	
C_c	1,204

Analyse granulométrique par voie fluide : fraction 0,040 µm - 2000 µm

Echantillon :	INDONESIE/11/PANTAI/U-01/140-160/T.Yan W. ISKANDARSYAH
Date :	23/01/2012 12:01
Opérateur :	MT
Fichier :	U01-007

Commentaires :	prof. : 140-160 cm Destruction MO à H2O2 -élimination des ions floculants - hexa + US

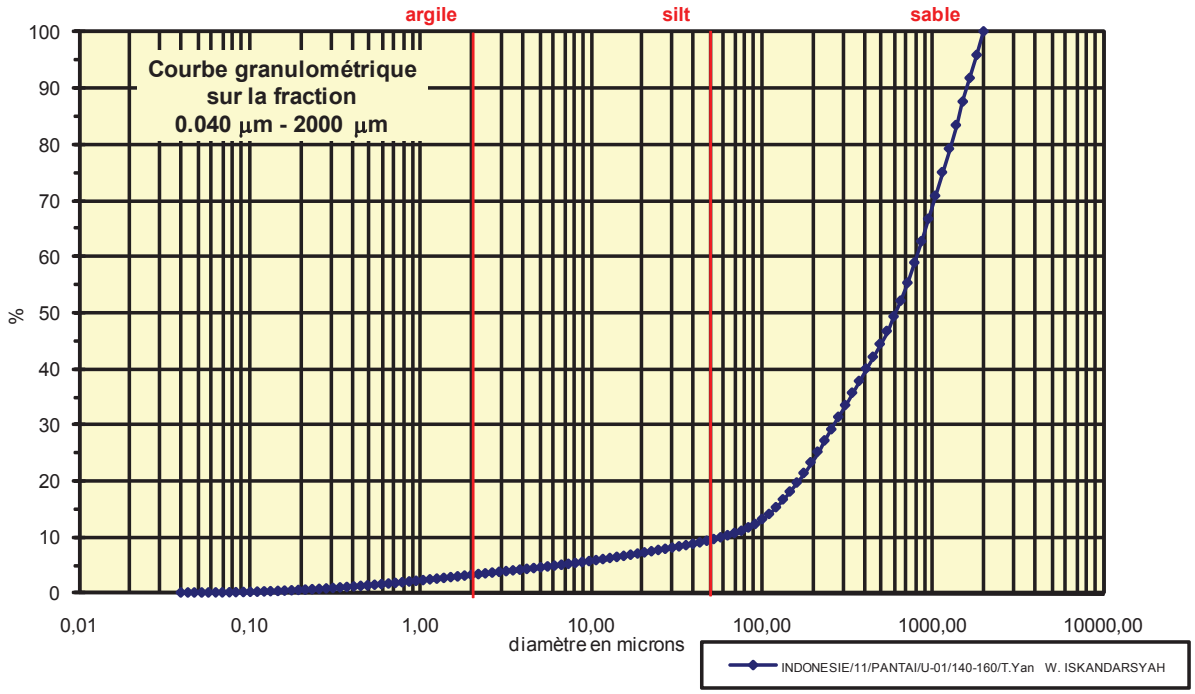

Fractiles	Taille (µm)	Taille (ϕ)
d_5	6,761	7,21
d_{10}	57,770	4,11
d_{16}	121,800	3,04
d_{25}	194,200	2,36
d_{30}	256,800	1,96
d_{50}	594,900	0,75
d_{60}	786,900	0,35
d_{75}	1143,000	-0,19
d_{84}	1377,000	-0,46
d_{90}	1512,000	-0,60
d_{95}	1660,000	-0,73

% Argile inférieur à 2µ	**A**	**3,01**
% Silts de 2µ à 50µ	**LT**	**6,21**
limons fins 2µ à 20µ	LF	3,93
limons grossiers 20µ à 50µ	LG	2,28
% Sables 50µ à 2000 µ	**ST**	**90,78**
sables fins 50µ à 200µ	SF	13,98
sables fins 50µ à 100µ	SF1	2,98
sables fins 100µ à 200 µ	SF2	11,00
sables grossiers 200µ à 2000µ	SG	76,80
sables grossiers 200µ à 500µ	SG1	21,10
sables grossiers 500µ à 1000µ	SG2	22,30
sables grossiers 1000µ à 2000µ	SG3	33,40

Indice de classement	
Trask, S_o	2,426
Krumbein, Q_d	-1,279
Inman, σ_ϕ	-1,749
Folk & Ward, σ_ϕ	-2,078
Hazen, C_u	13,621

Moyenne	
Trask, M	668,600
Inman, M_ϕ	1,288
Folk & Ward, M_z	1,108

Coefficient de dissymétrie	
Skew ness, S_{k-1}	0,627
Skew ness, S_{k-2}	0,792
Inman, $\alpha_{\phi-1}$	-0,308
Inman, $\alpha_{\phi-2}$	-1,423
Folk & Ward, Sk_I	-0,467

Coefficient d'acuité (Kurtosis)	
Krumbein & Petijohn, K	0,326
Inman, K_ϕ	1,269
Folk & Ward, K_G	1,272

Coefficient de courbure	
C_c	1,451

Analyse granulométrique par voie fluide : fraction 0,040 µm - 2000 µm

Echantillon :	INDONESIE/11/PANTAI/U-01/LEMPUNG/175-200/T.Yan W. ISKANDARSYAH
Date :	23/01/2012 14:46
Opérateur :	MT
Fichier :	U01-008

Commentaires :	prof. : 175-200 cm Destruction MO à H2O2 -élimination des ions floculants - hexa + US

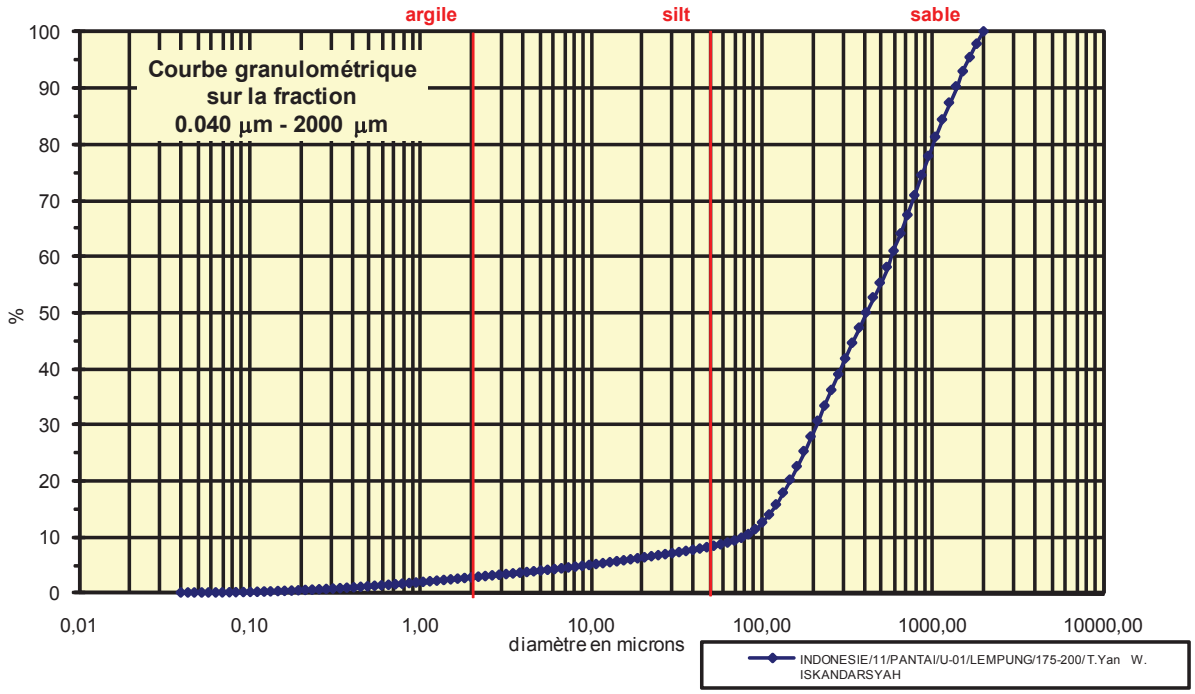

Fractiles	Taille (µm)	Taille (ϕ)
d_5	9,819	6,67
d_{10}	76,430	3,71
d_{16}	121,800	3,04
d_{25}	161,200	2,63
d_{30}	194,200	2,36
d_{50}	409,600	1,29
d_{60}	541,900	0,88
d_{75}	863,900	0,21
d_{84}	1041,000	-0,06
d_{90}	1255,000	-0,33
d_{95}	1512,000	-0,60

% Argile inférieur à 2µ	**A**	**2,58**
% Silts de 2µ à 50µ	**LT**	**5,49**
limons fins 2µ à 20µ	LF	3,52
limons grossiers 20µ à 50µ	LG	1,97
% Sables 50µ à 2000 µ	**ST**	**91,93**
sables fins 50µ à 200µ	SF	19,73
sables fins 50µ à 100µ	SF1	3,23
sables fins 100µ à 200 µ	SF2	16,50
sables grossiers 200µ à 2000µ	SG	72,20
sables grossiers 200µ à 500µ	SG1	27,40
sables grossiers 500µ à 1000µ	SG2	22,60
sables grossiers 1000µ à 2000µ	SG3	22,20

Indice de classement	
Trask, S_o	2,315
Krumbein, Q_d	-1,211
Inman, σ_ϕ	-1,548
Folk & Ward, σ_ϕ	-1,875
Hazen, C_u	7,090

Moyenne	
Trask, M	512,550
Inman, M_ϕ	1,490
Folk & Ward, M_z	1,422

Coefficient de dissymétrie	
Skew ness, S_{k-1}	0,830
Skew ness, S_{k-2}	0,911
Inman, $\alpha_{\phi-1}$	-0,131
Inman, $\alpha_{\phi-2}$	-1,130
Folk & Ward, Sk_I	-0,306

Coefficient d'acuité (Kurtosis)	
Krumbein & Petijohn, K	0,298
Inman, K_ϕ	1,348
Folk & Ward, K_G	1,230

Coefficient de courbure	
C_c	0,911

Analyse granulométrique par voie fluide : fraction 0,040 µm - 2000 µm

Echantillon :	INDONESIE/11/PANTAI/U-01/PASIR/200-210/T.Yan W. ISKANDARSYAH
Date :	23/01/2012 15:20
Opérateur :	MT
Fichier :	U01-009

Commentaires :	prof. : 200-210 cm Destruction MO à H2O2 -élimination des ions floculants - hexa + US

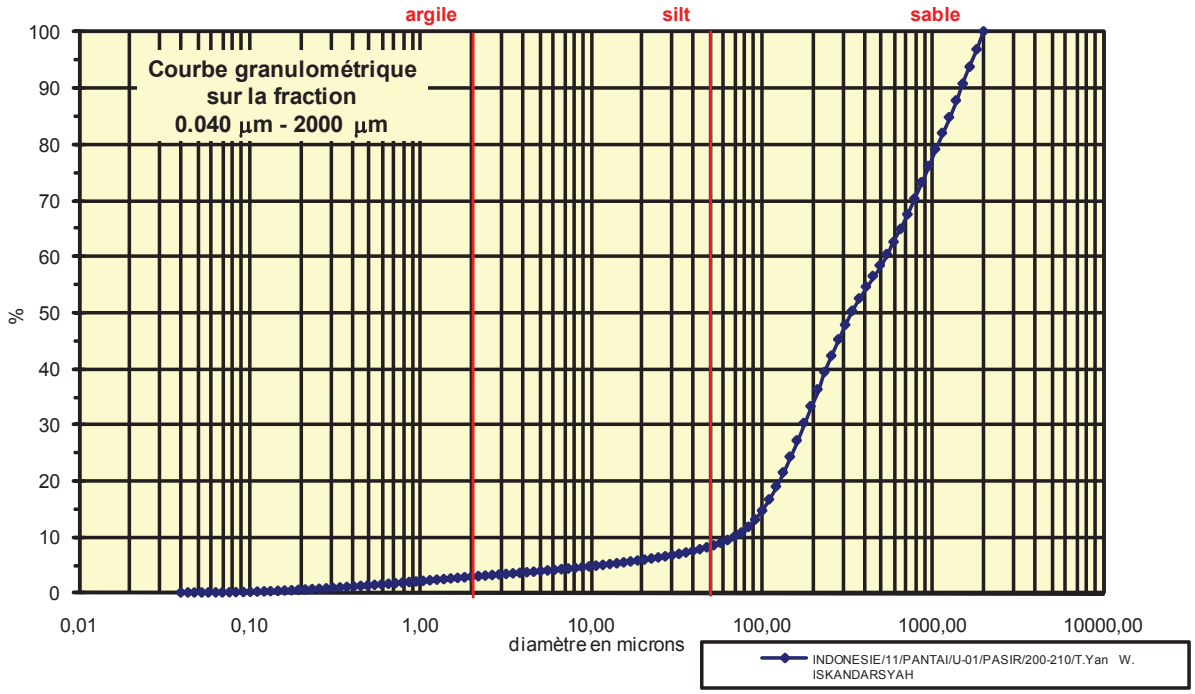

Fractiles	Taille (µm)	Taille (ϕ)
d_5	11,830	6,40
d_{10}	69,620	3,84
d_{16}	101,100	3,31
d_{25}	146,800	2,77
d_{30}	161,200	2,63
d_{50}	309,600	1,69
d_{60}	493,600	1,02
d_{75}	863,900	0,21
d_{84}	1143,000	-0,19
d_{90}	1377,000	-0,46
d_{95}	1660,000	-0,73

% Argile inférieur à 2µ	**A**	**2,71**
% Silts de 2µ à 50µ	**LT**	**5,34**
limons fins 2µ à 20µ	LF	2,99
limons grossiers 20µ à 50µ	LG	2,35
% Sables 50µ à 2000 µ	**ST**	**91,95**
sables fins 50µ à 200µ	SF	25,15
sables fins 50µ à 100µ	SF1	4,95
sables fins 100µ à 200 µ	SF2	20,20
sables grossiers 200µ à 2000µ	SG	66,80
sables grossiers 200µ à 500µ	SG1	25,10
sables grossiers 500µ à 1000µ	SG2	17,70
sables grossiers 1000µ à 2000µ	SG3	24,00

Indice de classement	
Trask, S_o	2,426
Krumbein, Q_d	-1,279
Inman, σ_ϕ	-1,749
Folk & Ward, σ_ϕ	-1,955
Hazen, C_u	7,090

Moyenne	
Trask, M	505,350
Inman, M_ϕ	1,557
Folk & Ward, M_z	1,602

Coefficient de dissymétrie	
Skew ness, S_{k-1}	1,323
Skew ness, S_{k-2}	1,150
Inman, $\alpha_{\phi-1}$	0,077
Inman, $\alpha_{\phi-2}$	-0,654
Folk & Ward, Sk_i	-0,122

Coefficient d'acuité (Kurtosis)	
Krumbein & Petijohn, K	0,274
Inman, K_ϕ	1,038
Folk & Ward, K_G	1,143

Coefficient de courbure	
C_c	0,756

Analyse granulométrique par voie fluide : fraction 0,040 µm - 2000 µm

Echantillon :	INDONESIE/11/PANTAI/U-01/210-280/T.Yan W. ISKANDARSYAH
Date :	23/01/2012 15:33
Opérateur :	MT
Fichier :	U01-010

Commentaires :	prof. : 210-280 cm Destruction MO à H2O2 -élimination des ions floculants - hexa + US

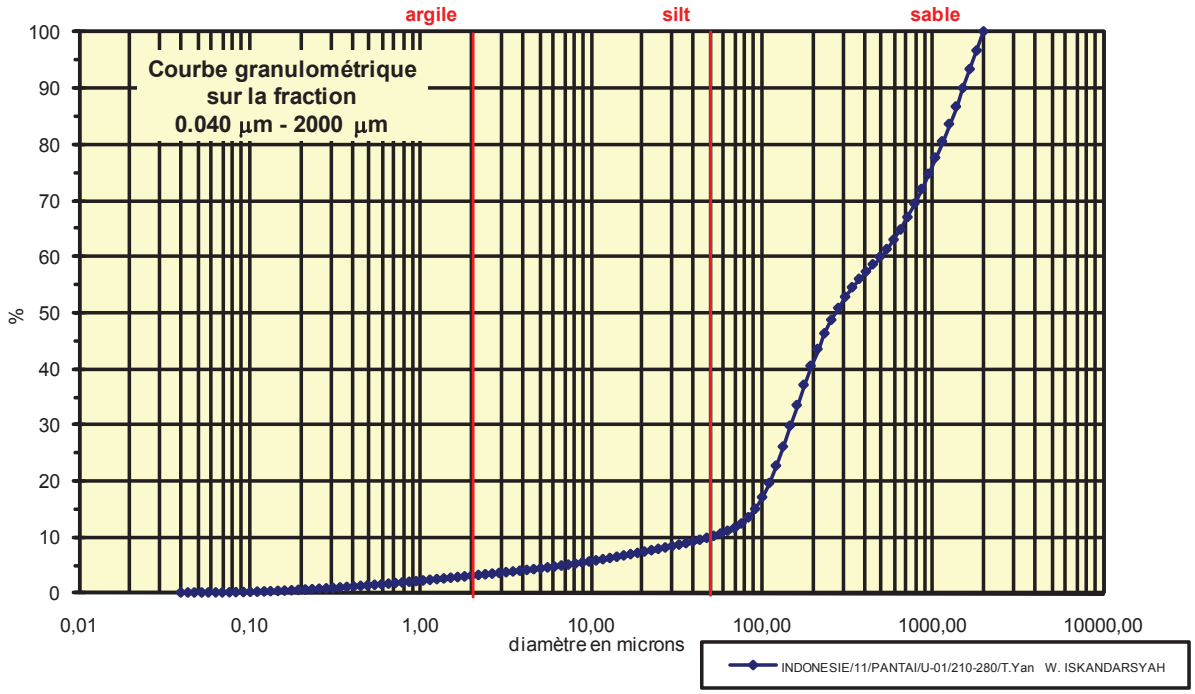

Fractiles	Taille (µm)	Taille (ϕ)
d_5	7,421	7,07
d_{10}	47,930	4,38
d_{16}	92,090	3,44
d_{25}	121,800	3,04
d_{30}	146,800	2,77
d_{50}	256,800	1,96
d_{60}	493,600	1,02
d_{75}	948,200	0,08
d_{84}	1255,000	-0,33
d_{90}	1512,000	-0,60
d_{95}	1660,000	-0,73

% Argile inférieur à 2µ	**A**	**2,87**
% Silts de 2µ à 50µ	**LT**	**6,87**
limons fins 2µ à 20µ	LF	4,19
limons grossiers 20µ à 50µ	LG	2,68
% Sables 50µ à 2000 µ	**ST**	**90,26**
sables fins 50µ à 200µ	SF	30,66
sables fins 50µ à 100µ	SF1	5,16
sables fins 100µ à 200 µ	SF2	25,50
sables grossiers 200µ à 2000µ	SG	59,60
sables grossiers 200µ à 500µ	SG1	19,40
sables grossiers 500µ à 1000µ	SG2	14,80
sables grossiers 1000µ à 2000µ	SG3	25,40

Indice de classement	
Trask, S_o	2,790
Krumbein, Q_d	-1,480
Inman, σ_ϕ	-1,884
Folk & Ward, σ_ϕ	-2,125
Hazen, C_u	10,298

Moyenne	
Trask, M	535,000
Inman, M_ϕ	1,557
Folk & Ward, M_z	1,691

Coefficient de dissymétrie	
Skew ness, S_{k1}	1,751
Skew ness, S_{k2}	1,323
Inman, $\alpha_{\phi-1}$	0,215
Inman, $\alpha_{\phi-2}$	-0,642
Folk & Ward, Sk_I	-0,048

Coefficient d'acuité (Kurtosis)	
Krumbein & Petijohn, K	0,282
Inman, K_ϕ	1,071
Folk & Ward, K_G	1,080

Coefficient de courbure	
C_c	0,911

Analyse granulométrique par voie fluide : fraction 0,040 µm - 2000 µm

Echantillon :	INDONESIE/12/LABAN-UJUNG KULON/U-01/PANTAI/T.YAN W.ISKANDARSYAH
Date :	04/03/2013 12:13
Opérateur :	MT
Fichier :	U01-011

Commentaires :	prof. 0 cm destruction MO à H2O2 - élimination des ions floculants - hexa +US

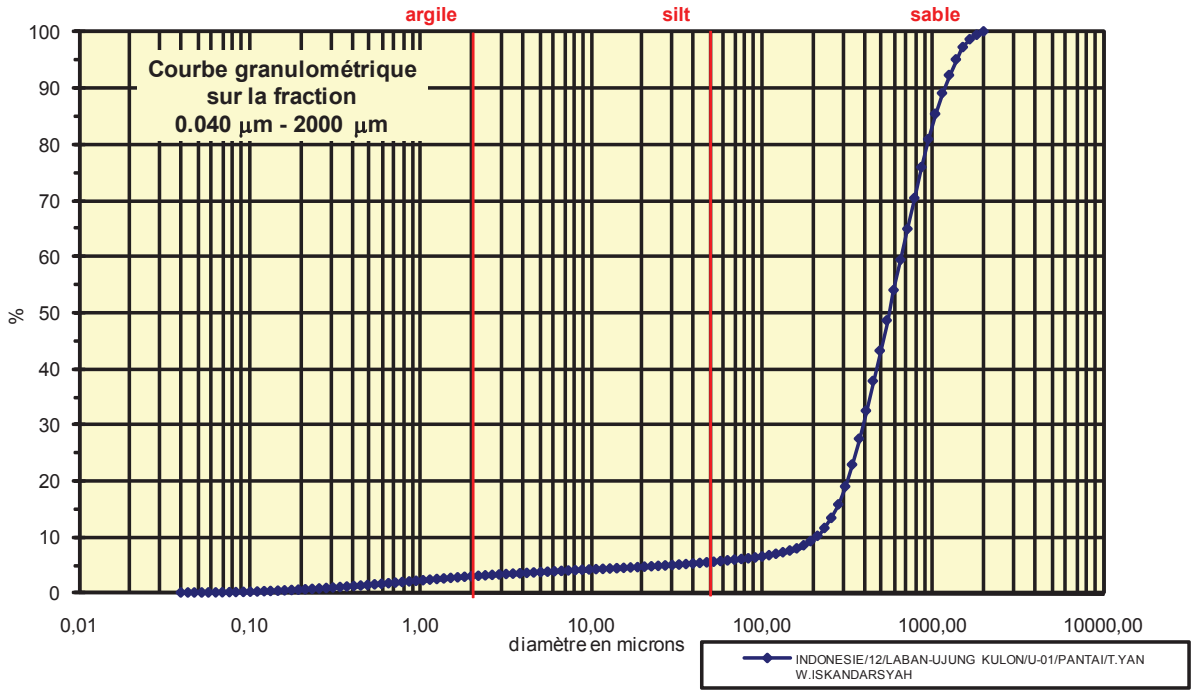

Fractiles	Taille (µm)	Taille (ϕ)
d_5	33,000	4,92
d_{10}	194,200	2,36
d_{16}	282,100	1,83
d_{25}	339,800	1,56
d_{30}	373,100	1,42
d_{50}	541,900	0,88
d_{60}	653,000	0,61
d_{75}	786,900	0,35
d_{84}	948,200	0,08
d_{90}	1143,000	-0,19
d_{95}	1377,000	-0,46

% Argile inférieur à 2µ	**A**	**2,80**
% Silts de 2µ à 50µ	**LT**	**2,57**
limons fins 2µ à 20µ	LF	1,72
limons grossiers 20µ à 50µ	LG	0,85
% Sables 50µ à 2000 µ	**ST**	**94,63**
sables fins 50µ à 200µ	SF	3,79
sables fins 50µ à 100µ	SF1	0,87
sables fins 100µ à 200 µ	SF2	2,92
sables grossiers 200µ à 2000µ	SG	90,84
sables grossiers 200µ à 500µ	SG1	33,94
sables grossiers 500µ à 1000µ	SG2	37,70
sables grossiers 1000µ à 2000µ	SG3	19,20

Indice de classement	
Trask, S_o	1,522
Krumbein, Q_d	-0,606
Inman, σ_ϕ	-0,874
Folk & Ward, σ_ϕ	-1,253
Hazen, C_u	3,363

Moyenne	
Trask, M	563,350
Inman, M_ϕ	0,951
Folk & Ward, M_z	0,929

Coefficient de dissymétrie	
Skew ness, S_{k-1}	0,911
Skew ness, S_{k-2}	0,954
Inman, $\alpha_{\phi-1}$	-0,077
Inman, $\alpha_{\phi-2}$	-1,539
Folk & Ward, Sk_I	-0,289

Coefficient d'acuité (Kurtosis)	
Krumbein & Petijohn, K	0,236
Inman, K_ϕ	2,078
Folk & Ward, K_G	1,821

Coefficient de courbure	
C_c	1,098

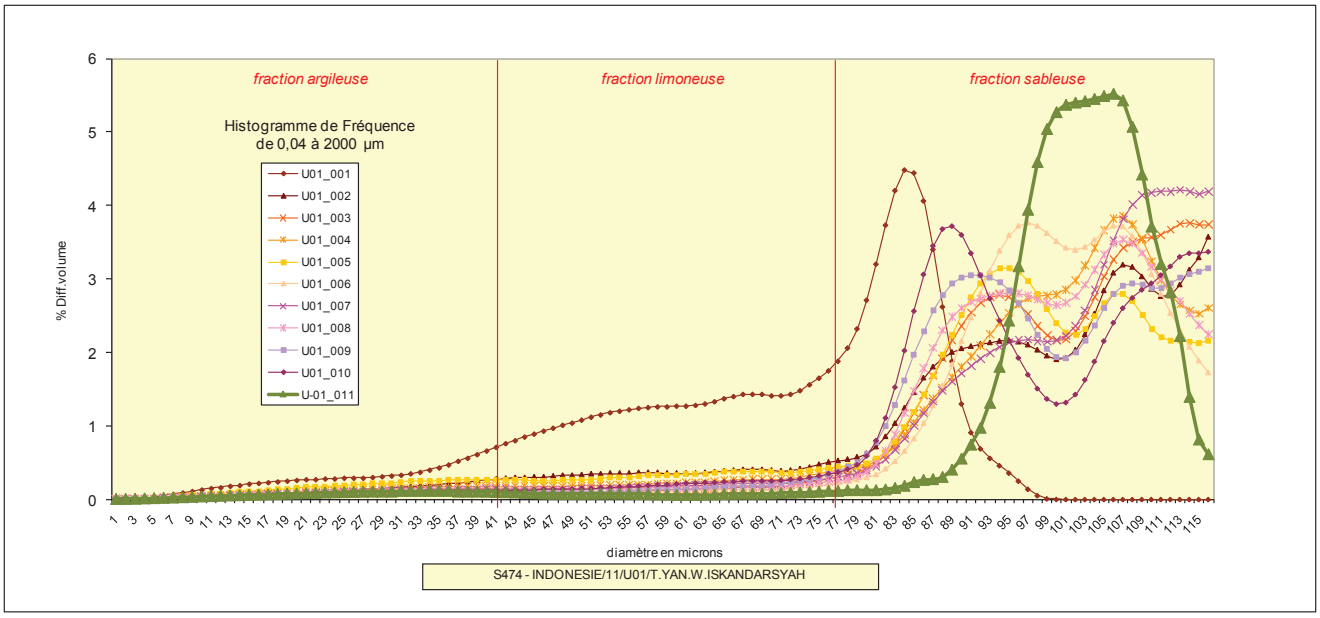
fraction argileuse
fraction limoneuse
fraction sableuse
Histogramme de Fréquence
de 0,04 à 2000 µm
U01_001
U01_002
U01_003
U01_004
U01_005
U01_006
U01_007
U01_008
U01_009
U01_010
U-01_011
% Diff volume
diamètre en microns
S474 - INDONESIE/11/U01/T.YAN.W.ISKANDARSYAH

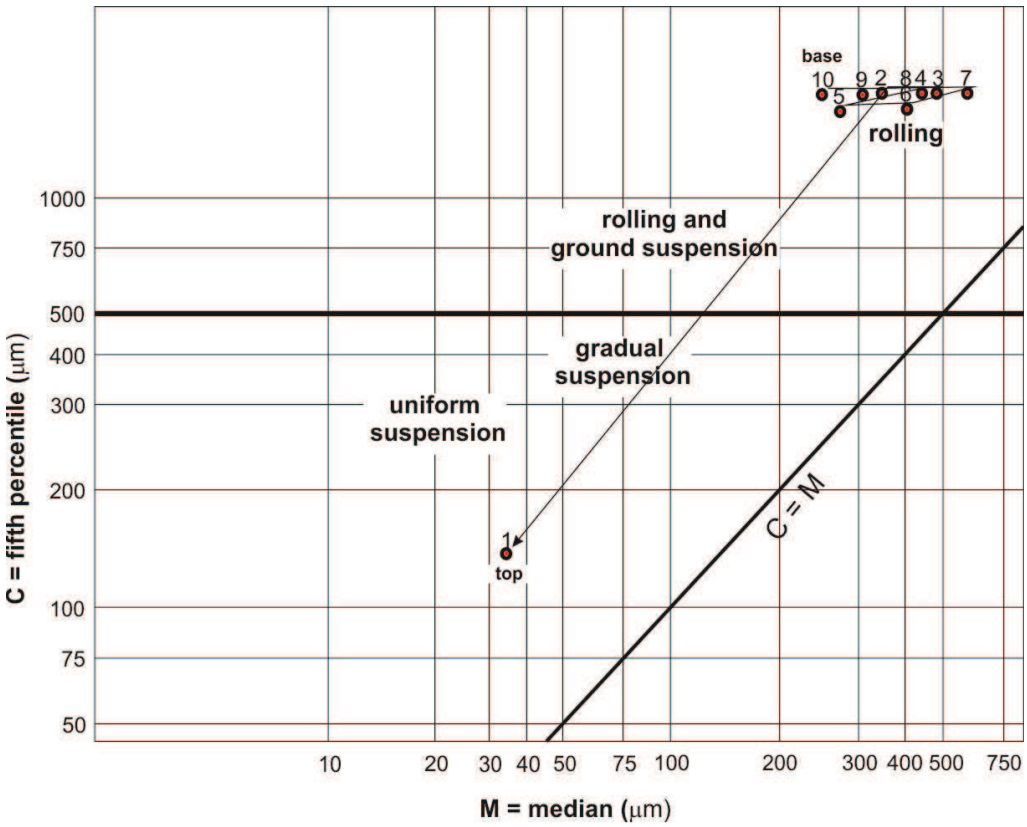
base
10 9 2 8 4 3 7
5 6
rolling
rolling and
ground suspension
gradual
suspension
uniform
suspension
1
top
C = M
1000
750
500
400
300
200
100
75
50
C = fifth percentile (μm)
10 20 30 40 50 75 100 200 300 400 500 750
M = median (μm)

Analyse granulométrique par voie fluide : fraction 0,040 µm - 2000 µm

Echantillon :	INDONESIE/12/.LABAN/U-02/001/soil/T.YAN W.ISKANDARSYAH
Date :	22/10/2013 16:32
Opérateur :	MT
Fichier :	U02-001

Commentaires :	prof. 0-15 cm 27/05/12 Destruction MO à H2O2-élimination des ions floculants - Hexa+US

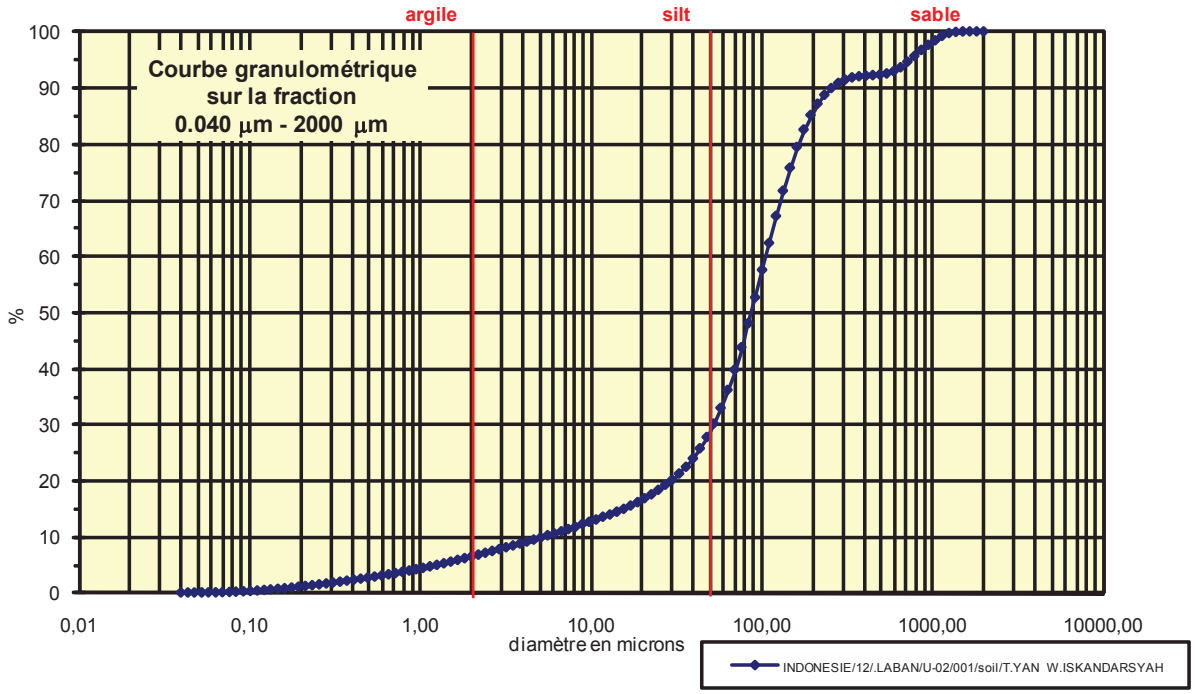

Fractiles	Taille (µm)	Taille (ϕ)
d_5	1,261	9,63
d_{10}	5,111	7,61
d_{16}	17,180	5,86
d_{25}	39,770	4,65
d_{30}	47,930	4,38
d_{50}	83,900	3,58
d_{60}	101,100	3,31
d_{75}	133,700	2,90
d_{84}	176,800	2,50
d_{90}	256,800	1,96
d_{95}	716,900	0,48

% Argile inférieur à 2µ	**A**	**6,12**
% Silts de 2µ à 50µ	**LT**	**21,58**
limons fins 2µ à 20µ	LF	9,98
limons grossiers 20µ à 50µ	LG	11,60
% Sables 50µ à 2000 µ	**ST**	**72,30**
sables fins 50µ à 200µ	SF	57,40
sables fins 50µ à 100µ	SF1	24,90
sables fins 100µ à 200 µ	SF2	32,50
sables grossiers 200µ à 2000µ	SG	14,90
sables grossiers 200µ à 500µ	SG1	7,20
sables grossiers 500µ à 1000µ	SG2	5,30
sables grossiers 1000µ à 2000µ	SG3	2,40

Indice de classement	
Trask, S_o	1,834
Krumbein, Q_d	-0,875
Inman, σ_ϕ	-1,682
Folk & Ward, σ_ϕ	-2,227
Hazen, C_u	19,781

Moyenne	
Trask, M	86,735
Inman, M_ϕ	4,181
Folk & Ward, M_z	3,979

Coefficient de dissymétrie	
Skew ness, S_{k1}	0,755
Skew ness, S_{k2}	0,869
Inman, $\alpha_{\phi-1}$	-0,361
Inman, $\alpha_{\phi-2}$	-0,880
Folk & Ward, Sk_I	-0,342

Coefficient d'acuité (Kurtosis)	
Krumbein & Petijohn, K	0,187
Inman, K_ϕ	1,721
Folk & Ward, K_G	2,144

Coefficient de courbure	
C_c	4,446

Analyse granulométrique par voie fluide : fraction 0,040 µm - 2000 µm

Echantillon :	INDONESIE/12/.LABAN/U-02/002/silty soil/T.YAN W.ISKANDARSYAH
Date :	22/10/2013 16:44
Opérateur :	MT
Fichier :	U02-002

Commentaires :	prof. 15-30 cm 27/05/12 Destruction MO à H2O2-élimination des ions floculants - Hexa+US

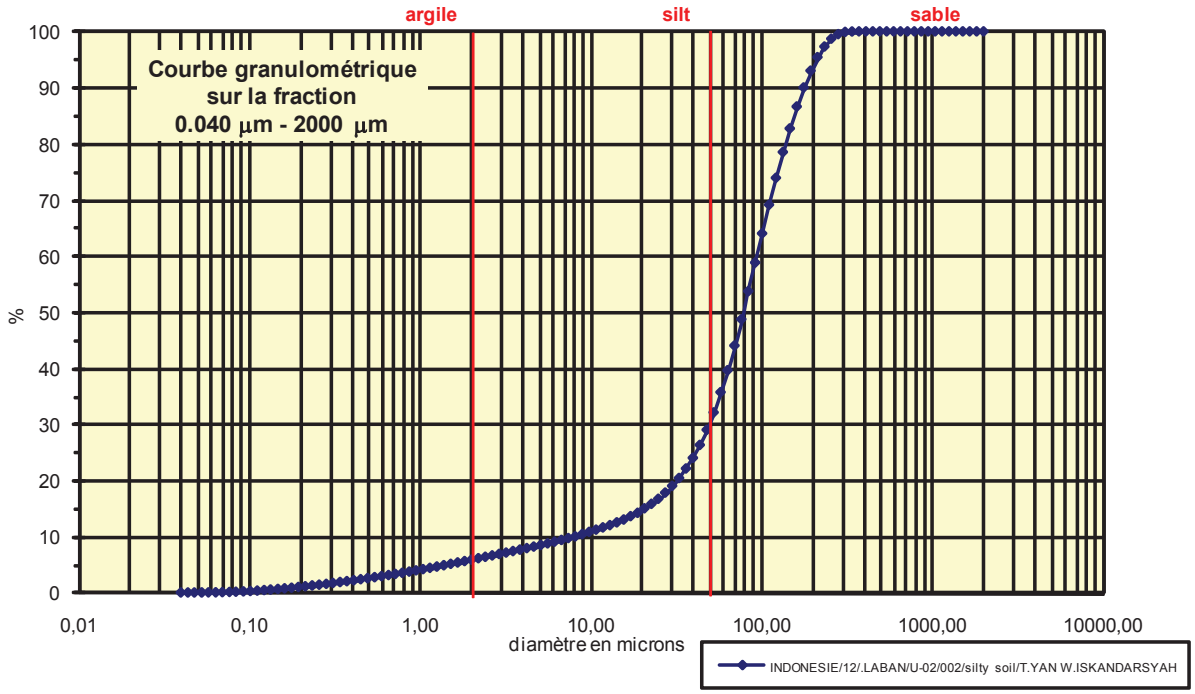

Fractiles	Taille (µm)	Taille (ϕ)
d_5	1,385	9,50
d_{10}	8,147	6,94
d_{16}	22,730	5,46
d_{25}	39,770	4,65
d_{30}	47,930	4,38
d_{50}	76,430	3,71
d_{60}	92,090	3,44
d_{75}	121,800	3,04
d_{84}	146,800	2,77
d_{90}	176,800	2,50
d_{95}	194,200	2,36

% Argile inférieur à 2µ	**A**	**5,60**
% Silts de 2µ à 50µ	**LT**	**23,40**
limons fins 2µ à 20µ	LF	8,60
limons grossiers 20µ à 50µ	LG	14,80
% Sables 50µ à 2000 µ	**ST**	**71,00**
sables fins 50µ à 200µ	SF	64,00
sables fins 50µ à 100µ	SF1	29,80
sables fins 100µ à 200 µ	SF2	34,20
sables grossiers 200µ à 2000µ	SG	7,00
sables grossiers 200µ à 500µ	SG1	7,00
sables grossiers 500µ à 1000µ	SG2	0,00
sables grossiers 1000µ à 2000µ	SG3	0,00

Indice de classement	
Trask, S_o	1,750
Krumbein, Q_d	-0,807
Inman, σ_ϕ	-1,346
Folk & Ward, σ_ϕ	-1,753
Hazen, C_u	11,304

Moyenne	
Trask, M	80,785
Inman, M_ϕ	4,114
Folk & Ward, M_z	3,979

Coefficient de dissymétrie	
Skew ness, S_{k-1}	0,829
Skew ness, S_{k-2}	0,911
Inman, $\alpha_{\phi-1}$	-0,300
Inman, $\alpha_{\phi-2}$	-1,650
Folk & Ward, Sk_I	-0,461

Coefficient d'acuité (Kurtosis)	
Krumbein & Petijohn, K	0,243
Inman, K_ϕ	1,650
Folk & Ward, K_G	1,810

Coefficient de courbure	
C_c	3,062

Analyse granulométrique par voie fluide : fraction 0,040 µm - 2000 µm

Echantillon :	INDONESIE/12/.LABAN/U-02/003/silty soil/T.YAN W.ISKANDARSYAH
Date :	22/10/2013 16:53
Opérateur :	MT
Fichier :	U02-003

Commentaires :	prof. 30-40 cm 27/05/12 Destruction MO à H2O2-élimination des ions floculants - Hexa+US

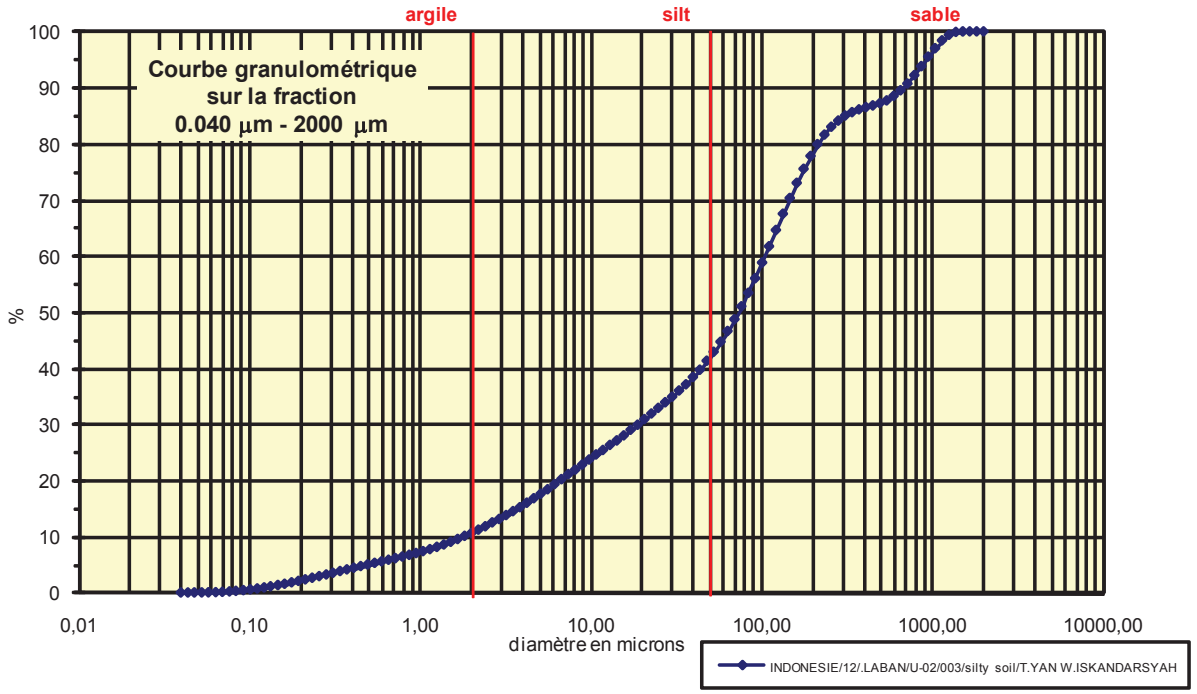

Fractiles	Taille (µm)	Taille (ϕ)
d_5	0,496	10,98
d_{10}	1,669	9,23
d_{16}	4,241	7,88
d_{25}	10,780	6,54
d_{30}	18,860	5,73
d_{50}	69,620	3,84
d_{60}	101,100	3,31
d_{75}	161,200	2,63
d_{84}	256,800	1,96
d_{90}	653,000	0,61
d_{95}	863,900	0,21

% Argile inférieur à 2µ	**A**	**10,10**
% Silts de 2µ à 50µ	**LT**	**31,20**
limons fins 2µ à 20µ	LF	19,80
limons grossiers 20µ à 50µ	LG	11,40
% Sables 50µ à 2000 µ	**ST**	**58,70**
sables fins 50µ à 200µ	SF	36,50
sables fins 50µ à 100µ	SF1	14,70
sables fins 100µ à 200 µ	SF2	21,80
sables grossiers 200µ à 2000µ	SG	22,20
sables grossiers 200µ à 500µ	SG1	9,40
sables grossiers 500µ à 1000µ	SG2	8,30
sables grossiers 1000µ à 2000µ	SG3	4,50

Indice de classement	
Trask, S_o	3,867
Krumbein, Q_d	-1,951
Inman, σ_ϕ	-2,960
Folk & Ward, σ_ϕ	-3,111
Hazen, C_u	60,575

Moyenne	
Trask, M	85,990
Inman, M_ϕ	4,921
Folk & Ward, M_z	4,562

Coefficient de dissymétrie	
Skew ness, S_{k-1}	0,359
Skew ness, S_{k-2}	0,599
Inman, $\alpha_{\phi-1}$	-0,364
Inman, $\alpha_{\phi-2}$	-0,591
Folk & Ward, Sk_i	-0,344

Coefficient d'acuité (Kurtosis)	
Krumbein & Petijohn, K	0,115
Inman, K_ϕ	0,819
Folk & Ward, K_G	1,131

Coefficient de courbure	
C_c	2,108

Analyse granulométrique par voie fluide : fraction 0,040 µm - 2000 µm

Echantillon :	INDONESIE/12/.LABAN/U-02/004/sand/T.YAN W.ISKANDARSYAH
Date :	22/10/2013 18:31
Opérateur :	MT
Fichier :	U02-004

Commentaires :	prof. 40-60 cm 27/05/12 Destruction MO à H2O2-élimination des ions floculants - Hexa+US

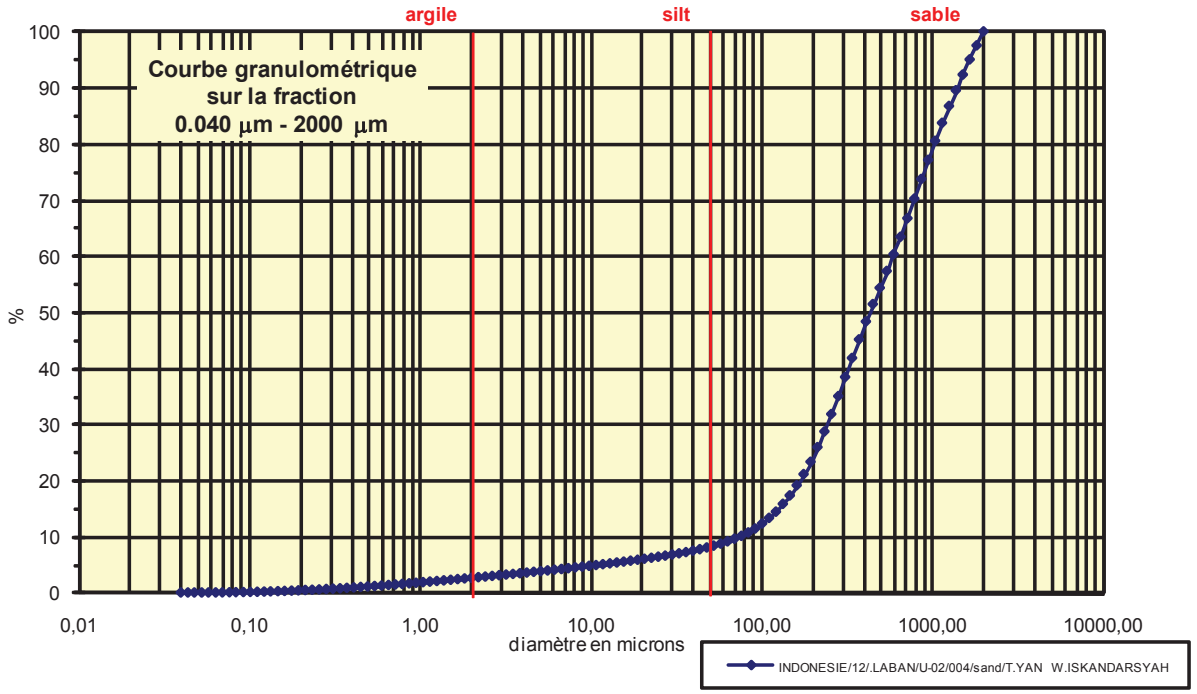

Fractiles	Taille (µm)	Taille (ϕ)
d_5	10,780	6,54
d_{10}	69,620	3,84
d_{16}	133,700	2,90
d_{25}	194,200	2,36
d_{30}	234,100	2,09
d_{50}	409,600	1,29
d_{60}	541,900	0,88
d_{75}	863,900	0,21
d_{84}	1143,000	-0,19
d_{90}	1377,000	-0,46
d_{95}	1660,000	-0,73

% Argile inférieur à 2µ	**A**	**2,50**
% Silts de 2µ à 50µ	**LT**	**5,52**
limons fins 2µ à 20µ	LF	3,34
limons grossiers 20µ à 50µ	LG	2,18
% Sables 50µ à 2000 µ	**ST**	**91,98**
sables fins 50µ à 200µ	SF	15,28
sables fins 50µ à 100µ	SF1	3,38
sables fins 100µ à 200 µ	SF2	11,90
sables grossiers 200µ à 2000µ	SG	76,70
sables grossiers 200µ à 500µ	SG1	31,00
sables grossiers 500µ à 1000µ	SG2	22,80
sables grossiers 1000µ à 2000µ	SG3	22,90

Indice de classement	
Trask, S_o	2,109
Krumbein, Q_d	-1,077
Inman, σ_ϕ	-1,548
Folk & Ward, σ_ϕ	-1,875
Hazen, C_u	7,784

Moyenne	
Trask, M	529,050
Inman, M_ϕ	1,355
Folk & Ward, M_z	1,333

Coefficient de dissymétrie	
Skew ness, S_{k-1}	1,000
Skew ness, S_{k-2}	1,000
Inman, $\alpha_{\phi-1}$	-0,044
Inman, $\alpha_{\phi-2}$	-1,043
Folk & Ward, Sk_i	-0,244

Coefficient d'acuité (Kurtosis)	
Krumbein & Petijohn, K	0,256
Inman, K_ϕ	1,347
Folk & Ward, K_G	1,383

Coefficient de courbure	
C_c	1,453

Analyse granulométrique par voie fluide : fraction 0,040 µm - 2000 µm

Echantillon :	INDONESIE/12/.LABAN/U-02/005/T.YAN W.ISKANDARSYAH
Date :	22/10/2013 18:31
Opérateur :	MT
Fichier :	U02-005

Commentaires :	prof. 60-90 cm 27/05/12 Destruction MO à H2O2-élimination des ions floculants - Hexa+US

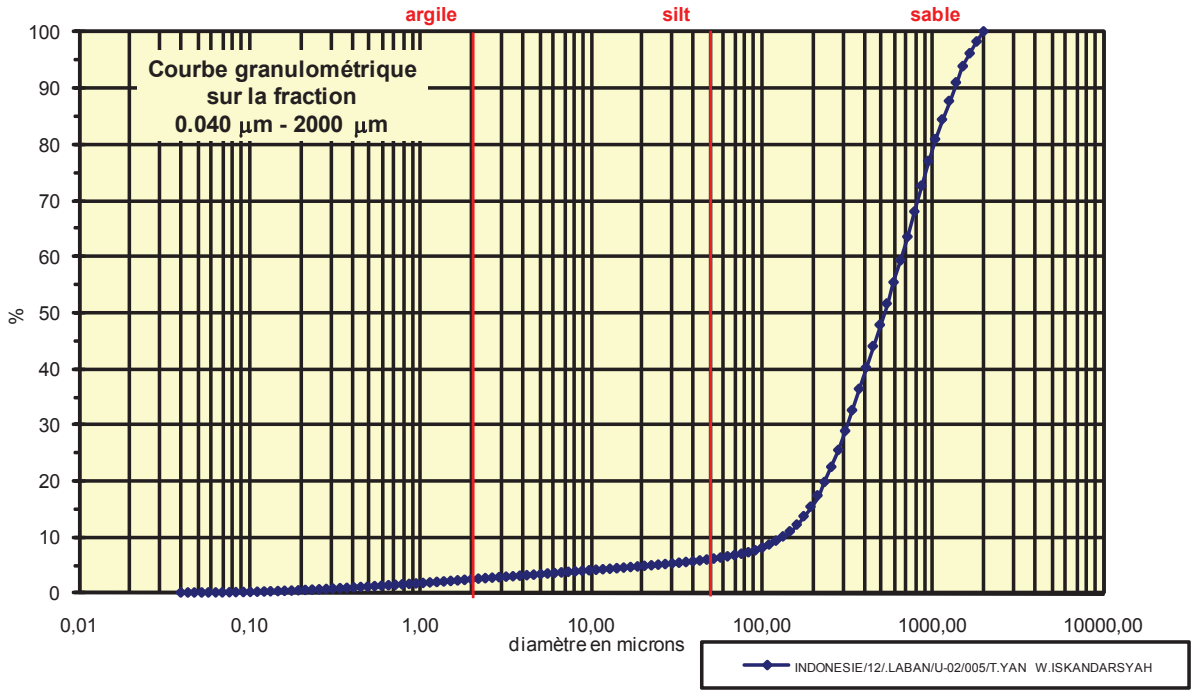

Fractiles	Taille (µm)	Taille (ϕ)
d_5	24,950	5,32
d_{10}	133,700	2,90
d_{16}	194,200	2,36
d_{25}	256,800	1,96
d_{30}	309,600	1,69
d_{50}	493,600	1,02
d_{60}	653,000	0,61
d_{75}	863,900	0,21
d_{84}	1041,000	-0,06
d_{90}	1255,000	-0,33
d_{95}	1512,000	-0,60

% Argile inférieur à 2µ	**A**	**2,26**
% Silts de 2µ à 50µ	**LT**	**3,61**
limons fins 2µ à 20µ	LF	2,38
limons grossiers 20µ à 50µ	LG	1,23
% Sables 50µ à 2000 µ	**ST**	**94,13**
sables fins 50µ à 200µ	SF	9,43
sables fins 50µ à 100µ	SF1	1,65
sables fins 100µ à 200 µ	SF2	7,78
sables grossiers 200µ à 2000µ	SG	84,70
sables grossiers 200µ à 500µ	SG1	32,40
sables grossiers 500µ à 1000µ	SG2	29,20
sables grossiers 1000µ à 2000µ	SG3	23,10

Indice de classement	
Trask, S_o	1,834
Krumbein, Q_d	-0,875
Inman, σ_ϕ	-1,211
Folk & Ward, σ_ϕ	-1,503
Hazen, C_u	4,884

Moyenne	
Trask, M	560,350
Inman, M_ϕ	1,153
Folk & Ward, M_z	1,108

Coefficient de dissymétrie	
Skew ness, S_{k-1}	0,911
Skew ness, S_{k-2}	0,954
Inman, $\alpha_{\phi-1}$	-0,111
Inman, $\alpha_{\phi-2}$	-1,111
Folk & Ward, Sk_I	-0,283

Coefficient d'acuité (Kurtosis)	
Krumbein & Petijohn, K	0,271
Inman, K_ϕ	1,444
Folk & Ward, K_G	1,387

Coefficient de courbure	
C_c	1,098

Analyse granulométrique par voie fluide : fraction 0,040 µm - 2000 µm

Echantillon :	INDONESIE/12/.LABAN/U-02/006/T.YAN W.ISKANDARSYAH
Date :	22/10/2013 18:37
Opérateur :	MT
Fichier :	U02-006

Commentaires :	prof. 90-120 cm 27/05/12 Destruction MO à H2O2-élimination des ions floculants - Hexa+US

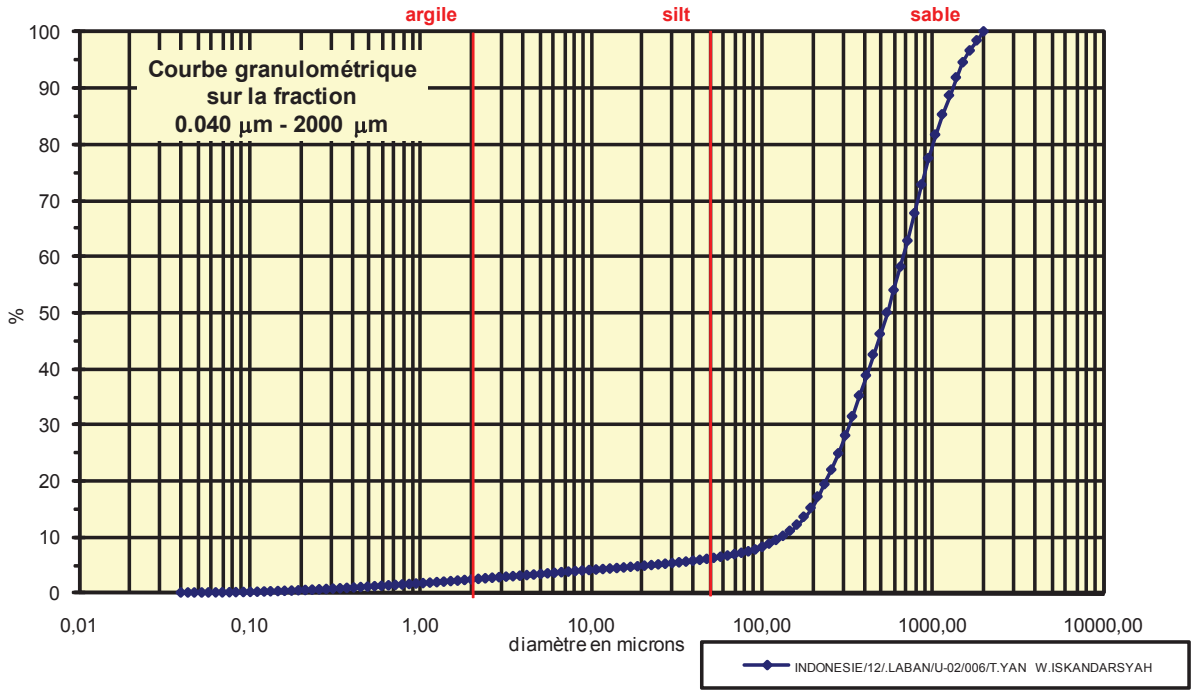

Fractiles	Taille (µm)	Taille (ϕ)
d_5	22,730	5,46
d_{10}	121,800	3,04
d_{16}	194,200	2,36
d_{25}	282,100	1,83
d_{30}	309,600	1,69
d_{50}	541,900	0,88
d_{60}	653,000	0,61
d_{75}	863,900	0,21
d_{84}	1041,000	-0,06
d_{90}	1255,000	-0,33
d_{95}	1512,000	-0,60

% Argile inférieur à 2µ	**A**	**2,23**
% Silts de 2µ à 50µ	**LT**	**3,76**
limons fins 2µ à 20µ	LF	2,44
limons grossiers 20µ à 50µ	LG	1,32
% Sables 50µ à 2000 µ	**ST**	**94,01**
sables fins 50µ à 200µ	SF	9,11
sables fins 50µ à 100µ	SF1	1,68
sables fins 100µ à 200 µ	SF2	7,43
sables grossiers 200µ à 2000µ	SG	84,90
sables grossiers 200µ à 500µ	SG1	31,00
sables grossiers 500µ à 1000µ	SG2	31,30
sables grossiers 1000µ à 2000µ	SG3	22,60

Indice de classement	
Trask, S_o	1,750
Krumbein, Q_d	-0,807
Inman, σ_ϕ	-1,211
Folk & Ward, σ_ϕ	-1,523
Hazen, C_u	5,361

Moyenne	
Trask, M	573,000
Inman, M_ϕ	1,153
Folk & Ward, M_z	1,063

Coefficient de dissymétrie	
Skew ness, S_{k-1}	0,830
Skew ness, S_{k-2}	0,911
Inman, $\alpha_{\phi-1}$	-0,222
Inman, $\alpha_{\phi-2}$	-1,278
Folk & Ward, Sk_I	-0,367

Coefficient d'acuité (Kurtosis)	
Krumbein & Petijohn, K	0,257
Inman, K_ϕ	1,500
Folk & Ward, K_G	1,537

Coefficient de courbure	
C_c	1,205

Analyse granulométrique par voie fluide : fraction 0,040 µm - 2000 µm

Echantillon :	INDONESIE/12/.LABAN/U-02/007/T.YAN W.ISKANDARSYAH
Date :	22/10/2013 18:46
Opérateur :	MT
Fichier :	U02-007

Commentaires :	prof. 120-150 cm 27/05/12 Destruction MO à H2O2-élimination des ions floculants - Hexa+US

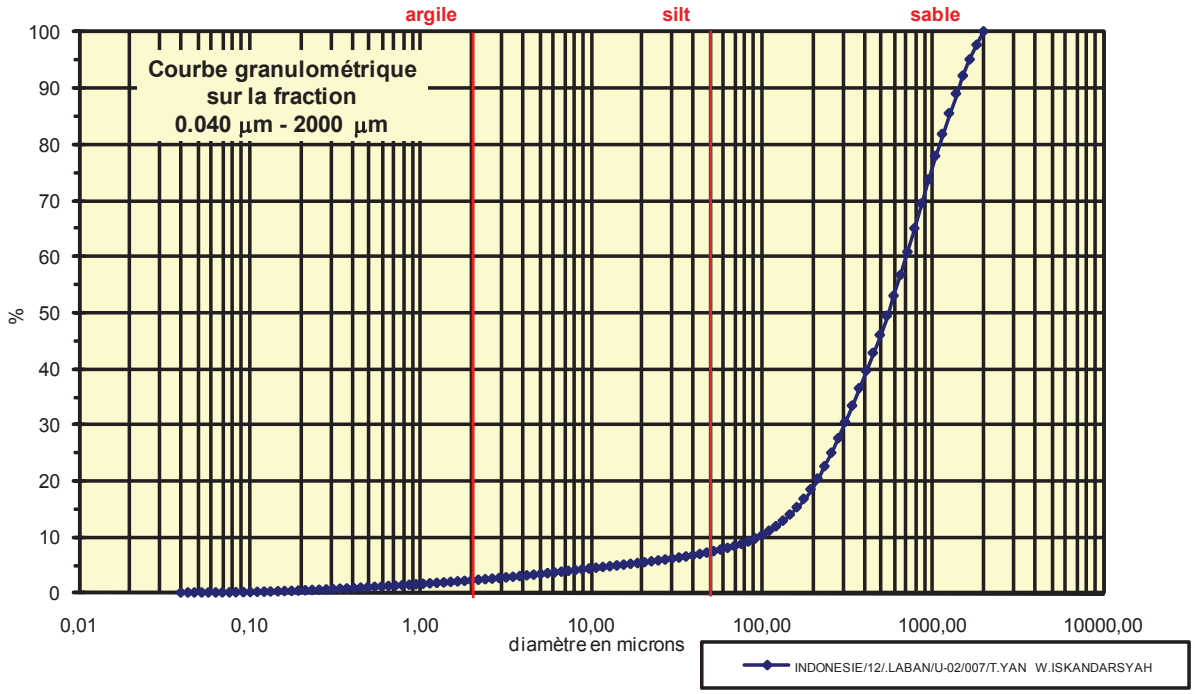

Fractiles	Taille (µm)	Taille (ϕ)
d_5	15,650	6,00
d_{10}	92,090	3,44
d_{16}	161,200	2,63
d_{25}	256,800	1,96
d_{30}	282,100	1,83
d_{50}	541,900	0,88
d_{60}	653,000	0,61
d_{75}	948,200	0,08
d_{84}	1143,000	-0,19
d_{90}	1377,000	-0,46
d_{95}	1660,000	-0,73

% Argile inférieur à 2µ	**A**	**2,07**
% Silts de 2µ à 50µ	**LT**	**5,03**
limons fins 2µ à 20µ	LF	3,18
limons grossiers 20µ à 50µ	LG	1,85
% Sables 50µ à 2000 µ	**ST**	**92,90**
sables fins 50µ à 200µ	SF	11,30
sables fins 50µ à 100µ	SF1	2,52
sables fins 100µ à 200 µ	SF2	8,78
sables grossiers 200µ à 2000µ	SG	81,60
sables grossiers 200µ à 500µ	SG1	27,50
sables grossiers 500µ à 1000µ	SG2	27,70
sables grossiers 1000µ à 2000µ	SG3	26,40

Indice de classement	
Trask, S_o	1,922
Krumbein, Q_d	-0,942
Inman, σ_ϕ	-1,413
Folk & Ward, σ_ϕ	-1,726
Hazen, C_u	7,091

Moyenne	
Trask, M	602,500
Inman, M_ϕ	1,220
Folk & Ward, M_z	1,108

Coefficient de dissymétrie	
Skew ness, S_{k-1}	0,829
Skew ness, S_{k-2}	0,911
Inman, $\alpha_{\phi-1}$	-0,238
Inman, $\alpha_{\phi-2}$	-1,238
Folk & Ward, Sk_i	-0,379

Coefficient d'acuité (Kurtosis)	
Krumbein & Petijohn, K	0,269
Inman, K_ϕ	1,381
Folk & Ward, K_G	1,463

Coefficient de courbure	
C_c	1,323

Analyse granulométrique par voie fluide : fraction 0,040 µm - 2000 µm

Echantillon :	INDONESIE/12/.LABAN/U-02/008/T.YAN W.ISKANDARSYAH
Date :	9:39 23 Oct 2013
Opérateur :	MT
Fichier :	U02-008

Commentaires :	prof. 150-170 cm 27/05/12 Destruction MO à H2O2-élimination des ions floculants - Hexa+US

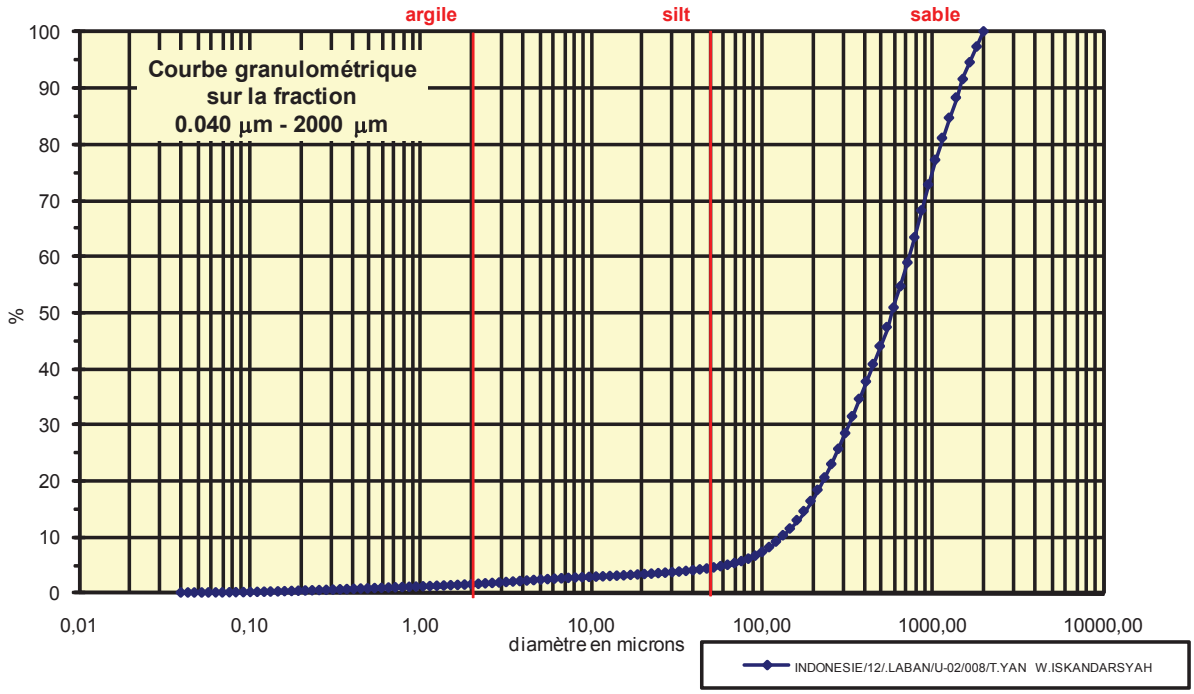

Fractiles	Taille (µm)	Taille (ϕ)
d_5	63,410	3,98
d_{10}	121,800	3,04
d_{16}	176,800	2,50
d_{25}	256,800	1,96
d_{30}	309,600	1,69
d_{50}	541,900	0,88
d_{60}	716,900	0,48
d_{75}	948,200	0,08
d_{84}	1143,000	-0,19
d_{90}	1377,000	-0,46
d_{95}	1660,000	-0,73

% Argile inférieur à 2µ	**A**	**1,41**
% Silts de 2µ à 50µ	**LT**	**2,87**
limons fins 2µ à 20µ	LF	1,80
limons grossiers 20µ à 50µ	LG	1,07
% Sables 50µ à 2000 µ	**ST**	**95,72**
sables fins 50µ à 200µ	SF	12,02
sables fins 50µ à 100µ	SF1	2,28
sables fins 100µ à 200 µ	SF2	9,74
sables grossiers 200µ à 2000µ	SG	83,70
sables grossiers 200µ à 500µ	SG1	27,60
sables grossiers 500µ à 1000µ	SG2	28,80
sables grossiers 1000µ à 2000µ	SG3	27,30

Indice de classement	
Trask, S_o	1,922
Krumbein, Q_d	-0,942
Inman, σ_ϕ	-1,346
Folk & Ward, σ_ϕ	-1,387
Hazen, C_u	5,886

Moyenne	
Trask, M	602,500
Inman, M_ϕ	1,153
Folk & Ward, M_z	1,064

Coefficient de dissymétrie	
Skew ness, S_{k-1}	0,829
Skew ness, S_{k-2}	0,911
Inman, $\alpha_{\phi-1}$	-0,200
Inman, $\alpha_{\phi-2}$	-0,550
Folk & Ward, Sk_I	-0,257

Coefficient d'acuité (Kurtosis)	
Krumbein & Petijohn, K	0,275
Inman, K_ϕ	0,749
Folk & Ward, K_G	1,024

Coefficient de courbure	
C_c	1,098

Analyse granulométrique par voie fluide : fraction 0,040 µm - 2000 µm

Echantillon :	INDONESIE/12/.LABAN/U-02/009/sand/T.YAN W.ISKANDARSYAH
Date :	9:49 23 Oct 2013
Opérateur :	MT
Fichier :	U02-009

Commentaires :	prof. 170-190 cm 27/05/12 Destruction MO à H2O2-élimination des ions floculants - Hexa+US

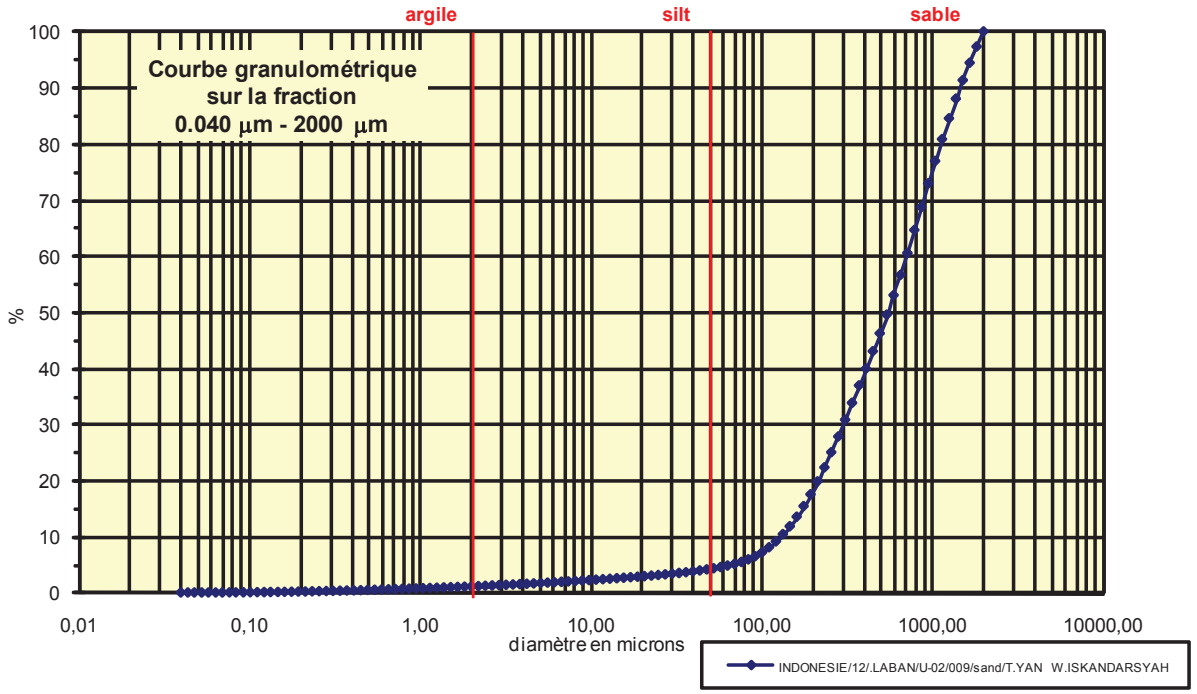

Fractiles	Taille (µm)	Taille (ϕ)
d_5	63,410	3,98
d_{10}	121,800	3,04
d_{16}	176,800	2,50
d_{25}	256,800	1,96
d_{30}	282,100	1,83
d_{50}	541,900	0,88
d_{60}	653,000	0,61
d_{75}	948,200	0,08
d_{84}	1143,000	-0,19
d_{90}	1377,000	-0,46
d_{95}	1660,000	-0,73

% Argile inférieur à 2µ	**A**	**1,04**
% Silts de 2µ à 50µ	**LT**	**3,08**
limons fins 2µ à 20µ	LF	1,77
limons grossiers 20µ à 50µ	LG	1,31
% Sables 50µ à 2000 µ	**ST**	**95,88**
sables fins 50µ à 200µ	SF	13,38
sables fins 50µ à 100µ	SF1	2,35
sables fins 100µ à 200 µ	SF2	11,03
sables grossiers 200µ à 2000µ	SG	82,50
sables grossiers 200µ à 500µ	SG1	28,70
sables grossiers 500µ à 1000µ	SG2	26,70
sables grossiers 1000µ à 2000µ	SG3	27,10

Indice de classement	
Trask, S_o	1,922
Krumbein, Q_d	-0,942
Inman, σ_ϕ	-1,346
Folk & Ward, σ_ϕ	-1,387
Hazen, C_u	5,361

Moyenne	
Trask, M	602,500
Inman, M_ϕ	1,153
Folk & Ward, M_z	1,064

Coefficient de dissymétrie	
Skew ness, S_{k-1}	0,829
Skew ness, S_{k-2}	0,911
Inman, $\alpha_{\phi-1}$	-0,200
Inman, $\alpha_{\phi-2}$	-0,550
Folk & Ward, Sk_i	-0,257

Coefficient d'acuité (Kurtosis)	
Krumbein & Petijohn, K	0,275
Inman, K_ϕ	0,749
Folk & Ward, K_G	1,024

Coefficient de courbure	
C_c	1,001

Analyse granulométrique par voie fluide : fraction 0,040 µm - 2000 µm

Echantillon :	INDONESIE/12/.LABAN/U-02/010/clay/T.YAN W.ISKANDARSYAH
Date :	9:58 23 Oct 2013
Opérateur :	MT
Fichier :	U02-010

Commentaires :	prof. 190-210 cm 27/05/12 Destruction MO à H2O2-élimination des ions floculants - Hexa+US

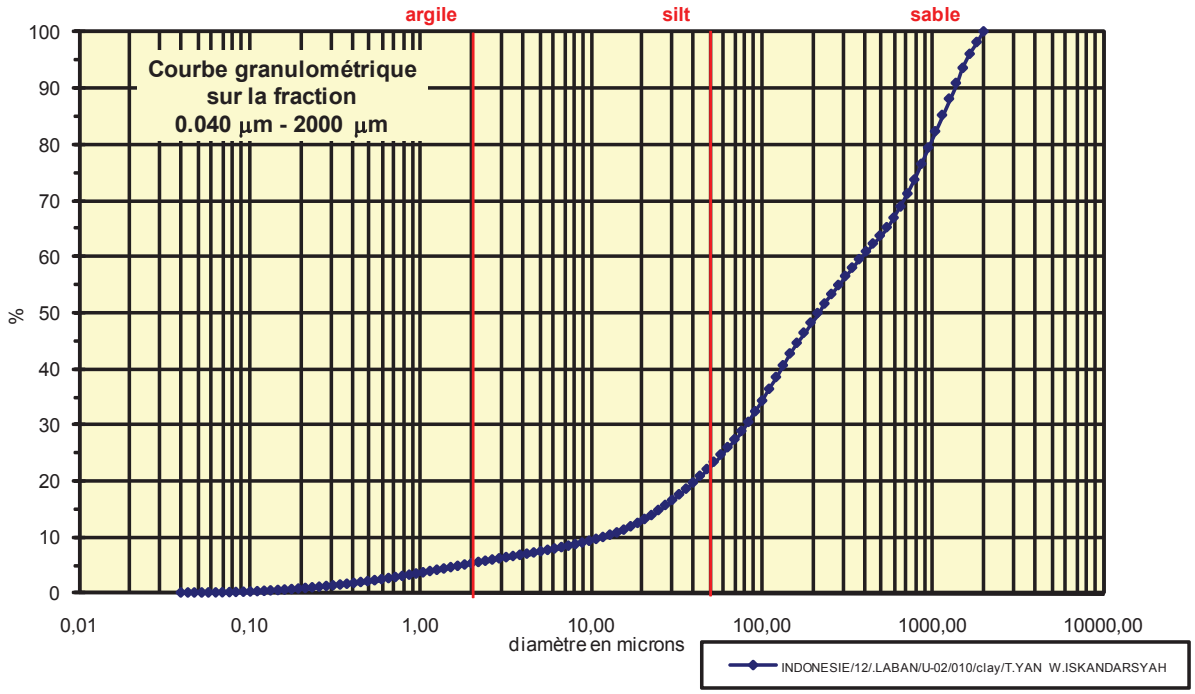

Fractiles	Taille (µm)	Taille (ϕ)
d_5	1,832	9,09
d_{10}	11,830	6,40
d_{16}	27,380	5,19
d_{25}	57,770	4,11
d_{30}	76,430	3,71
d_{50}	213,200	2,23
d_{60}	373,100	1,42
d_{75}	786,900	0,35
d_{84}	1041,000	-0,06
d_{90}	1255,000	-0,33
d_{95}	1512,000	-0,60

% Argile inférieur à 2µ	**A**	**4,99**
% Silts de 2µ à 50µ	**LT**	**17,01**
limons fins 2µ à 20µ	LF	7,41
limons grossiers 20µ à 50µ	LG	9,60
% Sables 50µ à 2000 µ	**ST**	**78,00**
sables fins 50µ à 200µ	SF	26,10
sables fins 50µ à 100µ	SF1	10,30
sables fins 100µ à 200 µ	SF2	15,80
sables grossiers 200µ à 2000µ	SG	51,90
sables grossiers 200µ à 500µ	SG1	15,50
sables grossiers 500µ à 1000µ	SG2	15,70
sables grossiers 1000µ à 2000µ	SG3	20,70

Indice de classement	
Trask, S_o	3,691
Krumbein, Q_d	-1,884
Inman, σ_ϕ	-2,624
Folk & Ward, σ_ϕ	-2,780
Hazen, C_u	31,538

Moyenne	
Trask, M	422,335
Inman, M_ϕ	2,566
Folk & Ward, M_z	2,454

Coefficient de dissymétrie	
Skew ness, S_{k-1}	1,000
Skew ness, S_{k-2}	1,000
Inman, $\alpha_{\phi-1}$	-0,128
Inman, $\alpha_{\phi-2}$	-0,769
Folk & Ward, Sk_i	-0,272

Coefficient d'acuité (Kurtosis)	
Krumbein & Petijohn, K	0,293
Inman, K_ϕ	0,846
Folk & Ward, K_G	1,054

Coefficient de courbure	
C_c	1,323

Analyse granulométrique par voie fluide : fraction 0,040 µm - 2000 µm

Echantillon :	INDONESIE/12/.LABAN/U-02/011/T.YAN W.ISKANDARSYAH
Date :	23/10/2013 10:12
Opérateur :	MT
Fichier :	U02-011

Commentaires :	prof. 210-240 cm 27/05/12 Destruction MO à H2O2-élimination des ions floculants - Hexa+US

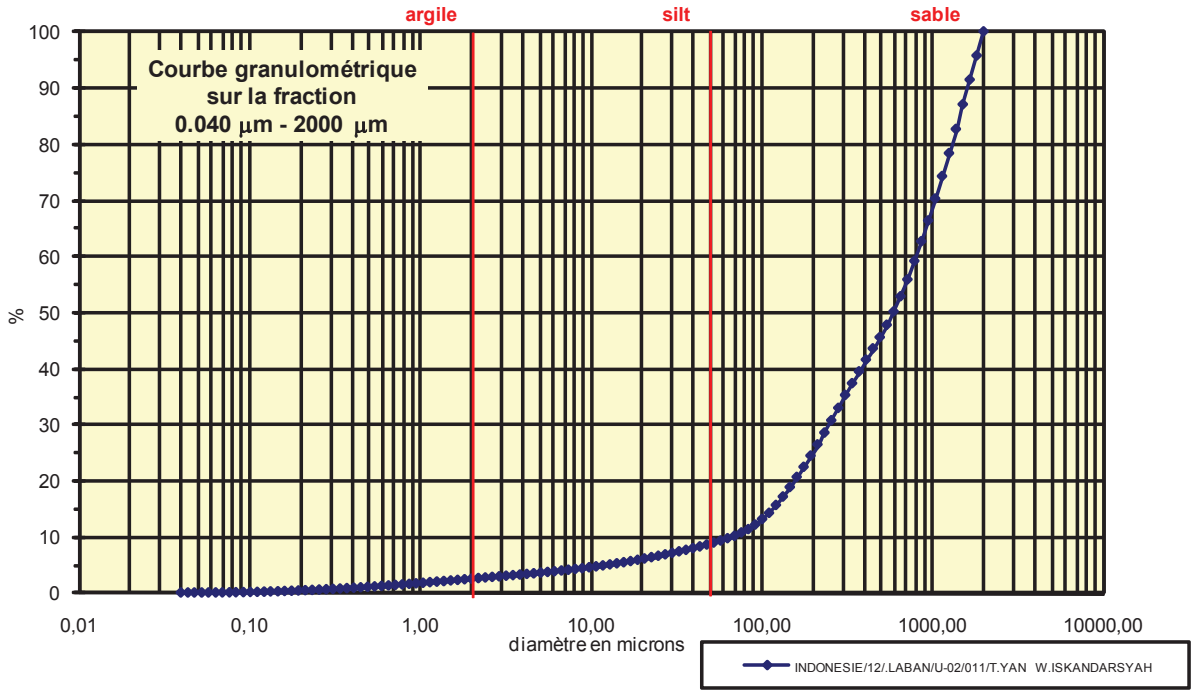

Fractiles	Taille (µm)	Taille (ϕ)
d_5	11,830	6,40
d_{10}	63,410	3,98
d_{16}	121,800	3,04
d_{25}	194,200	2,36
d_{30}	234,100	2,09
d_{50}	541,900	0,88
d_{60}	786,900	0,35
d_{75}	1143,000	-0,19
d_{84}	1377,000	-0,46
d_{90}	1512,000	-0,60
d_{95}	1660,000	-0,73

% Argile inférieur à 2µ	**A**	**2,36**
% Silts de 2µ à 50µ	**LT**	**6,19**
limons fins 2µ à 20µ	LF	3,47
limons grossiers 20µ à 50µ	LG	2,72
% Sables 50µ à 2000 µ	**ST**	**91,45**
sables fins 50µ à 200µ	SF	15,85
sables fins 50µ à 100µ	SF1	3,55
sables fins 100µ à 200 µ	SF2	12,30
sables grossiers 200µ à 2000µ	SG	75,60
sables grossiers 200µ à 500µ	SG1	21,10
sables grossiers 500µ à 1000µ	SG2	20,80
sables grossiers 1000µ à 2000µ	SG3	33,70

Indice de classement	
Trask, S_o	2,426
Krumbein, Q_d	-1,279
Inman, σ_ϕ	-1,749
Folk & Ward, σ_ϕ	-1,955
Hazen, C_u	12,410

Moyenne	
Trask, M	668,600
Inman, M_ϕ	1,288
Folk & Ward, M_z	1,153

Coefficient de dissymétrie	
Skew ness, S_{k-1}	0,756
Skew ness, S_{k-2}	0,869
Inman, $\alpha_{\phi-1}$	-0,231
Inman, $\alpha_{\phi-2}$	-1,115
Folk & Ward, Sk_I	-0,389

Coefficient d'acuité (Kurtosis)	
Krumbein & Petijohn, K	0,327
Inman, K_ϕ	1,038
Folk & Ward, K_G	1,143

Coefficient de courbure	
C_c	1,098

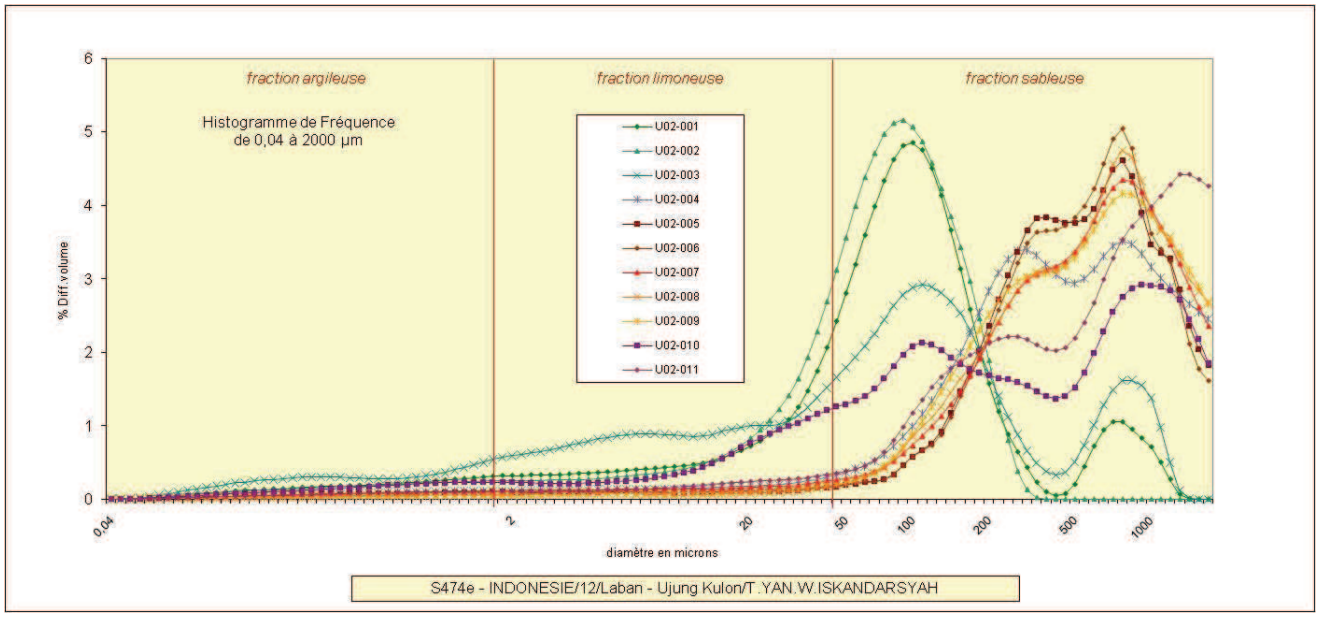
fraction argileuse
fraction limoneuse
fraction sableuse
Histogramme de Fréquence
de 0,04 à 2000 µm
U02-001
U02-002
U02-003
U02-004
U02-005
U02-006
U02-007
U02-008
U02-009
U02-010
U02-011
% Diff.volume
0
1
2
3
4
5
6
0,04
2
20
50
100
200
500
1000
diamètre en microns
S474e - INDONESIE/12/Laban - Ujung Kulon/T.YAN.W.ISKANDARSYAH

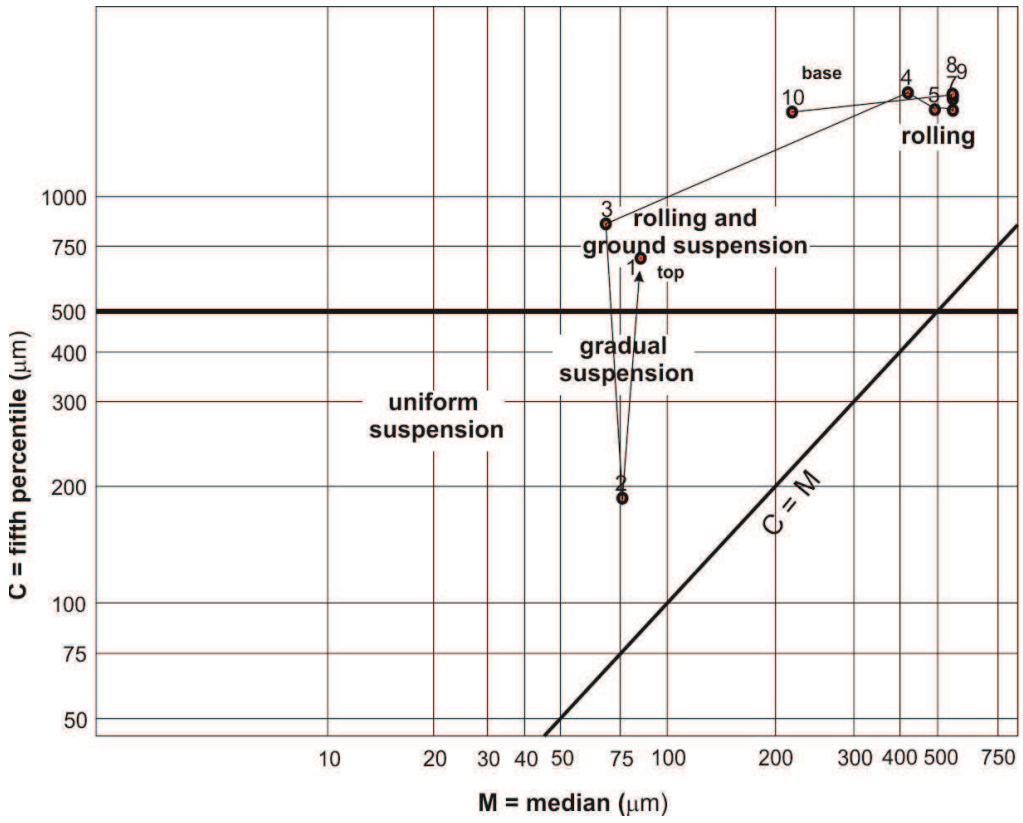
base
10
4
8
9
7
5
6
rolling
3
rolling and
ground suspension
1
top
gradual
suspension
uniform
suspension
2
C = M
1000
750
500
400
300
200
100
75
50
C = fifth percentile (μm)
10
20
30
40
50
75
100
200
300
400
500
750
M = median (μm)

Analyse granulométrique par voie fluide : fraction 0,040 µm - 2000 µm

Echantillon :	INDONESIE/12/LABAN/U-03/01/T.YAN W.ISKANDARSYAH
Date :	11/07/2013 16:04
Opérateur :	MT
Fichier :	U03-001

Commentaires :	prof. 0-15 cm 26/05/12 Destruction MO à H2O2-élimination des ions floculants - Hexa+US

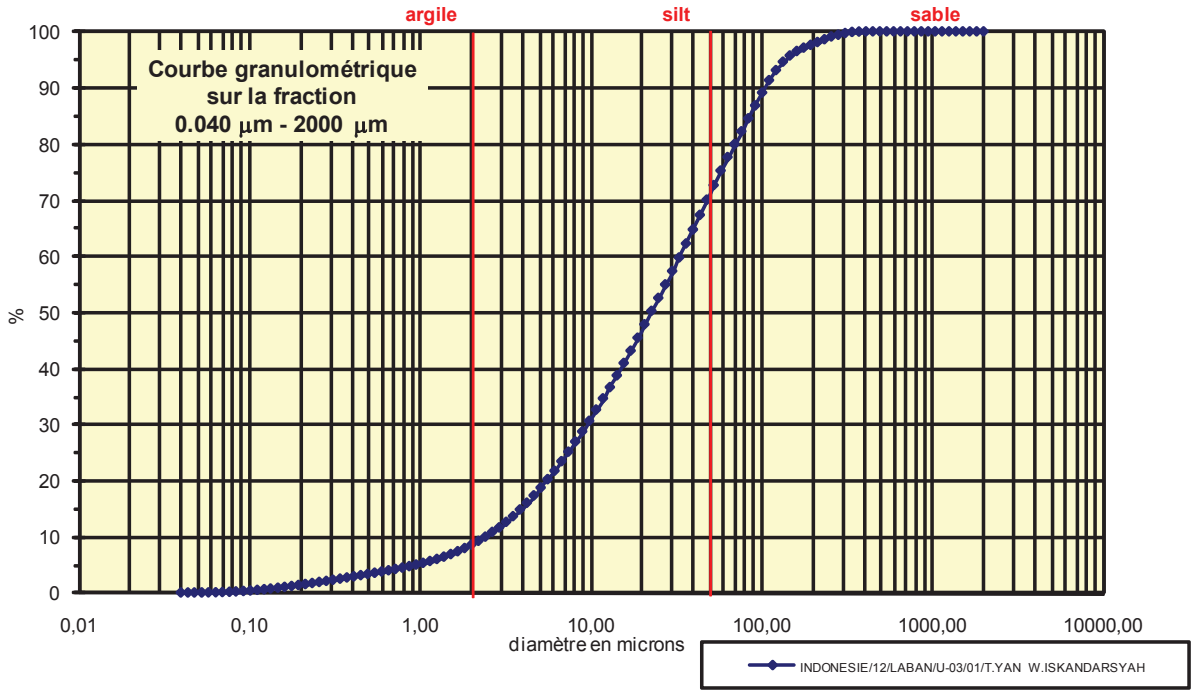

Fractiles	Taille (µm)	Taille (ϕ)
d_5	0,953	10,04
d_{10}	2,423	8,69
d_{16}	4,241	7,88
d_{25}	6,761	7,21
d_{30}	8,944	6,80
d_{50}	20,700	5,59
d_{60}	33,000	4,92
d_{75}	52,630	4,25
d_{84}	76,430	3,71
d_{90}	101,100	3,31
d_{95}	133,700	2,90

% Argile inférieur à 2µ	**A**	**7,92**
% Silts de 2µ à 50µ	**LT**	**62,08**
limons fins 2µ à 20µ	LF	37,48
limons grossiers 20µ à 50µ	LG	24,60
% Sables 50µ à 2000 µ	**ST**	**30,00**
sables fins 50µ à 200µ	SF	27,60
sables fins 50µ à 100µ	SF1	16,80
sables fins 100µ à 200 µ	SF2	10,80
sables grossiers 200µ à 2000µ	SG	2,40
sables grossiers 200µ à 500µ	SG1	2,40
sables grossiers 500µ à 1000µ	SG2	0,00
sables grossiers 1000µ à 2000µ	SG3	0,00

Indice de classement	
Trask, S_o	2,790
Krumbein, Q_d	-1,480
Inman, σ_ϕ	-2,086
Folk & Ward, σ_ϕ	-2,124
Hazen, C_u	13,619

Moyenne	
Trask, M	29,696
Inman, M_ϕ	5,796
Folk & Ward, M_z	5,728

Coefficient de dissymétrie	
Skew ness, S_{k-1}	0,830
Skew ness, S_{k-2}	0,911
Inman, $\alpha_{\phi-1}$	-0,097
Inman, $\alpha_{\phi-2}$	-0,419
Folk & Ward, Sk_I	-0,171

Coefficient d'acuité (Kurtosis)	
Krumbein & Petijohn, K	0,232
Inman, K_ϕ	0,710
Folk & Ward, K_G	0,987

Coefficient de courbure	
C_c	1,000

Analyse granulométrique par voie fluide : fraction 0,040 µm - 2000 µm

Echantillon :	INDONESIE/12/LABAN/U-03/02/T.YAN W.ISKANDARSYAH
Date :	11/07/2013 16:13
Opérateur :	MT
Fichier :	U03-002

Commentaires :	prof. 15-30 cm 26/05/12 Destruction MO à H2O2-élimination des ions floculants - Hexa+US

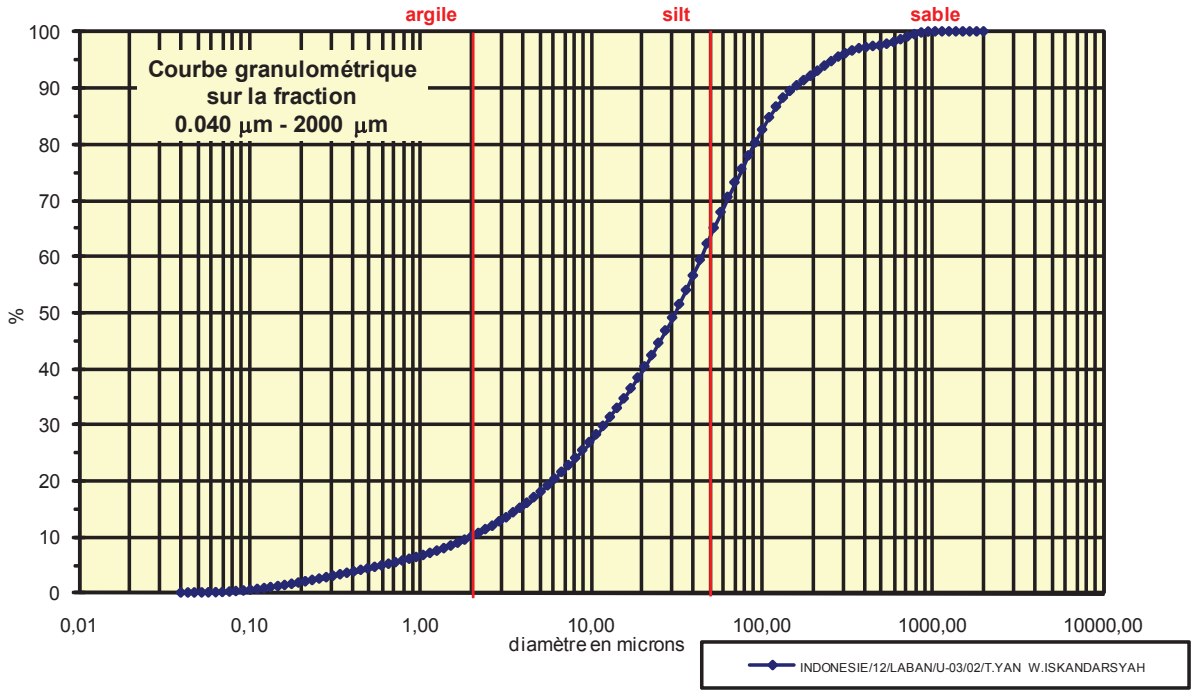

Fractiles	Taille (µm)	Taille (ϕ)
d_5	0,598	10,71
d_{10}	2,010	8,96
d_{16}	4,241	7,88
d_{25}	8,147	6,94
d_{30}	11,830	6,40
d_{50}	30,070	5,06
d_{60}	43,660	4,52
d_{75}	69,620	3,84
d_{84}	101,100	3,31
d_{90}	146,800	2,77
d_{95}	256,800	1,96

% Argile inférieur à 2µ	**A**	**9,42**
% Silts de 2µ à 50µ	**LT**	**52,78**
limons fins 2µ à 20µ	LF	28,88
limons grossiers 20µ à 50µ	LG	23,90
% Sables 50µ à 2000 µ	**ST**	**37,80**
sables fins 50µ à 200µ	SF	29,90
sables fins 50µ à 100µ	SF1	18,00
sables fins 100µ à 200 µ	SF2	11,90
sables grossiers 200µ à 2000µ	SG	7,90
sables grossiers 200µ à 500µ	SG1	5,40
sables grossiers 500µ à 1000µ	SG2	2,47
sables grossiers 1000µ à 2000µ	SG3	0,03

Indice de classement	
Trask, S_o	2,923
Krumbein, Q_d	-1,548
Inman, σ_ϕ	-2,288
Folk & Ward, σ_ϕ	-2,469
Hazen, C_u	21,721

Moyenne	
Trask, M	38,884
Inman, M_ϕ	5,594
Folk & Ward, M_z	5,414

Coefficient de dissymétrie	
Skew ness, S_{k-1}	0,627
Skew ness, S_{k-2}	0,792
Inman, $\alpha_{\phi-1}$	-0,235
Inman, $\alpha_{\phi-2}$	-0,559
Folk & Ward, Sk_i	-0,264

Coefficient d'acuité (Kurtosis)	
Krumbein & Petijohn, K	0,212
Inman, K_ϕ	0,912
Folk & Ward, K_G	1,158

Coefficient de courbure	
C_c	1,595

Analyse granulométrique par voie fluide : fraction 0,040 µm - 2000 µm

Echantillon :	INDONESIE/12/LABAN/U-03/03/T.YAN W.ISKANDARSYAH
Date :	11/07/2013 16:34
Opérateur :	MT
Fichier :	U03-003

Commentaires :	prof. 30-60 cm 26/05/12 Destruction MO à H2O2-élimination des ions floculants - Hexa+US

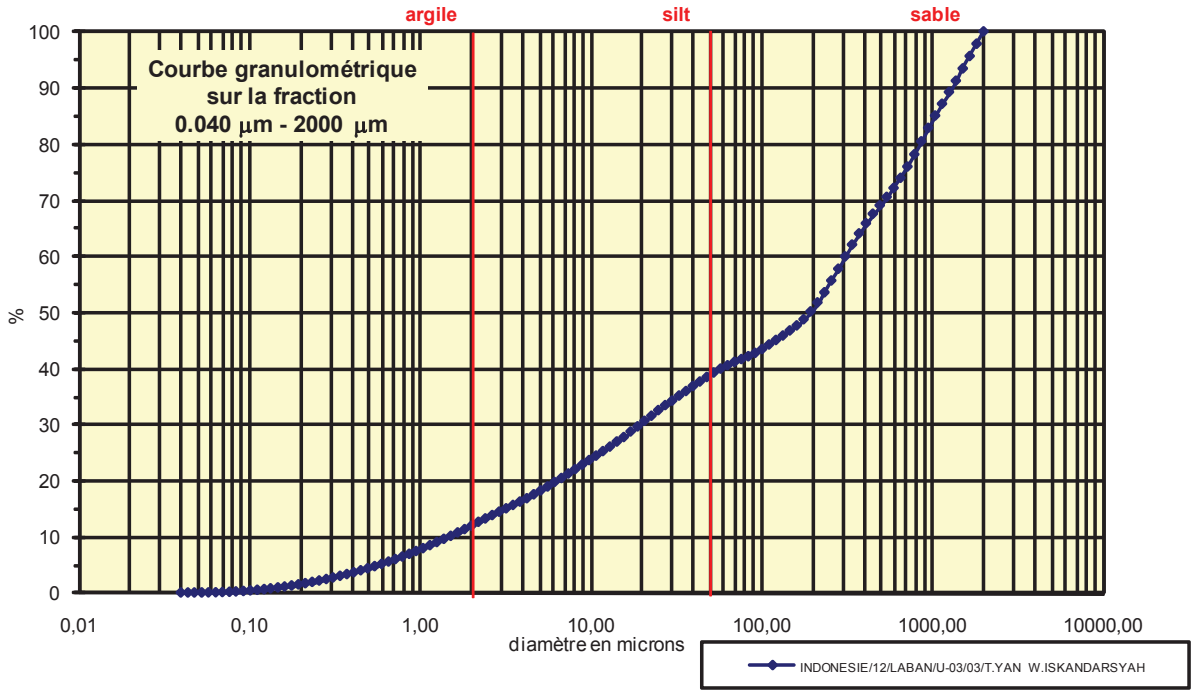

Fractiles	Taille (µm)	Taille (ϕ)
d_5	0,545	10,84
d_{10}	1,385	9,50
d_{16}	3,519	8,15
d_{25}	10,780	6,54
d_{30}	18,860	5,73
d_{50}	176,800	2,50
d_{60}	309,600	1,69
d_{75}	653,000	0,61
d_{84}	948,200	0,08
d_{90}	1255,000	-0,33
d_{95}	1512,000	-0,60

% Argile inférieur à 2µ	**A**	**11,30**
% Silts de 2µ à 50µ	**LT**	**27,10**
limons fins 2µ à 20µ	LF	18,30
limons grossiers 20µ à 50µ	LG	8,80
% Sables 50µ à 2000 µ	**ST**	**61,60**
sables fins 50µ à 200µ	SF	11,70
sables fins 50µ à 100µ	SF1	4,30
sables fins 100µ à 200 µ	SF2	7,40
sables grossiers 200µ à 2000µ	SG	49,90
sables grossiers 200µ à 500µ	SG1	18,90
sables grossiers 500µ à 1000µ	SG2	13,80
sables grossiers 1000µ à 2000µ	SG3	17,20

Indice de classement	
Trask, S_o	7,783
Krumbein, Q_d	-2,960
Inman, σ_ϕ	-4,037
Folk & Ward, σ_ϕ	-3,751
Hazen, C_u	223,538

Moyenne	
Trask, M	331,890
Inman, M_ϕ	4,114
Folk & Ward, M_z	3,576

Coefficient de dissymétrie	
Skew ness, S_{k-1}	0,225
Skew ness, S_{k-2}	0,475
Inman, $\alpha_{\phi-1}$	-0,400
Inman, $\alpha_{\phi-2}$	-0,650
Folk & Ward, Sk_I	-0,429

Coefficient d'acuité (Kurtosis)	
Krumbein & Petijohn, K	0,256
Inman, K_ϕ	0,417
Folk & Ward, K_G	0,792

Coefficient de courbure	
C_c	0,830

Analyse granulométrique par voie fluide : fraction 0,040 µm - 2000 µm

Echantillon :	INDONESIE/12/LABAN/U-03/04/T.YAN W.ISKANDARSYAH
Date :	11/07/2013 16:45
Opérateur :	MT
Fichier :	U03-004

Commentaires :	prof. 60-90 cm 26/05/12 Destruction MO à H2O2-élimination des ions floculants - Hexa+US

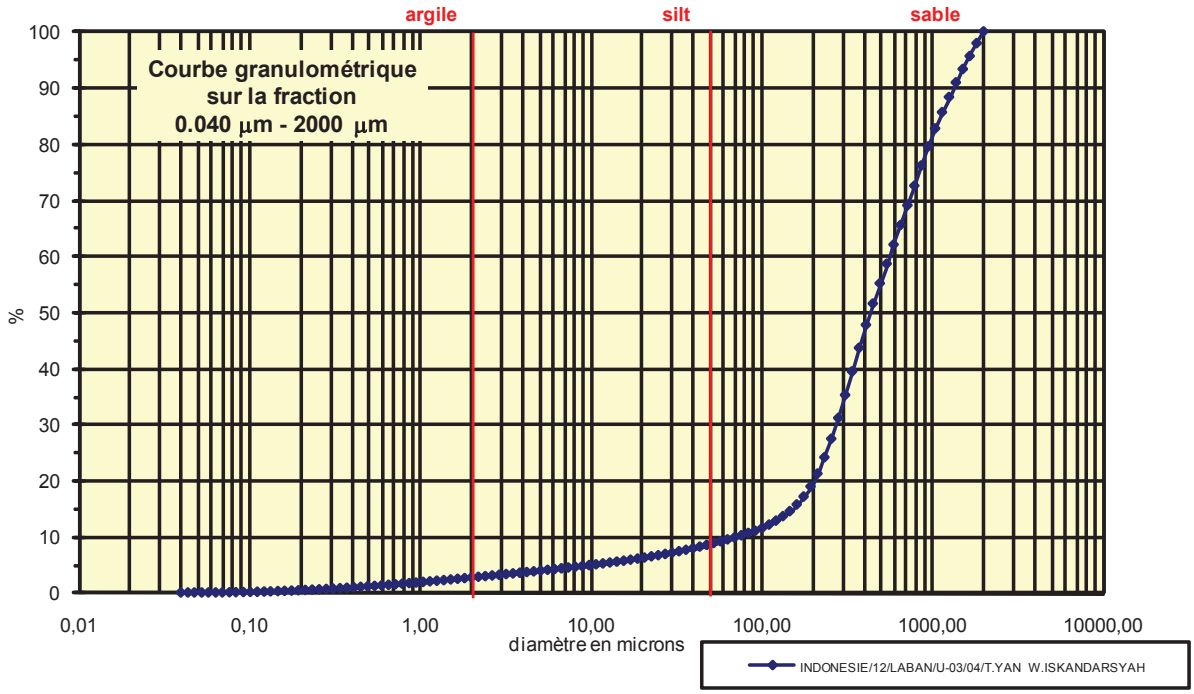

Fractiles	Taille (µm)	Taille (ϕ)
d_5	9,819	6,67
d_{10}	69,620	3,84
d_{16}	161,200	2,63
d_{25}	234,100	2,09
d_{30}	256,800	1,96
d_{50}	409,600	1,29
d_{60}	541,900	0,88
d_{75}	786,900	0,35
d_{84}	1041,000	-0,06
d_{90}	1255,000	-0,33
d_{95}	1512,000	-0,60

% Argile inférieur à 2µ	**A**	**2,56**
% Silts de 2µ à 50µ	**LT**	**5,93**
limons fins 2µ à 20µ	LF	3,48
limons grossiers 20µ à 50µ	LG	2,45
% Sables 50µ à 2000 µ	**ST**	**91,51**
sables fins 50µ à 200µ	SF	10,41
sables fins 50µ à 100µ	SF1	2,51
sables fins 100µ à 200 µ	SF2	7,90
sables grossiers 200µ à 2000µ	SG	81,10
sables grossiers 200µ à 500µ	SG1	36,20
sables grossiers 500µ à 1000µ	SG2	24,40
sables grossiers 1000µ à 2000µ	SG3	20,50

Indice de classement	
Trask, S_o	1,833
Krumbein, Q_d	-0,875
Inman, σ_ϕ	-1,346
Folk & Ward, σ_ϕ	-1,774
Hazen, C_u	7,784

Moyenne	
Trask, M	510,500
Inman, M_ϕ	1,288
Folk & Ward, M_z	1,288

Coefficient de dissymétrie	
Skew ness, S_{k-1}	1,098
Skew ness, S_{k-2}	1,048
Inman, $\alpha_{\phi-1}$	0,000
Inman, $\alpha_{\phi-2}$	-1,300
Folk & Ward, Sk_I	-0,241

Coefficient d'acuité (Kurtosis)	
Krumbein & Petijohn, K	0,233
Inman, K_ϕ	1,700
Folk & Ward, K_G	1,703

Coefficient de courbure	
C_c	1,748

Analyse granulométrique par voie fluide : fraction 0,040 µm - 2000 µm

Echantillon :	INDONESIE/12/LABAN/U-03/05/T.YAN W.ISKANDARSYAH
Date :	11/07/2013 16:53
Opérateur :	MT
Fichier :	U03-005

Commentaires :	prof. 90-120 cm 26/05/12 Destruction MO à H2O2-élimination des ions floculants - Hexa+US

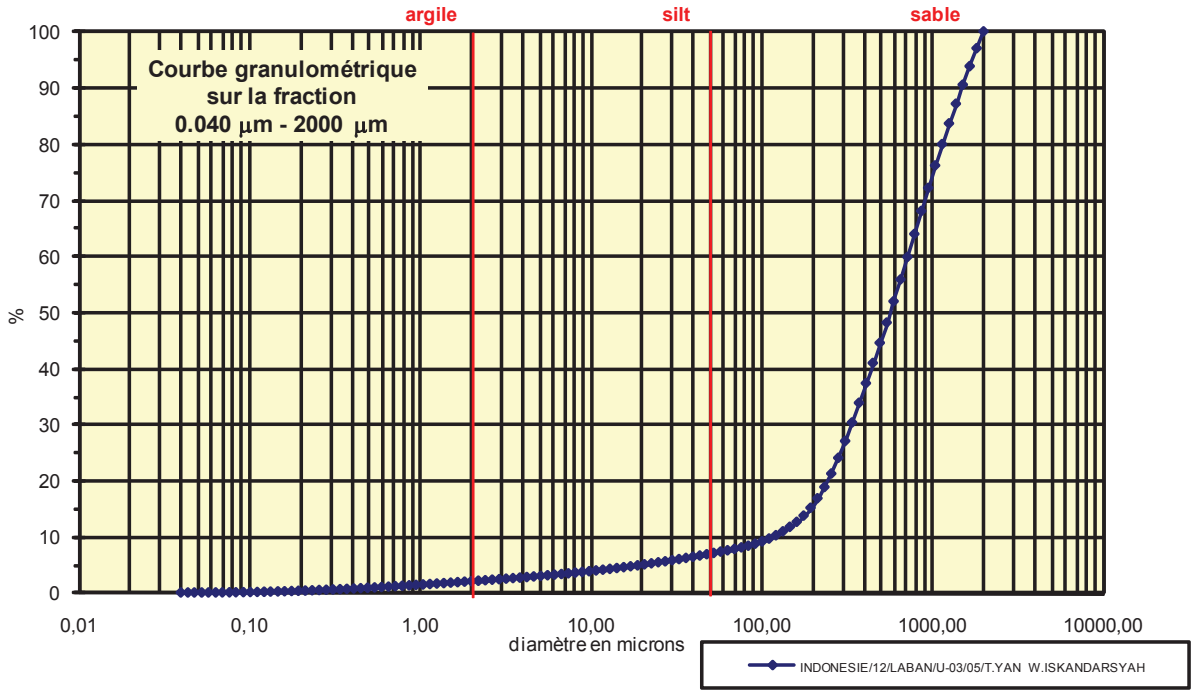

Fractiles	Taille (µm)	Taille (ϕ)
d_5	18,860	5,73
d_{10}	111,000	3,17
d_{16}	194,200	2,36
d_{25}	282,100	1,83
d_{30}	309,600	1,69
d_{50}	541,900	0,88
d_{60}	716,900	0,48
d_{75}	948,200	0,08
d_{84}	1255,000	-0,33
d_{90}	1377,000	-0,46
d_{95}	1660,000	-0,73

% Argile inférieur à 2µ	**A**	**1,93**
% Silts de 2µ à 50µ	**LT**	**4,89**
limons fins 2µ à 20µ	LF	2,91
limons grossiers 20µ à 50µ	LG	1,98
% Sables 50µ à 2000 µ	**ST**	**93,18**
sables fins 50µ à 200µ	SF	8,28
sables fins 50µ à 100µ	SF1	1,88
sables fins 100µ à 200 µ	SF2	6,40
sables grossiers 200µ à 2000µ	SG	84,90
sables grossiers 200µ à 500µ	SG1	29,40
sables grossiers 500µ à 1000µ	SG2	27,60
sables grossiers 1000µ à 2000µ	SG3	27,90

Indice de classement	
Trask, S_o	1,833
Krumbein, Q_d	-0,874
Inman, σ_ϕ	-1,346
Folk & Ward, σ_ϕ	-1,652
Hazen, C_u	6,459

Moyenne	
Trask, M	615,150
Inman, M_ϕ	1,018
Folk & Ward, M_z	0,974

Coefficient de dissymétrie	
Skew ness, S_{k-1}	0,911
Skew ness, S_{k-2}	0,954
Inman, $\alpha_{\phi-1}$	-0,100
Inman, $\alpha_{\phi-2}$	-1,200
Folk & Ward, Sk_I	-0,300

Coefficient d'acuité (Kurtosis)	
Krumbein & Petijohn, K	0,263
Inman, K_ϕ	1,400
Folk & Ward, K_G	1,514

Coefficient de courbure	
C_c	1,205

Analyse granulométrique par voie fluide : fraction 0,040 µm - 2000 µm

Echantillon :	INDONESIE/12/LABAN/U-03/06/T.YAN W.ISKANDARSYAH
Date :	11/07/2013 17:04
Opérateur :	MT
Fichier :	U03-006

Commentaires :	prof. 120-130 cm 26/05/12 Destruction MO à H2O2-élimination des ions floculants - Hexa+US

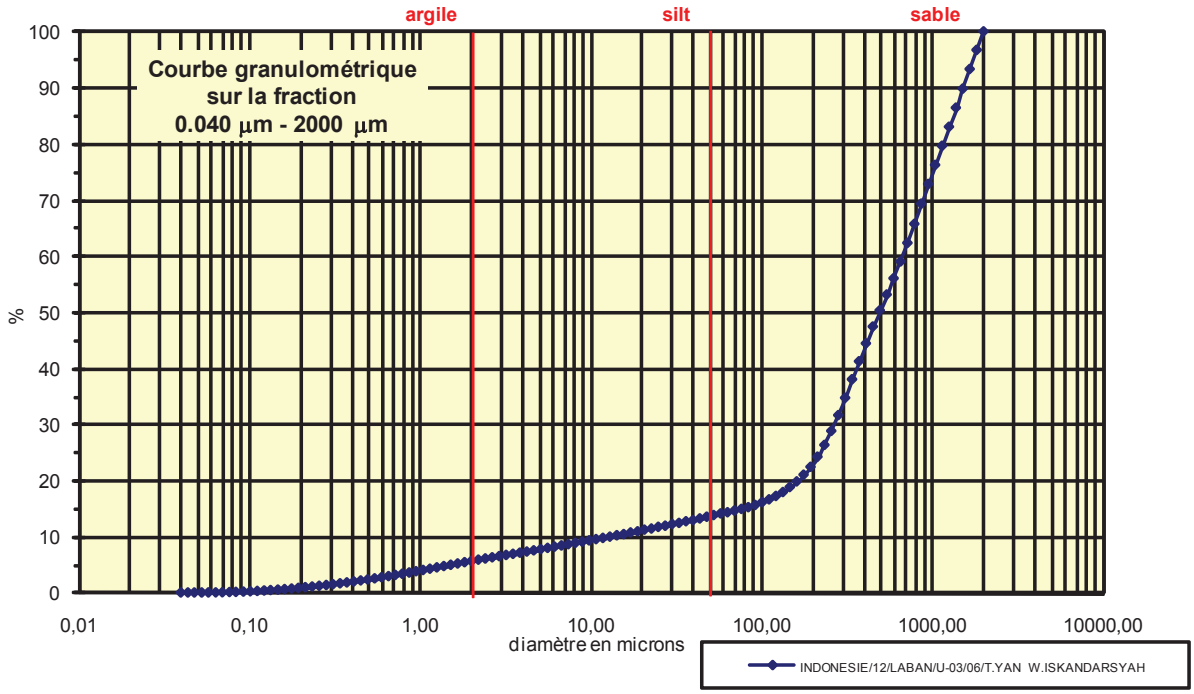

Fractiles	Taille (µm)	Taille (ϕ)
d_5	1,520	9,36
d_{10}	12,990	6,27
d_{16}	92,090	3,44
d_{25}	213,200	2,23
d_{30}	256,800	1,96
d_{50}	449,700	1,15
d_{60}	653,000	0,61
d_{75}	948,200	0,08
d_{84}	1255,000	-0,33
d_{90}	1512,000	-0,60
d_{95}	1660,000	-0,73

% Argile inférieur à 2µ	**A**	**5,40**
% Silts de 2µ à 50µ	**LT**	**8,10**
limons fins 2µ à 20µ	LF	5,50
limons grossiers 20µ à 50µ	LG	2,60
% Sables 50µ à 2000 µ	**ST**	**86,50**
sables fins 50µ à 200µ	SF	8,90
sables fins 50µ à 100µ	SF1	2,10
sables fins 100µ à 200 µ	SF2	6,80
sables grossiers 200µ à 2000µ	SG	77,60
sables grossiers 200µ à 500µ	SG1	27,90
sables grossiers 500µ à 1000µ	SG2	22,50
sables grossiers 1000µ à 2000µ	SG3	27,20

Indice de classement	
Trask, S_o	2,109
Krumbein, Q_d	-1,076
Inman, σ_ϕ	-1,884
Folk & Ward, σ_ϕ	-2,471
Hazen, C_u	50,269

Moyenne	
Trask, M	580,700
Inman, M_ϕ	1,557
Folk & Ward, M_z	1,422

Coefficient de dissymétrie	
Skew ness, S_{k-1}	1,000
Skew ness, S_{k-2}	1,000
Inman, $\alpha_{\phi-1}$	-0,214
Inman, $\alpha_{\phi-2}$	-1,678
Folk & Ward, Sk_I	-0,420

Coefficient d'acuité (Kurtosis)	
Krumbein & Petijohn, K	0,245
Inman, K_ϕ	1,678
Folk & Ward, K_G	1,921

Coefficient de courbure	
C_c	7,774

Analyse granulométrique par voie fluide : fraction 0,040 µm - 2000 µm

Echantillon :	INDONESIE/12/LABAN/U-03/07/T.YAN W.ISKANDARSYAH
Date :	11/07/2013 17:13
Opérateur :	MT
Fichier :	U03-007

Commentaires :	prof. 130-150 cm 26/05/12 Destruction MO à H2O2-élimination des ions floculants - Hexa+US

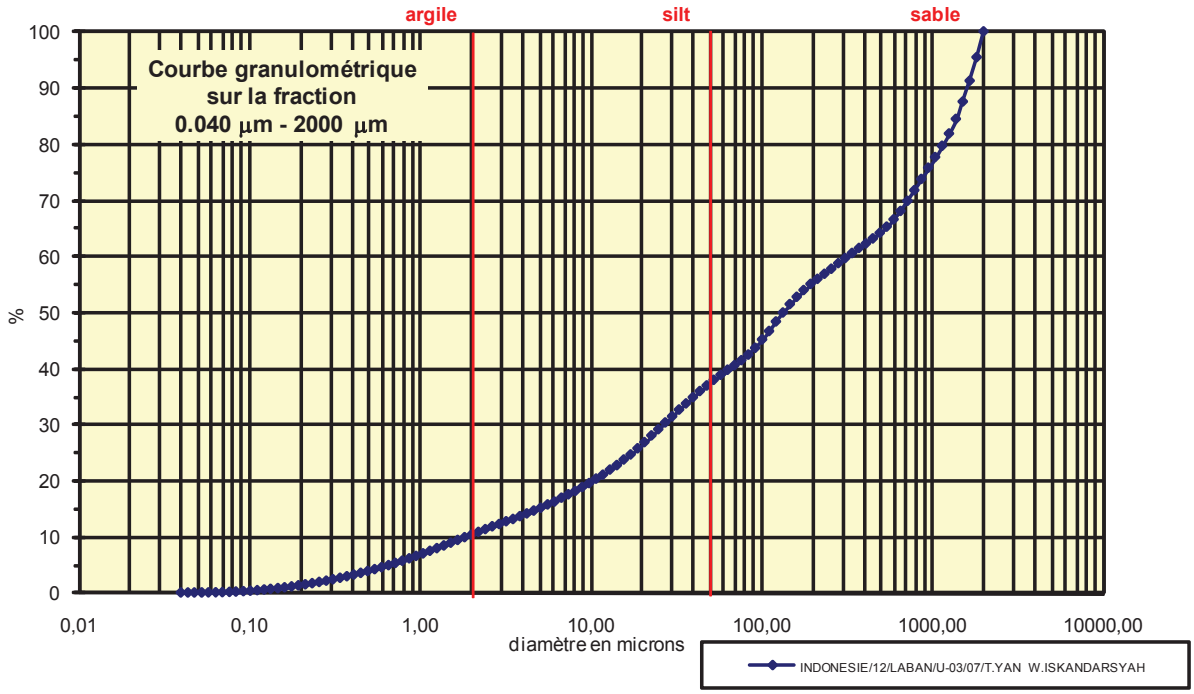

Fractiles	Taille (µm)	Taille (ϕ)
d_5	0,657	10,57
d_{10}	1,832	9,09
d_{16}	5,611	7,48
d_{25}	17,180	5,86
d_{30}	24,950	5,32
d_{50}	133,700	2,90
d_{60}	309,600	1,69
d_{75}	863,900	0,21
d_{84}	1255,000	-0,33
d_{90}	1512,000	-0,60
d_{95}	1660,000	-0,73

% Argile inférieur à 2µ	**A**	**9,86**
% Silts de 2µ à 50µ	**LT**	**27,04**
limons fins 2µ à 20µ	LF	15,84
limons grossiers 20µ à 50µ	LG	11,20
% Sables 50µ à 2000 µ	**ST**	**63,10**
sables fins 50µ à 200µ	SF	18,10
sables fins 50µ à 100µ	SF1	6,70
sables fins 100µ à 200 µ	SF2	11,40
sables grossiers 200µ à 2000µ	SG	45,00
sables grossiers 200µ à 500µ	SG1	9,10
sables grossiers 500µ à 1000µ	SG2	11,60
sables grossiers 1000µ à 2000µ	SG3	24,30

Indice de classement	
Trask, S_o	7,091
Krumbein, Q_d	-2,826
Inman, σ_ϕ	-3,903
Folk & Ward, σ_ϕ	-3,664
Hazen, C_u	168,996

Moyenne	
Trask, M	440,540
Inman, M_ϕ	3,575
Folk & Ward, M_z	3,351

Coefficient de dissymétrie	
Skew ness, S_{k-1}	0,830
Skew ness, S_{k-2}	0,911
Inman, $\alpha_{\phi-1}$	-0,172
Inman, $\alpha_{\phi-2}$	-0,517
Folk & Ward, Sk_I	-0,265

Coefficient d'acuité (Kurtosis)	
Krumbein & Petijohn, K	0,280
Inman, K_ϕ	0,448
Folk & Ward, K_G	0,820

Coefficient de courbure	
C_c	1,098

Analyse granulométrique par voie fluide : fraction 0,040 µm - 2000 µm

Echantillon :	INDONESIE/12/LABAN/U-03/08/T.YAN W.ISKANDARSYAH
Date :	11/07/2013 17:26
Opérateur :	MT
Fichier :	U03-008

Commentaires :	prof. 150-170 cm 26/05/12 Destruction MO à H2O2-élimination des ions floculants - Hexa+US

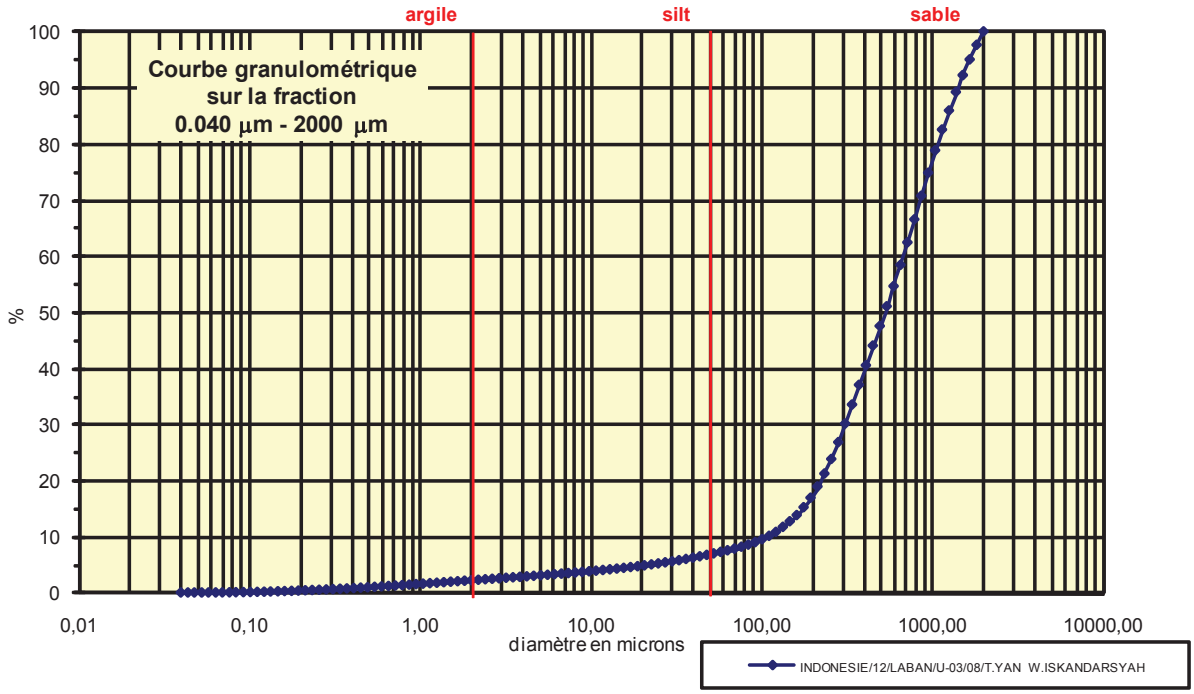

Fractiles	Taille (µm)	Taille (ϕ)
d_5	20,700	5,59
d_{10}	101,100	3,31
d_{16}	176,800	2,50
d_{25}	256,800	1,96
d_{30}	282,100	1,83
d_{50}	493,600	1,02
d_{60}	653,000	0,61
d_{75}	948,200	0,08
d_{84}	1143,000	-0,19
d_{90}	1377,000	-0,46
d_{95}	1660,000	-0,73

% Argile inférieur à 2µ	**A**	**2,10**
% Silts de 2µ à 50µ	**LT**	**4,60**
limons fins 2µ à 20µ	LF	2,58
limons grossiers 20µ à 50µ	LG	2,02
% Sables 50µ à 2000 µ	**ST**	**93,30**
sables fins 50µ à 200µ	SF	10,20
sables fins 50µ à 100µ	SF1	2,28
sables fins 100µ à 200 µ	SF2	7,92
sables grossiers 200µ à 2000µ	SG	83,10
sables grossiers 200µ à 500µ	SG1	30,60
sables grossiers 500µ à 1000µ	SG2	27,30
sables grossiers 1000µ à 2000µ	SG3	25,20

Indice de classement	
Trask, S_o	1,922
Krumbein, Q_d	-0,942
Inman, σ_ϕ	-1,346
Folk & Ward, σ_ϕ	-1,632
Hazen, C_u	6,459

Moyenne	
Trask, M	602,500
Inman, M_ϕ	1,153
Folk & Ward, M_z	1,109

Coefficient de dissymétrie	
Skew ness, S_{k-1}	0,999
Skew ness, S_{k-2}	1,000
Inman, $\alpha_{\phi-1}$	-0,100
Inman, $\alpha_{\phi-2}$	-1,049
Folk & Ward, Sk_I	-0,273

Coefficient d'acuité (Kurtosis)	
Krumbein & Petijohn, K	0,271
Inman, K_ϕ	1,349
Folk & Ward, K_G	1,376

Coefficient de courbure	
C_c	1,205

Analyse granulométrique par voie fluide : fraction 0,040 µm - 2000 µm

Echantillon :	INDONESIE/12/LABAN/U-03/009/T.YAN W.ISKANDARSYAH
Date :	22/10/2013 14:14
Opérateur :	MT
Fichier :	U03-009

Commentaires :	prof. 170-180 cm 26/05/12 Destruction MO à H2O2-élimination des ions floculants - Hexa+US

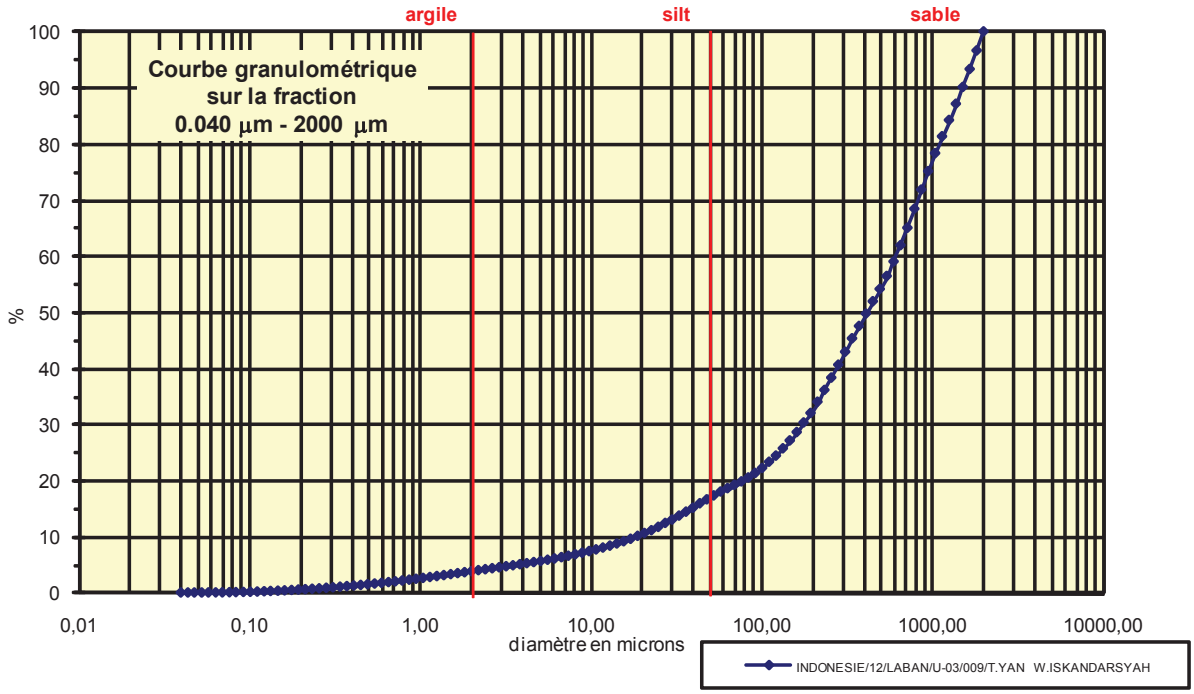

Fractiles	Taille (µm)	Taille (ϕ)
d_5	3,519	8,15
d_{10}	17,180	5,86
d_{16}	43,660	4,52
d_{25}	121,800	3,04
d_{30}	161,200	2,63
d_{50}	409,600	1,29
d_{60}	594,900	0,75
d_{75}	863,900	0,21
d_{84}	1143,000	-0,19
d_{90}	1377,000	-0,46
d_{95}	1660,000	-0,73

% Argile inférieur à 2µ	**A**	**3,62**
% Silts de 2µ à 50µ	**LT**	**12,98**
limons fins 2µ à 20µ	LF	6,48
limons grossiers 20µ à 50µ	LG	6,50
% Sables 50µ à 2000 µ	**ST**	**83,40**
sables fins 50µ à 200µ	SF	15,40
sables fins 50µ à 100µ	SF1	4,70
sables fins 100µ à 200 µ	SF2	10,70
sables grossiers 200µ à 2000µ	SG	68,00
sables grossiers 200µ à 500µ	SG1	22,10
sables grossiers 500µ à 1000µ	SG2	21,00
sables grossiers 1000µ à 2000µ	SG3	24,90

Indice de classement	
Trask, S_o	2,663
Krumbein, Q_d	-1,413
Inman, σ_ϕ	-2,355
Folk & Ward, σ_ϕ	-2,523
Hazen, C_u	34,627

Moyenne	
Trask, M	492,850
Inman, M_ϕ	2,162
Folk & Ward, M_z	1,871

Coefficient de dissymétrie	
Skew ness, S_{k-1}	0,627
Skew ness, S_{k-2}	0,792
Inman, $\alpha_{\phi-1}$	-0,371
Inman, $\alpha_{\phi-2}$	-1,028
Folk & Ward, Sk_I	-0,458

Coefficient d'acuité (Kurtosis)	
Krumbein & Petijohn, K	0,273
Inman, K_ϕ	0,886
Folk & Ward, K_G	1,288

Coefficient de courbure	
C_c	2,543

Analyse granulométrique par voie fluide : fraction 0,040 µm - 2000 µm

Echantillon :	INDONESIE/12/LABAN/U-03/010/sand/T.YAN W.ISKANDARSYAH
Date :	22/10/2013 18:48
Opérateur :	MT
Fichier :	U03-010

Commentaires :	prof. 180-210 cm 26/05/12 Destruction MO à H2O2-élimination des ions floculants - Hexa+US

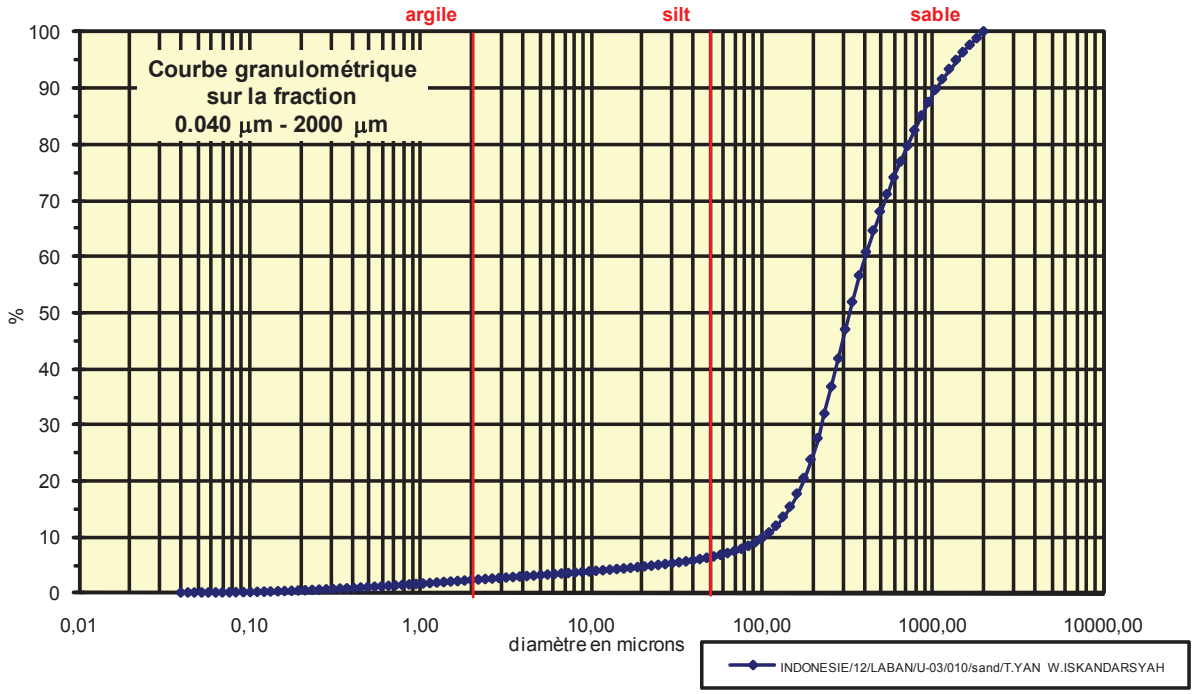

Fractiles	Taille (µm)	Taille (ϕ)
d_5	24,950	5,32
d_{10}	101,100	3,31
d_{16}	146,800	2,77
d_{25}	194,200	2,36
d_{30}	213,200	2,23
d_{50}	309,600	1,69
d_{60}	373,100	1,42
d_{75}	594,900	0,75
d_{84}	786,900	0,35
d_{90}	1041,000	-0,06
d_{95}	1377,000	-0,46

% Argile inférieur à 2µ	**A**	**2,13**
% Silts de 2µ à 50µ	**LT**	**4,05**
limons fins 2µ à 20µ	LF	2,39
limons grossiers 20µ à 50µ	LG	1,66
% Sables 50µ à 2000 µ	**ST**	**93,82**
sables fins 50µ à 200µ	SF	17,52
sables fins 50µ à 100µ	SF1	2,77
sables fins 100µ à 200 µ	SF2	14,75
sables grossiers 200µ à 2000µ	SG	76,30
sables grossiers 200µ à 500µ	SG1	44,20
sables grossiers 500µ à 1000µ	SG2	19,50
sables grossiers 1000µ à 2000µ	SG3	12,60

Indice de classement	
Trask, S_o	1,750
Krumbein, Q_d	-0,808
Inman, σ_ϕ	-1,211
Folk & Ward, σ_ϕ	-1,482
Hazen, C_u	3,690

Moyenne	
Trask, M	394,550
Inman, M_ϕ	1,557
Folk & Ward, M_z	1,602

Coefficient de dissymétrie	
Skew ness, S_{k1}	1,205
Skew ness, S_{k2}	1,098
Inman, $\alpha_{\phi-1}$	0,111
Inman, $\alpha_{\phi-2}$	-0,611
Folk & Ward, Sk_I	-0,072

Coefficient d'acuité (Kurtosis)	
Krumbein & Petijohn, K	0,213
Inman, K_ϕ	1,389
Folk & Ward, K_G	1,468

Coefficient de courbure	
C_c	1,205

Analyse granulométrique par voie fluide : fraction 0,040 µm - 2000 µm

Echantillon :	INDONESIE/12/LABAN/U-03/011/clay/T.YAN W.ISKANDARSYAH
Date :	22/10/2013 18:40
Opérateur :	MT
Fichier :	U03-011

Commentaires :	prof. 180-210 cm 26/05/12 Destruction MO à H2O2-élimination des ions floculants - Hexa+US

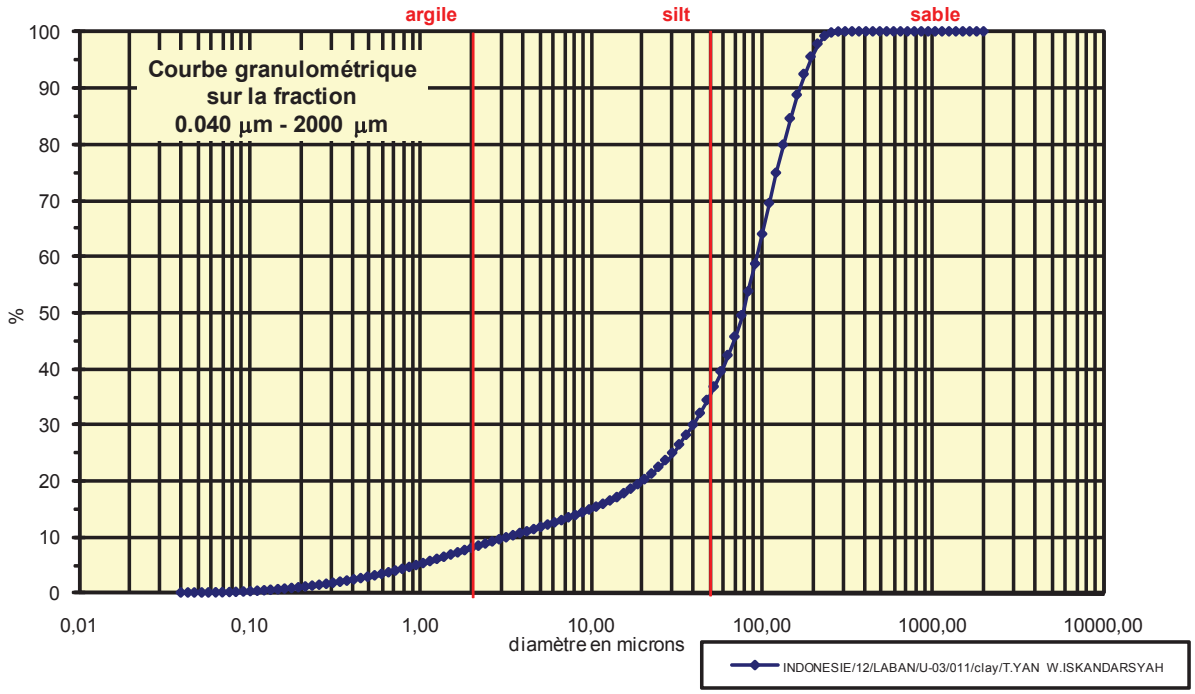

Fractiles	Taille (µm)	Taille (ϕ)
d_5	0,953	10,04
d_{10}	3,206	8,29
d_{16}	11,830	6,40
d_{25}	30,070	5,06
d_{30}	39,770	4,65
d_{50}	76,430	3,71
d_{60}	92,090	3,44
d_{75}	121,800	3,04
d_{84}	133,700	2,90
d_{90}	161,200	2,63
d_{95}	176,800	2,50

% Argile inférieur à 2µ	**A**	**7,56**
% Silts de 2µ à 50µ	**LT**	**26,74**
limons fins 2µ à 20µ	LF	11,74
limons grossiers 20µ à 50µ	LG	15,00
% Sables 50µ à 2000 µ	**ST**	**65,70**
sables fins 50µ à 200µ	SF	61,20
sables fins 50µ à 100µ	SF1	24,30
sables fins 100µ à 200 µ	SF2	36,90
sables grossiers 200µ à 2000µ	SG	4,50
sables grossiers 200µ à 500µ	SG1	4,50
sables grossiers 500µ à 1000µ	SG2	0,00
sables grossiers 1000µ à 2000µ	SG3	0,00

Indice de classement	
Trask, S_o	2,013
Krumbein, Q_d	-1,009
Inman, σ_ϕ	-1,749
Folk & Ward, σ_ϕ	-2,016
Hazen, C_u	28,724

Moyenne	
Trask, M	75,935
Inman, M_ϕ	4,652
Folk & Ward, M_z	4,338

Coefficient de dissymétrie	
Skew ness, S_{k-1}	0,627
Skew ness, S_{k-2}	0,792
Inman, $\alpha_{\phi-1}$	-0,539
Inman, $\alpha_{\phi-2}$	-1,462
Folk & Ward, Sk_i	-0,609

Coefficient d'acuité (Kurtosis)	
Krumbein & Petijohn, K	0,290
Inman, K_ϕ	1,154
Folk & Ward, K_G	1,530

Coefficient de courbure	
C_c	5,357

Analyse granulométrique par voie fluide : fraction 0,040 µm - 2000 µm

Echantillon :	INDONESIE/12/LABAN/U-03/012/A/T.YAN W.ISKANDARSYAH
Date :	22/10/2013 14:22
Opérateur :	MT
Fichier :	U03-012

Commentaires :	prof. 210-225 cm 26/05/12 Destruction MO à H2O2-élimination des ions floculants - Hexa+US

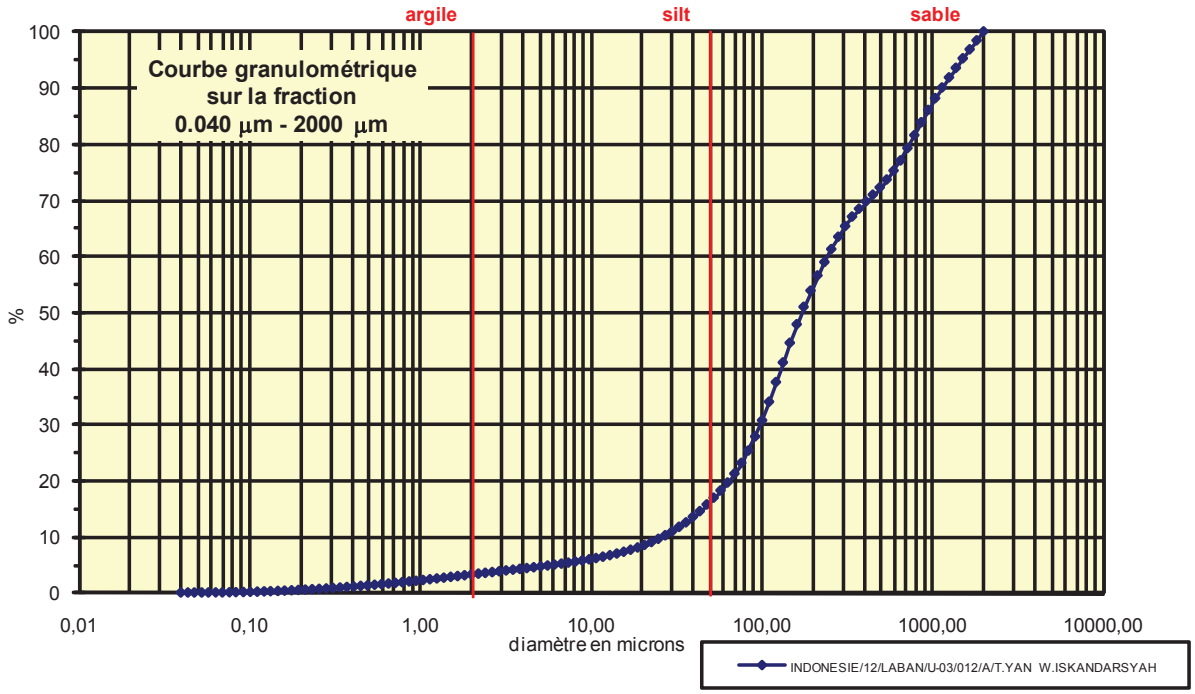

Fractiles	Taille (µm)	Taille (ϕ)
d_5	6,158	7,34
d_{10}	24,950	5,32
d_{16}	47,930	4,38
d_{25}	76,430	3,71
d_{30}	92,090	3,44
d_{50}	161,200	2,63
d_{60}	234,100	2,09
d_{75}	541,900	0,88
d_{84}	863,900	0,21
d_{90}	1143,000	-0,19
d_{95}	1377,000	-0,46

% Argile inférieur à 2µ	**A**	**3,07**
% Silts de 2µ à 50µ	**LT**	**12,63**
limons fins 2µ à 20µ	LF	4,96
limons grossiers 20µ à 50µ	LG	7,67
% Sables 50µ à 2000 µ	**ST**	**84,30**
sables fins 50µ à 200µ	SF	38,10
sables fins 50µ à 100µ	SF1	12,10
sables fins 100µ à 200 µ	SF2	26,00
sables grossiers 200µ à 2000µ	SG	46,20
sables grossiers 200µ à 500µ	SG1	18,40
sables grossiers 500µ à 1000µ	SG2	13,80
sables grossiers 1000µ à 2000µ	SG3	14,00

Indice de classement	
Trask, S_o	2,663
Krumbein, Q_d	-1,413
Inman, σ_ϕ	-2,086
Folk & Ward, σ_ϕ	-2,226
Hazen, C_u	9,383

Moyenne	
Trask, M	309,165
Inman, M_ϕ	2,297
Folk & Ward, M_z	2,409

Coefficient de dissymétrie	
Skew ness, S_{k-1}	1,594
Skew ness, S_{k-2}	1,262
Inman, $\alpha_{\phi-1}$	0,161
Inman, $\alpha_{\phi-2}$	-0,387
Folk & Ward, Sk_i	-0,023

Coefficient d'acuité (Kurtosis)	
Krumbein & Petijohn, K	0,208
Inman, K_ϕ	0,871
Folk & Ward, K_G	1,132

Coefficient de courbure	
C_c	1,452

Analyse granulométrique par voie fluide : fraction 0,040 µm - 2000 µm

Echantillon :	INDONESIE/12/.LABAN/U-03/013/B/T.YAN W.ISKANDARSYAH
Date :	22/10/2013 14:30
Opérateur :	MT
Fichier :	U03-013

Commentaires :	prof. 225-240 cm 26/05/12 Destruction MO à H2O2-élimination des ions floculants - Hexa+US

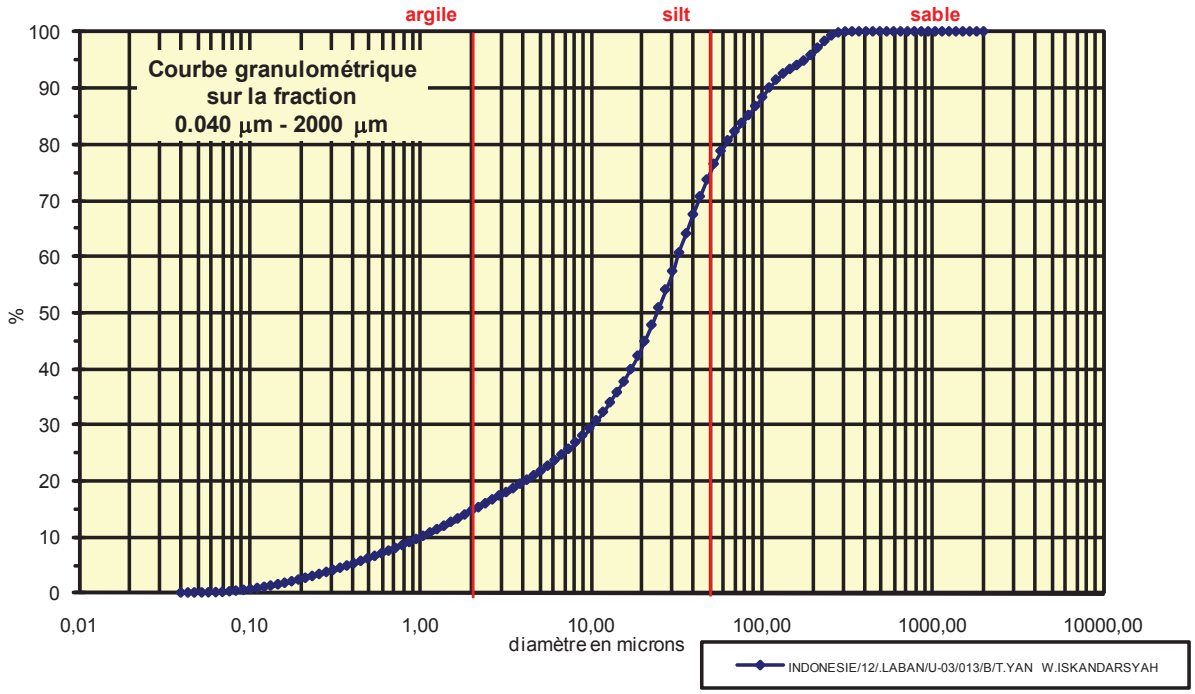

Fractiles	Taille (µm)	Taille (ϕ)
d_5	0,375	11,38
d_{10}	0,953	10,04
d_{16}	2,423	8,69
d_{25}	6,761	7,21
d_{30}	9,819	6,67
d_{50}	22,730	5,46
d_{60}	30,070	5,06
d_{75}	47,930	4,38
d_{84}	76,430	3,71
d_{90}	111,000	3,17
d_{95}	176,800	2,50

% Argile inférieur à 2µ	**A**	**13,90**
% Silts de 2µ à 50µ	**LT**	**59,70**
limons fins 2µ à 20µ	LF	28,30
limons grossiers 20µ à 50µ	LG	31,40
% Sables 50µ à 2000 µ	**ST**	**26,40**
sables fins 50µ à 200µ	SF	22,20
sables fins 50µ à 100µ	SF1	13,10
sables fins 100µ à 200 µ	SF2	9,10
sables grossiers 200µ à 2000µ	SG	4,20
sables grossiers 200µ à 500µ	SG1	4,20
sables grossiers 500µ à 1000µ	SG2	0,00
sables grossiers 1000µ à 2000µ	SG3	0,00

Indice de classement	
Trask, S_o	2,663
Krumbein, Q_d	-1,413
Inman, σ_ϕ	-2,490
Folk & Ward, σ_ϕ	-2,590
Hazen, C_u	31,553

Moyenne	
Trask, M	27,346
Inman, M_ϕ	6,199
Folk & Ward, M_z	5,953

Coefficient de dissymétrie	
Skew ness, S_{k-1}	0,627
Skew ness, S_{k-2}	0,792
Inman, $\alpha_{\phi-1}$	-0,297
Inman, $\alpha_{\phi-2}$	-0,595
Folk & Ward, Sk_i	-0,315

Coefficient d'acuité (Kurtosis)	
Krumbein & Petijohn, K	0,187
Inman, K_ϕ	0,784
Folk & Ward, K_G	1,288

Coefficient de courbure	
C_c	3,364

Analyse granulométrique par voie fluide : fraction 0,040 µm - 2000 µm

Echantillon :	INDONESIE/12/.LABAN/U-03/014/T.YAN W.ISKANDARSYAH
Date :	22/10/2013 16:20
Opérateur :	MT
Fichier :	U03-014

Commentaires :	prof. 240-270 cm 26/05/12 Destruction MO à H2O2-élimination des ions floculants - Hexa+US

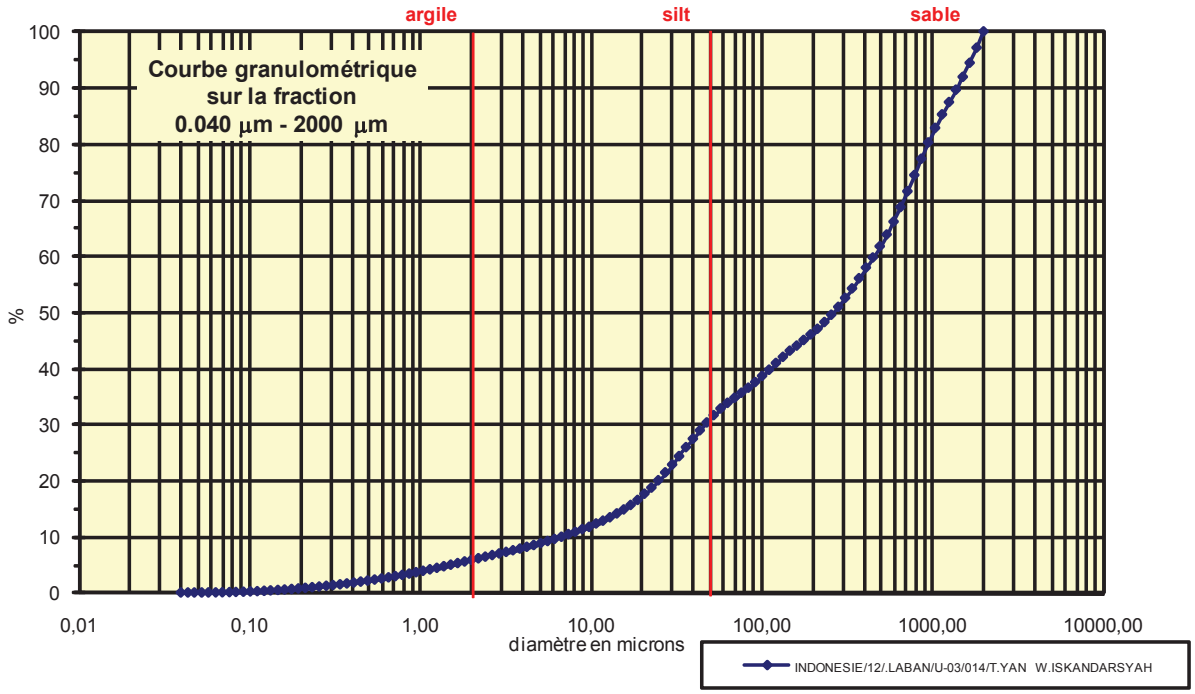

Fractiles	Taille (µm)	Taille (ϕ)
d_5	1,520	9,36
d_{10}	6,761	7,21
d_{16}	17,180	5,86
d_{25}	33,000	4,92
d_{30}	43,660	4,52
d_{50}	256,800	1,96
d_{60}	449,700	1,15
d_{75}	786,900	0,35
d_{84}	1041,000	-0,06
d_{90}	1377,000	-0,46
d_{95}	1660,000	-0,73

% Argile inférieur à 2µ	**A**	**5,53**
% Silts de 2µ à 50µ	**LT**	**24,77**
limons fins 2µ à 20µ	LF	10,97
limons grossiers 20µ à 50µ	LG	13,80
% Sables 50µ à 2000 µ	**ST**	**69,70**
sables fins 50µ à 200µ	SF	15,70
sables fins 50µ à 100µ	SF1	7,20
sables fins 100µ à 200 µ	SF2	8,50
sables grossiers 200µ à 2000µ	SG	54,00
sables grossiers 200µ à 500µ	SG1	15,70
sables grossiers 500µ à 1000µ	SG2	18,50
sables grossiers 1000µ à 2000µ	SG3	19,80

Indice de classement	
Trask, S_o	4,883
Krumbein, Q_d	-2,288
Inman, σ_ϕ	-2,961
Folk & Ward, σ_ϕ	-3,010
Hazen, C_u	66,514

Moyenne	
Trask, M	409,950
Inman, M_ϕ	2,903
Folk & Ward, M_z	2,589

Coefficient de dissymétrie	
Skew ness, S_{k-1}	0,394
Skew ness, S_{k-2}	0,628
Inman, $\alpha_{\phi-1}$	-0,318
Inman, $\alpha_{\phi-2}$	-0,795
Folk & Ward, Sk_i	-0,392

Coefficient d'acuité (Kurtosis)	
Krumbein & Petijohn, K	0,275
Inman, K_ϕ	0,705
Folk & Ward, K_G	0,904

Coefficient de courbure	
C_c	0,627

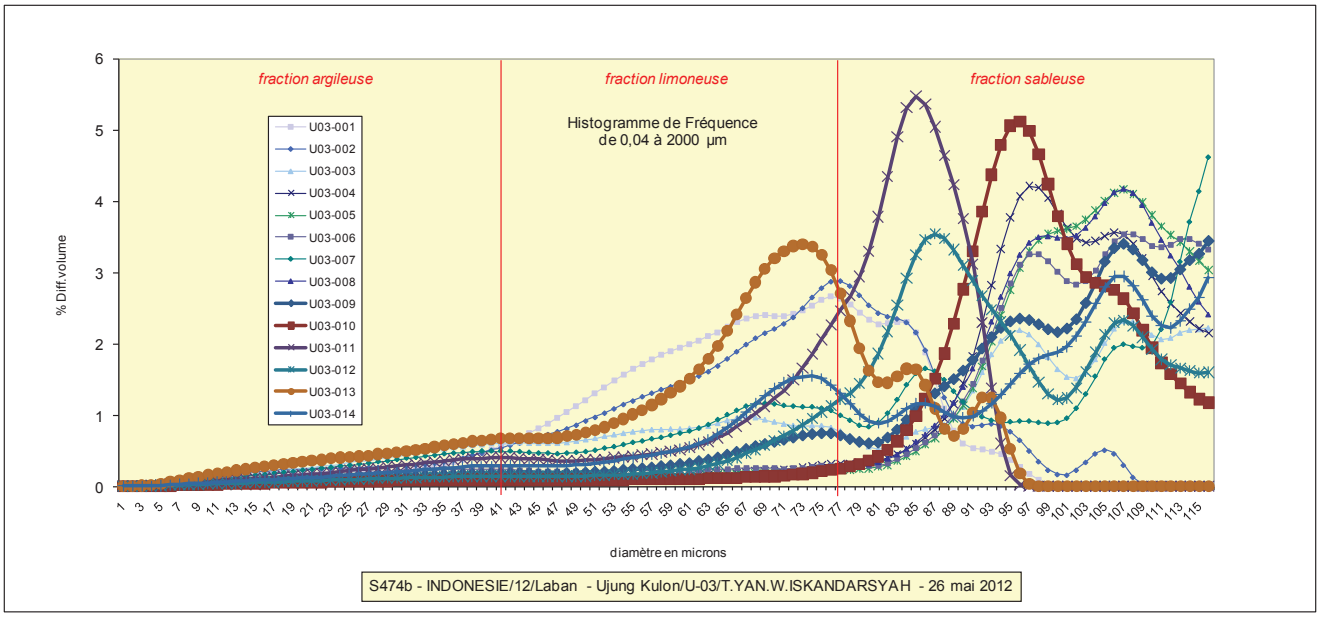
fraction argileuse
fraction limoneuse
fraction sableuse
Histogramme de Fréquence
de 0,04 à 2000 µm
U03-001
U03-002
U03-003
U03-004
U03-005
U03-006
U03-007
U03-008
U03-009
U03-010
U03-011
U03-012
U03-013
U03-014
% Diff.volume
diamètre en microns
S474b - INDONESIE/12/Laban - Ujung Kulon/U-03/T.YAN.W.ISKANDARSYAH - 26 mai 2012

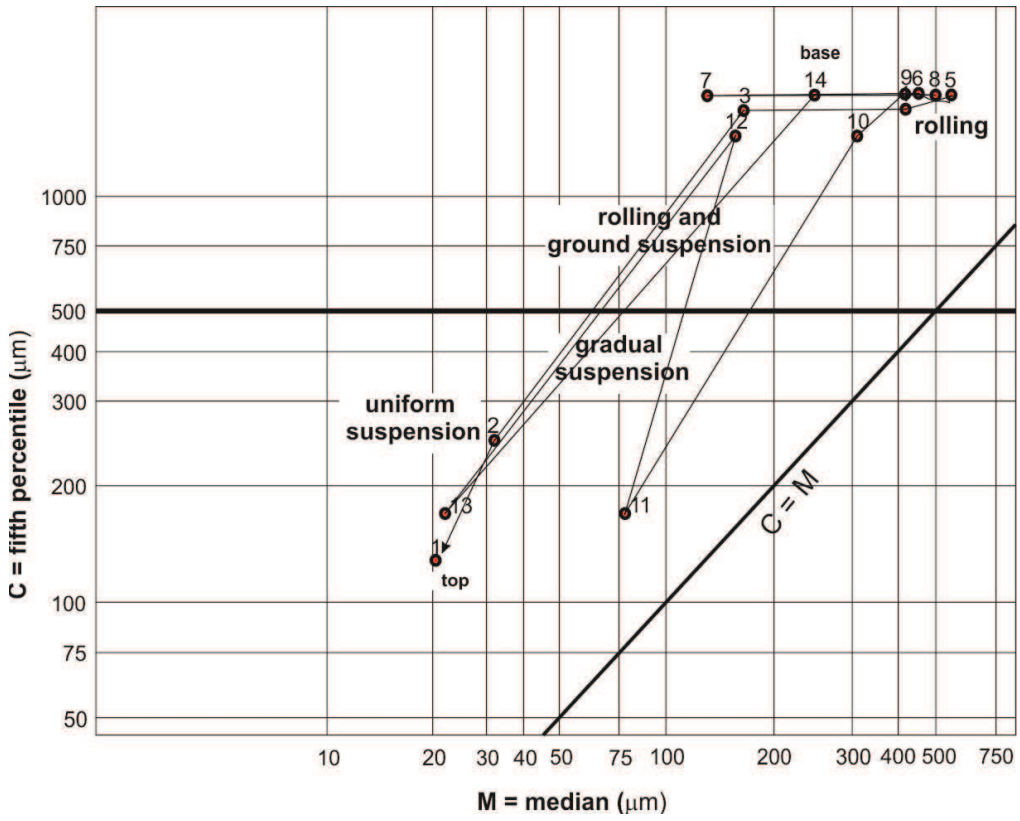
base
7
14
96 8 5
3
12
10
rolling
rolling and
ground suspension
gradual
suspension
uniform
suspension
2
13
1
top
11
C = M
1000
750
500
400
300
200
100
75
50
C = fifth percentile (μm)
10
20
30
40
50
75
100
200
300
400
500
750
M = median (μm)

Analyse granulométrique par voie fluide : fraction 0,040 µm - 2000 µm

Echantillon :	INDONESIE/12/LABAN/U-04/01/T.YAN W.ISKANDARSYAH
Date :	10/07/2013 16:22
Opérateur :	MT
Fichier :	U04-001

Commentaires :	prof. 0-15 cm 25/05/12 0

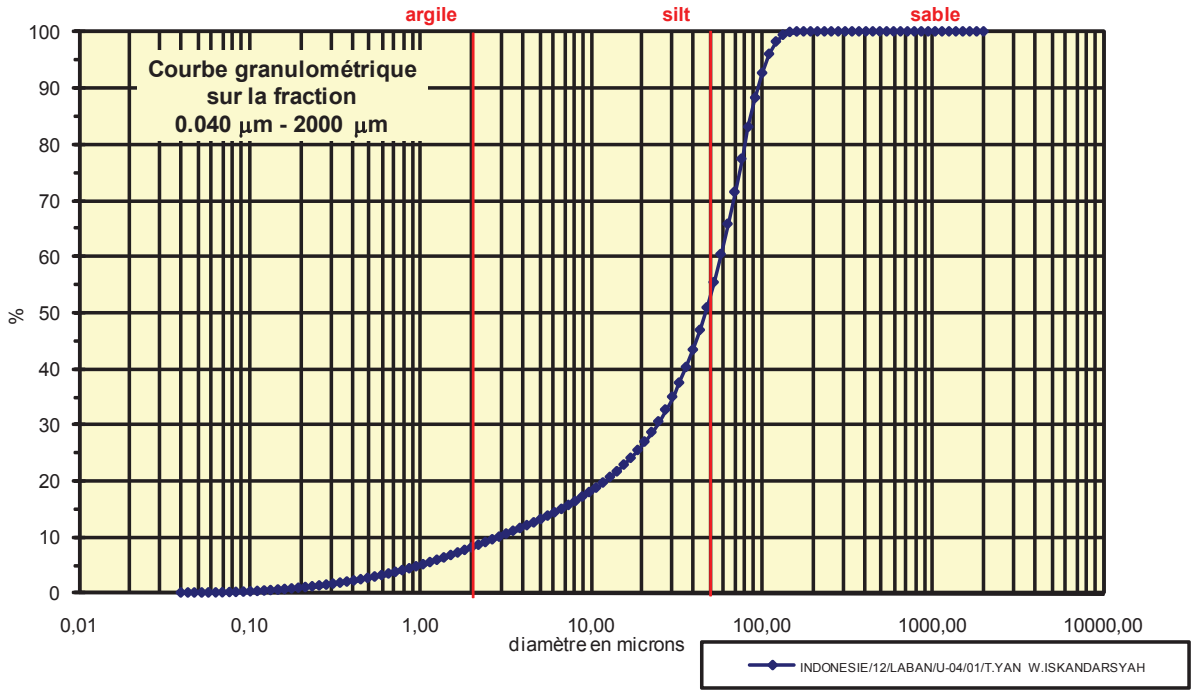

Fractiles	Taille (µm)	Taille (ϕ)
d_5	0,953	10,04
d_{10}	2,920	8,42
d_{16}	7,421	7,07
d_{25}	17,180	5,86
d_{30}	22,730	5,46
d_{50}	43,660	4,52
d_{60}	52,630	4,25
d_{75}	69,620	3,84
d_{84}	83,900	3,58
d_{90}	92,090	3,44
d_{95}	101,100	3,31

% Argile inférieur à 2µ	**A**	**7,59**
% Silts de 2µ à 50µ	**LT**	**43,21**
limons fins 2µ à 20µ	LF	17,81
limons grossiers 20µ à 50µ	LG	25,40
% Sables 50µ à 2000 µ	**ST**	**49,20**
sables fins 50µ à 200µ	SF	49,20
sables fins 50µ à 100µ	SF1	37,40
sables fins 100µ à 200 µ	SF2	11,80
sables grossiers 200µ à 2000µ	SG	0,00
sables grossiers 200µ à 500µ	SG1	0,00
sables grossiers 500µ à 1000µ	SG2	0,00
sables grossiers 1000µ à 2000µ	SG3	0,00

Indice de classement	
Trask, S_o	2,013
Krumbein, Q_d	-1,009
Inman, σ_ϕ	-1,749
Folk & Ward, σ_ϕ	-1,894
Hazen, C_u	18,024

Moyenne	
Trask, M	43,400
Inman, M_ϕ	5,325
Folk & Ward, M_z	5,056

Coefficient de dissymétrie	
Skew ness, S_{k-1}	0,627
Skew ness, S_{k-2}	0,792
Inman, $\alpha_{\phi-1}$	-0,461
Inman, $\alpha_{\phi-2}$	-1,231
Folk & Ward, Sk_i	-0,551

Coefficient d'acuité (Kurtosis)	
Krumbein & Petijohn, K	0,294
Inman, K_ϕ	0,923
Folk & Ward, K_G	1,366

Coefficient de courbure	
C_c	3,362

Analyse granulométrique par voie fluide : fraction 0,040 µm - 2000 µm

Echantillon :	INDONESIE/12/LABAN/U-04/02/T.YAN W.ISKANDARSYAH
Date :	10/07/2013 16:28
Opérateur :	MT
Fichier :	U04-002

Commentaires :	prof. 15-30 cm 25/05/12 0

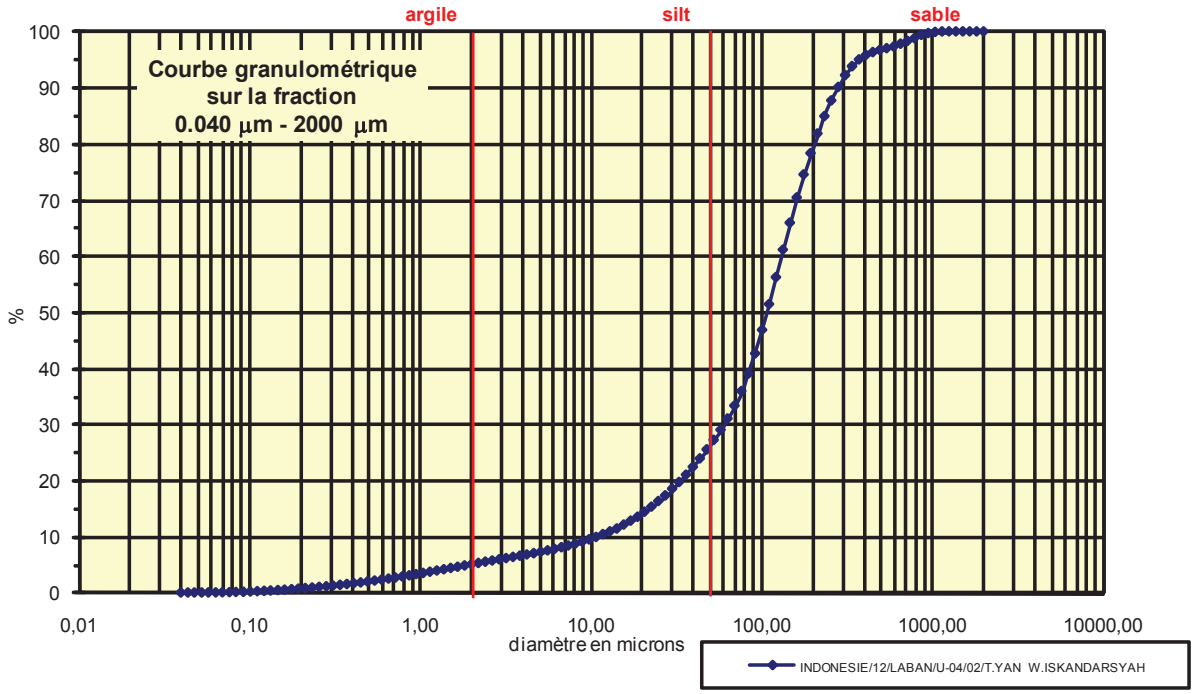

Fractiles	Taille (µm)	Taille (ϕ)
d_5	1,832	9,09
d_{10}	10,780	6,54
d_{16}	22,730	5,46
d_{25}	43,660	4,52
d_{30}	57,770	4,11
d_{50}	101,100	3,31
d_{60}	121,800	3,04
d_{75}	176,800	2,50
d_{84}	213,200	2,23
d_{90}	256,800	1,96
d_{95}	373,100	1,42

% Argile inférieur à 2µ	**A**	**4,82**
% Silts de 2µ à 50µ	**LT**	**20,68**
limons fins 2µ à 20µ	LF	8,68
limons grossiers 20µ à 50µ	LG	12,00
% Sables 50µ à 2000 µ	**ST**	**74,50**
sables fins 50µ à 200µ	SF	52,80
sables fins 50µ à 100µ	SF1	17,10
sables fins 100µ à 200 µ	SF2	35,70
sables grossiers 200µ à 2000µ	SG	21,70
sables grossiers 200µ à 500µ	SG1	18,40
sables grossiers 500µ à 1000µ	SG2	3,00
sables grossiers 1000µ à 2000µ	SG3	0,30

Indice de classement	
Trask, S_o	2,012
Krumbein, Q_d	-1,009
Inman, σ_ϕ	-1,615
Folk & Ward, σ_ϕ	-1,970
Hazen, C_u	11,299

Moyenne	
Trask, M	110,230
Inman, M_ϕ	3,844
Folk & Ward, M_z	3,665

Coefficient de dissymétrie	
Skew ness, S_{k-1}	0,755
Skew ness, S_{k-2}	0,869
Inman, $\alpha_{\phi-1}$	-0,333
Inman, $\alpha_{\phi-2}$	-1,208
Folk & Ward, Sk_I	-0,421

Coefficient d'acuité (Kurtosis)	
Krumbein & Petijohn, K	0,271
Inman, K_ϕ	1,375
Folk & Ward, K_G	1,558

Coefficient de courbure	
C_c	2,542

Analyse granulométrique par voie fluide : fraction 0,040 µm - 2000 µm

Echantillon :	INDONESIE/12/LABAN/U-04/03/T.YAN W.ISKANDARSYAH
Date :	10/07/2013 16:34
Opérateur :	MT
Fichier :	U04-003

Commentaires :	prof. 30-60 cm 25/05/12 0

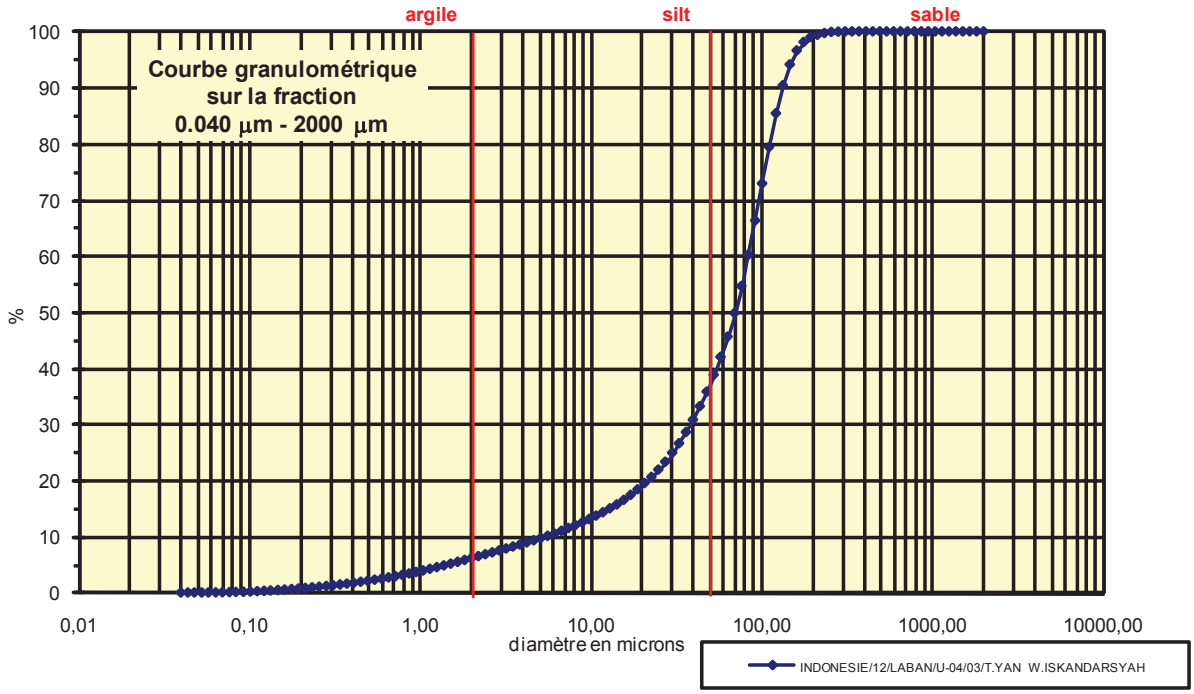

Fractiles	Taille (µm)	Taille (ϕ)
d_5	1,385	9,50
d_{10}	5,111	7,61
d_{16}	14,260	6,13
d_{25}	30,070	5,06
d_{30}	36,240	4,79
d_{50}	69,620	3,84
d_{60}	76,430	3,71
d_{75}	101,100	3,31
d_{84}	111,000	3,17
d_{90}	121,800	3,04
d_{95}	146,800	2,77

% Argile inférieur à 2µ	**A**	**5,80**
% Silts de 2µ à 50µ	**LT**	**30,00**
limons fins 2µ à 20µ	LF	12,60
limons grossiers 20µ à 50µ	LG	17,40
% Sables 50µ à 2000 µ	**ST**	**64,20**
sables fins 50µ à 200µ	SF	63,20
sables fins 50µ à 100µ	SF1	30,50
sables fins 100µ à 200 µ	SF2	32,70
sables grossiers 200µ à 2000µ	SG	1,00
sables grossiers 200µ à 500µ	SG1	1,00
sables grossiers 500µ à 1000µ	SG2	0,00
sables grossiers 1000µ à 2000µ	SG3	0,00

Indice de classement	
Trask, S_o	1,834
Krumbein, Q_d	-0,875
Inman, σ_ϕ	-1,480
Folk & Ward, σ_ϕ	-1,759
Hazen, C_u	14,954

Moyenne	
Trask, M	65,585
Inman, M_ϕ	4,652
Folk & Ward, M_z	4,383

Coefficient de dissymétrie	
Skew ness, S_{k-1}	0,627
Skew ness, S_{k-2}	0,792
Inman, $\alpha_{\phi-1}$	-0,545
Inman, $\alpha_{\phi-2}$	-1,545
Folk & Ward, Sk_i	-0,613

Coefficient d'acuité (Kurtosis)	
Krumbein & Petijohn, K	0,304
Inman, K_ϕ	1,273
Folk & Ward, K_G	1,576

Coefficient de courbure	
C_c	3,362

Analyse granulométrique par voie fluide : fraction 0,040 µm - 2000 µm

Echantillon :	INDONESIE/12/LABAN/U-04/04/T.YAN W.ISKANDARSYAH
Date :	10/07/2013 16:47
Opérateur :	MT
Fichier :	U04-004

Commentaires :	prof. 80 cm 25/05/12 0

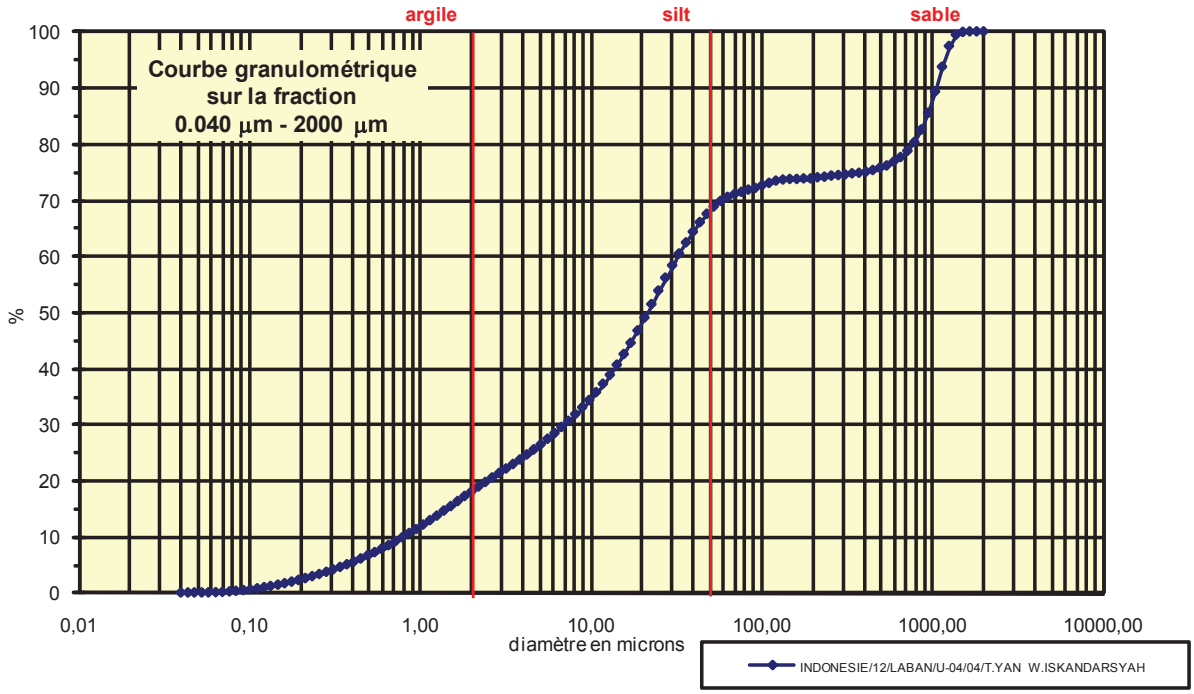

Fractiles	Taille (µm)	Taille (ϕ)
d_5	0,342	11,51
d_{10}	0,791	10,30
d_{16}	1,520	9,36
d_{25}	4,241	7,88
d_{30}	6,761	7,21
d_{50}	20,700	5,59
d_{60}	30,070	5,06
d_{75}	409,600	1,29
d_{84}	863,900	0,21
d_{90}	1041,000	-0,06
d_{95}	1143,000	-0,19

% Argile inférieur à 2µ	**A**	**17,20**
% Silts de 2µ à 50µ	**LT**	**50,30**
limons fins 2µ à 20µ	LF	29,50
limons grossiers 20µ à 50µ	LG	20,80
% Sables 50µ à 2000 µ	**ST**	**32,50**
sables fins 50µ à 200µ	SF	6,30
sables fins 50µ à 100µ	SF1	4,60
sables fins 100µ à 200 µ	SF2	1,70
sables grossiers 200µ à 2000µ	SG	26,20
sables grossiers 200µ à 500µ	SG1	1,90
sables grossiers 500µ à 1000µ	SG2	9,80
sables grossiers 1000µ à 2000µ	SG3	14,50

Indice de classement	
Trask, S_o	9,828
Krumbein, Q_d	-3,297
Inman, σ_ϕ	-4,575
Folk & Ward, σ_ϕ	-4,061
Hazen, C_u	38,015

Moyenne	
Trask, M	206,921
Inman, M_ϕ	4,786
Folk & Ward, M_z	5,056

Coefficient de dissymétrie	
Skew ness, S_{k-1}	4,054
Skew ness, S_{k-2}	2,013
Inman, $\alpha_{\phi-1}$	0,177
Inman, $\alpha_{\phi-2}$	-0,014
Folk & Ward, Sk_i	0,083

Coefficient d'acuité (Kurtosis)	
Krumbein & Petijohn, K	0,195
Inman, K_ϕ	0,279
Folk & Ward, K_G	0,728

Coefficient de courbure	
C_c	1,922

Analyse granulométrique par voie fluide : fraction 0,040 µm - 2000 µm

Echantillon :	INDONESIE/12/LABAN/U-04/05/T.YAN W.ISKANDARSYAH
Date :	10/07/2013 16:56
Opérateur :	MT
Fichier :	U04-005

Commentaires :	prof. 60-90 cm 25/05/12 0

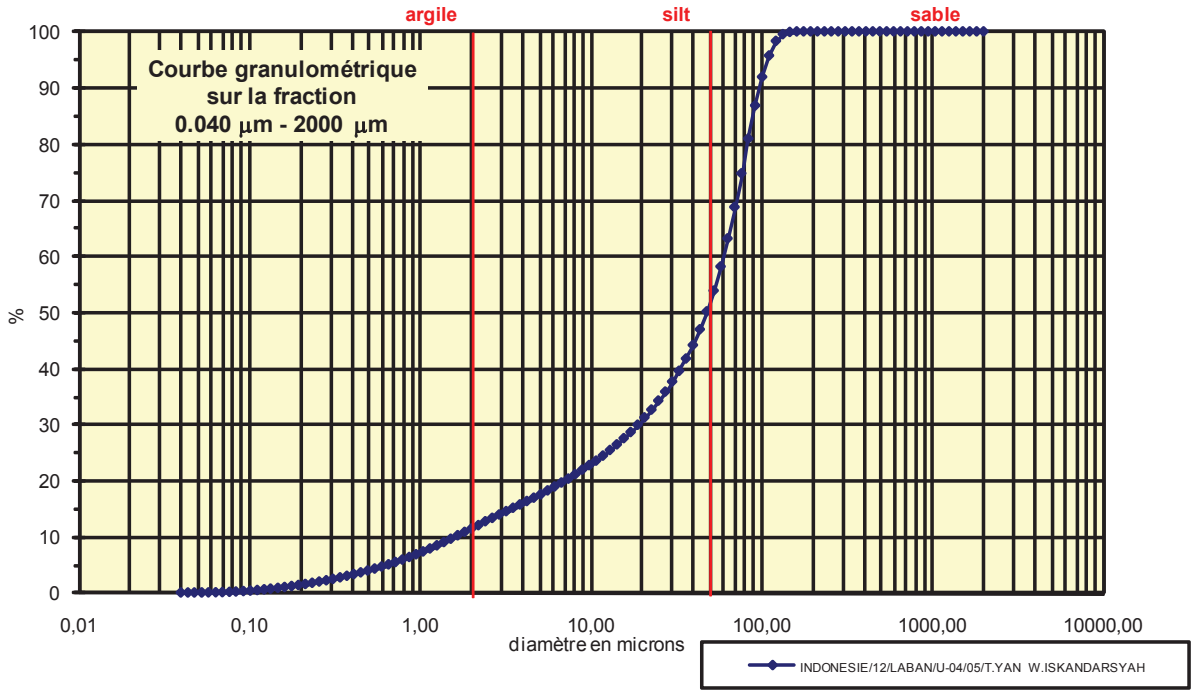

Fractiles	Taille (µm)	Taille (ϕ)
d_5	0,598	10,71
d_{10}	1,520	9,36
d_{16}	3,862	8,02
d_{25}	11,830	6,40
d_{30}	18,860	5,73
d_{50}	43,660	4,52
d_{60}	57,770	4,11
d_{75}	76,430	3,71
d_{84}	83,900	3,58
d_{90}	92,090	3,44
d_{95}	101,100	3,31

% Argile inférieur à 2µ	**A**	**10,80**
% Silts de 2µ à 50µ	**LT**	**39,30**
limons fins 2µ à 20µ	LF	19,10
limons grossiers 20µ à 50µ	LG	20,20
% Sables 50µ à 2000 µ	**ST**	**49,90**
sables fins 50µ à 200µ	SF	49,90
sables fins 50µ à 100µ	SF1	36,70
sables fins 100µ à 200 µ	SF2	13,20
sables grossiers 200µ à 2000µ	SG	0,00
sables grossiers 200µ à 500µ	SG1	0,00
sables grossiers 500µ à 1000µ	SG2	0,00
sables grossiers 1000µ à 2000µ	SG3	0,00

Indice de classement	
Trask, S_o	2,542
Krumbein, Q_d	-1,346
Inman, σ_ϕ	-2,221
Folk & Ward, σ_ϕ	-2,232
Hazen, C_u	38,007

Moyenne	
Trask, M	44,130
Inman, M_ϕ	5,796
Folk & Ward, M_z	5,370

Coefficient de dissymétrie	
Skew ness, S_{k-1}	0,474
Skew ness, S_{k-2}	0,689
Inman, $\alpha_{\phi-1}$	-0,576
Inman, $\alpha_{\phi-2}$	-1,121
Folk & Ward, Sk_i	-0,624

Coefficient d'acuité (Kurtosis)	
Krumbein & Petijohn, K	0,357
Inman, K_ϕ	0,667
Folk & Ward, K_G	1,127

Coefficient de courbure	
C_c	4,051

Analyse granulométrique par voie fluide : fraction 0,040 µm - 2000 µm

Echantillon :	INDONESIE/12/LABAN/U-04/06/T.YAN W.ISKANDARSYAH
Date :	10/07/2013 17:01
Opérateur :	MT
Fichier :	U04-006

Commentaires :	prof. 90-100 cm 26/05/12 0

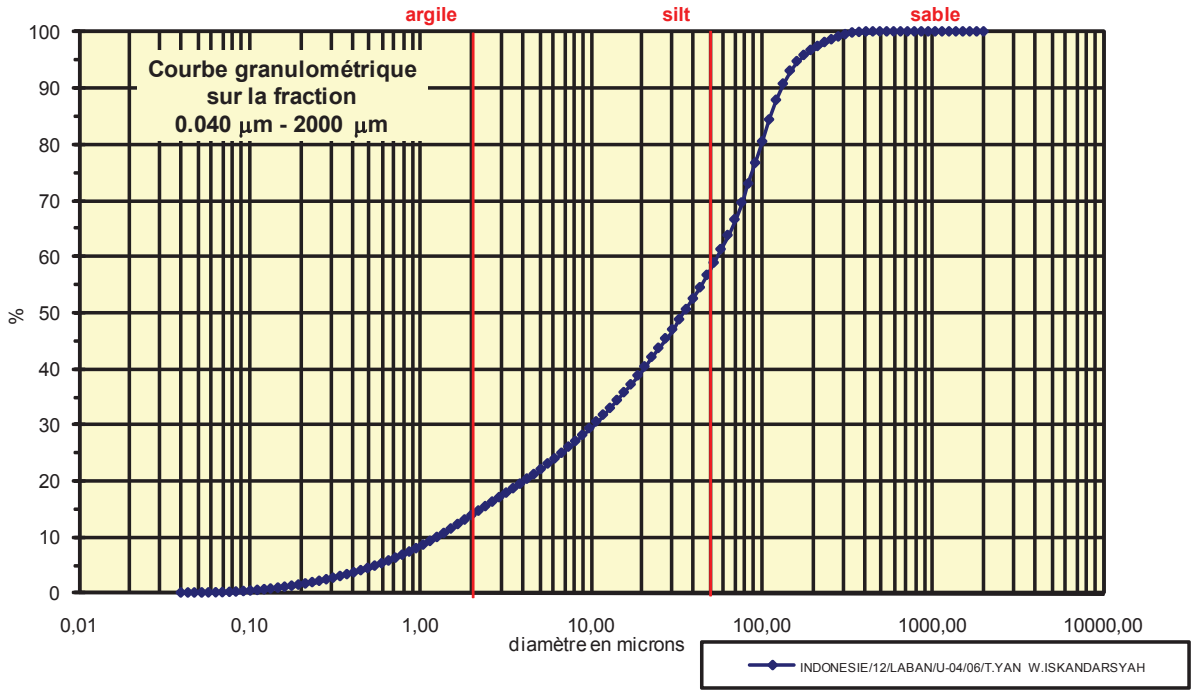

Fractiles	Taille (µm)	Taille (ϕ)
d_5	0,545	10,84
d_{10}	1,261	9,63
d_{16}	2,423	8,69
d_{25}	6,761	7,21
d_{30}	9,819	6,67
d_{50}	33,000	4,92
d_{60}	52,630	4,25
d_{75}	83,900	3,58
d_{84}	101,100	3,31
d_{90}	121,800	3,04
d_{95}	161,200	2,63

% Argile inférieur à 2µ	**A**	**13,00**
% Silts de 2µ à 50µ	**LT**	**43,60**
limons fins 2µ à 20µ	LF	25,70
limons grossiers 20µ à 50µ	LG	17,90
% Sables 50µ à 2000 µ	**ST**	**43,40**
sables fins 50µ à 200µ	SF	40,10
sables fins 50µ à 100µ	SF1	20,00
sables fins 100µ à 200 µ	SF2	20,10
sables grossiers 200µ à 2000µ	SG	3,30
sables grossiers 200µ à 500µ	SG1	3,30
sables grossiers 500µ à 1000µ	SG2	0,00
sables grossiers 1000µ à 2000µ	SG3	0,00

Indice de classement	
Trask, S_o	3,523
Krumbein, Q_d	-1,817
Inman, σ_ϕ	-2,691
Folk & Ward, σ_ϕ	-2,589
Hazen, C_u	41,737

Moyenne	
Trask, M	45,331
Inman, M_ϕ	5,998
Folk & Ward, M_z	5,639

Coefficient de dissymétrie	
Skew ness, S_{k-1}	0,521
Skew ness, S_{k-2}	0,722
Inman, $\alpha_{\phi-1}$	-0,400
Inman, $\alpha_{\phi-2}$	-0,675
Folk & Ward, Sk_i	-0,421

Coefficient d'acuité (Kurtosis)	
Krumbein & Petijohn, K	0,320
Inman, K_ϕ	0,525
Folk & Ward, K_G	0,926

Coefficient de courbure	
C_c	1,453

Analyse granulométrique par voie fluide : fraction 0,040 µm - 2000 µm

Echantillon :	INDONESIE/12/LABAN/U-04/07/T.YAN W.ISKANDARSYAH
Date :	11/07/2013 10:25
Opérateur :	MT
Fichier :	U04-007

Commentaires :	prof. 100-120 cm 26/05/12 Destruction MO à H2O2-élimination des ions floculants - Hexa+US

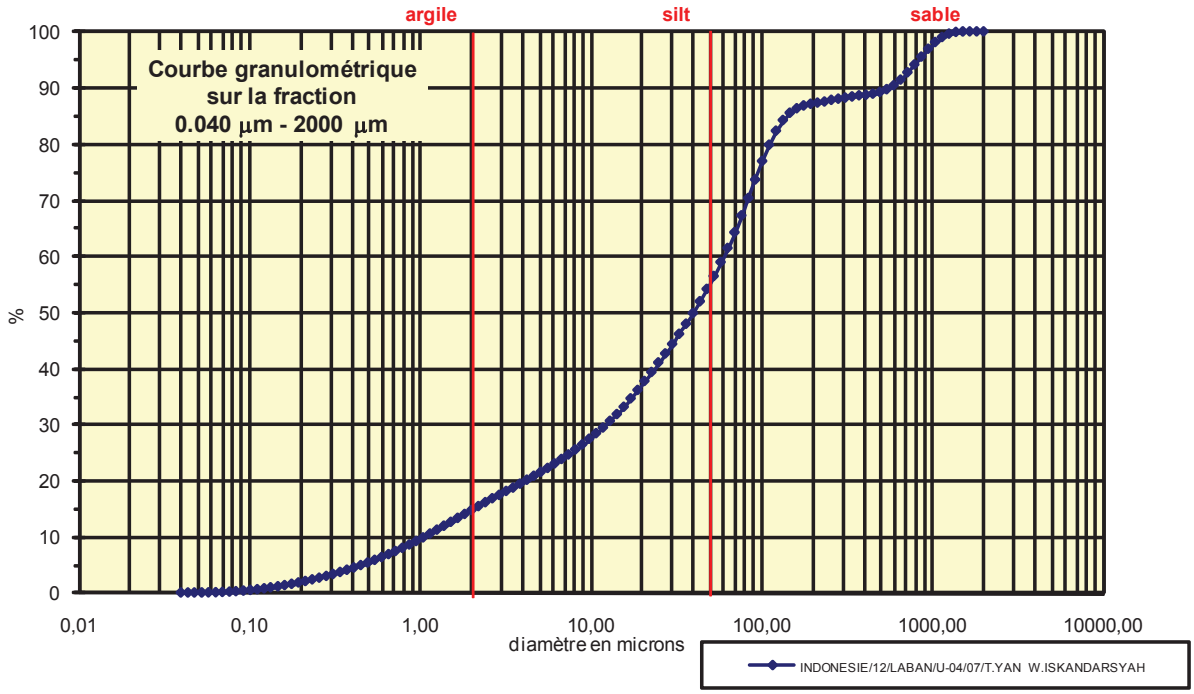

Fractiles	Taille (µm)	Taille (ϕ)
d_5	0,452	11,11
d_{10}	1,047	9,90
d_{16}	2,207	8,82
d_{25}	7,421	7,07
d_{30}	11,830	6,40
d_{50}	39,770	4,65
d_{60}	57,770	4,11
d_{75}	92,090	3,44
d_{84}	121,800	3,04
d_{90}	541,900	0,88
d_{95}	786,900	0,35

% Argile inférieur à 2µ	**A**	**14,00**
% Silts de 2µ à 50µ	**LT**	**40,10**
limons fins 2µ à 20µ	LF	22,10
limons grossiers 20µ à 50µ	LG	18,00
% Sables 50µ à 2000 µ	**ST**	**45,90**
sables fins 50µ à 200µ	SF	33,00
sables fins 50µ à 100µ	SF1	19,50
sables fins 100µ à 200 µ	SF2	13,50
sables grossiers 200µ à 2000µ	SG	12,90
sables grossiers 200µ à 500µ	SG1	2,10
sables grossiers 500µ à 1000µ	SG2	7,70
sables grossiers 1000µ à 2000µ	SG3	3,10

Indice de classement	
Trask, S_o	3,523
Krumbein, Q_d	-1,817
Inman, σ_ϕ	-2,893
Folk & Ward, σ_ϕ	-3,078
Hazen, C_u	55,177

Moyenne	
Trask, M	49,756
Inman, M_ϕ	5,931
Folk & Ward, M_z	5,504

Coefficient de dissymétrie	
Skew ness, S_{k-1}	0,432
Skew ness, S_{k-2}	0,657
Inman, $\alpha_{\phi-1}$	-0,442
Inman, $\alpha_{\phi-2}$	-0,372
Folk & Ward, Sk_i	-0,321

Coefficient d'acuité (Kurtosis)	
Krumbein & Petijohn, K	0,078
Inman, K_ϕ	0,861
Folk & Ward, K_G	1,214

Coefficient de courbure	
C_c	2,314

Analyse granulométrique par voie fluide : fraction 0,040 µm - 2000 µm

Echantillon :	INDONESIE/12/LABAN/U-04/08/T.YAN W.ISKANDARSYAH
Date :	11/07/2013 13:58
Opérateur :	MT
Fichier :	U04-008

Commentaires :	prof. 120-130 cm 26/05/12 Destruction MO à H2O2-élimination des ions floculants - Hexa+US

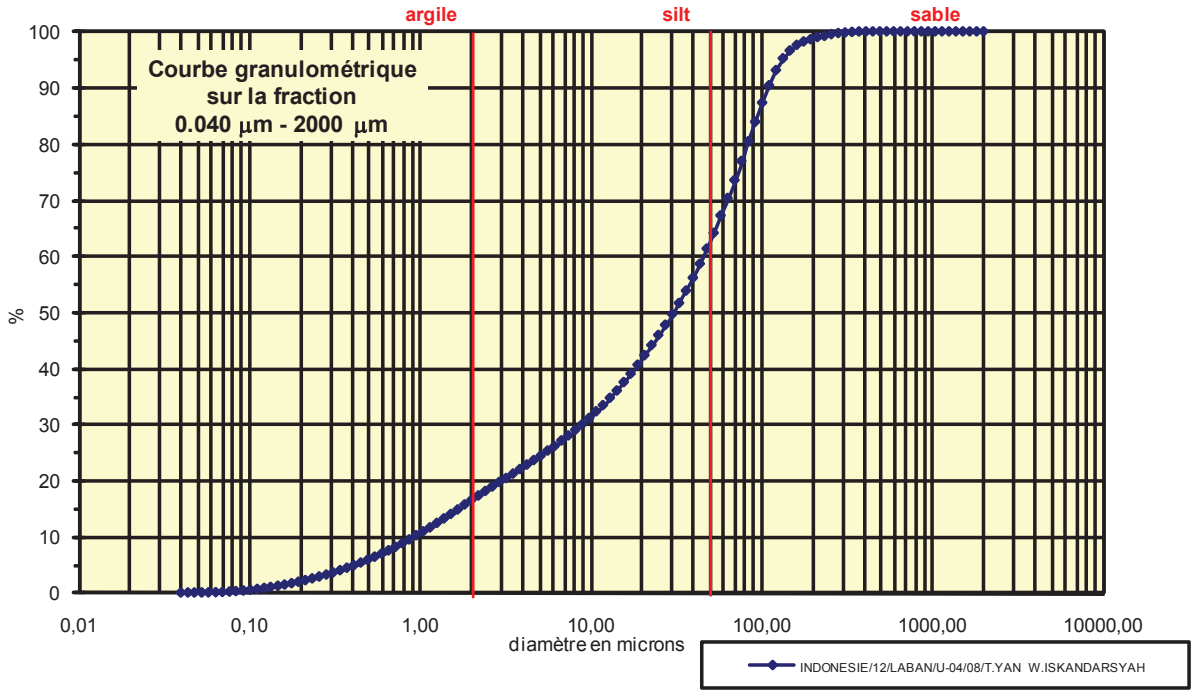

Fractiles	Taille (µm)	Taille (ϕ)
d_5	0,412	11,25
d_{10}	0,869	10,17
d_{16}	1,832	9,09
d_{25}	5,111	7,61
d_{30}	8,944	6,80
d_{50}	30,070	5,06
d_{60}	43,660	4,52
d_{75}	69,620	3,84
d_{84}	92,090	3,44
d_{90}	101,100	3,31
d_{95}	121,800	3,04

% Argile inférieur à 2µ	**A**	**15,70**
% Silts de 2µ à 50µ	**LT**	**45,60**
limons fins 2µ à 20µ	LF	24,90
limons grossiers 20µ à 50µ	LG	20,70
% Sables 50µ à 2000 µ	**ST**	**38,70**
sables fins 50µ à 200µ	SF	37,30
sables fins 50µ à 100µ	SF1	22,60
sables fins 100µ à 200 µ	SF2	14,70
sables grossiers 200µ à 2000µ	SG	1,40
sables grossiers 200µ à 500µ	SG1	1,40
sables grossiers 500µ à 1000µ	SG2	0,00
sables grossiers 1000µ à 2000µ	SG3	0,00

Indice de classement	
Trask, S_o	3,691
Krumbein, Q_d	-1,884
Inman, σ_ϕ	-2,826
Folk & Ward, σ_ϕ	-2,656
Hazen, C_u	50,242

Moyenne	
Trask, M	37,366
Inman, M_ϕ	6,267
Folk & Ward, M_z	5,863

Coefficient de dissymétrie	
Skew ness, S_{k-1}	0,394
Skew ness, S_{k-2}	0,627
Inman, $\alpha_{\phi-1}$	-0,429
Inman, $\alpha_{\phi-2}$	-0,738
Folk & Ward, Sk_i	-0,468

Coefficient d'acuité (Kurtosis)	
Krumbein & Petijohn, K	0,322
Inman, K_ϕ	0,452
Folk & Ward, K_G	0,893

Coefficient de courbure	
C_c	2,108

Analyse granulométrique par voie fluide : fraction 0,040 µm - 2000 µm

Echantillon :	INDONESIE/12/LABAN/U-04/09/T.YAN W.ISKANDARSYAH
Date :	11/07/2013 14:11
Opérateur :	MT
Fichier :	U04-009

Commentaires :	prof. 130-150 cm 26/05/12 Destruction MO à H2O2-élimination des ions floculants - Hexa+US

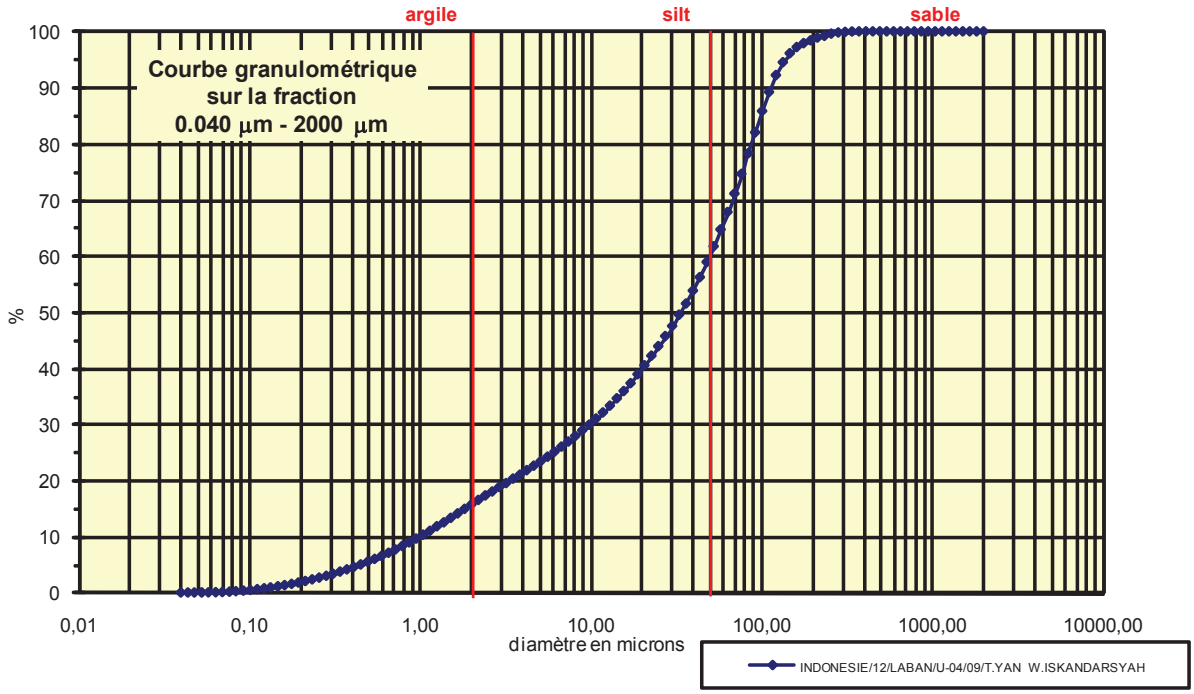

Fractiles	Taille (µm)	Taille (ϕ)
d_5	0,452	11,11
d_{10}	0,953	10,04
d_{16}	2,010	8,96
d_{25}	5,611	7,48
d_{30}	9,819	6,67
d_{50}	33,000	4,92
d_{60}	47,930	4,38
d_{75}	76,430	3,71
d_{84}	92,090	3,44
d_{90}	111,000	3,17
d_{95}	133,700	2,90

% Argile inférieur à 2µ	**A**	**14,90**
% Silts de 2µ à 50µ	**LT**	**44,00**
limons fins 2µ à 20µ	LF	24,00
limons grossiers 20µ à 50µ	LG	20,00
% Sables 50µ à 2000 µ	**ST**	**41,10**
sables fins 50µ à 200µ	SF	39,50
sables fins 50µ à 100µ	SF1	23,10
sables fins 100µ à 200 µ	SF2	16,40
sables grossiers 200µ à 2000µ	SG	1,60
sables grossiers 200µ à 500µ	SG1	1,60
sables grossiers 500µ à 1000µ	SG2	0,00
sables grossiers 1000µ à 2000µ	SG3	0,00

Indice de classement	
Trask, S_o	3,691
Krumbein, Q_d	-1,884
Inman, σ_ϕ	-2,759
Folk & Ward, σ_ϕ	-2,623
Hazen, C_u	50,294

Moyenne	
Trask, M	41,021
Inman, M_ϕ	6,200
Folk & Ward, M_z	5,774

Coefficient de dissymétrie	
Skew ness, S_{k-1}	0,394
Skew ness, S_{k-2}	0,628
Inman, $\alpha_{\phi-1}$	-0,463
Inman, $\alpha_{\phi-2}$	-0,756
Folk & Ward, Sk_i	-0,486

Coefficient d'acuité (Kurtosis)	
Krumbein & Petijohn, K	0,322
Inman, K_ϕ	0,488
Folk & Ward, K_G	0,893

Coefficient de courbure	
C_c	2,111

Analyse granulométrique par voie fluide : fraction 0,040 µm - 2000 µm

Echantillon :	INDONESIE/12/LABAN/U-04/10/T.YAN W.ISKANDARSYAH
Date :	11/07/2013 14:19
Opérateur :	MT
Fichier :	U04-010

Commentaires :	prof. 150-160 cm 26/05/12 Destruction MO à H2O2-élimination des ions floculants - Hexa+US

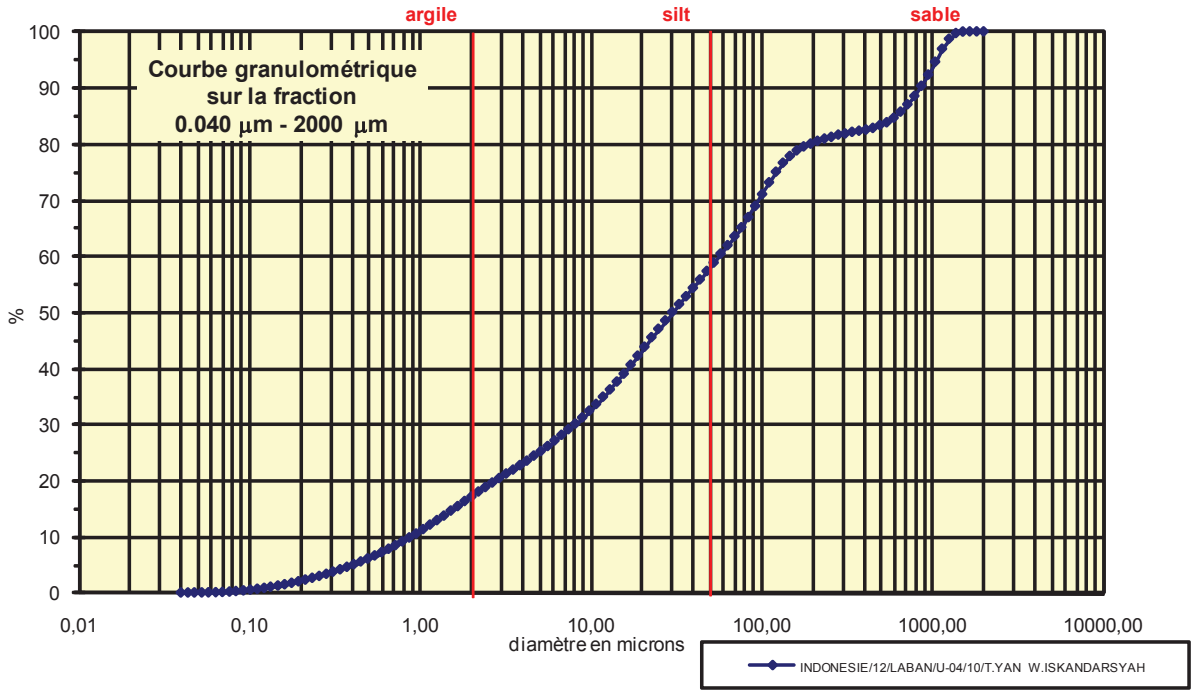

Fractiles	Taille (µm)	Taille (ϕ)
d_5	0,375	11,38
d_{10}	0,869	10,17
d_{16}	1,669	9,23
d_{25}	4,656	7,75
d_{30}	7,421	7,07
d_{50}	30,070	5,06
d_{60}	52,630	4,25
d_{75}	121,800	3,04
d_{84}	541,900	0,88
d_{90}	786,900	0,35
d_{95}	1041,000	-0,06

% Argile inférieur à 2µ	**A**	**16,30**
% Silts de 2µ à 50µ	**LT**	**41,00**
limons fins 2µ à 20µ	LF	25,90
limons grossiers 20µ à 50µ	LG	15,10
% Sables 50µ à 2000 µ	**ST**	**42,70**
sables fins 50µ à 200µ	SF	22,70
sables fins 50µ à 100µ	SF1	11,60
sables fins 100µ à 200 µ	SF2	11,10
sables grossiers 200µ à 2000µ	SG	20,00
sables grossiers 200µ à 500µ	SG1	3,30
sables grossiers 500µ à 1000µ	SG2	9,00
sables grossiers 1000µ à 2000µ	SG3	7,70

Indice de classement	
Trask, S_o	5,115
Krumbein, Q_d	-2,355
Inman, σ_ϕ	-4,171
Folk & Ward, σ_ϕ	-3,819
Hazen, C_u	60,564

Moyenne	
Trask, M	63,228
Inman, M_ϕ	5,055
Folk & Ward, M_z	5,055

Coefficient de dissymétrie	
Skew ness, S_{k-1}	0,627
Skew ness, S_{k-2}	0,792
Inman, $\alpha_{\phi-1}$	0,000
Inman, $\alpha_{\phi-2}$	-0,145
Folk & Ward, Sk_i	-0,053

Coefficient d'acuité (Kurtosis)	
Krumbein & Petijohn, K	0,075
Inman, K_ϕ	0,371
Folk & Ward, K_G	0,995

Coefficient de courbure	
C_c	1,204

Analyse granulométrique par voie fluide : fraction 0,040 µm - 2000 µm

Echantillon :	INDONESIE/12/LABAN/U-04/11/T.YAN W.ISKANDARSYAH
Date :	11/07/2013 14:30
Opérateur :	MT
Fichier :	U04-011

Commentaires :	prof. 160-170 cm 26/05/12 Destruction MO à H2O2-élimination des ions floculants - Hexa+US

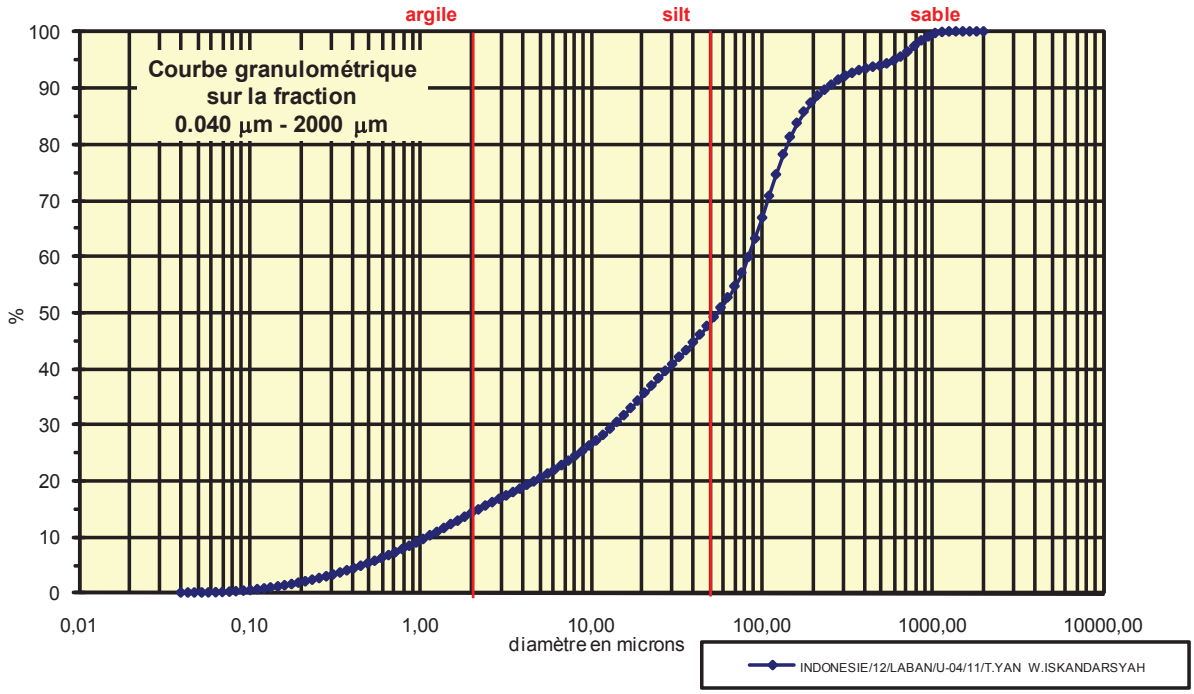

Fractiles	Taille (µm)	Taille (ϕ)
d_5	0,452	11,11
d_{10}	1,047	9,90
d_{16}	2,423	8,69
d_{25}	8,147	6,94
d_{30}	12,990	6,27
d_{50}	52,630	4,25
d_{60}	83,900	3,58
d_{75}	121,800	3,04
d_{84}	161,200	2,63
d_{90}	234,100	2,09
d_{95}	594,900	0,75

% Argile inférieur à 2µ	**A**	**13,50**
% Silts de 2µ à 50µ	**LT**	**34,00**
limons fins 2µ à 20µ	LF	20,70
limons grossiers 20µ à 50µ	LG	13,30
% Sables 50µ à 2000 µ	**ST**	**52,50**
sables fins 50µ à 200µ	SF	39,80
sables fins 50µ à 100µ	SF1	15,60
sables fins 100µ à 200 µ	SF2	24,20
sables grossiers 200µ à 2000µ	SG	12,70
sables grossiers 200µ à 500µ	SG1	6,60
sables grossiers 500µ à 1000µ	SG2	5,20
sables grossiers 1000µ à 2000µ	SG3	0,90

Indice de classement	
Trask, S_o	3,867
Krumbein, Q_d	-1,951
Inman, σ_ϕ	-3,028
Folk & Ward, σ_ϕ	-3,084
Hazen, C_u	80,134

Moyenne	
Trask, M	64,974
Inman, M_ϕ	5,661
Folk & Ward, M_z	5,190

Coefficient de dissymétrie	
Skew ness, S_{k-1}	0,358
Skew ness, S_{k-2}	0,599
Inman, $\alpha_{\phi-1}$	-0,467
Inman, $\alpha_{\phi-2}$	-0,556
Folk & Ward, Sk_i	-0,396

Coefficient d'acuité (Kurtosis)	
Krumbein & Petijohn, K	0,244
Inman, K_ϕ	0,711
Folk & Ward, K_G	1,088

Coefficient de courbure	
C_c	1,921

Analyse granulométrique par voie fluide : fraction 0,040 µm - 2000 µm

Echantillon :	INDONESIE/12/LABAN/U-04/12/T.YAN W.ISKANDARSYAH
Date :	11/07/2013 14:39
Opérateur :	MT
Fichier :	U04-012

Commentaires :	prof. 160-170 cm 26/05/12 Destruction MO à H2O2-élimination des ions floculants - Hexa+US

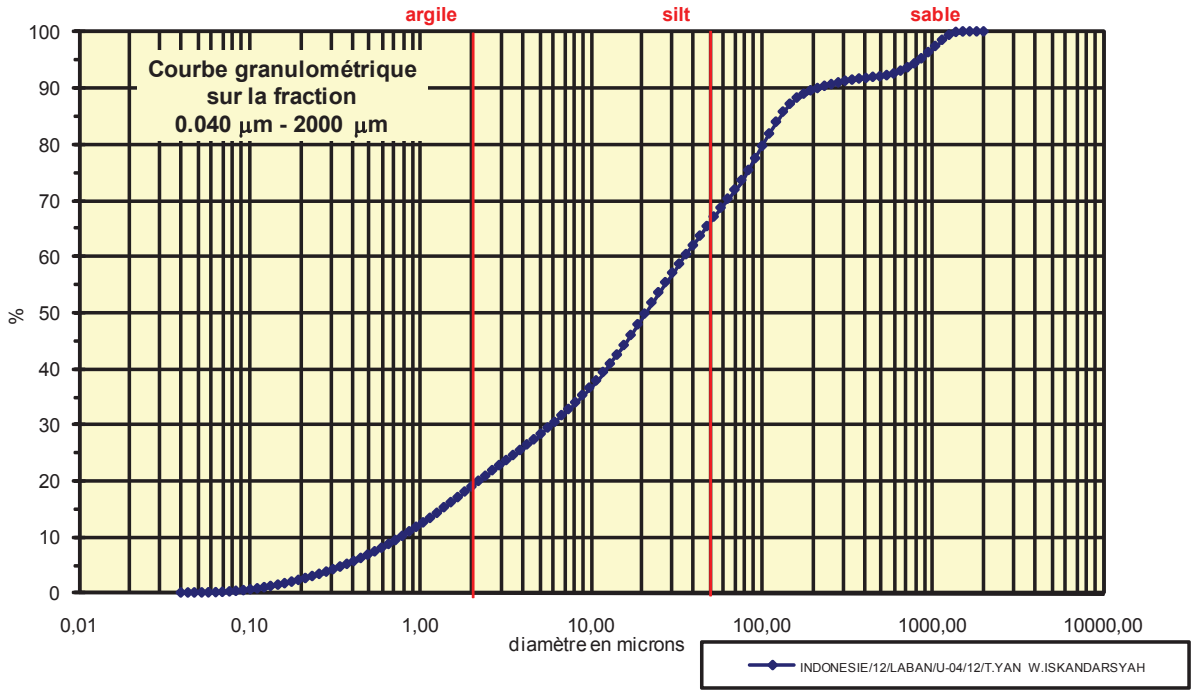

Fractiles	Taille (µm)	Taille (ϕ)
d_5	0,342	11,51
d_{10}	0,721	10,44
d_{16}	1,385	9,50
d_{25}	3,519	8,15
d_{30}	5,611	7,48
d_{50}	20,700	5,59
d_{60}	33,000	4,92
d_{75}	76,430	3,71
d_{84}	121,800	3,04
d_{90}	213,200	2,23
d_{95}	786,900	0,35

% Argile inférieur à 2µ	**A**	**18,00**
% Silts de 2µ à 50µ	**LT**	**47,30**
limons fins 2µ à 20µ	LF	29,80
limons grossiers 20µ à 50µ	LG	17,50
% Sables 50µ à 2000 µ	**ST**	**34,70**
sables fins 50µ à 200µ	SF	24,20
sables fins 50µ à 100µ	SF1	12,10
sables fins 100µ à 200 µ	SF2	12,10
sables grossiers 200µ à 2000µ	SG	10,50
sables grossiers 200µ à 500µ	SG1	2,50
sables grossiers 500µ à 1000µ	SG2	4,30
sables grossiers 1000µ à 2000µ	SG3	3,70

Indice de classement	
Trask, S_o	4,660
Krumbein, Q_d	-2,220
Inman, σ_ϕ	-3,229
Folk & Ward, σ_ϕ	-3,307
Hazen, C_u	45,770

Moyenne	
Trask, M	39,975
Inman, M_ϕ	6,267
Folk & Ward, M_z	6,043

Coefficient de dissymétrie	
Skew ness, S_{k-1}	0,628
Skew ness, S_{k-2}	0,792
Inman, $\alpha_{\phi-1}$	-0,208
Inman, $\alpha_{\phi-2}$	-0,104
Folk & Ward, Sk_i	-0,134

Coefficient d'acuité (Kurtosis)	
Krumbein & Petijohn, K	0,172
Inman, K_ϕ	0,729
Folk & Ward, K_G	1,031

Coefficient de courbure	
C_c	1,323

Analyse granulométrique par voie fluide : fraction 0,040 µm - 2000 µm

Echantillon :	INDONESIE/12/LABAN/U-04/13/T.YAN W.ISKANDARSYAH
Date :	11/07/2013 14:48
Opérateur :	MT
Fichier :	U04-013

Commentaires :	prof. 170-180 cm 26/05/12 Destruction MO à H2O2-élimination des ions floculants - Hexa+US

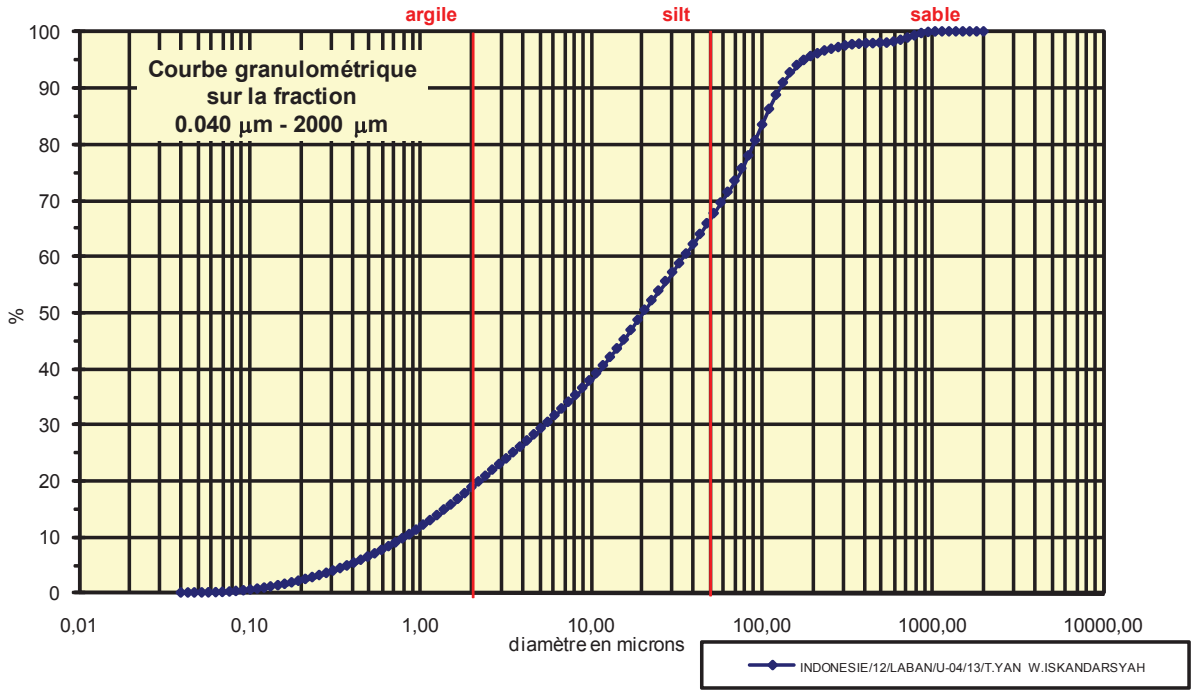

Fractiles	Taille (µm)	Taille (ϕ)
d_5	0,375	11,38
d_{10}	0,791	10,30
d_{16}	1,520	9,36
d_{25}	3,519	8,15
d_{30}	5,111	7,61
d_{50}	18,860	5,73
d_{60}	33,000	4,92
d_{75}	69,620	3,84
d_{84}	101,100	3,31
d_{90}	121,800	3,04
d_{95}	176,800	2,50

% Argile inférieur à 2µ	**A**	**17,70**
% Silts de 2µ à 50µ	**LT**	**48,10**
limons fins 2µ à 20µ	LF	30,90
limons grossiers 20µ à 50µ	LG	17,20
% Sables 50µ à 2000 µ	**ST**	**34,20**
sables fins 50µ à 200µ	SF	29,80
sables fins 50µ à 100µ	SF1	14,80
sables fins 100µ à 200 µ	SF2	15,00
sables grossiers 200µ à 2000µ	SG	4,40
sables grossiers 200µ à 500µ	SG1	2,40
sables grossiers 500µ à 1000µ	SG2	1,90
sables grossiers 1000µ à 2000µ	SG3	0,10

Indice de classement	
Trask, S_o	4,448
Krumbein, Q_d	-2,153
Inman, σ_ϕ	-3,028
Folk & Ward, σ_ϕ	-2,859
Hazen, C_u	41,719

Moyenne	
Trask, M	36,570
Inman, M_ϕ	6,334
Folk & Ward, M_z	6,132

Coefficient de dissymétrie	
Skew ness, S_{k-1}	0,689
Skew ness, S_{k-2}	0,830
Inman, $\alpha_{\phi-1}$	-0,200
Inman, $\alpha_{\phi-2}$	-0,400
Folk & Ward, Sk_I	-0,236

Coefficient d'acuité (Kurtosis)	
Krumbein & Petijohn, K	0,273
Inman, K_ϕ	0,467
Folk & Ward, K_G	0,845

Coefficient de courbure	
C_c	1,001

Analyse granulométrique par voie fluide : fraction 0,040 µm - 2000 µm

Echantillon :	INDONESIE/12/LABAN/U-04/14/T.YAN W.ISKANDARSYAH
Date :	11/07/2013 14:59
Opérateur :	MT
Fichier :	U04-014

Commentaires :	prof. 180-210 cm 26/05/12 Destruction MO à H2O2-élimination des ions floculants - Hexa+US

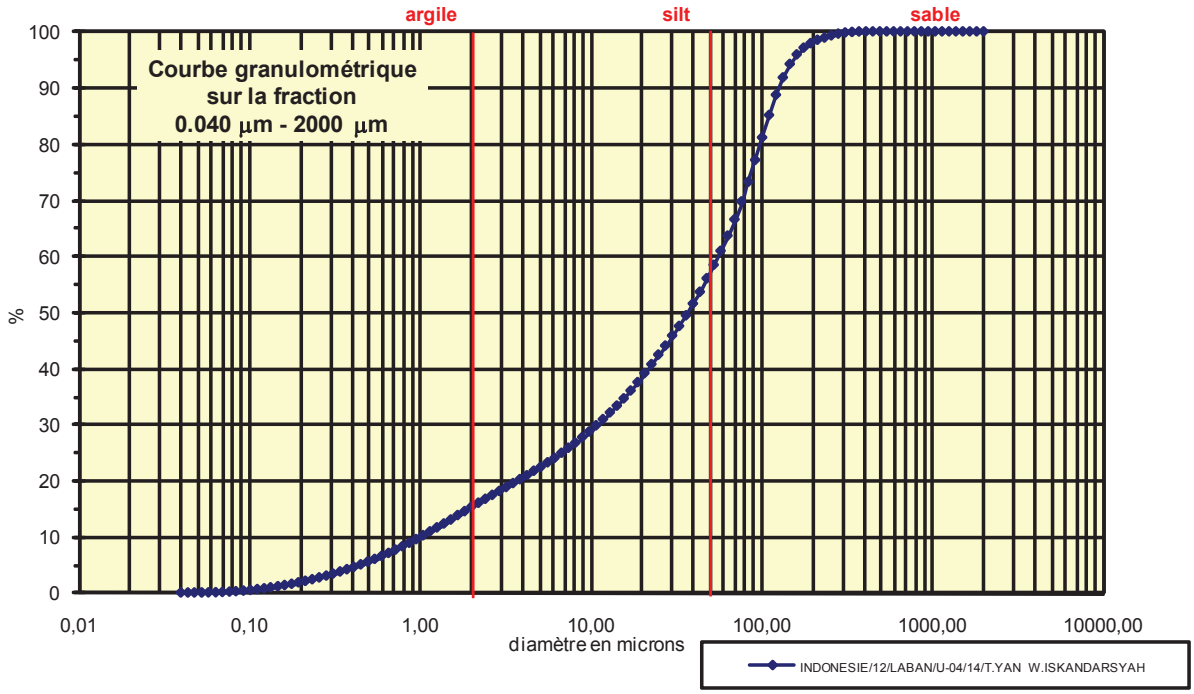

Fractiles	Taille (µm)	Taille (ϕ)
d_5	0,412	11,25
d_{10}	0,953	10,04
d_{16}	2,207	8,82
d_{25}	6,761	7,21
d_{30}	10,780	6,54
d_{50}	36,240	4,79
d_{60}	52,630	4,25
d_{75}	83,900	3,58
d_{84}	101,100	3,31
d_{90}	121,800	3,04
d_{95}	146,800	2,77

% Argile inférieur à 2µ	**A**	**14,50**
% Silts de 2µ à 50µ	**LT**	**41,50**
limons fins 2µ à 20µ	LF	23,00
limons grossiers 20µ à 50µ	LG	18,50
% Sables 50µ à 2000 µ	**ST**	**44,00**
sables fins 50µ à 200µ	SF	41,90
sables fins 50µ à 100µ	SF1	21,10
sables fins 100µ à 200 µ	SF2	20,80
sables grossiers 200µ à 2000µ	SG	2,10
sables grossiers 200µ à 500µ	SG1	2,10
sables grossiers 500µ à 1000µ	SG2	0,00
sables grossiers 1000µ à 2000µ	SG3	0,00

Indice de classement	
Trask, S_o	3,523
Krumbein, Q_d	-1,817
Inman, σ_ϕ	-2,759
Folk & Ward, σ_ϕ	-2,664
Hazen, C_u	55,226

Moyenne	
Trask, M	45,331
Inman, M_ϕ	6,065
Folk & Ward, M_z	5,639

Coefficient de dissymétrie	
Skew ness, S_{k-1}	0,432
Skew ness, S_{k-2}	0,657
Inman, $\alpha_{\phi-1}$	-0,463
Inman, $\alpha_{\phi-2}$	-0,805
Folk & Ward, Sk_i	-0,494

Coefficient d'acuité (Kurtosis)	
Krumbein & Petijohn, K	0,319
Inman, K_ϕ	0,536
Folk & Ward, K_G	0,956

Coefficient de courbure	
C_c	2,317

Analyse granulométrique par voie fluide : fraction 0,040 µm - 2000 µm

Echantillon :	INDONESIE/12/LABAN/U-04/15/T.YAN W.ISKANDARSYAH
Date :	11/07/2013 15:07
Opérateur :	MT
Fichier :	U04-015

Commentaires :	prof. 200-210 cm 26/05/12 Destruction MO à H2O2-élimination des ions floculants - Hexa+US

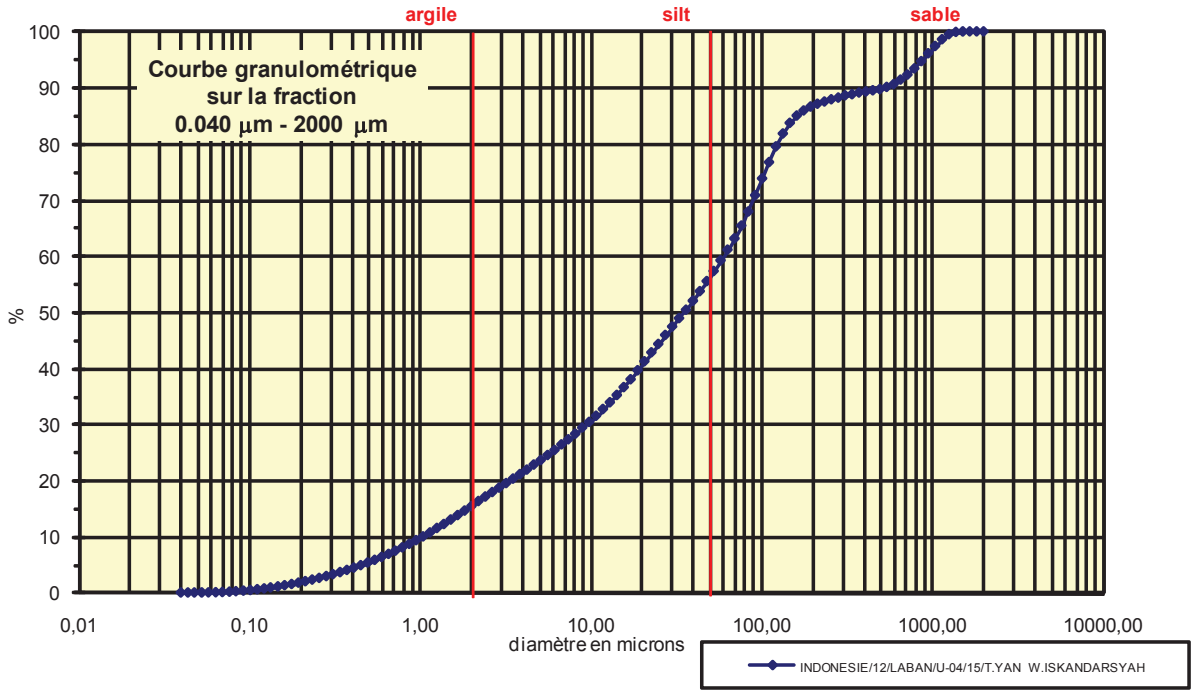

Fractiles	Taille (µm)	Taille (ϕ)
d_5	0,452	11,11
d_{10}	1,047	9,90
d_{16}	2,010	8,96
d_{25}	5,611	7,48
d_{30}	8,944	6,80
d_{50}	33,000	4,92
d_{60}	57,770	4,11
d_{75}	101,100	3,31
d_{84}	146,800	2,77
d_{90}	493,600	1,02
d_{95}	863,900	0,21

% Argile inférieur à 2µ	**A**	**14,60**
% Silts de 2µ à 50µ	**LT**	**40,90**
limons fins 2µ à 20µ	LF	25,00
limons grossiers 20µ à 50µ	LG	15,90
% Sables 50µ à 2000 µ	**ST**	**44,50**
sables fins 50µ à 200µ	SF	31,10
sables fins 50µ à 100µ	SF1	15,30
sables fins 100µ à 200 µ	SF2	15,80
sables grossiers 200µ à 2000µ	SG	13,40
sables grossiers 200µ à 500µ	SG1	3,10
sables grossiers 500µ à 1000µ	SG2	6,40
sables grossiers 1000µ à 2000µ	SG3	3,90

Indice de classement	
Trask, S_o	4,245
Krumbein, Q_d	-2,086
Inman, σ_ϕ	-3,095
Folk & Ward, σ_ϕ	-3,199
Hazen, C_u	55,177

Moyenne	
Trask, M	53,356
Inman, M_ϕ	5,863
Folk & Ward, M_z	5,549

Coefficient de dissymétrie	
Skew ness, S_{k-1}	0,521
Skew ness, S_{k-2}	0,722
Inman, $\alpha_{\phi-1}$	-0,304
Inman, $\alpha_{\phi-2}$	-0,239
Folk & Ward, Sk_i	-0,220

Coefficient d'acuité (Kurtosis)	
Krumbein & Petijohn, K	0,097
Inman, K_ϕ	0,761
Folk & Ward, K_G	1,071

Coefficient de courbure	
C_c	1,323

Analyse granulométrique par voie fluide : fraction 0,040 µm - 2000 µm

Echantillon :	INDONESIE/12/LABAN/U-04/16/T.YAN W.ISKANDARSYAH
Date :	11/07/2013 16:13
Opérateur :	MT
Fichier :	U04-016

Commentaires :	prof. 210-240 cm 26/05/12 Destruction MO à H2O2-élimination des ions floculants - Hexa+US

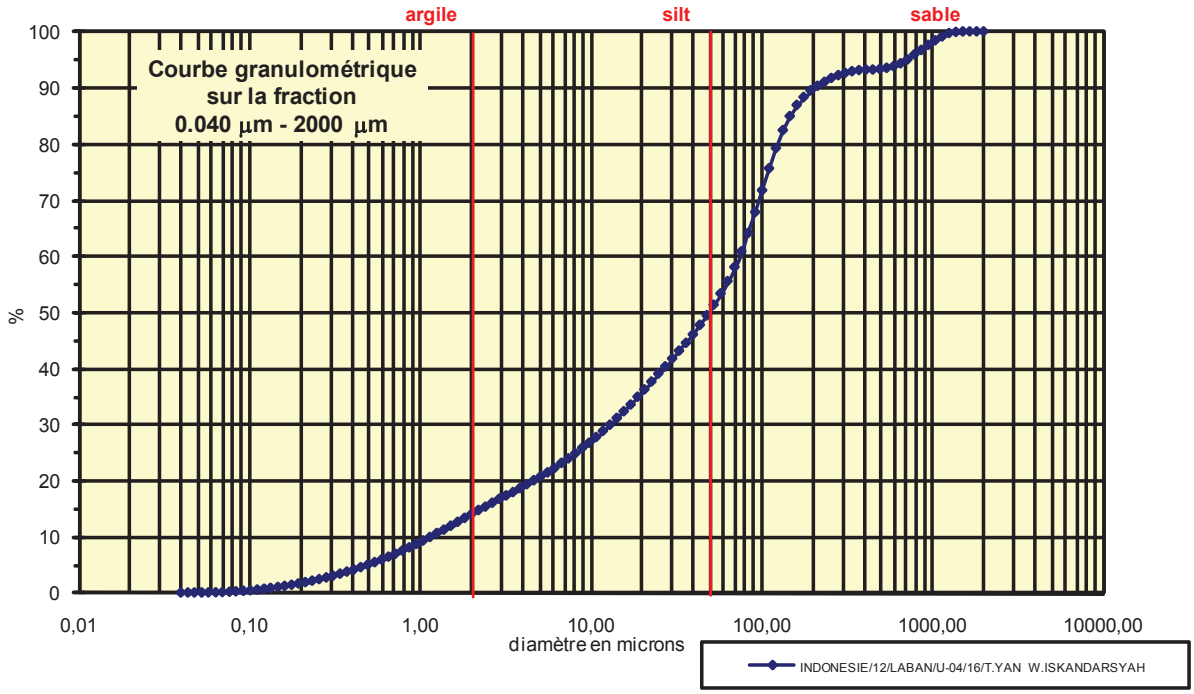

Fractiles	Taille (µm)	Taille (ϕ)
d_5	0,496	10,98
d_{10}	1,149	9,77
d_{16}	2,660	8,55
d_{25}	8,147	6,94
d_{30}	12,990	6,27
d_{50}	47,930	4,38
d_{60}	69,620	3,84
d_{75}	101,100	3,31
d_{84}	133,700	2,90
d_{90}	194,200	2,36
d_{95}	716,900	0,48

% Argile inférieur à 2µ	**A**	**13,30**
% Silts de 2µ à 50µ	**LT**	**36,10**
limons fins 2µ à 20µ	LF	21,60
limons grossiers 20µ à 50µ	LG	14,50
% Sables 50µ à 2000 µ	**ST**	**50,60**
sables fins 50µ à 200µ	SF	40,10
sables fins 50µ à 100µ	SF1	18,40
sables fins 100µ à 200 µ	SF2	21,70
sables grossiers 200µ à 2000µ	SG	10,50
sables grossiers 200µ à 500µ	SG1	3,80
sables grossiers 500µ à 1000µ	SG2	4,30
sables grossiers 1000µ à 2000µ	SG3	2,40

Indice de classement	
Trask, S_o	3,523
Krumbein, Q_d	-1,817
Inman, σ_ϕ	-2,826
Folk & Ward, σ_ϕ	-3,003
Hazen, C_u	60,592

Moyenne	
Trask, M	54,624
Inman, M_ϕ	5,729
Folk & Ward, M_z	5,280

Coefficient de dissymétrie	
Skew ness, S_{k-1}	0,359
Skew ness, S_{k-2}	0,599
Inman, $\alpha_{\phi-1}$	-0,476
Inman, $\alpha_{\phi-2}$	-0,476
Folk & Ward, Sk_i	-0,366

Coefficient d'acuité (Kurtosis)	
Krumbein & Petijohn, K	0,241
Inman, K_ϕ	0,857
Folk & Ward, K_G	1,184

Coefficient de courbure	
C_c	2,109

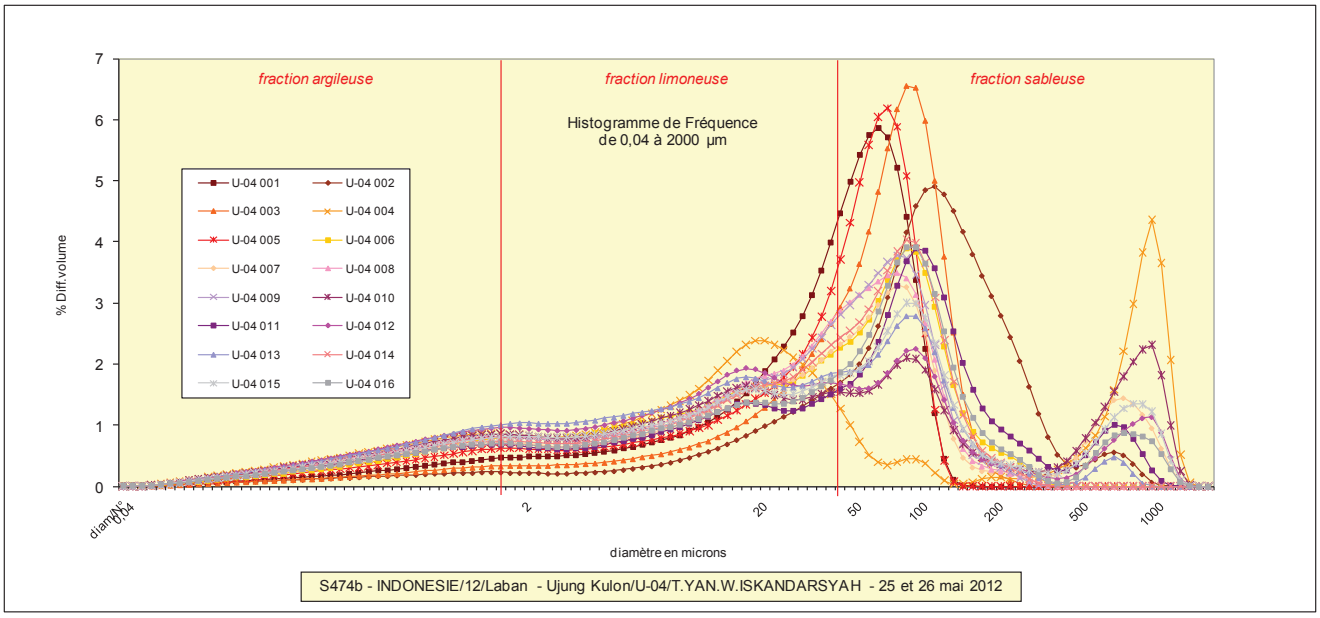
fraction argileuse
fraction limoneuse
fraction sableuse
Histogramme de Fréquence
de 0,04 à 2000 µm
U-04 001
U-04 002
U-04 003
U-04 004
U-04 005
U-04 006
U-04 007
U-04 008
U-04 009
U-04 010
U-04 011
U-04 012
U-04 013
U-04 014
U-04 015
U-04 016
% Diff.volume
diamètre en microns
S474b - INDONESIE/12/Laban - Ujung Kulon/U-04/T.YAN.W.ISKANDARSYAH - 25 et 26 mai 2012

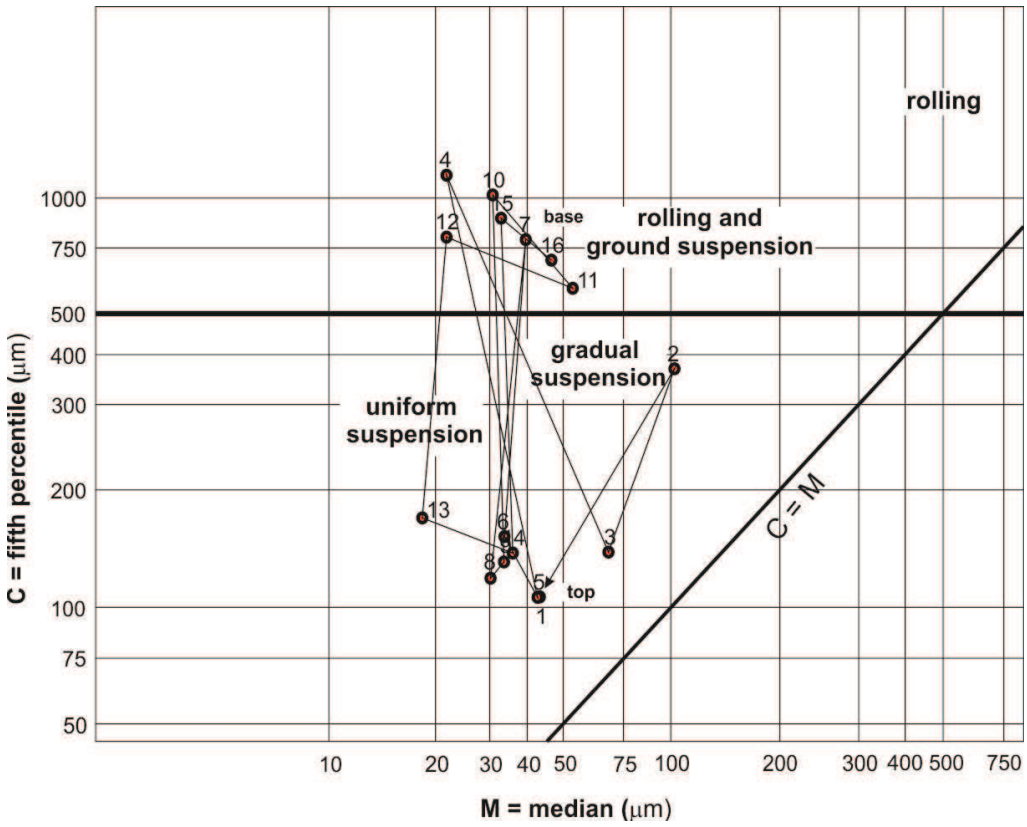
rolling
rolling and
ground suspension
base
gradual
suspension
uniform
suspension
C = M
top
C = fifth percentile (μm)
M = median (μm)
1000
750
500
400
300
200
100
75
50
10
20
30
40
50
75
100
200
300
400
500
750

Analyse granulométrique par voie fluide : fraction 0,040 µm - 2000 µm

Echantillon :	INDONESIE/12/LABAN/U-05/01/T.YAN W.ISKANDARSYAH
Date :	05/03/2013 11:11
Opérateur :	MT
Fichier :	U05-001

Commentaires :	prof. 0-15 cm 25/05/12 SILTY SOIL destruction MO à H2O2 - élimination des ions floculants - hexa +US

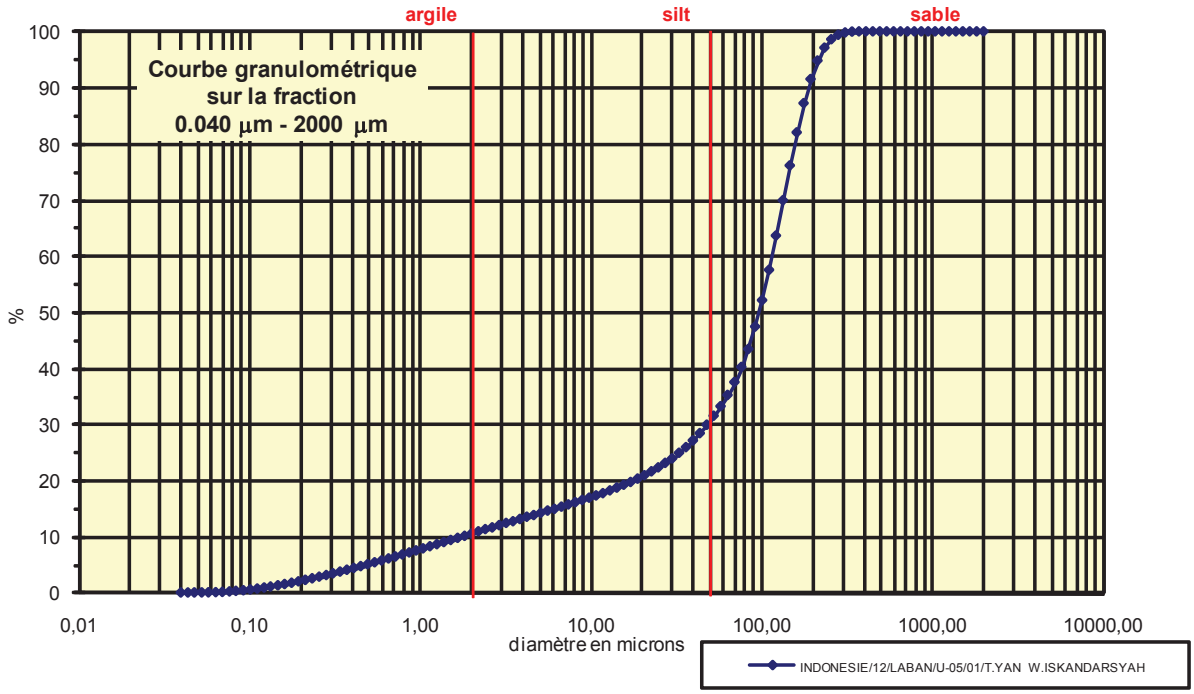

Fractiles	Taille (µm)	Taille (ϕ)
d_5	0,452	11,11
d_{10}	1,669	9,23
d_{16}	7,421	7,07
d_{25}	33,000	4,92
d_{30}	47,930	4,38
d_{50}	92,090	3,44
d_{60}	111,000	3,17
d_{75}	133,700	2,90
d_{84}	161,200	2,63
d_{90}	176,800	2,50
d_{95}	213,200	2,23

% Argile inférieur à 2µ	**A**	**10,10**
% Silts de 2µ à 50µ	**LT**	**19,80**
limons fins 2µ à 20µ	LF	10,20
limons grossiers 20µ à 50µ	LG	9,60
% Sables 50µ à 2000 µ	**ST**	**70,10**
sables fins 50µ à 200µ	SF	61,60
sables fins 50µ à 100µ	SF1	17,50
sables fins 100µ à 200 µ	SF2	44,10
sables grossiers 200µ à 2000µ	SG	8,50
sables grossiers 200µ à 500µ	SG1	8,50
sables grossiers 500µ à 1000µ	SG2	0,00
sables grossiers 1000µ à 2000µ	SG3	0,00

Indice de classement	
Trask, S_o	2,013
Krumbein, Q_d	-1,009
Inman, σ_ϕ	-2,221
Folk & Ward, σ_ϕ	-2,456
Hazen, C_u	66,507

Moyenne	
Trask, M	83,350
Inman, M_ϕ	4,854
Folk & Ward, M_z	4,383

Coefficient de dissymétrie	
Skew ness, S_{k-1}	0,520
Skew ness, S_{k-2}	0,721
Inman, $\alpha_{\phi-1}$	-0,636
Inman, $\alpha_{\phi-2}$	-1,454
Folk & Ward, Sk_i	-0,682

Coefficient d'acuité (Kurtosis)	
Krumbein & Petijohn, K	0,287
Inman, K_ϕ	1,000
Folk & Ward, K_G	1,803

Coefficient de courbure	
C_c	12,400

Analyse granulométrique par voie fluide : fraction 0,040 µm - 2000 µm

Echantillon :	INDONESIE/12/LABAN/U-05/02/T.YAN W.ISKANDARSYAH
Date :	05/03/2013 11:20
Opérateur :	MT
Fichier :	U05-002

Commentaires :	prof. 15-30 cm 25/05/12 SANDY SOIL destruction MO à H2O2 - élimination des ions floculants - hexa +US

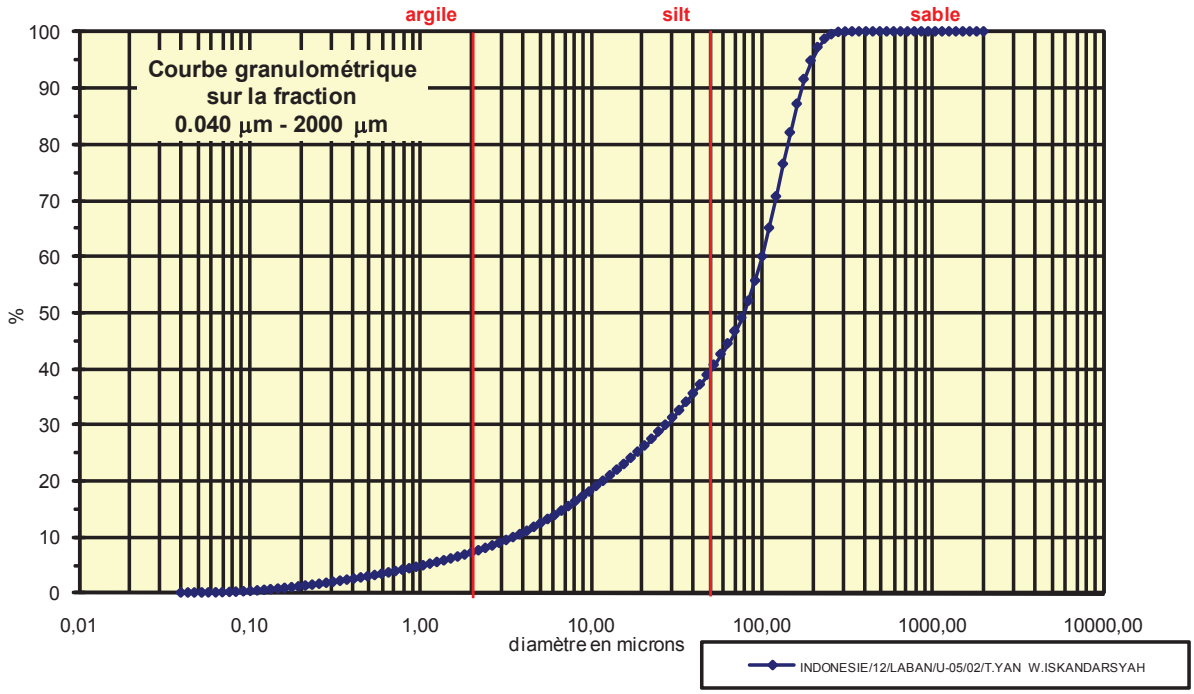

Fractiles	Taille (µm)	Taille (ϕ)
d_5	1,047	9,90
d_{10}	3,519	8,15
d_{16}	7,421	7,07
d_{25}	17,180	5,86
d_{30}	27,380	5,19
d_{50}	76,430	3,71
d_{60}	101,100	3,31
d_{75}	121,800	3,04
d_{84}	146,800	2,77
d_{90}	161,200	2,63
d_{95}	194,200	2,36

% Argile inférieur à 2µ	**A**	**6,76**
% Silts de 2µ à 50µ	**LT**	**32,04**
limons fins 2µ à 20µ	LF	18,34
limons grossiers 20µ à 50µ	LG	13,70
% Sables 50µ à 2000 µ	**ST**	**61,20**
sables fins 50µ à 200µ	SF	56,00
sables fins 50µ à 100µ	SF1	16,80
sables fins 100µ à 200 µ	SF2	39,20
sables grossiers 200µ à 2000µ	SG	5,20
sables grossiers 200µ à 500µ	SG1	5,20
sables grossiers 500µ à 1000µ	SG2	0,00
sables grossiers 1000µ à 2000µ	SG3	0,00

Indice de classement	
Trask, S_o	2,663
Krumbein, Q_d	-1,413
Inman, σ_ϕ	-2,153
Folk & Ward, σ_ϕ	-2,218
Hazen, C_u	28,730

Moyenne	
Trask, M	69,490
Inman, M_ϕ	4,921
Folk & Ward, M_z	4,517

Coefficient de dissymétrie	
Skew ness, S_{k-1}	0,358
Skew ness, S_{k-2}	0,599
Inman, $\alpha_{\phi-1}$	-0,563
Inman, $\alpha_{\phi-2}$	-1,125
Folk & Ward, Sk_i	-0,603

Coefficient d'acuité (Kurtosis)	
Krumbein & Petijohn, K	0,332
Inman, K_ϕ	0,750
Folk & Ward, K_G	1,093

Coefficient de courbure	
C_c	2,107

Analyse granulométrique par voie fluide : fraction 0,040 µm - 2000 µm

Echantillon :	INDONESIE/12/LABAN/U-05/03/T.YAN W.ISKANDARSYAH
Date :	05/03/2013 11:32
Opérateur :	MT
Fichier :	U05-003

Commentaires :	prof. 30-60 cm 25/05/12 destruction MO à H2O2 - élimination des ions floculants - hexa +US

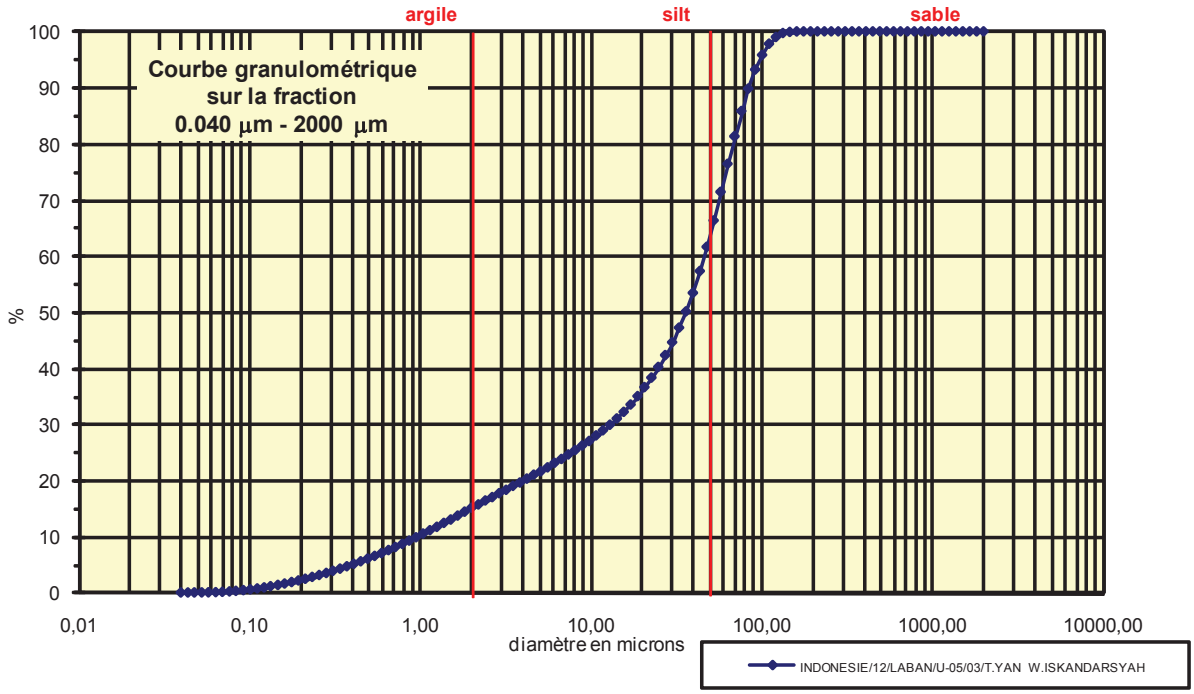

Fractiles	Taille (µm)	Taille (ϕ)
d_5	0,375	11,38
d_{10}	0,953	10,04
d_{16}	2,207	8,82
d_{25}	7,421	7,07
d_{30}	12,990	6,27
d_{50}	33,000	4,92
d_{60}	43,660	4,52
d_{75}	57,770	4,11
d_{84}	69,620	3,84
d_{90}	83,900	3,58
d_{95}	92,090	3,44

% Argile inférieur à 2µ	**A**	**14,40**
% Silts de 2µ à 50µ	**LT**	**47,20**
limons fins 2µ à 20µ	LF	20,60
limons grossiers 20µ à 50µ	LG	26,60
% Sables 50µ à 2000 µ	**ST**	**38,40**
sables fins 50µ à 200µ	SF	38,40
sables fins 50µ à 100µ	SF1	31,60
sables fins 100µ à 200 µ	SF2	6,80
sables grossiers 200µ à 2000µ	SG	0,00
sables grossiers 200µ à 500µ	SG1	0,00
sables grossiers 500µ à 1000µ	SG2	0,00
sables grossiers 1000µ à 2000µ	SG3	0,00

Indice de classement	
Trask, S_o	2,790
Krumbein, Q_d	-1,480
Inman, σ_ϕ	-2,490
Folk & Ward, σ_ϕ	-2,448
Hazen, C_u	45,813

Moyenne	
Trask, M	32,596
Inman, M_ϕ	6,334
Folk & Ward, M_z	5,863

Coefficient de dissymétrie	
Skew ness, S_{k-1}	0,394
Skew ness, S_{k-2}	0,627
Inman, $\alpha_{\phi-1}$	-0,567
Inman, $\alpha_{\phi-2}$	-1,000
Folk & Ward, Sk_i	-0,597

Coefficient d'acuité (Kurtosis)	
Krumbein & Petijohn, K	0,304
Inman, K_ϕ	0,595
Folk & Ward, K_G	1,099

Coefficient de courbure	
C_c	4,055

Analyse granulométrique par voie fluide : fraction 0,040 µm - 2000 µm

Echantillon :	INDONESIE/12/LABAN/U-05/04/T.YAN W.ISKANDARSYAH
Date :	05/03/2013 11:40
Opérateur :	MT
Fichier :	U05-004

Commentaires :	prof. 60-90 cm 25/05/12 destruction MO à H2O2 - élimination des ions floculants - hexa +US

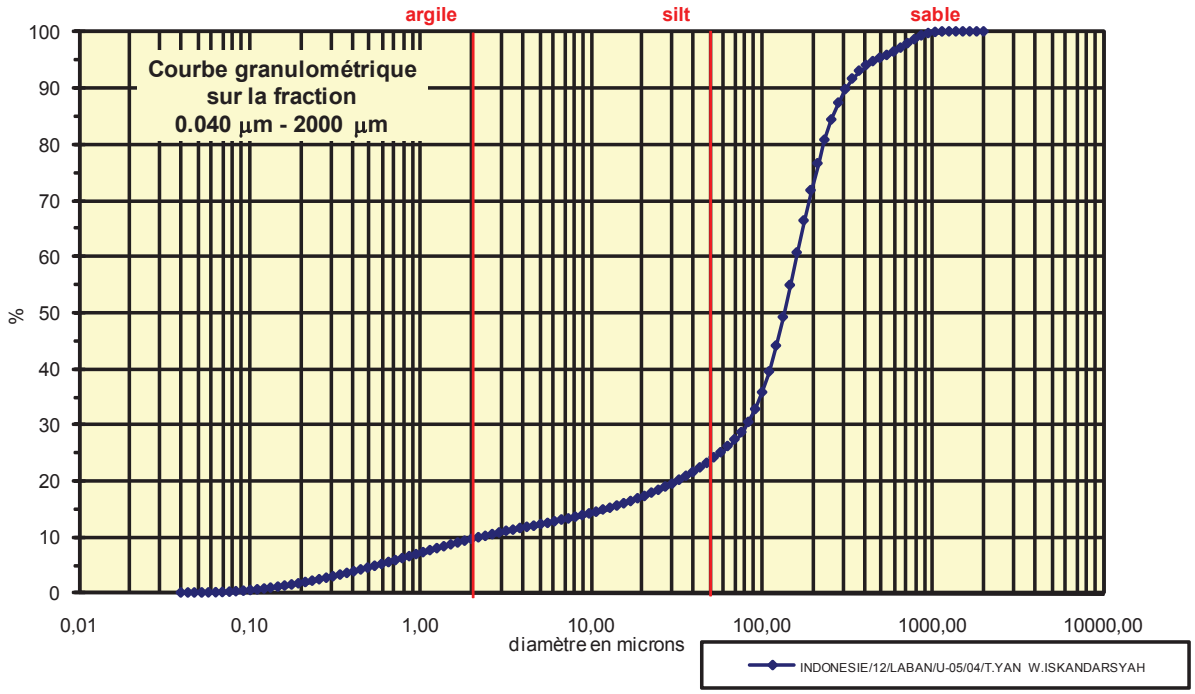

Fractiles	Taille (µm)	Taille (ϕ)
d_5	0,545	10,84
d_{10}	2,207	8,82
d_{16}	15,650	6,00
d_{25}	57,770	4,11
d_{30}	76,430	3,71
d_{50}	133,700	2,90
d_{60}	146,800	2,77
d_{75}	194,200	2,36
d_{84}	234,100	2,09
d_{90}	309,600	1,69
d_{95}	449,700	1,15

% Argile inférieur à 2µ	**A**	**9,24**
% Silts de 2µ à 50µ	**LT**	**13,86**
limons fins 2µ à 20µ	LF	7,56
limons grossiers 20µ à 50µ	LG	6,30
% Sables 50µ à 2000 µ	**ST**	**76,90**
sables fins 50µ à 200µ	SF	48,60
sables fins 50µ à 100µ	SF1	9,60
sables fins 100µ à 200 µ	SF2	39,00
sables grossiers 200µ à 2000µ	SG	28,30
sables grossiers 200µ à 500µ	SG1	23,60
sables grossiers 500µ à 1000µ	SG2	4,40
sables grossiers 1000µ à 2000µ	SG3	0,30

Indice de classement	
Trask, S_o	1,833
Krumbein, Q_d	-0,875
Inman, σ_ϕ	-1,951
Folk & Ward, σ_ϕ	-2,444
Hazen, C_u	66,516

Moyenne	
Trask, M	125,985
Inman, M_ϕ	4,046
Folk & Ward, M_z	3,665

Coefficient de dissymétrie	
Skew ness, S_{k1}	0,628
Skew ness, S_{k2}	0,792
Inman, $\alpha_{\phi-1}$	-0,586
Inman, $\alpha_{\phi-2}$	-1,586
Folk & Ward, Sk_i	-0,612

Coefficient d'acuité (Kurtosis)	
Krumbein & Petijohn, K	0,222
Inman, K_ϕ	1,482
Folk & Ward, K_G	2,270

Coefficient de courbure	
C_c	18,030

Analyse granulométrique par voie fluide : fraction 0,040 µm - 2000 µm

Echantillon :	INDONESIE/12/LABAN/U-05/05/T.YAN W.ISKANDARSYAH
Date :	05/03/2013 11:51
Opérateur :	MT
Fichier :	U05-005

Commentaires :	prof. 90-100 cm 25/05/12 SANDY SOIL destruction MO à H2O2 - élimination des ions floculants - hexa +US

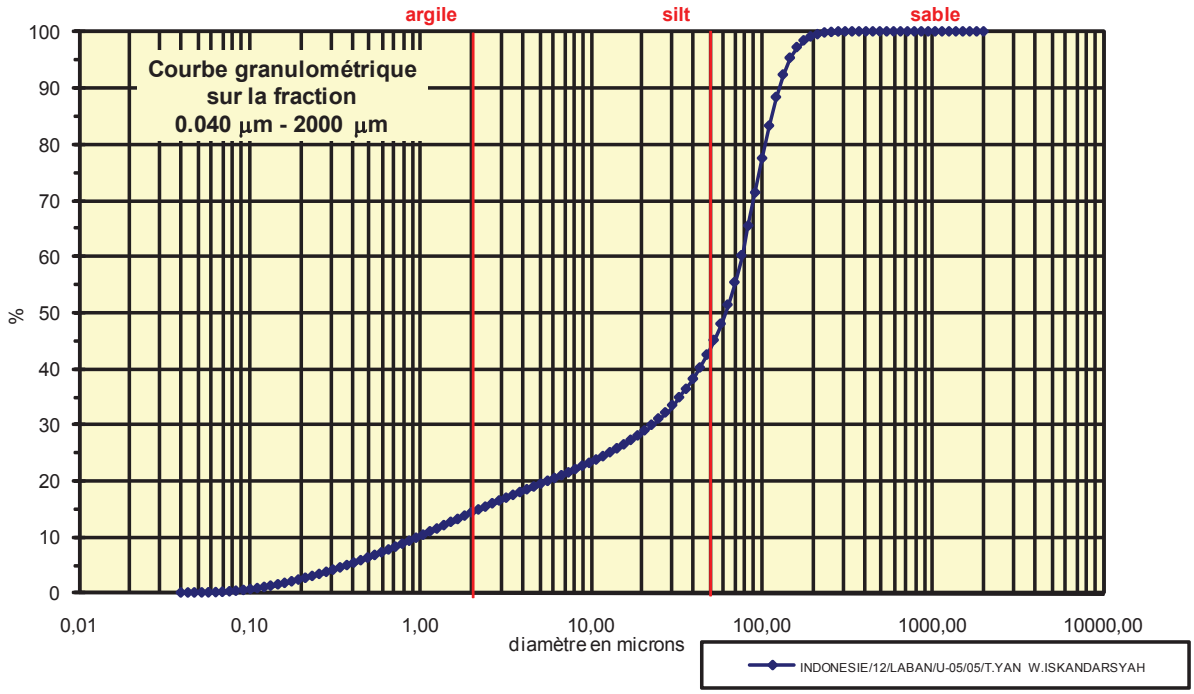

Fractiles	Taille (µm)	Taille (ϕ)
d_5	0,375	11,38
d_{10}	0,953	10,04
d_{16}	2,660	8,55
d_{25}	12,990	6,27
d_{30}	22,730	5,46
d_{50}	57,770	4,11
d_{60}	69,620	3,84
d_{75}	92,090	3,44
d_{84}	111,000	3,17
d_{90}	121,800	3,04
d_{95}	133,700	2,90

% Argile inférieur à 2µ	**A**	**13,70**
% Silts de 2µ à 50µ	**LT**	**28,70**
limons fins 2µ à 20µ	LF	14,30
limons grossiers 20µ à 50µ	LG	14,40
% Sables 50µ à 2000 µ	**ST**	**57,60**
sables fins 50µ à 200µ	SF	56,70
sables fins 50µ à 100µ	SF1	28,90
sables fins 100µ à 200 µ	SF2	27,80
sables grossiers 200µ à 2000µ	SG	0,90
sables grossiers 200µ à 500µ	SG1	0,90
sables grossiers 500µ à 1000µ	SG2	0,00
sables grossiers 1000µ à 2000µ	SG3	0,00

Indice de classement	
Trask, S_o	2,663
Krumbein, Q_d	-1,413
Inman, σ_ϕ	-2,691
Folk & Ward, σ_ϕ	-2,630
Hazen, C_u	73,054

Moyenne	
Trask, M	52,540
Inman, M_ϕ	5,863
Folk & Ward, M_z	5,280

Coefficient de dissymétrie	
Skew ness, S_{k-1}	0,358
Skew ness, S_{k-2}	0,599
Inman, $\alpha_{\phi-1}$	-0,650
Inman, $\alpha_{\phi-2}$	-1,125
Folk & Ward, Sk_i	-0,682

Coefficient d'acuité (Kurtosis)	
Krumbein & Petijohn, K	0,327
Inman, K_ϕ	0,575
Folk & Ward, K_G	1,230

Coefficient de courbure	
C_c	7,787

Analyse granulométrique par voie fluide : fraction 0,040 µm - 2000 µm

Echantillon :	INDONESIE/12/LABAN/U-05/06/T.YAN W.ISKANDARSYAH
Date :	05/03/2013 12:00
Opérateur :	MT
Fichier :	U05-006

Commentaires :	prof. 100-120 cm 25/05/12 SAND destruction MO à H2O2 - élimination des ions floculants - hexa +US

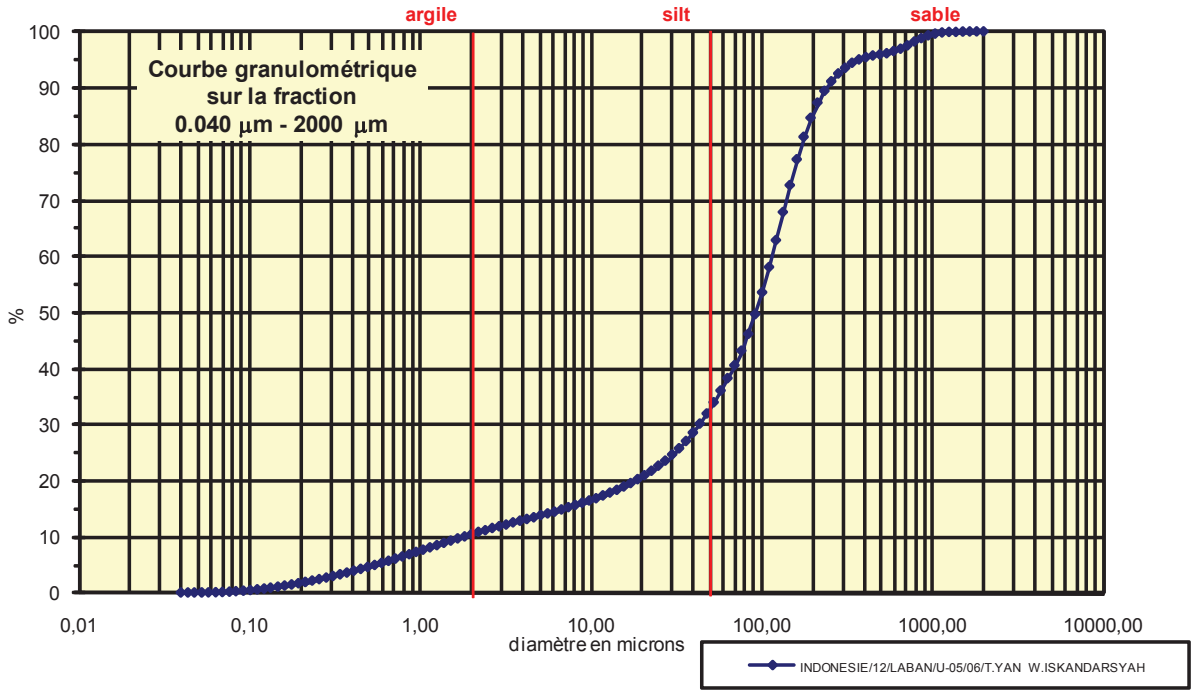

Fractiles	Taille (µm)	Taille (ϕ)
d_5	0,545	10,84
d_{10}	1,832	9,09
d_{16}	8,944	6,80
d_{25}	30,070	5,06
d_{30}	39,770	4,65
d_{50}	92,090	3,44
d_{60}	111,000	3,17
d_{75}	146,800	2,77
d_{84}	176,800	2,50
d_{90}	234,100	2,09
d_{95}	373,100	1,42

% Argile inférieur à 2µ	**A**	**10,00**
% Silts de 2µ à 50µ	**LT**	**21,90**
limons fins 2µ à 20µ	LF	10,20
limons grossiers 20µ à 50µ	LG	11,70
% Sables 50µ à 2000 µ	**ST**	**68,10**
sables fins 50µ à 200µ	SF	52,70
sables fins 50µ à 100µ	SF1	17,70
sables fins 100µ à 200 µ	SF2	35,00
sables grossiers 200µ à 2000µ	SG	15,40
sables grossiers 200µ à 500µ	SG1	11,30
sables grossiers 500µ à 1000µ	SG2	3,40
sables grossiers 1000µ à 2000µ	SG3	0,70

Indice de classement	
Trask, S_o	2,210
Krumbein, Q_d	-1,144
Inman, σ_ϕ	-2,153
Folk & Ward, σ_ϕ	-2,503
Hazen, C_u	60,590

Moyenne	
Trask, M	88,435
Inman, M_ϕ	4,652
Folk & Ward, M_z	4,248

Coefficient de dissymétrie	
Skew ness, S_{k-1}	0,521
Skew ness, S_{k-2}	0,721
Inman, $\alpha_{\phi-1}$	-0,563
Inman, $\alpha_{\phi-2}$	-1,250
Folk & Ward, Sk_i	-0,567

Coefficient d'acuité (Kurtosis)	
Krumbein & Petijohn, K	0,251
Inman, K_ϕ	1,188
Folk & Ward, K_G	1,688

Coefficient de courbure	
C_c	7,778

Analyse granulométrique par voie fluide : fraction 0,040 µm - 2000 µm

Echantillon :	INDONESIE/12/LABAN/U-05/07/T.YAN W.ISKANDARSYAH
Date :	05/03/2013 12:09
Opérateur :	MT
Fichier :	U05-007

Commentaires :	prof. 120-150 cm 25/05/12 destruction MO à H2O2 - élimination des ions floculants - hexa +US

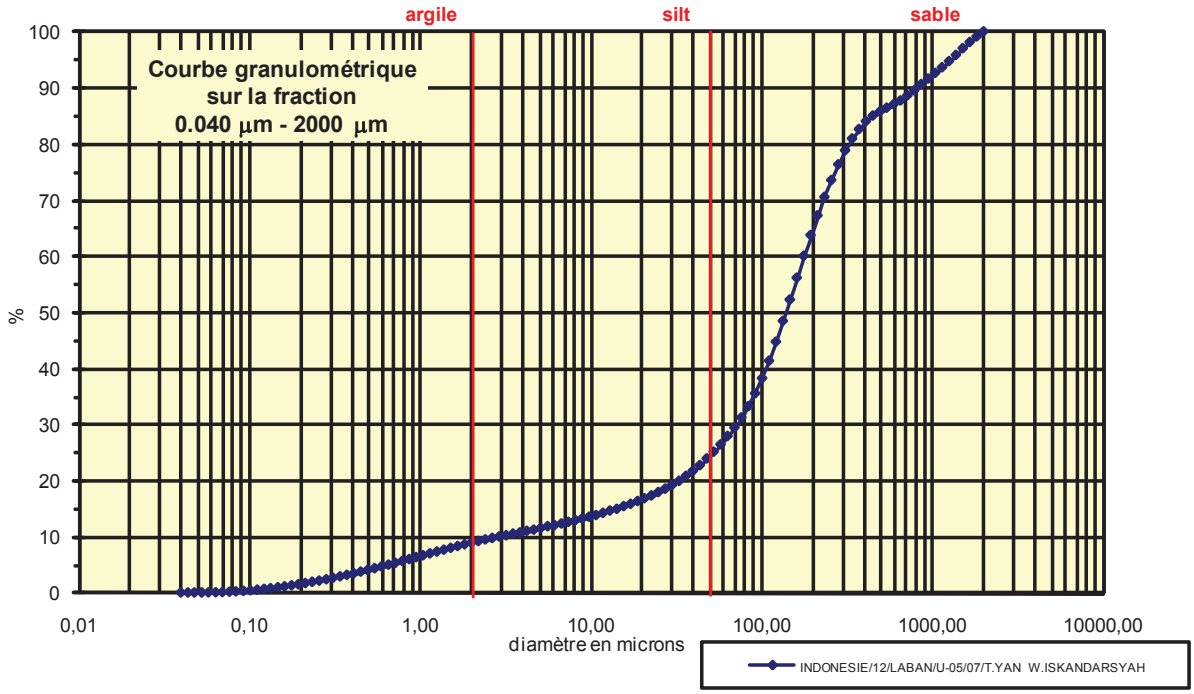

Fractiles	Taille (µm)	Taille (ϕ)
d_5	0,657	10,57
d_{10}	2,920	8,42
d_{16}	17,180	5,86
d_{25}	47,930	4,38
d_{30}	69,620	3,84
d_{50}	133,700	2,90
d_{60}	176,800	2,50
d_{75}	256,800	1,96
d_{84}	409,600	1,29
d_{90}	786,900	0,35
d_{95}	1255,000	-0,33

% Argile inférieur à 2µ	**A**	**8,59**
% Silts de 2µ à 50µ	**LT**	**15,31**
limons fins 2µ à 20µ	LF	7,71
limons grossiers 20µ à 50µ	LG	7,60
% Sables 50µ à 2000 µ	**ST**	**76,10**
sables fins 50µ à 200µ	SF	39,80
sables fins 50µ à 100µ	SF1	11,60
sables fins 100µ à 200 µ	SF2	28,20
sables grossiers 200µ à 2000µ	SG	36,30
sables grossiers 200µ à 500µ	SG1	22,00
sables grossiers 500µ à 1000µ	SG2	5,90
sables grossiers 1000µ à 2000µ	SG3	8,40

Indice de classement	
Trask, S_o	2,315
Krumbein, Q_d	-1,211
Inman, σ_ϕ	-2,288
Folk & Ward, σ_ϕ	-2,795
Hazen, C_u	60,548

Moyenne	
Trask, M	152,365
Inman, M_ϕ	3,575
Folk & Ward, M_z	3,351

Coefficient de dissymétrie	
Skew ness, S_{k-1}	0,689
Skew ness, S_{k-2}	0,830
Inman, $\alpha_{\phi-1}$	-0,294
Inman, $\alpha_{\phi-2}$	-0,970
Folk & Ward, Sk_i	-0,351

Coefficient d'acuité (Kurtosis)	
Krumbein & Petijohn, K	0,133
Inman, K_ϕ	1,382
Folk & Ward, K_G	1,845

Coefficient de courbure	
C_c	9,389

Analyse granulométrique par voie fluide : fraction 0,040 µm - 2000 µm

Echantillon :	INDONESIE/12/LABAN/U-05/08/T.YAN W.ISKANDARSYAH
Date :	05/03/2013 12:18
Opérateur :	MT
Fichier :	U05-008

Commentaires :	prof. 150-160 cm 25/05/12 destruction MO à H2O2 - élimination des ions floculants - hexa +US

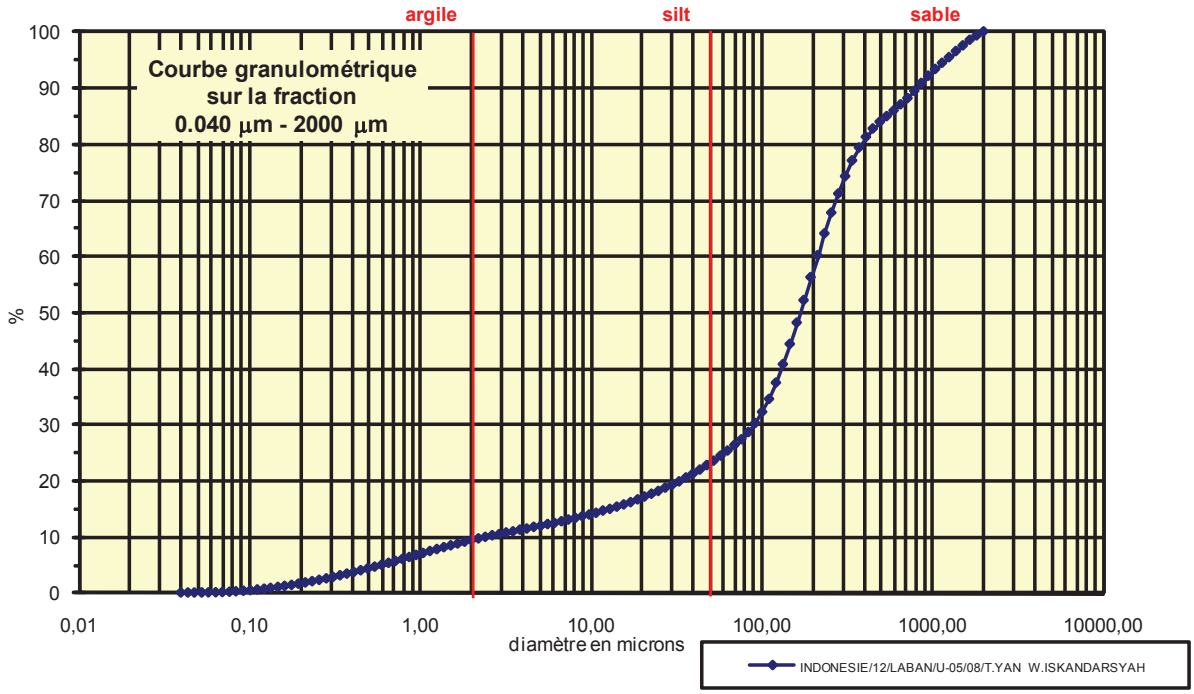

Fractiles	Taille (µm)	Taille (ϕ)
d_5	0,598	10,71
d_{10}	2,423	8,69
d_{16}	15,650	6,00
d_{25}	57,770	4,11
d_{30}	83,900	3,58
d_{50}	161,200	2,63
d_{60}	194,200	2,36
d_{75}	309,600	1,69
d_{84}	493,600	1,02
d_{90}	786,900	0,35
d_{95}	1143,000	-0,19

% Argile inférieur à 2µ	**A**	**9,05**
% Silts de 2µ à 50µ	**LT**	**13,65**
limons fins 2µ à 20µ	LF	7,55
limons grossiers 20µ à 50µ	LG	6,10
% Sables 50µ à 2000 µ	**ST**	**77,30**
sables fins 50µ à 200µ	SF	33,50
sables fins 50µ à 100µ	SF1	7,50
sables fins 100µ à 200 µ	SF2	26,00
sables grossiers 200µ à 2000µ	SG	43,80
sables grossiers 200µ à 500µ	SG1	27,70
sables grossiers 500µ à 1000µ	SG2	8,20
sables grossiers 1000µ à 2000µ	SG3	7,90

Indice de classement	
Trask, S_o	2,315
Krumbein, Q_d	-1,211
Inman, σ_ϕ	-2,490
Folk & Ward, σ_ϕ	-2,896
Hazen, C_u	80,149

Moyenne	
Trask, M	183,685
Inman, M_ϕ	3,508
Folk & Ward, M_z	3,216

Coefficient de dissymétrie	
Skew ness, S_{k1}	0,688
Skew ness, S_{k2}	0,830
Inman, $\alpha_{\phi-1}$	-0,351
Inman, $\alpha_{\phi-2}$	-1,054
Folk & Ward, Sk_I	-0,416

Coefficient d'acuité (Kurtosis)	
Krumbein & Petijohn, K	0,161
Inman, K_ϕ	1,189
Folk & Ward, K_G	1,844

Coefficient de courbure	
C_c	14,960

Analyse granulométrique par voie fluide : fraction 0,040 µm - 2000 µm

Echantillon :	INDONESIE/12/LABAN/U-05/09/T.YAN W.ISKANDARSYAH
Date :	10/07/2013 12:35
Opérateur :	MT
Fichier :	U05-009

Commentaires :	prof. 160 cm 25/05/12 0

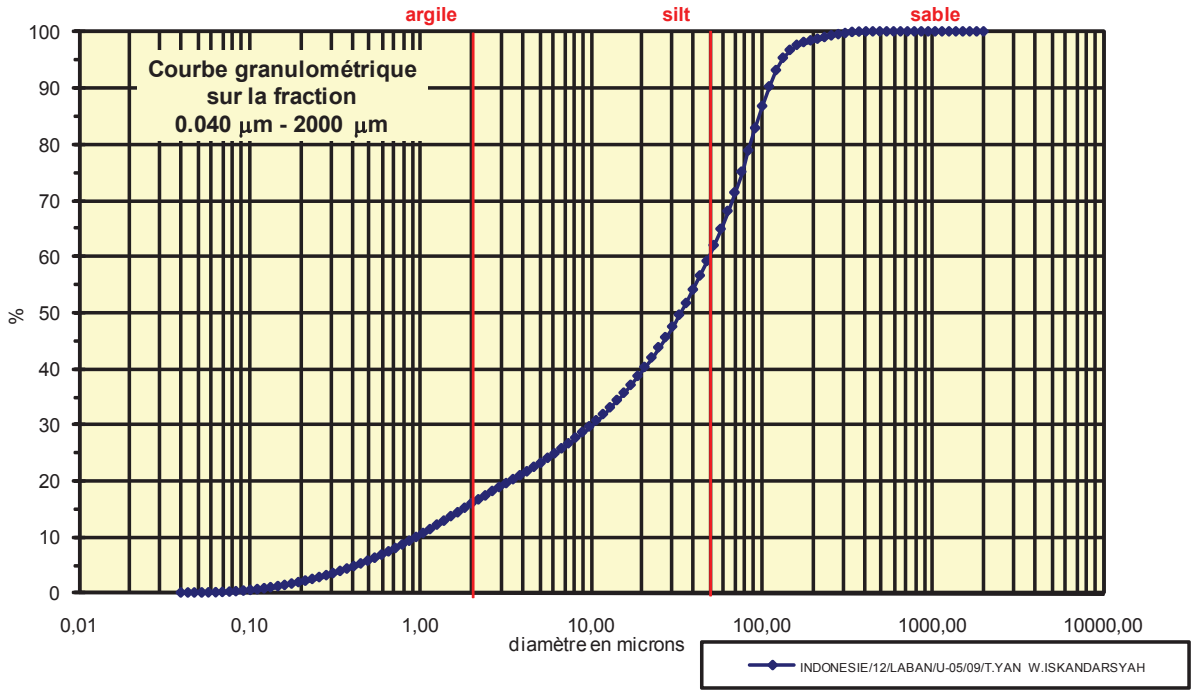

Fractiles	Taille (µm)	Taille (ϕ)
d_5	0,412	11,25
d_{10}	0,953	10,04
d_{16}	2,010	8,96
d_{25}	6,158	7,34
d_{30}	9,819	6,67
d_{50}	33,000	4,92
d_{60}	47,930	4,38
d_{75}	76,430	3,71
d_{84}	92,090	3,44
d_{90}	101,100	3,31
d_{95}	121,800	3,04

% Argile inférieur à 2µ	**A**	**15,10**
% Silts de 2µ à 50µ	**LT**	**44,00**
limons fins 2µ à 20µ	LF	23,50
limons grossiers 20µ à 50µ	LG	20,50
% Sables 50µ à 2000 µ	**ST**	**40,90**
sables fins 50µ à 200µ	SF	39,30
sables fins 50µ à 100µ	SF1	23,70
sables fins 100µ à 200 µ	SF2	15,60
sables grossiers 200µ à 2000µ	SG	1,60
sables grossiers 200µ à 500µ	SG1	1,60
sables grossiers 500µ à 1000µ	SG2	0,00
sables grossiers 1000µ à 2000µ	SG3	0,00

Indice de classement	
Trask, S_o	3,523
Krumbein, Q_d	-1,817
Inman, σ_ϕ	-2,759
Folk & Ward, σ_ϕ	-2,623
Hazen, C_u	50,294

Moyenne	
Trask, M	41,294
Inman, M_ϕ	6,200
Folk & Ward, M_z	5,774

Coefficient de dissymétrie	
Skew ness, S_{k-1}	0,432
Skew ness, S_{k-2}	0,657
Inman, $\alpha_{\phi-1}$	-0,463
Inman, $\alpha_{\phi-2}$	-0,805
Folk & Ward, Sk_i	-0,502

Coefficient d'acuité (Kurtosis)	
Krumbein & Petijohn, K	0,351
Inman, K_ϕ	0,487
Folk & Ward, K_G	0,926

Coefficient de courbure	
C_c	2,111

Analyse granulométrique par voie fluide : fraction 0,040 µm - 2000 µm

Echantillon :	INDONESIE/12/LABAN/U-05/10/T.YAN W.ISKANDARSYAH
Date :	10/07/2013 12:53
Opérateur :	MT
Fichier :	U05-010

Commentaires :	prof. 160-170 cm 25/05/12 0

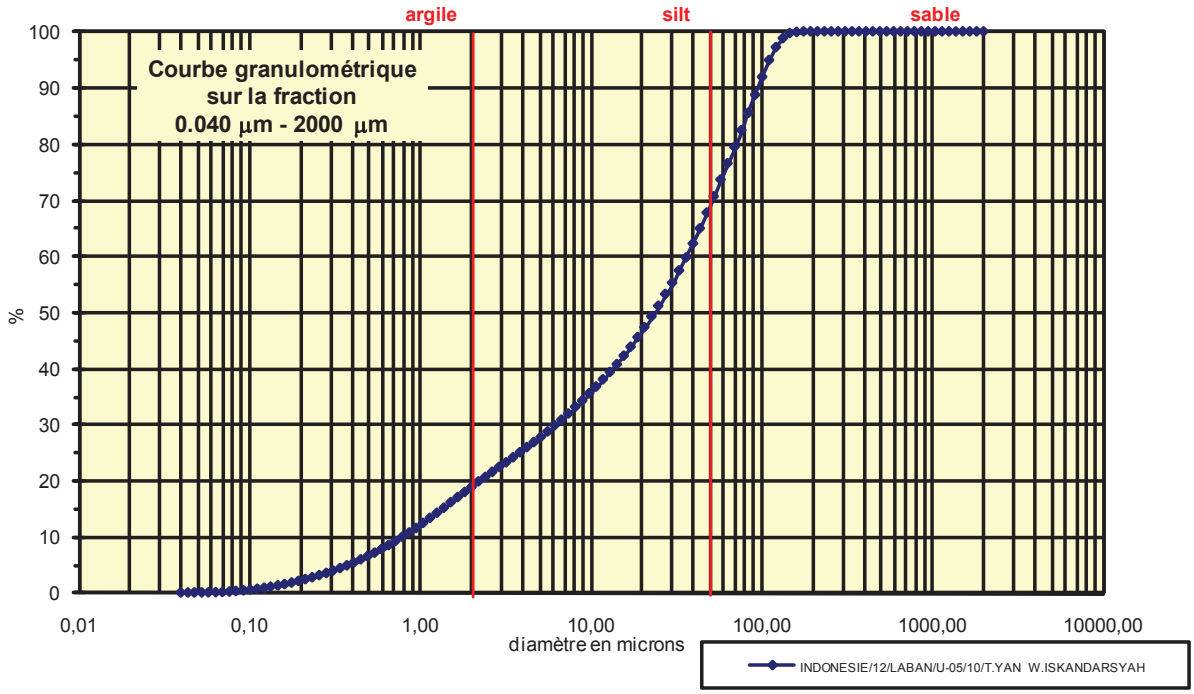

Fractiles	Taille (µm)	Taille (ϕ)
d_5	0,375	11,38
d_{10}	0,791	10,30
d_{16}	1,385	9,50
d_{25}	3,862	8,02
d_{30}	6,158	7,34
d_{50}	22,730	5,46
d_{60}	36,240	4,79
d_{75}	57,770	4,11
d_{84}	76,430	3,71
d_{90}	92,090	3,44
d_{95}	111,000	3,17

% Argile inférieur à 2µ	**A**	**17,90**
% Silts de 2µ à 50µ	**LT**	**49,80**
limons fins 2µ à 20µ	LF	27,60
limons grossiers 20µ à 50µ	LG	22,20
% Sables 50µ à 2000 µ	**ST**	**32,30**
sables fins 50µ à 200µ	SF	32,30
sables fins 50µ à 100µ	SF1	21,00
sables fins 100µ à 200 µ	SF2	11,30
sables grossiers 200µ à 2000µ	SG	0,00
sables grossiers 200µ à 500µ	SG1	0,00
sables grossiers 500µ à 1000µ	SG2	0,00
sables grossiers 1000µ à 2000µ	SG3	0,00

Indice de classement	
Trask, S_o	3,868
Krumbein, Q_d	-1,951
Inman, σ_ϕ	-2,893
Folk & Ward, σ_ϕ	-2,690
Hazen, C_u	45,815

Moyenne	
Trask, M	30,816
Inman, M_ϕ	6,603
Folk & Ward, M_z	6,222

Coefficient de dissymétrie	
Skew ness, S_{k-1}	0,432
Skew ness, S_{k-2}	0,657
Inman, $\alpha_{\phi-1}$	-0,395
Inman, $\alpha_{\phi-2}$	-0,628
Folk & Ward, Sk_i	-0,419

Coefficient d'acuité (Kurtosis)	
Krumbein & Petijohn, K	0,295
Inman, K_ϕ	0,419
Folk & Ward, K_G	0,862

Coefficient de courbure	
C_c	1,323

Analyse granulométrique par voie fluide : fraction 0,040 µm - 2000 µm

Echantillon :	INDONESIE/12/LABAN/U-05/11/T.YAN W.ISKANDARSYAH
Date :	10/07/2013 13:00
Opérateur :	MT
Fichier :	U05-011

Commentaires :	prof. 170-180 cm 25/05/12 0

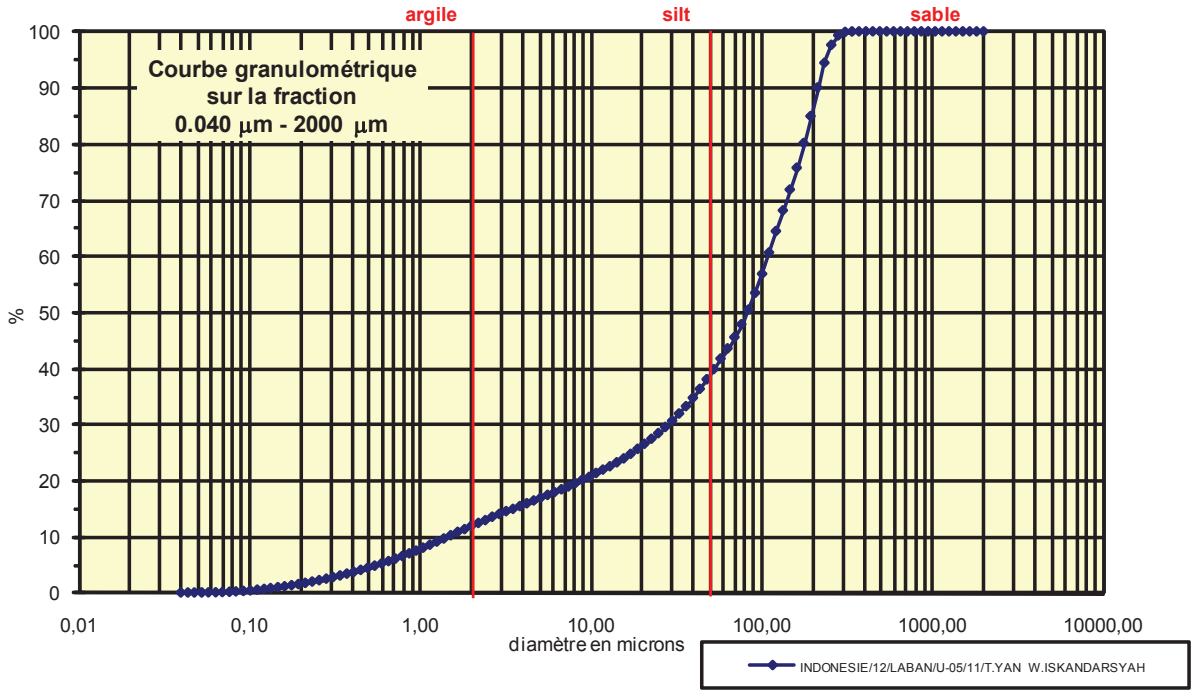

Fractiles	Taille (µm)	Taille (ϕ)
d_5	0,545	10,84
d_{10}	1,385	9,50
d_{16}	4,241	7,88
d_{25}	17,180	5,86
d_{30}	27,380	5,19
d_{50}	76,430	3,71
d_{60}	101,100	3,31
d_{75}	146,800	2,77
d_{84}	176,800	2,50
d_{90}	213,200	2,23
d_{95}	234,100	2,09

% Argile inférieur à 2µ	**A**	**11,30**
% Silts de 2µ à 50µ	**LT**	**26,70**
limons fins 2µ à 20µ	LF	14,30
limons grossiers 20µ à 50µ	LG	12,40
% Sables 50µ à 2000 µ	**ST**	**62,00**
sables fins 50µ à 200µ	SF	46,90
sables fins 50µ à 100µ	SF1	15,40
sables fins 100µ à 200 µ	SF2	31,50
sables grossiers 200µ à 2000µ	SG	15,10
sables grossiers 200µ à 500µ	SG1	15,10
sables grossiers 500µ à 1000µ	SG2	0,00
sables grossiers 1000µ à 2000µ	SG3	0,00

Indice de classement	
Trask, S_o	2,923
Krumbein, Q_d	-1,548
Inman, σ_ϕ	-2,691
Folk & Ward, σ_ϕ	-2,671
Hazen, C_u	72,996

Moyenne	
Trask, M	81,990
Inman, M_ϕ	5,191
Folk & Ward, M_z	4,697

Coefficient de dissymétrie	
Skew ness, S_{k-1}	0,432
Skew ness, S_{k-2}	0,657
Inman, $\alpha_{\phi-1}$	-0,550
Inman, $\alpha_{\phi-2}$	-1,025
Folk & Ward, Sk_i	-0,591

Coefficient d'acuité (Kurtosis)	
Krumbein & Petijohn, K	0,306
Inman, K_ϕ	0,625
Folk & Ward, K_G	1,158

Coefficient de courbure	
C_c	5,354

Analyse granulométrique par voie fluide : fraction 0,040 µm - 2000 µm

Echantillon :	INDONESIE/12/LABAN/U-05/12/T.YAN W.ISKANDARSYAH
Date :	10/07/2013 14:32
Opérateur :	MT
Fichier :	U05-012

Commentaires :	prof. 180-190 cm 25/05/12 0

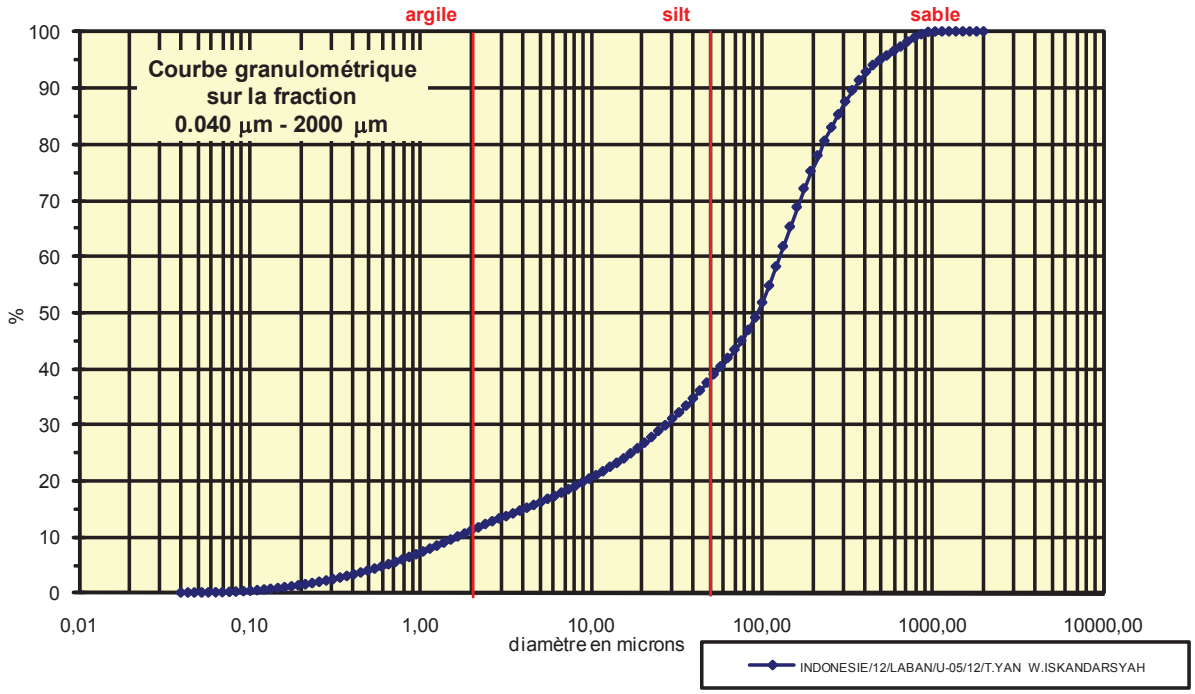

Fractiles	Taille (µm)	Taille (ϕ)
d_5	0,598	10,71
d_{10}	1,669	9,23
d_{16}	4,656	7,75
d_{25}	17,180	5,86
d_{30}	27,380	5,19
d_{50}	92,090	3,44
d_{60}	121,800	3,04
d_{75}	176,800	2,50
d_{84}	256,800	1,96
d_{90}	339,800	1,56
d_{95}	493,600	1,02

% Argile inférieur à 2µ	**A**	**10,50**
% Silts de 2µ à 50µ	**LT**	**26,90**
limons fins 2µ à 20µ	LF	15,20
limons grossiers 20µ à 50µ	LG	11,70
% Sables 50µ à 2000 µ	**ST**	**62,60**
sables fins 50µ à 200µ	SF	37,70
sables fins 50µ à 100µ	SF1	11,60
sables fins 100µ à 200 µ	SF2	26,10
sables grossiers 200µ à 2000µ	SG	24,90
sables grossiers 200µ à 500µ	SG1	19,80
sables grossiers 500µ à 1000µ	SG2	5,00
sables grossiers 1000µ à 2000µ	SG3	0,10

Indice de classement	
Trask, S_o	3,208
Krumbein, Q_d	-1,682
Inman, σ_ϕ	-2,893
Folk & Ward, σ_ϕ	-2,914
Hazen, C_u	72,978

Moyenne	
Trask, M	96,990
Inman, M_ϕ	4,854
Folk & Ward, M_z	4,383

Coefficient de dissymétrie	
Skew ness, S_{k-1}	0,358
Skew ness, S_{k-2}	0,598
Inman, $\alpha_{\phi-1}$	-0,489
Inman, $\alpha_{\phi-2}$	-0,837
Folk & Ward, Sk_I	-0,494

Coefficient d'acuité (Kurtosis)	
Krumbein & Petijohn, K	0,236
Inman, K_ϕ	0,675
Folk & Ward, K_G	1,181

Coefficient de courbure	
C_c	3,688

Analyse granulométrique par voie fluide : fraction 0,040 µm - 2000 µm

Echantillon :	INDONESIE/12/LABAN/U-05/13/T.YAN W.ISKANDARSYAH
Date :	10/07/2013 14:41
Opérateur :	MT
Fichier :	U05-013

Commentaires :	prof. 190-200 cm 25/05/12 0

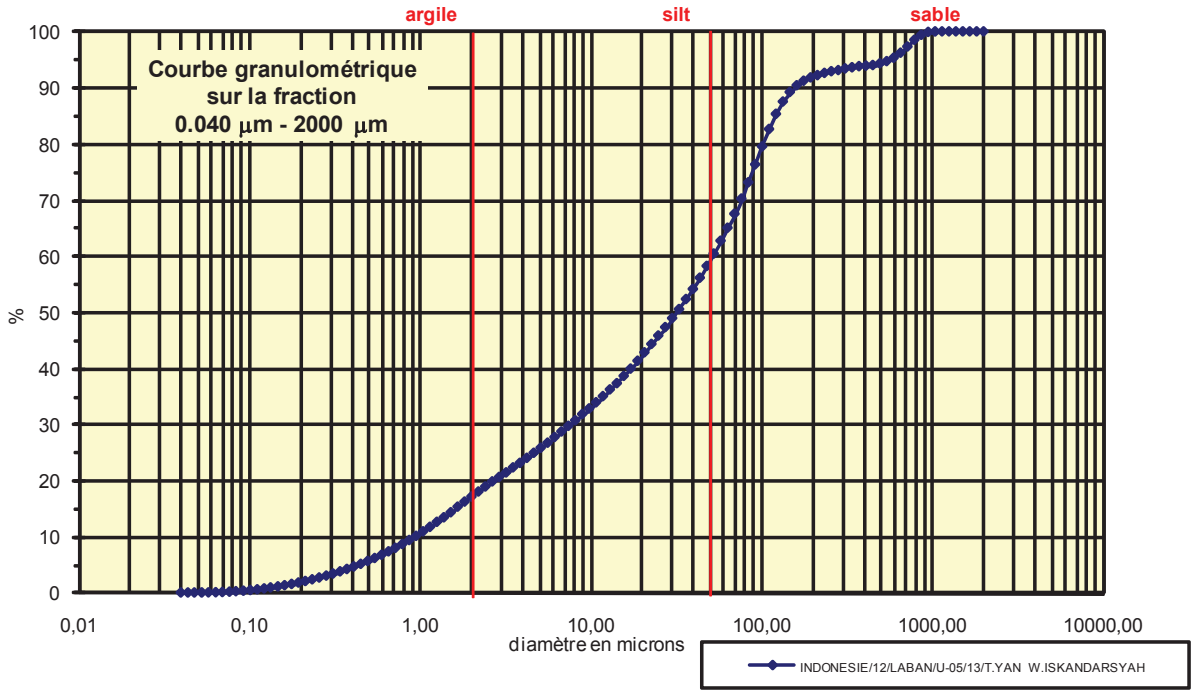

Fractiles	Taille (µm)	Taille (ϕ)
d_5	0,412	11,25
d_{10}	0,869	10,17
d_{16}	1,669	9,23
d_{25}	4,656	7,75
d_{30}	7,421	7,07
d_{50}	30,070	5,06
d_{60}	47,930	4,38
d_{75}	83,900	3,58
d_{84}	111,000	3,17
d_{90}	146,800	2,77
d_{95}	541,900	0,88

% Argile inférieur à 2µ	**A**	**16,20**
% Silts de 2µ à 50µ	**LT**	**42,00**
limons fins 2µ à 20µ	LF	25,10
limons grossiers 20µ à 50µ	LG	16,90
% Sables 50µ à 2000 µ	**ST**	**41,80**
sables fins 50µ à 200µ	SF	33,60
sables fins 50µ à 100µ	SF1	18,10
sables fins 100µ à 200 µ	SF2	15,50
sables grossiers 200µ à 2000µ	SG	8,20
sables grossiers 200µ à 500µ	SG1	2,50
sables grossiers 500µ à 1000µ	SG2	5,60
sables grossiers 1000µ à 2000µ	SG3	0,10

Indice de classement	
Trask, S_o	4,245
Krumbein, Q_d	-2,086
Inman, σ_ϕ	-3,028
Folk & Ward, σ_ϕ	-3,084
Hazen, C_u	55,155

Moyenne	
Trask, M	44,278
Inman, M_ϕ	6,199
Folk & Ward, M_z	5,818

Coefficient de dissymétrie	
Skew ness, S_{k-1}	0,432
Skew ness, S_{k-2}	0,657
Inman, $\alpha_{\phi-1}$	-0,378
Inman, $\alpha_{\phi-2}$	-0,333
Folk & Ward, Sk_I	-0,286

Coefficient d'acuité (Kurtosis)	
Krumbein & Petijohn, K	0,272
Inman, K_ϕ	0,711
Folk & Ward, K_G	1,018

Coefficient de courbure	
C_c	1,322

Analyse granulométrique par voie fluide : fraction 0,040 µm - 2000 µm

Echantillon :	INDONESIE/12/LABAN/U-05/14/T.YAN W.ISKANDARSYAH
Date :	10/07/2013 15:31
Opérateur :	MT
Fichier :	U05-014

Commentaires :	prof. 200-210 cm 25/05/12 0

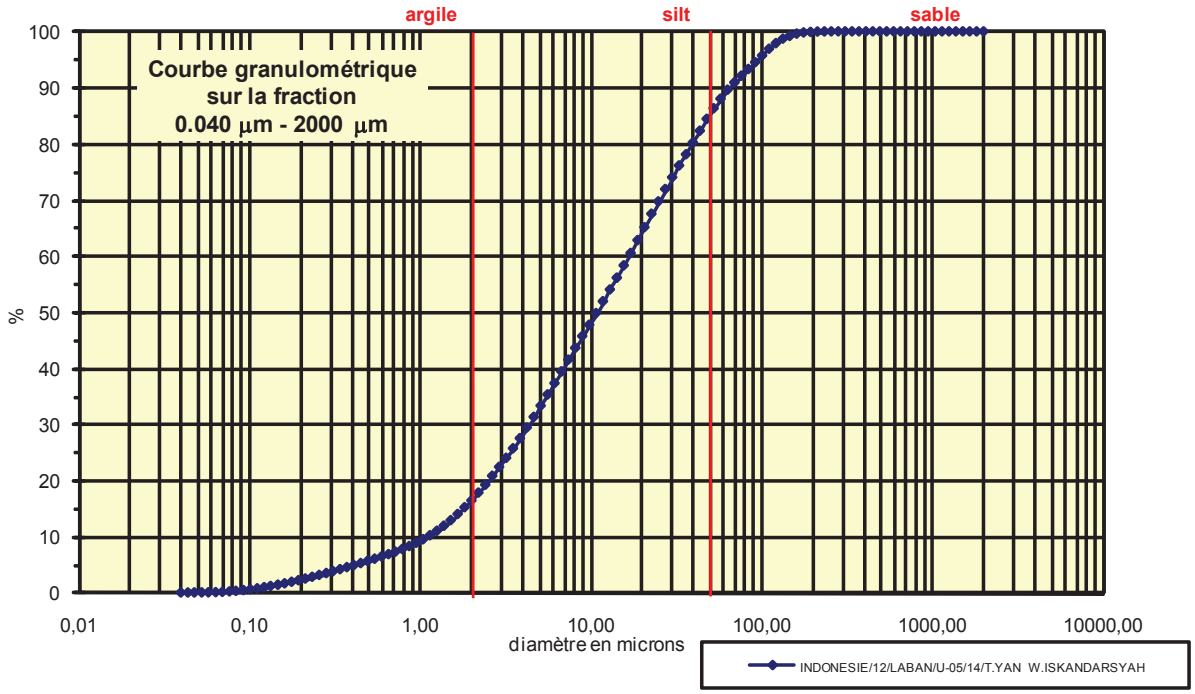

Fractiles	Taille (µm)	Taille (ϕ)
d_5	0,412	11,25
d_{10}	1,047	9,90
d_{16}	1,832	9,09
d_{25}	3,206	8,29
d_{30}	4,241	7,88
d_{50}	10,780	6,54
d_{60}	15,650	6,00
d_{75}	30,070	5,06
d_{84}	43,660	4,52
d_{90}	63,410	3,98
d_{95}	92,090	3,44

% Argile inférieur à 2µ	**A**	**15,20**
% Silts de 2µ à 50µ	**LT**	**69,20**
limons fins 2µ à 20µ	LF	47,60
limons grossiers 20µ à 50µ	LG	21,60
% Sables 50µ à 2000 µ	**ST**	**15,60**
sables fins 50µ à 200µ	SF	15,50
sables fins 50µ à 100µ	SF1	10,10
sables fins 100µ à 200 µ	SF2	5,40
sables grossiers 200µ à 2000µ	SG	0,10
sables grossiers 200µ à 500µ	SG1	0,10
sables grossiers 500µ à 1000µ	SG2	0,00
sables grossiers 1000µ à 2000µ	SG3	0,00

Indice de classement	
Trask, S_o	3,063
Krumbein, Q_d	-1,615
Inman, σ_ϕ	-2,287
Folk & Ward, σ_ϕ	-2,326
Hazen, C_u	14,947

Moyenne	
Trask, M	16,638
Inman, M_ϕ	6,805
Folk & Ward, M_z	6,715

Coefficient de dissymétrie	
Skew ness, S_{k-1}	0,830
Skew ness, S_{k-2}	0,911
Inman, $\alpha_{\phi-1}$	-0,118
Inman, $\alpha_{\phi-2}$	-0,353
Folk & Ward, Sk_I	-0,162

Coefficient d'acuité (Kurtosis)	
Krumbein & Petijohn, K	0,215
Inman, K_ϕ	0,706
Folk & Ward, K_G	0,990

Coefficient de courbure	
C_c	1,098

Analyse granulométrique par voie fluide : fraction 0,040 µm - 2000 µm

Echantillon :	INDONESIE/12/LABAN/U-05/15/T.YAN W.ISKANDARSYAH
Date :	10/07/2013 15:43
Opérateur :	MT
Fichier :	U05-015

Commentaires :	prof. 210-240 cm 25/05/12 0

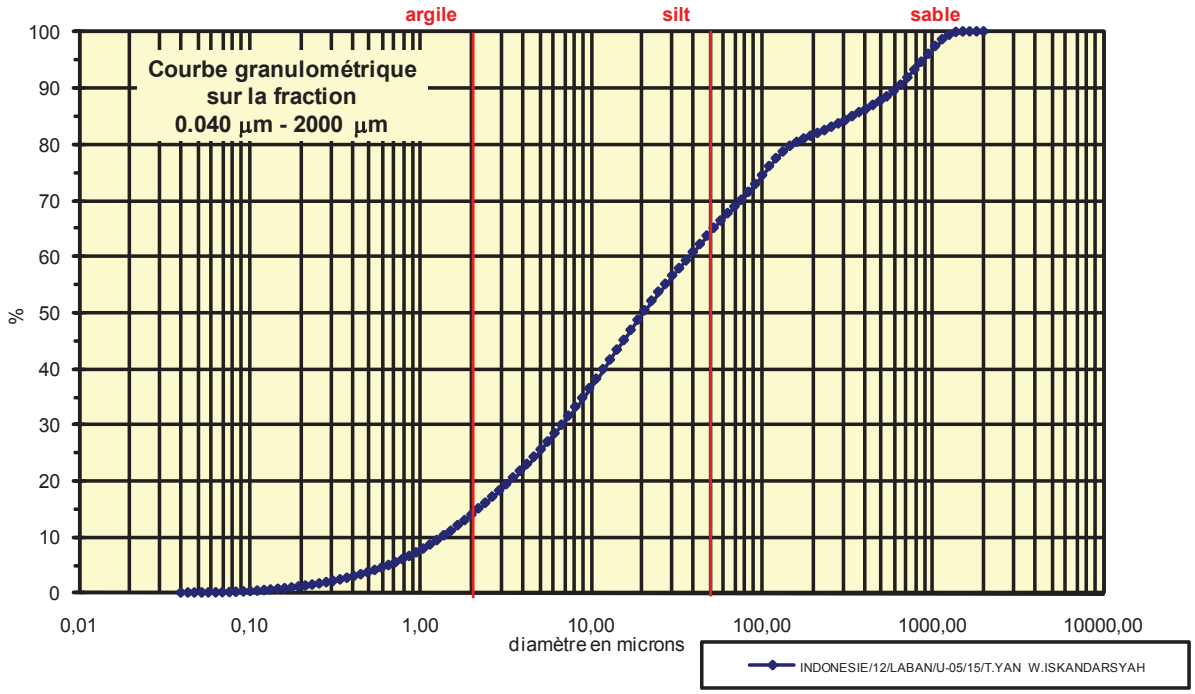

Fractiles	Taille (µm)	Taille (ϕ)
d_5	0,657	10,57
d_{10}	1,261	9,63
d_{16}	2,423	8,69
d_{25}	4,656	7,75
d_{30}	6,761	7,21
d_{50}	18,860	5,73
d_{60}	36,240	4,79
d_{75}	101,100	3,31
d_{84}	282,100	1,83
d_{90}	594,900	0,75
d_{95}	863,900	0,21

% Argile inférieur à 2µ	**A**	**12,90**
% Silts de 2µ à 50µ	**LT**	**50,70**
limons fins 2µ à 20µ	LF	35,70
limons grossiers 20µ à 50µ	LG	15,00
% Sables 50µ à 2000 µ	**ST**	**36,40**
sables fins 50µ à 200µ	SF	17,80
sables fins 50µ à 100µ	SF1	9,20
sables fins 100µ à 200 µ	SF2	8,60
sables grossiers 200µ à 2000µ	SG	18,60
sables grossiers 200µ à 500µ	SG1	6,20
sables grossiers 500µ à 1000µ	SG2	8,40
sables grossiers 1000µ à 2000µ	SG3	4,00

Indice de classement	
Trask, S_o	4,660
Krumbein, Q_d	-2,220
Inman, σ_ϕ	-3,432
Folk & Ward, σ_ϕ	-3,286
Hazen, C_u	28,739

Moyenne	
Trask, M	52,878
Inman, M_ϕ	5,257
Folk & Ward, M_z	5,414

Coefficient de dissymétrie	
Skew ness, S_{k-1}	1,323
Skew ness, S_{k-2}	1,150
Inman, $\alpha_{\phi-1}$	0,137
Inman, $\alpha_{\phi-2}$	0,098
Folk & Ward, Sk_i	0,101

Coefficient d'acuité (Kurtosis)	
Krumbein & Petijohn, K	0,081
Inman, K_ϕ	0,510
Folk & Ward, K_G	0,956

Coefficient de courbure	
C_c	1,000

Analyse granulométrique par voie fluide : fraction 0,040 µm - 2000 µm

Echantillon :	INDONESIE/12/LABAN/U-05/16/T.YAN W.ISKANDARSYAH
Date :	10/07/2013 15:58
Opérateur :	MT
Fichier :	U05-016

Commentaires :	prof. 240-270 cm 25/05/12 0

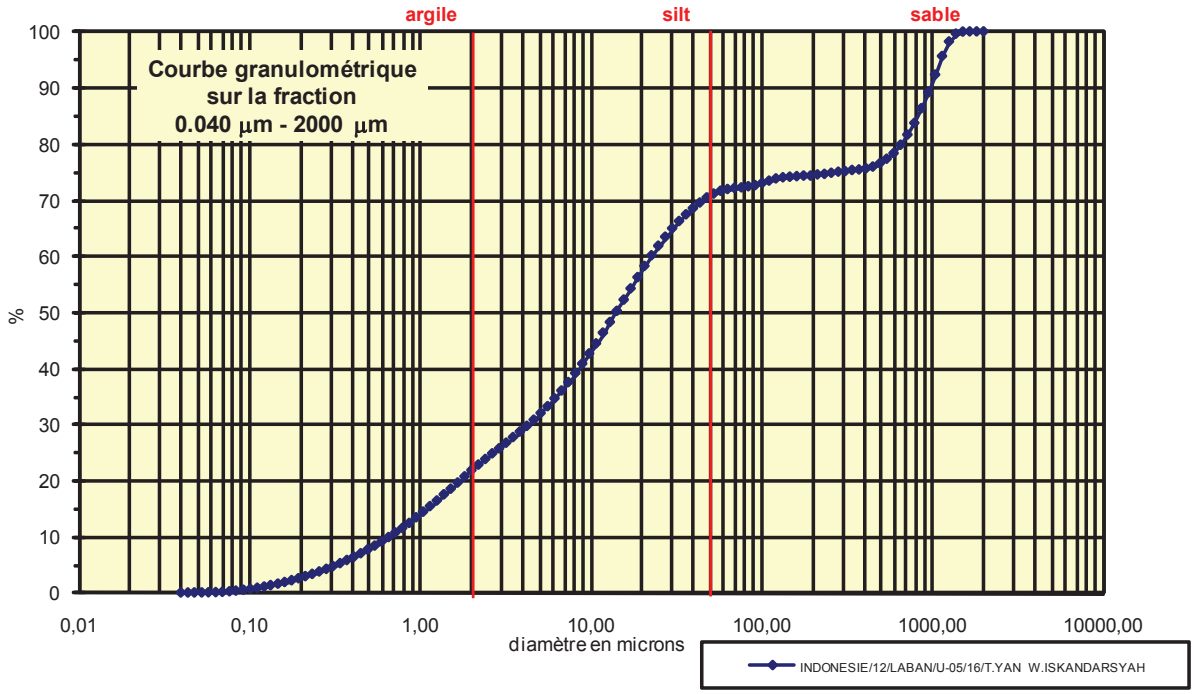

Fractiles	Taille (µm)	Taille (ϕ)
d_5	0,311	11,65
d_{10}	0,657	10,57
d_{16}	1,149	9,77
d_{25}	2,660	8,55
d_{30}	4,241	7,88
d_{50}	12,990	6,27
d_{60}	20,700	5,59
d_{75}	282,100	1,83
d_{84}	786,900	0,35
d_{90}	948,200	0,08
d_{95}	1041,000	-0,06

% Argile inférieur à 2µ	**A**	**20,70**
% Silts de 2µ à 50µ	**LT**	**49,70**
limons fins 2µ à 20µ	LF	35,50
limons grossiers 20µ à 50µ	LG	14,20
% Sables 50µ à 2000 µ	**ST**	**29,60**
sables fins 50µ à 200µ	SF	3,90
sables fins 50µ à 100µ	SF1	2,20
sables fins 100µ à 200 µ	SF2	1,70
sables grossiers 200µ à 2000µ	SG	25,70
sables grossiers 200µ à 500µ	SG1	2,20
sables grossiers 500µ à 1000µ	SG2	12,60
sables grossiers 1000µ à 2000µ	SG3	10,90

Indice de classement	
Trask, S_o	10,298
Krumbein, Q_d	-3,364
Inman, σ_ϕ	-4,710
Folk & Ward, σ_ϕ	-4,129
Hazen, C_u	31,507

Moyenne	
Trask, M	142,380
Inman, M_ϕ	5,056
Folk & Ward, M_z	5,459

Coefficient de dissymétrie	
Skew ness, S_{k-1}	4,447
Skew ness, S_{k-2}	2,109
Inman, $\alpha_{\phi-1}$	0,257
Inman, $\alpha_{\phi-2}$	0,100
Folk & Ward, Sk_i	0,169

Coefficient d'acuité (Kurtosis)	
Krumbein & Petijohn, K	0,147
Inman, K_ϕ	0,243
Folk & Ward, K_G	0,713

Coefficient de courbure	
C_c	1,323

Analyse granulométrique par voie fluide : fraction 0,040 µm - 2000 µm

Echantillon :	INDONESIE/12/LABAN/U-05/17/T.YAN W.ISKANDARSYAH
Date :	10/07/2013 16:09
Opérateur :	MT
Fichier :	U05-017

Commentaires :	prof. 270-295 cm 25/05/12 0

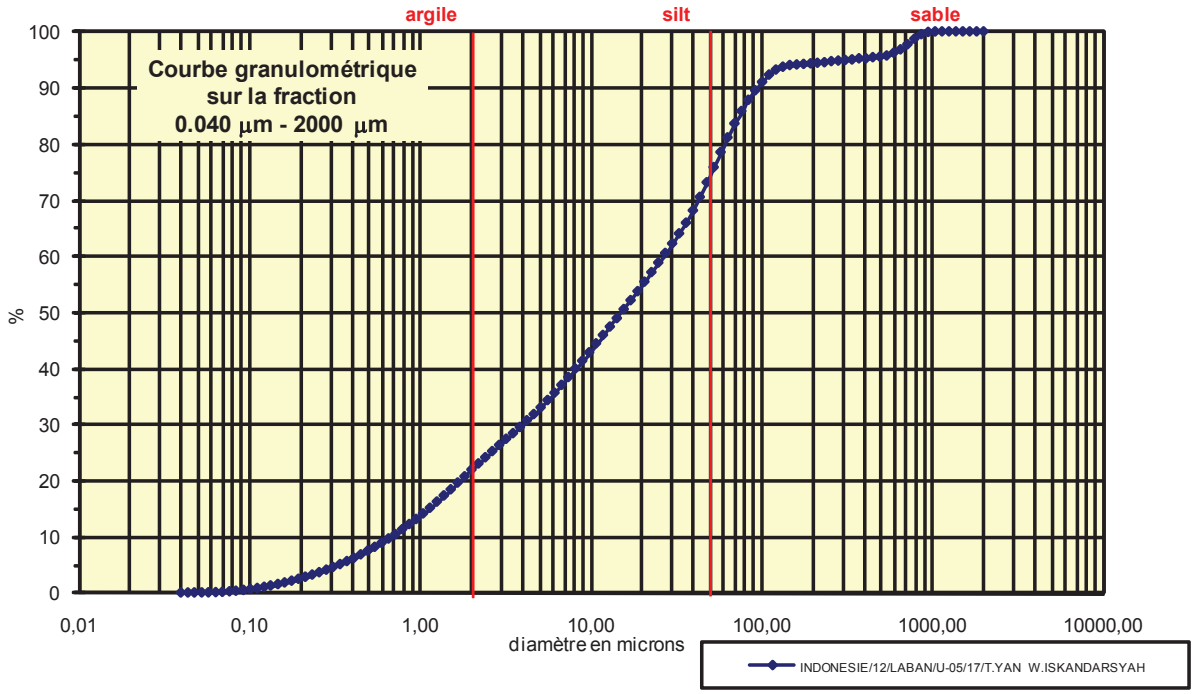

Fractiles	Taille (µm)	Taille (ϕ)
d_5	0,311	11,65
d_{10}	0,657	10,57
d_{16}	1,149	9,77
d_{25}	2,423	8,69
d_{30}	3,862	8,02
d_{50}	14,260	6,13
d_{60}	24,950	5,32
d_{75}	47,930	4,38
d_{84}	69,620	3,84
d_{90}	92,090	3,44
d_{95}	339,800	1,56

% Argile inférieur à 2µ	**A**	**20,70**
% Silts de 2µ à 50µ	**LT**	**52,40**
limons fins 2µ à 20µ	LF	33,00
limons grossiers 20µ à 50µ	LG	19,40
% Sables 50µ à 2000 µ	**ST**	**26,90**
sables fins 50µ à 200µ	SF	21,20
sables fins 50µ à 100µ	SF1	16,40
sables fins 100µ à 200 µ	SF2	4,80
sables grossiers 200µ à 2000µ	SG	5,70
sables grossiers 200µ à 500µ	SG1	1,20
sables grossiers 500µ à 1000µ	SG2	4,40
sables grossiers 1000µ à 2000µ	SG3	0,10

Indice de classement	
Trask, S_o	4,448
Krumbein, Q_d	-2,153
Inman, σ_ϕ	-2,961
Folk & Ward, σ_ϕ	-3,010
Hazen, C_u	37,976

Moyenne	
Trask, M	25,177
Inman, M_ϕ	6,805
Folk & Ward, M_z	6,581

Coefficient de dissymétrie	
Skew ness, S_{k-1}	0,571
Skew ness, S_{k-2}	0,756
Inman, $\alpha_{\phi-1}$	-0,227
Inman, $\alpha_{\phi-2}$	-0,159
Folk & Ward, Sk_i	-0,160

Coefficient d'acuité (Kurtosis)	
Krumbein & Petijohn, K	0,249
Inman, K_ϕ	0,705
Folk & Ward, K_G	0,961

Coefficient de courbure	
C_c	0,910

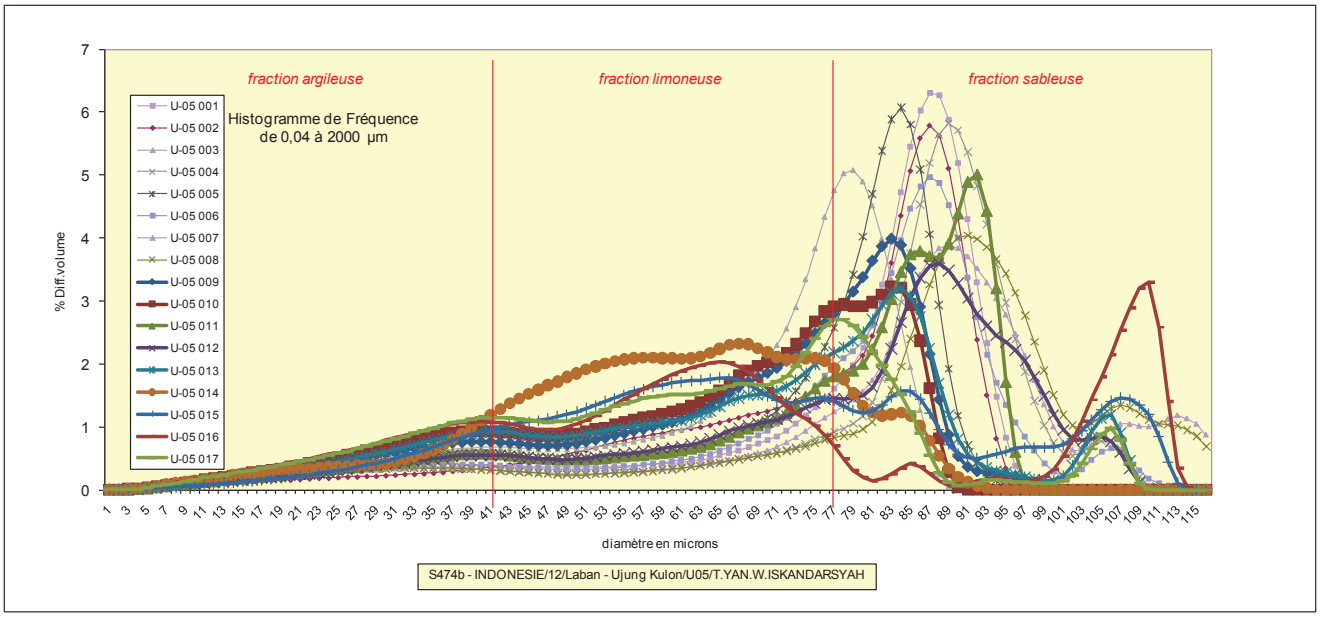
fraction argileuse
fraction limoneuse
fraction sableuse
Histogramme de Fréquence
de 0,04 à 2000 µm
U-05 001
U-05 002
U-05 003
U-05 004
U-05 005
U-05 006
U-05 007
U-05 008
U-05 009
U-05 010
U-05 011
U-05 012
U-05 013
U-05 014
U-05 015
U-05 016
U-05 017
% Diff.volume
diamètre en microns
S474b - INDONESIE/12/Laban - Ujung Kulon/U05/T.YAN.W.ISKANDARSYAH

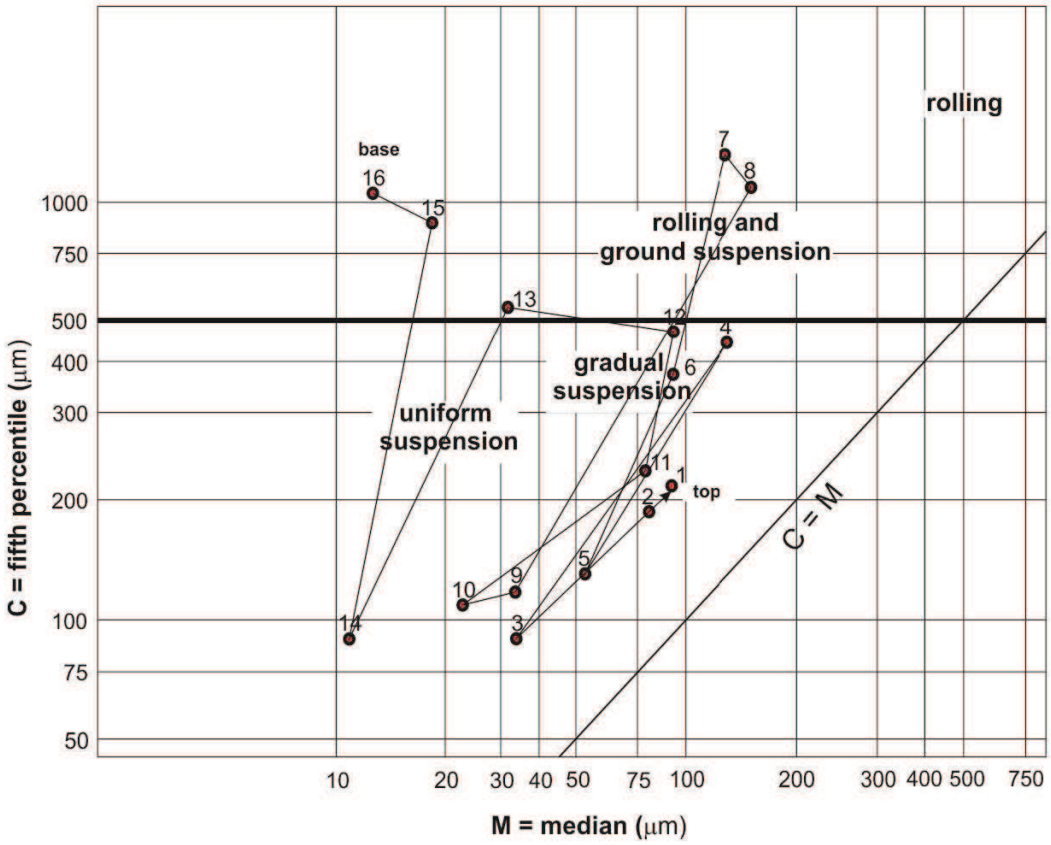
rolling
base
16
15
7
8
rolling and
ground suspension
13
12
4
gradual
suspension
6
uniform
suspension
11
1
top
2
C = M
5
10
9
14
3
1000
750
500
400
300
200
100
75
50
C = fifth percentile (μm)
10
20
30
40
50
75
100
200
300
400
500
750
M = median (μm)

Analyse granulométrique par voie fluide : fraction 0,040 µm - 2000 µm

Echantillon :	INDONESIE/12/LABAN/U-06/1/T.YAN W.ISKANDARSYAH
Date :	04/03/2013 15:01
Opérateur :	MT
Fichier :	U06-001

Commentaires :	prof. 0-3 cm 24/05/12 destruction MO à H2O2 - élimination des ions floculants - hexa +US

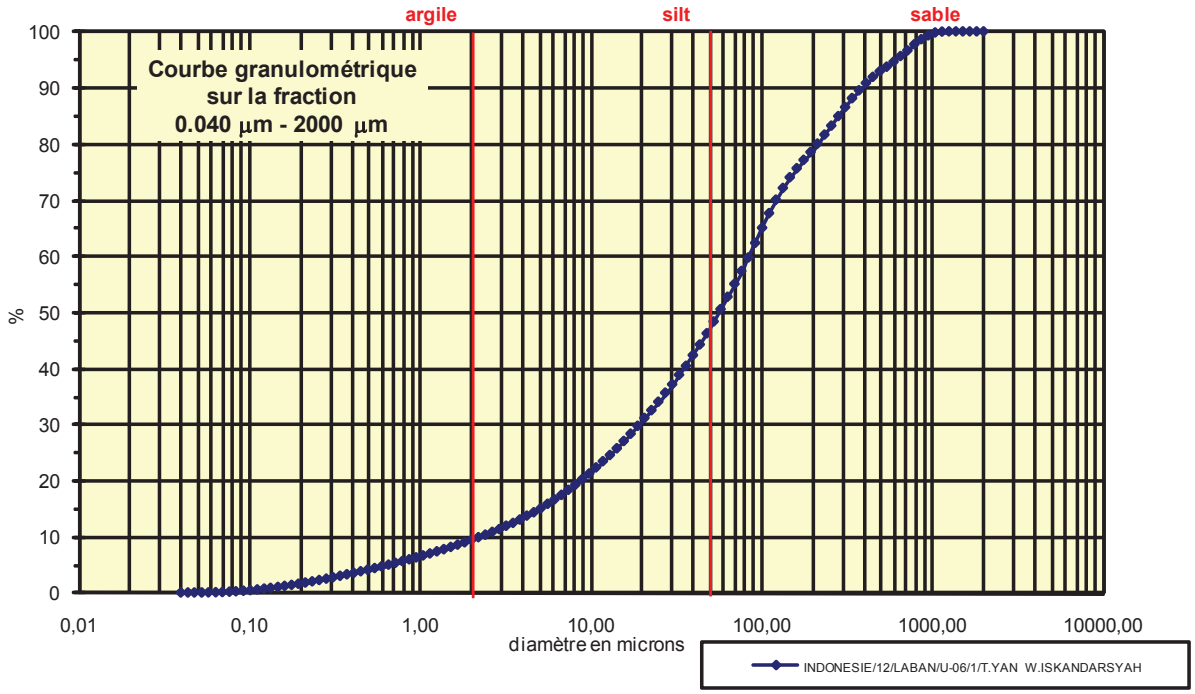

Fractiles	Taille (µm)	Taille (ϕ)
d_5	0,657	10,57
d_{10}	2,207	8,82
d_{16}	5,611	7,48
d_{25}	12,990	6,27
d_{30}	18,860	5,73
d_{50}	52,630	4,25
d_{60}	83,900	3,58
d_{75}	146,800	2,77
d_{84}	256,800	1,96
d_{90}	373,100	1,42
d_{95}	594,900	0,75

% Argile inférieur à 2µ	**A**	**8,96**
% Silts de 2µ à 50µ	**LT**	**37,24**
limons fins 2µ à 20µ	LF	20,74
limons grossiers 20µ à 50µ	LG	16,50
% Sables 50µ à 2000 µ	**ST**	**53,80**
sables fins 50µ à 200µ	SF	32,30
sables fins 50µ à 100µ	SF1	16,10
sables fins 100µ à 200 µ	SF2	16,20
sables grossiers 200µ à 2000µ	SG	21,50
sables grossiers 200µ à 500µ	SG1	14,40
sables grossiers 500µ à 1000µ	SG2	6,40
sables grossiers 1000µ à 2000µ	SG3	0,70

Indice de classement	
Trask, S_o	3,362
Krumbein, Q_d	-1,749
Inman, σ_ϕ	-2,758
Folk & Ward, σ_ϕ	-2,867
Hazen, C_u	38,015

Moyenne	
Trask, M	79,895
Inman, M_ϕ	4,719
Folk & Ward, M_z	4,562

Coefficient de dissymétrie	
Skew ness, S_{k-1}	0,688
Skew ness, S_{k-2}	0,830
Inman, $\alpha_{\phi-1}$	-0,171
Inman, $\alpha_{\phi-2}$	-0,512
Folk & Ward, Sk_i	-0,229

Coefficient d'acuité (Kurtosis)	
Krumbein & Petijohn, K	0,180
Inman, K_ϕ	0,781
Folk & Ward, K_G	1,151

Coefficient de courbure	
C_c	1,921

Analyse granulométrique par voie fluide : fraction 0,040 µm - 2000 µm

Echantillon :	INDONESIE/12/LABAN/U-06/2/T.YAN W.ISKANDARSYAH
Date :	04/03/2013 15:13
Opérateur :	MT
Fichier :	U06-002

Commentaires :	prof. 3-20 cm 24/05/12 destruction MO à H2O2 - élimination des ions floculants - hexa +US

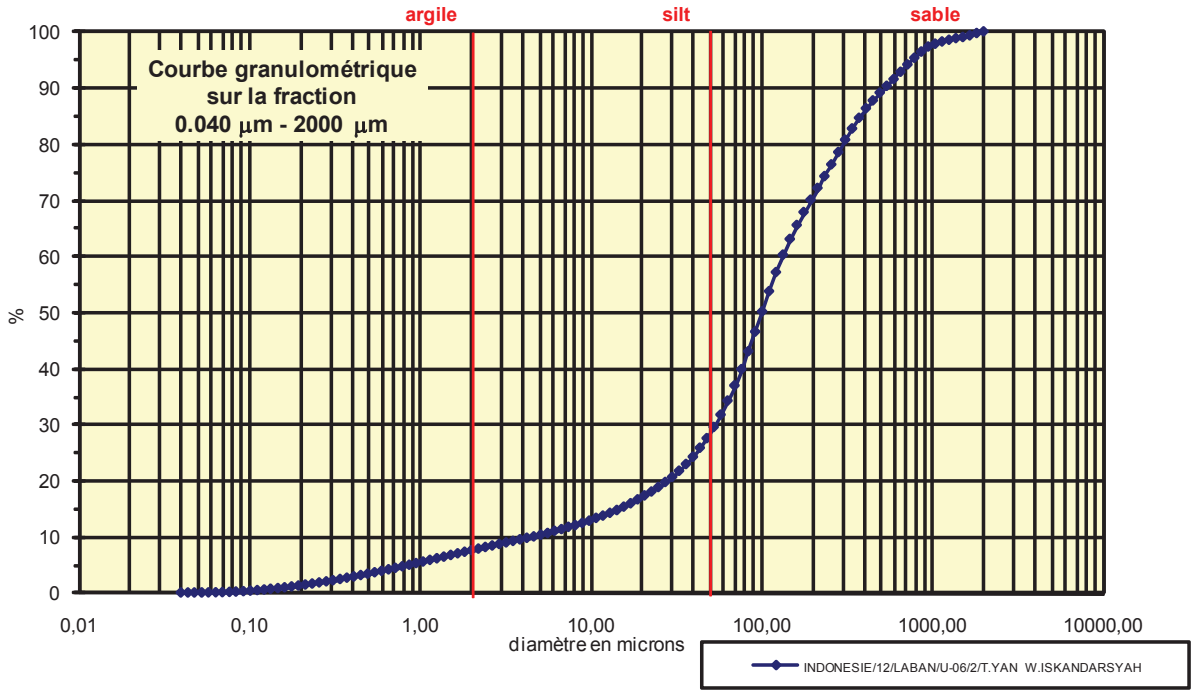

Fractiles	Taille (µm)	Taille (ϕ)
d_5	0,869	10,17
d_{10}	4,656	7,75
d_{16}	17,180	5,86
d_{25}	39,770	4,65
d_{30}	52,630	4,25
d_{50}	92,090	3,44
d_{60}	121,800	3,04
d_{75}	234,100	2,09
d_{84}	339,800	1,56
d_{90}	493,600	1,02
d_{95}	716,900	0,48

% Argile inférieur à 2µ	**A**	**7,26**
% Silts de 2µ à 50µ	**LT**	**20,24**
limons fins 2µ à 20µ	LF	9,34
limons grossiers 20µ à 50µ	LG	10,90
% Sables 50µ à 2000 µ	**ST**	**72,50**
sables fins 50µ à 200µ	SF	42,50
sables fins 50µ à 100µ	SF1	19,00
sables fins 100µ à 200 µ	SF2	23,50
sables grossiers 200µ à 2000µ	SG	30,00
sables grossiers 200µ à 500µ	SG1	19,10
sables grossiers 500µ à 1000µ	SG2	8,20
sables grossiers 1000µ à 2000µ	SG3	2,70

Indice de classement	
Trask, S_o	2,426
Krumbein, Q_d	-1,279
Inman, σ_ϕ	-2,153
Folk & Ward, σ_ϕ	-2,544
Hazen, C_u	26,160

Moyenne	
Trask, M	136,935
Inman, M_ϕ	3,710
Folk & Ward, M_z	3,620

Coefficient de dissymétrie	
Skew ness, S_{k1}	1,098
Skew ness, S_{k2}	1,048
Inman, $\alpha_{\phi-1}$	-0,125
Inman, $\alpha_{\phi-2}$	-0,875
Folk & Ward, Sk_I	-0,257

Coefficient d'acuité (Kurtosis)	
Krumbein & Petijohn, K	0,199
Inman, K_ϕ	1,250
Folk & Ward, K_G	1,553

Coefficient de courbure	
C_c	4,884

Analyse granulométrique par voie fluide : fraction 0,040 µm - 2000 µm

Echantillon :	INDONESIE/12/LABAN/U-06/3/T.YAN W.ISKANDARSYAH
Date :	04/03/2013 15:29
Opérateur :	MT
Fichier :	U06-003

Commentaires :	prof. 20-30 cm 24/05/12 destruction MO à H2O2 - élimination des ions floculants - hexa +US

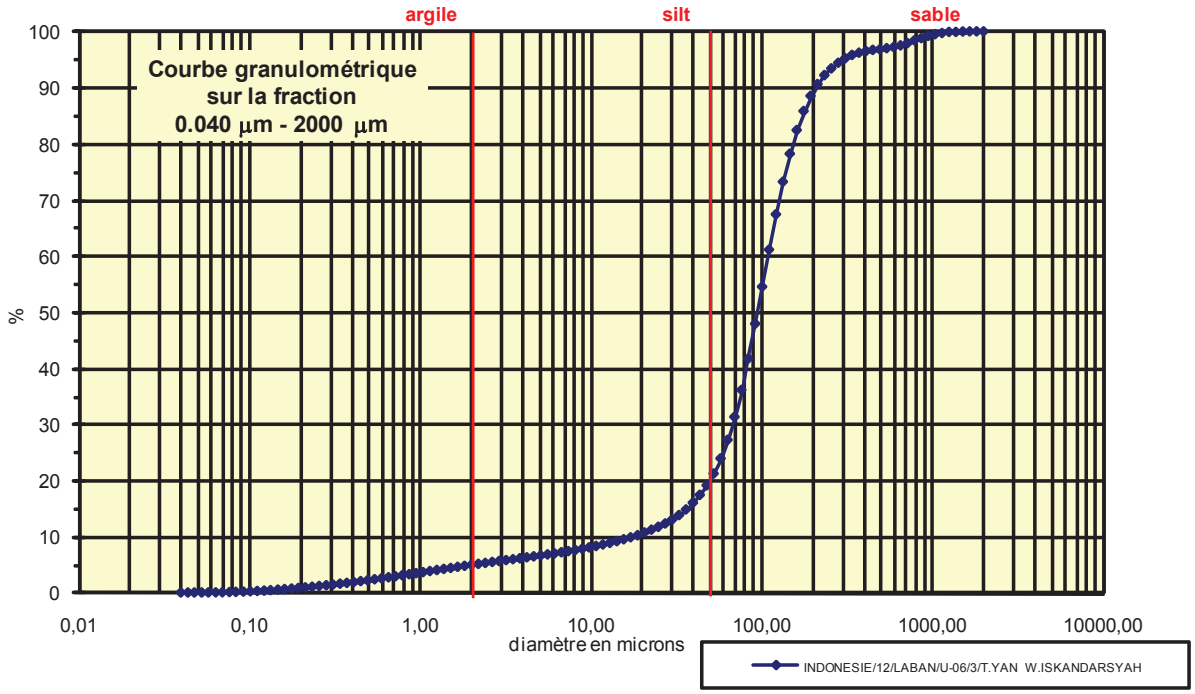

Fractiles	Taille (µm)	Taille (ϕ)
d_5	2,010	8,96
d_{10}	17,180	5,86
d_{16}	39,770	4,65
d_{25}	57,770	4,11
d_{30}	63,410	3,98
d_{50}	92,090	3,44
d_{60}	101,100	3,31
d_{75}	133,700	2,90
d_{84}	161,200	2,63
d_{90}	194,200	2,36
d_{95}	282,100	1,83

% Argile inférieur à 2µ	**A**	**4,75**
% Silts de 2µ à 50µ	**LT**	**14,35**
limons fins 2µ à 20µ	LF	5,45
limons grossiers 20µ à 50µ	LG	8,90
% Sables 50µ à 2000 µ	**ST**	**80,90**
sables fins 50µ à 200µ	SF	69,40
sables fins 50µ à 100µ	SF1	28,80
sables fins 100µ à 200 µ	SF2	40,60
sables grossiers 200µ à 2000µ	SG	11,50
sables grossiers 200µ à 500µ	SG1	8,30
sables grossiers 500µ à 1000µ	SG2	2,40
sables grossiers 1000µ à 2000µ	SG3	0,80

Indice de classement	
Trask, S_o	1,521
Krumbein, Q_d	-0,605
Inman, σ_ϕ	-1,010
Folk & Ward, σ_ϕ	-1,586
Hazen, C_u	5,885

Moyenne	
Trask, M	95,735
Inman, M_ϕ	3,643
Folk & Ward, M_z	3,575

Coefficient de dissymétrie	
Skew ness, S_{k1}	0,911
Skew ness, S_{k2}	0,954
Inman, $\alpha_{\phi-1}$	-0,200
Inman, $\alpha_{\phi-2}$	-1,933
Folk & Ward, Sk_I	-0,374

Coefficient d'acuité (Kurtosis)	
Krumbein & Petijohn, K	0,214
Inman, K_ϕ	2,533
Folk & Ward, K_G	2,415

Coefficient de courbure	
C_c	2,315

Analyse granulométrique par voie fluide : fraction 0,040 µm - 2000 µm

Echantillon :	INDONESIE/12/LABAN/U-06/4/T.YAN W.ISKANDARSYAH
Date :	04/03/2013 15:40
Opérateur :	MT
Fichier :	U06-004

Commentaires :	prof. 30-38 cm 24/05/12 destruction MO à H2O2 - élimination des ions floculants - hexa +US

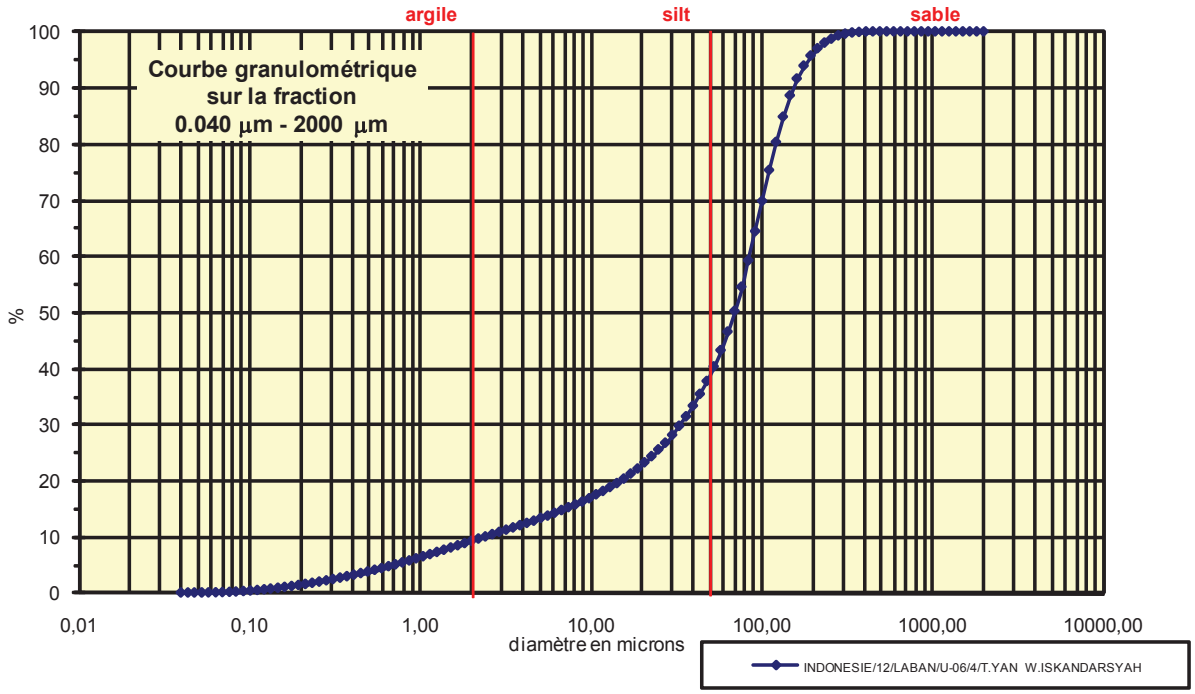

Fractiles	Taille (µm)	Taille (ϕ)
d_5	0,657	10,57
d_{10}	2,423	8,69
d_{16}	8,147	6,94
d_{25}	22,730	5,46
d_{30}	33,000	4,92
d_{50}	63,410	3,98
d_{60}	83,900	3,58
d_{75}	101,100	3,31
d_{84}	121,800	3,04
d_{90}	146,800	2,77
d_{95}	176,800	2,50

% Argile inférieur à 2µ	**A**	**8,82**
% Silts de 2µ à 50µ	**LT**	**28,88**
limons fins 2µ à 20µ	LF	13,28
limons grossiers 20µ à 50µ	LG	15,60
% Sables 50µ à 2000 µ	**ST**	**62,30**
sables fins 50µ à 200µ	SF	58,00
sables fins 50µ à 100µ	SF1	26,70
sables fins 100µ à 200 µ	SF2	31,30
sables grossiers 200µ à 2000µ	SG	4,30
sables grossiers 200µ à 500µ	SG1	4,30
sables grossiers 500µ à 1000µ	SG2	0,00
sables grossiers 1000µ à 2000µ	SG3	0,00

Indice de classement	
Trask, S_o	2,109
Krumbein, Q_d	-1,077
Inman, σ_ϕ	-1,951
Folk & Ward, σ_ϕ	-2,199
Hazen, C_u	34,626

Moyenne	
Trask, M	61,915
Inman, M_ϕ	4,988
Folk & Ward, M_z	4,652

Coefficient de dissymétrie	
Skew ness, S_{k-1}	0,572
Skew ness, S_{k-2}	0,756
Inman, $\alpha_{\phi-1}$	-0,517
Inman, $\alpha_{\phi-2}$	-1,310
Folk & Ward, Sk_i	-0,575

Coefficient d'acuité (Kurtosis)	
Krumbein & Petijohn, K	0,271
Inman, K_ϕ	1,069
Folk & Ward, K_G	1,536

Coefficient de courbure	
C_c	5,357

Analyse granulométrique par voie fluide : fraction 0,040 µm - 2000 µm

Echantillon :	INDONESIE/12/LABAN/U-06/5/T.YAN W.ISKANDARSYAH
Date :	04/03/2013 15:50
Opérateur :	MT
Fichier :	U06-005

Commentaires :	prof. 38-41 cm 24/05/12 destruction MO à H2O2 - élimination des ions floculants - hexa +US

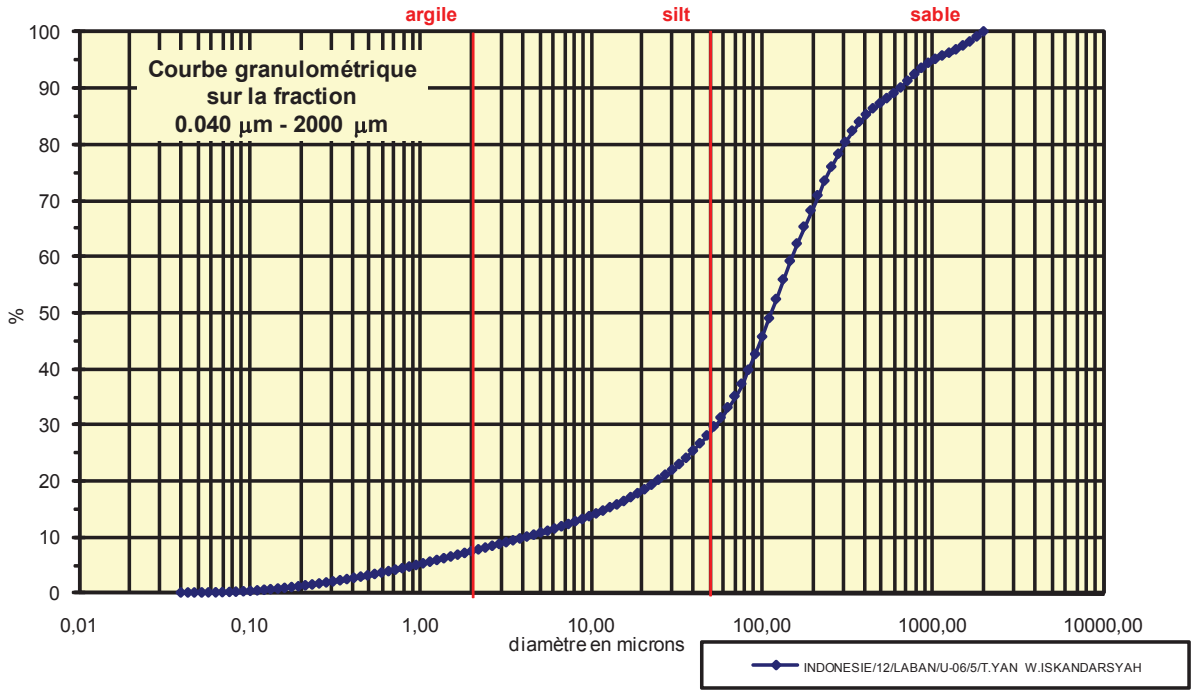

Fractiles	Taille (µm)	Taille (ϕ)
d_5	0,953	10,04
d_{10}	4,241	7,88
d_{16}	14,260	6,13
d_{25}	36,240	4,79
d_{30}	52,630	4,25
d_{50}	111,000	3,17
d_{60}	146,800	2,77
d_{75}	234,100	2,09
d_{84}	373,100	1,42
d_{90}	653,000	0,61
d_{95}	948,200	0,08

% Argile inférieur à 2µ	**A**	**7,05**
% Silts de 2µ à 50µ	**LT**	**20,95**
limons fins 2µ à 20µ	LF	10,65
limons grossiers 20µ à 50µ	LG	10,30
% Sables 50µ à 2000 µ	**ST**	**72,00**
sables fins 50µ à 200µ	SF	40,10
sables fins 50µ à 100µ	SF1	14,50
sables fins 100µ à 200 µ	SF2	25,60
sables grossiers 200µ à 2000µ	SG	31,90
sables grossiers 200µ à 500µ	SG1	19,10
sables grossiers 500µ à 1000µ	SG2	7,20
sables grossiers 1000µ à 2000µ	SG3	5,60

Indice de classement	
Trask, S_o	2,542
Krumbein, Q_d	-1,346
Inman, σ_ϕ	-2,355
Folk & Ward, σ_ϕ	-2,686
Hazen, C_u	34,614

Moyenne	
Trask, M	135,170
Inman, M_ϕ	3,777
Folk & Ward, M_z	3,575

Coefficient de dissymétrie	
Skew ness, S_{k-1}	0,689
Skew ness, S_{k-2}	0,830
Inman, $\alpha_{\phi-1}$	-0,257
Inman, $\alpha_{\phi-2}$	-0,800
Folk & Ward, Sk_i	-0,318

Coefficient d'acuité (Kurtosis)	
Krumbein & Petijohn, K	0,152
Inman, K_ϕ	1,115
Folk & Ward, K_G	1,516

Coefficient de courbure	
C_c	4,449

Analyse granulométrique par voie fluide : fraction 0,040 µm - 2000 µm

Echantillon :	INDONESIE/12/LABAN/U-06/6/T.YAN W.ISKANDARSYAH
Date :	04/03/2013 15:57
Opérateur :	MT
Fichier :	U06-006

Commentaires :	prof. 41-44 cm 24/05/12 destruction MO à H2O2 - élimination des ions floculants - hexa +US

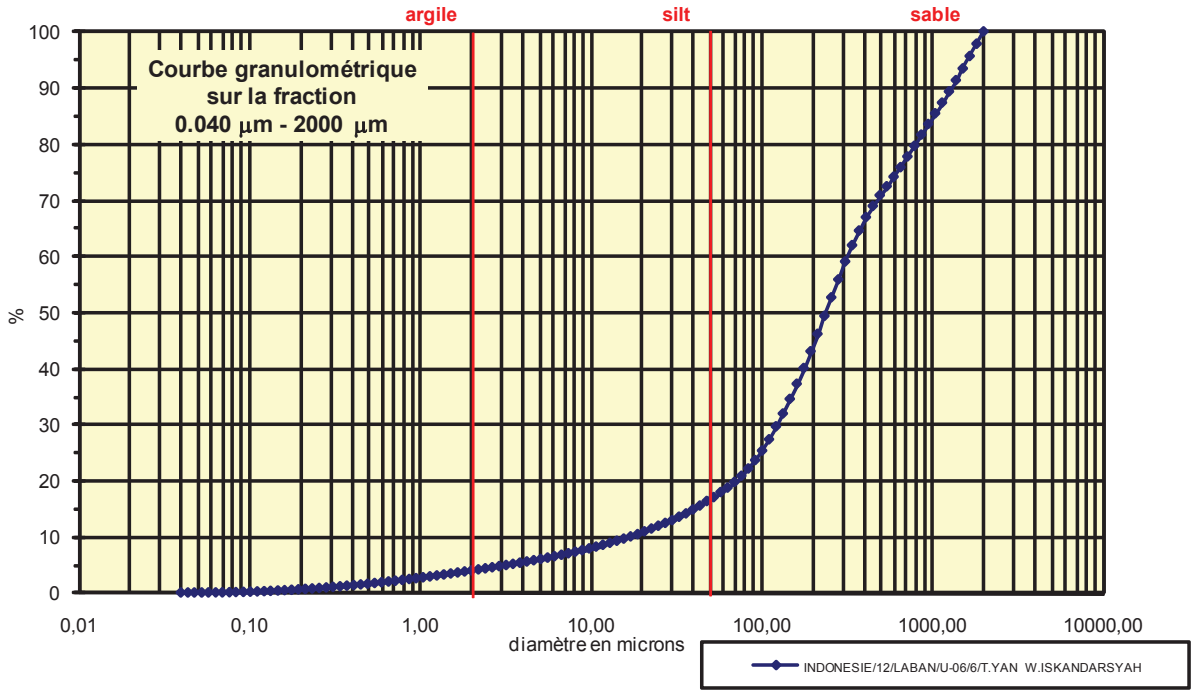

Fractiles	Taille (µm)	Taille (ϕ)
d_5	3,206	8,29
d_{10}	17,180	5,86
d_{16}	43,660	4,52
d_{25}	92,090	3,44
d_{30}	121,800	3,04
d_{50}	234,100	2,09
d_{60}	309,600	1,69
d_{75}	594,900	0,75
d_{84}	948,200	0,08
d_{90}	1255,000	-0,33
d_{95}	1512,000	-0,60

% Argile inférieur à 2µ	**A**	**3,75**
% Silts de 2µ à 50µ	**LT**	**12,55**
limons fins 2µ à 20µ	LF	6,65
limons grossiers 20µ à 50µ	LG	5,90
% Sables 50µ à 2000 µ	**ST**	**83,70**
sables fins 50µ à 200µ	SF	26,70
sables fins 50µ à 100µ	SF1	7,30
sables fins 100µ à 200 µ	SF2	19,40
sables grossiers 200µ à 2000µ	SG	57,00
sables grossiers 200µ à 500µ	SG1	27,80
sables grossiers 500µ à 1000µ	SG2	12,70
sables grossiers 1000µ à 2000µ	SG3	16,50

Indice de classement	
Trask, S_o	2,542
Krumbein, Q_d	-1,346
Inman, σ_ϕ	-2,220
Folk & Ward, σ_ϕ	-2,456
Hazen, C_u	18,021

Moyenne	
Trask, M	343,495
Inman, M_ϕ	2,297
Folk & Ward, M_z	2,230

Coefficient de dissymétrie	
Skew ness, S_{k-1}	1,000
Skew ness, S_{k-2}	1,000
Inman, $\alpha_{\phi-1}$	-0,091
Inman, $\alpha_{\phi-2}$	-0,788
Folk & Ward, Sk_I	-0,243

Coefficient d'acuité (Kurtosis)	
Krumbein & Petijohn, K	0,203
Inman, K_ϕ	1,000
Folk & Ward, K_G	1,352

Coefficient de courbure	
C_c	2,789

Analyse granulométrique par voie fluide : fraction 0,040 µm - 2000 µm

Echantillon :	INDONESIE/12/LABAN/U-06/7/T.YAN W.ISKANDARSYAH
Date :	04/03/2013 16:09
Opérateur :	MT
Fichier :	U06-007

Commentaires :	prof. 44-55 cm 24/05/12 destruction MO à H2O2 - élimination des ions floculants - hexa +US

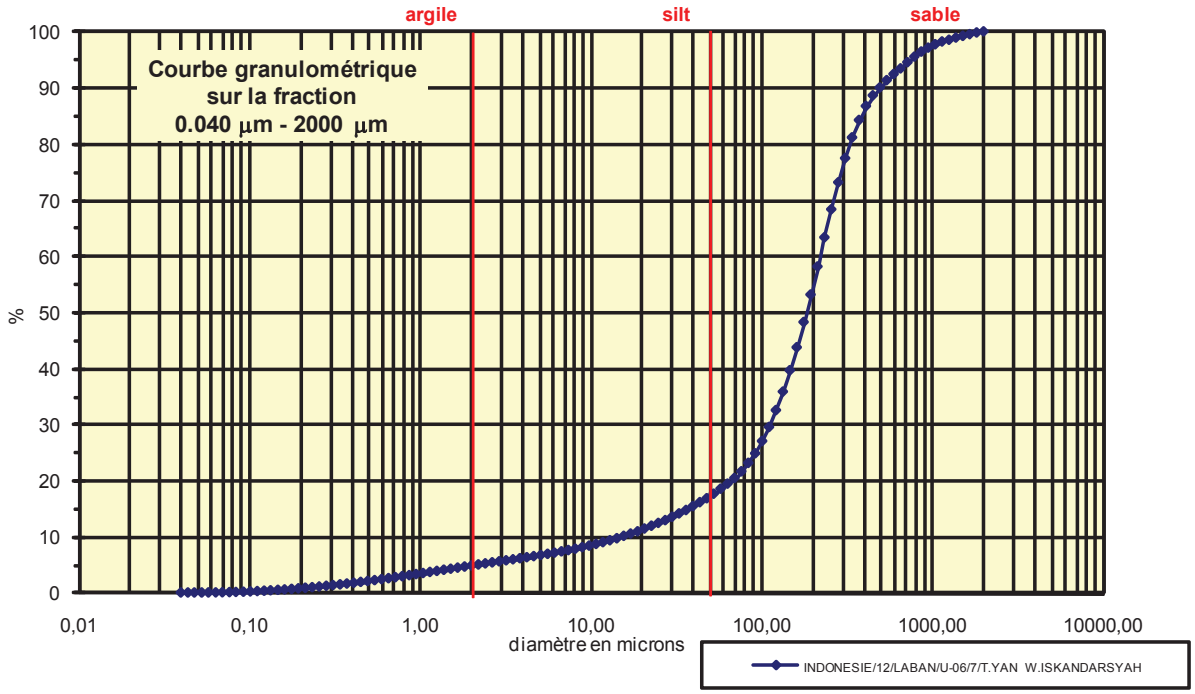

Fractiles	Taille (µm)	Taille (ϕ)
d_5	2,207	8,82
d_{10}	14,260	6,13
d_{16}	39,770	4,65
d_{25}	92,090	3,44
d_{30}	111,000	3,17
d_{50}	176,800	2,50
d_{60}	213,200	2,23
d_{75}	282,100	1,83
d_{84}	339,800	1,56
d_{90}	493,600	1,02
d_{95}	716,900	0,48

% Argile inférieur à 2µ	**A**	**4,62**
% Silts de 2µ à 50µ	**LT**	**12,18**
limons fins 2µ à 20µ	LF	6,28
limons grossiers 20µ à 50µ	LG	5,90
% Sables 50µ à 2000 µ	**ST**	**83,20**
sables fins 50µ à 200µ	SF	36,30
sables fins 50µ à 100µ	SF1	8,00
sables fins 100µ à 200 µ	SF2	28,30
sables grossiers 200µ à 2000µ	SG	46,90
sables grossiers 200µ à 500µ	SG1	36,90
sables grossiers 500µ à 1000µ	SG2	7,10
sables grossiers 1000µ à 2000µ	SG3	2,90

Indice de classement	
Trask, S_o	1,750
Krumbein, Q_d	-0,808
Inman, σ_ϕ	-1,547
Folk & Ward, σ_ϕ	-2,038
Hazen, C_u	14,951

Moyenne	
Trask, M	187,095
Inman, M_ϕ	3,105
Folk & Ward, M_z	2,903

Coefficient de dissymétrie	
Skew ness, S_{k1}	0,831
Skew ness, S_{k2}	0,912
Inman, $\alpha_{\phi-1}$	-0,391
Inman, $\alpha_{\phi-2}$	-1,391
Folk & Ward, Sk_I	-0,453

Coefficient d'acuité (Kurtosis)	
Krumbein & Petijohn, K	0,198
Inman, K_ϕ	1,696
Folk & Ward, K_G	2,117

Coefficient de courbure	
C_c	4,053

Analyse granulométrique par voie fluide : fraction 0,040 µm - 2000 µm

Echantillon :	INDONESIE/12/LABAN/U-06/8/T.YAN W.ISKANDARSYAH
Date :	04/03/2013 16:19
Opérateur :	MT
Fichier :	U06-008

Commentaires :	prof. 55-75 cm 24/05/12 destruction MO à H2O2 - élimination des ions floculants - hexa +US

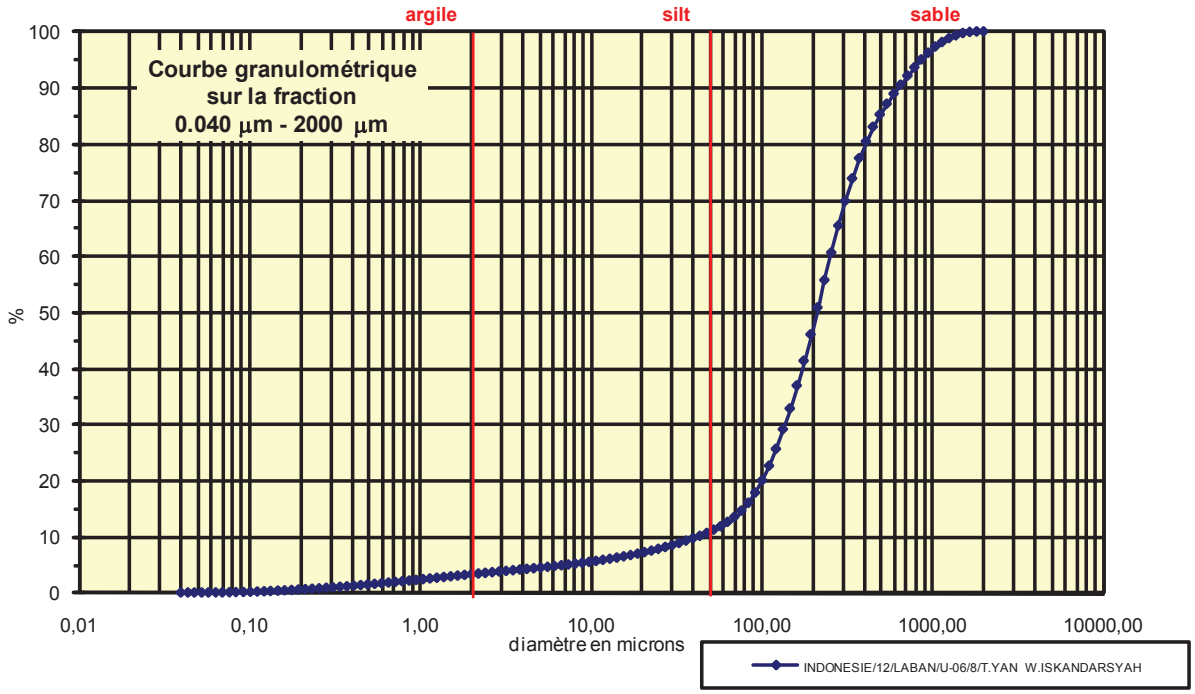

Fractiles	Taille (µm)	Taille (ϕ)
d_5	7,421	7,07
d_{10}	39,770	4,65
d_{16}	83,900	3,58
d_{25}	111,000	3,17
d_{30}	133,700	2,90
d_{50}	194,200	2,36
d_{60}	234,100	2,09
d_{75}	339,800	1,56
d_{84}	449,700	1,15
d_{90}	594,900	0,75
d_{95}	863,900	0,21

% Argile inférieur à 2µ	**A**	**3,13**
% Silts de 2µ à 50µ	**LT**	**7,47**
limons fins 2µ à 20µ	LF	3,79
limons grossiers 20µ à 50µ	LG	3,68
% Sables 50µ à 2000 µ	**ST**	**89,40**
sables fins 50µ à 200µ	SF	35,40
sables fins 50µ à 100µ	SF1	7,20
sables fins 100µ à 200 µ	SF2	28,20
sables grossiers 200µ à 2000µ	SG	54,00
sables grossiers 200µ à 500µ	SG1	39,20
sables grossiers 500µ à 1000µ	SG2	11,00
sables grossiers 1000µ à 2000µ	SG3	3,80

Indice de classement	
Trask, S_o	1,750
Krumbein, Q_d	-0,807
Inman, σ_ϕ	-1,211
Folk & Ward, σ_ϕ	-1,645
Hazen, C_u	5,886

Moyenne	
Trask, M	225,400
Inman, M_ϕ	2,364
Folk & Ward, M_z	2,364

Coefficient de dissymétrie	
Skew ness, S_{k-1}	1,000
Skew ness, S_{k-2}	1,000
Inman, $\alpha_{\phi-1}$	0,000
Inman, $\alpha_{\phi-2}$	-1,055
Folk & Ward, Sk_i	-0,186

Coefficient d'acuité (Kurtosis)	
Krumbein & Petijohn, K	0,206
Inman, K_ϕ	1,833
Folk & Ward, K_G	1,743

Coefficient de courbure	
C_c	1,920

Analyse granulométrique par voie fluide : fraction 0,040 µm - 2000 µm

Echantillon :	INDONESIE/12/LABAN/U-06/9/T.YAN W.ISKANDARSYAH
Date :	04/03/2013 16:27
Opérateur :	MT
Fichier :	U06-009

Commentaires :	prof. 75-87 cm 24/05/12 SAND destruction MO à H2O2 - élimination des ions floculants - hexa +US

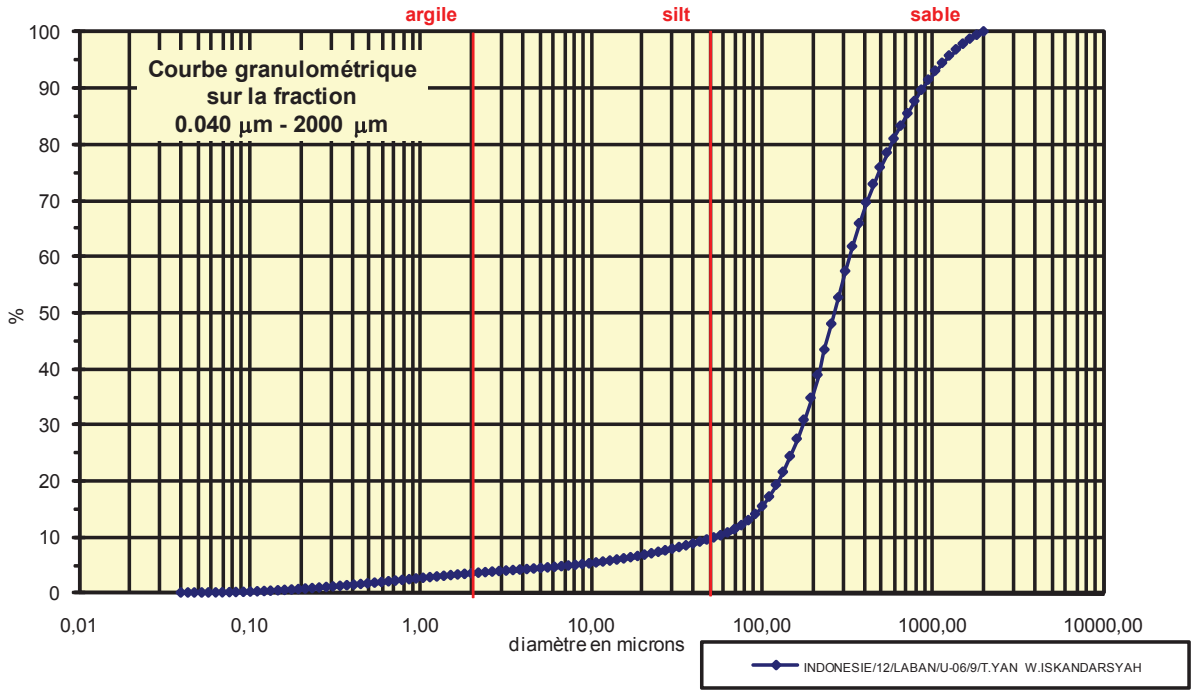

Fractiles	Taille (µm)	Taille (ϕ)
d_5	8,147	6,94
d_{10}	52,630	4,25
d_{16}	101,100	3,31
d_{25}	146,800	2,77
d_{30}	161,200	2,63
d_{50}	256,800	1,96
d_{60}	309,600	1,69
d_{75}	449,700	1,15
d_{84}	653,000	0,61
d_{90}	863,900	0,21
d_{95}	1143,000	-0,19

% Argile inférieur à 2µ	**A**	**3,32**
% Silts de 2µ à 50µ	**LT**	**6,12**
limons fins 2µ à 20µ	LF	3,19
limons grossiers 20µ à 50µ	LG	2,93
% Sables 50µ à 2000 µ	**ST**	**90,56**
sables fins 50µ à 200µ	SF	25,26
sables fins 50µ à 100µ	SF1	4,56
sables fins 100µ à 200 µ	SF2	20,70
sables grossiers 200µ à 2000µ	SG	65,30
sables grossiers 200µ à 500µ	SG1	41,10
sables grossiers 500µ à 1000µ	SG2	15,60
sables grossiers 1000µ à 2000µ	SG3	8,60

Indice de classement	
Trask, S_o	1,750
Krumbein, Q_d	-0,808
Inman, σ_ϕ	-1,346
Folk & Ward, σ_ϕ	-1,753
Hazen, C_u	5,883

Moyenne	
Trask, M	298,250
Inman, M_ϕ	1,960
Folk & Ward, M_z	1,961

Coefficient de dissymétrie	
Skew ness, S_{k-1}	1,001
Skew ness, S_{k-2}	1,001
Inman, $\alpha_{\phi-1}$	0,001
Inman, $\alpha_{\phi-2}$	-1,049
Folk & Ward, Sk_i	-0,198

Coefficient d'acuité (Kurtosis)	
Krumbein & Petijohn, K	0,187
Inman, K_ϕ	1,650
Folk & Ward, K_G	1,810

Coefficient de courbure	
C_c	1,595

Analyse granulométrique par voie fluide : fraction 0,040 µm - 2000 µm

Echantillon :	INDONESIE/12/LABAN/U-06/10/T.YAN W.ISKANDARSYAH
Date :	9:59 5 Mar 2013
Opérateur :	MT
Fichier :	U06-010

Commentaires :	prof. 75-87cm 24/05/12 CLAY destruction MO à H2O2 - élimination des ions floculants - hexa +US

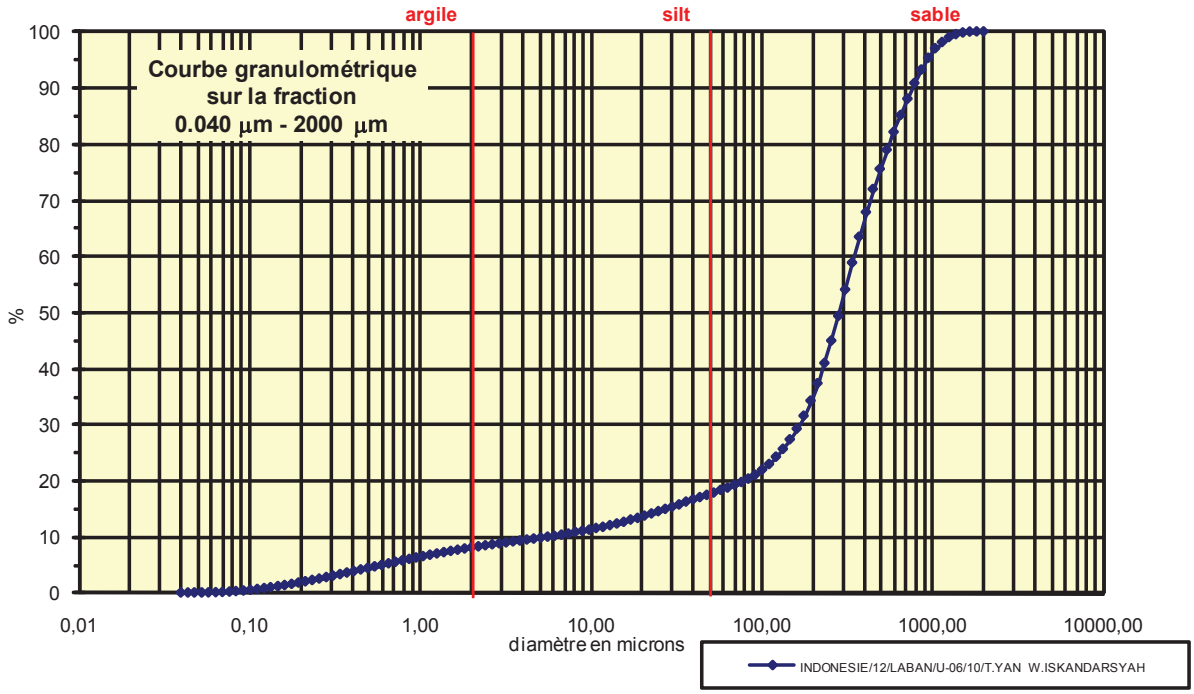

Fractiles	Taille (µm)	Taille (ϕ)
d_5	0,598	10,71
d_{10}	5,611	7,48
d_{16}	33,000	4,92
d_{25}	121,800	3,04
d_{30}	161,200	2,63
d_{50}	282,100	1,83
d_{60}	339,800	1,56
d_{75}	449,700	1,15
d_{84}	594,900	0,75
d_{90}	716,900	0,48
d_{95}	863,900	0,21

% Argile inférieur à 2µ	**A**	**7,84**
% Silts de 2µ à 50µ	**LT**	**9,56**
limons fins 2µ à 20µ	LF	5,46
limons grossiers 20µ à 50µ	LG	4,10
% Sables 50µ à 2000 µ	**ST**	**82,60**
sables fins 50µ à 200µ	SF	16,80
sables fins 50µ à 100µ	SF1	3,60
sables fins 100µ à 200 µ	SF2	13,20
sables grossiers 200µ à 2000µ	SG	65,80
sables grossiers 200µ à 500µ	SG1	41,30
sables grossiers 500µ à 1000µ	SG2	19,80
sables grossiers 1000µ à 2000µ	SG3	4,70

Indice de classement	
Trask, S_o	1,921
Krumbein, Q_d	-0,942
Inman, σ_ϕ	-2,086
Folk & Ward, σ_ϕ	-2,633
Hazen, C_u	60,560

Moyenne	
Trask, M	285,750
Inman, M_ϕ	2,835
Folk & Ward, M_z	2,499

Coefficient de dissymétrie	
Skew ness, S_{k1}	0,688
Skew ness, S_{k2}	0,830
Inman, $\alpha_{\phi-1}$	-0,484
Inman, $\alpha_{\phi-2}$	-1,742
Folk & Ward, Sk_i	-0,588

Coefficient d'acuité (Kurtosis)	
Krumbein & Petijohn, K	0,230
Inman, K_ϕ	1,516
Folk & Ward, K_G	2,283

Coefficient de courbure	
C_c	13,629

Analyse granulométrique par voie fluide : fraction 0,040 µm - 2000 µm

Echantillon :	INDONESIE/12/LABAN/U-06/11/T.YAN W.ISKANDARSYAH
Date :	9:57 5 Mar 2013
Opérateur :	MT
Fichier :	U06-011

Commentaires :	prof. 87-117 cm 24/05/12 SAND destruction MO à H2O2 - élimination des ions floculants - hexa +US

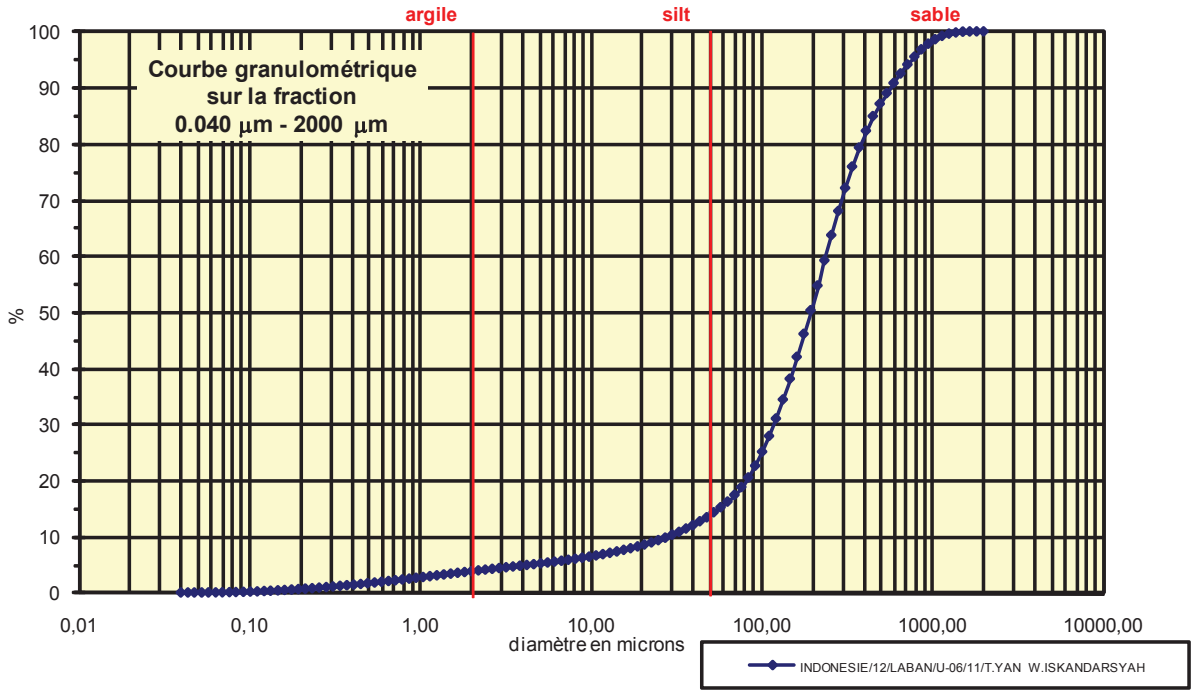

Fractiles	Taille (µm)	Taille (ϕ)
d_5	4,241	7,88
d_{10}	27,380	5,19
d_{16}	57,770	4,11
d_{25}	92,090	3,44
d_{30}	111,000	3,17
d_{50}	176,800	2,50
d_{60}	234,100	2,09
d_{75}	309,600	1,69
d_{84}	409,600	1,29
d_{90}	541,900	0,88
d_{95}	716,900	0,48

% Argile inférieur à 2µ	**A**	**3,65**
% Silts de 2µ à 50µ	**LT**	**9,75**
limons fins 2µ à 20µ	LF	4,56
limons grossiers 20µ à 50µ	LG	5,19
% Sables 50µ à 2000 µ	**ST**	**86,60**
sables fins 50µ à 200µ	SF	36,90
sables fins 50µ à 100µ	SF1	9,20
sables fins 100µ à 200 µ	SF2	27,70
sables grossiers 200µ à 2000µ	SG	49,70
sables grossiers 200µ à 500µ	SG1	36,80
sables grossiers 500µ à 1000µ	SG2	10,70
sables grossiers 1000µ à 2000µ	SG3	2,20

Indice de classement	
Trask, S_o	1,834
Krumbein, Q_d	-0,875
Inman, σ_ϕ	-1,413
Folk & Ward, σ_ϕ	-1,828
Hazen, C_u	8,550

Moyenne	
Trask, M	200,845
Inman, M_ϕ	2,701
Folk & Ward, M_z	2,634

Coefficient de dissymétrie	
Skew ness, S_{k-1}	0,912
Skew ness, S_{k-2}	0,955
Inman, $\alpha_{\phi-1}$	-0,142
Inman, $\alpha_{\phi-2}$	-1,190
Folk & Ward, Sk_i	-0,298

Coefficient d'acuité (Kurtosis)	
Krumbein & Petijohn, K	0,211
Inman, K_ϕ	1,619
Folk & Ward, K_G	1,734

Coefficient de courbure	
C_c	1,922

Analyse granulométrique par voie fluide : fraction 0,040 µm - 2000 µm

Echantillon :	INDONESIE/12/LABAN/U-06/12/T.YAN W.ISKANDARSYAH
Date :	05/03/2013 10:06
Opérateur :	MT
Fichier :	U06-012

Commentaires :	prof. 87-117 cm 24/05/12 CLAY destruction MO à H2O2 - élimination des ions floculants - hexa +US

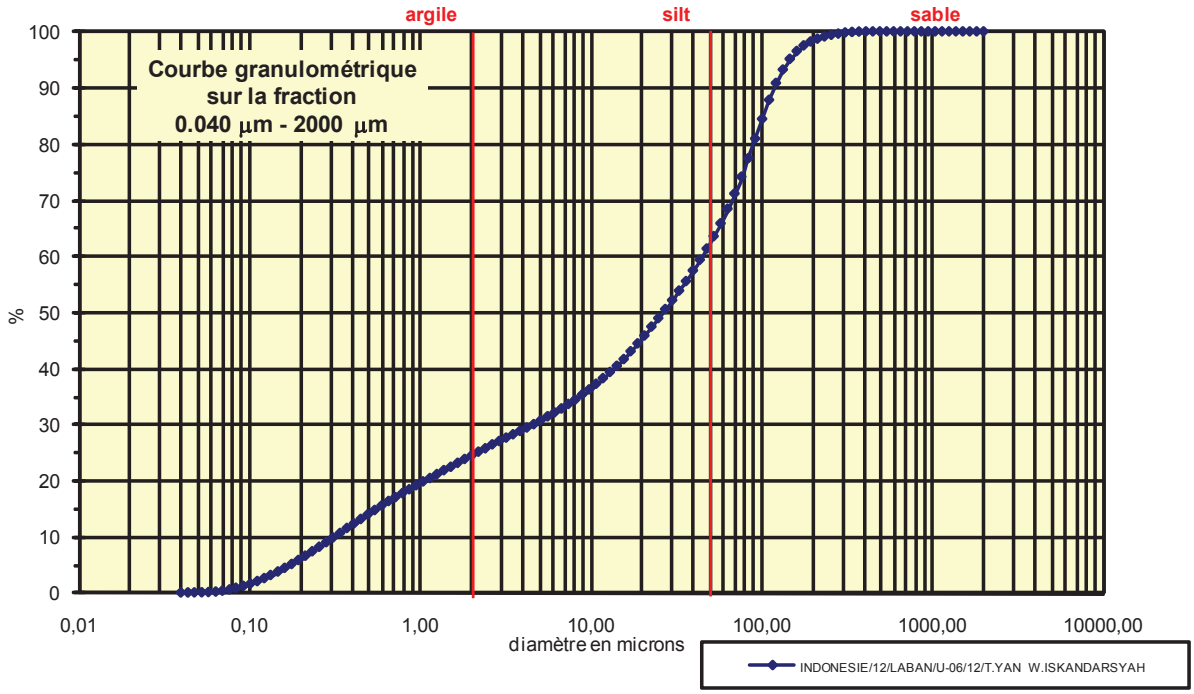

Fractiles	Taille (µm)	Taille (ϕ)
d_5	0,162	12,59
d_{10}	0,311	11,65
d_{16}	0,598	10,71
d_{25}	2,010	8,96
d_{30}	4,656	7,75
d_{50}	24,950	5,32
d_{60}	43,660	4,52
d_{75}	76,430	3,71
d_{84}	92,090	3,44
d_{90}	111,000	3,17
d_{95}	133,700	2,90

% Argile inférieur à 2µ	**A**	**23,80**
% Silts de 2µ à 50µ	**LT**	**37,50**
limons fins 2µ à 20µ	LF	20,60
limons grossiers 20µ à 50µ	LG	16,90
% Sables 50µ à 2000 µ	**ST**	**38,70**
sables fins 50µ à 200µ	SF	36,90
sables fins 50µ à 100µ	SF1	19,60
sables fins 100µ à 200 µ	SF2	17,30
sables grossiers 200µ à 2000µ	SG	1,80
sables grossiers 200µ à 500µ	SG1	1,80
sables grossiers 500µ à 1000µ	SG2	0,00
sables grossiers 1000µ à 2000µ	SG3	0,00

Indice de classement	
Trask, S_o	6,166
Krumbein, Q_d	-2,624
Inman, σ_ϕ	-3,633
Folk & Ward, σ_ϕ	-3,285
Hazen, C_u	140,386

Moyenne	
Trask, M	39,220
Inman, M_ϕ	7,074
Folk & Ward, M_z	6,491

Coefficient de dissymétrie	
Skew ness, S_{k-1}	0,247
Skew ness, S_{k-2}	0,497
Inman, $\alpha_{\phi-1}$	-0,481
Inman, $\alpha_{\phi-2}$	-0,667
Folk & Ward, Sk_i	-0,491

Coefficient d'acuité (Kurtosis)	
Krumbein & Petijohn, K	0,336
Inman, K_ϕ	0,333
Folk & Ward, K_G	0,757

Coefficient de courbure	
C_c	1,597

Analyse granulométrique par voie fluide : fraction 0,040 µm - 2000 µm

Echantillon :	INDONESIE/12/LABAN/U-06/13/T.YAN W.ISKANDARSYAH
Date :	05/03/2013 10:17
Opérateur :	MT
Fichier :	U06-013

Commentaires :	prof. 117-147 cm 24/05/12 SAND destruction MO à H2O2 - élimination des ions floculants - hexa +US

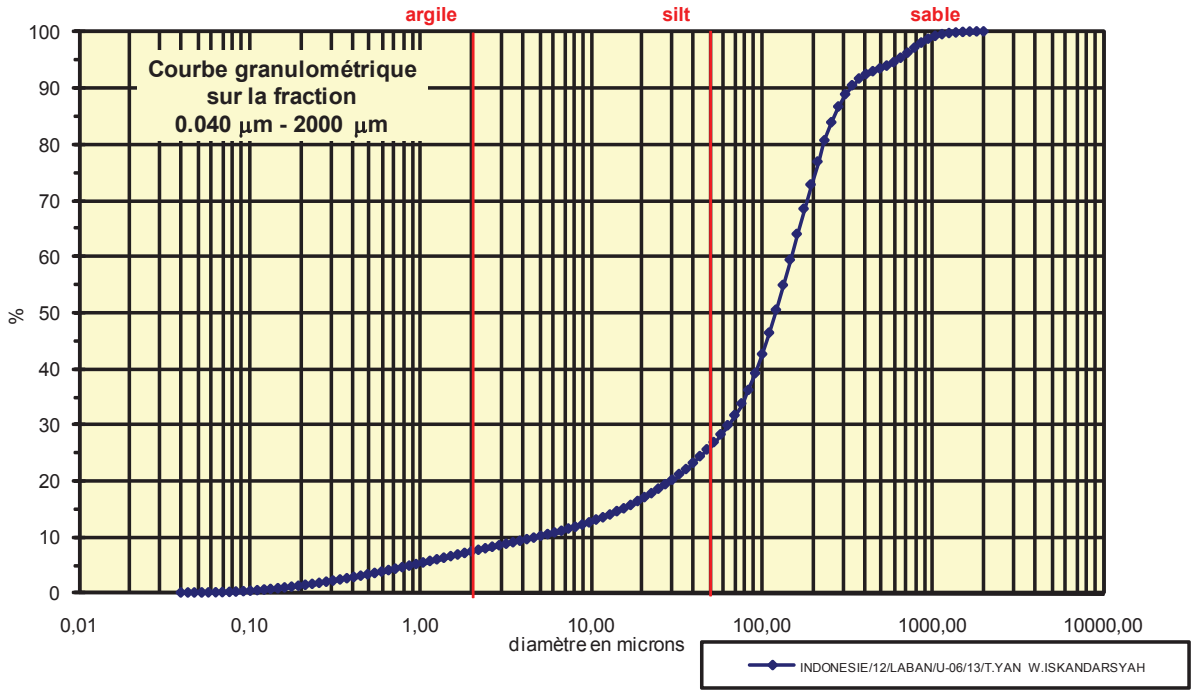

Fractiles	Taille (µm)	Taille (ϕ)
d_5	0,869	10,17
d_{10}	4,656	7,75
d_{16}	17,180	5,86
d_{25}	43,660	4,52
d_{30}	63,410	3,98
d_{50}	111,000	3,17
d_{60}	146,800	2,77
d_{75}	194,200	2,36
d_{84}	256,800	1,96
d_{90}	309,600	1,69
d_{95}	594,900	0,75

% Argile inférieur à 2µ	**A**	**7,05**
% Silts de 2µ à 50µ	**LT**	**18,45**
limons fins 2µ à 20µ	LF	9,25
limons grossiers 20µ à 50µ	LG	9,20
% Sables 50µ à 2000 µ	**ST**	**74,50**
sables fins 50µ à 200µ	SF	47,20
sables fins 50µ à 100µ	SF1	13,60
sables fins 100µ à 200 µ	SF2	33,60
sables grossiers 200µ à 2000µ	SG	27,30
sables grossiers 200µ à 500µ	SG1	20,70
sables grossiers 500µ à 1000µ	SG2	5,30
sables grossiers 1000µ à 2000µ	SG3	1,30

Indice de classement	
Trask, S_o	2,109
Krumbein, Q_d	-1,077
Inman, σ_ϕ	-1,951
Folk & Ward, σ_ϕ	-2,403
Hazen, C_u	31,529

Moyenne	
Trask, M	118,930
Inman, M_ϕ	3,912
Folk & Ward, M_z	3,665

Coefficient de dissymétrie	
Skew ness, S_{k-1}	0,688
Skew ness, S_{k-2}	0,830
Inman, $\alpha_{\phi-1}$	-0,380
Inman, $\alpha_{\phi-2}$	-1,172
Folk & Ward, Sk_i	-0,433

Coefficient d'acuité (Kurtosis)	
Krumbein & Petijohn, K	0,247
Inman, K_ϕ	1,414
Folk & Ward, K_G	1,793

Coefficient de courbure	
C_c	5,883

Analyse granulométrique par voie fluide : fraction 0,040 µm - 2000 µm

Echantillon :	INDONESIE/12/LABAN/U-06/14/T.YAN W.ISKANDARSYAH
Date :	05/03/2013 10:30
Opérateur :	MT
Fichier :	U06-014

Commentaires :	prof. 117-147 cm 24/05/12 CLAY destruction MO à H2O2 - élimination des ions floculants - hexa +US

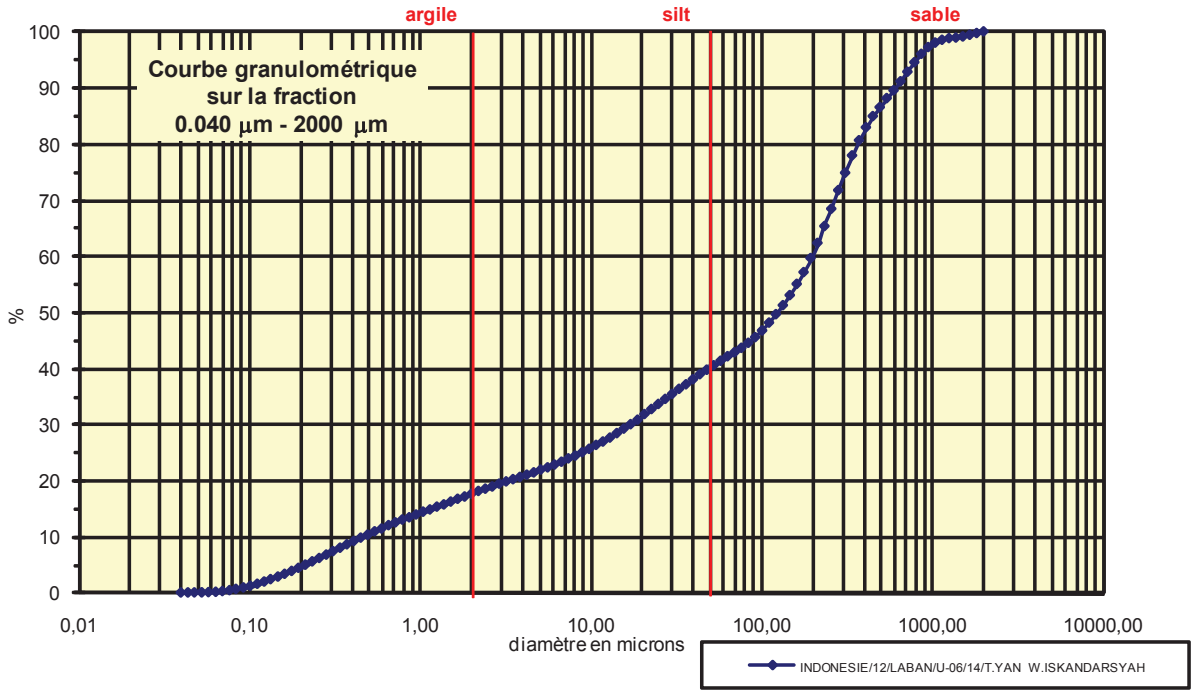

Fractiles	Taille (µm)	Taille (ϕ)
d_5	0,214	12,19
d_{10}	0,452	11,11
d_{16}	1,385	9,50
d_{25}	8,944	6,80
d_{30}	17,180	5,86
d_{50}	121,800	3,04
d_{60}	194,200	2,36
d_{75}	309,600	1,69
d_{84}	409,600	1,29
d_{90}	594,900	0,75
d_{95}	786,900	0,35

% Argile inférieur à 2µ	**A**	**17,10**
% Silts de 2µ à 50µ	**LT**	**22,60**
limons fins 2µ à 20µ	LF	13,70
limons grossiers 20µ à 50µ	LG	8,90
% Sables 50µ à 2000 µ	**ST**	**60,30**
sables fins 50µ à 200µ	SF	19,90
sables fins 50µ à 100µ	SF1	5,80
sables fins 100µ à 200 µ	SF2	14,10
sables grossiers 200µ à 2000µ	SG	40,40
sables grossiers 200µ à 500µ	SG1	26,90
sables grossiers 500µ à 1000µ	SG2	10,70
sables grossiers 1000µ à 2000µ	SG3	2,80

Indice de classement	
Trask, S_o	5,883
Krumbein, Q_d	-2,557
Inman, σ_ϕ	-4,104
Folk & Ward, σ_ϕ	-3,847
Hazen, C_u	429,646

Moyenne	
Trask, M	159,272
Inman, M_ϕ	5,392
Folk & Ward, M_z	4,607

Coefficient de dissymétrie	
Skew ness, S_{k-1}	0,187
Skew ness, S_{k-2}	0,432
Inman, $\alpha_{\phi-1}$	-0,574
Inman, $\alpha_{\phi-2}$	-0,787
Folk & Ward, Sk_i	-0,560

Coefficient d'acuité (Kurtosis)	
Krumbein & Petijohn, K	0,253
Inman, K_ϕ	0,443
Folk & Ward, K_G	0,949

Coefficient de courbure	
C_c	3,362

Analyse granulométrique par voie fluide : fraction 0,040 µm - 2000 µm

Echantillon :	INDONESIE/12/LABAN/U-06/15/T.YAN W.ISKANDARSYAH
Date :	05/03/2013 10:42
Opérateur :	MT
Fichier :	U06-015

Commentaires :	prof. 147-177 cm 24/05/12 destruction MO à H2O2 - élimination des ions floculants - hexa +US

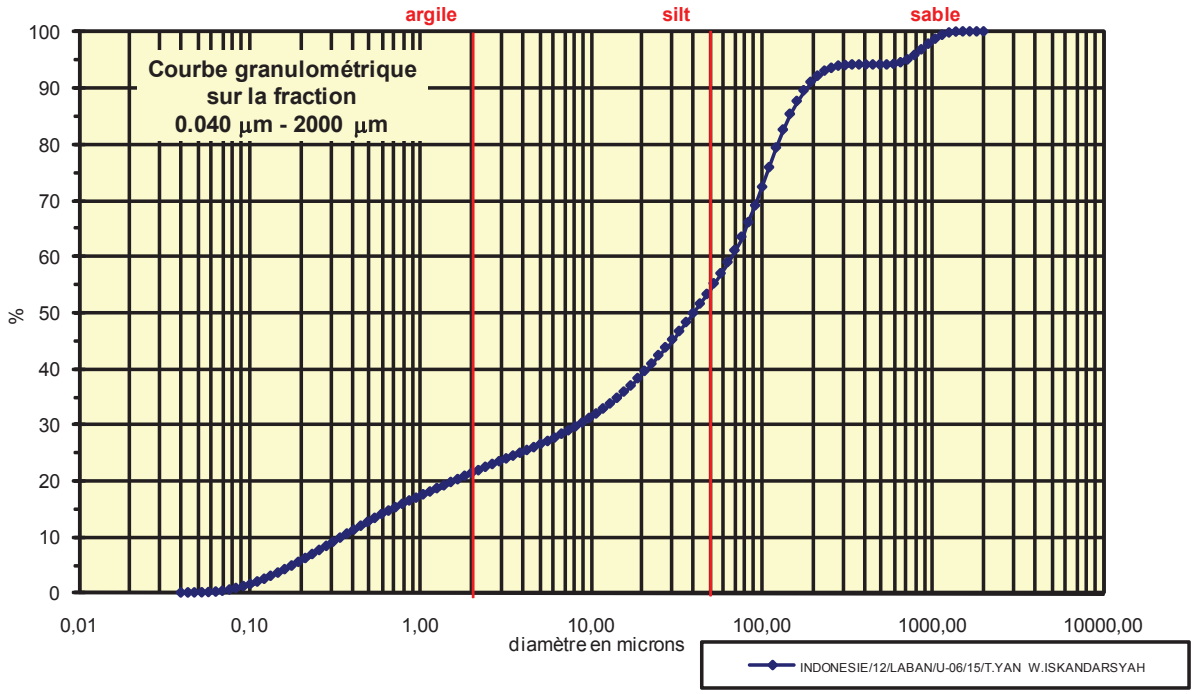

Fractiles	Taille (µm)	Taille (ϕ)
d_5	0,178	12,46
d_{10}	0,342	11,51
d_{16}	0,791	10,30
d_{25}	3,862	8,02
d_{30}	8,147	6,94
d_{50}	39,770	4,65
d_{60}	63,410	3,98
d_{75}	101,100	3,31
d_{84}	133,700	2,90
d_{90}	176,800	2,50
d_{95}	716,900	0,48

% Argile inférieur à 2µ	**A**	**20,80**
% Silts de 2µ à 50µ	**LT**	**32,40**
limons fins 2µ à 20µ	LF	17,40
limons grossiers 20µ à 50µ	LG	15,00
% Sables 50µ à 2000 µ	**ST**	**46,80**
sables fins 50µ à 200µ	SF	37,80
sables fins 50µ à 100µ	SF1	15,80
sables fins 100µ à 200 µ	SF2	22,00
sables grossiers 200µ à 2000µ	SG	9,00
sables grossiers 200µ à 500µ	SG1	3,10
sables grossiers 500µ à 1000µ	SG2	3,70
sables grossiers 1000µ à 2000µ	SG3	2,20

Indice de classement	
Trask, S_o	5,116
Krumbein, Q_d	-2,355
Inman, σ_ϕ	-3,701
Folk & Ward, σ_ϕ	-3,665
Hazen, C_u	185,409

Moyenne	
Trask, M	52,481
Inman, M_ϕ	6,603
Folk & Ward, M_z	5,953

Coefficient de dissymétrie	
Skew ness, S_{k-1}	0,247
Skew ness, S_{k-2}	0,497
Inman, $\alpha_{\phi-1}$	-0,527
Inman, $\alpha_{\phi-2}$	-0,491
Folk & Ward, Sk_i	-0,415

Coefficient d'acuité (Kurtosis)	
Krumbein & Petijohn, K	0,276
Inman, K_ϕ	0,618
Folk & Ward, K_G	1,042

Coefficient de courbure	
C_c	3,061

Analyse granulométrique par voie fluide : fraction 0,040 µm - 2000 µm

Echantillon :	INDONESIE/12/LABAN/U-06/16/T.YAN W.ISKANDARSYAH
Date :	05/03/2013 10:50
Opérateur :	MT
Fichier :	U06-016

Commentaires :	prof. 177-207 cm 24/05/12 destruction MO à H2O2 - élimination des ions floculants - hexa +US

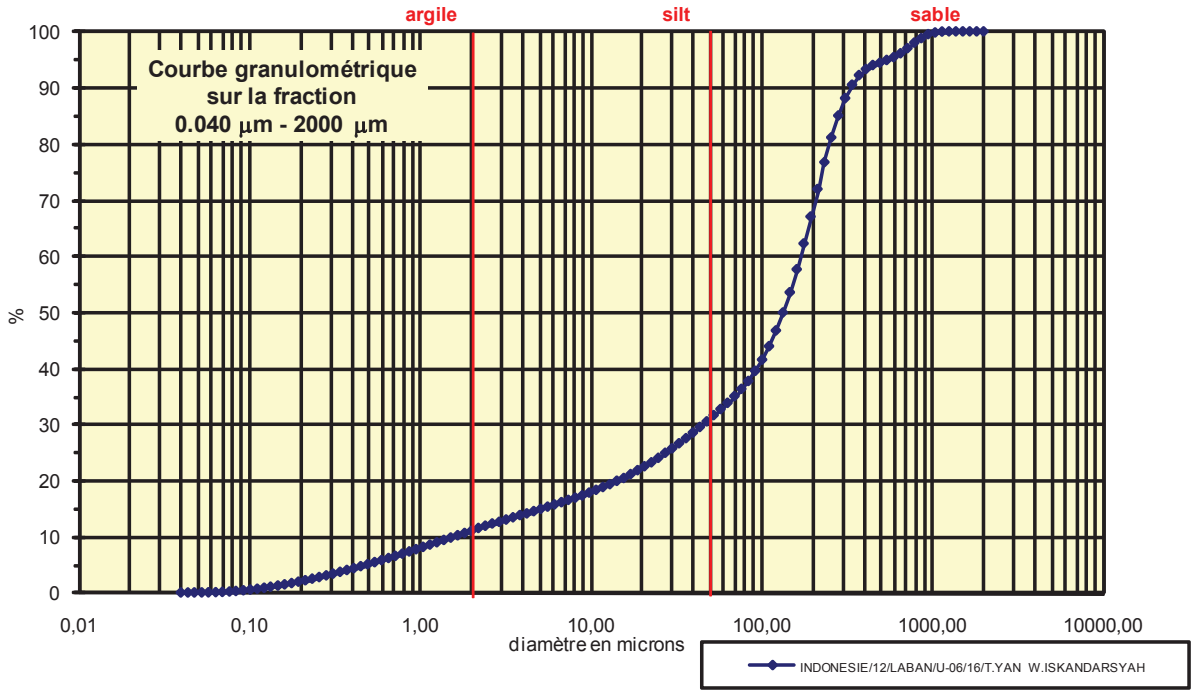

Fractiles	Taille (µm)	Taille (ϕ)
d_5	0,452	11,11
d_{10}	1,520	9,36
d_{16}	6,158	7,34
d_{25}	27,380	5,19
d_{30}	43,660	4,52
d_{50}	133,700	2,90
d_{60}	161,200	2,63
d_{75}	213,200	2,23
d_{84}	256,800	1,96
d_{90}	309,600	1,69
d_{95}	541,900	0,88

% Argile inférieur à 2µ	**A**	**10,60**
% Silts de 2µ à 50µ	**LT**	**19,90**
limons fins 2µ à 20µ	LF	11,20
limons grossiers 20µ à 50µ	LG	8,70
% Sables 50µ à 2000 µ	**ST**	**69,50**
sables fins 50µ à 200µ	SF	36,50
sables fins 50µ à 100µ	SF1	9,00
sables fins 100µ à 200 µ	SF2	27,50
sables grossiers 200µ à 2000µ	SG	33,00
sables grossiers 200µ à 500µ	SG1	27,40
sables grossiers 500µ à 1000µ	SG2	5,10
sables grossiers 1000µ à 2000µ	SG3	0,50

Indice de classement	
Trask, S_o	2,790
Krumbein, Q_d	-1,481
Inman, σ_ϕ	-2,691
Folk & Ward, σ_ϕ	-2,895
Hazen, C_u	106,053

Moyenne	
Trask, M	120,290
Inman, M_ϕ	4,652
Folk & Ward, M_z	4,069

Coefficient de dissymétrie	
Skew ness, S_{k-1}	0,327
Skew ness, S_{k-2}	0,571
Inman, $\alpha_{\phi-1}$	-0,650
Inman, $\alpha_{\phi-2}$	-1,150
Folk & Ward, Sk_i	-0,628

Coefficient d'acuité (Kurtosis)	
Krumbein & Petijohn, K	0,302
Inman, K_ϕ	0,900
Folk & Ward, K_G	1,416

Coefficient de courbure	
C_c	7,780

Analyse granulométrique par voie fluide : fraction 0,040 µm - 2000 µm

Echantillon :	INDONESIE/12/LABAN/U-06/17/T.YAN W.ISKANDARSYAH
Date :	05/03/2013 11:03
Opérateur :	MT
Fichier :	U06-017

Commentaires :	prof. 207-237 cm 24/05/12 destruction MO à H2O2 - élimination des ions floculants - hexa +US

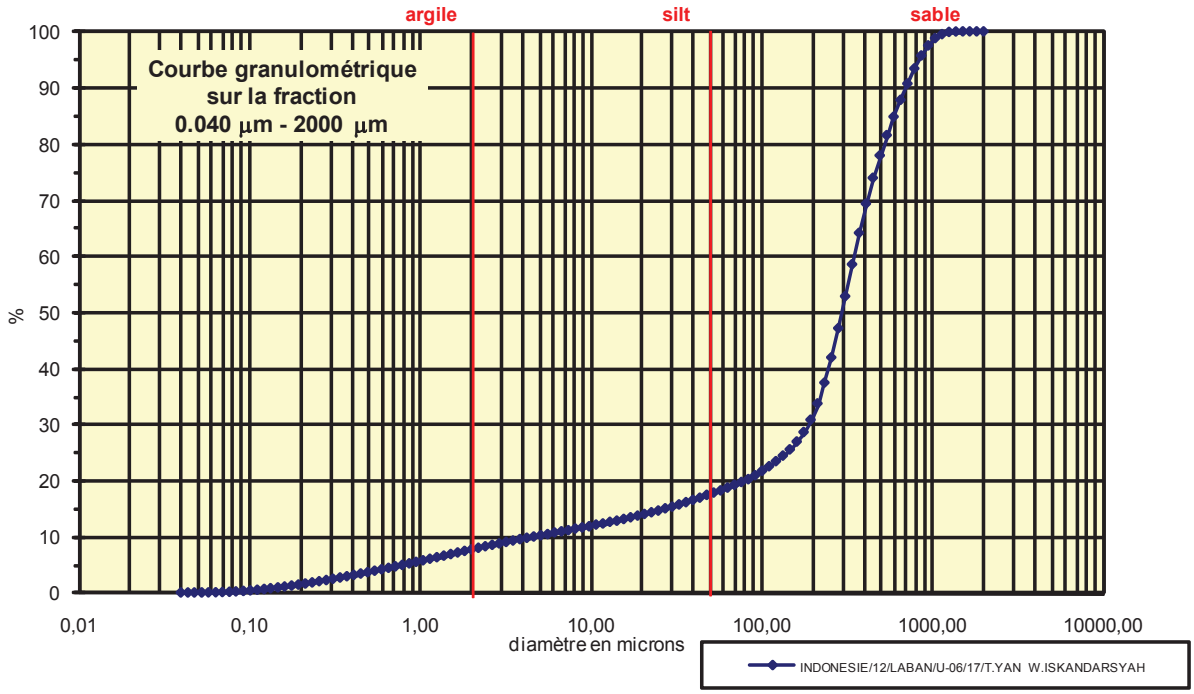

Fractiles	Taille (µm)	Taille (ϕ)
d_5	0,791	10,30
d_{10}	4,656	7,75
d_{16}	33,000	4,92
d_{25}	133,700	2,90
d_{30}	176,800	2,50
d_{50}	282,100	1,83
d_{60}	339,800	1,56
d_{75}	449,700	1,15
d_{84}	541,900	0,88
d_{90}	653,000	0,61
d_{95}	786,900	0,35

% Argile inférieur à 2µ	**A**	**7,41**
% Silts de 2µ à 50µ	**LT**	**9,99**
limons fins 2µ à 20µ	LF	6,29
limons grossiers 20µ à 50µ	LG	3,70
% Sables 50µ à 2000 µ	**ST**	**82,60**
sables fins 50µ à 200µ	SF	13,40
sables fins 50µ à 100µ	SF1	3,50
sables fins 100µ à 200 µ	SF2	9,90
sables grossiers 200µ à 2000µ	SG	69,20
sables grossiers 200µ à 500µ	SG1	47,10
sables grossiers 500µ à 1000µ	SG2	19,60
sables grossiers 1000µ à 2000µ	SG3	2,50

Indice de classement	
Trask, S_o	1,834
Krumbein, Q_d	-0,875
Inman, σ_ϕ	-2,019
Folk & Ward, σ_ϕ	-2,518
Hazen, C_u	72,981

Moyenne	
Trask, M	291,700
Inman, M_ϕ	2,903
Folk & Ward, M_z	2,544

Coefficient de dissymétrie	
Skew ness, S_{k-1}	0,756
Skew ness, S_{k-2}	0,869
Inman, $\alpha_{\phi-1}$	-0,533
Inman, $\alpha_{\phi-2}$	-1,733
Folk & Ward, Sk_i	-0,618

Coefficient d'acuité (Kurtosis)	
Krumbein & Petijohn, K	0,244
Inman, K_ϕ	1,466
Folk & Ward, K_G	2,332

Coefficient de courbure	
C_c	19,757

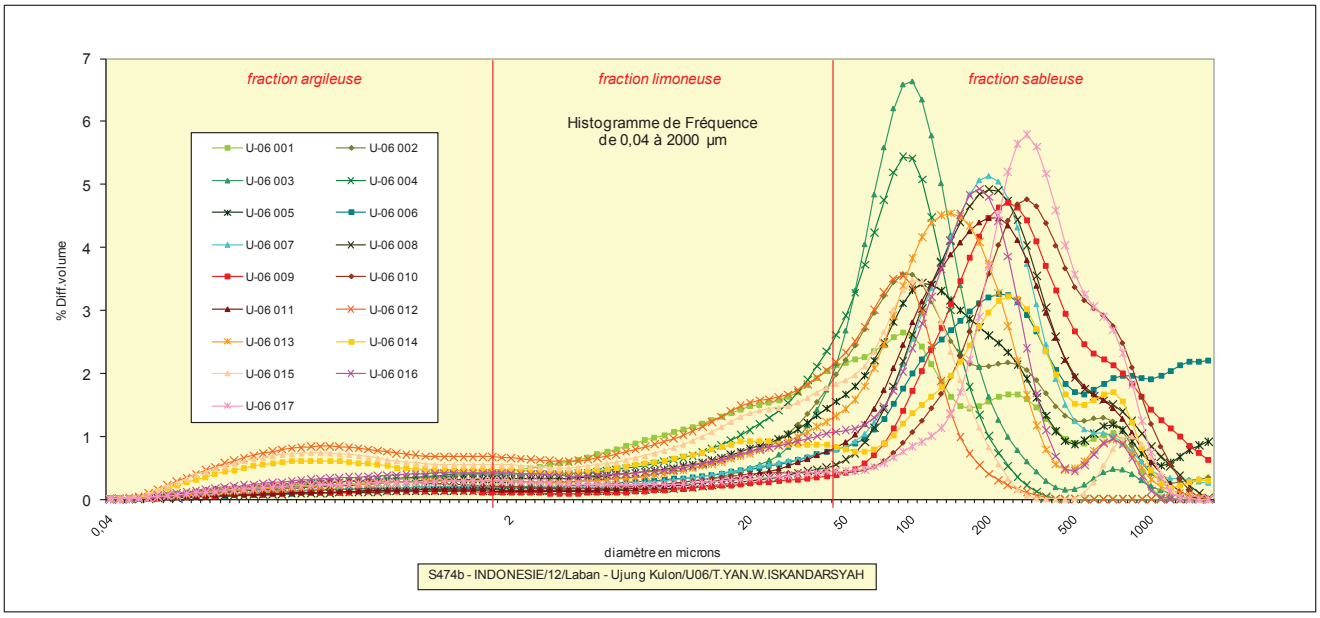
fraction argileuse
fraction limoneuse
fraction sableuse
Histogramme de Fréquence
de 0,04 à 2000 µm
U-06 001
U-06 002
U-06 003
U-06 004
U-06 005
U-06 006
U-06 007
U-06 008
U-06 009
U-06 010
U-06 011
U-06 012
U-06 013
U-06 014
U-06 015
U-06 016
U-06 017
% Diff volume
0
1
2
3
4
5
6
7
0,04
2
20
50
100
200
500
1000
diamètre en microns
S474b - INDONESIE/12/Laban - Ujung Kulon/U06/T.YAN.W.ISKANDARSYAH

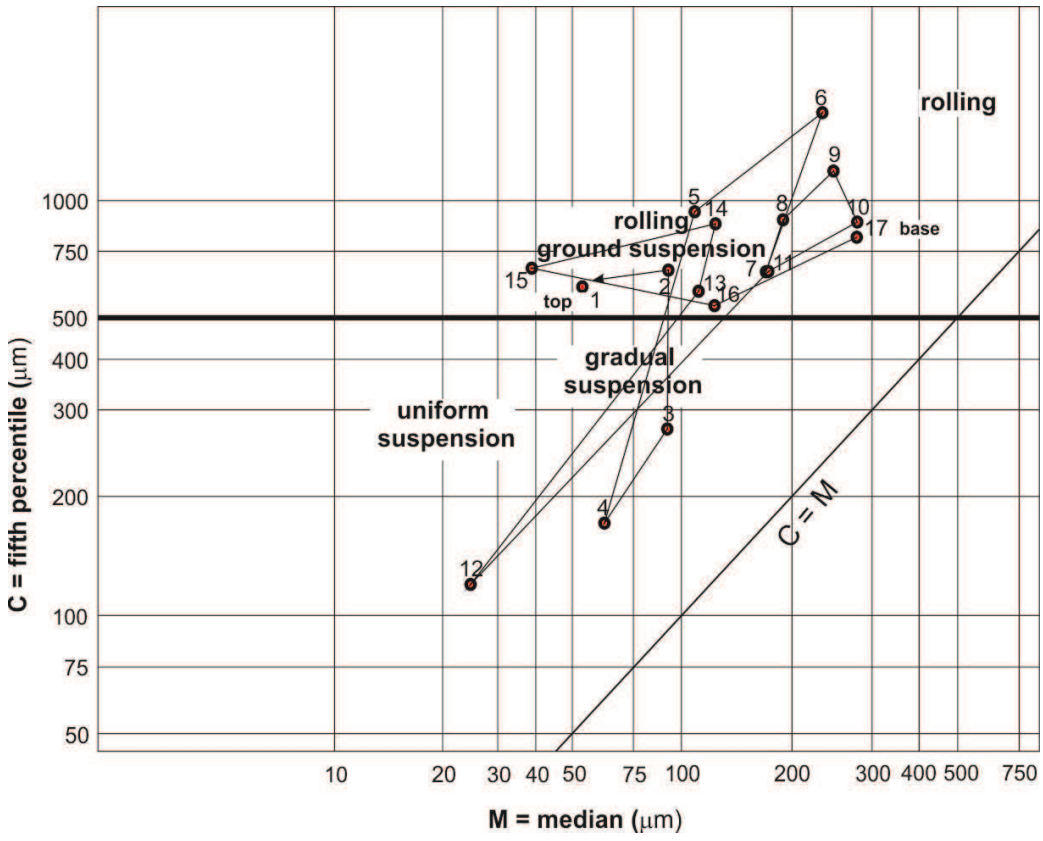
rolling
rolling
ground suspension
gradual
suspension
uniform
suspension
top
base
C = M
C = fifth percentile (μm)
M = median (μm)
1000
750
500
400
300
200
100
75
50
10
20
30
40
50
75
100
200
300
400
500
750
1
2
3
4
5
6
7
8
9
10
11
12
13
14
15
16
17

Analyse granulométrique par voie fluide : fraction 0,040 µm - 2000 µm

Echantillon :	INDONESIE/11/PANTAI/U-08/0-35/T.Yan W. ISKANDARSYAH
Date :	18/01/2012 12:36
Opérateur :	MT
Fichier :	U08-001

Commentaires :	prof. : 0 - 35 cm Destruction MO à H2O2 -élimination des ions floculants - hexa + US

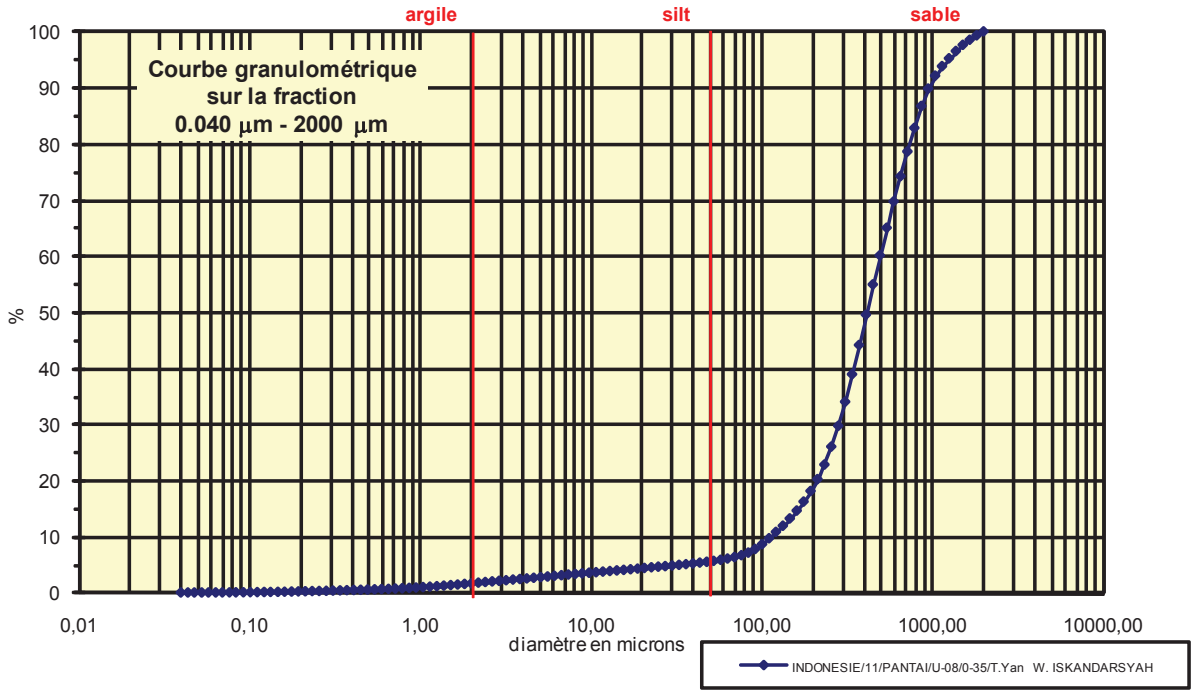

Fractiles	Taille (µm)	Taille (ϕ)
d_5	33,000	4,92
d_{10}	111,000	3,17
d_{16}	161,200	2,63
d_{25}	234,100	2,09
d_{30}	282,100	1,83
d_{50}	409,600	1,29
d_{60}	449,700	1,15
d_{75}	653,000	0,61
d_{84}	786,900	0,35
d_{90}	948,200	0,08
d_{95}	1143,000	-0,19

% Argile inférieur à 2µ	**A**	**1,53**
% Silts de 2µ à 50µ	**LT**	**3,94**
limons fins 2µ à 20µ	LF	2,73
limons grossiers 20µ à 50µ	LG	1,21
% Sables 50µ à 2000 µ	**ST**	**94,53**
sables fins 50µ à 200µ	SF	12,63
sables fins 50µ à 100µ	SF1	2,29
sables fins 100µ à 200 µ	SF2	10,34
sables grossiers 200µ à 2000µ	SG	81,90
sables grossiers 200µ à 500µ	SG1	42,00
sables grossiers 500µ à 1000µ	SG2	29,70
sables grossiers 1000µ à 2000µ	SG3	10,20

Indice de classement	
Trask, S_o	1,670
Krumbein, Q_d	-0,740
Inman, σ_ϕ	-1,144
Folk & Ward, σ_ϕ	-1,347
Hazen, C_u	4,051

Moyenne	
Trask, M	443,550
Inman, M_ϕ	1,489
Folk & Ward, M_z	1,422

Coefficient de dissymétrie	
Skew ness, S_{k-1}	0,911
Skew ness, S_{k-2}	0,955
Inman, $\alpha_{\phi-1}$	-0,176
Inman, $\alpha_{\phi-2}$	-0,941
Folk & Ward, Sk_i	-0,299

Coefficient d'acuité (Kurtosis)	
Krumbein & Petijohn, K	0,250
Inman, K_ϕ	1,236
Folk & Ward, K_G	1,416

Coefficient de courbure	
C_c	1,594

Analyse granulométrique par voie fluide : fraction 0,040 µm - 2000 µm

Echantillon :	INDONESIE/11/PANTAI/U-08/35-70/T.Yan W. ISKANDARSYAH
Date :	18/01/2012 15:07
Opérateur :	MT
Fichier :	U08-002

Commentaires :	prof. : 35-70 cm Destruction MO à H2O2 -élimination des ions floculants - hexa + US

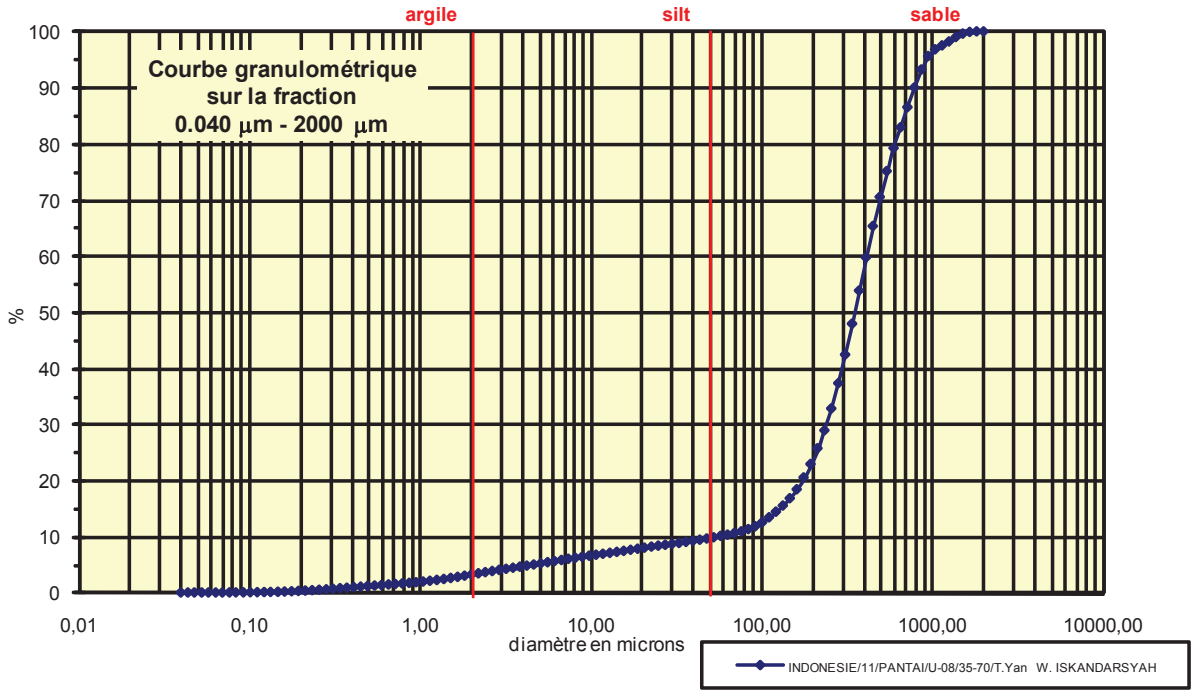

Fractiles	Taille (µm)	Taille (ϕ)
d_5	4,656	7,75
d_{10}	52,630	4,25
d_{16}	133,700	2,90
d_{25}	194,200	2,36
d_{30}	234,100	2,09
d_{50}	339,800	1,56
d_{60}	409,600	1,29
d_{75}	493,600	1,02
d_{84}	653,000	0,61
d_{90}	786,900	0,35
d_{95}	863,900	0,21

% Argile inférieur à 2µ	**A**	**3,00**
% Silts de 2µ à 50µ	**LT**	**6,62**
limons fins 2µ à 20µ	LF	4,80
limons grossiers 20µ à 50µ	LG	1,82
% Sables 50µ à 2000 µ	**ST**	**90,38**
sables fins 50µ à 200µ	SF	13,28
sables fins 50µ à 100µ	SF1	2,18
sables fins 100µ à 200 µ	SF2	11,10
sables grossiers 200µ à 2000µ	SG	77,10
sables grossiers 200µ à 500µ	SG1	47,60
sables grossiers 500µ à 1000µ	SG2	25,10
sables grossiers 1000µ à 2000µ	SG3	4,40

Indice de classement	
Trask, S_o	1,594
Krumbein, Q_d	-0,673
Inman, σ_ϕ	-1,144
Folk & Ward, σ_ϕ	-1,714
Hazen, C_u	7,783

Moyenne	
Trask, M	343,900
Inman, M_ϕ	1,759
Folk & Ward, M_z	1,692

Coefficient de dissymétrie	
Skew ness, S_{k1}	0,830
Skew ness, S_{k2}	0,911
Inman, $\alpha_{\phi-1}$	-0,176
Inman, $\alpha_{\phi-2}$	-2,117
Folk & Ward, Sk_I	-0,409

Coefficient d'acuité (Kurtosis)	
Krumbein & Petijohn, K	0,204
Inman, K_ϕ	2,293
Folk & Ward, K_G	2,295

Coefficient de courbure	
C_c	2,542

Analyse granulométrique par voie fluide : fraction 0,040 µm - 2000 µm

Echantillon :	INDONESIE/11/PANTAI/U-08/70-105/T.Yan W. ISKANDARSYAH
Date :	18/01/2012 15:30
Opérateur :	MT
Fichier :	U08-003

Commentaires :	prof. : 70-105 cm Destruction MO à H2O2 -élimination des ions floculants - hexa + US

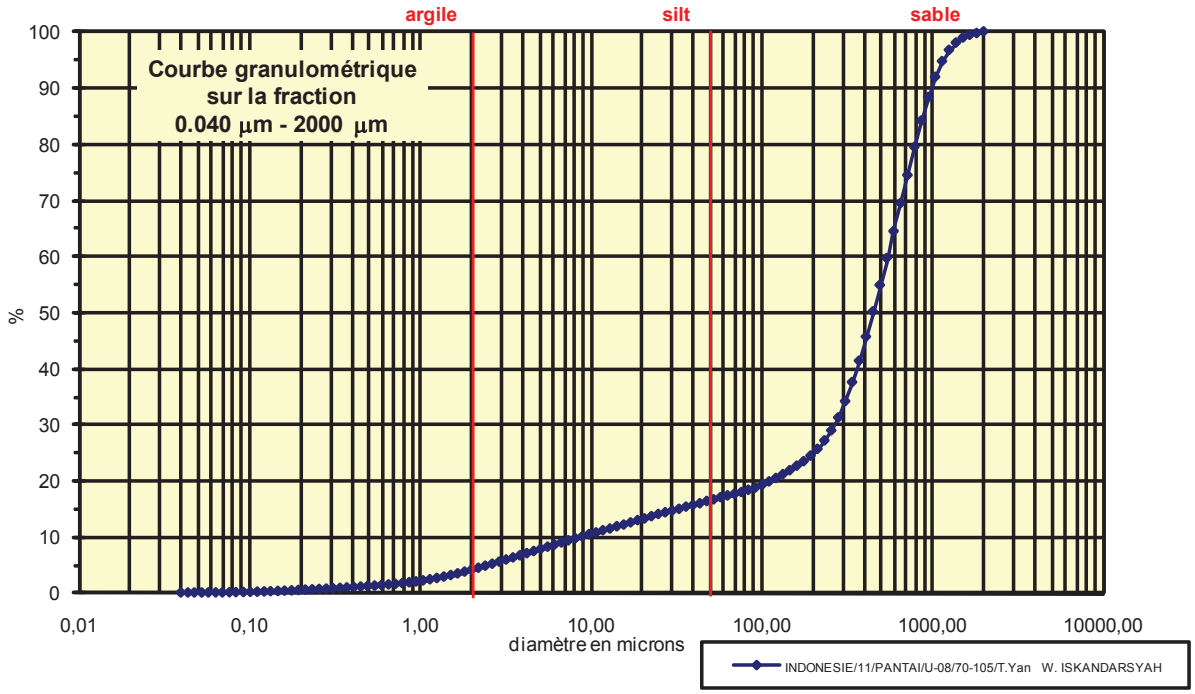

Fractiles	Taille (µm)	Taille (ϕ)
d_5	2,423	8,69
d_{10}	8,944	6,80
d_{16}	43,660	4,52
d_{25}	194,200	2,36
d_{30}	256,800	1,96
d_{50}	409,600	1,29
d_{60}	541,900	0,88
d_{75}	716,900	0,48
d_{84}	786,900	0,35
d_{90}	948,200	0,08
d_{95}	1143,000	-0,19

% Argile inférieur à 2µ	**A**	**3,73**
% Silts de 2µ à 50µ	**LT**	**12,57**
limons fins 2µ à 20µ	LF	9,17
limons grossiers 20µ à 50µ	LG	3,40
% Sables 50µ à 2000 µ	**ST**	**83,70**
sables fins 50µ à 200µ	SF	8,10
sables fins 50µ à 100µ	SF1	2,40
sables fins 100µ à 200 µ	SF2	5,70
sables grossiers 200µ à 2000µ	SG	75,60
sables grossiers 200µ à 500µ	SG1	30,40
sables grossiers 500µ à 1000µ	SG2	33,50
sables grossiers 1000µ à 2000µ	SG3	11,70

Indice de classement	
Trask, S_o	1,921
Krumbein, Q_d	-0,942
Inman, σ_ϕ	-2,086
Folk & Ward, σ_ϕ	-2,389
Hazen, C_u	60,588

Moyenne	
Trask, M	455,550
Inman, M_ϕ	2,432
Folk & Ward, M_z	2,050

Coefficient de dissymétrie	
Skew ness, S_{k-1}	0,830
Skew ness, S_{k-2}	0,911
Inman, $\alpha_{\phi-1}$	-0,548
Inman, $\alpha_{\phi-2}$	-1,419
Folk & Ward, Sk_i	-0,608

Coefficient d'acuité (Kurtosis)	
Krumbein & Petijohn, K	0,278
Inman, K_ϕ	1,129
Folk & Ward, K_G	1,932

Coefficient de courbure	
C_c	13,606

Analyse granulométrique par voie fluide : fraction 0,040 µm - 2000 µm

Echantillon :	INDONESIE/11/PANTAI/U-08/105-120/T.Yan W. ISKANDARSYAH
Date :	18/01/2012 15:42
Opérateur :	MT
Fichier :	U08-004

Commentaires :	prof. : 105-120 cm Destruction MO à H2O2 -élimination des ions floculants - hexa + US

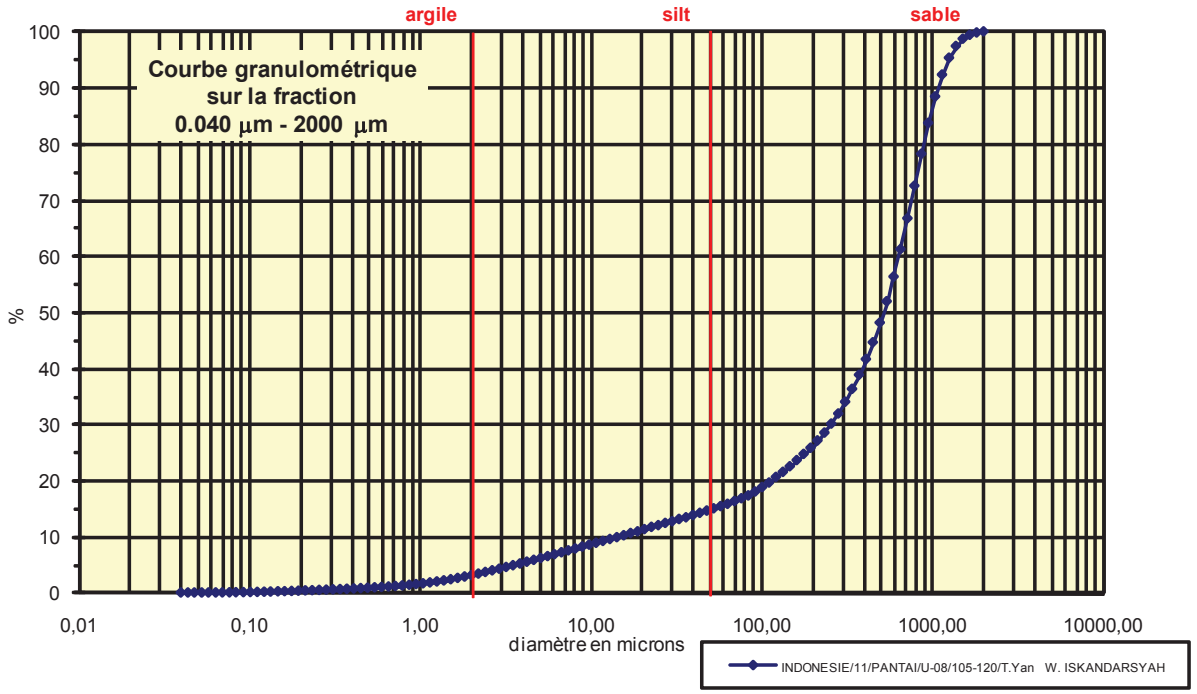

Fractiles	Taille (µm)	Taille (ϕ)
d_5	3,519	8,15
d_{10}	14,260	6,13
d_{16}	63,410	3,98
d_{25}	176,800	2,50
d_{30}	234,100	2,09
d_{50}	493,600	1,02
d_{60}	594,900	0,75
d_{75}	786,900	0,35
d_{84}	948,200	0,08
d_{90}	1041,000	-0,06
d_{95}	1143,000	-0,19

% Argile inférieur à 2µ	**A**	**2,85**
% Silts de 2µ à 50µ	**LT**	**11,75**
limons fins 2µ à 20µ	LF	8,05
limons grossiers 20µ à 50µ	LG	3,70
% Sables 50µ à 2000 µ	**ST**	**85,40**
sables fins 50µ à 200µ	SF	11,20
sables fins 50µ à 100µ	SF1	3,40
sables fins 100µ à 200 µ	SF2	7,80
sables grossiers 200µ à 2000µ	SG	74,20
sables grossiers 200µ à 500µ	SG1	22,30
sables grossiers 500µ à 1000µ	SG2	35,60
sables grossiers 1000µ à 2000µ	SG3	16,30

Indice de classement	
Trask, S_o	2,110
Krumbein, Q_d	-1,077
Inman, σ_ϕ	-1,951
Folk & Ward, σ_ϕ	-2,240
Hazen, C_u	41,718

Moyenne	
Trask, M	481,850
Inman, M_ϕ	2,028
Folk & Ward, M_z	1,691

Coefficient de dissymétrie	
Skew ness, S_{k-1}	0,571
Skew ness, S_{k-2}	0,756
Inman, $\alpha_{\phi-1}$	-0,517
Inman, $\alpha_{\phi-2}$	-1,517
Folk & Ward, Sk_i	-0,613

Coefficient d'acuité (Kurtosis)	
Krumbein & Petijohn, K	0,297
Inman, K_ϕ	1,138
Folk & Ward, K_G	1,587

Coefficient de courbure	
C_c	6,460

Analyse granulométrique par voie fluide : fraction 0,040 µm - 2000 µm

Echantillon :	INDONESIE/11/PANTAI/U-08/120-140/T.Yan W. ISKANDARSYAH
Date :	18/01/2012 15:57
Opérateur :	MT
Fichier :	U08-005

Commentaires :	prof. : 120-140 cm Destruction MO à H2O2 -élimination des ions floculants - hexa + US

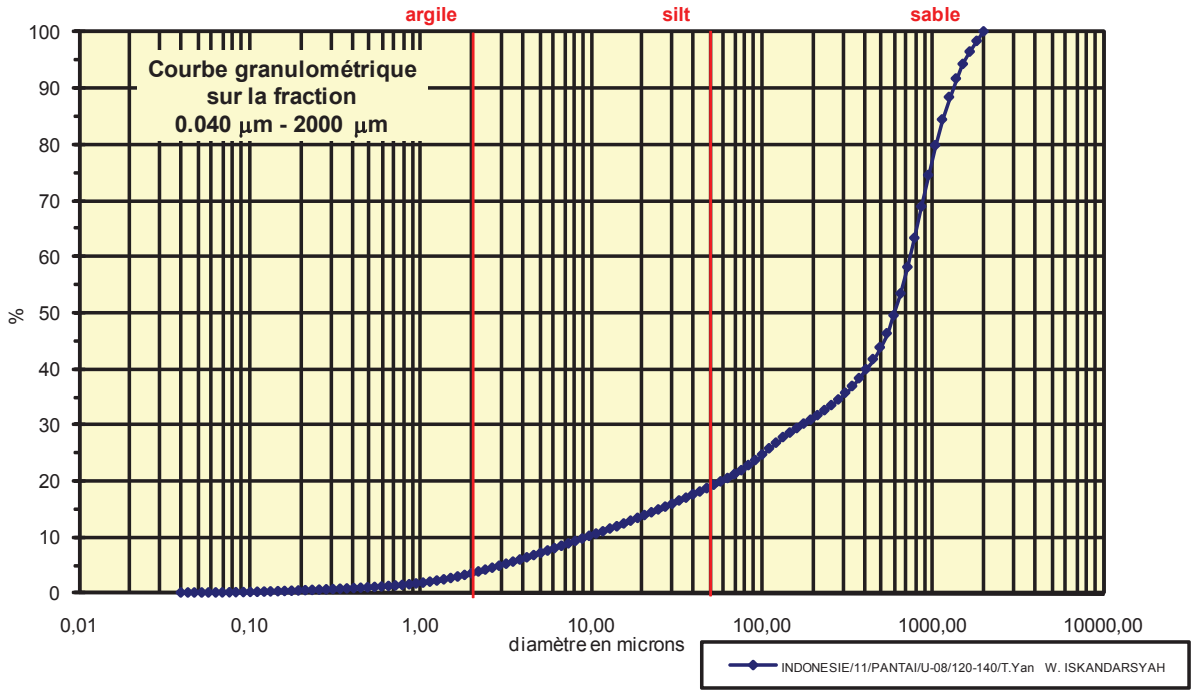

Fractiles	Taille (µm)	Taille (ϕ)
d_5	2,920	8,42
d_{10}	8,944	6,80
d_{16}	30,070	5,06
d_{25}	101,100	3,31
d_{30}	161,200	2,63
d_{50}	594,900	0,75
d_{60}	716,900	0,48
d_{75}	948,200	0,08
d_{84}	1041,000	-0,06
d_{90}	1255,000	-0,33
d_{95}	1512,000	-0,60

% Argile inférieur à 2µ	**A**	**3,13**
% Silts de 2µ à 50µ	**LT**	**15,47**
limons fins 2µ à 20µ	LF	10,17
limons grossiers 20µ à 50µ	LG	5,30
% Sables 50µ à 2000 µ	**ST**	**81,40**
sables fins 50µ à 200µ	SF	12,20
sables fins 50µ à 100µ	SF1	5,00
sables fins 100µ à 200 µ	SF2	7,20
sables grossiers 200µ à 2000µ	SG	69,20
sables grossiers 200µ à 500µ	SG1	12,90
sables grossiers 500µ à 1000µ	SG2	30,70
sables grossiers 1000µ à 2000µ	SG3	25,60

Indice de classement	
Trask, S_o	3,062
Krumbein, Q_d	-1,615
Inman, σ_ϕ	-2,557
Folk & Ward, σ_ϕ	-2,644
Hazen, C_u	80,154

Moyenne	
Trask, M	524,650
Inman, M_ϕ	2,499
Folk & Ward, M_z	1,916

Coefficient de dissymétrie	
Skew ness, S_{k-1}	0,271
Skew ness, S_{k-2}	0,520
Inman, $\alpha_{\phi-1}$	-0,684
Inman, $\alpha_{\phi-2}$	-1,237
Folk & Ward, Sk_I	-0,693

Coefficient d'acuité (Kurtosis)	
Krumbein & Petijohn, K	0,340
Inman, K_ϕ	0,763
Folk & Ward, K_G	1,144

Coefficient de courbure	
C_c	4,053

Analyse granulométrique par voie fluide : fraction 0,040 µm - 2000 µm

Echantillon :	INDONESIE/11/PANTAI/U-08/140-156/T.Yan W. ISKANDARSYAH
Date :	18/01/2012 16:36
Opérateur :	MT
Fichier :	U08-006

Commentaires :	prof. : 140-156 cm Destruction MO à H2O2 -élimination des ions floculants - hexa + US

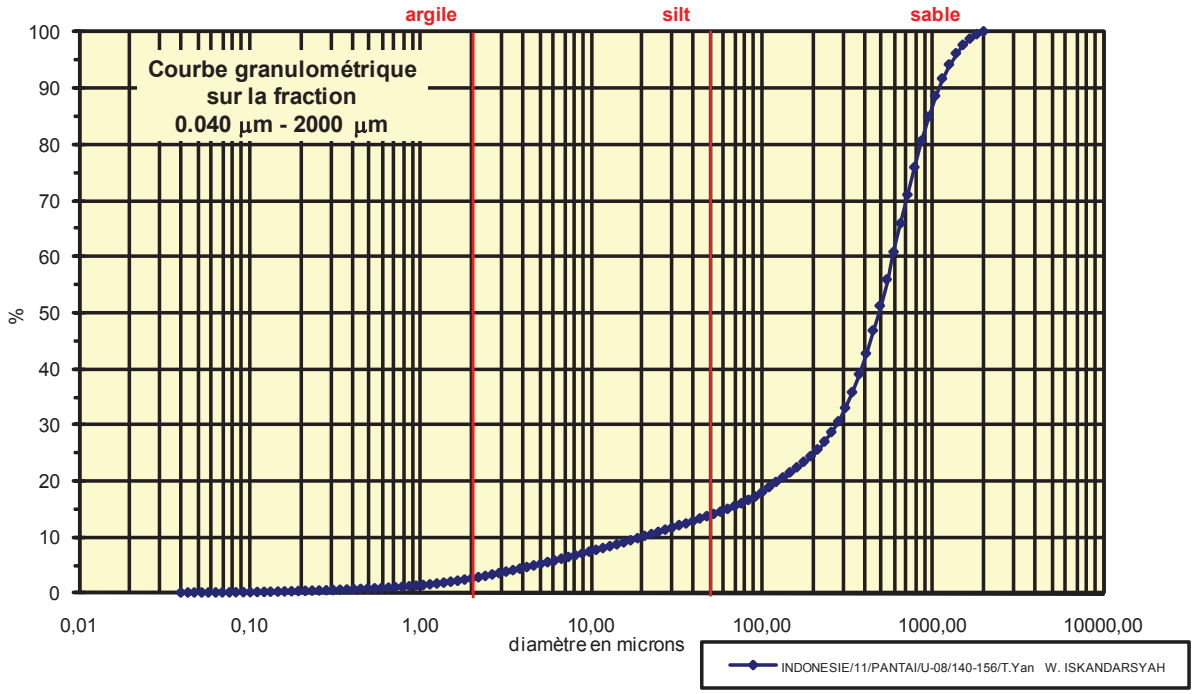

Fractiles	Taille (µm)	Taille (ϕ)
d_5	4,656	7,75
d_{10}	18,860	5,73
d_{16}	76,430	3,71
d_{25}	194,200	2,36
d_{30}	256,800	1,96
d_{50}	449,700	1,15
d_{60}	541,900	0,88
d_{75}	716,900	0,48
d_{84}	863,900	0,21
d_{90}	1041,000	-0,06
d_{95}	1255,000	-0,33

% Argile inférieur à 2µ	**A**	**2,30**
% Silts de 2µ à 50µ	**LT**	**11,30**
limons fins 2µ à 20µ	LF	7,38
limons grossiers 20µ à 50µ	LG	3,92
% Sables 50µ à 2000 µ	**ST**	**86,40**
sables fins 50µ à 200µ	SF	10,70
sables fins 50µ à 100µ	SF1	3,50
sables fins 100µ à 200 µ	SF2	7,20
sables grossiers 200µ à 2000µ	SG	75,70
sables grossiers 200µ à 500µ	SG1	26,80
sables grossiers 500µ à 1000µ	SG2	33,70
sables grossiers 1000µ à 2000µ	SG3	15,20

Indice de classement	
Trask, S_o	1,921
Krumbein, Q_d	-0,942
Inman, σ_ϕ	-1,749
Folk & Ward, σ_ϕ	-2,098
Hazen, C_u	28,733

Moyenne	
Trask, M	455,550
Inman, M_ϕ	1,960
Folk & Ward, M_z	1,691

Coefficient de dissymétrie	
Skew ness, S_{k-1}	0,688
Skew ness, S_{k-2}	0,830
Inman, $\alpha_{\phi-1}$	-0,462
Inman, $\alpha_{\phi-2}$	-1,461
Folk & Ward, Sk_i	-0,547

Coefficient d'acuité (Kurtosis)	
Krumbein & Petijohn, K	0,256
Inman, K_ϕ	1,308
Folk & Ward, K_G	1,756

Coefficient de courbure	
C_c	6,453

Analyse granulométrique par voie fluide : fraction 0,040 µm - 2000 µm

Echantillon :	INDONESIE/11/PANTAI/U-08/156-175/T.Yan W. ISKANDARSYAH
Date :	18/01/2012 16:47
Opérateur :	MT
Fichier :	U08-007

Commentaires :	prof. : 156-175 cm Destruction MO à H2O2 -élimination des ions floculants - hexa + US

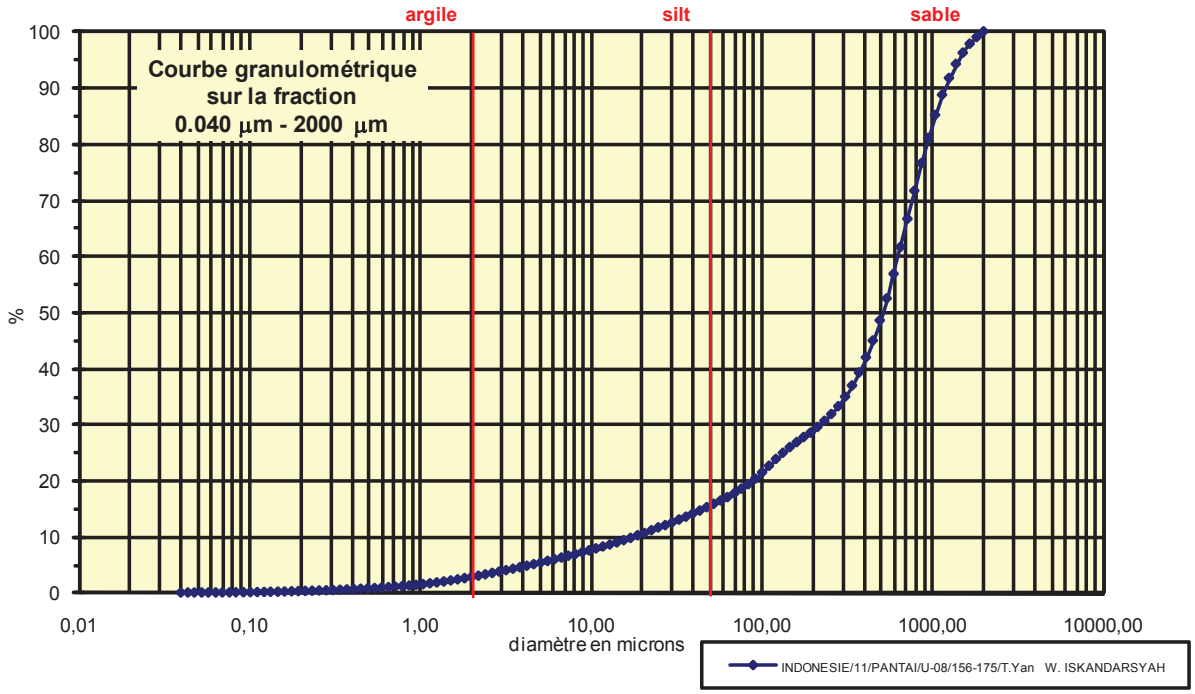

Fractiles	Taille (µm)	Taille (ϕ)
d_5	4,241	7,88
d_{10}	17,180	5,86
d_{16}	52,630	4,25
d_{25}	133,700	2,90
d_{30}	213,200	2,23
d_{50}	493,600	1,02
d_{60}	594,900	0,75
d_{75}	786,900	0,35
d_{84}	948,200	0,08
d_{90}	1143,000	-0,19
d_{95}	1377,000	-0,46

% Argile inférieur à 2µ	**A**	**2,55**
% Silts de 2µ à 50µ	**LT**	**12,65**
limons fins 2µ à 20µ	LF	7,65
limons grossiers 20µ à 50µ	LG	5,00
% Sables 50µ à 2000 µ	**ST**	**84,80**
sables fins 50µ à 200µ	SF	13,30
sables fins 50µ à 100µ	SF1	5,10
sables fins 100µ à 200 µ	SF2	8,20
sables grossiers 200µ à 2000µ	SG	71,50
sables grossiers 200µ à 500µ	SG1	20,00
sables grossiers 500µ à 1000µ	SG2	32,50
sables grossiers 1000µ à 2000µ	SG3	19,00

Indice de classement	
Trask, S_o	2,426
Krumbein, Q_d	-1,279
Inman, σ_ϕ	-2,086
Folk & Ward, σ_ϕ	-2,307
Hazen, C_u	34,627

Moyenne	
Trask, M	460,300
Inman, M_ϕ	2,162
Folk & Ward, M_z	1,781

Coefficient de dissymétrie	
Skew ness, S_{k-1}	0,432
Skew ness, S_{k-2}	0,657
Inman, $\alpha_{\phi-1}$	-0,548
Inman, $\alpha_{\phi-2}$	-1,290
Folk & Ward, Sk_I	-0,597

Coefficient d'acuité (Kurtosis)	
Krumbein & Petijohn, K	0,290
Inman, K_ϕ	1,000
Folk & Ward, K_G	1,337

Coefficient de courbure	
C_c	4,447

Analyse granulométrique par voie fluide : fraction 0,040 µm - 2000 µm

Echantillon :	INDONESIE/11/PANTAI/U-08/175-210/T.Yan W. ISKANDARSYAH
Date :	18/01/2012 17:39
Opérateur :	MT
Fichier :	U08-008

Commentaires :	prof. : 175-210 cm Destruction MO à H2O2 -élimination des ions floculants - hexa + US

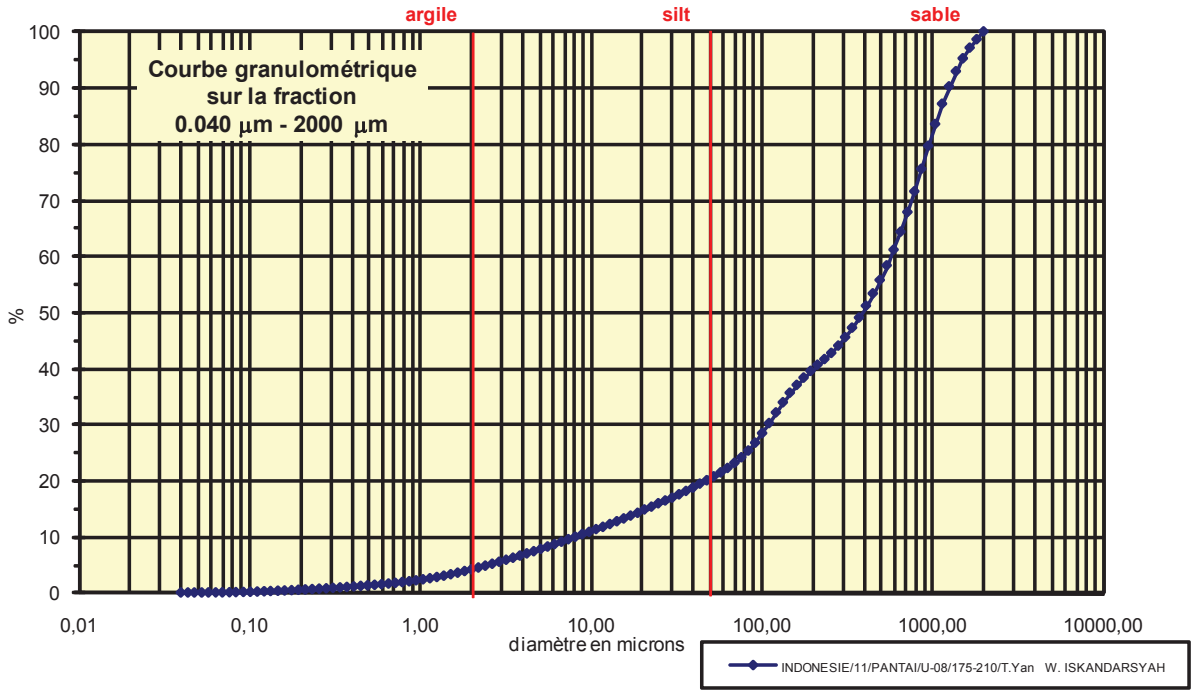

Fractiles	Taille (µm)	Taille (ϕ)
d_5	2,423	8,69
d_{10}	8,147	6,94
d_{16}	24,950	5,32
d_{25}	76,430	3,71
d_{30}	101,100	3,31
d_{50}	373,100	1,42
d_{60}	541,900	0,88
d_{75}	786,900	0,35
d_{84}	1041,000	-0,06
d_{90}	1143,000	-0,19
d_{95}	1377,000	-0,46

% Argile inférieur à 2µ	**A**	**3,82**
% Silts de 2µ à 50µ	**LT**	**16,18**
limons fins 2µ à 20µ	LF	10,38
limons grossiers 20µ à 50µ	LG	5,80
% Sables 50µ à 2000 µ	**ST**	**80,00**
sables fins 50µ à 200µ	SF	19,50
sables fins 50µ à 100µ	SF1	6,70
sables fins 100µ à 200 µ	SF2	12,80
sables grossiers 200µ à 2000µ	SG	60,50
sables grossiers 200µ à 500µ	SG1	16,20
sables grossiers 500µ à 1000µ	SG2	23,90
sables grossiers 1000µ à 2000µ	SG3	20,40

Indice de classement	
Trask, S_o	3,209
Krumbein, Q_d	-1,682
Inman, σ_ϕ	-2,691
Folk & Ward, σ_ϕ	-2,732
Hazen, C_u	66,515

Moyenne	
Trask, M	431,665
Inman, M_ϕ	2,633
Folk & Ward, M_z	2,230

Coefficient de dissymétrie	
Skew ness, S_{k-1}	0,432
Skew ness, S_{k-2}	0,657
Inman, $\alpha_{\phi-1}$	-0,450
Inman, $\alpha_{\phi-2}$	-1,000
Folk & Ward, Sk_i	-0,519

Coefficient d'acuité (Kurtosis)	
Krumbein & Petijohn, K	0,313
Inman, K_ϕ	0,700
Folk & Ward, K_G	1,115

Coefficient de courbure	
C_c	2,315

Analyse granulométrique par voie fluide : fraction 0,040 µm - 2000 µm

Echantillon :	INDONESIE/11/PANTAI/U-08/210-245/T.Yan W. ISKANDARSYAH
Date :	18/01/2012 17:53
Opérateur :	MT
Fichier :	U08-009

Commentaires :	prof. : 210-245 cm Destruction MO à H2O2 -élimination des ions floculants - hexa + US

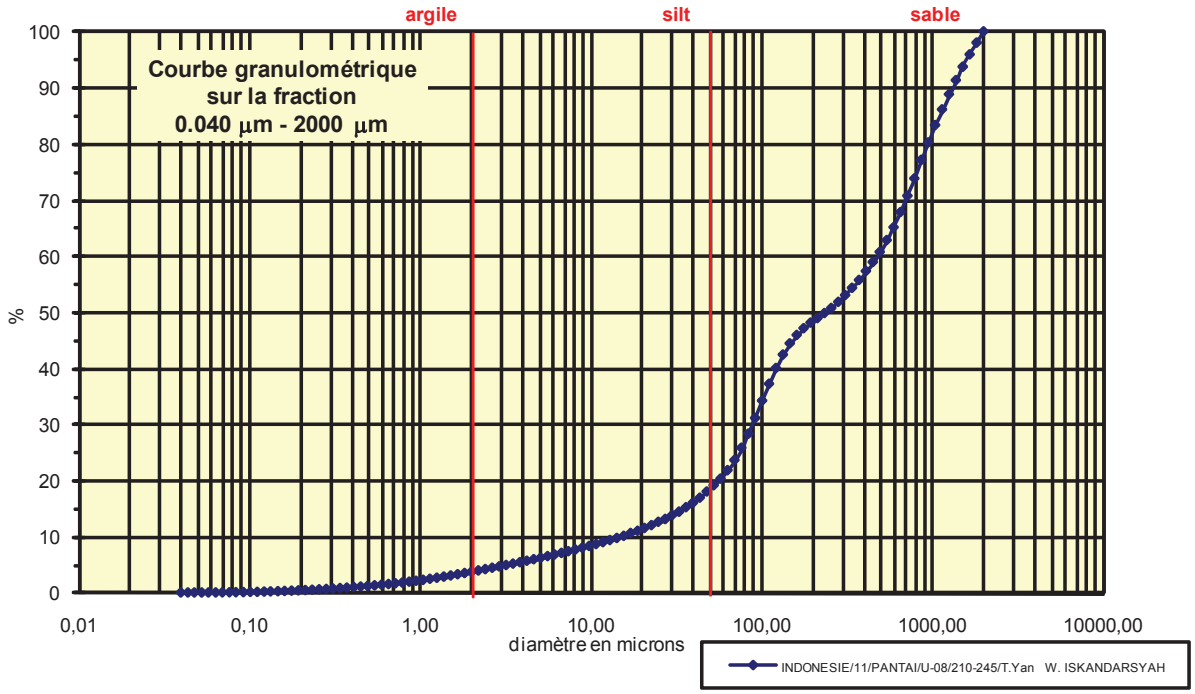

Fractiles	Taille (µm)	Taille (ϕ)
d_5	3,206	8,29
d_{10}	14,260	6,13
d_{16}	39,770	4,65
d_{25}	69,620	3,84
d_{30}	83,900	3,58
d_{50}	234,100	2,09
d_{60}	449,700	1,15
d_{75}	786,900	0,35
d_{84}	1041,000	-0,06
d_{90}	1255,000	-0,33
d_{95}	1512,000	-0,60

% Argile inférieur à 2µ	**A**	**3,47**
% Silts de 2µ à 50µ	**LT**	**14,53**
limons fins 2µ à 20µ	LF	7,53
limons grossiers 20µ à 50µ	LG	7,00
% Sables 50µ à 2000 µ	**ST**	**82,00**
sables fins 50µ à 200µ	SF	30,10
sables fins 50µ à 100µ	SF1	13,10
sables fins 100µ à 200 µ	SF2	17,00
sables grossiers 200µ à 2000µ	SG	51,90
sables grossiers 200µ à 500µ	SG1	12,60
sables grossiers 500µ à 1000µ	SG2	19,50
sables grossiers 1000µ à 2000µ	SG3	19,80

Indice de classement	
Trask, S_o	3,362
Krumbein, Q_d	-1,749
Inman, σ_ϕ	-2,355
Folk & Ward, σ_ϕ	-2,523
Hazen, C_u	31,536

Moyenne	
Trask, M	428,260
Inman, M_ϕ	2,297
Folk & Ward, M_z	2,230

Coefficient de dissymétrie	
Skew ness, S_{k-1}	1,000
Skew ness, S_{k-2}	1,000
Inman, $\alpha_{\phi-1}$	-0,086
Inman, $\alpha_{\phi-2}$	-0,743
Folk & Ward, Sk_i	-0,240

Coefficient d'acuité (Kurtosis)	
Krumbein & Petijohn, K	0,289
Inman, K_ϕ	0,886
Folk & Ward, K_G	1,040

Coefficient de courbure	
C_c	1,098

Analyse granulométrique par voie fluide : fraction 0,040 µm - 2000 µm

Echantillon :	INDONESIE/11/PANTAI/U-08/245-259/T.Yan W. ISKANDARSYAH
Date :	19/01/2012 14:14
Opérateur :	MT
Fichier :	U08-010

Commentaires :	prof. : 245-259 cm Destruction MO à H2O2 -élimination des ions floculants - hexa + US

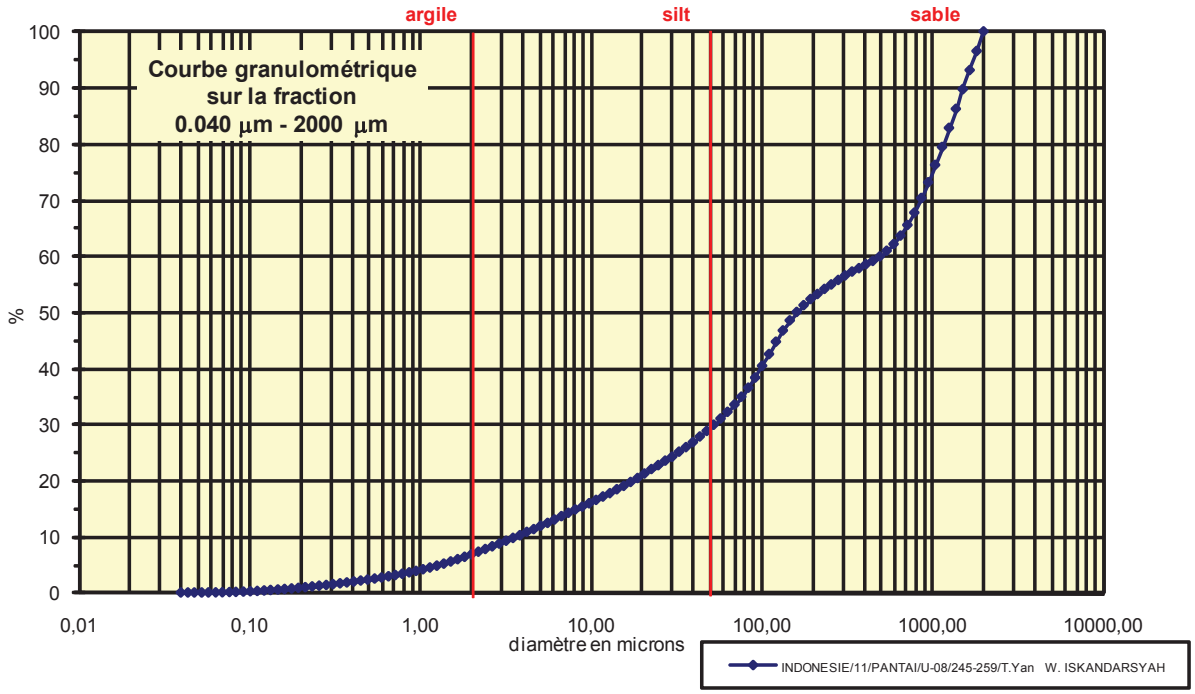

Fractiles	Taille (µm)	Taille (ϕ)
d_5	1,261	9,63
d_{10}	3,519	8,15
d_{16}	9,819	6,67
d_{25}	30,070	5,06
d_{30}	52,630	4,25
d_{50}	161,200	2,63
d_{60}	493,600	1,02
d_{75}	948,200	0,08
d_{84}	1255,000	-0,33
d_{90}	1512,000	-0,60
d_{95}	1660,000	-0,73

% Argile inférieur à 2µ	**A**	**6,36**
% Silts de 2µ à 50µ	**LT**	**22,44**
limons fins 2µ à 20µ	LF	14,04
limons grossiers 20µ à 50µ	LG	8,40
% Sables 50µ à 2000 µ	**ST**	**71,20**
sables fins 50µ à 200µ	SF	23,50
sables fins 50µ à 100µ	SF1	9,50
sables fins 100µ à 200 µ	SF2	14,00
sables grossiers 200µ à 2000µ	SG	47,70
sables grossiers 200µ à 500µ	SG1	7,60
sables grossiers 500µ à 1000µ	SG2	13,20
sables grossiers 1000µ à 2000µ	SG3	26,90

Indice de classement	
Trask, S_o	5,615
Krumbein, Q_d	-2,489
Inman, σ_ϕ	-3,499
Folk & Ward, σ_ϕ	-3,320
Hazen, C_u	140,267

Moyenne	
Trask, M	489,135
Inman, M_ϕ	3,171
Folk & Ward, M_z	2,992

Coefficient de dissymétrie	
Skew ness, S_{k1}	1,097
Skew ness, S_{k2}	1,047
Inman, $\alpha_{\phi-1}$	-0,154
Inman, $\alpha_{\phi-2}$	-0,519
Folk & Ward, Sk_I	-0,252

Coefficient d'acuité (Kurtosis)	
Krumbein & Petijohn, K	0,304
Inman, K_ϕ	0,481
Folk & Ward, K_G	0,853

Coefficient de courbure	
C_c	1,595

Analyse granulométrique par voie fluide : fraction 0,040 µm - 2000 µm

Echantillon :	INDONESIE/11/PANTAI/U08/259-280/T.Yan W. ISKANDARSYAH
Date :	24/01/2012 15:30
Opérateur :	MT
Fichier :	U08-011

Commentaires :	prof. : 259-280 cm Destruction MO à H2O2 -élimination des ions floculants - hexa + US

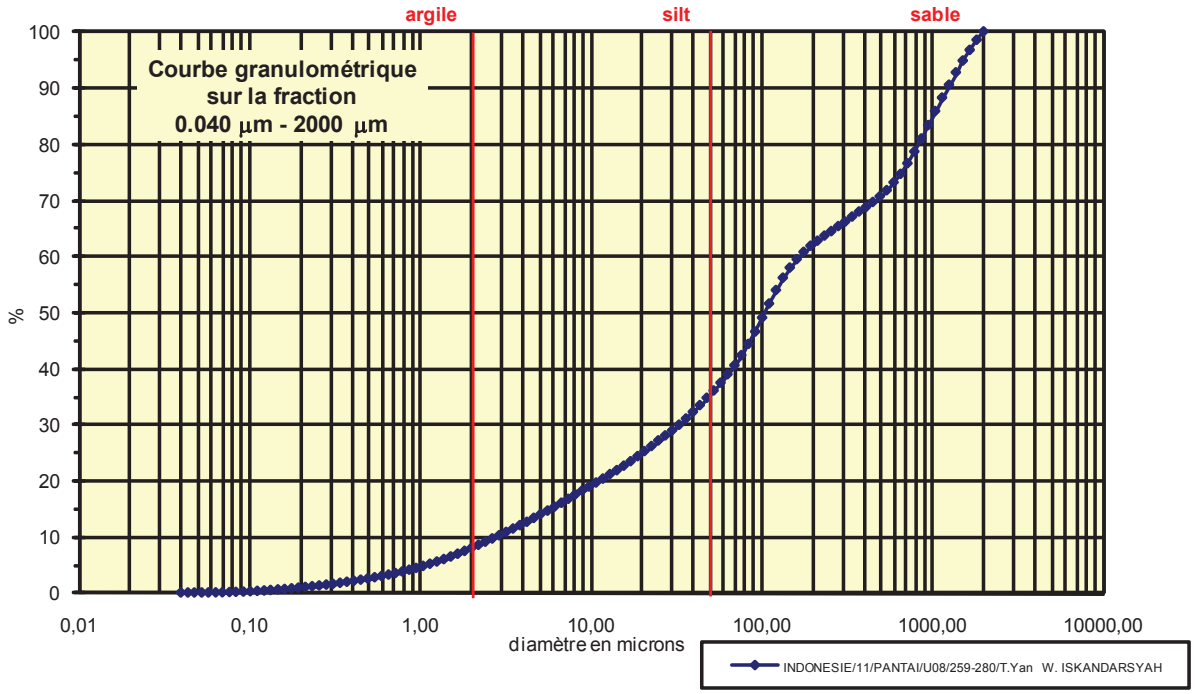

Fractiles	Taille (µm)	Taille (ϕ)
d_5	1,047	9,90
d_{10}	2,660	8,55
d_{16}	6,761	7,21
d_{25}	18,860	5,73
d_{30}	33,000	4,92
d_{50}	101,100	3,31
d_{60}	161,200	2,63
d_{75}	653,000	0,61
d_{84}	948,200	0,08
d_{90}	1143,000	-0,19
d_{95}	1512,000	-0,60

% Argile inférieur à 2µ	**A**	**7,42**
% Silts de 2µ à 50µ	**LT**	**27,28**
limons fins 2µ à 20µ	LF	16,88
limons grossiers 20µ à 50µ	LG	10,40
% Sables 50µ à 2000 µ	**ST**	**65,30**
sables fins 50µ à 200µ	SF	27,10
sables fins 50µ à 100µ	SF1	11,80
sables fins 100µ à 200 µ	SF2	15,30
sables grossiers 200µ à 2000µ	SG	38,20
sables grossiers 200µ à 500µ	SG1	8,80
sables grossiers 500µ à 1000µ	SG2	12,70
sables grossiers 1000µ à 2000µ	SG3	16,70

Indice de classement	
Trask, S_o	5,884
Krumbein, Q_d	-2,557
Inman, σ_ϕ	-3,566
Folk & Ward, σ_ϕ	-3,373
Hazen, C_u	60,602

Moyenne	
Trask, M	335,930
Inman, M_ϕ	3,643
Folk & Ward, M_z	3,530

Coefficient de dissymétrie	
Skew ness, S_{k-1}	1,205
Skew ness, S_{k-2}	1,098
Inman, $\alpha_{\phi-1}$	-0,094
Inman, $\alpha_{\phi-2}$	-0,377
Folk & Ward, Sk_i	-0,175

Coefficient d'acuité (Kurtosis)	
Krumbein & Petijohn, K	0,278
Inman, K_ϕ	0,472
Folk & Ward, K_G	0,841

Coefficient de courbure	
C_c	2,540

Analyse granulométrique par voie fluide : fraction 0,040 µm - 2000 µm

Echantillon :	INDONESIE/11/PANTAI/U-08/280-315/T.Yan W. ISKANDARSYAH
Date :	19/01/2012 14:29
Opérateur :	MT
Fichier :	U08-012

Commentaires :	prof. : 280-315 cm Destruction MO à H2O2 -élimination des ions floculants - hexa + US

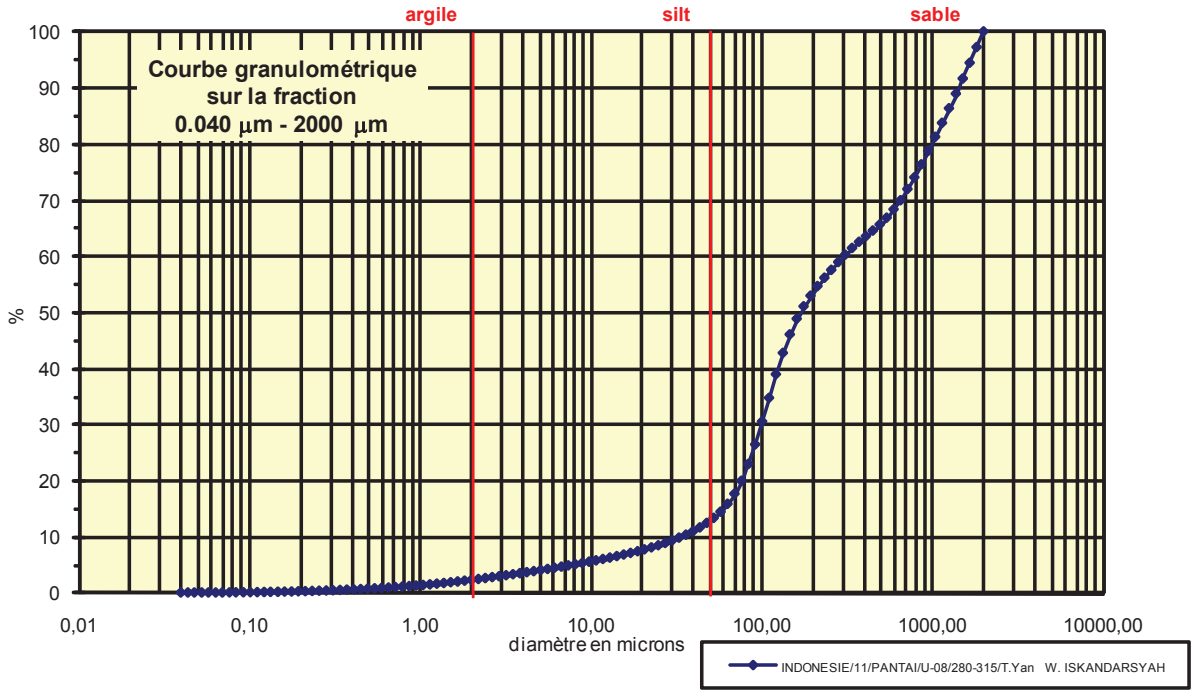

Fractiles	Taille (µm)	Taille (ϕ)
d_5	7,421	7,07
d_{10}	33,000	4,92
d_{16}	63,410	3,98
d_{25}	83,900	3,58
d_{30}	92,090	3,44
d_{50}	161,200	2,63
d_{60}	282,100	1,83
d_{75}	786,900	0,35
d_{84}	1143,000	-0,19
d_{90}	1377,000	-0,46
d_{95}	1660,000	-0,73

% Argile inférieur à 2µ	**A**	**2,11**
% Silts de 2µ à 50µ	**LT**	**10,29**
limons fins 2µ à 20µ	LF	5,25
limons grossiers 20µ à 50µ	LG	5,04
% Sables 50µ à 2000 µ	**ST**	**87,60**
sables fins 50µ à 200µ	SF	40,50
sables fins 50µ à 100µ	SF1	14,00
sables fins 100µ à 200 µ	SF2	26,50
sables grossiers 200µ à 2000µ	SG	47,10
sables grossiers 200µ à 500µ	SG1	12,70
sables grossiers 500µ à 1000µ	SG2	13,10
sables grossiers 1000µ à 2000µ	SG3	21,30

Indice de classement	
Trask, S_o	3,063
Krumbein, Q_d	-1,615
Inman, σ_ϕ	-2,086
Folk & Ward, σ_ϕ	-2,226
Hazen, C_u	8,548

Moyenne	
Trask, M	435,400
Inman, M_ϕ	1,893
Folk & Ward, M_z	2,140

Coefficient de dissymétrie	
Skew ness, S_{k-1}	2,541
Skew ness, S_{k-2}	1,594
Inman, $\alpha_{\phi-1}$	0,355
Inman, $\alpha_{\phi-2}$	-0,258
Folk & Ward, Sk_i	0,108

Coefficient d'acuité (Kurtosis)	
Krumbein & Petijohn, K	0,262
Inman, K_ϕ	0,871
Folk & Ward, K_G	0,991

Coefficient de courbure	
C_c	0,911

Analyse granulométrique par voie fluide : fraction 0,040 µm - 2000 µm

Echantillon :	INDONESIE/11/PANTAI/U-08/0/T.Yan W. ISKANDARSYAH
Date :	18/01/2012 12:28
Opérateur :	MT
Fichier :	U08-013

Commentaires :	prof. : 0 cm Destruction MO à H2O2 -élimination des ions floculants - hexa + US

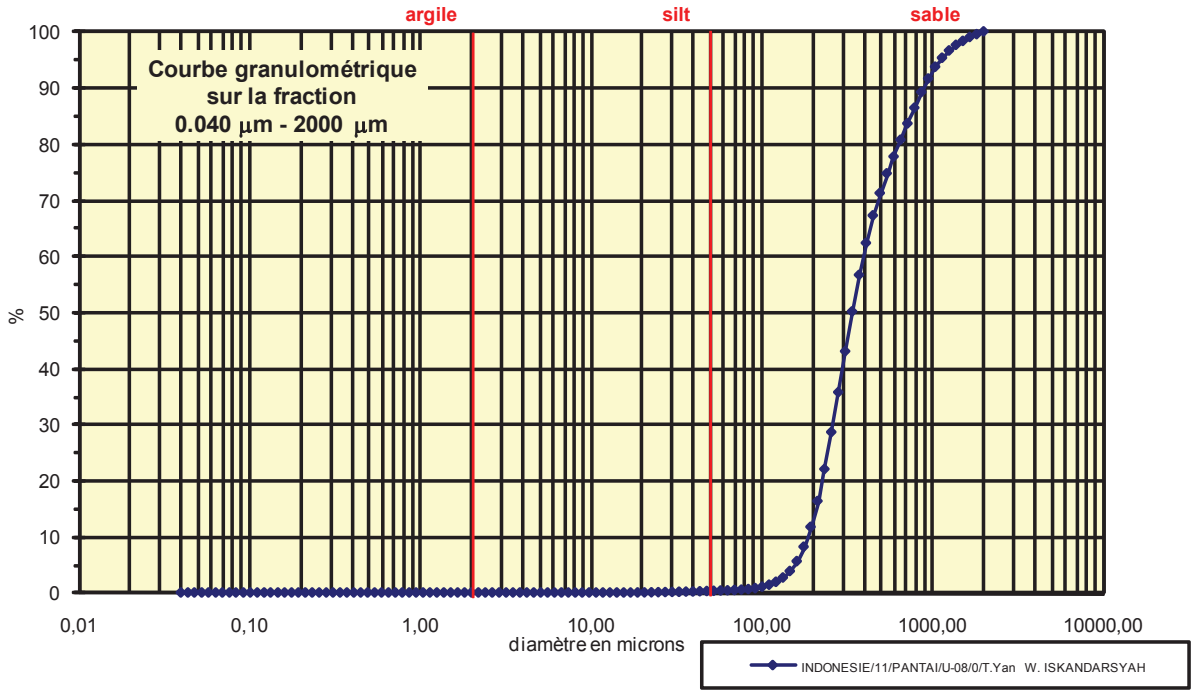

Fractiles	Taille (µm)	Taille (ϕ)
d_5	146,800	2,77
d_{10}	176,800	2,50
d_{16}	194,200	2,36
d_{25}	234,100	2,09
d_{30}	256,800	1,96
d_{50}	309,600	1,69
d_{60}	373,100	1,42
d_{75}	541,900	0,88
d_{84}	716,900	0,48
d_{90}	863,900	0,21
d_{95}	1041,000	-0,06

% Argile inférieur à 2µ	**A**	**0,00**
% Silts de 2µ à 50µ	**LT**	**0,26**
limons fins 2µ à 20µ	LF	0,01
limons grossiers 20µ à 50µ	LG	0,25
% Sables 50µ à 2000 µ	**ST**	**99,74**
sables fins 50µ à 200µ	SF	11,44
sables fins 50µ à 100µ	SF1	0,52
sables fins 100µ à 200 µ	SF2	10,92
sables grossiers 200µ à 2000µ	SG	88,30
sables grossiers 200µ à 500µ	SG1	59,50
sables grossiers 500µ à 1000µ	SG2	20,40
sables grossiers 1000µ à 2000µ	SG3	8,40

Indice de classement	
Trask, S_o	1,521
Krumbein, Q_d	-0,605
Inman, σ_ϕ	-0,942
Folk & Ward, σ_ϕ	-0,899
Hazen, C_u	2,110

Moyenne	
Trask, M	388,000
Inman, M_ϕ	1,422
Folk & Ward, M_z	1,512

Coefficient de dissymétrie	
Skew ness, S_{k-1}	1,323
Skew ness, S_{k-2}	1,150
Inman, $\alpha_{\phi-1}$	0,286
Inman, $\alpha_{\phi-2}$	0,357
Folk & Ward, Sk_I	0,262

Coefficient d'acuité (Kurtosis)	
Krumbein & Petijohn, K	0,224
Inman, K_ϕ	0,500
Folk & Ward, K_G	0,956

Coefficient de courbure	
C_c	1,000

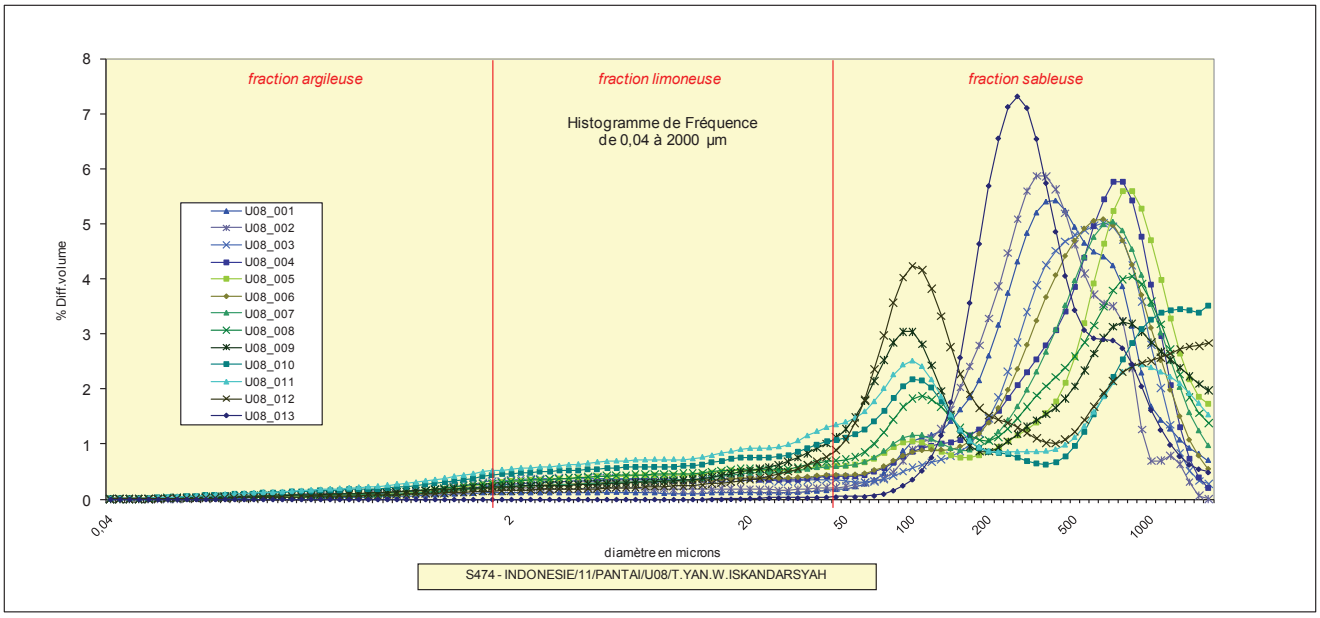
fraction argileuse
fraction limoneuse
fraction sableuse
Histogramme de Fréquence
de 0,04 à 2000 µm
% Diff volume
U08_001
U08_002
U08_003
U08_004
U08_005
U08_006
U08_007
U08_008
U08_009
U08_010
U08_011
U08_012
U08_013
0,04
2
20
50
100
200
500
1000
diamètre en microns
S474 - INDONESIE/11/PANTAI/U08/T.YAN.W.ISKANDARSYAH

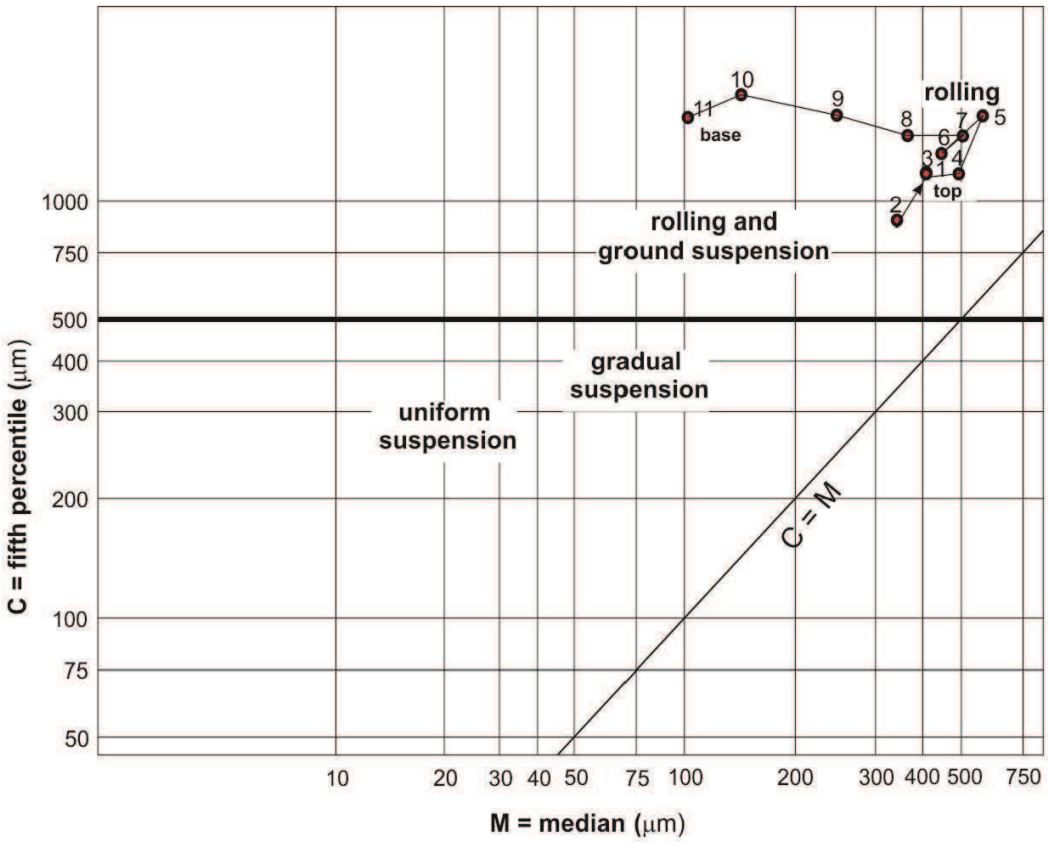
rolling
base
top
rolling and
ground suspension
gradual
suspension
uniform
suspension
C = M
C = fifth percentile (μm)
M = median (μm)
1000
750
500
400
300
200
100
75
50
10
20
30
40
50
75
100
200
300
400
500
750

Analyse granulométrique par voie fluide : fraction 0,040 µm - 2000 µm

Echantillon :	INDONESIE/12/KARANG RANJANG//U-07/T.YAN W.ISKANDARSYAH
Date :	04/03/2013 14:18
Opérateur :	MT
Fichier :	U07-001

Commentaires :	prof. 0 cm destruction MO à H2O2 - élimination des ions floculants - hexa +US

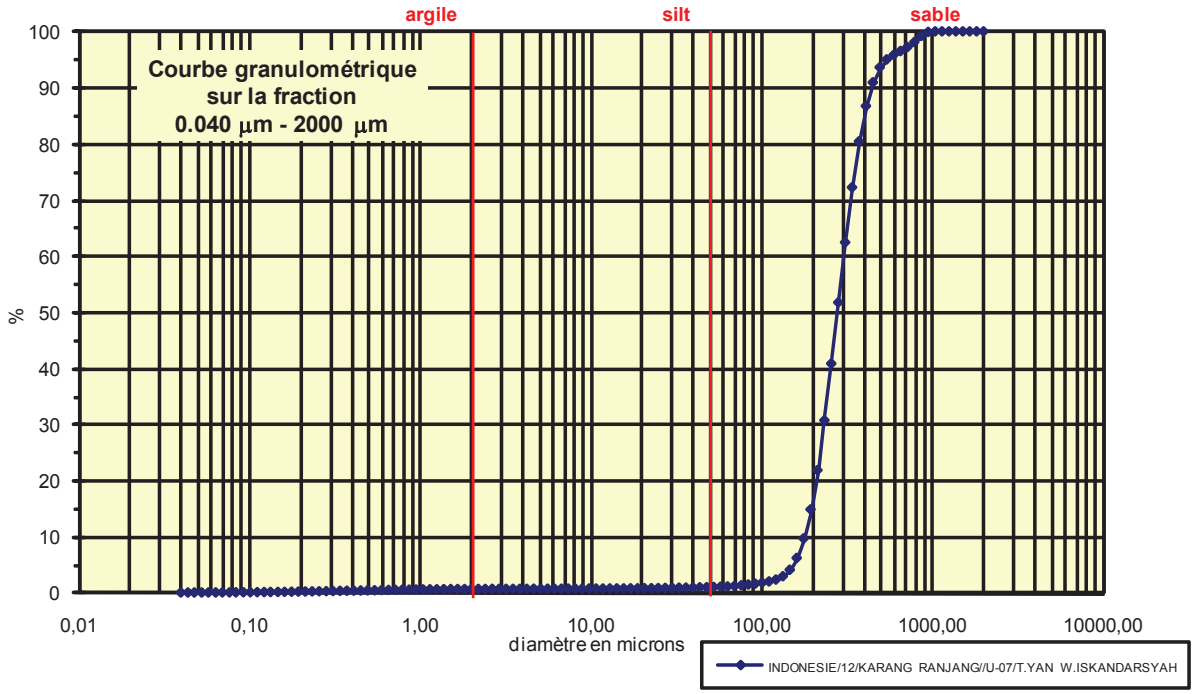

Fractiles	Taille (µm)	Taille (ϕ)
d_5	146,800	2,77
d_{10}	176,800	2,50
d_{16}	194,200	2,36
d_{25}	213,200	2,23
d_{30}	213,200	2,23
d_{50}	256,800	1,96
d_{60}	282,100	1,83
d_{75}	339,800	1,56
d_{84}	373,100	1,42
d_{90}	409,600	1,29
d_{95}	541,900	0,88

% Argile inférieur à 2µ	**A**	**0,61**
% Silts de 2µ à 50µ	**LT**	**0,34**
limons fins 2µ à 20µ	LF	0,14
limons grossiers 20µ à 50µ	LG	0,20
% Sables 50µ à 2000 µ	**ST**	**99,05**
sables fins 50µ à 200µ	SF	13,85
sables fins 50µ à 100µ	SF1	0,63
sables fins 100µ à 200 µ	SF2	13,22
sables grossiers 200µ à 2000µ	SG	85,20
sables grossiers 200µ à 500µ	SG1	78,80
sables grossiers 500µ à 1000µ	SG2	6,30
sables grossiers 1000µ à 2000µ	SG3	0,10

Indice de classement	
Trask, S_o	1,262
Krumbein, Q_d	-0,336
Inman, σ_ϕ	-0,471
Folk & Ward, σ_ϕ	-0,521
Hazen, C_u	1,596

Moyenne	
Trask, M	276,500
Inman, M_ϕ	1,893
Folk & Ward, M_z	1,916

Coefficient de dissymétrie	
Skew ness, S_{k-1}	1,099
Skew ness, S_{k-2}	1,048
Inman, $\alpha_{\phi-1}$	0,144
Inman, $\alpha_{\phi-2}$	0,287
Folk & Ward, Sk_i	0,144

Coefficient d'acuité (Kurtosis)	
Krumbein & Petijohn, K	0,272
Inman, K_ϕ	1,000
Folk & Ward, K_G	1,148

Coefficient de courbure	
C_c	0,911

Analyse granulométrique par voie fluide : fraction 0,040 µm - 2000 µm

Echantillon :	INDONESIE/12/KARANG RANJANG//U-07/T.YAN W.ISKANDARSYAH
Date :	04/03/2013 14:31
Opérateur :	MT
Fichier :	U07-002

Commentaires :	prof. 0 cm 24/05/12 Sand dune destruction MO à H2O2 - élimination des ions floculants - hexa +US

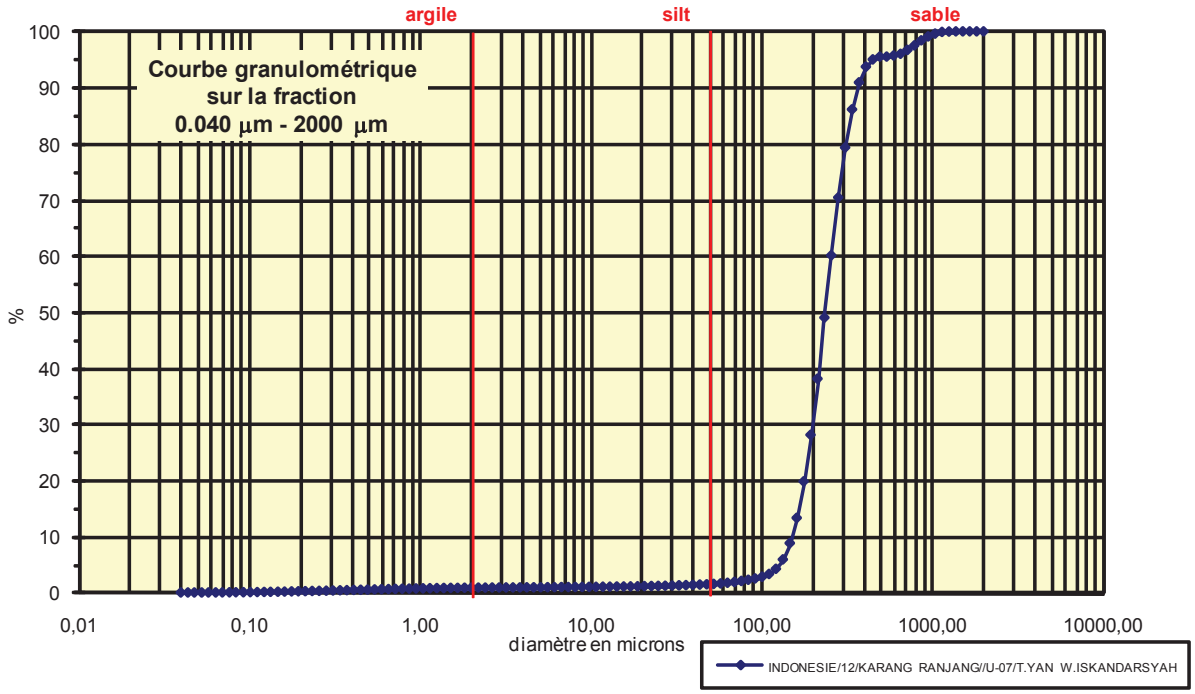

Fractiles	Taille (µm)	Taille (ϕ)
d_5	121,800	3,04
d_{10}	146,800	2,77
d_{16}	161,200	2,63
d_{25}	176,800	2,50
d_{30}	194,200	2,36
d_{50}	234,100	2,09
d_{60}	234,100	2,09
d_{75}	282,100	1,83
d_{84}	309,600	1,69
d_{90}	339,800	1,56
d_{95}	449,700	1,15

% Argile inférieur à 2µ	**A**	**0,85**
% Silts de 2µ à 50µ	**LT**	**0,61**
limons fins 2µ à 20µ	LF	0,26
limons grossiers 20µ à 50µ	LG	0,35
% Sables 50µ à 2000 µ	**ST**	**98,54**
sables fins 50µ à 200µ	SF	26,64
sables fins 50µ à 100µ	SF1	1,04
sables fins 100µ à 200 µ	SF2	25,60
sables grossiers 200µ à 2000µ	SG	71,90
sables grossiers 200µ à 500µ	SG1	67,40
sables grossiers 500µ à 1000µ	SG2	3,60
sables grossiers 1000µ à 2000µ	SG3	0,90

Indice de classement	
Trask, S_o	1,263
Krumbein, Q_d	-0,337
Inman, σ_ϕ	-0,471
Folk & Ward, σ_ϕ	-0,521
Hazen, C_u	1,595

Moyenne	
Trask, M	229,450
Inman, M_ϕ	2,162
Folk & Ward, M_z	2,140

Coefficient de dissymétrie	
Skew ness, S_{k-1}	0,910
Skew ness, S_{k-2}	0,954
Inman, $\alpha_{\phi-1}$	-0,143
Inman, $\alpha_{\phi-2}$	-0,001
Folk & Ward, Sk_I	-0,072

Coefficient d'acuité (Kurtosis)	
Krumbein & Petijohn, K	0,273
Inman, K_ϕ	1,001
Folk & Ward, K_G	1,146

Coefficient de courbure	
C_c	1,097

Analyse granulométrique par voie fluide : fraction 0,040 µm - 2000 µm

Echantillon :	INDONESIE/11/TANJUNG/ALANG-ALANG/U09/0/T.Yan W. ISKANDARSYAH
Date :	24/01/2012 14:09
Opérateur :	MT
Fichier :	U09-001

Commentaires :	prof. : 0 cm Destruction MO à H2O2 -élimination des ions floculants - hexa + US

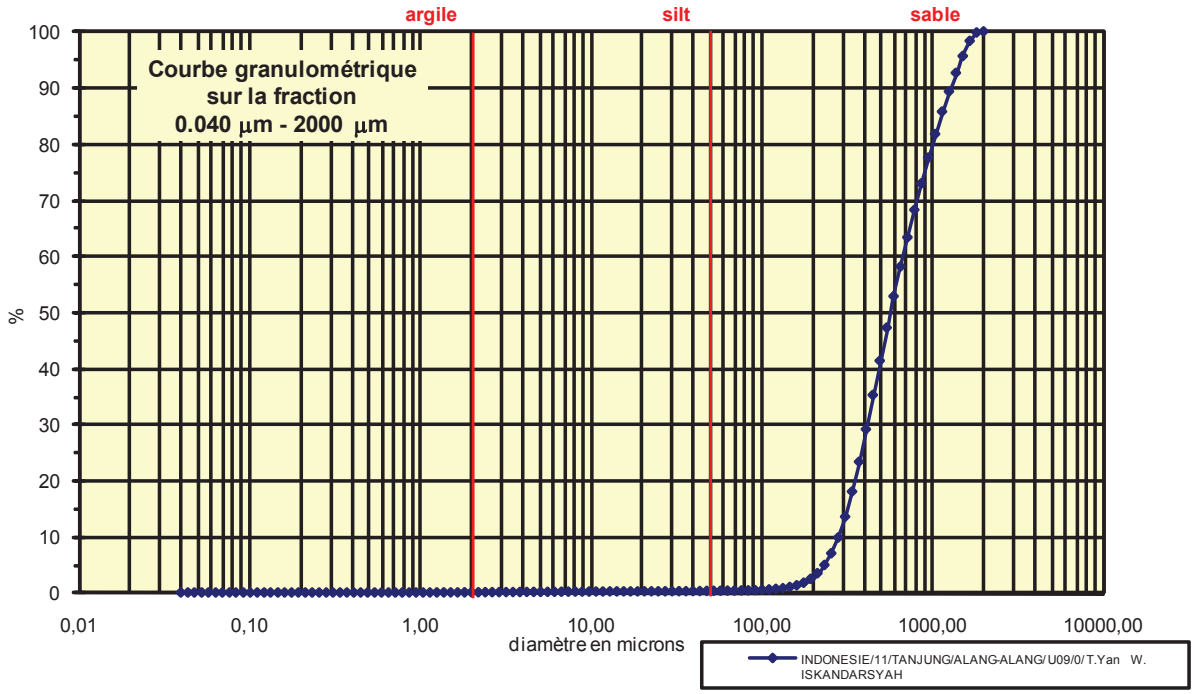

Fractiles	Taille (µm)	Taille (ϕ)
d_5	234,100	2,09
d_{10}	282,100	1,83
d_{16}	309,600	1,69
d_{25}	373,100	1,42
d_{30}	409,600	1,29
d_{50}	541,900	0,88
d_{60}	653,000	0,61
d_{75}	863,900	0,21
d_{84}	1041,000	-0,06
d_{90}	1255,000	-0,33
d_{95}	1377,000	-0,46

% Argile inférieur à 2µ	**A**	**0,03**
% Silts de 2µ à 50µ	**LT**	**0,25**
limons fins 2µ à 20µ	LF	0,17
limons grossiers 20µ à 50µ	LG	0,08
% Sables 50µ à 2000 µ	**ST**	**99,72**
sables fins 50µ à 200µ	SF	2,15
sables fins 50µ à 100µ	SF1	0,14
sables fins 100µ à 200 µ	SF2	2,01
sables grossiers 200µ à 2000µ	SG	97,57
sables grossiers 200µ à 500µ	SG1	38,87
sables grossiers 500µ à 1000µ	SG2	36,20
sables grossiers 1000µ à 2000µ	SG3	22,50

Indice de classement	
Trask, S_o	1,522
Krumbein, Q_d	-0,606
Inman, σ_ϕ	-0,875
Folk & Ward, σ_ϕ	-0,825
Hazen, C_u	2,315

Moyenne	
Trask, M	618,500
Inman, M_ϕ	0,817
Folk & Ward, M_z	0,839

Coefficient de dissymétrie	
Skew ness, S_{k-1}	1,098
Skew ness, S_{k-2}	1,048
Inman, $\alpha_{\phi-1}$	0,077
Inman, $\alpha_{\phi-2}$	0,077
Folk & Ward, Sk_I	0,065

Coefficient d'acuité (Kurtosis)	
Krumbein & Petijohn, K	0,252
Inman, K_ϕ	0,461
Folk & Ward, K_G	0,865

Coefficient de courbure	
C_c	0,911

Analyse granulométrique par voie fluide : fraction 0,040 µm - 2000 µm

Echantillon :	INDONESIE/12/CIGENTER/U-10/001/T.YAN W.ISKANDARSYAH
Date :	23/10/2013 10:21
Opérateur :	MT
Fichier :	U10-001

Commentaires :	prof.100-120 cm 27/05/12 Destruction MO à H2O2-élimination des ions floculants - Hexa+US

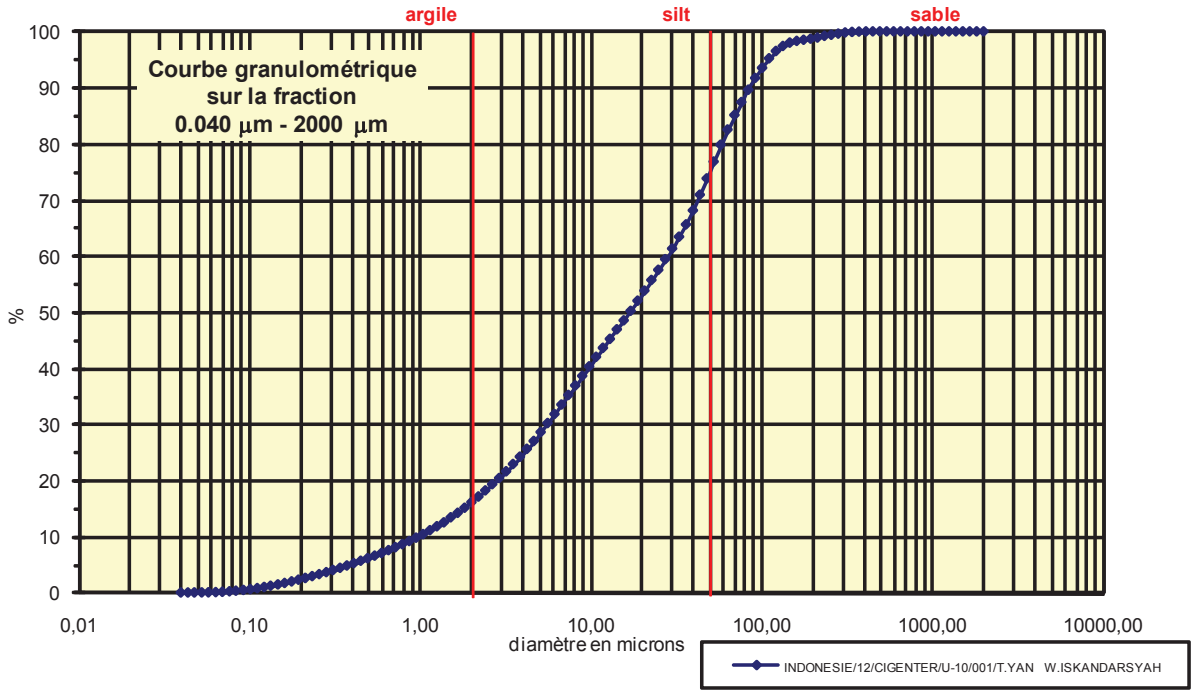

Fractiles	Taille (µm)	Taille (ϕ)
d_5	0,375	11,38
d_{10}	0,953	10,04
d_{16}	1,832	9,09
d_{25}	3,862	8,02
d_{30}	5,111	7,61
d_{50}	15,650	6,00
d_{60}	27,380	5,19
d_{75}	47,930	4,38
d_{84}	63,410	3,98
d_{90}	83,900	3,58
d_{95}	101,100	3,31

% Argile inférieur à 2µ	**A**	**15,10**
% Silts de 2µ à 50µ	**LT**	**58,70**
limons fins 2µ à 20µ	LF	36,90
limons grossiers 20µ à 50µ	LG	21,80
% Sables 50µ à 2000 µ	**ST**	**26,20**
sables fins 50µ à 200µ	SF	24,90
sables fins 50µ à 100µ	SF1	17,90
sables fins 100µ à 200 µ	SF2	7,00
sables grossiers 200µ à 2000µ	SG	1,30
sables grossiers 200µ à 500µ	SG1	1,30
sables grossiers 500µ à 1000µ	SG2	0,00
sables grossiers 1000µ à 2000µ	SG3	0,00

Indice de classement	
Trask, S_o	3,523
Krumbein, Q_d	-1,817
Inman, σ_ϕ	-2,557
Folk & Ward, σ_ϕ	-2,502
Hazen, C_u	28,730

Moyenne	
Trask, M	25,896
Inman, M_ϕ	6,536
Folk & Ward, M_z	6,356

Coefficient de dissymétrie	
Skew ness, S_{k-1}	0,756
Skew ness, S_{k-2}	0,869
Inman, $\alpha_{\phi-1}$	-0,210
Inman, $\alpha_{\phi-2}$	-0,526
Folk & Ward, Sk_i	-0,272

Coefficient d'acuité (Kurtosis)	
Krumbein & Petijohn, K	0,266
Inman, K_ϕ	0,579
Folk & Ward, K_G	0,911

Coefficient de courbure	
C_c	1,001

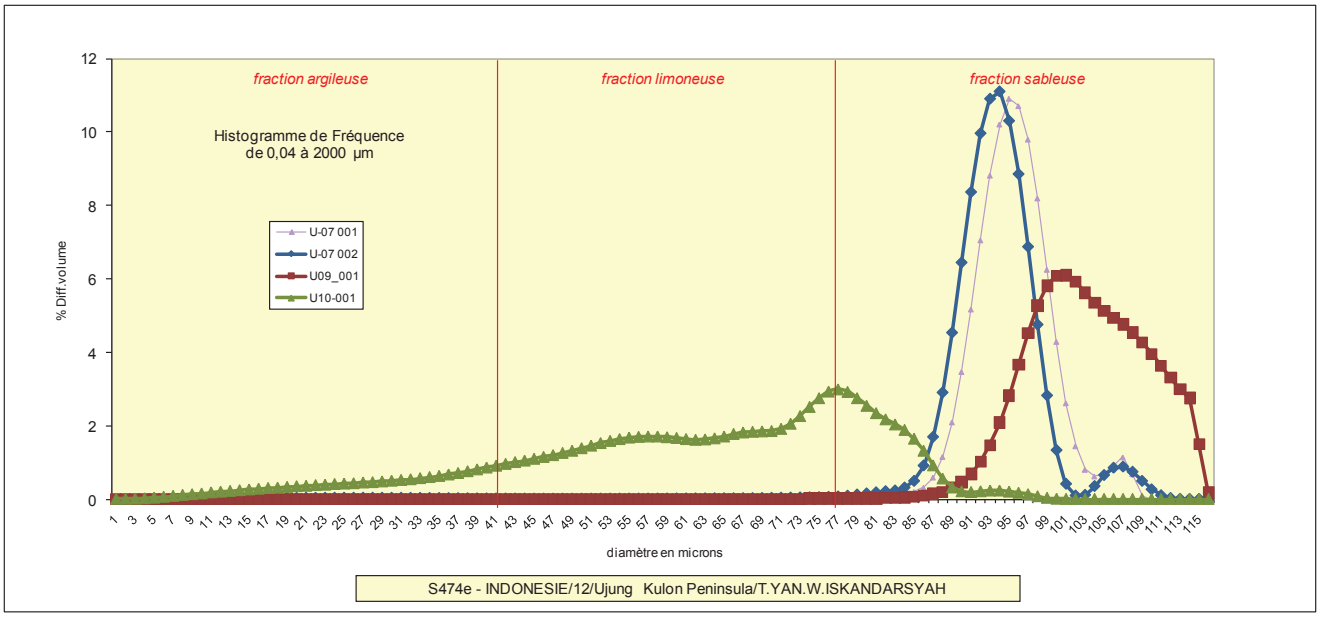
fraction argileuse
fraction limoneuse
fraction sableuse
Histogramme de Fréquence
de 0,04 à 2000 µm
U-07 001
U-07 002
U09_001
U10-001
% Diff volume
diamètre en microns
S474e - INDONESIE/12/Ujung Kulon Peninsula/T.YAN.W.ISKANDARSYAH

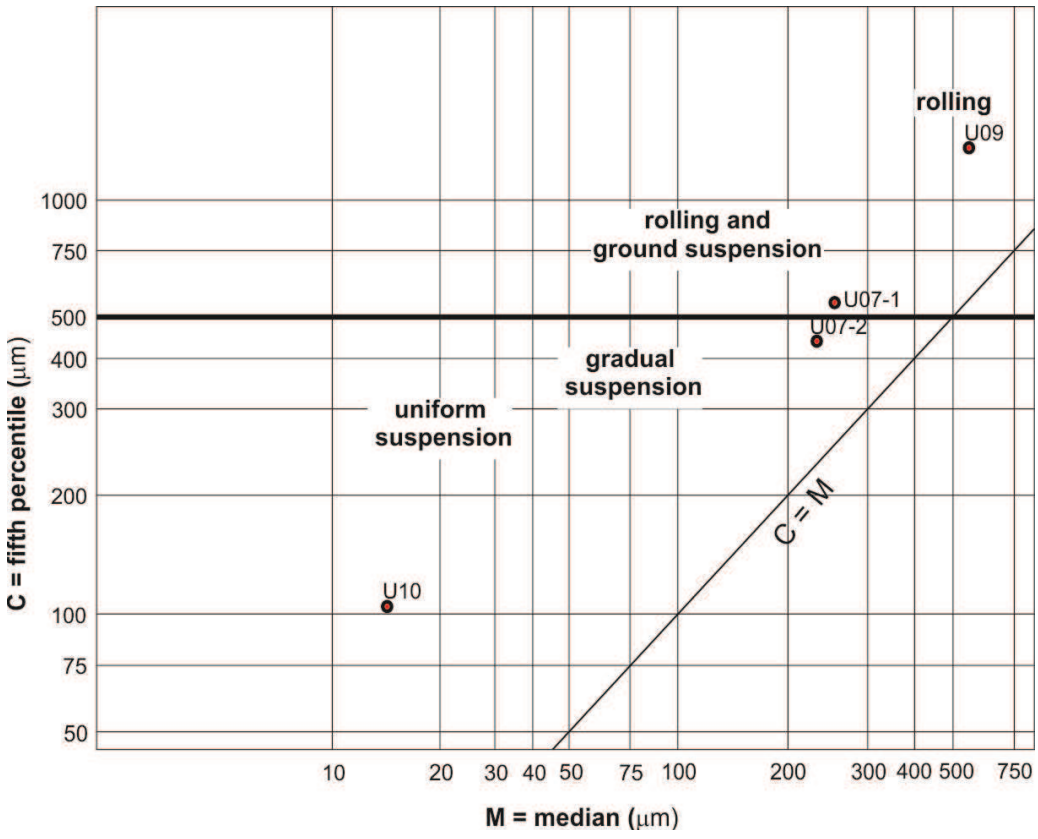
rolling
U09
rolling and
ground suspension
U07-1
U07-2
gradual
suspension
uniform
suspension
C = M
U10
1000
750
500
400
300
200
100
75
50
C = fifth percentile (μm)
10
20
30
40
50
75
100
200
300
400
500
750
M = median (μm)

Analyse granulométrique par voie fluide : fraction 0,040 µm - 2000 µm

Echantillon :	INDONESIE/11/Tamanjaya/U13/Tuff Pasir/70-100/T.Yan W. ISKANDARSYAH
Date :	24/07/2013 15:03
Opérateur :	MT
Fichier :	U13-001

Commentaires :	0 Destruction MO à H2O2 - élimination des ions floculants - hexa+us

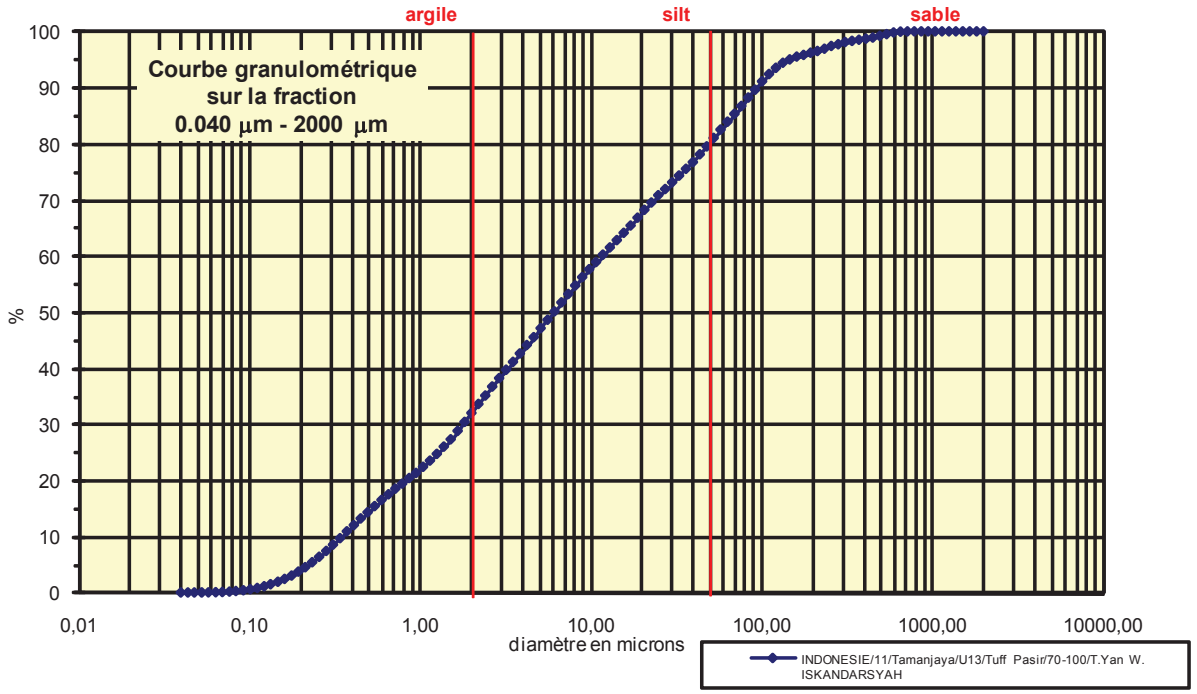

Fractiles	Taille (µm)	Taille (ϕ)
d_5	0,214	12,19
d_{10}	0,342	11,51
d_{16}	0,545	10,84
d_{25}	1,261	9,63
d_{30}	1,669	9,23
d_{50}	5,611	7,48
d_{60}	10,780	6,54
d_{75}	33,000	4,92
d_{84}	63,410	3,98
d_{90}	92,090	3,44
d_{95}	146,800	2,77

% Argile inférieur à 2µ	**A**	**30,40**
% Silts de 2µ à 50µ	**LT**	**49,10**
limons fins 2µ à 20µ	LF	36,40
limons grossiers 20µ à 50µ	LG	12,70
% Sables 50µ à 2000 µ	**ST**	**20,50**
sables fins 50µ à 200µ	SF	16,70
sables fins 50µ à 100µ	SF1	10,10
sables fins 100µ à 200 µ	SF2	6,60
sables grossiers 200µ à 2000µ	SG	3,80
sables grossiers 200µ à 500µ	SG1	3,00
sables grossiers 500µ à 1000µ	SG2	0,80
sables grossiers 1000µ à 2000µ	SG3	0,00

Indice de classement	
Trask, S_o	5,116
Krumbein, Q_d	-2,355
Inman, σ_ϕ	-3,431
Folk & Ward, σ_ϕ	-3,143
Hazen, C_u	31,520

Moyenne	
Trask, M	17,131
Inman, M_ϕ	7,410
Folk & Ward, M_z	7,433

Coefficient de dissymétrie	
Skew ness, S_{k-1}	1,322
Skew ness, S_{k-2}	1,150
Inman, $\alpha_{\phi-1}$	0,020
Inman, $\alpha_{\phi-2}$	0,000
Folk & Ward, Sk_i	0,010

Coefficient d'acuité (Kurtosis)	
Krumbein & Petijohn, K	0,173
Inman, K_ϕ	0,373
Folk & Ward, K_G	0,820

Coefficient de courbure	
C_c	0,756

Analyse granulométrique par voie fluide : fraction 0,040 µm - 2000 µm

Echantillon :	INDONESIE/11/Tamanjaya/U13/Pasir Lempung/170-200/T.Yan W. ISKANDARSYAH
Date :	24/07/2013 15:16
Opérateur :	MT
Fichier :	U13-002

Commentaires :	0 Destruction MO à H2O2 - élimination des ions floculants - hexa+us

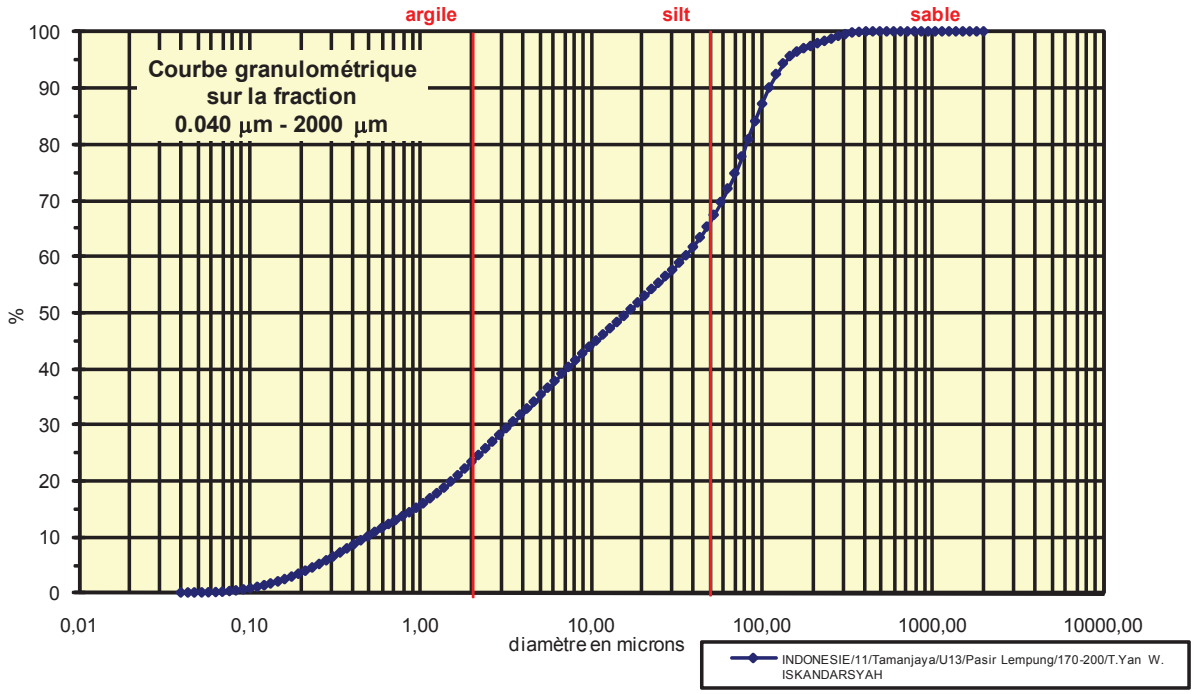

Fractiles	Taille (µm)	Taille (ϕ)
d_5	0,235	12,06
d_{10}	0,496	10,98
d_{16}	1,047	9,90
d_{25}	2,207	8,82
d_{30}	3,206	8,29
d_{50}	15,650	6,00
d_{60}	33,000	4,92
d_{75}	69,620	3,84
d_{84}	92,090	3,44
d_{90}	111,000	3,17
d_{95}	133,700	2,90

% Argile inférieur à 2µ	**A**	**22,10**
% Silts de 2µ à 50µ	**LT**	**43,10**
limons fins 2µ à 20µ	LF	29,60
limons grossiers 20µ à 50µ	LG	13,50
% Sables 50µ à 2000 µ	**ST**	**34,80**
sables fins 50µ à 200µ	SF	32,20
sables fins 50µ à 100µ	SF1	18,80
sables fins 100µ à 200 µ	SF2	13,40
sables grossiers 200µ à 2000µ	SG	2,60
sables grossiers 200µ à 500µ	SG1	2,60
sables grossiers 500µ à 1000µ	SG2	0,00
sables grossiers 1000µ à 2000µ	SG3	0,00

Indice de classement	
Trask, S_o	5,617
Krumbein, Q_d	-2,490
Inman, σ_ϕ	-3,229
Folk & Ward, σ_ϕ	-3,001
Hazen, C_u	66,532

Moyenne	
Trask, M	35,914
Inman, M_ϕ	6,670
Folk & Ward, M_z	6,446

Coefficient de dissymétrie	
Skew ness, S_{k-1}	0,627
Skew ness, S_{k-2}	0,792
Inman, $\alpha_{\phi-1}$	-0,208
Inman, $\alpha_{\phi-2}$	-0,459
Folk & Ward, Sk_I	-0,266

Coefficient d'acuité (Kurtosis)	
Krumbein & Petijohn, K	0,305
Inman, K_ϕ	0,417
Folk & Ward, K_G	0,753

Coefficient de courbure	
C_c	0,628

Analyse granulométrique par voie fluide : fraction 0,040 µm - 2000 µm

Echantillon :	INDONESIE/11/Tamanjaya/U13/Pantai/0/T.Yan W. ISKANDARSYAH
Date :	24/07/2013 14:55
Opérateur :	MT
Fichier :	U13-003

Commentaires :	0 Destruction MO à H2O2 - élimination des ions floculants - hexa+us

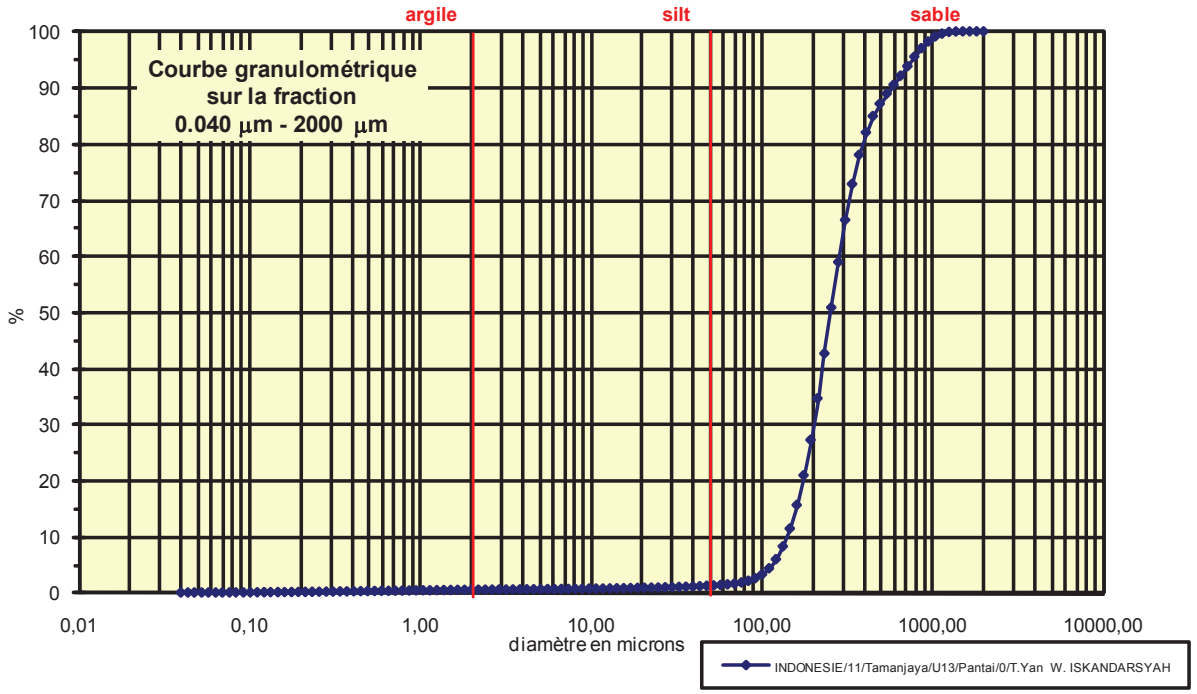

Fractiles	Taille (µm)	Taille (ϕ)
d_5	111,000	3,17
d_{10}	133,700	2,90
d_{16}	161,200	2,63
d_{25}	176,800	2,50
d_{30}	194,200	2,36
d_{50}	234,100	2,09
d_{60}	282,100	1,83
d_{75}	339,800	1,56
d_{84}	409,600	1,29
d_{90}	541,900	0,88
d_{95}	716,900	0,48

% Argile inférieur à 2µ	**A**	**0,47**
% Silts de 2µ à 50µ	**LT**	**0,72**
limons fins 2µ à 20µ	LF	0,35
limons grossiers 20µ à 50µ	LG	0,37
% Sables 50µ à 2000 µ	**ST**	**98,81**
sables fins 50µ à 200µ	SF	26,01
sables fins 50µ à 100µ	SF1	1,35
sables fins 100µ à 200 µ	SF2	24,66
sables grossiers 200µ à 2000µ	SG	72,80
sables grossiers 200µ à 500µ	SG1	59,90
sables grossiers 500µ à 1000µ	SG2	11,10
sables grossiers 1000µ à 2000µ	SG3	1,80

Indice de classement	
Trask, S_o	1,386
Krumbein, Q_d	-0,471
Inman, σ_ϕ	-0,673
Folk & Ward, σ_ϕ	-0,744
Hazen, C_u	2,110

Moyenne	
Trask, M	258,300
Inman, M_ϕ	1,960
Folk & Ward, M_z	2,005

Coefficient de dissymétrie	
Skew ness, S_{k-1}	1,096
Skew ness, S_{k-2}	1,047
Inman, $\alpha_{\phi-1}$	0,200
Inman, $\alpha_{\phi-2}$	0,400
Folk & Ward, Sk_I	0,200

Coefficient d'acuité (Kurtosis)	
Krumbein & Petijohn, K	0,200
Inman, K_ϕ	1,000
Folk & Ward, K_G	1,170

Coefficient de courbure	
C_c	1,000

Analyse granulométrique par voie fluide : fraction 0,040 µm - 2000 µm

Echantillon :	INDONESIE/11/Sumur/U17/0-3/T.Yan W. ISKANDARSYAH
Date :	24/07/2013 12:11
Opérateur :	MT
Fichier :	U17-001

Commentaires :	0 Destruction MO à H2O2 - élimination des ions floculants - hexa+us

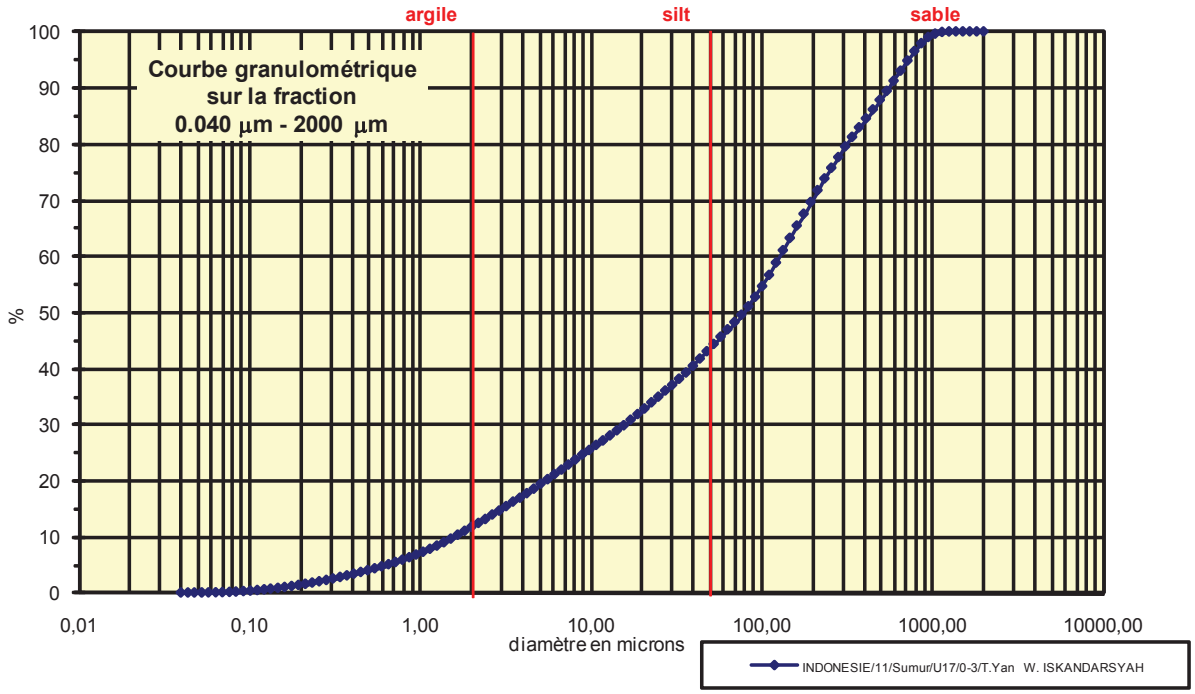

Fractiles	Taille (µm)	Taille (ϕ)
d_5	0,598	10,71
d_{10}	1,520	9,36
d_{16}	3,206	8,29
d_{25}	8,944	6,80
d_{30}	15,650	6,00
d_{50}	76,430	3,71
d_{60}	121,800	3,04
d_{75}	234,100	2,09
d_{84}	373,100	1,42
d_{90}	541,900	0,88
d_{95}	716,900	0,48

% Argile inférieur à 2µ	**A**	**11,00**
% Silts de 2µ à 50µ	**LT**	**32,00**
limons fins 2µ à 20µ	LF	20,80
limons grossiers 20µ à 50µ	LG	11,20
% Sables 50µ à 2000 µ	**ST**	**57,00**
sables fins 50µ à 200µ	SF	26,60
sables fins 50µ à 100µ	SF1	9,70
sables fins 100µ à 200 µ	SF2	16,90
sables grossiers 200µ à 2000µ	SG	30,40
sables grossiers 200µ à 500µ	SG1	18,20
sables grossiers 500µ à 1000µ	SG2	11,20
sables grossiers 1000µ à 2000µ	SG3	1,00

Indice de classement	
Trask, S_o	5,116
Krumbein, Q_d	-2,355
Inman, σ_ϕ	-3,431
Folk & Ward, σ_ϕ	-3,265
Hazen, C_u	80,132

Moyenne	
Trask, M	121,522
Inman, M_ϕ	4,854
Folk & Ward, M_z	4,472

Coefficient de dissymétrie	
Skew ness, S_{k-1}	0,358
Skew ness, S_{k-2}	0,599
Inman, $\alpha_{\phi-1}$	-0,333
Inman, $\alpha_{\phi-2}$	-0,549
Folk & Ward, Sk_i	-0,351

Coefficient d'acuité (Kurtosis)	
Krumbein & Petijohn, K	0,208
Inman, K_ϕ	0,490
Folk & Ward, K_G	0,890

Coefficient de courbure	
C_c	1,323

Analyse granulométrique par voie fluide : fraction 0,040 µm - 2000 µm

Echantillon :	INDONESIE/11/Sumur/U17/10-20/T.Yan W. ISKANDARSYAH
Date :	24/07/2013 14:38
Opérateur :	MT
Fichier :	U17-002

Commentaires :	0 Destruction MO à H2O2 - élimination des ions floculants - hexa+us

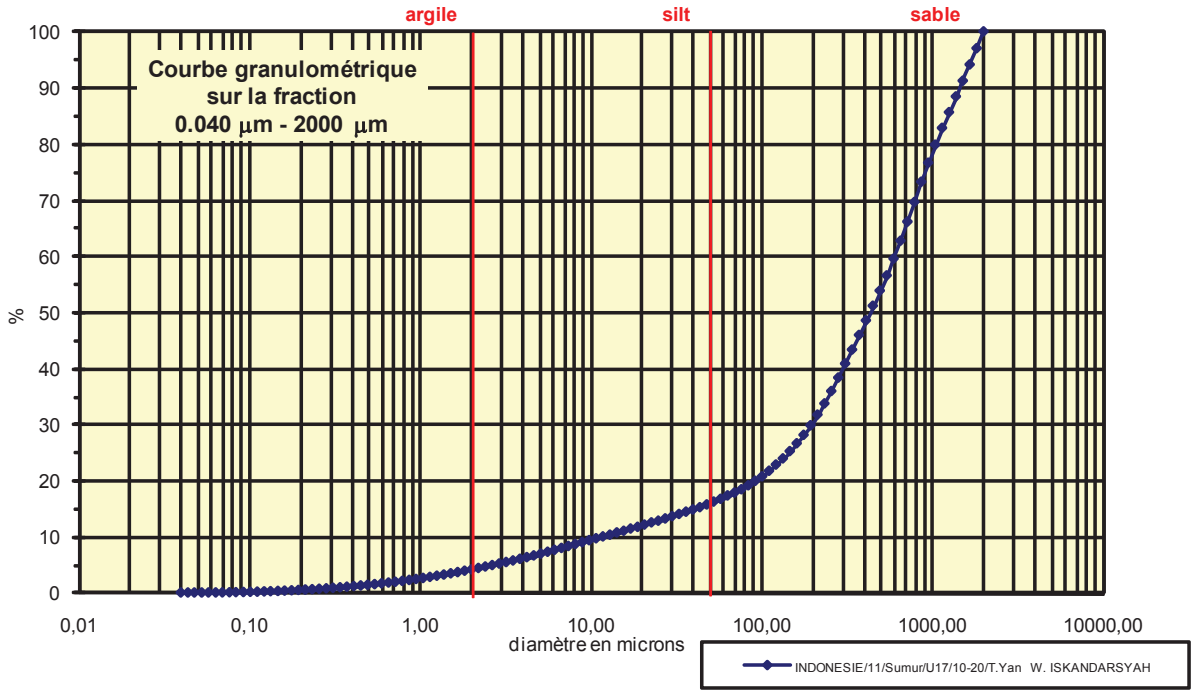

Fractiles	Taille (µm)	Taille (ϕ)
d_5	2,660	8,55
d_{10}	11,830	6,40
d_{16}	47,930	4,38
d_{25}	133,700	2,90
d_{30}	194,200	2,36
d_{50}	409,600	1,29
d_{60}	594,900	0,75
d_{75}	863,900	0,21
d_{84}	1143,000	-0,19
d_{90}	1377,000	-0,46
d_{95}	1660,000	-0,73

% Argile inférieur à 2µ	**A**	**3,88**
% Silts de 2µ à 50µ	**LT**	**11,82**
limons fins 2µ à 20µ	LF	7,82
limons grossiers 20µ à 50µ	LG	4,00
% Sables 50µ à 2000 µ	**ST**	**84,30**
sables fins 50µ à 200µ	SF	14,10
sables fins 50µ à 100µ	SF1	4,20
sables fins 100µ à 200 µ	SF2	9,90
sables grossiers 200µ à 2000µ	SG	70,20
sables grossiers 200µ à 500µ	SG1	24,00
sables grossiers 500µ à 1000µ	SG2	22,80
sables grossiers 1000µ à 2000µ	SG3	23,40

Indice de classement	
Trask, S_o	2,542
Krumbein, Q_d	-1,346
Inman, σ_ϕ	-2,288
Folk & Ward, σ_ϕ	-2,551
Hazen, C_u	50,287

Moyenne	
Trask, M	498,800
Inman, M_ϕ	2,095
Folk & Ward, M_z	1,826

Coefficient de dissymétrie	
Skew ness, S_{k-1}	0,688
Skew ness, S_{k-2}	0,830
Inman, $\alpha_{\phi-1}$	-0,353
Inman, $\alpha_{\phi-2}$	-1,147
Folk & Ward, Sk_I	-0,459

Coefficient d'acuité (Kurtosis)	
Krumbein & Petijohn, K	0,267
Inman, K_ϕ	1,029
Folk & Ward, K_G	1,414

Coefficient de courbure	
C_c	5,359

Analyse granulométrique par voie fluide : fraction 0,040 µm - 2000 µm

Echantillon :	INDONESIE/11/Sumur/U17/20-30/T.Yan W. ISKANDARSYAH
Date :	24/07/2013 14:47
Opérateur :	MT
Fichier :	U17-003

Commentaires :	0 Destruction MO à H2O2 - élimination des ions floculants - hexa+us

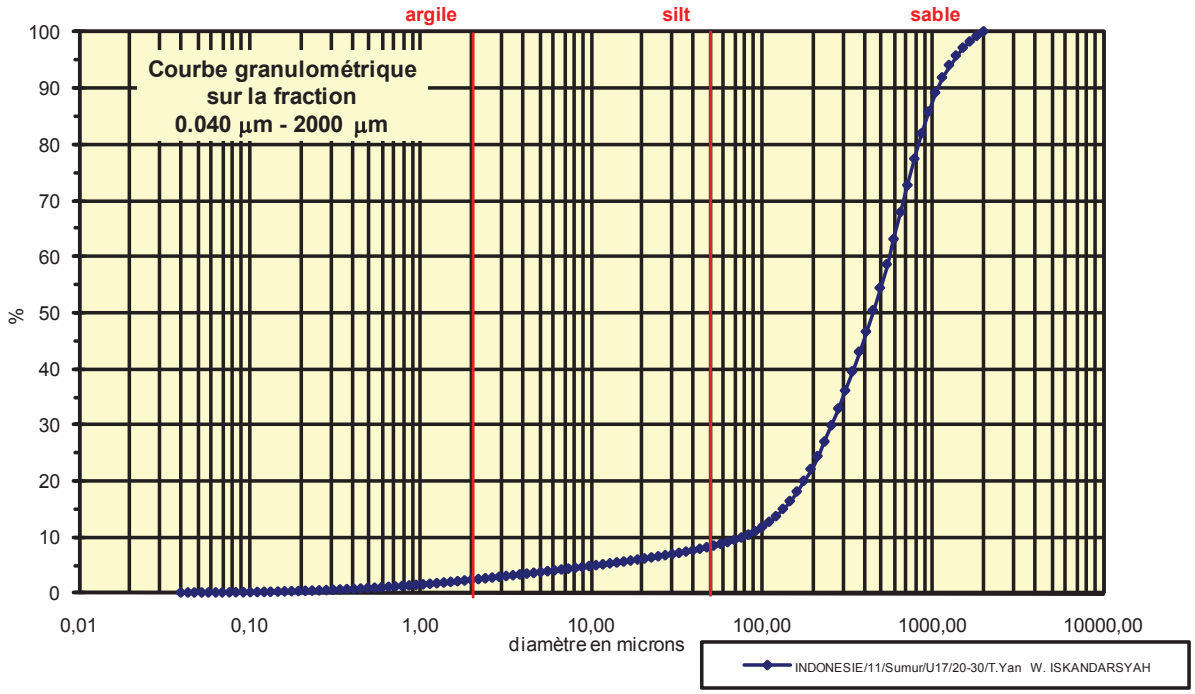

Fractiles	Taille (µm)	Taille (ϕ)
d_5	10,780	6,54
d_{10}	76,430	3,71
d_{16}	133,700	2,90
d_{25}	213,200	2,23
d_{30}	256,800	1,96
d_{50}	409,600	1,29
d_{60}	541,900	0,88
d_{75}	716,900	0,48
d_{84}	863,900	0,21
d_{90}	1041,000	-0,06
d_{95}	1255,000	-0,33

% Argile inférieur à 2µ	**A**	**2,14**
% Silts de 2µ à 50µ	**LT**	**5,92**
limons fins 2µ à 20µ	LF	3,73
limons grossiers 20µ à 50µ	LG	2,19
% Sables 50µ à 2000 µ	**ST**	**91,94**
sables fins 50µ à 200µ	SF	13,94
sables fins 50µ à 100µ	SF1	2,84
sables fins 100µ à 200 µ	SF2	11,10
sables grossiers 200µ à 2000µ	SG	78,00
sables grossiers 200µ à 500µ	SG1	32,30
sables grossiers 500µ à 1000µ	SG2	31,40
sables grossiers 1000µ à 2000µ	SG3	14,30

Indice de classement	
Trask, S_o	1,834
Krumbein, Q_d	-0,875
Inman, σ_ϕ	-1,346
Folk & Ward, σ_ϕ	-1,713
Hazen, C_u	7,090

Moyenne	
Trask, M	465,050
Inman, M_ϕ	1,557
Folk & Ward, M_z	1,467

Coefficient de dissymétrie	
Skew ness, S_{k-1}	0,911
Skew ness, S_{k-2}	0,954
Inman, $\alpha_{\phi-1}$	-0,200
Inman, $\alpha_{\phi-2}$	-1,349
Folk & Ward, Sk_i	-0,365

Coefficient d'acuité (Kurtosis)	
Krumbein & Petijohn, K	0,261
Inman, K_ϕ	1,550
Folk & Ward, K_G	1,608

Coefficient de courbure	
C_c	1,592

Analyse granulométrique par voie fluide : fraction 0,040 µm - 2000 µm

Echantillon :	INDONESIE/11/U17/30-40/T.Yan W. ISKANDARSYAH
Date :	24/01/2012 12:59
Opérateur :	MT
Fichier :	U17-004

Commentaires :	prof. : 30-40 cm Destruction MO à H2O2 -élimination des ions floculants - hexa + US

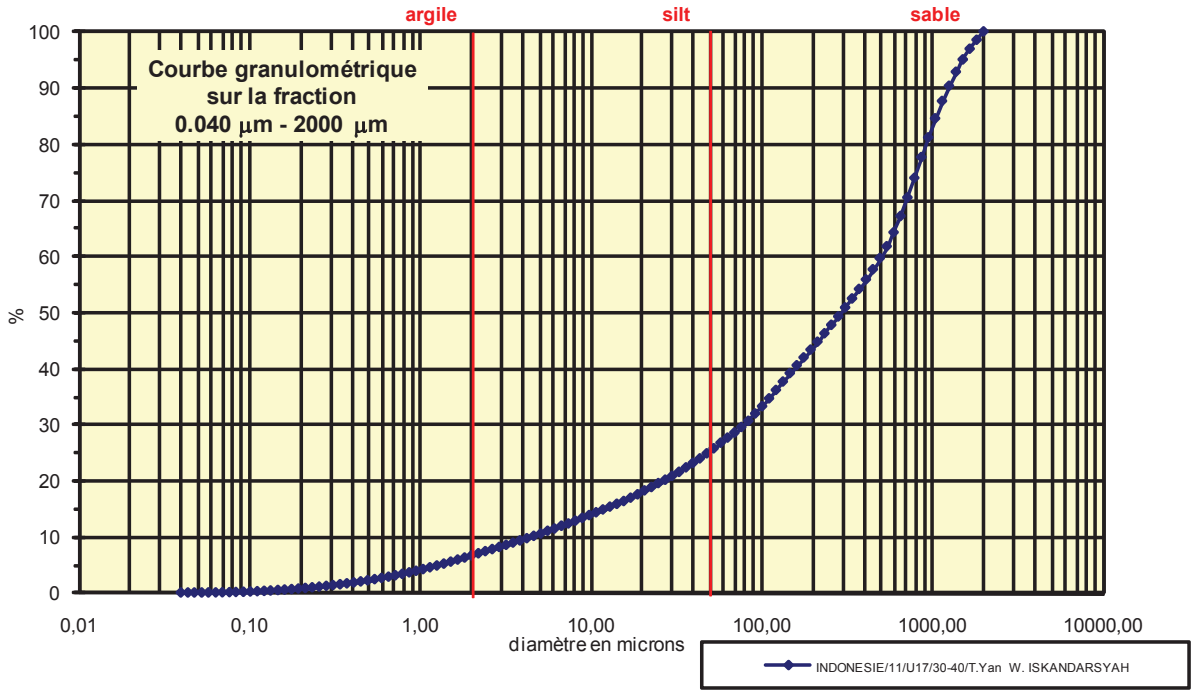

Fractiles	Taille (µm)	Taille (ϕ)
d_5	1,261	9,63
d_{10}	4,241	7,88
d_{16}	14,260	6,13
d_{25}	47,930	4,38
d_{30}	76,430	3,71
d_{50}	282,100	1,83
d_{60}	493,600	1,02
d_{75}	786,900	0,35
d_{84}	948,200	0,08
d_{90}	1143,000	-0,19
d_{95}	1512,000	-0,60

% Argile inférieur à 2µ	**A**	**6,23**
% Silts de 2µ à 50µ	**LT**	**18,57**
limons fins 2µ à 20µ	LF	11,27
limons grossiers 20µ à 50µ	LG	7,30
% Sables 50µ à 2000 µ	**ST**	**75,20**
sables fins 50µ à 200µ	SF	18,50
sables fins 50µ à 100µ	SF1	7,10
sables fins 100µ à 200 µ	SF2	11,40
sables grossiers 200µ à 2000µ	SG	56,70
sables grossiers 200µ à 500µ	SG1	16,30
sables grossiers 500µ à 1000µ	SG2	21,50
sables grossiers 1000µ à 2000µ	SG3	18,90

Indice de classement	
Trask, S_o	4,052
Krumbein, Q_d	-2,019
Inman, σ_ϕ	-3,028
Folk & Ward, σ_ϕ	-3,063
Hazen, C_u	116,388

Moyenne	
Trask, M	417,415
Inman, M_ϕ	3,104
Folk & Ward, M_z	2,678

Coefficient de dissymétrie	
Skew ness, S_{k1}	0,474
Skew ness, S_{k2}	0,688
Inman, $\alpha_{\phi-1}$	-0,422
Inman, $\alpha_{\phi-2}$	-0,889
Folk & Ward, Sk_I	-0,474

Coefficient d'acuité (Kurtosis)	
Krumbein & Petijohn, K	0,324
Inman, K_ϕ	0,689
Folk & Ward, K_G	1,038

Coefficient de courbure	
C_c	2,791

Analyse granulométrique par voie fluide : fraction 0,040 µm - 2000 µm

Echantillon :	INDONESIE/11/U17/45-55/T.Yan W. ISKANDARSYAH
Date :	24/01/2012 13:31
Opérateur :	MT
Fichier :	U17-005

Commentaires :	prof. : 45-55 cm Destruction MO à H2O2 -élimination des ions floculants - hexa + US

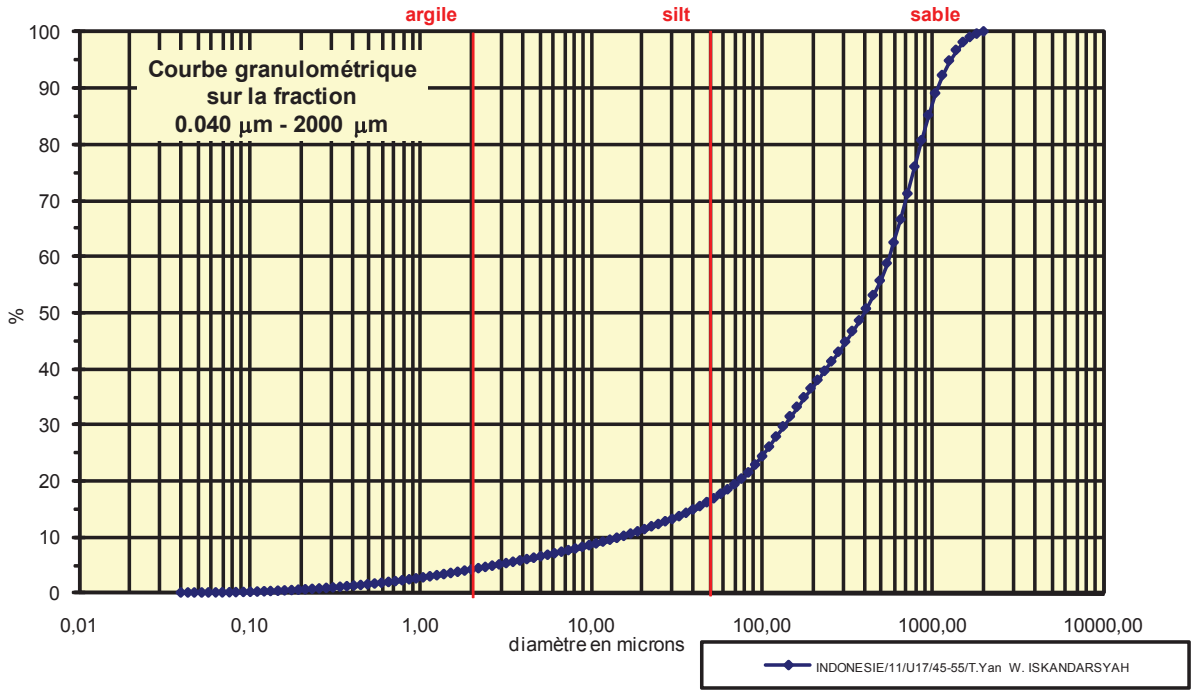

Fractiles	Taille (µm)	Taille (ϕ)
d_5	2,660	8,55
d_{10}	14,260	6,13
d_{16}	43,660	4,52
d_{25}	101,100	3,31
d_{30}	133,700	2,90
d_{50}	373,100	1,42
d_{60}	541,900	0,88
d_{75}	716,900	0,48
d_{84}	863,900	0,21
d_{90}	1041,000	-0,06
d_{95}	1255,000	-0,33

% Argile inférieur à 2µ	**A**	**3,90**
% Silts de 2µ à 50µ	**LT**	**12,20**
limons fins 2µ à 20µ	LF	7,00
limons grossiers 20µ à 50µ	LG	5,20
% Sables 50µ à 2000 µ	**ST**	**83,90**
sables fins 50µ à 200µ	SF	20,30
sables fins 50µ à 100µ	SF1	6,70
sables fins 100µ à 200 µ	SF2	13,60
sables grossiers 200µ à 2000µ	SG	63,60
sables grossiers 200µ à 500µ	SG1	19,20
sables grossiers 500µ à 1000µ	SG2	29,50
sables grossiers 1000µ à 2000µ	SG3	14,90

Indice de classement	
Trask, S_o	2,663
Krumbein, Q_d	-1,413
Inman, σ_ϕ	-2,153
Folk & Ward, σ_ϕ	-2,422
Hazen, C_u	38,001

Moyenne	
Trask, M	409,000
Inman, M_ϕ	2,364
Folk & Ward, M_z	2,050

Coefficient de dissymétrie	
Skew ness, S_{k-1}	0,521
Skew ness, S_{k-2}	0,722
Inman, $\alpha_{\phi-1}$	-0,437
Inman, $\alpha_{\phi-2}$	-1,250
Folk & Ward, Sk_i	-0,522

Coefficient d'acuité (Kurtosis)	
Krumbein & Petijohn, K	0,300
Inman, K_ϕ	1,062
Folk & Ward, K_G	1,288

Coefficient de courbure	
C_c	2,313

Analyse granulométrique par voie fluide : fraction 0,040 µm - 2000 µm

Echantillon :	INDONESIE/11/Sumur/U17/0/Pantai/T.Yan W. ISKANDARSYAH
Date :	24/07/2013 12:12
Opérateur :	MT
Fichier :	U17-006

Commentaires :	0 Destruction MO à H2O2 - élimination des ions floculants - hexa+us

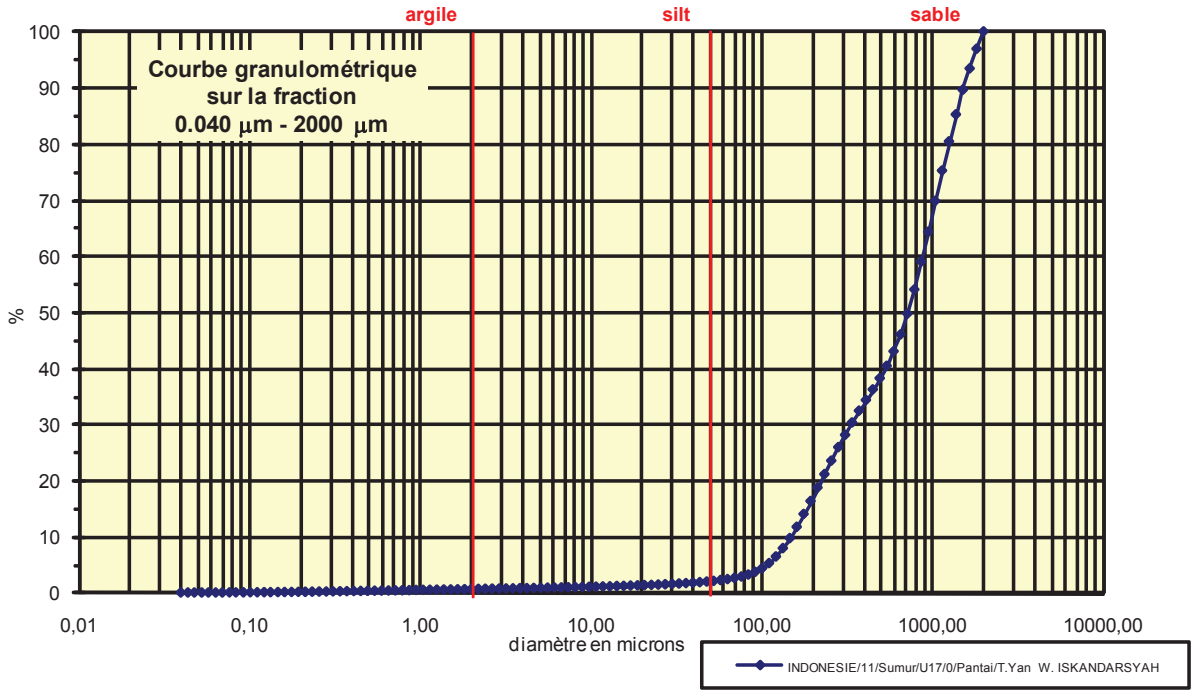

Fractiles	Taille (µm)	Taille (ϕ)
d_5	101,100	3,31
d_{10}	146,800	2,77
d_{16}	176,800	2,50
d_{25}	256,800	1,96
d_{30}	309,600	1,69
d_{50}	716,900	0,48
d_{60}	863,900	0,21
d_{75}	1041,000	-0,06
d_{84}	1255,000	-0,33
d_{90}	1512,000	-0,60
d_{95}	1660,000	-0,73

% Argile inférieur à 2µ	**A**	**0,59**
% Silts de 2µ à 50µ	**LT**	**1,36**
limons fins 2µ à 20µ	LF	0,68
limons grossiers 20µ à 50µ	LG	0,68
% Sables 50µ à 2000 µ	**ST**	**98,05**
sables fins 50µ à 200µ	SF	14,35
sables fins 50µ à 100µ	SF1	1,73
sables fins 100µ à 200 µ	SF2	12,62
sables grossiers 200µ à 2000µ	SG	83,70
sables grossiers 200µ à 500µ	SG1	21,90
sables grossiers 500µ à 1000µ	SG2	26,10
sables grossiers 1000µ à 2000µ	SG3	35,70

Indice de classement	
Trask, S_o	2,013
Krumbein, Q_d	-1,010
Inman, σ_ϕ	-1,414
Folk & Ward, σ_ϕ	-1,319
Hazen, C_u	5,885

Moyenne	
Trask, M	648,900
Inman, M_ϕ	1,086
Folk & Ward, M_z	0,884

Coefficient de dissymétrie	
Skew ness, S_{k1}	0,520
Skew ness, S_{k2}	0,721
Inman, $\alpha_{\phi-1}$	-0,429
Inman, $\alpha_{\phi-2}$	-0,571
Folk & Ward, Sk_i	-0,414

Coefficient d'acuité (Kurtosis)	
Krumbein & Petijohn, K	0,287
Inman, K_ϕ	0,428
Folk & Ward, K_G	0,819

Coefficient de courbure	
C_c	0,756

Analyse granulométrique par voie fluide : fraction 0,040 µm - 2000 µm

Echantillon :	INDONESIE/11/ATAS/U20/0-10/T.Yan W. ISKANDARSYAH
Date :	24/01/2012 12:17
Opérateur :	MT
Fichier :	U20-001

Commentaires :	prof. : 0-10 cm Destruction MO à H2O2 -élimination des ions floculants - hexa + US

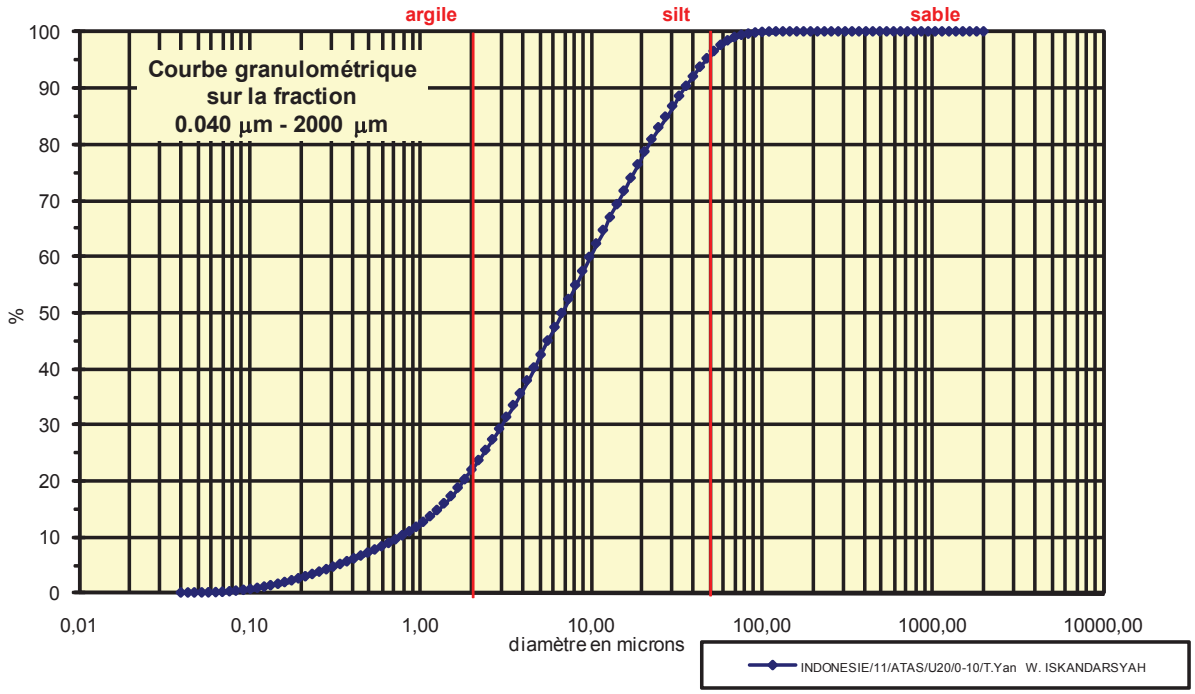

Fractiles	Taille (µm)	Taille (ϕ)
d_5	0,311	11,65
d_{10}	0,721	10,44
d_{16}	1,385	9,50
d_{25}	2,207	8,82
d_{30}	2,920	8,42
d_{50}	6,761	7,21
d_{60}	9,819	6,67
d_{75}	17,180	5,86
d_{84}	24,950	5,32
d_{90}	33,000	4,92
d_{95}	43,660	4,52

% Argile inférieur à 2µ	**A**	**20,20**
% Silts de 2µ à 50µ	**LT**	**75,00**
limons fins 2µ à 20µ	LF	56,10
limons grossiers 20µ à 50µ	LG	18,90
% Sables 50µ à 2000 µ	**ST**	**4,80**
sables fins 50µ à 200µ	SF	4,80
sables fins 50µ à 100µ	SF1	4,60
sables fins 100µ à 200 µ	SF2	0,20
sables grossiers 200µ à 2000µ	SG	0,00
sables grossiers 200µ à 500µ	SG1	0,00
sables grossiers 500µ à 1000µ	SG2	0,00
sables grossiers 1000µ à 2000µ	SG3	0,00

Indice de classement	
Trask, S_o	2,790
Krumbein, Q_d	-1,480
Inman, σ_ϕ	-2,086
Folk & Ward, σ_ϕ	-2,124
Hazen, C_u	13,619

Moyenne	
Trask, M	9,694
Inman, M_ϕ	7,410
Folk & Ward, M_z	7,343

Coefficient de dissymétrie	
Skew ness, S_{k-1}	0,829
Skew ness, S_{k-2}	0,911
Inman, $\alpha_{\phi-1}$	-0,097
Inman, $\alpha_{\phi-2}$	-0,420
Folk & Ward, Sk_I	-0,171

Coefficient d'acuité (Kurtosis)	
Krumbein & Petijohn, K	0,232
Inman, K_ϕ	0,710
Folk & Ward, K_G	0,987

Coefficient de courbure	
C_c	1,204

Analyse granulométrique par voie fluide : fraction 0,040 µm - 2000 µm

Echantillon :	INDONESIE/11/TENGAH/U20/20-30/T.Yan W. ISKANDARSYAH
Date :	24/01/2012 12:01
Opérateur :	MT
Fichier :	U20-02

Commentaires :	prof. : 20-30 cm Destruction MO à H2O2 -élimination des ions floculants - hexa + US

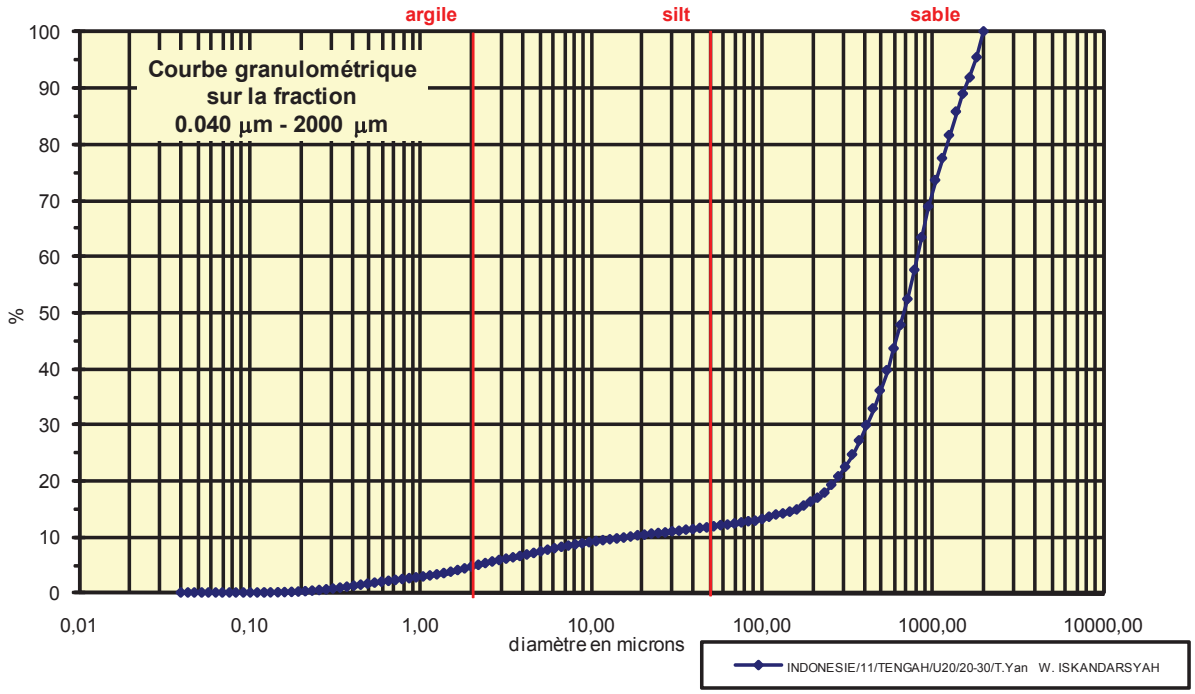

Fractiles	Taille (µm)	Taille (ϕ)
d_5	2,207	8,82
d_{10}	17,180	5,86
d_{16}	176,800	2,50
d_{25}	339,800	1,56
d_{30}	409,600	1,29
d_{50}	653,000	0,61
d_{60}	786,900	0,35
d_{75}	1041,000	-0,06
d_{84}	1255,000	-0,33
d_{90}	1512,000	-0,60
d_{95}	1660,000	-0,73

% Argile inférieur à 2µ	**A**	**4,30**
% Silts de 2µ à 50µ	**LT**	**7,30**
limons fins 2µ à 20µ	LF	5,90
limons grossiers 20µ à 50µ	LG	1,40
% Sables 50µ à 2000 µ	**ST**	**88,40**
sables fins 50µ à 200µ	SF	4,60
sables fins 50µ à 100µ	SF1	1,20
sables fins 100µ à 200 µ	SF2	3,40
sables grossiers 200µ à 2000µ	SG	83,80
sables grossiers 200µ à 500µ	SG1	19,80
sables grossiers 500µ à 1000µ	SG2	32,80
sables grossiers 1000µ à 2000µ	SG3	31,20

Indice de classement	
Trask, S_o	1,750
Krumbein, Q_d	-0,808
Inman, σ_ϕ	-1,414
Folk & Ward, σ_ϕ	-2,155
Hazen, C_u	45,803

Moyenne	
Trask, M	690,400
Inman, M_ϕ	1,086
Folk & Ward, M_z	0,929

Coefficient de dissymétrie	
Skew ness, S_{k-1}	0,830
Skew ness, S_{k-2}	0,911
Inman, $\alpha_{\phi-1}$	-0,333
Inman, $\alpha_{\phi-2}$	-2,427
Folk & Ward, Sk_I	-0,526

Coefficient d'acuité (Kurtosis)	
Krumbein & Petijohn, K	0,235
Inman, K_ϕ	2,379
Folk & Ward, K_G	2,424

Coefficient de courbure	
C_c	12,410

Analyse granulométrique par voie fluide : fraction 0,040 µm - 2000 µm

Echantillon :	INDONESIE/11/BAWAH/U20/40-50/T.Yan W. ISKANDARSYAH
Date :	23/01/2012 16:34
Opérateur :	MT
Fichier :	U20-003

Commentaires :	prof. : 40 -50 cm Destruction MO à H2O2 -élimination des ions floculants - hexa + US

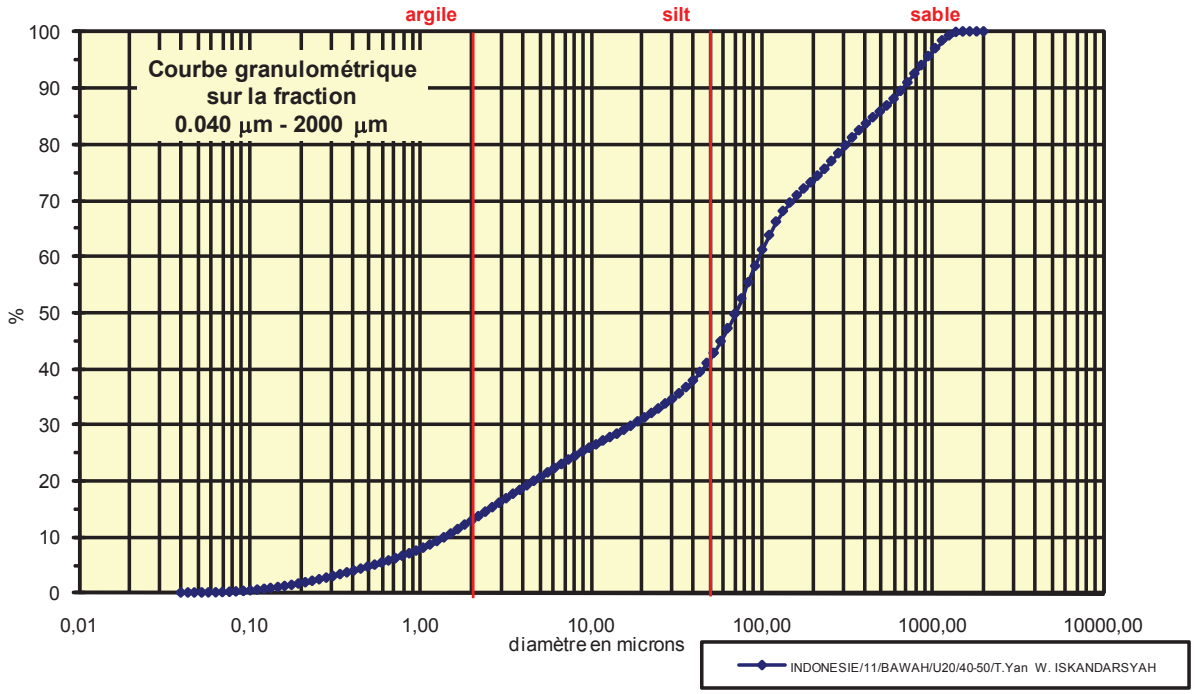

Fractiles	Taille (µm)	Taille (ϕ)
d_5	0,545	10,84
d_{10}	1,385	9,50
d_{16}	2,920	8,42
d_{25}	8,147	6,94
d_{30}	17,180	5,86
d_{50}	69,620	3,84
d_{60}	92,090	3,44
d_{75}	213,200	2,23
d_{84}	409,600	1,29
d_{90}	653,000	0,61
d_{95}	863,900	0,21

% Argile inférieur à 2µ	**A**	**12,10**
% Silts de 2µ à 50µ	**LT**	**28,80**
limons fins 2µ à 20µ	LF	18,40
limons grossiers 20µ à 50µ	LG	10,40
% Sables 50µ à 2000 µ	**ST**	**59,10**
sables fins 50µ à 200µ	SF	32,20
sables fins 50µ à 100µ	SF1	17,30
sables fins 100µ à 200 µ	SF2	14,90
sables grossiers 200µ à 2000µ	SG	26,90
sables grossiers 200µ à 500µ	SG1	12,60
sables grossiers 500µ à 1000µ	SG2	9,90
sables grossiers 1000µ à 2000µ	SG3	4,40

Indice de classement	
Trask, S_o	5,116
Krumbein, Q_d	-2,355
Inman, σ_ϕ	-3,566
Folk & Ward, σ_ϕ	-3,394
Hazen, C_u	66,491

Moyenne	
Trask, M	110,674
Inman, M_ϕ	4,854
Folk & Ward, M_z	4,517

Coefficient de dissymétrie	
Skew ness, S_{k-1}	0,358
Skew ness, S_{k-2}	0,599
Inman, $\alpha_{\phi-1}$	-0,283
Inman, $\alpha_{\phi-2}$	-0,472
Folk & Ward, Sk_I	-0,300

Coefficient d'acuité (Kurtosis)	
Krumbein & Petijohn, K	0,157
Inman, K_ϕ	0,490
Folk & Ward, K_G	0,925

Coefficient de courbure	
C_c	2,314

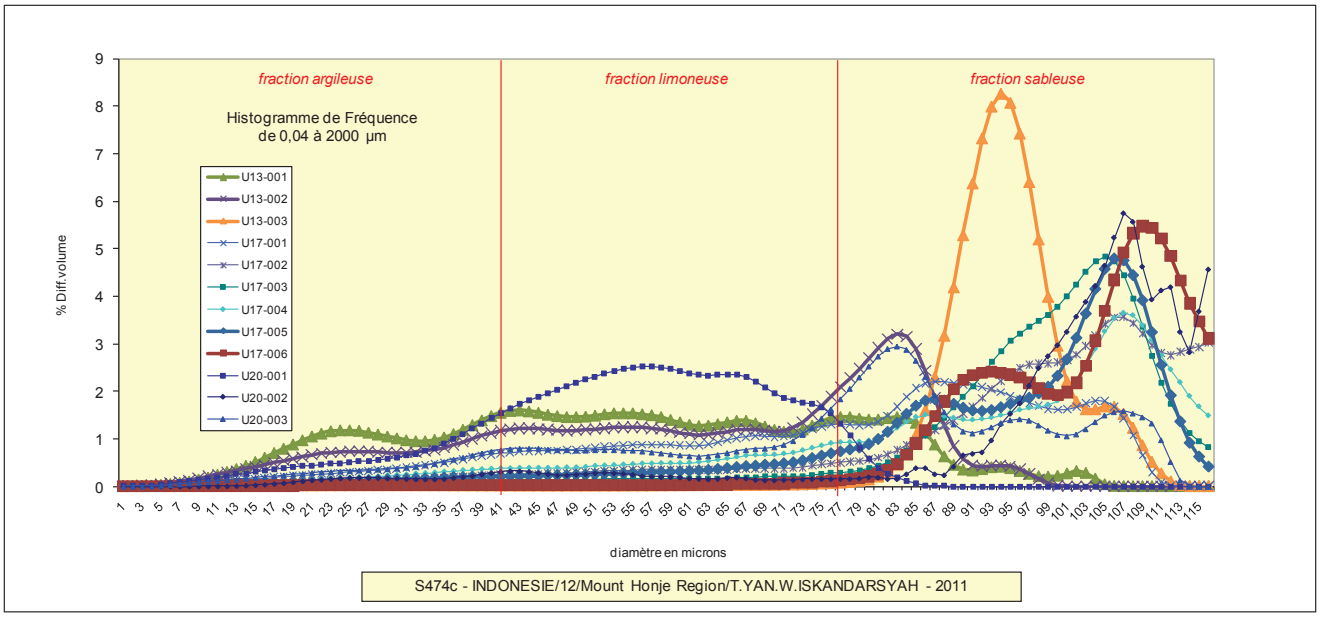
fraction argileuse
fraction limoneuse
fraction sableuse
Histogramme de Fréquence
de 0,04 à 2000 µm
U13-001
U13-002
U13-003
U17-001
U17-002
U17-003
U17-004
U17-005
U17-006
U20-001
U20-002
U20-003
% Diff.volume
diamètre en microns
S474c - INDONESIE/12/Mount Honje Region/T.YAN.W.ISKANDARSYAH - 2011

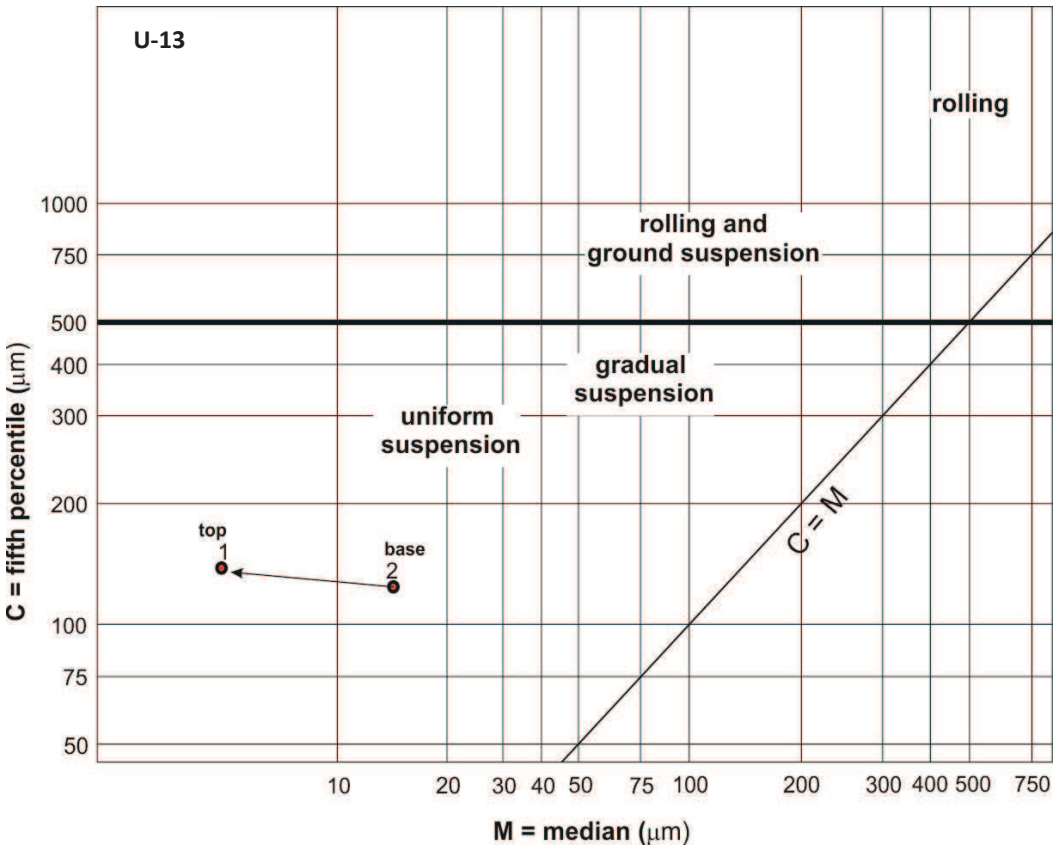
U-13
rolling
rolling and
ground suspension
gradual
suspension
uniform
suspension
top
1
base
2
C = M
C = fifth percentile (μm)
M = median (μm)
1000
750
500
400
300
200
100
75
50
10
20
30
40
50
75
100
200
300
400
500
750

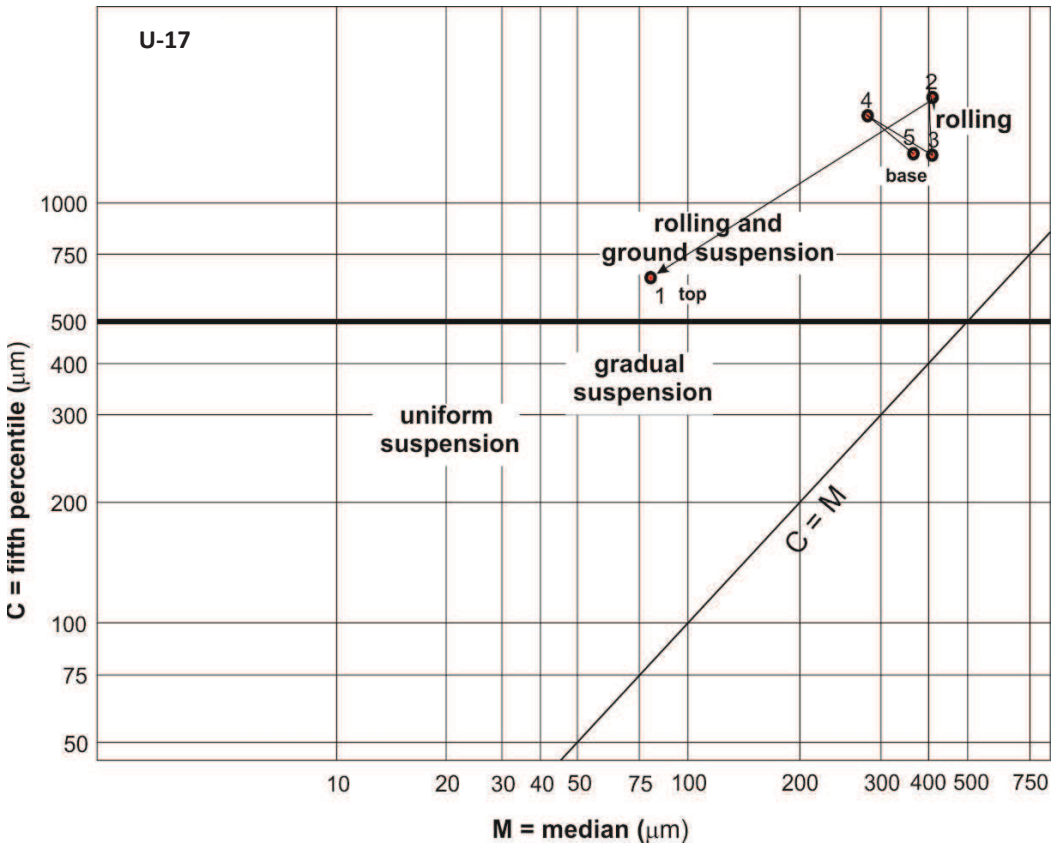
U-17
rolling
base
rolling and
ground suspension
1 top
gradual
suspension
uniform
suspension
C = M
C = fifth percentile (μm)
M = median (μm)
1000
750
500
400
300
200
100
75
50
10
20
30
40
50
75
100
200
300
400
500
750

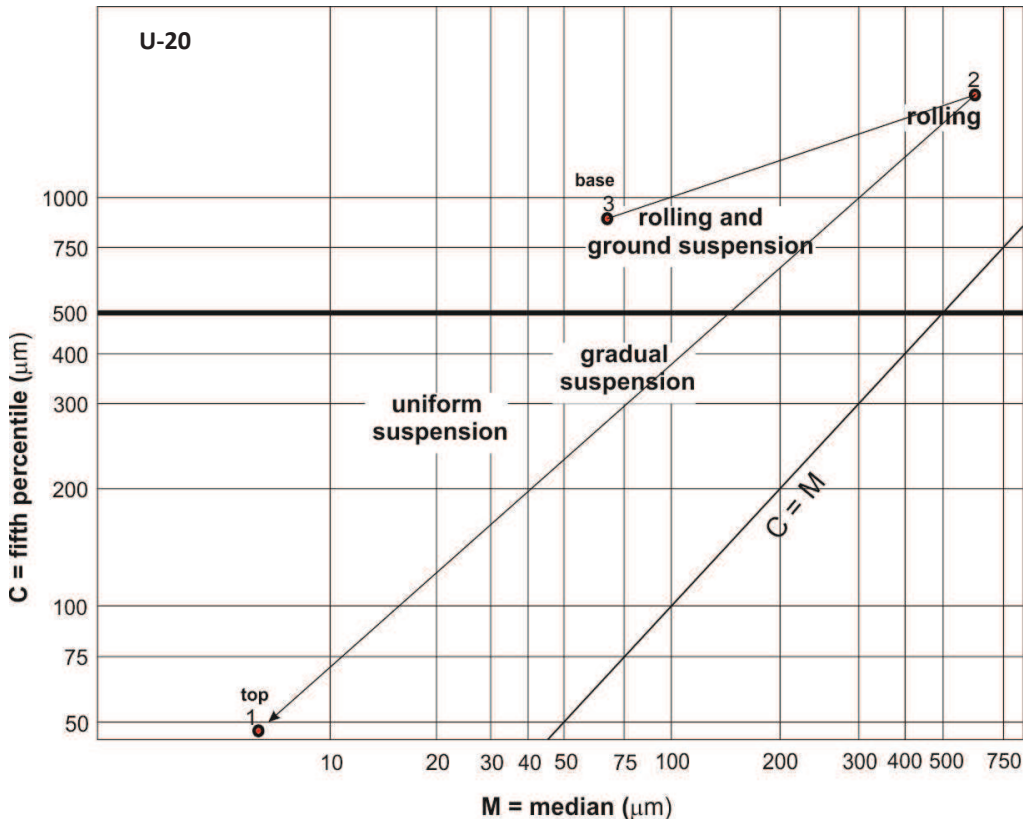
U-20
2
rolling
base
3
rolling and
ground suspension
gradual
suspension
uniform
suspension
C = M
top
1
C = fifth percentile (μm)
1000
750
500
400
300
200
100
75
50
10
20
30
40
50
75
100
200
300
400
500
750
M = median (μm)

2. FORAMINIFERAL IDENTIFICATION

	Benthic foraminifera : *Ammobaculites agglutinans* **d'Orbigny** 1134 meter below sea level Photograph was taken from microfossil within soil in U-04 (0-30 cm)
	Benthic foraminifera : *Amphicoryna proxima* **Silvestri** 171 – 180 meter below sea level Photograph was taken from microfossil within coral sand in U-04 (150-180 cm)
	Benthic foraminifera : *Amphicoryna separans* **Brady** 495 meter below sea level Photograph was taken from microfossil within gravel in U-04 (180-210 cm)
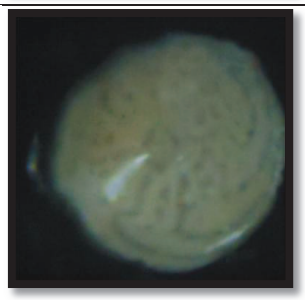	Benthic foraminifera : *Amphistegina lessonii* **d'Orbigny** 29,25– 45,7 meter below sea level Photograph was taken from microfossil within sand in U-04 (90 -120 cm)
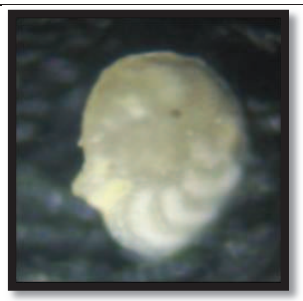	Benthic foraminifera : *Amphistegina quoyii* **d'Orbigny** 28.8 – 45 meter below sea level Photograph was taken from microfossil within soil in U-04 (0-30 cm)

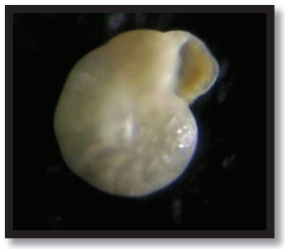	Benthic foraminifera : *Anomalina colligera* **Chapman and Parr.** 378 meter below sea level Photograph was taken from microfossil within U-05 (150-180 cm)
	Benthic foraminifera : *Anomalina globulosa* **Chapman and Parr.** 3690 meter below sea level Photograph was taken from microfossil within U-05 (270-295 cm)
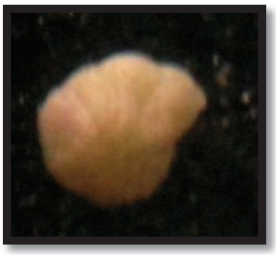	Benthic foraminifera : *Anomalinella rostrata* **Brady** 66.6 meter below sea level Photograph was taken from microfossil within U-05 (150-180 cm)
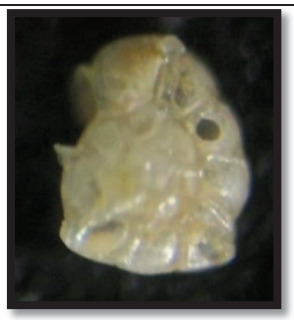	Benthic foraminifera : *Asterorotalia trispinosa* **Thalmann** Depth ?? Photograph was taken from microfossil within sand soil in U-05 (90-120 cm)
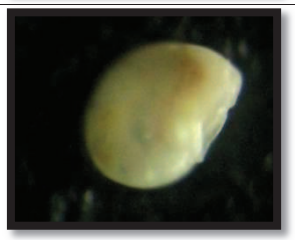	Benthic foraminifera : *Astrononion fijiense* **Cushman & Edwards** 378 meter below sea level Photograph was taken from microfossil within U-05 (210-240 cm)
	Benthic foraminifera : *Bigenerina nodosaria* **d'Orbigny** 140 – 220 meter below sea level Photograph was taken from microfossil within sand in U-04 (90-120 cm)

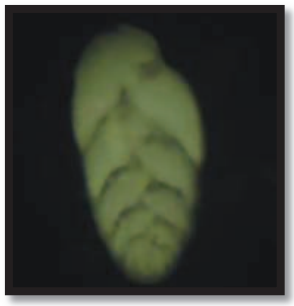	Benthic foraminifera : *Bolivina nitida* **Brady** 279 meter below sea level Photograph was taken from microfossil within soil in U-04 (0-30 cm)
	Benthic foraminifera : *Bolivina spathulata* **Williamson** 334,52 meter below sea level Photograph was taken from microfossil within soil in U-04 (0-30 cm)
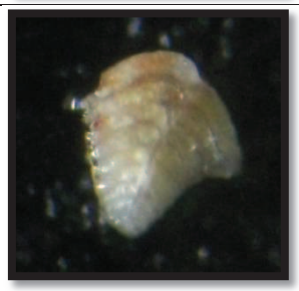	Benthic foraminifera : *Bolivinella elegans* **Parr.** 279 meter below sea level Photograph was taken from microfossil within U-05 (270-295 cm)
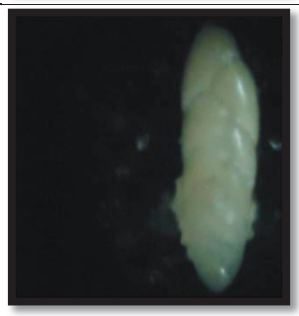	Benthic foraminifera : *Bolivinellina translucens* **Phleger and F.L. Parker** 91,40 meter below sea level Photograph was taken from microfossil within U-04 (60-90 cm)
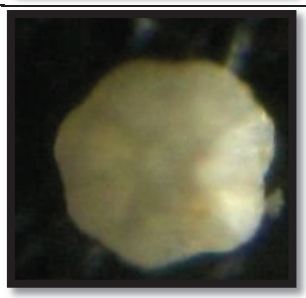	Benthic foraminifera : *Buccella frigid* **Cushman** 100,54 meter below sea level Photograph was taken from microfossil within U-05 (90-120 cm)
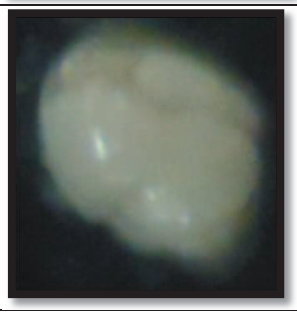	Benthic foraminifera : *Bulimina marginata* **d'Orbigny** 2979,64 meter below sea level Photograph was taken from microfossil within sand in U-04 (90-120 cm)

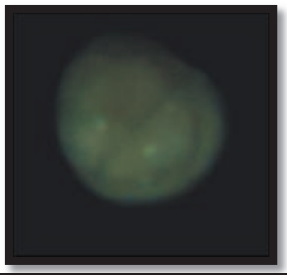	Benthic foraminifera : *Bulimina pupoides* **d'Orbigny** 630,66 meter below sea level Photograph was taken from microfossil within soil in U-04 (0-30 cm)
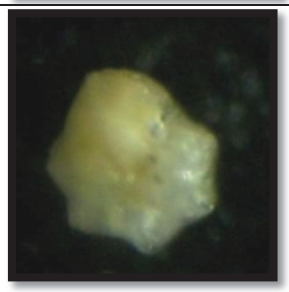	Benthic foraminifera : *Calcarina calcar* **d'Orbigny** 10,97 meter below sea level Photograph was taken from microfossil within sand in U-05 (90-120 cm)
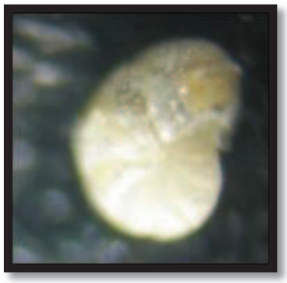	Benthic foraminifera : *Calcarina venusta* **Brady** 14,4 meter below sea level Photograph was taken from microfossil within soil in U-04 (0-30 cm)
	Benthic foraminifera : *Cancris auriculus* **Fichtel & Moll** 0 – 200 meter below sea level Photograph was taken from microfossil within soil in U-04 (0-30 cm)
	Benthic foraminifera : *Cancris oblongus* **Williamson** 702 meter below sea level Photograph was taken from microfossil within soil in U-04 (0-30 cm)
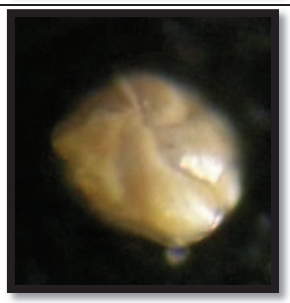	Benthic foraminifera : *Cassidulina teretis* **Tappan** 2979,64 meter below sea level Photograph was taken from microfossil within sand in U-05 (90-120 cm)

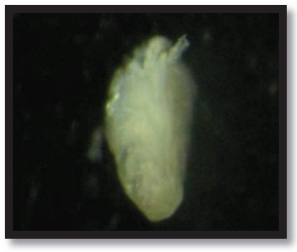	Benthic foraminifera : *Chrysalidinella dimorpha* **Brady** 72 meter below sea level Photograph was taken from microfossil within fragment in U-05 (240-270 cm)
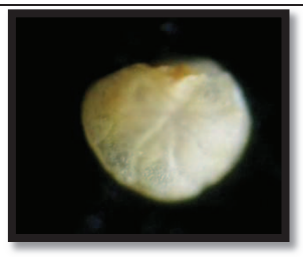	Benthic foraminifera : *Cibicides subhaidingerii* **Parr.** 279 meter below sea level Photograph was taken from microfossil within fragment in U-05 (180-210 cm)
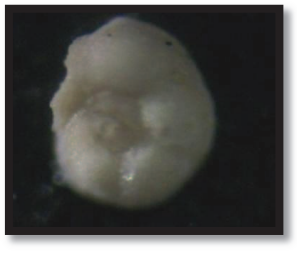	Benthic foraminifera : *Conorboides advena* **Cushman** 28,8 – 45 meter below sea level Photograph was taken from microfossil within fragment in U-05 (180-210 cm)
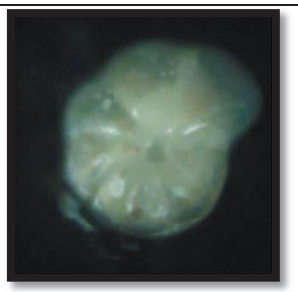	Benthic foraminifera : *Cyclammina trullissata* **Brady** 702 meter below sea level Photograph was taken from microfossil within U-04 (60-90 cm)
	Benthic foraminifera : *Dentalina subsoluta* **Cushman** 822,6 meter below sea level Photograph was taken from microfossil within sand in U-04 (90-120 cm)
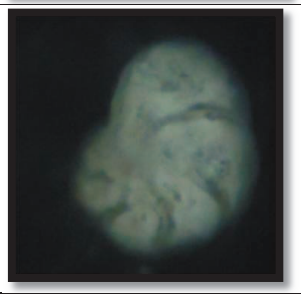	Benthic foraminifera : *Discorbinella bodjongensis* LEROY 30,38 meter below sea level Photograph was taken from microfossil within sand in U-04 (90-120 cm)

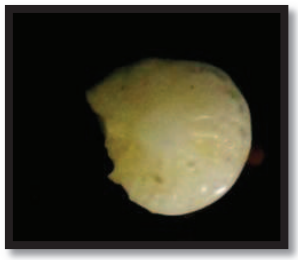	Benthic foraminifera : *Elphidium crispum* **Linnaeus** 12,79 – 14,62 meter below sea level Photograph was taken from microfossil within U-05 (150-180 cm)
	Benthic foraminifera : *Elphidium lesonii* **d'Orbigny** 10,97 meter below sea level Photograph was taken from microfossil within U-05 (150-180 cm)
	Benthic foraminifera : *Elphidium macellum* **Fichtel & Moll** 50 – 150 meter below sea level Photograph was taken from microfossil within gravel in U-04 (180-210 cm)
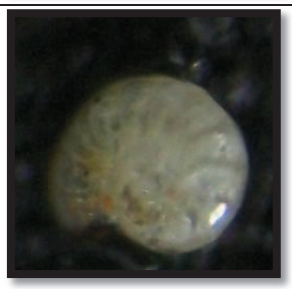	Benthic foraminifera : *Elphidium orbidulare* **Brady** 1137,6 meter below sea level Photograph was taken from microfossil within sand soil in U-05 (90-120 cm)
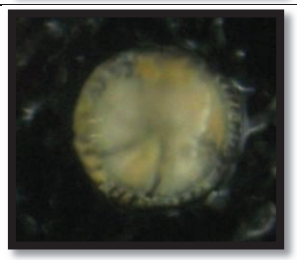	Benthic foraminifera : *Eponides (?) procera* **Brady** 378 meter below sea level Photograph was taken from microfossil within sand soil in U-05 (90-120 cm)
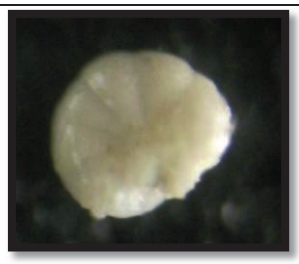	Benthic foraminifera : *Eponides schreibersi* **d' Orbigny** 279 meter below sea level Photograph was taken from microfossil within U-05 (210-240 cm)

	Benthic foraminifera : *Eponides schreibersi* **d'Orbigny** 270 meter below sea level Photograph was taken from microfossil within soil in U-04 (0-30 cm)
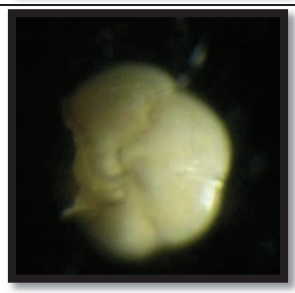	Benthic foraminifera : *Eponides (?) tenera* **Brady** 216 meter below sea level Photograph was taken from microfossil within U-05 (180-210 cm)
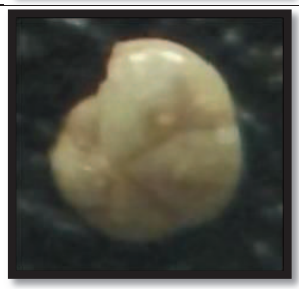	Benthic foraminifera : *Eponides umbonatus* **Reuss** 315 meter below sea level Photograph was taken from microfossil within silty soil in U-04 (0-30 cm)
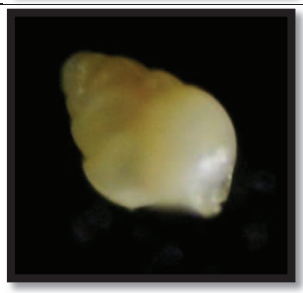	Benthic foraminifera : *Euuvigerina peregrina* **Cushman** 712,92 meter below sea level Photograph was taken from microfossil within U-05 (150-180 cm)
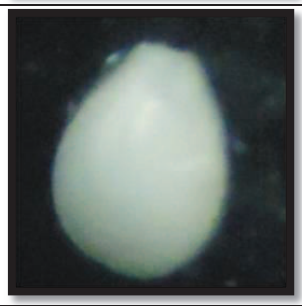	Benthic foraminifera : *Fissurina circularis* **Todd** 79,25 meter below sea level Photograph was taken from microfossil within silty sand in U-04 (90-120 cm)
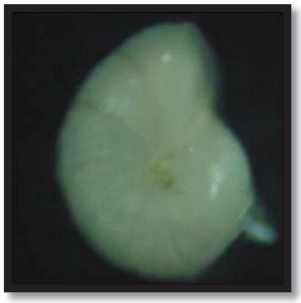	Benthic foraminifera : *Gavelinonion barleeanum* **Williamson** 702 meter below sea level Photograph was taken from microfossil within U-04 (120-150 cm)

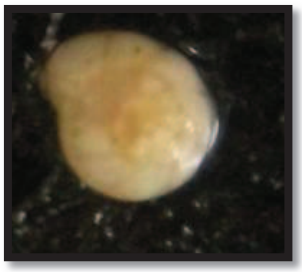	Benthic foraminifera : *Gyroidina neosoldanii* **Brotzen** 2610 meter below sea level Photograph was taken from microfossil within U-05 (150-180 cm)
	Benthic foraminifera : *Hogliindina elegans* **d'Orbigny** 180 – 270 meter below sea level Photograph was taken from microfossil within U-04 (120-150 cm)
	Benthic foraminifera : *Hyalinea balthica* **Schroeter** 2979,64 meter below sea level Photograph was taken from microfossil within U-05 (150-180 cm)
	Benthic foraminifera : *Hypermina cylindrica* PARR 35,75 meter below sea level Photograph was taken from microfossil within U-04 (150-180 cm)
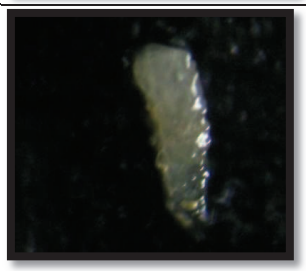	Benthic foraminifera : *Jaculella acuta* **Brady** 630 meter below sea level Photograph was taken from microfossil within U-05 (180-210 cm)
	Benthic foraminifera : *Karreriella bradyi* **Cushman** 2475 meter below sea level Photograph was taken from microfossil within gravel in U-04 (180-210 cm)

	Benthic foraminifera : *Lagena gracilima* **Seguenza** 150 – 725 meter below sea level Photograph was taken from microfossil within U-04 (60-90 cm)
	Benthic foraminifera : *Lagena hispidula* **Cushman** 3960 meter below sea level Photograph was taken from microfossil within silty sand in U-04 (150-180 cm)
	Benthic foraminifera : *Lagena laevis* **Montagu** 279 meter below sea level Photograph was taken from microfossil within U-05 (180-210 cm)
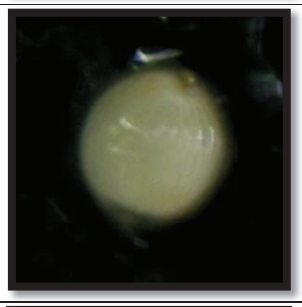	Benthic foraminifera : *Lagena sulcata* **Walker and Jacob** 36 – 108 meter below sea level Photograph was taken from microfossil within U-05 (180-210 cm)
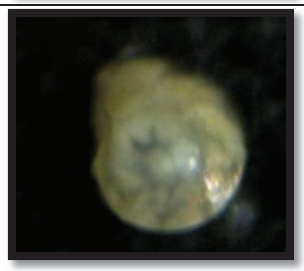	Benthic foraminifera : *Lenticulina calcar* **Linnaeus** 810 meter below sea level Photograph was taken from microfossil within U-05 (150-180 cm)
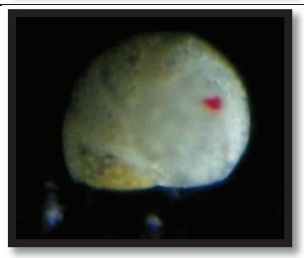	Benthic foraminifera : *Lenticulina Formosa* **Cushman** 810 meter below sea level Photograph was taken from microfossil within U-05 (150-180 cm)

	Benthic foraminifera : *Loxostomum sp*. **Nov** 25,2 meter below sea level Photograph was taken from microfossil within soil in U-04 (0-30 cm)
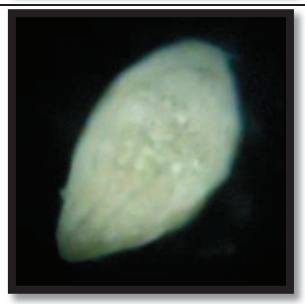	Benthic foraminifera : *Loxostomina mayori* **Cushman** 207,26 meter below sea level Photograph was taken from microfossil within U-04 (> 80 cm)
	Benthic foraminifera : *Neoconorbina terquemi* **Rzehak** 60 – 150 meter below sea level Photograph was taken from microfossil within silty soil in U-04 (90-120 cm)
	Benthic foraminifera : *Neouvigerina porrecta* **Brady** 279 meter below sea level Photograph was taken from microfossil within silty soil in U-04 (90-120 cm)
	Benthic foraminifera : *Nonion cf. asterizans* **Fichtel and Moll** 20,11 meter below sea level Photograph was taken from microfossil within sand in U-05 (90-120 cm)

	Benthic foraminifera : *Nonion scaphum* **Fichtel and Moll** 630,66 meter below sea level Photograph was taken from microfossil within U-05 (150-180 cm)
	Benthic foraminifera : *Operculina ammonoides* **Gronovius** 27 – 36 meter below sea level Photograph was taken from microfossil within U-04 (60-90 cm)
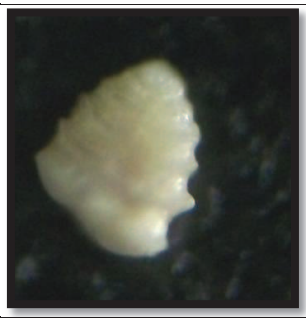	Benthic foraminifera : *Patellinella jugosa* **Brady** 283,34 meter below sea level Photograph was taken from microfossil within sand in U-05 (90-120 cm)
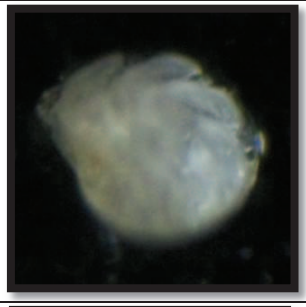	Benthic foraminifera : *Planulina ariminensis* **d'Orbigny** 639,8 meter below sea level Photograph was taken from microfossil within sand in U-05 (90-120 cm)
	Benthic foraminifera : *Planulina wuellerstorfi* **Schwager** 502,7 meter below sea level Photograph was taken from microfossil within sand in U-04 (90-120 cm)
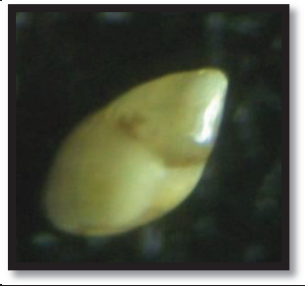	Benthic foraminifera : *Pleurostomella brevis* **Schwager** 235,81 meter below sea level Photograph was taken from microfossil within U-05 (120-150 cm)

	Benthic foraminifera : *Quinqueloculina auberiana* **d'Orbigny** 702 meter below sea level Photograph was taken from microfossil within U-04 (60-90 cm)
	Benthic foraminifera : *Quinqueloqulina pygmaea* **Reuss** 29,25 – 45,7 meter below sea level Photograph was taken from microfossil within U-05 (150-180 cm)
	Benthic foraminifera : *Quinqueloqulina seminulum* **Linnaeus** 82,26 – 109,68 meter below sea level Photograph was taken from microfossil within U-04 (210-240 cm)
	Benthic foraminifera : *Quinqueloculina tropicalis* **Cushman** 66,6 meter below sea level Photograph was taken from microfossil within fragment in U-05 (240-270 cm)
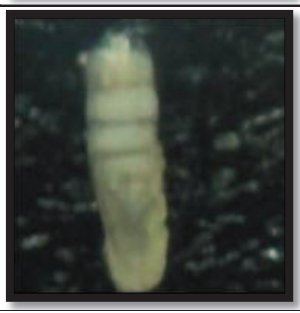	Benthic foraminifera : *Rectobolivina columellaris* **Brady** 1116 meter below sea level Photograph was taken from microfossil within gravel in U-04 (180-210 cm)
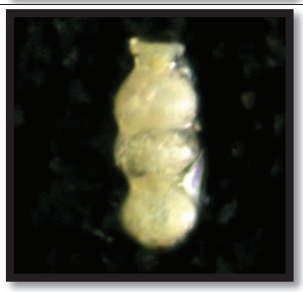	Benthic foraminifera : *Rectobolivina virgula* **Brady** 66,6 meter below sea level Photograph was taken from microfossil within U-05 (180-210 cm)

	Benthic foraminifera : *Rectoglandulina comatula* **Cushman** 783 meter below sea level Photograph was taken from microfossil within silty soil in U-04 (90-120 cm)
	Benthic foraminifera : *Reophax nodulosus* **Brady** 3420 meter below sea level Photograph was taken from microfossil within U-05 (150-180 cm)
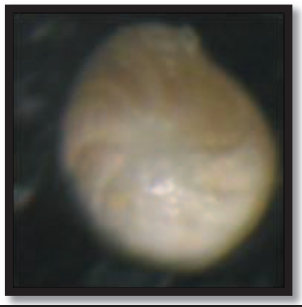	Benthic foraminifera : *Robulus thalmani* **Hessland** 712,92 meter below sea level Photograph was taken from microfossil within soil in U-04 (0-30 cm)
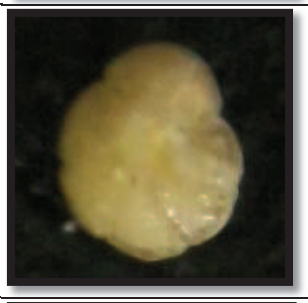	Benthic foraminifera : *Rosalina sp.* **Nov.** 27 meter below sea level Photograph was taken from microfossil within U-05 (150-180 cm)
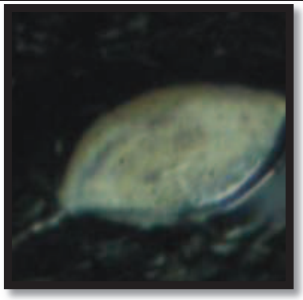	Benthic foraminifera : *Sigmoilina tenuis* **Czjzek** 2610 meter below sea level Photograph was taken from microfossil within soil in U-04 (0-30 cm)
	Benthic foraminifera : *Siphotextularia crispata* **Brady** 30,6 meter below sea level Photograph was taken from microfossil within U-04 (120-150 cm)

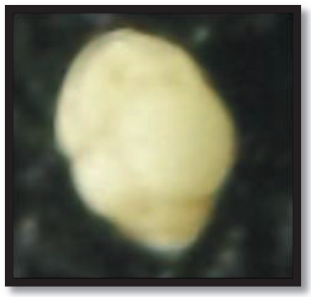	Benthic foraminifera : *Sphaeroidina bulloides* **d'Orbigny** 1215 meter below sea level Photograph was taken from microfossil within U-04 (> 80 cm)
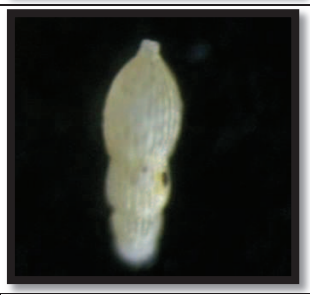	Benthic foraminifera : *Stilostomella fistuca* **Schwager** 232,2 meter below sea level Photograph was taken from microfossil within U-05 (240-270 cm)
	Benthic foraminifera : *Streblus becarii* **Linnaeus** 14,63 meter below sea level Photograph was taken from microfossil within U-04 (120-150 cm)
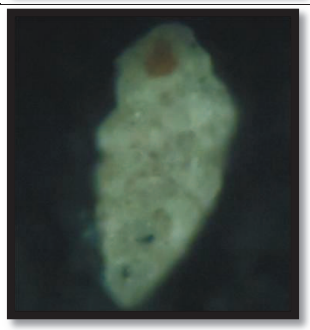	Benthic foraminifera : *Textularia agglutinans* **d'Orbigny** 10 – 200 meter below sea level Photograph was taken from microfossil within sand in U-04 (90-120 cm)
	Benthic foraminifera : *Textularia agglutinans* D'ORBIGNY 10 – 200 meter below sea level Photograph was taken from microfossil within U-04 (120-150 cm)

	Benthic foraminifera : *Trifarina bradyi* **Cushman** 292,48 meter below sea level Photograph was taken from microfossil within silty soil in U-04 (90-120 cm)
	Benthic foraminifera : *Tubinella funalis* **Brady** 91,4 – 274,2 meter below sea level Photograph was taken from microfossil within sand in U-05 (90-120 cm)
	Benthic foraminifera : *Uvigerina conariensis* **d'Orbigny** 3420 meter below sea level Photograph was taken from microfossil within sand in U-04 (90-120 cm)
	Benthic foraminifera : *Uvigerina cushmani* **Todd** 135 meter below sea level Photograph was taken from microfossil within U-04 (210-240 cm)
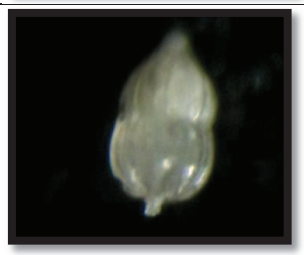	Benthic foraminifera : *Uvigerina peregrina* **CUSHMAN** 214,5 meter below sea level Photograph was taken from microfossil within U-05 (240-270 cm)

3. ANISOTROPY OF MAGNETIC SUSCEPTIBILITY (AMS)

Code of Samples	Location & Sampled Layers	Depth Interval (cm)	Mean Depth (cm)
U-01 004	Laban 4	90 - 92	91
U-01 006	Laban 5	125 - 127	126
U-01 007	Laban 6	154 - 156	155
U-01 008	Laban 7	180 - 182	181
U-01 009	Laban 8	201 - 203	202
U-01 010-a	Laban 9a	216 - 218	217
U-01 010-b	Laban 9b	230 - 232	231
U-03 002-a	Laban D-SA	14.5 - 16.5	15.5
U-03 002-b	Laban D-SB	17.5 - 19.5	18.5
U-03 002-c	Laban D-SC	20 - 22	21
U-03 002-d	Laban D-SD	22.5 - 24.5	23.5
U-03 002-e	Laban D-SE	28 - 30	29
U-03 003	Laban D-SF	44 - 46	45
U-04 002-a	Laban C 1	14 - 16	15
U-04 002-b	Laban C 2	20 - 22	21
U-04 003-a	Laban C 3	39 - 41	40
U-04 003-b	Laban C 4	45 - 47	46
U-04 003-c	Laban C 5	47.5 - 49.5	48.5
U-04 003-d	Laban C 6	50 - 52	51
U-04 003-e	Laban C 7	53 - 55	54
U-04 005-a	Laban C 8	70 - 72	71
U-04 005-b	Laban C 9	83 - 85	84
U-04 007-a	Laban C 10	99 - 101	100
U-04 007-b	Laban C 11	103 - 105	104
U-04 007-c	Laban C 12	109 - 111	110
U-04 007-d	Laban C 13	113 - 115	114
U-04 009-a	Laban C 14	132.5 - 134.5	133.5
U-04 009-b	Laban C 15	135 - 137	136
U-04 009-c	Laban C 16	138 - 140	139
U-04 009-d	Laban C 17	141.5 - 143.5	142.5
U-04 011	Laban C 18	162.5 - 164.5	163.5
U-04 013	Laban C 19	171 - 173	172
U-04 014	Laban C 20	192 - 194	193
U-04 015-a	Laban C 21	199 - 201	200
U-04 015-b	Laban C 22	202.5 - 204.5	203.5
U-04 016-a	Laban C 23	221 - 223	222
U-04 016-b	Laban C 24	224 - 226	225
U-04 016-c	Laban C 25	226.5 - 228.5	227.5
U-04 016-d	Laban C 26	229 - 231	230
U-04 016-e	Laban C 27	231.5 - 233.5	232.5
U-05 002	Laban B 1	22 - 24	23
U-05 003-a	Laban B 2	39 - 41	40
U-05 003-b	Laban B 3	46 - 48	47
U-05 003-c	Laban B 4	50 - 52	51
U-05 004-a	Laban B 5	70 - 72	71

Code of Samples	Location & Sampled Layers	Depth Interval (cm)	Mean Depth (cm)
U-05 004-b	Laban B 6	78 - 80	79
U-05 004-c	Laban B 7	81 - 83	82
U-05 005-a	Laban B 8	96 - 98	97
U-05 005-b	Laban B 9	99 - 101	100
U-05 006	Laban B 10	102 - 104	103
U-05 007	Laban B 11	121 - 123	122
U-05 012	Laban B 12	188 - 190	189
U-05 013	Laban B 13	195 - 197	196
U-05 017-a	Laban B 14	281 - 283	282
U-05 017-b	Laban B 15	284 - 286	285
U-06 002-a	Laban A 1	6.5 - 8.5	7.5
U-06 002-b	Laban A 2	11 - 13	12
U-06 003	Laban A 3	27 - 29	28
U-06 004	Laban A 4	32 - 34	33
U-06 005	Laban A 5	37 - 39	38
U-06 006	Laban A 6	42 - 44	43
U-06 007	Laban A 7	47 - 49	48
U-06 008-a	Laban A 8	59 - 61	60
U-06 008-b	Laban A 9	62 - 64	63
U-06 008-c	Laban A 10	65 - 67	66
U-06 008-d	Laban A 11	69 - 71	70
U-06 011	Laban A 12	100 - 102	101
U-06 012	Laban A 13	106 - 108	107
U-08 007-a	Cidaun 1	165 - 167	166
U-08 007-b	Cidaun 2	169 - 171	170
U-08 008	Cidaun 3	193 - 195	194
U-17 002-a	Sumur 1	16 - 18	17
U-17 002-b	Sumur 2	18.5 - 20.5	19.5
U-17 003-a	Sumur 3	21 - 23	22
U-17 003-b	Sumur 4	25.5 - 27.5	26.5
U-17 003-c	Sumur 5	26 - 28	27
U-17 004	Sumur 6	30.5 - 32.5	31.5
U-17 005-a	Sumur 10	45 - 47	46
U-17 005-b	Sumur 11	55 - 57	56
U-17 005-c	Sumur 12	70 - 72	71

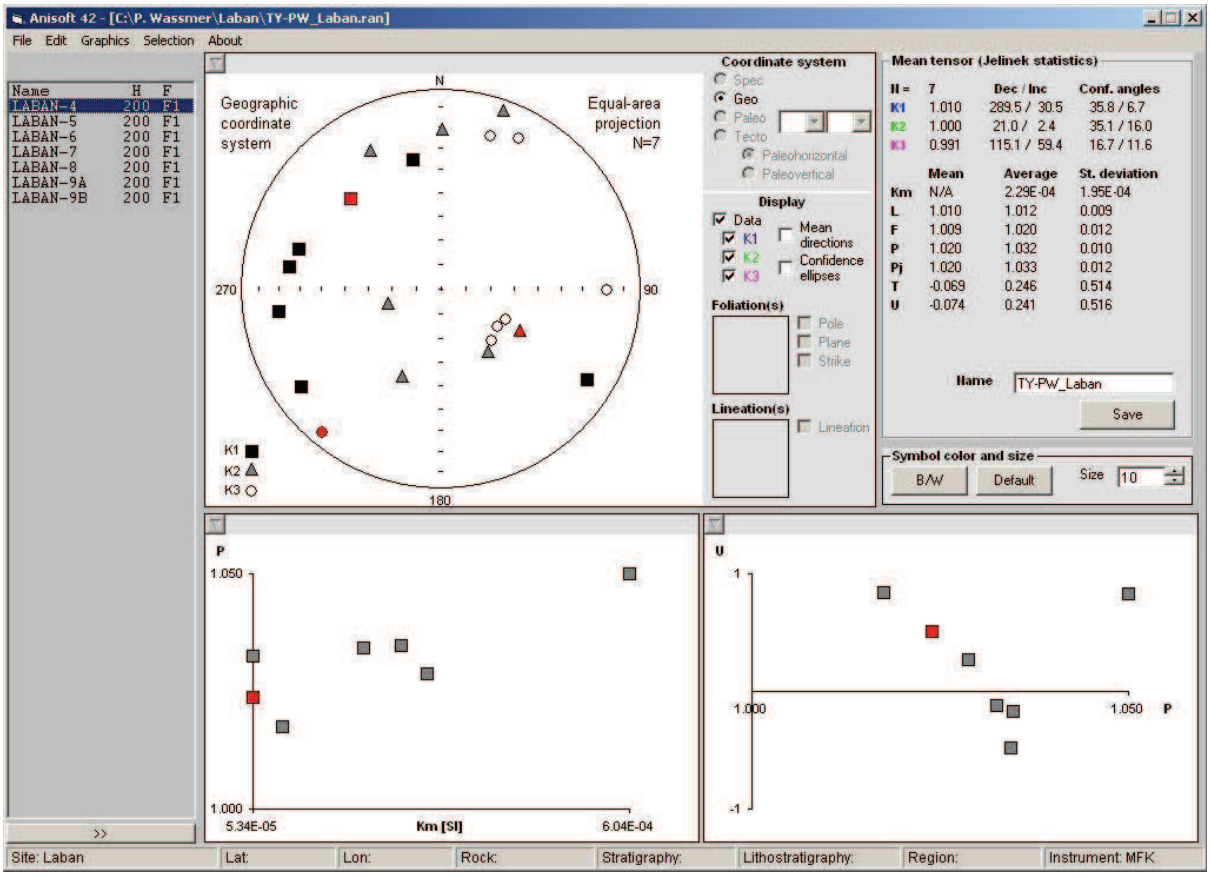
Anisoft 42 - [C:\P. Wassmer\Laban\TY-PW_Laban.ran]
File Edit Graphics Selection About
Name H F
LABAN-4 200 F1
LABAN-5 200 F1
LABAN-6 200 F1
LABAN-7 200 F1
LABAN-8 200 F1
LABAN-9A 200 F1
LABAN-9B 200 F1
Geographic coordinate system
Equal-area projection N=7
N
90
180
270
K1
K2
K3
Coordinate system
Spec
Geo
Paleo
Tecto
Paleohorizontal
Paleovertical
Display
Data
K1
K2
K3
Mean directions
Confidence ellipses
Foliation(s)
Pole
Plane
Strike
Lineation(s)
Lineation
Mean tensor (Jelinek statistics)
II = 7 Dec / Inc Conf. angles
K1 1.010 289.5 / 30.5 35.8 / 6.7
K2 1.000 21.0 / 2.4 35.1 / 16.0
K3 0.991 115.1 / 59.4 16.7 / 11.6
Mean Average St. deviation
Km N/A 2.29E-04 1.95E-04
L 1.010 1.012 0.009
F 1.009 1.020 0.012
P 1.020 1.032 0.010
Pj 1.020 1.033 0.012
T -0.069 0.246 0.514
U -0.074 0.241 0.516
Name TY-PW_Laban
Save
Symbol color and size
B/W
Default
Size 10
P
1.050
1.000
5.34E-05
Km [SI]
6.04E-04
U
1
-1
1.000
1.050
P
Site: Laban
Lat:
Lon:
Rock:
Stratigraphy:
Lithostratigraphy:
Region:
Instrument: MFK

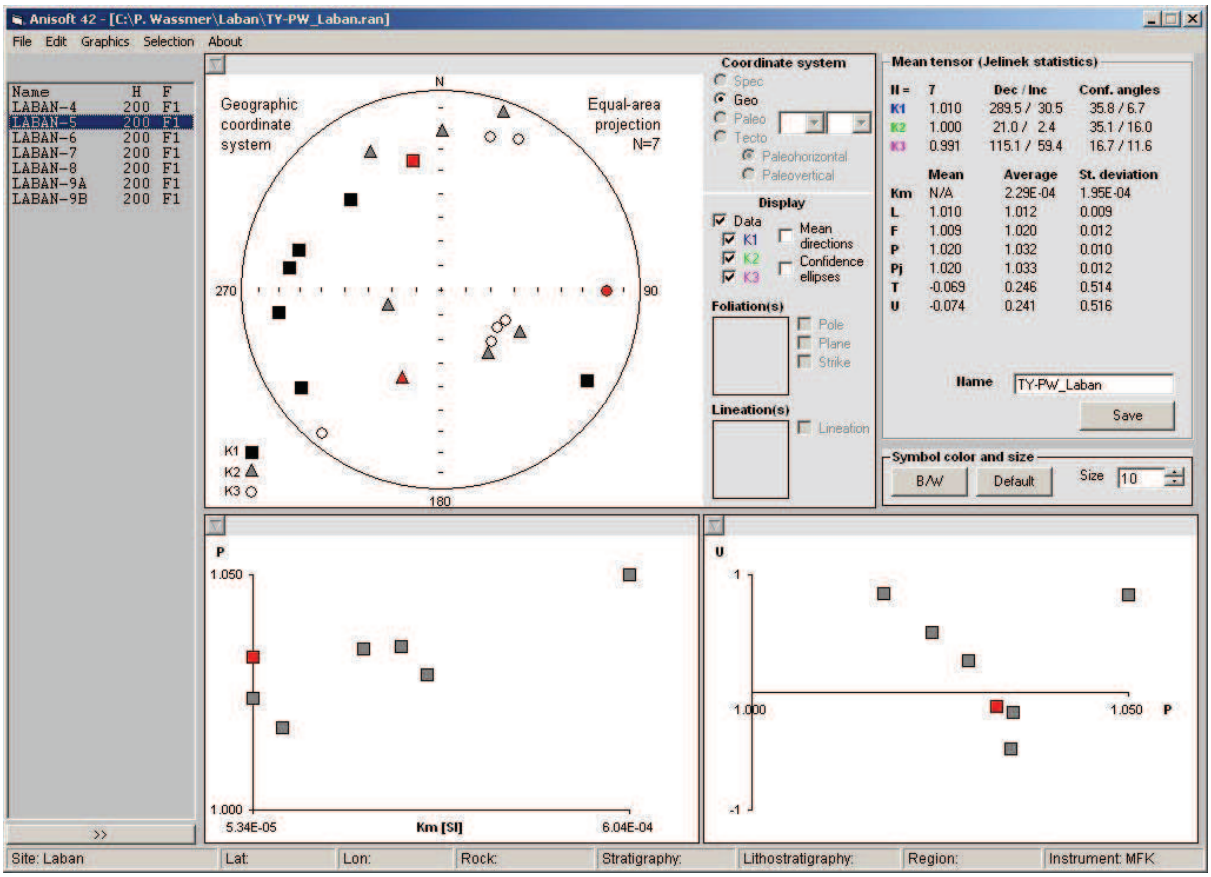
Anisoft 42 - [C:\P. Wassmer\Laban\TY-PW_Laban.ran]
File Edit Graphics Selection About
Name H F
LABAN-4 200 F1
LABAN-5 200 F1
LABAN-6 200 F1
LABAN-7 200 F1
LABAN-8 200 F1
LABAN-9A 200 F1
LABAN-9B 200 F1
Geographic coordinate system
Equal-area projection N=7
N
90
180
270
K1
K2
K3
Coordinate system
Spec
Geo
Paleo
Tecto
Paleohorizontal
Paleovertical
Display
Data
K1
K2
K3
Mean directions
Confidence ellipses
Foliation(s)
Pole
Plane
Strike
Lineation(s)
Lineation
Mean tensor (Jelinek statistics)
II = 7 Dec / Inc Conf. angles
K1 1.010 289.5 / 30.5 35.8 / 6.7
K2 1.000 21.0 / 2.4 35.1 / 16.0
K3 0.991 115.1 / 59.4 16.7 / 11.6
Mean Average St. deviation
Km N/A 2.29E-04 1.95E-04
L 1.010 1.012 0.009
F 1.009 1.020 0.012
P 1.020 1.032 0.010
Pj 1.020 1.033 0.012
T -0.069 0.246 0.514
U -0.074 0.241 0.516
Name TY-PW_Laban
Save
Symbol color and size
B/W
Default
Size 10
P
1.050
1.000
5.34E-05
Km [SI]
6.04E-04
U
1
-1
1.000
1.050
P
Site: Laban
Lat:
Lon:
Rock:
Stratigraphy:
Lithostratigraphy:
Region:
Instrument: MFK

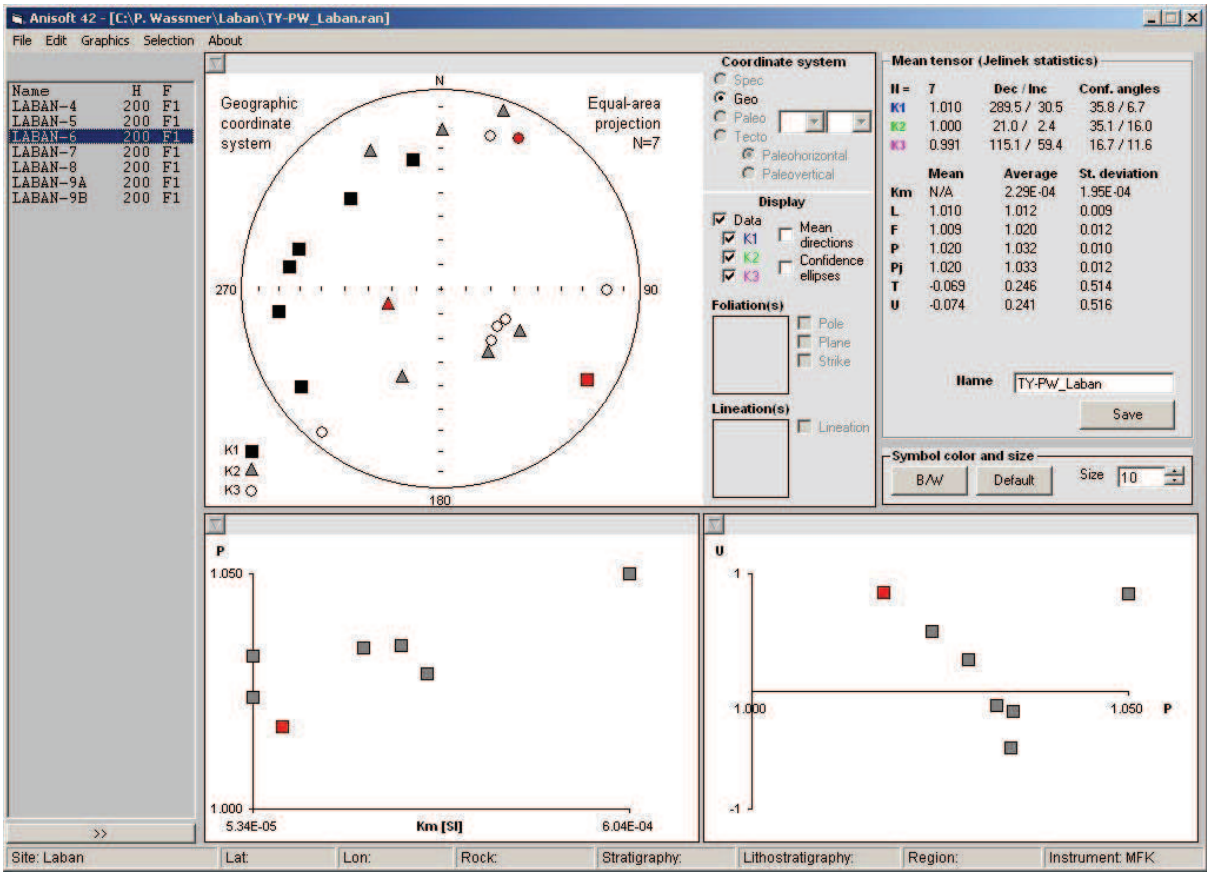
Anisoft 42 - [C:\P. Wassmer\Laban\TY-PW_Laban.ran]
File Edit Graphics Selection About
Name H F
LABAN-4 200 F1
LABAN-5 200 F1
LABAN-6 200 F1
LABAN-7 200 F1
LABAN-8 200 F1
LABAN-9A 200 F1
LABAN-9B 200 F1
Geographic coordinate system
Equal-area projection N=7
N
90
180
270
K1
K2
K3
Coordinate system
Spec
Geo
Paleo
Tecto
Paleohorizontal
Paleovertical
Display
Data
K1
K2
K3
Mean directions
Confidence ellipses
Foliation(s)
Pole
Plane
Strike
Lineation(s)
Lineation
Mean tensor (Jelinek statistics)
II = 7 Dec / Inc Conf. angles
K1 1.010 289.5 / 30.5 35.8 / 6.7
K2 1.000 21.0 / 2.4 35.1 / 16.0
K3 0.991 115.1 / 59.4 16.7 / 11.6
Mean Average St. deviation
Km N/A 2.29E-04 1.95E-04
L 1.010 1.012 0.009
F 1.009 1.020 0.012
P 1.020 1.032 0.010
Pj 1.020 1.033 0.012
T -0.069 0.246 0.514
U -0.074 0.241 0.516
Name TY-PW_Laban
Save
Symbol color and size
B/W
Default
Size 10
P
1.050
1.000
5.34E-05
Km [SI]
6.04E-04
U
1
-1
Site: Laban
Lat:
Lon:
Rock:
Stratigraphy:
Lithostratigraphy:
Region:
Instrument: MFK

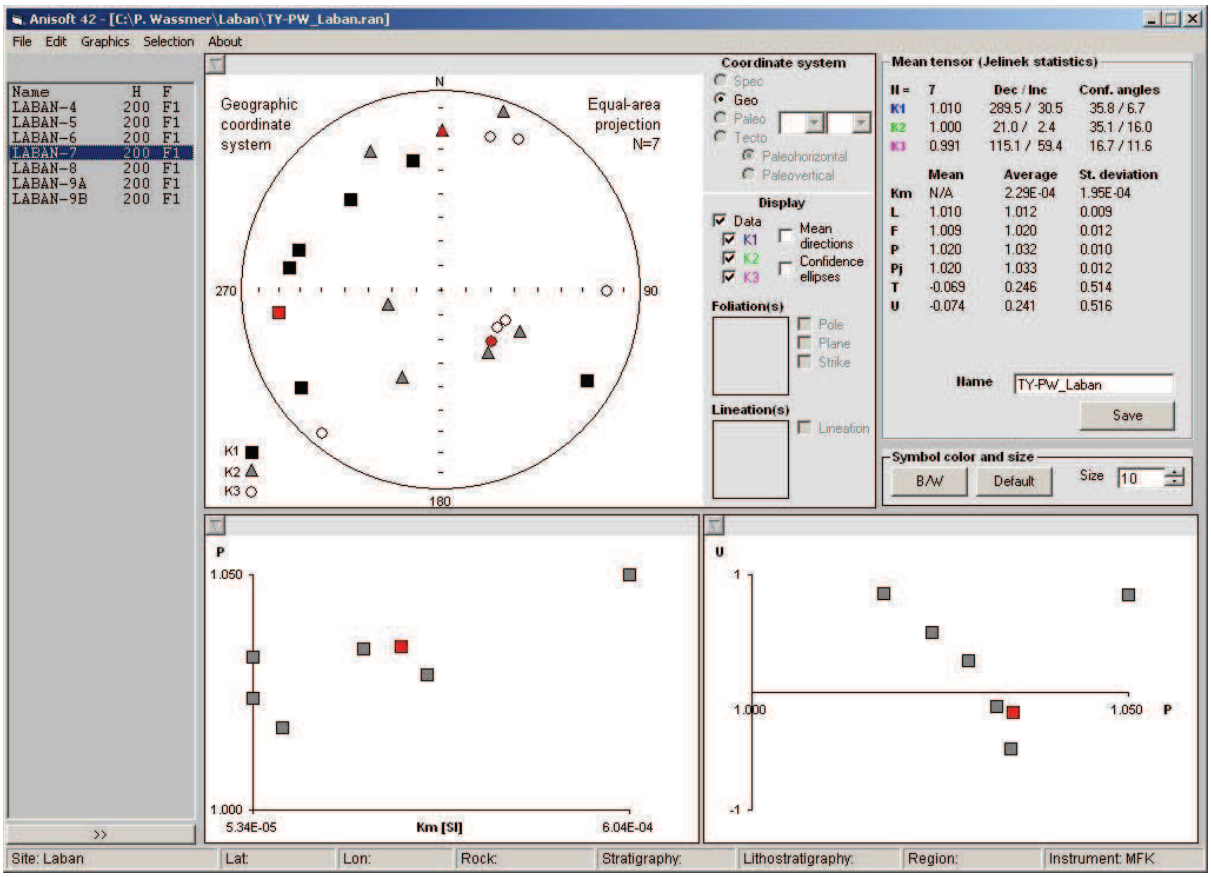
Anisoft 42 - [C:\P. Wassmer\Laban\TY-PW_Laban.ran]
File Edit Graphics Selection About
Name H F
LABAN-4 200 F1
LABAN-5 200 F1
LABAN-6 200 F1
LABAN-7 200 F1
LABAN-8 200 F1
LABAN-9A 200 F1
LABAN-9B 200 F1
Geographic coordinate system
Equal-area projection N=7
N
90
180
270
K1
K2
K3
Coordinate system
Spec
Geo
Paleo
Tecto
Paleohorizontal
Paleovertical
Display
Data
K1
K2
K3
Mean directions
Confidence ellipses
Foliation(s)
Pole
Plane
Strike
Lineation(s)
Lineation
Mean tensor (Jelinek statistics)
II = 7 Dec / Inc Conf. angles
K1 1.010 289.5 / 30.5 35.8 / 6.7
K2 1.000 21.0 / 2.4 35.1 / 16.0
K3 0.991 115.1 / 59.4 16.7 / 11.6
Mean Average St. deviation
Km N/A 2.29E-04 1.95E-04
L 1.010 1.012 0.009
F 1.009 1.020 0.012
P 1.020 1.032 0.010
Pj 1.020 1.033 0.012
T -0.069 0.246 0.514
U -0.074 0.241 0.516
Name TY-PW_Laban
Save
Symbol color and size
B/W
Default
Size 10
P
1.050
1.000
5.34E-05
Km [SI]
6.04E-04
U
1
-1
Site: Laban
Lat:
Lon:
Rock:
Stratigraphy:
Lithostratigraphy:
Region:
Instrument: MFK

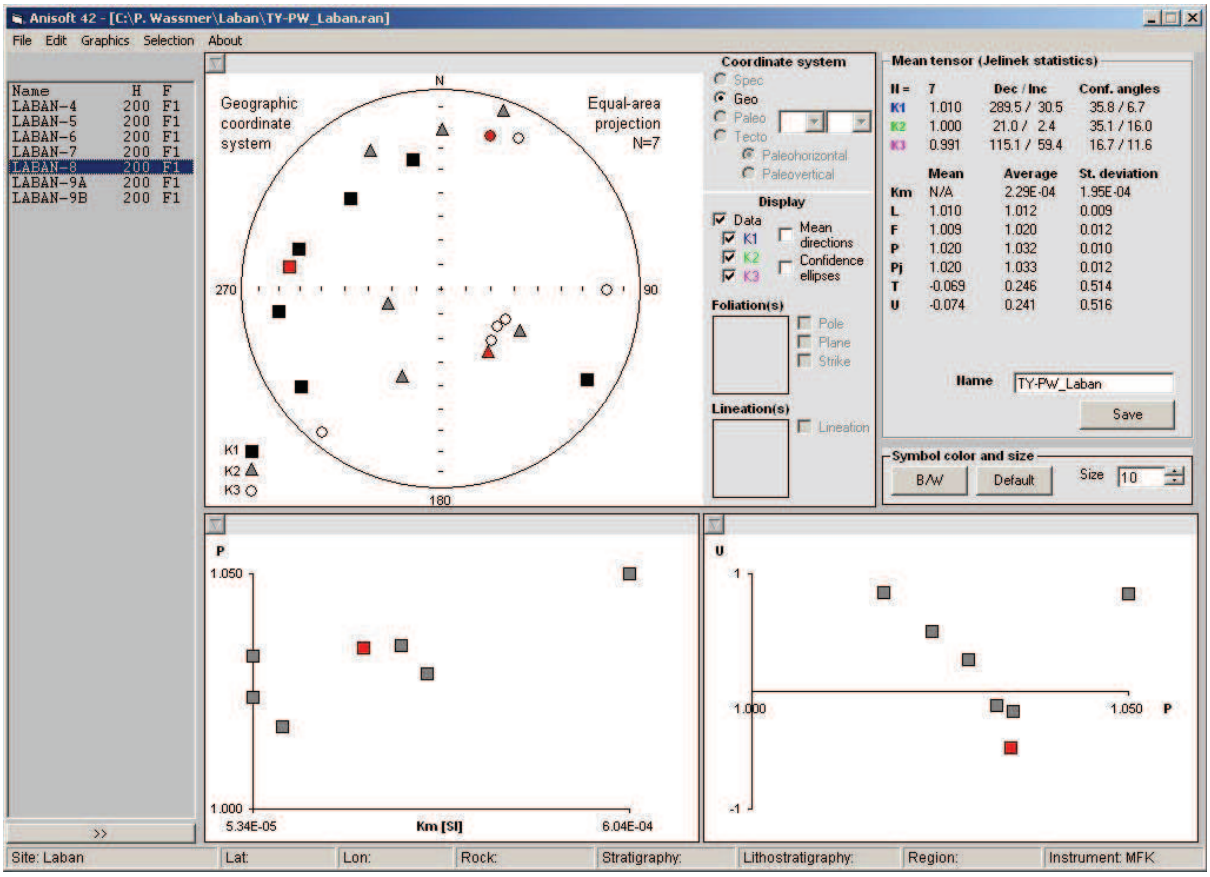
Anisoft 42 - [C:\P. Wassmer\Laban\TY-PW_Laban.ran]
File Edit Graphics Selection About
Name H F
LABAN-4 200 F1
LABAN-5 200 F1
LABAN-6 200 F1
LABAN-7 200 F1
LABAN-8 200 F1
LABAN-9A 200 F1
LABAN-9B 200 F1
Geographic coordinate system
Equal-area projection N=7
N
90
180
270
K1
K2
K3
Coordinate system
Spec
Geo
Paleo
Tecto
Paleohorizontal
Paleovertical
Display
Data
K1
K2
K3
Mean directions
Confidence ellipses
Foliation(s)
Pole
Plane
Strike
Lineation(s)
Lineation
Mean tensor (Jelinek statistics)
Dec / Inc
Conf. angles
Mean
Average
St. deviation
Km N/A 2.29E-04 1.95E-04
L 1.010 1.012 0.009
F 1.009 1.020 0.012
P 1.020 1.032 0.010
Pj 1.020 1.033 0.012
T -0.069 0.246 0.514
U -0.074 0.241 0.516
Name TY-PW_Laban
Save
Symbol color and size
B/W
Default
Size 10
P
1.050
1.000
5.34E-05
Km [SI]
6.04E-04
U
1
-1
Site: Laban
Lat:
Lon:
Rock:
Stratigraphy:
Lithostratigraphy:
Region:
Instrument: MFK

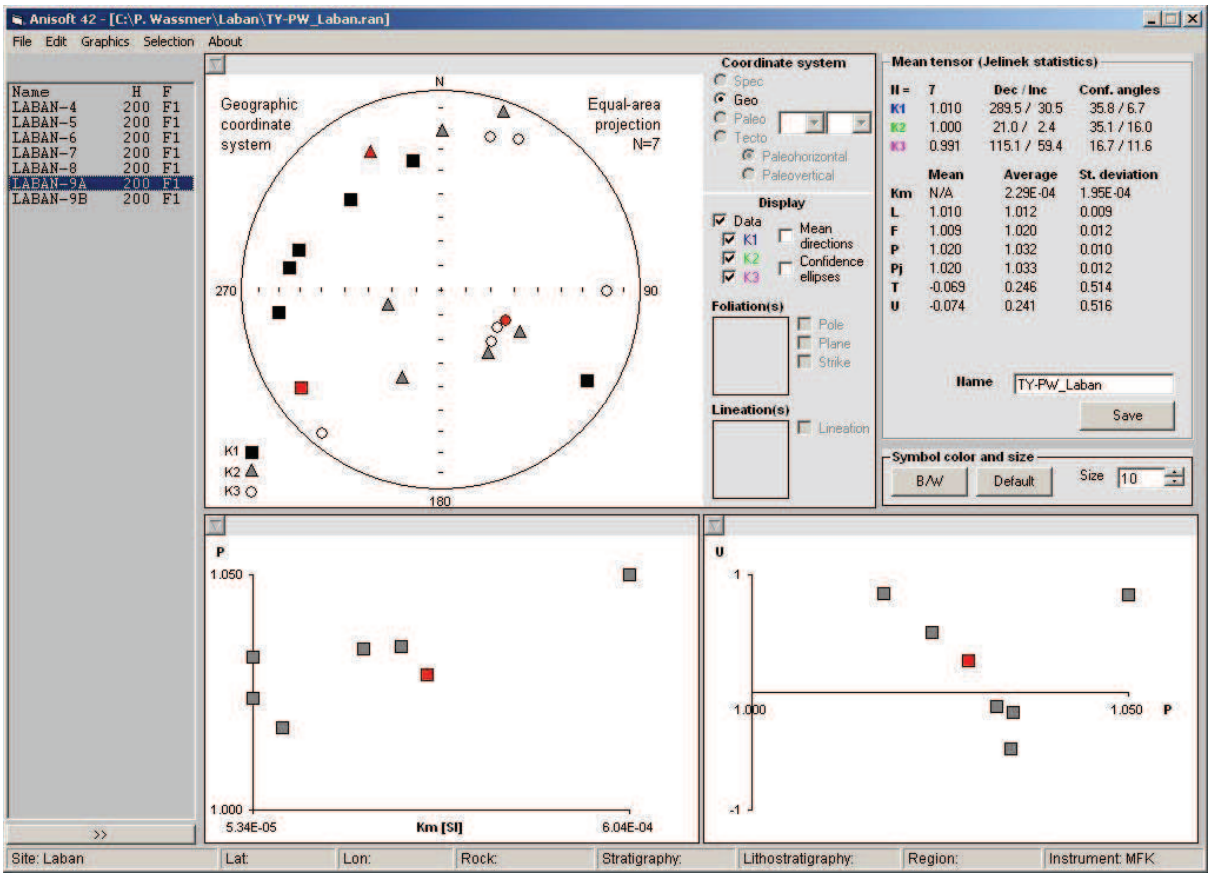
Anisoft 42 - [C:\P. Wassmer\Laban\TY-PW_Laban.ran]
File Edit Graphics Selection About
Name H F
LABAN-4 200 F1
LABAN-5 200 F1
LABAN-6 200 F1
LABAN-7 200 F1
LABAN-8 200 F1
LABAN-9A 200 F1
LABAN-9B 200 F1
Geographic coordinate system
Equal-area projection N=7
N
90
180
270
K1
K2
K3
Coordinate system
Spec
Geo
Paleo
Tecto
Paleohorizontal
Paleovertical
Display
Data
K1
K2
K3
Mean directions
Confidence ellipses
Foliation(s)
Pole
Plane
Strike
Lineation(s)
Lineation
Mean tensor (Jelinek statistics)
Dec / Inc
Conf. angles
Mean
Average
St. deviation
Km N/A 2.29E-04 1.95E-04
L 1.010 1.012 0.009
F 1.009 1.020 0.012
P 1.020 1.032 0.010
Pj 1.020 1.033 0.012
T -0.069 0.246 0.514
U -0.074 0.241 0.516
Name TY-PW_Laban
Save
Symbol color and size
B/W
Default
Size 10
P
1.050
1.000
5.34E-05
Km [SI]
6.04E-04
U
1
-1
Site: Laban
Lat:
Lon:
Rock:
Stratigraphy:
Lithostratigraphy:
Region:
Instrument: MFK

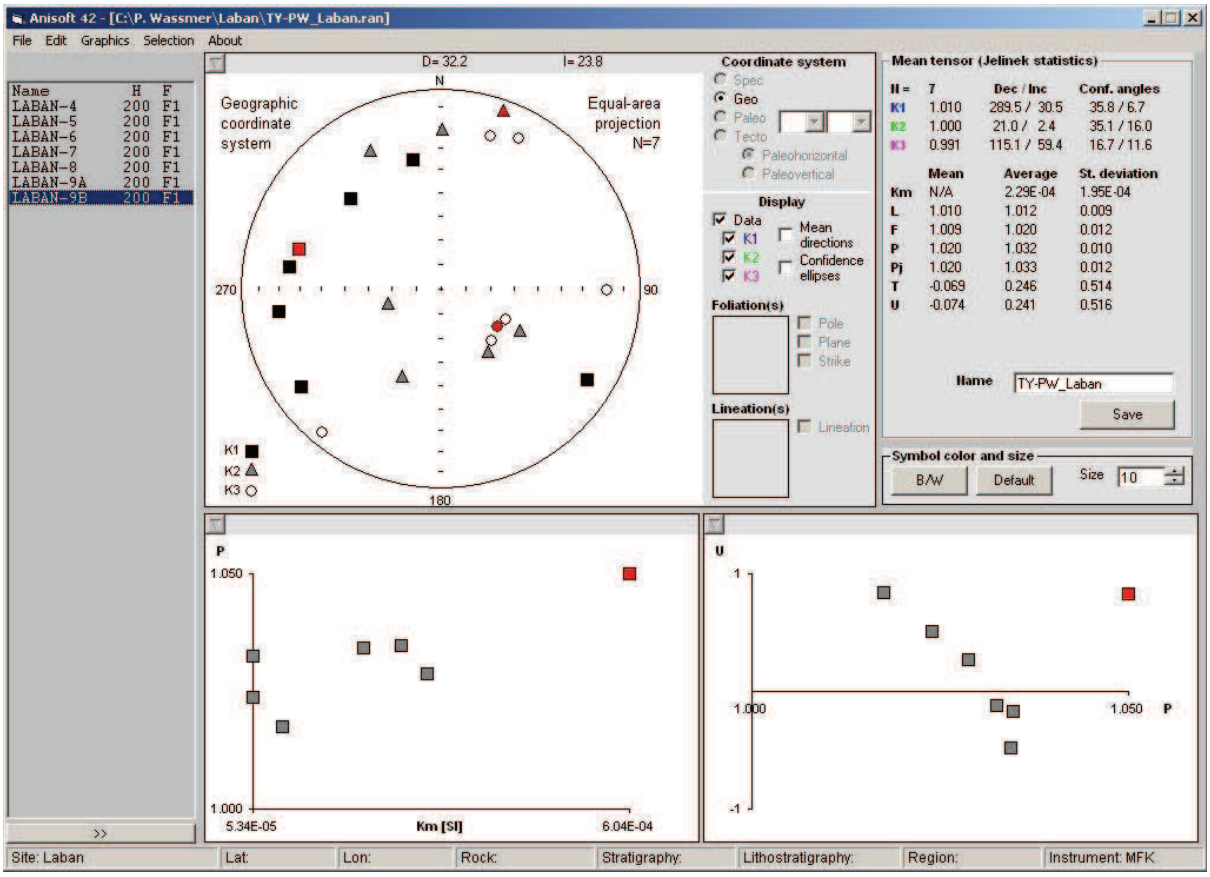
Anisoft 42 - [C:\P. Wassmer\Laban\TY-PW_Laban.ran]
File Edit Graphics Selection About
Name H F
LABAN-4 200 F1
LABAN-5 200 F1
LABAN-6 200 F1
LABAN-7 200 F1
LABAN-8 200 F1
LABAN-9A 200 F1
LABAN-9B 200 F1
D= 32.2 I= 23.8
Geographic coordinate system
Equal-area projection N=7
N
90
180
270
K1
K2
K3
Coordinate system
Spec
Geo
Paleo
Tecto
Paleohorizontal
Paleovertical
Display
Data
K1
K2
K3
Mean directions
Confidence ellipses
Foliation(s)
Pole
Plane
Strike
Lineation(s)
Lineation
Mean tensor (Jelinek statistics)
II = 7 Dec / Inc Conf. angles
K1 1.010 289.5 / 30.5 35.8 / 6.7
K2 1.000 21.0 / 2.4 35.1 / 16.0
K3 0.991 115.1 / 59.4 16.7 / 11.6
Mean Average St. deviation
Km N/A 2.29E-04 1.95E-04
L 1.010 1.012 0.009
F 1.009 1.020 0.012
P 1.020 1.032 0.010
Pj 1.020 1.033 0.012
T -0.069 0.246 0.514
U -0.074 0.241 0.516
Name TY-PW_Laban
Save
Symbol color and size
B/W
Default
Size 10
P
1.050
1.000
5.34E-05
Km [SI]
6.04E-04
U
1
1.000
-1
1.050
P
Site: Laban
Lat:
Lon:
Rock:
Stratigraphy:
Lithostratigraphy:
Region:
Instrument: MFK

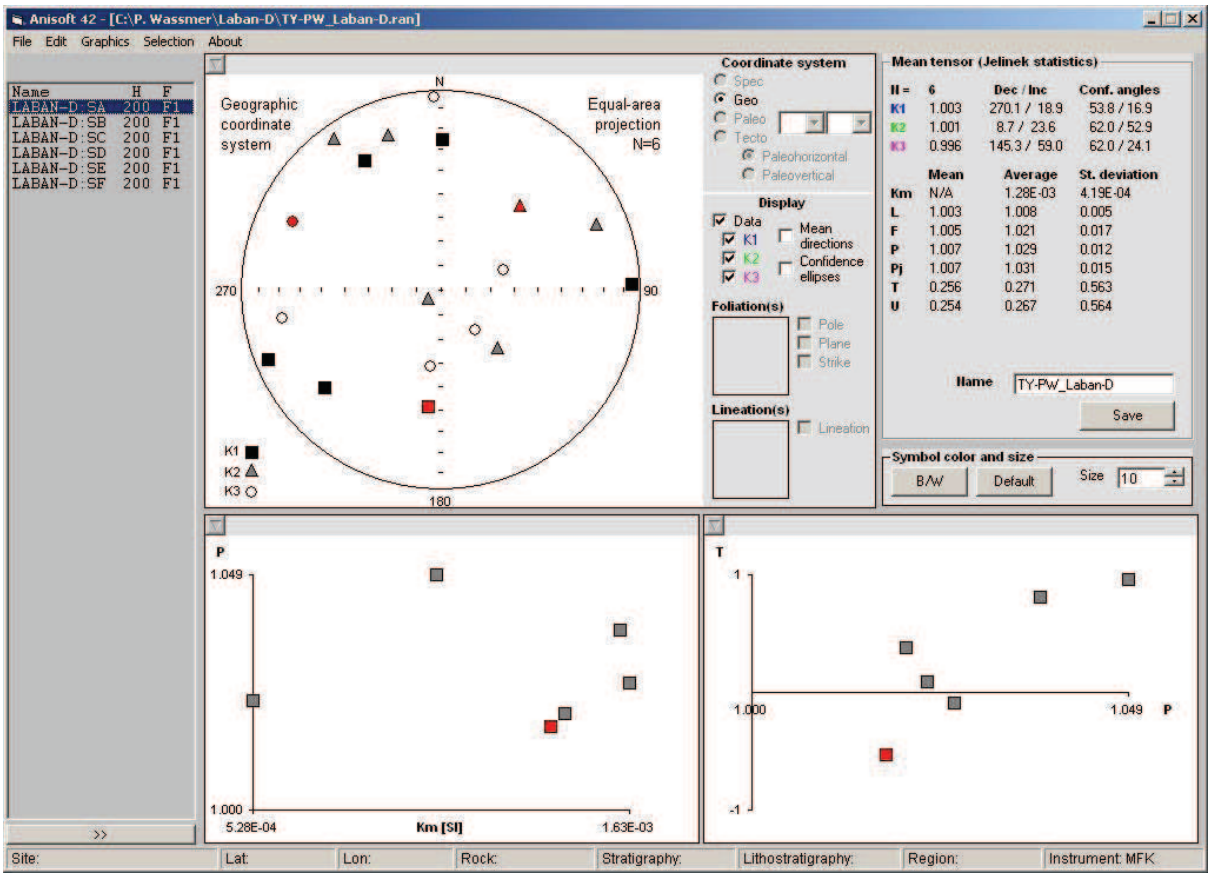
Anisoft 42 - [C:\P. Wassmer\Laban-D\TY-PW_Laban-D.ran]
File Edit Graphics Selection About
Name H F
LABAN-D:SA 200 F1
LABAN-D:SB 200 F1
LABAN-D:SC 200 F1
LABAN-D:SD 200 F1
LABAN-D:SE 200 F1
LABAN-D:SF 200 F1
Geographic coordinate system
Equal-area projection N=6
N
90
180
270
K1
K2
K3
Coordinate system
Spec
Geo
Paleo
Tecto
Paleohorizontal
Paleovertical
Display
Data
K1
K2
K3
Mean directions
Confidence ellipses
Foliation(s)
Pole
Plane
Strike
Lineation(s)
Lineation
Mean tensor (Jelinek statistics)
II = 6 Dec / Inc Conf. angles
K1 1.003 270.1 / 18.9 53.8 / 16.9
K2 1.001 8.7 / 23.6 62.0 / 52.9
K3 0.996 145.3 / 59.0 62.0 / 24.1
Mean Average St. deviation
Km N/A 1.28E-03 4.19E-04
L 1.003 1.008 0.005
F 1.005 1.021 0.017
P 1.007 1.029 0.012
Pj 1.007 1.031 0.015
T 0.256 0.271 0.563
U 0.254 0.267 0.564
Name TY-PW_Laban-D
Save
Symbol color and size
B/W
Default
Size 10
P
1.049
1.000
5.28E-04
Km [SI]
1.63E-03
T
1
1.000
-1
1.049
P
Site:
Lat:
Lon:
Rock:
Stratigraphy:
Lithostratigraphy:
Region:
Instrument: MFK

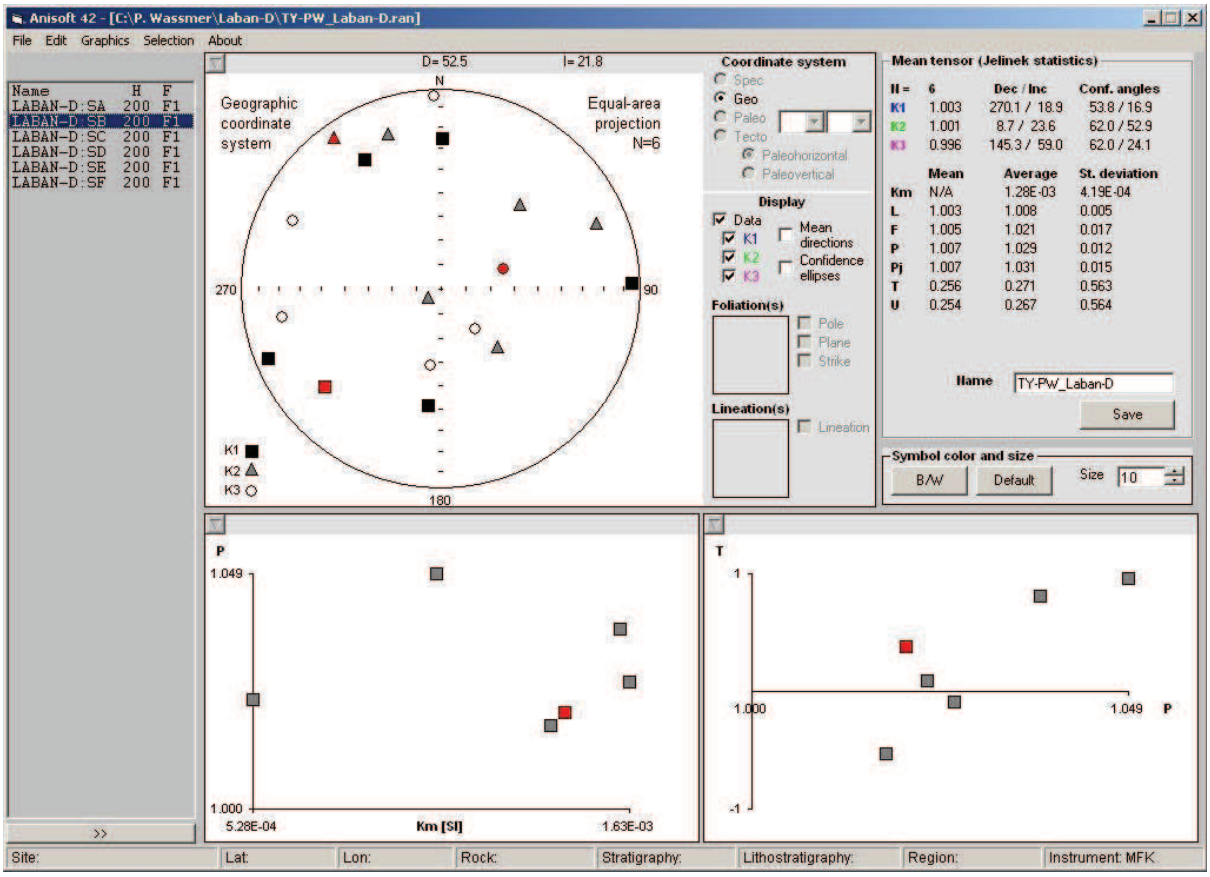
Anisoft 42 - [C:\P. Wassmer\Laban-D\TY-PW_Laban-D.ran]
File Edit Graphics Selection About
Name H F
LABAN-D:SA 200 F1
LABAN-D:SB 200 F1
LABAN-D:SC 200 F1
LABAN-D:SD 200 F1
LABAN-D:SE 200 F1
LABAN-D:SF 200 F1
D= 52.5 I= 21.8
Geographic coordinate system
Equal-area projection N=6
N
270
90
180
K1
K2
K3
Coordinate system
Spec
Geo
Paleo
Tecto
Paleohorizontal
Paleovertical
Display
Data
K1
K2
K3
Mean directions
Confidence ellipses
Foliation(s)
Pole
Plane
Strike
Lineation(s)
Lineation
Mean tensor (Jelinek statistics)
II = 6 Dec / Inc Conf. angles
K1 1.003 270.1 / 18.9 53.8 / 16.9
K2 1.001 8.7 / 23.6 62.0 / 52.9
K3 0.996 145.3 / 59.0 62.0 / 24.1
Mean Average St. deviation
Km N/A 1.28E-03 4.19E-04
L 1.003 1.008 0.005
F 1.005 1.021 0.017
P 1.007 1.029 0.012
Pj 1.007 1.031 0.015
T 0.256 0.271 0.563
U 0.254 0.267 0.564
Name TY-PW_Laban-D
Save
Symbol color and size
B/W
Default
Size 10
P
1.049
1.000
5.28E-04
Km [SI]
1.63E-03
T
1
1.000
1.049
P
-1
Site:
Lat:
Lon:
Rock:
Stratigraphy:
Lithostratigraphy:
Region:
Instrument: MFK

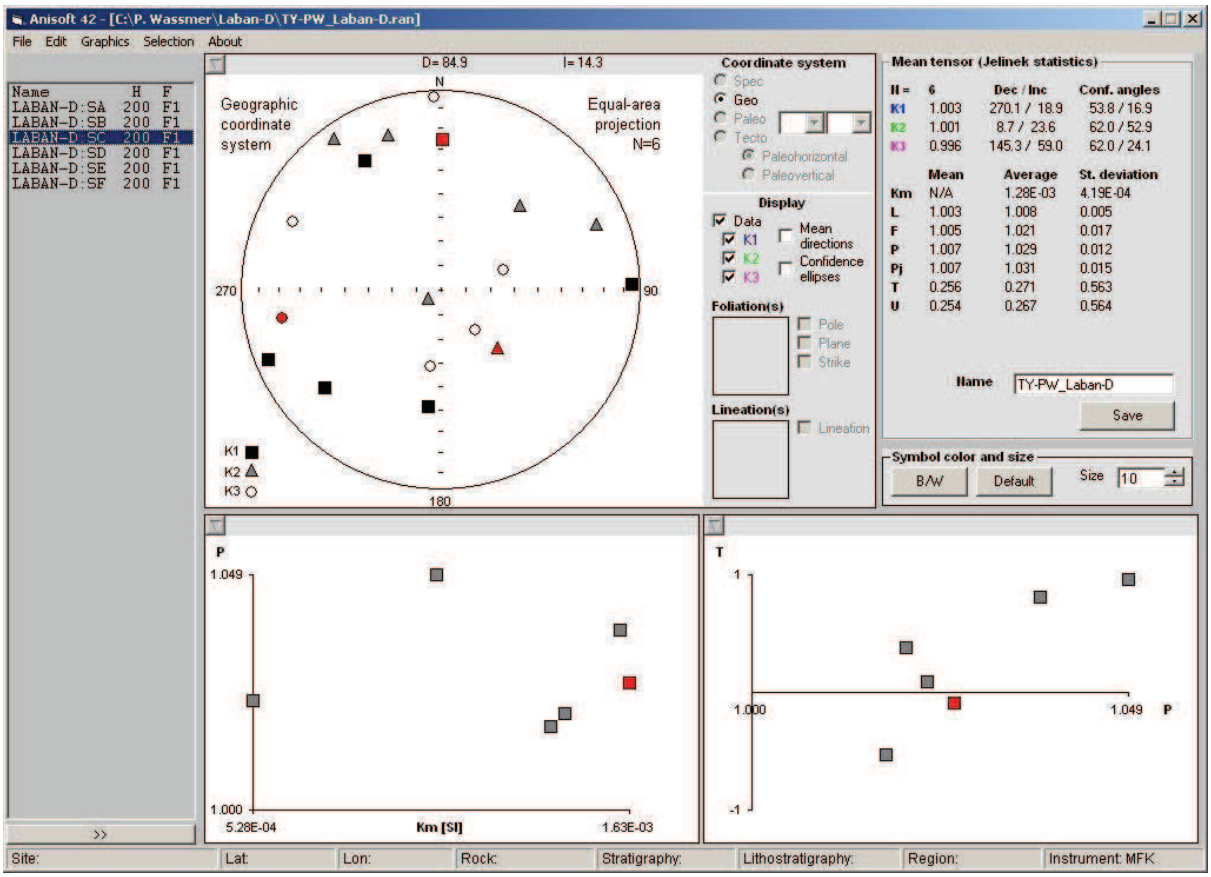
Anisoft 42 - [C:\P. Wassmer\Laban-D\TY-PW_Laban-D.ran]
File Edit Graphics Selection About
Name H F
LABAN-D:SA 200 F1
LABAN-D:SB 200 F1
LABAN-D:SC 200 F1
LABAN-D:SD 200 F1
LABAN-D:SE 200 F1
LABAN-D:SF 200 F1
D= 84.9 I= 14.3
Geographic coordinate system
Equal-area projection N=6
N
270
90
180
K1
K2
K3
Coordinate system
Spec
Geo
Paleo
Tecto
Paleohorizontal
Paleovertical
Display
Data
K1
K2
K3
Mean directions
Confidence ellipses
Foliation(s)
Pole
Plane
Strike
Lineation(s)
Lineation
Mean tensor (Jelinek statistics)
II = 6 Dec / Inc Conf. angles
K1 1.003 270.1 / 18.9 53.8 / 16.9
K2 1.001 8.7 / 23.6 62.0 / 52.9
K3 0.996 145.3 / 59.0 62.0 / 24.1
Mean Average St. deviation
Km N/A 1.28E-03 4.19E-04
L 1.003 1.008 0.005
F 1.005 1.021 0.017
P 1.007 1.029 0.012
Pj 1.007 1.031 0.015
T 0.256 0.271 0.563
U 0.254 0.267 0.564
Name TY-PW_Laban-D
Save
Symbol color and size
B/W
Default
Size 10
P
1.049
1.000
5.28E-04
Km [SI]
1.63E-03
T
1
1.000
1.049
P
-1
Site:
Lat:
Lon:
Rock:
Stratigraphy:
Lithostratigraphy:
Region:
Instrument: MFK

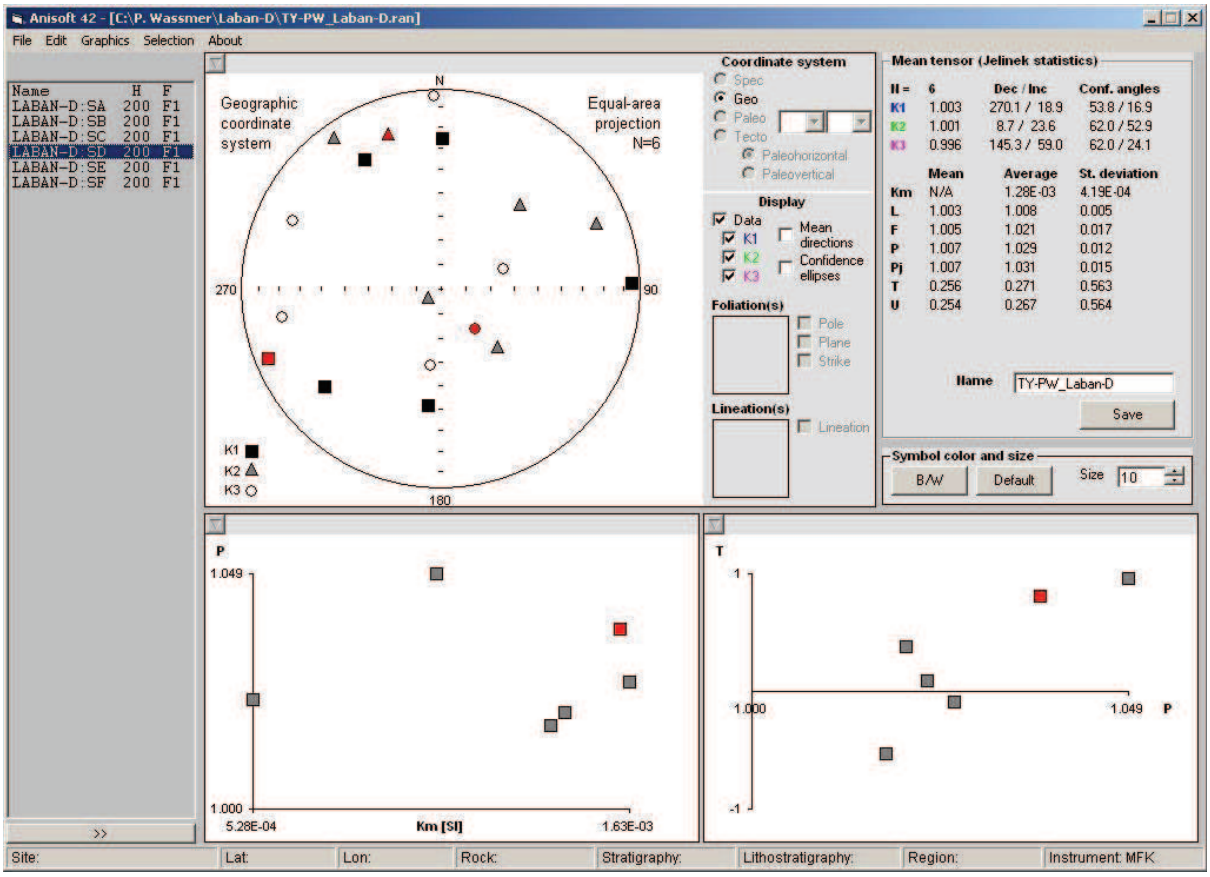
Anisoft 42 - [C:\P. Wassmer\Laban-D\TY-PW_Laban-D.ran]
File Edit Graphics Selection About
Name H F
LABAN-D:SA 200 F1
LABAN-D:SB 200 F1
LABAN-D:SC 200 F1
LABAN-D:SD 200 F1
LABAN-D:SE 200 F1
LABAN-D:SF 200 F1
Geographic coordinate system
Equal-area projection N=6
N
270
90
180
K1
K2
K3
Coordinate system
Spec
Geo
Paleo
Tecto
Paleohorizontal
Paleovertical
Display
Data
K1
K2
K3
Mean directions
Confidence ellipses
Foliation(s)
Pole
Plane
Strike
Lineation(s)
Lineation
Mean tensor (Jelinek statistics)
II = 6 Dec / Inc Conf. angles
K1 1.003 270.1 / 18.9 53.8 / 16.9
K2 1.001 8.7 / 23.6 62.0 / 52.9
K3 0.996 145.3 / 59.0 62.0 / 24.1
Mean Average St. deviation
Km N/A 1.28E-03 4.19E-04
L 1.003 1.008 0.005
F 1.005 1.021 0.017
P 1.007 1.029 0.012
Pj 1.007 1.031 0.015
T 0.256 0.271 0.563
U 0.254 0.267 0.564
Name TY-PW_Laban-D
Save
Symbol color and size
B/W
Default
Size 10
P
1.049
1.000
5.28E-04
Km [SI]
1.63E-03
T
1
1.000
1.049
P
-1
Site:
Lat:
Lon:
Rock:
Stratigraphy:
Lithostratigraphy:
Region:
Instrument: MFK

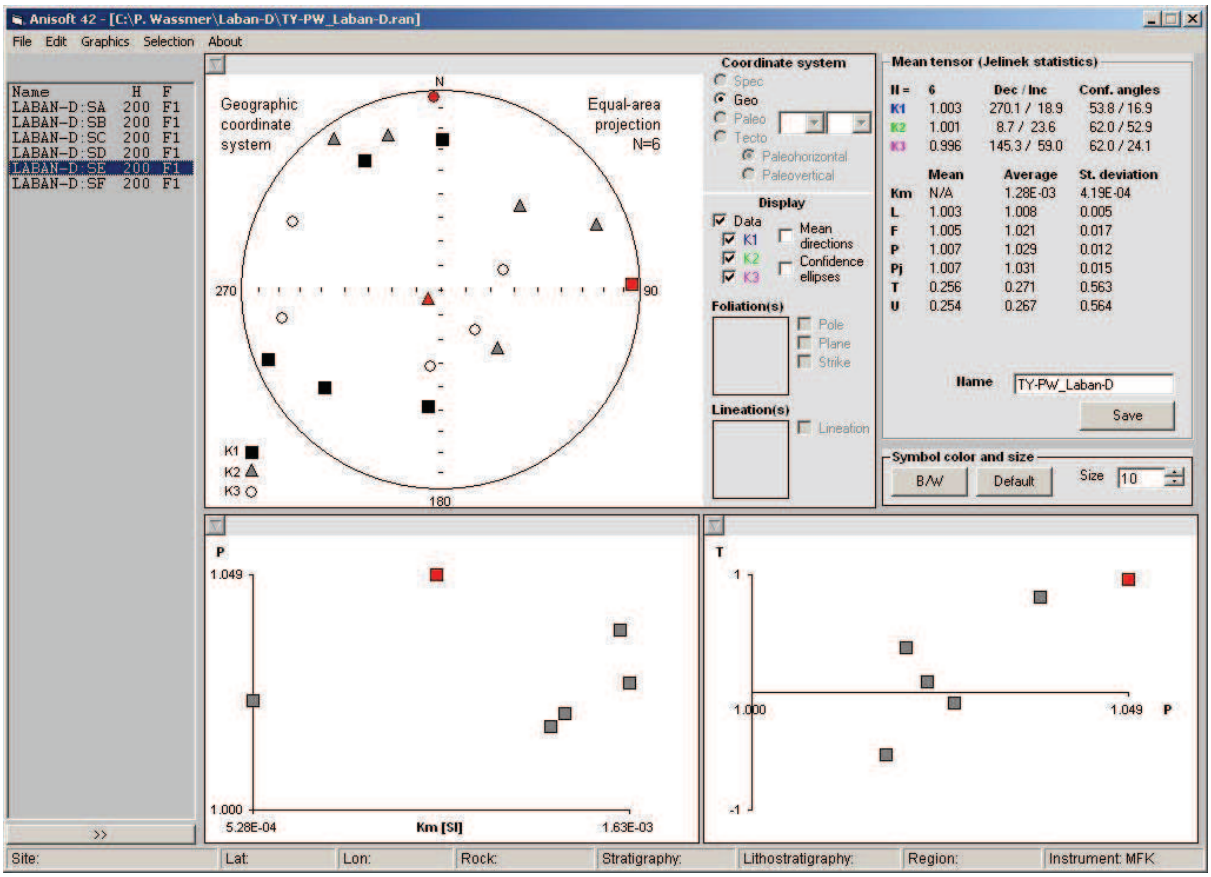
Anisoft 42 - [C:\P. Wassmer\Laban-D\TY-PW_Laban-D.ran]
File Edit Graphics Selection About
Name H F
LABAN-D:SA 200 F1
LABAN-D:SB 200 F1
LABAN-D:SC 200 F1
LABAN-D:SD 200 F1
LABAN-D:SE 200 F1
LABAN-D:SF 200 F1
Geographic coordinate system
Equal-area projection N=6
N
270
90
180
K1
K2
K3
Coordinate system
Spec
Geo
Paleo
Tecto
Paleohorizontal
Paleovertical
Display
Data
K1
K2
K3
Mean directions
Confidence ellipses
Foliation(s)
Pole
Plane
Strike
Lineation(s)
Lineation
Mean tensor (Jelinek statistics)
II = 6 Dec / Inc Conf. angles
K1 1.003 270.1 / 18.9 53.8 / 16.9
K2 1.001 8.7 / 23.6 62.0 / 52.9
K3 0.996 145.3 / 59.0 62.0 / 24.1
Mean Average St. deviation
Km N/A 1.28E-03 4.19E-04
L 1.003 1.008 0.005
F 1.005 1.021 0.017
P 1.007 1.029 0.012
Pj 1.007 1.031 0.015
T 0.256 0.271 0.563
U 0.254 0.267 0.564
Name TY-PW_Laban-D
Save
Symbol color and size
B/W
Default
Size 10
P
1.049
1.000
5.28E-04
Km [SI]
1.63E-03
T
1
1.000
1.049
P
-1
Site:
Lat:
Lon:
Rock:
Stratigraphy:
Lithostratigraphy:
Region:
Instrument: MFK

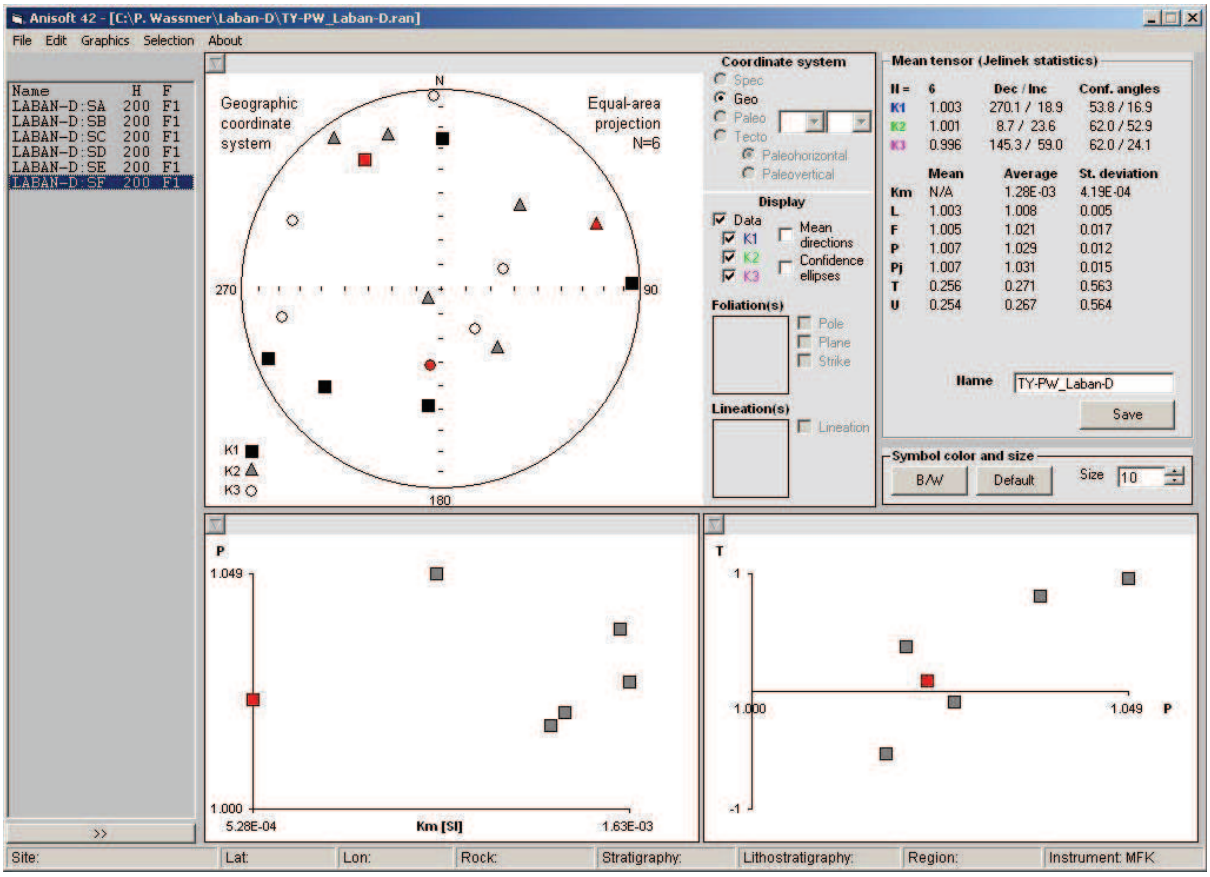
Anisoft 42 - [C:\P. Wassmer\Laban-D\TY-PW_Laban-D.ran]
File Edit Graphics Selection About
Name H F
LABAN-D:SA 200 F1
LABAN-D:SB 200 F1
LABAN-D:SC 200 F1
LABAN-D:SD 200 F1
LABAN-D:SE 200 F1
LABAN-D:SF 200 F1
Geographic coordinate system
Equal-area projection N=6
N
90
180
270
K1
K2
K3
Coordinate system
Spec
Geo
Paleo
Tecto
Paleohorizontal
Paleovertical
Display
Data
K1
K2
K3
Mean directions
Confidence ellipses
Foliation(s)
Pole
Plane
Strike
Lineation(s)
Lineation
Mean tensor (Jelinek statistics)
II = 6 Dec / Inc Conf. angles
K1 1.003 270.1 / 18.9 53.8 / 16.9
K2 1.001 8.7 / 23.6 62.0 / 52.9
K3 0.996 145.3 / 59.0 62.0 / 24.1
Mean Average St. deviation
Km N/A 1.28E-04 4.19E-04
L 1.003 1.008 0.005
F 1.005 1.021 0.017
P 1.007 1.029 0.012
Pj 1.007 1.031 0.015
T 0.256 0.271 0.563
U 0.254 0.267 0.564
Name TY-PW_Laban-D
Save
Symbol color and size
B/W
Default
Size 10
P
1.049
1.000
5.28E-04
Km [SI]
1.63E-03
T
1
1.000
1.049
P
-1
Site:
Lat:
Lon:
Rock:
Stratigraphy:
Lithostratigraphy:
Region:
Instrument: MFK

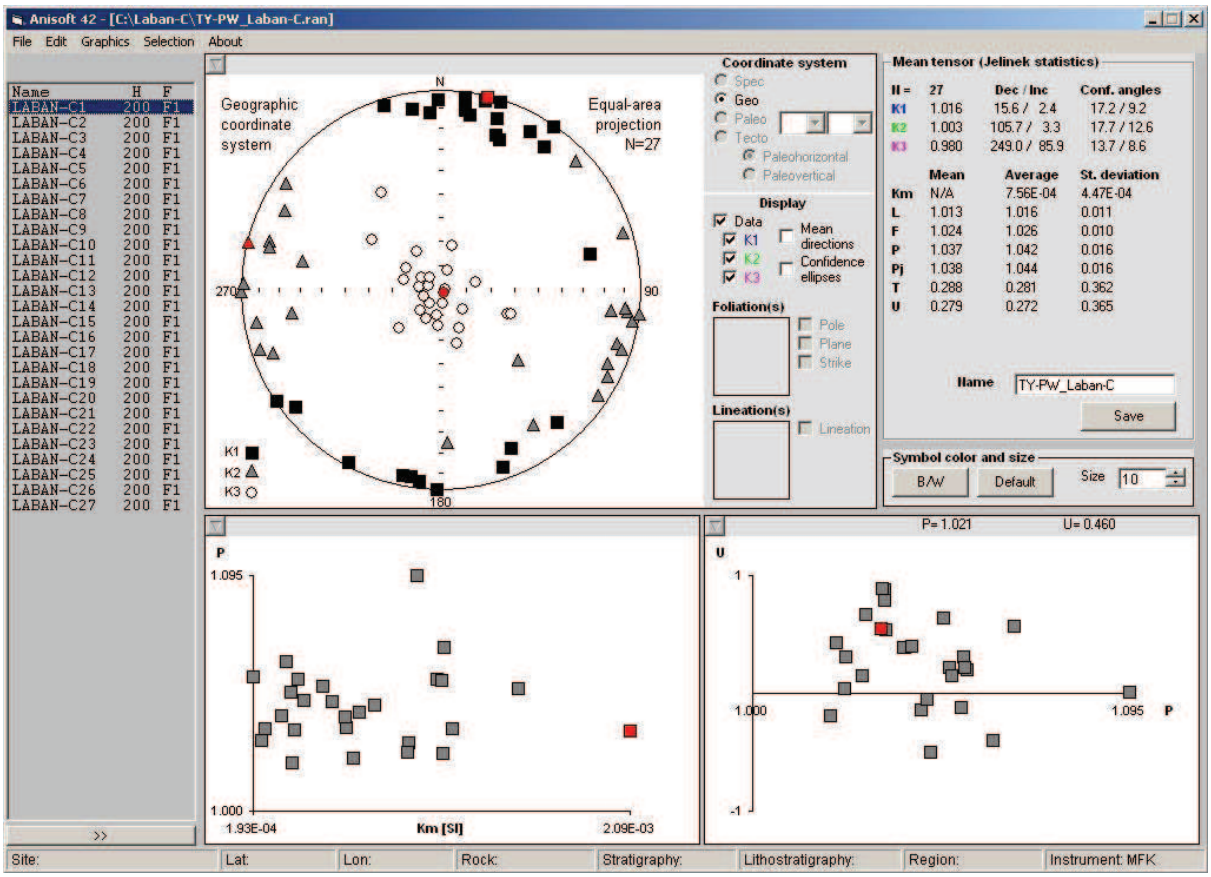
Anisoft 42 - [C:\Laban-C\TY-PW_Laban-C.ran]
File Edit Graphics Selection About
Name H F
LABAN-C1 200 F1
LABAN-C2 200 F1
LABAN-C3 200 F1
LABAN-C4 200 F1
LABAN-C5 200 F1
LABAN-C6 200 F1
LABAN-C7 200 F1
LABAN-C8 200 F1
LABAN-C9 200 F1
LABAN-C10 200 F1
LABAN-C11 200 F1
LABAN-C12 200 F1
LABAN-C13 200 F1
LABAN-C14 200 F1
LABAN-C15 200 F1
LABAN-C16 200 F1
LABAN-C17 200 F1
LABAN-C18 200 F1
LABAN-C19 200 F1
LABAN-C20 200 F1
LABAN-C21 200 F1
LABAN-C22 200 F1
LABAN-C23 200 F1
LABAN-C24 200 F1
LABAN-C25 200 F1
LABAN-C26 200 F1
LABAN-C27 200 F1
Geographic coordinate system
Equal-area projection N=27
N
90
180
270
K1
K2
K3
Coordinate system
Spec
Geo
Paleo
Tecto
Paleohorizontal
Paleovertical
Display
Data
K1
K2
K3
Mean directions
Confidence ellipses
Foliation(s)
Pole
Plane
Strike
Lineation(s)
Lineation
Mean tensor (Jelinek statistics)
II = 27 Dec / Inc Conf. angles
K1 1.016 15.6 / 2.4 17.2 / 9.2
K2 1.003 105.7 / 3.3 17.7 / 12.6
K3 0.980 249.0 / 85.9 13.7 / 8.6
Mean Average St. deviation
Km N/A 7.56E-04 4.47E-04
L 1.013 1.016 0.011
F 1.024 1.026 0.010
P 1.037 1.042 0.016
Pj 1.038 1.044 0.016
T 0.288 0.281 0.362
U 0.279 0.272 0.365
Name TY-PW_Laban-C
Save
Symbol color and size
B/W
Default
Size 10
P= 1.021
U= 0.460
P
1.095
1.000
1.93E-04
Km [SI]
2.09E-03
U
1
1.000
1.095
P
-1
Site:
Lat:
Lon:
Rock:
Stratigraphy:
Lithostratigraphy:
Region:
Instrument: MFK

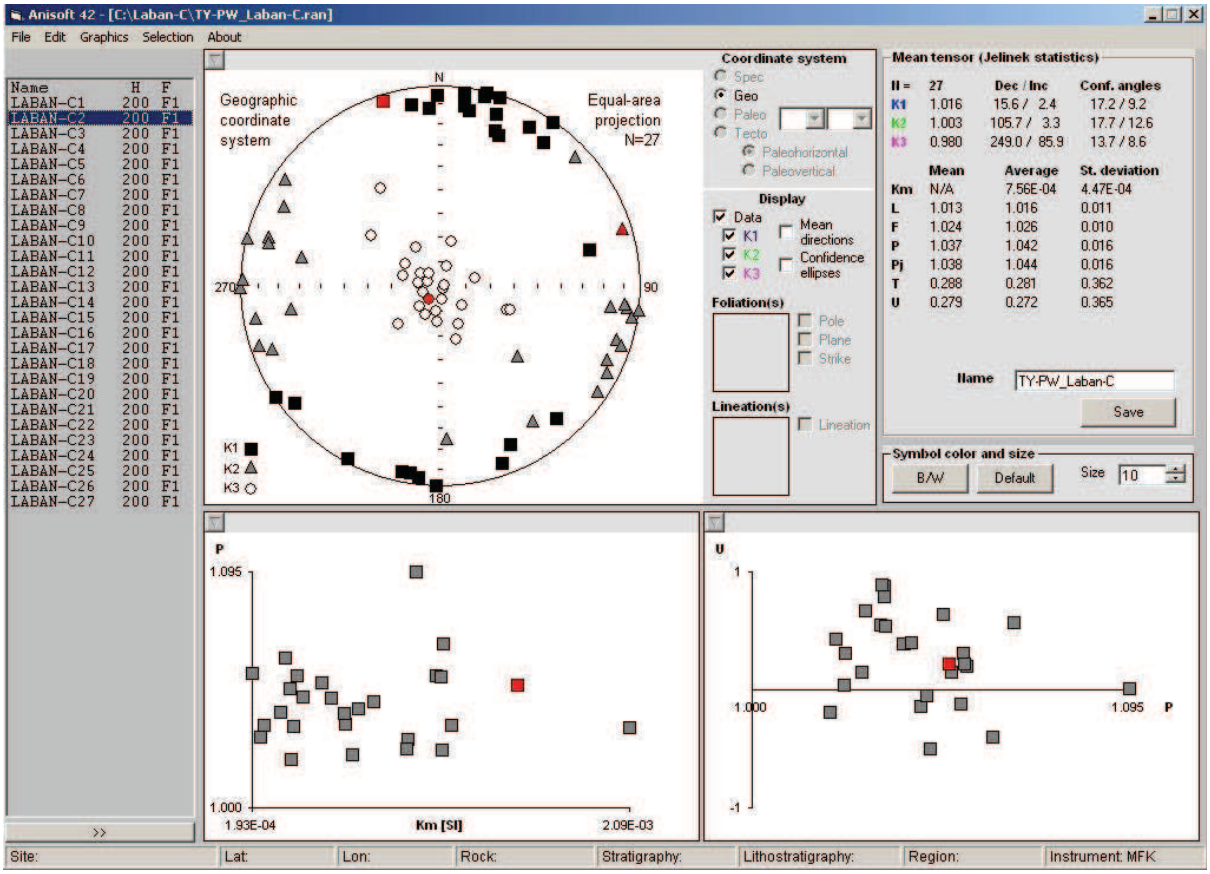
Anisoft 42 - [C:\Laban-C\TY-PW_Laban-C.ran]
File Edit Graphics Selection About
Name H F
LABAN-C1 200 F1
LABAN-C2 200 F1
LABAN-C3 200 F1
LABAN-C4 200 F1
LABAN-C5 200 F1
LABAN-C6 200 F1
LABAN-C7 200 F1
LABAN-C8 200 F1
LABAN-C9 200 F1
LABAN-C10 200 F1
LABAN-C11 200 F1
LABAN-C12 200 F1
LABAN-C13 200 F1
LABAN-C14 200 F1
LABAN-C15 200 F1
LABAN-C16 200 F1
LABAN-C17 200 F1
LABAN-C18 200 F1
LABAN-C19 200 F1
LABAN-C20 200 F1
LABAN-C21 200 F1
LABAN-C22 200 F1
LABAN-C23 200 F1
LABAN-C24 200 F1
LABAN-C25 200 F1
LABAN-C26 200 F1
LABAN-C27 200 F1
Geographic coordinate system
Equal-area projection N=27
N
90
180
270
K1
K2
K3
Coordinate system
Spec
Geo
Paleo
Tecto
Paleohorizontal
Paleovertical
Display
Data
K1
K2
K3
Mean directions
Confidence ellipses
Foliation(s)
Pole
Plane
Strike
Lineation(s)
Lineation
Mean tensor (Jelinek statistics)
II = 27 Dec / Inc Conf. angles
K1 1.016 15.6 / 2.4 17.2 / 9.2
K2 1.003 105.7 / 3.3 17.7 / 12.6
K3 0.980 249.0 / 85.9 13.7 / 8.6
Mean Average St. deviation
Km N/A 7.56E-04 4.47E-04
L 1.013 1.016 0.011
F 1.024 1.026 0.010
P 1.037 1.042 0.016
Pj 1.038 1.044 0.016
T 0.288 0.281 0.362
U 0.279 0.272 0.365
Name TY-PW_Laban-C
Save
Symbol color and size
B/W
Default
Size 10
P
1.095
1.000
1.93E-04
Km [SI]
2.09E-03
U
1
-1
1.000
1.095
P
Site:
Lat:
Lon:
Rock:
Stratigraphy:
Lithostratigraphy:
Region:
Instrument: MFK

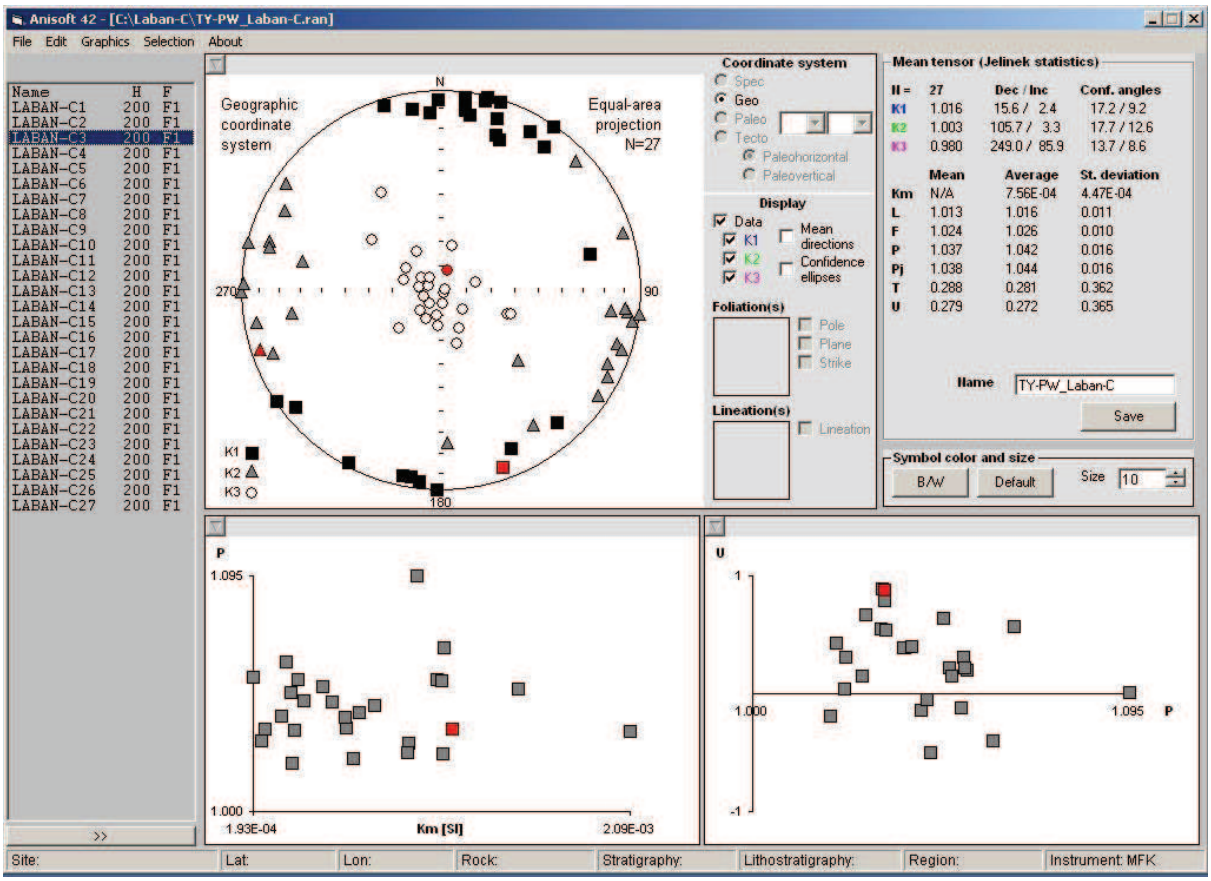
Anisoft 42 - [C:\Laban-C\TY-PW_Laban-C.ran]
File Edit Graphics Selection About
Name H F
LABAN-C1 200 F1
LABAN-C2 200 F1
LABAN-C3 200 F1
LABAN-C4 200 F1
LABAN-C5 200 F1
LABAN-C6 200 F1
LABAN-C7 200 F1
LABAN-C8 200 F1
LABAN-C9 200 F1
LABAN-C10 200 F1
LABAN-C11 200 F1
LABAN-C12 200 F1
LABAN-C13 200 F1
LABAN-C14 200 F1
LABAN-C15 200 F1
LABAN-C16 200 F1
LABAN-C17 200 F1
LABAN-C18 200 F1
LABAN-C19 200 F1
LABAN-C20 200 F1
LABAN-C21 200 F1
LABAN-C22 200 F1
LABAN-C23 200 F1
LABAN-C24 200 F1
LABAN-C25 200 F1
LABAN-C26 200 F1
LABAN-C27 200 F1
Geographic coordinate system
Equal-area projection N=27
N
90
180
270
K1
K2
K3
Coordinate system
Spec
Geo
Paleo
Tecto
Paleohorizontal
Paleovertical
Display
Data
K1
K2
K3
Mean directions
Confidence ellipses
Foliation(s)
Pole
Plane
Strike
Lineation(s)
Lineation
Mean tensor (Jelinek statistics)
II = 27 Dec / Inc Conf. angles
K1 1.016 15.6 / 2.4 17.2 / 9.2
K2 1.003 105.7 / 3.3 17.7 / 12.6
K3 0.980 249.0 / 85.9 13.7 / 8.6
Mean Average St. deviation
Km N/A 7.56E-04 4.47E-04
L 1.013 1.016 0.011
F 1.024 1.026 0.010
P 1.037 1.042 0.016
Pj 1.038 1.044 0.016
T 0.288 0.281 0.362
U 0.279 0.272 0.365
Name TY-PW_Laban-C
Save
Symbol color and size
B/W
Default
Size 10
P
1.095
1.000
1.93E-04
Km [SI]
2.09E-03
U
1
-1
1.000
1.095
P
Site:
Lat:
Lon:
Rock:
Stratigraphy:
Lithostratigraphy:
Region:
Instrument: MFK

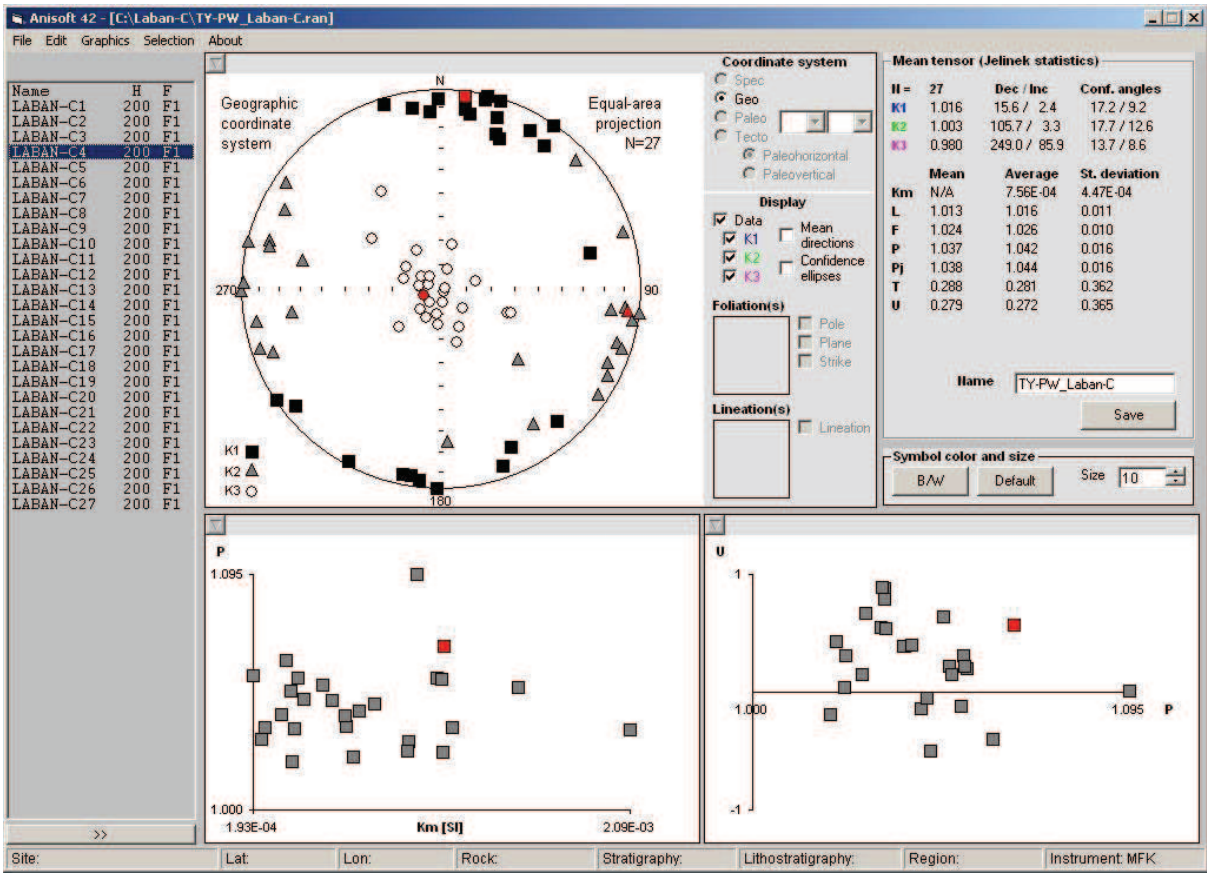
Anisoft 42 - [C:\Laban-C\TY-PW_Laban-C.ran]
File Edit Graphics Selection About
Name H F
LABAN-C1 200 F1
LABAN-C2 200 F1
LABAN-C3 200 F1
LABAN-C4 200 F1
LABAN-C5 200 F1
LABAN-C6 200 F1
LABAN-C7 200 F1
LABAN-C8 200 F1
LABAN-C9 200 F1
LABAN-C10 200 F1
LABAN-C11 200 F1
LABAN-C12 200 F1
LABAN-C13 200 F1
LABAN-C14 200 F1
LABAN-C15 200 F1
LABAN-C16 200 F1
LABAN-C17 200 F1
LABAN-C18 200 F1
LABAN-C19 200 F1
LABAN-C20 200 F1
LABAN-C21 200 F1
LABAN-C22 200 F1
LABAN-C23 200 F1
LABAN-C24 200 F1
LABAN-C25 200 F1
LABAN-C26 200 F1
LABAN-C27 200 F1
Geographic coordinate system
Equal-area projection N=27
N
90
180
270
K1
K2
K3
Coordinate system
Spec
Geo
Paleo
Tecto
Paleohorizontal
Paleovertical
Display
Data
K1
K2
K3
Mean directions
Confidence ellipses
Foliation(s)
Pole
Plane
Strike
Lineation(s)
Lineation
Mean tensor (Jelinek statistics)
II = 27 Dec / Inc Conf. angles
K1 1.016 15.6 / 2.4 17.2 / 9.2
K2 1.003 105.7 / 3.3 17.7 / 12.6
K3 0.980 249.0 / 85.9 13.7 / 8.6
Mean Average St. deviation
Km N/A 7.56E-04 4.47E-04
L 1.013 1.016 0.011
F 1.024 1.026 0.010
P 1.037 1.042 0.016
Pj 1.038 1.044 0.016
T 0.288 0.281 0.362
U 0.279 0.272 0.365
Name TY-PW_Laban-C
Save
Symbol color and size
B/W
Default
Size 10
P
1.095
1.000
1.93E-04
Km [SI]
2.09E-03
U
1
-1
Site:
Lat:
Lon:
Rock:
Stratigraphy:
Lithostratigraphy:
Region:
Instrument: MFK

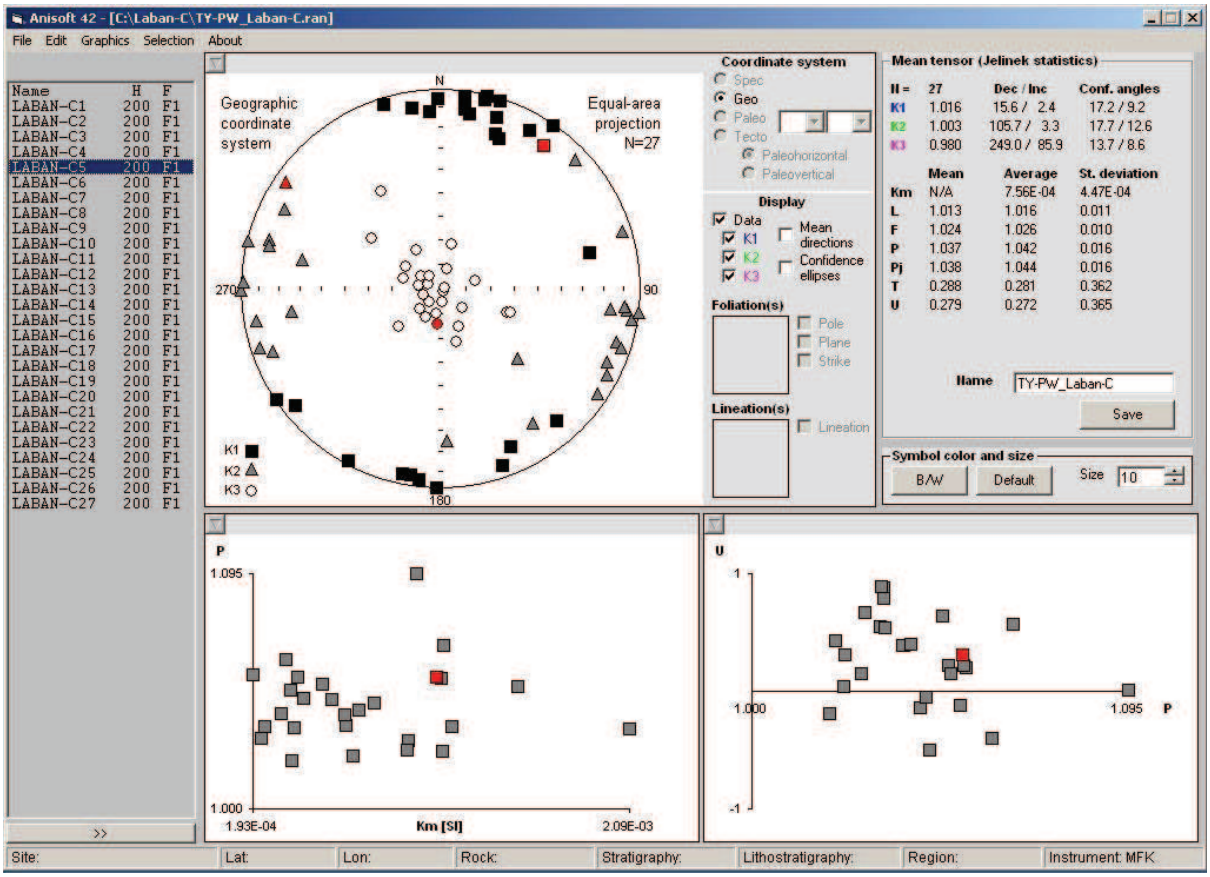
Anisoft 42 - [C:\Laban-C\TY-PW_Laban-C.ran]
File Edit Graphics Selection About
Name H F
LABAN-C1 200 F1
LABAN-C2 200 F1
LABAN-C3 200 F1
LABAN-C4 200 F1
LABAN-C5 200 F1
LABAN-C6 200 F1
LABAN-C7 200 F1
LABAN-C8 200 F1
LABAN-C9 200 F1
LABAN-C10 200 F1
LABAN-C11 200 F1
LABAN-C12 200 F1
LABAN-C13 200 F1
LABAN-C14 200 F1
LABAN-C15 200 F1
LABAN-C16 200 F1
LABAN-C17 200 F1
LABAN-C18 200 F1
LABAN-C19 200 F1
LABAN-C20 200 F1
LABAN-C21 200 F1
LABAN-C22 200 F1
LABAN-C23 200 F1
LABAN-C24 200 F1
LABAN-C25 200 F1
LABAN-C26 200 F1
LABAN-C27 200 F1
Geographic coordinate system
Equal-area projection N=27
N
90
180
270
K1
K2
K3
Coordinate system
Spec
Geo
Paleo
Tecto
Paleohorizontal
Paleovertical
Display
Data
K1
K2
K3
Mean directions
Confidence ellipses
Foliation(s)
Pole
Plane
Strike
Lineation(s)
Lineation
Mean tensor (Jelinek statistics)
II = 27 Dec / Inc Conf. angles
K1 1.016 15.6 / 2.4 17.2 / 9.2
K2 1.003 105.7 / 3.3 17.7 / 12.6
K3 0.980 249.0 / 85.9 13.7 / 8.6
Mean Average St. deviation
Km N/A 7.56E-04 4.47E-04
L 1.013 1.016 0.011
F 1.024 1.026 0.010
P 1.037 1.042 0.016
Pj 1.038 1.044 0.016
T 0.288 0.281 0.362
U 0.279 0.272 0.365
Name TY-PW_Laban-C
Save
Symbol color and size
B/W
Default
Size 10
P
1.095
1.000
1.93E-04
Km [SI]
2.09E-03
U
1
-1
Site:
Lat:
Lon:
Rock:
Stratigraphy:
Lithostratigraphy:
Region:
Instrument: MFK

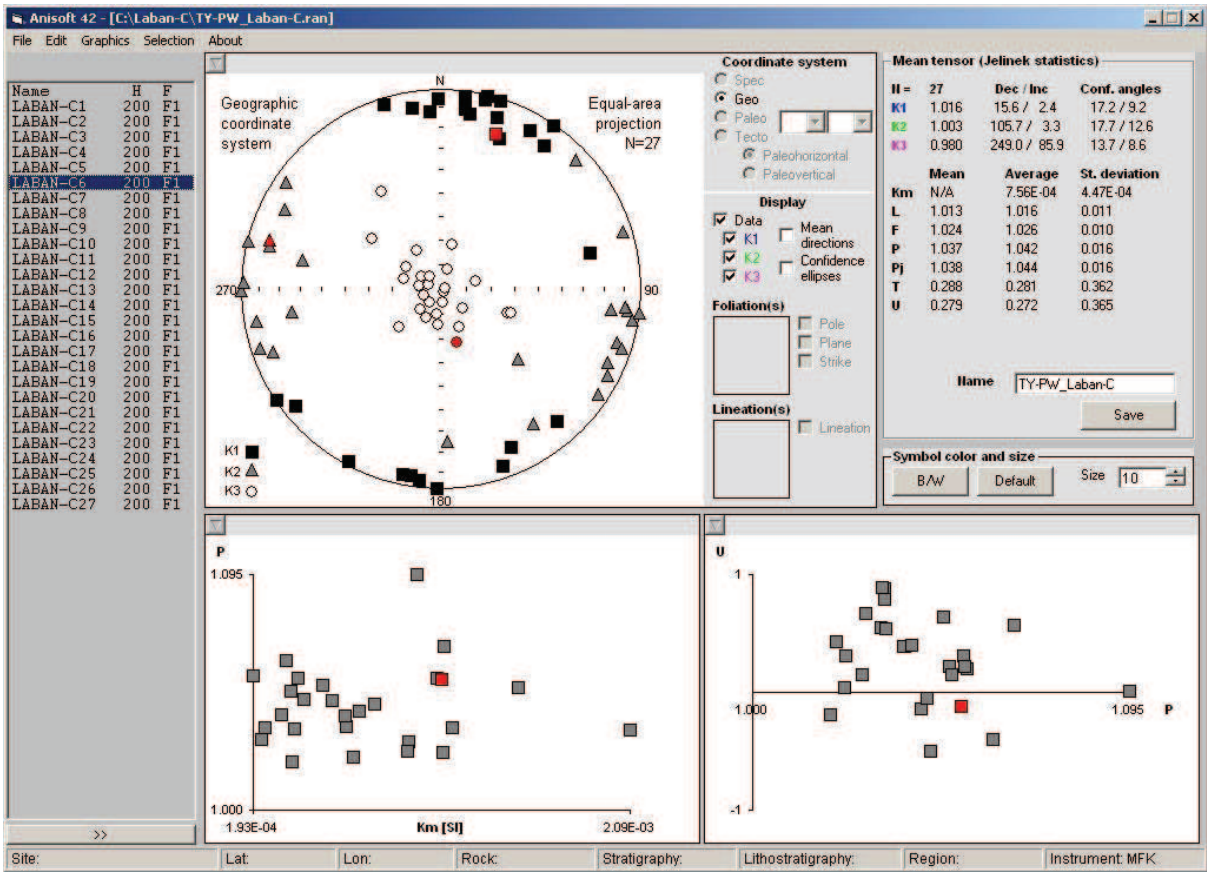
Anisoft 42 - [C:\Laban-C\TY-PW_Laban-C.ran]
File Edit Graphics Selection About
Name H F
LABAN-C1 200 F1
LABAN-C2 200 F1
LABAN-C3 200 F1
LABAN-C4 200 F1
LABAN-C5 200 F1
LABAN-C6 200 F1
LABAN-C7 200 F1
LABAN-C8 200 F1
LABAN-C9 200 F1
LABAN-C10 200 F1
LABAN-C11 200 F1
LABAN-C12 200 F1
LABAN-C13 200 F1
LABAN-C14 200 F1
LABAN-C15 200 F1
LABAN-C16 200 F1
LABAN-C17 200 F1
LABAN-C18 200 F1
LABAN-C19 200 F1
LABAN-C20 200 F1
LABAN-C21 200 F1
LABAN-C22 200 F1
LABAN-C23 200 F1
LABAN-C24 200 F1
LABAN-C25 200 F1
LABAN-C26 200 F1
LABAN-C27 200 F1
Geographic coordinate system
Equal-area projection N=27
N
90
180
270
K1
K2
K3
Coordinate system
Spec
Geo
Paleo
Tecto
Paleohorizontal
Paleovertical
Display
Data
K1
K2
K3
Mean directions
Confidence ellipses
Foliation(s)
Pole
Plane
Strike
Lineation(s)
Lineation
Mean tensor (Jelinek statistics)
II = 27 Dec / Inc Conf. angles
K1 1.016 15.6 / 2.4 17.2 / 9.2
K2 1.003 105.7 / 3.3 17.7 / 12.6
K3 0.980 249.0 / 85.9 13.7 / 8.6
Mean Average St. deviation
Km N/A 7.56E-04 4.47E-04
L 1.013 1.016 0.011
F 1.024 1.026 0.010
P 1.037 1.042 0.016
Pj 1.038 1.044 0.016
T 0.288 0.281 0.362
U 0.279 0.272 0.365
Name TY-PW_Laban-C
Save
Symbol color and size
B/W
Default
Size 10
P
1.095
1.000
1.93E-04
Km [SI]
2.09E-03
U
1
-1
Site:
Lat:
Lon:
Rock:
Stratigraphy:
Lithostratigraphy:
Region:
Instrument: MFK

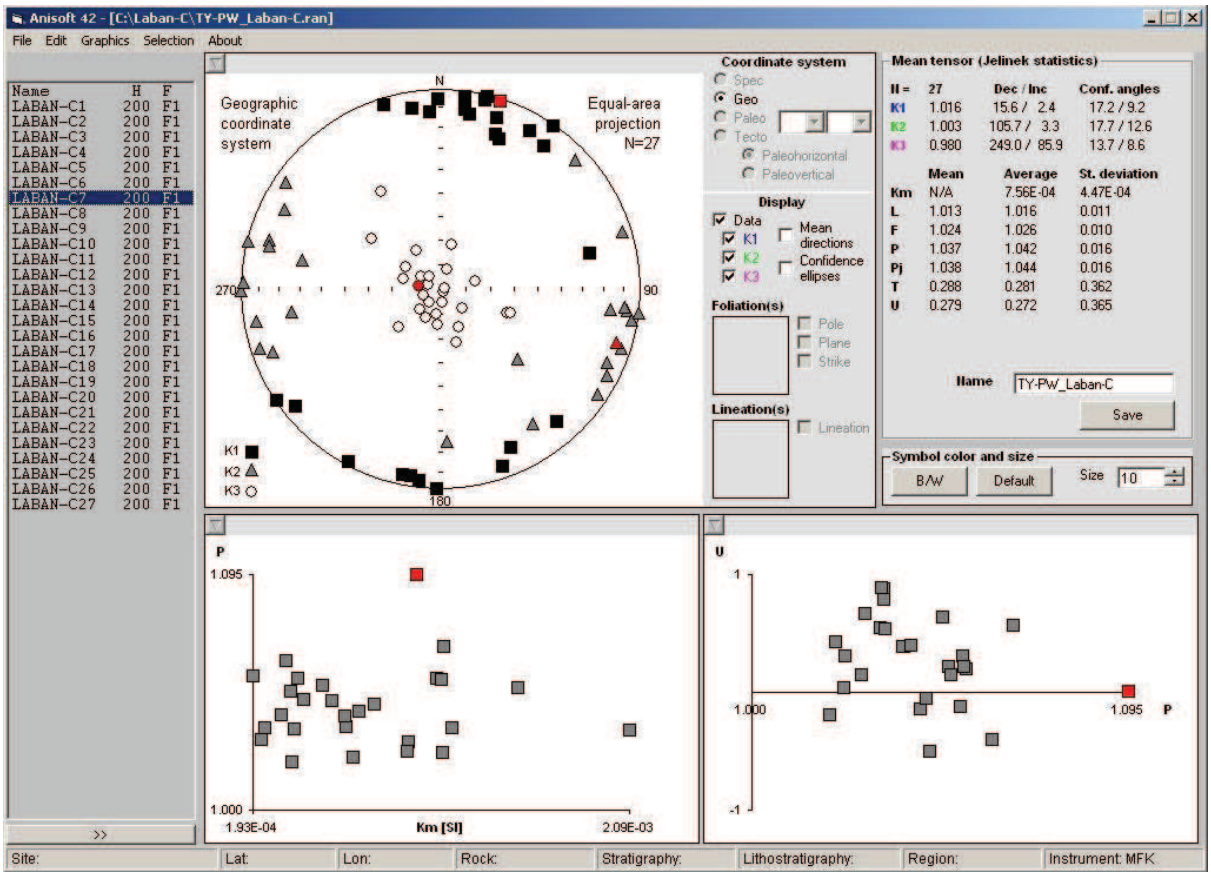
Anisoft 42 - [C:\Laban-C\TY-PW_Laban-C.ran]
File Edit Graphics Selection About
Name H F
LABAN-C1 200 F1
LABAN-C2 200 F1
LABAN-C3 200 F1
LABAN-C4 200 F1
LABAN-C5 200 F1
LABAN-C6 200 F1
LABAN-C7 200 F1
LABAN-C8 200 F1
LABAN-C9 200 F1
LABAN-C10 200 F1
LABAN-C11 200 F1
LABAN-C12 200 F1
LABAN-C13 200 F1
LABAN-C14 200 F1
LABAN-C15 200 F1
LABAN-C16 200 F1
LABAN-C17 200 F1
LABAN-C18 200 F1
LABAN-C19 200 F1
LABAN-C20 200 F1
LABAN-C21 200 F1
LABAN-C22 200 F1
LABAN-C23 200 F1
LABAN-C24 200 F1
LABAN-C25 200 F1
LABAN-C26 200 F1
LABAN-C27 200 F1
Geographic coordinate system
Equal-area projection N=27
N
90
180
270
K1
K2
K3
Coordinate system
Spec
Geo
Paleo
Tecto
Paleohorizontal
Paleovertical
Display
Data
K1
K2
K3
Mean directions
Confidence ellipses
Foliation(s)
Pole
Plane
Strike
Lineation(s)
Lineation
Mean tensor (Jelinek statistics)
II = 27 Dec / Inc Conf. angles
K1 1.016 15.6 / 2.4 17.2 / 9.2
K2 1.003 105.7 / 3.3 17.7 / 12.6
K3 0.980 249.0 / 85.9 13.7 / 8.6
Mean Average St. deviation
Km N/A 7.56E-04 4.47E-04
L 1.013 1.016 0.011
F 1.024 1.026 0.010
P 1.037 1.042 0.016
Pj 1.038 1.044 0.016
T 0.288 0.281 0.362
U 0.279 0.272 0.365
Name TY-PW_Laban-C
Save
Symbol color and size
B/W
Default
Size 10
P
1.095
1.000
1.93E-04
Km [SI]
2.09E-03
U
1
-1
Site:
Lat:
Lon:
Rock:
Stratigraphy:
Lithostratigraphy:
Region:
Instrument: MFK

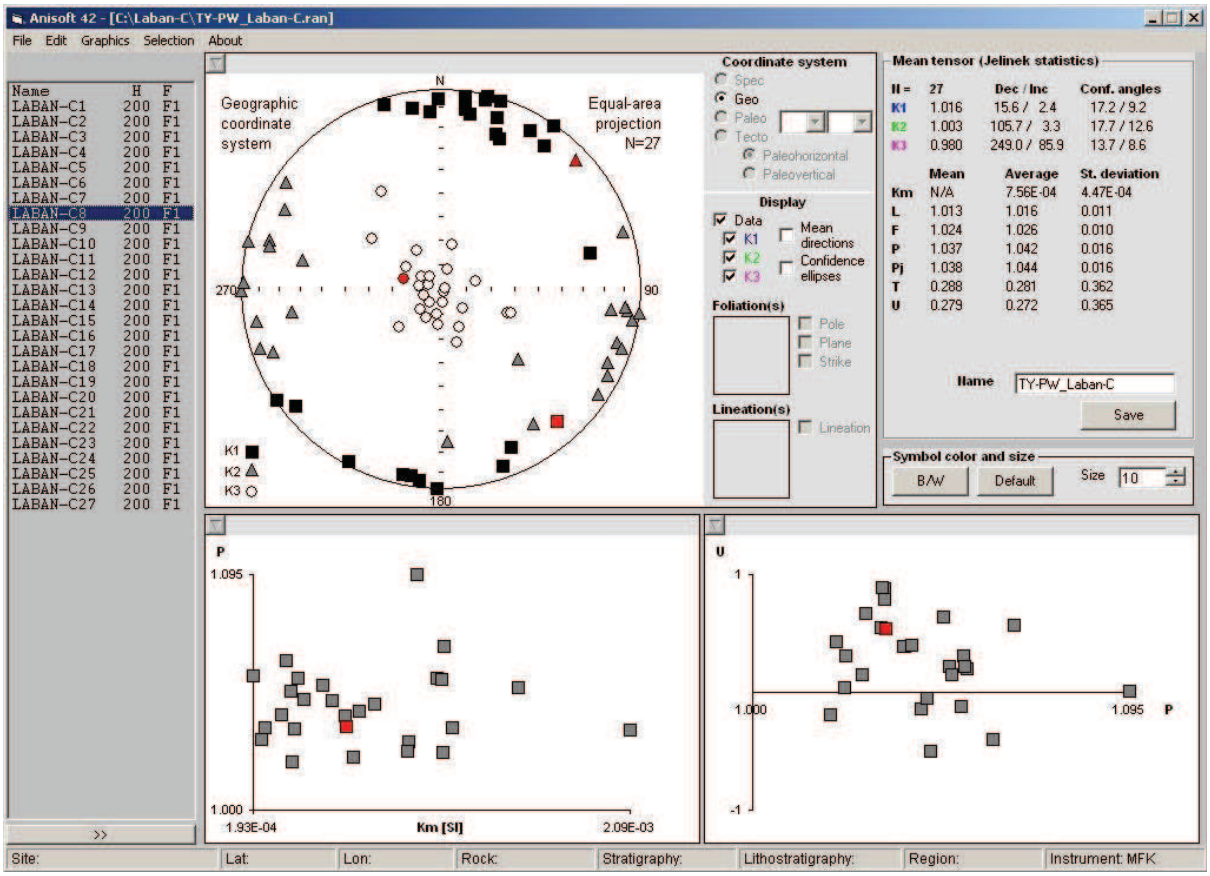
Anisoft 42 - [C:\Laban-C\TY-PW_Laban-C.ran]
File Edit Graphics Selection About
Name H F
LABAN-C1 200 F1
LABAN-C2 200 F1
LABAN-C3 200 F1
LABAN-C4 200 F1
LABAN-C5 200 F1
LABAN-C6 200 F1
LABAN-C7 200 F1
LABAN-C8 200 F1
LABAN-C9 200 F1
LABAN-C10 200 F1
LABAN-C11 200 F1
LABAN-C12 200 F1
LABAN-C13 200 F1
LABAN-C14 200 F1
LABAN-C15 200 F1
LABAN-C16 200 F1
LABAN-C17 200 F1
LABAN-C18 200 F1
LABAN-C19 200 F1
LABAN-C20 200 F1
LABAN-C21 200 F1
LABAN-C22 200 F1
LABAN-C23 200 F1
LABAN-C24 200 F1
LABAN-C25 200 F1
LABAN-C26 200 F1
LABAN-C27 200 F1
Geographic coordinate system
Equal-area projection N=27
N
90
180
270
K1
K2
K3
Coordinate system
Spec
Geo
Paleo
Tecto
Paleohorizontal
Paleovertical
Display
Data
K1
K2
K3
Mean directions
Confidence ellipses
Foliation(s)
Pole
Plane
Strike
Lineation(s)
Lineation
Mean tensor (Jelinek statistics)
II = 27 Dec / Inc Conf. angles
K1 1.016 15.6 / 2.4 17.2 / 9.2
K2 1.003 105.7 / 3.3 17.7 / 12.6
K3 0.980 249.0 / 85.9 13.7 / 8.6
Mean Average St. deviation
Km N/A 7.56E-04 4.47E-04
L 1.013 1.016 0.011
F 1.024 1.026 0.010
P 1.037 1.042 0.016
Pj 1.038 1.044 0.016
T 0.288 0.281 0.362
U 0.279 0.272 0.365
Name TY-PW_Laban-C
Save
Symbol color and size
B/W
Default
Size 10
P
1.095
1.000
1.93E-04
Km [SI]
2.09E-03
U
1
-1
Site:
Lat:
Lon:
Rock:
Stratigraphy:
Lithostratigraphy:
Region:
Instrument: MFK

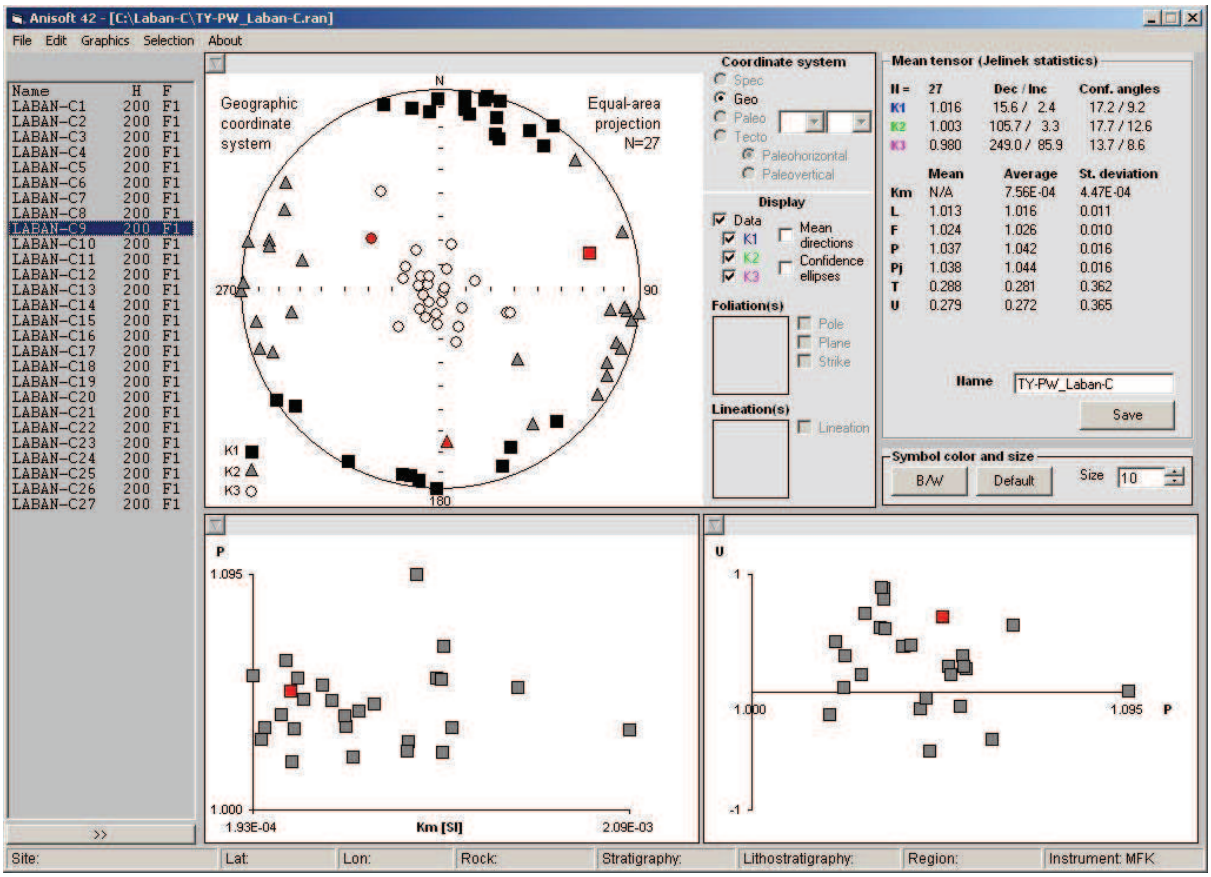
Anisoft 42 - [C:\Laban-C\TY-PW_Laban-C.ran]
File Edit Graphics Selection About
Name H F
LABAN-C1 200 F1
LABAN-C2 200 F1
LABAN-C3 200 F1
LABAN-C4 200 F1
LABAN-C5 200 F1
LABAN-C6 200 F1
LABAN-C7 200 F1
LABAN-C8 200 F1
LABAN-C9 200 F1
LABAN-C10 200 F1
LABAN-C11 200 F1
LABAN-C12 200 F1
LABAN-C13 200 F1
LABAN-C14 200 F1
LABAN-C15 200 F1
LABAN-C16 200 F1
LABAN-C17 200 F1
LABAN-C18 200 F1
LABAN-C19 200 F1
LABAN-C20 200 F1
LABAN-C21 200 F1
LABAN-C22 200 F1
LABAN-C23 200 F1
LABAN-C24 200 F1
LABAN-C25 200 F1
LABAN-C26 200 F1
LABAN-C27 200 F1
Geographic coordinate system
Equal-area projection N=27
N
90
180
270
K1
K2
K3
Coordinate system
Spec
Geo
Paleo
Tecto
Paleohorizontal
Paleovertical
Display
Data
K1
K2
K3
Mean directions
Confidence ellipses
Foliation(s)
Pole
Plane
Strike
Lineation(s)
Lineation
Mean tensor (Jelinek statistics)
II = 27 Dec / Inc Conf. angles
K1 1.016 15.6 / 2.4 17.2 / 9.2
K2 1.003 105.7 / 3.3 17.7 / 12.6
K3 0.980 249.0 / 85.9 13.7 / 8.6
Mean Average St. deviation
Km N/A 7.56E-04 4.47E-04
L 1.013 1.016 0.011
F 1.024 1.026 0.010
P 1.037 1.042 0.016
Pj 1.038 1.044 0.016
T 0.288 0.281 0.362
U 0.279 0.272 0.365
Name TY-PW_Laban-C
Save
Symbol color and size
B/W
Default
Size 10
P
1.095
1.000
1.93E-04
Km [SI]
2.09E-03
U
1
-1
Site:
Lat:
Lon:
Rock:
Stratigraphy:
Lithostratigraphy:
Region:
Instrument: MFK

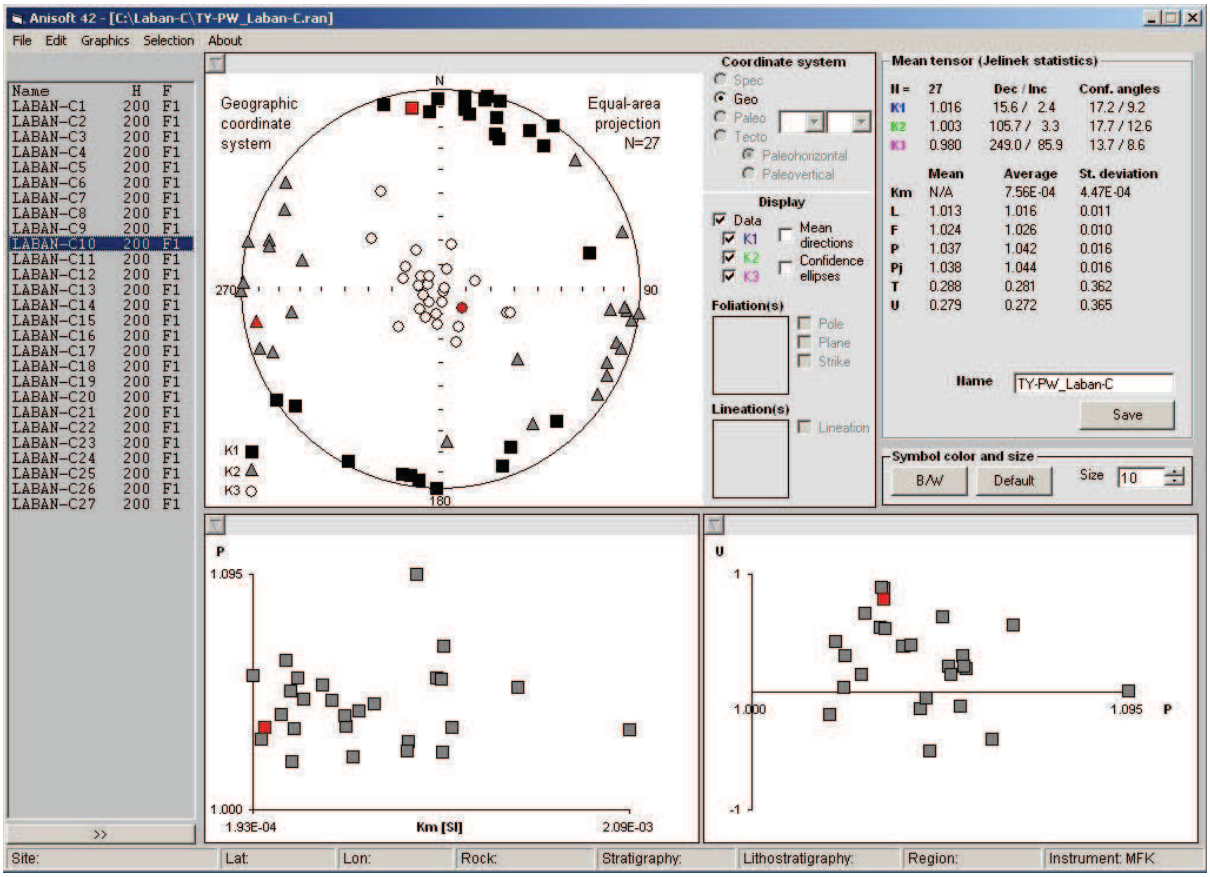
Anisoft 42 - [C:\Laban-C\TY-PW_Laban-C.ran]
File Edit Graphics Selection About
Name H F
LABAN-C1 200 F1
LABAN-C2 200 F1
LABAN-C3 200 F1
LABAN-C4 200 F1
LABAN-C5 200 F1
LABAN-C6 200 F1
LABAN-C7 200 F1
LABAN-C8 200 F1
LABAN-C9 200 F1
LABAN-C10 200 F1
LABAN-C11 200 F1
LABAN-C12 200 F1
LABAN-C13 200 F1
LABAN-C14 200 F1
LABAN-C15 200 F1
LABAN-C16 200 F1
LABAN-C17 200 F1
LABAN-C18 200 F1
LABAN-C19 200 F1
LABAN-C20 200 F1
LABAN-C21 200 F1
LABAN-C22 200 F1
LABAN-C23 200 F1
LABAN-C24 200 F1
LABAN-C25 200 F1
LABAN-C26 200 F1
LABAN-C27 200 F1
Geographic coordinate system
Equal-area projection N=27
N
90
180
270
K1
K2
K3
Coordinate system
Spec
Geo
Paleo
Tecto
Paleohorizontal
Paleovertical
Display
Data
K1
K2
K3
Mean directions
Confidence ellipses
Foliation(s)
Pole
Plane
Strike
Lineation(s)
Lineation
Mean tensor (Jelinek statistics)
II = 27 Dec / Inc Conf. angles
K1 1.016 15.6 / 2.4 17.2 / 9.2
K2 1.003 105.7 / 3.3 17.7 / 12.6
K3 0.980 249.0 / 85.9 13.7 / 8.6
Mean Average St. deviation
Km N/A 7.56E-04 4.47E-04
L 1.013 1.016 0.011
F 1.024 1.026 0.010
P 1.037 1.042 0.016
Pj 1.038 1.044 0.016
T 0.288 0.281 0.362
U 0.279 0.272 0.365
Name TY-PW_Laban-C
Save
Symbol color and size
B/W
Default
Size 10
P
1.095
1.000
1.93E-04
Km [SI]
2.09E-03
U
1
-1
Site:
Lat:
Lon:
Rock:
Stratigraphy:
Lithostratigraphy:
Region:
Instrument: MFK

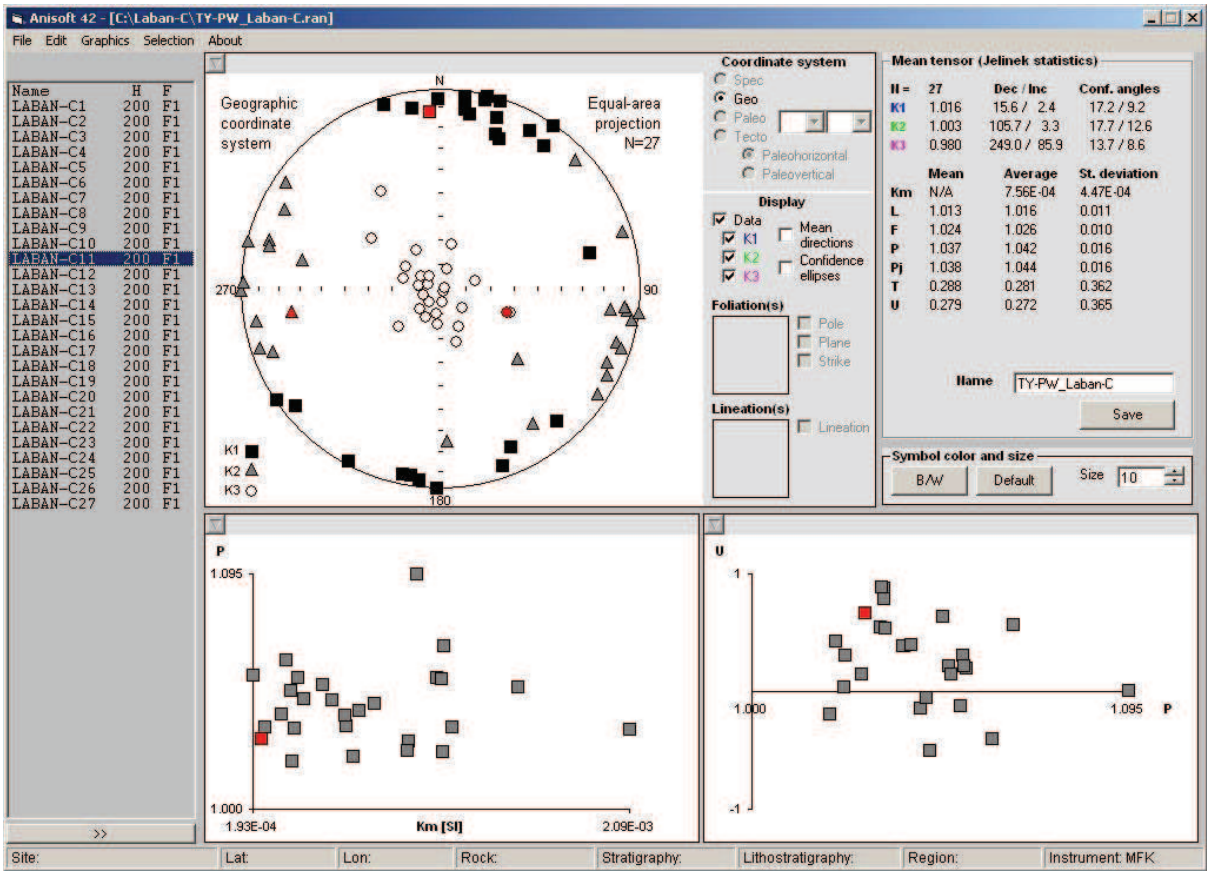
Anisoft 42 - [C:\Laban-C\TY-PW_Laban-C.ran]
File Edit Graphics Selection About
Name H F
LABAN-C1 200 F1
LABAN-C2 200 F1
LABAN-C3 200 F1
LABAN-C4 200 F1
LABAN-C5 200 F1
LABAN-C6 200 F1
LABAN-C7 200 F1
LABAN-C8 200 F1
LABAN-C9 200 F1
LABAN-C10 200 F1
LABAN-C11 200 F1
LABAN-C12 200 F1
LABAN-C13 200 F1
LABAN-C14 200 F1
LABAN-C15 200 F1
LABAN-C16 200 F1
LABAN-C17 200 F1
LABAN-C18 200 F1
LABAN-C19 200 F1
LABAN-C20 200 F1
LABAN-C21 200 F1
LABAN-C22 200 F1
LABAN-C23 200 F1
LABAN-C24 200 F1
LABAN-C25 200 F1
LABAN-C26 200 F1
LABAN-C27 200 F1
Geographic coordinate system
Equal-area projection N=27
N
90
180
270
K1
K2
K3
Coordinate system
Spec
Geo
Paleo
Tecto
Paleohorizontal
Paleovertical
Display
Data
K1
K2
K3
Mean directions
Confidence ellipses
Foliation(s)
Pole
Plane
Strike
Lineation(s)
Lineation
Mean tensor (Jelinek statistics)
II = 27 Dec / Inc Conf. angles
K1 1.016 15.6 / 2.4 17.2 / 9.2
K2 1.003 105.7 / 3.3 17.7 / 12.6
K3 0.980 249.0 / 85.9 13.7 / 8.6
Mean Average St. deviation
Km N/A 7.56E-04 4.47E-04
L 1.013 1.016 0.011
F 1.024 1.026 0.010
P 1.037 1.042 0.016
Pj 1.038 1.044 0.016
T 0.288 0.281 0.362
U 0.279 0.272 0.365
Name TY-PW_Laban-C
Save
Symbol color and size
B/W
Default
Size 10
P
1.095
1.000
1.93E-04
Km [SI]
2.09E-03
U
1
-1
Site:
Lat:
Lon:
Rock:
Stratigraphy:
Lithostratigraphy:
Region:
Instrument: MFK

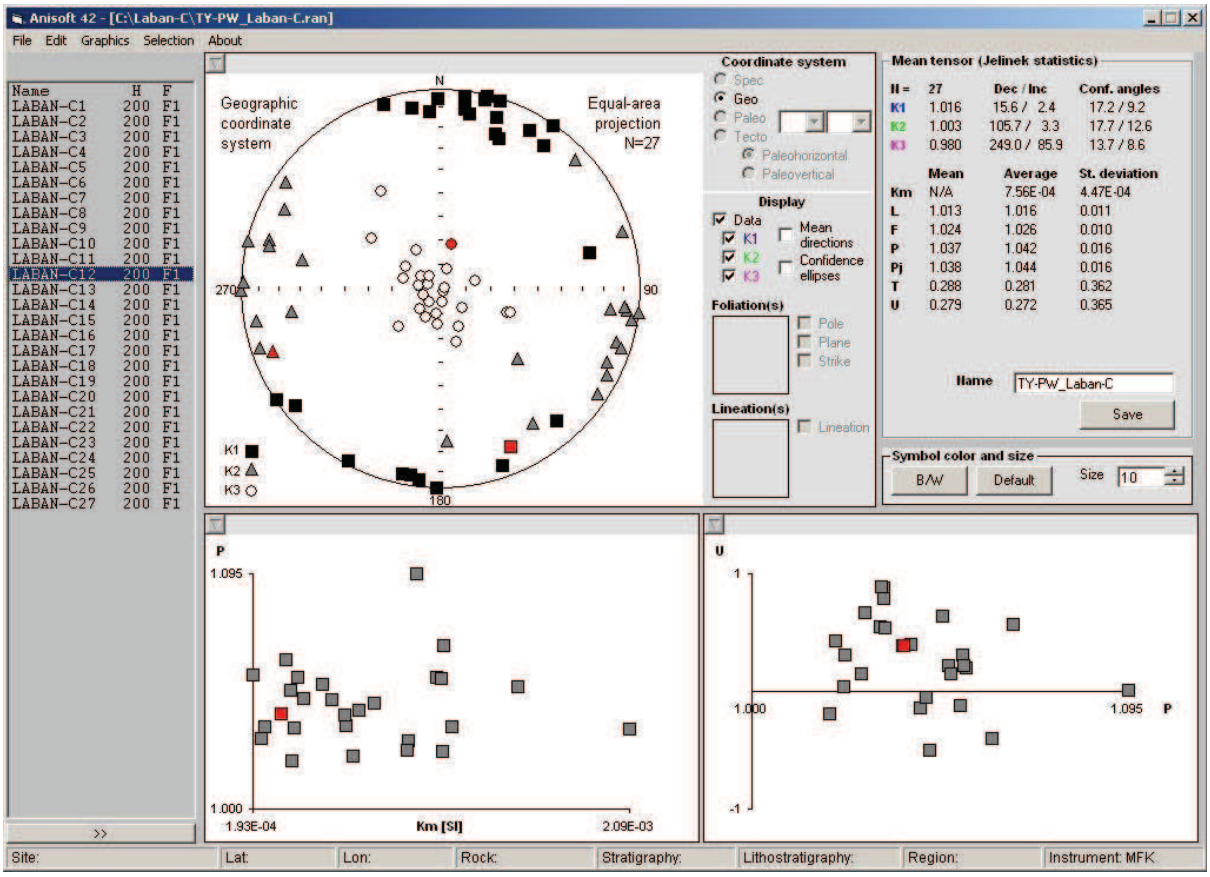
Anisoft 42 - [C:\Laban-C\TY-PW_Laban-C.ran]
File Edit Graphics Selection About
Name H F
LABAN-C1 200 F1
LABAN-C2 200 F1
LABAN-C3 200 F1
LABAN-C4 200 F1
LABAN-C5 200 F1
LABAN-C6 200 F1
LABAN-C7 200 F1
LABAN-C8 200 F1
LABAN-C9 200 F1
LABAN-C10 200 F1
LABAN-C11 200 F1
LABAN-C12 200 F1
LABAN-C13 200 F1
LABAN-C14 200 F1
LABAN-C15 200 F1
LABAN-C16 200 F1
LABAN-C17 200 F1
LABAN-C18 200 F1
LABAN-C19 200 F1
LABAN-C20 200 F1
LABAN-C21 200 F1
LABAN-C22 200 F1
LABAN-C23 200 F1
LABAN-C24 200 F1
LABAN-C25 200 F1
LABAN-C26 200 F1
LABAN-C27 200 F1
Geographic coordinate system
Equal-area projection N=27
N
90
180
270
K1
K2
K3
Coordinate system
Spec
Geo
Paleo
Tecto
Paleohorizontal
Paleovertical
Display
Data
K1
K2
K3
Mean directions
Confidence ellipses
Foliation(s)
Pole
Plane
Strike
Lineation(s)
Lineation
Mean tensor (Jelinek statistics)
II = 27 Dec / Inc Conf. angles
K1 1.016 15.6 / 2.4 17.2 / 9.2
K2 1.003 105.7 / 3.3 17.7 / 12.6
K3 0.980 249.0 / 85.9 13.7 / 8.6
Mean Average St. deviation
Km N/A 7.56E-04 4.47E-04
L 1.013 1.016 0.011
F 1.024 1.026 0.010
P 1.037 1.042 0.016
Pj 1.038 1.044 0.016
T 0.288 0.281 0.362
U 0.279 0.272 0.365
Name TY-PW_Laban-C
Save
Symbol color and size
B/W
Default
Size 10
P
1.095
1.000
1.93E-04
Km [SI]
2.09E-03
U
1
-1
Site:
Lat:
Lon:
Rock:
Stratigraphy:
Lithostratigraphy:
Region:
Instrument: MFK

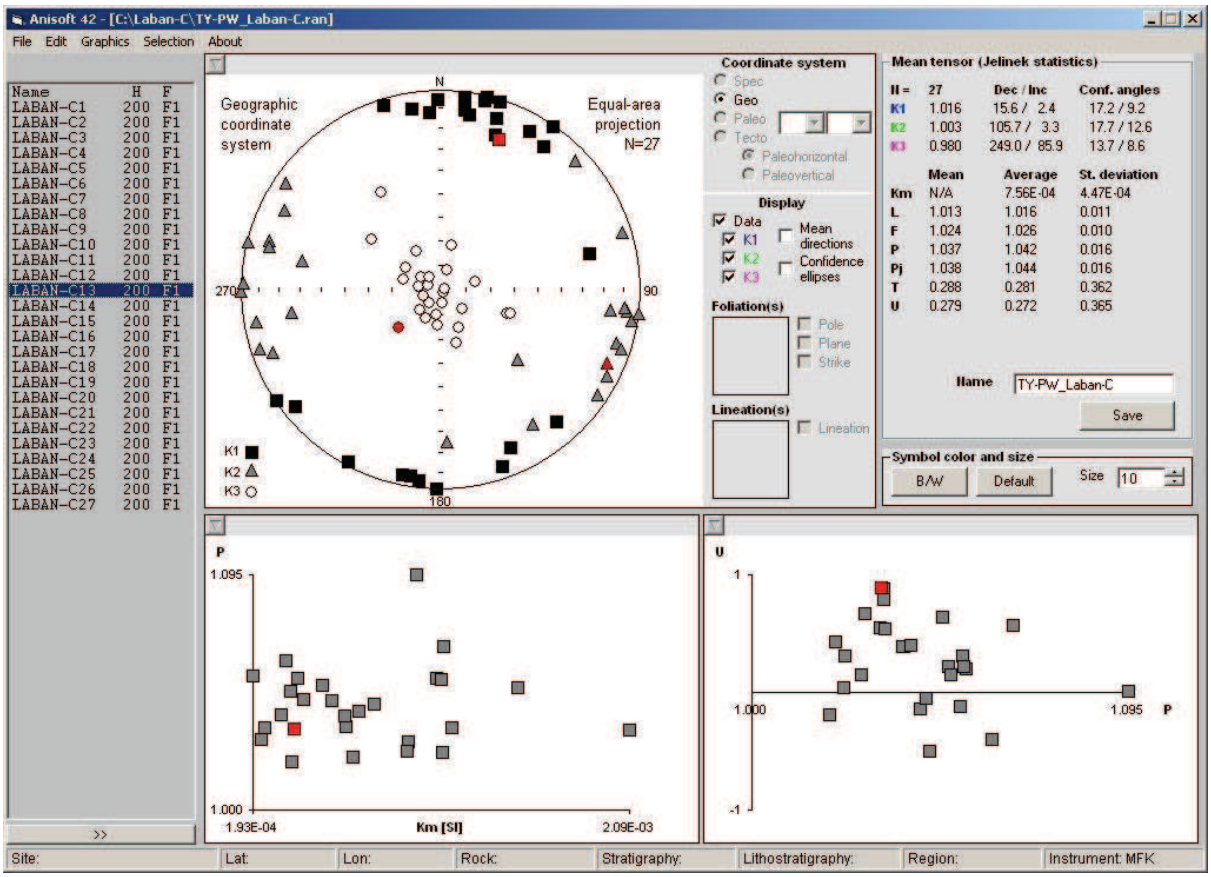
Anisoft 42 - [C:\Laban-C\TY-PW_Laban-C.ran]
File Edit Graphics Selection About
Name H F
LABAN-C1 200 F1
LABAN-C2 200 F1
LABAN-C3 200 F1
LABAN-C4 200 F1
LABAN-C5 200 F1
LABAN-C6 200 F1
LABAN-C7 200 F1
LABAN-C8 200 F1
LABAN-C9 200 F1
LABAN-C10 200 F1
LABAN-C11 200 F1
LABAN-C12 200 F1
LABAN-C13 200 F1
LABAN-C14 200 F1
LABAN-C15 200 F1
LABAN-C16 200 F1
LABAN-C17 200 F1
LABAN-C18 200 F1
LABAN-C19 200 F1
LABAN-C20 200 F1
LABAN-C21 200 F1
LABAN-C22 200 F1
LABAN-C23 200 F1
LABAN-C24 200 F1
LABAN-C25 200 F1
LABAN-C26 200 F1
LABAN-C27 200 F1
Geographic coordinate system
Equal-area projection N=27
N
90
180
270
K1
K2
K3
Coordinate system
Spec
Geo
Paleo
Tecto
Paleohorizontal
Paleovertical
Display
Data
K1
K2
K3
Mean directions
Confidence ellipses
Foliation(s)
Pole
Plane
Strike
Lineation(s)
Lineation
Mean tensor (Jelinek statistics)
II = 27 Dec / Inc Conf. angles
K1 1.016 15.6 / 2.4 17.2 / 9.2
K2 1.003 105.7 / 3.3 17.7 / 12.6
K3 0.980 249.0 / 85.9 13.7 / 8.6
Mean Average St. deviation
Km N/A 7.56E-04 4.47E-04
L 1.013 1.016 0.011
F 1.024 1.026 0.010
P 1.037 1.042 0.016
Pj 1.038 1.044 0.016
T 0.288 0.281 0.362
U 0.279 0.272 0.365
Name TY-PW_Laban-C
Save
Symbol color and size
B/W
Default
Size 10
P
1.095
1.000
1.93E-04
Km [SI]
2.09E-03
U
1
-1
Site:
Lat:
Lon:
Rock:
Stratigraphy:
Lithostratigraphy:
Region:
Instrument: MFK

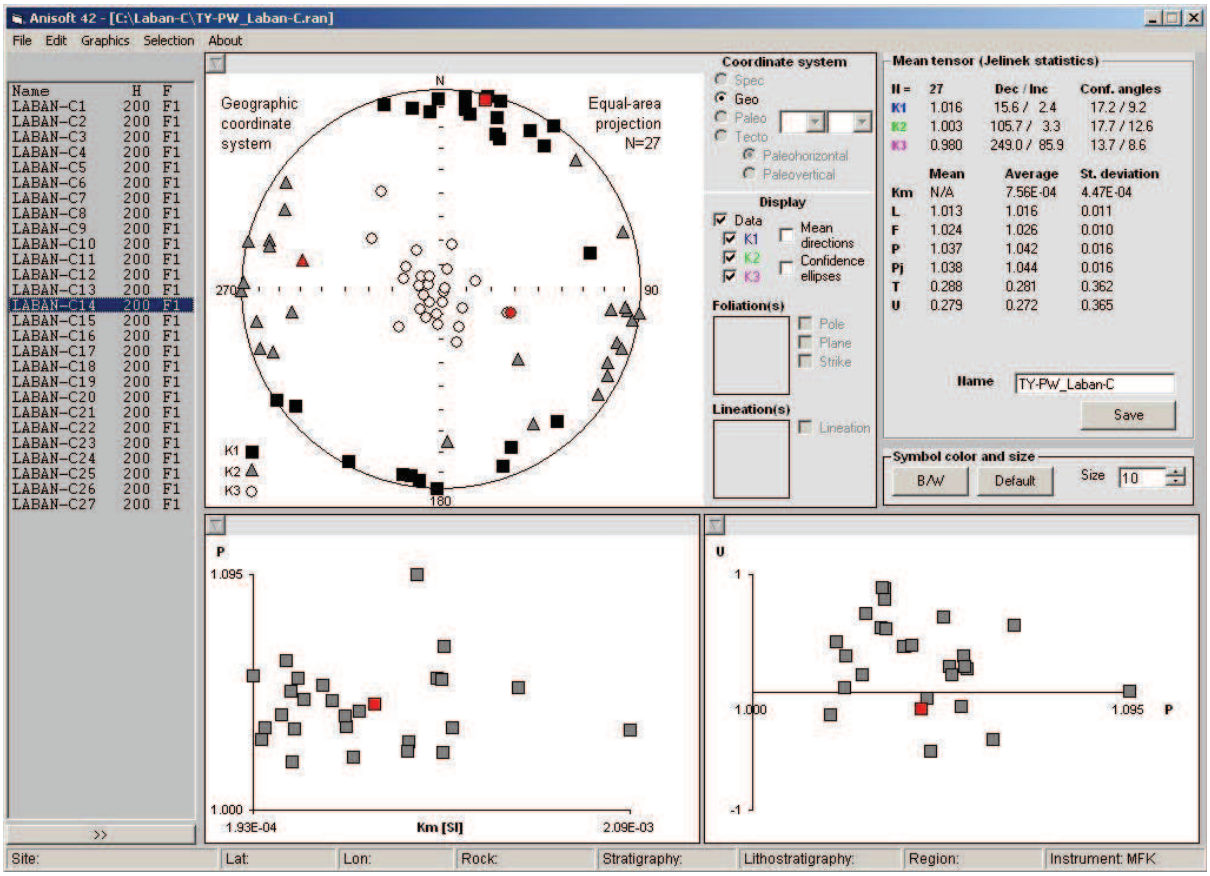
Anisoft 42 - [C:\Laban-C\TY-PW_Laban-C.ran]
File Edit Graphics Selection About
Name H F
LABAN-C1 200 F1
LABAN-C2 200 F1
LABAN-C3 200 F1
LABAN-C4 200 F1
LABAN-C5 200 F1
LABAN-C6 200 F1
LABAN-C7 200 F1
LABAN-C8 200 F1
LABAN-C9 200 F1
LABAN-C10 200 F1
LABAN-C11 200 F1
LABAN-C12 200 F1
LABAN-C13 200 F1
LABAN-C14 200 F1
LABAN-C15 200 F1
LABAN-C16 200 F1
LABAN-C17 200 F1
LABAN-C18 200 F1
LABAN-C19 200 F1
LABAN-C20 200 F1
LABAN-C21 200 F1
LABAN-C22 200 F1
LABAN-C23 200 F1
LABAN-C24 200 F1
LABAN-C25 200 F1
LABAN-C26 200 F1
LABAN-C27 200 F1
Geographic coordinate system
Equal-area projection N=27
N
90
180
270
K1
K2
K3
Coordinate system
Spec
Geo
Paleo
Tecto
Paleohorizontal
Paleovertical
Display
Data
K1
K2
K3
Mean directions
Confidence ellipses
Foliation(s)
Pole
Plane
Strike
Lineation(s)
Lineation
Mean tensor (Jelinek statistics)
II = 27 Dec / Inc Conf. angles
K1 1.016 15.6 / 2.4 17.2 / 9.2
K2 1.003 105.7 / 3.3 17.7 / 12.6
K3 0.980 249.0 / 85.9 13.7 / 8.6
Mean Average St. deviation
Km N/A 7.56E-04 4.47E-04
L 1.013 1.016 0.011
F 1.024 1.026 0.010
P 1.037 1.042 0.016
Pj 1.038 1.044 0.016
T 0.288 0.281 0.362
U 0.279 0.272 0.365
Name TY-PW_Laban-C
Save
Symbol color and size
B/W
Default
Size 10
P
1.095
1.000
1.93E-04
Km [SI]
2.09E-03
U
1
-1
1.000
1.095
P
Site:
Lat:
Lon:
Rock:
Stratigraphy:
Lithostratigraphy:
Region:
Instrument: MFK

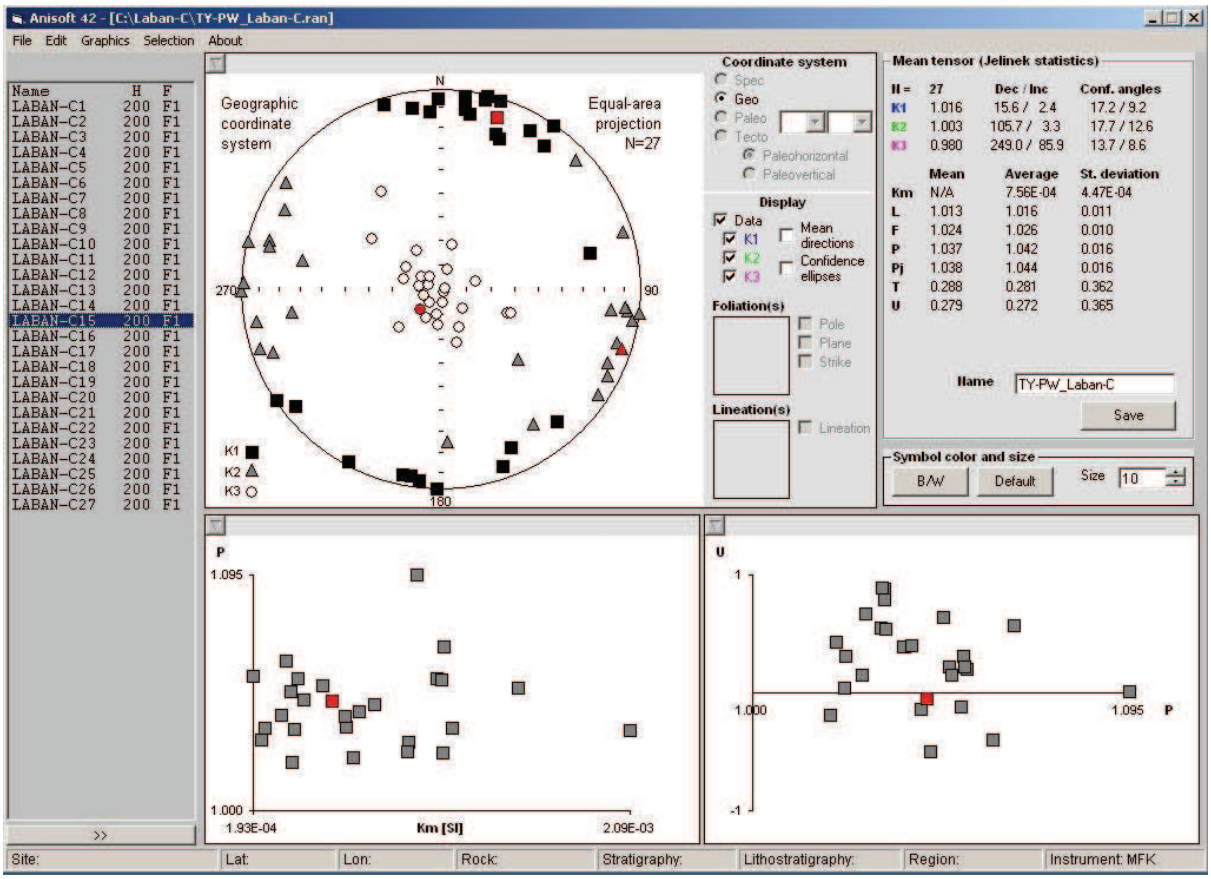
Anisoft 42 - [C:\Laban-C\TY-PW_Laban-C.ran]
File Edit Graphics Selection About
Name H F
LABAN-C1 200 F1
LABAN-C2 200 F1
LABAN-C3 200 F1
LABAN-C4 200 F1
LABAN-C5 200 F1
LABAN-C6 200 F1
LABAN-C7 200 F1
LABAN-C8 200 F1
LABAN-C9 200 F1
LABAN-C10 200 F1
LABAN-C11 200 F1
LABAN-C12 200 F1
LABAN-C13 200 F1
LABAN-C14 200 F1
LABAN-C15 200 F1
LABAN-C16 200 F1
LABAN-C17 200 F1
LABAN-C18 200 F1
LABAN-C19 200 F1
LABAN-C20 200 F1
LABAN-C21 200 F1
LABAN-C22 200 F1
LABAN-C23 200 F1
LABAN-C24 200 F1
LABAN-C25 200 F1
LABAN-C26 200 F1
LABAN-C27 200 F1
Geographic coordinate system
Equal-area projection N=27
N
90
180
270
K1
K2
K3
Coordinate system
Spec
Geo
Paleo
Tecto
Paleohorizontal
Paleovertical
Display
Data
K1
K2
K3
Mean directions
Confidence ellipses
Foliation(s)
Pole
Plane
Strike
Lineation(s)
Lineation
Mean tensor (Jelinek statistics)
II = 27 Dec / Inc Conf. angles
K1 1.016 15.6 / 2.4 17.2 / 9.2
K2 1.003 105.7 / 3.3 17.7 / 12.6
K3 0.980 249.0 / 85.9 13.7 / 8.6
Mean Average St. deviation
Km N/A 7.56E-04 4.47E-04
L 1.013 1.016 0.011
F 1.024 1.026 0.010
P 1.037 1.042 0.016
Pj 1.038 1.044 0.016
T 0.288 0.281 0.362
U 0.279 0.272 0.365
Name TY-PW_Laban-C
Save
Symbol color and size
B/W
Default
Size 10
P
1.095
1.000
1.93E-04
Km [SI]
2.09E-03
U
1
-1
1.000
1.095
P
Site:
Lat:
Lon:
Rock:
Stratigraphy:
Lithostratigraphy:
Region:
Instrument: MFK

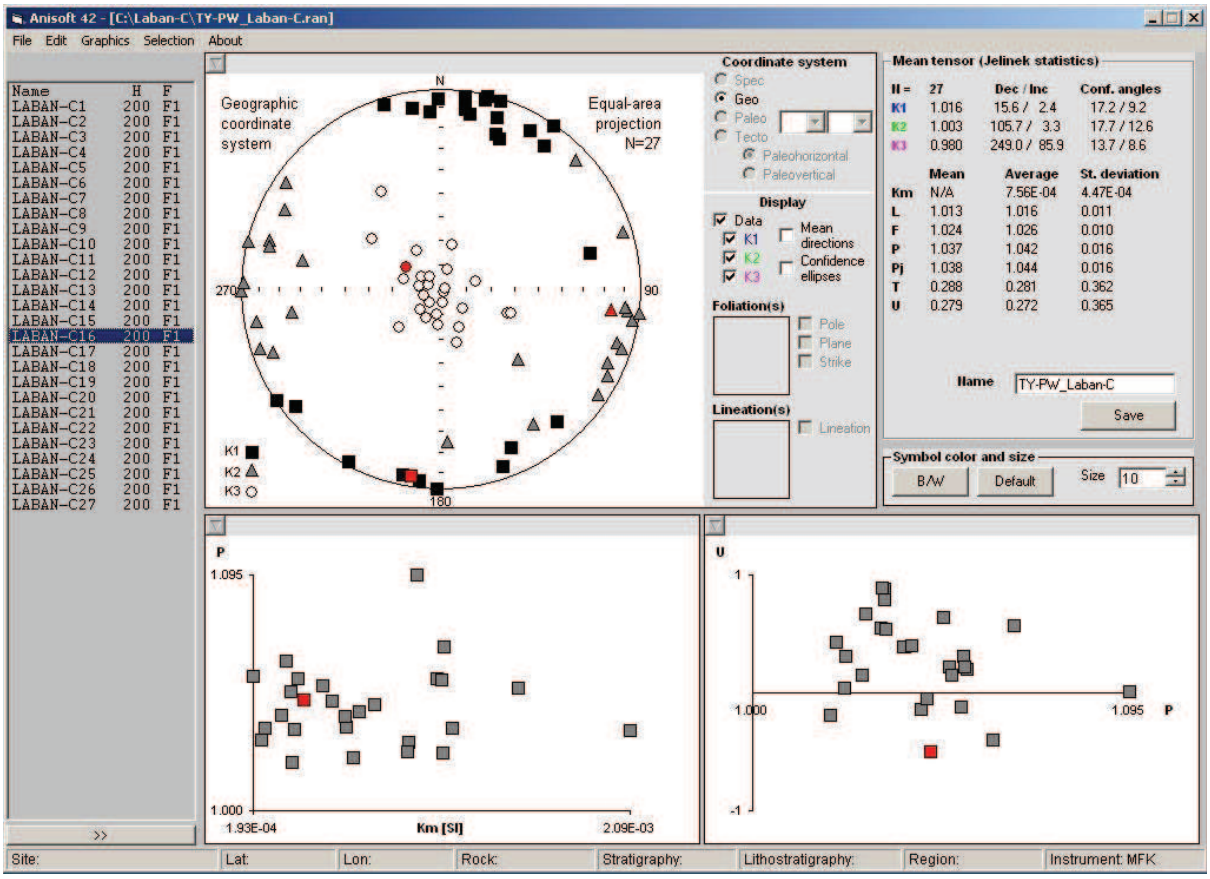
Anisoft 42 - [C:\Laban-C\TY-PW_Laban-C.ran]
File Edit Graphics Selection About
Name H F
LABAN-C1 200 F1
LABAN-C2 200 F1
LABAN-C3 200 F1
LABAN-C4 200 F1
LABAN-C5 200 F1
LABAN-C6 200 F1
LABAN-C7 200 F1
LABAN-C8 200 F1
LABAN-C9 200 F1
LABAN-C10 200 F1
LABAN-C11 200 F1
LABAN-C12 200 F1
LABAN-C13 200 F1
LABAN-C14 200 F1
LABAN-C15 200 F1
LABAN-C16 200 F1
LABAN-C17 200 F1
LABAN-C18 200 F1
LABAN-C19 200 F1
LABAN-C20 200 F1
LABAN-C21 200 F1
LABAN-C22 200 F1
LABAN-C23 200 F1
LABAN-C24 200 F1
LABAN-C25 200 F1
LABAN-C26 200 F1
LABAN-C27 200 F1
Geographic coordinate system
Equal-area projection N=27
N
90
180
270
K1
K2
K3
Coordinate system
Spec
Geo
Paleo
Tecto
Paleohorizontal
Paleovertical
Display
Data
K1
K2
K3
Mean directions
Confidence ellipses
Foliation(s)
Pole
Plane
Strike
Lineation(s)
Lineation
Mean tensor (Jelinek statistics)
II = 27 Dec / Inc Conf. angles
K1 1.016 15.6 / 2.4 17.2 / 9.2
K2 1.003 105.7 / 3.3 17.7 / 12.6
K3 0.980 249.0 / 85.9 13.7 / 8.6
Mean Average St. deviation
Km N/A 7.56E-04 4.47E-04
L 1.013 1.016 0.011
F 1.024 1.026 0.010
P 1.037 1.042 0.016
Pj 1.038 1.044 0.016
T 0.288 0.281 0.362
U 0.279 0.272 0.365
Name TY-PW_Laban-C
Save
Symbol color and size
B/W
Default
Size 10
P
1.095
1.000
1.93E-04
Km [SI]
2.09E-03
U
1
-1
1.000
1.095
P
Site:
Lat:
Lon:
Rock:
Stratigraphy:
Lithostratigraphy:
Region:
Instrument: MFK

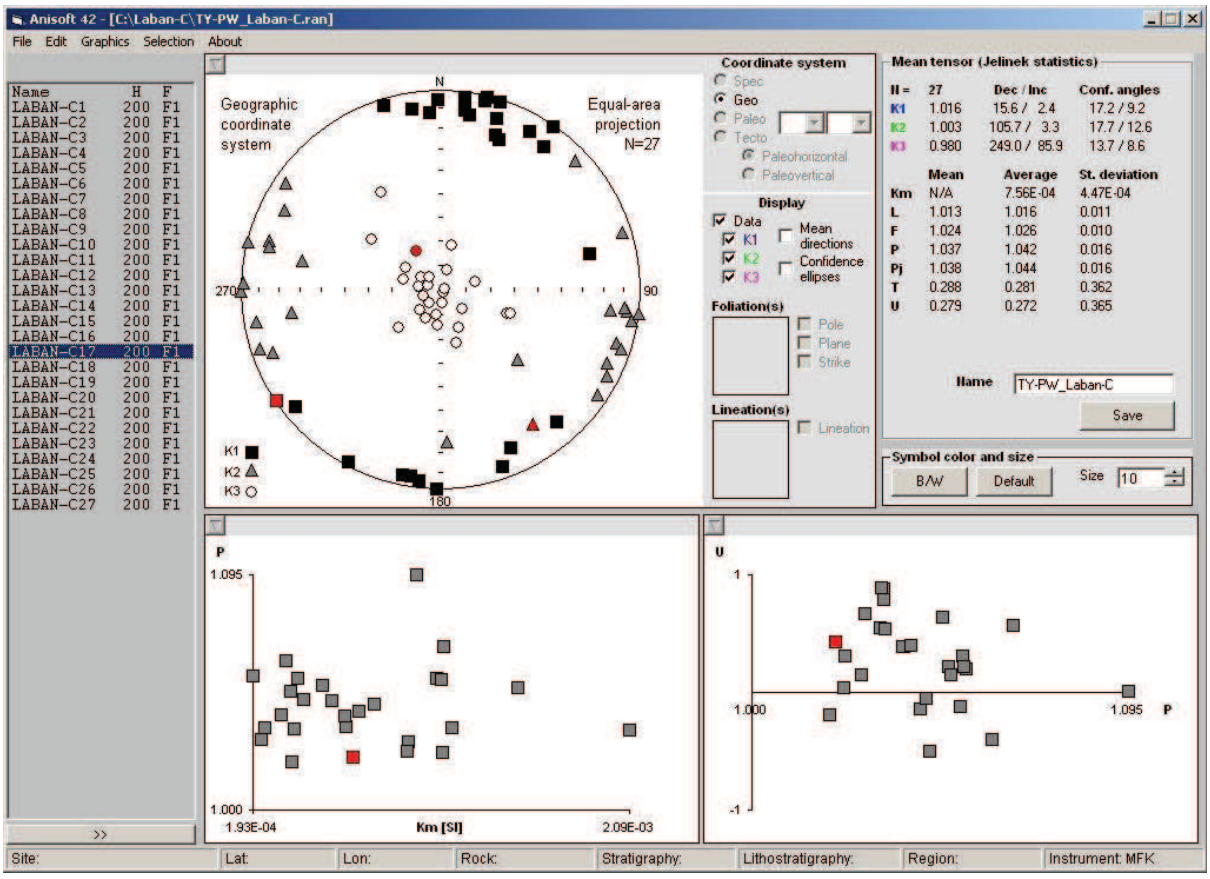
Anisoft 42 - [C:\Laban-C\TY-PW_Laban-C.ran]
File Edit Graphics Selection About
Name H F
LABAN-C1 200 F1
LABAN-C2 200 F1
LABAN-C3 200 F1
LABAN-C4 200 F1
LABAN-C5 200 F1
LABAN-C6 200 F1
LABAN-C7 200 F1
LABAN-C8 200 F1
LABAN-C9 200 F1
LABAN-C10 200 F1
LABAN-C11 200 F1
LABAN-C12 200 F1
LABAN-C13 200 F1
LABAN-C14 200 F1
LABAN-C15 200 F1
LABAN-C16 200 F1
LABAN-C17 200 F1
LABAN-C18 200 F1
LABAN-C19 200 F1
LABAN-C20 200 F1
LABAN-C21 200 F1
LABAN-C22 200 F1
LABAN-C23 200 F1
LABAN-C24 200 F1
LABAN-C25 200 F1
LABAN-C26 200 F1
LABAN-C27 200 F1
Geographic coordinate system
Equal-area projection N=27
N
90
180
270
K1
K2
K3
Coordinate system
Spec
Geo
Paleo
Tecto
Paleohorizontal
Paleovertical
Display
Data
K1
K2
K3
Mean directions
Confidence ellipses
Foliation(s)
Pole
Plane
Strike
Lineation(s)
Lineation
Mean tensor (Jelinek statistics)
II = 27 Dec / Inc Conf. angles
K1 1.016 15.6 / 2.4 17.2 / 9.2
K2 1.003 105.7 / 3.3 17.7 / 12.6
K3 0.980 249.0 / 85.9 13.7 / 8.6
Mean Average St. deviation
Km N/A 7.56E-04 4.47E-04
L 1.013 1.016 0.011
F 1.024 1.026 0.010
P 1.037 1.042 0.016
Pj 1.038 1.044 0.016
T 0.288 0.281 0.362
U 0.279 0.272 0.365
Name TY-PW_Laban-C
Save
Symbol color and size
B/W
Default
Size 10
P
1.095
1.000
1.93E-04
Km [SI]
2.09E-03
U
1
-1
1.000
1.095
P
Site:
Lat:
Lon:
Rock:
Stratigraphy:
Lithostratigraphy:
Region:
Instrument: MFK

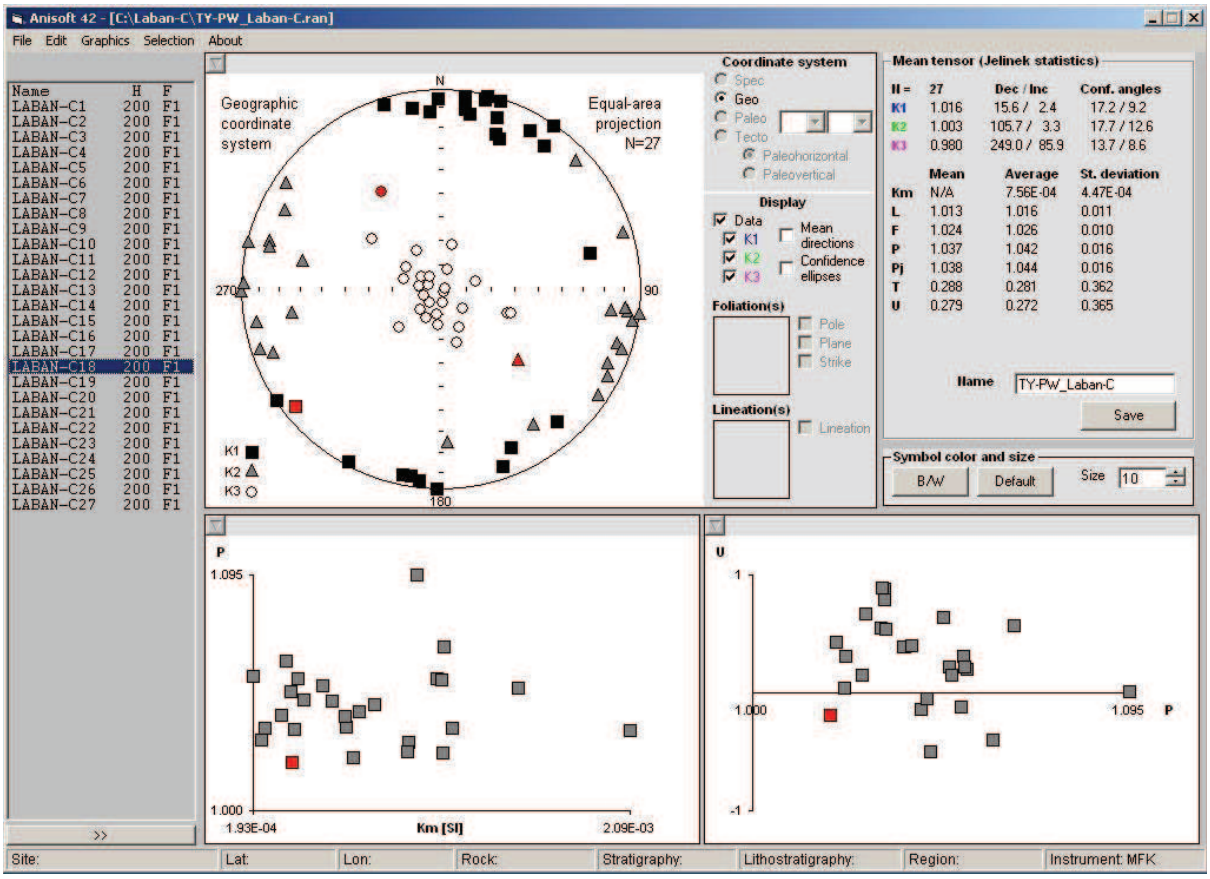
Anisoft 42 - [C:\Laban-C\TY-PW_Laban-C.ran]
File Edit Graphics Selection About
Name H F
LABAN-C1 200 F1
LABAN-C2 200 F1
LABAN-C3 200 F1
LABAN-C4 200 F1
LABAN-C5 200 F1
LABAN-C6 200 F1
LABAN-C7 200 F1
LABAN-C8 200 F1
LABAN-C9 200 F1
LABAN-C10 200 F1
LABAN-C11 200 F1
LABAN-C12 200 F1
LABAN-C13 200 F1
LABAN-C14 200 F1
LABAN-C15 200 F1
LABAN-C16 200 F1
LABAN-C17 200 F1
LABAN-C18 200 F1
LABAN-C19 200 F1
LABAN-C20 200 F1
LABAN-C21 200 F1
LABAN-C22 200 F1
LABAN-C23 200 F1
LABAN-C24 200 F1
LABAN-C25 200 F1
LABAN-C26 200 F1
LABAN-C27 200 F1
Geographic coordinate system
Equal-area projection N=27
N
90
180
270
K1
K2
K3
Coordinate system
Spec
Geo
Paleo
Tecto
Paleohorizontal
Paleovertical
Display
Data
K1
K2
K3
Mean directions
Confidence ellipses
Foliation(s)
Pole
Plane
Strike
Lineation(s)
Lineation
Mean tensor (Jelinek statistics)
II = 27 Dec / Inc Conf. angles
K1 1.016 15.6 / 2.4 17.2 / 9.2
K2 1.003 105.7 / 3.3 17.7 / 12.6
K3 0.980 249.0 / 85.9 13.7 / 8.6
Mean Average St. deviation
Km N/A 7.56E-04 4.47E-04
L 1.013 1.016 0.011
F 1.024 1.026 0.010
P 1.037 1.042 0.016
Pj 1.038 1.044 0.016
T 0.288 0.281 0.362
U 0.279 0.272 0.365
Name TY-PW_Laban-C
Save
Symbol color and size
B/W
Default
Size 10
P
1.095
1.000
1.93E-04
Km [SI]
2.09E-03
U
1
-1
Site:
Lat:
Lon:
Rock:
Stratigraphy:
Lithostratigraphy:
Region:
Instrument: MFK

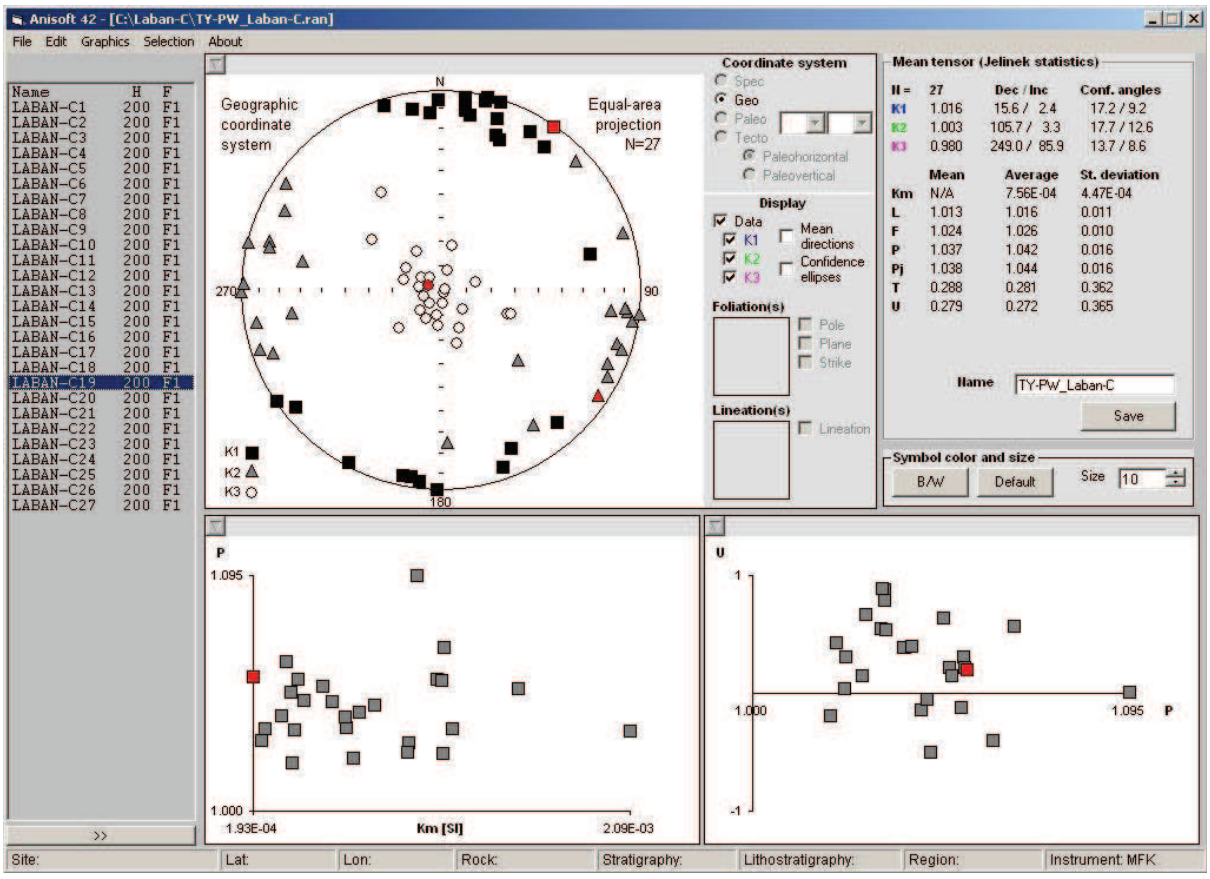
Anisoft 42 - [C:\Laban-C\TY-PW_Laban-C.ran]
File Edit Graphics Selection About
Name H F
LABAN-C1 200 F1
LABAN-C2 200 F1
LABAN-C3 200 F1
LABAN-C4 200 F1
LABAN-C5 200 F1
LABAN-C6 200 F1
LABAN-C7 200 F1
LABAN-C8 200 F1
LABAN-C9 200 F1
LABAN-C10 200 F1
LABAN-C11 200 F1
LABAN-C12 200 F1
LABAN-C13 200 F1
LABAN-C14 200 F1
LABAN-C15 200 F1
LABAN-C16 200 F1
LABAN-C17 200 F1
LABAN-C18 200 F1
LABAN-C19 200 F1
LABAN-C20 200 F1
LABAN-C21 200 F1
LABAN-C22 200 F1
LABAN-C23 200 F1
LABAN-C24 200 F1
LABAN-C25 200 F1
LABAN-C26 200 F1
LABAN-C27 200 F1
Geographic coordinate system
Equal-area projection N=27
N
90
180
270
K1
K2
K3
Coordinate system
Spec
Geo
Paleo
Tecto
Paleohorizontal
Paleovertical
Display
Data
K1
K2
K3
Mean directions
Confidence ellipses
Foliation(s)
Pole
Plane
Strike
Lineation(s)
Lineation
Mean tensor (Jelinek statistics)
II = 27 Dec / Inc Conf. angles
K1 1.016 15.6 / 2.4 17.2 / 9.2
K2 1.003 105.7 / 3.3 17.7 / 12.6
K3 0.980 249.0 / 85.9 13.7 / 8.6
Mean Average St. deviation
Km N/A 7.56E-04 4.47E-04
L 1.013 1.016 0.011
F 1.024 1.026 0.010
P 1.037 1.042 0.016
Pj 1.038 1.044 0.016
T 0.288 0.281 0.362
U 0.279 0.272 0.365
Name TY-PW_Laban-C
Save
Symbol color and size
B/W
Default
Size 10
P
1.095
1.000
1.93E-04
Km [SI]
2.09E-03
U
1
-1
Site:
Lat:
Lon:
Rock:
Stratigraphy:
Lithostratigraphy:
Region:
Instrument: MFK

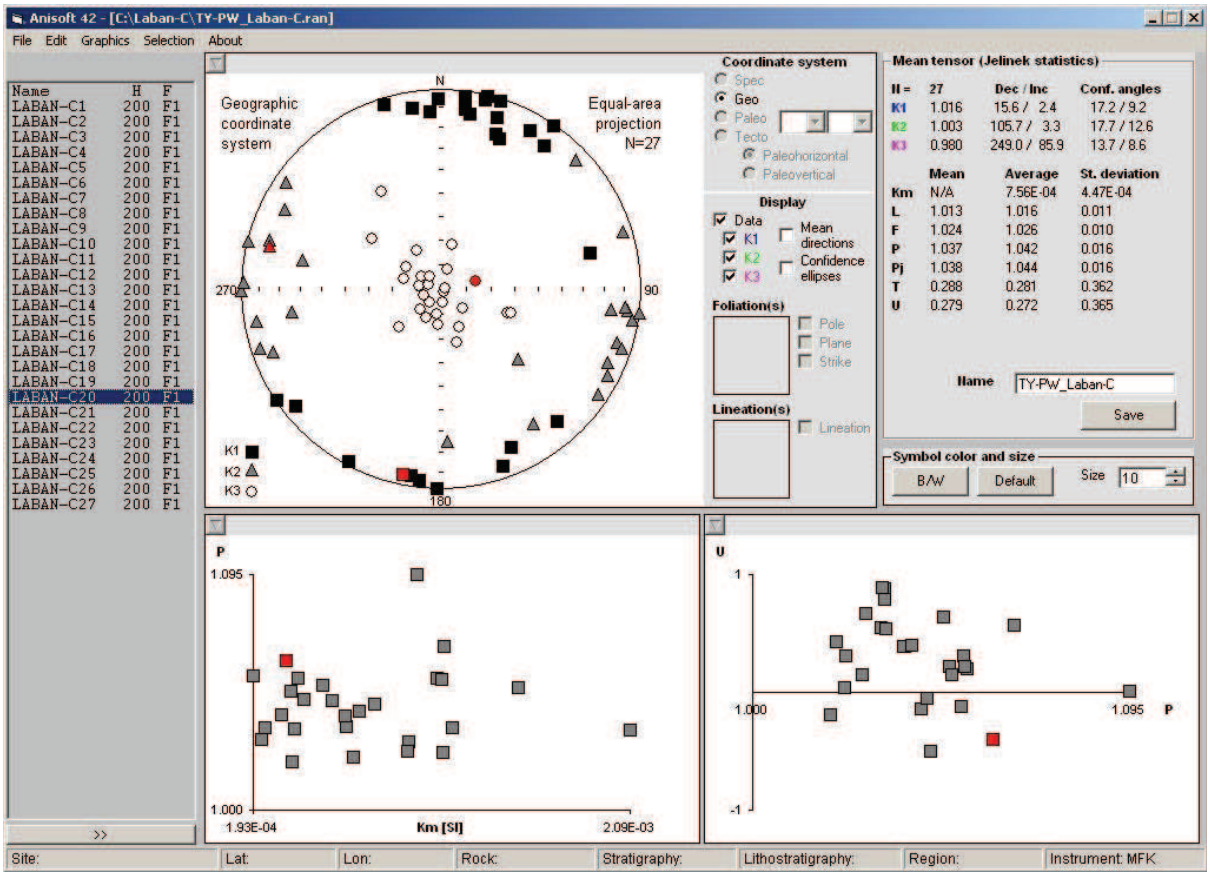
Anisoft 42 - [C:\Laban-C\TY-PW_Laban-C.ran]
File Edit Graphics Selection About
Name H F
LABAN-C1 200 F1
LABAN-C2 200 F1
LABAN-C3 200 F1
LABAN-C4 200 F1
LABAN-C5 200 F1
LABAN-C6 200 F1
LABAN-C7 200 F1
LABAN-C8 200 F1
LABAN-C9 200 F1
LABAN-C10 200 F1
LABAN-C11 200 F1
LABAN-C12 200 F1
LABAN-C13 200 F1
LABAN-C14 200 F1
LABAN-C15 200 F1
LABAN-C16 200 F1
LABAN-C17 200 F1
LABAN-C18 200 F1
LABAN-C19 200 F1
LABAN-C20 200 F1
LABAN-C21 200 F1
LABAN-C22 200 F1
LABAN-C23 200 F1
LABAN-C24 200 F1
LABAN-C25 200 F1
LABAN-C26 200 F1
LABAN-C27 200 F1
Geographic coordinate system
Equal-area projection N=27
N
90
180
270
K1
K2
K3
Coordinate system
Spec
Geo
Paleo
Tecto
Paleohorizontal
Paleovertical
Display
Data
K1
K2
K3
Mean directions
Confidence ellipses
Foliation(s)
Pole
Plane
Strike
Lineation(s)
Lineation
Mean tensor (Jelinek statistics)
II = 27 Dec / Inc Conf. angles
K1 1.016 15.6 / 2.4 17.2 / 9.2
K2 1.003 105.7 / 3.3 17.7 / 12.6
K3 0.980 249.0 / 85.9 13.7 / 8.6
Mean Average St. deviation
Km N/A 7.56E-04 4.47E-04
L 1.013 1.016 0.011
F 1.024 1.026 0.010
P 1.037 1.042 0.016
Pj 1.038 1.044 0.016
T 0.288 0.281 0.362
U 0.279 0.272 0.365
Name TY-PW_Laban-C
Save
Symbol color and size
B/W
Default
Size 10
P
1.095
1.000
1.93E-04
Km [SI]
2.09E-03
U
1
-1
1.000
1.095
P
Site:
Lat:
Lon:
Rock:
Stratigraphy:
Lithostratigraphy:
Region:
Instrument: MFK

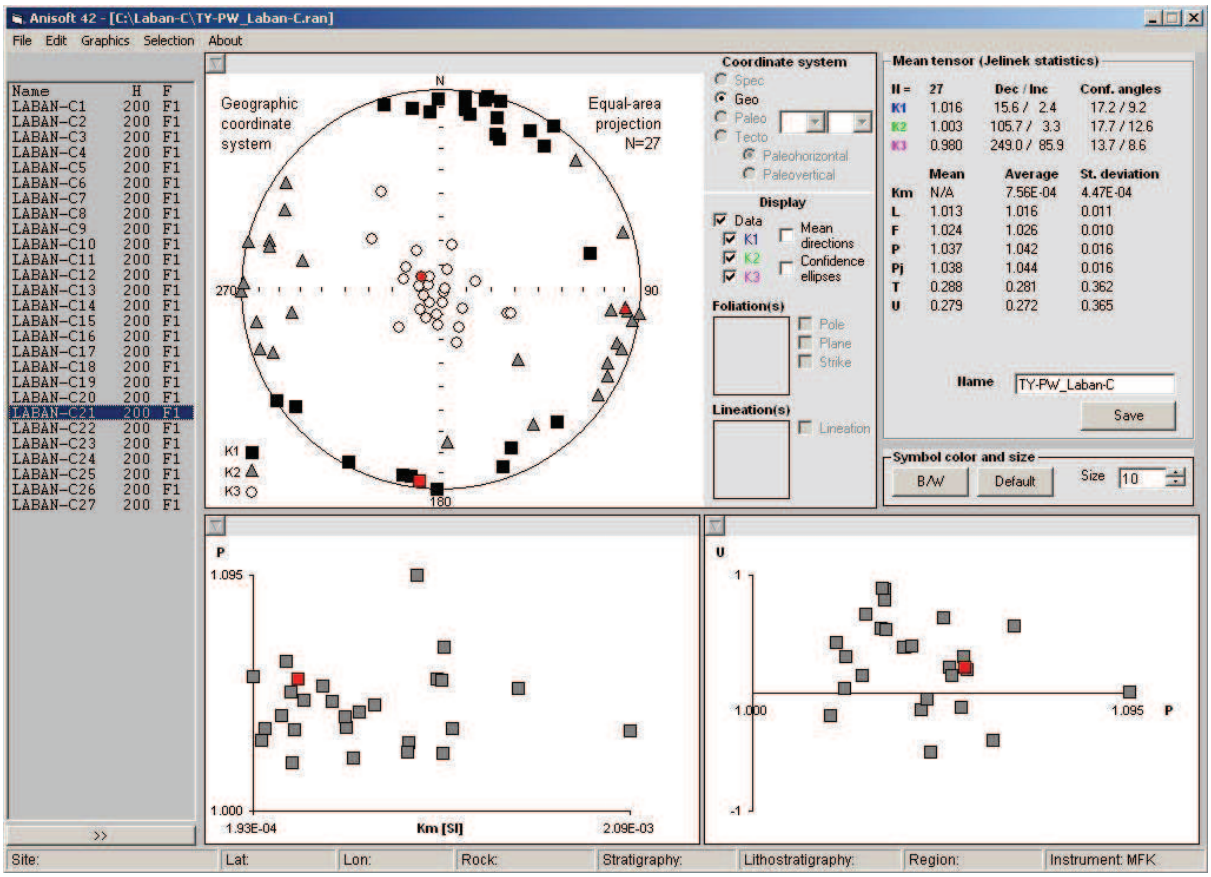
Anisoft 42 - [C:\Laban-C\TY-PW_Laban-C.ran]
File Edit Graphics Selection About
Name H F
LABAN-C1 200 F1
LABAN-C2 200 F1
LABAN-C3 200 F1
LABAN-C4 200 F1
LABAN-C5 200 F1
LABAN-C6 200 F1
LABAN-C7 200 F1
LABAN-C8 200 F1
LABAN-C9 200 F1
LABAN-C10 200 F1
LABAN-C11 200 F1
LABAN-C12 200 F1
LABAN-C13 200 F1
LABAN-C14 200 F1
LABAN-C15 200 F1
LABAN-C16 200 F1
LABAN-C17 200 F1
LABAN-C18 200 F1
LABAN-C19 200 F1
LABAN-C20 200 F1
LABAN-C21 200 F1
LABAN-C22 200 F1
LABAN-C23 200 F1
LABAN-C24 200 F1
LABAN-C25 200 F1
LABAN-C26 200 F1
LABAN-C27 200 F1
Geographic coordinate system
Equal-area projection N=27
N
90
180
270
K1
K2
K3
Coordinate system
Spec
Geo
Paleo
Tecto
Paleohorizontal
Paleovertical
Display
Data
K1
K2
K3
Mean directions
Confidence ellipses
Foliation(s)
Pole
Plane
Strike
Lineation(s)
Lineation
Mean tensor (Jelinek statistics)
II = 27 Dec / Inc Conf. angles
K1 1.016 15.6 / 2.4 17.2 / 9.2
K2 1.003 105.7 / 3.3 17.7 / 12.6
K3 0.980 249.0 / 85.9 13.7 / 8.6
Mean Average St. deviation
Km N/A 7.56E-04 4.47E-04
L 1.013 1.016 0.011
F 1.024 1.026 0.010
P 1.037 1.042 0.016
Pj 1.038 1.044 0.016
T 0.288 0.281 0.362
U 0.279 0.272 0.365
Name TY-PW_Laban-C
Save
Symbol color and size
B/W
Default
Size 10
P
1.095
1.000
1.93E-04
Km [SI]
2.09E-03
U
1
-1
1.000
1.095
P
Site:
Lat:
Lon:
Rock:
Stratigraphy:
Lithostratigraphy:
Region:
Instrument: MFK

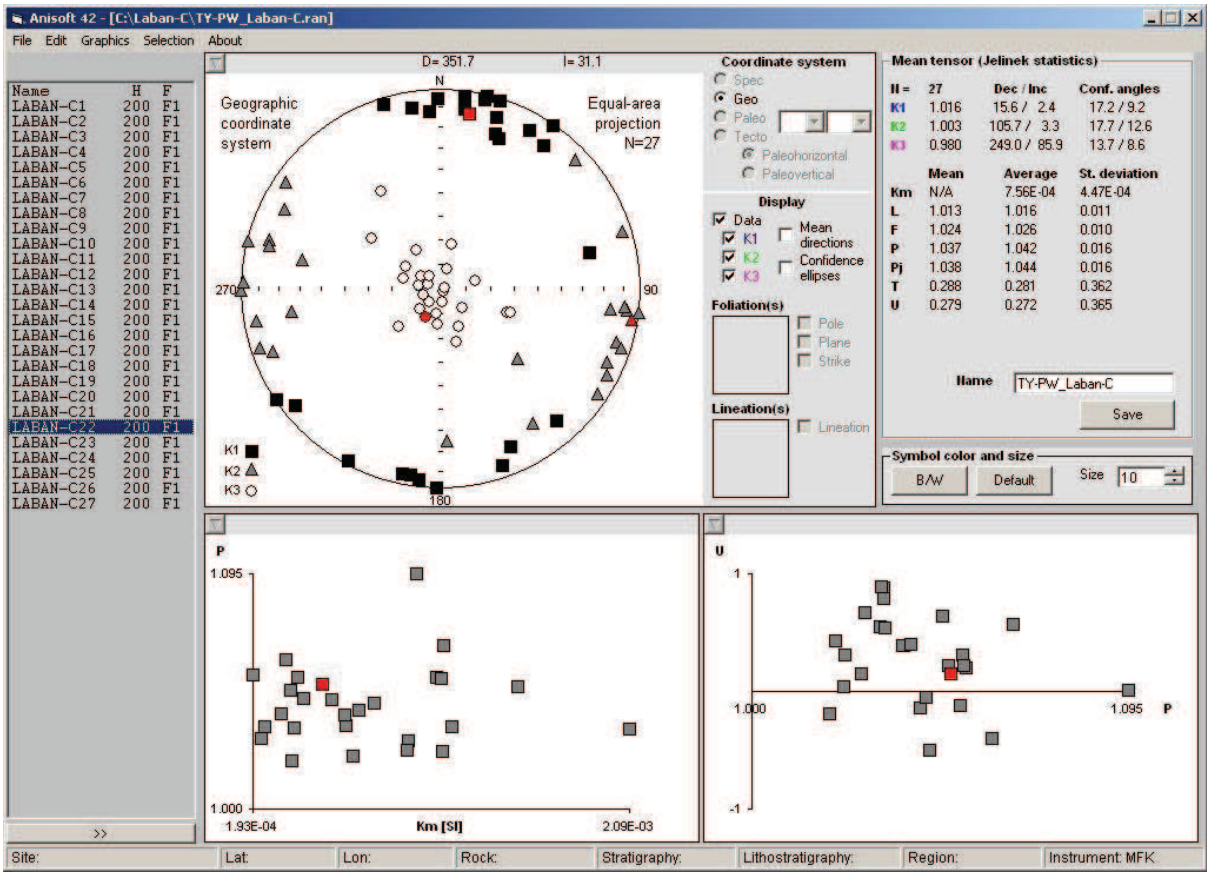
Anisoft 42 - [C:\Laban-C\TY-PW_Laban-C.ran]
File Edit Graphics Selection About
Name H F
LABAN-C1 200 F1
LABAN-C2 200 F1
LABAN-C3 200 F1
LABAN-C4 200 F1
LABAN-C5 200 F1
LABAN-C6 200 F1
LABAN-C7 200 F1
LABAN-C8 200 F1
LABAN-C9 200 F1
LABAN-C10 200 F1
LABAN-C11 200 F1
LABAN-C12 200 F1
LABAN-C13 200 F1
LABAN-C14 200 F1
LABAN-C15 200 F1
LABAN-C16 200 F1
LABAN-C17 200 F1
LABAN-C18 200 F1
LABAN-C19 200 F1
LABAN-C20 200 F1
LABAN-C21 200 F1
LABAN-C22 200 F1
LABAN-C23 200 F1
LABAN-C24 200 F1
LABAN-C25 200 F1
LABAN-C26 200 F1
LABAN-C27 200 F1
D= 351.7 I= 31.1
Geographic coordinate system
Equal-area projection N=27
N
90
180
270
K1
K2
K3
Coordinate system
Spec
Geo
Paleo
Tecto
Paleohorizontal
Paleovertical
Display
Data
K1
K2
K3
Mean directions
Confidence ellipses
Foliation(s)
Pole
Plane
Strike
Lineation(s)
Lineation
Mean tensor (Jelinek statistics)
II = 27 Dec / Inc Conf. angles
K1 1.016 15.6 / 2.4 17.2 / 9.2
K2 1.003 105.7 / 3.3 17.7 / 12.6
K3 0.980 249.0 / 85.9 13.7 / 8.6
Mean Average St. deviation
Km N/A 7.56E-04 4.47E-04
L 1.013 1.016 0.011
F 1.024 1.026 0.010
P 1.037 1.042 0.016
Pj 1.038 1.044 0.016
T 0.288 0.281 0.362
U 0.279 0.272 0.365
Name TY-PW_Laban-C
Save
Symbol color and size
B/W
Default
Size 10
P
1.095
1.000
1.93E-04
Km [SI]
2.09E-03
U
1
-1
Site:
Lat:
Lon:
Rock:
Stratigraphy:
Lithostratigraphy:
Region:
Instrument: MFK

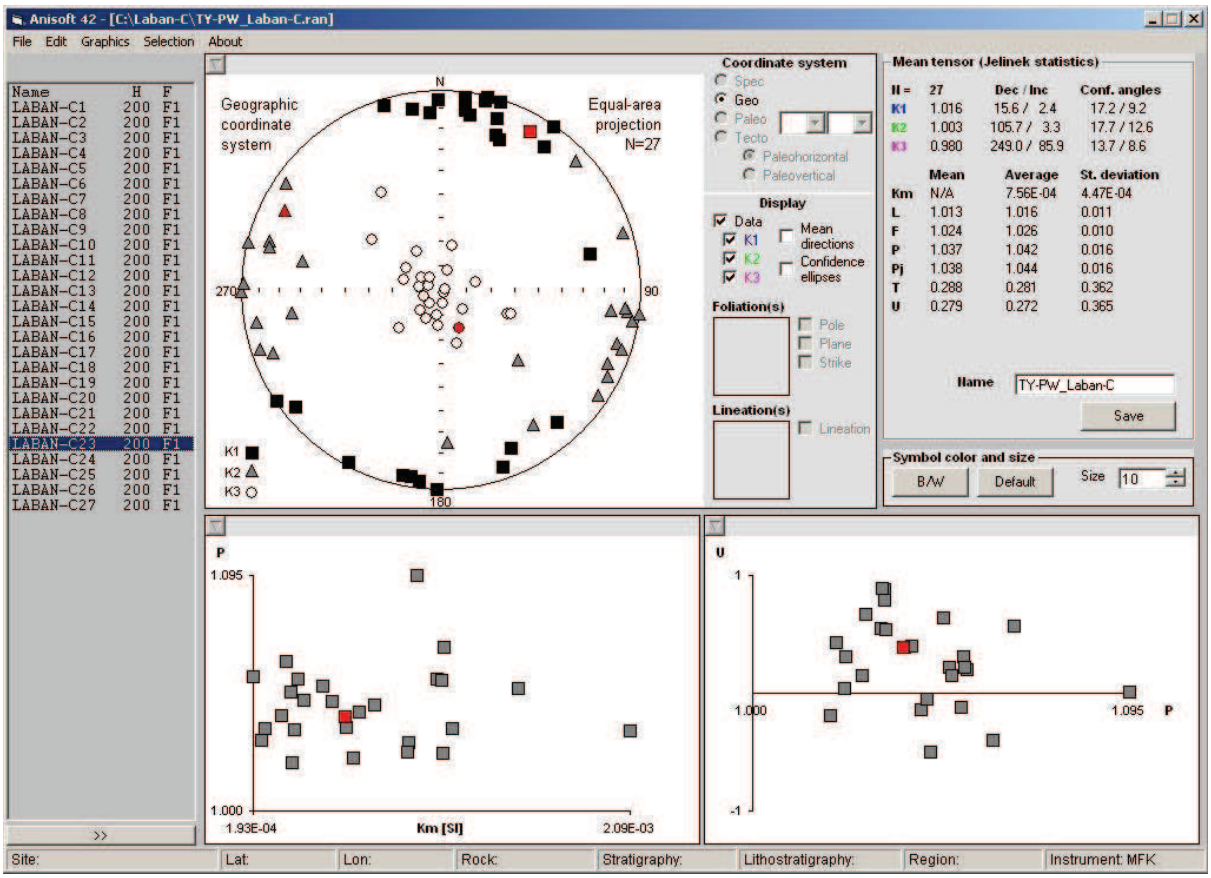
Anisoft 42 - [C:\Laban-C\TY-PW_Laban-C.ran]
File Edit Graphics Selection About
Name H F
LABAN-C1 200 F1
LABAN-C2 200 F1
LABAN-C3 200 F1
LABAN-C4 200 F1
LABAN-C5 200 F1
LABAN-C6 200 F1
LABAN-C7 200 F1
LABAN-C8 200 F1
LABAN-C9 200 F1
LABAN-C10 200 F1
LABAN-C11 200 F1
LABAN-C12 200 F1
LABAN-C13 200 F1
LABAN-C14 200 F1
LABAN-C15 200 F1
LABAN-C16 200 F1
LABAN-C17 200 F1
LABAN-C18 200 F1
LABAN-C19 200 F1
LABAN-C20 200 F1
LABAN-C21 200 F1
LABAN-C22 200 F1
LABAN-C23 200 F1
LABAN-C24 200 F1
LABAN-C25 200 F1
LABAN-C26 200 F1
LABAN-C27 200 F1
Geographic coordinate system
Equal-area projection N=27
N
90
180
270
K1
K2
K3
Coordinate system
Spec
Geo
Paleo
Tecto
Paleohorizontal
Paleovertical
Display
Data
K1
K2
K3
Mean directions
Confidence ellipses
Foliation(s)
Pole
Plane
Strike
Lineation(s)
Lineation
Mean tensor (Jelinek statistics)
II = 27 Dec / Inc Conf. angles
K1 1.016 15.6 / 2.4 17.2 / 9.2
K2 1.003 105.7 / 3.3 17.7 / 12.6
K3 0.980 249.0 / 85.9 13.7 / 8.6
Mean Average St. deviation
Km N/A 7.56E-04 4.47E-04
L 1.013 1.016 0.011
F 1.024 1.026 0.010
P 1.037 1.042 0.016
Pj 1.038 1.044 0.016
T 0.288 0.281 0.362
U 0.279 0.272 0.365
Name TY-PW_Laban-C
Save
Symbol color and size
B/W
Default
Size 10
P
1.095
1.000
1.93E-04
Km [SI]
2.09E-03
U
1
-1
Site:
Lat:
Lon:
Rock:
Stratigraphy:
Lithostratigraphy:
Region:
Instrument: MFK

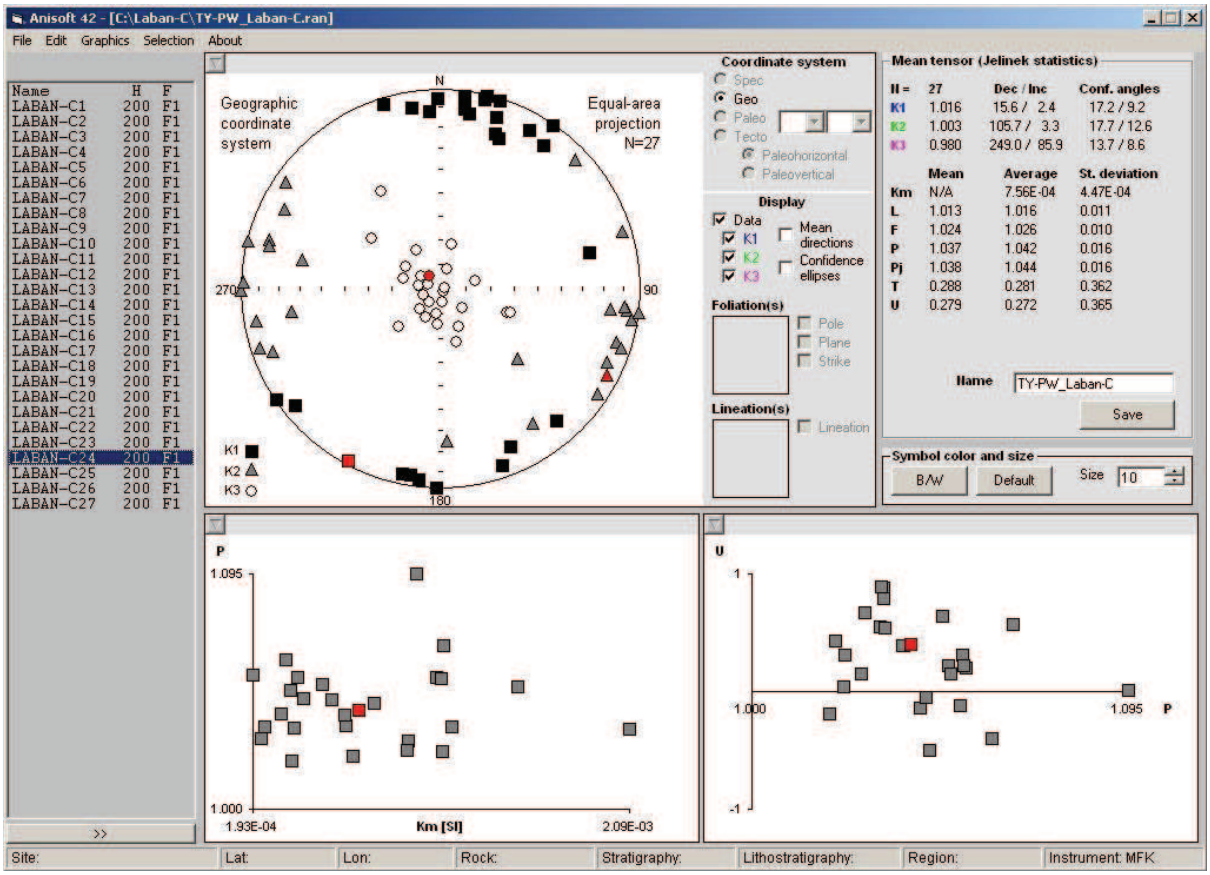
Anisoft 42 - [C:\Laban-C\TY-PW_Laban-C.ran]
File Edit Graphics Selection About
Name H F
LABAN-C1 200 F1
LABAN-C2 200 F1
LABAN-C3 200 F1
LABAN-C4 200 F1
LABAN-C5 200 F1
LABAN-C6 200 F1
LABAN-C7 200 F1
LABAN-C8 200 F1
LABAN-C9 200 F1
LABAN-C10 200 F1
LABAN-C11 200 F1
LABAN-C12 200 F1
LABAN-C13 200 F1
LABAN-C14 200 F1
LABAN-C15 200 F1
LABAN-C16 200 F1
LABAN-C17 200 F1
LABAN-C18 200 F1
LABAN-C19 200 F1
LABAN-C20 200 F1
LABAN-C21 200 F1
LABAN-C22 200 F1
LABAN-C23 200 F1
LABAN-C24 200 F1
LABAN-C25 200 F1
LABAN-C26 200 F1
LABAN-C27 200 F1
Geographic coordinate system
Equal-area projection N=27
N
90
180
270
K1
K2
K3
Coordinate system
Spec
Geo
Paleo
Tecto
Paleohorizontal
Paleovertical
Display
Data
K1
K2
K3
Mean directions
Confidence ellipses
Foliation(s)
Pole
Plane
Strike
Lineation(s)
Lineation
Mean tensor (Jelinek statistics)
II = 27 Dec / Inc Conf. angles
K1 1.016 15.6 / 2.4 17.2 / 9.2
K2 1.003 105.7 / 3.3 17.7 / 12.6
K3 0.980 249.0 / 85.9 13.7 / 8.6
Mean Average St. deviation
Km N/A 7.56E-04 4.47E-04
L 1.013 1.016 0.011
F 1.024 1.026 0.010
P 1.037 1.042 0.016
Pj 1.038 1.044 0.016
T 0.288 0.281 0.362
U 0.279 0.272 0.365
Name TY-PW_Laban-C
Save
Symbol color and size
B/W
Default
Size 10
P
1.095
1.000
1.93E-04
Km [SI]
2.09E-03
U
1
-1
Site:
Lat:
Lon:
Rock:
Stratigraphy:
Lithostratigraphy:
Region:
Instrument: MFK

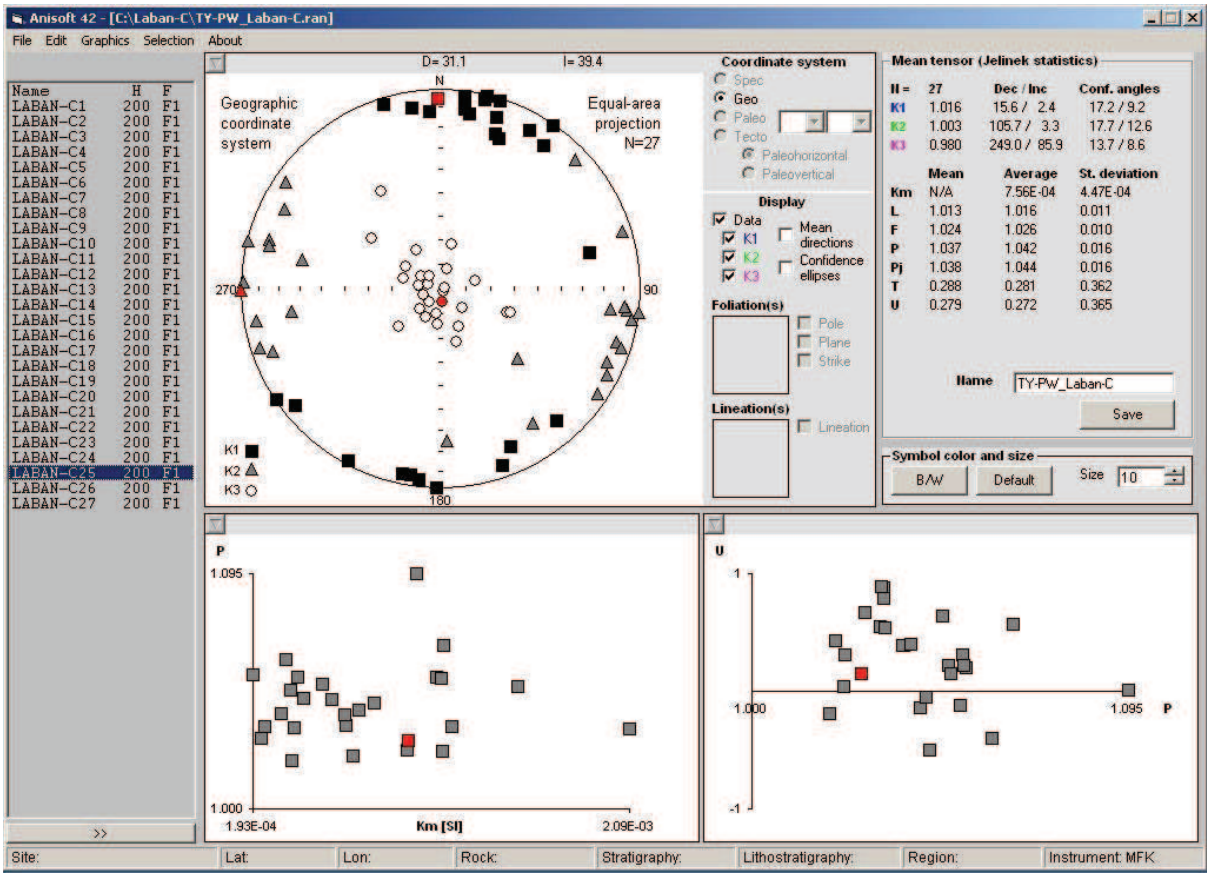
Anisoft 42 - [C:\Laban-C\TY-PW_Laban-C.ran]
File Edit Graphics Selection About
D= 31.1 I= 39.4
Name H F
LABAN-C1 200 F1
LABAN-C2 200 F1
LABAN-C3 200 F1
LABAN-C4 200 F1
LABAN-C5 200 F1
LABAN-C6 200 F1
LABAN-C7 200 F1
LABAN-C8 200 F1
LABAN-C9 200 F1
LABAN-C10 200 F1
LABAN-C11 200 F1
LABAN-C12 200 F1
LABAN-C13 200 F1
LABAN-C14 200 F1
LABAN-C15 200 F1
LABAN-C16 200 F1
LABAN-C17 200 F1
LABAN-C18 200 F1
LABAN-C19 200 F1
LABAN-C20 200 F1
LABAN-C21 200 F1
LABAN-C22 200 F1
LABAN-C23 200 F1
LABAN-C24 200 F1
LABAN-C25 200 F1
LABAN-C26 200 F1
LABAN-C27 200 F1
Geographic coordinate system
Equal-area projection N=27
N
90
180
270
K1
K2
K3
Coordinate system
Spec
Geo
Paleo
Tecto
Paleohorizontal
Paleovertical
Display
Data
K1
K2
K3
Mean directions
Confidence ellipses
Foliation(s)
Pole
Plane
Strike
Lineation(s)
Lineation
Mean tensor (Jelinek statistics)
II = 27 Dec / Inc Conf. angles
K1 1.016 15.6 / 2.4 17.2 / 9.2
K2 1.003 105.7 / 3.3 17.7 / 12.6
K3 0.980 249.0 / 85.9 13.7 / 8.6
Mean Average St. deviation
Km N/A 7.56E-04 4.47E-04
L 1.013 1.016 0.011
F 1.024 1.026 0.010
P 1.037 1.042 0.016
Pj 1.038 1.044 0.016
T 0.288 0.281 0.362
U 0.279 0.272 0.365
Name TY-PW_Laban-C
Save
Symbol color and size
B/W
Default
Size 10
P
1.095
1.000
1.93E-04
Km [SI]
2.09E-03
U
1
-1
Site:
Lat:
Lon:
Rock:
Stratigraphy:
Lithostratigraphy:
Region:
Instrument: MFK

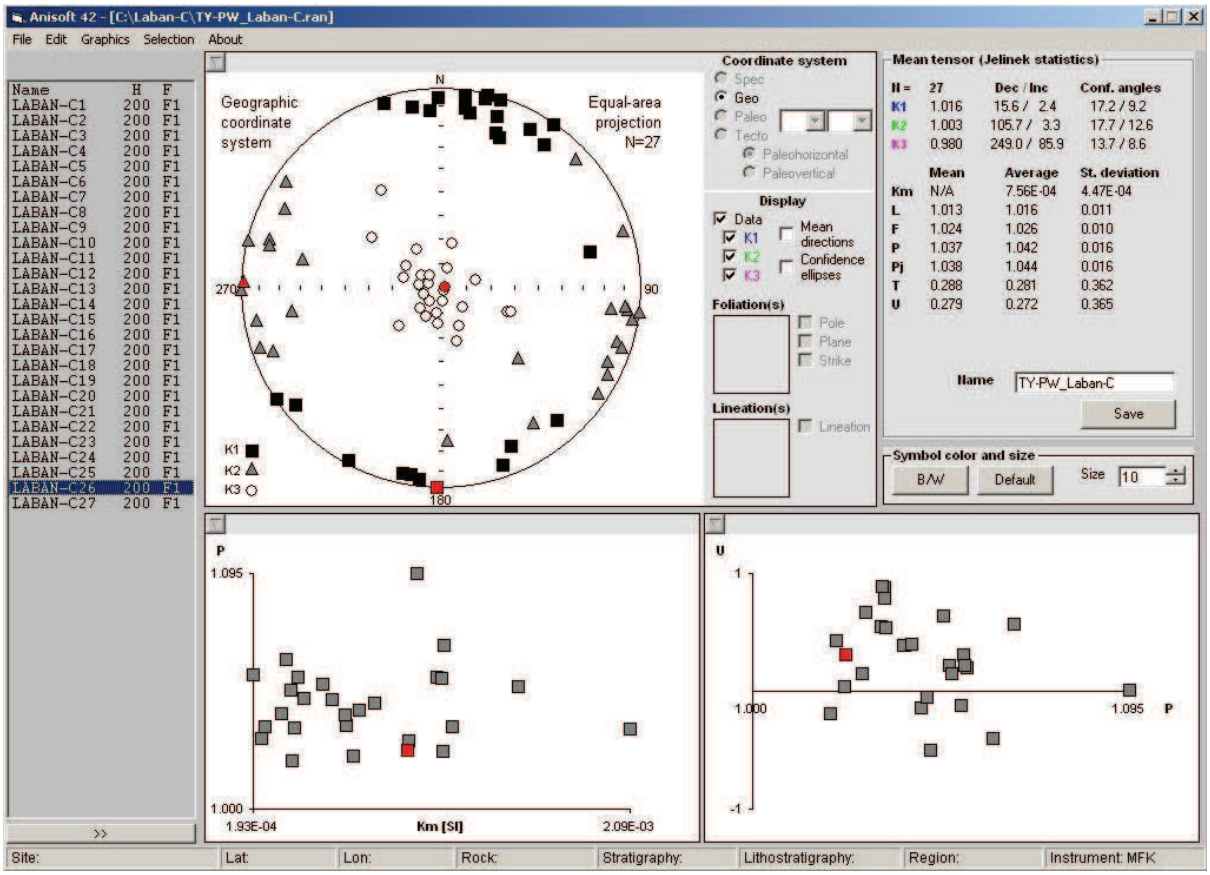
Anisoft 42 - [C:\Laban-C\TY-PW_Laban-C.ran]
File Edit Graphics Selection About
Name H F
LABAN-C1 200 F1
LABAN-C2 200 F1
LABAN-C3 200 F1
LABAN-C4 200 F1
LABAN-C5 200 F1
LABAN-C6 200 F1
LABAN-C7 200 F1
LABAN-C8 200 F1
LABAN-C9 200 F1
LABAN-C10 200 F1
LABAN-C11 200 F1
LABAN-C12 200 F1
LABAN-C13 200 F1
LABAN-C14 200 F1
LABAN-C15 200 F1
LABAN-C16 200 F1
LABAN-C17 200 F1
LABAN-C18 200 F1
LABAN-C19 200 F1
LABAN-C20 200 F1
LABAN-C21 200 F1
LABAN-C22 200 F1
LABAN-C23 200 F1
LABAN-C24 200 F1
LABAN-C25 200 F1
LABAN-C26 200 F1
LABAN-C27 200 F1
Geographic coordinate system
Equal-area projection N=27
N
90
180
270
K1
K2
K3
Coordinate system
Spec
Geo
Paleo
Tecto
Paleohorizontal
Paleovertical
Display
Data
K1
K2
K3
Mean directions
Confidence ellipses
Foliation(s)
Pole
Plane
Strike
Lineation(s)
Lineation
Mean tensor (Jelinek statistics)
II = 27 Dec / Inc Conf. angles
K1 1.016 15.6 / 2.4 17.2 / 9.2
K2 1.003 105.7 / 3.3 17.7 / 12.6
K3 0.980 249.0 / 85.9 13.7 / 8.6
Mean Average St. deviation
Km N/A 7.56E-04 4.47E-04
L 1.013 1.016 0.011
F 1.024 1.026 0.010
P 1.037 1.042 0.016
Pj 1.038 1.044 0.016
T 0.288 0.281 0.362
U 0.279 0.272 0.365
Name TY-PW_Laban-C
Save
Symbol color and size
B/W
Default
Size 10
P
1.095
1.000
1.93E-04
Km [SI]
2.09E-03
U
1
-1
Site:
Lat:
Lon:
Rock:
Stratigraphy:
Lithostratigraphy:
Region:
Instrument: MFK

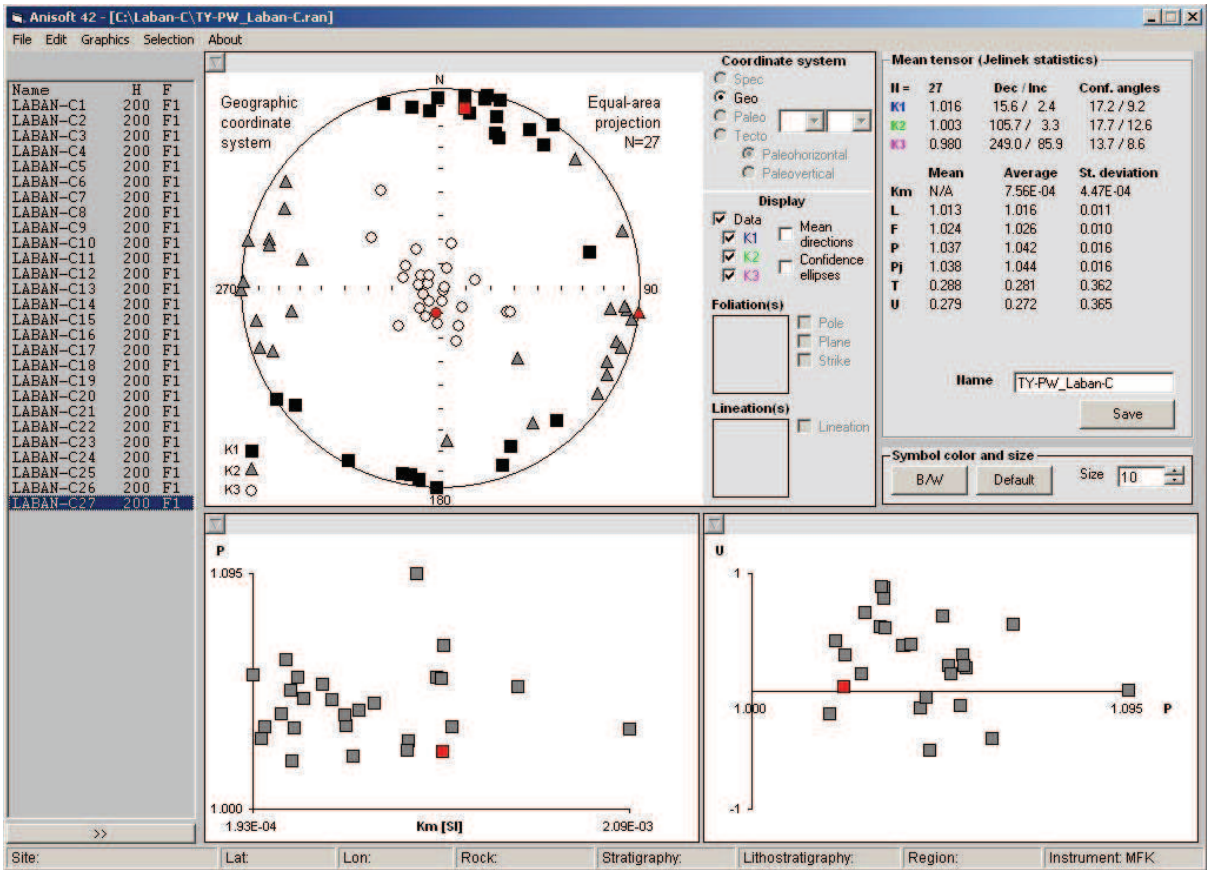
Anisoft 42 - [C:\Laban-C\TY-PW_Laban-C.ran]
File Edit Graphics Selection About
Name H F
LABAN-C1 200 F1
LABAN-C2 200 F1
LABAN-C3 200 F1
LABAN-C4 200 F1
LABAN-C5 200 F1
LABAN-C6 200 F1
LABAN-C7 200 F1
LABAN-C8 200 F1
LABAN-C9 200 F1
LABAN-C10 200 F1
LABAN-C11 200 F1
LABAN-C12 200 F1
LABAN-C13 200 F1
LABAN-C14 200 F1
LABAN-C15 200 F1
LABAN-C16 200 F1
LABAN-C17 200 F1
LABAN-C18 200 F1
LABAN-C19 200 F1
LABAN-C20 200 F1
LABAN-C21 200 F1
LABAN-C22 200 F1
LABAN-C23 200 F1
LABAN-C24 200 F1
LABAN-C25 200 F1
LABAN-C26 200 F1
LABAN-C27 200 F1
Geographic coordinate system
Equal-area projection N=27
N
90
180
270
K1
K2
K3
Coordinate system
Spec
Geo
Paleo
Tecto
Paleohorizontal
Paleovertical
Display
Data
K1
K2
K3
Mean directions
Confidence ellipses
Foliation(s)
Pole
Plane
Strike
Lineation(s)
Lineation
Mean tensor (Jelinek statistics)
II = 27 Dec / Inc Conf. angles
K1 1.016 15.6 / 2.4 17.2 / 9.2
K2 1.003 105.7 / 3.3 17.7 / 12.6
K3 0.980 249.0 / 85.9 13.7 / 8.6
Mean Average St. deviation
Km N/A 7.56E-04 4.47E-04
L 1.013 1.016 0.011
F 1.024 1.026 0.010
P 1.037 1.042 0.016
Pj 1.038 1.044 0.016
T 0.288 0.281 0.362
U 0.279 0.272 0.365
Name TY-PW_Laban-C
Save
Symbol color and size
B/W
Default
Size 10
P
1.095
1.000
1.93E-04
Km [SI]
2.09E-03
U
1
-1
Site:
Lat:
Lon:
Rock:
Stratigraphy:
Lithostratigraphy:
Region:
Instrument: MFK

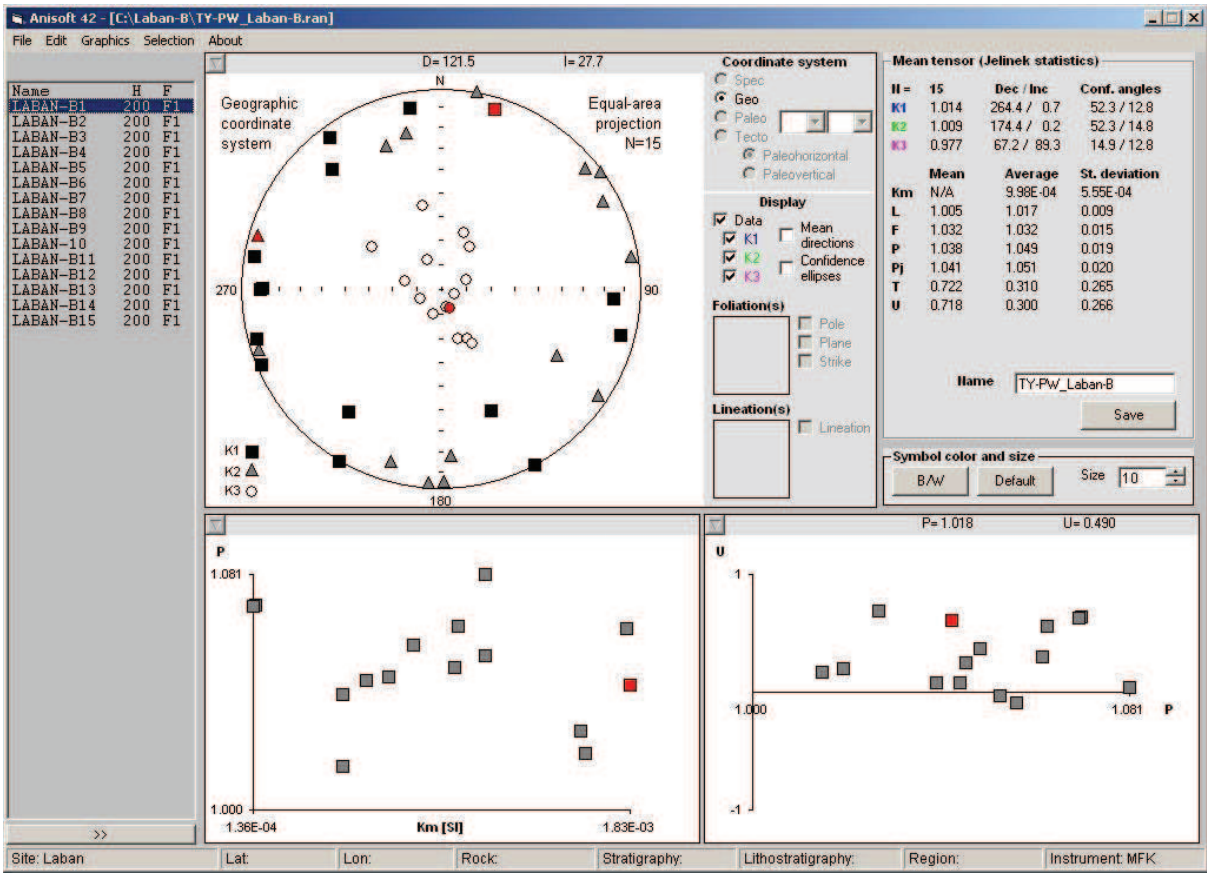
Anisoft 42 - [C:\Laban-B\TY-PW_Laban-B.ran]
File Edit Graphics Selection About
Name H F
LABAN-B1 200 F1
LABAN-B2 200 F1
LABAN-B3 200 F1
LABAN-B4 200 F1
LABAN-B5 200 F1
LABAN-B6 200 F1
LABAN-B7 200 F1
LABAN-B8 200 F1
LABAN-B9 200 F1
LABAN-10 200 F1
LABAN-B11 200 F1
LABAN-B12 200 F1
LABAN-B13 200 F1
LABAN-B14 200 F1
LABAN-B15 200 F1
D= 121.5 I= 27.7
Geographic coordinate system
Equal-area projection N=15
N
270
90
180
K1
K2
K3
Coordinate system
Spec
Geo
Paleo
Tecto
Paleohorizontal
Paleovertical
Display
Data
K1
K2
K3
Mean directions
Confidence ellipses
Foliation(s)
Pole
Plane
Strike
Lineation(s)
Lineation
Mean tensor (Jelinek statistics)
II = 15 Dec / Inc Conf. angles
K1 1.014 264.4 / 0.7 52.3 / 12.8
K2 1.009 174.4 / 0.2 52.3 / 14.8
K3 0.977 67.2 / 89.3 14.9 / 12.8
Mean Average St. deviation
Km N/A 9.98E-04 5.55E-04
L 1.005 1.017 0.009
F 1.032 1.032 0.015
P 1.038 1.049 0.019
Pj 1.041 1.051 0.020
T 0.722 0.310 0.265
U 0.718 0.300 0.266
Name TY-PW_Laban-B
Save
Symbol color and size
B/W
Default
Size 10
P
1.081
1.000
1.36E-04
Km [SI]
1.83E-03
P= 1.018 U= 0.490
U
1
1.000
-1
1.081
P
Site: Laban
Lat:
Lon:
Rock:
Stratigraphy:
Lithostratigraphy:
Region:
Instrument: MFK

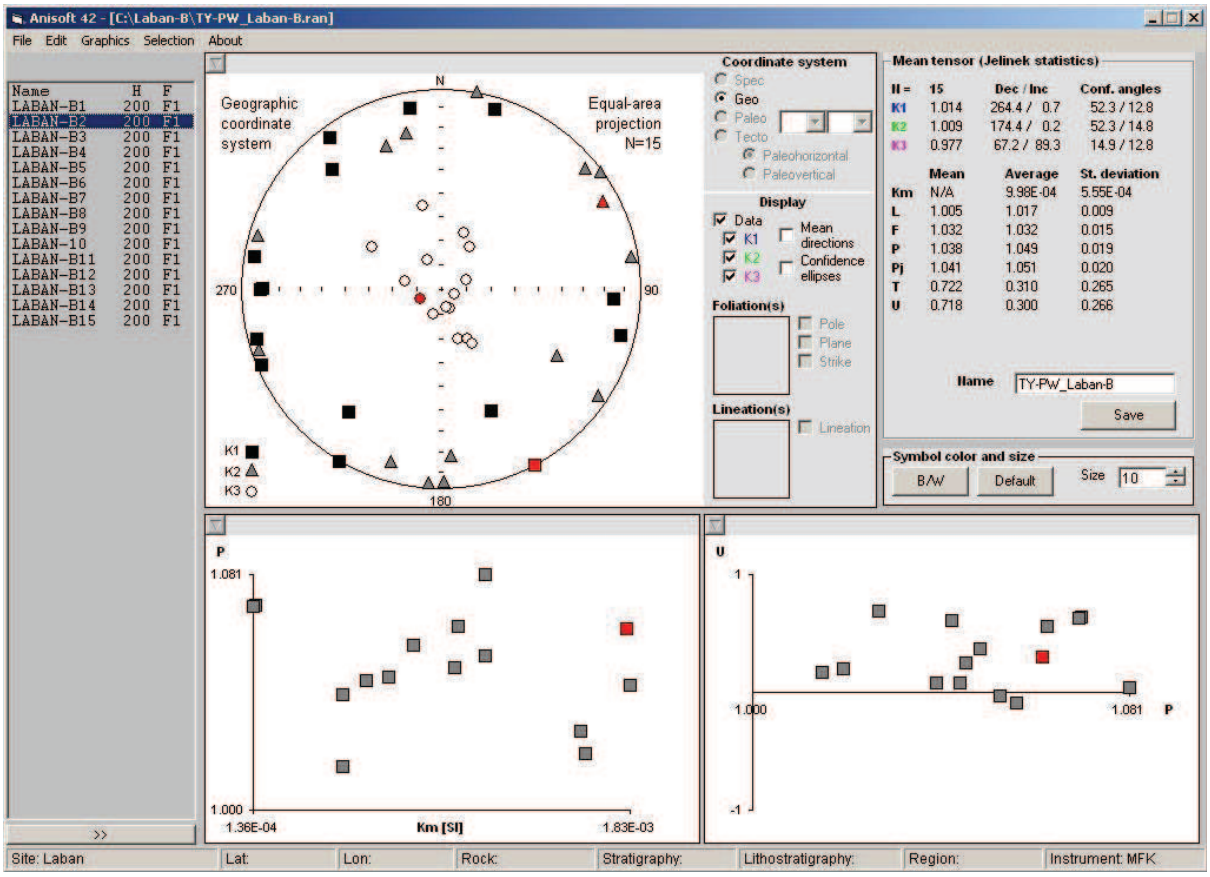
Anisoft 42 - [C:\Laban-B\TY-PW_Laban-B.ran]
File Edit Graphics Selection About
Name H F
LABAN-B1 200 F1
LABAN-B2 200 F1
LABAN-B3 200 F1
LABAN-B4 200 F1
LABAN-B5 200 F1
LABAN-B6 200 F1
LABAN-B7 200 F1
LABAN-B8 200 F1
LABAN-B9 200 F1
LABAN-10 200 F1
LABAN-B11 200 F1
LABAN-B12 200 F1
LABAN-B13 200 F1
LABAN-B14 200 F1
LABAN-B15 200 F1
Geographic coordinate system
Equal-area projection N=15
N
270
90
180
K1
K2
K3
Coordinate system
Spec
Geo
Paleo
Tecto
Paleohorizontal
Paleovertical
Display
Data
K1
K2
K3
Mean directions
Confidence ellipses
Foliation(s)
Pole
Plane
Strike
Lineation(s)
Lineation
Mean tensor (Jelinek statistics)
II = 15 Dec / Inc Conf. angles
K1 1.014 264.4 / 0.7 52.3 / 12.8
K2 1.009 174.4 / 0.2 52.3 / 14.8
K3 0.977 67.2 / 89.3 14.9 / 12.8
Mean Average St. deviation
Km N/A 9.98E-04 5.55E-04
L 1.005 1.017 0.009
F 1.032 1.032 0.015
P 1.038 1.049 0.019
Pj 1.041 1.051 0.020
T 0.722 0.310 0.265
U 0.718 0.300 0.266
Name TY-PW_Laban-B
Save
Symbol color and size
B/W
Default
Size 10
P
1.081
1.000
1.36E-04
Km [SI]
1.83E-03
U
1
1.000
-1
1.081
P
Site: Laban
Lat:
Lon:
Rock:
Stratigraphy:
Lithostratigraphy:
Region:
Instrument: MFK

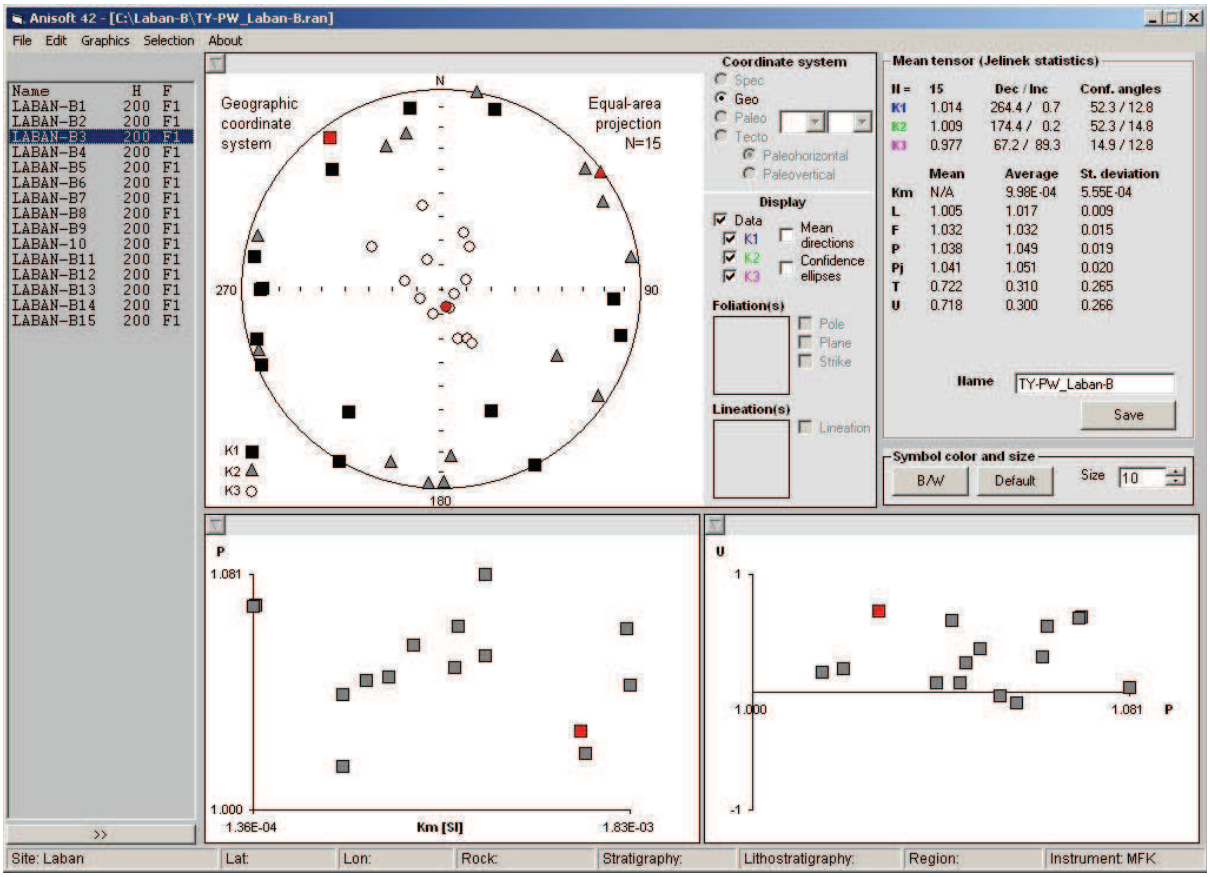
Anisoft 42 - [C:\Laban-B\TY-PW_Laban-B.ran]
File Edit Graphics Selection About
Name H F
LABAN-B1 200 F1
LABAN-B2 200 F1
LABAN-B3 200 F1
LABAN-B4 200 F1
LABAN-B5 200 F1
LABAN-B6 200 F1
LABAN-B7 200 F1
LABAN-B8 200 F1
LABAN-B9 200 F1
LABAN-10 200 F1
LABAN-B11 200 F1
LABAN-B12 200 F1
LABAN-B13 200 F1
LABAN-B14 200 F1
LABAN-B15 200 F1
Geographic coordinate system
Equal-area projection N=15
N
90
180
270
K1
K2
K3
Coordinate system
Spec
Geo
Paleo
Tecto
Paleohorizontal
Paleovertical
Display
Data
K1
K2
K3
Mean directions
Confidence ellipses
Foliation(s)
Pole
Plane
Strike
Lineation(s)
Lineation
Mean tensor (Jelinek statistics)
Dec / Inc
Conf. angles
K1 1.014 264.4 / 0.7 52.3 / 12.8
K2 1.009 174.4 / 0.2 52.3 / 14.8
K3 0.977 67.2 / 89.3 14.9 / 12.8
Mean
Average
St. deviation
Km N/A 9.98E-04 5.55E-04
L 1.005 1.017 0.009
F 1.032 1.032 0.015
P 1.038 1.049 0.019
Pj 1.041 1.051 0.020
T 0.722 0.310 0.265
U 0.718 0.300 0.266
Name
TY-PW_Laban-B
Save
Symbol color and size
B/W
Default
Size
10
P
1.081
1.000
1.36E-04
Km [SI]
1.83E-03
U
1
-1
1.000
1.081
P
Site: Laban
Lat:
Lon:
Rock:
Stratigraphy:
Lithostratigraphy:
Region:
Instrument: MFK

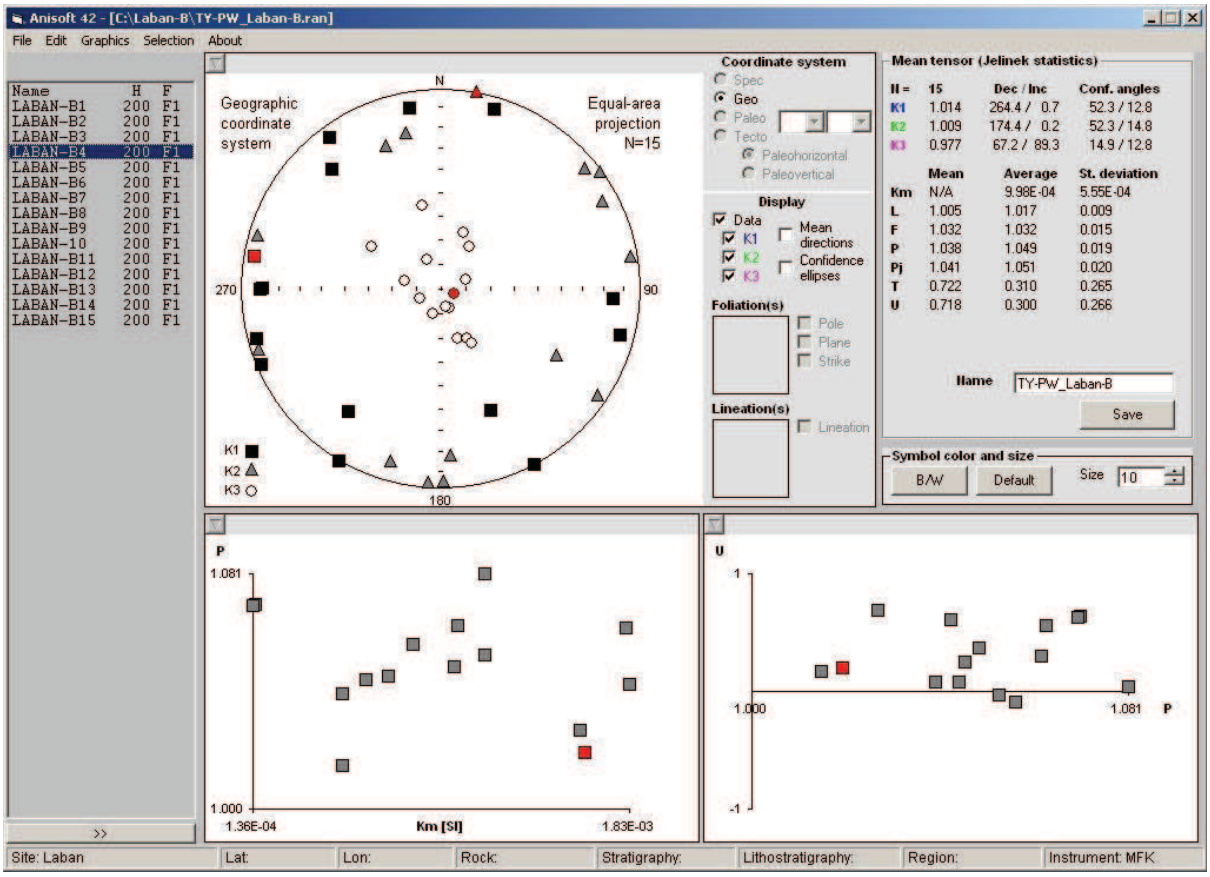
Anisoft 42 - [C:\Laban-B\TY-PW_Laban-B.ran]
File Edit Graphics Selection About
Name H F
LABAN-B1 200 F1
LABAN-B2 200 F1
LABAN-B3 200 F1
LABAN-B4 200 F1
LABAN-B5 200 F1
LABAN-B6 200 F1
LABAN-B7 200 F1
LABAN-B8 200 F1
LABAN-B9 200 F1
LABAN-10 200 F1
LABAN-B11 200 F1
LABAN-B12 200 F1
LABAN-B13 200 F1
LABAN-B14 200 F1
LABAN-B15 200 F1
Geographic coordinate system
Equal-area projection N=15
N
90
180
270
K1
K2
K3
Coordinate system
Spec
Geo
Paleo
Tecto
Paleohorizontal
Paleovertical
Display
Data
K1
K2
K3
Mean directions
Confidence ellipses
Foliation(s)
Pole
Plane
Strike
Lineation(s)
Lineation
Mean tensor (Jelinek statistics)
Dec / Inc
Conf. angles
K1 1.014 264.4 / 0.7 52.3 / 12.8
K2 1.009 174.4 / 0.2 52.3 / 14.8
K3 0.977 67.2 / 89.3 14.9 / 12.8
Mean
Average
St. deviation
Km N/A 9.98E-04 5.55E-04
L 1.005 1.017 0.009
F 1.032 1.032 0.015
P 1.038 1.049 0.019
Pj 1.041 1.051 0.020
T 0.722 0.310 0.265
U 0.718 0.300 0.266
Name
TY-PW_Laban-B
Save
Symbol color and size
B/W
Default
Size
10
P
1.081
1.000
1.36E-04
Km [SI]
1.83E-03
U
1
-1
1.000
1.081
P
Site: Laban
Lat:
Lon:
Rock:
Stratigraphy:
Lithostratigraphy:
Region:
Instrument: MFK

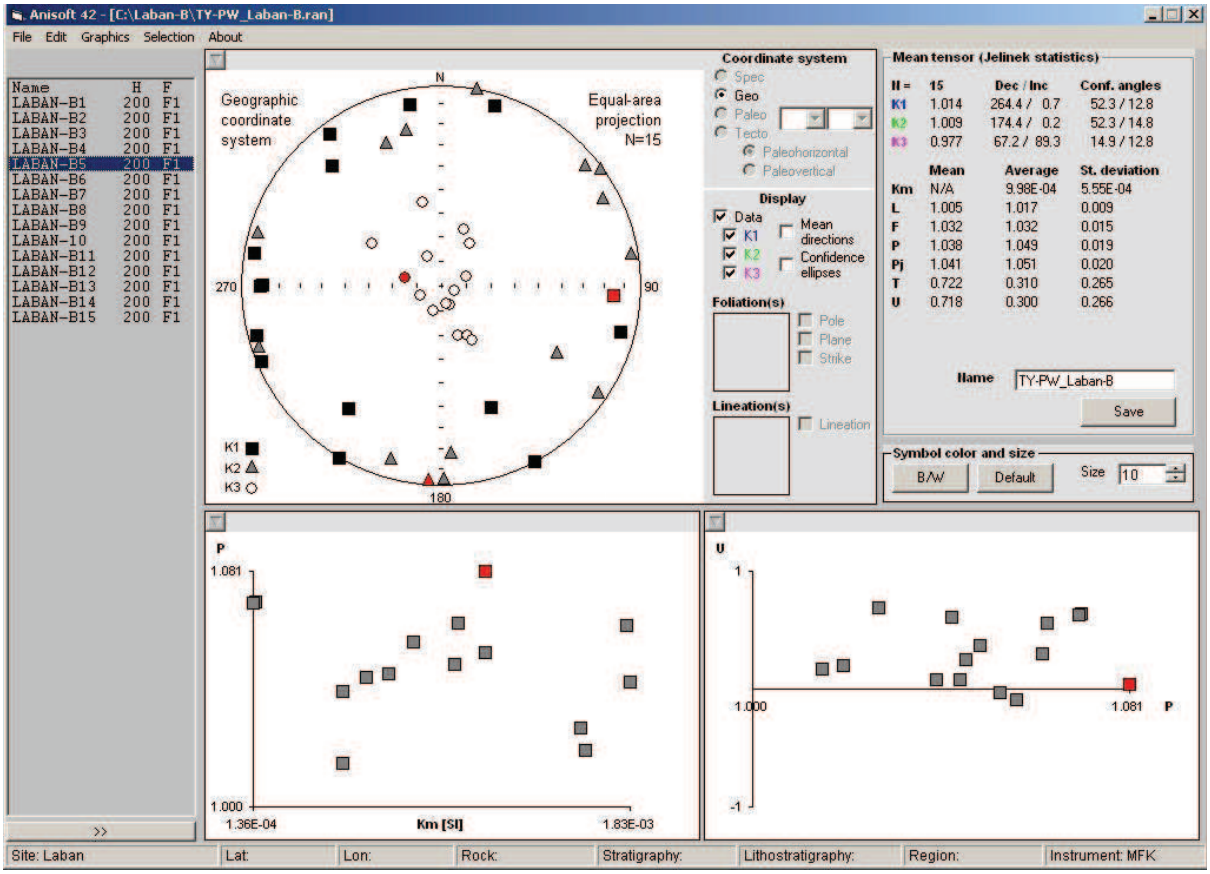
Anisoft 42 - [C:\Laban-B\TY-PW_Laban-B.ran]
File Edit Graphics Selection About
Name H F
LABAN-B1 200 F1
LABAN-B2 200 F1
LABAN-B3 200 F1
LABAN-B4 200 F1
LABAN-B5 200 F1
LABAN-B6 200 F1
LABAN-B7 200 F1
LABAN-B8 200 F1
LABAN-B9 200 F1
LABAN-10 200 F1
LABAN-B11 200 F1
LABAN-B12 200 F1
LABAN-B13 200 F1
LABAN-B14 200 F1
LABAN-B15 200 F1
Geographic coordinate system
Equal-area projection N=15
N
270
90
180
K1
K2
K3
Coordinate system
Spec
Geo
Paleo
Tecto
Paleohorizontal
Paleovertical
Display
Data
K1
K2
K3
Mean directions
Confidence ellipses
Foliation(s)
Pole
Plane
Strike
Lineation(s)
Lineation
Mean tensor (Jelinek statistics)
II = 15 Dec / Inc Conf. angles
K1 1.014 264.4 / 0.7 52.3 / 12.8
K2 1.009 174.4 / 0.2 52.3 / 14.8
K3 0.977 67.2 / 89.3 14.9 / 12.8
Mean Average St. deviation
Km N/A 9.98E-04 5.55E-04
L 1.005 1.017 0.009
F 1.032 1.032 0.015
P 1.038 1.049 0.019
Pj 1.041 1.051 0.020
T 0.722 0.310 0.265
U 0.718 0.300 0.266
Name TY-PW_Laban-B
Save
Symbol color and size
B/W
Default
Size 10
P
1.081
1.000
1.36E-04
Km [SI]
1.83E-03
U
1
1.000
1.081
P
-1
Site: Laban
Lat:
Lon:
Rock:
Stratigraphy:
Lithostratigraphy:
Region:
Instrument: MFK

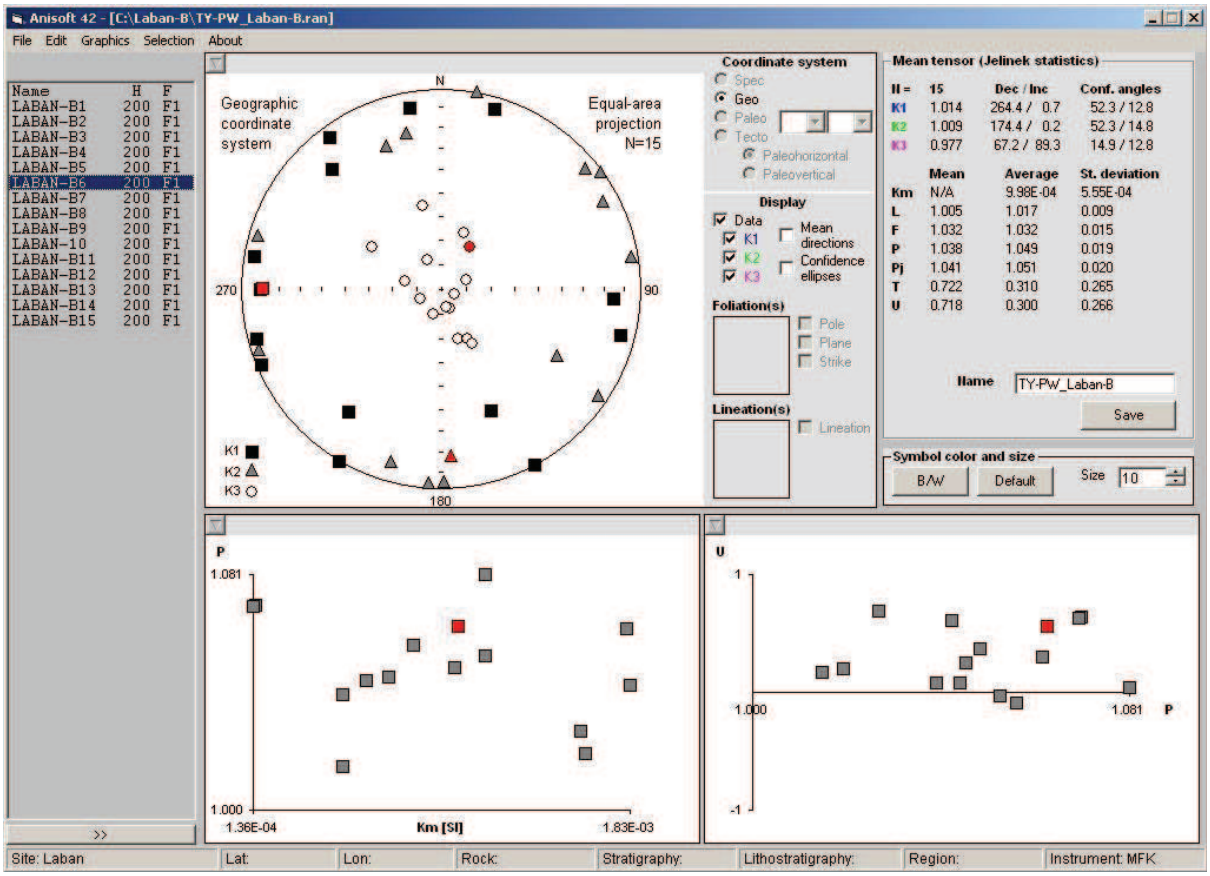
Anisoft 42 - [C:\Laban-B\TY-PW_Laban-B.ran]
File Edit Graphics Selection About
Name H F
LABAN-B1 200 F1
LABAN-B2 200 F1
LABAN-B3 200 F1
LABAN-B4 200 F1
LABAN-B5 200 F1
LABAN-B6 200 F1
LABAN-B7 200 F1
LABAN-B8 200 F1
LABAN-B9 200 F1
LABAN-10 200 F1
LABAN-B11 200 F1
LABAN-B12 200 F1
LABAN-B13 200 F1
LABAN-B14 200 F1
LABAN-B15 200 F1
Geographic coordinate system
Equal-area projection N=15
N
270
90
180
K1
K2
K3
Coordinate system
Spec
Geo
Paleo
Tecto
Paleohorizontal
Paleovertical
Display
Data
K1
K2
K3
Mean directions
Confidence ellipses
Foliation(s)
Pole
Plane
Strike
Lineation(s)
Lineation
Mean tensor (Jelinek statistics)
II = 15 Dec / Inc Conf. angles
K1 1.014 264.4 / 0.7 52.3 / 12.8
K2 1.009 174.4 / 0.2 52.3 / 14.8
K3 0.977 67.2 / 89.3 14.9 / 12.8
Mean Average St. deviation
Km N/A 9.98E-04 5.55E-04
L 1.005 1.017 0.009
F 1.032 1.032 0.015
P 1.038 1.049 0.019
Pj 1.041 1.051 0.020
T 0.722 0.310 0.265
U 0.718 0.300 0.266
Name TY-PW_Laban-B
Save
Symbol color and size
B/W
Default
Size 10
P
1.081
1.000
1.36E-04
Km [SI]
1.83E-03
U
1
1.000
1.081
P
-1
Site: Laban
Lat:
Lon:
Rock:
Stratigraphy:
Lithostratigraphy:
Region:
Instrument: MFK

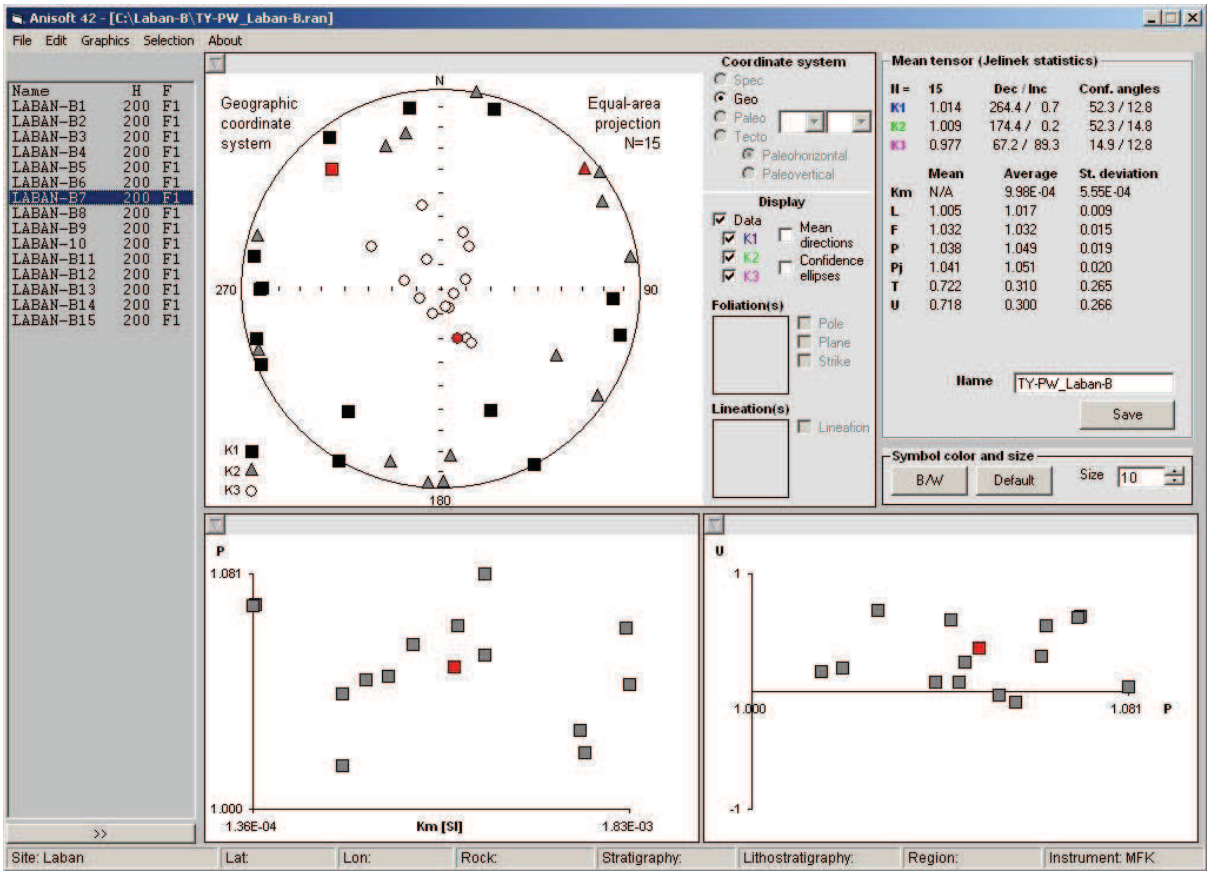
Anisoft 42 - [C:\Laban-B\TY-PW_Laban-B.ran]
File Edit Graphics Selection About
Name H F
LABAN-B1 200 F1
LABAN-B2 200 F1
LABAN-B3 200 F1
LABAN-B4 200 F1
LABAN-B5 200 F1
LABAN-B6 200 F1
LABAN-B7 200 F1
LABAN-B8 200 F1
LABAN-B9 200 F1
LABAN-10 200 F1
LABAN-B11 200 F1
LABAN-B12 200 F1
LABAN-B13 200 F1
LABAN-B14 200 F1
LABAN-B15 200 F1
Geographic coordinate system
Equal-area projection N=15
N
270
90
180
K1
K2
K3
Coordinate system
Spec
Geo
Paleo
Tecto
Paleohorizontal
Paleovertical
Display
Data
K1
K2
K3
Mean directions
Confidence ellipses
Foliation(s)
Pole
Plane
Strike
Lineation(s)
Lineation
Mean tensor (Jelinek statistics)
II = 15 Dec / Inc Conf. angles
K1 1.014 264.4 / 0.7 52.3 / 12.8
K2 1.009 174.4 / 0.2 52.3 / 14.8
K3 0.977 67.2 / 89.3 14.9 / 12.8
Mean Average St. deviation
Km N/A 9.98E-04 5.55E-04
L 1.005 1.017 0.009
F 1.032 1.032 0.015
P 1.038 1.049 0.019
Pj 1.041 1.051 0.020
T 0.722 0.310 0.265
U 0.718 0.300 0.266
Name TY-PW_Laban-B
Save
Symbol color and size
B/W
Default
Size 10
P
1.081
1.000
1.36E-04
Km [SI]
1.83E-03
U
1
1.000
1.081
P
-1
Site: Laban
Lat:
Lon:
Rock:
Stratigraphy:
Lithostratigraphy:
Region:
Instrument: MFK

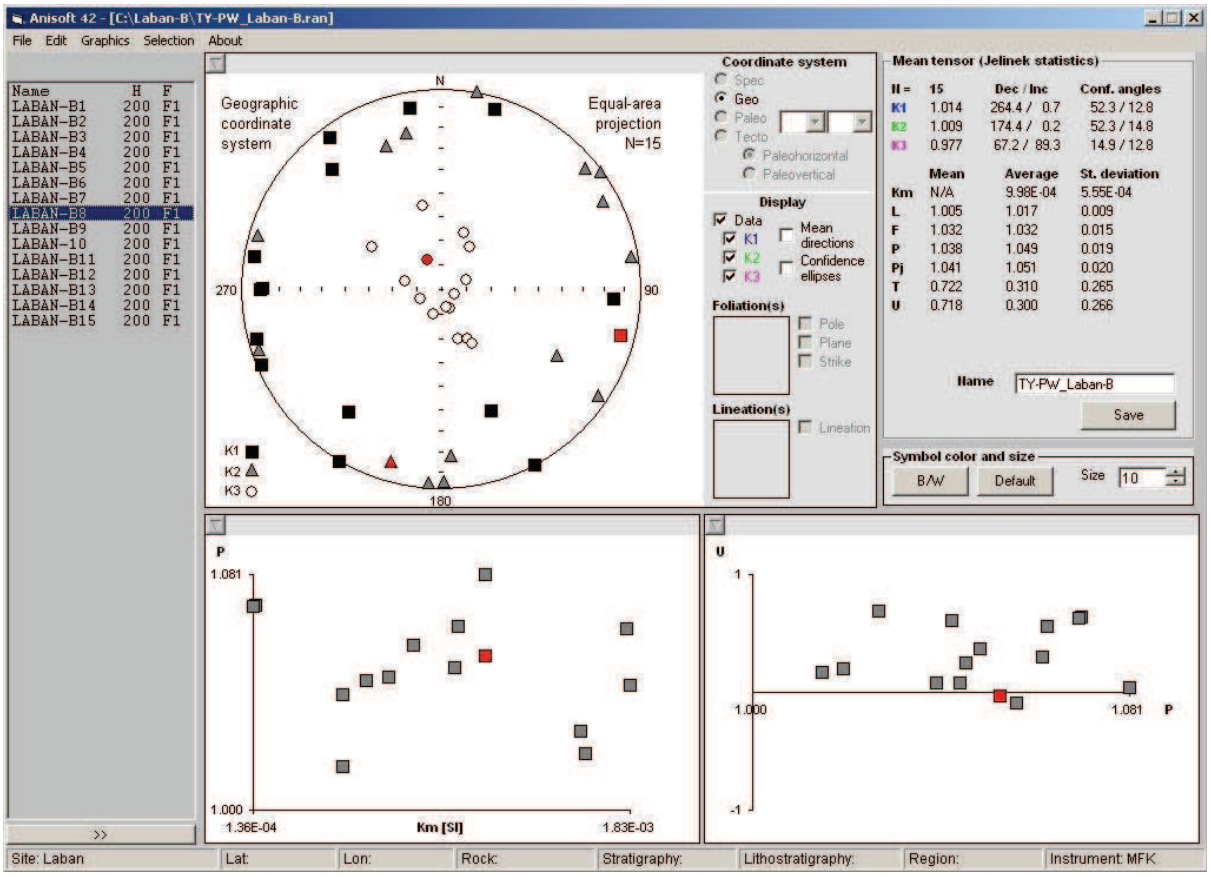
Anisoft 42 - [C:\Laban-B\TY-PW_Laban-B.ran]
File Edit Graphics Selection About
Name H F
LABAN-B1 200 F1
LABAN-B2 200 F1
LABAN-B3 200 F1
LABAN-B4 200 F1
LABAN-B5 200 F1
LABAN-B6 200 F1
LABAN-B7 200 F1
LABAN-B8 200 F1
LABAN-B9 200 F1
LABAN-10 200 F1
LABAN-B11 200 F1
LABAN-B12 200 F1
LABAN-B13 200 F1
LABAN-B14 200 F1
LABAN-B15 200 F1
Geographic coordinate system
Equal-area projection N=15
N
270
90
180
K1
K2
K3
Coordinate system
Spec
Geo
Paleo
Tecto
Paleohorizontal
Paleovertical
Display
Data
K1
K2
K3
Mean directions
Confidence ellipses
Foliation(s)
Pole
Plane
Strike
Lineation(s)
Lineation
Mean tensor (Jelinek statistics)
II = 15 Dec / Inc Conf. angles
K1 1.014 264.4 / 0.7 52.3 / 12.8
K2 1.009 174.4 / 0.2 52.3 / 14.8
K3 0.977 67.2 / 89.3 14.9 / 12.8
Mean Average St. deviation
Km N/A 9.98E-04 5.55E-04
L 1.005 1.017 0.009
F 1.032 1.032 0.015
P 1.038 1.049 0.019
Pj 1.041 1.051 0.020
T 0.722 0.310 0.265
U 0.718 0.300 0.266
Name TY-PW_Laban-B
Save
Symbol color and size
B/W
Default
Size 10
P
1.081
1.000
1.36E-04
Km [SI]
1.83E-03
U
1
1.000
1.081
P
-1
Site: Laban
Lat:
Lon:
Rock:
Stratigraphy:
Lithostratigraphy:
Region:
Instrument: MFK

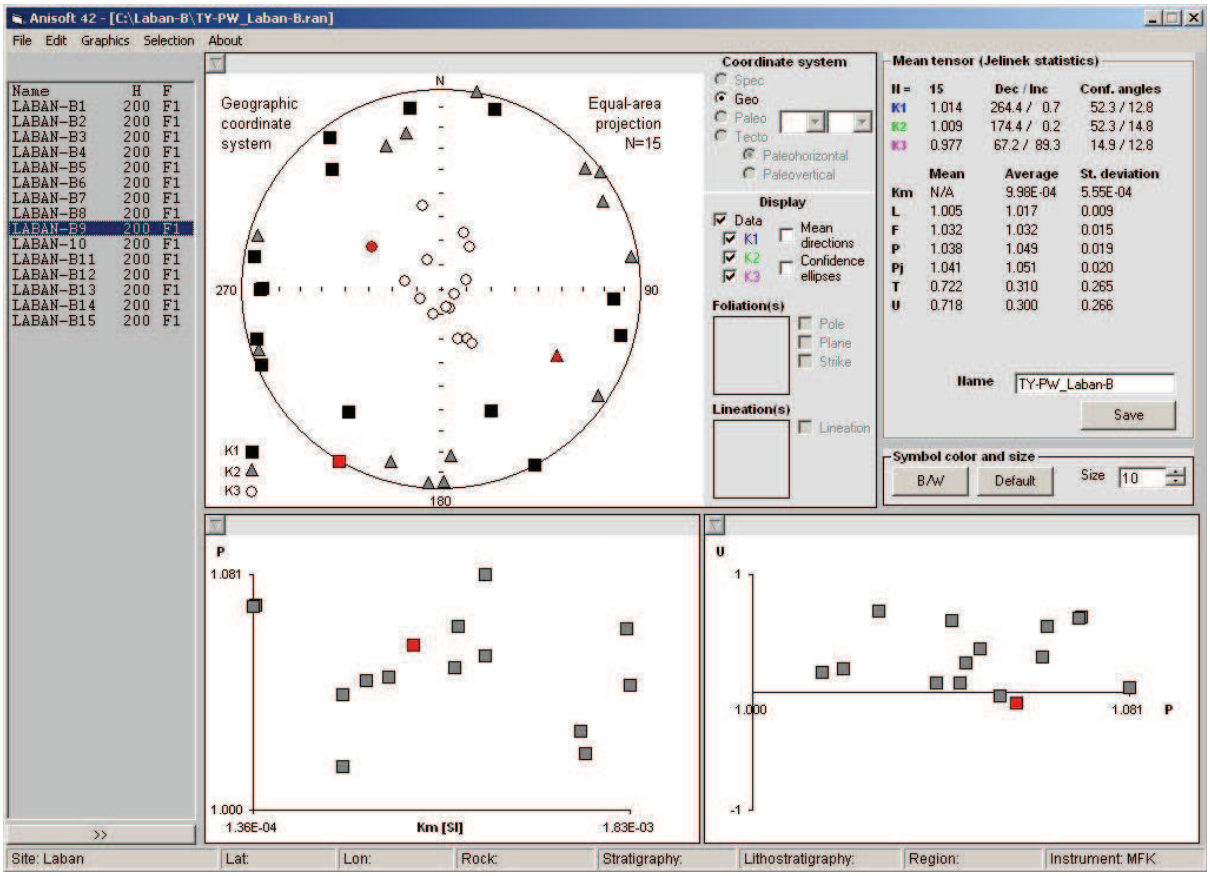
Anisoft 42 - [C:\Laban-B\TY-PW_Laban-B.ran]
File Edit Graphics Selection About
Name H F
LABAN-B1 200 F1
LABAN-B2 200 F1
LABAN-B3 200 F1
LABAN-B4 200 F1
LABAN-B5 200 F1
LABAN-B6 200 F1
LABAN-B7 200 F1
LABAN-B8 200 F1
LABAN-B9 200 F1
LABAN-10 200 F1
LABAN-B11 200 F1
LABAN-B12 200 F1
LABAN-B13 200 F1
LABAN-B14 200 F1
LABAN-B15 200 F1
Geographic coordinate system
Equal-area projection N=15
N
90
180
270
K1
K2
K3
Coordinate system
Spec
Geo
Paleo
Tecto
Paleohorizontal
Paleovertical
Display
Data
K1
K2
K3
Mean directions
Confidence ellipses
Foliation(s)
Pole
Plane
Strike
Lineation(s)
Lineation
Mean tensor (Jelinek statistics)
II = 15 Dec / Inc Conf. angles
K1 1.014 264.4 / 0.7 52.3 / 12.8
K2 1.009 174.4 / 0.2 52.3 / 14.8
K3 0.977 67.2 / 89.3 14.9 / 12.8
Mean Average St. deviation
Km N/A 9.98E-04 5.55E-04
L 1.005 1.017 0.009
F 1.032 1.032 0.015
P 1.038 1.049 0.019
Pj 1.041 1.051 0.020
T 0.722 0.310 0.265
U 0.718 0.300 0.266
Name TY-PW_Laban-B
Save
Symbol color and size
B/W
Default
Size 10
P
1.081
1.000
1.36E-04
Km [SI]
1.83E-03
U
1
1.000
1.081
P
-1
Site: Laban
Lat:
Lon:
Rock:
Stratigraphy:
Lithostratigraphy:
Region:
Instrument: MFK

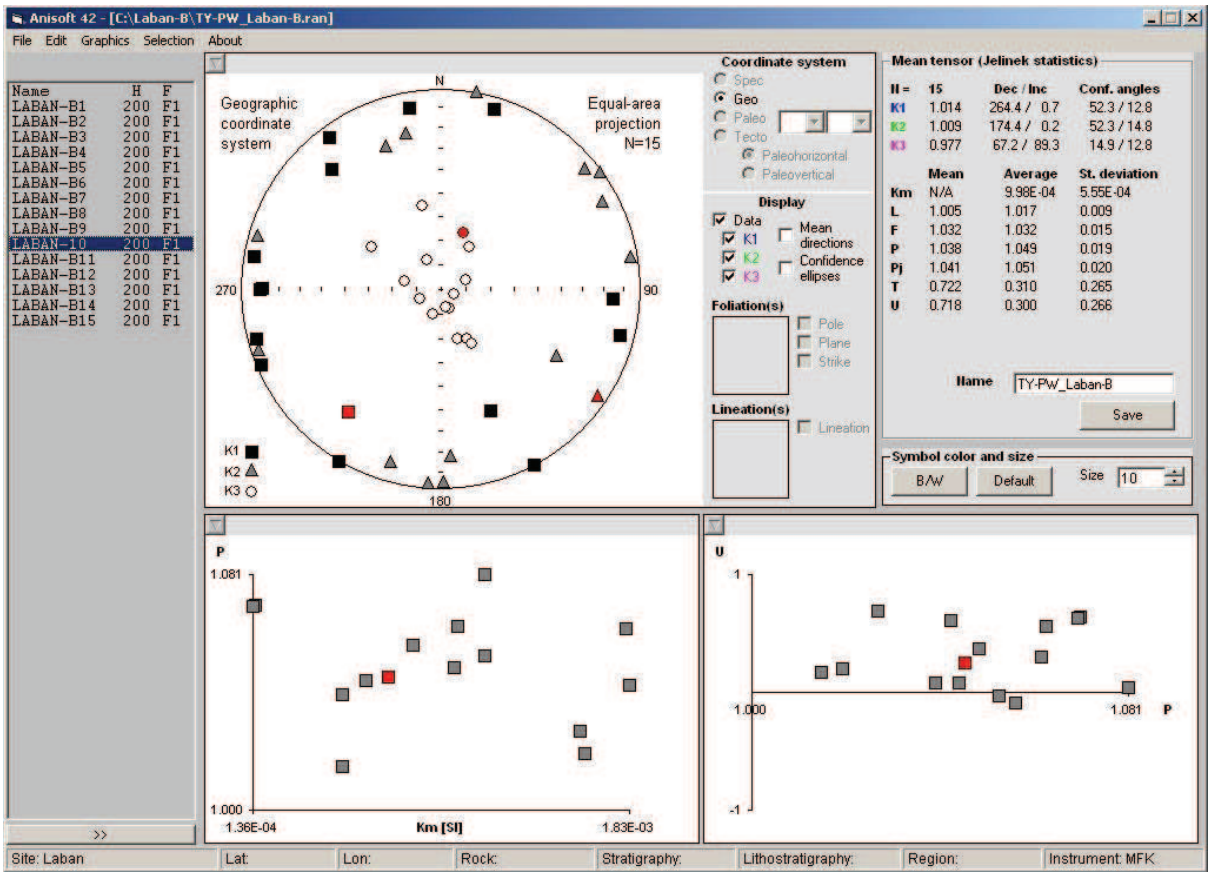
Anisoft 42 - [C:\Laban-B\TY-PW_Laban-B.ran]
File Edit Graphics Selection About
Name H F
LABAN-B1 200 F1
LABAN-B2 200 F1
LABAN-B3 200 F1
LABAN-B4 200 F1
LABAN-B5 200 F1
LABAN-B6 200 F1
LABAN-B7 200 F1
LABAN-B8 200 F1
LABAN-B9 200 F1
LABAN-10 200 F1
LABAN-B11 200 F1
LABAN-B12 200 F1
LABAN-B13 200 F1
LABAN-B14 200 F1
LABAN-B15 200 F1
Geographic coordinate system
Equal-area projection N=15
N
90
180
270
K1
K2
K3
Coordinate system
Spec
Geo
Paleo
Tecto
Paleohorizontal
Paleovertical
Display
Data
K1
K2
K3
Mean directions
Confidence ellipses
Foliation(s)
Pole
Plane
Strike
Lineation(s)
Lineation
Mean tensor (Jelinek statistics)
II = 15 Dec / Inc Conf. angles
K1 1.014 264.4 / 0.7 52.3 / 12.8
K2 1.009 174.4 / 0.2 52.3 / 14.8
K3 0.977 67.2 / 89.3 14.9 / 12.8
Mean Average St. deviation
Km N/A 9.98E-04 5.55E-04
L 1.005 1.017 0.009
F 1.032 1.032 0.015
P 1.038 1.049 0.019
Pj 1.041 1.051 0.020
T 0.722 0.310 0.265
U 0.718 0.300 0.266
Name TY-PW_Laban-B
Save
Symbol color and size
B/W
Default
Size 10
P
1.081
1.000
1.36E-04
Km [SI]
1.83E-03
U
1
1.000
1.081
P
-1
Site: Laban
Lat:
Lon:
Rock:
Stratigraphy:
Lithostratigraphy:
Region:
Instrument: MFK

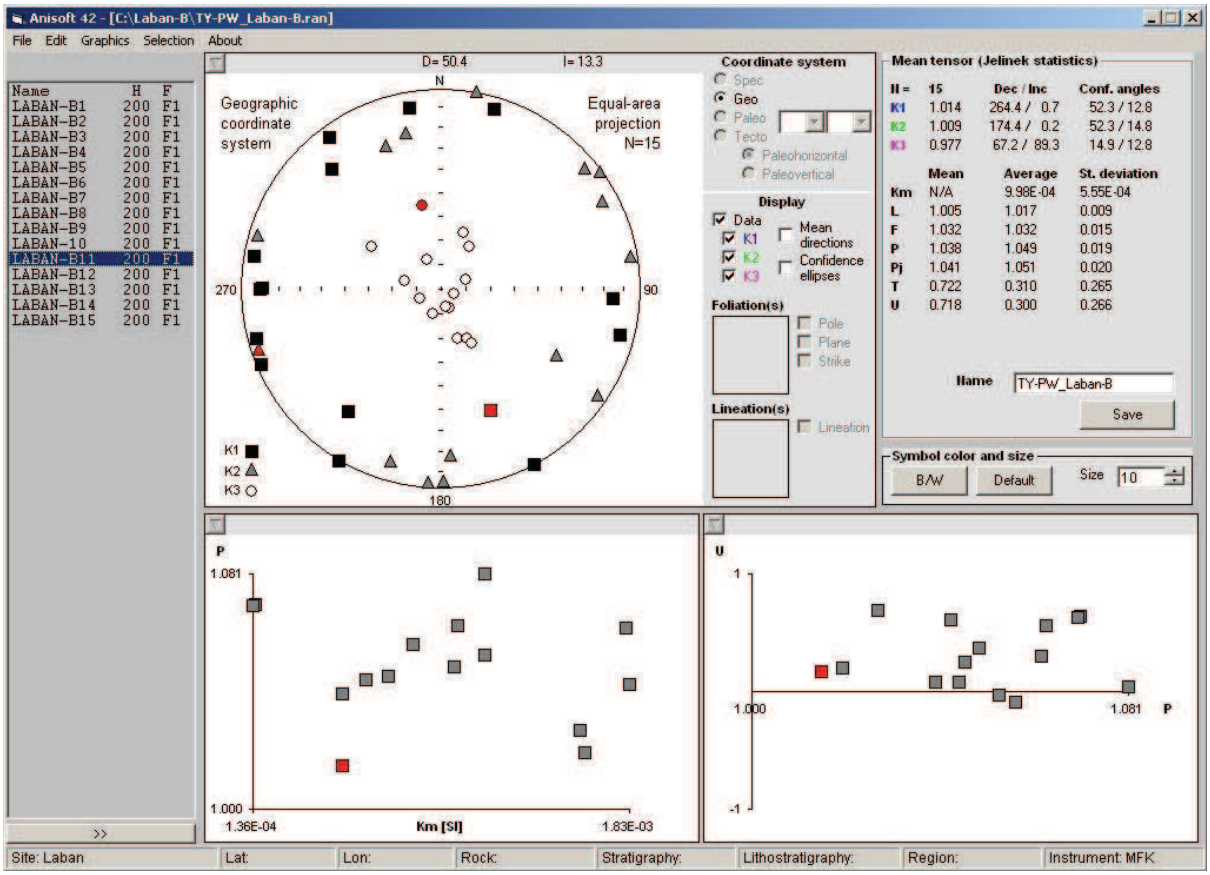
Anisoft 42 - [C:\Laban-B\TY-PW_Laban-B.ran]
File Edit Graphics Selection About
Name H F
LABAN-B1 200 F1
LABAN-B2 200 F1
LABAN-B3 200 F1
LABAN-B4 200 F1
LABAN-B5 200 F1
LABAN-B6 200 F1
LABAN-B7 200 F1
LABAN-B8 200 F1
LABAN-B9 200 F1
LABAN-10 200 F1
LABAN-B11 200 F1
LABAN-B12 200 F1
LABAN-B13 200 F1
LABAN-B14 200 F1
LABAN-B15 200 F1
D= 50.4 I= 13.3
Geographic coordinate system
Equal-area projection N=15
N
270
90
180
K1
K2
K3
Coordinate system
Spec
Geo
Paleo
Tecto
Paleohorizontal
Paleovertical
Display
Data
K1
K2
K3
Mean directions
Confidence ellipses
Foliation(s)
Pole
Plane
Strike
Lineation(s)
Lineation
Mean tensor (Jelinek statistics)
II = 15 Dec / Inc Conf. angles
K1 1.014 264.4 / 0.7 52.3 / 12.8
K2 1.009 174.4 / 0.2 52.3 / 14.8
K3 0.977 67.2 / 89.3 14.9 / 12.8
Mean Average St. deviation
Km N/A 9.98E-04 5.55E-04
L 1.005 1.017 0.009
F 1.032 1.032 0.015
P 1.038 1.049 0.019
Pj 1.041 1.051 0.020
T 0.722 0.310 0.265
U 0.718 0.300 0.266
Name TY-PW_Laban-B
Save
Symbol color and size
B/W
Default
Size 10
P
1.081
1.000
1.36E-04
Km [SI]
1.83E-03
U
1
1.000
1.081
P
-1
Site: Laban
Lat:
Lon:
Rock:
Stratigraphy:
Lithostratigraphy:
Region:
Instrument: MFK

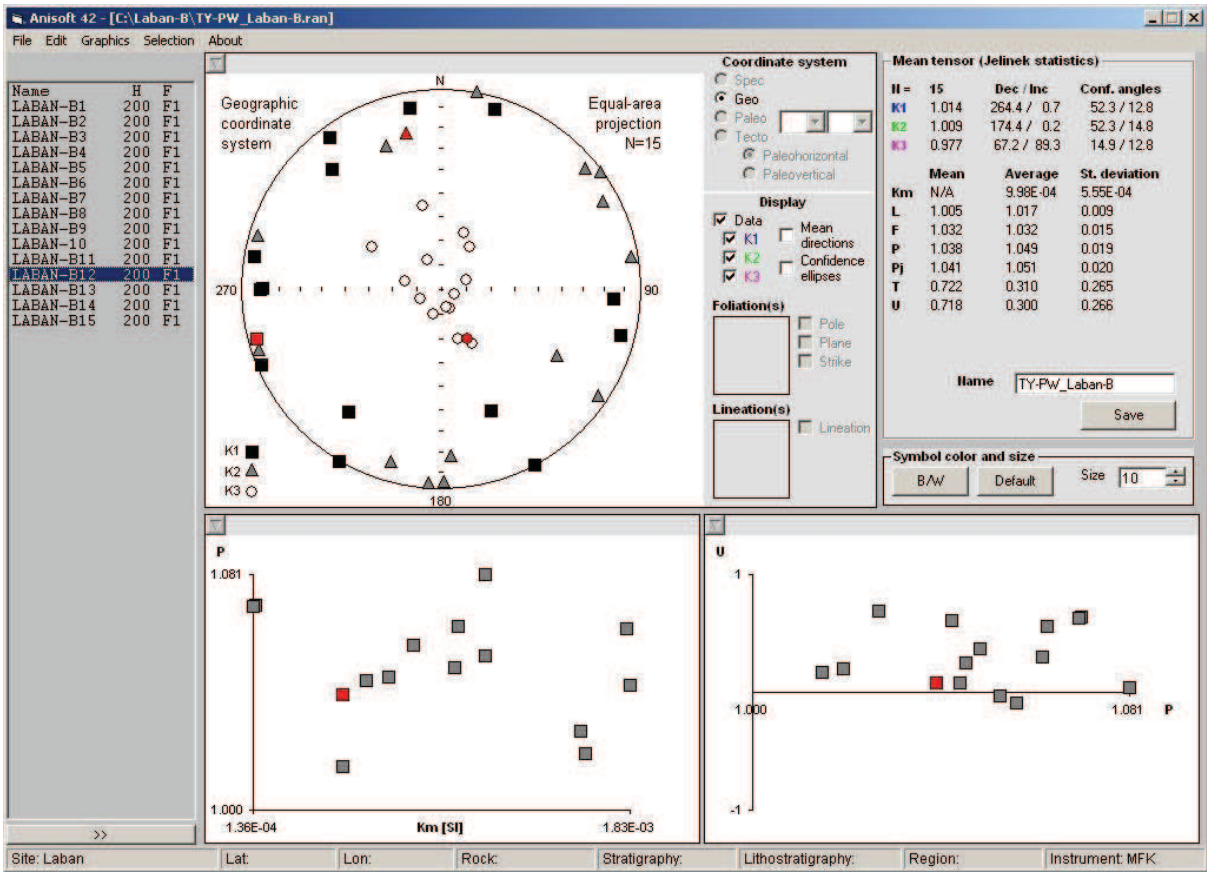
Anisoft 42 - [C:\Laban-B\TY-PW_Laban-B.ran]
File Edit Graphics Selection About
Name H F
LABAN-B1 200 F1
LABAN-B2 200 F1
LABAN-B3 200 F1
LABAN-B4 200 F1
LABAN-B5 200 F1
LABAN-B6 200 F1
LABAN-B7 200 F1
LABAN-B8 200 F1
LABAN-B9 200 F1
LABAN-10 200 F1
LABAN-B11 200 F1
LABAN-B12 200 F1
LABAN-B13 200 F1
LABAN-B14 200 F1
LABAN-B15 200 F1
Geographic coordinate system
Equal-area projection N=15
N
270
90
180
K1
K2
K3
Coordinate system
Spec
Geo
Paleo
Tecto
Paleohorizontal
Paleovertical
Display
Data
K1
K2
K3
Mean directions
Confidence ellipses
Foliation(s)
Pole
Plane
Strike
Lineation(s)
Lineation
Mean tensor (Jelinek statistics)
II = 15 Dec / Inc Conf. angles
K1 1.014 264.4 / 0.7 52.3 / 12.8
K2 1.009 174.4 / 0.2 52.3 / 14.8
K3 0.977 67.2 / 89.3 14.9 / 12.8
Mean Average St. deviation
Km N/A 9.98E-04 5.55E-04
L 1.005 1.017 0.009
F 1.032 1.032 0.015
P 1.038 1.049 0.019
Pj 1.041 1.051 0.020
T 0.722 0.310 0.265
U 0.718 0.300 0.266
Name TY-PW_Laban-B
Save
Symbol color and size
B/W
Default
Size 10
P
1.081
1.000
1.36E-04
Km [SI]
1.83E-03
U
1
1.000
1.081
P
-1
Site: Laban
Lat:
Lon:
Rock:
Stratigraphy:
Lithostratigraphy:
Region:
Instrument: MFK

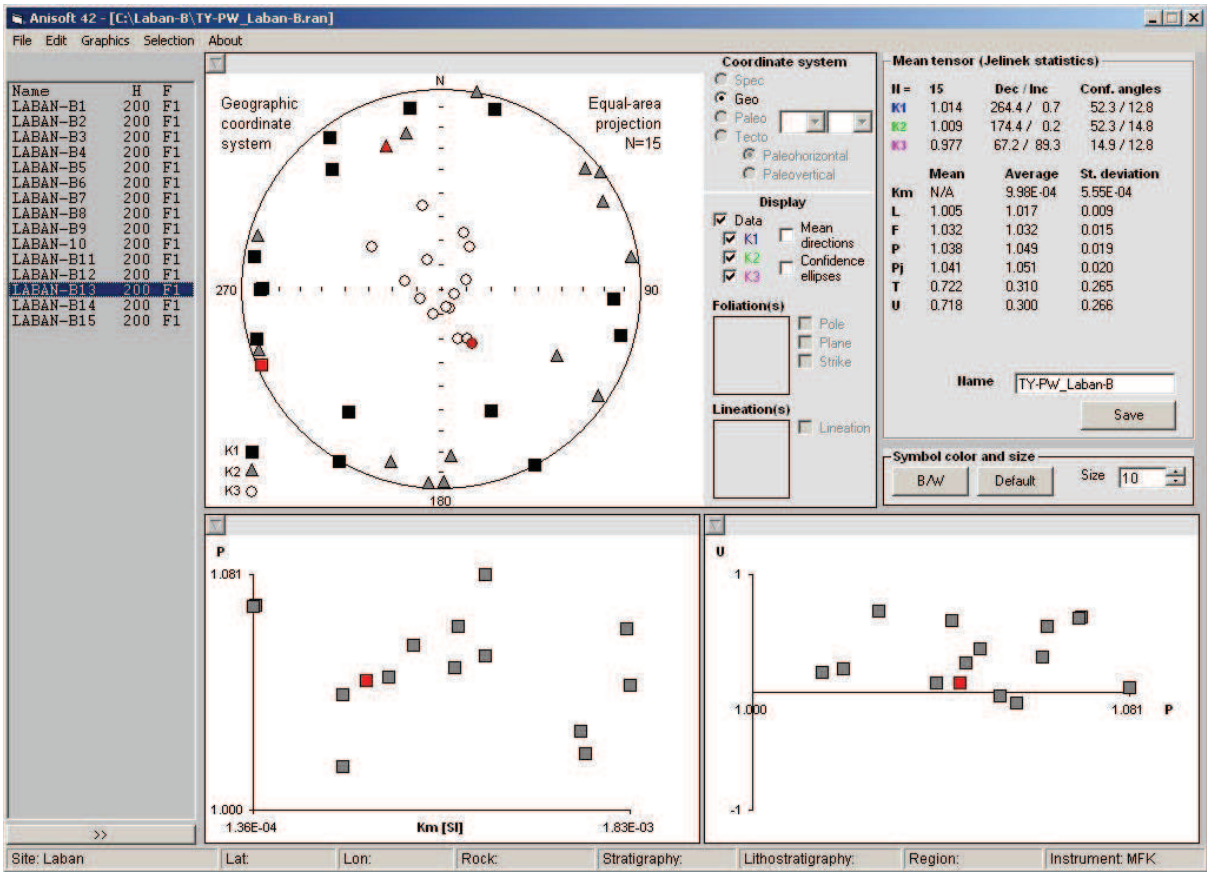
Anisoft 42 - [C:\Laban-B\TY-PW_Laban-B.ran]
File Edit Graphics Selection About
Name H F
LABAN-B1 200 F1
LABAN-B2 200 F1
LABAN-B3 200 F1
LABAN-B4 200 F1
LABAN-B5 200 F1
LABAN-B6 200 F1
LABAN-B7 200 F1
LABAN-B8 200 F1
LABAN-B9 200 F1
LABAN-10 200 F1
LABAN-B11 200 F1
LABAN-B12 200 F1
LABAN-B13 200 F1
LABAN-B14 200 F1
LABAN-B15 200 F1
Geographic coordinate system
Equal-area projection N=15
N
90
180
270
K1
K2
K3
Coordinate system
Spec
Geo
Paleo
Tecto
Paleohorizontal
Paleovertical
Display
Data
K1
K2
K3
Mean directions
Confidence ellipses
Foliation(s)
Pole
Plane
Strike
Lineation(s)
Lineation
Mean tensor (Jelinek statistics)
II = 15 Dec / Inc Conf. angles
K1 1.014 264.4 / 0.7 52.3 / 12.8
K2 1.009 174.4 / 0.2 52.3 / 14.8
K3 0.977 67.2 / 89.3 14.9 / 12.8
Mean Average St. deviation
Km N/A 9.98E-04 5.55E-04
L 1.005 1.017 0.009
F 1.032 1.032 0.015
P 1.038 1.049 0.019
Pj 1.041 1.051 0.020
T 0.722 0.310 0.265
U 0.718 0.300 0.266
Name TY-PW_Laban-B
Save
Symbol color and size
B/W
Default
Size 10
P
1.081
1.000
1.36E-04
Km [SI]
1.83E-03
U
1
1.000
1.081
P
-1
Site: Laban
Lat:
Lon:
Rock:
Stratigraphy:
Lithostratigraphy:
Region:
Instrument: MFK

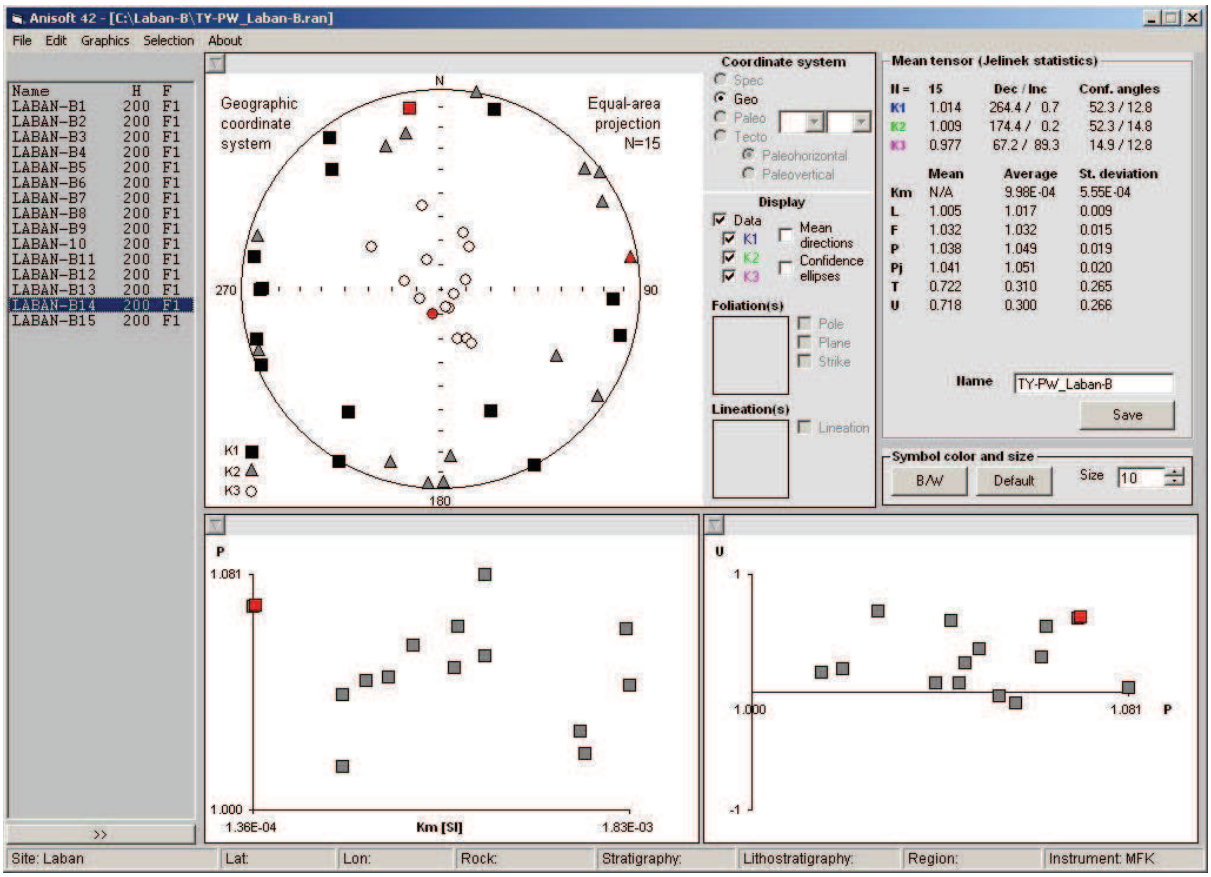
Anisoft 42 - [C:\Laban-B\TY-PW_Laban-B.ran]
File Edit Graphics Selection About
Name H F
LABAN-B1 200 F1
LABAN-B2 200 F1
LABAN-B3 200 F1
LABAN-B4 200 F1
LABAN-B5 200 F1
LABAN-B6 200 F1
LABAN-B7 200 F1
LABAN-B8 200 F1
LABAN-B9 200 F1
LABAN-10 200 F1
LABAN-B11 200 F1
LABAN-B12 200 F1
LABAN-B13 200 F1
LABAN-B14 200 F1
LABAN-B15 200 F1
Geographic coordinate system
Equal-area projection N=15
N
90
180
270
K1
K2
K3
Coordinate system
Spec
Geo
Paleo
Tecto
Paleohorizontal
Paleovertical
Display
Data
K1
K2
K3
Mean directions
Confidence ellipses
Foliation(s)
Pole
Plane
Strike
Lineation(s)
Lineation
Mean tensor (Jelinek statistics)
II = 15 Dec / Inc Conf. angles
K1 1.014 264.4 / 0.7 52.3 / 12.8
K2 1.009 174.4 / 0.2 52.3 / 14.8
K3 0.977 67.2 / 89.3 14.9 / 12.8
Mean Average St. deviation
Km N/A 9.98E-04 5.55E-04
L 1.005 1.017 0.009
F 1.032 1.032 0.015
P 1.038 1.049 0.019
Pj 1.041 1.051 0.020
T 0.722 0.310 0.265
U 0.718 0.300 0.266
Name TY-PW_Laban-B
Save
Symbol color and size
B/W
Default
Size 10
P
1.081
1.000
1.36E-04
Km [SI]
1.83E-03
U
1
1.000
1.081
P
-1
Site: Laban
Lat:
Lon:
Rock:
Stratigraphy:
Lithostratigraphy:
Region:
Instrument: MFK

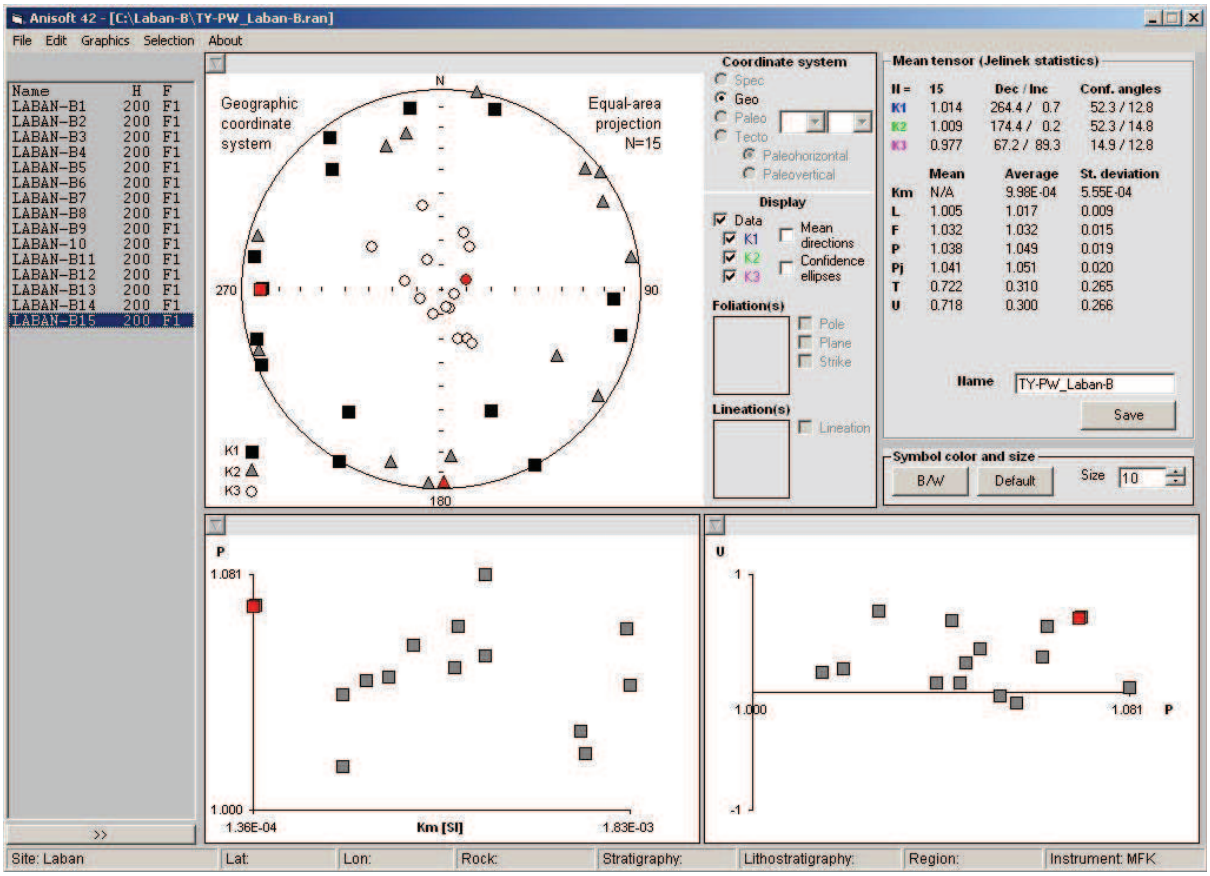
Anisoft 42 - [C:\Laban-B\TY-PW_Laban-B.ran]
File Edit Graphics Selection About
Name H F
LABAN-B1 200 F1
LABAN-B2 200 F1
LABAN-B3 200 F1
LABAN-B4 200 F1
LABAN-B5 200 F1
LABAN-B6 200 F1
LABAN-B7 200 F1
LABAN-B8 200 F1
LABAN-B9 200 F1
LABAN-10 200 F1
LABAN-B11 200 F1
LABAN-B12 200 F1
LABAN-B13 200 F1
LABAN-B14 200 F1
LABAN-B15 200 F1
Geographic coordinate system
Equal-area projection N=15
N
90
180
270
K1
K2
K3
Coordinate system
Spec
Geo
Paleo
Tecto
Paleohorizontal
Paleovertical
Display
Data
K1
K2
K3
Mean directions
Confidence ellipses
Foliation(s)
Pole
Plane
Strike
Lineation(s)
Lineation
Mean tensor (Jelinek statistics)
II = 15 Dec / Inc Conf. angles
K1 1.014 264.4 / 0.7 52.3 / 12.8
K2 1.009 174.4 / 0.2 52.3 / 14.8
K3 0.977 67.2 / 89.3 14.9 / 12.8
Mean Average St. deviation
Km N/A 9.98E-04 5.55E-04
L 1.005 1.017 0.009
F 1.032 1.032 0.015
P 1.038 1.049 0.019
Pj 1.041 1.051 0.020
T 0.722 0.310 0.265
U 0.718 0.300 0.266
Name TY-PW_Laban-B
Save
Symbol color and size
B/W
Default
Size 10
P
1.081
1.000
1.36E-04
Km [SI]
1.83E-03
U
1
1.000
-1
1.081
P
Site: Laban
Lat:
Lon:
Rock:
Stratigraphy:
Lithostratigraphy:
Region:
Instrument: MFK

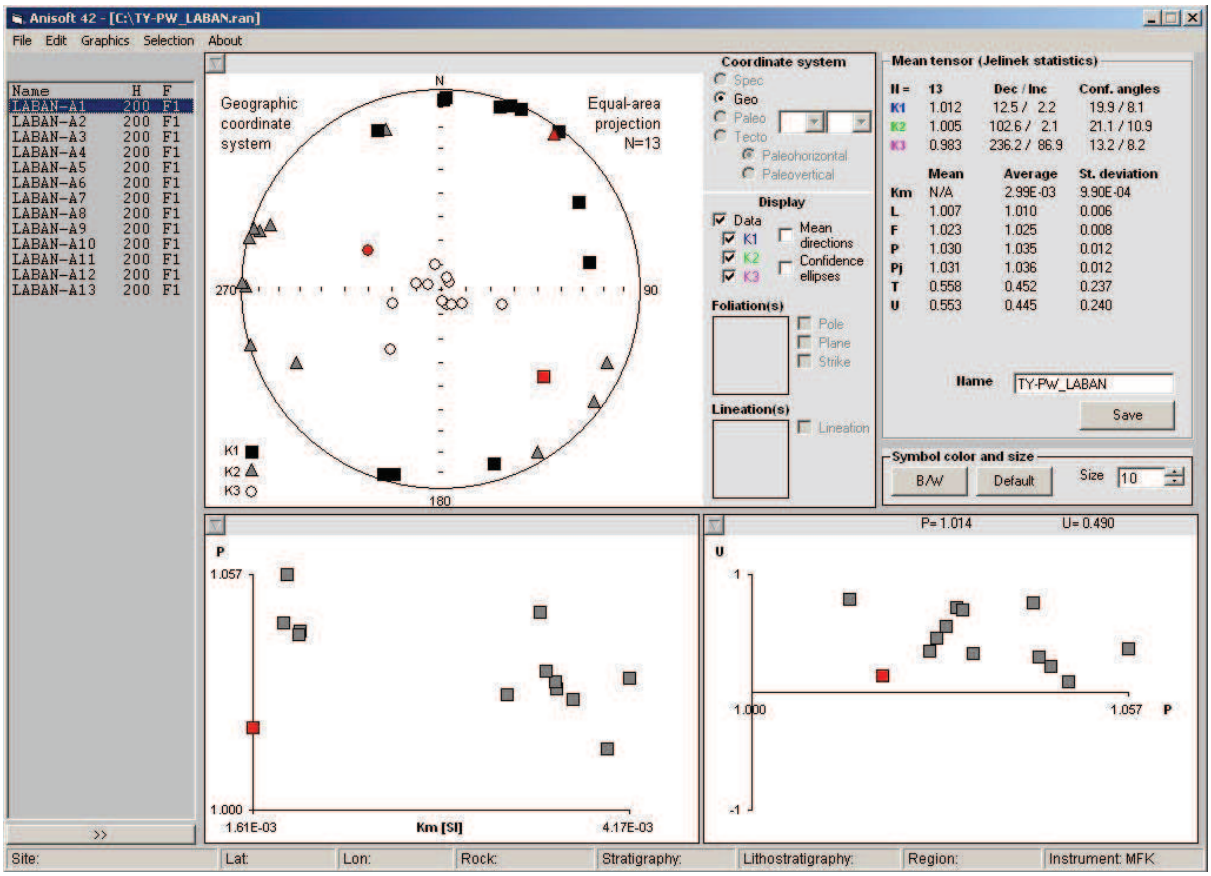
Anisoft 42 - [C:\TY-PW_LABAN.ran]
File Edit Graphics Selection About
Name H F
LABAN-A1 200 F1
LABAN-A2 200 F1
LABAN-A3 200 F1
LABAN-A4 200 F1
LABAN-A5 200 F1
LABAN-A6 200 F1
LABAN-A7 200 F1
LABAN-A8 200 F1
LABAN-A9 200 F1
LABAN-A10 200 F1
LABAN-A11 200 F1
LABAN-A12 200 F1
LABAN-A13 200 F1
Geographic coordinate system
Equal-area projection N=13
N
90
180
270
K1
K2
K3
Coordinate system
Spec
Geo
Paleo
Tecto
Paleohorizontal
Paleovertical
Display
Data
K1
K2
K3
Mean directions
Confidence ellipses
Foliation(s)
Pole
Plane
Strike
Lineation(s)
Lineation
Mean tensor (Jelinek statistics)
II = 13 Dec / Inc Conf. angles
K1 1.012 12.5 / 2.2 19.9 / 8.1
K2 1.005 102.6 / 2.1 21.1 / 10.9
K3 0.983 236.2 / 86.9 13.2 / 8.2
Mean Average St. deviation
Km N/A 2.99E-03 9.90E-04
L 1.007 1.010 0.006
F 1.023 1.025 0.008
P 1.030 1.035 0.012
Pj 1.031 1.036 0.012
T 0.558 0.452 0.237
U 0.553 0.445 0.240
Name TY-PW_LABAN
Save
Symbol color and size
B/W
Default
Size 10
P= 1.014
U= 0.490
P
1.057
1.000
1.61E-03
Km [SI]
4.17E-03
U
1
1.000
-1
1.057
P
Site:
Lat:
Lon:
Rock:
Stratigraphy:
Lithostratigraphy:
Region:
Instrument: MFK

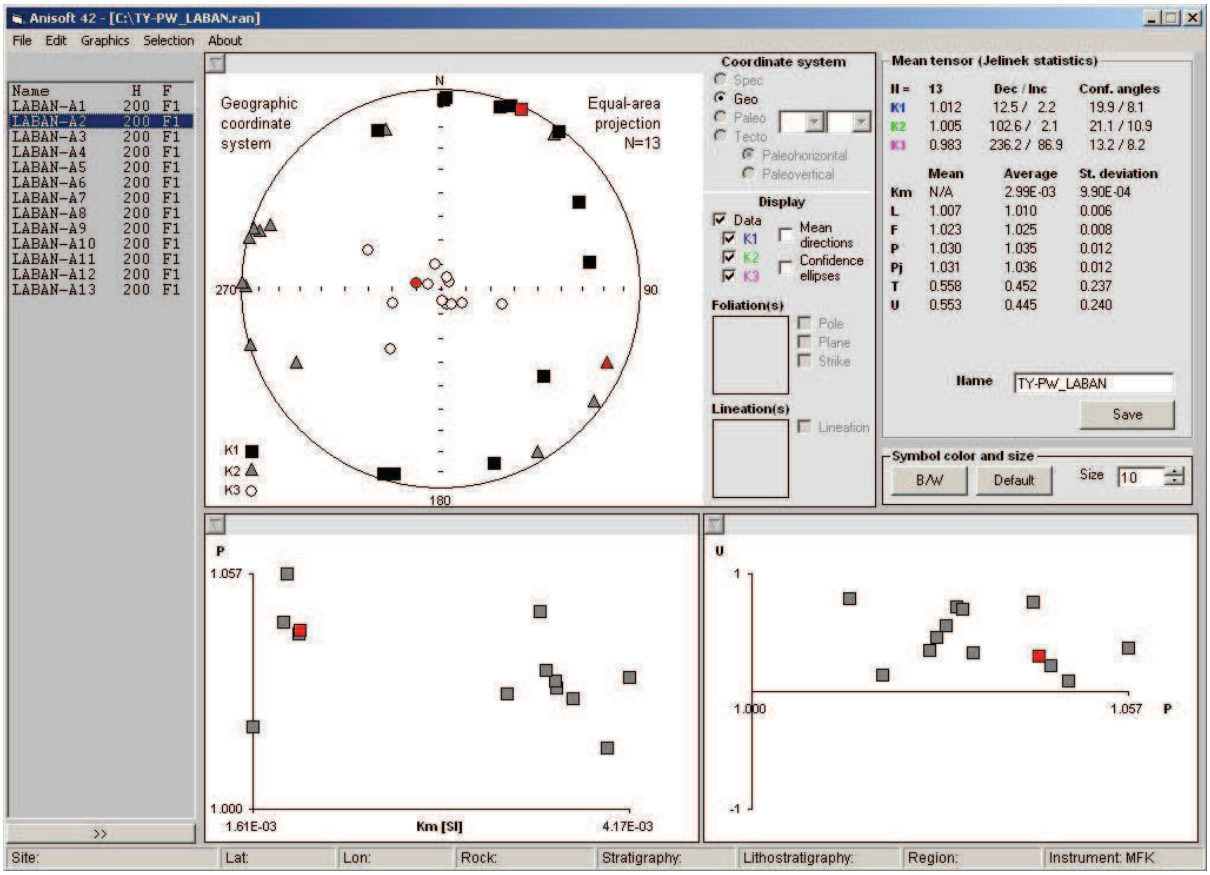
Anisoft 42 - [C:\TY-PW_LABAN.ran]
File Edit Graphics Selection About
Name H F
LABAN-A1 200 F1
LABAN-A2 200 F1
LABAN-A3 200 F1
LABAN-A4 200 F1
LABAN-A5 200 F1
LABAN-A6 200 F1
LABAN-A7 200 F1
LABAN-A8 200 F1
LABAN-A9 200 F1
LABAN-A10 200 F1
LABAN-A11 200 F1
LABAN-A12 200 F1
LABAN-A13 200 F1
Geographic coordinate system
Equal-area projection N=13
N
90
180
270
K1
K2
K3
Coordinate system
Spec
Geo
Paleo
Tecto
Paleohorizontal
Paleovertical
Display
Data
K1
K2
K3
Mean directions
Confidence ellipses
Foliation(s)
Pole
Plane
Strike
Lineation(s)
Lineation
Mean tensor (Jelinek statistics)
II = 13 Dec / Inc Conf. angles
K1 1.012 12.5 / 2.2 19.9 / 8.1
K2 1.005 102.6 / 2.1 21.1 / 10.9
K3 0.983 236.2 / 86.9 13.2 / 8.2
Mean Average St. deviation
Km N/A 2.99E-03 9.90E-04
L 1.007 1.010 0.006
F 1.023 1.025 0.008
P 1.030 1.035 0.012
Pj 1.031 1.036 0.012
T 0.558 0.452 0.237
U 0.553 0.445 0.240
Name TY-PW_LABAN
Save
Symbol color and size
B/W
Default
Size 10
P
1.057
1.000
1.61E-03
Km [SI]
4.17E-03
U
1
1.000
1.057
P
-1
Site:
Lat:
Lon:
Rock:
Stratigraphy:
Lithostratigraphy:
Region:
Instrument: MFK

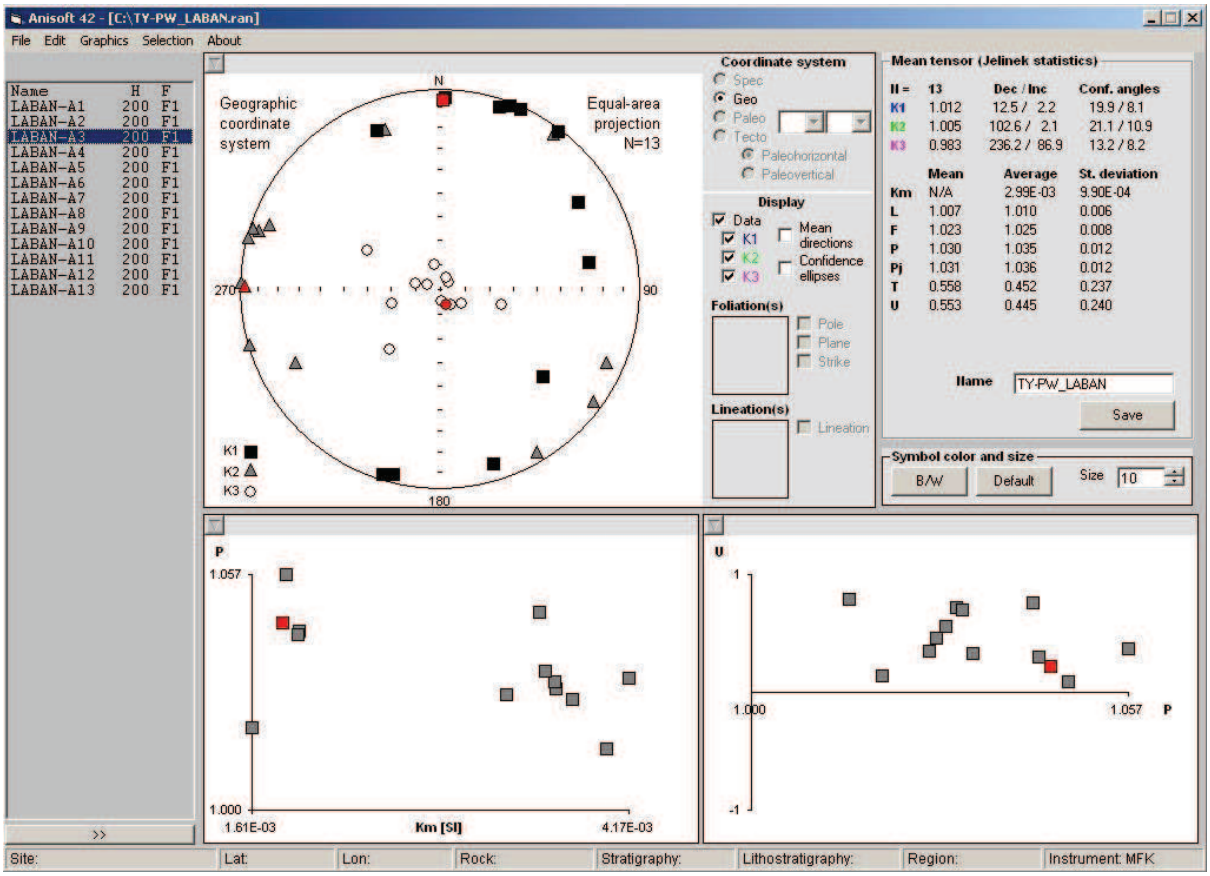
Anisoft 42 - [C:\TY-PW_LABAN.ran]
File Edit Graphics Selection About
Name H F
LABAN-A1 200 F1
LABAN-A2 200 F1
LABAN-A3 200 F1
LABAN-A4 200 F1
LABAN-A5 200 F1
LABAN-A6 200 F1
LABAN-A7 200 F1
LABAN-A8 200 F1
LABAN-A9 200 F1
LABAN-A10 200 F1
LABAN-A11 200 F1
LABAN-A12 200 F1
LABAN-A13 200 F1
Geographic coordinate system
Equal-area projection N=13
N
90
180
270
K1
K2
K3
Coordinate system
Spec
Geo
Paleo
Tecto
Paleohorizontal
Paleovertical
Display
Data
K1
K2
K3
Mean directions
Confidence ellipses
Foliation(s)
Pole
Plane
Strike
Lineation(s)
Lineation
Mean tensor (Jelinek statistics)
II = 13 Dec / Inc Conf. angles
K1 1.012 12.5 / 2.2 19.9 / 8.1
K2 1.005 102.6 / 2.1 21.1 / 10.9
K3 0.983 236.2 / 86.9 13.2 / 8.2
Mean Average St. deviation
Km N/A 2.99E-03 9.90E-04
L 1.007 1.010 0.006
F 1.023 1.025 0.008
P 1.030 1.035 0.012
Pj 1.031 1.036 0.012
T 0.558 0.452 0.237
U 0.553 0.445 0.240
Name TY-PW_LABAN
Save
Symbol color and size
B/W
Default
Size 10
P
1.057
1.000
1.61E-03
Km [SI]
4.17E-03
U
1
1.000
1.057
P
-1
Site:
Lat:
Lon:
Rock:
Stratigraphy:
Lithostratigraphy:
Region:
Instrument: MFK

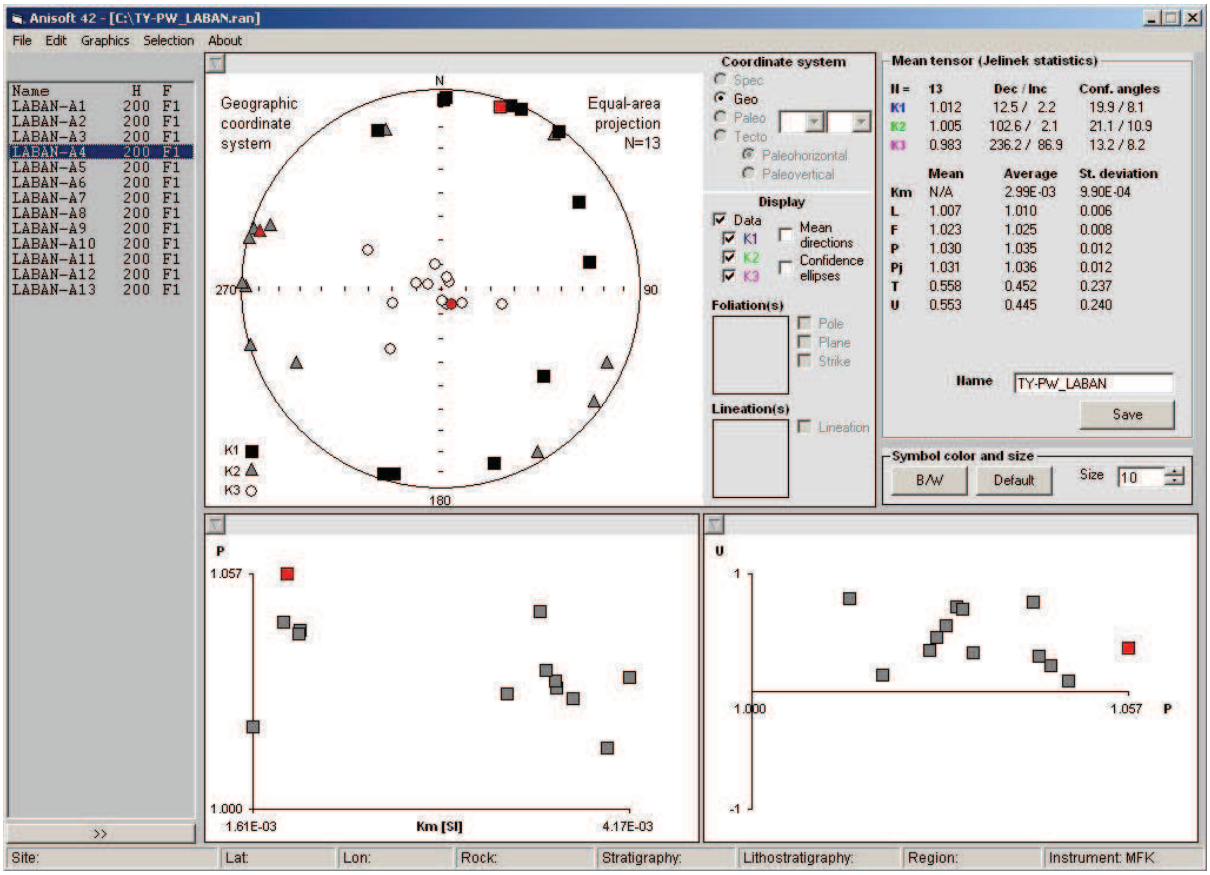
Anisoft 42 - [C:\TY-PW_LABAN.ran]
File Edit Graphics Selection About
Name H F
LABAN-A1 200 F1
LABAN-A2 200 F1
LABAN-A3 200 F1
LABAN-A4 200 F1
LABAN-A5 200 F1
LABAN-A6 200 F1
LABAN-A7 200 F1
LABAN-A8 200 F1
LABAN-A9 200 F1
LABAN-A10 200 F1
LABAN-A11 200 F1
LABAN-A12 200 F1
LABAN-A13 200 F1
Geographic coordinate system
Equal-area projection N=13
N
90
180
270
K1
K2
K3
Coordinate system
Spec
Geo
Paleo
Tecto
Paleohorizontal
Paleovertical
Display
Data
K1
K2
K3
Mean directions
Confidence ellipses
Foliation(s)
Pole
Plane
Strike
Lineation(s)
Lineation
Mean tensor (Jelinek statistics)
II = 13 Dec / Inc Conf. angles
K1 1.012 12.5 / 2.2 19.9 / 8.1
K2 1.005 102.6 / 2.1 21.1 / 10.9
K3 0.983 236.2 / 86.9 13.2 / 8.2
Mean Average St. deviation
Km N/A 2.99E-03 9.90E-04
L 1.007 1.010 0.006
F 1.023 1.025 0.008
P 1.030 1.035 0.012
Pj 1.031 1.036 0.012
T 0.558 0.452 0.237
U 0.553 0.445 0.240
Name TY-PW_LABAN
Save
Symbol color and size
B/W
Default
Size 10
P
1.057
1.000
1.61E-03
Km [SI]
4.17E-03
U
1
1.000
1.057
P
-1
Site:
Lat:
Lon:
Rock:
Stratigraphy:
Lithostratigraphy:
Region:
Instrument: MFK

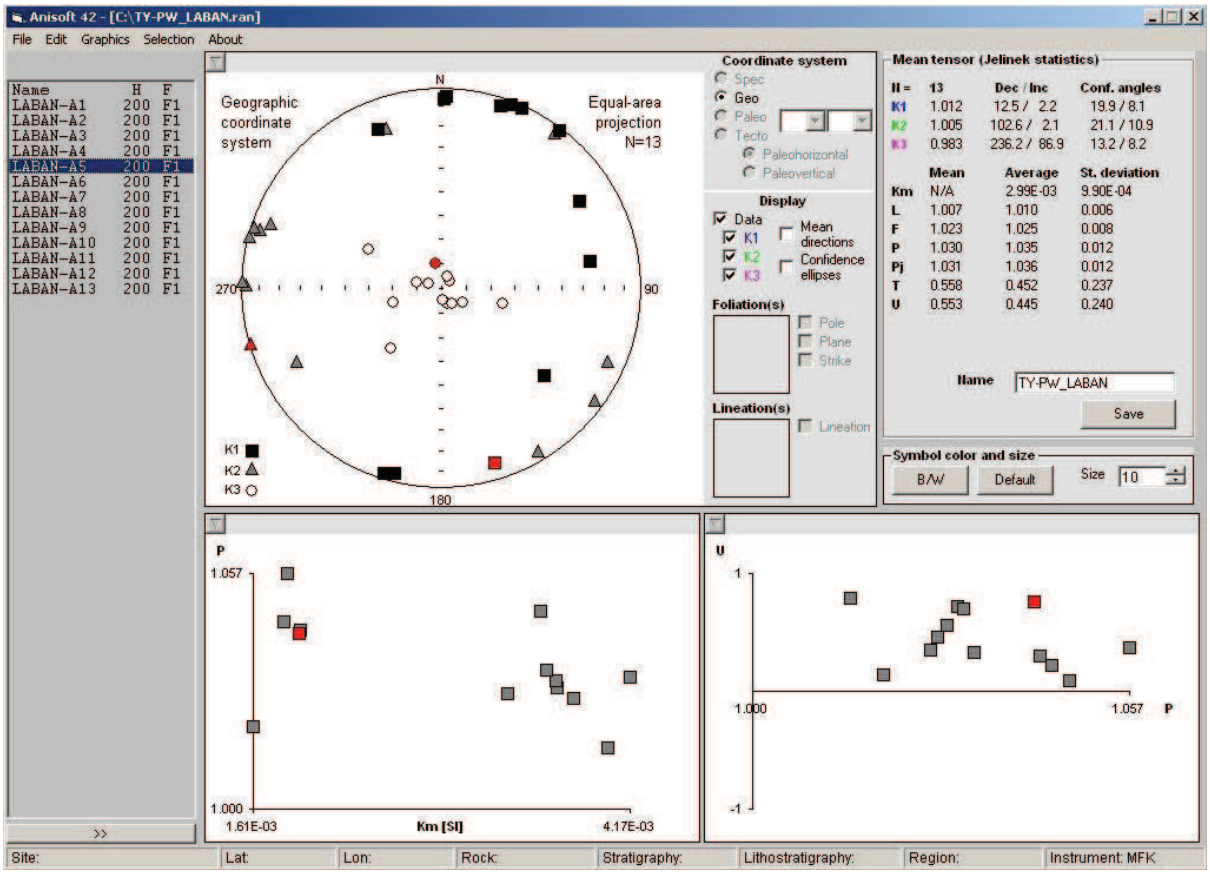
Anisoft 42 - [C:\TY-PW_LABAN.ran]
File Edit Graphics Selection About
Name H F
LABAN-A1 200 F1
LABAN-A2 200 F1
LABAN-A3 200 F1
LABAN-A4 200 F1
LABAN-A5 200 F1
LABAN-A6 200 F1
LABAN-A7 200 F1
LABAN-A8 200 F1
LABAN-A9 200 F1
LABAN-A10 200 F1
LABAN-A11 200 F1
LABAN-A12 200 F1
LABAN-A13 200 F1
Geographic coordinate system
Equal-area projection N=13
N
90
180
270
K1
K2
K3
Coordinate system
Spec
Geo
Paleo
Tecto
Paleohorizontal
Paleovertical
Display
Data
K1
K2
K3
Mean directions
Confidence ellipses
Foliation(s)
Pole
Plane
Strike
Lineation(s)
Lineation
Mean tensor (Jelinek statistics)
II = 13 Dec / Inc Conf. angles
K1 1.012 12.5 / 2.2 19.9 / 8.1
K2 1.005 102.6 / 2.1 21.1 / 10.9
K3 0.983 236.2 / 86.9 13.2 / 8.2
Mean Average St. deviation
Km N/A 2.99E-03 9.90E-04
L 1.007 1.010 0.006
F 1.023 1.025 0.008
P 1.030 1.035 0.012
Pj 1.031 1.036 0.012
T 0.558 0.452 0.237
U 0.553 0.445 0.240
Name TY-PW_LABAN
Save
Symbol color and size
B/W
Default
Size 10
P
1.057
1.000
1.61E-03
Km [SI]
4.17E-03
U
1
1.000
1.057
P
-1
Site:
Lat:
Lon:
Rock:
Stratigraphy:
Lithostratigraphy:
Region:
Instrument: MFK

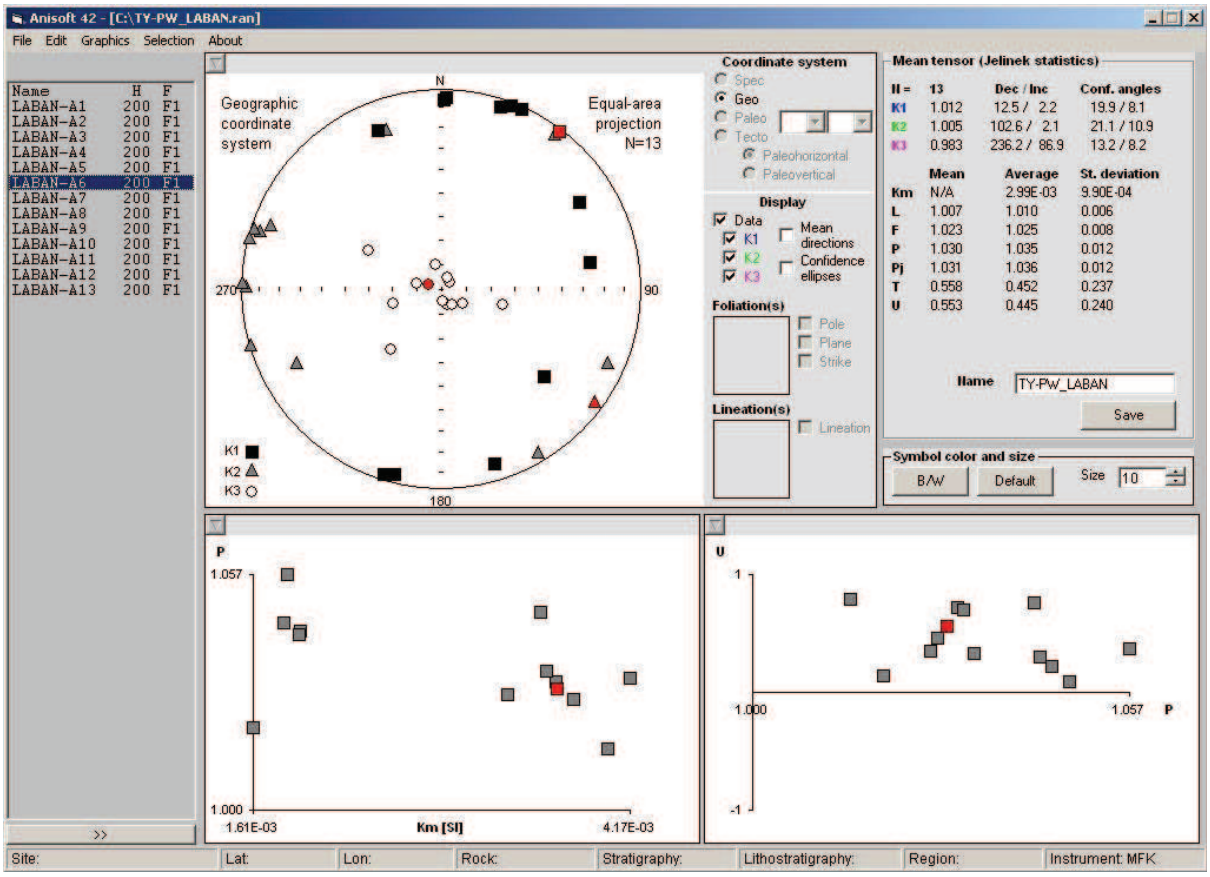
Anisoft 42 - [C:\TY-PW_LABAN.ran]
File Edit Graphics Selection About
Name H F
LABAN-A1 200 F1
LABAN-A2 200 F1
LABAN-A3 200 F1
LABAN-A4 200 F1
LABAN-A5 200 F1
LABAN-A6 200 F1
LABAN-A7 200 F1
LABAN-A8 200 F1
LABAN-A9 200 F1
LABAN-A10 200 F1
LABAN-A11 200 F1
LABAN-A12 200 F1
LABAN-A13 200 F1
Geographic coordinate system
Equal-area projection N=13
N
90
180
270
K1
K2
K3
Coordinate system
Spec
Geo
Paleo
Tecto
Paleohorizontal
Paleovertical
Display
Data
K1
K2
K3
Mean directions
Confidence ellipses
Foliation(s)
Pole
Plane
Strike
Lineation(s)
Lineation
Mean tensor (Jelinek statistics)
II = 13 Dec / Inc Conf. angles
K1 1.012 12.5 / 2.2 19.9 / 8.1
K2 1.005 102.6 / 2.1 21.1 / 10.9
K3 0.983 236.2 / 86.9 13.2 / 8.2
Mean Average St. deviation
Km N/A 2.99E-03 9.90E-04
L 1.007 1.010 0.006
F 1.023 1.025 0.008
P 1.030 1.035 0.012
Pj 1.031 1.036 0.012
T 0.558 0.452 0.237
U 0.553 0.445 0.240
Name TY-PW_LABAN
Save
Symbol color and size
B/W
Default
Size 10
P
1.057
1.000
1.61E-03
Km [SI]
4.17E-03
U
1
1.000
1.057
P
-1
Site:
Lat:
Lon:
Rock:
Stratigraphy:
Lithostratigraphy:
Region:
Instrument: MFK

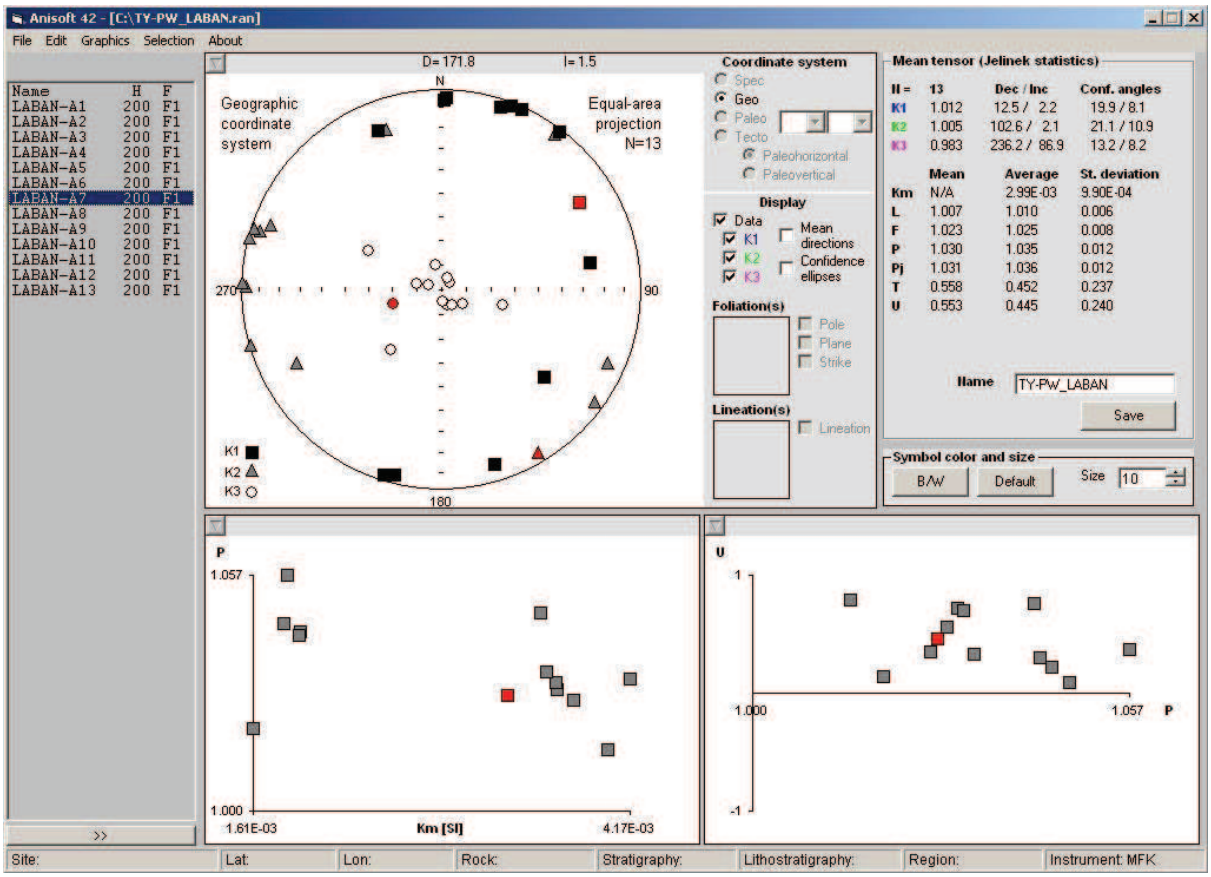
Anisoft 42 - [C:\TY-PW_LABAN.ran]
File Edit Graphics Selection About
D= 171.8 I= 1.5
Name H F
LABAN-A1 200 F1
LABAN-A2 200 F1
LABAN-A3 200 F1
LABAN-A4 200 F1
LABAN-A5 200 F1
LABAN-A6 200 F1
LABAN-A7 200 F1
LABAN-A8 200 F1
LABAN-A9 200 F1
LABAN-A10 200 F1
LABAN-A11 200 F1
LABAN-A12 200 F1
LABAN-A13 200 F1
Geographic coordinate system
Equal-area projection N=13
N
90
180
270
K1
K2
K3
Coordinate system
Spec
Geo
Paleo
Tecto
Paleohorizontal
Paleovertical
Display
Data
K1
K2
K3
Mean directions
Confidence ellipses
Foliation(s)
Pole
Plane
Strike
Lineation(s)
Lineation
Mean tensor (Jelinek statistics)
II = 13 Dec / Inc Conf. angles
K1 1.012 12.5 / 2.2 19.9 / 8.1
K2 1.005 102.6 / 2.1 21.1 / 10.9
K3 0.983 236.2 / 86.9 13.2 / 8.2
Mean Average St. deviation
Km N/A 2.99E-03 9.90E-04
L 1.007 1.010 0.006
F 1.023 1.025 0.008
P 1.030 1.035 0.012
Pj 1.031 1.036 0.012
T 0.558 0.452 0.237
U 0.553 0.445 0.240
Name TY-PW_LABAN
Save
Symbol color and size
B/W
Default
Size 10
P
1.057
1.000
1.61E-03
Km [SI]
4.17E-03
U
1
1.000
1.057
P
-1
Site:
Lat:
Lon:
Rock:
Stratigraphy:
Lithostratigraphy:
Region:
Instrument: MFK

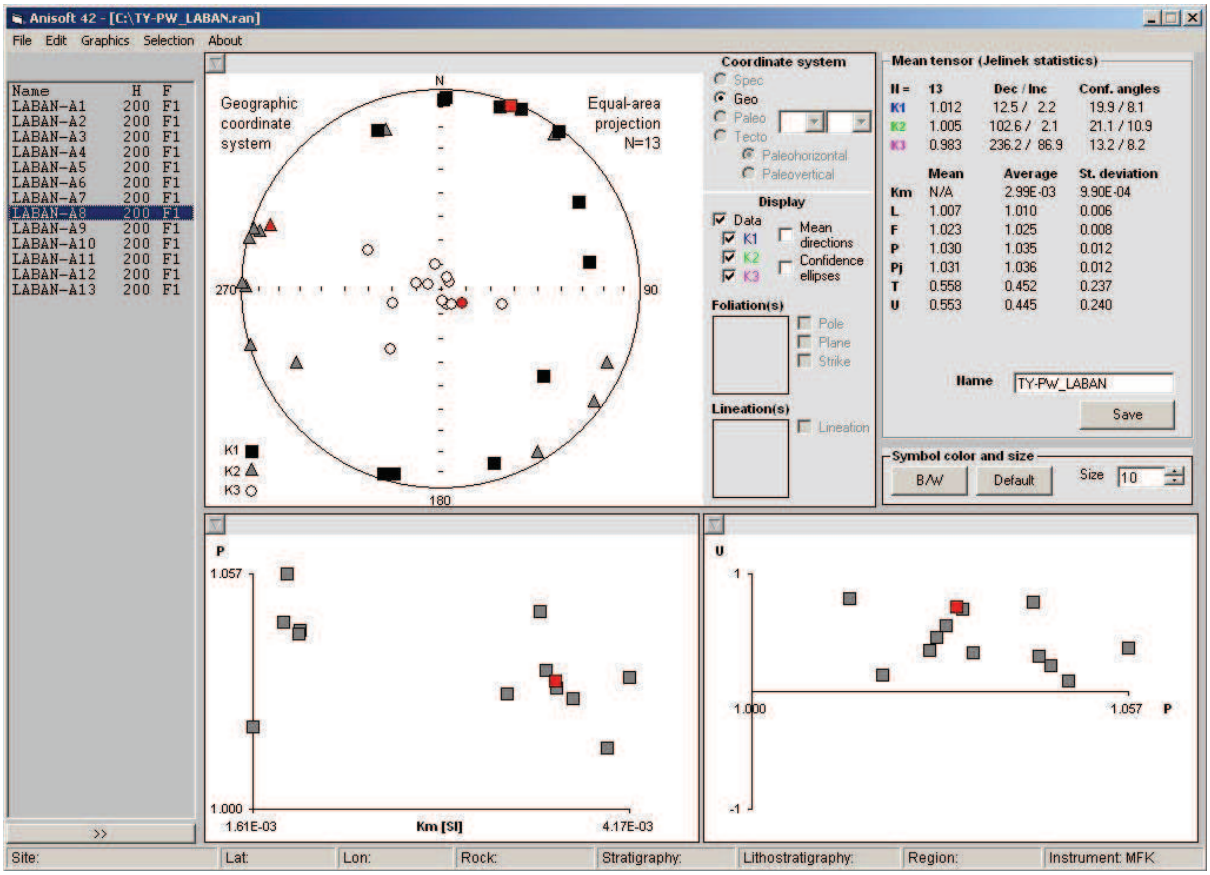
Anisoft 42 - [C:\TY-PW_LABAN.ran]
File Edit Graphics Selection About
Name H F
LABAN-A1 200 F1
LABAN-A2 200 F1
LABAN-A3 200 F1
LABAN-A4 200 F1
LABAN-A5 200 F1
LABAN-A6 200 F1
LABAN-A7 200 F1
LABAN-A8 200 F1
LABAN-A9 200 F1
LABAN-A10 200 F1
LABAN-A11 200 F1
LABAN-A12 200 F1
LABAN-A13 200 F1
Geographic coordinate system
Equal-area projection N=13
N
90
180
270
K1
K2
K3
Coordinate system
Spec
Geo
Paleo
Tecto
Paleohorizontal
Paleovertical
Display
Data
K1
K2
K3
Mean directions
Confidence ellipses
Foliation(s)
Pole
Plane
Strike
Lineation(s)
Lineation
Mean tensor (Jelinek statistics)
II = 13 Dec / Inc Conf. angles
K1 1.012 12.5 / 2.2 19.9 / 8.1
K2 1.005 102.6 / 2.1 21.1 / 10.9
K3 0.983 236.2 / 86.9 13.2 / 8.2
Mean Average St. deviation
Km N/A 2.99E-03 9.90E-04
L 1.007 1.010 0.006
F 1.023 1.025 0.008
P 1.030 1.035 0.012
Pj 1.031 1.036 0.012
T 0.558 0.452 0.237
U 0.553 0.445 0.240
Name TY-PW_LABAN
Save
Symbol color and size
B/W
Default
Size 10
P
1.057
1.000
1.61E-03
Km [SI]
4.17E-03
U
1
1.000
1.057
P
-1
Site:
Lat:
Lon:
Rock:
Stratigraphy:
Lithostratigraphy:
Region:
Instrument: MFK

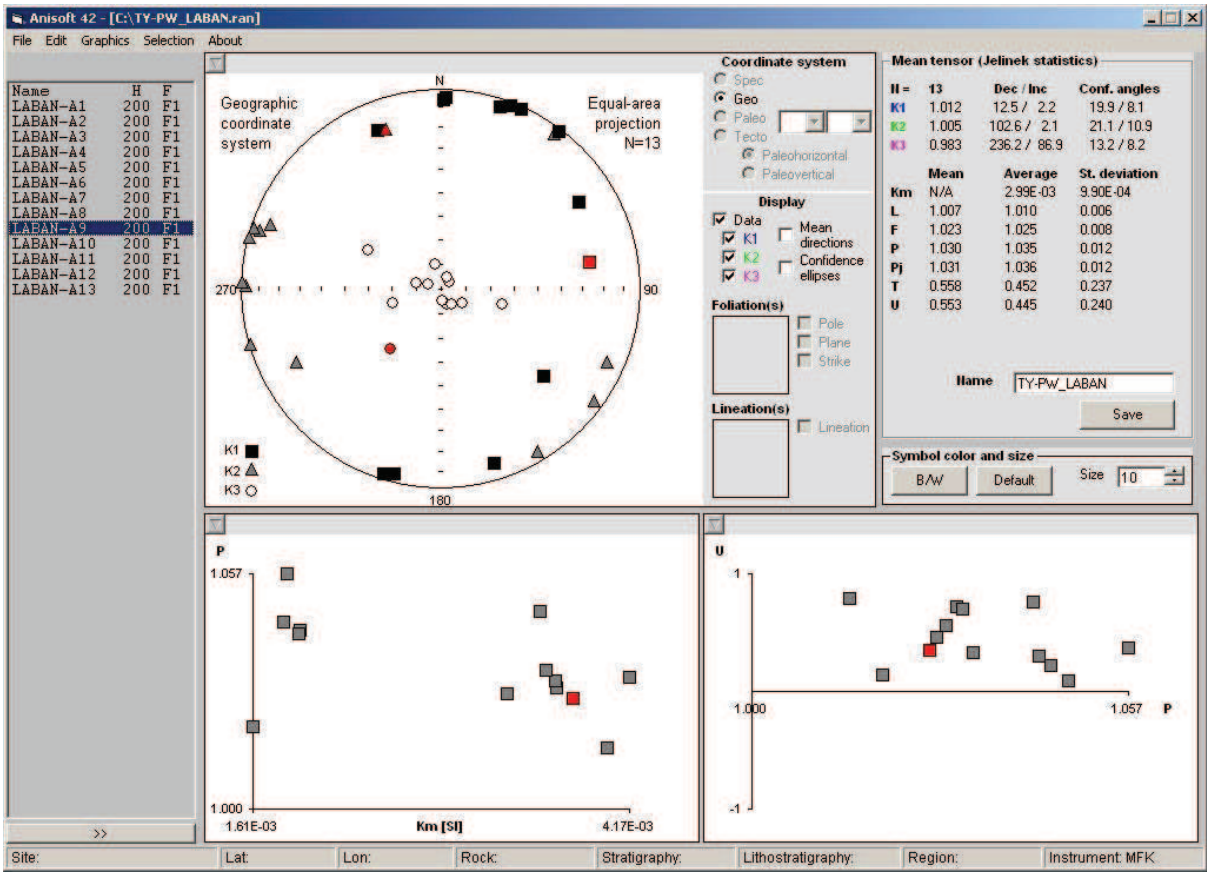
Anisoft 42 - [C:\TY-PW_LABAN.ran]
File Edit Graphics Selection About
Name H F
LABAN-A1 200 F1
LABAN-A2 200 F1
LABAN-A3 200 F1
LABAN-A4 200 F1
LABAN-A5 200 F1
LABAN-A6 200 F1
LABAN-A7 200 F1
LABAN-A8 200 F1
LABAN-A9 200 F1
LABAN-A10 200 F1
LABAN-A11 200 F1
LABAN-A12 200 F1
LABAN-A13 200 F1
Geographic coordinate system
Equal-area projection N=13
N
90
180
270
K1
K2
K3
Coordinate system
Spec
Geo
Paleo
Tecto
Paleohorizontal
Paleovertical
Display
Data
K1
K2
K3
Mean directions
Confidence ellipses
Foliation(s)
Pole
Plane
Strike
Lineation(s)
Lineation
Mean tensor (Jelinek statistics)
II = 13 Dec / Inc Conf. angles
K1 1.012 12.5 / 2.2 19.9 / 8.1
K2 1.005 102.6 / 2.1 21.1 / 10.9
K3 0.983 236.2 / 86.9 13.2 / 8.2
Mean Average St. deviation
Km N/A 2.99E-03 9.90E-04
L 1.007 1.010 0.006
F 1.023 1.025 0.008
P 1.030 1.035 0.012
Pj 1.031 1.036 0.012
T 0.558 0.452 0.237
U 0.553 0.445 0.240
Name TY-PW_LABAN
Save
Symbol color and size
B/W
Default
Size 10
P
1.057
1.000
1.61E-03
Km [SI]
4.17E-03
U
1
1.000
1.057
P
-1
Site:
Lat:
Lon:
Rock:
Stratigraphy:
Lithostratigraphy:
Region:
Instrument: MFK

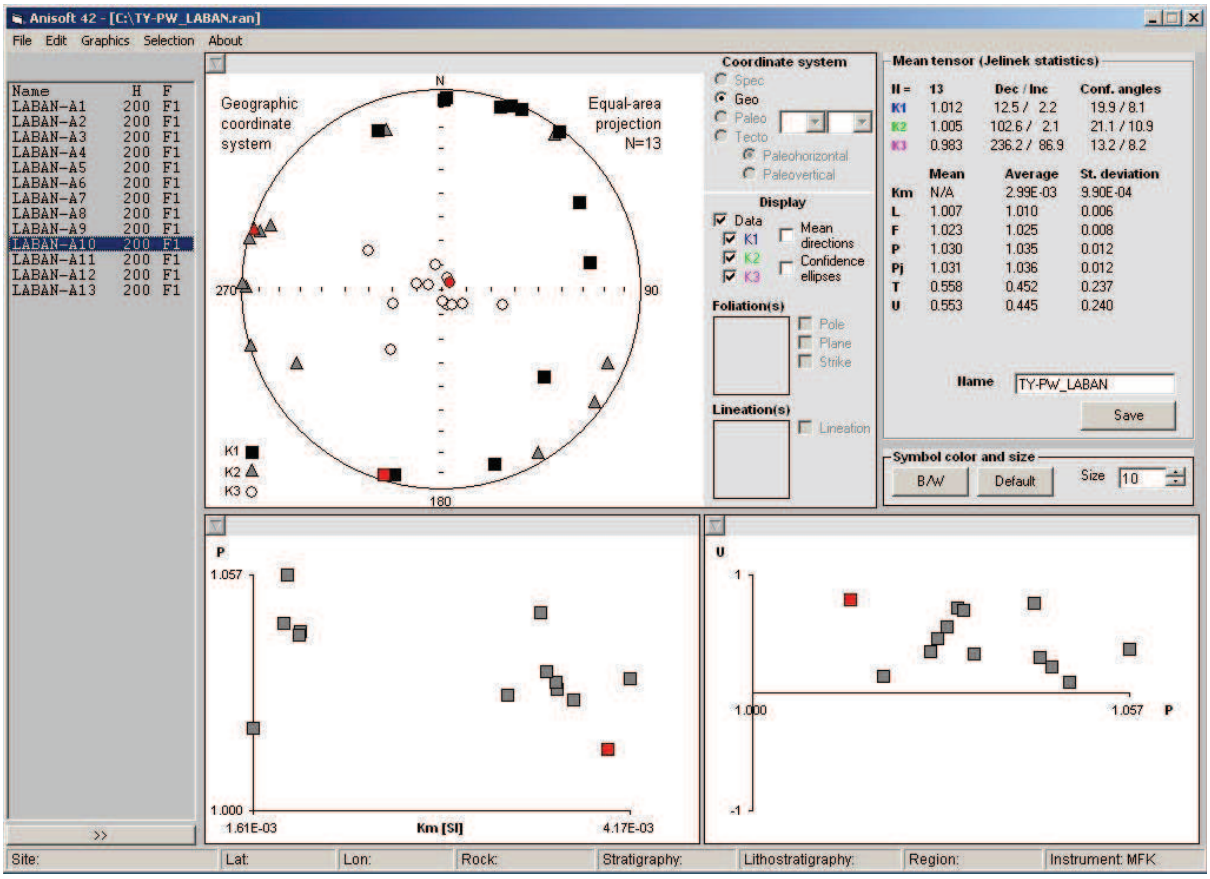
Anisoft 42 - [C:\TY-PW_LABAN.ran]
File Edit Graphics Selection About
Name H F
LABAN-A1 200 F1
LABAN-A2 200 F1
LABAN-A3 200 F1
LABAN-A4 200 F1
LABAN-A5 200 F1
LABAN-A6 200 F1
LABAN-A7 200 F1
LABAN-A8 200 F1
LABAN-A9 200 F1
LABAN-A10 200 F1
LABAN-A11 200 F1
LABAN-A12 200 F1
LABAN-A13 200 F1
Geographic coordinate system
Equal-area projection N=13
N
90
180
270
K1
K2
K3
Coordinate system
Spec
Geo
Paleo
Tecto
Paleohorizontal
Paleovertical
Display
Data
K1
K2
K3
Mean directions
Confidence ellipses
Foliation(s)
Pole
Plane
Strike
Lineation(s)
Lineation
Mean tensor (Jelinek statistics)
II = 13 Dec / Inc Conf. angles
K1 1.012 12.5 / 2.2 19.9 / 8.1
K2 1.005 102.6 / 2.1 21.1 / 10.9
K3 0.983 236.2 / 86.9 13.2 / 8.2
Mean Average St. deviation
Km N/A 2.99E-03 9.90E-04
L 1.007 1.010 0.006
F 1.023 1.025 0.008
P 1.030 1.035 0.012
Pj 1.031 1.036 0.012
T 0.558 0.452 0.237
U 0.553 0.445 0.240
Name TY-PW_LABAN
Save
Symbol color and size
B/W
Default
Size 10
P
1.057
1.000
1.61E-03
Km [SI]
4.17E-03
U
1
1.000
1.057
P
-1
Site:
Lat:
Lon:
Rock:
Stratigraphy:
Lithostratigraphy:
Region:
Instrument: MFK

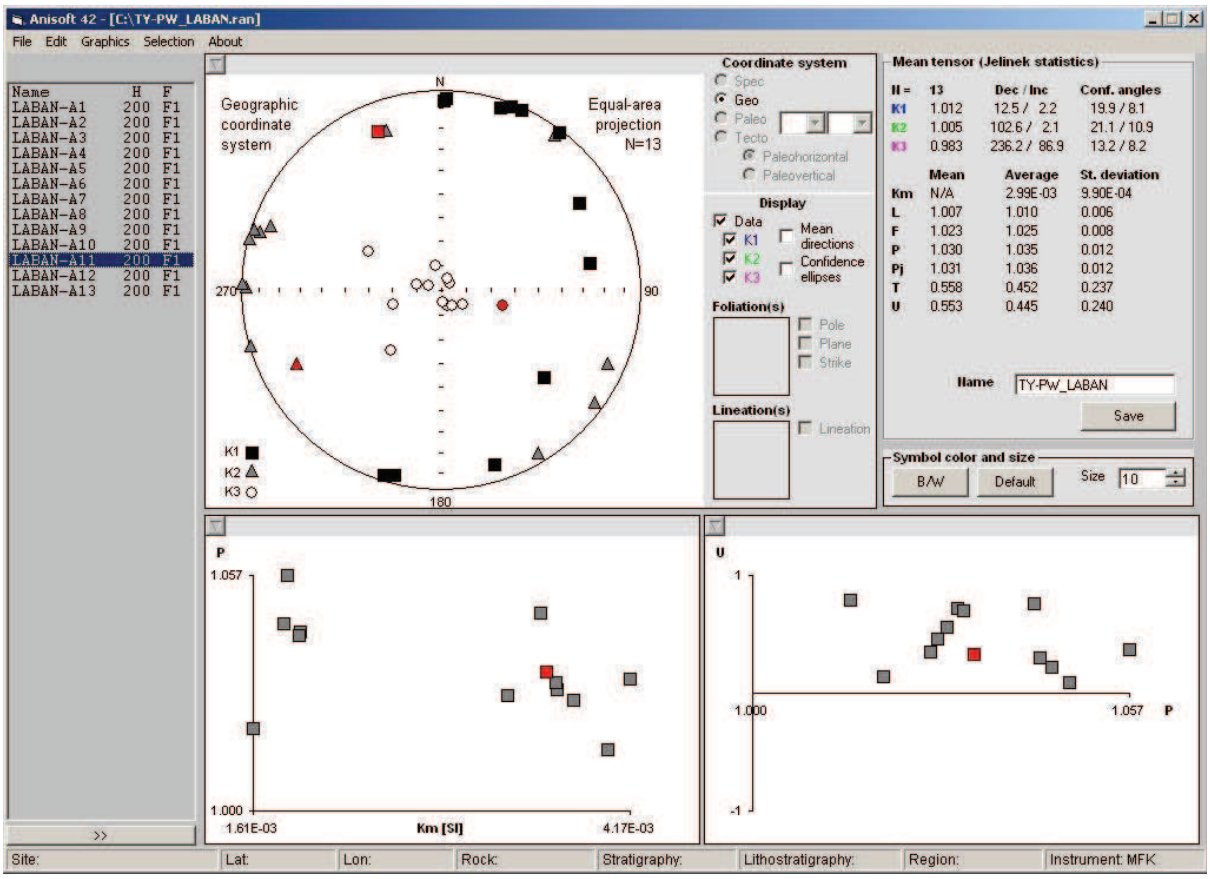
Anisoft 42 - [C:\TY-PW_LABAN.ran]
File Edit Graphics Selection About
Name H F
LABAN-A1 200 F1
LABAN-A2 200 F1
LABAN-A3 200 F1
LABAN-A4 200 F1
LABAN-A5 200 F1
LABAN-A6 200 F1
LABAN-A7 200 F1
LABAN-A8 200 F1
LABAN-A9 200 F1
LABAN-A10 200 F1
LABAN-A11 200 F1
LABAN-A12 200 F1
LABAN-A13 200 F1
Geographic coordinate system
Equal-area projection N=13
N
90
180
270
K1
K2
K3
Coordinate system
Spec
Geo
Paleo
Tecto
Paleohorizontal
Paleovertical
Display
Data
K1
K2
K3
Mean directions
Confidence ellipses
Foliation(s)
Pole
Plane
Strike
Lineation(s)
Lineation
Mean tensor (Jelinek statistics)
II = 13 Dec / Inc Conf. angles
K1 1.012 12.5 / 2.2 19.9 / 8.1
K2 1.005 102.6 / 2.1 21.1 / 10.9
K3 0.983 236.2 / 86.9 13.2 / 8.2
Mean Average St. deviation
Km N/A 2.99E-03 9.90E-04
L 1.007 1.010 0.006
F 1.023 1.025 0.008
P 1.030 1.035 0.012
Pj 1.031 1.036 0.012
T 0.558 0.452 0.237
U 0.553 0.445 0.240
Name TY-PW_LABAN
Save
Symbol color and size
B/W
Default
Size 10
P
1.057
1.000
1.61E-03
Km [SI]
4.17E-03
U
1
1.000
1.057
P
-1
Site:
Lat:
Lon:
Rock:
Stratigraphy:
Lithostratigraphy:
Region:
Instrument: MFK

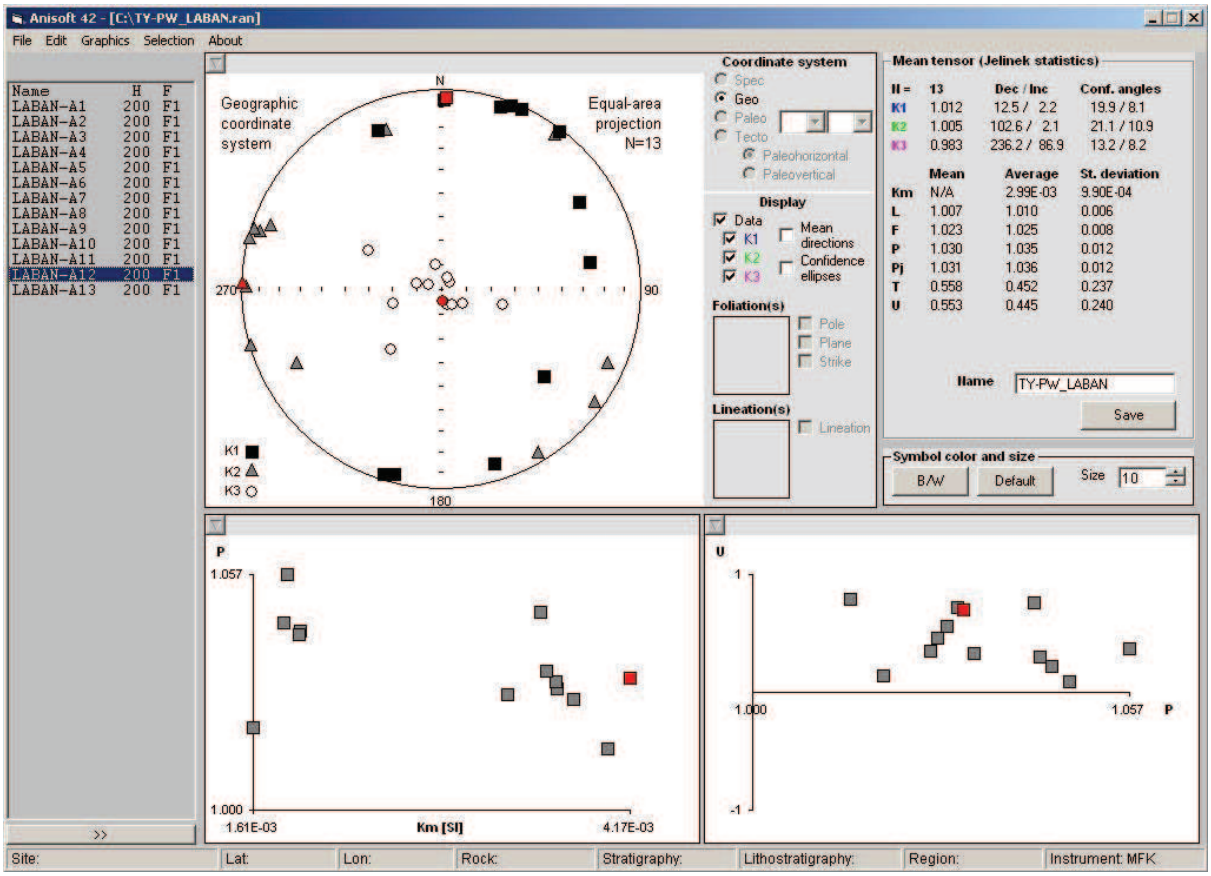
Anisoft 42 - [C:\TY-PW_LABAN.ran]
File Edit Graphics Selection About
Name H F
LABAN-A1 200 F1
LABAN-A2 200 F1
LABAN-A3 200 F1
LABAN-A4 200 F1
LABAN-A5 200 F1
LABAN-A6 200 F1
LABAN-A7 200 F1
LABAN-A8 200 F1
LABAN-A9 200 F1
LABAN-A10 200 F1
LABAN-A11 200 F1
LABAN-A12 200 F1
LABAN-A13 200 F1
Geographic coordinate system
Equal-area projection N=13
N
90
180
270
K1
K2
K3
Coordinate system
Spec
Geo
Paleo
Tecto
Paleohorizontal
Paleovertical
Display
Data
K1
K2
K3
Mean directions
Confidence ellipses
Foliation(s)
Pole
Plane
Strike
Lineation(s)
Lineation
Mean tensor (Jelinek statistics)
II = 13 Dec / Inc Conf. angles
K1 1.012 12.5 / 2.2 19.9 / 8.1
K2 1.005 102.6 / 2.1 21.1 / 10.9
K3 0.983 236.2 / 86.9 13.2 / 8.2
Mean Average St. deviation
Km N/A 2.99E-03 9.90E-04
L 1.007 1.010 0.006
F 1.023 1.025 0.008
P 1.030 1.035 0.012
Pj 1.031 1.036 0.012
T 0.558 0.452 0.237
U 0.553 0.445 0.240
Name TY-PW_LABAN
Save
Symbol color and size
B/W
Default
Size 10
P
1.057
1.000
1.61E-03
Km [SI]
4.17E-03
U
1
1.000
1.057
P
-1
Site:
Lat:
Lon:
Rock:
Stratigraphy:
Lithostratigraphy:
Region:
Instrument: MFK

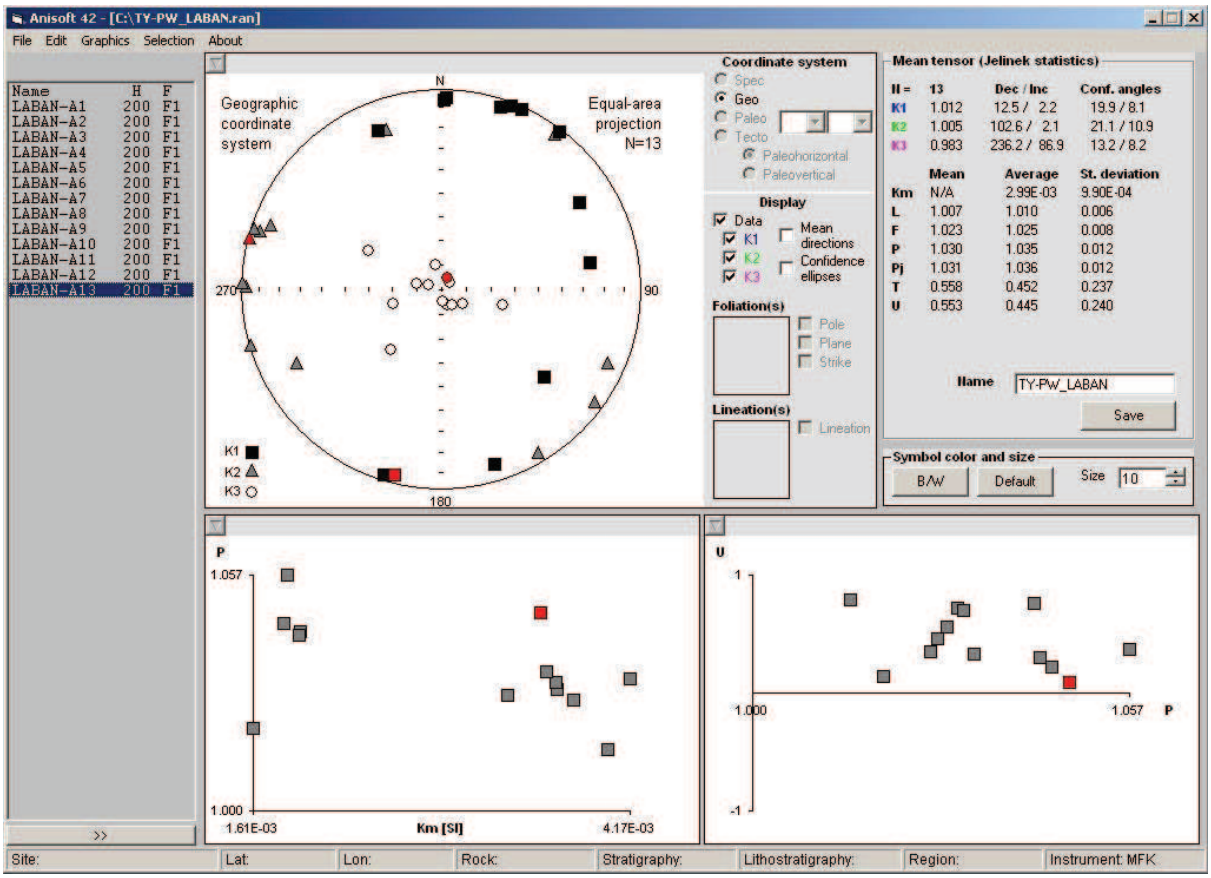
Anisoft 42 - [C:\TY-PW_LABAN.ran]
File Edit Graphics Selection About
Name H F
LABAN-A1 200 F1
LABAN-A2 200 F1
LABAN-A3 200 F1
LABAN-A4 200 F1
LABAN-A5 200 F1
LABAN-A6 200 F1
LABAN-A7 200 F1
LABAN-A8 200 F1
LABAN-A9 200 F1
LABAN-A10 200 F1
LABAN-A11 200 F1
LABAN-A12 200 F1
LABAN-A13 200 F1
Geographic coordinate system
Equal-area projection N=13
N
90
180
270
K1
K2
K3
Coordinate system
Spec
Geo
Paleo
Tecto
Paleohorizontal
Paleovertical
Display
Data
K1
K2
K3
Mean directions
Confidence ellipses
Foliation(s)
Pole
Plane
Strike
Lineation(s)
Lineation
Mean tensor (Jelinek statistics)
II = 13 Dec / Inc Conf. angles
K1 1.012 12.5 / 2.2 19.9 / 8.1
K2 1.005 102.6 / 2.1 21.1 / 10.9
K3 0.983 236.2 / 86.9 13.2 / 8.2
Mean Average St. deviation
Km N/A 2.99E-03 9.90E-04
L 1.007 1.010 0.006
F 1.023 1.025 0.008
P 1.030 1.035 0.012
Pj 1.031 1.036 0.012
T 0.558 0.452 0.237
U 0.553 0.445 0.240
Name TY-PW_LABAN
Save
Symbol color and size
B/W
Default
Size 10
P
1.057
1.000
1.61E-03
Km [SI]
4.17E-03
U
1
1.000
1.057
P
-1
Site:
Lat:
Lon:
Rock:
Stratigraphy:
Lithostratigraphy:
Region:
Instrument: MFK

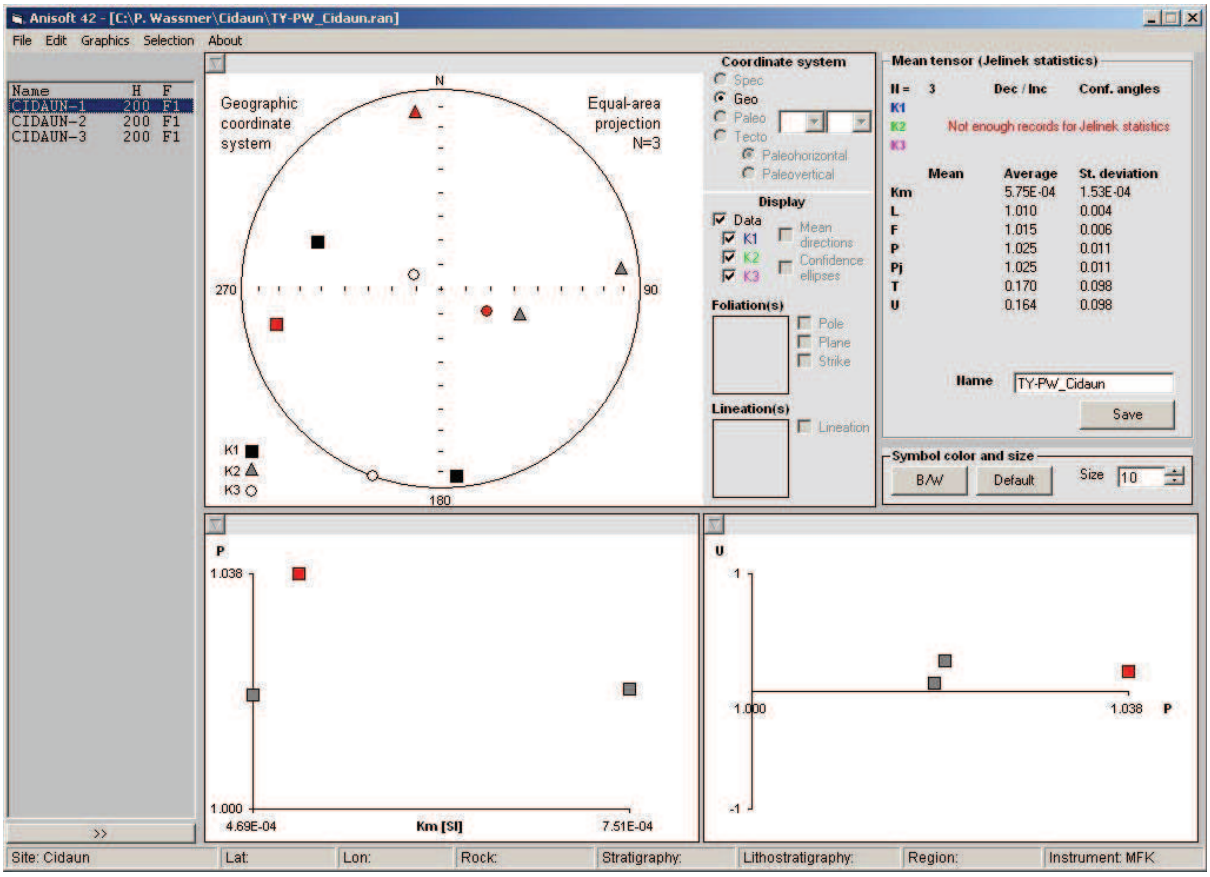
Anisoft 42 - [C:\P. Wassmer\Cidaun\TY-PW_Cidaun.ran]
File Edit Graphics Selection About
Name H F
CIDAUN-1 200 F1
CIDAUN-2 200 F1
CIDAUN-3 200 F1
Geographic coordinate system
Equal-area projection N=3
N
270
90
180
K1
K2
K3
Coordinate system
Spec
Geo
Paleo
Tecto
Paleohorizontal
Paleovertical
Display
Data
K1
K2
K3
Mean directions
Confidence ellipses
Foliation(s)
Pole
Plane
Strike
Lineation(s)
Lineation
Mean tensor (Jelinek statistics)
II = 3
Dec / Inc
Conf. angles
K1
K2
K3
Not enough records for Jelinek statistics
Mean
Average
St. deviation
Km 5.75E-04 1.53E-04
L 1.010 0.004
F 1.015 0.006
P 1.025 0.011
Pj 1.025 0.011
T 0.170 0.098
U 0.164 0.098
Name TY-PW_Cidaun
Save
Symbol color and size
B/W
Default
Size 10
P
1.038
1.000
4.69E-04
Km [SI]
7.51E-04
U
1
1.000
1.038
P
-1
Site: Cidaun
Lat:
Lon:
Rock:
Stratigraphy:
Lithostratigraphy:
Region:
Instrument: MFK

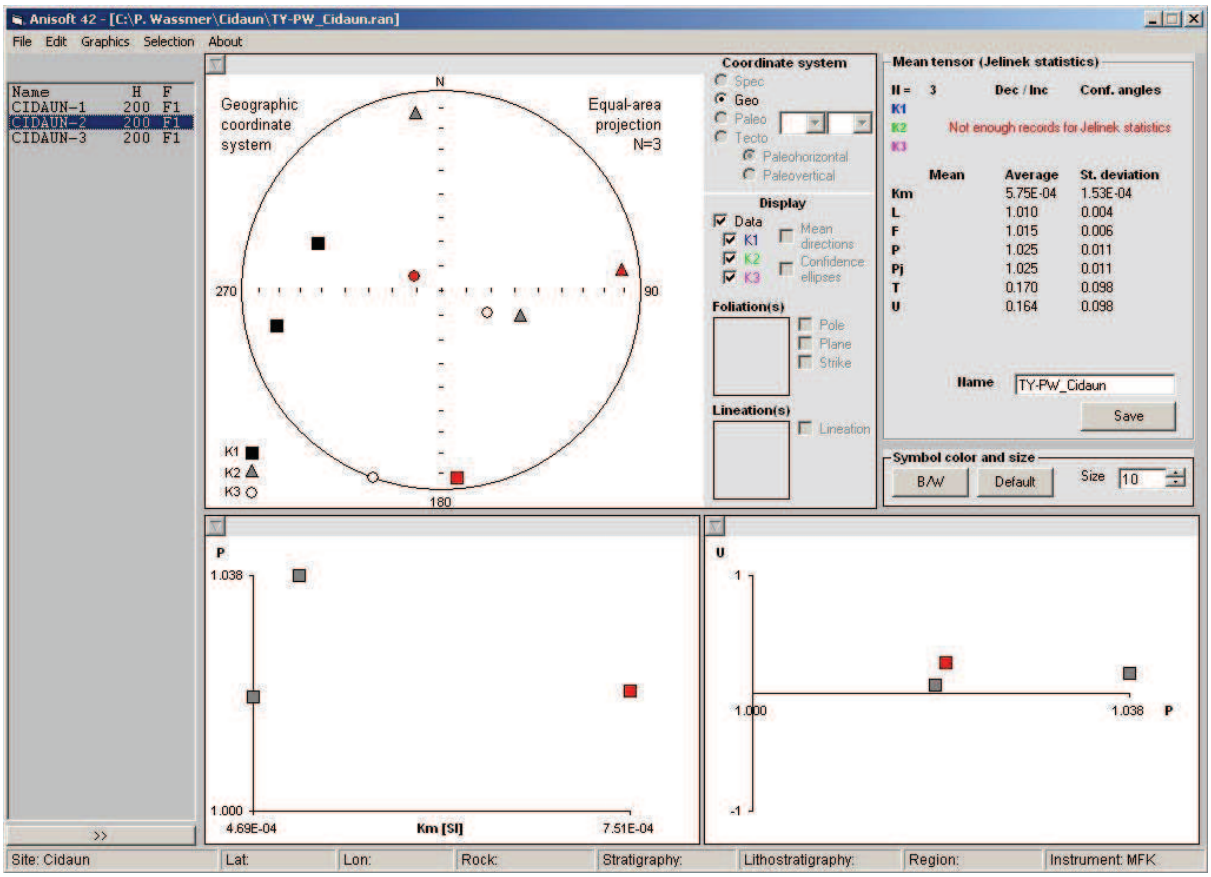
Anisoft 42 - [C:\P. Wassmer\Cidaun\TY-PW_Cidaun.ran]
File Edit Graphics Selection About
Name H F
CIDAUN-1 200 F1
CIDAUN-2 200 F1
CIDAUN-3 200 F1
Geographic coordinate system
Equal-area projection N=3
N
270
90
180
K1
K2
K3
Coordinate system
Spec
Geo
Paleo
Tecto
Paleohorizontal
Paleovertical
Display
Data
K1
K2
K3
Mean directions
Confidence ellipses
Foliation(s)
Pole
Plane
Strike
Lineation(s)
Lineation
Mean tensor (Jelinek statistics)
II = 3
Dec / Inc
Conf. angles
K1
K2
K3
Not enough records for Jelinek statistics
Mean
Average
St. deviation
Km 5.75E-04 1.53E-04
L 1.010 0.004
F 1.015 0.006
P 1.025 0.011
Pj 1.025 0.011
T 0.170 0.098
U 0.164 0.098
Name TY-PW_Cidaun
Save
Symbol color and size
B/W
Default
Size 10
P
1.038
1.000
4.69E-04
Km [SI]
7.51E-04
U
1
1.000
1.038
P
-1
Site: Cidaun
Lat:
Lon:
Rock:
Stratigraphy:
Lithostratigraphy:
Region:
Instrument: MFK

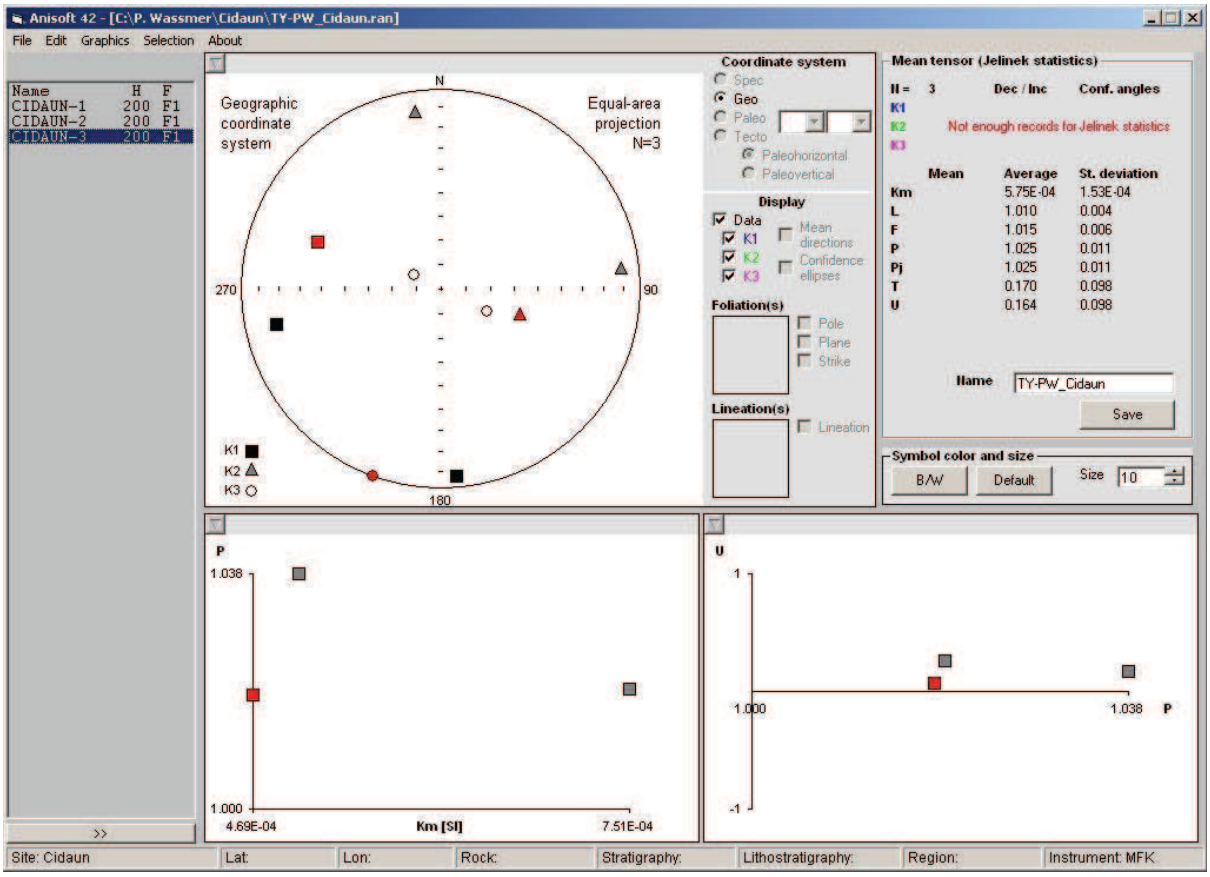
Anisoft 42 - [C:\P. Wassmer\Cidaun\TY-PW_Cidaun.ran]
File Edit Graphics Selection About
Name H F
CIDAUN-1 200 F1
CIDAUN-2 200 F1
CIDAUN-3 200 F1
Geographic coordinate system
Equal-area projection
N=3
N
270
90
180
K1
K2
K3
Coordinate system
Spec
Geo
Paleo
Tecto
Paleohorizontal
Paleovertical
Display
Data
K1
K2
K3
Mean directions
Confidence ellipses
Foliation(s)
Pole
Plane
Strike
Lineation(s)
Lineation
Mean tensor (Jelinek statistics)
II = 3
Dec / Inc
Conf. angles
K1
K2
K3
Not enough records for Jelinek statistics
Mean
Average
St. deviation
Km 5.75E-04 1.53E-04
L 1.010 0.004
F 1.015 0.006
P 1.025 0.011
Pj 1.025 0.011
T 0.170 0.098
U 0.164 0.098
Name TY-PW_Cidaun
Save
Symbol color and size
B/W
Default
Size 10
P
1.038
1.000
4.69E-04
Km [SI]
7.51E-04
U
1
1.000
1.038
P
-1
Site: Cidaun
Lat:
Lon:
Rock:
Stratigraphy:
Lithostratigraphy:
Region:
Instrument: MFK

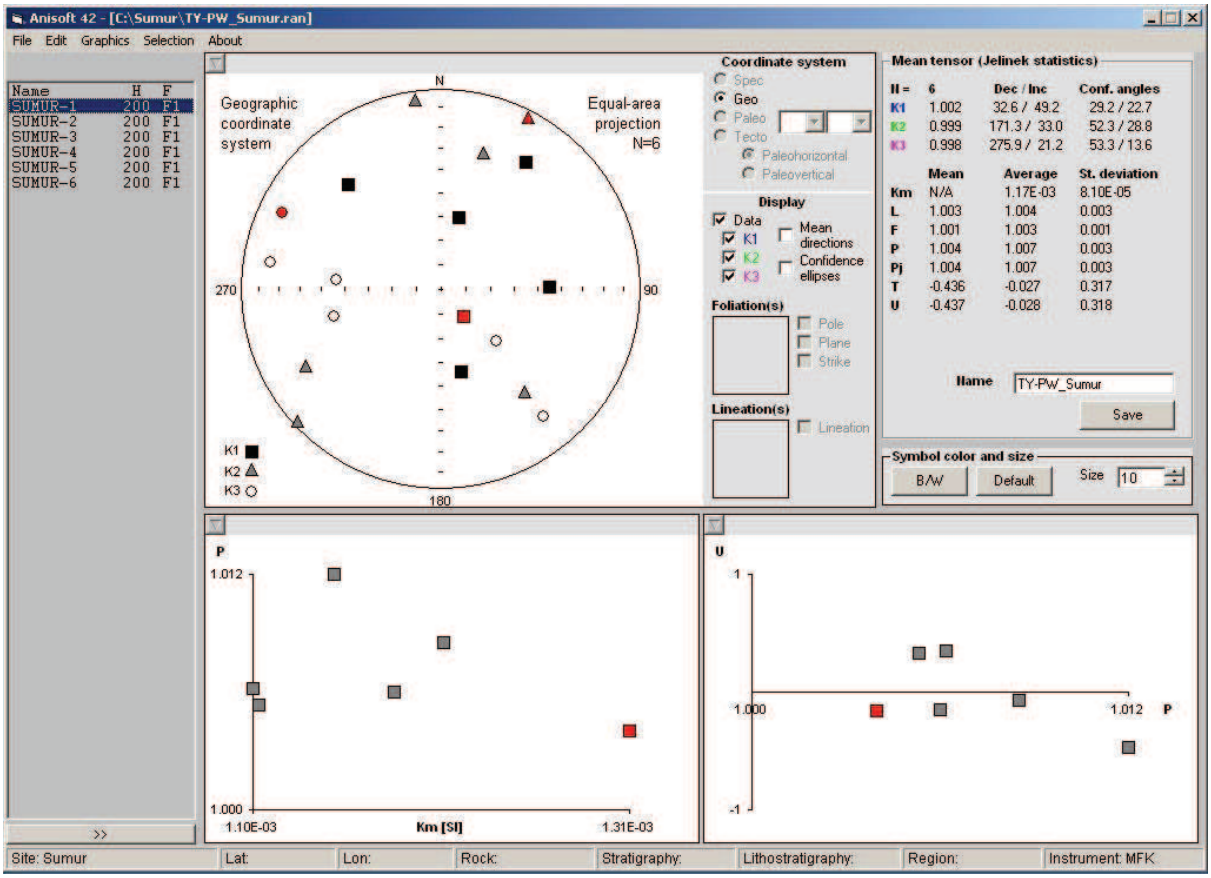
Anisoft 42 - [C:\Sumur\TY-PW_Sumur.ran]
File Edit Graphics Selection About
Name H F
SUMUR-1 200 F1
SUMUR-2 200 F1
SUMUR-3 200 F1
SUMUR-4 200 F1
SUMUR-5 200 F1
SUMUR-6 200 F1
Geographic coordinate system
Equal-area projection
N=6
N
270
90
180
K1
K2
K3
Coordinate system
Spec
Geo
Paleo
Tecto
Paleohorizontal
Paleovertical
Display
Data
K1
K2
K3
Mean directions
Confidence ellipses
Foliation(s)
Pole
Plane
Strike
Lineation(s)
Lineation
Mean tensor (Jelinek statistics)
II = 6
Dec / Inc
Conf. angles
K1 1.002 32.6 / 49.2 29.2 / 22.7
K2 0.999 171.3 / 33.0 52.3 / 28.8
K3 0.998 275.9 / 21.2 53.3 / 13.6
Mean
Average
St. deviation
Km N/A 1.17E-03 8.10E-05
L 1.003 1.004 0.003
F 1.001 1.003 0.001
P 1.004 1.007 0.003
Pj 1.004 1.007 0.003
T -0.436 -0.027 0.317
U -0.437 -0.028 0.318
Name TY-PW_Sumur
Save
Symbol color and size
B/W
Default
Size 10
P
1.012
1.000
1.10E-03
Km [SI]
1.31E-03
U
1
1.000
1.012
P
-1
Site: Sumur
Lat:
Lon:
Rock:
Stratigraphy:
Lithostratigraphy:
Region:
Instrument: MFK

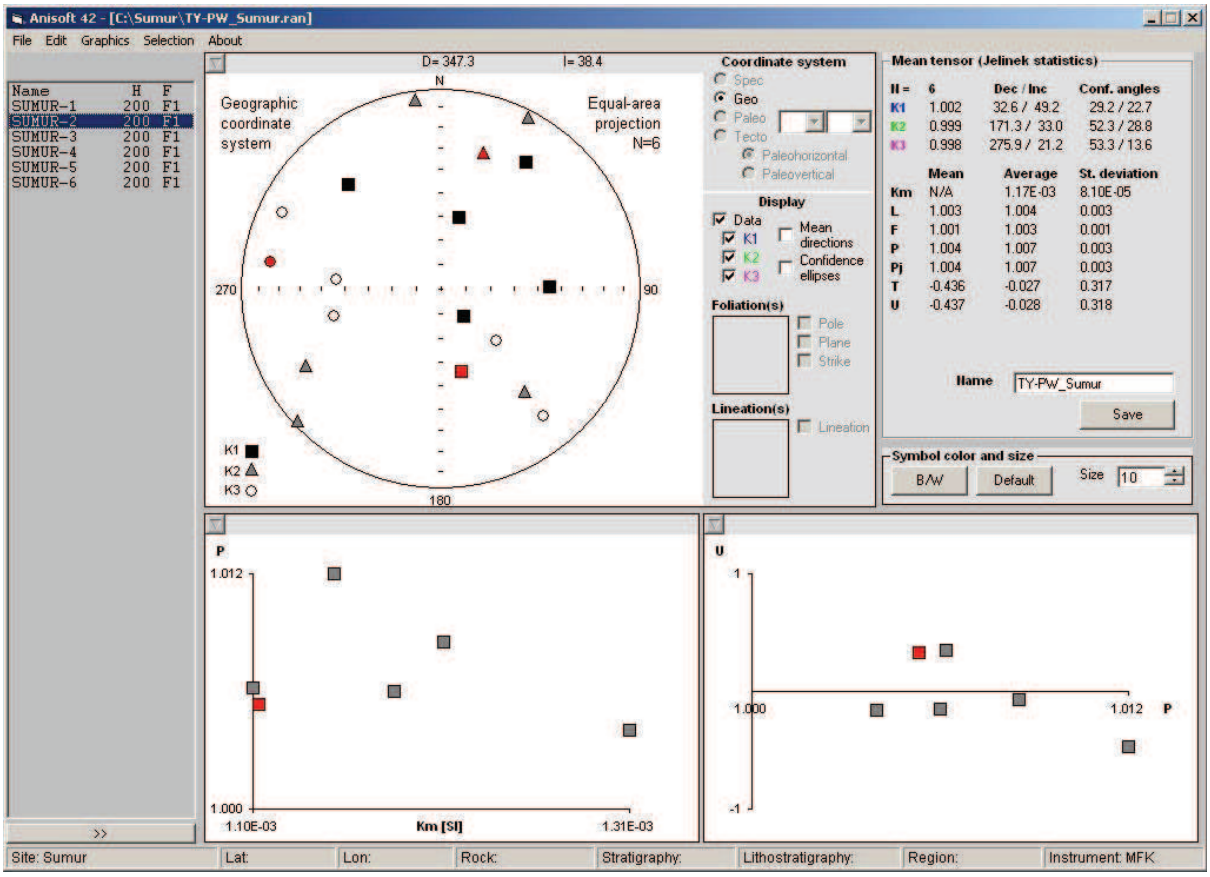
Anisoft 42 - [C:\Sumur\TY-PW_Sumur.ran]
File Edit Graphics Selection About
Name H F
SUMUR-1 200 F1
SUMUR-2 200 F1
SUMUR-3 200 F1
SUMUR-4 200 F1
SUMUR-5 200 F1
SUMUR-6 200 F1
D= 347.3 I= 38.4
Geographic coordinate system
Equal-area projection N=6
N
90
180
270
K1
K2
K3
Coordinate system
Spec
Geo
Paleo
Tecto
Paleohorizontal
Paleovertical
Display
Data
K1
K2
K3
Mean directions
Confidence ellipses
Foliation(s)
Pole
Plane
Strike
Lineation(s)
Lineation
Mean tensor (Jelinek statistics)
II = 6 Dec / Inc Conf. angles
K1 1.002 32.6 / 49.2 29.2 / 22.7
K2 0.999 171.3 / 33.0 52.3 / 28.8
K3 0.998 275.9 / 21.2 53.3 / 13.6
Mean Average St. deviation
Km N/A 1.17E-03 8.10E-05
L 1.003 1.004 0.003
F 1.001 1.003 0.001
P 1.004 1.007 0.003
Pj 1.004 1.007 0.003
T -0.436 -0.027 0.317
U -0.437 -0.028 0.318
Name TY-PW_Sumur
Save
Symbol color and size
B/W
Default
Size 10
P
1.012
1.000
1.10E-03
Km [SI]
1.31E-03
U
1
1.000
1.012
P
-1
Site: Sumur
Lat:
Lon:
Rock:
Stratigraphy:
Lithostratigraphy:
Region:
Instrument: MFK

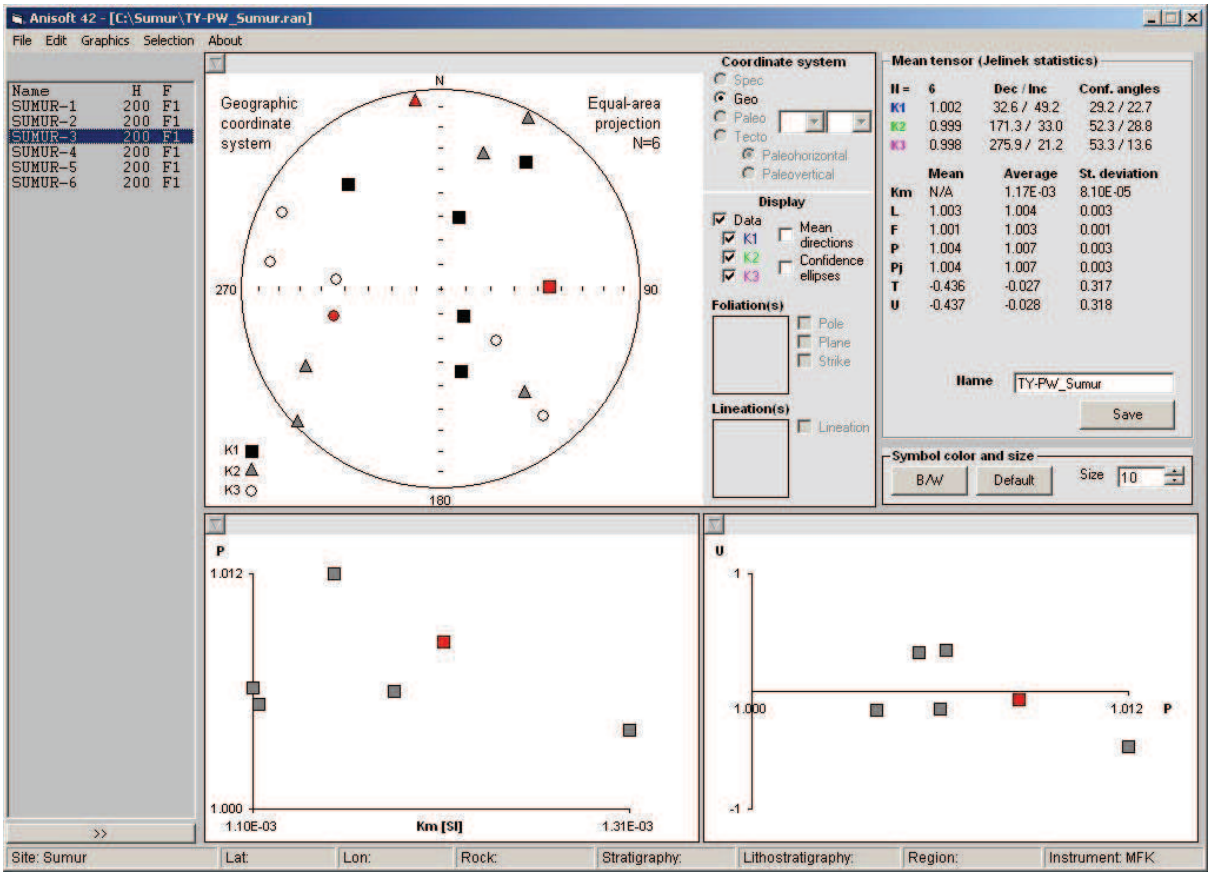
Anisoft 42 - [C:\Sumur\TY-PW_Sumur.ran]
File Edit Graphics Selection About
Name H F
SUMUR-1 200 F1
SUMUR-2 200 F1
SUMUR-3 200 F1
SUMUR-4 200 F1
SUMUR-5 200 F1
SUMUR-6 200 F1
Geographic coordinate system
Equal-area projection N=6
N
90
180
270
K1
K2
K3
Coordinate system
Spec
Geo
Paleo
Tecto
Paleohorizontal
Paleovertical
Display
Data
K1
K2
K3
Mean directions
Confidence ellipses
Foliation(s)
Pole
Plane
Strike
Lineation(s)
Lineation
Mean tensor (Jelinek statistics)
II = 6 Dec / Inc Conf. angles
K1 1.002 32.6 / 49.2 29.2 / 22.7
K2 0.999 171.3 / 33.0 52.3 / 28.8
K3 0.998 275.9 / 21.2 53.3 / 13.6
Mean Average St. deviation
Km N/A 1.17E-03 8.10E-05
L 1.003 1.004 0.003
F 1.001 1.003 0.001
P 1.004 1.007 0.003
Pj 1.004 1.007 0.003
T -0.436 -0.027 0.317
U -0.437 -0.028 0.318
Name TY-PW_Sumur
Save
Symbol color and size
B/W
Default
Size 10
P
1.012
1.000
1.10E-03
Km [SI]
1.31E-03
U
1
1.000
1.012
P
-1
Site: Sumur
Lat:
Lon:
Rock:
Stratigraphy:
Lithostratigraphy:
Region:
Instrument: MFK

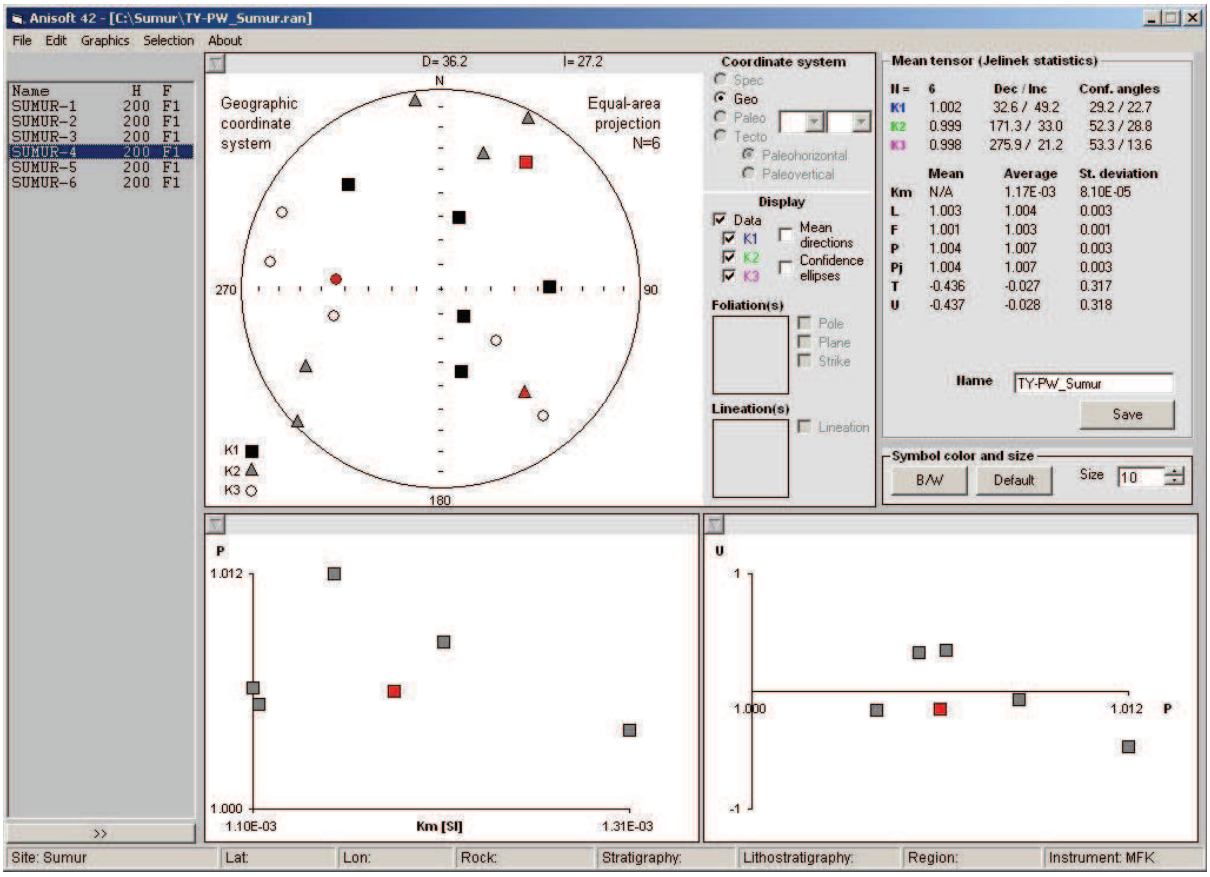
Anisoft 42 - [C:\Sumur\TY-PW_Sumur.ran]
File Edit Graphics Selection About
Name H F
SUMUR-1 200 F1
SUMUR-2 200 F1
SUMUR-3 200 F1
SUMUR-4 200 F1
SUMUR-5 200 F1
SUMUR-6 200 F1
D= 36.2 I= 27.2
Geographic coordinate system
Equal-area projection N=6
N
270
90
180
K1
K2
K3
Coordinate system
Spec
Geo
Paleo
Tecto
Paleohorizontal
Paleovertical
Display
Data
K1
K2
K3
Mean directions
Confidence ellipses
Foliation(s)
Pole
Plane
Strike
Lineation(s)
Lineation
Mean tensor (Jelinek statistics)
II = 6 Dec / Inc Conf. angles
K1 1.002 32.6 / 49.2 29.2 / 22.7
K2 0.999 171.3 / 33.0 52.3 / 28.8
K3 0.998 275.9 / 21.2 53.3 / 13.6
Mean Average St. deviation
Km N/A 1.17E-03 8.10E-05
L 1.003 1.004 0.003
F 1.001 1.003 0.001
P 1.004 1.007 0.003
Pj 1.004 1.007 0.003
T -0.436 -0.027 0.317
U -0.437 -0.028 0.318
Name TY-PW_Sumur
Save
Symbol color and size
B/W
Default
Size 10
P
1.012
1.000
1.10E-03
Km [SI]
1.31E-03
U
1
1.000
1.012
P
-1
Site: Sumur
Lat:
Lon:
Rock:
Stratigraphy:
Lithostratigraphy:
Region:
Instrument: MFK

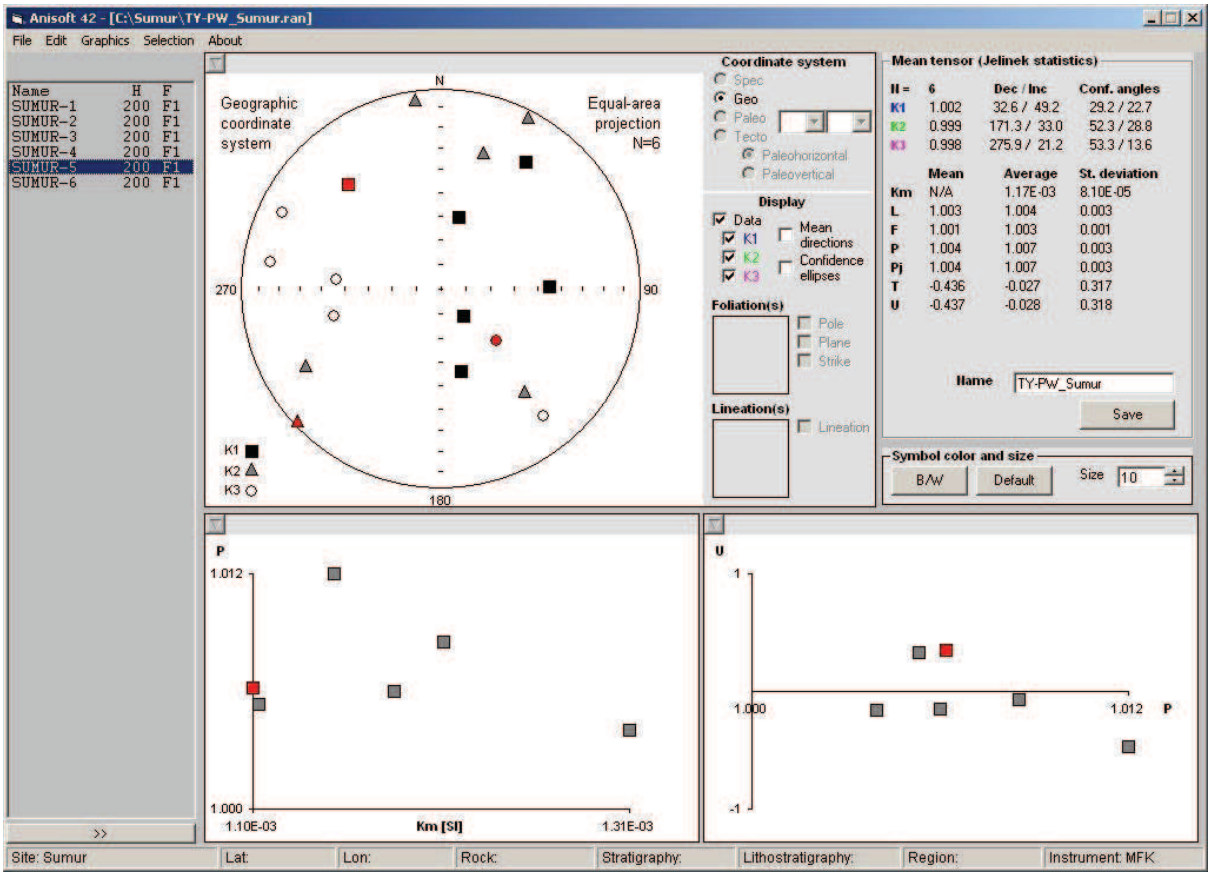
Anisoft 42 - [C:\Sumur\TY-PW_Sumur.ran]
File Edit Graphics Selection About
Name H F
SUMUR-1 200 F1
SUMUR-2 200 F1
SUMUR-3 200 F1
SUMUR-4 200 F1
SUMUR-5 200 F1
SUMUR-6 200 F1
Geographic coordinate system
Equal-area projection N=6
N
270
90
180
K1
K2
K3
Coordinate system
Spec
Geo
Paleo
Tecto
Paleohorizontal
Paleovertical
Display
Data
K1
K2
K3
Mean directions
Confidence ellipses
Foliation(s)
Pole
Plane
Strike
Lineation(s)
Lineation
Mean tensor (Jelinek statistics)
II = 6 Dec / Inc Conf. angles
K1 1.002 32.6 / 49.2 29.2 / 22.7
K2 0.999 171.3 / 33.0 52.3 / 28.8
K3 0.998 275.9 / 21.2 53.3 / 13.6
Mean Average St. deviation
Km N/A 1.17E-03 8.10E-05
L 1.003 1.004 0.003
F 1.001 1.003 0.001
P 1.004 1.007 0.003
Pj 1.004 1.007 0.003
T -0.436 -0.027 0.317
U -0.437 -0.028 0.318
Name TY-PW_Sumur
Save
Symbol color and size
B/W
Default
Size 10
P
1.012
1.000
1.10E-03
Km [SI]
1.31E-03
U
1
1.000
1.012
P
-1
Site: Sumur
Lat:
Lon:
Rock:
Stratigraphy:
Lithostratigraphy:
Region:
Instrument: MFK

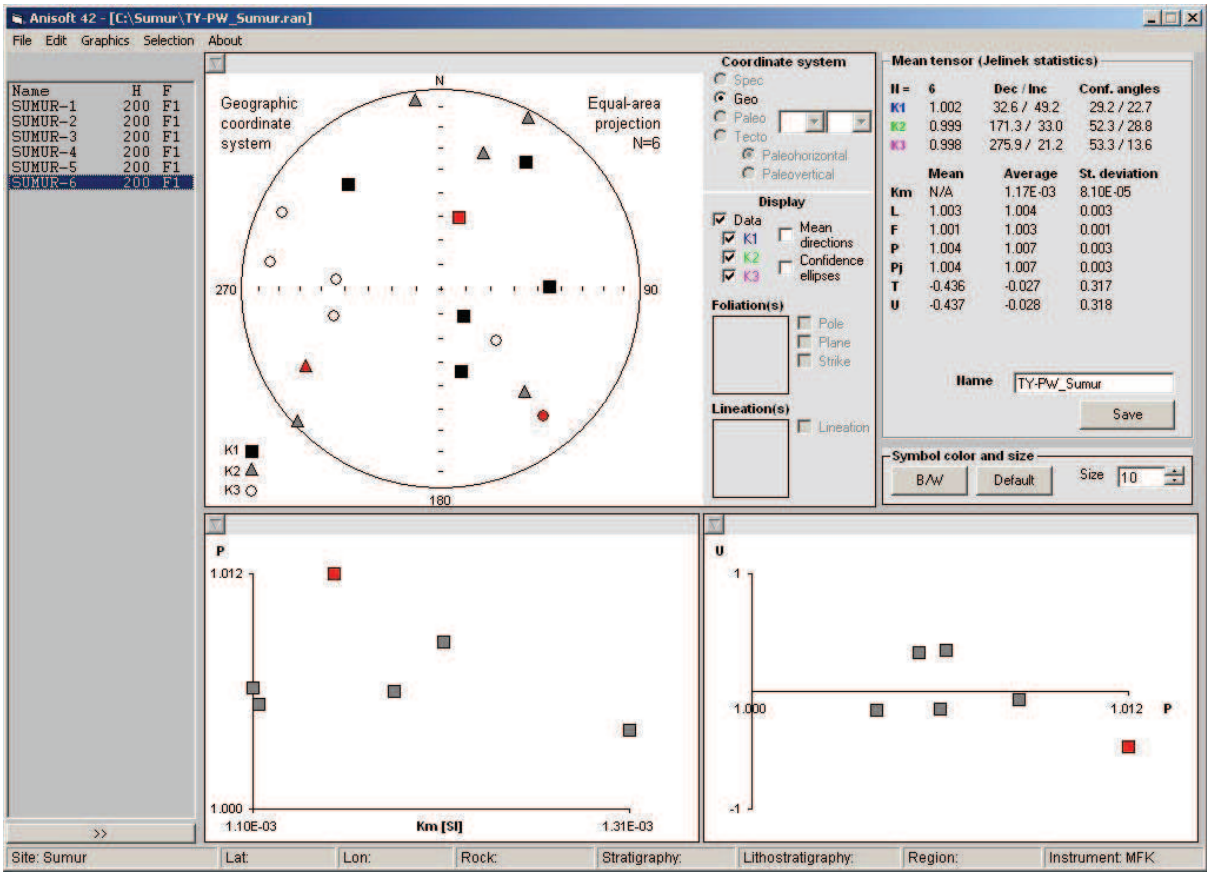
Anisoft 42 - [C:\Sumur\TY-PW_Sumur.ran]
File Edit Graphics Selection About
Name H F
SUMUR-1 200 F1
SUMUR-2 200 F1
SUMUR-3 200 F1
SUMUR-4 200 F1
SUMUR-5 200 F1
SUMUR-6 200 F1
Geographic coordinate system
Equal-area projection
N=6
N
90
180
270
K1
K2
K3
Coordinate system
Spec
Geo
Paleo
Tecto
Paleohorizontal
Paleovertical
Display
Data
K1
K2
K3
Mean directions
Confidence ellipses
Foliation(s)
Pole
Plane
Strike
Lineation(s)
Lineation
Mean tensor (Jelinek statistics)
II = 6 Dec / Inc Conf. angles
K1 1.002 32.6 / 49.2 29.2 / 22.7
K2 0.999 171.3 / 33.0 52.3 / 28.8
K3 0.998 275.9 / 21.2 53.3 / 13.6
Mean Average St. deviation
Km N/A 1.17E-03 8.10E-05
L 1.003 1.004 0.003
F 1.001 1.003 0.001
P 1.004 1.007 0.003
Pj 1.004 1.007 0.003
T -0.436 -0.027 0.317
U -0.437 -0.028 0.318
Name TY-PW_Sumur
Save
Symbol color and size
B/W
Default
Size 10
P
1.012
1.000
1.10E-03
Km [SI]
1.31E-03
U
1
1.000
1.012
P
-1
Site: Sumur
Lat:
Lon:
Rock:
Stratigraphy:
Lithostratigraphy:
Region:
Instrument: MFK

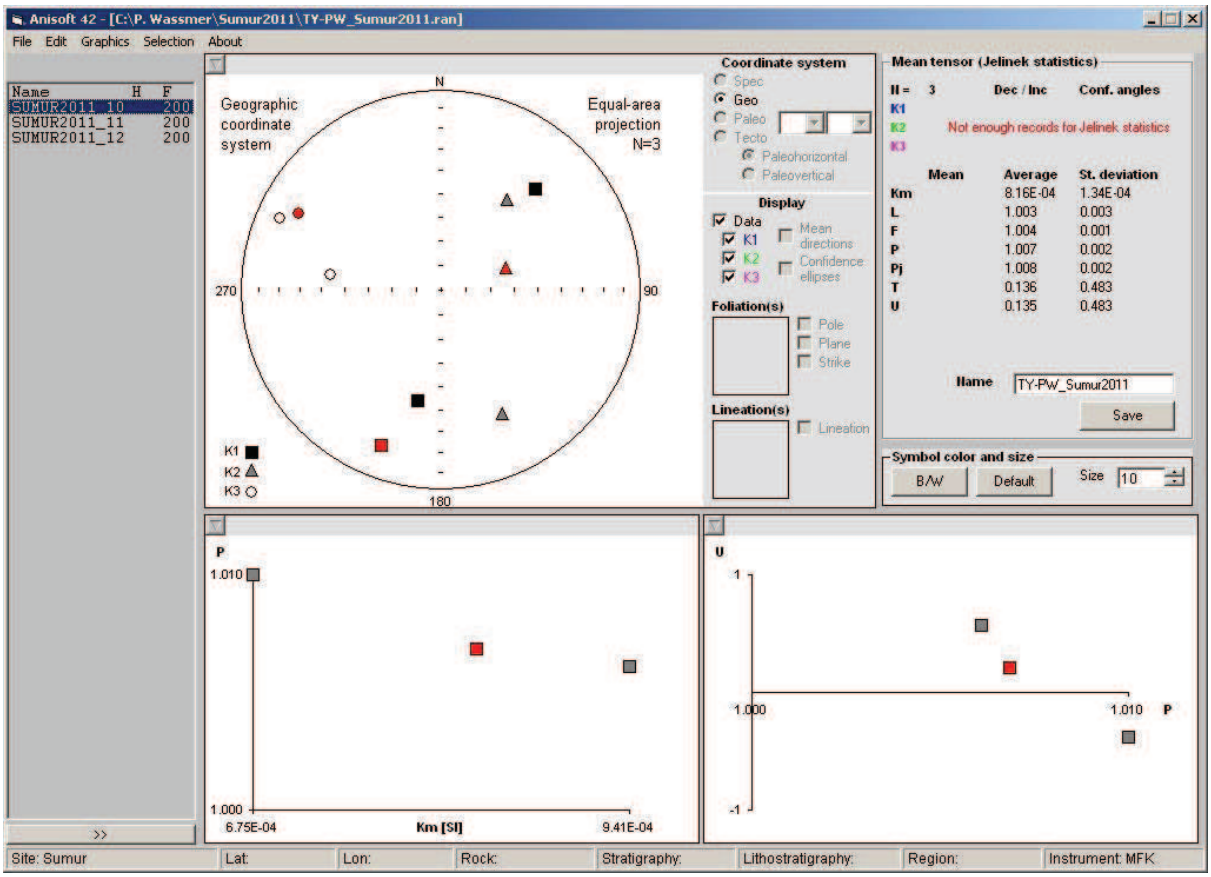
Anisoft 42 - [C:\P. Wassmer\Sumur2011\TY-PW_Sumur2011.ran]
File Edit Graphics Selection About
Name H F
SUMUR2011_10 200
SUMUR2011_11 200
SUMUR2011_12 200
Geographic coordinate system
Equal-area projection
N=3
N
90
180
270
K1
K2
K3
Coordinate system
Spec
Geo
Paleo
Tecto
Paleohorizontal
Paleovertical
Display
Data
K1
K2
K3
Mean directions
Confidence ellipses
Foliation(s)
Pole
Plane
Strike
Lineation(s)
Lineation
Mean tensor (Jelinek statistics)
II = 3 Dec / Inc Conf. angles
K1
K2 Not enough records for Jelinek statistics
K3
Mean Average St. deviation
Km 8.16E-04 1.34E-04
L 1.003 0.003
F 1.004 0.001
P 1.007 0.002
Pj 1.008 0.002
T 0.136 0.483
U 0.135 0.483
Name TY-PW_Sumur2011
Save
Symbol color and size
B/W
Default
Size 10
P
1.010
1.000
6.75E-04
Km [SI]
9.41E-04
U
1
1.000
1.010
P
-1
Site: Sumur
Lat:
Lon:
Rock:
Stratigraphy:
Lithostratigraphy:
Region:
Instrument: MFK

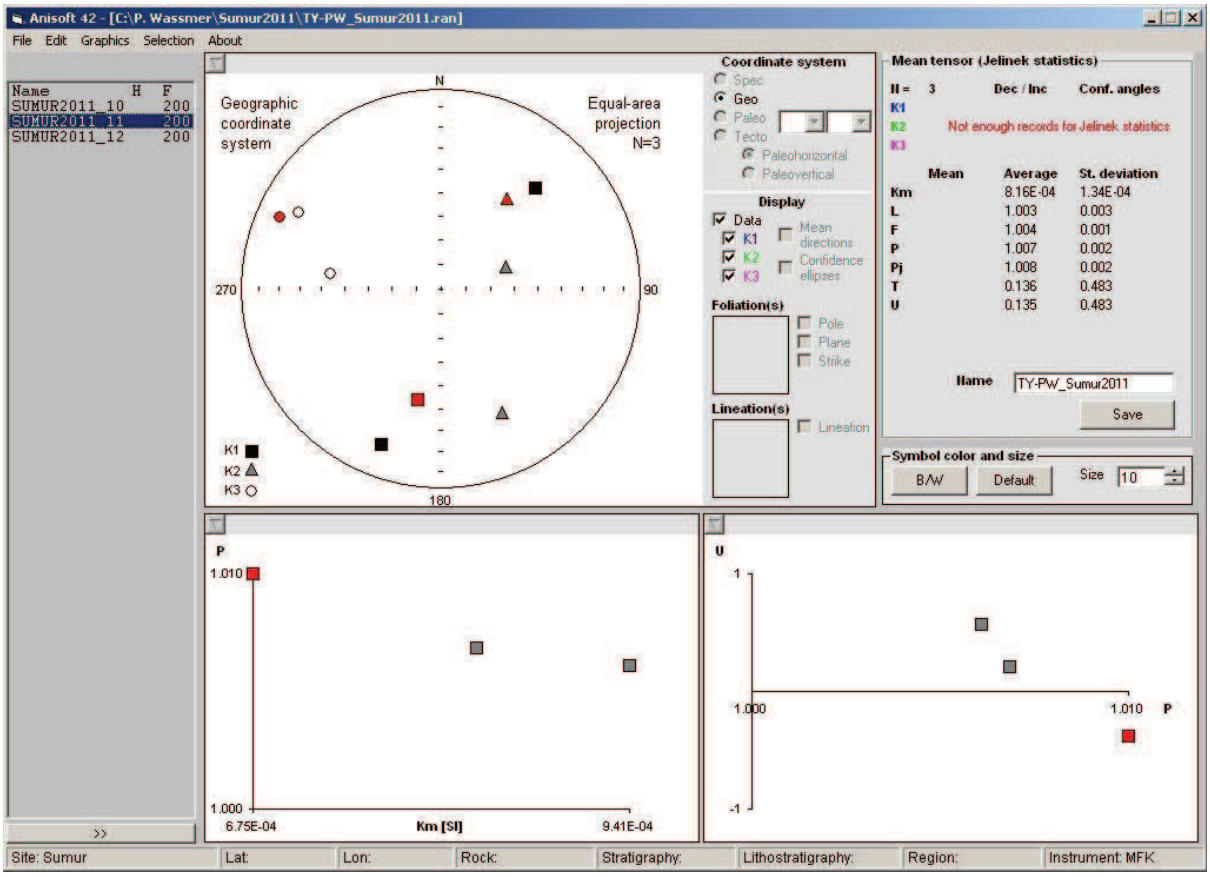
Anisoft 42 - [C:\P. Wassmer\Sumur2011\TY-PW_Sumur2011.ran]
File Edit Graphics Selection About
Name H F
SUMUR2011_10 200
SUMUR2011_11 200
SUMUR2011_12 200
Geographic coordinate system
Equal-area projection N=3
N
270
90
180
K1
K2
K3
Coordinate system
Spec
Geo
Paleo
Tecto
Paleohorizontal
Paleovertical
Display
Data
K1
K2
K3
Mean directions
Confidence ellipses
Foliation(s)
Pole
Plane
Strike
Lineation(s)
Lineation
Mean tensor (Jelinek statistics)
II = 3
Dec / Inc
Conf. angles
K1
K2
K3
Not enough records for Jelinek statistics
Mean
Average
St. deviation
Km 8.16E-04 1.34E-04
L 1.003 0.003
F 1.004 0.001
P 1.007 0.002
Pj 1.008 0.002
T 0.136 0.483
U 0.135 0.483
Name TY-PW_Sumur2011
Save
Symbol color and size
B/W
Default
Size 10
P
1.010
1.000
6.75E-04
Km [SI]
9.41E-04
U
1
1.000
1.010
P
-1
Site: Sumur
Lat:
Lon:
Rock:
Stratigraphy:
Lithostratigraphy:
Region:
Instrument: MFK

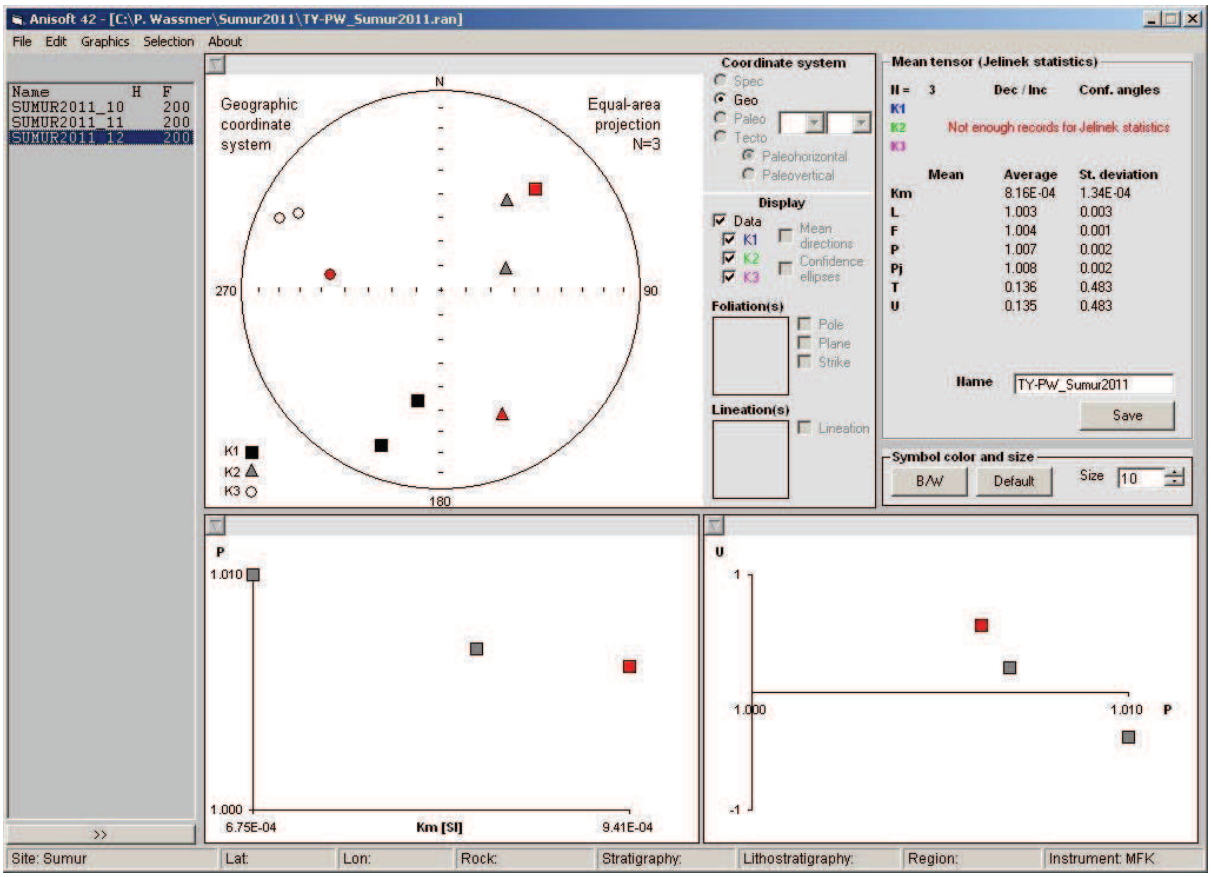
Anisoft 42 - [C:\P. Wassmer\Sumur2011\TY-PW_Sumur2011.ran]
File Edit Graphics Selection About
Name H F
SUMUR2011_10 200
SUMUR2011_11 200
SUMUR2011_12 200
Geographic coordinate system
Equal-area projection N=3
N
270
90
180
K1
K2
K3
Coordinate system
Spec
Geo
Paleo
Tecto
Paleohorizontal
Paleovertical
Display
Data
K1
K2
K3
Mean directions
Confidence ellipses
Foliation(s)
Pole
Plane
Strike
Lineation(s)
Lineation
Mean tensor (Jelinek statistics)
II = 3
Dec / Inc
Conf. angles
K1
K2
K3
Not enough records for Jelinek statistics
Mean
Average
St. deviation
Km 8.16E-04 1.34E-04
L 1.003 0.003
F 1.004 0.001
P 1.007 0.002
Pj 1.008 0.002
T 0.136 0.483
U 0.135 0.483
Name TY-PW_Sumur2011
Save
Symbol color and size
B/W
Default
Size 10
P
1.010
1.000
6.75E-04
Km [SI]
9.41E-04
U
1
1.000
1.010
P
-1
Site: Sumur
Lat:
Lon:
Rock:
Stratigraphy:
Lithostratigraphy:
Region:
Instrument: MFK

Bull Volcanol (2014) 76:814
DOI 10.1007/s00445-014-0814-x

RESEARCH ARTICLE

Coupling eruption and tsunami records: the Krakatau 1883 case study, Indonesia

Raphaël Paris · Patrick Wassmer · Franck Lavigne · Alexander Belousov · Marina Belousova · Yan Iskandarsyah · Mhammed Benbakkar · Budianto Ontowirjo · Nelly Mazzoni

Received: 14 October 2013 / Accepted: 18 February 2014

Abstract The well-documented 1883 eruption of Krakatau volcano (Indonesia) offers an opportunity to couple the eruption's history with the tsunami record. The aim of this paper is not to re-analyse the scenario for the 1883 eruption but to demonstrate that the study of tsunami deposits provides information for reconstructing past eruptions. Indeed, though the characteristics of volcanogenic tsunami deposits are similar to those of other tsunami deposits, they may include juvenile material (e.g. fresh pumice) or be interbedded with distal pyroclastic deposits (ash fall, surges), due to their simultaneity with the eruption. Five kinds of sedimentary and volcanic facies related to the 1883 events were identified along the coasts of Java and Sumatra: (1) bioclastic tsunami sands and (2) pumiceous tsunami sands, deposited respectively before and during the Plinian phase (26–27 August); (3) rounded pumice lapilli reworked by tsunami; (4) pumiceous ash fall deposits and (5) pyroclastic surge deposits (only in Sumatra). The stratigraphic record on the coasts of Java and Sumatra, which agrees particularly well with observations of the 1883 events, is tentatively linked to the proximal stratigraphy of the eruption.

Editorial responsibility: S. Self

Electronic supplementary material The online version of this article (doi:10.1007/s00445-014-0814-x) contains supplementary material, which is available to authorized users.

R. Paris · M. Benbakkar
Clermont Université, Université Blaise Pascal, BP 10448, 63000 Clermont-Ferrand, France

R. Paris (✉) · M. Benbakkar
Magmas et Volcans, CNRS, UMR 6524, 63038 Clermont-Ferrand, France
e-mail: R.Paris@opgc.univ-bpclermont.fr

P. Wassmer · F. Lavigne
UMR 8591, Laboratoire de Géographie Physique, CNRS, 92195 Meudon, France

P. Wassmer
Faculté de Géographie et d'Aménagement, Université de Strasbourg, Strasbourg, France

F. Lavigne
Université Paris 1 Panthéon-Sorbonne, PRES HESAM, Meudon, France

A. Belousov · M. Belousova
Institute of Volcanology and Seismology, Petropavlosk-Kamchatsky, Russia

Y. Iskandarsyah
Laboratorium Geologi Lingkungan dan Hidrogeologi, Fakultas Teknik Geologi, Universitas Padjadjaran (UNPAD), Bandung, Indonesia

Y. Iskandarsyah
Laboratoire Image, Ville, Environnement (LIVE), UMR 7362 CNRS, Université de Strasbourg, Strasbourg, France

N. Mazzoni
Clermont Université, GEOLAB, Université Blaise Pascal, BP 10448, 63000 Clermont-Ferrand, France

N. Mazzoni
GEOLAB, UMR 6042, CNRS, 63057 Clermont-Ferrand, France

B. Ontowirjo
BPDP BPPT, Jakarta 10340, Indonesia

Published online: 08 March 2014

Keywords Volcanic tsunami · Tsunami deposits · 1883 Krakatau eruption · Pyroclastic fall · Pyroclastic surge · Indonesia

Introduction

Past volcanic eruptions can be reconstructed by analysing historical documents and characterising primary volcanic products in terms of thickness, componentry, texture, fragmentation, temperature of emplacement, crystal chronometry, etc. When tsunami waves are generated during a volcanic eruption, some primary volcanic deposits should be stratigraphically associated with tsunami deposits, thus adding more constraints for ordering the succession of the events and for geological interpretations. The generation of so-called volcanic tsunami by eruptive, intrusive and gravitational processes is more than anecdotal, and tsunami are implied in producing several of the worst volcanic disasters (Latter 1981; Dzurisin 2000), including those of the Late Bronze Age eruption of Santorini Island in the Aegean Sea, the 1792 flank collapse of Mayuyama dome near Unzen volcano in Japan and the 1883 eruption of Krakatau volcano in Indonesia. Volcanic tsunamis are characterised by short-period waves and greater dispersion compared to earthquake-generated tsunamis, but they clearly expand the potential damage area of many volcanoes (Paris et al. 2013). The aim of this contribution is to document the sedimentary record of the 1883 Krakatau tsunamis on Java and Sumatra coasts (Fig. 1), and to demonstrate that tsunami deposits have the potential to allow complete reconstruction of past eruptions and their tsunamigenic processes.

The 1883 eruption and tsunamis that devastated the coasts of the Sunda Strait are particularly well documented, thanks to hundreds of observations and eyewitness accounts that were collected during and after the disaster (Verbeek 1886; Symons 1888; Simkin and Fiske 1983). The eruptive processes and the source and time propagation of the tsunamis have been widely debated on the basis of observations, analysis of near-field (<20 km from Krakatau volcano) pyroclastic deposits, tide and pressure gauge records and numerical modelling (Verbeek 1886; Stehn 1929; Williams 1941; Ewing and Press 1955; Latter 1981; Self and Rampino 1981; Yokoyama 1981, 1987; Camus and Vincent 1983; Francis 1985; Self 1992; Nomanbhoy and Satake 1995; Carey et al. 1996; Mandeville et al. 1996a, b; Choi et al. 2003; Pelinovsky et al. 2005; Maeno and Imamura 2011). This paper does not attempt to re-analyse the 1883 eruption and question the source of the tsunamis. It is now commonly accepted that (1) tsunamis occurred throughout the paroxysmal August 26–27 eruption; (2) several processes could have produced tsunamis (emplacement of pyroclastic flow entering seawater, caldera collapse, shock wave produced by large explosion); (3) most of the pyroclastic flows were discharged into the sea with water depths up to 40 m, thus (4) generating tsunamis of increasing magnitude from the afternoon 26 August to the morning 27 August and (5) pyroclastic surges travelled over water and impacted the southern coast of Sumatra.

The temporal order of the different processes is recorded in the strata of the proximal pyroclastic deposits (Stehn 1929; Williams 1941; Self and Rampino 1981; Mandeville et al. 1996b). Moderate explosive activity from May 20 to early August is represented by ash fall deposits overlying the 1883 soil horizon. Onset of the Plinian August 26–27 phase is evidenced by coarse pumice fall deposits interbedded with surge and small pyroclastic flow deposits. In the early morning of 27 August, activity shifted from a convecting to a collapsing column, thus producing massive accumulations of pyroclastic flow deposits. Co-ignimbrite lag breccias in the upper part of the 1883 stratigraphic record might reflect the onset of caldera collapse. Investigations by Carey et al. (1996) and Mandeville et al. (1996b) on the islands north of Krakatau (Sebesi, Sebuku, Lagoendi) and offshore (GCUDA cores) illustrate the segregation of pyroclastic flows into a subaqueous high-concentration component and a dilute component travelling over water up to 80 km from the volcano. The culminating 10:00 AM explosion was followed by mud rain that lasted more than 7 h (Verbeek 1886). Mud rain was interpreted by Self and Rampino (1981) as a consequence of phreatomagmatic explosions when pyroclastic flows were discharged into the sea, but Carey et al. (1996) argued for a large co-ignimbrite ash plume.

Less attention was paid to the deposits left inland by the tsunami waves. Coral boulders interpreted as 1883 remnants were mentioned on the coasts of Java and Sumatra (Fig. 1), from Ujung Kulon Peninsula (Umbgrove 1947; Verstappen 1956) to Anyer (Verbeek 1886; Setjadmadja 2007) and Gubug Garam (Setjadmadja 2007). Photographs from the archives of the Royal Institute for the Tropics, Amsterdam, illustrate devastated landscapes covered by debris (coral boulders, pumices, fragments of buildings, trees, etc.). Remnants of a lighthouse (so-called 4th Point Java) were found up to 4 km inland along the Cikoneng River (near Anyer, Java). The largest coral boulder reported in Anyer by Verbeek (1886) had an approximate weight of 200 t, which is in the range of the largest coral boulders moved by tsunamis (e.g. Terry et al. 2013). Ongkosongo (1983) and Bronto (1990) briefly

Fig. 1 Maps showing distribution of 1883 Krakatau tsunami, pyroclastic surge and ash fall deposits in Sunda Strait region (Indonesia), after previous works on tsunami deposits by Williams (1941), Ongkosongo (1983), Bronto (1990), Carey et al. (2001) and Van der Berg et al. (2003). Distribution of coral boulders after Umbgrove (1947), Verstappen (1956) and Setjadmadja (2007). Typical tsunami wave propagation time in Sunda Strait (in minutes) was estimated by Yokoyama (1981), Giachetti et al. (2012) and Maeno and Imamura (2011)

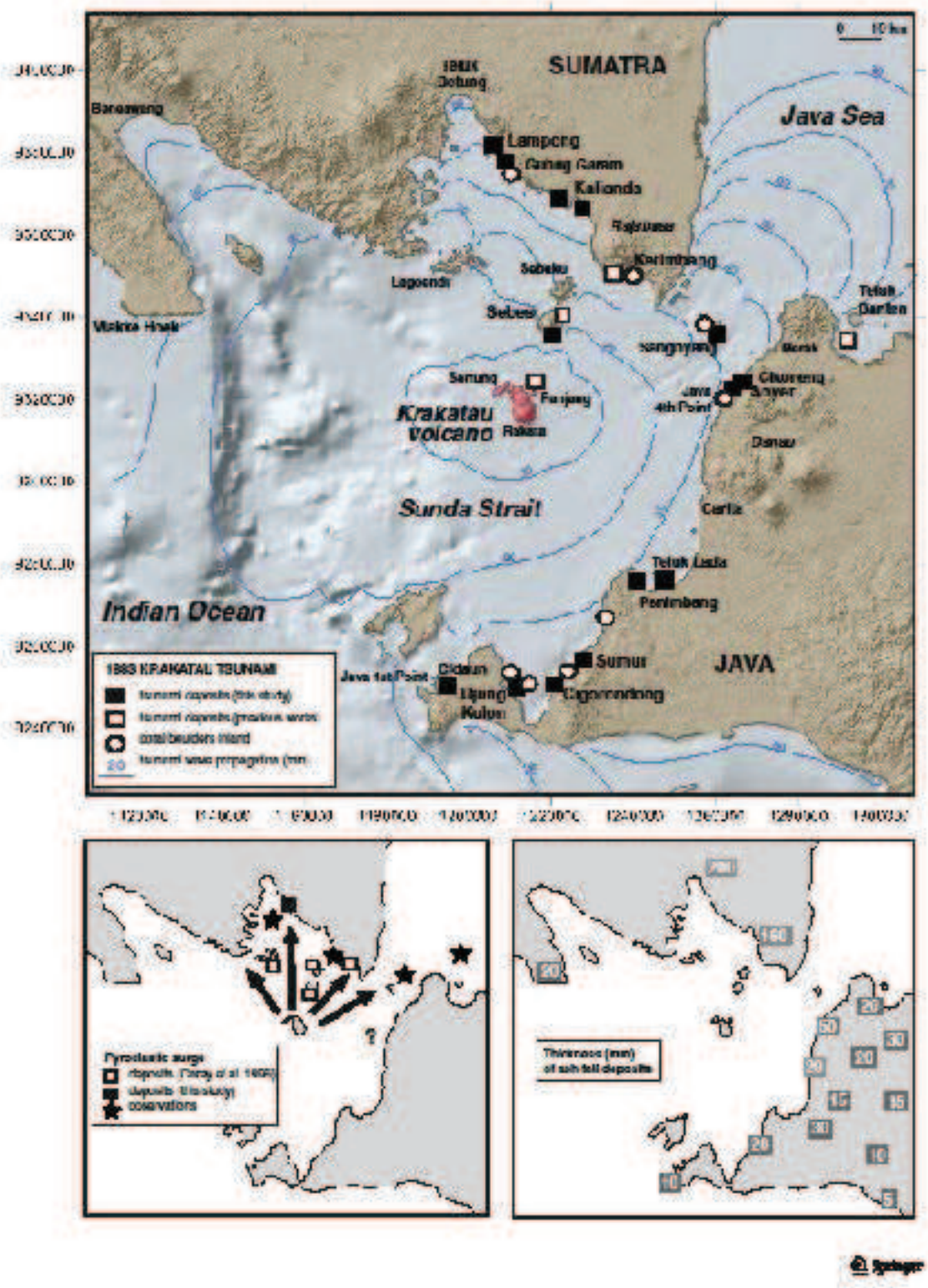
SUMATRA
Java Sea
Indian Ocean
Sunda Strait
Krakatau volcano
Anak Krakatau
Rakata
Sertung
Panjang
Lampung
Kalianda
Labuhan
Sebesi
Merak
Tanjung Lesung
Carita
Telukbetung
Penimbang
Sumur
JAVA
Cilacap
Ujung Kulon
1883 KRAKATAU TSUNAMI
coral boulders inland
Pyroclastic surge
observations
Thickness (mm) of ash fall deposits

described the 1883 tsunami deposits in Java and Sumatra as unsorted and structureless gravel overlying pyroclastic deposits, but few details are given on the composition and emplacement of the deposits. Carey et al. (1996, 2001) studied the 1884 pyroclastic flow deposits on the islands south of Krakatau (Sebesi, Sebuku). Units of rounded pumice lapilli intercalated between the pyroclastic flow deposits are interpreted as floating pumice rafts reworked and left inland by tsunami. They also mentioned poorly sorted, silty to sandy deposits with corals and pumice on Sebesi Island and Sumatra (Fig. 1). Williams (1941) mentioned "a compact unit consisting of lithic blocks, sediments, coral and shells" on Rakata, Panjang (Lang) and Sertung (Verlaten) islands, but he did not suggest a possible tsunami origin. This unit does not appear on the stratigraphic columns described by other authors (e.g. Stehn 1929; Mandeville et al. 1996a, b). The 1883 Krakatau main tsunami (originated at 10:00 AM of 27 August) is apparently recorded in submarine cores off Teluk Banten (Java Sea), as evidenced by Van den Berg et al. (2003) who identified a poorly sorted, sandy layer with abundant bioclasts, pumices and the typical 1883 crystal assemblage (plagioclase, green augite, brown hypersthene and magnetite). Land-derived components were laterally transported into the shallow bay by the tsunami backwash (outflow).

Methods

Observations of the 1883 events compiled in the reports of Verbeek (1886) and Symons (1888), and in the more recent review of Simkin and Fiske (1983) were entered into a georeferenced database with links to the original text and integrated into a GIS (Geographic Information System). Data can be sorted by thematic, geographical or chronological requests (e.g. all tephra fall information in Java from 4:00 to 9:00 PM of 26 August 1883). Thematic files were prepared to be viewed with Google Earth (e.g. .kml files of tsunami observations, tephra falls, explosions etc.). The scenario of the events at a precise location can thus be compared with the stratigraphic record. The main types of observation were distinguished: earthquakes, eruptive activity at the vents (e.g. explosions, pyroclastic flows), airwaves (generated by the major explosion), pyroclastic falls, mud rain, darkness, optical effects, thunder/lightning, smell of gas, floating pumice, tsunami, destruction of objects and fatalities. ArcGIS shapefiles and Google Earth .kml files will be soon available at http://www.obs.univ-lyon1.fr/labo/fr/anne/pponsard/index.php.

Four surveys were carried out along the coasts of the Sunda Strait in January 2009, August 2010, August 2011 and October 2011, from Bandar Lampung (present name of Teluk Betung, Sumatra) to Ujung Kulon National Park (Java), including Sanghyang, Sebesi and Sertung islands (Fig. 1). More than 50 trenches were dug or refreshed, and hundreds of samples collected. Well-preserved sedimentary sequences deposited by the 1883 events were found at only 15 sites. Indeed, the 1883 tsunami and primary volcanic deposits are not preserved everywhere, and are often reworked through bioturbation, slope processes, fish farming, tourist resorts, agriculture and industries (e.g. Merak, Labuhan, Bandar Lampung). All samples were analysed using a binocular microscope for estimating the proportions of marine bioclasts and 1883 volcanic juveniles (pumice, glass shards and fresh crystals). We also sampled pyroclastic deposits of the 1883 eruption in Panjang and Rakata islands (Fig. 1).

Tsunami deposits are usually characterised using a multidisciplinary approach, including sedimentological, micropalaeontological, geochronological and geochemical methods (e.g. Dawson and Stewart 2007; Bourgeois 2009; Goff et al. 2012; Kortekaas et al. 2011). Cuven et al. (2013) used a combination of sedimentological (grain size, sorting, anisotropy of magnetic susceptibility), micromorphological (X-ray tomography and radiography, thin sections) and geochemical analysis (X-ray microfluorescence, ICP-AES, loss on ignition) to provide a comprehensive reconstruction of the different phases of the 1755 tsunami deposition and flow dynamics in Andalusia (Spain). The same suite of methods cannot be applied entirely to the 1883 Krakatau tsunami deposits. Grain size distributions were obtained for some selected units (e.g. sandy deposits in West Java, pumice lapilli in Sumatra), but most of the sediments sampled had a wide range of clast size (from silts to cobbles) and clast shape (e.g. coral gravels) and were not processed for granulometry. Because of the mixture of clasts, we made the choice not to undertake X-ray tomography (cores in carbon tubes) or macroscopic observations (half cores) such as:

We were able to collect samples for anisotropy of magnetic susceptibility (AMS) at only four sites, because for AMS the sediments must be fine (clay, silt and fine sand fractions) and have good cohesion. Samples were collected along vertical sections into 2-cm sided boxes, as described in Wassmer et al. (2010), who demonstrated that AMS can be used on unconsolidated tsunami deposits to gain information about sediment fabrics and depositional processes. Each sample was analysed in 15 directions using a Kappabridge KLY-2 in order to determine the magnitude and direction of the maximum, intermediate, and minimum AMS axes. The anisotropy of each sample (i.e. each cube box) can be visualised by a triaxial ellipsoid (the maximum, intermediate and minimum axes corresponding to principal eigenvectors). The projection of AMS linear axes on a diagram of the lower hemisphere equal-areas gives information on the influence of paleocurrents on the preferential orientation of the long axis of particles (grains). The calculation of AMS parameters such as magnetic lineation (L), foliation (F), alignment parameter (Ta) and shape parameter (T) allow relationships between

magnetic fabrics and depositional processes to be evaluated. The alignment parameter represents the development of a linear fabric and thus increases with bottom current strength. The shape parameter describes the geometry of the AMS ellipsoid, which is oblate for $T>0$ (settling mode) or prolate for $T<0$ (traction mode). It has been demonstrated that the mean orientation of the grains long axes (and thus the maximum tensor axis K_{max}) is parallel to flow direction for moderate currents and settling from suspension (e.g., Wassmer et al. 2010). For stronger currents with dominant traction (bed load), the long axes of prolate particles (and the K_{max}) tends to be orientated perpendicular to flow direction.

Seventeen bulk samples of tsunami deposits, 13 samples of 1883 pyroclastic deposits (selected pumices) and four samples of older regional ignimbrites were analysed by ICP-AES (Jobin-Yvon ULTIMA C) for concentrations of major elements. This method allows (1) comparison with XRF analyses of 1883 whole-rock samples published by Self (1992) and Mandeville et al. (1996a, b), (2) and distinguishing between the 1883 Krakatau pumice and other regional sources of pumice that crop out along the coasts of Java and Sumatra (e.g. Danau caldera, Rajabasa volcano). Water, organic and carbonate content were estimated by loss on ignition (LOI) for 12 h at 105 °C, 4 h at 550 °C and 2 h at 950 °C, respectively.

Results

Stratigraphy and composition of the deposits

Stratigraphic sections are described by geographical sectors, from the westernmost point of Java (Ujung Kulon) to Lampung Bay (Sumatra). In all the sections described, pumices, glass shards, dark alteration and fresh crystals were identified. Three kinds of pumices can be distinguished: (1) highly vesicular white pumice emitted during the climactic stage (27 August 1883), representing 85 % of the erupted products (Mandeville et al. 1996a); (2) highly vesicular light pink to dark grey pumice and (3) banded pumice. The most abundant crystals are tabular plagioclase and orthopyroxene (rhombic brown hypersthene, up to 4 mm in length and bronzite), but there are also monoclinic clinopyroxene and oxides (titanomagnetite, ilmenite), as in the 1883 primary pyroclastic deposits (Verbeek 1886; Williams 1941; Camus et al. 1987; Mandeville et al. 1996a). These criteria helped us identify 1883 primary or reworked volcanic deposits in the stratigraphy.

Ujung Kulon

Trenches 250 m from the north eastern shoreline of the Ujung Kulon National Park (West Java, Fig. 1) display the following stratigraphy, from base to top (Fig. 2a). At a depth of 50 cm, coral cobbles and gravels are mixed with medium-grained sands and marine bioclasts (4 wt% carbonates estimated by LOI at 950 °C). Sand grains are subrounded to subangular and their dominant shiny surfaces indicate that the main sediment source was a beach (Cailleux and Tricart 1959). We were not able to dig deeper and reach the 1883 surface. From 45 to 32 cm depth, this medium-grained sand is considerably enriched in dark heavy minerals. A 3-cm thick unit of lenticular coarse sand with fresh crystals, shells and coral fragments was found at a depth of 40 cm (12 wt% LOI at 950 °C). Above (32 cm) is a 10-cm thick unit of poorly sorted coarse sands, rich in bioclasts (mostly shell and coral fragments, 9 wt% LOI at 950 °C), in a clayey matrix including very fine pumices in low abundance. At 20-cm depth, a discontinuous layer of light grey ash with rounded pumice lapilli and fresh crystals. It is overlain by a unit of coarse sand with abundant fine pumice (48 % of the grains), fresh crystals (30 %) and bioclasts (22 %, using the binocular microscope; 13 wt% LOI at 950 °C). Coral boulders up to 80 cm wide rise from the top of this sequence, covered by the post-1883 soil.

Other sites were investigated further north (Citadau, Fig. 2b). The stratigraphy of the 3.5-m thick sequence can be simplified as a succession of (1) volcanic pumiceous ash and lapilli and (2) sand units with coral gravels, showing enrichment in volcanic material upward. Sand units between 315 and 745 cm deep are very poorly sorted, enriched in coral and shell fragments and have rip-up clasts of clay at the base (Fig. 2b). These first sands are overlain by a grey ash (245–210 cm) with numerous dark minerals and charcoal fragments. The second sand unit is composed of a lower layer (210–180 cm) of fine sands with marine bioclasts and pumiceous ash and an upper layer (180–156 cm) of fine sand mixed with brown silt. From 156 to 125 cm, there is a light grey ash, with pumice lapilli and other fragments of volcanic rock (rhyolite). The third sand unit (125–45 cm) is yellowish, poorly sorted, mixed with pumiceous ash and lapilli, and marine bioclasts. Three layers can be distinguished, with an increasing abundance of pumice and decreasing abundance of bioclasts upward.

Sumur

A 380-m-long transect of 10 trenches was established near the village of Sumur (Fig. 1), from the coast to vegetated dunes near the road. The orientation of the transect (NNW-SSE) corresponds to the inferred flow direction of a tsunami coming from Krakatau volcano. Deposits of the 1883 events are here intercalated between the coral calcirudite and dune sands. The stratigraphy can be summarised as follows (Fig. 3): (1) bioclastic very coarse sand to gravel, without any evidence of fresh volcanic material; (2) coarse sand with marine bioclasts (40–50 %) and fine pumice (40 %) in a clayey ashy matrix (corresponding to weathered volcanic ash); (3) discontinuous yellowish fine sand with abundant pumice but less bioclasts

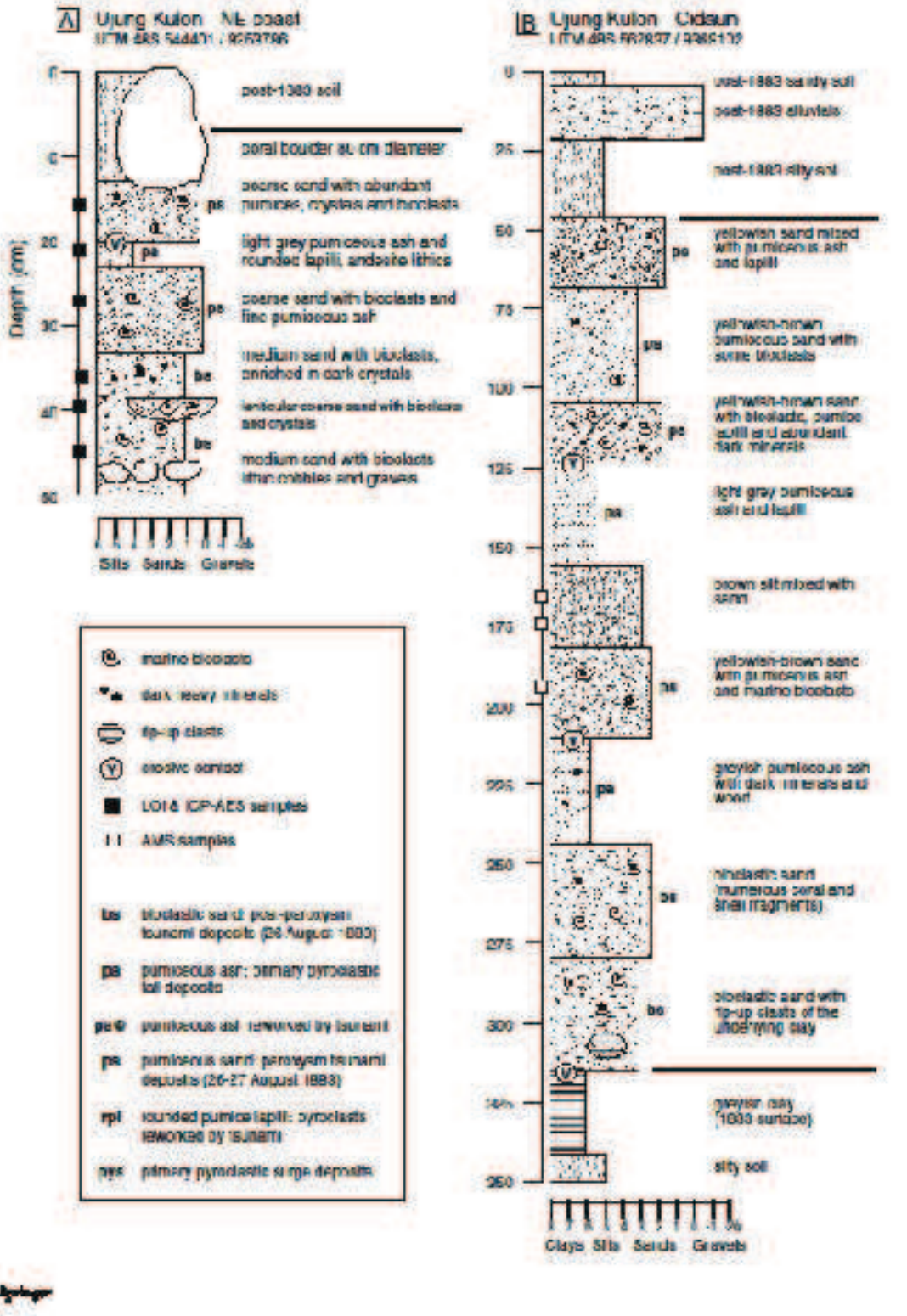
A Ujung Kulon NE coast
B Ujung Kulon Cidaun
Depth (cm)
post-1883 soil
coral boulder 40 cm diameter
coarse sand with abundant pumices, crystals and bioclasts
light grey pumiceous ash and rounded lapilli, andesite lithics
coarse sand with bioclasts and fine pumiceous ash
medium sand with bioclasts, enriched in dark crystals
lenticular coarse sand with bioclasts and crystals
medium sand with bioclasts, shin pebbles and gravels
Silts Sands Gravels
marine bioclasts
dark heavy minerals
rip-up clasts
erosive contact
LOI & ICP-AES samples
AMS samples
bioclastic sand (pre-peryaam tsunami deposits (26 August 1883)
pumiceous ash: primary pyroclastic fall deposits
pumiceous ash reworked by tsunami
pumiceous sand: peryaam tsunami deposits (26-27 August 1883)
rounded pumice lapilli: pyroclasts reworked by tsunami
primary pyroclastic surge deposits
post-1883 silty soil
yellowish sand mixed with pumiceous ash and lapilli
yellowish-brown pumiceous sand with some bioclasts
yellowish-brown sand with bioclasts, pumice lapilli and abundant dark minerals
light gray pumiceous ash and lapilli
brown silt mixed with sand
yellowish-brown sand with pumiceous ash and marine bioclasts
grayish pumiceous ash with dark minerals and wood
bioclastic sand (numerous coral and shell fragments)
bioclastic sand with rip-up clasts of the underlying clay
gray clay (1883 surface)
silty soil
Clays Silts Sands Gravels

◀ Fig. 2 Stratigraphic logs of Ujung Kulon peninsula (SW Java). The 1883 sequence is delimited by *thick lines* when lower and upper contacts are observable (see text for details)

(<20 %) and wood; and (4) thick unit (20–30 cm) of coarse sand to gravel with abundant pumice (including rounded lapilli), glass shards, obsidian and coarse bioclasts (<25 %). Juvenile volcanic material (i.e. from the 1883 eruption) represents up to 80 % of this fourth unit. A rounded cobble of irregularly vesicular pumice was found in unit 4 at 380 m from the shoreline (Fig. 4). Units 1, 2 and 4 are particularly rich in marine macrofauna, especially gastropods (e.g. *Cancellaria*, *Conidae*, *Columbella*, *Architectonica*, *Natica*, *Tridacna*). All units identified are poorly sorted, with inverse grading observed in units 1 (30–70 cm) and 4 (45–75 cm).

Ciperumbang

On the road from Sumur to Ciperumbang (UTM 48S, 339370/9253857), trenches revealed the presence of a 70-cm thick tephra unit between a depth of 80 and 100 cm. It is a white pumiceous ash with angular lapilli and fresh crystals (mostly plagioclase). No vertical grading was detected. Below the tephra, we found a thick unit of yellowish coarse sand with coarse bioclasts, shrapnel and very fine pumices. Above Sumur, the substratum is a coral calcirudite. The tephra unit is overlain by coarse sand with pumiceous ash, light grey rounded pumice lapilli and wood fragments. Surprisingly, we could not find marine bioclasts in this upper unit. As in Ujung Kulon, coral boulders (up to 2 m) are set in the uppermost part of the sequence.

Pantai Anyang

A sequence of pumiceous sands is preserved near the shore 15 km WSW of Tanjung Lesung (Fig. 1). Fossilising the 1883 soil (Fig. 4). The lower part of the sequence is a thick (~20 cm), massive sand unit with a bimodal grain size distribution (sample 1 in Fig. 4; 50 % medium-sized beach sand mixed with 40 % very fine pumices). The upper part is

Fig. 3 Stratigraphic log of Sumur section (SW Java). Photograph: pumice bomb found in the upper pumiceous sand unit. See Fig. 2 for legend

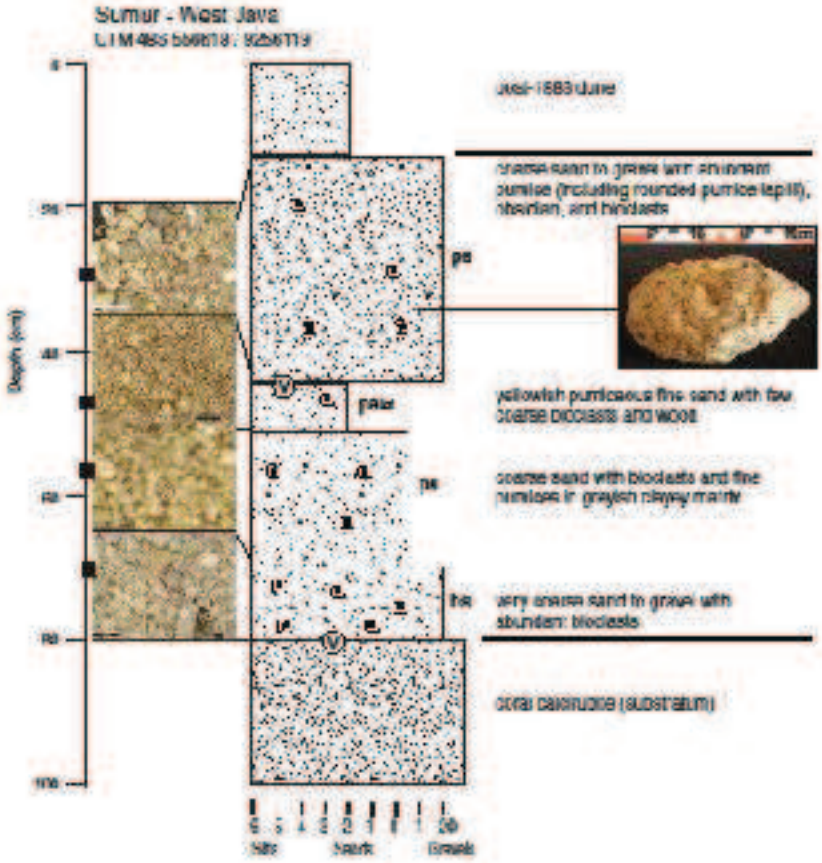

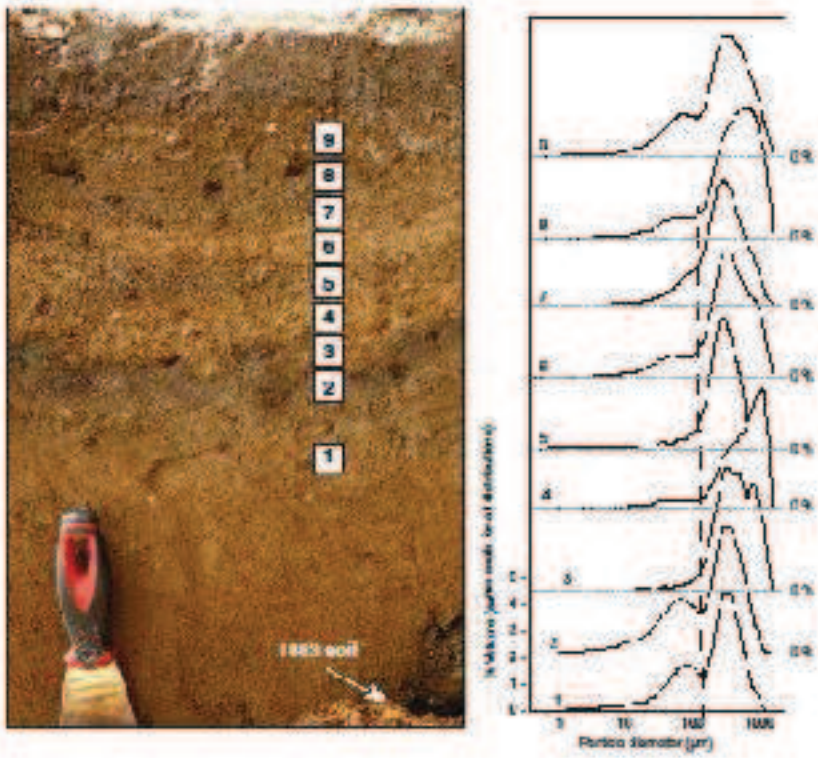

Fig. 4 Sampling and grain size distribution (GSD) of 1883 tsunami deposits near Pari island (West Java, UTM 488, 9279486/9279487). Two populations can be distinguished in the GSD (separated by *dashed line*): fine volcanic ash in the coarse silt to very fine sand fraction, and medium to coarse sand from the beach, with coarse bioclastic shells >1 mm. Grain size analysis was carried out using a laser diffraction particle analyser (Coulter LS 100)

a lens-shaped accumulation of coarse sand with bioclasts and small rounded pumice lapilli (e.g. samples 4 and 5), more or less enriched in very fine ash which forms clayey aggregates (e.g. sample 2). The contact between the lower and upper part of the sequence is associated with a very fine deposition of ash and charcoal, eroded by the upper laminated sands. Grain size distributions and observations with the binocular microscope allow two populations to be distinguished: (1) fine volcanic ash in the coarse silt to very fine sand fractions and (2) medium to coarse sand from the beach with coarse bioclasts (shells >1 mm).

A marine gravel was found at 1.8 m above sea level (s.s.l.) on a rocky platform 8 km west of Anyer/Carita (UTM: 488, 581630/9279586). The platform is made of siltstone (greyish volcanic ash) eroded by the overlying gravel. Rip-up clasts of siltstone are numerous at the base of the gravel, which contains many kinds of coral and shells. The thickness and clast size of the gravel decrease landward from 1 m thick at the rocky point to less than 10 cm inland (3.5 m s.s.l.) where the gravel turns to coarse bioclastic sand. It is, however, difficult to conclusively prove the presence of 1883 volcanic products in these deposits because older greyish ash from the underlying platform is abundant.

Anyer

The 1883 tsunami deposits around Anyer's lighthouse were briefly described by Ongkosongo (1983) and Bronto (1990). The typical sequence displays a basal unit of coarse sand with pumices (70–80 %), fresh crystals (10–15 %), coarse bioclasts (10–15 %) and lithics (5–10 %), lying directly on the substratum (calcarenite and coral platform). This coarse sand unit is yellowish at the base and brownish at the top. A horizon of angular blocks occurs in the middle part (Fig. 5a). The second unit is a light-grey coarse sand enriched in very fine white ash, rounded pumice lapilli and wood. It is ~10 cm thick (at a depth of 30–40 cm) and its upper part was eroded before deposition of the overlying gravel, with evidence of sand incorporation into the gravel. The top gravel unit also contains abundant juvenile grains (pumice, 70–80 %, glass shards, 5 %, fresh crystals, 10–15 %; obsidian, <3 %) together with lithic clasts (10 %) including bricks from the lighthouse, minor bioclasts (<5 %) and charcoal (<2 %). Several types of pumice are present in this third unit (white to light grey homogeneous highly vesicular pumice, light brown to yellowish pumice, banded pumices).

Sections including deposits of the 1883 events are also preserved along the Cikoneng River and its tributaries up to

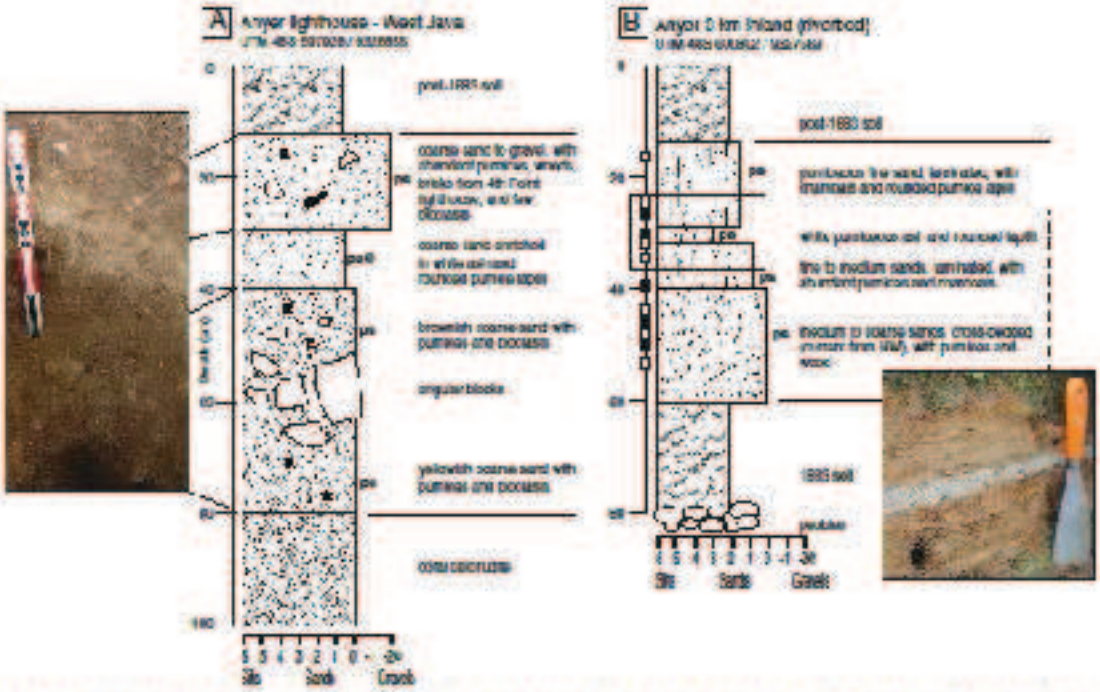

Fig. 5 Stratigraphic logs of Anyer coastal section a located near 4th Point Java Lighthouse (at 100 m from the present-day shoreline), and distal section b located 3 km inland in a riverbed (Cikoneng). White pumiceous ash of pumicystal phase (early morning August 27) is better preserved inland (Fig. 5b) than on the coastal sections (Fig. 5a). See Fig. 2 for legend

4 km inland (Eronto 1990). In this paragraph, we describe a section located 3 km inland along a riverbed. The 1883 deposits overlie a soil and rounded pebbles from the riverbed (Fig. 5b). The first unit is a ~20 cm thick sequence of cross-bedded sands with 50 % pumice (including pumice with veins of dense obsidian) and wood fragments. Cross-bedding indicates a current directed towards the NW. The great majority of the grains are angular to subangular and their surface is not shiny, suggesting a fluvial origin rather than marine (Cailleux and Tricart 1959). The transition from cross-stratified to laminated sands (of same composition+ charcoal) marks a change in flow dynamics at ~40 cm bottom depth (Fig. 5b). At ~32 cm, there is a 4-cm-thick continuous layer of white pumiceous ash and rounded lapilli. The tephra layer is eroded beneath a thick unit of laminated fine pumiceous sand (95 % varied pumices). The white, highly vesicular pumices are coarser than the other types of pumices. No marine macrofauna was detected using the binocular microscope. This is confirmed by the very low LOI at 950 °C (<1.3 wt%).

Sanghyang Island

Sanghyang Island (Fig. 1) is located in the middle of the narrowest path of the Sunda Strait between Java and Sumatra, 50 km ENE from the volcano. Coral boulders up to 4 m wide are dispersed in the forest and mangroves. The most complete of our sections is a 4 m pit at 430 m from the shoreline (UTM 48S, 594243/9341627), where the coral platform and bioclastic sands are covered by a 2-m-thick massive coral gravel. At 1 m deep, the gravel is overlain by white pumiceous fine sand mixed with coral and wood, followed by a sequence of coarse bioclastic sand with less than 20 % very fine pumice. This top unit is inversely graded, from coarse sand at −70 cm to gravel at −20 cm. We also noted that the topographic lows of the island are often filled by accumulations of rounded pumice lapilli (up to pebble size).

Kalianda

Northwest of Kalianda city (Fig. 1), traces of the 1883 eruption and tsunamis can be found everywhere around tourist resorts and mangroves up to 1 km inland: pumice lapilli and coral in the soil, coral gravel and bioclastic sands with pumice, glass shards and other bioclasts (shells), accumulations of pumice (usually below the coral gravel in the mangroves). These pumice deposits are up to 1 m thick

and the dominant population is rounded lapilli, as on Sanghyang Island.

One of the most complete sequences along the Sumatra coast was found in a sand quarry located 3 km NW of Kalianda city (250 m inland, 5 m a.s.l.). The 1883 sequence is up to 220 cm thick and cuts into paleo-dunes (Fig. 6). The first unit resembles the underlying bioclastic sand from the dune, but its composition is different since it incorporates fresh crystals and rare pumice, wood and organic matter (4.7 wt% LOI at 550 °C compared to 1.8 wt% in the dune). This sand is then covered by volcanic ash (greyish silty clay) which is characterised by its bimodal grain-size distribution: very fine pumices <100 μm and subrounded pumices typically 1 mm in diameter. The ash is eroded beneath and reworked into another sand unit. The contact displays scour-and-fill features, plastic deformation of the ash layer into pipes and rip-up clasts in the sand. The composition of this second sand unit is close to that of the first one, with fewer bioclasts (2.5 wt% LOI at 950 °C, compared to 35 wt%), and more heavy minerals and pumice. It is draped by a thick unit of rounded pumice lapilli with charcoal and tree moulds. The uppermost dark silty sand unit is unusual: it is a mixture of very fine pumiceous ash, fresh crystals, bioclasts (coral, shells—11 % LOI at 950 °C) and abundant fine fragments of charred wood.

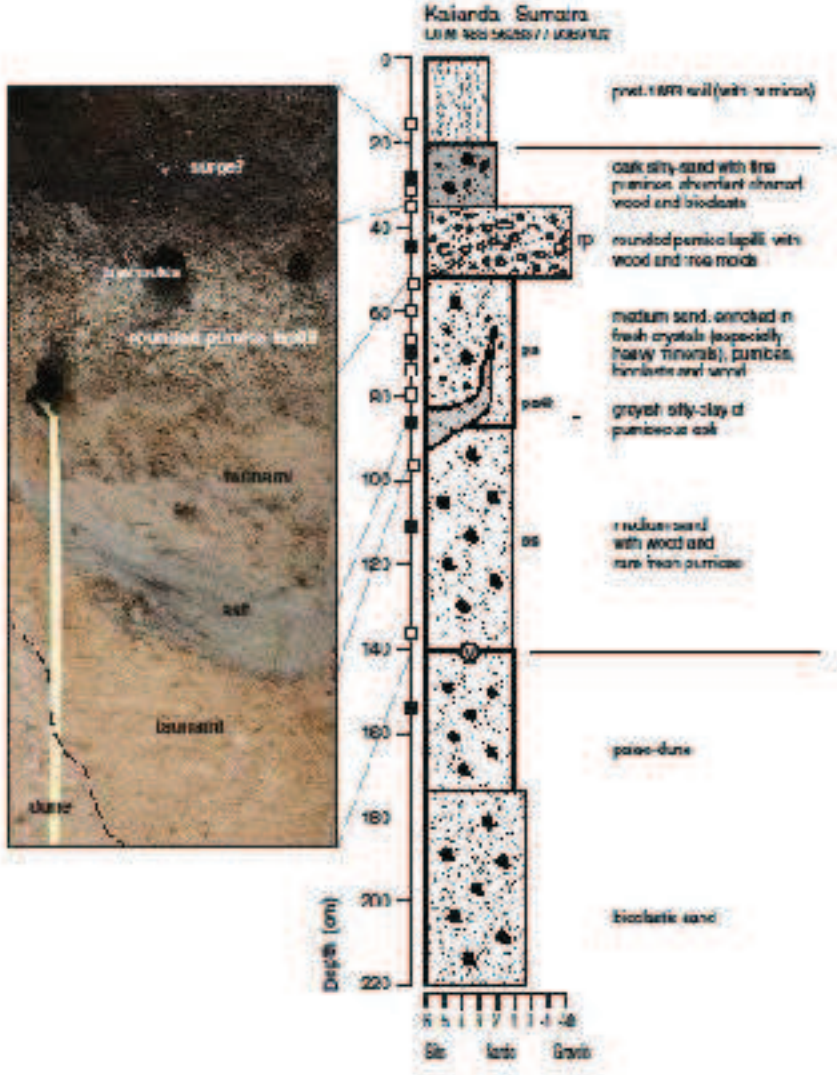

Fig. 6 Stratigraphic log of Kalianda section (quarry, 7 km N of Kalianda). Reworking of the greyish ash layer (at depth 90 cm) by tsunami is evidenced by pipes and rip-up clasts in the pumiceous sand. See Fig. 2 for legend

Lampung Bay

Halfway between Kalianda and Bandar Lampung (Fig. 1) a coastal platform gently sloping landward provides good areas for preserving tsunami deposits. In the village of Gubug Garam (300 m from the present-day shoreline), the sequence is slightly different to that at Kalianda. Bioclastic sands predating the 1883 events are increasingly reworked upwards and enriched in pumice and fresh crystals (Fig. 7). The overlying pumiceous ash unit (a greyish silty clay) here incorporates lenses of rounded pumice lapilli. The upper part of the ash progressively evolves into a brown silty clay, very rich in pumices, with both terrestrial and marine bioclasts. The upper 20 cm of the section are reworked and thus difficult to interpret.

In this same area, many sections were accessible during the building of the Tahuran PLTU power plant. The typical sequence starts with coarse bioclastic sand enriched in pumice and fip-up clasts from the underlying soil. Above is a layer of light grey primary ash (no bioclasts or wood), eroded beneath the upper pumiceous sand (>70 % volcanic juveniles) which is normally graded. Many kinds of pumice were observed in this unit: massive, fibrous and banded, with or without veins of dense obsidian. The coarse pumices in the sand units are rounded, whereas all pumices in the ash layer are angular to sub-angular. Sand pipes extending upward from the lower sand unit go through the ash and up to the upper sand unit. Finally, coral boulders less than 1 m wide can be found on top of the sequence, buried in the soil and underlying deposits. Traces of the 1883 tsunami are limited to the coastal platform, with the deposition limit at 700 m inland (<10 m a.s.l.), where slopes become steeper.

The most complete sequence (Fig. 8) displays more than 70 cm of 1883 "event deposits" above 1 m of laterite soil (without any evidence of tephra or tsunamis prior to 1883). The lower half of the sequence is similar to the previous sections of the same area: (1) lower unit of coarse sand with abundant pumice, marine bioclasts and rip-up clasts from the underlying soil; (2) greyish pumiceous ash (up to lapilli size), eroded by (3) the upper pumiceous silty sand (as evidenced by fip-up clasts of greyish ash in the pumiceous sand). The upper part of the sequence displays successively (4) rounded pumice lapilli infilling the irregular surface of the upper pumiceous sand, and (5) 30 cm of light grey primary silt-to-sand size volcanic ash (reworked by pedogenesis only in its uppermost part). This final ash unit is organised into three subunits—a lower massive facies, an intermediate cross-bedded facies (eroding the massive facies) and an upper planar bedded facies. Bedforms illustrated in Fig. 8 are oriented oblique to a flow coming from the South (section is oriented WSW-ENE).

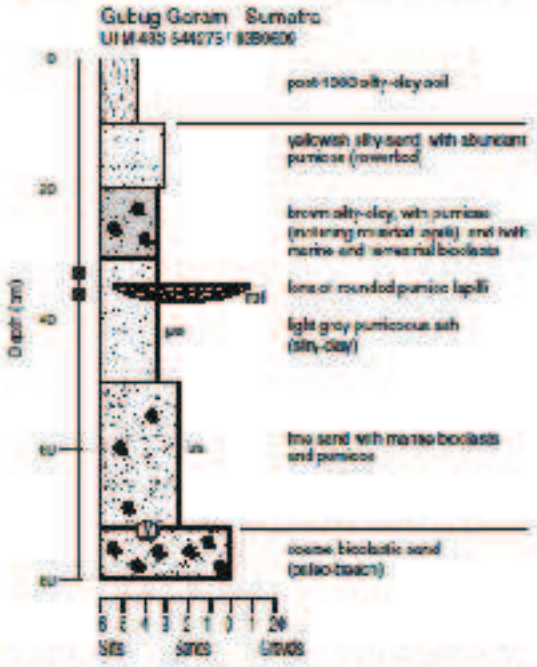

Fig. 7 Stratigraphic log of Gubug Garam section (village, Lampung Bay, East Sumatra). See Fig. 2 for legend

Sebesi Island

Sebesi is located only 17 km North of Krakatau (Fig. 1). The island was completely devastated by pyroclastic flows and surges. Products of the 1883 climactic stage are preserved as a massive 0.5- to 3-m thick unit of light grey to white pumice, with clasts ranging from fine ash to boulders up to 30 cm, including coral blocks. A better sorted and finer basal facies can be observed at some outcrops. On the eastern shore of the island (UTM 48S, 556816.9342020), a brownish coral-enriched unit is intercalated between the 1883 ashfall (soil or coral beach) and the pyroclastic flow deposits of the 1883 climactic stage. These observations are concordant with the sections described by Carey et al. (1996) on the eastern shore of Sebesi Island. The brownish coral-bearing unit has an irregular thickness (10–80 cm), a sharp basal contact, includes fragments of pumice and has a matrix that is not vesicular. Elongate clasts tend to have their long axes aligned horizontally.

Anisotropy of magnetic susceptibility

Ten samples were collected for AMS analysis in Kalianda (Fig. 9). The bioclastic sand unit (Fig. 6, depth 90–150 cm) is characterised by dominant reverse imbrication increasing upward (pro site clipboards, lower below) and a significant anticlockwise tilting of the K_{max} tensors (landward fabric). The pumiceous sand unit

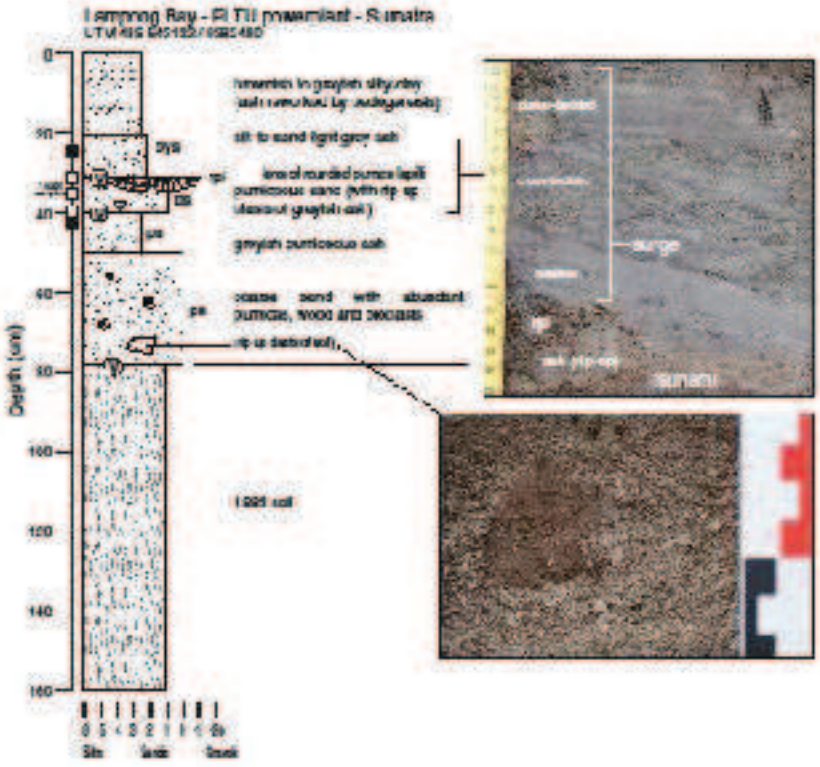

Fig. 8 Stratigraphic log of Lamprong section (PLTU powerplant near Tabaran). Photographs: rip-up clasts of soil in the lower pumiceous sand (below), and ballistic in the pyroclastic surge deposit (cross bedding corresponds to oblique diastem-set structures dipping from an upper-flow regime). See Fig. 2 for legend

(50–30 cm) shows a succession of traction followed by settling (peak of foliation at 70 cm). The uppermost dark silty sand (35–20 cm) has a moderate linear fabric and an oblate ellipsoid of anisotropy. Orientation of the 10 K_{max} tensors is concordant with a flow oriented S-N to SSW-NNE (Fig. 10), which corresponds to the direction of Krakatau volcano.

Coastal sections in Anyer (Fig. 5a) were not sampled for AMS because of the coarse grain-size of the sediments. Finer pumiceous sands in the sections found 3 km inland in the riverbeds (Fig. 5b) were suitable for AMS analysis. Samples of the lower cross-bedded pumiceous sand (60–40 cm) have K_{max} tensors oriented N-S (Fig. 10), i.e. almost perpendicular to the Krakatau direction and the present-day riverbed. This is surprising considering that the deposition was dominated by settling (oblate ellipsoids). The tsunami flow may have been initially channelled by a riverbed oriented N-S, even if the present-day riverbed is now oriented WSW-ENE. In contrast, two samples of pumiceous sands have K_{max} tensors oriented W-E (at 15 and 34 cm depth). The white pumiceous ash intercalated between the pumiceous sands (Fig. 5b, depth 40 cm) displays unusual AMS parameters—highly linear fabric, flat oblate ellipsoids, with both foliation and lineation higher than in the under- and over-lying pumiceous sands (Fig. 9).

Three samples are correlated from a bioclastic sand unit at Cidaun (Fig. 2, depth 210–156 cm). Deposition was dominated by settling ($T>0$ and foliation>lineation). Orientation and declination of the AMS tensors suggest that the lower yellowish-brown bioclastic sand (210–180 cm) was deposited by a flow coming from the E (Fig. 10). The upper brown silt (180–156 cm) has K_{max} tensors oriented successively N-S (170 cm) and E-W (156 cm). These variations likely reflect the influence of coastal morphology (V-shaped bays, islands) on flow direction.

In Lamprong (Fig. 8), seven samples of the upper pumiceous sand (Fig. 8, depth 24–46 cm) were analysed for AMS, thus giving the opportunity to assess vertical variations of sediment fabrics and depositional processes in a single unit. The lower pumiceous sand (80–50 cm) is coarser and thus not suitable for this kind of sampling. Vertical variations of grain size in the upper pumiceous sand suggest a single phase of

Fig. 9 AMS parameters of the 1883 Krakatau tsunami deposits in Lamprong (Fig. 8), Kalanda (Fig. 6) and Cikereng (Fig. 5b). The shape parameter describes the geometry of the AMS ellipsoid, which is oblate for $T>0$ (settling mode, dominant foliation) or prolate for $T<0$ (traction mode, dominant lineation). The alignment parameter represents the development of a linear fabric and thus increases with bottom current strength

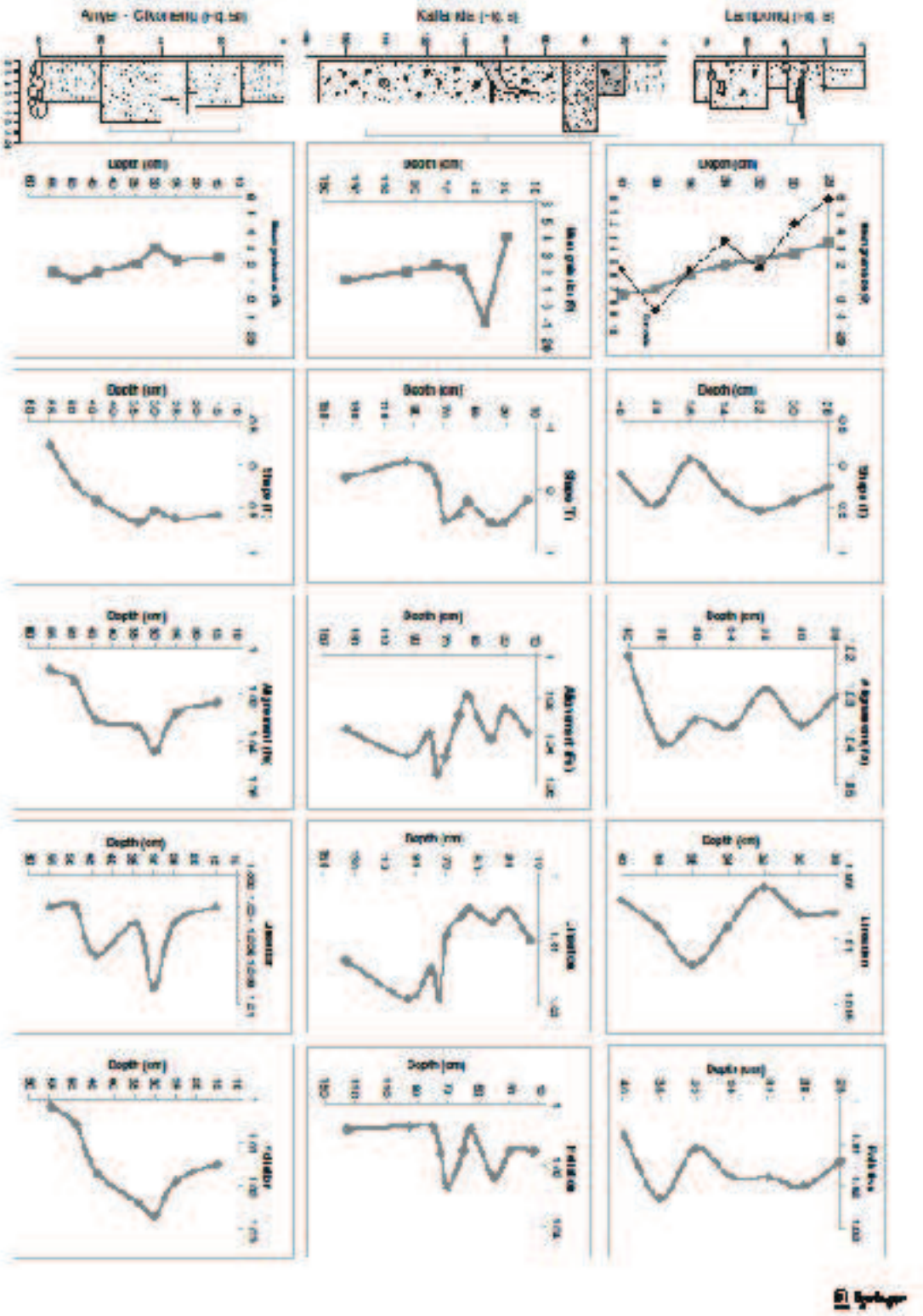

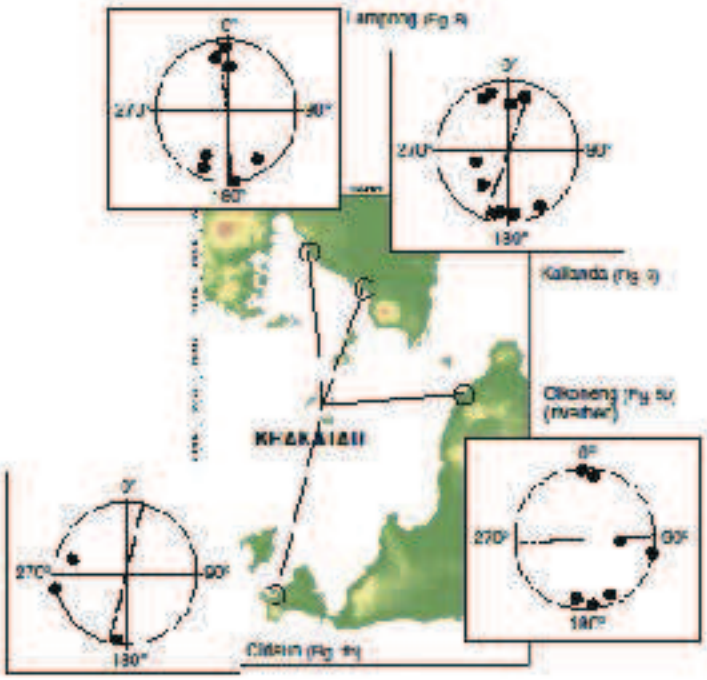

Fig. 10 Projections of AMS (anisotropy of magnetic susceptibility) maximum tensor axes (K_{max}) onto a diagram of the lower hemisphere equal area. *Dashed lines* in the diagrams indicate direction of Krakatau volcano from sampling site

settling, characterised by normal grading and upward sorting from base to top of the unit (Fig. 9), but AMS parameters reveal changes in flow dynamics which were not detectable in the field. Six of the seven ellipsoids are oblate, thus confirming that settling was the dominant mode (Fig. 9). Traction dominates for one sample (at 38 cm deep, peak of alignment parameter and lineation), but the prolate shape of the ellipsoid is not pronounced. The vertical variations of the alignment parameter display two peaks of increased linear fabric. The orientations of the maximum tensor axes (K_{max}) range from SSW-NNE to SSE-NNW, alternately sliting southward and northward (Fig. 10), thus suggesting an oscillatory flow. This area is characterised by a narrow coastal plain which slopes gently seawards and is delimited by steep slopes to the north, thus limiting tsunami propagation inland and generating turnaround periods (e.g. Dawson 1996). Similar flow behaviour was described by Paris et al. (2007) for the 2004 Indian Ocean tsunami in a similar topographic setting.

Major element composition

From the stratigraphic logs presented above, observations using a binocular microscope and major element compositions (ESM 1), we can distinguish seven sedimentary and volcanic facies: primary pyroclastic deposits (punicoous ash and lapilli), rounded pumice lapilli, bioclastic sands, quartz-dominated sands and punicoous sands.

Quartz-dominated sands (70–80 wt% SiO_2, <10 wt% CaO) were found only in Ujung Kulon (Java). Bioclastic sands contain >40 wt% CaO and <40 wt% SiO_2, whereas the punicoous sands have 40–60 wt% SiO_2 and <30 wt% of CaO (Fig. 11). These proportions agree with the binocular microscope observations and LOI at 950 °C. Bioclastic sands have up to 30 % bioclasts and 3.5 wt% LOI at 950 °C. Punicoous sands have <20 % bioclasts and <2% wt% LOI at 950 °C, but >40 % juvenile clasts (punicoous ash, fresh

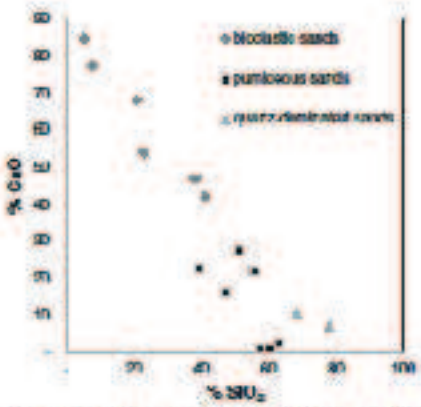

Fig. 11 Major element variation diagram for SiO_2 versus CaO for 1883 Krakatau tsunami deposits. Values recalculated to volatile-free oxide mass of 100 wt%

crystals, glass shards). Proportions of other major elements mostly depend on the variable incorporation of volcanic juvenile material, local sedimentary setting (e.g. TiO_2, Al_2O_3, MnO), and post-1883 weathering and leaching of the deposits (Fe_2O_3, Na_2O, K_2O). Strontium mainly originates from marine calcibiota (e.g. Chagué-Goff 2010) and is therefore higher in bioclastic sands. Barium content is generally higher in the 1883 primary pyroclastic deposits and pumiceous sands than in bioclastic sands.

Major element composition of the pumiceous sand (ESM 1) is transitional between the bioclastic sands and the 1883 pyroclastic deposits identified along the different sections (ESM 2). Comparison with samples collected near Krakatau volcano (Mandeville et al. 1996a and this study) confirms that the distal pyroclastic deposits described in this paper were clearly produced by the 1883 eruption of Krakatau volcano (ESM 2). Figure 12 shows that they differ from pumice fall deposits and ignimbrites of Rajabasa volcano (Eastern Sumatra) and Danau caldera (Western Java), two major sources of pumice in the region. The presence of shades to lithics in some pumiceous sediments is confirmed by higher Mg and Ca proportions (e.g. EA1 3a; greyish pumiceous ash at a depth of 85 cm in Fig. 6). Post-depositional weathering is evidenced by higher FeO and lower alkalis (e.g. Sumur and Ujung Kulon samples). The reworking of some ash fall deposits by tsunami waves led to the addition of biogenic Ca (e.g. SUS1; yellowish pumiceous ash at a depth of 50 cm in Fig. 3).

Discussion

Interpretation of the sedimentary and volcanic facies

Pre-Plinian phase tsunami deposit: bioclastic sands and gravels

Coral gravel and bioclastic sand facies (Table 1) are found in the lower part of many sections (e.g. Ujung Kulon, Sumur and Kalianda, Figs. 2, 3 and 6). These deposits resemble many tsunami deposits described in the literature (e.g. Goff et al. 2012; Cuven et al. 2013): basal erosional features and rip-up clasts from the substratum (soil), a large size fractions (from very fine sands to pluricentimetre boulders) present in some samples, poor sorting, lateral and longitudinal variations of thickness and internal organisation, both uniform and laminated facies, units enriched in heavy minerals and numerous marine bioclasts (up to 50 % of the clasts and 25 wt% LOI at 930 °C). Landward thinning and fining is often reported for tsunami deposits, but this is far from systematic for the 1883 tsunami deposits. However, poor preservation of the 1883 deposits does not allow longitudinal trends to be correctly evaluated, either in terms of thickness or grain size.

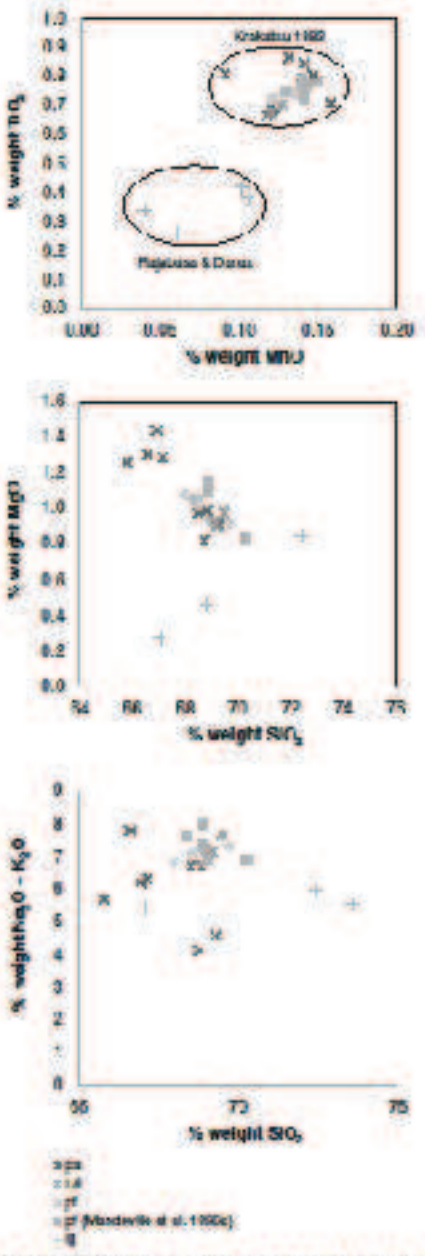

Fig. 12 Major-element variation diagrams for a SiO_2 versus alkalis (NaO + K_2O), b SiO_2 versus MgO and c MnO versus TiO$_2$. Values recalculated to volatile-free oxide sum of 100 wt%. Sample codes *pu* are pumiceous ash interbedded with 1883 tsunami deposits, *ypf* are mottled pumice lapilli (1883 tsunami deposits), *pf* are 1883 pyroclastic flow deposits sampled in Panjang and Rakata islands (including samples from Mandeville et al. 1996a), *rj* are ignimbrites from Rajabasa volcano (East Sumatra) and Danau caldera (West Java)

Table 1 Characteristics of the sedimentary facies associated with the 1883 Krakatau eruption and tsunamis along the coasts of the Sunda Strait (Indonesia)

	Bioclastic sand	Pumiceous sand	Pumiceous ash	Cross-bedded ash	Rounded pumice lapilli
Thickness (cm)	10–50	10–40	5–20	10–15	5–20
Grain size	Fine sand to gravel	Silt to coarse sand	Ash, lapilli, rare bombs	Ash (silt to sand)	Lapilli
Bedding	Massive	Massive, laminated	Massive	Massive, undercuts	Massive
Sorting	Poor to very poor	Poor to moderate	Well sorted	Moderate	Moderate
Fabric	Clast supported	Clasts to matrix supported	Matrix supported	Matrix supported	Clast supported
Volcanic juveniles (%)	<40	30–90	100	100	100
Bioclasts (%)	<50	<20	0	0	0
wt% LOI 950 °C	<35	<25	<1	0	0
wt% LOI 550 °C	2–6	1–6	1–5	<4	<4
Sample code	bs	ps	pa	pya	rp^1
Location	Java, Sumatra	Java, Sumatra	Java, Sumatra	Sumatra only	Sumatra only
Interpretation	Tsunami (pumiceous sand)	Tsunami (Plinian pumiceous)	Ash fall	Pyroclastic surge	Tsunami backwash

Compared to other coastal sediments (beach, dune sands) predating the 1883 eruption, tsunami bioclastic sands are enriched in heavy minerals (Ujung Kulon, Carita) and organic matter (e.g. pre-tsunami dune sand in Kalianda has a LOI at 550 °C of <2 wt%, and overlying tsunami sand 4.7 wt%, typically 2–6 wt% for tsunami deposits).

The proportion of juvenile clasts (pumices, fresh crystals) from the 1883 eruption ranges between 0 and 40 % in the bioclastic sand facies, which is interpreted as being the result of tsunami waves reaching the coasts of Java and Sumatra before the onset of ash falls related to the 26–27 August Plinian phase. Eruption-tsunami deposits that lack or are poor in juvenile grains have previously been described in Japan and Turkey. Nishimura and Miyaji (1995) found sand and gravel beneath fine ash (blast) and massive pumice (Plinian fall) deposits from the AD 1640 eruption of Komagatake volcano (southern Hokkaido). The sand unit is characterised by landward thinning and fining and overlies a clearly eroded underlying soil. Minoura et al. (2000) described a tsunami deposit on the Aegean coast of Turkey without juvenile material, and overlain by felsic ash fall deposits from the Minoan eruption of Santorini, although this interpretation remains controversial (e.g. Sewell 2001).

Pyroclastic fall deposits, pumiceous ash

The 1883 pyroclastic fall deposits are preserved as pumiceous ash interbedded between tsunami deposits everywhere around Sunda Strait. Their thickness is usually less than 10 cm and their colour varies from yellowish to greyish, light grey or white. The dominant grain size is ash, but lapilli are quite common and there are, rarely, bombs (e.g. Sumur).

However, the apparent pyroclastic fall deposits are not always primary, and we found evidence of reworking by later tsunami waves—presence of marine bioclasts (e.g. Sumur, 1 wt% LOI at 950 °C), abundance of non-volcanic material (e.g. Anyer) and erosion of rounded pumice lapilli in volcanic sea layers (e.g. Ujung Kulon) (see discussion below on the interpretation of rounded pumice lapilli). Rip-up clasts of the underlying greyish ash were found in pumiceous tsunami sands at a depth of 36 cm in Lampong (Fig. 8). In Kalianda, pipes and slabs of greyish ash are incorporated into the overlying tsunami sand (Fig. 8). The ash deposit was thus muddy (wet) when the tsunami came. This can be explained by the intense rain falls reported by Verbeek (1886) in the area during the night of 26–27 August.

Due to this reworking, it is not possible to reconstruct isopachs of the 1883 pyroclastic falls in Java and Sumatra from the deposits alone. Nevertheless, the thicknesses measured along the sections broadly correspond to those reported or measured by Verbeek (1886)—4–6 cm in Anyer (see Figs. 1 and 5b, depth 28–31 cm, for a comparison), 2 cm in Sumur and Ujung Kulon (Fig. 3a, depth 70–71 cm), 16 cm in Kalianda (Fig. 6, depth 86–88 cm) and 20 cm in Lampong Bay (Fig. 7, depth 32–50 cm; Fig. 8, depth 40–50 cm).

Plinian phase tsunami deposits, pumiceous sands

Following the increasing intensity of pyroclastic falls in the late afternoon of 26 August and night of 26–27 August, the proportion of juvenile clasts increases from the base to the top of the sections, and tsunami deposits in the upper part of the sections are characterised by their pumiceous texture (e.g. Cidaun; Fig. 2). These deposits, named pumiceous sands, present many of the diagnostic criteria of tsunami deposits (e.g. rip-up clasts of underlying ash fall deposits), but their proportion of fine pumiceous ash and lapilli is higher than 20 %, reaching up to 90 %. In the stratigraphy, pumiceous sands overlie pyroclastic fall deposits (Figs. 2, 3, 5, 6 and 8). The abundance of pumices in the tsunami pumiceous sand is

the result of bulking through incorporation of freshly deposited pyroclastic fall deposits into the tsunami flow.

Pumiceous sands are a diagnostic facies of volcanic tsunamis. Waythomas and Neal (1998) described ash fall deposits from the Aniakchak caldera-forming eruption (ca. 3.5 ka) reworked into overlying tsunami pumiceous sands. The most recent example was the 1994 Rabaul eruption (Papua New Guinea), during which tsunamis were generated by pyroclastic flows (Bourke and McKee 1995), and where up to three pumiceous sand units are interbedded with primary volcanic deposits (pumiceous ash and lapilli fall, surge deposits; Nishimura et al. 2005).

Bioclasts are less abundant in the pumiceous sand facies (<20 % clasts, <25 % LOI at 950 °C) than in the bioclastic sand facies. The source of marine bioclasts available offshore is progressively reduced by successive tsunamis. For instance, the lower bioclastic sand (Fig. 3a, depth 40–80 cm) and upper pumiceous sand in Anyer (depth 12–29 cm) have 15 and <5 % bioclasts, respectively. Nevertheless, we do not always observe this upward decrease. In Ujung Kulon, the abundance of bioclasts displays two variations from base to top of the sections: 6–12 % LOI at 950 °C in the bioclastic sands (Fig. 2a, depth 23–45 cm), 13 % in the pumiceous sand (depth 12–20 cm).

Pumice fall deposits reworked by tsunami: rounded pumice lapilli

The rounded pumice lapilli described on the Sumatra coast (this study) and by Carey et al. (2001) on Sebesi Island are better sorted than pyroclastic flow deposits in Krakatau Sertung (proximal facies) and Sebesi (20 km from Krakatau volcano), and coarser-grained than the pyroclastic deposits in Sebesi (Fig. 13). Thus, rounded lapilli are not the distal complement of proximal pyroclastic flow deposits. At all sites, the rounded pumice lapilli are depleted in crystals and lithic fragments, thus ruling out pyroclastic falls and surges as depositional mechanisms. Carey et al. (2001) concluded that these rounded pumice lapilli were originally deposited on the sea surface during fallout, thus forming pumice rafts, then abraded (rounded) during tsunami runup, and finally left inland during tsunami backwash (return flow). In terms of stratigraphy, the rounded pumice lapilli consist of a 20-cm-thick unit above pumiceous tsunami sand at Kalianda (Fig. 6). They were thus deposited during the Plinian phase of the eruption. At the Lampong sections, they are found as a discontinuous layer on top of pumiceous tsunami sand and below surge deposits (Fig. 8, depth 30 cm). The surge reached the coast of Sumatra at 10:30 AM of 27 August, just after the largest 10:00 AM explosion (Carey et al. 1996). At Gubug Garam, the rounded pumice lapilli appear as a small lens penetrating a pumiceous ash fall unit (Fig. 7). In Sebesi Island, Carey et al. (1996, 2001) mentioned the rounded pumice lapilli intercalated between greyish ash units interpreted as pyroclastic flow and surge deposits. The rounded pumice lapilli sampled along the coasts of Sumatra are finer grained than the ones studied by Carey et al. (1996, 2001) at Sebesi Island (Fig. 13).

Floating pumice rafts and deposits of rounded pumice lapilli were described by Bourke and McKee (1995) and Nishimura et al. (2005) during the 1994 Rabaul eruption and related tsunamis (Papua New Guinea). On the north-eastern coast of New Zealand, tsunami washover lobes are associated with rounded pumice lapilli (de Lange and Moon 2007). Freundt et al. (2007) mentioned pumice lenses in a tsunami sand sheet between two pyroclastic flows of the Masaya Holocene eruption (Lake Managua, Nicaragua).

Pyroclastic surge deposits

The 1883 tsunami deposits frequently contain wood fragments (small branches, bark, leaves and roots). In some units, wood was charred and now preserved as charcoal, both in Java and Sumatra. It can be found in the bioclastic sand facies (e.g. PL31, Lampong), pumiceous sand facies (e.g. Anyer) and rounded pumice lapilli (e.g. Kalianda). Two hypotheses may explain the presence of charred wood in the 1883 deposits: (1) wood previously charred (for instance by anthropic activities) and then transported by the tsunami and (2) pyroclastic surges instantaneously charring vegetation on Sumatra and Java coasts.

There is strong evidence that surges travelled distances of up to 65 km and reached the southern coast of Sumatra at 10:30 A.M., 30 min after the culminating 10:00 AM explosion of 27 August (Fig. 1): hundreds of people were burnt and 1,000 people were killed in the Kalumbang district, people on ships described "hot sulphurous winds" or "hurricane winds" followed by violent mud rains (Verbeek 1886). Survivors in Teluk Betung (now Bandar Lampung) also mentioned violent winds. There is no description or geological evidence of surge on the coasts of Java, but "hurricane winds" were felt aboard the *HMS Sense* north of Merak (Java Sea, at 30 km from Krakatau). Mandeville et al. (1994) estimated the emplacement temperature of submarine pyroclastic flows to range between 350 and 550 °C (using partial thermoremanent magnetization) at distances up to 15 km north of from the volcano. The temperature of the flow traveling over the sea was still hot enough to char wood on Sumatra coasts, but not intense enough to sinter coral, yielding a maximum temperature of 200 °C. This is concordant with the absence of surface reflectance on charred wood sampled in Sumatra (Scott and Gaispool 2005; Hudspith et al. 2010).

The uppermost light grey ash unit found at Lampong (Fig. 8) is interpreted as a pyroclastic surge deposit. It displays the typical vertical succession of a lower massive facies to an intermediate cross-bedded facies, and an upper planar-bedded facies (e.g. Wohletz and Sheridan 1979; Fisher and

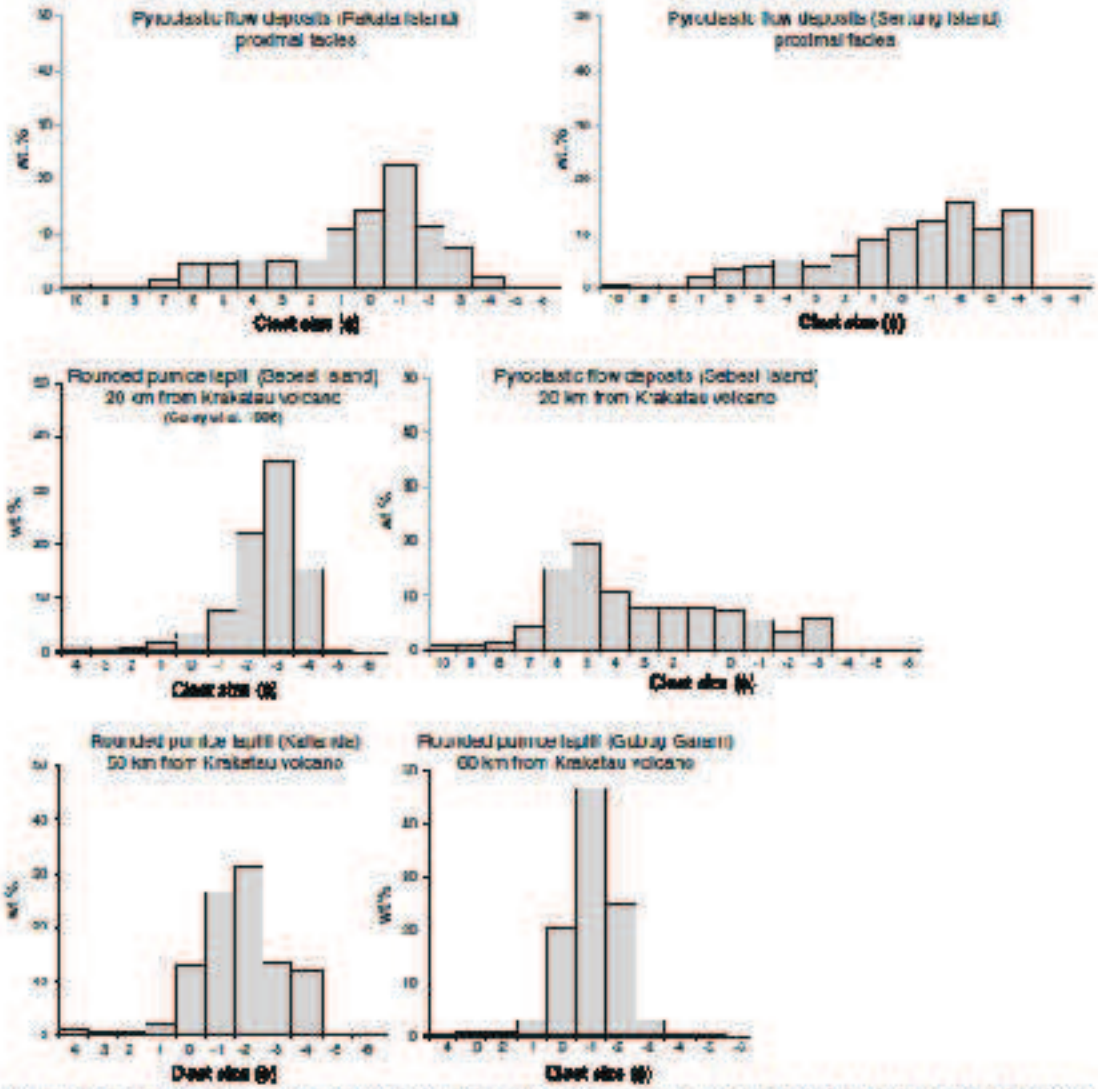

Fig. 13 Grain size distributions of pyroclastic flow deposits near the 1883 active vents (Sertung, Rakata islands) and at 20 km from the volcano (sampled on rounded pumice lapillis at Kalianda and Lampung (Sumatra coast)

Schmincke 1984). Cross-bedding resembles the chute-and-pool structures described by Schmincke et al. (1973), suggesting a supercritical flow regime, associated with grain-size sorting between sand and silt fractions of pumice. The sharp transition between the cross-bedded and the plane-bedded facies marks an abrupt decrease in flow power. Orientation of the bedforms is appropriate for a flow coming from the South. This is the first geological evidence of pyroclastic surge deposits related to the 1883 Krakatau eruption on the coasts of Sumatra. The uppermost dark silty sand found at Kalianda (Fig. 6, depth 35–20 cm) has a pumiceous ashy matrix and is very rich in charcoal. It might be considered to indicate the passage of the surge but the abundance of marine bioclasts suggests that it is reworked.

Mud rain?

The culminating 10:00 A.M explosion was followed by mud rain that lasted more than 2 h, both in Sumatra and Java (Verbeek 1886). The uppermost units of the 1883 sequence and post-1883 soils are usually reworked, and there is no clear evidence of the mud rain in the stratigraphic record. The

brown silty clay overlying greyish pumiceous ash and rounded pumice lapilli at Cubug Garam (Fig. 7) contains pumices (including rounded lapilli), but also coral fragments, and both marine and terrestrial bioclasts. This unit is here inferred to represent a tsunami backwash deposit, rather than mud rain.

Observations versus stratigraphy

South-western Java (Ujung Kulon, Sumur)

In the Ujung Kulon area (Java's First Point), pumiceous ash and bombs started to fall at 6:10 PM on 26 August, followed by ash only around 7:30 PM and wet ash in the early morning of 27 August (~4:20 AM). Ash fall deposits were found preserved in the sections we trenched in Ujung Kulon (Fig. 2a), Cuhan (Fig. 2b) and Sumur (Fig. 3). We found evidence of tsunamis below (bioclastic sand followed by pumiceous sand) and above (pumiceous sand only) the ash fall deposits, both in Ujung Kulon (Fig. 2a) and Sumur (Fig. 3). The Cuhan section suggests that at least three tsunamis reached the eastern coast of the Ujung Kulon peninsula, interbedded with ash fall deposits (Fig. 2b). The transition from bioclastic sands to pumiceous sands marks the onset of ash falls on the south-western coasts of Java (evening of 26 August). The light grey colour and high vesiculation of ash at 25 cm (Fig. 2a) and 140 cm (Fig. 2b) corresponds to the early morning of 27 August paroxysm.

According to the reports, Java's First Point was not affected by "unusual" waves before the major tsunami of 27 August at 11:00 AM, but the lighthouse was located on the south-western side of the peninsula (Indian Ocean coast). Tsunamis were reported in Viktor Hoek and Benewang (western Sumatra) during the evening of 26 August and early morning of 27 August (Latter 1981).

Western Java (Anyer, Sanghyang Island)

Batavia's tide gauge (Tandjong Priok) started to record tsunami waves at 6:10 PM on 26 August, thus illustrating the threshold was passed in the propagation of tsunamis northwards (Batavia being located 130 km from the volcano, on the northern coast of Java). Latter (1981) linked this first tsunami in Batavia to the 3:34 PM explosion.

Tsunamis reported in Anyer before 9:40 PM on 26 August are described as small agitations of sea level, but explosions in the evening generated 1–2 m high tsunamis, for example at Carita (Cyringin, 30 km SSW of Anyer). These tsunamis are not recorded individually in the sections described, and their traces might have been eroded by subsequent tsunamis. The pumiceous sands in the lower part of the Anyer section (Fig. 5a, depth >40 cm) were most probably deposited by the early morning 27 August tsunamis, at the beginning of the climactic stage of the eruption (~5:30 AM). In the early morning of 27 August, volcanic activity shifted from a convecting column, with localised pyroclastic flows, to a collapsing column (Self 1992). The production of large-volume pyroclastic flows resulted in an increasing amplitude of tsunami waves. According to Latter (1981), the 5:05 AM explosion generated a tsunami that propagated in all directions. Merak, Cyringin and Anyer were devastated by tsunami waves between 6:04 and 9:00 AM, leaving few survivors. Verbeek (1886) then noted a sudden increase in the intensity of ash falls at 9:30 AM in the Anyer area. The units of light grey pumiceous ash interclated between pumiceous tsunami sands (Fig. 5a, depth 30–40 cm, Fig. 5b, depth 29–31 cm) could represent the sixth stage phase of ash falls. The culminating tsunami occurred at ~10:20 in Anyer and 11:00 in Java's First Point. Waves were as high as the coconut trees in Merak, and destroyed the lighthouse at Java's 4th Point (Anyer). Bricks of the lighthouse were found in the upper pumiceous sand up to 4 km inland (Fig. 5a, depth 13–30 cm; Fig. 5b, depth 15–28 cm).

A similar stratigraphy is found in Sanghyang Island, but the tsunami deposits there are less rich in pumice than in Anyer. The 10:30 AM tsunami might be attested by bioclastic sands lying on white pumiceous fine sand, and the earlier tsunamis left a 2 m-thick coral breccia (7:30 or 9:00 AM tsunamis in Merak?). The relatively low pumice abundance in the Sanghyang Island deposits is consistent with the late arrival of ash falls in the Merak area (no ash falls before 10:30 AM in Merak, based on Verbeek 1886).

Eastern Sumatra (Kalianda, Lampung Bay)

Ketimbang and Kalianda were damaged by tsunamis sooner than elsewhere in Sumatra and Java. Ketimbang was evacuated after 8:00 PM on 26 August and devastated before 6:30 AM on 27 August. Verbeek (1886) mentioned successively: ash falls with pumice bombs during the night 26–27 August, then an intense "rain" of lapilli and bombs at 9:00–10:00 AM (the possible source of the rounded pumice lapilli), a short phase of fine ash at ~12:00 AM, followed by cold ash or mud rain until 28 August. This scenario agrees particularly well with the stratigraphic record in Kalianda (Fig. 6). The lower tsunami sands (depth 88–140 cm) have low pumice abundance and could be the result of the tsunamis on the evening of 26 August, prior to the main ash falls (depth 70–88 cm). The upper sand of pumiceous sand erosionally overlies the wet ash fall deposits and ends with deposits of rounded pumice lapilli (depth 35–55 cm).

The most complete section trenched along the coasts of Lampung Bay (Fig. 8) displays from base to top (1) a thick pumiceous tsunami sand with rip-up clasts of the underlying soil, (2) wet ash fall deposits, (3) a second unit of pumiceous tsunami sands with rip-up clasts of ash fall deposits and lenses of pumice rounded lapilli and (4) a cross-stratified surge

deposit. This stratigraphy can be compared with observations in Teluk Betung (Fig. 1), where the first damaging tsunami occurred at 6:30 AM (27 August). A second tsunami is reported at ~7:00 AM in Lampong Bay (by the ship

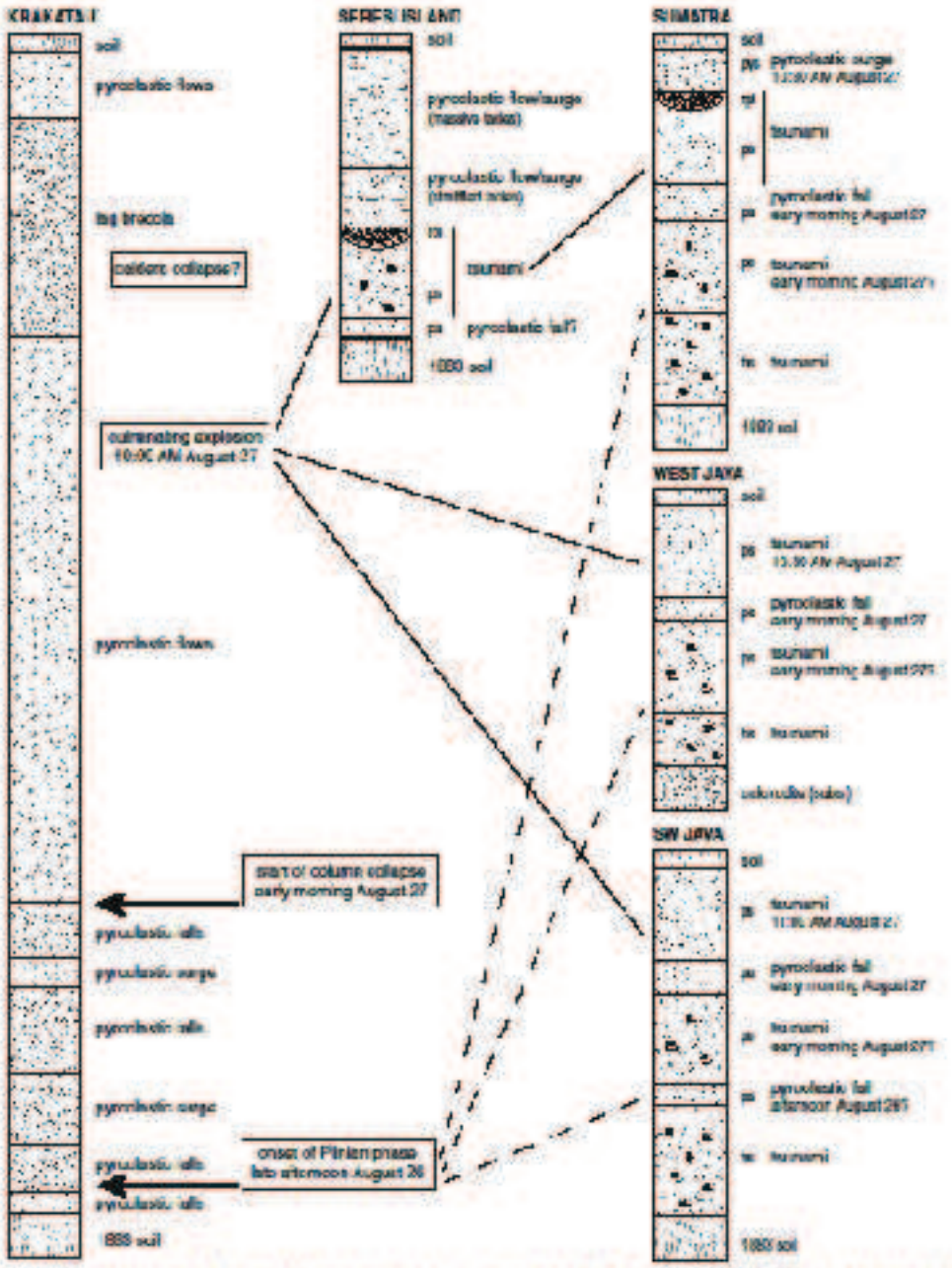

Fig. 14 Integrative stratigraphic columns for 1883 Krakatau pyroclastic deposits and tsunami deposits, from the proximal zone (Panjang, Rakata and Sertung islands—Stehn 1929; Self and Rampino 1981; Mandeville et al. 1996), to Sebesi (30 km from the volcano—Carey et al. 1996) and Sumatra and Java coasts (40–70 km from the volcano—this study). Sedimentary and volcanic facies—fs fine lithic sand, ps pumiceous sand, pl rounded pumice lapilli, pyp pyroclastic surge. Not to scale

London), reaching Teluk Betung at 7:45 AM. It is impossible to state which one of these tsunamis produced the lower pumiceous sand (Fig. 8, depth 30–80 cm). The intensity of ash falls increased after 7:00 AM, shifting to mud rains between 10:45 and 12:45 A.M. The timing of the major tsunami following the 10:00 A.M explosions not documented in Lampung Bay, because most of the people there were killed by earlier tsunamis or evacuated to higher ground. As at Kalianda, this tsunami is evidenced by an upper unit of pumiceous sand and rounded pumice lapilli (Fig. 8, depth 30–40 cm).

The pyroclastic surge was felt shortly after the tsunami (e.g. account by the ship *Charles Bal*, from near Sanghyang Island). This agrees with the stratigraphic position of the upper tsunami sand and rounded pumice lapilli under the surge deposits in Lampong (Fig. 4) and Sebesi (Carey et al. 1996). Considering that the tsunami waves reached the coasts of Sumatra and Java after 30–40 min of propagation (Verbeek 1886; Simkin and Fiske 1983), we can estimate that the surge travelled over seawater at a velocity of less than 30 m/s (if the surge and tsunami shared the same source). The ships *London* and *Charles Bal*, both located 65 km from the volcano, felt the effects of the surge at ~10:30 AM, yielding an average velocity of 36 m/s. Pumice rafts may have locally increased seawater viscosity and density, favouring the transport of pyroclastic surges across the sea, as suggested by Allen and Cas (2001) for the Kos Plateau Tuff across the Aegean Sea.

Conclusions

The tsunamigenic 1883 eruption of Krakatau volcano represents an emblematic case study for coupling eruptive history (through stratigraphy and observations) and the sedimentary record of tsunamis. Our sedimentological approach to the tsunami deposits interbedded with primary or reworked pyroclastic deposits demonstrates that past eruptions can be reconstructed using their tsunami record. Five kinds of sedimentary and volcanic facies were identified: (1) bioclastic sands deposited by tsunamis before the Plinian phase of the eruption, (2) pumiceous tsunami sands indicating the onset of the Plinian phase, (3) rounded pumice lapilli corresponding to pyroclastic falls reworked by tsunami (and most probably deposited by the backwash), (4) pumiceous ash fall deposits (primary or reworked) and (5) pyroclastic surge deposits overlying the uppermost tsunami deposits only in Sumatra.

The stratigraphic record agrees quite well with the observations and allows a scenario to be reconstructed for each eruption. Figure 4 displays a tentative synthesis of the proximal and distal stratigraphy of the 1883 eruption and tsunamis. Links are proposed between the beginning of the Plinian phase in the late afternoon of August 26, pyroclastic fall deposits on the coasts of Java and Sumatra, and the enrichment of the tsunami deposits in pumice (pumice sand facies). Thicknesses of ash fall deposits measured along the sections are concordant with thicknesses reported by Verbeek (1886). Tsunami observed before the paroxysm (bioclastic sand facies) might have been generated by precursory pyroclastic flows or subsidence of the volcanic edifice. There are no tsunamis recorded above the surge deposits in Sumatra, i.e. no tsunamis after the main explosion (10:00 AM August 27). The temperature of the flow travelling over the sea at 30–36 km was still hot enough to char wood fragments (without surface reflectance), but not marine shells and corals, yielding a maximum temperature of 200 °C. The final phase of the eruption and formation of the submarine caldera might have generated tsunamis, but they are not recorded along the coastal sections described here.

Volcanic tsunamis expand the potential damage area of many underwater and coastal volcanoes, and must be considered in terms of volcanic hazard assessment. Learning from past tsunamigenic eruptions helps understand the relationships between the eruptive processes, thresholds in eruptive activity and the timeframe and magnitude of tsunamis. Using current knowledge, tsunamis happening during a volcanic eruption are unpredictable, and sometimes numerous, yet volcanic monitoring is often unsuited to dealing with tsunamis.

Acknowledgements This work was funded by French ANR (*Agence Nationale de la Recherche*) program "Young Scientists" 2006–project VITESS (Volcano Induced Tsunamis: Sedimentary Signature and numerical Simulation) whose leader was Raphaël Paris. The authors are also grateful to Jean-Marc Tétot (SEM, Clermont-Ferrand), Marc Desmet and Martine Tronquart (AMS and grain size analyses, Strasbourg), Claudia Vinzia Sequenzia, Eko Yulianto and Brian Atwater (for giving unpublished manuscript or coral location), and David Dubluchet (for building the trench file). The authors thank Scott Bryan, Adam Switzer and an anonymous reviewer for their careful reviews, as well as Steve Self and James White. This is Laboratory of Excellence ClerVolc contribution n° 60.

References

Allen SR, Cas RAF (2001) Transport of pyroclastic flows across the sea during the explosive, rhyolitic eruption of the Kos Plateau Tuff, Greece. Bull Volcanol 62:441–456

Bagiel JE (2000) Volcanic tsunamis. In: Sigurdsson H, Houghton B, McNutt SR, Rymer H, Stix J (eds) Encyclopedia of volcanoes. Academic Press, New York, pp 1005–1013

Blong RJ, McKee CO (1995) The Rabaul eruption 1994—destruction of a town. Natural Hazards Research Center, Macquarie University, Australia, 52 p

Bourgeois J (2009) Geologic effects and records of tsunamis. In: Robinson AR, Bernard EN (eds) The sea, vol 15: tsunamis. Harvard: Harvard University Press, pp 55–91

Bronto S (1990) Gunung Krakatau, Bentuk Dasarnya Volkanologi, Edisi Khusus No 113, Direktorat Vulkanologi, Sh. unpublished.

Cantet A, Incant J (1995) Constitutions et tremblements de terre. CDU, Paris, 576 p

Camus G, Vincent PM (1983) Discussion of a new hypothesis for the Krakatau volcanic eruption in 1883. J Volcanol Geotherm Res 19: 167–173
Camus G, Gourgaud A, Vincent PM (1987) Petrologic evolution of Krakatau (Indonesia): implications for a future activity. J Volcanol Geotherm Res 33:299–316
Carey S, Sigurdsson H, Mandeville C, Bronto S (1996) Pyroclastic flows and surges over water: an example from the 1883 Krakatau eruption. Bull Volcanol 57:493–511
Carey S, Morelli D, Sigurdsson H, Bursik S (2001) Tsunami deposits from major explosive eruptions: an example from the 1883 eruption of Krakatau. Geology 29(8):747–750
Chagué-Goff C (2010) Chemical signature of palaeotsunamis: a first case proxy? Mar Geol 271:67–71
Choi BH, Pelinovsky E, Lee YO, Lee JS (2003) Simulation of the trans-oceanic tsunami propagation due to the 1883 Krakatau volcanic eruption. Nat Hazards Earth Syst Sci 3:321–332
Cisneros S, Paris R, Fauvel S, Mee Koinark Z, Benbakkar M, Schneider JL, Billy I (2013) High-resolution analysis of a tsunami deposit: case study from the 1755 Lisbon tsunami in southwestern Spain. Mar Geol 337:98–111
Dawson AG (1996) The geological significance of tsunamites. Zeitschrift fr Geomorphologie Suppl Band 102:199–210
Dawson AG, Stewart I (2007) Tsunami deposits in the geological record. Sediment Geol 200:166–183
de Lange WP, Moon VG (2005) Tsunami washover deposits, Tawharanui, New Zealand. Sediment Geol 200:232–247
Ewing M, Press F (1955) Tide-gage disturbance from the great eruption of Krakatoa. Trans Am Geophys Union 36(1):53–66
Fisher RV, Schmincke HU (1984) Pyroclastic rocks. Springer, Berlin, 472 p
Francis PW (1985) The origin of the 1883 Krakatau tsunamis. J Volcanol Geotherm Res 25:349–363
Freundt A, Strauch W, Kutterolf S, Schmincke HU (2007) Volcanogenic tsunamis in lakes: examples from Nicaragua and general implications. Pure Appl Geophys 164:527–565
Giachetti T, Paris R, Kelfoun K, Ontowirjo B (2012) Tsunami hazard related to a flank collapse of Anak Krakatau volcano, Sunda Strait, Indonesia. Geological Society, London, Special Publication 361:79–85
Goff JR, Chagué-Goff C, Nichol SL, Jaffe B, Dominey-Howes D (2012) Progress in palaeotsunami research. Sediment Geol 243–244:70–88
Hadnutt VA, Bursik MC, Wilson CJN, Cobbold ME (2010) Clast-clast wear by volcanic processes: an example from the Taupo ignimbrite, New Zealand. Palaeogeogr Palaeoclimatol Palaeoecol 291: 46–58
Keating BH, Helsley CE, Warrick M, Walker D (2011) Tsunami deposit research: fidelity of the tsunami record, ephemeral nature, tsunami deposit characteristics, resuspension of sediments by last waves, and boulder movement. In: Mörner NA (Ed.) The tsunami threat—Research and Technology. InTech, 714 p
Latter JN (1981) Tsunamis of volcanic origin: summary of causes with particular reference to Krakatau, 1883. Bull Volcanol 44(3):467–490
Maeno F, Imamura F (2011) Tsunami generation by a rapid entrance of pyroclastic flow into the sea during the 1883 Krakatau eruption, Indonesia. J Geophys Res 116, B09205
Mandeville CW, Carey S, Sigurdsson H, King J (1994) Paleomagnetic evidence of high-temperature emplacement of the 1883 subaqueous pyroclastic flows from Krakatau volcano, Indonesia. J Geophys Res 99:9487–9504
Mandeville CW, Carey S, Sigurdsson H (1996a) Magma mixing, fractional crystallization and volatile degassing during the 1883 eruption of Krakatau volcano, Indonesia. J Volcanol Geotherm Res 74:243–274
Mandeville CW, Carey S, Sigurdsson H (1996b) Sedimentology of the Krakatau 1883 submarine pyroclastic deposits. Bull Volcanol 57: 512–529
Minoura K, Imamura F, Kuran U, Nakamura T, Papadopoulos GA, Takahashi T, Yalciner AC (2000) Discovery of Minoan tsunami deposits. Geology 28(1):59–62
Nishimura Y, Miyaji N (1995) Tsunami deposits from the 1993 Southwest Hokkaido earthquake and the 1640 Hokkaido Komagatake eruption. Northern Japan. Pure Appl Geophys 144: 715–733
Nishimura Y, Nakagawa M, Kudoh J, Wakana J (2005) Timing and scale of tsunamis caused by the 1994 Rabaul eruption, East New Britain, Papua New Guinea. In: Satake K (ed) Tsunamis: case studies and recent developments. Springer, New York, pp 45–66
Nomanbhoy N, Satake K (1995) Generation mechanism of tsunamis from the 1883 Krakatau eruption. Geophys Res Lett 22(13):509–512
Ongkosongo OSR (1981) Coastal geomorphology of Ujung Kulon, West Java, with special emphasis on the tsunamis of the 1883 Krakatau tsunamis activity. Symposium on 100th year Development of Krakatau and its surroundings, August 21–27, 1983, Jakarta, Indonesia
Paris R, Lavigne F, Wassmer P, Sartohadi J (2007) Coastal sedimentation associated with the December 26, 2004 tsunami in Lhok Ngo, west Banda Aceh (Sumatra, Indonesia). Mar Geol 238:93–106
Paris R, Switzer AD, Belousova M, Belousov A, Ontowirjo B, Whelley PL, Ulvrova M (2014) Volcanic tsunamis: a review of source mechanisms, past events and hazards in Southeast Asia (Indonesia, Philippines, Papua New Guinea). Natural Hazards. doi:10.1007/s11069-013-0822-8
Pelinovsky E, Choi BH, Stepanov A, Talipova T, Kim HS (2005) Analysis of tide-gauge records of the 1883 Krakatau tsunami. In: Satake K (ed) Tsunamis: case studies and recent developments. Springer, New York, pp 57–78
Schmincke HU, Fisher RV, Waters AC (1973) Antidune and chute and pool structures in the base surge deposits of the Laacher See area, Germany. Sedimentology 20:553–574
Scott AC, Glasspool IJ (2005) Charcoal reflectance as a proxy for the emplacement temperature of pyroclastic flow deposits. Geology 33(7):589–592
Self S (1992) Krakatau revisited: the course of events and interpretation of the 1883 eruption. Geo Journal 28:109–121
Self S, Rampino MR (1981) The 1883 eruption of Krakatau. Nature 294: 699–704
Setiyantidi CM (2007) Boulder deposition associated with the 1883 Krakatau tsunami in Java and Sumatra. Unpublished MS Thesis, Asian Institute of Technology, Bangkok
Sewell DN (2001) Earth, air, fire and water: An elemental analysis of the Minoan eruption of Santorini volcano in the Late Bronze Age. Unpublished PhD Thesis, University of Reading, 427 p
Simkin T, Fiske RS (1983) Krakatau 1883: the volcanic eruption and its effects. Smithsonian Institution Press, Washington DC, 464 p
Stehn CE (1929) The geology and volcanism of the Krakatau group. Proceedings of the Fourth Pacific Science Congress, Batavia, pp 1–55
Symons GJ (1888) The eruption of Krakatau and subsequent phenomena: report of the Krakatau Committee of the Royal Society. Trubner, London
Terry JP, Tam AYA, Fagentu S (2013) Boulder-like coral boulders—evidence for high-energy marine inundation events on tropical coastlines. Springer Briefs in Earth Science, 102 p
Umbgrove JHF (1947) Coral reefs of the East Indies. Bull Geol Soc Am 58:729–778

Van den Berg GJ, Boer W de, Haas H, van Weering TCE, van Wijhe R (2003) Shallow marine tsunami deposits in Teluk Banten (NW Java, Indonesia), generated by the 1883 Krakatau eruption. Mar Geol 197:3–24

Verbeek RM (1886) Krakatau. Batavia, Imprimerie de l'Etat. 567 p

Verstappen HT (1956) Landscape development of the Ujung Kulon Game Reserve. Penggarus Alam 36:37–51

Wassmer P, Schneider JL, Fortrège AV, Lavigne F, Paris R, Gomez C (2010) Use of anisotropy of magnetic susceptibility (AMS) in the study of tsunami deposits: application to the 2004 deposits on the eastern coast of Banda Aceh, North Sumatra, Indonesia. Mar Geol 275:255–272

Waythomas CF, Neal CA (1998) Tsunami generation by pyroclastic flow during the 3500-year BP caldera-forming eruption of Aniakchak volcano, Alaska. Bull Volcanol 60:314–334

Williams H (1941) Calderas and their origin. Univ Calif Publ Geol Sci 25:239–346

Wohletz KH, Sheridan MF (1979) A model of pyroclastic surge. Geol Soc Amer Spec Pap 180:177–193

Yokoyama I (1981) A geophysical interpretation of the 1883 Krakatau eruption. J Volcanol Geotherm Res 9:359–378

Yokoyama I (1987) A scenario of the 1883 Krakatau tsunami. J Volcanol Geotherm Res 34:123–134